Transactions of the ASME®

Journal of Applied Mechanics

Published Quarterly by The American Society of Mechanical Engineers

VOLUME 64 • NUMBER 3 • SEPTEMBER 1997

Transactions of the ASME, Journal of Applied Mechanics (ISSN 0021-8936) is published quarterly (Mar., June, Sept., Dec.) for $210.00 per year by The American Society of Mechanical Engineers, 345 East 47th Street, New York, NY 10017. Periodicals postage paid at New York, NY and additional mailing office. POSTMASTER: Send address changes to Transactions of the ASME, Journal of Applied Mechanics, c/o THE AMERICAN SOCIETY OF MECHANICAL ENGINEERS, 22 Law Drive, Box 2300, Fairfield, NJ 07007-2300. **CHANGES OF ADDRESS** must be received at Society headquarters seven weeks before they are to be effective. Please send old label and new address. **PRICES:** To members, $40.00, annually: to nonmembers, $210.00. Add $30.00 for postage to countries outside the United States and Canada.

TECHNICAL PAPERS

(Contents continued on outside back cover)

CONTENTS (CONTINUED)

BRIEF NOTES

DISCUSSION

ANNOUNCEMENTS AND SPECIAL NOTICES

The Surface Crack Problem for a Plate With Functionally Graded Properties

F. Erdogan
Fellow ASME

B. H. Wu

Department of Mechanical Engineering and Mechanics,
Lehigh University,
Bethlehem, PA 18015

In this study the plane elasticity problem for a nonhomogeneous layer containing a crack perpendicular to the boundaries is considered. It is assumed that the Young's modulus of the medium varies continuously in the thickness direction. The problem is solved under three different loading conditions, namely fixed grip, membrane loading, and bending applied to the layer away from the crack region. Mode I stress intensity factors are presented for embedded as well as edge cracks for various values of dimensionless parameters representing the size and the location of the crack and the material nonhomogeneity. Some sample results are also given for the crack-opening displacement and the stress distribution.

1 Introduction

In today's highly demanding technological environment, one of the main challenges in new material design appears to be combining seemingly irreconcilable thermomechanical and strength properties in the same component. For example, in high-temperature applications the material is required to have high heat and corrosion resistance as well as high mechanical toughness and heat conductivity. Similarly, in such components as gears and bearings, it may not be possible to find the required degree of high wear resistance and high toughness in the same homogeneous material. In very high-temperature applications the potential of basically homogeneous materials appears to be limited and in recent years the new trends in material design seem to be toward coating the main load-bearing component, generally a superalloy, by a heat-resistant layer, generally a ceramic (Batakis and Vogan, 1985; Houck, 1987). However, from a structural view point these homogeneous thermal barrier coatings have certain disadvantages such as high thermal and residual stresses and relatively poor bonding strength. As a result, generally the layered medium becomes very susceptible to cracking and spallation. One concept that seems to be quite effective against these shortcomings is replacing the homogeneous coating by, or introducing between the coating and the substrate, a metal/ceramic composite layer with a composition varying continuously from 100 percent metal near the substrate to 100 percent ceramic near the surface. These new materials, called functionally graded materials (FGMs), have recently been introduced primarily to take advantage of the heat and corrosion resistance of ceramics and the mechanical strength of metals, and at the same time, to reduce the magnitude of residual and thermal stresses (Hirano and Yamada, 1988, Hirano et al., 1988, Niino and Maeda, 1990); see also Yamanouchi et al., 1990, and Holt et al., 1992 for review, applications, and extensive references).

In designing components involving FGMs, an important aspect of the problem is the fracture mechanics which requires the calculation of the crack driving forces such as the stress intensity factors on one hand and the resistance characterization of the material on the other. In this study the plane elasticity problem for a nonhomogeneous layer containing an internal or an edge crack perpendicular to the boundaries is considered (Fig. 1). It is assumed that the elastic properties of the medium vary continuously in thickness direction and the loading is perpendicular to the plane of the crack. In addition to representing a relatively common structural component, the part/crack geometry and loading conditions considered in this study may be particularly useful in the fracture mechanics characterization of FGMs. The previous studies on the plane elastic mode I crack problems in FGMs deal mostly with unbounded media and, therefore, are not very suitable for material characterization (Delale and Erdogan, 1983; Erdogan et al., 1991; Konda and Erdogan, 1994; Ozturk and Erdogan, 1993).

2 Formulation of the Problem

The problem under consideration is described in Fig. 1. The external loads are assumed to be such that the plane of the crack is a plane of symmetry and the crack problem is one of mode I. Thus, in analyzing the problem it is sufficient to consider one-half ($y > 0$) of the medium only. Also, through a proper superposition, the problem is assumed to have been reduced to a perturbation problem in which the crack surface tractions are the only nonzero external loads. The previous studies indicate that the influence of the Poisson's ratio on the stress intensity factors is not very significant (Delale and Erdogan, 1983; Konda and Erdogan, 1994). Therefore, to make the analysis tractable, it is further assumed that the Poisson's ratio of the graded medium is constant and the shear modulus is given by the following two-parameter expression:

$$\mu(x) = \mu_o e^{\beta x} \tag{1}$$

where β is a positive or negative constant. The equations of plane elasticity for the nonhomogeneous medium may then be expressed as

$$(\kappa+1)\frac{\partial^2 u}{\partial x^2} + (\kappa-1)\frac{\partial^2 u}{\partial y^2} + 2\frac{\partial^2 v}{\partial x \partial y} + \beta(\kappa+1)\frac{\partial u}{\partial x} + \beta(3-\kappa)\frac{\partial v}{\partial y} = 0,$$

$$(\kappa+1)\frac{\partial^2 v}{\partial y^2} + (\kappa-1)\frac{\partial^2 v}{\partial x^2} + 2\frac{\partial^2 u}{\partial x \partial y} + \beta(\kappa-1)\left(\frac{\partial v}{\partial x} + \frac{\partial u}{\partial y}\right) = 0, \quad (2a,b)$$

Contributed by the Applied Mechanics Division of THE AMERICAN SOCIETY OF MECHANICAL ENGINEERS for publication in the ASME JOURNAL OF APPLIED MECHANICS.

Discussion on the paper should be addressed to the Technical Editor, Professor Lewis T. Wheeler, Department of Mechanical Engineering, University of Houston, Houston, TX 77204-4792, and will be accepted until four months after final publication of the paper itself in the ASME JOURNAL OF APPLIED MECHANICS.

Manuscript received by the ASME Applied Mechanics Division, June 24, 1994; final revision, Apr. 14, 1997. Associate Technical Editor: M. Taya.

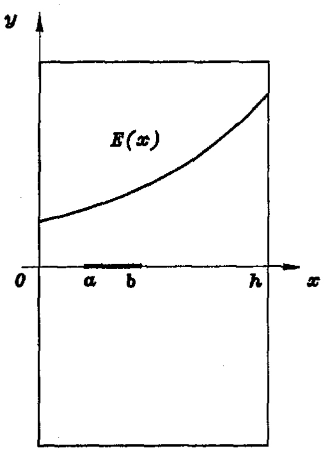

Fig. 1 Geometry of the crack problem in a layer with graded properties

$$\sigma_{xx} = \frac{\mu}{\kappa - 1}\left[(1+\kappa)\frac{\partial u}{\partial x} + (3-\kappa)\frac{\partial v}{\partial y}\right],$$

$$\sigma_{yy} = \frac{\mu}{\kappa - 1}\left[(3-\kappa)\frac{\partial u}{\partial x} + (1+\kappa)\frac{\partial v}{\partial y}\right],$$

$$\sigma_{xy} = \mu\left(\frac{\partial u}{\partial y} + \frac{\partial v}{\partial x}\right), \qquad (3a\text{–}c)$$

where u and v are the x and y components of the displacement vector, σ_{ij}, $(i, j = x, y)$ are the stress components, and $\kappa = 3 - 4\nu$ for plane strain and $\kappa = (3-\nu)/(1+\nu)$ for plane stress, ν being the Poisson's ratio. The mixed boundary value problem shown in Fig. 1 must be solved under the following conditions:

$$\sigma_{xx}(0, y) = 0, \quad \sigma_{xy}(0, y) = 0, \quad 0 < y < \infty, \qquad (4a,b)$$

$$\sigma_{xx}(h, y) = 0, \quad \sigma_{xy}(h, y) = 0, \quad 0 \le y < \infty, \qquad (5a,b)$$

$$\sigma_{xy}(x, 0) = 0, \quad 0 < x < h, \qquad (6)$$

$$\sigma_{yy}(x, 0) = p(x), \quad a < x < b,$$

$$v(x, 0) = 0, \quad 0 < x < a, \quad b < x < h, \qquad (7a,b)$$

where $p(x)$ is a known function.

We will now assume the solution of (2) in the following form:

$$u(x,y) = \frac{1}{2\pi}\int_{-\infty}^{\infty} f_1(y,\alpha)e^{-i\alpha x}d\alpha + \frac{2}{\pi}\int_0^{\infty} f_2(x,\alpha)\cos\alpha y d\alpha,$$

$$v(x, y) = \frac{1}{2\pi}\int_{-\infty}^{\infty} g_1(y, \alpha)e^{-i\alpha x}d\alpha$$

$$+ \frac{2}{\pi}\int_0^{\infty} g_2(x, \alpha)\sin\alpha y d\alpha. \qquad (8a,b)$$

From (2) and (8) it may be shown that

$$g_1(y, \alpha) = \sum_{j=1}^{4} D_j(\alpha)e^{n_j y},$$

$$f_1(y, \alpha) = \sum_{j=1}^{4} m_j D_j(\alpha)e^{n_j y}, \qquad (9a,b)$$

$$n_1 = -n_4 = -\frac{\gamma}{2} - \frac{1}{2}\sqrt{\gamma^2 + 4(\alpha^2 + i\beta\alpha)},$$

$$n_2 = -n_3 = \frac{\gamma}{2} - \frac{1}{2}\sqrt{\gamma^2 + 4(\alpha^2 + i\beta\alpha)}, \qquad (10a,b)$$

$$\gamma = \beta\sqrt{(3-\kappa)/(1+\kappa)}, \qquad (11)$$

$$m_j = \frac{(\kappa-1)(\alpha^2 + i\beta\alpha) - (\kappa+1)n_j^2}{[\beta(\kappa-1) - 2i\alpha]n_j}, \quad (j = 1, ., 4) \qquad (12)$$

$$g_2(x, \alpha) = \sum_{j=1}^{4} A_j(\alpha)e^{p_j x},$$

$$f_2(x, \alpha) = \sum_{j=1}^{4} q_j A_j(\alpha)e^{p_j x}, \qquad (13a,b)$$

$$p_1 = -\frac{\beta}{2} - \frac{1}{2}\sqrt{\beta^2 + 4\alpha^2 + 4i\gamma\alpha},$$

$$p_2 = -\frac{\beta}{2} - \frac{1}{2}\sqrt{\beta^2 + 4\alpha^2 - 4i\gamma\alpha},$$

$$p_3 = -\frac{\beta}{2} + \frac{1}{2}\sqrt{\beta^2 + 4\alpha^2 + 4i\gamma\alpha},$$

$$p_4 = -\frac{\beta}{2} + \frac{1}{2}\sqrt{\beta^2 + 4\alpha^2 - 4i\gamma\alpha}, \qquad (14a\text{–}d)$$

$$q_j = \frac{(\kappa-1)(\beta + p_j)p_j - (\kappa+1)\alpha^2}{\alpha[2p_j + \beta(\kappa-1)]},$$

$$(j = 1, \ldots, 4). \qquad (15)$$

Since the stresses vanish as $y \to \infty$, from (9) and (10) it may be seen that

$$D_3(\alpha) = 0, \quad D_4(\alpha) = 0. \qquad (16a,b)$$

We now introduce the new unknown function

$$g(x) = \frac{\partial}{\partial x}v(x, 0). \qquad (17)$$

By using (6) and (7b) and by substituting from (17) and (9a) into (8b), we obtain

$$D_1(\alpha) = \frac{(m_2 n_2 - i\alpha)i}{(m_2 n_2 - m_1 n_1)\alpha}\int_a^b g(t)e^{i\alpha t}dt,$$

$$D_2(\alpha) = -\frac{(m_1 n_1 - i\alpha)i}{(m_2 n_2 - m_1 n_1)\alpha}\int_a^b g(t)e^{i\alpha t}dt. \qquad (18a,b)$$

Similarly, using (8), (9), (13), (3), and (18), from the homogeneous conditions (4) and (5) it follows that

$$\sum_{j=1}^{4}[(1+\kappa)q_j p_j + (3-\kappa)\alpha]A_j = \int_a^b F_1(\alpha, t)g(t)dt,$$

$$\sum_{j=1}^{4}(p_j - \alpha q_j)A_j = \int_a^b F_2(\alpha, t)g(t)dt,$$

$$\sum_{j=1}^{4}[(1+\kappa)q_j p_j + (3-\kappa)\alpha]e^{p_j h}A_j = \int_a^b F_3(\alpha, t)g(t)dt,$$

$$\sum_{j=1}^{4}[(p_j - \alpha q_j)e^{p_j h}A_j = \int_a^b F_4(\alpha, t)g(t)dt, \qquad (19a\text{–}d)$$

giving

$$A_j(\alpha) = \int_a^b C_j(\alpha, t)g(t)dt, \quad (j = 1, ., 4) \qquad (20)$$

where the functions F_j and C_j, $(j = 1, \ldots, 4)$ are given in the Appendix. Note that $g(t)$ is the only unknown function which may be determined from (7a).

3 Derivation of the Integral Equation

From the formulation given in the previous section σ_{yy} may be expressed in terms of A_i and D_j as follows:

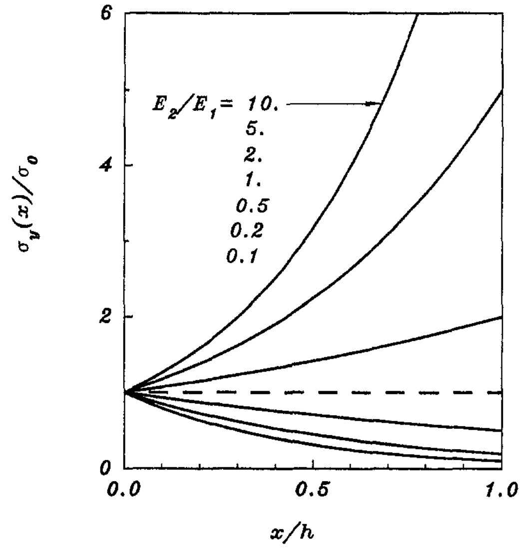

Fig. 2 The stress distribution in the uncracked layer under fixed grip loading $\sigma_0 = E_1\epsilon_0/(1-\nu^2)$

$$
\sigma_{yy}(x, y) = \frac{\mu(x)}{\kappa - 1}\left\{\frac{1}{2\pi}\int_{-\infty}^{\infty}\sum_{j=1}^{2}[(1+\kappa)n_j - (3-\kappa)i\alpha m_j]D_j e^{n_j y - i\alpha x}d\alpha + \frac{2}{\pi}\int_0^{\infty}\sum_{j=1}^{4}[(1+\kappa)\alpha + (3-\kappa)q_j p_j]A_j e^{p_j x}\cos\alpha y d\alpha\right\}. \quad (21)
$$

Substituting from (18), (20), and (21) into (7a), we obtain

$$
\int_a^b [h_1(x, t) + h_2(x, t)]g(t)dt = \frac{\kappa - 1}{\mu(x)}p(x), \quad a < x < b, \quad (22)
$$

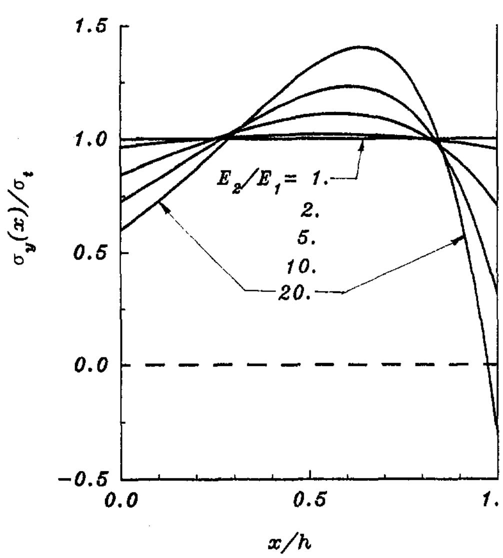

Fig. 3 The stress distribution in the uncracked layer under membrane loading, $\sigma_t = N/h$

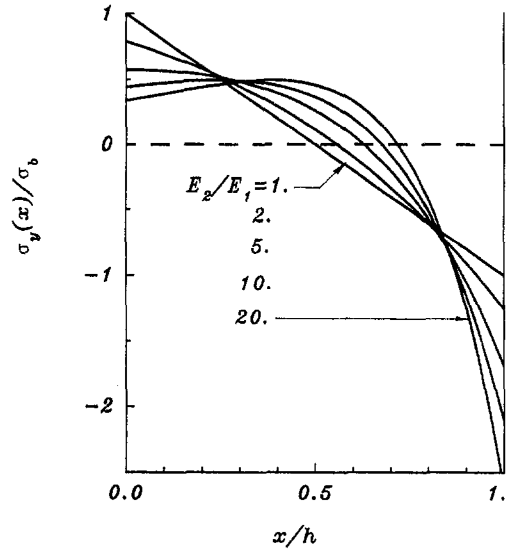

Fig. 4 The stress distribution in the uncracked layer under bending, $\sigma_b = 6M/h^2$

$$
h_1(x, t) = \lim_{y \to +0}\frac{1}{2\pi}\int_{-\infty}^{\infty}K_1(y, \alpha)e^{i\alpha(t-x)}d\alpha,
$$

$$
h_2(x, t) = \lim_{y \to +0}\frac{1}{2\pi}\int_{-\infty}^{\infty}K_2(x, t, \alpha)\cos\alpha y d\alpha, \quad (23a,b)
$$

$$
K_1(y, \alpha) = \frac{i}{\alpha(m_2 n_2 - m_1 n_1)}\{[(1+\kappa)n_1 - (3-\kappa)i\alpha m_1](m_2 n_2 - i\alpha)e^{n_1 y} + [(1+\kappa)n_2 - (3-\kappa)i\alpha m_2](i\alpha - m_1 n_1)e^{n_2 y}\},
$$

$$
K_2(x, t, \alpha) = \sum_{j=1}^{4}[(1+\kappa)\alpha + (3-\kappa)q_j p_j]e^{p_j x}C_j(\alpha, t). \quad (24a,b)
$$

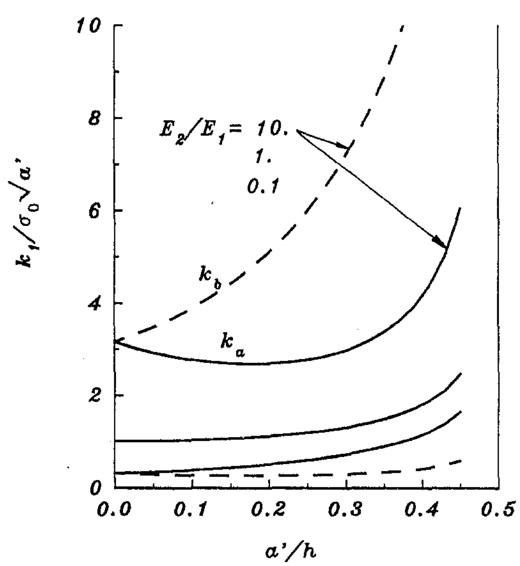

Fig. 5 The stress intensity factors for a symmetrically located internal crack in a graded layer under fixed grip loading, $(a+b)/2 = h/2$, $(b-a)/2 = a'$, $\sigma_0 = E_1\epsilon_0/(1-\nu^2)$; solid lines refer to $k_1(a)$ and dashed lines to $k_1(b)$

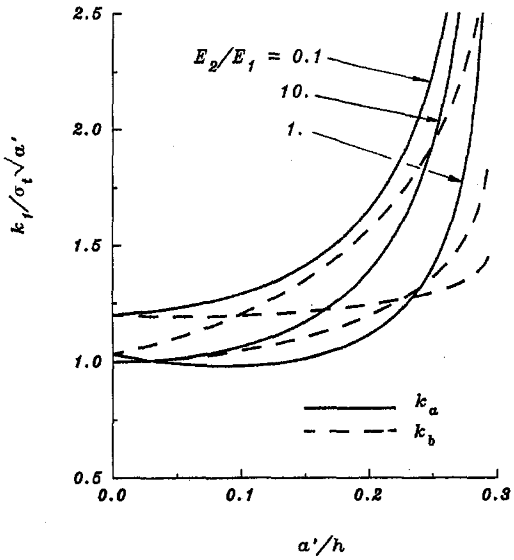

Fig. 6 The stress intensity factors for an internal crack in a graded layer under membrane loading, $(a + b)/2 = 0.3h$, $a' = (b - a)/2$, $\sigma_t = N/h$

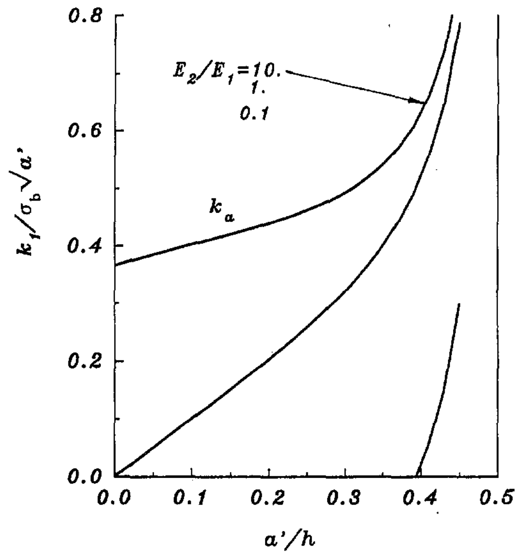

Fig. 7 The stress intensity factor for an internal crack in a graded layer under bending, $(a + b)/2 = h/2$, $a' = (b - a)/2$, $\sigma_b = 6M/h^2$

Observing that for $|\alpha| \to \infty$ the asymptotic value of K_1 is

$$K_{1\infty}(y, \alpha) = -4i \frac{\kappa - 1}{\kappa + 1} \frac{|\alpha|}{\alpha} e^{-|\alpha|y}, \qquad (25)$$

by adding and subtracting $K_{1\infty}$ to and from the integrand, from (23a) we find

$$h_1(x, t) = \frac{4(\kappa - 1)}{\pi(\kappa + 1)} \left(\frac{1}{t - x} + k_1(x, t) \right), \qquad (26)$$

$$k_1(x, t) = \frac{\kappa + 1}{8(\kappa - 1)} \int_{-\infty}^{\infty} [K_1(0, \alpha) - K_{1\infty}(0, \alpha)] e^{i\alpha(t-x)} d\alpha. \qquad (27)$$

Note that the singular term $(t - x)^{-1}$ in the kernel $h_1(x, t)$ is associated with an embedded crack in an elastic medium and leads to the standard square-root singularity for the unknown function $g(t)$. It may easily be shown that for $a > 0$ and $b < h$, $h_2(x, t)$ and $k_1(x, t)$ remain bounded in the closed interval $a \le (x, t) \le b$. However, for the case of an edge crack, at $a = 0$ or $b = h$ $g(t)$ is known to be nonsingular and the kernel $h_2(x, t)$ must contribute singular terms to make this possible. These singular terms may again be separated by examining the asymptotic behavior of the integrand $K_2(x, t, \alpha)$ in (23b) for $\alpha \to \infty$. Thus, after some lengthy analysis the asymptotic value of K_2 for $\alpha \to \infty$ was found to be[1]

$$K_{2\infty}(x, t, \alpha) = \frac{8(\kappa - 1)}{\kappa + 1} [2\alpha^2 xt - \alpha(x + 3t) + 2] e^{-\alpha(t+x)} - [2\alpha^2(h - x)(h - t) - \alpha(h - x) - 3\alpha(h - t) + 2] e^{-\alpha(2h-x-t)}. \qquad (28)$$

Substituting $y = 0$ and evaluating the integrals, from (23b) and (28) the singular and bounded terms in h_2 may be obtained as follows:

$$h_2(x, t) = \frac{4(\kappa - 1)}{\pi(\kappa + 1)} [k_s(x, t) + k_b(x, t)], \qquad (29)$$

$$k_s(x, t) = -\frac{1}{t + x} + \frac{6x}{(t + x)^2} - \frac{4x^2}{(t + x)^3} + \frac{1}{2h - x - t} - \frac{6(h - x)}{(2h - x - t)^2} + \frac{4(h - x)^2}{(2h - x - t)^3}, \qquad (30)$$

$$k_b(x, t) = \frac{\kappa + 1}{8(\kappa - 1)} \int_0^{\infty} [K_2(x, t, \alpha) - K_{2\infty}(x, t, \alpha)] d\alpha. \qquad (31)$$

The integral Eq. (22) may then be expressed as

$$\frac{1}{\pi} \int_a^b \left[\frac{1}{t - x} + k_s(x, t) + k_1(x, t) + k_b(x, t) \right] g(t) dt = \frac{1 + \kappa}{4\mu(x)} p(x), \quad a < x < b. \qquad (32)$$

In solving the edge crack problem ($a = 0$) the last three terms

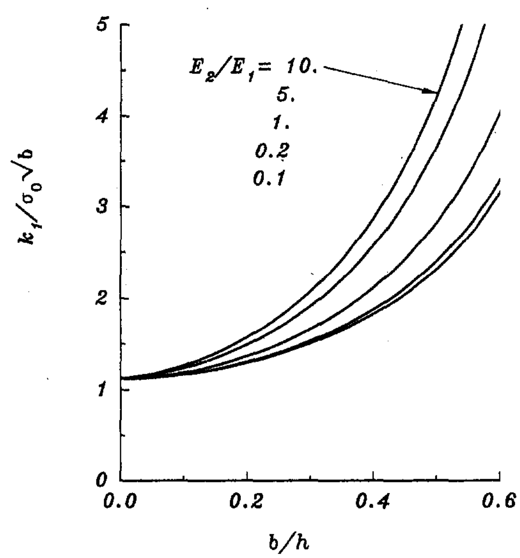

Fig. 8 Stress intensity factor for an edge crack in a graded layer under fixed grip loading, $a = 0$, $\sigma_0 = E_1\epsilon_0(1 - \nu^2)$

[1] In determining $K_{2\infty}$ most of the analysis was performed by using MAPLE and the related integrals were evaluated by using contour integration.

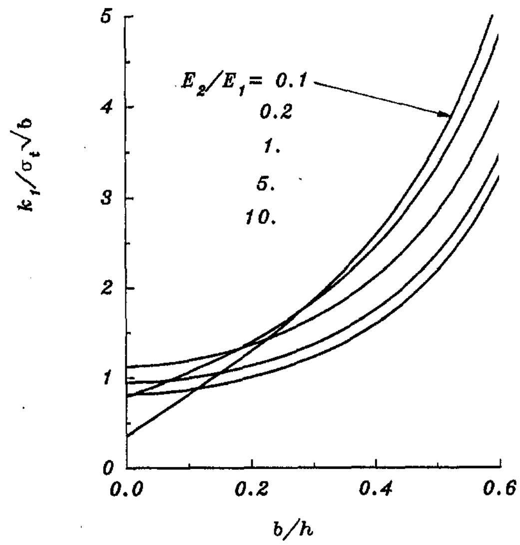

Fig. 9 Stress intensity factor for an edge crack in a graded layer under membrane loading, $a = 0$, $\sigma_t = N/h$

in (30) may be treated as Fredholm kernels. However, in the "free end" problem $a = 0$ and $b = h$, (32) is still valid, but all six terms in (30) as well as $(t - x)^{-1}$ have to be treated as singular kernels (Bakioglu and Erdogan, 1977; Gupta and Erdogan, 1974).

4 On the Solution of the Integral Equation

For the case of an embedded crack, $a > 0$, $b < h$, the solution of (32) is quite straightforward. First the interval is normalized by defining

$$t = \frac{b-a}{2}r + \frac{b+a}{2}, \quad x = \frac{b-a}{2}s + \frac{b+a}{2},$$

$$g(t) = \phi(r), \quad p(x) = f(s). \tag{33}$$

Then, observing that the fundamental solution of (32) is $(1 - r^2)^{-1/2}$, the unknown function is expressed as

$$\phi(r) = \frac{1}{\sqrt{1-r^2}} \sum_0^\infty B_n T_n(r), \quad -1 < r < 1, \tag{34}$$

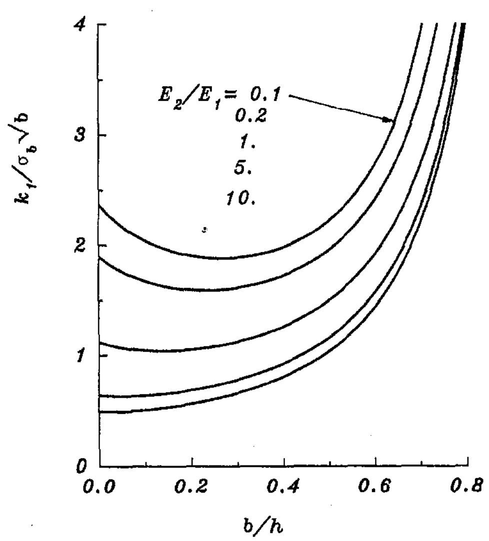

Fig. 10 Stress intensity factor for an edge crack in a graded layer under bending, $a = 0$, $\sigma_b = 6M/h^2$

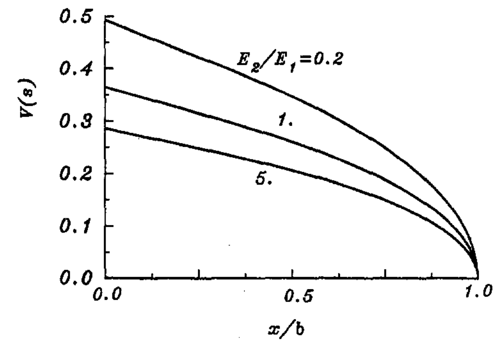

Fig. 11 Crack surface displacement for an edge crack in a graded layer under fixed grip loading for various values of the nonhomogeneity parameter E_2/E_1, $b/h = 0.2$, $V(s) = v(x, 0)/2h\epsilon_0$

where T_n is the Chebyshev polynomial of the first kind and B_1, $B_2, \ldots$ are unknown constants. In this case from (7b) and (17) it follows that ϕ must satisfy the following single valuedness condition:

$$\int_{-1}^{1} \phi(r)dr = 0. \tag{35}$$

By using the orthogonality conditions for T_n, from (34) and (35) it may be seen that $B_0 = 0$. The remaining constants are then determined by substituting from (33) and (34) into (32) and by using a convenient collocation method.

After determining $B_1, B_2, \ldots$ the stress intensity factors and the crack surface displacement may be evaluated from

$$k_1(a) = \lim_{x \to a} \frac{4\mu(x)}{1+\kappa} \sqrt{2(x-a)}g(x) = \frac{4\mu(a)}{1+\kappa}\sqrt{\frac{b-a}{2}} \sum_1^\infty (-1)^n B_n,$$

$$k_1(b) = -\lim_{x \to b} \frac{4\mu(x)}{1+\kappa} \sqrt{2(b-x)}g(x) = -\frac{4\mu(b)}{1+\kappa}\sqrt{\frac{b-a}{2}} \sum_1^\infty B_n, \tag{36a,b}$$

$$v(x, 0) = -\frac{b-a}{2}\sqrt{1-s^2} \sum_1^\infty \frac{B_n}{n} U_{n-1}(s), \tag{37}$$

where U_n is the Chebyshev polynomial of the second kind.

In the edge crack problem, $a = 0$, we again normalize the interval by defining

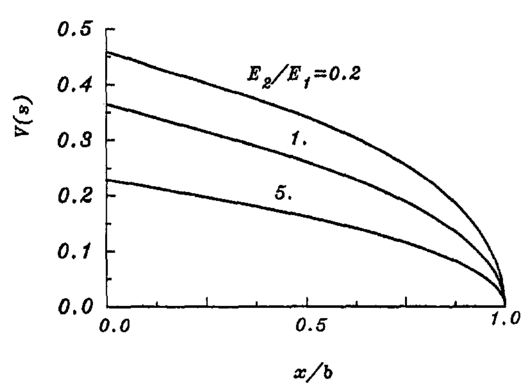

Fig. 12 Crack surface displacement for an edge crack in a graded layer under membrane loading, $b/h = 0.2$, $V(s) = [E_1/(1 - \nu^2)][v(x, 0)]/2h\sigma_t$

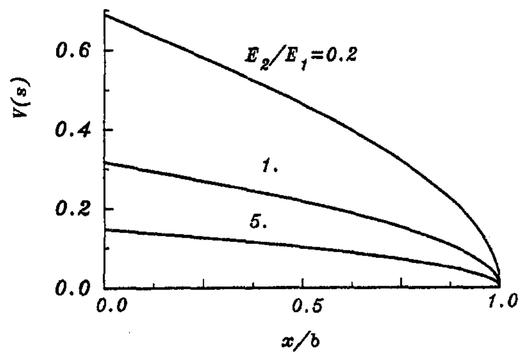

Fig. 13 Crack surface displacement for an edge crack in a graded layer under bending, $b/h = 0.2$, $V(s) = [E_1/(1-\nu^2)][v(x,0)]/2h\sigma_b$

$$t = \frac{b}{2}(1+r), \quad x = \frac{b}{2}(1+s),$$

$$g(t) = \phi(r), \quad p(x) = f(s). \tag{38}$$

In this case from the generalized Cauchy kernel given by (30) it can be shown that the weight function of the solution is $(1-r)^{-1/2}$. We then express the solution as follows:

$$\phi(r) = \frac{1}{\sqrt{1-r}} \sum_0^\infty A_n T_n(r), \quad -1 < r < 1. \tag{39}$$

For $a = 0$, in the integral Eq. (32), the Cauchy kernel $(t-x)^{-1}$ and the first three terms of $k_s(x,t)$ are singular. However, it should be observed that at $t = 0$ the sum of these four singular kernels is zero. The singular terms in (32) may be evaluated by observing that (Kaya and Erdogan, 1987)

$$\int_{-1}^{1} \frac{T_n(\tau)d\tau}{\sqrt{1-\tau}(\tau-\sigma)} = \int_{-1}^{1} \frac{T_n(\tau) - T_n(\sigma)}{\sqrt{1-\tau}(\tau-\sigma)} d\tau$$

$$+ T_n(\sigma) \int_{-1}^{1} \frac{d\tau}{\sqrt{1-\tau}(\tau-\sigma)}, \tag{40}$$

where σ is real, on the right-hand side at $\tau = \sigma$ the first integral is bounded, and the second integral is given by

$$\int_{-1}^{1} \frac{d\tau}{\sqrt{1-\tau}(\tau-\sigma)} = \frac{\log|B(\sigma)|}{\sqrt{1-\sigma}}, \quad \sigma < 1, \tag{41}$$

$$B(\sigma) = \frac{1 + \sqrt{(1-\sigma)/2}}{1 - \sqrt{(1-\sigma)/2}}, \tag{42}$$

$$\int_{-1}^{1} \frac{d\tau}{\sqrt{1-\tau}(\tau-\sigma)^m} = -\frac{(-1)^m\sqrt{2}}{(m-1)(1-\sigma)(1+\sigma)^{m-1}}$$

$$+ \frac{2m-3}{2(m-1)(1-\sigma)} \int_{-1}^{1} \frac{d\tau}{\sqrt{1-\tau}(\tau-\sigma)^{m-1}}$$

$$\sigma < 1, \quad m = 2, 3, \ldots. \tag{43}$$

In (43), the strongly singular integrals are treated in the Hadamard sense (Kaya and Erdogan, 1987). Note that after normalizing (32), σ is either s or $-(s+2)$ and $-1 < s < 1$. All other bounded integrals in (32) are evaluated by using Gaussian quadrature and the resulting functional equation is solved for $A_1, \ldots, A_N$ by collocation.

In this case, too, once the coefficients A_n are determined, the unknown function is obtained essentially in closed form and the stress intensity factor and the crack surface displacement may be expressed as

$$k_1(b) = -\lim_{x\to b} \frac{4\mu(x)}{1+\kappa} \sqrt{2(b-x)}\, g(x)$$

$$= -\frac{4\mu(b)}{1+\kappa} \sqrt{b} \sum_0^\infty A_n, \tag{44}$$

$$v(x,0) = -\frac{b}{\sqrt{2}} \sum_0^\infty A_n \left[\frac{\sin(n-\frac{1}{2})\theta}{n-\frac{1}{2}} + \frac{\sin(n+\frac{1}{2})\theta}{n+\frac{1}{2}} \right], \tag{45}$$

$$\cos\theta = (2x-b)/b. \tag{46}$$

5 Results and Discussion

The mode I crack problem described in Fig. 1 is solved for $a = 0$ and $a > 0$ under three loading conditions. The first is a "fixed grip" loading with $\epsilon_{yy}(x, \mp\infty) = \epsilon_0$ for which the crack surface traction defined by (7a) becomes

$$p(x) = -\sigma_y(x) = -\frac{8\mu(x)}{1+\kappa}\epsilon_0 \tag{47}$$

for both plane-strain ($\epsilon_{zz} = 0$) and plane-stress ($\sigma_{zz} = 0$) conditions. Observing that $\mu(x) = \mu_0 \exp(\beta x)$ and κ = constant, in this problem we define the normalizing stress as

$$\sigma_0 = \frac{8\mu_0}{1+\kappa}\epsilon_0 = \frac{E_1}{1-\nu^2}\epsilon_0 \tag{48}$$

where $E(x) = E_1 \exp(\beta x)$ and for plane stress $E_1/(1-\nu^2)$ should be replaced by E_1.

The second loading is a "membrane" resultant $N_{yy} = N$ applied along $x = h/2$ away from the crack region, and the third is bending $M_{zz} = M$. For these two loading conditions the normalizing stresses are defined by

$$\sigma_t = N/h, \quad \sigma_b = 6M/h^2. \tag{49a,b}$$

In the last two cases the compatibility condition $\partial^2\epsilon_{yy}/\partial x^2 = 0$ would give

$$\sigma_y(x) = \frac{8\mu(x)}{1+\kappa}(Ax + B) \tag{50}$$

where the constants A and B are determined from

$$\int_0^h \sigma_y(x)dx = N, \quad \int_0^h \sigma_y(x)xdx = M \tag{51a,b}$$

by assuming $M = 0$ for membrane loading and $N = 0$ for bending. The crack surface traction $p(x)$ would then be obtained by letting $p(x) = -\sigma_y(x)$. The results given in this study are calculated under plane-strain conditions.

For the nonhomogeneous medium considered it is assumed that ν is constant and $E(x)$ or $\mu(x)$ is characterized by two parameters which are selected to be $E_1 = E(0)$ and $E_2 = E(h)$ giving

$$\beta h = \log(E_2/E_1). \tag{52}$$

Figures 2–4 show some sample results for the stress in the uncracked medium obtained from (47) and (50) for various values of the material nonhomogeneity parameter E_2/E_1. Note that the results given for $E_2/E_1 = 1, 2, 5, 10, 20$ in Figs. 3 and 4 may also be interpreted for $E_2/E_1 = 1, 0.5, 0.2, 0.1, 0.05$, respectively. Under membrane loading the ends are free to rotate and, as a result, the stress distribution exhibits some bending effects which, depending on E_2/E_1, can be quite severe (Fig. 3).

Some examples for the stress intensity factors in the nonhomogeneous layer containing an embedded crack (i.e., $a > 0$, $b < h$, Fig. 1) are shown in Figs. 5–7. In these figures $a' = (b-a)/2$ is the half-crack length and $k_a = k_1(a)/\sigma_i\sqrt{a'}$, $k_b =$

Table 1 The normalized stress intensity factors $k_1/\sigma_o\sqrt{b}$, $k_1/\sigma_t\sqrt{b}$ and $k_1/\sigma_b\sqrt{b}$ resulting from, respectively, a fixed grip loading, membrane loading and bending of a graded layer containing an edge crack, $\sigma_0 = E_1\epsilon_0/(1-\nu^2)$, $\sigma_t = N/h$, $\sigma_b = 6M/h^2$.

b/h	$E_2/E_1 = 0.1$			$E_2/E_1 = 0.2$			$E_2/E_1 = 0.5$		
	$\frac{k_1}{\sigma_0\sqrt{b}}$	$\frac{k_1}{\sigma_t\sqrt{b}}$	$\frac{k_1}{\sigma_b\sqrt{b}}$	$\frac{k_1}{\sigma_0\sqrt{b}}$	$\frac{k_1}{\sigma_t\sqrt{b}}$	$\frac{k_1}{\sigma_b\sqrt{b}}$	$\frac{k_1}{\sigma_0\sqrt{b}}$	$\frac{k_1}{\sigma_t\sqrt{b}}$	$\frac{k_1}{\sigma_b\sqrt{b}}$
0.1	1.1648	0.8129	2.0427	1.1670	1.0553	1.6743	1.1766	1.1897	1.2840
0.2	1.2963	1.2965	1.9040	1.3058	1.3956	1.5952	1.3336	1.4150	1.2618
0.3	1.5083	1.8581	1.8859	1.5330	1.8395	1.6122	1.5922	1.7559	1.3128
0.4	1.8246	2.5699	1.9778	1.8751	2.4436	1.7210	1.9872	2.2598	1.4398
0.5	2.3140	3.5701	2.2151	2.4031	3.3266	1.9534	2.6032	3.0331	1.6744
0.6	3.1544	5.1880	2.7170	3.2981	4.7614	2.4037	3.6359	4.3187	2.0992
0.7	4.9305	8.4818	3.8953	5.0272	7.5248	3.3536	5.6098	6.7657	2.9407
	$E_2/E_1 = 0.6$			$E_2/E_1 = 0.7$			$E_2/E_1 = 0.8$		
0.1	1.1795	1.1967	1.2173	1.1821	1.1984	1.1635	1.1846	1.1970	1.1187
0.2	1.3414	1.4068	1.2041	1.3485	1.3974	1.1572	1.3553	1.3874	1.1180
0.3	1.6080	1.7330	1.2604	1.6224	1.7122	1.2177	1.6358	1.6933	1.1818
0.4	2.0163	2.2214	1.3903	2.0429	2.1886	1.3498	2.0673	2.1599	1.3157
0.5	2.6551	2.9774	1.6254	2.7024	2.9308	1.5854	2.7460	2.8908	1.5517
0.6	3.7285	4.2403	2.0477	3.8131	4.1765	2.0059	3.8914	4.1220	1.9707
0.7	5.7801	6.6494	2.8791	5.9381	6.5562	2.8301	6.0853	6.4785	2.7894
0.8	10.7542	12.4850	4.9108	11.0734	12.3056	4.8310	11.3788	12.1640	4.7683
	$E_2/E_1 = 0.9$			$E_2/E_1 = 2$			$E_2/E_1 = 3$		
0.1	1.1870	1.1937	1.0804	1.2066	1.2187	0.8502	1.2190	1.0738	0.7504
0.2	1.3615	1.3773	1.0845	1.4132	1.2821	0.8801	1.4461	1.2197	0.7898
0.3	1.6482	1.6760	1.1510	1.7503	1.5437	0.9612	1.8154	1.4690	0.8760
0.4	2.0902	2.1345	1.2864	2.2764	1.9573	1.1037	2.3953	1.8654	1.0205
0.5	2.7860	2.8560	1.5229	3.1196	2.6233	1.3406	3.3339	2.5082	1.2568
0.6	3.9651	4.0755	1.9408	4.5706	3.7702	1.7512	4.9660	3.6238	1.6640
0.7	6.2264	6.4150	2.7563	7.3973	6.0025	2.5452	8.1791	5.8121	2.4495
0.8	11.6862	12.0639	4.7241	14.2834	11.4297	4.4475	16.0887	11.1735	4.3373
	$E_2/E_1 = 4$			$E_2/E_1 = 5$			$E_2/E_1 = 10$		
0.1	1.2289	1.0286	0.6856	1.2372	0.9908	0.6385	1.2664	0.8631	0.5082
0.2	1.4724	1.1713	0.7305	1.4946	1.1318	0.6871	1.5740	1.0019	0.5648
0.3	1.8676	1.4137	0.8195	1.9118	1.3697	0.7778	2.0723	1.2291	0.6588
0.4	2.4912	1.7996	0.9650	2.5730	1.7483	0.9236	2.8736	1.5884	0.8043
0.5	3.5080	2.4276	1.2003	3.6573	2.3656	1.1518	4.2140	2.1762	1.0350
0.6	5.2903	3.5226	1.6043	5.5704	3.4454	1.5597	6.6319	3.2124	1.4286
0.7	8.8280	5.6818	2.3848	9.3936	5.5830	2.3360	11.5755	5.2865	2.1915
0.8	17.6120	11.0041	4.2649	18.9549	10.8775	4.2109	24.2450	10.5008	4.0512

$k_1(b)/\sigma_i\sqrt{a'}$, $(i = o, t, b)$ are the normalized stress intensity factors. In Figs. 5 and 7 the crack is located symmetrically; that is, $a + b = h$, and therefore the stress intensity factors become unbounded as $a' \to h/2$. In all cases as a' approaches zero we have $k_1(a) \to \sigma_y(x)\sqrt{a'}$, where $x = (b + a)/2$ and $\sigma_y(x)$ is the stress in the uncracked medium shown, for example, in Figs. 2–4. For reference, in each case the figures also show the results for the corresponding homogeneous layer, $E_1 = E_2$. Note that under constant strain loading as may be seen from Fig. 2 the crack surface traction for $E_2/E_1 = 10$ is considerably greater than that for $E_2/E_1 = 0.1$, whereas the normalizing stress intensity factor is the same in both cases. This essentially is the reason for the differences in the stress intensity factors shown in Fig. 5.

In the example showing the results for bending (Fig. 7), $k_1(b) < 0$ and, therefore, only $k_1(a)$ is given. Because of this, these results are meaningful only if they are superimposed on other solutions in such a way that the resulting stress intensity factors are positive.

Figure 6 shows the embedded crack results for $(b - a)/2 = 0.3h$. Note that $a'/h = 0.3$ corresponds to $a = 0$ for which $k_1(a)$ becomes unbounded and $k_1(b)$ would be the edge crack result at $b/h = 0.6$. The limiting values of $k_1(b)$ calculated from the edge crack solution are

E_2/E_1:	0.1	1	10
$k_1(b)/\sigma_t\sqrt{a'}$:	7.337	5.704	4.543
$k_1(b)/\sigma_t\sqrt{b}$:	5.188	4.033	3.212

At $a'/h = 0.3$ even though $k_1(b)$ is bounded, because of the sudden change in the crack configuration going from embedded to an edge crack, its derivative with respect to a'/h becomes unbounded and, consequently, $k_1(b)$ becomes rather ill-defined.

The final set of results shown in Figs. 8–10 present the stress intensity factors for the important case of an edge crack in a nonhomogeneous layer. The results for constant strain or fixed grip loading are shown in Fig. 8. Note that the stress $\sigma_0 = E_1\epsilon_0/(1 - \nu^2)$ is the value of $\sigma_y(x)$ at $x = 0$. Thus, for all values of E_2/E_1, as $b/h \to 0$, $k_1/\sigma_0\sqrt{b}$ would approach 1.1215, the edge crack solution for a homogeneous half-plane. Also, the magnitude of the crack surface tractions and, as a result, the stress intensity factor increases, with increasing stiffness ratio E_2/E_1, and $k_1(b)$ becomes unbounded as $b/h \to 1$.

The stress intensity factor for an edge crack in a graded layer under membrane loading and bending are given in Figs. 9 and 10, respectively. Note that the limiting values of $k_1(b)$ for $b \to 0$ are given by $k_1(b) = 1.1215\sigma_y(0)\sqrt{b}$ where $\sigma_y(x)$ is the stress in the uncracked medium shown in Figs. 3 and 4. In these problems, too, $k_1(b)$ becomes unbounded as b approaches h.

Finally, some sample results for the crack surface displacement $v(x, 0)$ for $b/h = 0.2$ and $E_2/E_1 = 0.2$, 1, 5 are shown in Figs. 11–13. For the three loading conditions very near the crack tip $x = b$ the relative values of the crack surface curvature are seen to follow the relative magnitudes of the corresponding stress intensity factors given in Figs. 8–10.

Comparing the results given in Figs. 2–10 for nonhomogeneous and homogeneous layers, it is clear that the material nonhomogeneity has quite considerable influence on the stress distribution and the stress intensity factors.

Additional results for stress intensity factors are given in Table 1. These results may be quite useful for determining the stress intensity factors by means of a suitable interpolation in a given practical application. They also provide the necessary information to be used in a possible application of the line spring model for estimating the stress intensity factors in three-dimensional surface crack problems for FGM plates.

Acknowledgments

This study was supported by the National Science Foundation under the Grant MSS-9114439 and by the Air Force Office of Scientific Research under the Grant F49620-93-1-0252.

References

Bakioglu, M., and Erdogan, F., 1977, "The Crack-Contact and the Free-End Problem for a Strip Under Residual Stress," ASME Journal of Applied Mechanics, Vol. 44, pp. 41–46.

Batakis, A. P., and Vogan, J. W., 1985, "Rocket Thrust Chamber Thermal Barrier Coatings," NASA CR-1750222.

Delale, F., and Erdogan, F., 1983, "The Crack Problem for a Nonhomogeneous Plane," ASME Journal of Applied Mechanics, Vol. 50, pp. 609–614.

Gupta, G. D., and Erdogan, F., 1974, "The Problem of Edge Cracks in an Infinite Strip," ASME Journal of Applied Mechanics, Vol. 41, pp. 1001–1006.

Hirano, T., and Yamada, T., 1988, "Multi-Paradigm Expert System Architecture Based Upon the Inverse Design Concept," Int. Workshop on Artificial Intelligence for Industrial Applications, Hitachi, Japan.

Hirano, T., Yamada, T., Teraki, J., Niino, M., and Kumakawa, A., 1988, "A Study of Functionally Gradient Material Design System for a Thrust Chamber," *Proc. 16th Int. Symp. on Space Technology and Science,* Sapporo, Japan.

Holt, J., Koizumi, M., Hirai, T., and Munir, Z., eds., 1992, *Functionally Gradient Materials,* Ceramic Transactions, Vol. 34, American Ceramic Society, Westerville, OH.

Houck, D. L., ed., 1987, *Thermal Spray: Advances in Coatings Technology,* Proc. of the National Thermal Spray Conference, ASM International.

Kaya, A. C., and Erdogan, F., 1987, "On the Solution of Integral Equations with Strongly Singular Kernels," *Quarterly of Applied Mathematics,* Vol. 45, pp. 105–122.

Konda, N., and Erdogan, F., 1994, "The Mixed Mode Crack Problem in a Nonhomogeneous Elastic Medium," *Engineering Fracture Mechanics,* Vol. 47, pp. 533–545.

Niino, M., and Maeda, S., 1990, "Recent Development Status of Functionally Gradient Materials," *ISIJ International,* Vol. 30, pp. 699–703.

Ozturk, M., and Erdogan, F., 1993, "The Axisymmetric Crack Problem in a Nonhomogeneous Medium," ASME Journal of Applied Mechanics, Vol. 44, pp. 631–636.

Yamanouchi, M., Koizumi, M., Hirai, T., and Shiota, I., eds., 1990, *FGM-90,* Proc. First Int. Symp. on Functionally Gradient Materials, FGM Forum, Tokyo, Japan.

APPENDIX

Expressions for the functions $F_1, \ldots, F_4$ and $C_1, \ldots, C_4$

$$F_1(\alpha, t) = \frac{i}{2\pi}\int_{-\infty}^{\infty}\frac{1}{\rho}e^{i\rho t}\left\{[(3-\kappa)n_1 - (1+\kappa)i\rho m_1]\right.$$
$$\times\frac{n_1(m_2n_2 - i\rho)}{(\alpha^2+n_1^2)(m_2n_2 - m_1n_1)} + [(3-\kappa)n_2$$
$$\left.-(1+\kappa)i\rho m_2]\frac{n_2(i\rho - m_1n_1)}{(a^2+n_2^2)(m_2n_2-m_1n_1)}\right\}d\rho, \quad \text{(A1)}$$

$$F_2(\alpha, t) = -\frac{i}{2\pi}\int_{-\infty}^{\infty}\frac{1}{\rho}e^{i\rho t}\left[\frac{\alpha(m_2n_2 - i\rho)(m_1n_1 - i\rho)}{(\alpha^2+n_1^2)(m_2n_2-m_1n_1)}\right.$$
$$\left.+\frac{\alpha(i\rho - m_1n_1)(m_2n_2 - i\rho)}{(\alpha^2+n_2^2)(m_2n_2-m_1n_1)}\right]d\rho, \quad \text{(A2)}$$

$$F_3(\alpha, t) = \frac{i}{2\pi}\int_{-\infty}^{\infty}\frac{1}{\rho}e^{i\rho(t-h)}\left\{[(3-\kappa)n_1 - (1+\kappa)i\rho m_1]\right.$$
$$\times\frac{n_1(m_2n_2 - i\rho)}{(\alpha^2+n_1^2)(m_2n_2-m_1n_1)} + [(3-\kappa)n_2 - (1+\kappa)i\rho m_2]$$
$$\left.\times\frac{n_2(i\rho - m_1n_1)}{(\alpha^2+n_2^2)(m_2n_2-m_1n_1)}\right\}d\rho, \quad \text{(A3)}$$

$$F_4(\alpha, t) = -\frac{i}{2\pi}\int_{-\infty}^{\infty}\frac{1}{\rho}e^{i\rho(t-h)}\left[\frac{\alpha(m_2n_2 - i\rho)(m_1n_1 - i\rho)}{(\alpha^2+n_1^2)(m_2n_2-m_1n_1)}\right.$$
$$\left.+\frac{\alpha(i\rho - m_1n_1)(m_2n_2 - i\rho)}{(\alpha^2+n_2^2)(m_2n_2-m_1n_1)}\right]d\rho. \quad \text{(A4)}$$

$$C_i(\alpha, t) = \sum_{j=1}^{4} b_{ij}(\alpha)F_j(\alpha, t), \quad (i = 1, \ldots, 4) \quad \text{(A5)}$$

where the matrix (b_{ij}) is the inverse of (a_{ij}) given by

$$a_{1j}(\alpha) = (1+\kappa)q_jp_j + (3-\kappa)\alpha, \quad a_{2j}(\alpha) = p_j - \alpha q_j,$$
$$a_{3j}(\alpha) = [(1+\kappa)q_jp_j + (3-\kappa)\alpha]e^{p_jh},$$
$$a_{4j}(\alpha) = (p_j - \alpha q_j)e^{p_jh}. \quad \text{(A6)}$$

Note that in (A1)–(A6) m_i and n_i are functions of ρ and p_j and q_j are functions of α (see Eqs. 10–15). By using the theory of residues, the integrals in (A1)–(A4) may be evaluated as follows:

$$F_1(\alpha, t) = -\frac{\kappa-1}{\kappa+1}\frac{\alpha^2e^{-t(\lambda_1-\beta/2)}}{\lambda_1\lambda_2(\lambda_1^2+\lambda_2^2)}[(2\lambda_1^2+2\lambda_2^2-\lambda_1\beta)$$
$$\times\sin(\lambda_2t) - \beta\lambda_2\cos(\lambda_2t)], \quad \text{(A7)}$$

$$F_2(\alpha, t)$$
$$= \frac{2}{\kappa+1}\frac{\alpha^2e^{-t(\lambda_1-\beta/2)}}{\lambda_1\lambda_2(\lambda_1^2+\lambda_2^2)}\left[\lambda_1\left(\lambda_1^2+\lambda_2^2-\frac{\beta^2}{4}\right)\sin(\lambda_2t)\right.$$
$$\left.-\lambda_2\left(\lambda_1^2+\lambda_2^2+\frac{\beta^2}{4}\right)\cos(\lambda_2t)\right], \quad \text{(A8)}$$

$$F_3(\alpha, t) = \frac{\kappa-1}{\kappa+1}\frac{\alpha^2e^{-(h-t)(\lambda_1+\beta/2)}}{\lambda_1\lambda_2(\lambda_1^2+\lambda_2^2)}[(2\lambda_1^2+2\lambda_2^2+\lambda_1\beta)$$
$$\times\sin(\lambda_2(h-t)) + \beta\lambda_2\cos(\lambda_2(h-t))], \quad \text{(A9)}$$

$$F_4(\alpha, t) = \frac{2}{\kappa+1}\frac{\alpha e^{-(h-t)(\lambda_1+\beta/2)}}{\lambda_1\lambda_2(\lambda_1^2+\lambda_2^2)}\left[\lambda_1\left(\lambda_1^2+\lambda_2^2-\frac{\beta^2}{4}\right)\right.$$
$$\times\sin\left(\lambda_2(h-t)\right) - \lambda_2\left(\lambda_1^2+\lambda_2^2+\frac{\beta^2}{4}\right)$$
$$\left.\times\cos(\lambda_2(h-t))\right], \quad \text{(A10)}$$

$$\lambda_1 = +\sqrt{\frac{R_1+R_2}{2}}, \quad \lambda_2 = +\sqrt{\frac{R_1-R_2}{2}},$$
$$R_1 = +\sqrt{\left(\alpha^2+\frac{\beta^2}{4}\right)^2 + \frac{3-\kappa}{1+\kappa}\alpha^2\beta^2},$$
$$R_2 = \alpha^2 + \frac{\beta^2}{4}. \quad \text{(A11)}$$

The Elastic Field Resulting From Elliptical Hertzian Contact of Transversely Isotropic Bodies: Closed-Form Solutions for Normal and Shear Loading

M. T. Hanson
Mem. ASME.

I. W. Puja

Department of Engineering Mechanics,
University of Kentucky,
Lexington, KY 40506-0046

This analysis presents the elastic field in a half-space caused by an ellipsoidal variation of normal traction on the surface. Coulomb friction is assumed and thus the shear traction on the surface is taken as a friction coefficient multiplied by the normal pressure. Hence the shear traction is also of an ellipsoidal variation. The half-space is transversely isotropic, where the planes of isotropy are parallel to the surface. A potential function method is used where the elastic field is written in three harmonic functions. The known point force potential functions are utilized to find the solution for ellipsoidal loading by quadrature. The integrals for the derivatives of the potential functions resulting from ellipsoidal loading are evaluated in terms of elementary functions and incomplete elliptic integrals of the first and second kinds. The elastic field is given in closed-form expressions for both normal and shear loading.

1 Introduction

The stress field generated by elliptical Hertzian contact for isotropic elastic materials has been thoroughly investigated. The solutions for several cases have been obtained. Haines and Ollerton (1963) studied elliptical contact stress under radial and tangential load. Solutions for various cases of the elliptical contact stress can also be found in the books by Gladwell (1980), Johnson (1985), and Hills et al. (1993). These solutions are extremely important since the elliptical contact problem arises often in engineering applications. For example the contact area between a ball rolling in a non conforming groove is an ellipse and a railway wheel moving along a convex rail head, or crossed cylinders also have elliptical contact geometries (Hills et al., 1993).

The evaluation of the elastic field throughout the contacting bodies for elliptical Hertzian contact has been obtained by Bryant and Keer (1982) for isotropy. Their solutions included slip and stick zones, based on the results of Cattaneo (1938). Sackfield and Hills (1983a, b) also evaluated the stress field for elliptical Hertzian contact under normal loading and shear loading. Although the Sackfield and Hills solutions were written in a different form, it can be shown numerically that the stress field for normal and shear traction are identical to the Bryant and Keer solutions. More concise formulas for the stress field are given by Sackfield et al. (1993). For a special case, when the minor and major axis of the ellipse are the same, the problem may be considered as spherical Hertzian contact. The case for normal contact stress was first considered by Huber (1904). Hamilton and Goodman (1966) have also examined the problem including shear traction, where they express the elastic field in terms of complex variables. Hamilton (1983) overcame the complication and gave real explicit expressions for the stress field. Sackfield and Hills (1983c) obtained the stress field for this problem by limiting the corresponding elliptical contact problems solved previously. Hanson and Johnson (1993) revisited this problem and gave the expressions for the elastic fields in a more convenient form. They also gave the relations showing equivalence between the different forms of the solutions.

With recent developments in composite materials (where the materials no longer obey an isotropic constitutive law) and their applications, it is important to develop methods of stress analysis for them also. At the present time, analytical solutions to orthotropic or more general anisotropy is still beyond our abilities. However, it has been shown that transverse isotropy solutions are obtainable in analytic form. Chen (1969) has obtained the subsurface elastic field in a transversely isotropic half space in contact with an elastic spherical indenter. Dahan and Zarka (1977) also evaluated the elastic field for spherical Hertzian contact (without traction) for transverse isotropy using Hankel transforms. Keer and Mowry (1979) extended the analysis to shear loading including regions of stick and slip. Hanson (1992) recently evaluated the elastic field for spherical Hertzian contact including sliding friction in a more convenient form. He also gave the comparation with those results previously obtained.

In the present paper, the elastic field for elliptical Hertzian contact including sliding traction for a transversely isotropic material is evaluated. Assuming Coulomb friction, the sliding traction is taken to be directly proportional to the contact pressure. The conventional assumption that the addition of a tangential load has no effect on the contact dimension or the Hertzian pressure is also adopted. Here the boundary value problem is solved using the potential method for transverse isotropy which was first given by Elliot (1948) and is used in the form by Fabrikant (1989). The potential functions are determined by integrating the point force Green's functions over the elliptical contact area. The partial derivatives of the potential functions needed to determine the elastic field are evaluated using Luré's method (1964). This method is based on the fact that the solutions of the Laplace equation in an elliptical coordinate system can be written in terms of three Lame functions. Complete

Contributed by the Applied Mechanics Division of THE AMERICAN SOCIETY OF MECHANICAL ENGINEERS for publication in the ASME JOURNAL OF APPLIED MECHANICS.

Discussion on this paper should be addressed to the Technical Editor, Professor Lewis T. Wheeler, Department of Mechancial Engineering, University of Houston, Houston, TX 77204-4792, and will be accepted until four months after final publication of the paper itself in the ASME JOURNAL OF APPLIED MECHANICS.

Manuscript received by the ASME Applied Mechanics Division, Dec. 18, 1995; final revision, Aug. 20, 1996. Associate Technical Editor: X. Markenscoff.

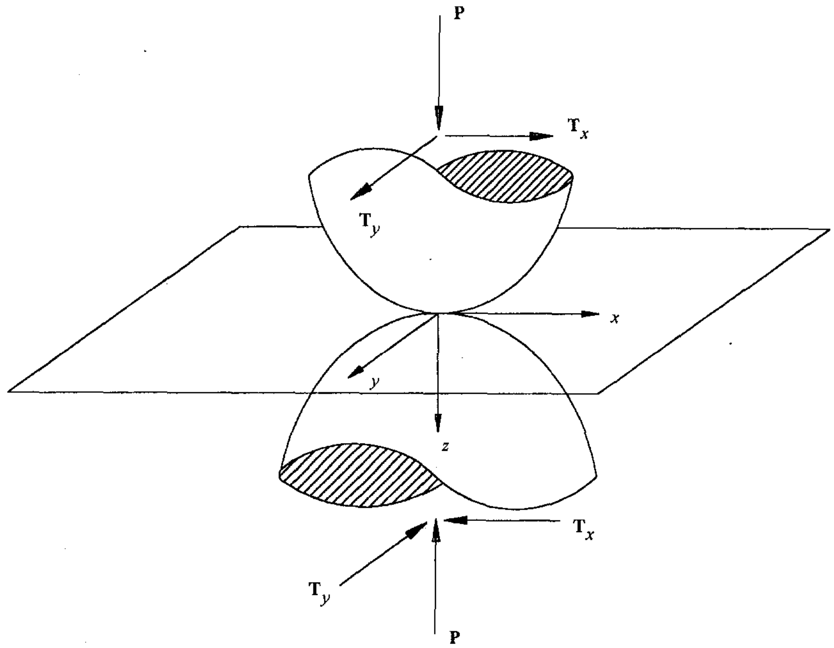

Fig. 1 Normal and tangential loading of two transversely isotropic bodies

evaluation for the partial derivatives of the potential functions are given in Appendix A for normal loading and in Appendix B for sliding traction. Finally, the elastic fields are expressed in terms of incomplete elliptic integrals and elementary functions which contain the Cartesian and ellipsoidal coordinates. Those expressions are given in Section 4 for normal loading and in Section 6 for sliding traction.

From the solution derived here it can be shown that the limiting form to a circular contact area will give the known results (Hanson, 1992). Using the limiting form of the expressions for isotropy (Appendix A in Hanson, 1993), it can also be shown that the present results will analytically agree with the Bryant and Keer (1983) solutions.

2 The Boundary Value Problem

Consider the state of stress when two identically curved transversely isotropic bodies are pressed together by a normal load and then a tangential force is applied as shown in Fig. 1. Here we note that the x and y coordinates are aligned with the principle directions of curvature. The radius of curvature being larger in the x direction. The dimensions of the contact area are considered to be sufficiently small compared with those of the contacting bodies. Assuming the simplifications introduced by Hertz (1882) and Mindlin (1949) we require the solution to the problem of an elastic half-space with the contact pressure and traction applied within an elliptical region Ω. Using Coulomb friction, the boundary conditions on the surface $z = 0$ for the half-space $z > 0$ (lower body) can be written as

$$\sigma_{zz} = -p_0 \sqrt{1 - \frac{x^2}{a^2} - \frac{y^2}{a^2(1-e^2)}}\,;$$
$$\tau_{xz} = f_x\sigma_{zz}; \quad \tau_{yz} = f_y\sigma_{zz}, \qquad (1)$$

for $x^2/a^2 + y^2/b^2 \le 1$. All surface tractions outside the elliptical contact area are zero. Here p_0 is the maximum Hertzian contact stress; f_x and f_y are the coefficients of friction in the x and y directions; $e^2 = 1 - (b/a)^2$, where a is the length of the major axis oriented along the x direction, and b is the length of the minor axis in the y direction as shown in Fig. 2.

The objective of this analysis is to obtain the expressions for the elastic field in the body $z > 0$. For this it is useful if the elliptical coordinate system (ξ, ζ, η) is used. These elliptic coordinates are determined as the roots of the polynomial equation in s given by

$$\frac{x^2}{a^2s^2} + \frac{y^2}{a^2(s^2-e^2)} + \frac{z^2}{a^2(s^2-1)} - 1 = 0, \qquad (2)$$

where $1 \le \xi^2 < \infty$, $e^2 \le \zeta^2 \le 1$, $0 \le \eta^2 \le e^2$. Note that when ξ = constant, the three confocal surfaces which pass through every point of space is an ellipsoid. The ellipsoid corresponding to $\xi = 1$ degenerates into an elliptic disc in the plane $z = 0$ with semi-axis a and $b = a\sqrt{1-e^2}$ (Galin, 1961). The differential relations between the parameter ξ and the Cartesian system can be written as

$$\frac{\partial\xi}{\partial x} = \frac{x}{\xi^3\mathbf{D}^2}, \quad \frac{\partial\xi}{\partial y} = \frac{y}{\xi(\xi^2-e^2)\mathbf{D}^2}, \quad \frac{\partial\xi}{\partial z} = \frac{z}{\xi(\xi^2-1)\mathbf{D}^2},$$
$$\mathbf{D}^2 = \frac{x^2}{\xi^4} + \frac{y^2}{(\xi^2-e^2)^2} + \frac{z^2}{(\xi^2-1)^2}$$
$$= a^2\frac{(\xi^2-\zeta^2)(\xi^2-\eta^2)}{\xi^2(\xi^2-e^2)(\xi^2-1)}. \qquad (3)$$

These relations will be needed for evaluation of the partial derivatives of the potential functions.

3 Potentials for Transverse Isotropy

Consider the transversely isotropic half-space region $z > 0$ where the surface $z = 0$ is parallel to the plane of isotropy. Using cylindrical coordinates, a point force is applied on the surface $z = 0$ at ρ_0, ϕ_0 with components T_x, T_y, and P in the x, y, and z directions as shown in Fig. 3. The potential functions for these fundamental point force solutions were given by Fabrikant (1989). For the point normal force P the potentials are

$$F_j(\rho, \phi, z; \rho_0, \phi_0) = \frac{H\gamma_j}{(m_j-1)} P \ln(R_j + z_j), \quad j = 1, 2,$$
$$F_3(\rho, \phi, z; \rho_0, \phi_0) = 0,$$
$$R_j^2 = \rho^2 + \rho_0^2 - 2\rho\rho_0\cos(\phi-\phi_0) + z_j^2, \quad z_j = \frac{z}{\gamma_j},$$
$$j = 1, 2, 3, \quad (4)$$

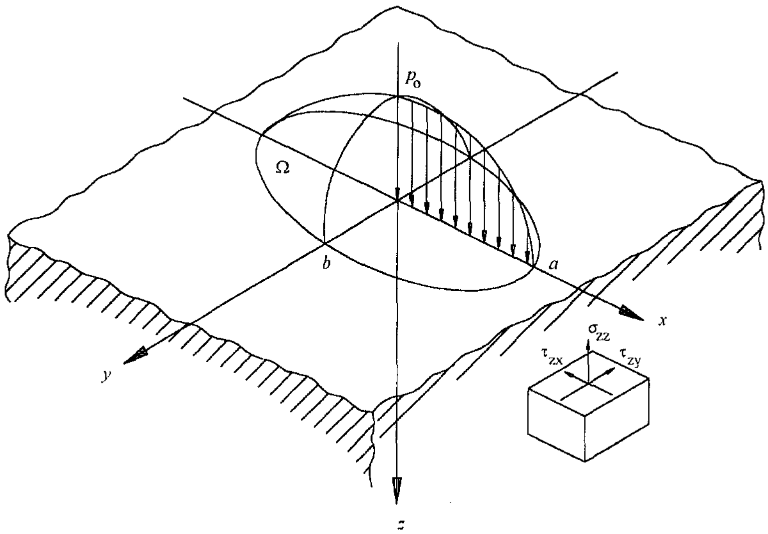

Fig. 2 Ellipsoidal variation of normal traction

where H, m_1, m_2, and γ_j are material parameters related to the five elastic constants A_{11}, A_{13}, A_{33}, A_{44}, and A_{66} (see Fabrikant, 1989). The potentials for concentrated shear loading are given as

$$F_1(\rho, \phi, z; \rho_0, \phi_0) = \frac{H\gamma_1}{(m_1 - 1)} \frac{\gamma_2}{2} (T\bar{\Lambda} + \bar{T}\Lambda)\chi(z_1),$$

$$F_2(\rho, \phi, z; \rho_0, \phi_0) = \frac{H\gamma_2}{(m_2 - 1)} \frac{\gamma_1}{2} (T\bar{\Lambda} + \bar{T}\Lambda)\chi(z_2),$$

$$F_3(\rho, \phi, z; \rho_0, \phi_0) = \frac{i\gamma_3}{4\pi A_{44}} (T\bar{\Lambda} - \bar{T}\Lambda)\chi(z_3), \quad (5)$$

where $T = T_x + iT_y$ is the complex shear force, an overbar indicates complex conjugation and the function $\chi(z_j)$ is defined as

$$\chi(z_j) = z_j \ln (R_j + z_j) - R_j, \quad j = 1, 2, 3. \quad (6)$$

The elastic displacements are denoted by $u^c = u + iv$ and w in the x, y, and z directions and $\sigma_1 = \sigma_{xx} + \sigma_{yy}$, $\sigma_2 = \sigma_{xx} - \sigma_{yy} + 2i\tau_{xy}$, and $\tau_z = \tau_{xz} + i\tau_{yz}$ are the stress components (see Fabrikant, 1989). Furthermore the differential operators Λ, Λ^2, Λ^3, and Δ are defined as

$$\Lambda = \frac{\partial}{\partial x} + i\frac{\partial}{\partial y}, \quad \Lambda^2 = \frac{\partial^2}{\partial x^2} - \frac{\partial^2}{\partial y^2} + i2\frac{\partial^2}{\partial x \partial y},$$

$$\Lambda^3 = \left(\frac{\partial^3}{\partial x^3} - 3\frac{\partial^3}{\partial x \partial y^2}\right) + i\left(3\frac{\partial^3}{\partial x^2 \partial y} - \frac{\partial^3}{\partial y^3}\right),$$

$$\Delta = \Lambda\bar{\Lambda} = \frac{\partial^2}{\partial x^2} + \frac{\partial^2}{\partial y^2}. \quad (7)$$

4 The Elastic Field for Normal Loading

Consider a half-space with the surface being free of shear stress and a normal contact pressure is applied within an elliptical region. The potential functions can be obtained by replacing the force P in Eq. (4) with $f_c(\rho_0, \phi_0)\rho_0 d\rho_0 d\phi_0$ and integrating the result over the elliptical contact area Ω. Here $f_c(\rho_0, \phi_0)$ is the elliptical Hertzian contact stress. The potential functions become

$$F_j(\rho, \phi, z) = \frac{p_0 H\gamma_j}{(m_j - 1)} \psi(\rho, \phi, z_j), \quad j = 1, 2,$$

$$F_3(\rho, \phi, z) = 0,$$

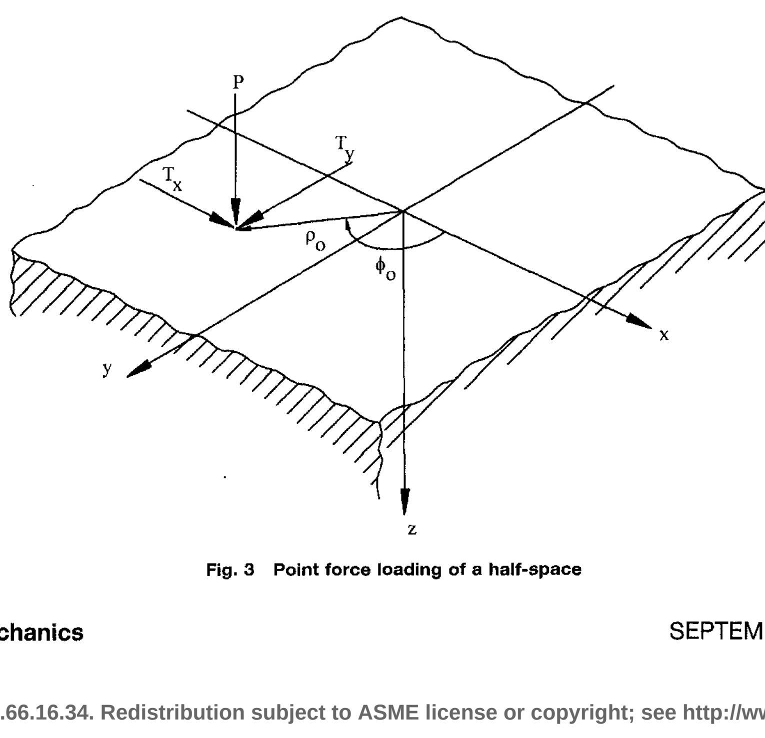

Fig. 3 Point force loading of a half-space

$$\psi(\rho, \phi, z) = \int_0^{2\pi} \int_0^{C(\phi_0)} \tilde{f}_c(\rho_0, \phi_0) \ln(R + z)\rho_0 d\rho_0 d\phi_0,$$

$$R^2 = \rho^2 + \rho_0^2 - 2\rho\rho_0 \cos(\phi - \phi_0) + z^2, \quad (8)$$

where p_0 is the maximum Hertz pressure and $\tilde{f}_c(\rho_0, \phi_0)$ is the nondimensional pressure variation given as

$$\tilde{f}_c(\rho_0, \phi_0) = \left\{1 - \frac{\rho_0^2 \cos^2\phi_0}{a^2} - \frac{\rho_0^2 \sin^2\phi_0}{a^2(1-e^2)}\right\}^{1/2}. \quad (9)$$

Here $C(\phi_0)$ is the boundary of the contact region Ω.

To determine the elastic field the partial derivatives of the potential functions (8) are needed. Using Luré's (1964) analysis, the first partial derivative with respect to z can be written in a single integral form as

$$\frac{\partial\psi(\rho, \phi, z)}{\partial z} = \pi a(1-e^2)^{1/2} \int_\xi^\infty \frac{d\lambda}{\Delta(\lambda)} \times \left\{1 - \frac{x^2}{a^2\lambda^2} - \frac{y^2}{a^2(\lambda^2 - e^2)} - \frac{z^2}{a^2(\lambda^2-1)}\right\}, \quad (10)$$

where $\Delta(\lambda) = \{(\lambda^2 - e^2)(\lambda^2 - 1)\}^{1/2}$. The evaluation of this integral and the other derivatives needed for the elastic field are given in Appendix A. Using those results the expressions for the elastic field are as follows:

$$u^c = -\frac{2\pi H p_0}{a}(1-e^2)^{1/2} \sum_{j=1}^{2} \frac{\gamma_j}{(m_j - 1)} \times \{x[z_j\psi_1(\xi_j) - aI_{11}] + iy[z_j\psi_2(\xi_j) - aI_{12}]\},$$

$$w = \frac{\pi H p_0}{a}(1-e^2)^{1/2} \sum_{j=1}^{2} \frac{m_j}{(m_j-1)} \times \{a^2\mathbf{F}(\varphi_j, e) - x^2\psi_1(\xi_j) - y^2\psi_2(\xi_j) - z_j^2\psi_3(\xi_j)\},$$

$$\sigma_1 = -4\pi A_{66} H p_0 (1-e^2)^{1/2} \sum_{j=1}^{2} \frac{\{\gamma_j^2 - (1+m_j)\gamma_3^2\}}{\gamma_j(m_j-1)} \frac{z_j}{a}\psi_3(\xi_j),$$

$$\sigma_{zz} = \frac{p_0(1-e^2)^{1/2}}{a(\gamma_1 - \gamma_2)} \sum_{j=1}^{2} (-1)^j \gamma_j z_j \psi_3(\xi_j),$$

$$\sigma_2 = -\frac{4\pi A_{66} H p_0}{a^2}(1-e^2)^{1/2} \sum_{j=1}^{2} \frac{\gamma_j}{(m_j-1)} \times \{a z_j[\psi_1(\xi_j) - \psi_2(\xi_j)] + x^2 I_8 - y^2 I_3 + a^2(I_{12} - I_{11}) + i2xyI_4\},$$

$$\tau_z = \frac{p_0(1-e^2)^{1/2}}{a(\gamma_1 - \gamma_2)} \sum_{j=1}^{2} (-1)^j \{x\psi_1(\xi_j) + iy\psi_2(\xi_j)\}. \quad (11)$$

5 Elastic Contact Parameters

On the surface $z = 0$, when the coordinate ξ and ζ equal one, the polynomial in Eq. (2) becomes an ellipse E_0 with semi-axes a and $a(1-e^2)^{1/2}$

$$\frac{x^2}{a^2} + \frac{y^2}{a^2(1-e^2)} - 1 = 0 \quad (E_0). \quad (12)$$

It was noted before that on the surface $z = 0$, the ellipsoid ξ = constant degenerates for $\xi = 1$ into an elliptic disk bounded by E_0 on which $\zeta = 1$. Thus the contact area is an elliptic disk bounded by an ellipse E_0. The surface $\zeta = 1$ represents the part of the plane $z = 0$ outside the ellipse E_0 (Luré, 1964).

Let the two contacting bodies be denoted by 1 and 2. The z-axis (z_1 and z_2 for body 1 and 2) is affixed to each body with the positive direction pointing inward and starting from the initial point of contact. If the normal surface displacement in the z direction for each body is denoted as w_1 and w_2, the following relation holds in the region of contact (Timoshenko and Goodier, 1951)

$$w_1 + w_2 = \alpha - Ax^2 - By^2, \quad (13)$$

where α is the relative approach. A and B are constants depending on the magnitudes of the principal curvatures of the two surfaces in contact and on the angle between the planes of principal curvatures of the two surfaces. If the axis of the principal curvature of each surface are inclined to each other by an angle ω, then A and B are determined from the equations

$$A + B = \frac{1}{2}\left\{\frac{1}{R_1} + \frac{1}{R_1'} + \frac{1}{R_2} + \frac{1}{R_2'}\right\},$$

$$B - A = \frac{1}{2}\left\{\left(\frac{1}{R_1} - \frac{1}{R_1'}\right)^2 + \left(\frac{1}{R_2} - \frac{1}{R_2'}\right)^2 + 2\left(\frac{1}{R_1} - \frac{1}{R_1'}\right)\left(\frac{1}{R_2} - \frac{1}{R_2'}\right)\cos 2\omega\right\}^{1/2}, \quad (14)$$

where R_1 and R_1' denote the principal radii of curvature at the point of contact for body 1 and R_2, R_2' for body 2.

To obtained the displacement in the contact area we need to evaluate the functions ψ_1, ψ_2, and ψ_3 as $z \to 0$ and $\xi = 1$. Noting that when $z \to 0$, $z_j \to 0$ as well, it can be verified that ψ_1, ψ_2 can be expressed in terms of complete elliptic integrals of the first and second kind as

$$\psi_1(1) = \frac{1}{e^2}\{\mathbf{F}(e) - \mathbf{E}(e)\} = \mathbf{D}(e),$$

$$\psi_2(1) = \frac{1}{e^2(1-e^2)}\{\mathbf{E}(e) - (1-e^2)\mathbf{F}(e)\} = \frac{\mathbf{B}(e)}{(1-e^2)}. \quad (15)$$

From Eq. (A16), it is seen that when $\xi \to 1$, ψ_3 tends to infinity. However, the displacements and stresses are bounded along the contact surface because in the expressions for the elastic field this function is either multiplied by z_j or z_j^2 which tend to zero. This limit can be evaluated using Eq. (A14), and it is readily apparent that

$$\lim_{\substack{z_j \to 0 \\ \xi_j \to 1}} z_j^2 \psi_3(\xi_j) = 0,$$

$$\lim_{\substack{z_j \to 0 \\ \xi_j \to 1}} z_j \psi_3(\xi_j) = \frac{a}{(1-e^2)^{1/2}}\left\{1 - \frac{x^2}{a^2} - \frac{y^2}{a^2(1-e^2)}\right\}^{1/2}. \quad (16)$$

Using the above analysis the normal displacements inside the contact region for each body can be found as

$$w_1 = \frac{\pi H_1 p_0}{a}(1-e^2)^{1/2} \times \left\{a^2\mathbf{F}(e) - x^2\mathbf{D}(e) - \frac{y^2}{(1-e^2)}\mathbf{B}(e)\right\},$$

$$w_2 = \frac{\pi H_2 p_0}{a}(1-e^2)^{1/2} \times \left\{a^2\mathbf{F}(e) - x^2\mathbf{D}(e) - \frac{y^2}{(1-e^2)}\mathbf{B}(e)\right\}, \quad (17)$$

where H_1 and H_2 are material parameters for each body, while $\mathbf{B}(e)$ and $\mathbf{D}(e)$ are defined in Eq. (15). Substitution of Eq. (17)

into (13) provides the relative approach and the relations for the constants A and B as

$$\alpha = \pi b p_0 (H_1 + H_2) \mathbf{F}(e),$$

$$A = \pi p_0 (H_1 + H_2) \frac{b}{a^2 e^2} \{\mathbf{F}(e) - \mathbf{E}(e)\},$$

$$B = \pi p_0 (H_1 + H_2) \frac{1}{b e^2} \{\mathbf{E}(e) - (1 - e^2)\mathbf{F}(e)\}, \quad (18)$$

where $b = a(1 - e^2)^{1/2}$.

To find the shape and size of the contact ellipse, one can first determine the axial ratio (b/a) which can be found numerically from the equation given next,

$$\frac{B}{A} = \frac{(b/a)^{-2}\mathbf{E}(e) - \mathbf{F}(e)}{\{\mathbf{F}(e) - \mathbf{E}(e)\}},$$

$$e = \left(1 - \frac{b^2}{a^2}\right)^{1/2}, \quad b \le a. \quad (19)$$

The major semi-axis a of the ellipse of contact may then be obtained from Eq. (18)

$$a^3 = \frac{3P(H_1 + H_2)}{2(b/a)^2 (B + A)} \mathbf{E}(e), \quad (20)$$

where P is the total contact force given by $P = (\frac{2}{3}) a b p_0$. In the isotropic limit $H_1 = (1 - \nu_1^2)/(\pi E_1)$, $H_2 = (1 - \nu_2^2)/(\pi E_2)$ and the results in Dyson (1965) and Johnson (1985) are recovered.

The solution method to obtain the contact dimensions from Eqs. (19) and (20) can be accomplished by a numerical procedure. Dyson (1965) has produced an approximate empirical analytical expression in terms of the ratio (A/B) to replace the elliptic integrals in Eq. (19). An iterative procedure was published by Hamrock et al. (1974) to obtain the contact dimensions. Brewe et al. (1977) introduced a linear regression by the method of least squares to solve for the contact dimensions. Instead of using a numerical procedure, a solution method with the aid of charts can also be used. Those methods can be found in the available literature (Jones, 1946; Harris, 1966; Walowitt and Anno, 1975; Thimoshenko and Goodier, 1970; Roark and Young 1975).

6 The Elastic Field for Shear Loading

Now consider the half-space as free of normal stress and a shear contact stress is applied within the elliptical region Ω. Assuming Coulomb friction, the distribution of the shear stress inside the contact region Ω is proportional to the contact pressure. The magnitude of the maximum shear contact stress now becomes $f p_0$. Here $f = f_x + i f_y$ is the complex coefficient of friction. The three potential functions can be obtained by replacing the complex force T in Eq. (5) with $f p_0 \tilde{f}_c(\rho_0, \phi_0) \rho_0 d\rho_0 d\phi_0$ and integrating the result over the elliptical contact area Ω. The potential functions for this problem can be written as

$$F_1(\rho, \phi, z) = \frac{H\gamma_1\gamma_2 p_0}{2(m_1 - 1)} (f\bar{\Lambda} + \bar{f}\Lambda)\chi(\rho, \phi, z_1),$$

$$F_2(\rho, \phi, z) = \frac{H\gamma_1\gamma_2 p_0}{2(m_2 - 1)} (f\bar{\Lambda} + \bar{f}\Lambda)\chi(\rho, \phi, z_2),$$

$$F_3(\rho, \phi, z) = \frac{i\gamma_3 p_0}{4\pi A_{44}} (f\bar{\Lambda} - \bar{f}\Lambda)\chi(\rho, \phi, z_3), \quad (21)$$

where

$$\chi(\rho, \phi, z) = z\psi(\rho, \phi, z) - \Phi(\rho, \phi, z),$$

$$\Phi(\rho, \phi, z) = \int_0^{2\pi} \int_0^{C(\phi_0)} \left\{1 - \frac{\rho_0^2 \cos^2\phi_0}{a^2} - \frac{\rho_0^2 \sin^2\phi_0}{a^2(1 - e^2)}\right\}^{1/2} R\rho_0 d\rho_0 d\phi_0. \quad (22)$$

It is important to point out that the derivative of $\Phi(\rho, \phi, z)$ is related to the potential function for normal loading by the equation

$$\frac{\partial\Phi(\rho, \phi, z)}{\partial z} = z \frac{\partial\psi(\rho, \phi, z)}{\partial z}. \quad (23)$$

It is also true that $\chi(\rho, \phi, z)$ is the integral of $\psi(\rho, \phi, z)$ with respect to z, so one may write the first partial derivative with respect to z as

$$\frac{\partial\chi(\rho, \phi, z)}{\partial z} = \frac{\partial}{\partial z}\{z\psi(\rho, \phi, z) - \Phi(\rho, \phi, z)\} = \psi(\rho, \phi, z). \quad (24)$$

To determine the expressions for the subsurface displacements and stresses, the partial derivatives for the potential functions in Eq. (21) must be found. Their evaluation are given in Appendix B. Using these results the expressions for the elastic field can be written as

$$\begin{aligned}
u^c = {} & \frac{\pi H\gamma_1\gamma_2 p_0 (1 - e^2)^{1/2}}{2a^2} \sum_{j=1}^{2} \frac{1}{(m_j - 1)} \\
& \times \{-fa[a^2\mathbf{F}(\varphi_j, e) - x^2\psi_1(\xi_j) - y^2\psi_2(\xi_j) - z_j^2\psi_3(\xi_j)] \\
& + \bar{f}[a(a^2 - z_j^2)\psi_1(\xi_j) + a[z_j^2 - a^2(1 - e^2)]\psi_2(\xi_j) \\
& - 3ay^2 I_1 + a(y^2 - x^2)I_2 + 2y^2 z_j I_3 - 2x^2 z_j I_8 + 3ax^2 I_9 \\
& + 2a^2 z_j (I_{11} - I_{12}) + i4xy(aI_2 - z_j I_4)]\} \\
& - \frac{\gamma_3 p_0 (1 - e^2)^{1/2}}{4a^2 A_{44}} \{-fa[a^2\mathbf{F}(\varphi_3, e) - x^2\psi_1(\xi_3) \\
& - y^2\psi_2(\xi_3) - z_\xi^2\psi_3(\xi_3)] - \bar{f}[a(a^2 - z_3^2)\psi_1(\xi_3) \\
& + a[z_3^2 - a^2(1 - e^2)]\psi_2(\xi_3) - 3ay^2 I_1 \\
& + a(y^2 - x^2)I_2 + 2y^2 z_3 I_3 - 2x^2 z_3 I_8 + 3ax^2 I_9 \\
& + 2a^2 z_3 (I_{11} - I_{12}) + i4xy(aI_2 - z_3 I_4)]\},
\end{aligned}$$

$$w = -\frac{2\pi H\gamma_1\gamma_2 p_0}{a} (1 - e^2)^{1/2} \sum_{j=1}^{2} \frac{m_j}{(m_j - 1)\gamma_j} \times \{x f_x [z_j\psi_1(\xi_j) - aI_{11}] + y f_y [z_j\psi_2(\xi_j) - aI_{12}]\},$$

$$\sigma_1 = \frac{4\pi H A_{66}\gamma_1\gamma_2 p_0}{a} (1 - e^2)^{1/2} \sum_{j=1}^{2} \frac{\{\gamma_j^2 - (1 + m_j)\gamma_3^2\}}{\gamma_j^2 (m_j - 1)} \times \{x f_x \psi_1(\xi_j) + y f_y \psi_2(\xi_j)\},$$

$$\sigma_{zz} = \frac{\gamma_1\gamma_2 p_0}{a(\gamma_1 - \gamma_2)} (1 - e^2)^{1/2} \sum_{j=1}^{2} (-1)^{j+1} \times \{x f_x \psi_1(\xi_j) + y f_y \psi_2(\xi_j)\},$$

$$\sigma_2 = \frac{2\pi A_{66} H\gamma_1\gamma_2 p_0}{a^2} (1 - e^2)^{1/2} \sum_{j=1}^{2} \frac{1}{(m_j - 1)}$$

$$\times \left\{ fa[x\psi_1(\xi_j) + iy\psi_2(\xi_j)] \right.$$

$$+ \bar{f} \left[\frac{x}{a} \{ 3a^2(I_9 - I_2) + 3az_j(I_4 - I_8) - x^2 I_{10} + 3y^2 I_6 \} \right.$$

$$\left.\left. + i \frac{y}{a} \{ 3a^2(I_2 - I_1) + 3az_j(I_3 - I_4) - 3x^2 I_7 + y^2 I_5 \} \right] \right\}$$

$$- \frac{p_0(1 - e^2)^{1/2}}{a^2 \gamma_3} \left\{ fa[x\psi_1(\xi_3) + iy\psi_2(\xi_3)] \right.$$

$$- \bar{f} \left[\frac{x}{a} \{ 3a^2(I_9 - I_2) + 3az_3(I_4 - I_8) - x^2 I_{10} + 3y^2 I_6 \} \right.$$

$$\left.\left. + i \frac{y}{a} \{ 3a^2(I_2 - I_1) + 3az_3(I_3 - I_4) - 3x^2 I_7 + y^2 I_5 \} \right] \right\},$$

$$\tau_z = \frac{\gamma_1 \gamma_2 p_0 (1 - e^2)^{1/2}}{2a^2(\gamma_1 - \gamma_2)} \sum_{j=1}^{2} \frac{(-1)^{j+1}}{\gamma_j}$$
$$\times \{ faz_j \psi_3(\xi_j) - \bar{f}[az_j \{ \psi_1(\xi_j) - \psi_2(\xi_j) \}$$
$$- a^2(I_{11} - I_{12}) + x^2 I_8 - y^2 I_3 + i2xyI_4] \}$$
$$- \frac{p_0}{2a^2}(1 - e^2)^{1/2} \{ faz_3 \psi_3(\xi_3)$$
$$+ \bar{f}[az_3 \{ \psi_1(\xi_3) - \psi_2(\xi_3) \}$$
$$- a^2(I_{11} - I_{12}) + x^2 I_8 - y^2 I_3 + i2xyI_4] \}. \quad (25)$$

7 Discussions

The present analysis has derived the elastic field in a transversely isotropic half-space loaded by an ellipsoidal distribution of normal or shear traction. The present results for transverse isotropy appear to be new while the problem has been solved previously in two different forms for an isotropic material.

One solution has been presented by Bryant and Keer (1982). The method used presently to evaluate the derivatives of the potential functions was analogous to that used by them. Hence all of the functions used in the present paper are consistent with the ones defined in their paper. It is noted here that the results in Bryant and Keer (1982) provided the elastic field but the individual derivatives of the potential functions were not included as they are presently in Appendix A and B. By using a limiting form of the transversely isotropic elastic field, the isotropic results can also be obtained from the present expressions. The limiting forms of the double sums for normal and shear loading are presented in Hanson and Johnson (1993). Using this limiting procedure the present analytical results provide an isotropic elastic field in agreement with Bryant and Keer (1982). Here it is noted that Eq. (10*b*) of their paper has a misprint in the expression for the stress σ_y^y. The last term in this expression should be divided by ρ^4 to make it correct and consistent with Bryant (1981).

A solution for isotropy in a different form has also been provided by Sackfield and Hills (1983a, 1983b, 1983c, 1993). The present authors have not made an analytical comparison between these two different isotropic solutions; however, a numerical analysis showed that they produced identical results.

Acknowledgment

It is gratefully acknowledged that support during the course of this research was received from the National Science Foundation under grant No. MSS-9210531.

References

Bryant, M. D., and Keer, L. M., 1982, "Rough Contact Between Elastically and Geometrically Identical Curved Bodies," ASME JOURNAL OF APPLIED MECHANICS, Vol. 49, pp. 345–352.

Bryant, M. D., 1981, "Some Aspects of Elastic Bodies in Contact," Doctoral Dissertation, Northwestern University.

Brewe, D. E., and Hamrock, B. J., 1977, "Simplified Solution for Elliptical-Contact Deformation Between two Elastic Solids," ASME *Journal of Lubrication Technology*, Vol. 99, pp. 485–487.

Cattaneo, C., 1938, "Sul Contatto di Due Corpi Elasticy: Distribuzione Locale Degli Storzi," *Rendiconti dell Accademia Nazionale dei Lincei*, Vol. 27, Series b, pp. 342–348; 434–436; 474–478.

Chen, W. T., 1969, "Stresses in Some Anisotropic Bodies Due to Indentation and Sliding," *Int. J. of Solid Structures*, Vol. 5., pp. 191–214.

Dahan, M., and Zarka, J., 1977, "Elastic Contact Between a Sphere and a Semi Infinite Transversely Isotropic Body," *Int. J. of Solid Structures*, Vol. 13., pp. 229–238.

Dyson, A., 1965, "Approximate Calculations of Hertzian Compressive Stresses and Contact Dimensions," *Journal of Mechanical Engineering Sciences*, Vol. 7 No. 2, pp. 224–227.

Elliot, H. A., 1948, "Three-Dimensional Stress Distributions in Hexagonal Aeolotropic Crystals," *Proceedings of the Cambridge Philosophical Society*, Vol. 44, pp. 522–533.

Fabrikant, V. I., 1989, *Applications of Potential Theory in Mechanics: A Selection of New Results*, Kluwer, The Netherlands.

Galin, L. A., 1961, *Contact Problems in the Theory of Elasticity* (Translated by H. Moss), North Carolina State College.

Gladwell, G. M. L., 1980, *Contact Problems in the Classical Theory of Elasticity*, Sijthoff & Noordhoff, The Netherlands.

Haines, D. J., and Ollerton, E., 1963, "Contact Stress Distributions on Elliptical Contact Surfaces Subjected to Radial and Tangential Forces," *Proc. Instn. Mech. Engrs.*, Vol. 177, pp. 95–114.

Hamilton, G. M., and Goodman, L. E., 1966, "The Stress Field Created by a Circular Sliding Contact," ASME JOURNAL OF APPLIED MECHANICS, Vol. 33, pp. 371–376.

Hamilton, G. M., 1983, "Explicit Equations for the Stress Beneath a Sliding Spherical Contact," *Proc. Instn. Mech. Engr.*, Vol. 197, pp. 53–59.

Hamrock, B. J., and Dowson, D., 1974, "Numerical Evaluation of the Surface Deformation of Elastic Solids Subjected to a Hertzian Contact Stress," NASA TN D-7774.

Hanson, M. T., 1992, "The Elastic Field for Spherical Hertzian Contact Including Sliding Friction for Transverse Isotropy," ASME *Journal of Tribology*, Vol. 114, pp. 606–611.

Hanson, M. T., and Johnson, T., 1993, "The Elastic Field for Spherical Hertzian Contact of Isotropic Bodies Revisited: Some Alternative Expressions," ASME *Journal of Tribology*, Vol. 115, pp. 327–332.

Harris, T. A., 1966, *Rolling Bearing Analysis*, John Wiley and Sons, New York.

Hertz, H., 1882, "Uber die Beruhrung Fester Elasticher Korper," *J.f.d. Reine u. Angewandte Math.*, Vol. 92, pp. 156–171.

Hills, D. A., Nowell, D., and Sackfield, A., 1993, *Mechanics of Elastic Contacts*, Butterworth-Heinemann, in press.

Huber, M. T., 1904, "Zur Theorie der Beruhung Fester Elastischer Korper," *Annalen der Physik*, Leipzig, Germany, Vol. 14, pp. 153–163.

Johnson, K. L., 1985, *Contact Mechanics*, Cambridge University Press, Cambridge, UK.

Jones, A. B., 1946, "Analysis of Stress and Deflections," *New Departure Engineering Data*, Vol. I and II, General Motors, Inc.

Keer, L. M., and Mowry, D. B., 1979, "The Stress Field Created by a Circular Sliding Contact on Transversely Isotropic Spheres," *Int. J. of Solid Structures*, Vol. 15., pp. 33–39.

Luré, A. I., 1964, *Three Dimensional Problems of the Theory of elasticity*, Interscience Publishers, pp. 259–313.

Mindlin, R. D., 1949, "Compliance of Elastic Bodies in Contact," ASME JOURNAL OF APPLIED MECHANICS, Vol. 16, pp. 259–268.

Roark, R. J., and Young, W. C., 1975, *Formula For Stress and Strain*, 5th ed., McGraw-Hill, New York, pp. 516–518.

Sackfield, A., and Hills, D. A., 1983a, "Some Useful Results in the Classical Hertz Contact Problem," *Journal of Strain Analysis*, Vol. 18, pp. 101–105.

Sackfield, A., and Hills, D. A., 1983b, "Some Useful Results in Tangentially Loaded Hertzian Contact Problem," *Journal of Strain Analysis*, Vol. 18, pp. 107–110.

Sackfield, A., and Hills, D. A., 1983c, "A Note on The Hertz Contact Problem: A Correlation of Standard Formulae," *Journal of Strain Analysis*, Vol. 18, pp. 195–197.

Sackfield, A., Hills, D. A., and Nowell, D., 1993, "The Stress Field Induced by a General Elliptical Hertzian," ASME *Journal of Tribology*, Vol. 115, pp. 705–706.

Timoshenko, S., and Goodier, J. N., 1970, *Theory of Elasticity*, 3rd ed., McGraw-Hill, New York, pp. 409–420.

Walowit, J. A., and Anno, J. N., 1975, *Modern Developments in Lubrication Mechanics*, Wiley Applied Science Publishers, pp. 81–84.

APPENDIX A

Partial Derivatives of the Potential Function for Normal Loading

The expression for the harmonic potential function for normal loading is given in Eq. (8) as

$$\psi(\rho, \phi, z) = \int_0^{2\pi} \int_0^{C(\phi_0)} \sqrt{1 - \frac{\rho_0^2 \cos^2 \phi_0}{a^2} - \frac{\rho_0^2 \sin^2 \phi_0}{a^2(1-e^2)}} \times \ln(R+z)\rho_0 d\rho_0 d\phi_0. \quad (A1)$$

The partial derivatives of the potential function are needed to obtained the elastic field. Those derivatives can be evaluated as follows:

$$\frac{\partial\psi(\rho, \phi, z)}{\partial z} = \pi(1-e^2)^{1/2} \times \left\{ a\mathbf{F}(\varphi, e) - \frac{x^2}{a}\psi_1(\xi) - \frac{y^2}{a}\psi_2(\xi) - \frac{z^2}{a}\psi_3(\xi) \right\}, \quad (A2)$$

$$\frac{\partial^2\psi(\rho, \phi, z)}{\partial z^2} = -2\pi \frac{z}{a}(1-e^2)^{1/2}\psi_3(\xi), \quad (A3)$$

$$\frac{\partial^2\psi(\rho, \phi, z)}{\partial x \partial z} = -2\pi \frac{x}{a}(1-e^2)^{1/2}\psi_1(\xi), \quad (A4)$$

$$\frac{\partial^2\psi(\rho, \phi, z)}{\partial y \partial z} = -2\pi \frac{y}{a}(1-e^2)^{1/2}\psi_2(\xi), \quad (A5)$$

$$\frac{\partial\psi(\rho, \phi, z)}{\partial x} = -2\pi \frac{x}{a}(1-e^2)^{1/2}\{z\psi_1(\xi) - aI_{11}\}, \quad (A6)$$

$$\frac{\partial\psi(\rho, \phi, z)}{\partial y} = -2\pi \frac{y}{a}(1-e^2)^{1/2}\{z\psi_2(\xi) - aI_{12}\}, \quad (A7)$$

$$\frac{\partial^2\psi(\rho, \phi, z)}{\partial x^2} = -\frac{2\pi}{a^2}(1-e^2)^{1/2}\{az\psi_1(\xi) - a^2 I_{11} + x^2 I_8\}, \quad (A8)$$

$$\frac{\partial^2\psi(\rho, \phi, z)}{\partial y^2} = -\frac{2\pi}{a^2}(1-e^2)^{1/2}\{az\psi_2(\xi) - a^2 I_{12} + y^2 I_3\}, \quad (A9)$$

$$\frac{\partial^2\psi(\rho, \phi, z)}{\partial x \partial y} = -\frac{2\pi xy}{a^2}(1-e^2)^{1/2} I_4, \quad (A10)$$

$$\Lambda \frac{\partial\psi(\rho, \phi, z)}{\partial z} = -\frac{2\pi}{a}(1-e^2)^{1/2}\{x\psi_1(\xi) + iy\psi_2(\xi)\}, \quad (A11)$$

$$\Lambda\psi(\rho, \phi, z) = -\frac{2\pi}{a}(1-e^2)^{1/2} \times \{x[z\psi_1(\xi) - aI_{11}] + iy[z\psi_2(\xi) - aI_{12}]\}, \quad (A12)$$

$$\Lambda^2\psi(\rho, \phi, z) = -\frac{2\pi}{a^2}(1-e^2)^{1/2}\{az[\psi_1(\xi) - \psi_2(\xi)] - a^2(I_{11} - I_{12}) + x^2 I_8 - y^2 I_3 + i2xyI_4\}, \quad (A13)$$

$$\psi_1(\xi) = \frac{1}{e^2}\{\mathbf{F}(\varphi, e) - \mathbf{E}(\varphi, e)\}, \quad (A14)$$

$$\psi_2(\xi) = \frac{1}{e^2(1-e^2)}\{\mathbf{E}(\varphi, e) - (1-e^2)\mathbf{F}(\varphi, e)\} - \frac{1}{\xi(1-e^2)}\left(\frac{\xi^2-1}{\xi^2-e^2}\right)^{1/2}, \quad (A15)$$

$$\psi_3(\xi) = -\frac{\mathbf{E}(\varphi, e)}{1-e^2} + \frac{1}{\xi(1-e^2)}\left(\frac{\xi^2-e^2}{\xi^2-1}\right)^{1/2}, \quad (A16)$$

$$\mathbf{F}(\varphi, e) = \int_0^{\varphi} \frac{d\theta}{(1-e^2\sin^2\theta)^{1/2}}, \quad (A17)$$

$$\mathbf{E}(\varphi, e) = \int_0^{\varphi} (1-e^2\sin^2\theta)^{1/2} d\theta, \quad (A18)$$

$$\varphi = \sin^{-1}(1/\xi), \quad (A19)$$

$$I_{11} = \frac{1}{2e^2}\left\{ \frac{C}{e^2} J_{14} - \left(\frac{\mathcal{B}}{e^2} + \frac{\mathcal{A}}{2}\right) J_{24} - \Phi_2(\xi, x, y; e) \right\}, \quad (A20)$$

$$I_{12} = \frac{1}{2e^2}\left\{ \frac{\mathcal{B}}{e^2} J_{24} + \left(\frac{B}{2} - \frac{C}{e^2}\right) J_{14} + \Phi_1(\xi, x, y; e) \right\}, \quad (A21)$$

$$I_3 = \begin{cases} \dfrac{1}{2C}\left\{ \Phi_1(\xi, x, y; e) + \dfrac{B}{2} S(\xi, x, y; e) \right\}; & e^2 > 0, y \neq 0 \\ \dfrac{1}{3B}\left\{ -\dfrac{2}{B}\Phi_3(\xi, x; e) + \dfrac{\chi_1(\xi, x; e)}{(\xi^2-e^2)^2} \right\}; & y = 0, x^2 \neq a^2e^2, \\ \dfrac{1}{4(\xi^2-e^2)^2}; & y = 0, x = a^2e^2 \end{cases} \quad (A22)$$

$$I_4 = \frac{1}{2e^2}\{J_{14} - J_{24}\}, \quad (A23)$$

$$I_8 = \begin{cases} \dfrac{1}{2\mathcal{B}}\left\{ \Phi_2(\xi, x, y; e) - \dfrac{\mathcal{A}}{2}\mathcal{L}_0(\xi, x, y) \right\}; & e^2 > 0, x^2 > 0 \\ \dfrac{1}{3\mathcal{A}}\left\{ -\dfrac{2}{\mathcal{A}}\Phi_4(\xi, y; e) + \dfrac{\chi_2(\xi, y; e)}{\xi^4} \right\}; & x = 0, \mathcal{A} < 0 \end{cases}, \quad (A24)$$

$$J_{14} = \begin{cases} -S(\xi, x, y; e); & e^2 > 0, y \neq 0 \\ \dfrac{2}{B}\Phi_3(\xi, x; e); & y = 0, x^2 \neq a^2e^2 \\ \dfrac{1}{\xi^2-e^2}; & y = 0, x^2 = a^2e^2 \end{cases}, \quad (A25)$$

$$J_{24} = \begin{cases} -\mathcal{L}_0(\xi, x, y); & e^2 > 0, x^2 > 0 \\ \dfrac{2}{\mathcal{A}}\Phi_4(\xi, y; e); & x = 0, \mathcal{A} < 0 \end{cases}, \quad (A26)$$

$$S(\xi, x, y; e) = \frac{1}{\sqrt{-C}}\left\{ \sin^{-1}\frac{B(\xi^2-e^2) + 2C}{(\xi^2-e^2)D} - \sin^{-1}\frac{B}{D} \right\}, \quad (A27)$$

$$\mathcal{L}_0(\xi, x, y) = \begin{cases} \dfrac{1}{\sqrt{\mathcal{B}}}\log\dfrac{2\sqrt{\mathcal{B}}\chi_0(\xi, x, y) + 2\mathcal{B} + \xi^2\mathcal{A}}{\xi^2(2\sqrt{\mathcal{B}} + \mathcal{A})} \\ \dfrac{1}{e^2}\log\dfrac{\xi^2-e^2}{\xi^2}; & y = 0, x^2 = a^2e^2 > 0 \end{cases}, \quad (A28)$$

$$B = e^2 - \frac{x^2}{a^2} - \frac{y^2}{a^2},\ C = -e^2\frac{y^2}{a^2},\ D = \sqrt{B^2 - 4C}, \quad \text{(A29)}$$

$$\mathcal{A} = -\left\{e^2 + \frac{x^2}{a^2} + \frac{y^2}{a^2}\right\},\quad \mathcal{B} = e^2\frac{x^2}{a^2}, \quad \text{(A30)}$$

$$\Phi_1(\xi, x, y; e) = \frac{\chi_0(\xi, x, y; e)}{\xi^2 - e^2} - 1,$$

$$\Phi_2(\xi, x, y; e) = \frac{\chi_0(\xi, x, y; e)}{\xi^2} - 1,$$

$$\Phi_3(\xi, x; e) = \frac{\chi_1(\xi, x; e)}{\xi^2 - e^2} - 1,$$

$$\Phi_4(\xi, y; e) = \frac{\chi_2(\xi, y; e)}{\xi^2} - 1, \quad \text{(A31)}$$

$$\chi_0(\xi, x, y; e) = \{\xi^4 + \mathcal{A}\xi^2 + \mathcal{B}\}^{1/2},$$

$$\chi_1(\xi, x; e) = \left\{(\xi^2 - e^2)\left(\xi^2 - \frac{x^2}{a^2}\right)\right\}^{1/2},$$

$$\chi_2(\xi, y; e) = \xi\left\{\xi^2 - e^2 - \frac{y^2}{a^2}\right\}^{1/2}. \quad \text{(A32)}$$

APPENDIX B

Partial Derivatives of the Potential Functions for Shear Loading

The potential function for shear loading is related to the potential function for normal loading by (see Section 6)

$$\chi(\rho, \phi, z) = z\psi(\rho, \phi, z) - \Phi(\rho, \phi, z),$$

$$\frac{\partial\Phi(\rho, \phi, z)}{\partial z} = z\frac{\partial}{\partial z}\psi(\rho, \phi, z). \quad \text{(B1)}$$

To determine the elastic field for shear loading, the partial derivatives of the potential function $\chi(\rho, \phi, z)$ are needed. The complete partial derivatives may be computed as

$$\Lambda\partial\chi(\rho, \phi, z)/\partial z = -\frac{2\pi}{a}(1 - e^2)^{1/2} \times \{x[z\psi_1(\xi) - aI_{11}] + iy[z\psi_2(\xi) - aI_{12}]\}, \quad \text{(B2)}$$

$$\bar{\Lambda}\partial\chi(\rho, \phi, z)/\partial z = -\frac{2\pi}{a}(1 - e^2)^{1/2} \times \{x[z\psi_1(\xi) - aI_{11}] - iy[z\psi_2(\xi) - aI_{12}]\}, \quad \text{(B3)}$$

$$\Lambda\partial^2\chi(\rho, \phi, z)/\partial z^2 = -\frac{2\pi}{a}(1 - e^2)^{1/2}\{x\psi_1(\xi) + iy\psi_2(\xi)\}, \quad \text{(B4)}$$

$$\bar{\Lambda}\partial^2\chi(\rho, \phi, z)/\partial z^2 = -\frac{2\pi}{a}(1 - e^2)^{1/2}\{x\psi_1(\xi) - iy\psi_2(\xi)\}, \quad \text{(B5)}$$

$$\Lambda\bar{\Lambda}\partial\chi(\rho, \phi, z)/\partial z = 2\pi(1 - e^2)^{1/2}\frac{z}{a}\psi_3(\xi), \quad \text{(B6)}$$

$$\Lambda^2\partial\chi(\rho, \phi, z)/\partial z = -\frac{2\pi}{a^2}(1 - e^2)^{1/2}\{az[\psi_1(\xi) - \psi_2(\xi)] - a^2(I_{11} - I_{12}) + x^2I_8 - y^2I_3 + i4xyI_4\}, \quad \text{(B7)}$$

$$\Lambda\bar{\Lambda}\chi(\rho, \phi, z) = -\frac{\pi}{a}(1 - e^2)^{1/2} \times \{a^2\mathbf{F}(\varphi, e) - x^2\psi_1(\xi) - y^2\psi_2(\xi) - z^2\psi_3(\xi)\}, \quad \text{(B8)}$$

$$\Lambda\Delta\chi(\rho, \phi, z) = \frac{2\pi}{a}(1 - e^2)^{1/2}\{x\psi_1(\xi) + iy\psi_2(\xi)\}, \quad \text{(B9)}$$

$$\frac{\partial\Phi(\rho, \phi, z)}{\partial x} = -\frac{\pi x}{a}(1 - e^2)^{1/2}\{z^2\psi_1(\xi) - a^2[\mathbf{F}(\varphi, e) - \psi_1(\xi)] + x^2I_9 + y^2I_2\}, \quad \text{(B10)}$$

$$\frac{\partial^2\Phi(\rho, \phi, z)}{\partial x^2} = -\frac{\pi}{a}(1 - e^2)^{1/2}\{z^2\psi_1(\xi) - a^2[\mathbf{F}(\varphi, e) - \psi_1(\xi)] + 3x^2I_9 + y^2I_2\}, \quad \text{(B11)}$$

$$\frac{\partial\Phi(\rho, \phi, z)}{\partial y} = -\frac{\pi y}{a}(1 - e^2)^{1/2}\left\{z^2\psi_2(\xi) + a^2\left[\frac{\Delta(\xi)}{\xi(\xi^2 - e^2)} - \psi_2(\xi)\right] + x^2I_2 + y^2I_1\right\}, \quad \text{(B12)}$$

$$\frac{\partial^2\Phi(\rho, \phi, z)}{\partial y^2} = -\frac{\pi}{a}(1 - e^2)^{1/2}\left\{z^2\psi_2(\xi) + a^2\left[\frac{\Delta(\xi)}{\xi(\xi^2 - e^2)} - \psi_2(\xi)\right] + x^2I_2 + 3y^2I_1\right\}, \quad \text{(B13)}$$

$$\frac{\partial^2\Phi(\rho, \phi, z)}{\partial x\partial y} = -\frac{\pi xy}{a}(1 - e^2)^{1/2}I_2, \quad \text{(B14)}$$

$$\Lambda^2\chi(\rho, \phi, z) = \frac{\pi}{a^2}(1 - e^2)^{1/2}\{a(a^2 - z^2)\psi_1(\xi) + a[z^2 - a^2(1 - e^2)]\psi_2(\xi) - 3ay^2I_1 + a(y^2 - x^2)I_2 + 2y^2zI_3 - 2x^2zI_8 + 3ax^2I_9 + 2z(I_{11} - I_{12}) + i4xy(aI_2 - zI_4)\}, \quad \text{(B15)}$$

$$\frac{\partial^3\psi(\rho, \phi, z)}{\partial x^3} = -2\pi\frac{x}{a^2}(1 - e^2)^{1/2} \times \left\{3I_8 + \frac{x^2}{az}I_{10} - \frac{x^2(\xi^2 - 1)^{1/2}}{\xi^7\Delta(\xi)\gamma(x, y, \xi)\mathbf{D}^2}\right\}, \quad \text{(B16)}$$

$$\frac{\partial^3\psi(\rho, \phi, z)}{\partial y^3} = -2\pi\frac{y}{a^2}(1 - e^2)^{1/2} \times \left\{3I_3 + \frac{y^2}{az}I_5 - \frac{y^2(\xi^2 - 1)^{1/2}}{\xi(\xi^2 - e^2)^3\Delta(\xi)\gamma(x, y, \xi)\mathbf{D}^2}\right\}, \quad \text{(B17)}$$

$$\frac{\partial^3\psi(\rho, \phi, z)}{\partial x^2\partial y} = -2\pi\frac{y}{a^2}(1 - e^2)^{1/2} \times \left\{I_4 + \frac{x^2}{az}I_7 - \frac{x^2(\xi^2 - 1)^{1/2}}{\xi^5(\xi^2 - e^2)\Delta(\xi)\gamma(x, y, \xi)\mathbf{D}^2}\right\}, \quad \text{(B18)}$$

$$\frac{\partial^3\psi(\rho, \phi, z)}{\partial x\partial y^2} = -2\pi\frac{x}{a^2}(1 - e^2)^{1/2}\left\{I_4 + \frac{y^2}{2az}J_{15} - \frac{y^2(\xi^2 - 1)^{1/2}}{\xi^3(\xi^2 - e^2)^2\Delta(\xi)\gamma(x, y, \xi)\mathbf{D}^2}\right\}, \quad \text{(B19)}$$

$$\frac{\partial^3\Phi(\rho,\phi,z)}{\partial x^3} = -2\pi\frac{x}{a}(1-e^2)^{1/2}\left\{3I_9 - \frac{x^2(\xi^2-1)}{\xi^7\Delta(\xi)\mathbf{D}^2}\right\}, \quad \text{(B20)}$$

$$\frac{\partial^3\Phi(\rho,\phi,z)}{\partial y^3} = -2\pi\frac{y}{a}(1-e^2)^{1/2} \times \left\{3I_1 - \frac{y^2(\xi^2-1)}{\xi(\xi^2-e^2)^3\Delta(\xi)\mathbf{D}^2}\right\}, \quad \text{(B21)}$$

$$\frac{\partial^3\Phi(\rho,\phi,z)}{\partial x^2\partial y} = -2\pi\frac{y}{a}(1-e^2)^{1/2} \times \left\{I_2 - \frac{x^2(\xi^2-1)}{\xi^5(\xi^2-e^2)\Delta(\xi)\mathbf{D}^2}\right\}, \quad \text{(B22)}$$

$$\frac{\partial^3\Phi(\rho,\phi,z)}{\partial x\partial y^2} = -2\pi\frac{x}{a}(1-e^2)^{1/2} \times \left\{I_2 - \frac{y^2(\xi^2-1)}{\xi^3(\xi^2-e^2)^2\Delta(\xi)\mathbf{D}^2}\right\}, \quad \text{(B23)}$$

$$\Lambda^3\chi(\rho,\phi,z) = 2\pi(1-e^2)^{1/2} \times\left[\frac{x}{a}\left\{3I_9 - 3I_2 - \frac{3z}{a}I_8 + \frac{3z}{a}I_4 - \frac{x^2}{a^2}I_{10} + \frac{3y^2}{a^2}I_6\right\} + i\frac{y}{a}\left\{3I_2 - 3I_1 - \frac{3z}{a}I_4 - \frac{3x^2}{a^2}I_7 + \frac{3z}{a}I_3 + \frac{y^2}{a^2}I_5\right\}\right], \quad \text{(B24)}$$

$$I_5 = \tfrac{1}{2}(J_{15} + e^2J_{25}), \quad \text{(B25)}$$

$$I_7 = \begin{cases} \dfrac{z}{a}\left\{\dfrac{1}{\mathcal{B}\mathcal{D}^2}\left[\mathcal{A} - \dfrac{\mathcal{A}\xi^2 - 2\mathcal{B} + \mathcal{A}^2}{\chi_0(\xi,x,y;e)}\right] + \dfrac{\mathcal{L}_0(\xi,x,y)}{2\mathcal{B}}\right\}; & e^2>0,\ x^2>0 \\[2ex] \dfrac{z}{3\mathcal{A}a}\left\{\dfrac{8}{\mathcal{A}^2} - \left[\dfrac{8\xi^2}{\mathcal{A}^2} + \dfrac{4}{\mathcal{A}} - \dfrac{1}{\xi^2}\right]\dfrac{1}{\chi_2(\xi,y;e)}\right\}; & x=0,\ \mathcal{A}<0 \end{cases}, \quad \text{(B26)}$$

$$I_{10} = I_7 - e^2J_{110}, \quad \text{(B27)}$$

$$J_{110} = \begin{cases} \dfrac{z}{2a\mathcal{B}^2}\left\{\dfrac{\mathcal{B}}{\xi^2\chi_0(\xi,x,y;e)} - \dfrac{3\mathcal{A}^2-8\mathcal{B}}{\mathcal{D}^2} + \dfrac{(3\mathcal{A}^2-8\mathcal{B})\xi^2 + (3\mathcal{A}^2-10\mathcal{B})\mathcal{A}}{\mathcal{D}^2\chi_0(\xi,x,y;e)} - \dfrac{3}{2}\mathcal{A}\mathcal{L}_0(\xi,x,y)\right\}; & e^2>0, x^2>0 \\[2ex] \dfrac{z}{5a\mathcal{A}}\left\{\dfrac{1}{\chi_2(\xi,y;e)}\left(\dfrac{16\xi^2}{\mathcal{A}^3} + \dfrac{8}{\mathcal{A}^2} - \dfrac{2}{\mathcal{A}\xi^2} + \dfrac{1}{\xi^4}\right) - \dfrac{16}{\mathcal{A}^3}\right\}; & x=0, \mathcal{A}<0 \end{cases}, \quad \text{(B28)}$$

$$J_{15} = \begin{cases} \dfrac{z}{a}\left\{-\dfrac{2[B(\xi^2-e^2) - 2C + B^2]}{CD^2\chi_0(\xi,x,y;e)} + \dfrac{2B}{CD^2} - \dfrac{1}{C}S(\xi,x,y;e)\right\}; & e^2>0,\ y\neq 0 \\[2ex] \dfrac{2z}{Ba}\left\{\dfrac{8}{3B^2} - \dfrac{1}{3}\left[\dfrac{8(\xi^2-e^2)}{B^2} + \dfrac{4}{B} - \dfrac{1}{(\xi^2-e^2)}\right]\dfrac{1}{\chi_1(\xi,x,e)}\right\}; & y=0,\ x\neq a^2e^2 \\[2ex] \dfrac{z}{3a(\xi^2-e^2)^3}; & y=0,\ x^2=a^2e^2 \end{cases}, \quad \text{(B29)}$$

$$J_{25} = \begin{cases} \dfrac{z}{a}\left\{\dfrac{1}{C\chi_0(\xi,x,y;e)}\left(\dfrac{1}{(\xi^2-e^2)} + \dfrac{(3B^2-8C)(\xi^2-e^2) + (3B^2-10C)B}{CD^2}\right) - \dfrac{3B^2-8C}{C^2D^2} + \dfrac{3B}{2C^2}S(\xi,x,y;e)\right\}; & e^2>0, y\neq 0 \\[2ex] \dfrac{2z}{5aB}\left\{\dfrac{1}{\chi_1(\xi,x;e)}\left(\dfrac{1}{(\xi^2-e^2)^2} - \dfrac{2}{B(\xi^2-e^2)} + \dfrac{8}{B^2} + \dfrac{16(\xi^2-e^2)}{B^3}\right) - \dfrac{16}{B^3}\right\}; & y=0, x^2\neq a^2e^2 \\[2ex] \dfrac{z}{4a(\xi^2-e^2)^4}; & y=0, x^2=a^2e^2 \end{cases} \quad \text{(B30)}$$

$$\Delta(\xi) = [(\xi^2-e^2)(\xi^2-1)]^{1/2}, \quad \text{(B31)}$$

$$\gamma(x,y,\xi) = \left\{1 - \frac{x^2}{a^2\xi^2} - \frac{y^2}{a^2(\xi^2-e^2)}\right\}^{1/2}, \quad \text{(B32)}$$

$$\mathcal{D} = \sqrt{\mathcal{A}^2 - 4\mathcal{B}}. \quad \text{(B33)}$$

S. B. Park

G. P. Carman
Mem. ASME.

Mechanical, Aerospace and
Nuclear Engineering Department,
38-137m Engineering IV,
University of California,
Los Angeles, CA 90024

Minimizing Stress Levels in Piezoelectric Media Containing Elliptical Voids

In this paper we present an analytical solution to calculate the stress concentrations around an elliptical void in a piezoelectric medium subjected to electrical loading. We show that the stress concentrations can be eliminated if the material properties satisfy a certain mathematical relation. While a trivial solution exists for this problem, we demonstrate that other families of solutions exist (optimal) to minimize/eliminate the stresses. The optimal families are shown to be independent of geometry and therefore are universally applicable to a specific material system. The optimal families do not limit the deformation profile and represent admissible solutions to the problem. Numerical studies demonstrate that the entire stress field in the medium vanishes and not just at the critical locations as dictated by the mathematics. Finally, we numerically demonstrate that the optimal properties are also applicable to the crack problem.

Introduction

Piezoelectric ceramics are currently being used in a variety of active material applications. Some of these include reducing vibrations, alleviating flutter, and suppressing noise on aircraft. While these applications suggest that piezoceramics offer considerable benefits, the small displacements provided by the material limits its usefulness. To overcome this limitation, researchers are applying larger electric fields to the piezoceramics with strains an order of magnitude larger than offered in conventional operations. However, these larger strain actuators show considerable degradation during electric fatigue making their usefulness questionable in engineering applications. Therefore, a focused investigation needs to be conducted on understanding the property/structure interactions with the purpose of extending fatigue life.

While a number of experimental reports indicate that electric fatigue degenerates a piezoceramic, some offer conflicting explanations. Carl (1975) reported that microcracks form and grow along grain boundaries leading to the degradation of properties. Pan (1992) reported that fatigue degradation is related to domain pinning issues related to internal defect structures and could be eliminated by repoling the material. However, Jiang (1993) reported that electric fatigue of piezoceramics is related to the porosity of the ceramic with considerable more degradation measured in higher porosity materials. Recently, Wang et al. (1996) reported that significant fatigue degradation occurs in piezoceramics during electric fatigue and is functionally dependent on both the applied electric field and the operating temperature. Wang et al. (1996) also report that property degradation could not be eliminated by repoling the material. While there have been a number of reports on the fatigue process of piezoceramics, all suggest that fatigue mechanisms are related to internal defect structures. The fact that significant stress concentrations arise around internal inhomogenities suggests this is a major contributor to the fatigue process. In fact, Park et al. (1996b) experimentally demonstrated that damage initiates and grows around internal void-like defects. Since internal stresses around these anomalies are dependent upon the piezoelectric material properties, a focused study needs to be implemented on evaluating if optimal properties exist to minimize the local stress concentrations.

In regards to analytical studies related to electrical fatigue, fracture mechanics has been used. Using different approaches, researchers found that stress fields are decoupled with electric fields along the self-similar plane of the crack Parton (1988). That is, in the plane of the crack electric fields do not induce any stress concentration. This implies that stress intensity factors, which are widely used as a measure of fracture toughness (and fatigue life) for nonpiezoelectric materials, are independent of electric field. However, this fact is contradicted by experimental evidence available in the open literature. The total potential energy release rate was also proposed as a fracture criteria (Pak, 1990; Suo, 1992). According to this criterion, all electric fields theoretically retarded crack propagation, a fact contradicted by experiments. More recently the mechanical strain energy release rate was suggested (Park and Sun, 1995a, b) and successfully used to predict the experimentally observed relation between fracture toughness and electric field strength. While all of these studies provide useful information regarding stress concentrations around internal anomalies, they did not attempt to evaluate the property structure interactions with the purpose of finding optimal properties which would eliminate the critical stress fields causing fatigue degradation.

Based on this introduction, electric fatigue of piezoceramics is attributable to the presence of internal defects. Furthermore, most analytical studies investigating this phenomena have focused on evaluating the stress distribution due to defect geometry and not on evaluating property/structure interactions. Therefore, in this paper we present an analytical study to investigate electric field induce stresses around an arbitrary elliptical defect. Using a proposed criteria, we demonstrate that optimal properties exist to eliminate the stress fields around the defect and do not limit the deformation of the piezoceramic. These optimal properties are shown to be independent of defect geometry and are applicable to the crack problem.

Analytic Solution for Defects in a Piezoelectric Medium

Voids or defects present in piezoelectric ceramics may be thought as randomly distributed ellipsoidal shaped cavities (see

Contributed by the Applied Mechanics Division of THE AMERICAN SOCIETY OF MECHANICAL ENGINEERS for publication in the ASME JOURNAL OF APPLIED MECHANICS.

Discussion on this paper should be addressed to the Technical Editor, Professor Lewis T. Wheeler, Department of Mechanical Engineering, University of Houston, Houston, TX 77204-4792, and will be accepted until four months after final publication of the paper itself in the ASME JOURNAL OF APPLIED MECHANICS.

Manuscript received by the ASME Applied Mechanics Division, May 23, 1996; final revision, Nov. 1, 1996. Associate Technical Editor: R. Becker.

Fig. $1(a)$). The specific geometry of the ellipses can vary from a circular hole to a slit-like crack. Since in any given piezoceramic there exists essentially a random distribution of these cavities, it is important to understand the stress concentrations which arise around each. The internal defects can be analytically modeled as two-dimensional hole-like defects (see Fig. $1(b)$) for simplicity. If we wish to physically understand the basic relation between material properties and stress/electric field concentrations, we can assume that interaction effects are second order and thereby reduce the model to a single defect as a first-order approximation (see Fig. $1(c)$).

Following Lekhnitskii's (1981) complex potential formulation for anisotropic plates, Sosa (1991) obtained a closed-form solution for the problem of an elliptical defect embedded in a piezoelectric material. In this section, we briefly summarize the approach and results from the closed-form solution. Following this we present the formulation to predict optimal properties for the various elliptical cavities. Optimal in the current context implies that the electric-field-induced stresses around the cavities are eliminated. Park and Carman (1996a) previously explained the physical existence of optimal properties for circular shaped voids with parametric studies. They attributed the optimal properties to the local stresses generated by two competing physical phenomena related to either the shear strain piezoelectric coefficients or the longitudinal strain piezoelectric coefficients.

Consider a piezoelectric medium which has an elliptical hole at the center. Based on linear piezoelectricity, the constitutive relations can be written as

$$S_{ij} = s^{D}_{ijkl}\sigma_{kl} + g_{kij}D_k, \quad E_i = -g_{ikl}\sigma_{kl} + \beta^{\sigma}_{ikl}D_k \qquad (1)$$

where s^{D}_{ijkl} is the compliance tensor measured at constant electric displacement, g_{kij} is the piezoelectric stress tensor, and β^{σ}_{ik} is the dielectric impermeability tensor measured at constant stress. Although there are several different types of expression for the constitutive relations (Ikeda, 1990), the expression in Eq. (1), called g-form, which has stresses, σ_{kl}, and electric displacements, D_k, as independent variables was chosen to facilitate the development of complex stress potentials.

Equilibrium equations are written as

$$\sigma_{ij,j} = 0, \quad D_{i,i} = 0. \qquad (2)$$

Generally, the x_3-axis is used as the poling direction in the material principal axes, $x_1 - x_2 - x_3$. Most piezoelectric ceramics have a tetragonal structure and are transversely isotropic with the x_3-axis normal to the isotropic plane. For our problem, the $x_1 - x_3$ plane is the working plane and it will be denoted as the $x-y$ plane. By reducing the problem to a two-dimensional plane-strain plane strain case, the following conditions are imposed:

$$S_{22} = S_{32} = S_{12} = E_2 = 0. \qquad (3)$$

With some algebraic manipulations after applying Eq. (3) into Eq. (1), the two-dimensional constitutive relations can be obtained in the following reduced matrix form:

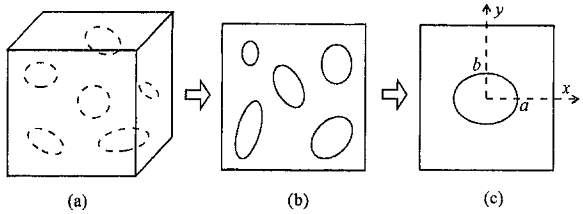

Fig. 1 Modeling of defects: (*a*) three-dimensional defects, (*b*) two-dimensional defects, (*c*) unit cell two-dimensional defect

$$\begin{Bmatrix} S_{xx} \\ S_{yy} \\ S_{xy} \end{Bmatrix} = \begin{bmatrix} a_{11} & a_{12} & 0 \\ a_{12} & a_{22} & 0 \\ 0 & 0 & a_{33} \end{bmatrix} \begin{Bmatrix} \sigma_{xx} \\ \sigma_{yy} \\ \sigma_{xy} \end{Bmatrix} + \begin{bmatrix} 0 & b_{21} \\ 0 & b_{22} \\ b_{13} & 0 \end{bmatrix} \begin{Bmatrix} D_x \\ D_y \end{Bmatrix} \qquad (4)$$

$$\begin{Bmatrix} E_x \\ E_y \end{Bmatrix} = -\begin{bmatrix} 0 & 0 & b_{13} \\ b_{21} & b_{22} & 0 \end{bmatrix} \begin{Bmatrix} \sigma_{xx} \\ \sigma_{yy} \\ \sigma_{xy} \end{Bmatrix} + \begin{bmatrix} \delta_{11} & 0 \\ 0 & \delta_{22} \end{bmatrix} \begin{Bmatrix} D_x \\ D_y \end{Bmatrix}. \qquad (5)$$

The constants of a_{ij}, b_{ij}, and δ_{ij} are reduced stiffness, piezoelectric coefficients, and permittivity values for a plane-strain problem.

The solution for the stress and electric displacement can be expressed as a function of φ_k as follows (Sosa, 1991):

$$\sigma_{xx} = 2\,\mathrm{Re} \sum_{k=1}^{3} \mu_k^2 \varphi_k'(z_k), \quad \sigma_{yy} = 2\,\mathrm{Re} \sum_{k=1}^{3} \varphi_k'(z_k),$$

$$\sigma_{xy} = -2\,\mathrm{Re} \sum_{k=1}^{3} \mu_k \varphi_k'(z_k)$$

$$D_x = 2\,\mathrm{Re} \sum_{k=1}^{3} \lambda_k \mu_k \varphi_k'(z_k), \quad D_y = -2\,\mathrm{Re} \sum_{k=1}^{3} \lambda_k \varphi_k'(z_k). \qquad (6)$$

In the current problem two boundary conditions must be stated. One is the far-field mechanical and electrical loading, and the other is the boundary conditions along the inner surface of the ellipse. Far-field loading can be denoted as

$$\sigma_{xx}^{\infty}, \quad \sigma_{xy}^{\infty}, \quad \sigma_{yy}^{\infty}, \quad D_x^{\infty}, \quad \text{and} \quad D_y^{\infty} \quad \text{at } z = \infty. \qquad (7)$$

The rim of the ellipse is traction free and to a first-order approximation it can be argued that the ellipse is electrically insulated. The validation of the latter boundary condition is justified by the fact that the dielectric permittivity of piezoelectric ceramics is three orders of magnitude higher than that of air or vacuum. Hence, boundary condition along the rim of ellipse, Γ, can be written as

$$\mathbf{t} = \mathbf{0} \quad \text{and} \quad \mathbf{D}\cdot\mathbf{n} = \mathbf{0} \quad \text{on } \Gamma \qquad (8)$$

where $\mathbf{t}$ is the traction vector and $\mathbf{n}$ is the normal vector of elliptical contour Γ. Using the boundary conditions of Eq. (7) with the Eq. (8), the full-field stress distributions can be calculated.

Applying the hole boundary conditions, the complex potential function can be obtained as

$$\varphi_k(z_k) = (UB_k + iB_k^*)z_k + \left(\sum_{j=1}^{3} \Lambda_{kj} l_j\right) \frac{z_k - \sqrt{z_k^2 - (a^2 + b^2\mu_k^2)}}{a + ib\mu_k} \qquad (9)$$

where B_k and B_k^* are real constants which can be determined by applying the far-field boundary conditions in Eq. (7). The l_j in Eq. (9) can be expressed as

$$l_1 = (-a\sigma_{yy}^{\infty} + ib\sigma_{xy}^{\infty})/2, \quad l_2 = (a\sigma_{xy}^{\infty} - ib\sigma_{xx}^{\infty})/2,$$

$$l_3 = (aD_y^{\infty} - ibD_x^{\infty})/2. \qquad (10)$$

Substituting Eq. (9) into Eq. (6), full-field solutions such as stresses and electric displacements can be obtained.

Optimal Properties

In the previous section a general solution for a piezoelectric medium containing an elliptical cavity was presented. In this section we will demonstrate that for a specific set of material constants the electric-field-induced stresses are eliminated in the medium. A trivial solution to this problem is that the piezoelectric coefficients are all zero. However, we will show that another family of solutions exists. For the current loading condition we focus our attention on far-field electrical loading and assume that the far-field mechanical loads are zero. When investigating the stress concentration in the medium related to this form of loading, the y component of the stress, i.e., σ_{yy}, is the pertinent one to study. The full-field σ_{yy} distribution for this loading is presented as follows:

$$\sigma_{yy} = 2 \text{ Re} \sum_{k=1}^{3} \left\{ (B_k + iB_k^*) + (\sum_{l=1}^{3} \Lambda_{kl} l_l) \frac{1}{a + i\mu_k b} \left[1 - \frac{z_k}{\sqrt{z_k^2 - (a^2 + \mu_k^2 b^2)}} \right] \right\} \quad (11)$$

where $z_k = x + \mu_k y$.

The largest stress concentration for this material would be expected to occur at the location $\theta = 0$ on the rim, i.e., $x = a$, $y = 0$. Using $z_k = a$ reduces Eq. (11) to

$$\sigma_{yy} (x = a, y = 0) = 2 \text{ Re} \sum_{k=1}^{3} \left\{ (B_k + iB_k^*) + (\sum_{j=1}^{3} \Lambda_{kj} l_j) \frac{1}{a + i\mu_k b} \left[1 - \frac{a}{b\sqrt{-\mu_k^2}} \right] \right\} \quad (12)$$

where

$$\sum_{k=1}^{3} B_k = \frac{\sigma_{yy}^{\infty}}{2}.$$

After further simplification, we obtain the following form for the stress distribution:

$$\sigma_{yy} (x = a, y = 0) = \sigma_{yy}^{\infty} + 2 \text{ Re} \sum_{k=1}^{3} \left\{ (\sum_{j=1}^{3} \Lambda_{kj} l_j) \frac{1}{a + i\mu_k b} \left(1 - \frac{a}{b\sqrt{-\mu_k^2}} \right) \right\}. \quad (13)$$

Considering only electrical loading, the far-field loading becomes

$$\sigma_{xx}^{\infty} = 0, \quad \sigma_{xy}^{\infty} = 0, \quad \sigma_{yy}^{\infty} = 0, \quad D_x^{\infty} = 0, \quad \text{and}$$
$$D_y^{\infty} = \text{constant} \quad \text{at } z = \infty. \quad (14)$$

The stress can therefore be represented as follows:

$$\sigma_{yy} (x = a, y = 0) = aD_y^{\infty} \text{ Re} \sum_{k=1}^{3} \left\{ \Lambda_{k3} \frac{1}{a + i\mu_k b} \left[1 - \frac{a}{b\sqrt{-\mu_k^2}} \right] \right\}. \quad (15)$$

Algebraic manipulation shows that μ_k are all purely imaginary when it is optimized or eliminated. Considering this, let $\mu_k = i\beta_k$ where β_k are real positive numbers. Then we have

$$\sigma_{yy} (x = a, y = 0) = -\frac{a}{b} D_y^{\infty} \text{ Re} \sum_{k=1}^{3} \left(\frac{\Lambda_{k3}}{\beta_k} \right). \quad (16)$$

Demanding that $\sigma_{yy} (x = a, y = 0) = 0$, it is obvious that the following relation holds:

$$\text{Re} \sum_{k=1}^{3} \left(\frac{\Lambda_{k3}}{\beta_k} \right) = 0. \quad (17)$$

One solution to Eq. (17) is that the piezoelectric coefficients are zero, a trivial solution. However, other admissible families exist to meet this criteria. Furthermore, the term Λ_{k3}/β_k is independent of geometry. Therefore, optimal properties for a given geometry are also optimal properties for any other geometry. Therefore, the optimal material properties reported by Park and Carman (1996a) for circular defects are also optimal for any arbitrary elliptical defects. In the limit, the ellipse approaches a crack and we find that the same optimal properties eliminate the stress field.

Results

In this section, we present analytical results for the electrical loading of a piezoceramic PZT-4 containing an elliptical hole. The electric field is applied in the negative y direction. Material properties for PZT-4 are provided in Table 1. Although analytic solutions were obtained using the g-form of a constitutive relation, e-form is used in this parametric analysis, Eq. (18).

$$\sigma_{ij} = C_{ijkl}^{E} S_{kl} + e_{kij} E_k, \quad D_i = e_{ikl} S_{kl} + \epsilon_{ik}^{S} E_k \quad (18)$$

where C_{ijkl}^{E} is the stiffness tensor measured at a constant electric field, e_{kij} is the piezoelectric tensor, and ϵ_{ik}^{S} is the dielectric permeability tensor measured at constant strain. The relationship between the e-form and g-form can be derived by simple manipulation listed in Table 1. Reduced notation is used in the presentation of results (i.e., $e_{i\alpha}$) where the first subscript ranges from 1 to 3 and is associated with the electric field and the second subscript ranges from 1 to 6 and is associated with the stress field.

In Fig. 2, we present results for the electric-field-induced hoop stresses at the rim of the void as a function of angle. Each curve shown in Fig. 2 represents a variation on the piezoelectric coefficient e_{15}. In this parametric study all other material constants remain fixed and are representative of PZT-4. The geometry of the ellipse studied in this figure is $b = a$, representative of a hole. The results indicate that as e_{15} changes, the magnitude of the stress at the rim varies, even in sign. For a value of $e_{15} = 10.75$, the hoop stress at the rim vanishes. Investigating the hoop stresses at other radial locations reveals that the stresses vanish everywhere in the medium. By varying e_{33}, we find that the stress vanishes for a value of $e_{33} = 20.15$. The optimal property for e_{31} is -9.63. Variations in both e_{31} and e_{33} cause pseudo linear changes in the stress. On the other hand, e_{15} causes nonlinear changes in the stress state.

Table 1 Material properties of PZT-4 piezoelectric ceramics (Jaffe and Berlincourt, 1965)

e-form	g-form	Two-dimensional g-form
$c_{11} = 14.02 \times 10^{10}$ (N/m²)	$s_{11} = 10.90 \times 10^{-12}$ (m²/N)	$a_{11} = 8.20 \times 10^{-12}$ (m²/N)
$c_{12} = 7.89 \times 10^{10}$	$s_{12} = -5.42 \times 10^{-12}$	$a_{12} = -3.14 \times 10^{-12}$
$c_{13} = 7.57 \times 10^{10}$	$s_{13} = -2.10 \times 10^{-12}$	$a_{22} = 7.50 \times 10^{-12}$
$c_{33} = 11.58 \times 10^{10}$	$s_{33} = 7.90 \times 10^{-12}$	$a_{33} = 20.88 \times 10^{-12}$
$c_{44} = 2.53 \times 10^{10}$	$s_{44} = 20.88 \times 10^{-12}$	
$e_{31} = -5.27$ (C/m²)	$g_{31} = -1.11 \times 10^{-2}$ (m²/C)	$b_{21} = -1.66 \times 10^{-2}$ (m²/C)
$e_{33} = 15.45$	$e_{33} = 2.61 \times 10^{-2}$	$b_{22} = 2.40 \times 10^{-2}$
$e_{15} = 13.00$	$e_{15} = 3.94 \times 10^{-2}$	$b_{13} = 3.94 \times 10^{-2}$
$\epsilon_{11} = 6.37 \times 10^{-9}$ (C/Vm)	$\beta_{11} = 8.29 \times 10^{7}$ (Vm/C)	$\delta_{11} = 8.29 \times 10^{7}$ (Vm/C)
$\epsilon_{33} = 5.52 \times 10^{-9}$	$\beta_{33} = 8.69 \times 10^{7}$	$\delta_{33} = 9.82 \times 10^{7}$

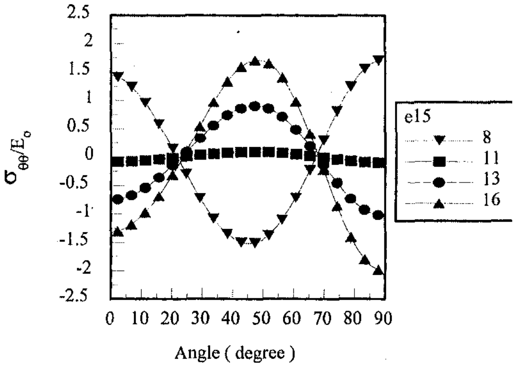

Fig. 2 Change of hoop stress distribution around the hole by varying e_{15}

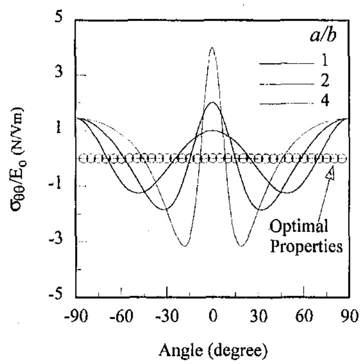

Fig. 5 Hoop stress distribution around the rim of ellipses with different *a*-to-*b* ratio

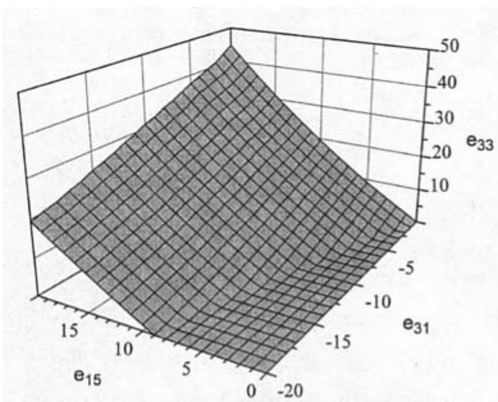

Fig. 3 Surface of optimal properties

Having shown that an optimal property exists for a circular hole, in Fig. 3 we present a design plot for optimal properties. In this figure the shaded region represents optimal properties for a piezoelectric medium containing an elliptical void. The three axis in the plot corresponds to the piezoelectric coefficients which optimize the properties. When constructing this plot the stiffness and permittivity values of the piezoceramic were taken to be those presented in Table 1. As can be seen when reviewing this graph the optimal surface appears to be two dimensional. To clarify this point we present sections of the graph in Fig. 4. This two-dimensional plot of the optimum properties shows that the variation between e_{15} and e_{31} is nearly linear for a wide range of e_{33} values. Furthermore, the spacing between the optimal curves presented in the figure indicates a slight nonlinear dependence upon variations in e_{33}. That is for small values of e_{33} the spacing between the curves is larger than for relatively larger values of e_{33}. A trivial solution to the problem is when all the piezoelectric coefficients are zero. That is when the electrical and mechanical fields decouple, the stress states vanish as they should.

To illustrate the influence these optimal properties have on an ellipse, we present analytical results in Fig. 5. The hoop stresses around the perimeter of an ellipse with different ratio of a/b are presented. The two symbols in the figure correspond to either a PZT-4 sample with properties listed in Table 1 or to an optimal piezoceramic defined in Fig. 4. As was proven analytically in Eq. (17), at $\theta = 0$ the optimal properties for the material cause this stress concentration to vanish regardless of geometry. This confirms the analytical result presented in Eq. (17) that the optimal values are independent of aspect ratio. Furthermore, as θ varies from 0 to 90 degrees the optimal properties also cause the hoop stress to vanish at all locations. This indicates that the entire stress state in the material is eliminated with the optimal values. This is a much stronger statement than implied by Eq. (17). That is, the optimal properties also cause the entire stress field to vanish for an arbitrary ellipse.

To investigate the influence of optimal properties on cracks, $a/b = \infty$, we present analytical results in Fig. 6. The hoop stress normalized by radius from the crack tip is plotted as a function of azimuth position. The two curves correspond to either a PZT-4 sample or an optimal material with properties defined by Fig. 4. At $\theta = 0$, the stresses vanish for either of the materials studied. That is, the stress fields decouple from the electric field regardless of the material properties in the self-similar plane as explained previously by Park and Sun (1995a). However, for the PZT-4 material the stress state does not arbitrarily vanish outside the self-similar plane. On the other hand, using the optimal material properties calculated using Eq. (17), the stresses vanish in the medium. Therefore, we conclude that the optimal properties are also applicable to the crack problem. Park and Carman (1996) indicated that optimal properties are achievable with appropriate modification during processing, a statement based on the analytical results generated on two dif-

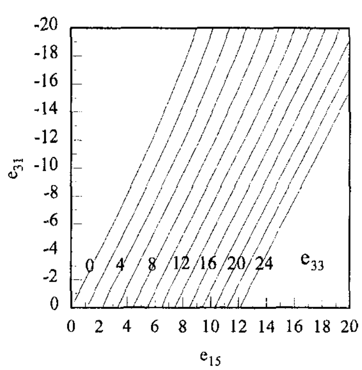

Fig. 4 Section portion of the optimal surface

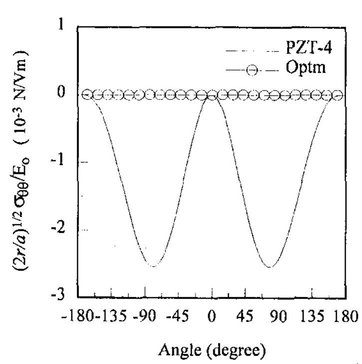

Fig. 6 Verification of effectiveness of optimal properties to cracks

ferent piezoelectric ceramics, that is PZT-5H and PZT-4. These results also demonstrated that optimal properties do not limit the deformation of the ceramic material.

Conclusion

In this paper we studied electric-field-induced stress concentrations in a piezoelectric medium with an elliptical shaped internal defect. Using an analytical constraint on the stress state in the medium we were able to eliminate the largest stress at the rim of the ellipse. The optimal properties predicted with this methodology were independent of geometry and was only a function of material properties. Numerical results demonstrated that the optimal properties also cause the entire stress field around the anomaly to vanish and not just at a specific location. This indicates that a porous medium with optimal properties behaves similar to a continuous medium. The optimal properties were also shown to be applicable to the crack problem in a piezoelectric medium. While this result does eliminate the stress concentration around the hole for linear ferroelectrics, cracking in many ferroelectric ceramics are due to nonlinear influences associated with polarization switching. The optimal properties proposed in this paper may not significantly influence the stress state for the nonlinear case (Wang et al., 1996).

Acknowledgment

This research work was supported by the Army Research Office under contract DAAH04-95-1-0095. Technical monitor is Dr. John Prater.

References

Carl, K., 1975, "Ferroelectric Properties and Fatiguing Effects of Modified $PbTiO_3$ Ceramics," *Ferroelectrics*, Vol. 9, pp. 23–32.

Ikeda, T., 1990, *Fundamentals of Piezoelectricity*, Oxford Science Publications, Oxford, UK.

Jaffe, H., and Berlincourt, D. A., 1965, "Piezoelectric Transducer Materials," *Proc. of the IEEE*, Vol. 53, No. 10, pp. 1372–1386.

Jiang, Q., and Cross, L. E., 1993, "Effects of Porosity on Electric Fatigue Behaviour in PLZT and PZT Ferroelectric Ceramics," *J. of Mat. Sci.*, Vol. 28, pp. 4536–4543.

Lekhnitskii, S. G., 1981, *Theory of Elasticity of an Anisotropic Body*, Mir, Moscow.

Pak, Y. E., 1990, "Crack Extension Force in a Piezoelectric Material," ASME JOURNAL OF APPLIED MECHANICS, Vol. 57, pp. 647–653.

Park, S. B., and Carman, G. P., 1996a, "Tailoring the Properties of Piezoelectric Ceramics: Analytical," *Int. J. Solids Structures*, accepted for publication.

Park, S. B., Park, S. S., and Carman, G. P., 1996b, "Measuring Strain Concentration During Mescopic Domain Reorientation in a Ferroelectric Ceramic," ASME *Journal of Engineering Materials and Technology*, submitted for publication.

Park, S. B., and Sun, C. T., 1995a, "Effect of Electric Field on Fracture of Piezoelectric Ceramics," *Int. J. Fracture*, Vol. 70, pp. 203–216.

Park, S. B., and Sun, C. T., 1995b, "Fracture Criteria for Piezoelectric Ceramics," *J. Am. Ceram. Soc.*, Vol. 78, pp. 1475–1480.

Pan, W., Yue, C-F., and Sun, S., 1992, "Domain Orientation Change Induced by Ferroelectric Fatigue Process in Lead Zirconate Titanate Ceramics," *Ferroelectrics*, Vol. 133, pp. 97–102.

Parton, V. Z., and Kudryavtsev, B. A., 1988, *Electromagnetoelasticity*, Gordon and Breach, New York.

Sosa, H. A., 1991, "Plane Problems in Piezoelectric Media with Defects," *Int. J. Solids Structures*, Vol. 28, pp. 491–505.

Suo, Z., Kuo, C.-M., Barnett, D. M., and Willis, J. R., 1992, "Fracture Mechanics for Piezoelectric Ceramics," *J. Mech. Phys. Solids*, Vol. 40, No. 4, pp. 739–765.

Wang, D., Carman, G. P., and Fotinich, Y., 1996, "Influence of Temperature on the Electro-Mechanical and Fatigue Behavior of Piezoelectric Ceramics," *J. of Applied Physics*, submitted for publication.

APPENDIX

Compatibility equations:

$$\frac{\partial^2 S_{xx}}{\partial y^2} + \frac{\partial^2 S_{yy}}{\partial x^2} - 2\frac{\partial^2 S_{xy}}{\partial x \partial y} = 0, \quad \frac{\partial E_x}{\partial y} - \frac{\partial E_y}{\partial x} = 0. \quad (A.1)$$

Stress functions and electric displacement functions which satisfy field equations:

$$\sigma_{xx} = \frac{\partial^2 U}{\partial y^2}, \quad \sigma_{yy} = \frac{\partial^2 U}{\partial x^2}, \quad \sigma_{xy} = -\frac{\partial^2 U}{\partial x \partial y},$$

$$D_x = \frac{\partial \psi}{\partial y}, \quad \text{and} \quad D_y = -\frac{\partial \psi}{\partial x} \quad (A.2)$$

where a complex variable, z, defined as $z = x + \mu y$.

Characteristic equation:

$$a_{11}\delta_{11}\mu^6 + (a_{11}\delta_{22} + 2a_{12}\delta_{11} + a_{33}\delta_{11} + b_{21}^2 + b_{13}^2 + 2b_{21}b_{13})\mu^4 + (a_{22}\delta_{11} + 2a_{12}\delta_{22} + a_{33}\delta_{22} + 2b_{21}b_{22} + 2b_{13}b_{22})\mu^2 + (a_{22}\delta_{22} + b_{22}^2) = 0. \quad (A.3)$$

General solution which satisfy compatibility condition:

$$\psi_k(z_k) = \lambda_k U_k'(z_k) \quad (A.4)$$

where

$$\lambda_k = -\frac{(b_{21} + b_{13})\mu_k^2 + b_{22}}{\delta_{11}\mu_k^2 + \delta_{22}}. \quad (A.5)$$

Complex function to reduce order of the derivative:

$$\varphi_k(z_k) = U_k'. \quad (A.6)$$

Simplified coefficients:

$$\Lambda = \frac{1}{\Delta}\begin{bmatrix} \mu_2\lambda_3 - \mu_3\lambda_2 & \lambda_2 - \lambda_3 & \mu_3 - \mu_2 \\ \mu_3\lambda_1 - \mu_1\lambda_3 & \lambda_3 - \lambda_1 & \mu_1 - \mu_3 \\ \mu_1\lambda_2 - \mu_2\lambda_1 & \lambda_1 - \lambda_2 & \mu_2 - \mu_1 \end{bmatrix} \quad (A.7)$$

and

$$\Delta = (\lambda_2 - \lambda_3)\mu_1 + (\lambda_3 - \lambda_1)\mu_2 + (\lambda_1 - \lambda_2)\mu_3.$$

I. Jasiuk
The George W. Woodruff School of Mechanical Engineering, Georgia Institute of Technology, Atlanta, GA 30332-0405
Mem. ASME

P. Y. Sheng
Energy Management Development, Product Development Vehicle Engineering, Chrystler Technology Center (contractor), Chrystler Corporation, CIMS 481-01-39, 800 Chrystler Drive East, Auburn Hills, MI 48326-2757

E. Tsuchida
Department of Mechanical Engineering, Saitama University, 255 Shimo-Okubo, Urawa 338, Japan

A Spherical Inclusion in an Elastic Half-Space Under Shear

We find the elastic fields in a half-space (matrix) having a spherical inclusion and subjected to either a remote shear stress parallel to its traction-free boundary or to a uniform shear transformation strain (eigenstrain) in the inclusion. The inclusion has distinct properties from those of the matrix, and the interface between the inclusion and the surrounding matrix is either perfectly bonded or is allowed to slip without friction. We obtain an analytical solution to this problem using displacement potentials in the forms of infinite integrals and infinite series. We include numerical examples which give the local elastic fields due to the inclusion and the traction-free surface.

Introduction

When an inclusion (inhomogeneity) is present in a matrix and a loading is applied, elastic stress fields are disturbed in the vicinity of the inclusion. These stresses depend on a number of factors which include the shape and location of the inclusion, the mismatch in the elastic constants of the inclusion and the matrix, the boundary conditions, and the loading.

Inclusion problems have been a focus of the micromechanics research for several decades (for a review of literature see, e.g., Mura, 1987). Most of these studies, however, considered the cases when the inclusion is placed in an infinitely extended material and a matrix-inclusion interface is perfectly bonded. In this paper we are interested in the case when the inclusion, with properties distinct from those of the matrix, is embedded near a surface of a half-space and the matrix-inclusion interface is either perfectly bonded or is allowed to slip.

In the terminology of Mura (1987) the *inclusion* denotes a subdomain in the matrix subjected to transformation strains (eigenstrains), while the *inhomogeneity* is a region with properties distinct from those of the matrix and subjected to a remote stress. In the above two paragraphs and the Abstract we used the term inclusion to denote both cases, for simplicity. In the remaining part of the Introduction we follow the Mura's terminology for the clarity of presentation.

The elasticity problems involving a half-space with a spherical (or spheroidal) inclusion, inhomogeneity or cavity have been studied by several researchers. Among them, Tsuchida and Nakahara (1970, 1972) solved the problem of a semi-infinite elastic body with a spherical cavity subjected to a remote all-around (equal biaxial) tension on the plane boundary or a uniform pressure on the surface of cavity. Tsutsui and Saito (1973) investigated the problem of a semi-infinite material containing a perfectly bonded spherical inhomogeneity under the all-around tension, while Tsuchida and Mura (1983) considered a similar problem involving a spheroidal inhomogeneity. Other related papers are due to Atsumi and Itou (1974), Tsuchida et al. (1973), and Tsuchida et al. (1982). The problem of a perfectly bonded ellipsoidal inclusion, having the same elastic constants as the half-space and subjected to dilatational strains, was solved by Seo and Mura (1979), and the similar problem but involving a spherical inclusion was studied by Mindlin and Cheng (1950) and Wachtman and Dundurs (1971). The spheroidal inclusion subjected to eigenstrains in the form of a uniform dilatation and an extension was considered by Yu and Sanday (1990). Jasiuk et al. (1991) solved the problem of a half-space containing a sliding spheroidal inhomogeneity under either an axisymmetric remote tension or an inclusion subjected to nonshear eigenstrain. All the above works involved axisymmetric loadings only.

Tsuchida and Nakahara (1974), using a combination of Boussinesq, Neuber, and Dougall displacement potentials, considered an asymmetric problem of a spherical cavity in a half-space subjected to either a uniaxial tension or a pure shear. Aderogba (1976) solved the problem of a perfectly bonded spherical inclusion in a semi-infinite solid, subjected to arbitrary eigenstrains, and Chiu (1978) investigated the corresponding problem involving a cuboidal inclusion. Yu and Sunday (1991, 1992) considered the problem of two half-spaces, either perfectly bonded or in frictionless contact with each other, with an inclusion (or inhomogeneity) embedded in one of the half-spaces. The inclusion, with distinct properties from those of the matrix, was of an arbitrary shape, perfectly bonded to the matrix, and subjected to either an arbitrary eigenstrain or a remote applied loading.

The corresponding two-dimensional problems involving a half-plane included a circular hole under a uniaxial tension solved by Jeffery (1920) and Mindlin (1948), a perfectly bonded circular inclusion subjected to an eigenstrain loading considered by Richardson (1969), and a perfectly bonded circular inhomogeneity under a remote uniaxial tension studied by Saleme (1958) and Shioya (1967). Also, Lee et al. (1992) addressed the case of a sliding circular inhomogeneity (and inclusion) in a half-plane under either a remote uniaxial tension or a nonshear eigenstrain loading.

Mindlin (1948) showed that the hoop stress becomes infinite as the hole approaches the traction-free surface as opposed to a finite value of stress concentration of 3 for the case of hole embedded in the infinite medium; Callias and Markenscoff (1989) studied the nature of this singularity analytically. Very

Contributed by the Applied Mechanics Division of THE AMERICAN SOCIETY OF MECHANICAL ENGINEERS for publication in the ASME JOURNAL OF APPLIED MECHANICS.

Discussion on this paper should be addressed to the Technical Editor, Professor Lewis T. Wheeler, Department of Mechanical Engineering, University of Houston, Houston, TX 77204-4792, and will be accepted until four months after final publication of the paper itself in the ASME JOURNAL OF APPLIED MECHANICS.

Manuscript received by the ASME Applied Mechanics Division, Sept. 7, 1993; final revision, Mar. 6, 1997. Associate Technical Editor: X. Markenscoff.

high stresses were also observed in the case of a stiff slipping inhomogeneity near the free surface by Lee et al. (1992).

In this paper we consider a spherical inclusion and inhomogeneity embedded near a traction-free surface of a half-space. Such a geometry may represent a near surface particle in a composite material, for example. The inhomogeneity is subjected to a remote pure shear stress parallel to the plane boundary while the inclusion, with the elastic properties distinct from those of the matrix, undergoes a pure shear eigenstrain. The interface between the inclusion (inhomogeneity) and the matrix is either perfectly bonded or allows slip without friction (shear tractions are zero) while maintaining continuity of normal displacements and tractions. This problem is related to earlier works involving a spheroidal slipping inclusion and inhomogeneity, under shear loading, embedded in an infinite matrix (Jasiuk et al., 1987; Sheng, 1992; Mura and Furuhashi, 1984). This is, however, the first study which investigates the joint effect of the traction-free surface and slipping matrix-inclusion interface under an asymmetric loading. We show that this situation gives rise to higher stress concentrations than in the case of the perfectly bonded and/or fully embedded inclusions. This problem is of importance in engineering design of as these high stresses, due to near surface inclusions and inhomogeneities, may initiate cracking and/or plasticity in composite materials under static as well as fatigue loadings.

In the analysis we use the displacement potentials in the forms of infinite series and infinite integrals. The method of solution is very similar to the one of Tsuchida et al. (1973, 1982), Tsuchida and Nakahara (1974), and Jasiuk et al. (1991). It is also similar to the one of Kouris and Mura (1989) who considered the hemispherical inclusion under an axisymmetric loading and used displacement potentials with a half-range expansion to satisfy a traction-free condition at a surface passing through the origin. However, since in our case the surface of the half-space does not pass through the center of the inclusion (the origin of coordinates) the integrals are used instead to cancel tractions at the surface.

An alternate method to this class of problems has been recently proposed by Yu and Sunday (1991, 1992) who employed the Green's function approach and the equivalent inclusion method of Eshelby (1957). Eshelby's method is easy to use when the eigenstrain is constant and the inclusion is embedded in the infinitely extended material. However, in the case of an inhomogeneous inclusion near a surface, the equivalent eigenstrains are nonuniform and expressed in the form of infinite number of terms in a polynomial (Moscovidis and Mura, 1975). Also, the sliding at the inclusion-matrix interface cannot be easily incorporated in that approach. Our method involves an infinite series of harmonic functions, which corresponds to the infinite number of eigenstrains. It can treat both perfect bonding and slipping conditions at the inclusion-matrix interface, but is more restrictive as it cannot deal with arbitrary shapes and requires a different set of potentials for different regular shapes (and different loadings). As our main interest is to study the effects of the matrix-inclusion interface of a spherical inclusion (and inhomogeneity) embedded near a surface, we choose our method for mathematical convenience.

Method of Solution

We consider a semi-infinite elastic material containing a spherical inclusion (inhomogeneity) of radius a, having different elastic constants from those of the matrix, as shown in Fig. 1. The loading is either a uniform pure shear stress, parallel to the traction-free boundary, applied at infinity for the inhomogeneity case, or an eigenstrain loading of shear type in the inclusion for the eigenstrain case.

These loading conditions can be expressed as $\sigma_{xx} = -\sigma_{yy} = p_0$ at infinity for the inhomogeneity case or

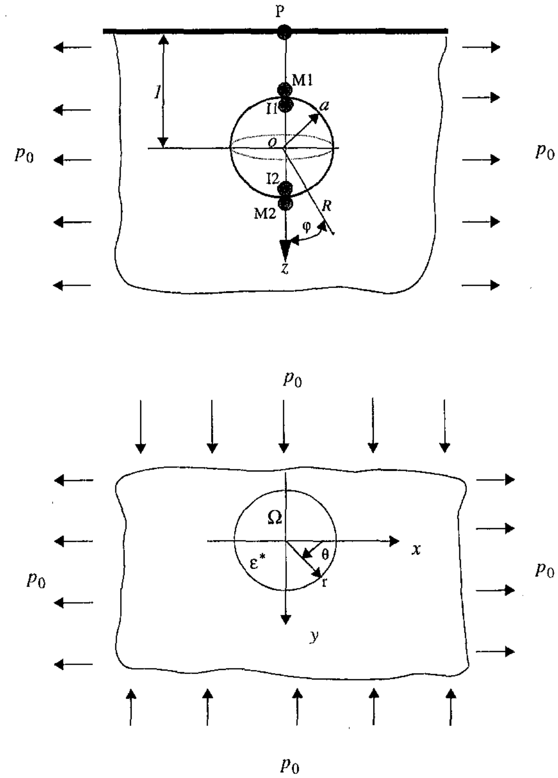

Fig. 1 The spherical inclusion (inhomogeneity) in a half-space

$$\bar{\epsilon}^*_{xx} = -\bar{\epsilon}^*_{yy} = \epsilon^* \tag{1}$$

for the inclusion case, where σ_{xx}, σ_{yy} are stresses, $\bar{\epsilon}^*_{xx}$, $\bar{\epsilon}^*_{yy}$ are eigenstrains, and p_0 and ϵ^* are constants. In our notation we denote the quantities in the inclusion (inhomogeneity) by a bar.

In the solution we use three coordinate systems, Cartesian (x, y, z), cylindrical (r, θ, z), and spherical (R, θ, φ). The relations among these systems are

$$x = r\cos\theta = R\sin\varphi\cos\theta$$

$$y = r\sin\theta = R\sin\varphi\sin\theta$$

$$z = R\cos\varphi. \tag{2}$$

We let the origin of coordinates be at the center of the spherical inclusion (and inhomogeneity) and the positive direction of the z-axis be downward and, without the loss of generality, we take the perpendicular distance from the origin of the inclusion to the traction-free surface as unity so that the plane boundary is located at $z = -1$.

The boundary conditions are as follows:

1 tractions at infinity are

$$\sigma_{xx} = -\sigma_{yy} = p_0 \tag{3}$$

for the remote shear loading, and vanishing tractions at infinity for the eigenstrain case;

2 the traction-free condition on the surface ($z = -1$) of the half-space

$$\sigma_{zz} = 0 \quad \sigma_{zr} = 0 \quad \sigma_{z\theta} = 0; \quad \text{and} \tag{4}$$

3 either perfect bonding boundary conditions at the particle-matrix interface ($r = a$)

$$u_R = \bar{u}_R \quad u_\theta = \bar{u}_\theta \quad u_\varphi = \bar{u}_\varphi$$

$$\sigma_{RR} = \bar{\sigma}_{RR} \quad \sigma_{R\theta} = \bar{\sigma}_{R\theta} \quad \sigma_{R\varphi} = \bar{\sigma}_{R\varphi} \tag{5}$$

or a frictionless slip at the interface with no separation in the normal direction

$$u_R = \bar{u}_R \quad \sigma_{RR} = \bar{\sigma}_{RR} \quad \sigma_{R\theta} = 0$$
$$\bar{\sigma}_{R\theta} = 0 \quad \sigma_{R\varphi} = 0 \quad \bar{\sigma}_{R\varphi} = 0. \qquad (6)$$

In the above expressions, u_i and σ_{ij} represent displacements and stresses, respectively.

In order to construct the solution to the above boundary value problems we use a combination of six harmonic displacement potential functions, ϕ_0, ϕ_1, ϕ_2, ϕ_3, ϕ_4, and λ_3. Among them, the set of ϕ_0, ϕ_1, ϕ_2, ϕ_3 is due to Papkovich and Neuber, the set of ϕ_0, ϕ_3, and λ_3 to Boussinesq, and the set of ϕ_0, ϕ_4, and λ_3 to Dougall. It should be pointed out that, since these potentials are not independent, our choice of the potentials is not unique and other combinations, specifically the fewer number of potentials, but at least three, can give the same solutions to the above two problems. We choose our combination for the mathematical convenience.

According to a superposition principle in linear elasticity, for the applied remote loading case, the stress and displacement fields in the matrix can be considered as sums of two parts, the undisturbed field in the absence of the inhomogeneity caused only by the applied loading at infinity and the local field due to the disturbance by the inhomogeneity. Similarly, for the eigenstrain case, the stress and displacement fields in the inclusion can be considered as sums of two parts, the inelastic field when the inclusion is allowed to deform freely due to eigenstrains without any constrain from the matrix and the field resulting from the elastic strains caused by the presence of the matrix.

For the matrix, the potential function which gives the elastic field due to the remote shear loading (3) in the absence of the inhomogeneity is

$$\phi_0 = \tfrac{1}{2}p_0(x^2 - y^2) = p_0\tfrac{1}{6}R^2P_2^2(\mu)\cos 2\theta \qquad (7)$$

where $\mu = \cos\varphi$ and $P_n^m(\mu)$ is the associated Legendre's function of the first kind of order n and degree m.

For the matrix, the potentials accounting for the disturbance due to the presence of the inclusion (inhomogeneity) are

$$\phi_0 = \sum_{m=2}^{\infty} C_m R^{-(m+1)}P_m^2(\mu)\cos 2\theta$$
$$\phi_1 = \sum_{m=1}^{\infty} D_m R^{-(m+1)}P_m^1(\mu)\cos\theta$$
$$\phi_2 = -\sum_{m=1}^{\infty} D_m R^{-(m+1)}P_m^1(\mu)\sin\theta$$
$$\phi_4 = -\sum_{m=2}^{\infty} \frac{D_m}{m-1} R^{-(m+1)}P_m^2(\mu)\cos 2\theta$$
$$\phi_3 = \sum_{m=2}^{\infty} E_n R^{-(n+1)}P_n^2(\mu)\cos 2\theta \qquad (8)$$

while the following potentials allow to satisfy the traction-free condition (4)

$$\phi_0 = \int_0^\infty \psi_3(\lambda)J_2(\lambda r)e^{-\lambda z}\cos 2\theta d\lambda$$
$$\phi_1 = \int_0^\infty \psi_4(\lambda)J_1(\lambda r)e^{-\lambda z}\cos\theta d\lambda$$
$$\phi_2 = -\int_0^\infty \psi_4(\lambda)J_1(\lambda r)e^{-\lambda z}\sin\theta d\lambda$$
$$\phi_3 = \int_0^\infty \lambda\psi_5(\lambda)J_2(\lambda r)e^{-\lambda z}\cos 2\theta d\lambda$$
$$\lambda_3 = \int_0^\infty \psi_6(\lambda)J_2(\lambda r)e^{-\lambda z}\sin 2\theta d\lambda. \qquad (9)$$

In the above equations C_m, D_m, and E_m are the unknown constants, ψ_3, ψ_4, ψ_5, and ψ_6 are the unknown functions which will be determined from the boundary conditions, and $J_n(\lambda r)$ is the Bessel function of the first kind of n order.

For the inclusion (inhomogeneity) region we choose the following displacement potentials:

$$\phi_0 = \sum_{n=2}^{\infty} \bar{C}_n R^n P_n^2(\mu)\cos 2\theta$$
$$\phi_1 = \sum_{n=1}^{\infty} \bar{D}_n R^n P_n^1(\mu)\cos\theta$$
$$\phi_2 = -\sum_{n=1}^{\infty} \bar{D}_n R^n P_n^1(\mu)\sin\theta$$
$$\phi_3 = \sum_{n=2}^{\infty} \bar{E}_n R^n P_n^2(\mu)\cos 2\theta. \qquad (10)$$

For the eigenstrain loading, given in Eq. (1), the undisturbed stresses in the inclusion are zero and the displacements, derived from displacement-strain relations, are as follows:

$$\bar{u}_R^* = \tfrac{1}{3}\epsilon^* RP_2^2(\mu)\cos 2\theta$$
$$\bar{u}_\theta^* = -\frac{1}{3\bar{\mu}}\epsilon^* RP_2^2(\mu)\sin 2\theta$$
$$\bar{u}_\varphi^* = -\tfrac{1}{6}\bar{\mu}\epsilon^* RP_2^{2\prime}(\mu)\cos 2\theta \qquad (11)$$

where $\bar{\mu} = \sin\varphi$.

Note that for the remote shear loading the potential function (7) yields the stresses $\sigma_{xx} = -\sigma_{yy} = p_0$ at infinity, while the other stress components are zero. The stresses derived from the potentials (8) and (9) vanish at infinity. Therefore, the total stresses in the matrix satisfy the boundary conditions at infinity (3). For the eigenstrain case for the matrix region we only use the potentials (8) and (9). These satisfy automatically traction-free boundary conditions at infinity.

The potentials (8)–(9) are expressed in spherical and cylindrical coordinates, respectively. In order to satisfy the traction-free boundary condition (4) on the surface $z = -1$, it is convenient to use cylindrical coordinates. With the aid of the relation,

$$\frac{P_n^m(\mu)}{R^{n+1}} = \frac{(-1)^{n-m}}{(n-m)!}\int_0^\infty \lambda^n J_m(\lambda r)e^{\lambda z}d\lambda \quad (z < 0), \qquad (12)$$

we can express potentials (8) in terms of cylindrical coordinates as

$$\phi_0 = \sum_{m=2}^{\infty} \hat{C}_m \int_0^\infty \lambda^m J_2(\lambda r)e^{\lambda z}\cos 2\theta d\lambda$$
$$\phi_1 = \sum_{m=1}^{\infty} \hat{D}_m \int_0^\infty \lambda^m J_1(\lambda r)e^{\lambda z}\cos\theta d\lambda$$
$$\phi_2 = -\sum_{m=1}^{\infty} \hat{D}_m \int_0^\infty \lambda^m J_1(\lambda r)e^{\lambda z}\sin\theta d\lambda$$
$$\phi_4 = -\sum_{m=2}^{\infty} \hat{D}_m \int_0^\infty \lambda^m J_2(\lambda r)e^{\lambda z}\cos 2\theta d\lambda$$
$$\phi_3 = \sum_{m=2}^{\infty} \hat{E}_m \int_0^\infty \lambda^m J_2(\lambda r)e^{\lambda z}\cos 2\theta d\lambda \qquad (13)$$

where

$$\hat{C}_n = C_n\frac{(-1)^n}{(n-2)!}$$

$$\hat{D}_n = D_n \frac{(-1)^n}{(n-1)!}$$

$$\hat{E}_n = E_n \frac{(-1)^n}{(n-2)!}. \quad (14)$$

Then, we substitute the potentials ϕ_0, ϕ_1, ϕ_2, ϕ_3, ϕ_4, and λ_3, given by (9) and (13), into the boundary conditions (4) at the surface ($z = -1$). The condition $(\sigma_{zz})_{z=-1} = 0$ is as follows:

$$(\sigma_{zz})_{z=-1} = \frac{\partial^2 \phi_0}{\partial z^2} + \left[r \frac{\partial^2 \phi_1}{\partial z^2} - 2\nu \frac{\partial \phi_1}{\partial r} \right] \cos\theta$$

$$+ 2\nu \frac{1}{r} \frac{\partial \phi_1}{\partial \theta} \sin\theta + \left[r \frac{\partial^2 \phi_2}{\partial z^2} - 2\nu \frac{\partial \phi_2}{\partial r} \right] \sin\theta$$

$$+ 2\nu \frac{1}{r} \frac{\partial \phi_2}{\partial \theta} \cos\theta + z \frac{\partial^2 \phi_3}{\partial z^2} - 2(1-\nu) \frac{\partial \phi_3}{\partial z}$$

$$- r \frac{\partial^2 \phi_4}{\partial r \partial z} - 2(2-\nu) \frac{\partial \phi_4}{\partial z} = 0. \quad (15)$$

We write the other two boundary conditions, given by (4), in a similar way. Then, we let the coefficients of terms involving $J_1(\lambda r)$, $J_2(\lambda r)$, and $J_2'(\lambda r)$ be zero and use the following relations:

(a) the Fourier-Bessel integral

$$f(x) = \int_0^\infty \int_0^\infty y t f(t) J_s(yt) J_s(yx) dy dt$$

$$(s > -1, x > 0); \quad (16)$$

(b) the transformation from the Legendre function to Bessel function given by the Eq. (12);

(c) the relation between Bessel and modified Bessel functions

$$\int_0^\infty \frac{x^{s+1}}{(x^2+y^2)^{t+1}} J_s(xb) dx = \frac{b^t y^{s-t} K_{s-t}(yb)}{2^t \Gamma(t+1)} \quad (17)$$

where $K_s(z)$ is a modified Bessel function of the second kind and $\Gamma(n)$ is a Gamma function;

(d) the definition of the modified Bessel function

$$K_{1/2}(\lambda) = K_{-1/2}(\lambda) = \sqrt{\frac{\pi}{2\lambda}} e^{-\lambda}; \quad \text{and} \quad (18)$$

(e) the recursion formula for the Gamma function

$$\Gamma(x+1) = x\Gamma(x) \quad (x > 0). \quad (19)$$

Then, the unknown functions ψ_3, ψ_4, ψ_5, and ψ_6, which satisfy the traction-free conditions at the surface ($z = -1$), given by (4), become

$$\psi_3(\lambda) = 2(-\lambda + 1 - 2\nu)^2 \hat{D}_1 e^{-2\lambda} + \sum_{n=2}^{\infty} [(-2\lambda + 3 - 4\nu)\hat{C}_m \lambda$$

$$+ 2(1-2\nu)(-2\lambda + 3 - 4\nu)\hat{D}_m$$

$$- 2\{2(1-\nu)(1-2\nu) - \lambda^2\}\hat{E}_m]\lambda^{m-1} e^{-2\lambda}$$

$$\psi_4(\lambda) = -\hat{D}_1 e^{-2\lambda}$$

$$\psi_5(\lambda) = -2(-\lambda + 1 - 2\nu)\hat{D}_{1e}^{-2\lambda}$$

$$+ \sum_{m=2}^{\infty} [-2\hat{C}_m \lambda - 4(1-2\nu)\hat{D}_m$$

$$+ (2\lambda + 3 - 4\nu)\hat{E}_m]\lambda^{m-1} e^{-2\lambda}$$

$$\psi_6(\lambda) = (1-2\nu) \sum_{m=2}^{\infty} \hat{D}_m \lambda^{m-1} e^{-2\lambda}. \quad (20)$$

Next, we use Eqs. (14) and express the unknown functions ψ_3, ψ_4, ψ_5, and ψ_6 in terms of the unknown constants C_m, D_m, and E_m, which are now the only unknowns in the harmonic potential functions (8) and (9) and will be determined from the boundary conditions at the particle-matrix interface given by either (5) or (6).

It is convenient to use the spherical coordinate system to satisfy the boundary conditions at the interface. We use the following relation to transform the potentials from the Bessel function form to the Legendre's function form using the mathematical relation

$$J_m(\lambda r) e^{-\lambda z} = \sum_{n=m}^{\infty} (-1)^{m+n} \frac{(\lambda R)^n}{(m+n)!} P_n^m(\mu). \quad (21)$$

Then, we rewrite the potentials (9) in the spherical coordinates as follows:

$$\phi_0 = \sum_{n=2}^{\infty} \xi_n R^n P_n^2(\mu) \cos 2\theta$$

$$\phi_1 = \sum_{n=1}^{\infty} \eta_n R^n P_n^1(\mu) \cos\theta$$

$$\phi_2 = -\sum_{n=1}^{\infty} \eta_n R^n P_n^1(\mu) \sin\theta$$

$$\phi_3 = \sum_{n=2}^{\infty} \zeta_n R^n P_n^2(\mu) \cos 2\theta$$

$$\lambda_3 = \sum_{n=2}^{\infty} \kappa_n R^n P_n^2(\mu) \sin 2\theta \quad (22)$$

where

$$\xi_n = \int_0^\infty \psi_3(\lambda) \frac{(-\lambda)^n}{(n+2)!} d\lambda$$

$$\eta_n = -\int_0^\infty \psi_4(\lambda) \frac{(-\lambda)^n}{(n+1)!} d\lambda$$

$$\zeta_n = -\int_0^\infty \psi_5(\lambda) \frac{(-\lambda)^{n+1}}{(n+2)!} d\lambda$$

$$\kappa_n = -\int_0^\infty \psi_6(\lambda) \frac{(-\lambda)^n}{(n+2)!} d\lambda. \quad (23)$$

After substituting ψ_3, ψ_4, ψ_5, and ψ_6 given by Eqs. (20) into (23), and using the formula

$$\int_0^\infty e^{-xc} x^b dx = \frac{\Gamma(b+1)}{c^{b+1}} \quad (c > 0, b > -1), \quad (24)$$

we have

$$\xi_n = -2\left[\gamma_{0,n+2} + \frac{2(1-2\nu)}{n+2} \gamma_{0,n+1} + \frac{(1-2\nu)^2}{(n+1)(n+2)} \gamma_{0,n} \right] D_1$$

$$+ \sum_{m=2}^{\infty} [2(n+3)\gamma_{m-2,n+3} + (3-4\nu)\gamma_{m-2,n+2}] C_m$$

$$+ \sum_{m=2}^{\infty} 2(1-2\nu) \left[\frac{-2}{n+2} \gamma_{m-1,n+1} - \frac{3-4\nu}{(n+2)(n+1)} \gamma_{m-1,n} \right] D_m$$

$$+ \sum_{m=2}^{\infty} 2\left[\frac{2(1-\nu)(1-2\nu)}{n+2} \gamma_{m-2,n+1} - (n+3)\gamma_{m-2,n+3} \right] E_m$$

$$\eta_n = D_1 \gamma_{0,n+1}$$

$$\zeta_n = -2\left[\gamma_{0,n+2} + \frac{1-2\nu}{n+2}\gamma_{0,n+1}\right]D_1$$
$$+ \sum_{m=2}^{\infty} 2(n+3)\gamma_{m-2,n+3}C_m - \sum_{m=2}^{\infty}\frac{4(1-2\nu)}{n+2}\gamma_{m-1,n+1}D_m$$
$$- \sum_{m=2}^{\infty}[2(n+3)\gamma_{m-2,n+3} - (3-4\nu)\gamma_{m-2,n+2}]E_m$$
$$\kappa_n = -\sum_{m=2}^{\infty}\frac{1-2\nu}{(n+2)(n+1)}\gamma_{m-1,n}D_m \quad (25)$$

where

$$\gamma_{p,q} = \frac{(-1)^{p+q}}{p!q!}\frac{(p+q)!}{2^{p+q+1}}. \quad (26)$$

Then, we express the displacements and stresses in terms of the potentials (8), (10), and (22), and either the undisturbed ones in the matrix, obtained from (7), or nonelastic ones in the inclusion, given by (11), into the boundary conditions (5) or (6), and use the recursion formulas for Legendre functions. Then, the condition of continuity of normal displacements $u_R = \bar{u}_R$ at $R = a$ becomes

$$-\frac{5-4\nu}{3a^2}D_1P_2^2(\mu) + \sum_{n=2}^{\infty}\Big[\{K^C_{n,n}C_n + K^D_{n,n+1}D_{n+1}$$
$$+ K^E_{n,n-1}E_{n-1} + K^E_{n,n+1}E_{n+1} + K^\xi_{n,n}\xi_n + K^\eta_{n,n-1}\eta_{n-1}$$
$$+ K^\eta_{n,n+1}\eta_{n+1} + K^\zeta_{n,n-1}\zeta_{n-1} + K^\zeta_{n,n+1}\zeta_{n+1} + K^\kappa_{n,n}\kappa_{n,n}\}$$
$$-\frac{1}{g}\{\bar{K}^C_{n,n}\bar{C}_n + \bar{K}^D_{n,n-1}\bar{D}_{n-1} + \bar{K}^D_{n,n+1}\bar{D}_{n+1}$$
$$+ \bar{K}^E_{n,n-1}\bar{E}_{n-1} + \bar{K}^E_{n,n+1}\bar{E}_{n+1}\}\Big]P_n^2(\mu)$$
$$= -\frac{1}{3}(p_0 - 2G\epsilon^*)aP_2^2(\mu) \quad (27)$$

where G is the shear modulus, and $g = \bar{G}/G$. The coefficients in Eq. (27) are defined as

$$K^C_{n,n} = -\frac{n+1}{a^{n+2}}$$
$$K^D_{n,n+1} = \frac{2(1-2\nu)}{na^{n+2}}$$
$$K^E_{n,n-1} = -\frac{(n+3-4\nu)(n-2)}{(2n-1)a^n}$$
$$K^E_{n,n+1} = -\frac{(n+5-4\nu)(n+3)}{(2n+3)a^{n+2}}$$
$$K^\xi_{n,n} = na^{n-1}$$
$$K^\eta_{n,n-1} = \frac{n-4+4\nu}{2n-1}a^{n-1}$$
$$K^\eta_{n,n+1} = -\frac{n-2+4\nu}{2n+3}a^{n+1}$$
$$K^\zeta_{n,n-1} = \frac{(n-4+4\nu)(n-2)}{2n-1}a^{n-1}$$
$$K^\zeta_{n,n+1} = \frac{(n-2+4\nu)(n+3)}{2n+3}a^{n+1}$$
$$K^\kappa_{n,n} = 4a^{n-1}. \quad (28)$$

We obtain similar expressions for the remaining conditions given by Eqs. (5) or (6). All terms denoted by a bar in Eq. (27) can be obtained from the corresponding terms without a bar by replacing ξ, η, ζ, and ν with C, D, E, and $\bar{\nu}$. For example, $\bar{K}^C_{n,n}$, $\bar{K}^D_{n,n-1}$, $\bar{K}^D_{n,n+1}$, $\bar{K}^E_{n,n-1}$ and $\bar{K}^E_{n,n+1}$ can be obtained from $K^\xi_{n,n}$, $K^\eta_{n,n-1}$, $K^\eta_{n,n+1}$, $K^\zeta_{n,n-1}$, and $K^\zeta_{n,n+1}$, respectively, by replacing ν with $\bar{\nu}$.

Using Eqs. (23), we reduce the unknown constants in the equations representing the boundary conditions at the interface to only C_n, D_n, E_n, $\bar{C}_n$, $\bar{D}_n$, and $\bar{E}_n$. Then, we equate the coefficients of $P_n^2(\mu)$ and $P_n^{2\prime}(\mu)$, where prime denotes the first derivative with respect to μ, on both sides of these equations for each n from $n = 2$ to $n \to \infty$, and obtain an infinite set of algebraic equations. Each of these sets contains six equations and six unknowns. For calculations we truncate this infinite set of equations at $n = N$. Therefore, there are $6N$ equations to be solved for the $6N$ unknowns. We truncate the series such that the boundary conditions (5) or (6) are satisfied to at least three significant figures. After these constants are evaluated, the stresses and displacements are known everywhere in the matrix and in the inclusion.

In the calculations, for the case of a perfectly bonded inclusion (and inhomogeneity), we set the constant D_1 to zero since D_1 and C_2 play the same role in the potentials and only one needs to be kept. Furthermore, we set the constants D_2 and E_2 to zero for both the perfectly bonded and slipping inclusion cases.

When the matrix is infinite (or the particle is very small), the analytical solution involves only a finite number of terms in the potential functions (8) and (10), and the potentials (9) do not enter. For the case of an infinite body containing a spherical cavity and subjected to uniform shear stresses $\sigma_{xx} = -\sigma_{yy} = p_0$ at infinity, the constants become

$$C_2 = \frac{1}{2(7-5\nu)}a^5$$
$$D_2 = -\frac{5}{2(7-5\nu)}a^3 \quad (29)$$

while the other constants vanish.

For the case of an infinite body containing a spherical inhomogeneity with a slipping interface and subjected to uniform shear stresses $\sigma_{xx} = -\sigma_{yy} = p_0$ at infinity the solution is

$$\bar{E}_3 = -\frac{70(1-\nu)g}{(17-19\nu)(7+5\bar{\nu})g + 4(7-5\nu)(7-4\bar{\nu})}\frac{1}{a^2}$$
$$\bar{D}_1 = 2\bar{E}_3$$
$$\bar{C}_2 = -\left(1+\frac{2\bar{\nu}}{7}\right)a^2\bar{E}_3$$
$$\bar{C}_4 = -\frac{4\bar{\nu}}{7}\bar{E}_3$$
$$D_1 = -\frac{3a^3}{7-5\nu}\left(\frac{5}{6} + \frac{2(7+5\bar{\nu})}{7}a^2\bar{E}_3\right)$$
$$C_2 = \frac{a^2}{24}(a^3 - 2(1+\nu)D_1) \quad (30)$$

with the other constants vanishing. This solution is in a form of finite series which is expected from the work of Ghahremani (1980). The solution for a perfectly bonded spherical inhomogeneity in an infinite space is also expressed in terms of finite series as shown by Goodier (1933).

Similarly, the solution for the spherical inclusion in an infinite space subjected to an eigenstrain loading case involves finite series for both perfect bonding and sliding cases.

Results and Discussion

We carry out the computations for various radii a of an inclusion (and an inhomogeneity) ranging from 0.2 to 0.99

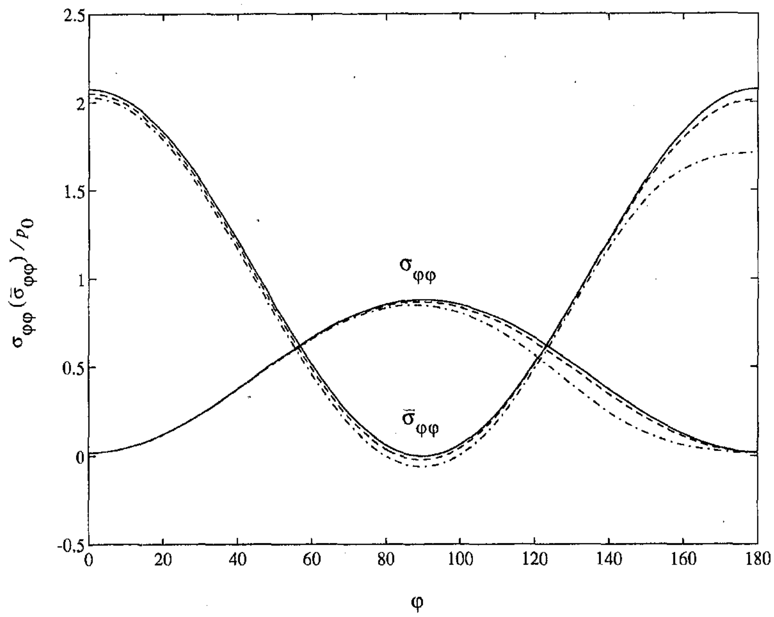

Fig. 2 The hoop stress $\sigma_{\varphi\varphi}(\bar{\sigma}_{\varphi\varphi})$ versus the angle φ for different radii a = 0.2 (solid line), 0.5 (dashed line), and 0.8 (dashdot line) when g = 100 and θ = 0 for the perfect bonding and remote shear loading case

(recall that the particle is located a unit distance from a traction-free surface so the larger the radius a the closer it is to the free surface) and for different ratios of shear moduli $g = \bar{G}/G$. We take the Poisson's ratio as $\nu = \bar{\nu} = 0.3$, for simplicity. We give the numerical results for the case of the inhomogeneity under a uniform remote shear loading, given by Eq. (3), in Figs. 2–6, and for the inclusion subjected to a uniform shear eigenstrain, given by Eq. (1), in Fig. 7.

Figure 2 shows hoop stresses $\sigma_{\varphi\varphi}$ and $\bar{\sigma}_{\varphi\varphi}$ along the interface (at $r = a$) of the perfectly bonded inhomogeneity versus an angle φ, taken from a positive z-axis, when the radius a = 0.2, 0.5 and 0.8 (plotted in solid, dashed and dashdot lines, respectively), $\theta = 0$, and $g = 100$. As expected, the radius has a small influence on the stresses $\sigma_{\varphi\varphi}$ and $\bar{\sigma}_{\varphi\varphi}$ when the angle φ is small and a larger effect when φ is close to 180 deg, which corresponds to a region near the traction-free surface. Around φ = 180 deg the stress $\bar{\sigma}_{\varphi\varphi}$ in the inhomogeneity is more influenced by the traction-free surface than the corresponding stress component $\sigma_{\varphi\varphi}$ in the matrix, and this effect is most pronounced at φ = 180 deg. Note that the stress $\bar{\sigma}_{\varphi\varphi}$ decreases as a increases (i.e., the inhomogeneity gets closer to the surface) for this combination of elastic constants. This is true for all $g > 1$ but when g decreases the effect of surface decreases, and for g = 1 is disappears as expected. However, when $g < 1$ and g decreases the effect is opposite and $\bar{\sigma}_{\varphi\varphi}$ increases due to the surface effect. Note that when g = 100 the stress $\bar{\sigma}_{\varphi\varphi}/p_0$ reaches the maximum at $\varphi = 0$ and is greater than unity as expected since the inhomogeneity is stiffer than the matrix and thus carries the

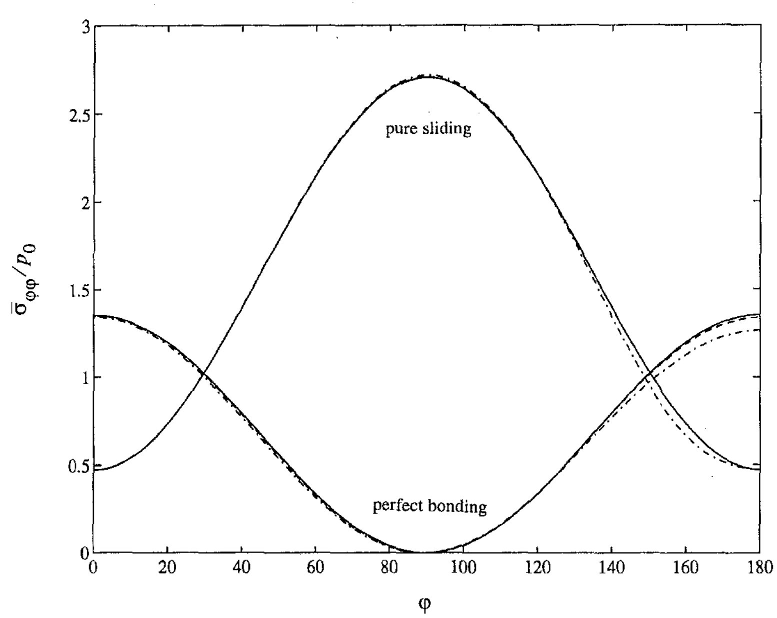

Fig. 3 The stress $\bar{\sigma}_{\varphi\varphi}$ versus angle φ for perfect bonding and sliding cases when g = 0.5, θ = 0, and different radii a = 0.2 (solid line), 0.5 (dashed line), and 0.8 (dashdot line) for the remote shear loading

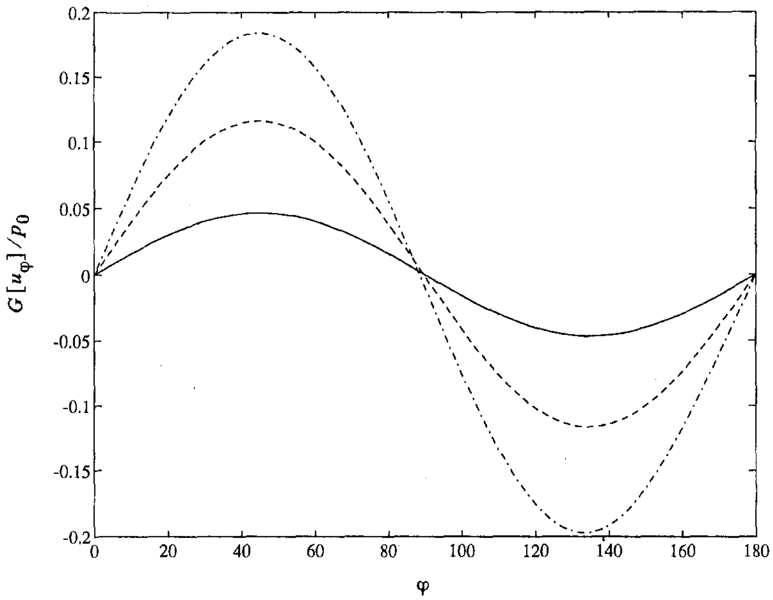

Fig. 4 The jump in displacement $[u_\varphi]$ versus angle φ for different radii $a = 0.2$ (solid line), 0.5 (dashed line), and 0.8 (dashdot line) when $g = 100$ and $\theta = 0$ for the slipping interface and remote shear loading case

load. At $\varphi = 180$ deg it is lower than at $\varphi = 0$ due to the traction-free surface effect.

$\sigma_{\varphi\varphi}/p_0$ in the matrix is smaller than unity when $g = 100$ as shown in Fig. 2 and this is true for any $g > 1$. It is interesting to note, however, that $\sigma_{\varphi\varphi}$ has a reverse image for smaller g. When $g < 1$ there is a stress concentration in $\sigma_{\varphi\varphi}$. When $g = 0.01$ $\sigma_{\varphi\varphi}/p_0 = 2.5$ for $a = 0.8$, $\sigma_{\varphi\varphi}/p_0$ is around 2.0 for $a = 0.5$, and 1.8 for $a = 0.2$ at $\varphi = 180$ deg, where it is maximum, while at $\varphi = 0$ it is around 1.8 for all three cases. Thus, the effect of the traction-free surface is pronounced for a close to unity for small g, and the presence of the free surface gives rise to higher stresses. When g is very small both perfect bonding and slipping interface conditions give very close results as expected since this is almost a cavity case; in this situation the stress $\bar{\sigma}_{\varphi\varphi}$ is very close to zero. For the sliding case $\bar{\sigma}_{\varphi\varphi}$ in the inhomogeneity is most affected by the surface of a half-space when g is large and 90 deg $< \varphi <$ 180 deg. $\sigma_{\varphi\varphi}$ in the matrix is rather insensitive to the traction-free surface when $g > 1$ but it is influenced by the surface only when $g < 1$ and for g very small coincides with the perfect bonding case as discussed above. These additional observations, included here, are based on Figs. 3–9 illustrating the cases of $g = 100$, 2, 0.5, and 0.01 for both interface conditions, given in Sheng (1995).

Figure 3 shows the stress $\bar{\sigma}_{\varphi\varphi}$ in the inhomogeneity along the interface (versus the angle φ) for both perfectly bonded and slipping interface cases when $g = 0.5$. We observe that the stress increases for the sliding case and decreases for the perfectly bonded case as φ increases from 0 to 90 deg, and vice versa from 90 deg to 180 deg, so that $\bar{\sigma}_{\varphi\varphi}$ reaches its maximum value at $\varphi = 0$ and the minimum value at $\varphi = 90$ deg for the

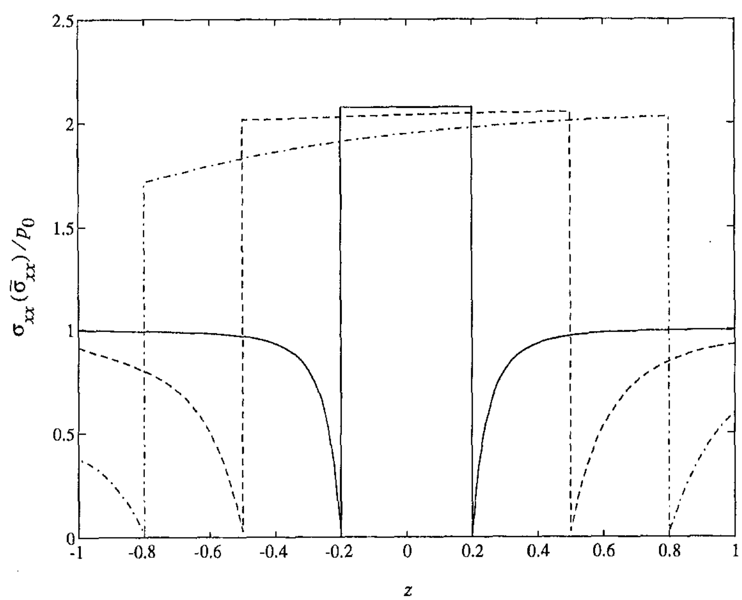

Fig. 5 The stress $\sigma_{xx}(\bar{\sigma}_{xx})$ along the z-axis for different radii $a = 0.2$ (solid line), 0.5 (dashed line), and 0.8 (dashdot line) when $g = 100$ and $\theta = 0$ for perfect bonding and remote shear loading case

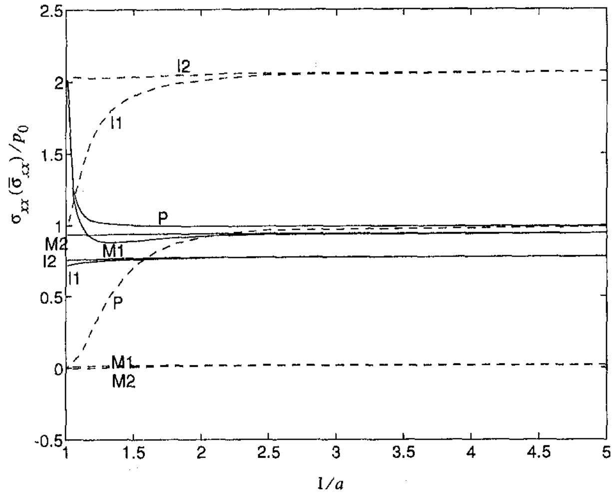

Fig. 6 The stress $\sigma_{xx}(\bar{\sigma}_{xx})$ at several points along the z-axis versus the radius of inclusion a for both perfect bonding (dashed lines) and slipping (solid lines) interface conditions when $g = 100$ for remote shear loading

perfectly bonded interface case, while the minimum is at $\varphi = 0$ and the maximum at $\varphi = 90$ deg for the sliding interface case. The maximum value of $\bar{\sigma}_{\varphi\varphi}$ in the slipping inclusion is about $2.7p_0$ for $g = 0.5$ and increases as g increases (for $g = 100$ it reaches $4.5p_0$). Thus, the stress concentration in the slipping inclusion is higher locally than for the perfectly bonded inclusion case. When $g \to 0$ both sets of curves become straight lines and coincide and $\bar{\sigma}_{\varphi\varphi} = 0$ as expected, since this is a limit case of a cavity.

Figure 4 illustrates the jump of the tangential displacement $[u_\varphi]$ along the inhomogeneity's interface for various radii $a = 0.2$, 0.5 and 0.8 (plotted in solid, dashed, and dashdot lines, respectively), $g = 100$, and $\theta = 0$ for the slipping interface case. Note that the jump in the displacement is higher for 90 deg $< \varphi <$ 180 deg (i.e., near the traction-free surface and increases when the inhomogeneity is closer to the free surface. This is true for any other ratio of shear moduli g, according to the results from our sample computations (Sheng, 1995). This is expected since the inhomogeneity can deform more freely near the traction-free surface.

Figure 5 illustrates stresses σ_{xx} and $\bar{\sigma}_{xx}$ along the z-axis from $z = -1$ to $z = 1$ when the inhomogeneity is perfectly bonded. The radius of the inhomogeneity takes on the values $a = 0.2$, 0.5 and 0.8 (plotted in solid, dashed, and dashdot lines, respectively), and $g = 100$. The stress $\bar{\sigma}_{xx}$ in the inhomogeneity (from $z = a$ to $z = -a$) decreases when the inhomogeneity is closer to the traction-free surface ($a = 0.8$) while the slope of $\bar{\sigma}_{xx}$ is almost zero when the radius is small ($a = 0.2$). This is not surprising since in the latter case we have almost nearly an infinite body containing the inhomogeneity and the stress $\bar{\sigma}_{xx}$ is almost nearly uniform in the particle as expected from Eshelby's (1957) solution. The curves have similar forms for other $g > 1$. Note that σ_{xx}/p_0 is less than unity for all $g > 1$ and it is lowest at $z = -a$. When $g < 1$ we have a bottom-up image and the stress concentration is in the matrix at the interface and it is maximum at $z = -a$. For example, when $g = 0.5$, σ_{xx}/p_0 is approximately 1.4 while for $g = 0.01$ it rises to 2.5. When $g = 1$ the curve is a straight line, as expected, since this is the case of a homogeneous material.

Figure 6 shows the stresses σ_{xx} and $\bar{\sigma}_{xx}$ at selected points P, M1, I1, I2, and M2 along the z-axis (see Fig. 1) when the radius a of the inhomogeneity varies continuously from 0.2 to 0.99 for both perfectly bonded (dashed curves) and slipping (solid curves) cases when $g = 100$. The point P is on the traction-free surface, M1 and M2 are in the matrix at the interface, I1 and I2 are in the inhomogeneity at the interface. In our notation 1 denotes the points at $z = -a$, while 2 denotes the points at $z = a$. It can be seen that the traction-free surface affects significantly the stresses σ_{xx} and $\bar{\sigma}_{xx}$ at point P for both interface cases, and at M1 for the sliding case and I1 for the perfect bonding case (i.e., at points close to the surface at the interface), but has a very small effect at points I2 and M2 (which are away from the surface), as expected. For the case of the perfectly bonded interface, σ_{xx} at M1 and M2 in the matrix is very small (almost zero for $g = 100$), but there is a stress concentration in $\bar{\sigma}_{xx}$ at I1 and I2 in the inhomogeneity (larger than $2p_0$ at I2). This is expected because when the particle is much stiffer than the matrix it carries most of the loading. It is interesting to note that the stress in the inhomogeneity at I1 decreases as $a \to 1$ and drops to about unity at $a = 1$. The stress σ_{xx} at point P decreases as the radius a increases and drops to zero at $a = 1$. This is also illustrated in Fig. 2. The inverse situation occurs when the inhomogeneity is softer than the matrix. Thus, for the stiff, perfectly bonded inhomogeneity case the stress in the particle is reduced due to the presence of the traction-free surface while the one in the matrix remains almost unchanged.

For the slipping inhomogeneity case, when the particle is away from the traction-free surface, the stresses σ_{xx} and $\bar{\sigma}_{xx}$ at these five points are smaller or equal to the applied stress. However, when the radius of the particle increases, there is a stress concentration σ_{xx} at points P and M1, which are the two points in the matrix closest to the surface, and it increases as the radius a increases (i.e., the inhomogeneity gets closer to the surface). Thus, there is a reverse behavior for the perfect bonding and sliding cases with the sliding case having the stress concentration in the matrix due to the surface. These conclusions are similar to those given in Lee et al. (1992) and Jasiuk et al. (1991) for different loadings and inhomogeneity geometries (note that Fig. 6 resembles very closely Fig. 2 in Lee et al., 1992).

Figure 7 illustrates the variation of stress σ_{xx} and $\bar{\sigma}_{xx}$ along the z-axis from $z = -1$ to $z = 1$, for the inclusion case when it undergoes the shear eigenstrain and is perfectly bonded to the matrix. The radius of the inclusion takes on the values of 0.2, 0.5, and 0.8 (plotted in solid, dashed, and dashdot lines, respectively), and $g = 100$. It is interesting to note that comparing the results to the corresponding case of inhomogeneity (with the same g), Fig. 7 has an inverse image. However, its shape is similar to the one for the case of a uniform shear loading when $g = 0.01$. Note that the stresses in the inclusion are nearly uniform when $a = 0.2$, as expected from the solution of Eshelby

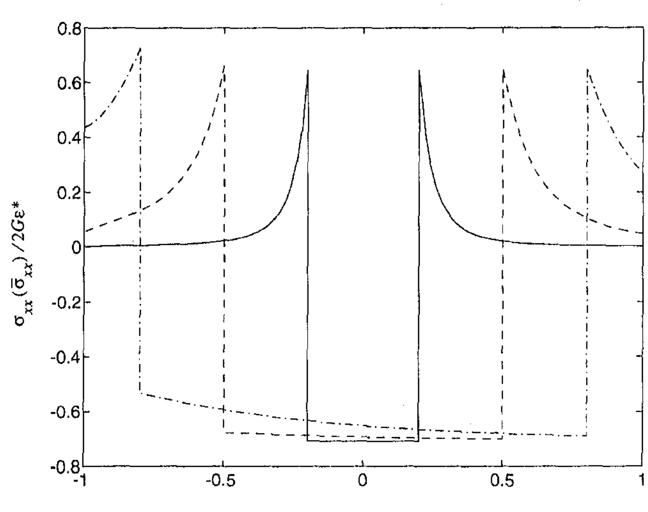

Fig. 7 The stress $\sigma_{xx}(\bar{\sigma}_{xx})$ along the z-axis for different radii $a = 0.2$ (solid line), 0.5 (dashed line), and 0.8 (dashdot line) when $g = 100$ and $\theta = 0$ for perfect bonding and eigenstrain case

(1957), and become nonuniform when a increases, i.e., the effect of surface enters. These observations are similar to those for Fig. 5. The stress in the inclusion is compressive and its absolute value decreases when it is closer to the surface and this effect becomes more pronounced as a increases. The stress in the matrix is tensile and it is higher in magnitude for the case when the inclusion is large, i.e., close to the surface; the maximum occurs at $z = -a$.

Conclusions

In this paper we solved two problems involving the spherical inhomogeneity under a remote shear loading and the spherical inclusion with an eigenstrain of shear type, both embedded in the half-space. In the analysis we used displacement potentials in the forms of infinite series and integrals.

In the numerical examples we studied the joint effect of the traction-free surface of the half-space and the interface conditions, perfect bonding and slipping, on the elastic stress fields. We have found that both effects were pronounced for certain mismatches in elastic moduli. For example, when the inhomogeneity was very compliant the stress fields rose due to the proximity of the traction-free surface and there was a stress concentration in the matrix. Also, for the slipping interface case there were stress concentrations in both the matrix and the inhomogeneity and they increased as we approached the traction-free surface of the half-space. When the inhomogeneity was perfectly bonded the stresses decreased due to the surface when the inhomogeneity was stiffer than the matrix.

Acknowledgments

This research was supported by the Research for Excellence Fund from State of Michigan and in part by the NSF grant number MSS 9402285.

References

Aderogba, K., 1976, "On Eigenstrains in a Semi-infinite Solid," *Mathematical Proceedings of the Cambridge Philosophical Society*, Vol. 80, pp. 555–562.

Atsumi, A., and Itou, S., 1974, "Stresses in a Transversely Isotropic Half Space having a Spherical Cavity," ASME JOURNAL OF APPLIED MECHANICS, Vol. 41, pp. 708–712.

Callias, C. J., and Markenscoff, X., 1989, "Singular Asymptotics Analysis for the Singularity at a Hole Near a Boundary," *Quarterly of Applied Mathematics*, Vol. 47, pp. 233–245.

Chui, Y. P., 1978, "On the Stress Field and Surface Deformation in a Half-Space with a Cuboidal Zone in which Initial Strains are Uniform," ASME JOURNAL OF APPLIED MECHANICS, Vol. 45, pp. 302–306.

Eshelby, J. D., 1957, "The Determination of the Elastic Field of an Ellipoidal Inclusion, and Related Problems," *Proceedings of the Royal Society, London*, Vol. A241, pp. 376–396.

Ghahremani, F., 1980, "Effect of Grain Boundary Sliding on Anelasticity of Polycrystals," *International Journal of Solids and Structures*, Vol. 16, pp. 825–845.

Goodier, J. N., 1933, "Concentration of Stress Around Spherical and Cylindrical Inclusions and Flaws," ASME JOURNAL OF APPLIED MECHANICS, Vol. 55, pp. A39–A44.

Jasiuk, I., Tsuchida, E., and Mura, T., 1991, "Spheroidal Sliding Inclusion in an Elastic Half-Space," ASME *Applied Mechanics Reviews*, Vol. 44, pp. 143–149.

Jasiuk, I., Tsuchida, E., and Mura, T., 1987, "The Sliding Inclusion under Shear," *International Journal of Solids and Structures*, Vol. 23, pp. 1373–1385.

Jeffery, G. B., 1920, "Plane Stress and Plane Strain in Bipolar Coordinates," *Transactions of Royal Society*, Vol. A221, pp. 265–293.

Kouris, D. A., and Mura, T., 1989, "The Elastic Field of a Hemispherical Inhomogeneity at the Free Surface of an Elastic Space," *Journal of the Mechanics and Physics of Solids*, Vol. 37, pp. 365–379.

Lee, M., Jasiuk, I., and Tsuchida, E., 1992, "The Sliding Circular Inclusion in an Elastic Half-Plane," ASME JOURNAL OF APPLIED MECHANICS, Vol. 59, pp. S57–S64.

Mindlin, R. D., 1948, "Stress Distribution Around a Hole near the Edge of a Plate Under Tension," *Proceedings of the Society for Experimental Stress Analysis*, Vol. 5, pp. 56–68.

Mindlin, R. D., and Cheng, D. H., 1950, "Thermoelastic Stress in the Semi-Infinite Solid," *Journal of Applied Physics*, Vol. 21, pp. 931–933.

Moscovidis, Z. A., and Mura, T., 1975, "Two-ellipsoidal Inhomogeneities by the Equivalent Inclusion Method," ASME JOURNAL OF APPLIED MECHANICS, Vol. 45, pp. 847–852.

Mura, T., 1987, *Micromechanics of Defects in Solids*, 2nd ed., Martinus Nijhoff, Dordrecht, The Netherlands.

Mura, T., and Furuhashi, R., 1984, "The Elastic Inclusion with a Sliding Interface," ASME JOURNAL OF APPLIED MECHANICS, Vol. 51, pp. 308–310.

Richardson, M. K., 1969, "Interference Stresses in a Half Plane Containing an Elastic Disk of the Same Material," ASME JOURNAL OF APPLIED MECHANICS, Vol. 36, pp. 128–130.

Saleme, E. M., 1958, "Stress Distribution Around a Circular Inclusion in a Semi-Infinite Elastic Plate," ASME JOURNAL OF APPLIED MECHANICS, Vol. 25, pp. 129–135.

Seo, K., and Mura, T., 1979, "The Elastic Field in a Half-Space due to Ellipsoidal Inclusions with Uniform Dilatational Eigenstrains," ASME JOURNAL OF APPLIED MECHANICS, Vol. 46, pp. 568–572.

Sheng, P. Y., 1992, "The Stress Field of a Spheroidal Sliding Inclusion under Shear," M.S. dissertation, Michigan State University.

Sheng, P. Y., 1995, "Analytical and Computational Approaches in Mechanics of Composite Materials," Ph.D. dissertation, Michigan State University.

Shioya, S., 1967, "On a Semi-infinite Thin Plate with a Circular Inclusion under Uniform Tension," *Bulletin of the JSME*, Vol. 10, pp. 1–9.

Tsuchida, E., and Mura, T., 1983, "The Stress Field in an Elastic Half Space having a Spheroidal Inhomogeneity under All-around Tension parallel to the Plane Boundary," ASME JOURNAL OF APPLIED MECHANICS, Vol. 50, pp. 807–816.

Tsuchida, E., and Nakahara, I., 1970, "Three-dimensional Stress Concentration Around a Spherical Cavity in a Semi-infinite Elastic Body," *Bulletin of the JSME*, Vol. 13, pp. 499–508.

Tsuchida, E., and Nakahara, I., 1972, "Stresses in a Semi-infinite Body Subjected to Uniform Pressure on the Surface of a Cavity and the Plane Boundary," *Bulletin of the JSME*, Vol. 15, pp. 1–10.

Tsuchida, E., and Nakahara, I., 1974, "Stress Concentration Around a Spherical Cavity in a Semi-infinite Body under Uniaxial Tension," *Bulletin of the JSME*, Vol. 17, pp. 1207–1217.

Tsuchida, E., Nakahara, I., and Kodama, M., 1973, "Stresses in a Semi-infinite Body having a Spherical Cavity Compressed by Rigid Body," *Proceedings of the 23rd Japan National Congress for Applied Mechanics*, Vol. 23, pp. 531–546.

Tsuchida, E., Saito, Y., Nakahara, I., and Kodama, M., 1982, "Stress Concentration around a Prolate Spheroidal Cavity in a Semi-infinite Elastic Body under All-around Tension," *Bulletin of the JSME*, Vol. 25, No. 202, pp. 493–500.

Tsutsui, S., and Saito, K., 1973, "On the Effect of a Free Surface and a Spherical Inhomogeneity on Stress Fields of a Semi-infinite Medium under Axi-symmetric Tension," *Proceedings of the 23rd Japan National Congress for Applied Mechanics*, Vol. 23, pp. 547–560.

Wachtman, J. B., and Dundurs, J., 1971, "Large Localized Surface Stresses Caused by Thermal Expansion Anisotropy," *Journal of the American Ceramic Society*, Vol. 54, pp. 525–526.

Yu, H. Y., and Sanday, S. C., 1990, "Axisymmetric Inclusion in a Half Space," ASME JOURNAL OF APPLIED MECHANICS, Vol. 57, pp. 74–77.

Yu, H. Y., and Sanday, S. C., 1991, "Elastic Fields in Joined Semi-Infinite Solids with an Inclusion," *Proceedings of the Royal Society, London*, Vol. A434, pp. 520–529.

Yu, H. Y., and Sanday, S. C., 1992, "Elastic Inclusions and Inhomogeneities in Bimaterials," *Proceedings of the Royal Society, London*, Vol. A439, pp. 659–667.

A Tensegrity Structure With Buckling Compression Elements: Application to Cell Mechanics

M. F. Coughlin

D. Stamenović [1]

Department of Biomedical Engineering,
Boston University,
44 Cummington Street,
Boston, MA 02215

A tensegrity structure composed of six slender struts interconnected with 24 linearly elastic cables is used as a model of cell deformability. Struts are allowed to buckle under compression and their post-buckling behavior is determined from an energy formulation of the classical pin-ended Euler column. At the reference state, the cables carry initial tension balanced by forces exerted by struts. The structure is stretched uniaxially and the stretching force versus axial extension relationships are obtained for different initial cable tensions by considering equilibrium at the joints. Structural stiffness is calculated as the ratio of stretching force to axial extension. Predicted dependences of structural stiffness on initial cable tension and on stretching force are consistent with behaviors observed in living cells. These predictions are both qualitatively and quantitatively superior to those obtained previously from the model in which the struts are viewed as rigid.

Introduction

Tensional integrity (tensegrity) architecture has been proposed to explain how various types of eukaryotic cells (e.g., endothelial, epithelial, fibroblast, smooth muscle, nerve cells, etc.) resist shape distortion (cf. Ingber, 1993). The concept of tensegrity was originally described by Buckminster Fuller (1961) as a new method in designing geodesic structures. In its simplest representation, tensegrity structures can be defined as the interaction between a set of isolated compression elements with a set of continuous tension elements in the aim to provide a stable volume and form in space (Pugh, 1976). Tension elements carry an initial force, conferring load supporting capability to the entire structure. The higher the initial force in the tension elements, the less deformable the structure, i.e., it is stiffer. Compression elements provide the initial force in the tension elements. Together they form a self-equilibrated mechanical system. In response to external forces, tensegrity structures exhibit a stiffening response, i.e., structural stiffness increases with increasing applied force (Wang et al., 1993; Stamenović et al., 1996).

In eukaryotic cells, filamentous biopolymers: actin filaments, microtubules, and intermediate filaments form a network, called the cytoskeleton (CSK), which extends from the cell membrane to the nucleus. It has been noted previously that the CSK lattice plays a major role in providing a cell's shape stability, and that it displays features that are consistent with tensegrity architecture (Ingber and Jamieson, 1985; Ingber, 1993; Wang et al., 1993; Thoumine et al., 1995). First, the CSK contains both tension and compression elements. Actin and intermediate filaments primarily carry tensile forces supported by microtubules which act as compression-resistant struts (Dennerll et al., 1988; Danowski, 1989; Amos and Amos, 1991; Kolodney and Wysolmerski, 1992, Ingber, 1993). In suspended (round) cells, the CSK filaments are believed to form a stable self-equilibrated system. However, in their natural state cells are spread over the extracellular matrix (ECM) to which they are attached through focal adhesion contacts. These are the sites of force transmission between the ECM, across the cell membrane, and tensile stress fibers of the CSK (Ingber, 1993). Thus, in spread cells, the CSK together with the ECM form a self-equilibrated system. A second feature of cells consistent with tensegrity is that they are initially tensed. For example, when cell's attachments to the ECM are severed, the cell rapidly retracts to a round configuration (Sims et al., 1992). Third, the more tensed cells exhibit higher stiffness. Shear measurements on isolated living cells, in which CSK tension has been altered either mechanically (Wang and Ingber, 1994) or pharmacologically (Hubmayr et al., 1996), reveal that more tensed cells are stiffer than less tensed cells. Finally, living cells exhibit stiffening. Data show that CSK shear stiffness increases approximately linearly with increasing applied shear stress (Wang et al., 1993; Wang and Ingber, 1994; Thoumine et al., 1995). This dependence appears to be a fundamental property of living cells and tissues.

We recently extended these qualitative notions into a formal structural analysis (Stamenović et al., 1996). We considered a simple tensegrity structure composed of six rigid struts interconnected with 24 linearly elastic cables (Fig. 1) as a representative model of cellular mechanics. The effect of the ECM on the force balance was bypassed, i.e., the initial tension in the cables was entirely balanced by compression in the struts. The structure was stretched uniaxially and stretching force versus axial extension relationships were obtained for different values of initial cable tension. It was found that structural stiffness, defined as the ratio of applied stretching force to axial extension, increases with increasing initial cable tension. Furthermore, the structure exhibits the stiffening effect, i.e., the structural stiffness increases with increasing stretching force. These features are consistent with the behavior observed in cells. On the other hand, some predicted features differ from those observed in cells. For example, the dependence of structure's stiffness on applied load is in general nonlinear whereas in cells it appears linear (Wang et al., 1993; Wang and Ingber, 1994; Thoumine et al., 1995). Second, the more tensed the structure, the less stiffening it exhibits, contrary to the behavior observed in cells where more distended cells exhibit greater stiffening than less distended ones (Wang and Ingber, 1994). Possible reasons for these discrepancies could be related to model assumptions. For example, it was assumed in the model that cables are extensible and

[1] To whom correspondence should be addressed.

Contributed by the Applied Mechanics Division of THE AMERICAN SOCIETY OF MECHANICAL ENGINEERS for publication in the ASME JOURNAL OF APPLIED MECHANICS.

Discussion on this paper should be addressed to the Technical Editor, Professor Lewis T. Wheeler, Department of Mechanical Engineering, University of Houston, Houston, TX 77204-4792, and will be accepted until four months after final publication of the paper itself in the ASME JOURNAL OF APPLIED MECHANICS.

Manuscript received by the ASME Applied Mechanics Division, July 29, 1996; final revision, Mar. 15, 1997. Associate Technical Editor: J. T. Jenkins.

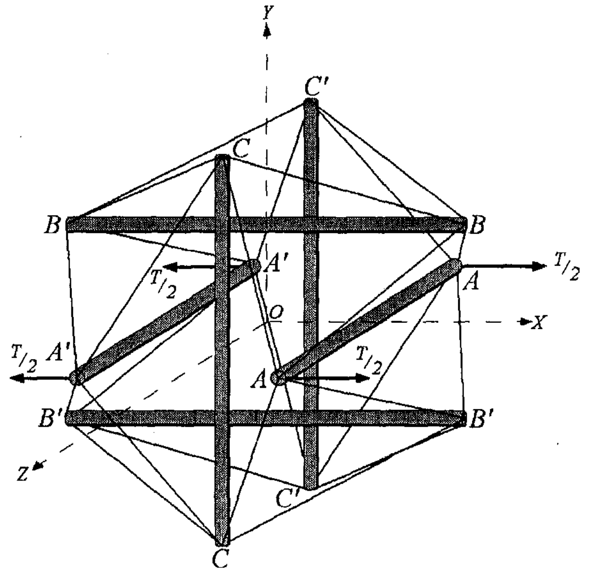

Fig. 1 **Six-strut tensegrity structure. Struts: $\overline{AA}$, $\overline{A'A'}$, $\overline{BB}$, $\overline{B'B'}$, $\overline{CC}$, $\overline{C'C'}$; cables: AB, AC, BC, $A'B$, $A'C$, $B'C$, AB', AC', BC', $A'B'$, $A'C'$, $B'C'$. Stretching force of magnitude $T/2$ (thick arrows) is applied at the endpoints A and A'.**

linearly elastic and that struts are rigid. Measurements on isolated CSK filaments indicate, however, that tension-bearing elements, actin filaments, are very little extensible and that compression-bearing elements, microtubules, buckle under compression (Gittes et al., 1993). According to these measurements, Young's moduli of actin filaments and microtubules are approximately 2.6 and 1.2 GPa, respectively, whereas bending stiffness of microtubules is on the order of 10^{-23} N·m^2. In comparison, the estimated Young's modulus of the endothelial cell does not exceed 10 Pa (Wang and Ingber, 1994). This huge difference in Young's moduli of CSK filaments and the cell suggest that mechanical properties of the filaments alone do not determine cell deformability. Based on our previous tensegrity analysis, we identified the CSK tension and architecture as key determinants of cell deformability (Stamenović et al., 1996). Our purpose here is to show that in addition to these two features, buckling of microtubules is also an important contributor to cell deformability. By allowing the struts in the six-strut tensegrity model to buckle, we could overcome some major shortcomings of the previous model. Moreover, by taking into account the measured values of the elastic moduli for actin filaments and microtubules, we could obtain quantitative predictions of forces and deformations encountered in living cells.

Model Formulation

The tensegrity structure shown in Fig. 1 is composed of six struts interconnected with 24 cable segments. The cables and struts are connected by pin-joints. Initially, the cables carry tensile forces balanced by compression in the struts. The struts are slender and buckle under compression. The origin O of a Cartesian coordinate system $OXYZ$ is placed at the center of the structure with the axes in the direction of the pairs of parallel struts (Fig. 1).

Geometrical Description. At the reference (initial) configuration, all the struts are of the same length (L_0). In the case that the struts are buckled, L_0 is the distance between the endpoints of each strut (chord-length). It is shown below that the corresponding length of the cable segments is $l_0 = \sqrt{3/8}L_0$ and the corresponding distance between the pairs of parallel strut chords is $s_0 = L_0/2$. The structure is stretched uniaxially (X-direction) by applying forces of magnitude $T/2$ at each endpoint of the struts $\overline{AA}$ and $\overline{A'A'}$ (Fig. 1). This causes (a) changes in the chord-lengths of the struts from L_0 to L_I (struts $\overline{AA}$ and $\overline{A'A'}$), L_{II} (struts $\overline{BB}$ and $\overline{B'B'}$), and L_{III} (struts $\overline{CC}$ and $\overline{C'C'}$), (b) changes in the distance between the pairs of parallel strut chords from s_0 to s_X (struts $\overline{AA}$ and $\overline{A'A'}$), s_Y (struts $\overline{BB}$ and $\overline{B'B'}$), and s_Z (struts $\overline{CC}$ and $\overline{C'C'}$), and (c) changes in the length of cable segments from l_0 to l_1 (segments $\overline{AB}$, $\overline{A'B}$, $\overline{AB'}$, $\overline{A'B'}$), l_2 (segments $\overline{AC}$, $\overline{A'C}$, $\overline{AC'}$, $\overline{A'C'}$), and l_3 (segments $\overline{BC}$, $\overline{B'C}$, $\overline{BC'}$, $\overline{B'C'}$). Changes in the distances between a pair of parallel strut chords, $\Delta s_\alpha \equiv s_\alpha - s_0 (\alpha = X, Y, Z)$, are referred to as extensions. Relationships between L_I, L_{II}, L_{III}, s_X, s_Y, s_Z, l_1, l_2, and l_3, are derived below.

Consider the portion of the structure inside the first quadrant of the $OXYZ$ coordinate system; $\overline{AB} = l_1$, $\overline{OA_X} = s_X/2$, $\overline{OB_Y} = s_Y/2$, $\overline{AA_X} = L_I/2$, $\overline{BB_Y} = L_{II}/2$ (Fig. 2). Thus,

$$l_1 = \sqrt{(\overline{BB_Y} - \overline{OA_X})^2 + (\overline{OB_Y})^2 + (\overline{AA_X})^2}$$
$$= \tfrac{1}{2}\sqrt{(L_{II} - s_X)^2 + s_Y^2 + L_I^2}. \quad (1)$$

Expressions for l_2 and l_3 are obtained in a similar manner.

$$l_2 = \tfrac{1}{2}\sqrt{s_X^2 + L_{III}^2 + (L_I - s_Z)^2} \quad (2)$$

$$l_3 = \tfrac{1}{2}\sqrt{L_{II}^2 + (L_{III} - s_Y)^2 + s_Z^2} \quad (3)$$

Equilibrium Equations. Equilibrium of the structure is determined by considering the balance of forces at each joint. These forces include the tensile forces F_1, F_2, and F_3 in cables with lengths l_1, l_2, and l_3, respectively, the compression forces P_I, P_{II}, and P_{III} exerted on struts with chord-lengths L_I, L_{II}, and L_{III}, respectively, and the external stretching force $T/2$ applied at the endpoints A and A' (Fig. 1). The following is obtained:

$$T = 2F_1\frac{s_X - L_{II}}{l_1} + 2F_2\frac{s_X}{l_2} \quad (4)$$

$$F_1\frac{s_Y}{l_1} = F_3\frac{L_{III} - s_Y}{l_3} \quad (5)$$

$$F_2\frac{L_I - s_Z}{l_2} = F_3\frac{s_Z}{l_3} \quad (6)$$

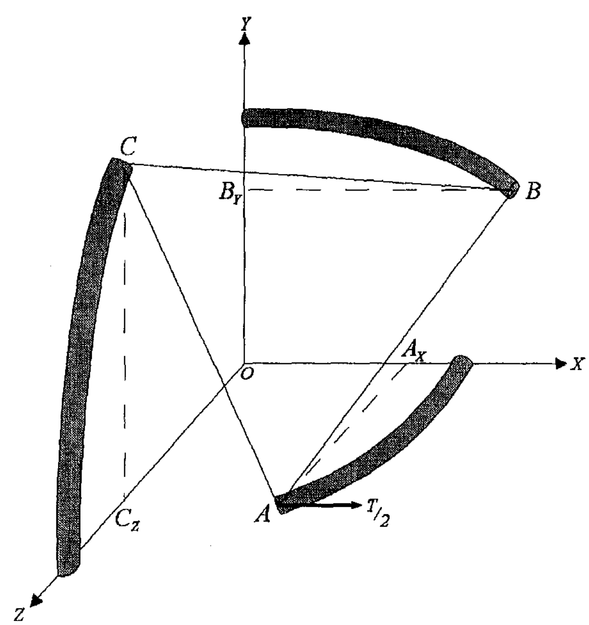

Fig. 2 **The portion of the six-strut tensegrity model from Fig. 1 inside the first quadrant of the $OXYZ$ coordinate system. The struts are buckled and dashed line segments $\overline{AA_X}$, $\overline{BB_Y}$, and $\overline{CC_Z}$ indicate halves of the chord-lengths.**

$$P_I = F_1 \frac{L_I}{l_1} + F_2 \frac{L_I - s_Z}{l_2} \tag{7}$$

$$P_{II} = F_1 \frac{L_{II} - s_X}{l_1} + F_3 \frac{L_{II}}{l_3} \tag{8}$$

$$P_{III} = F_2 \frac{L_{III}}{l_2} + F_3 \frac{L_{III} - s_Y}{l_3}. \tag{9}$$

Equations (4) and (7) represent the balance of forces at the joints A and A' in the X and Z-directions, respectively, Eqs. (5) and (8) represent the balance of forces at the joints B and B' in the Y and X-directions, respectively, and Eqs. (6) and (9) represent the balance of forces at the joints C and C' in the Z and Y-directions, respectively. Force balance at the joints in directions other than indicated above are satisfied by the symmetry of the structure.

Cable Elasticity. It is assumed that the cables are linearly elastic (i.e., Hookean) and carry only tensile forces. Hence, their force versus length relationships are as follows:

$$F_i = \begin{cases} E_c A_c \left(\dfrac{l_i}{l_r} - 1 \right) & \text{if} \quad l_i > l_r \\ 0 & \text{if} \quad l_i \le l_r \end{cases} \qquad (i = 1, 2, 3) \tag{10}$$

where E_c is the Young's modulus of the cable and A_c and l_r are its resting cross-sectional area and length, respectively ($l_r \le l_0$). Since actin filaments are viewed as tension supporting cables in the cell, values for E_c and A_c are taken from data for mechanical properties of isolated actin filaments, $E_c = 2.6$ GPa and $A_c = 18$ nm^2 (Gittes et al., 1993).

Strut Elasticity. The struts are viewed as elastic slender columns which carry compression forces (thrusts) exerted at their endpoints and no lateral forces. Below a critical value of thrust (P^C), the centerline of the strut remains straight and shortens with a linear response given by

$$P_M = E_s A_s \left(1 - \frac{L_M}{L_r} \right) \quad (M = I, II, III) \tag{11}$$

where E_s is the Young's modulus of the strut and A_s and L_r are its resting cross-sectional area and length, respectively ($L_r \ge L_0$). Since microtubules play the role of compression supporting struts in the cell, E_s and A_s are determined from data for mechanical properties of isolated microtubules, $E_s = 1.2$ GPa and $A_s = 190$ nm^2 (Gittes et al., 1993). For a $P_M \ge P^C$, the strut buckles. The post-buckling force-length relationship is determined based on an exact energy formulation of the classical pin-ended Euler strut (Thompson and Hunt, 1969). That is, the strut is considered simply supported, the axial thrust P_M retains its magnitude and direction during deformation and the length of the strut centerline remains constant during buckling.

To calculate the relationship between the thrust P_M and strut chord-length L_M, the shape of the centerline of the buckled strut (i.e., the elastica) is needed. The elastica is described by a function $w_M(x)$ that indicates the local deflection of the centerline from the chord in the buckled configuration ($0 \le x \le L_M$) as shown in Fig. 3. (In Fig. 3 and in further text the subscript M is omitted for simplicity.)

A continuum perturbation analysis is used to determine an expression for $w(x)$. It is given as a power series in the central deflexion $h \equiv w(L/2)$

$$w(x) = hw_1(x) + h^2 w_2(x) + h^3 w_3(x) + \ldots \tag{12}$$

where $w_j(x)$ ($j = 1, 2, 3, \ldots$) are trigonometric functions given in the Appendix. Thrust P is given as a Taylor series in h

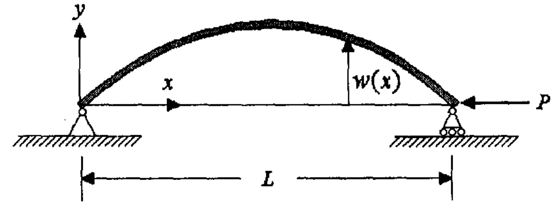

Fig. 3 Elastic column pinned at the endpoints during buckling by axial thrust P; L is the chord-length and $w(x)$ is local deflection ($0 \le x \le L$)

$$P = P^C + hP_1 + \frac{1}{2!} h^2 P_2 + \frac{1}{3!} h^3 P_3 + \ldots \tag{13}$$

where $P^C = \pi^2 B / L_r^2$ is the first critical load, B is bending stiffness of the strut, and each P_k ($k = 1, 2, 3, \ldots$) is associated with the corresponding $w_j(x)$ such that P^C corresponds to w_1, P_1 to w_2, P_2 to w_3, etc. The P_k's are constants depending only on L and B and are given in the Appendix. By substituting Eqs. (12) and (13) into the Euler equation for the strut (Appendix) and identifying terms of the same powers in h, a system of linear differential equations in $w_j(x)$ is obtained. A P_k is determined by finding the nontrivial solution $w_j(x)$ that satisfies the boundary conditions imposed on the ends of the struts (Appendix).

$$L_{el} = \int_0^L \sqrt{1 + w'(x)^2}\, dx \tag{14}$$

The chord-length L of the deformed strut was determined iteratively, using the condition that the total length of the elastica was a constant, equal to the resting length L_r. This procedure is described as follows. For a given thrust P, the central deflexion h is determined from Eq. (13) and an initial value of L that is guessed. These two values, h and L, are substituted into Eq. (12) and $w(x)$ is obtained. The total length of the elastica (L_{el}) is determined by numerical integration where prime denotes differentiation with respect to x. This procedure is repeated until the value of the chord-length is found such that L_{el} matches the known L_r. Computations are performed with Mathematica software. The value of bending stiffness measured in isolated microtubules, $B = 2.15 \times 10^{-23}$ N·m^2 (Gittes et al., 1993), is used. According to Thompson and Hunt (1969), if the expansion of the series (12) and (13) is carried out up to the seventh term ($j = 7$ and $k = 6$), the above procedure yields a good approximation of the thrust versus chord-length (P versus L) relationship for $h < L_r/3$. Thus, only values of h within this range are used in our calculations.

Reference Configuration. Before determining the stretching force versus axial extension relationships of the structure, it is necessary to determine its reference (initial) configuration. At the reference configuration the structure is symmetric, i.e., $L_I = L_{II} = L_{III} \equiv L_0$, $l_1 = l_2 = l_3 \equiv l_0$, $s_X = s_Y = s_Z \equiv s_0$, $P_I = P_{II} = P_{III} \equiv P_0$, and $F_1 = F_2 = F_3 \equiv F_0$. Taking this into account and setting $T = 0$, L_0 is determined directly from Eqs. (1)–(11) as follows. Equations (1)–(9) yield

$$s_0 = L_0/2 \tag{15a}$$

$$l_0 = \sqrt{3/8}\, L_0 \tag{15b}$$

$$P_0 = \sqrt{6}\, F_0. \tag{15c}$$

By substituting Eqs. (10) and (11) into Eq. (15c), L_0 is obtained for the case where the struts are not buckled initially

$$L_0 = \left(1 - \sqrt{6}\, \frac{A_c E_c}{A_s E_s}\, \epsilon \right) L_r, \tag{16}$$

where $\epsilon \equiv l_0/l_r - 1$ is the initial cable strain ($\epsilon \geq 0$). In the case where the struts buckle initially, only Eq. (10) is substituted into Eq. (15c),

$$P_0 = \sqrt{6} E_c A_c \epsilon, \tag{17}$$

and L_0 is determined from the thrust versus chord-length relationship for the post-buckling behavior. Values for E_c, A_c, E_s, and A_s given in the previous section are used, whereas values for ϵ and L_r are chosen arbitrarily (see below). Once L_0 is determined, s_0 and l_0 are obtained from equations (15a) and (15b), respectively, and l_r from l_0 and ϵ. These values are applied to obtain mechanical behavior of the structure during uniaxial stretching.

Structural Elasticity. The stretching force versus axial extension relationships for the model (T versus Δs_X) are obtained by solving Eqs. (1)–(11) simultaneously. In the case when the struts buckle, Eq. (11) is replaced by the P versus L relationship for the post-buckling behavior described above. Solutions are obtained for a given value of ϵ and L_r and a series of values of T, using a Newton-Raphson iterative method. The value of L_r and ϵ are chosen ad hoc; $L_r = 3$ μm and $\epsilon = 0$, 3×10^{-4} and 4×10^{-4}, $L_r = 10$ μm and $\epsilon = 0$, 3×10^{-5} and 4×10^{-5}, and $L_r = 40.85$ μm, and $\epsilon = 0$, 1.8×10^{-6} and 2.5×10^{-6}. The choice $L_r = 3$ μm is influenced by the length of the segments of microtubules observed in electron micrographs of the CSK (cf. Amos and Amos, 1991), whereas $L_r = 40.85$ μm is the average length of isolated microtubules in the experiments of Gittes et al. (1993). The value of T increases until a thrust (P_I, P_{II}, or P_{III}) exceeds the value which results in the central deflection $h \gtrsim L_r/3$. Once the T versus Δs_X relationship is obtained, the structural stiffness is determined as the ratio $K \equiv T/\Delta s_X$. The above calculations were performed using TK Solver Plus software.

Results and Discussion

Results of the above analysis are shown only for the model with struts of resting length $L_r = 3$ μm. Results obtained with the models with L_r's of 10 and 40.85 μm are qualitatively similar.

The post-buckling axial thrust versus chord-length behavior (P versus L) for a strut with a resting length $L_r = 3$ μm is shown in Fig. 4. Once the thrust reaches the critical value $P^C = 23.578$ pN, it increases nearly hyperbolically with decreasing chord-length. This relationship is used to calculate the response of the model to uniaxial stretching.

The behavior of the model during stretching is depicted in Figs. 5–8. The applied stretching force T increases nonlinearly with increasing axial extension Δs_X of the structure (Fig. 5). This dependence is greater at higher initial cable strain ϵ (i.e., higher initial cable tension F_0). It differs from the Hookean behavior of cables (10) and struts before buckling (11) as well as from the strut post-buckling behavior (Fig. 4). Thus, mechanical properties of individual structural components are not sole determinants of the structure's response to stretching. The structure's architecture and F_0 play important roles as well as shown in our earlier tensegrity analysis (Stamenović et al. 1996).

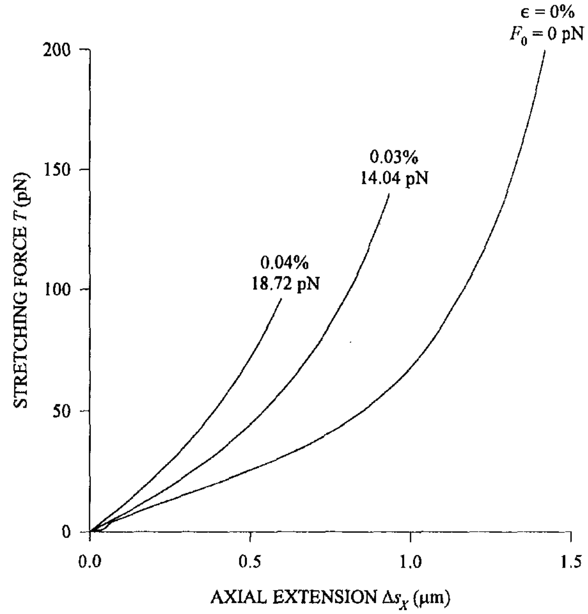

Fig. 5 Stretching force T versus axial extension Δs_X relationship for the six-strut tensegrity structure with struts of resting length $L_r = 3$ μm, for initial cable strain ϵ of 0, 0.03, and 0.04 percent, i.e., initial cable tension F_0 of 0, 14.04, and 18.72 pN, respectively.

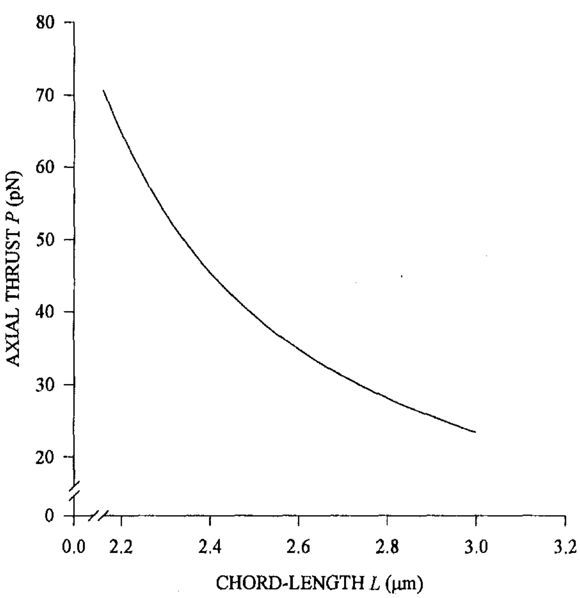

Fig. 4 Post-buckling axial thrust P versus chord-length L relationship for the pinned elastic column of resting length $L_r = 3$ μm

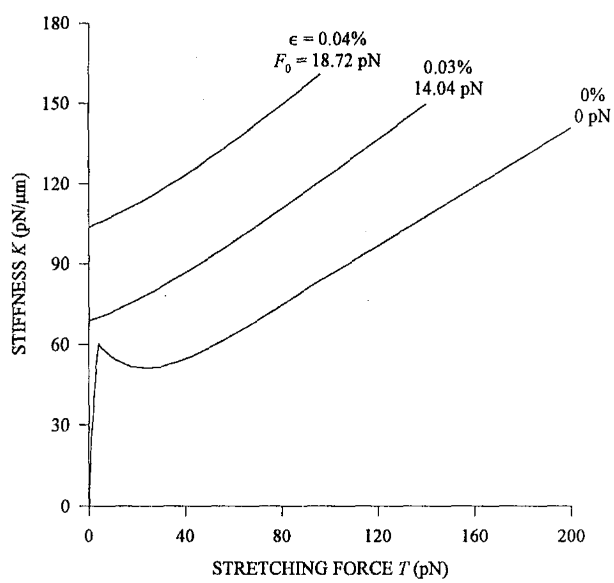

Fig. 6 Structural stiffness K versus stretching force T relationship for the six-strut tensegrity structure with struts of resting length $L_r = 3$ μm, for initial cable strains ϵ of 0, 0.03, and 0.04 percent, i.e., initial cable tension F_0 of 0, 14.04 and 18.72 pN, respectively.

From the T versus Δs_X relationship it is obtained that the structural stiffness K increases with increasing F_0, and at a given F_0, K increases with increasing T (i.e., stiffening) (Fig. 6). The dependence of K on T is nearly linear in the examined range of Δs_X, except in the case where $F_0 = 0$ with K exhibiting a peak during initial stretching (Fig. 6). This peak is related to the onset of buckling in the struts (see below). Results in Fig. 6 also show that the stiffening is somewhat greater at higher F_0, i.e., K versus T curves obtained at different F_0's exhibit a slight splay with increasing T.

The above findings are the most significant results of this analysis for a number of reasons. First, they are consistent with the behavior observed in living cells (Wang and Ingber, 1994; Thoumine et al., 1995; Hubmayr et al., 1996). Second, the apparent linearity and slight splay of the stiffening curves in Fig. 6 cannot be obtained from our previous tensegrity analysis where the struts are viewed as rigid (Stamenović et al., 1996). This in turn suggests that buckling of the CSK compression-bearing elements (i.e., microtubules) is a key determinant of cell deformability. Third, this stiffening response, which characterizes mechanical behavior of cells and tissues, has so far been predicted by either empirical relationships (cf. Mow et al., 1992) or phenomenological models (Frisén et al., 1969). Here it is derived starting from a physically plausible model and first principles. Finally, by identifying the cables as actin filaments and struts as microtubules, the present model predicts forces and deformation which are of the same order of magnitude as

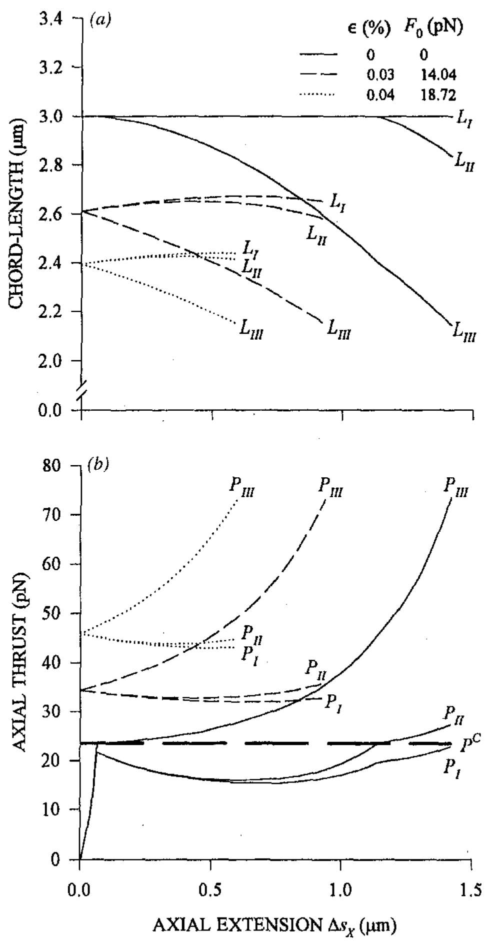

Fig. 7 Relationships of (a) chord-lengths L_I, L_{II}, and L_{III} and (b) corresponding thrusts P_I, P_{II}, and P_{III} versus axial extension Δs_X of the structure with struts of resting length $L_r = 3$ μm, for initial cable strains ϵ of 0, 0.03, and 0.04 percent, i.e., initial cable tension F_0 of 0, 14.04, and 18.72 pN, respectively. A heavy dashed line in panel (b) indicates the critical thrust $P^C = 23.578$ pN.

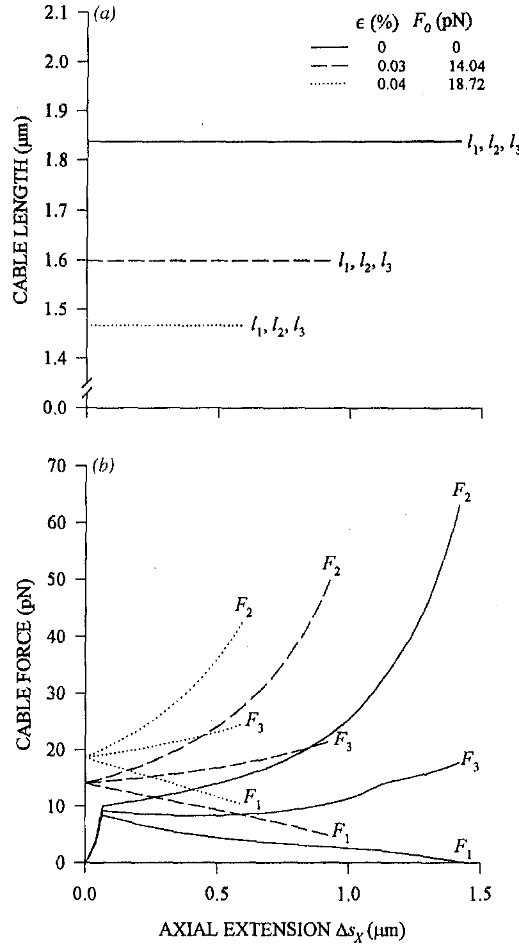

Fig. 8 Relationships of (a) cable lengths l_1, l_2, and l_3 (b) corresponding cable forces F_1, F_2, and F_3 versus axial extension Δs_X of the structure with struts of resting length $L_r = 3$ μm, for initial cable strains ϵ of 0, 0.03, and 0.04 percent, i.e., initial cable tension F_0 of 0, 14.04, and 18.72 pN, respectively.

those observed in cells (Dennerll et al., 1988; Wang and Ingber, 1994). The model with rigid struts, on the other hand, yields high overestimates of forces and deformations.

An important feature follows from the case where the model is not initially tensed (i.e., where $F_0 = 0$). In that case, the model lacks intrinsic resistance to shape distortion, i.e., $K = 0$ when $T = 0$ (Fig. 6). Thus, an $F_0 > 0$ is needed to provide an initial stiffness to the structure. This behavior characterizes many biological structures (e.g., cells, lungs, cartilage, plant leaves, spider webs) as well as nonbiological structures (e.g., soap foams, tents), all of which are known or are believed to lack shape stability unless initial tensed, and all of which appear to be designed according to the rules of tensegrity.

It is instructive to consider how the lengths and forces of individual members change during uniaxial stretching of the structure. Figures 7(*a*) and 7(*b*) depict the changes in chord-length and thrust of the struts, respectively. The values of chord-length and thrust at $\Delta s_X = 0$ are the initial chord-lengths L_0 (Fig. 7(*a*)) and the initial thrusts P_0 (Fig. 7(*b*)). Chord-lengths of each strut decrease with increasing initial cable tension F_0 (Fig. 7(*a*)). For $F_0 = 0$, only the struts with chord-length L_{III} buckles during initial stretching of the structure. The remaining struts shorten without buckling until Δs_X reaches ~1.16 μm when the buckling in the struts of length L_{II} occurs (Fig. 7(*a*)). The struts of length L_I do not buckle within the examined range of Δs_X. For ϵ of 0.03 and 0.04 percent (i.e., F_0 of 14.04 and 18.72 pN, respectively), all struts buckle even before imposing a T (Fig. 7(*a*)). At each of these F_0, the chord-length L_{III}

shortens with increasing Δs_X while the others, L_I and L_{II}, first increase slightly before shortening but the struts remain buckled all the time. The above features can be also seen from the plot of thrust exerted by the struts versus Δs_X, for different values of ϵ (Fig. 7(b)). The heavy dashed line in Fig. 7(b) indicates the critical load P^C in the struts. When the thrust force lies above this line, the strut is buckled and vice versa. The fact that in the initially tensed structure the struts buckle even before the stretching force is applied may explain the bent-shaped appearance of microtubules on the immunofluorescent views of the CSK (Amos and Amos, 1991).

During axial stretching of the structure, cables change their lengths very little as shown in Fig. 8(a). A better insight into changes of cable lengths can be obtained from the plots of cable forces versus axial extension Δs_X (Fig. 8(b)). For a given F_0, F_2 and F_3 increase with increasing Δs_X, indicating that the corresponding cable lengths l_2 and l_3 also increase. The opposite was found for F_1 which decreases with increasing Δs_X. Force F_1 does not reach a zero value within the examined range of Δs_X and hence, the corresponding cables do not attain the resting length l_r. The "kinks" in the force versus length relationships for $F_0 = 0$ (Fig. 8(b)) correspond to the onset of buckling in the struts.

It should be mentioned that the six-strut tensegrity structure has cubic symmetry and therefore it is anisotropic. Details about the degree of anisotropy can be found in Stamenović et al. (1996).

Concluding Remarks

The analysis presented in this study suggests that a simple tensegrity structure composed of linearly elastic cables and slender struts which buckle under compression can mimic the behavior observed in living cells exposed to mechanical stresses. Moreover, by identifying the tensile and compressive force-bearing components of the model with the corresponding elements in the CSK, it was possible to obtain quantitative predictions of forces and deformations which fall within the same order of magnitude as those observed in cells. The key features which determine the structure's response to stretching are initial cable tension, architecture and buckling of struts under compression. The buckling of the struts appears to be crucial for providing good correspondence between model behavior and observations in cells. Previous analysis which employed the same model but viewed the struts as rigid, yields less accurate qualitative and highly overestimated quantitative predictions of mechanical properties of the cell.

It is important to note that the simple static six-strut tensegrity structure employed in this study is only a crude representation of the CSK, which is an architecturally more complex dynamic structure, which expresses its mechanical behavior by interacting with the ECM. Here, the ECM was not explicitly considered. Even so, this simple model of the CSK could capture the main features that characterize a cell's response to mechanical stresses.

Acknowledgment

This study was supported by National Heart, Lung, and Blood Institute Grant HL-33009.

References

Amos, L. A., and Amos, W. B., 1991, *Molecules of the Cytoskeleton*, Guilford Press, New York.

Danowski, B. A., 1989, "Fibroblast contractility and actin organization are stimulated by microtubule inhibitors," *Journal of Cell Science*, Vol. 93, pp. 255–266.

Dennerll, T. J., Joshi, H. C., Steel, V. L., Buxbaum, R. E., and Heidemann, S. R., 1988, "Tension and compression in the cytoskeleton of PC-12 neurites II: Quantitative measurements," *Journal of Cell Biology*, Vol. 107, pp. 665–674.

Frisén, M., Mägi, M., Sonnerup, I., and Viidik, A., 1969, "Rheological analysis of soft collagenous tissue—I," *Journal of Biomechanics*, Vol. 2, pp. 13–20.

Fuller, B., 1961, "Tensegrity," *Portfolio Artnews Annual*, Vol. 4, pp. 112–127.

Gittes, F., Mickey, B., Nettleton, J., and Howard, J., 1993, "Flexural rigidity of microtubules and actin filaments measured from thermal fluctuations in shape," *Journal of Cell Biology*, Vol. 120, pp. 923–934.

Hubmayr, R. D., Shore, S. A., Fredberg, J. J., Planus, E., Panettieri, R. A., Jr., Moller, W., Heyder, J., and Wang, N., 1996, "Pharmacological activation changes stiffness of cultured human airway smooth muscle cells," *American Journal of Physiology*, Vol. 271 (*Cell Physiology*, Vol. 40), pp. C1660–C1668.

Ingber, D. E., 1993, "Cellular tensegrity: defining new rules of biological design that govern the cytoskeleton," *Journal of Cell Science*, Vol. 104, pp. 613–627.

Ingber, D. E., and Jamieson, J. D., 1985, "Cells as tensegrity structures: Architectural regulation of hystodifferentiation by physical forces transduced over basement membrane," *Gene Expression During Normal and Malignant Differentiation*, L. C. Anderson, C. G. Gahmberg, and P. Ekblom, eds., Academic Press, London, pp. 13–32.

Kolodney, M. S., and Wysolmerski, R. B., 1992, "Isometric contraction of fibroblasts and endothelial cells in tissue culture: A quantitative study," *Journal of Cell Biology*, Vol. 117, pp. 73–82.

Mow, V. C., Ratcliffe, A., and Poole, A. R., 1992, "Cartilage and diarthrodial joints as paradigms for hierarchical materials and structures," *Biomaterials*, Vol. 13, pp. 67–97.

Pugh, A., 1976, *Introduction to Tensegrity*, University of California Press, Berkeley, CA.

Sims, J. R., Karp, S., and Ingber, D. E., 1992, "Altering the cellular mechanical force balance results in integrated changes in cell, cytoskeletal and nuclear shape," *Journal of Cell Science*, Vol. 103, pp. 1215–1222.

Stamenović, D., Fredberg, J. J., Wang, N., Butler, J. P., and Ingber, D. E., 1996, "A microstructural approach to cytoskeletal mechanics based on tensegrity," *Journal of Theoretical Biology*, Vol. 181, pp. 125–136.

Thompson, J. M. T., and Hunt, G. W., 1969, "Comparative perturbation studies of the elastica," *International Journal of Mechanical Sciences*, Vol. 11, pp. 999–1014.

Thoumine, O., Ziegler, T., Girard, P. R., and Nerem, R. M., 1995, "Elongation of confluent endothelial cells in culture: The importance of fields of force in the associated alterations of their cytoskeletal structure," *Experimental Cell Research*, Vol. 219, pp. 427–441.

Wang, N., and Ingber, D. E., 1994, "Control of cytoskeletal mechanics by extracellular matrix, cell shape, and mechanical tension," *Biophysical Journal*, Vol. 66, pp. 2181–2189.

Wang, N., Butler, J. P., and Ingber, D. E., 1993, "Mechanotransduction across the cell surface and through the cytoskeleton," *Science*, Vol. 260, pp. 1124–1127.

APPENDIX

The Euler equation for the axially loaded pin-ended strut (Thompson and Hunt, 1969) is given by

$$\frac{w''''}{1 - w'^2} + \frac{4w'''w''w'}{(1 - w'^2)^2} + \frac{w''^3(1 + 3w'^2)}{(1 - w'^2)^3} + \frac{P}{B}\frac{w''}{(1 - w'^2)^{3/2}} = 0 \quad \text{(A1)}$$

where $w = w(x)$ and primes denote derivatives with respect to x. The boundary conditions are

$$w(0) = w''(0) = 0,$$

$$w(L) = w''(L) = 0.$$

The denominators of each term in Eq. (A1) can be expanded as a Binomial series giving the expanded form of the Euler equation

$$w''''[1 + w'^2 + w'^4 + \ldots] + 4w'''w''w'[1 + 2w'^2 + 3w'^4 + \ldots] + w''^3[1 + 6w'^2 + 15w'^4 + \ldots] + \frac{P}{B}w''[1 + \frac{3}{2}w'^2 + \frac{15}{8}w'^4 + \ldots] = 0. \quad \text{(A2)}$$

By substituting Eqs. (12) and (13) into Eq. (A2) and collecting like powers of h, a system of linear differential equations that can be solved sequentially is obtained. The coefficients of the first powers of h result in the equation

$$w_1'''' + \frac{P^C}{B} w_1'' = 0$$

with a solution

$$w_1(x) = \sin\left(\frac{\pi x}{L}\right).$$

In solving for $w_1(x)$, a nontrivial solution that satisfies the boundary conditions requires that

$$P^C = \left(\frac{\pi}{L}\right)^2 B.$$

The coefficients of h^2 and all even powers of h result in the same solutions

$$P_k = 0 \quad \text{for } k \text{ odd}$$

$$w_j(x) = 0 \quad \text{for } j \text{ even.}$$

The coefficients of h^3 result in

$$P_2 = \frac{1}{4} B\left(\frac{\pi}{L}\right)^4$$

$$w_3(x) = -\left(\frac{\pi}{8L}\right)^2\left(\sin\frac{\pi x}{L} + \sin\frac{3\pi x}{L}\right).$$

The coefficients of h^5 give

$$P_4 = \frac{57}{64} B\left(\frac{\pi}{L}\right)^6$$

$$w_5(x) = -\left(\frac{\pi}{8L}\right)^4\left(17\sin\frac{\pi x}{L} + 16\sin\frac{3\pi x}{L} - \sin\frac{5\pi x}{L}\right).$$

The coefficients of h^7 give

$$P_6 = \frac{1305}{128} B\left(\frac{\pi}{L}\right)^8$$

$$w_7(x) = \left(\frac{\pi}{8L}\right)^6\left(395\sin\frac{\pi x}{L} + 2\sin\frac{3\pi x}{L} - 32\sin\frac{5\pi x}{L} + \sin\frac{7\pi x}{L}\right).$$

Similar calculations can be made for coefficients of higher orders in h.

Dynamic Constitutive and Failure Behavior of a Two-Phase Tungsten Composite

M. Zhou
George W. Woodruff School of Mechanical Engineering, Georgia Institute of Technology, Atlanta, GA 30332-0405
Assoc. Mem. ASME

R. J. Clifton
Division of Engineering, Brown University, Providence, RI 02912
Mem. ASME.

The constitutive response and failure behavior of a W-Ni-Fe alloy over the strain rate range of 10^{-4} to 5×10^{5} s^{-1} is experimentally investigated. Experiments conducted are pressure-shear plate impact, torsional Kolsky bar, and quasi-static torsion. The material has a microstructure of hard tungsten grains embedded in a soft alloy matrix. Nominal shear stress-strain relations are obtained for deformations throughout the experiments and until after the initiation of localization. Shear bands form when the plastic strain becomes sufficiently large, involving both the grains and the matrix. The critical shear strain for shear band development under the high rate, high pressure conditions of pressure-shear is approximately 1–1.5 or 6–8 times that obtained in torsional Kolsky bar experiments which involve lower strain rates and zero pressure. Shear bands observed in the impact experiments show significantly more intensely localized deformation. Eventual failure through the shear band is a combination of grain-matrix separation, ductile matrix rupture, and grain fracture. In order to understand the effect of the composite microstructure and material inhomogeneity on deformation, two other materials are also used in the study. One is a pure tungsten and the other is an alloy of W, Ni, and Fe with the same composition as that of the matrix phase in the overall composite. The results show that the overall two-phase composite is more susceptible to the formation of shear bands than either of its constituents.

1 Introduction

Tungsten heavy alloys (WHA or tungsten composites) are characterized by high density, high strength, and high toughness resulting from their composite microstructures of hard tungsten grains embedded in a ductile matrix. Because of these properties and such qualities as good machinability, low cost, and nonradioactivity, they are candidate materials for kinetic energy penetrators. Traditionally, the mechanical properties of these materials have been studied by means of tensile and compressive tests under quasi-static or low strain rate conditions, Churn et al. (1984), O'Donnell et al. (1990), Rabin et al. (1988), Krock et al. (1963), and Krock (1964). However, WHA with different properties as characterized by such tests have demonstrated similar penetrating capabilities which are worse than that of depleted Uranium (see e.g., Magness (1992)), suggesting that the behavior of these materials under impact conditions are dominated by deformation and failure mechanisms not accounted for by such material properties as tensile strengths and ductility. Magness (1992) also reported that the performance of penetrator materials depends strongly on the formation of shear bands. Specifically, the localization of plastic deformation associated with the development of shear bands and the eventual material failure significantly improve the performance of these penetrators by allowing deformed materials to be discarded. Zurek et al. (1995) compared the behavior of a tungsten composite with that of a depleted Uranium over the strain rate range of 10^{-3} to 6000 s^{-1} and suggested that the enhanced susceptibility to shear localization of the Uranium is due to the existence of a soft high-temperature phase. Indeed, the dynamic process involves material deformation at high strain rates and high hydrostatic pressures. Under such conditions, more deformation and failure mechanisms are operative than those found in the quasi-static tests, including rate sensitivity, thermal softening, and the effect of inertia.

Investigations have indicated that WHA demonstrate significant rate sensitivity between low and moderate strain rates. Woodward et al. (1985) studied the effect of strain rate on the flow stress of three WHA over the range of 10^{-3} to 10^{3} s^{-1} and reported an increase of flow stress with increasing strain rate. Thermal softening was observed for strain rates greater than 2 s^{-1}. Coates et al. (1990a, 1990b, 1992) found a 25 percent increase in flow stress at a strain of 8 percent over the strain rate range of 10^{-4} to 7×10^{3} s^{-1} in alloys containing 90 percent to 97 percent W. Increasing strength and decreasing ductility with increasing strain rates in tensile and compression tests have also been reported by Meyer et al. (1983). Andrews et al. (1992) and Weerasooriya et al. (1992) studied the formation of shear bands in WHA using torsional Kolsky bar experiments. Shear bands observed under their test conditions have an average width of 50—100 μm and the critical strain at which shear bands form is approximately 0.15–0.25. Andrews et al. (1992) also found that the peak temperature in the shear bands is about 580°C and axial pressures delay the process of shear band formation. The behavior of tungsten composites at strain rates up to 8×10^{4} s^{-1} has also been analyzed by Baek et al. (1994), Belk et al. (1994), Weerasooriya (1994), Weerasooriya et al. (1994), Woodward et al. (1994), Tham et al. (1995), Yadav et al. (1995), and Zhao et al. (1995).

Higher strain rates and higher pressures exist in penetration. In order to improve the performance through revisions in material design and processing, it is necessary to characterize the material behavior under high-rate and high-pressure conditions similar to those in actual applications. This need calls for experiments that involve strain rates up to 10^{6} s^{-1} and pressures up to 8–10 GPa. Pressure-shear plate impact, as described by Clif-

Contributed by the Applied Mechanics Division of THE AMERICAN SOCIETY OF MECHANICAL ENGINEERS for publication in the ASME JOURNAL OF APPLIED MECHANICS.

Discussion on the paper should be addressed to the Technical Editor, Professor Lewis T. Wheeler, Department of Mechanical Engineering, University of Houston, Houston, TX 77204-4792, and will be accepted until four months after final publication of the paper itself in the ASME JOURNAL OF APPLIED MECHANICS.

Manuscript received by the ASME Applied Mechanics Division, Mar. 4, 1996; final revision, Nov. 4, 1996. Associate Technical Editor: W. N. Sharpe, Jr.

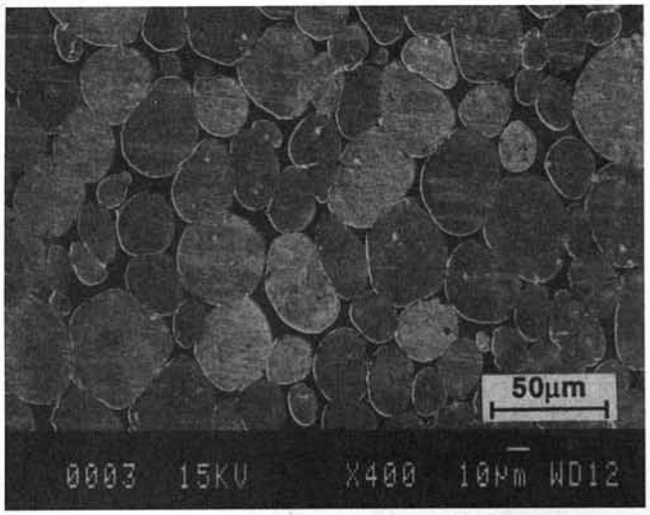

(a)

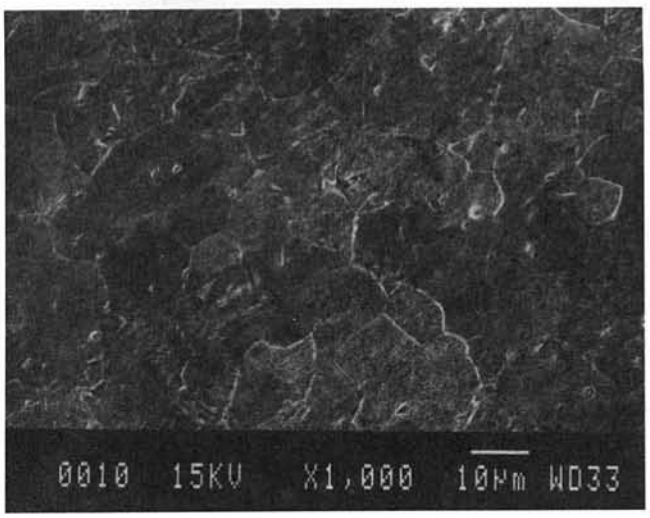

(b)

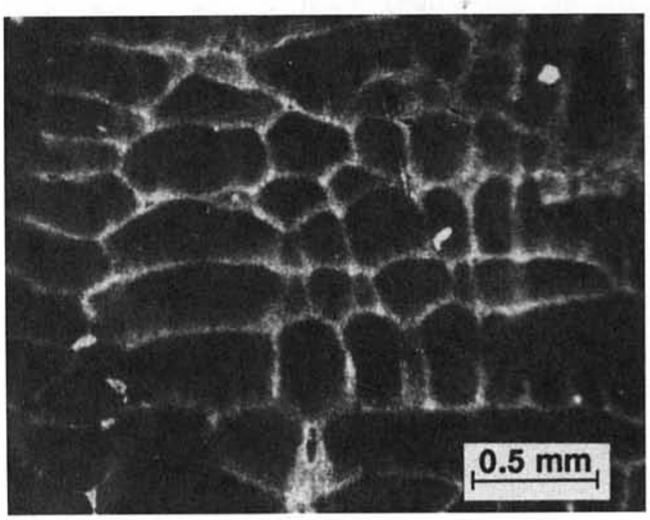

(c)

Fig. 1 Microstructures of materials used; (*a*) tungsten composite, (*b*) pure tungsten, and (*c*) matrix alloy

ton et al. (1985), provides an attractive means for achieving such strain rates and pressures under well-characterized plane-strain conditions. In this investigation, controlled shear band formation is studied using the pressure-shear configuration. In addition, constitutive responses at intermediate and quasi-static strain rates are studied using a torsional Kolsky bar apparatus. The combined pressure-shear impact, torsional Kolsky bar, and quasi-static torsion experiments allow material responses over the strain rate range of 10^{-4} to 10^{6} s^{-1} to be characterized.

2 Materials

Figure 1(*a*) shows the microstructure of the tungsten heavy alloy used in the study. This microstructure consists of tungsten grains embedded in a matrix phase of nickel, iron, and tungsten. This material contains 93wt%–W, 4.9wt%–Ni and 2.1wt%–Fe. In order to understand the effects of the two-phase microstructure and material inhomogeneities on the behavior of the alloy, a pure tungsten and a Ni-W-Fe alloy are used to determine the responses of the two constituent phases in the composite. The matrix alloy, having a composition of 50wt%–Ni, 25wt%–Fe, and 25wt%–W, is custom made to match the the composition of the matrix phase (Ekbom, 1981; O'Donnell et al., 1990; Hofmann et al., 1984) in the composite. All materials are sintered and cross-rolled along two perpendicular directions in the rolling plane to a thickness reduction of eight percent in each direction to obtain comparable dislocation structures so that direct comparisons could be made between the response of the WHA and its constituents. The microstructures of the pure tungsten and the matrix alloy are shown in Figs. 1(*b*) and 1(*c*), respectively.

3 Experiments

In the pressure-shear plate impact experiment, the specimen is a disk 50 μm to 200 μm in thickness. The specimen material is subjected to simple shear for 2 μs at nominal shear strain rates between 10^5 and 10^6 s^{-1}, under pressures on the order of 8–10 GPa. Because of its well-characterized plane-strain conditions, this experiment is an excellent configuration for studying material constitutive response at very high strain rates when uniform deformation is sustained in the specimen. This experiment also allows the onset of shear localization and the development of a shear band to be interpreted from the stress-time and stress-strain profiles. Since the specimen has no free surface, shear band initiation and development are insensitive to macroscopic geometrical defects, which may significantly influence the initiation and development of shear bands in other experimental configurations, such as torsional Kolsky bar (Mol-

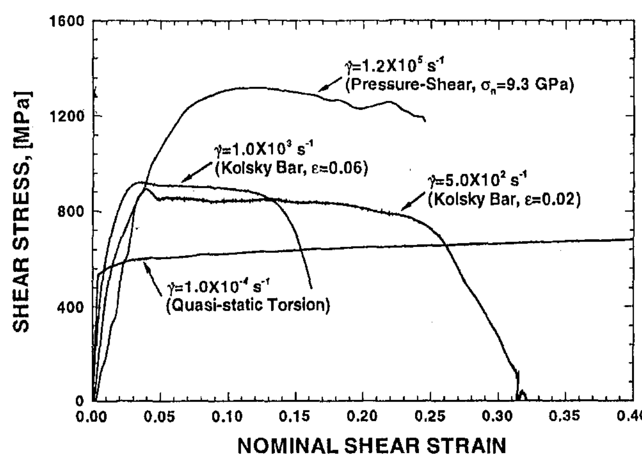

Fig. 2 Shear stress-strain curves of WHA obtained from pressure-shear plate impact, torsional Kolsky bar, and quasi-static torsion experiments

Table 1 Pressure-shear experiment on WHA, W, and matrix alloy

Shot #	Specimen Material	Projectile Velocity mm/μs	Skew Angle °	Normal Pressure MPa	Shear Stress MPa	Shear Rate $\times 10^5 s^{-1}$	Specimen Thickness μm	Shear Band
9109	WHA	0.181	21.5	8981	1100	0.14	1973	No
9201	WHA	0.188	22.0	9326	1300	1.2	201	No
9205	WHA	0.205	21.5	10689	1350	3.9	78	Yes
9206	WHA	0.202	26.6	9629	1300	5.4	87	Yes
9207	WHA	0.213	22.0	10555	1350	4.0	89	Yes
9209	WHA	0.205	18.0	10430	1290	3.5	61	No
9211	WHA	0.205	21.5	10174	1250	6.5	57	Yes
9303	WHA	0.198	22.9	9748	1320	4.2	79	Yes
9301	W	0.198	22.9	9733	1250	4.2	91	No
9302	W	0.206	22.9	10142	1320	2.5	151	No
9208	Matrix	0.200	18.0	10146	680	3.0	129	No
9212	Matrix	0.199	21.5	9910	780	9.0	55	No

inari et al., 1987). Table 1 summarizes the pressure-shear plate impact experiments conducted on the WHA, the pure tungsten, and the matrix alloy.

Torsional Kolsky bar experiments are conducted on the matrix alloy. In addition, data from similar experiments conducted by Andrews et al. (1992) on the same WHA are used in the discussions. This experiment has been described in, e.g., Hartley et al. (1985), Duffy et al. (1971), and Costin et al. (1979). Quasi-static torsion experiments are conducted on the torsional Kolsky bar apparatus with minor modifications. Table 2 summarizes the torsional Kolsky bar and quasistatic torsion experiments conducted on the matrix alloy. Tests at elevated temperatures of 200°C and 250°C were conducted to gain information on the temperature dependence of the stress-strain curves.

4 Experimental Results

4.1 Shear Band Formation and Strain-Rate Effect. Figure 2 shows the shear stress-strain curves of the WHA at different strain rates obtained by pressure-shear impact, torsional Kolsky bar, and quasi-static torsion. Over the strain rate range of 10^{-4} to 1.2×10^5 s^{-1} shown, the flow stress level increases 2.5 times (from 570 to 1360 MPa), suggesting a strong rate sensitivity of the stress-strain relation. The alloy shows strain hardening under the quasi-static strain rate. The curves at the higher strain rates indicate strain softening of the material. This decrease in stress with increasing strain is attributed to thermal softening due to heat generated by the plastic deformation and the lack of time for the heat to be diffused out of the specimen. The precipitous drops in stress shown by the Kolsky bar curves indicate the onset of shear localization. The critical strains at which shear bands form are between 0.12–0.25. The defect parameter ϵ, defined as the maximum wall thickness variation in the gauge section of the specimen divided by the average wall thickness, has a strong influence on the critical strain for shear localization. No sharp downturn in stress is seen in the curve obtained by pressure-shear impact although the overall rate of strain softening and the amount of accumulated shear strain are comparable to those in the Kolsky bar curves. This lack of quick loss of stress-carrying capability signifies that no localization has occurred, as confirmed by the deformed microstructure of the specimen (see the next section). The continuation of uniform deformation beyond the critical shear strains of the torsional experiments suggests that the formation of shear bands have been delayed under conditions of the impact experiment.

Shear localization is observed in impact experiments as the total amount of shear strain is increased by decreasing the specimen thickness and increasing impact velocity and impact angle. Figure 3 shows the stress-strain curves from three shots involving specimens 57–87 μm in thickness and impact angles of 18–26.6°. The sharp downturns in the curves of the two higher angle shots (9206 and 9211) signify the loss of stress-carrying capability associated with the onset of shear localization. The critical shear strains at the onset of localization are between 1–1.5. These values are six to eight times those obtained in the torsional Kolsky bar experiments (Fig. 2). Several factors may contribute to delaying shear band formation in pressure-shear

Table 2 Torsional experiments on matrix alloy

Specimen #	Test Temperature °C (K)	Nominal Shear Strain Rate s^{-1}	Flow Stress MPa	Defect Parameter ϵ	Shear Band
M1	250 (523)	1.3×10^3	430	0.118	No
M2	20 (293)	0.5×10^3	570	0.147	No
M3	200 (473)	1.5×10^3	490	0.123	No
M4	20 (293)	1.4×10^3	580	0.095	No
M6	20 (293)	2.7×10^3	590	0.054	No
M7	20 (293)	2.6×10^3	590	0.062	No
M8	250 (523)	2.7×10^3	400	0.130	No
M9	20 (293)	$\sim 1.0 \times 10^{-4}$	320	0.086	No
M11	20 (293)	$\sim 1.0 \times 10^{-4}$	350	0.120	No

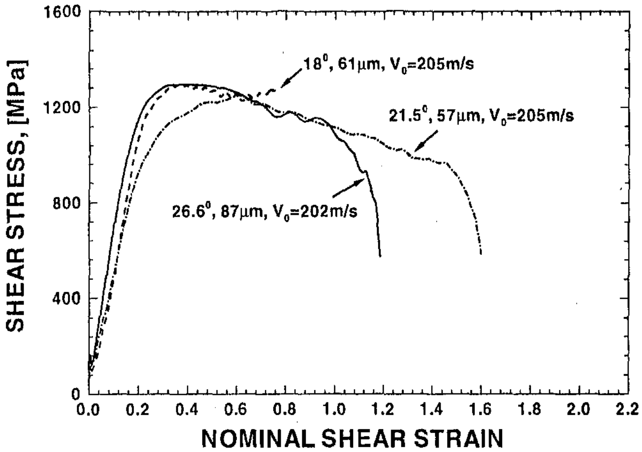

Fig. 3 Dynamic shear stress-strain curves of WHA obtained by pressure-shear plate impact

impact. Higher strain rates cause the material to flow at higher levels of stress. This increase in stress tends to stabilize the localization of deformation through higher flow stresses inside emerging shear bands where strain rates are higher. Normal pressures applied to the specimen during impact suppress the development of microvoids which would develop in the absence of pressure. This retardation reduces the additional softening caused by progressive microrupture. The normal pressure on the specimen makes the pressure-shear configuration insensitive to macroscopic geometric variations of the specimen. Such variations expedite the initiation and development of shear bands in the torsional Kolsky bar configuration (Molinari et al., 1987). Material inertia effect at high rates of deformation may also delay the development of shear bands.

4.2 Microscopic Observations. A series of scanning electron micrographs are obtained to show the deformation of the phases, the morphology of the shear bands, and the damage mechanisms that are responsible for eventual failure of the material inside the shear bands. The deformed microstructure of the specimen corresponding to the stress-strain curve in Fig. 2 that is obtained from pressure-shear impact is shown in Fig. 4. The elliptical grain shapes demonstrate the direction of the shear deformation. The deformation appears to be uniform across the thickness and no shear band is observed. This observation is consistent with the shape of the stress-stress curve in Fig. 2 which does not show a sharp drop in stress.

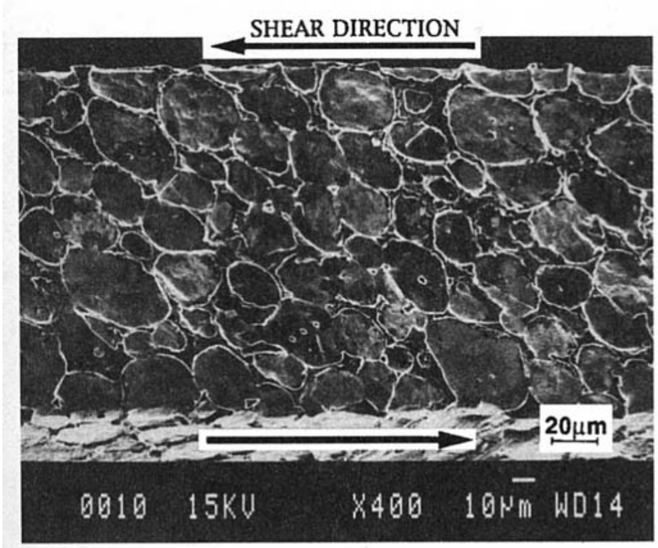

Fig. 4 Deformed microstructure of WHA after pressure-shear impact, V_0 = 188 ms^{-1}, θ = 22 deg, and h = 201 μm

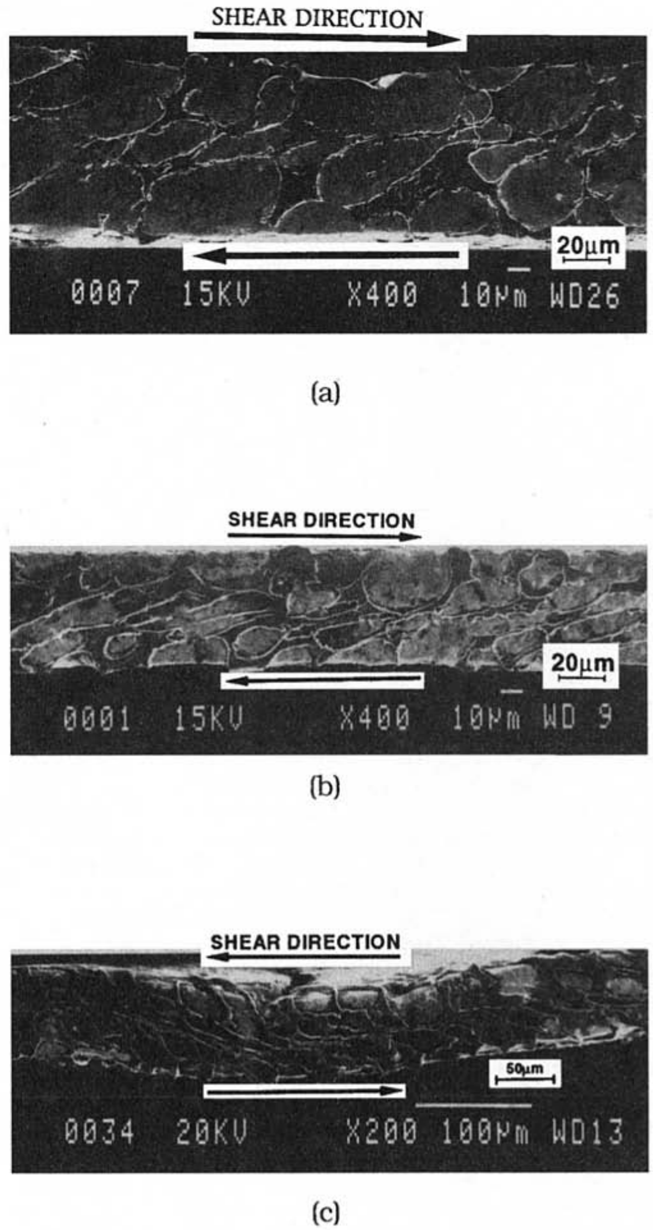

Fig. 5 Shear band morphologies in specimens after pressure-shear plate impact; (a) V_0 = 205 ms^{-1}, θ = 21.5 deg, and h = 78 μm, sheared for 1.44 μs, (b) V_0 = 205 ms^{-1}, θ = 21.5 deg, and h = 57 μm, sheared for 2 μs, and (c) V_0 = 202 ms^{-1}, θ = 26.6 deg, and h = 87 μm, sheared for 2 μs

Figure 5 shows shear band morphologies at different stages of development. The specimens are subjected to successively more intense shear loading. All three shots have similar impact velocities between 202–205 ms^{-1} and the specimens are 57–87 μm in thickness. Figure 5(a) shows the deformed microstructure of a specimen sheared for approximately 1.44 μs. The micrograph shows a nucleating band at the center of the specimen. A neck has formed in the tear-drop-shaped grain. Further development of the band would involve shearing of this grain and propagation on both sides of the nucleating band. Figure 5(b) shows the morphology of a developing shear band in a specimen sheared for 2 μs. The impact angle and the impact velocity are the same as those for Fig. 5(a). Heavily elongated grains in the middle of the specimen indicate the developing

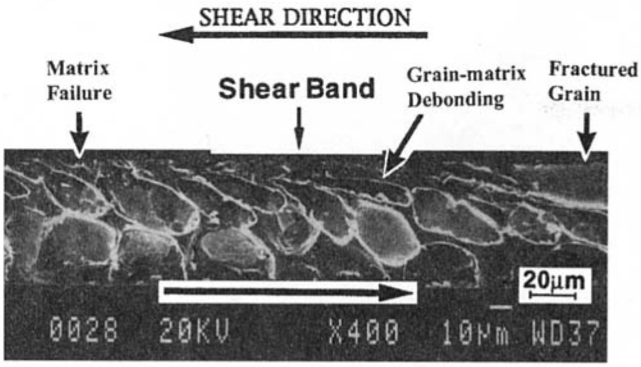

Fig. 6 A shear band that has led to fracture of a WHA specimen, V_0 = 213 ms^{-1}, θ = 22 deg, and h = 89 μm

shear band. The intensely sheared region involves both the W gains and the matrix. In Fig. 5(c), a shear band with more intensely localized deformation is seen. The micrograph shows deep etching of the grains so that the structure of the deformed matrix and grains is clearly revealed. The grains form tear-drop shapes near the middle of the band. The different distributions of deformation across the shear bands in Figs. 5(b) and 5(c) suggest that after the onset of shear localization further deformation occurs primarily in the center of the bands.

The shear bands in Fig. 5(b–c) have widths of approximately 5–10 μm. This is in sharp contrast to the widths of approximately 100 μm reported for torsional Kolsky bar experiments (Andrews et al., 1992). Although many factors may influence the width of shear bands, heat conduction over the time duration of the experiments sets one of the length scales for the localization of deformation. In the pressure-shear impact experiment, the specimen is sheared for 2 μs. The torsional Kolsky bar experiment subjects specimens to torsional loading of up to 600 μs in duration. At higher strain rates, shear bands develop over a shorter time. Consequently, heat conduction occurs over a shorter distance. The more localized high temperatures contribute to the formation of narrower shear bands. The shear bands in Fig. 5 also show more intense shear than what has been observed in the torsional Kolsky bar experiments (see Andrews et al. (1992) and Weerasooriya et al. (1992)). Prolonged shear band development occurs in pressure-shear impact partly because high pressures (9.62 GPa and 10.17 GPa for the two specimens in Figs. 5(b–c)) delay failure due to microvoids and microcracks. During the torsional Kolsky bar experiments, rupture occurs at relatively early stages of localized deformation in the absence of pressure.

The shear band in Fig. 5(c) indicates that more intense shear deformation occurs in the matrix. Parts of the grains that are involved in the shear band form thin tails. As the deformation continues, grain-matrix separation and matrix rupture may occur due to strain incompatibility. A shear band that has led to the failure of the composite is shown in Figure 6. Note that the original thickness of this specimen is approximately twice of that shown in the picture. Only one half is shown because fracture occurred through the shear band, in the middle of the specimen. The top surface of the piece shown is the center line of the shear band through which fracture occurred. Ductile rupture of the matrix, grain-matrix separation, and grain fracture can be seen. A fractograph of the ruptured shear band surface is shown in Fig. 7. The dark areas are the matrix and the light regions are the grains. The surface morphology indicates intense shearing at the center of the shear band. Note the fractured grain at A. Dark strips on the grain surfaces indicate grain-matrix contact before separation. Because of the high percentage of the fracture surface that carries the grain-matrix shear marks, grain-matrix separation appears to be the dominant failure mechanism. A group of light grains with no dark contact marks

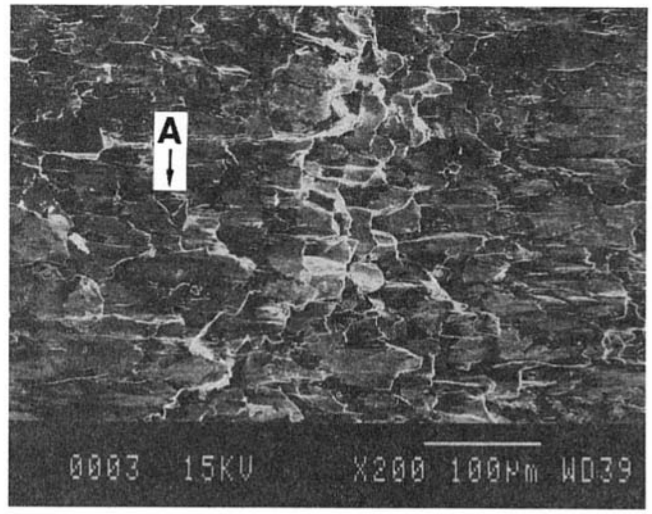

Fig. 7 Fractograph of the shear band surface, V_0 = 198 ms^{-1}, θ = 22.9 deg, and h = 79 μm

appear near the center of the fractograph. These grains are the remaining halves of fractured grains. It is not known whether the fracture surfaces represent certain crystallographic cleavage planes. A combination of ductile rupture of matrix, grain-matrix separations, and grain fracture appears to be responsible for the failure inside the shear band.

4.3 Role of Material Inhomogeneities in Shear Band Formation. The deformed microstructure of a tungsten specimen is shown in Fig. 8. This specimen shows intense shear deformation. The material near the top and lower faces experiences less severe shear because the conduction of heat into the flyer and anvil reduces the temperature increases and the amount of thermal softening near the surfaces. No shear band is observed for this material although the impact condition is comparable to those for the WHA specimen in Fig. 5(c). This result is in contrast to the shear band observed in Fig. 5(c) for the composite. Similarly, no shear bands were observed in the matrix alloy under similar impact conditions (see Table 1).

The stress-strain curves of pure tungsten, matrix alloy, and the composite obtained from impact experiments are summarized in Fig. 9. Similar stress levels are observed for the tungsten and the composite. The matrix, on the other hand, has lower flow stresses which are approximately one half of those for the tungsten and the composite. Neither the tungsten curve nor the

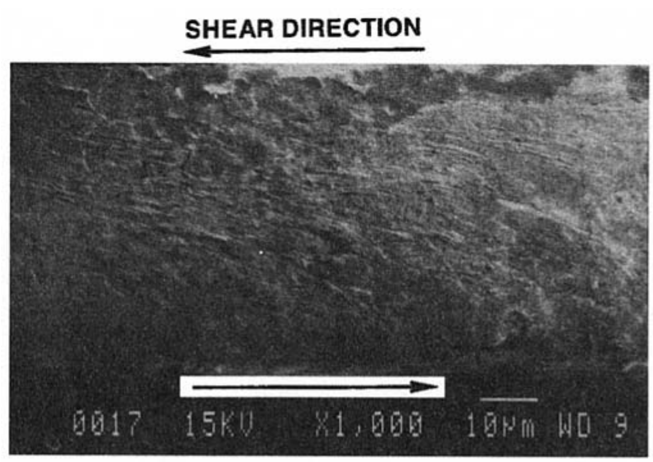

Fig. 8 Deformed microstructure of pure tungsten, V_0 = 198 ms^{-1}, θ = 22.9 deg, and h = 91 μm, sheared for 2 μs

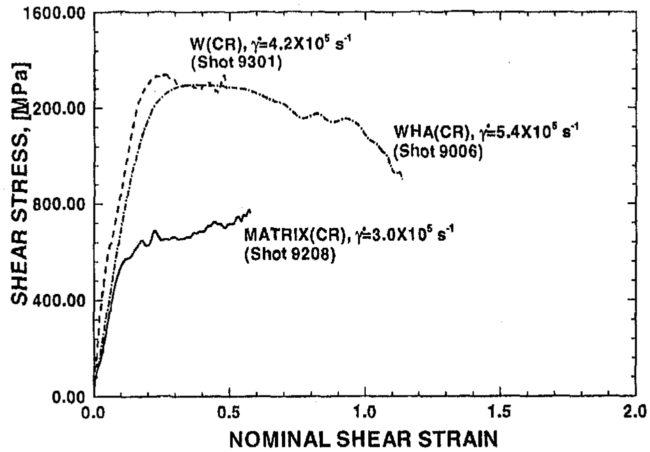

Fig. 9 Dynamic shear stress-strain curves of WHA, pure tungsten, and matrix alloy obtained from pressure-shear plate impact

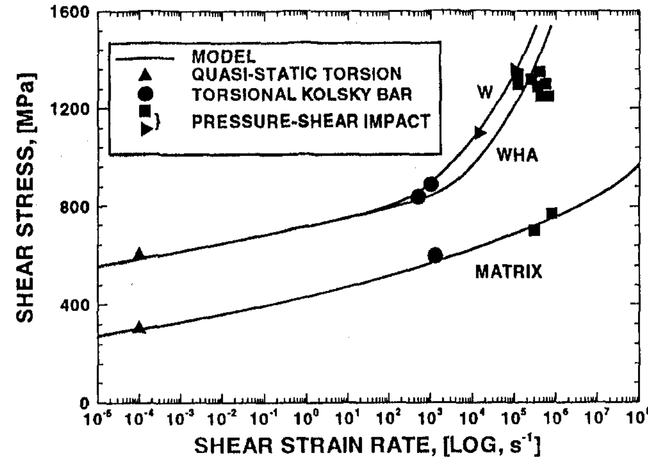

Fig. 11 Strain-rate sensitivities of WHA, pure tungsten, and matrix alloy

matrix curve shows a sharp downturn that indicates the loss of stress-carrying capability associated with the onset of localized deformation. The matrix shows strong strain hardening throughout the deformation. These curves, along with the results of microscopic examinations, suggest that material inhomogeneities inherit in the composite microstructure of WHA enhance the tendency for localization. The heterogeneous material distribution provides conditions under which nonuniform deformation develops more easily. This nonuniformity in turn expedites the initiation of shear bands in the composite, causing the composite to be more susceptible to shear localization than either of its constituent phases when they are tested separately. Numerical simulations of the pressure-shear impact experiments carried out in Zhou et al. (1994) showed that the material inhomogeneities inherit in the composite microstructure indeed dominate the course of shear band formation in WHA. The calculations also confirmed that the two constituent phases are more resistant to shear banding than the composite WHA.

Torsional Kolsky bar and quasistatic torsion experiments conducted on the matrix alloy demonstrate that deformation is essentially uniform in the specimen and no localization is observed. This result is in contrast to the observation of shear band formation in WHA in torsional Kolsky bar experiments reported by Andrews et al. (1992). These results are consistent with the results of pressure-shear plate impact, confirming the higher susceptibility to shear banding of the composite. Torsional experiments on pure tungsten were not successful due to its brittle response. The specimen fractured immediately upon loading. Substantial plastic deformation is achieved in pure tungsten only during pressure-shear plate impact. The presence of pressure is necessary to facilitate plastic deformation in brittle tungsten.

4.4 Material Response Characterization. Figure 10 summaries the stress-strain curves for the matrix alloy obtained from quasi-static torsion, torsional Kolsky bar and pressure-shear plate impact. Unlike the composite, the matrix alloy shows strain hardening under both quasistatic and dynamic conditions. This lack of strain softening can be explained as follows. The matrix alloy has a specific heat three times that of the WHA. Its flow stress and density are only approximately one half of those of the WHA. For the same amount of plastic strain, the temperature change would likely be only one third of that for the composite. In addition, the FCC lattice structure of the matrix gives it a higher rate of strain hardening due to its larger number of slip systems and the resulting higher rate of dislocation entanglement. In contract, pure tungsten has a BCC lattice structure and a relatively lower rate of strain hardening.

The strain-rate sensitivities of the WHA, the tungsten and the matrix alloy are shown in Fig. 11. The flow stresses plotted correspond to a shear strain of 0.45. It is noted that the matrix alloy exhibits a relatively weaker strain-rate dependence of flow stress at strain rates above 10^3 s^{-1}. The composite, on the other hand, shows a strong strain-rate sensitivity at high strain rates. The flow stress levels of pure tungsten are slightly higher than those of the composite.

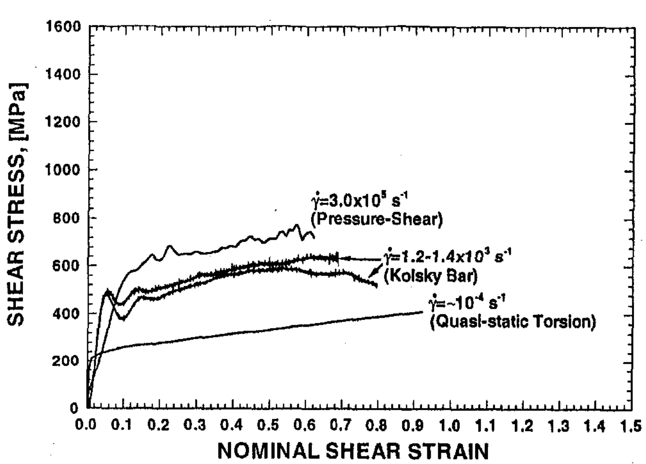

Fig. 10 Shear stress-strain curves of matrix alloy obtained from pressure-shear plate impact, torsional Kolsky bar, and quasi-static torsion

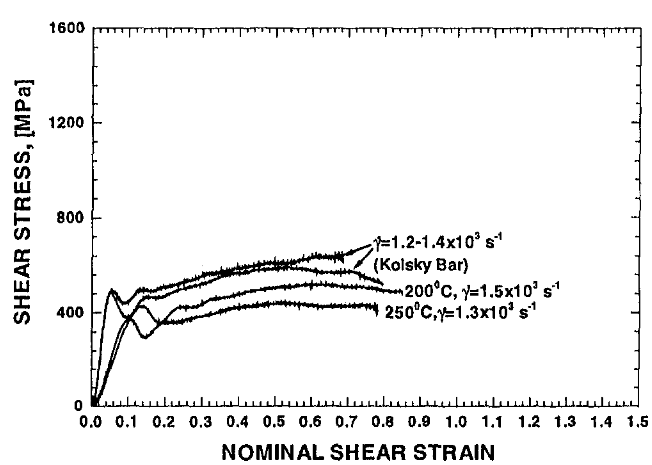

Fig. 12 Shear stress-strain curves of matrix alloy at room temperature, 200°C, and 250°C obtained from torsional Kolsky bar

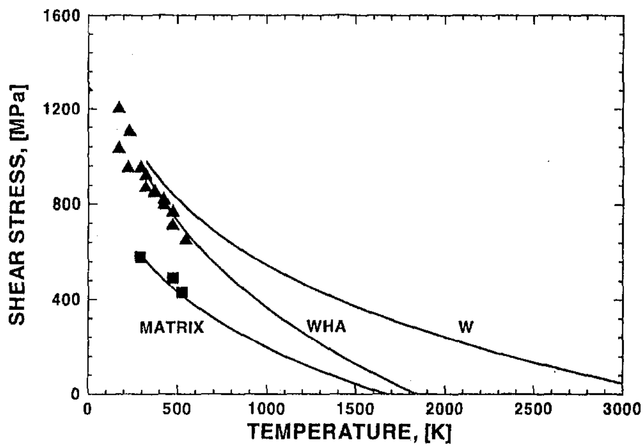

Fig. 13 Temperature dependence of flow stress for WHA, W, and matrix alloy

Figure 12 shows the shear stress-strain curves of the matrix alloy obtained from torsional Kolsky bar experiments at room temperature, 200°C and 250°C. Significant thermal softening is seen in this temperature range. The temperature dependence of flow stresses for the composite, pure tungsten, and the matrix alloy are summarized in Fig. 13. The data for WHA are reported by Andrews et al. (1992), Bose et al. (1988), and O'Donnell et al. (1990). Based on the data presented here, Zhou et al. (1994) used a characterization which accounts for viscoplasticity, strain hardening, and thermal softening for the responses of the tungsten and the matrix. This model characterization is indicated by the solid lines. There is a lack of data at high temperatures for all the materials studied. It is assumed that the materials lose all stress-carrying capabilities when the temperature reaches their corresponding melting points. Tungsten shows a much lower rate of thermal softening than the matrix partly because of its high melting temperature (approximately 3300 K versus 1750 K). Simulations of the pressure-shear plate impact experiments on WHA using this characterization of the constituents gave good predictions for the behavior of WHA.

5 Conclusions

1 The formation of shear bands in a tungsten heavy alloy is studied using pressure-shear plate impact. In the experiment, the material is subjected to simple shear at shear strain rates up to 7×10^5 s^{-1}. The experiment provides an opportunity to relate the shear band development to stress-strain profiles. Dynamic stress-strain relations obtained from the pressure-shear plate impact and torsional Kolsky bar experiments show that the alloy exhibits significant rate sensitivity and thermal softening due to plastic dissipation. Shear bands form when the plastic strain becomes sufficiently large. Significantly more intensely formed shear bands are observed in the pressure-shear impact experiments than those reported for torsional Kolsky bar experiments. The critical shear strain for shear band development is approximately 1–1.5 or 6–8 times that obtained in torsional Kolsky bar experiments.

2 Failure inside the shear bands during pressure-shear impact is a combination of grain-matrix separation, ductile matrix rupture, and grain fracture. Grain-matrix separation seems to be the dominant mechanism through which material failure occurs.

3 Impact experiments show that the flow strength of the WHA follows closely that of the tungsten grains. The matrix has a flow strength approximately one-half that of the WHA. Pure tungsten and the composite show stronger rate sensitivities than the matrix. Pure tungsten and WHA also show thermal softening during pressure-shear impact experiments while the matrix exhibits strain hardening for strain rates up to 3.0×10^5 s^{-1}.

4 The presence of different phases serves as a perturbation to deformation that enhances the initiation and development of shear bands. The composite microstructure causes the WHA to be more susceptible to shear banding than either of its constituents when tested separately.

Acknowledgment

This research was supported by the Army Research Office. Completion of the work was supported by the Office of Naval Research through grant N00014-96-1-1195 to Georgia Tech. We would like to thank Drs. T. W. Penrice and Steven Caldwell of Teledyne Firth Sterling for supplying the cross-rolled tungsten heavy alloy and matrix alloy, and Mr. Meinrad Ostermann of Teledyne Wah Chang for supplying the cross-rolled pure tungsten used in this investigation.

References

Andrews, E. W., Bower, A. F., and Duffy, J., 1992, "Shear Band Formation in a Tungsten Heavy Alloy," *Proc. Symposium on Shear Bands and Viscoplastic Theories, The 29th Annual Technical Meeting of the Society for Engineering Science,* Sep. 14–16, La Jolla, CA.

Baek, W. H., Hong, M.-H., Lee, S., and Chung, D.-T., 1994, "A Study of the Shear Localization Behavior of Tungsten Heavy Alloys," *Proc. of the 2nd International Conference on Tungsten and Refractory Metals,* A. Bose and R. Dowding, eds., Mclean, VA, pp. 463–471.

Belk, J. A., Waltson, C. H., Bentley, A. R., and Hogwood, M. C., 1994, "Dynamic Deformation Characteristics of Tungsten Alloys," *Proc. of the 2nd International Conference on Tungsten and Refractory Metals,* A. Bose and R. Dowding, eds., Mclean, VA, pp. 389–399.

Bose, A., Sims, D., and German, R. M., 1988, "Test Temperature and Strain Rate Effects on the Properties of a Tungsten Heavy Alloy," *Metallurgical Transactions A,* Vol. 19A, pp. 487–494.

Churn, K.-S., and German, R. M., 1984, "Fracture Behavior of W-Ni-Fe Heavy Alloys," *Metallurgical Transactions A,* Vol. 15A, pp. 331–338.

Clifton, R. J., and Klopp, R. W., 1985 "Pressure-Shear Plate Impact Testing," *Metals Handbook,* Vol. 8, 9th ed., Amer. Soc. Metals, pp. 230–239.

Coates, R. S., and Ramesh, K. T., 1990a, "The Rate-Dependent Deformation of a Tungsten Heavy Alloy," The Johns Hopkins University Report, No. DIL-9001, June, Baltimore, MD.

Coates, R. S., and Ramesh, K. T., 1990b, "The Deformation of Tungsten Alloys at High Strain Rates," The Johns Hopkins University Report, No. DIL-9002, Nov., Baltimore, MD.

Costin, L. S., Crisman, E. E., Hawley, R. H., and Duffy, J., 1979, "On the Localization of Plastic Flow in Mild Steel Tubes under Dynamic Torsional Loading," *Proc. 2nd Conf. on Mech. Properties of Materials at High Rates of Strain,* J. Harding, ed., The Institute of Physics, London, pp. 90–100.

Duffy, J., Campbell, J. D., and Hawley, R. H., 1971, "On the Use of a Torsional Split-Hopkinson Bar to Study Rate Effects in 1100-0 Aluminum," ASME JOURNAL OF APPLIED MECHANICS, Vol. 38, pp. 83–91.

Ekbom, L., 1981, "Microstructural Study of the Deformation and Fracture Behavior of a Sintered Tungsten-Base Composite," *Modern Developments in Powder Metallurgy,* Vol. 14, H. H. Hausner, H. W. Antes, and G. D. Smith, eds., Metal Powder Industries Federation, Princeton, NJ, pp. 177–188.

Hartley, K. A., Duffy, J., and Hawley, R. H., 1985, The Torsional Kolsky (Split-Hopkinson) Bar, *Metals Handbook,* Vol. 8, ASM, pp. 218–228.

Hofmann, H., and Petzow, G., 1984, "Influence of Sintering Atmosphere on Mechanical Properties of Tungsten Based Heavy Alloys," *Modern Developments in Powder Metallurgy,* Vol. 17, pp. 17–31.

Krock, R. H., and Shepard, L. A., 1963, "Mechanical Behavior of the Two-Phase Composite, Tungsten-Nickel-Iron," *Transactions of The Metallurgical Society of AIME,* Vol. 227, pp. 1127–1134.

Krock, R. H., 1964, "Effect of Composition and Temperature on the Dynamic Elastic Moduli of W-Ni-Fe Composite Materials," *Proc. ASTM,* Vol. 64, pp. 712–718.

Kumar, P., and Clifton, R. J., 1976, Optical Alignment of Impact Faces for Plate Impact Experiments, *J. Appl. Phy.,* Vol. 48, No. 3, pp. 1366–1367.

Lassila, D. H., and Connor, A., 1991, "Fracture Behavior of Warm Forged and CVD Tungsten," Lawrence Livermore National Laboratory Report, No. UCRL-JC-106552, *Proc. of the Symposium Tungsten Heavy Alloys—Recent Advances,* TMS/AIME Refractory Metals Committee, TMS/AIME 1991 Annual Meeting, New Orleans, LA.

Magness, L. S., 1992, "Properties and Performance of KE Penetrator Materials," *Proceedings of the First International Conference on Tungsten and Tungsten Alloys,* A. Bose and R. J. Dowding, eds., Nov. 15–18, Arlington VA, Metal Powder Industries Federation, pp. 15–22.

Meyer, L. W., Kunze, H.-D., and Staskewitsch, E., 1983, "Dynamic Strength and Ductility of a Tungsten-Alloy for KE-Penetrators in Swaged and Unswaged Condition under Various Loading," *Proc. 7th International Symposium on Ballistics,* The Hague, pp. 289–293.

Molinari, A., and Clifton, R. J., 1987, "Analytical Characterization of Shear Localization in Thermoviscoplastic Materials," ASME JOURNAL OF APPLIED MECHANICS, Vol. 54, pp. 806–812.

O'Donnell, R. G., and Woodward, R. L., 1990, "The Composition and Temperature Dependence of the Mechanical Properties of Tungsten Alloys," *Metallurgical Transactions A,* Vol. 21A, pp. 744–748.

Rabin, B. H., and German, R. M., 1988, "Microstructure Effects on Tensile Properties of Tungsten-Nickel-Iron Composites," *Metallurgical Transactions A,* Vol. 19A, pp. 1523–1532.

Ramesh, K. T., and Coates, R. S., 1992, "Microstructural Influences on the Dynamic Response of Tungsten Heavy Alloys," *Metallurgical Transactions A,* Vol. 23A, pp. 2625–2630.

Tham, R. H., and Hohler, V., 1995, "Dynamic Behavior of Novel Tungsten Penetrator Materials," *Proc. of the 3rd International Conference on Tungsten and Refractory Metals,* A. Bose and R. Dowding, eds., Mclean, VA, pp. 159–166.

Yadav, Y., and Ramesh, K. T., 1995, "The Mechanical Properties of Tungsten-based Composites at Very High Strain Rates," *Materials Science and Engineering,* Vol. A203, pp. 140–153.

Weerasooriya, T., 1994, "Effect of Sudden Change in Strain Rate on the Deformation and Failure Behavior of a Tungsten Heavy Alloy," *Proc. of the 2nd International Conference on Tungsten and Refractory Metals,* A. Bose and R. Dowding, eds., Mclean, VA, pp. 455–471.

Weerasooriya, T., Beaulieu, P. A., and Swanson, R., 1992, "Deformation and Failure Behavior of 93W-5Ni-2Fe at High Strain Rate Shear Loading," U.S. Army Materials Technology Laboratory Report, No. MTL TR 92-19, Watertown, MA.

Weerasooriya, Moy, P., and Dowding R. J., 1994, "Effect of W-W grain Contiguity on the High Shear Strain Rate Behavior of 93W-5Ni-2Fe Tungsten Heavy Alloy," *Proc. of the 2nd International Conference on Tungsten and Refractory Metals,* A. Bose and R. Dowding, eds., Mclean, VA, 401–409.

Woodward, R. L., Alkemade, S. J., and Magness, L. S., 1994, "Strain Localization and Fracture in Dynamic Dumbbell Compression of Tungsten Alloys," *Proc. of the 2nd International Conference on Tungsten and Refractory Metals,* A. Bose and R. Dowding, eds., Mclean, VA, pp. 431–445.

Woodward, R. L., Baldwin, N. J., Burch, I., and Baxter, B. J., 1985, "Effect of Strain Rate on the Flow Stress of Three Liquid Phase Sintered Tungsten Alloys," *Metallurgical Transactions A,* Vol. 16A, pp. 2031–2037.

Zhao, D., Valencia, J. J., and McCabe, T. J., 1995, "Mechanical and Microstructural Behavior of Tungsten Alloys during High Rate Deformation," *Proc. of the 3rd International Conference on Tungsten and Refractory Metals,* A. Bose and R. Dowding, eds., Mclean, VA, pp. 123–130.

Zhou, M., Needleman, A., and Clifton, R. J., 1994, "Finite Element Simulations of Dynamic Shear Localization," *Journal of Mechanics and Physics of Solids,* Vol. 42, No. 3, pp. 423–458.

Zurek, A. K., and Follansbee, P. S., 1995, "A Comparison of Shear Localization Susceptibility in U-0.75 Wt Pct Ti and W-Ni-Fe during High Strain Rate Deformation," *Metallurgical and Materials Transactions A,* Vol. 26A, pp. 1483–1490.

H. Nozaki
Faculty of Education,
Ibaraki University,
2-1-1 Bunkyo, Mito-shi,
310 Japan

M. Taya
Department of Mechanical Engineering,
University of Washington,
Box 352600,
Seattle, WA 98195
Fellow ASME

Elastic Fields in a Polygon-Shaped Inclusion With Uniform Eigenstrains

In this paper the elastic fields in an arbitrary, convex polygon-shaped inclusion with uniform eigenstrains are investigated under the condition of plane strain. Closed-form solutions are obtained for the elastic fields in a polygon-shaped inclusion. The applications to the evaluation of the effective elastic properties of composite materials with polygon-shaped reinforcements are also investigated for both dilute and dense systems. Numerical examples are presented for the strain field, strain energy, and stiffness of the composites with polygon shaped fibers. The results are also compared with some existing solutions.

1 Introduction

The elastic fields due to ellipsoidal inclusions in an infinitely extended media have been investigated by many authors following the pioneering work of Eshelby (Eshelby, 1957). However, little work has been done for nonellipsoidal inclusions. The elastic fields due to a cuboidal inclusion with uniform eigenstrains have been calculated by Faivre (1964), Sankaran and Laird (1976), Lee and Johnson (1977, 1978), and Chiu (1977, 1978). Owen (1972) and Chiu (1980) considered the problem of a rectangular inclusion in both infinite and half-spaces. Takao et al. (1981) investigated a cylindrical inclusion problem in an attempt to examine the hygrothermal effect in a fiber composite material. Nonellipsoidal inclusion problems are important for composite materials since some nonellipsoidal reinforcements are used, for examples, SiC whisker used in metal and ceramic matrix composites, and eutectics used in superconductor composites. Recently Mura et al. (1994) have examined the elastic field in a pentagonal star-shaped inclusion and claimed that the elastic field (stress and strain) inside the inclusion is uniform.

In this paper an arbitrary, convex polygon-shaped (n-sides) inclusion is investigated for the case where uniform eigenstrains are prescribed. In the following, we first show the elastic fields induced by the eigenstrains in the convex polygon-shaped inclusion can be obtained explicitly by the straightforward extension of a well-known procedure for an ellipsoidal inclusion (Mura, 1987). It should be noted here that "convexity" of an inclusion shape is required so as to maintain one-to-one mapping between the inclusion and unit sphere. Then, the strain concentration matrix (Dunn and Taya, 1992) is calculated to determine the overall elastic constants of composite materials reinforced by polygon-shaped fibers. Finally, numerical results are presented for the strain field, strain energy, and effective stiffness of composites with polygon-shaped fibers. The strain fields and strain energy are compared with the analytical ones by Chiu (1980) for $n = 4$ and Eshelby (1957) for $n \to \infty$. Dilute approximation and Mori-Tanaka mean field approaches are used to evaluate the overall stiffness of composites. A numerical integration formula is applied to obtain the strain energy and averaged Eshelby's tensor.

Contributed by the Applied Mechanics Division of THE AMERICAN SOCIETY OF MECHANICAL ENGINEERS for publication in the ASME JOURNAL OF APPLIED MECHANICS.

Discussion on this paper should be addressed to the Technical Editor, Professor Lewis T. Wheeler, Department of Mechanical Engineering, University of Houston, Houston, TX 77204-4792, and will be accepted until four months after final publication of the paper itself in the ASME JOURNAL OF APPLIED MECHANICS.

Manuscript received by the ASME Applied Mechanics Division, May 10, 1996; final revision, Oct. 8, 1996. Associate Technical Editor: L. T. Wheeler.

2 Computational Procedure

2.1 General Case. Consider an infinite, elastic, homogeneous, and isotropic domain D having an arbitrarily shaped convex inclusion Ω with uniform eigenstrain ϵ_{ij}^* in a Cartesian coordinate system (x_1', x_2', x_3'). The matrix domain is denoted as $D - \Omega$. The eigenstrain ϵ_{ij}^* is so defined that it assumes some constant value in Ω but vanishes in $D - \Omega$. For prescribed eigenstrain ϵ_{ij}^* in Ω, the resulting stress σ_{ij} is given by

$$\sigma_{ij} = C_{ijkl}(\epsilon_{kl} - \epsilon_{kl}^*) \quad \text{in} \quad D, \tag{1}$$

where C_{ijkl} is the elastic stiffness tensor of the matrix and ϵ_{kl} is the strain induced by the inclusion. Using Green's function $G_{ij}(\mathbf{x} - \mathbf{x}')$, the displacement field inside Ω can be written as (Mura, 1987)

$$u_i(\mathbf{x}) = -C_{jkmn}\epsilon_{mn}^* \int_\Omega G_{ij,k}(\mathbf{x} - \mathbf{x}')d\mathbf{x}' = \frac{\epsilon_{jk}^*}{8\pi(1-\nu)} \int_\Sigma r(\mathbf{l}, \mathbf{x}) g_{ijk}(\mathbf{l}) d\omega, \tag{2}$$

where ν is the Poisson's ratio of the matrix and $\mathbf{x}$, $\mathbf{x}'$ are the points inside Ω. $\mathbf{l} = (\mathbf{x}' - \mathbf{x})/|\mathbf{x}' - \mathbf{x}|$, $r(\mathbf{l}, \mathbf{x}) = |\mathbf{x}' - \mathbf{x}|$ and $d\omega$ is a surface element of a unit sphere Σ. $g_{ijk}(\mathbf{l})$ is a function defined by

$$g_{ijk}(\mathbf{l}) = (1 - 2\nu)(\delta_{ij}l_k + \delta_{ik}l_j - \delta_{jk}l_i) + 3l_il_jl_k. \tag{3}$$

Thus, if we find $r(\mathbf{l}, \mathbf{x})$, we can determine the displacement field inside any convex inclusion from (2) and the strain and stress fields using the standard displacement-strain relationships and Eq. (1).

2.2 Two-Dimensional Polygons. When the inclusion is a cylindrical inclusion in the x_3 direction extended from $x_3 = -\infty$ to $x_3 = \infty$ and the transverse section of which has an arbitrary convex polygon (n-sides) shape as shown in Fig. 1, the elastic displacement due to the inclusion is still given by Eq. (2). The volume element $d\mathbf{x}'$ in Eq. (2) is $dx_1'dx_2'dx_3'$ and the eigenstrain ϵ_{ij}^* is assumed to be independent of x_3. The integration with respect to x_3' involves only the Green's function and this integration requires the Green's function for two-dimensional plane-strain problems. For isotropic media, the Green's function for two-dimensional plane strain is (Mura et al., 1994)

$$G_{ij}^p(\mathbf{x} - \mathbf{x}') = [\bar{x}_i\bar{x}_j/r^2 - (3 - 4\nu)\delta_{ij}\log r]/8\pi(1-\nu)\mu, \tag{4}$$

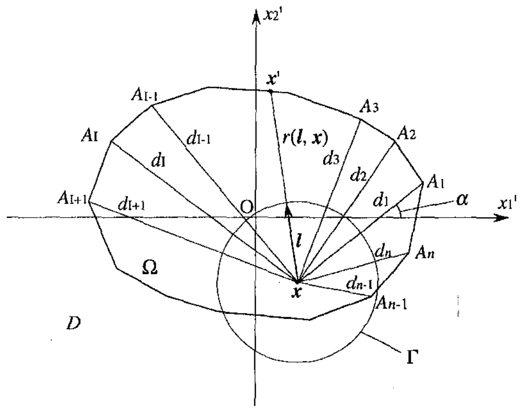

Fig. 1 Polygon-shaped inclusion Ω and unit circle Γ

with $\bar{x}_i = x_i' - x_i$ and $r^2 = (x_1 - x_1')^2 + (x_2 - x_2')^2 = |\mathbf{x}' - \mathbf{x}|^2 = |\mathbf{x} - \mathbf{x}'|^2$. In Eq. (4), μ is the shear modulus of the matrix. Now the integral (2) is reduced to a two-dimensional integral defined inside the polygon and further to a line integral along the unit circle Γ centered at point $\mathbf{x}$.

$$u_i(\mathbf{x}) = -C_{jkmn}\epsilon^*_{mn}\int_\Omega G^p_{ij,k}(\mathbf{x} - \mathbf{x}')d\mathbf{x}'$$

$$= -\frac{\epsilon^*_{jk}}{4\pi(1-\nu)}\int_\Gamma r(\mathbf{l}, \mathbf{x})g^p_{ijk}(\mathbf{l})d\omega. \quad (5)$$

In the above equation, $g^p_{ijk}(\mathbf{l})$ is defined by

$$g^p_{ijk}(\mathbf{l}) = (1 - 2\nu)(-\delta_{jk}l_i + \delta_{ij}l_k + \delta_{ik}l_j) + 2l_il_jl_k. \quad (6)$$

When $\mathbf{x}$ is located inside the inclusion, the integral in Eq. (5) is explicitly performed. $A_I(x_1^I, x_2^I)$ $(I = 1 \sim n)$ is a vertex of a polygon of n sides. When $\mathbf{x}'$ is on the side $\overline{A_IA_{I+1}}$ of the polygon, Fig. 1, $r(\mathbf{l}, \mathbf{x})$, the distance between $\mathbf{x}$ and $\mathbf{x}'$, is obtained by

$$r(\mathbf{l}, \mathbf{x}) = r_I(\mathbf{l}, \mathbf{x}) = -\frac{\alpha_Ix_1 + \beta_Ix_2 + \gamma_I}{\alpha_Il_1 + \beta_Il_2}, \quad (7)$$

where

$$\alpha_I = x_2^I - x_2^{I+1},$$
$$\beta_I = -(x_1^I - x_1^{I+1}),$$
$$\gamma_I = x_1^Ix_2^{I+1} - x_2^Ix_1^{I+1}. \quad (8)$$

Substituting Eq. (7) into Eq. (5), we obtain

$$u_i(\mathbf{x})$$
$$= -\frac{\epsilon^*_{ij}}{4\pi(1-\nu)}\left[\int_{\Gamma_1} r_1(\mathbf{l}, \mathbf{x})g_{ijk}(\mathbf{l})d\omega + \int_{\Gamma_2} r_2(\mathbf{l}, \mathbf{x})g_{ijk}(\mathbf{l})d\omega + \ldots + \int_{\Gamma_I} r_I(\mathbf{l}, \mathbf{x})g_{ijk}(\mathbf{l})d\omega + \ldots + \int_{\Gamma_n} r_n(\mathbf{l}, \mathbf{x})g_{ijk}(\mathbf{l})d\omega\right]$$

$$= -\frac{\epsilon^*_{ij}}{4\pi(1-\nu)}\sum_{I=1}^{n}\int_{\Theta_{I-1}(\mathbf{x})}^{\Theta_I(\mathbf{x})} r_I(\mathbf{l}, \mathbf{x})g_{ijk}(\mathbf{l})d\theta$$

$$= \frac{1}{4\pi(1-\nu)}\sum_{I=1}^{n}(\alpha_Ix_1 + \beta_Ix_2 + \gamma_I)\int_{\Theta_{I-1}(\mathbf{x})}^{\Theta_I(\mathbf{x})}\frac{\epsilon^*_{jk}g_{ijk}(\mathbf{l})}{\alpha_Il_1 + \beta_Il_2}d\theta, \quad (9)$$

where Γ_I $(I = 1 \sim n)$ is an arc segment of the unit circle Γ corresponding to the side $\overline{A_IA_{I+1}}$ of the polygon, $d\omega = 1 \cdot d\theta$ and $\Theta_I(\mathbf{x})$ is defined as

$$\Theta_I(\mathbf{x}) = \alpha(\mathbf{x}) + \sum_{J=1}^{I}\theta_J(\mathbf{x}),$$
$$\Theta_0(\mathbf{x}) = \alpha(\mathbf{x}),\ \Theta_n(x) = \alpha(\mathbf{x}) + 2\pi,$$
$$\alpha(\mathbf{x}) = \tan^{-1}\left[\frac{x_2 - x_2^1}{x_1 - x_1^1}\right]. \quad (10)$$

In Eq. (10), $\theta_I(\mathbf{x})$ is the angle corresponding to the arc segment Γ_I

$$\theta_I(\mathbf{x}) = \cos^{-1}\left[\frac{\{d_I(\mathbf{x})\}^2 + \{d_{I+1}(\mathbf{x})\}^2 - a_I^2}{2d_I(\mathbf{x})d_{I+1}(\mathbf{x})}\right],$$

$$d_I(\mathbf{x}) = \sqrt{(x_1 - x_1^I)^2 + (x_2 - x_2^I)^2},$$
$$a_I = \sqrt{(x_1^I - x_1^{I+1})^2 + (x_2^I - x_2^{I+1})^2}. \quad (11)$$

Using the integral formulae given in Appendix A, Eq. (9) is reduced to

$$u_i(\mathbf{x}) = D_{ijk}(\mathbf{x})\epsilon^*_{jk}, \quad (12)$$

where $D_{ijk}(\mathbf{x})$ is a third-order tensor given in Appendix B. The strain field inside Ω is obtained from Eq. (12)

$$\epsilon_{ij}(\mathbf{x}) = \tfrac{1}{2}(u_{i,j} + u_{j,i}) = S_{ijkl}(\mathbf{x})\epsilon^*_{kl}, \quad (13)$$

where $S_{ijkl}(\mathbf{x})$ is a fourth-order tensor given in Appendix C. $S_{ijkl}(\mathbf{x})$ is the Eshelby tensor for polygon-shaped inclusion. The stress field inside Ω, $\sigma_{ij}(\mathbf{x})$ is calculated by substituting Eq. (13) into Eq. (1).

The elastic strain energy in the infinite domain D is (Mura, 1987)

$$W^* = \tfrac{1}{2}\int_D \sigma_{ij}(\mathbf{x})\{\epsilon_{ij}(\mathbf{x}) - \epsilon^*_{ij}\}dD$$

$$= -\tfrac{1}{2}\int_\Omega \sigma_{ij}(\mathbf{x})\epsilon^*_{ij}dD. \quad (14)$$

The expression for $\sigma_{ij}(\mathbf{x})$ is so complicated that we are not able to perform the integral in Eq. (14) analytically. Thus we need to employ a numerical integration technique to evaluate the elastic strain energy (14).

3 Effective Stiffness of Composites Reinforced by Polygon-Shaped Fibers

3.1 Strain Concentration Matrix. Consider polygon-shaped fibers (elastic stiffness C^f_{ijkl}) embedded in an infinite body D (elastic stiffness C^m_{ijkl}) subjected to an uniform farfield strain ϵ^0_{ij}. The state of actual strain at any point in a composite material can be expressed by $\epsilon^0_{ij} + \epsilon_{ij}(\mathbf{x})$ where $\epsilon_{ij}(\mathbf{x})$ is the disturbance strain field due to the existence of fibers. Therefore the integration of the disturbance strain $\epsilon_{ij}(\mathbf{x})$ over the entire composite domain vanishes, i.e.,

$$\bar{\epsilon}^c_{ij} = \epsilon^0_{ij}, \quad (15)$$

where $\bar{\epsilon}^c_{ij}$ is the average strain field in the composite material. On the other hand, the average strain and stress fields in the composite material are expressed as

$$\bar{\epsilon}^c_{ij} = f\bar{\epsilon}^f_{ij} + (1-f)\bar{\epsilon}^m_{ij},$$
$$\bar{\sigma}^c_{ij} = f\bar{\sigma}^f_{ij} + (1-f)\bar{\sigma}^m_{ij}. \quad (16)$$

In the above equations, f is the volume fraction of fibers, $\bar{\epsilon}^i$ and $\bar{\sigma}^i$ $(i = c, f, m)$ are the average strain and stress fields (in composite material, fibers, and matrix), respectively. The stress-strain relations in each phase are defined by

$$\bar{\sigma}^c_{ij} = C^c_{ijkl}\bar{\epsilon}^c_{kl},$$
$$\bar{\sigma}^f_{ij} = C^f_{ijkl}\bar{\epsilon}^f_{kl},$$
$$\bar{\sigma}^m_{ij} = C^m_{ijkl}\bar{\epsilon}^m_{kl}. \quad (17)$$

From Eqs. (15), (16), and (17), we obtain the elastic stiffness tensor of the composite material as

$$C^c_{ijkl} = C^m_{ijkl} + f(C^f_{ijkl} - C^m_{ijkl})A_{ijkl}, \quad (18)$$

where A_{ijkl} is the strain concentration matrix (Dunn and Taya, 1992) which relates the average strain in fiber domain to that in the composite material, i.e.,

$$\bar{\epsilon}^f_{ij} = A_{ijkl}\bar{\epsilon}_{kl} = A_{ijkl}\epsilon^0_{kl}. \quad (19)$$

We can obtain A_{ijkl} for both dilute and dense systems by Eshelby's equivalent inclusion method.

3.2 Dilute System. First, we consider a composite material of which fiber volume fraction is low enough to ignore the interaction effects. The composite material is subjected to an uniform farfield strain ϵ^0_{ij} and we write for the total strain as

$$\epsilon^c_{ij}(\mathbf{x}) = \epsilon^0_{ij} + \epsilon_{ij}(\mathbf{x}), \quad (20)$$

where $\epsilon_{ij}(\mathbf{x})$ is the disturbance strain caused by the inhomogeneities. The effect of the inhomogeneities on the stress and strain distribution may be modeled with help of a eigenstrain $\epsilon^*_{ij}(\mathbf{x})$. This concept is based on the following equivalence:

$$\sigma^0_{ij} + \sigma_{ij}(\mathbf{x}) = C^f_{ijkl}(\epsilon^0_{kl} + \epsilon_{kl}(\mathbf{x}))$$
$$= C^m_{ijkl}(\epsilon^0_{kl} + \epsilon_{kl}(\mathbf{x}) - \epsilon^*_{kl}(\mathbf{x})) \quad \text{in} \quad \Omega. \quad (21)$$

where σ^0_{ij} is the uniform stress corresponding to the applied strain and they are related by

$$\sigma^0_{ij} = C^m_{ijkl}\epsilon^0_{kl}, \quad (22)$$

and $\sigma_{ij}(\mathbf{x})$ is the stress disturbance by the inhomogeneities. Averaging Eq. (21) over Ω, we obtain

$$C^f_{ijkl}(\epsilon^0_{kl} + \bar{\epsilon}_{kl}) = C^m_{ijkl}(\epsilon^0_{kl} + \bar{\epsilon}_{kl} - \bar{\epsilon}^*_{kl}). \quad (23)$$

Subtracting the uniform field, Eq. (22) from Eq. (21) we obtain

$$\bar{\sigma}_{ij} = C^m_{ijkl}(\bar{\epsilon}_{kl} - \bar{\epsilon}^*_{kl}). \quad (24)$$

Equation (24) is identical to Eq. (1) in form if Eq. (1) is averaged over Ω. Furthermore, if Eq. (13) is averaged over Ω, we have

$$\bar{\epsilon}_{kl} = \bar{S}_{klmn}\bar{\epsilon}^*_{mn} = \bar{S}_{klmn}\epsilon^*_{mn} \quad (25)$$

where ϵ^*_{ij} was assumed constant. Thus, as far as the averaged fields are concerned, we can use Eq. (25) to solve Eq. (23). In Eq. (25), $\bar{S}_{ijkl}$ is the averaged Eshelby tensor defined by

$$\bar{S}_{klmn} = \frac{1}{V_\Omega}\int_\Omega S_{klmn}(\mathbf{x})dV. \quad (26)$$

The average strain field in Ω is obtained as

$$\bar{\epsilon}^f_{ij} = \epsilon^0_{ij} + \bar{S}_{ijkl}\bar{\epsilon}^*_{kl}. \quad (27)$$

We can reduce Eq. (23) to

$$C^f_{ijkl}\bar{\epsilon}^f_{kl} = C^m_{ijkl}(\bar{\epsilon}^f_{kl} - \bar{\epsilon}^*_{kl}). \quad (28)$$

By eliminating $\bar{\epsilon}^*_{kl}$ with Eqs. (27) and (28), the relationship between the average strain in the fiber domain and that in the composite material is obtained as

$$\bar{\epsilon}^f_{ij} = A^{dil}_{ijkl}\epsilon^0_{kl}, \quad (29)$$

where

$$A^{dil}_{ijkl} = [I_{ijkl} + \bar{S}_{ijkl}(C^m_{ijkl})^{-1}(C^f_{ijkl} - C^m_{ijkl})]^{-1}. \quad (30)$$

3.3 Dense System. We adopt the Mori-Tanaka mean field approach (Mori and Tanaka, 1973) which is effective for any finite volume fraction of fibers f, $0 \leq f \leq 1$. The key assumption in the Mori-Tanaka theory is that the concentration factor A_{ijkl} is given by the solution for a single fiber embedded in an infinite matrix subjected to an applied elastic field equal to the as yet unknown average elastic field in the matrix. This solution is easily expressed as

$$\bar{\epsilon}^f_{ij} = A^{dil}_{ijkl}\bar{\epsilon}^m_{kl}, \quad (31)$$

where A^{dil}_{ijkl} is given by Eq. (30). With Eqs. (16), (19), and (31), the concentration factor, A^{MT}_{ijkl}, can be written in the form as first proposed by Benveniste (1987),

$$A^{MT}_{ijkl} = A^{dil}_{ijkl}[(1-f)I_{ijkl} + fA^{dil}_{ijkl}]^{-1}. \quad (32)$$

4 Numerical Results and Discussion

4.1 Strain Fields and Strain Energy in the Inclusion. Numerical examples of the strain (13) and the elastic strain energy (14) are shown in this section. We assume a regular polygon-shaped inclusion centered at the origin O of the Cartesian coordinate system as shown in Fig. 2. The Poisson's ratio of the matrix ν is assumed to be 0.3 throughout the computation. As will be mentioned further, the strain field inside the inclusion have logarithmic singularity at its corners. To evaluate the integrals of strain energy (14) and average Eshelby tensor (26) properly, we devide the polygon into triangles whose vertices are denoted by O, A_I, B_I or O, A_I, C_I ($I = 1 \sim n$) where B_I is the midpoint of a side $\overline{A_IA_{I+1}}$ and C_I is that of $\overline{A_{I-1}A_I}$. Transforming the triangles to a square of which vertices are (1, 1), (−1, 1), (−1, −1) and (1, −1) so as to correcpond $O \rightarrow (-1, 1)$, $B_I(C_I) \rightarrow (1, 1)$ and $A_I \rightarrow (-1, -1)$, (1, −1), standard Gaussian numerical integration formula has been used to evaluate the integral over the square. This transformation gives a Jacobian which contains nondimensional distance from A_I, a singular point, so that the logarithmic singularity at the corners of poligons is suppressed. The number of abscissas for numerical integration on each triangle was 100.

Figures 3 and 4 show the variation of the total strain fields $\epsilon_{11}(\mathbf{x})$, $\epsilon_{22}(\mathbf{x})$ in a regular n polygon-shaped inclusion along the x'_1-axis for a dilatational eigenstrain $(\epsilon^*_{11}, \epsilon^*_{12}, \epsilon^*_{22}) = (\epsilon_0, 0, \epsilon_0)$. The strain distributions are not uniform but approach to the Eshelby's solutions (dashed line) for circular inclusion of radius a with the increasing number of vertices n. The strain fields have logarithmic singularity at the corner of each polygon as pointed out by Chiu (1980) for a rectangular inclusion. Note that the values of strain fields in a regular n polygon-shaped

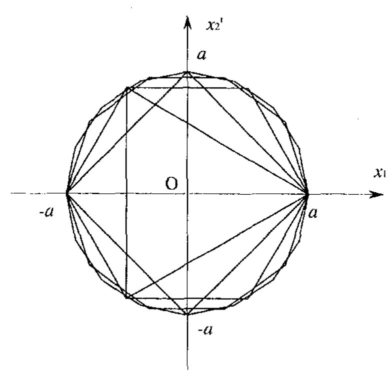

Fig. 2 Regular polygon-shaped inclusions

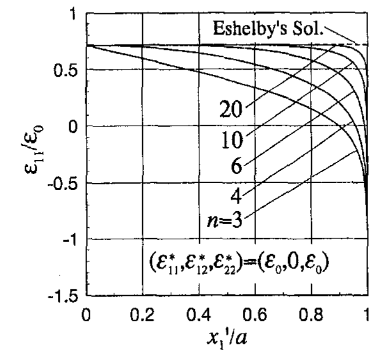

Fig. 3 Normalized total strain ϵ_{11}/ϵ_0 in regular polygon-shaped inclusions along the x_1'-axis for a dilational eigenstrain (ϵ_0, 0, ϵ_0)

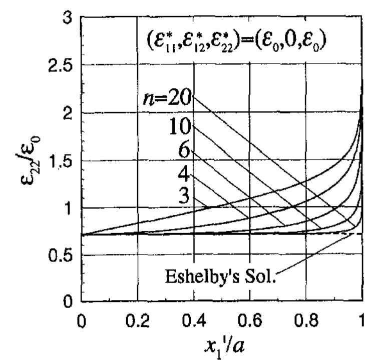

Fig. 4 Normalized total strain ϵ_{22}/ϵ_0 in regular polygon-shaped inclusions along the x_1'-axis for a dilational eigenstrain (ϵ_0, 0, ϵ_0)

inclusion for the given eigenstrain field coincide with Eshelby's solutions at its center. Figures 5 and 6 show the results for a uniaxial eigenstrain, $(\epsilon^*_{11}, \epsilon^*_{12}, \epsilon^*_{22}) = (\epsilon_0, 0, 0)$. In this case, the values of strains at its center take the same values with Eshelby's solution except for the case $n = 4$. The reason for the discrepancy between the present results and Chiu's solutions for $n = 4$ is that the square used in Chiu's model is parallel to the x_1' and x_2' axes, type II in Fig. 7, while the square used in the present model is type I as shown in Fig. 7 where the lines of the square are tilted at 45 deg with the x_1' and x_2'-axes. In addition, the uniaxial eigenstrain imposed is along the x_1' axis which is not parallel to the lines of the square used in the present computation, type I. We also computed the strain at the center of a type II square used by Chiu by using the present model and found the results coincide with those of Chiu (1980).

Figure 8 shows the variation of the normalized strain energy $\bar{W}^* = W^*(1 - \nu^2)/\epsilon_0^2 EV_\Omega$ for regular polygon-shaped inclusions with a dilational eigenstrain $(\epsilon^*_{11}, \epsilon^*_{12}, \epsilon^*_{22}) = (\epsilon_0, 0, \epsilon_0)$ versus the number of vertices n, where E is the Young's modulus of the matrix and V_Ω is the volume of inclusion. It is noted in Fig. 8 that the normalized strain energy for the square type II under the dilational eigenstrain ($n = 4$) coincides with Chiu's solution (1980). Figure 9 shows the results of normalized strain energy based on the present model for a uniaxial eigenstrain $(\epsilon^*_{11}, \epsilon^*_{12}, \epsilon^*_{22}) = (\epsilon_0, 0, 0)$ where the analytical results by Chiu (1980) for $n = 4$ are shown as an open square (□) $\bar{W}^* = 0.195$, and the present results for the square type I by an open diamond square (◇) $\bar{W}^* = 0.180$, while the Eshelby's results for a circular cylinder are $\bar{W}^* = 0.1875$. Thus the strain energy for a cylindrical inclusion lies between those of square type I and II. If the present model is applied to another tilted square (square type III, in Fig. 7) where the angle of tilt is 22.5 deg,

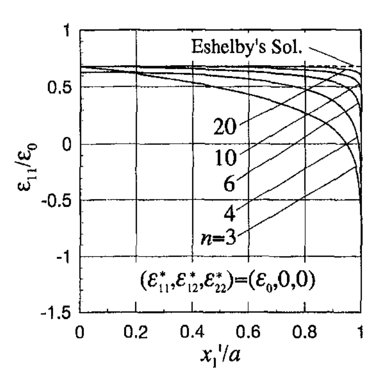

Fig. 5 Normalized total strain ϵ_{11}/ϵ_0 in regular polygon-shaped inclusions along the x_1'-axis for a uniaxial eigenstrain (ϵ_0, 0, 0)

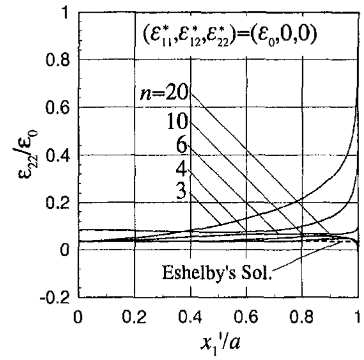

Fig. 6 Normalized total strain ϵ_{22}/ϵ_0 in regular polygon-shaped inclusions along the x_1'-axis for a uniaxial eigenstrain (ϵ_0, 0, 0)

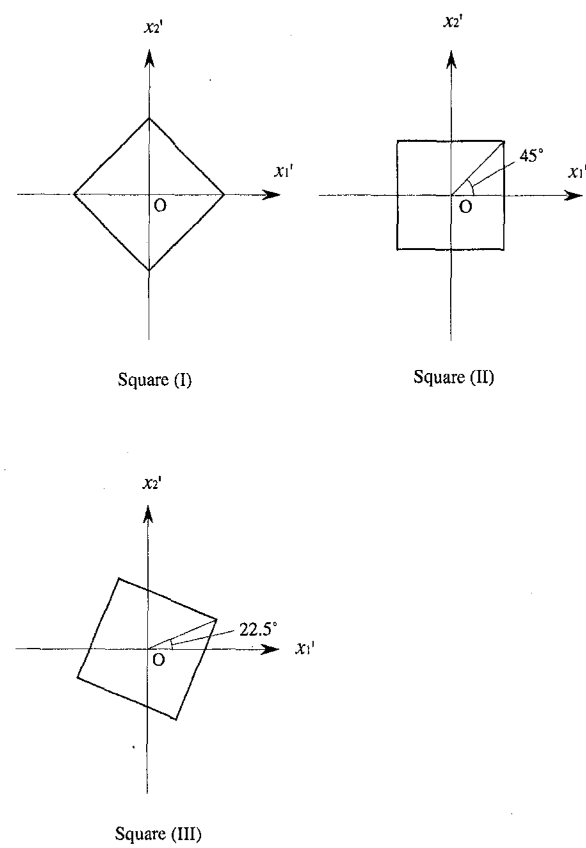

Fig. 7 Geometry of various types of square: type I (diamond square with tilt angle $\pi/4$), type II (regular square with zero tilt angle), type III (with $\pi/8$ tilt angle)

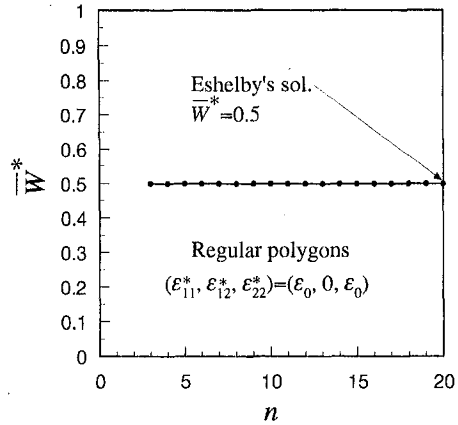

Fig. 8 Normalized elastic strain energy $\bar{W}^* = W^*(1-\nu^2)/\epsilon_0^2 EV_\Omega$ in an infinite body with a regular polygon-shaped inclusions of n sides for a dilational eigenstrain $(\epsilon_0, 0, \epsilon_0)$

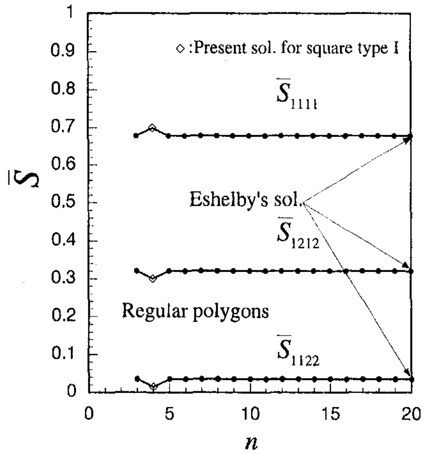

Fig. 10 Averaged Eshelby tensor $\bar{S}_{ijkl}$ for regular polygon-shaped inclusion versus n

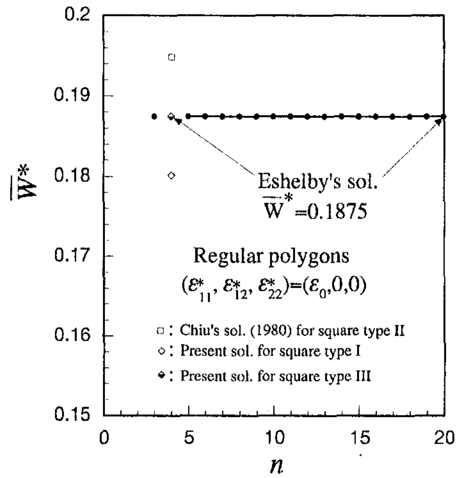

Fig. 9 Normalized elastic strain energy $\bar{W}^* = W^*(1-\nu^2)/\epsilon_0^2 EV_\Omega$ in an infinite body with a regular polygon-shaped inclusion of n sides for a uniaxial eigenstrain $(\epsilon_0, 0, 0)$

just a half of square type II, the strain energy of an infinite body containing the square inclusion of type III ◇ coincides with the Eshelby's results for a circular inclusion, i.e., $\bar{W}^* = 0.1875$. For square type III, the computed S_{1111}, S_{1122}, S_{2211}, and S_{2222} all coincides with the Eshelby's results for a circular inclusion, although the Eshelby's tensor for shear such as S_{1121} do not vanish. We computed $\bar{W}^*$ by using the present model for the square type II which was used by Chiu, and the result of $\bar{W}^*$ based on the present model coincide with Chiu's model: $\bar{W}^* = 0.195$. It should be noted that the values of the normalized strain energy of regular n-polygons approach to the Eshelby's solution of a circular cylinder as $n \to \infty$.

4.2 Stiffness of Composites With Polygon-Shaped Fibers. To obtain the effective stiffness of composites with polygon-shaped fibers, we first compute the averaged Eshelby's tensor in Eq. (23) numerically, using the same numerical integration procedure used for strain energy. Figure 10 shows the variation of averaged Eshelby tensor versus the number of vertices n for regular polygons where the present solutions for the square type I are shown by an open diamond square (◇). The averaged Eshelby tensor takes the same value as the one for a circular inclusion (Eshelby's solution) except for the case $n = 4$. This is similar to the case of the strain energy discussed above.

Table 1 shows the comparison between Eshelby tensor for a circular cylinder and averaged Eshelby tensor for square-shaped inclusions. It is noted in Table 1 that the values of S_{ijkl} for the square type I are those marked by an open diamond square (◇) in Fig. 10. We calculated the stiffness of an Al matrix composite reinforced with SiC square-shaped fibers by using Table 1 and the data of SiC and Al in Table 2, where indices 1 and 2 refer to the x_1' and x_2'-axes defined in Fig. 7, respectively. Figures 11 and 12 show the calculated stiffness tensor components C^c_{1111} and C^c_{1212} respectively, where subscripts 1 and 2 again refer to the x_1' and x_2' axes, respectively. It turns out that the stiffness for the square type I is larger

Table 1 Nonzero components of the averaged Eshelby's tensor for square-shaped inclusions

Eshelby's tensor	Circular cylinder	Square (I)	Square (II)
S_{1111}	0.678571	0.699546	0.657597
S_{1122}	0.035714	0.014740	0.056689
S_{1212}	0.321429	0.300454	0.342403

Table 2 Elastic stiffness of SiC and Al

Material	C_{1111} (GPa)	C_{1212} (GPa)
Al Matrix	110.5	26.5
SiC Fiber	474.2	188.1

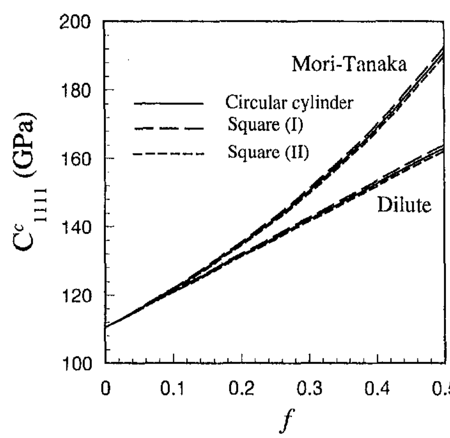

Fig. 11 Composite stiffness components C^c_{1111} versus volume fraction f

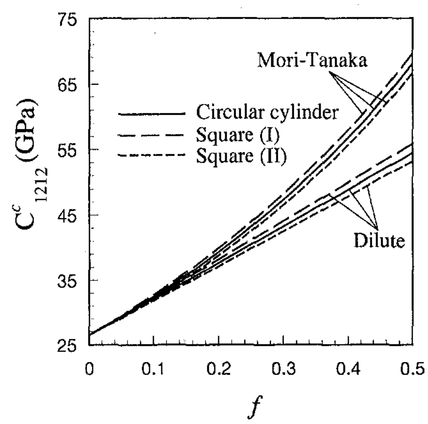

Fig. 12 Composite stiffness components C^c_{1212} versus volume fraction f

than that for circular cylinder, and the stiffness for the square type II is smaller than that for circular cylinder. The shape effect is larger on C^c_{1212} than C^c_{1111}. It should be noted here that the cross section of common SiC fiber is normally either circular or hexagonal. In these cases, the computation of the elastic constants of SiC fiber composites can be done by using the standard Eshelby's model where the values of S_{ijkl} are for a circular cylinder, which coincide with those for a fiber of hexagonal cross section. It should also be noted that a high performance transducer element is made of PZT fiber of square cross section embedded in epoxy matrix. The present model would be useful in analyzing the stress field in such a piezoelectric composite.

Acknowledgments

We express our deep thanks to Prof. T. Mura (Northwestern University) for his encouragement in this work, although our results turned out to be different from his. This work was supported in part by a grant from National Science Foundation to the University of Washington (CMS-9414696).

References

Benveniste, Y., 1987, "A New Approach to the Application of Mori-Tanaka's Theory in Composite Materials," *Mechanics of Materials*, Vol. 6, pp. 147–157.

Chiu, Y. P., 1977, "On the Stress field Due to Initial Strains in a Cuboid Surrounded by an Infinite Elastic Space," ASME JOURNAL OF APPLIED MECHANICS, Vol. 44, pp. 587–590.

Chiu, Y. P., 1978, "On the Stress Field and Surface Deformation in a Half Space With Cuboidal Zone in which Initial Strains Are Uniform," ASME JOURNAL OF APPLIED MECHANICS, Vol. 45, pp. 302–306.

Chiu, Y. P., 1980, "On the Internal Stresses in a Half Plane and a Layer Containing Localized Inelastic Strains or Inclusions," ASME JOURNAL OF APPLIED MECHANICS, Vol. 47, pp. 313–318.

Dunn, M. L., and Taya, M., 1992, "Micromechanics Predictions of the Effective Electroelastic Moduli of Piezoelectric Composites," *International Journal of Solids and Structures*, Vol. 30, No. 2, pp. 161–175.

Eshelby, J. D., 1957, "The Determination of the Elastic Field of an Ellipsoidal Inclusion and Related Problems," *Proceedings of the Royal Society, London*, Vol. A241, pp. 376–396.

Faivre, G., 1964, "Déformations de cohérence d'un précipité quadratique," *Physica Status Solidi*, Vol. 35, pp. 249–259.

Lee, J. K., and Johnson, W. C., 1977, "Elastic Strain Energy and Interactions of Thin Square Plates Which Have Undergone a Simple Shear," *Scripta Metallurgica*, Vol. 11, pp. 477–484.

Lee, J. K., and Johnson, W. C., 1978, "Calculation of the Elastic Strain Field of a Cuboidal Precipitate in an Anisotropic Matrix," *Physica Status Solidi*, Vol. 46, pp. 267–272.

Mori, T., and Tanaka, K., 1973, "Average Stress in Matrix and Average Elastic Energy of Materials with Misfitting Inclusions," *Acta Metall.* Vol. 21, pp. 571–574.

Mura, T., 1987, *Micromechanics of Defects in Solids*, 2nd ed., Martinus Nijhoff, Dordrecht, The Netherlands.

Mura, T., Shodja, H. M., Lin, T. Y., Safadi, A., and Makkawy, A., 1994, "The determination of the Elastic Field of a Pentagonal Star Shaped Inclusion," Bulletin of the Technical University of Istanbul for dedicating Dr. Erdogan and Dr. Suhubi's Anniversary.

Owen, D. R. J., 1972, "Analysis of Fibre-Reinforced Materials by an Initial Strain Method," *Fibre Science and Technology*, Vol. 5, pp. 37–59.

Sankaran, R., and Laird, C., 1976, "Deformation Field of a Misfitting Inclusion," *Journal of the Mechanics and Physics of Solids*, Vol. 24, pp. 251–262.

Takao, Y., Taya, M., and Chou, T. W., 1981, "Stress Field Due to a Cylindrical Inclusion With Constant Axial Eigenstrain in an Infinite Elastic Body," ASME JOURNAL OF APPLIED MECHANICS, Vol. 48, pp. 853–858.

APPENDIX A

Integral Formulae

To perform the integral in Eq. (9), the following formulae are used:

$$\int \frac{\cos\theta}{a\cos\theta + b\sin\theta}\,d\theta = \frac{a\theta + b\log|a\cos\theta + b\sin\theta|}{a^2+b^2},$$

$$\int \frac{\sin\theta}{a\cos\theta + b\sin\theta}\,d\theta = \frac{b\theta - a\log|a\cos\theta + b\sin\theta|}{a^2+b^2},$$

$$\int \frac{\cos^3\theta}{a\cos\theta + b\sin\theta}\,d\theta = \frac{2a\theta(a^2+3b^2) + (a^2+b^2)(b\cos 2\theta + a\sin 2\theta)}{4(a^2+b^2)^2} + \frac{b^3\log|a\cos\theta + b\sin\theta|}{(a^2+b^2)^2},$$

$$\int \frac{\cos^2\theta\sin\theta}{a\cos\theta + b\sin\theta}\,d\theta = \frac{2b\theta(b^2-a^2) - (a^2+b^2)(a\cos 2\theta - b\sin 2\theta)}{4(a^2+b^2)^2} - \frac{ab^2\log|a\cos\theta + b\sin\theta|}{(a^2+b^2)^2},$$

$$\int \frac{\cos\theta\sin^2\theta}{a\cos\theta + b\sin\theta}\,d\theta = \frac{2a\theta(a^2-b^2) - (a^2+b^2)(b\cos 2\theta + a\sin 2\theta)}{4(a^2+b^2)^2} + \frac{a^2b\log|a\cos\theta + b\sin\theta|}{(a^2+b^2)^2},$$

$$\int \frac{\sin^3\theta}{a\cos\theta + b\sin\theta}\,d\theta = \frac{2b\theta(3a^2+b^2) + (a^2+b^2)(a\cos 2\theta - b\sin 2\theta)}{4(a^2+b^2)^2} - \frac{a^3\log|a\cos\theta + b\sin\theta|}{(a^2+b^2)^2}. \quad \text{(A1)}$$

APPENDIX B

Third-Order Tensor $D_{ijk}(\mathbf{x})$ for Displacements

In equation (12), the components of $D_{ijk}(\mathbf{x})$ are

$$D_{ijk}(\mathbf{x}) = \frac{1}{4\pi(1-\nu)}\sum_{I=1}^{n}(\alpha_I x_1 + \beta_I x_2 + \gamma_I) \times [F^I_{ijk}(\Theta_I(\mathbf{x})) - F^I_{ijk}(\Theta_{I-1}(\mathbf{x}))], \quad \text{(A2)}$$

where

$$F^I_{111}(\theta) = (1 - 2\nu)\left\{\frac{\alpha_I\theta + \beta_I \log|\alpha_I\cos\theta + \beta_I\sin\theta|}{\alpha_I^2 + \beta_I^2}\right\}$$

$$+ \frac{2\alpha_I\theta(\alpha_I^2 + 3\beta_I^2) + (\alpha_I^2 + \beta_I^2)(\beta_I\cos 2\theta + \alpha_I\sin 2\theta)}{2(\alpha_I^2 + \beta_I^2)^2}$$

$$+ \frac{2\beta_I^3 \log|\alpha_I\cos\theta + \beta_I\sin\theta|}{(\alpha_I^2 + \beta_I^2)^2},$$

$$F^I_{112}(\theta) = (1 - 2\nu)\left\{\frac{\beta_I\theta - \alpha_I \log|\alpha_I\cos\theta + \beta_I\sin\theta|}{\alpha_I^2 + \beta_I^2}\right\}$$

$$+ \frac{2\beta_I\theta(\beta_I^2 - \alpha_I^2) - (\alpha_I^2 + \beta_I^2)(\alpha_I\cos 2\theta - \beta_I\sin 2\theta)}{2(\alpha_I^2 + \beta_I^2)^2}$$

$$- \frac{2\alpha_I\beta_I^2 \log|\alpha_I\cos\theta + \beta_I\sin\theta|}{(\alpha_I^2 + \beta_I^2)^2},$$

$$F^I_{121}(\theta) = F^I_{112}(\theta),$$

$$F^I_{122}(\theta) = -(1 - 2\nu)\left\{\frac{\alpha_I\theta + \beta_I \log|\alpha_I\cos\theta + \beta_I\sin\theta|}{\alpha_I^2 + \beta_I^2}\right\}$$

$$+ \frac{2\alpha_I\theta(\alpha_I^2 - \beta_I^2) - (\alpha_I^2 + \beta_I^2)(\beta_I\cos 2\theta + \alpha_I\sin 2\theta)}{2(\alpha_I^2 + \beta_I^2)^2}$$

$$+ \frac{2\alpha_I^2\beta_I \log|\alpha_I\cos\theta + \beta_I\sin\theta|}{(\alpha_I^2 + \beta_I^2)^2},$$

$$F^I_{211}(\theta) = -(1 - 2\nu)\left\{\frac{\beta_I\theta - \alpha_I \log|\alpha_I\cos\theta + \beta_I\sin\theta|}{\alpha_I^2 + \beta_I^2}\right\}$$

$$+ \frac{2\beta_I\theta(\beta_I^2 - \alpha_I^2) - (\alpha_I^2 + \beta_I^2)(\alpha_I\cos 2\theta - \beta_I\sin 2\theta)}{2(\alpha_I^2 + \beta_I^2)^2}$$

$$- \frac{2\alpha\beta_I^2 \log|\alpha_I\cos\theta + \beta_I\sin\theta|}{(\alpha_I^2 + \beta_I^2)^2},$$

$$F^I_{212}(\theta) = (1 - 2\nu)\left\{\frac{\alpha_I\theta + \beta_I \log|\alpha_I\cos\theta + \beta_I\sin\theta|}{\alpha_I^2 + \beta_I^2}\right\}$$

$$+ \frac{2\alpha_I\theta(\alpha_I^2 - \beta_I^2) - (\alpha_I^2 + \beta_I^2)(\beta_I\cos 2\theta + \alpha_I\sin 2\theta)}{2(\alpha_I^2 + \beta_I^2)^2}$$

$$+ \frac{2\alpha_I^2\beta_I \log|\alpha_I\cos\theta + \beta_I\sin\theta|}{(\alpha_I^2 + \beta_I^2)^2},$$

$$F^I_{221}(\theta) = F^2_{212}(\theta),$$

$$F^I_{222}(\theta) = (1 - 2\nu)\left\{\frac{\beta_I\theta - \alpha_I \log|\alpha_I\cos\theta + \beta_I\sin\theta|}{\alpha_I^2 + \beta_I^2}\right\}$$

$$+ \frac{2\beta_I\theta(3\alpha_I^2 + \beta_I^2) + (\alpha_I^2 + \beta_I^2)(\alpha_I\cos 2\theta - \beta_I\sin 2\theta)}{2(\alpha_I^2 + \beta_I^2)^2}$$

$$- \frac{2\alpha_I^3 \log|\alpha_I\cos\theta + \beta_I\sin\theta|}{(\alpha_I^2 + \beta_I^2)^2}. \quad \text{(A3)}$$

APPENDIX C

Eshelby's Tensor $S_{ijkl}(\mathbf{x})$, for Polygon-Shaped Inclusions

In Eq. (14), the components of $S_{ijkl}(\mathbf{x})$ are

$$S_{ijkl}(\mathbf{x}) = \tfrac{1}{2}(D_{ikl,j} + D_{jkl,i}) = \frac{1}{4\pi(1-\nu)}$$

$$\times \sum_{I=1}^{n} [E^I_{ijkl}(\Theta_I(\mathbf{x}), \mathbf{x}) - E^I_{ijkl}(\Theta_{I-1}(\mathbf{x}), \mathbf{x})], \quad \text{(A4)}$$

where $S_{ijkl} = S_{jikl} = S_{ijlk}$, $E^I_{ijkl}(\theta, \mathbf{x})$ are

$$E^I_{1111}(\theta, \mathbf{x}) = \alpha_I F^I_{111}(\theta) + (\alpha_I x_1 + \beta_I x_2 + \gamma_I)B^I_{111}(\theta)H_1(\theta),$$

$$E^I_{1112}(\theta, \mathbf{x}) = \alpha_I F^I_{112}(\theta) + (\alpha_I x_1 + \beta_I x_2 + \gamma_I)B^I_{112}(\theta)H_1(\theta),$$

$$E^I_{1121}(\theta, \mathbf{x}) = E^I_{1112}(\theta, \mathbf{x}),$$

$$E^I_{1122}(\theta, \mathbf{x}) = \alpha_I F^I_{122}(\theta) + (\alpha_I x_1 + \beta_I x_2 + \gamma_I)B^I_{122}(\theta)H_1(\theta),$$

$$E^I_{1211}(\theta, \mathbf{x}) = \tfrac{1}{2}\{\alpha_I F^I_{211}(\theta) + \beta_I F^I_{111}(\theta)$$

$$+ (\alpha_I x_1 + \beta_I x_2 + \gamma_I)(B^I_{111}(\theta)H_2(\theta) + B^I_{211}(\theta)H_1(\theta))\},$$

$$E^I_{1212}(\theta, \mathbf{x}) = \tfrac{1}{2}\{\alpha_I F^I_{212}(\theta) + \beta_I F^I_{112}(\theta)$$

$$+ (\alpha_I x_1 + \beta_I x_2 + \gamma_I)(B^I_{112}(\theta)H_2(\theta) + B^I_{212}(\theta)H_1(\theta))\},$$

$$E^I_{1221}(\theta, \mathbf{x}) = E^I_{1212}(\theta, \mathbf{x}),$$

$$E^I_{1222}(\theta, \mathbf{x}) = \tfrac{1}{2}\{\alpha_I F^I_{222}(\theta) + \beta_I F^I_{122}(\theta)$$

$$+ (\alpha_I x_1 + \beta_I x_2 + \gamma_I)(B^I_{122}(\theta)H_2(\theta) + B^I_{222}(\theta)H_1(\theta))\},$$

$$E^I_{2111}(\theta, \mathbf{x}) = E^I_{1211}(\theta, \mathbf{x}),$$

$$E^I_{2112}(\theta, \mathbf{x}) = E^I_{1212}(\theta, \mathbf{x}),$$

$$E^I_{2121}(\theta, \mathbf{x}) = E^I_{1212}(\theta, \mathbf{x}),$$

$$E^I_{2122}(\theta, \mathbf{x}) = E^I_{1222}(\theta, \mathbf{x}),$$

$$E^I_{2211}(\theta, \mathbf{x}) = \beta_I F^I_{211}(\theta) + (\alpha_I x_1 + \beta_I x_2 + \gamma_I)B^I_{211}(\theta)H_2(\theta),$$

$$E^I_{2212}(\theta, \mathbf{x}) = \beta_I F^I_{212}(\theta) + (\alpha_I x_1 + \beta_I x_2 + \gamma_I)B^I_{212}(\theta)H_2(\theta),$$

$$E^I_{2221}(\theta, \mathbf{x}) = E^I_{2212}(\theta, \mathbf{x}),$$

$$E^I_{2222}(\theta, \mathbf{x}) = \beta_I F^I_{222}(\theta)$$

$$+ (\alpha_I x_1 + \beta_I x_2 + \gamma_I)B^I_{222}(\theta)H_2(\theta), \quad \text{(A5)}$$

where $B^I_{jkl}(\theta)$ and $H_j(\theta)$ are

$$B^I_{111}(\theta) = \frac{(1-2\nu)\cos\theta + 2\cos^3\theta}{\alpha_I\cos\theta + \beta_I\sin\theta},$$

$$B^I_{112}(\theta) = \frac{(1-2\nu)\sin\theta + 2\cos^2\theta\sin\theta}{\alpha_I\cos\theta + \beta_I\sin\theta},$$

$$B^I_{122}(\theta) = -\frac{(1-2\nu)\cos\theta - 2\cos^2\theta\sin\theta}{\alpha_I\cos\theta + \beta_I\sin\theta},$$

$$B^I_{211}(\theta) = -\frac{(1-2\nu)\sin\theta - 2\cos^2\theta\sin\theta}{\alpha_I\cos\theta + \beta_I\sin\theta},$$

$$B^I_{212}(\theta) = \frac{(1-2\nu)\cos\theta + 2\cos\theta\sin^2\theta}{\alpha_I\cos\theta + \beta_I\sin\theta},$$

$$B^I_{222}(\theta) = \frac{(1-2\nu)\sin\theta + 2\sin^3\theta}{\alpha_I\cos\theta + \beta_I\sin\theta}, \quad \text{(A6)}$$

$$H_1(\Theta(\mathbf{x})) = \frac{\partial\Theta(\mathbf{x})}{\partial x_1}$$

$$= -\frac{x_2 - x_2^1}{d_1^2}$$

$$- \sum_{J=1}^{I} \frac{1}{\sqrt{(2d_J d_{J+1})^2 - (d_J^2 + d_{J+1}^2 - a_J^2)^2}}$$

$$\times \left\{2(x_1 - x_1^J) + 2(x_1 - x_1^{J+1})\right.$$

$$\left. - (d_J^2 + d_{J+1}^2 - a_J^2)\left(\frac{x_1 - x_1^{J+1}}{d_{J+1}^2} + \frac{x_1 - x_1^J}{d_J^2}\right)\right\},$$

$$H_2(\Theta(\mathbf{x})) = \frac{\partial \Theta(\mathbf{x})}{\partial x_2}$$

$$= \frac{x_1 - x_1^1}{d_1^2}$$

$$- \sum_{J=1}^{I} \frac{1}{\sqrt{(2d_J d_{J+1})^2 - (d_J^2 + d_{J+1}^2 - a_J^2)^2}}$$

$$\times \left\{ 2(x_2 - x_2^J) + 2(x_2 - x_2^{J+1}) \right.$$

$$- (d_J^2 + d_{J+1}^2 - a_J^2)$$

$$\left. \times \left(\frac{x_2 - x_2^{J+1}}{d_{J+1}^2} + \frac{x_2 - x_2^J}{d_J^2} \right) \right\}. \quad \text{(A7)}$$

A Yield Criterion for Porous Ductile Media at High Strain Rate

Ze-Ping Wang

Qing Jiang

Department of Engineering Mechanics,
University of Nebraska,
Lincoln, NE 68588-0347

An approximate yield criterion for porous ductile media at high strain rate is developed adopting energy principles. A new concept that the macroscopic stresses are composed of two parts, representing dynamic and quasi-static components, is proposed. It is found that the dynamic part of the macroscopic stresses controls the movement of the dynamic yield surface in stress space, while the quasi-static part determines the shape of the dynamic yield surface. The matrix material is idealized as rigid-perfectly plastic and obeying the von Mises yield. An approximate velocity field for the matrix is employed to derive the dynamic yield function. Numerical results show that the dynamic yield function is dependent not only on the rate of deformation but also on the distribution of initial micro-damage, which are different from that of the quasi-static condition. It is indicated that inertial effects play a very important role in the dynamic behavior of the yield function. However, it is also shown that when the rate of deformation is low ($\leq 10^3$/sec), inertial effects become vanishingly small, and the dynamic yield function in this case reduces to the Gurson model.

1 Introduction

It is quite evident that the process of fracture of ductile materials under intense dynamic loading is mainly characterized by inertial effects (kinetic energy of void growth) which is different from that of quasi-static loading (Rajendran and Fyfe, 1982; Meyers and Aimone, 1983; Carroll et al., 1986; Wang, 1994). In addition, the influence of the thermal effect (adiabatic heating), generated by high rate of deformation, and the rate-dependent effect on evolution of dynamic damage is also important (Meyers and Aimone, 1983; Wang, 1994).

Carroll and Holt (1972) proposed a model of dynamic void growth in the case of spherical geometry subjected to spherical symmetric tension pressure, in which inertial effects were considered. The material was assumed to be rate independent and ideally plastic. This model has been modified by considering the influence of deviatoric stress (Butcher et al., 1974), viscosity (Johnson, 1981), and strain hardening (Perzyna, 1986). Curran and co-workers (Curran et al., 1987) established a computational model called NAG (nucleation and growth) for ductile dynamic fracture. In the model, two internal state variables N (the number of microvoids) and R (average radius of microvoids) were introduced to describe the process of dynamic fracture in solids. However, the influence of inertial effects on void growth was not included in their model. Wang (1994) developed a model of void growth in ductile porous materials under intense dynamic loading. In his model, the influence of the inertial, thermal, and rate-dependent effects on void growth were taken into account.

Gurson (1977) first developed approximate yield criteria and flow rules for ductile porous materials. In the Gurson model, the matrix material is idealized as rigid-perfectly plastic and obeying the von Mises yield criterion. The main advantage of the Gurson model is its simplicity and its ability to provide direct calculation of the microparameters, which are essential in predicting failure. The Gurson model has widely been used in the predictions of the behavior in porous ductile media under quasi-static loading (Tvergaard 1990). The Gurson theory has also been used to model the process of dynamic ductile fracture by Rajendran and Fyfe (1982), Johnson and Addessio (1988), and Worswick and Pick (1995). But the predictions were not as good as expected.

The purpose of this work is to develop an approximate dynamic yield criterion which is a dynamic extension of the Gurson model and from which the dynamic constitutive relationships can be derived for porous ductile materials. In the present work, our attention is restricted to consider the inertial term. No attempt is made to include rate-dependent and thermal effects.

2 Dynamic Yield Function

Consider a representative macroscopic volume element (RVE) containing a distribution of spherical voids of mean radius a and mean spacing b. The solid surrounding the void is idealized as homogeneous, incompressible, rigid-plastic, von Mises material, and the dilatation is due completely to void growth. Throughout this paper, the adjective "macroscopic" refers to average values of physical quantities (stress, rate of deformation, etc.) which represent the aggregate behavior. The macroscopic stress and rate of deformation acting on the RVE are denoted by Σ_{ij} and $\dot{E}_{ij}$, respectively. The corresponding microscopic stress and rate of deformation (in the matrix material) are σ_{ij} and $\dot{\epsilon}_{ij}$. For the purpose of analysis, the representative volume element is idealized as a single void in a rigid-plastic cell (as shown in Fig. 1) with volume, V. The volume of the matrix material in the cell is denoted by V_M. The void volume fraction f, which is defined as $f = V_M/V$, of the cell equals that of the aggregate (in this way, some account is taken of the interaction of neighboring voids). Take the void and the matrix material to be a system with outer radius b and inner radius a.

The macroscopic rate of deformation is defined, as in Gurson (1977), in terms of the velocity field on the surface of the unit cell

Contributed by the Applied Mechanics Division of The American Society of Mechanical Engineers for publication in the ASME Journal of Applied Mechanics.

Discussion on this paper should be addressed to the Technical Editor, Professor Lewis T. Wheeler, Department of Mechanical Engineering, University of Houston, Houston, TX 77204-4792, and will be accepted until four months after final publication of the paper itself in the ASME Journal of Applied Mechanics.

Manuscript received by the ASME Applied Mechanics Division, July 17, 1995; final revision, Feb. 19, 1997 Associate Technical Editor: R. Becker.

$$\dot{E}_{ij} = \frac{1}{V}\int_S \frac{1}{2}(v_i n_j + v_j n_i)dS, \tag{1}$$

where v_j is the microscopic velocity field, S is its outer surface, and $\mathbf{n}$ is the unit outward normal on S. For the true stress field σ_{ij} and the true strain-rate $\dot{\epsilon}_{ij}$, the following conditions should be satisfied:

$$v_i = \dot{E}_{ij}x_j \text{ on } S \text{ (Cartesian coordinates)}, \tag{2}$$

$$\sigma_{ij,j} = \rho_s \dot{v}_i \text{ in } \Omega \text{ (Cartesian coordinates)}, \tag{3}$$

where x_j is the position of a material point in cartesian coordinates, and $(\ )_{,j}$ denotes differentiation in the coordinate system. Indices i, j rang from 1 to 3, and summation convention is adopted for repeated indices, the overdot denotes the time rate of change, and ρ_s is the density of the matrix material.

Energy conservation requires that

$$W = I_i + I_k, \tag{4}$$

where W is the work done by the external applied stress Σ_{ij}, while I_i and I_k denote deformation energy and kinetic energy of the system, respectively. Differentiating Eq. (5) with respect to time t gives

$$\dot{W} = \dot{I}_i + \dot{I}_k, \tag{5}$$

with

$$\dot{W} = \Sigma_{ij}\dot{E}_{ij}, \tag{6a}$$

$$\dot{I}_i = \frac{1}{V}\int_{V_M} \sigma_{ij}\dot{\epsilon}_{ij}dV, \tag{6b}$$

$$\dot{I}_k = \frac{\rho_s}{V}\frac{d}{dt}\left(\int_{V_m}\frac{1}{2}v_k v_k dV\right), \tag{6c}$$

where v_k is the component of the actual velocity field in the matrix material which is characterized by its generation of the minimum of the dissipation $\dot{W}$. In this case, Gurson (1977) proved that the yield locus of Σ_{ij} has the properties of convexity and normality. That is

$$\Sigma_{ij} = \frac{\partial \dot{W}}{\partial \dot{E}_{ij}}. \tag{7}$$

Gurson's result was obtained in the quasi-static condition. In what follows we can prove that the approximate actual velocity field also minimize $\dot{I}_i + \dot{I}_k$ so that Eq. (7) can be suitable for the dynamic loading.

Axisymmetric motion with symmetric axis x_3 is considered in the present work. The macroscopic rate of deformation is described by

$$\dot{E}_{11} = \dot{E}_{22} \neq 0, \quad |\dot{E}_{33}| \geq |\dot{E}_{11}|, \quad \dot{E}_{ij} = 0\ (i \neq j). \tag{8}$$

The situation where $|\dot{E}_{33}| < |\dot{E}_{11}|$ may be analyzed in a similar manner.

The rate of deformation $\dot{\epsilon}_{ij}$, in the matrix material expressed in spherical polar coordinate as shown in Fig. 1, is given by

$$\dot{\epsilon}_{rr} = \frac{\partial v_r}{\partial r}, \tag{9a}$$

$$\dot{\epsilon}_{\theta\theta} = \frac{1}{r}\frac{\partial v_\theta}{\partial \theta} + \frac{v_r}{r}, \tag{9b}$$

$$\dot{\epsilon}_{\varphi\varphi} = ctg\,\theta\frac{v_\theta}{r} + \frac{v_r}{r}, \tag{9c}$$

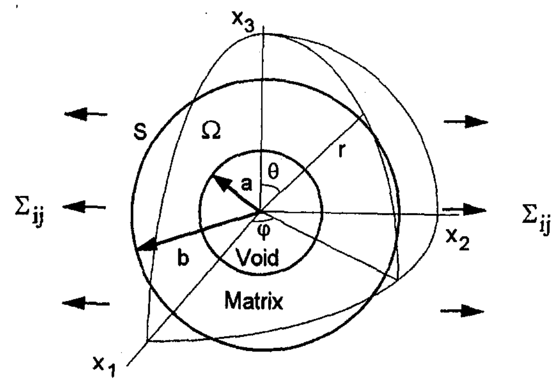

Fig. 1 A rigid-plastic spherical cell

$$\dot{\epsilon}_{r\theta} = \frac{1}{2}\left(\frac{\partial v_\theta}{\partial r} - \frac{v_\theta}{r} + \frac{1}{r}\frac{\partial v_r}{\partial \theta}\right), \tag{9d}$$

where v_r and v_θ are components of the velocity field $\mathbf{v}$.

The velocity field $\mathbf{v}$ is assumed to be broken up into three parts (as in references (Gurson, 1977; Sun and Huang, 1992)),

$$\mathbf{v} = \mathbf{v}^s + \mathbf{v}^v + \mathbf{v}^*, \tag{10}$$

where

$$v_i^s = \dot{E}'_{ij}x_j, \tag{11a}$$

$$v_i^v = \frac{1}{3}\dot{E}_{kk}\left(\frac{b}{r}\right)^3 x_i, \tag{11b}$$

$\dot{E}'_{ij}$ and $\dot{E}_{kk}$ denote the deviatoric and dilatant parts of the macroscopic rate of deformation $\dot{E}_{ij}$, respectively. $\mathbf{v}^*$ is an additional velocity field given by (Sun and Huang, 1992)

$$v_r^* = -\frac{1}{r^2\sin\theta}\frac{\partial\eta(r,\theta)}{\partial\theta}, \tag{12a}$$

$$v_\theta^* = \frac{1}{r\sin\theta}\frac{\partial\eta(r,\theta)}{\partial r}, \tag{12b}$$

$\eta(r, \theta)$ is given by

$$\eta(r,\theta) = \frac{3}{2}\dot{E}_e(b-r)^2\sin\theta\sum_{k=2,4,\cdots}R_k(r)P_{k,\theta}(\cos\theta),$$

$$R_k(r) = \sum_{l=0,\pm1,\pm2,\cdots} a_{kl}r^l, \tag{13}$$

where $P_k(\cos\theta)$ is the Legendre polynomial of k, $\dot{E}_e = (\frac{2}{3}\dot{E}'_{ij}\dot{E}'_{ij})^{1/2} = \frac{2}{3}(\dot{E}_{33} - \dot{E}_{11})$ is the macroscopic effective rate of deformation. Parameters a_{kl} are chosen so that minimize $\dot{W}$. The velocity field $\mathbf{v}$ (Eq. (10)) obviously satisfies the boundary condition (2) and the incompressible condition.

The parameters a_{lk} in Eq. (13) could be determined by minimizing $\dot{I}_i + \dot{I}_k$. Let $(\dot{I}_i + \dot{I}_k)_0$ expresses the one given by the velocity field $\mathbf{v}^s + \mathbf{v}^v$, while $\dot{I}_i + \dot{I}_k$ is determined by $\mathbf{v}^s + \mathbf{v}^v + \mathbf{v}^*$. The steepest descent algorithm is used to determine the parameters a_{lk} by minimizing $\dot{I}_i + \dot{I}_k$. The numerical results for copper-like material with $\sigma_0 = 0.26$ GPa, $\rho_s = 8.92$ g/cm^3, $a_0 = 0.00019$ cm, $f_0 = 0.0001$ show that $|(\dot{I}_i + \dot{I}_k)/(\dot{I}_i + \dot{I}_k)_0| \leq 0.9823$ for the condition of ($\dot{E}_m = \dot{E}_e = 10^5$/sec, $\ddot{E}_m = \ddot{E}_e = 0$) and $|(\dot{I}_i + \dot{I}_k)/(\dot{I}_i + \dot{I}_k)_0| \leq 0.9714$ for the condition of ($\dot{E}_m = \dot{E}_e = 10^5$/sec, $\ddot{E}_m = \ddot{E}_e = 0.1/\text{sec}^2$). Numerical calculation shows that $\mathbf{v}^*$ has little contribution to the value of $\dot{I}_i + \dot{I}_k$. So we can take approximately the velocity field,

$$\mathbf{v} = \mathbf{v}^s + \mathbf{v}^v, \tag{14}$$

as the actual velocity field, i.e.,

$$v_r \approx \frac{C_0}{r^2} + \frac{1}{4}\dot{E}_e r(1 + 3\cos 2\theta), \tag{15a}$$

$$v_\theta \approx -\tfrac{3}{4}\dot{E}_e r \sin 2\theta, \tag{15b}$$

where $C_0 = b^3\dot{E}_m$, $\dot{E}_m = \frac{1}{3}\dot{E}_{kk}$.

Substitution of Eq. (15) into Eq. (9) gives

$$\dot{\epsilon}_{rr} = -\frac{2C_0}{r^3} + \frac{1}{4}\dot{E}_e(1 + 3\cos 2\theta), \tag{16a}$$

$$\dot{\epsilon}_{\theta\theta} = \frac{C_0}{r^3} + \frac{1}{4}\dot{E}_e(1 - 3\cos 2\theta), \tag{16b}$$

$$\dot{\epsilon}_{\varphi\varphi} = \frac{C_0}{r^3} - \frac{1}{2}\dot{E}_e, \tag{16c}$$

$$\dot{\epsilon}_{r\theta} = -\tfrac{3}{4}\dot{E}_e \sin 2\theta. \tag{16d}$$

The effective rate of deformation $\dot{\epsilon}_e$ in the matrix material can be expressed by

$$\dot{\epsilon}_e = \left(\frac{4C_0^2}{r^6} - \frac{C_0\dot{E}_e h(\theta)}{r^3} + \dot{E}_e^2\right)^{1/2}, \tag{17}$$

where $h(\theta) = 1 + 3\cos 2\theta$.

By virtue of Eq. (17), the rate of deformation energy of the system $\dot{I}_i$ can be expressed as

$$\dot{I}_i = \frac{3\sigma_0}{2b^3}\int_0^\pi \int_a^b \left[\frac{4C_0^2}{r^6} - h(\theta)\frac{C_0\dot{E}_e}{r^3} + \dot{E}_e^2\right]^{1/2} \times \sin\theta r^2 d\theta dr. \tag{18}$$

By introducing variables ω, ω^*, and x such that

$$\omega = \frac{2}{3}\frac{\dot{V}}{\dot{E}_e V} = \frac{2\dot{E}_m}{\dot{E}_e}, \quad \omega^* = \frac{\omega}{f}, \quad x = \omega\left(\frac{b}{r}\right)^3, \tag{19}$$

Eq. (18) can be rewritten as

$$\dot{I}_i = \tfrac{1}{2}\sigma_0\dot{E}_e U(\omega, f), \tag{20}$$

where

$$U(\omega, f) = \omega\int_\omega^{\omega^*}\left[1 - \tfrac{1}{2}h(\theta)x + x^2\right]^{1/2} x^{-2}dx. \tag{21}$$

Since

$$-1 \le \frac{2x}{1 + x^2} \le 1, \quad -\frac{1}{2} \le \frac{h(\theta)}{4} \le 1, \tag{22}$$

we have

$$\left(1 - \frac{1}{2}h(\theta)x + x^2\right)^{1/2} = (1 + x^2)^{1/2}\left[1 - \frac{1}{4}h(\theta)\frac{x}{1 + x^2} - \frac{1}{32}h^2(\theta)\left(\frac{x}{1 + x^2}\right)^2 + \cdots\right]$$
$$\approx (1 + x^2)^{1/2}\left[1 - \frac{1}{4}h(\theta)\frac{x}{1 + x^2}\right]. \tag{23}$$

Substitution of Eq. (23) into Eq. (21) gives

$$U(\omega, f) \approx 2\omega\left[\frac{\sqrt{1 + \omega^2}}{\omega} - \frac{\sqrt{1 + \omega^{*2}}}{\omega^*} + \ln\frac{\omega^* + \sqrt{1 + \omega^{*2}}}{\omega + \sqrt{1 + \omega^2}}\right]. \tag{24}$$

Using Eq. (15), the rate of kinetic energy of the system $\dot{I}_k$ can be expressed as

$$\dot{I}_k = a_0^2\rho_s\left(\frac{1 - f_0}{f_0}\right)^{2/3}(1 - f)^{-2/3}\left\{\frac{1}{4}\dot{E}_m[f_1(f)\dot{E}_m^2 + f_2(f)\dot{E}_e^2] + 3[f_3(f)\dot{E}_m\ddot{E}_m + f_4(f)\dot{E}_e\ddot{E}_e]\right\}, \tag{25}$$

with

$$f_1(f) = 2(6f^{-1/3} - f^{-4/3} - 5), \tag{26a}$$

$$f_2(f) = 1 - f^{2/3}, \tag{26b}$$

$$f_3(f) = f^{-1/3} - 1, \tag{26c}$$

$$f_4(f) = \tfrac{1}{10}(1 - f^{5/3}), \tag{26d}$$

where a_0 and f_0 denote the initial radius of a void and the initial void volume fraction, respectively.

Components of the macroscopic stresses can be obtained by

$$\Sigma_{11} = \Sigma_{22} = \frac{1}{2}\frac{\partial\dot{W}}{\partial\dot{E}_{11}}, \tag{27a}$$

$$\Sigma_{33} = \frac{\partial\dot{W}}{\partial\dot{E}_{33}}, \tag{27b}$$

After some manipulation, we have

$$\Sigma_m = \tfrac{1}{3}(\Sigma_{11} + \Sigma_{22} + \Sigma_{33}) = \Sigma_m^s + \Sigma_m^d, \tag{28a}$$

$$\Sigma_e = \Sigma_{33} - \Sigma_{11} = \Sigma_e^s + \Sigma_e^d, \tag{28b}$$

with

$$\Sigma_m^s = \frac{2}{3}\sigma_0 \ln\frac{\omega^* + \sqrt{1 + \omega^{*2}}}{\omega + \sqrt{1 + \omega^2}}, \tag{29a}$$

$$\Sigma_e^s = \sigma_0\omega\left(\frac{\sqrt{1 + \omega^2}}{\omega} - \frac{\sqrt{1 + \omega^{*2}}}{\omega^*}\right), \tag{29b}$$

$$\Sigma_m^d = \frac{1}{12}a_0^2\rho_s\left(\frac{1 - f_0}{f_0}\right)^{2/3}(1 - f)^{-2/3} \times [3f_1(f)\dot{E}_m^2 + f_2(f)\dot{E}_e^2 + 12f_3(f)\ddot{E}_m], \tag{30a}$$

$$\Sigma_e^d = \frac{1}{2}a_0^2\rho_s\left(\frac{1 - f_0}{f_0}\right)^{2/3}(1 - f)^{-2/3} \times [f_2(f)\dot{E}_m\dot{E}_e + 6f_4(f)\ddot{E}_e], \tag{30b}$$

where Σ_m and Σ_e are the macroscopic mean and effective stresses, respectively. Equations (28)–(30) indicate that the macroscopic stresses are divided into two parts, the quasi-static part represented by superscript "s" and the dynamic part denoted by superscript "d," due to inertial effects.

By eliminating parameters ω and ω^* in Eq. (29), the expression of a dynamic yield function (yield criterion) can be obtained,

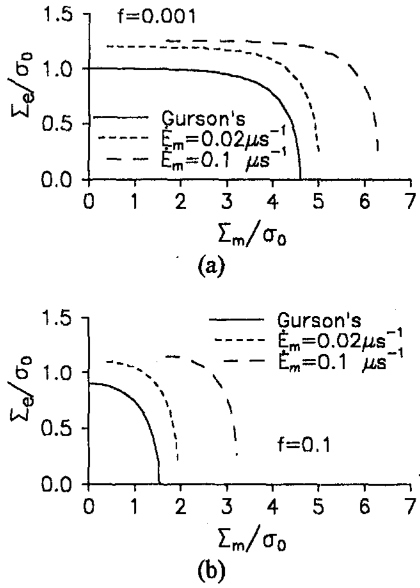

Fig. 2 The movements of the dynamic yield surface in stress space with different values of f and $\dot{E}_m$ for the case of $\dot{E}_e = \dot{E}_m$

$$\Phi(\Sigma_{ij}, \dot{E}_{ij}, \ddot{E}_{ij}, f) = \left(\frac{\Sigma_e - \Sigma_e^d}{\sigma_0}\right)^2 + 2f\cosh\left(\frac{3}{2}\frac{\Sigma_m - \Sigma_m^d}{\sigma_0}\right) - (1 + f^2) = 0. \quad (31)$$

3 Dynamic Freatures of Yield Function

Computed results of Eqs. (29)–(30) indicate that when $\dot{E}_m \le 10^3$/sec, $\Sigma_m^d \ll \Sigma_m^s$ and $\Sigma_e^d \ll \Sigma_e^s$. In this case, $\Sigma_m \approx \Sigma_m^s$, $\Sigma_e \approx \Sigma_e^s$. However, as the rate of deformation is greater than 10^3/sec, the dynamic part of the macroscopic stresses becomes significant. Σ_m^d and Σ_e^d increase rapidly with the increasing rate of deformation. The dynamic yield function Eq. (31) reveals that in stress space, the coordinates of the center of the dynamic yield surface $\Phi(\Sigma_{ij}, \dot{E}_{ij}, \ddot{E}_{ij}, f)$ are determined by Σ_m^d/σ_0 and Σ_e^d/σ_0. The distance between the original point of the coordinate and the center of the dynamic yield surface in stress space, d, is given by

$$d = [(\Sigma_m^d/\sigma_0)^2 + (\Sigma_e^d/\sigma_0)^2]^{1/2}. \quad (32)$$

A copper-like material is chosen for numerical analysis. In order to investigate dependence of the dynamic yield function (Eq. (31)) on the void volume fraction f and the dilatant rate of deformation $\dot{E}_m$, a simple situation, $\dot{E}_e = \dot{E}_m$, is employed to carry out numerical analysis (as shown in Fig. 2). It is shown that the distance d moved by the dynamic yield surface increases as $\dot{E}_m$ increases for the same value of the void volume fraction f.

To investigate the dependence of the movement behavior of the dynamic yield function in stress space on the rate of deformation and the size of voids, numerical computations have been carried out for the case of $\dot{E}_e = \dot{E}_m$, which are displayed in Fig. 3. Figure 3 indicates that the distance d of movement of the dynamic yield surface has a very strong rate dependence. d decreases with increasing f. It is also sensitive to the void volume fraction f.

Numerical investigations of the dependence of d on the initial radius a_0 of a void and the initial void volume fraction f_0 have also been performed, and are shown in Figs. 4–5. Computational results indicate that d is quite sensitive to a_0 especially for small values of f. In addition, it can be seen clearly from Fig. 5, that d is also dependent on the initial value of the void volume fraction f_0. But dependence of d on f_0 is relatively weak when compared with that of a_0.

4 Finite-Difference Calculation

As an application of the foregoing theory, a spallation experiment on copper is calculated. The experimental setup, the manganin pressure gauge record as well as the predicted result, are shown in Fig. 6.

The two-dimensional flow equations in terms of the macroscopic Lagrangian position coordinate X_i are

$$\dot{V}/V = U_{k,k}, \quad (33)$$

$$\rho \dot{U}_i = \Sigma_{ij,j}, \quad (34)$$

$$\rho \dot{E}_I = \Sigma_m \dot{V}/V + (\Sigma_{ij} - \delta_{ij}\Sigma_{kk})\dot{E}_{ij}, \quad (35)$$

with

$$\rho = (1 - f)\rho_s, \quad (36)$$

where U_i is component of the average velocity field, $\dot{V}$ is the rate of the average relative specific volume, E_I is the average specific internal energy, and ρ is the average density of the porous ductile material.

The macroscopic rate of deformation is written as the sum of an elastic part and a plastic part,

$$\dot{E}_{ij} = \dot{E}_{ij}^e + \dot{E}_{ij}^p. \quad (37)$$

$\dot{E}_{ij}^e$ is given by

$$\dot{E}_{ij}^e = \frac{1}{2\mu}\dot{\Sigma}_{ij} + \frac{1}{3}\left(\frac{1}{2K} - \frac{1}{2\mu}\right)\delta_{ij}\dot{\Sigma}_{kk}, \quad (38)$$

where μ and K are the elastic shear and bulk modulus, respectively, δ_{ij} is Kronecker delta. The dynamic yield function Eq. (31) is taken as the plastic potential such that

$$\dot{E}_{ij}^p = \Lambda \frac{\partial \Phi}{\partial \Sigma_{ij}}. \quad (39)$$

The parameter Λ is determined from the equivalent plastic work expression, $\Sigma_{ij}\dot{E}_{ij}^p \approx (1 - f)\sigma_e\dot{\epsilon} + \frac{1}{2}\rho \dot{U}_k U_k$,

$$\Lambda = \frac{(1 - f)\sigma_e\dot{\epsilon} + \frac{1}{2}\rho\dot{U}_k U_k}{\Sigma_{kl}\dfrac{\partial\Phi}{\partial\Sigma_{kl}}}, \quad (40)$$

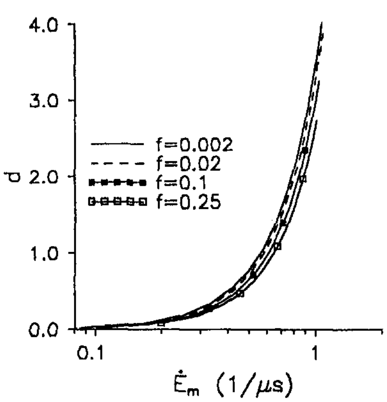

Fig. 3 The distance d of movement of the dynamic yield surface as a function of $\dot{E}_m$ and f. The curves are computed for the case of $\dot{E}_e = \dot{E}_m$ with $f_0 = 0.0001$, $a_0 = 0.0019$ cm, $\rho_s = 8.92$ g/cm^3, and $\sigma_0 = 0.26$ GPa.

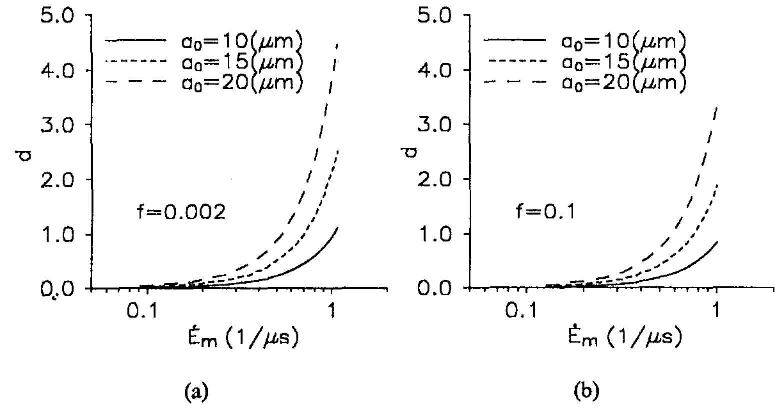

Fig. 4 Dependence of d on a_0 for different values of f with $f_0 = 0.0001$ and $\rho_s = 8.92$ g/cm^3

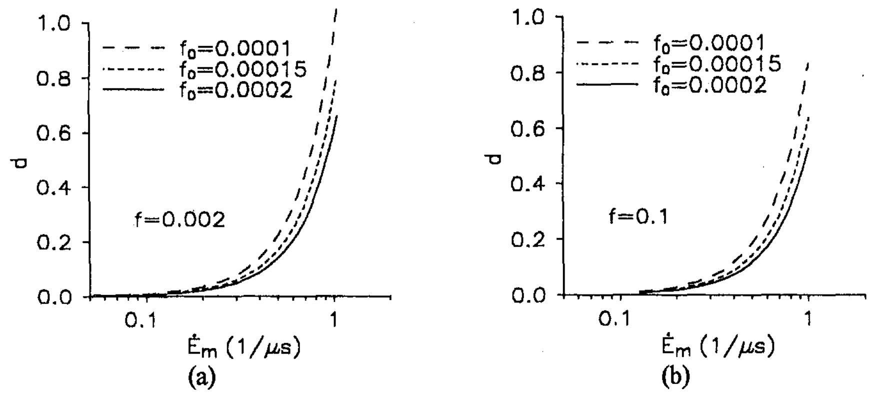

Fig. 5 Dependence of d on f_0 for different values of f with $a_0 = 0.001$ cm and $\rho_s = 8.92$ g/cm^3

with

$$\sigma_e = \sigma_0 \left(\frac{\dot\epsilon}{\dot\epsilon_0}\right)^m, \tag{41}$$

where σ_e is the effective stress in the matrix material, $\dot\epsilon_0$ is a reference strain rate, and m is the exponent coefficient which is taken so small ($m = 0.01$) that the behavior of the matrix acts as rigid-perfectly plastic.

The fracture criterion of a critical void volume fraction $f_{\rm crit}$ is adopted. That is, if the void volume fraction $f \geq f_{\rm crit}$, the mesh is taken to be failure. The rate of void growth is given by

$$\dot f \approx (1 - f)\dot E^p_{kk}. \tag{42}$$

The predicted result comparing with the experimental result is shown in Fig. 6. It seems that the predicted void growth is slightly slower than the record. The reason, we think, is that the thermal effect (adiabatic heating) is not considered in the constitutive relationships, since the thermal effect would decrease stress level and increase void growth. Anyway, as a whole, application of the dynamic damage analysis to the spalling process in copper gives a reasonable good representation of the data with the material parameters $\mu = 46.6$ GPa, $K = 139.7$ GPa, and $f_{\rm crit} = 0.3$.

5 Discussion

5.1 Some Special Cases. For the condition of pure dilatant deformation ($\ddot E_e$, $\dot E_e = 0$), from Eq. ($30a$), we can obtain a growth equation of a void,

$$\Sigma_m - \frac{2}{3}\sigma_0 \ln\frac{1}{f} = \frac{1}{3} a_0^2 \rho_s \left(\frac{1-f_0}{f_0}\right)^{2/3} (1-f)^{-8/3} \times [(f^{-1/3} + f - f^{2/3} - 1)\ddot f + \frac{1}{6}(12 f^{-1/3} - f^{-4/3} - 11)\dot f^2]. \tag{43}$$

This is exactly the same as that derived by Carroll and Holt (1972).

Numerical analyses indicate that as the rate of deformation $\leq 10^3$/sec, inertial effects can be ignored. Therefore, the dynamic yield criterion (Eq. (31)) reduces to the quasi-static criterion,

$$\Phi(\Sigma_{ij}, \sigma_0, f) = \left(\frac{\Sigma_e}{\sigma_0}\right)^2 + 2f\cosh\left(\frac{3}{2}\frac{\Sigma_m}{\sigma_0}\right) - (1 + f^2) = 0 \tag{44}$$

which is the Gurson model (Gurson, 1977).

5.2 Inertial Effects. It is evident that inertial effects play an important rule in the mechanical response of solids under intense dynamic loading (Rajendran and Fyfe, 1982; Meyers and Aimone, 1983; Regazzoni, et al., 1986; Carroll at al., 1986; Ortiz and Molmari, 1992; Wang, 1994). As a consequence of its influence on stability, inertial enhances ductility and exhibits the potentially stabilizing effect at the microscale. Experimental evidence suggests that there exists a threshold tensile stress at which fracture initiation takes place. However, a material can

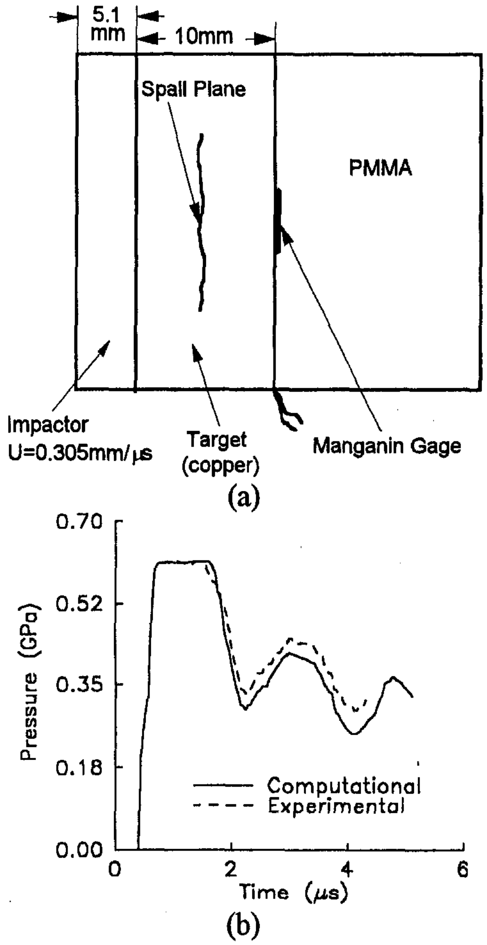

Fig. 6 (*a*) **The experimental setup.** (*b*) **A comparison between the prediction of the model (Eq. (31)) and the experimental data in sapallation in copper. ---- the data and —— the computed.**

bear tensile stresses considerably larger than such threshold stress without causing fracture. This is due to inertia or kinetics associated with the micromechanisms controlling the spall type of fracture. Experimental results indicate that in general, the threshold tensile stresses ($\Sigma^d_{\rm crit}$) for spall fracture are 3 ~ 5 times as large as those ($\Sigma^s_{\rm crit}$) of quasistatic loading. For example, for polycrystalline alumina, $\Sigma^d_{\rm crit} \approx 3\Sigma^s_{\rm crit}$ (Munson and Lawrence, 1979), and for copper, $\Sigma^d_{\rm crit} \approx 5\Sigma^s_{\rm crit}$ (Grady, 1988). The influence of inertial effects on the evolution of a void is resisting void growth (Johnson, 1981; Meyers and Aimone, 1983). Worwick and Pick (1995) modeled the processes of ductile fracture occurring during symmetric Taylor cylinder impact tests on leaded brass in great detail using the Gurson constitutive model implemented within the DYNA2D finite element code. Numerical results showed that the predicted void growth exceeded that observed experimentally and the predicted extent of void coalescence was too large. The problem Worwick and Pick met is that resistance of inertia on void growth was not taken into account, since the Gruson constitutive model is only suitable for the quasi-static condition due to inertial term being not included.

5.3 Comparisons With Other Models. The model describing dynamic growth of a void in porous ductile materials proposed by Carroll and Holt (1972), and later modified by Butcher and co-workers (1974), Johnson (1981), and Perzyna (1986), in fact, is only an evolution equation of void growth under high rate loading, rather than a constitutive model for porous ductile materials at high strain rate. So is our previous model (Wang, 1994). The original Carroll-Holt model is, as proved in the above content, a special result (under hydrostatic case, $\dot{E}_e = \ddot{E}_e = 0$) of the model developed here. Curran, Seaman, and Shockey (1987) carried out a systematic study of dynamic fracture in ductile and brittle solids and developed computational models for ductile and brittle fracture called NAG (nucleation and growth) models. The model features have been taken mainly from detailed observations of samples partially fractured during impacts rather than the theoretical analysis of microstructure of materials. The NAG models have sufficient generality to include the statistical distribution of one or more variables such as porosity, void density etc., but require numerous phenomenological constants that are difficult to obtain. In their models, inertial effects were not included.

An advantage of the model developed in the present work comparing with other models of dynamic growth of a void such as the Carroll-Holt model (1972) and our previous model (Wang, 1994) is that the present model is a macroscopic constitutive model for porous ductile materials at high strain rate which can describe the overall behavior of porous ductile materials under intense dynamic loading, not merely an evolution equation of dynamic growth of a void. For the special situation such as hydrostatic dynamic loading, the present model can reduce to an evolution equation of dynamic growth of a void which is the same as the Carroll-Holt model. As for comparison with NAG models (Curran et al., 1987), the present model is much more simpler than NAG model. There are only a few parameters to be determined. Meanwhile the present model can describe the continuum constitutive behavior in terms of the properties and structure of the microconstituents.

The dynamic yield function (Eq. (31)) actually is a dynamic extension of the Gurson model at high strain rate. Inertial effects on the constitutive behavior of porous ductile materials are emphasized and investigated in detail. The key point different from the Gurson model is that the filed variables in the matrix material are required to satisfy $\sigma_{ij,j} = \rho_s \dot{v}_i$. The terms $\rho_s \dot{v}_i$ called inertial terms represent the dynamic response characteristics of materials. The difference of descriptions between dynamic and quasi-static behavior of materials is whether considering inertial terms ($\rho_s \dot{v}_i$) or not. In the Gurson model, $\rho_s \dot{v}_i$ are not included.

To derive the dynamic yield criterion (Eq. (31)), an assumption that the form of velocity field of matrix material adopted in quasistatic deformation analysis is available for the case of high strain rate. Although the form of velocity field in the matrix is assumed to be the same as that of quasistatic case, the velocity field is required to satisfy the field equation $\sigma_{ij,j} = \rho_s \dot{v}_i$, which is different from the quasi-static field. The assumption we adopt is also employed by many investigators in intense dynamic deformation analysis (Carroll et al., 1972, 1986; Rajendran and Fyfe, 1982; Regazzoni, et al., 1986; Ortiz and Molinari, 1992). Numerical estimation carried out in the present work verifies that the approximate velocity field (Eq. (15)) is accurate enough to be taken as the true field. Using the approximate velocity field, the approximate yield function, which has the same form as the Gurson model, is derived.

A new concept that the macroscopic stresses are comprised of two parts, the quasistatic part Σ^s_m and Σ^s_e, and the dynamic part Σ^d_m and Σ^d_e due to inertial effects, is proposed in this work. The dynamic part of the macroscopic stresses represents the dynamic features of mechanical response of porous ductile materials. However, as the macroscopic rate of deformation $\le 10^3$/sec, Σ^d_m and Σ^d_e are vanishingly small comparing with Σ^s_m and Σ^s_e, i.e., $\Sigma_m \approx \Sigma^s_m$ and $\Sigma_e \approx \Sigma^s_e$. This is in consistence with the actual stress status in materials. Therefore, without deleting Σ^d_m and Σ^d_e from the dynamic yield function, Eq. (31) is also suitable for the quasistatic situation.

In the present work, our attention is restricted to consider a rigid-perfectly plastic material which is assumed to obey the von Mises yield. The influence of the strain-rate hardening of the matrix material and the thermal effect (adiabatic heating) generated by high rate of deformation on the dynamic behavior of porous ductile media is not taken into account. These effects will be investigated in our future work.

6 Conclusions

An approximate dynamic yield criterion for porous ductile media is developed by means of energy principles for a rate-independent rigid-perfectly plastic matrix material obeying the von Mises yield. Numerical analysis has been carried out in detail to investigate various features of the dynamic yield function. A new concept that the macroscopic stresses are comprised of two parts, the quasi-static part Σ_m^s and Σ_e^s, and the dynamic part Σ_m^d and Σ_e^d due to inertial effects, is proposed in this work. An interesting and important fact is found that the movement of the dynamic yield surface in stress space is only controlled by the dynamic part of the macroscopic stresses, Σ_m^d and Σ_e^d, while its shape is only determined by the quasi-static part of the macroscopic stresses, Σ_m^s and Σ_e^s. Analysis shows that when the rate of deformation $\leq 10^3$/sec, inertial effects become vanishing small due to $\Sigma_m^d \ll \Sigma_m^s$ and $\Sigma_e^d \ll \Sigma_e^s$, and the dynamic yield criterion in this case reduces to the Gurson yield criterion (a quasi-static yield criterion). To check the validation of the foregoing theory, a spalling experiment in copper is simulated. The prediction of the model is reasonably good.

Numerical analysis of the model proposed here reveal the following additional features of the dynamic yield function which are different from that of the quasistatic yield function: (1) the dynamic yield function is rate dependent; (2) inertial effects play an important role in the dynamic yield function when the rate of deformation is very high ($\geq 10^4$ sec^{-1}); (3) the influence of the distribution of the initial micro-damage in porous ductile materials on the dynamic yield is significant.

References

Butcher, B. M., Carroll, M. M., and Holt, A. C., 1974, "Shock-wave Compaction of Porous Aluminum," *J. Appl. Phys.*, Vol. 45, pp. 3864–3875.

Carroll, M. M., and Holt, A. C., 1972, "Static and Dynamic Pore-collapse Relations for Ductile Porous Materials," *J. Appl. Phys.*, Vol. 43, pp. 1626–1636.

Carroll, M. M., Kim, K. T., and Nesterenko, V. F., 1986, "The Effect of Temperature on Viscoplastic Pore Collapse," *J. Appl. Phys.*, Vol. 59, pp. 1962–1967.

Curran, D. R., Seaman, L., and Shockey, D. A., 1987, "Dynamic Failure of Solids," *Phys. Rep.*, Vol. 147, pp. 254–388.

Grady, D. E., 1988, "The Spall Strength of Condensed Matter," *J. Mech. Phys. Solids*, Vol. 36, pp. 353–384.

Gurson, A. L., 1977, "Continuum Theory of Ductile Rupture by Void Nucleation and Growth: Part I—Yield Criteria and Flow Rules for Porous Ductile Media," *J. Eng. Mater. Tech.*, Vol. 99, pp. 2–15.

Johnson, J. N., 1981, "Dynamic Fracture and Spallation in Ductile Solids," *J. Appl. Phys.*, Vol. 52, pp. 2812–2825.

Johnson, J. N., and Addessio, F. L., 1988, "Tensile Plasticity and Ductile Fracture," *J. Appl. Phys.*, Vol. 64, pp. 6699–6712.

Meyers, M. A., and Aimone, C. T., 1983, "Dynamic Failure (Spalling) of Metals," *Prog. Mater. Sci.*, Vol. 28, pp. 1–96.

Munson, D. E., and Lawrence, R. J., 1979, "Dynamic Deformation of Polycrystalline Alumina," *J. Appl. Phys.*, Vol. 50, pp. 6272–6282.

Ortiz, M., and Molinari, A., 1992, "Effect of Strain Hardening and Rate Sensitivity on the Dynamic Growth of a Void in a Plastic Material," ASME JOURNAL OF APPLIED MECHANICS, Vol. 59, pp. 48–53.

Perzyna, P., 1986, "Internal State Variable Description of Dynamic Fracture of Ductile Solids," *Int. J. Solids Struct.*, Vol. 22, pp. 797–818.

Rajendran, A. M., and Fyfe, I. M., 1982, "Inertial Effects on the Ductile Failure of Thin Rings," *J. Appl. Phys.* Vol. 49, pp. 31–36.

Regazzoni, G., Johnson, J. N., and Follansbee, P. S., 1986, "Theoretical Study of the Dynamic Tensile Test," ASME JOURNAL OF APPLIED MECHANICS, Vol. 53, pp. 519–528.

Sun, L. Z., and Huang, Z. P., 1992, "Dynamic Void Growth in Rate-sensitive Plastic Solids," *Int. J. Plasticity*, Vol. 8, pp. 903–924.

Tvergaard, V., 1990, "Material Failure by Void Growth and Coalescence," *Adv. Appl. Mech.*, Vol. 27, pp. 83–151.

Wang, Ze-Ping, 1994, "Growth of Voids in Porous Ductile Materials at High Strain Rate," *J. Appl. Phys.*, Vol. 76, pp. 1535–1542.

Worswick, M. J., and Pick, R. J., 1995, "Void Growth and Coalescence during High Velocity Impact," *Mech. Mater.*, Vol. 19, pp. 293–309.

Optimal Bounds on Plastic Deformations for Bodies Constituted of Temperature-Dependent Elastic Hardening Material

F. Giambanco
Associate Professor of Structural Mechanics, Mem. ASME.

L. Palizzolo
Assistant Professor of Structural Mechanics.

Dipartimento di Ingegneria Strutturale & Geotecnica, Universita di Palermo Viale delle Scienze, 90128 Palermo, Italy

Bounds are investigated on the plastic deformations in a continuous solid body produced during the transient phase by cyclic loading not exceeding the shakedown limit. The constitutive model employs internal variables to describe temperature-dependent elastic-plastic material response with hardening. A deformation bounding theorem is proved. Bounds turn out to depend on some fictitious self-stresses and mechanical internal variables evaluated in the whole structure. An optimization problem, aimed to make the bound most stringent, is formulated. The Euler-Lagrange equations related to this last problem are deduced and they show that the relevant optimal bound has a local character, i.e., it depends just on some fictitious plastic deformations produced in the same region of the body where the bounded real plastic deformations are considered. The bounding technique is also generalized to the case of loads arbitrarily varying in a given domain. An application is worked out.

1 Introduction

In many cases of practical interest, structures are required to operate beyond their elastic limit under the action of loads that vary within given ranges, but with time histories not specified. Under such conditions, the so-called shakedown limit load multiplier provides an effective safety factor for the relevant structure. When the load multiplier is below the shakedown limit (but above the elastic limit), the structural response to the loads manifests itself with an initial elastic plastic phase, during which some finite amount of plastic deformations (depending on the actual load history) is produced, with no further plastic deformations whatever the subsequent loads. Such desirable behavior of the structure, usually referred to as shakedown (or adaptation), can no longer occur for load multipliers that are above the shakedown limit, since in the latter case, plastic deformations may not cease and the structure is exposed to a certain inadaptation collapse, either incremental collapse (or ratchetting) with consequent plastic strain growth, or alternating plasticity collapse (or plastic shakedown) with ensuing fatigue failure (see, e.g., Koiter, 1960; Martin, 1975; König, 1987; Gokhfeld and Cherniavsky, 1980).

The assessment of the shakedown limit load multiplier for a given structure subjected to loads varying in a given domain can be achieved by methods based on one of the two basic shakedown theorems, namely the statical and kinematical theorems; related numerical procedures have been developed for various structural models and with different approximation levels (see, e.g., Koiter, 1960; Corradi and Zavelani Rossi, 1974; Cohn and Maier, 1977; Gokhfeld and Cherniavsky, 1980; Polizzotto, 1982; König, 1987). In particular, the shakedown limit load multiplier problem has also been studied for material models with internal variables (see, e.g., Maier, 1987; Maier and Novati, 1987, 1990; Polizzotto et al., 1991).

Since plastic deformations occurring in the initial phase of the structural response, although finite, may indeed exceed some tolerance limits (e.g., ductility limits), the computation of suitably chosen measures of these plastic deformations may be very useful.

The exact computation of the plastic deformation related to the transient phase may be effected by a step-by-step analysis, which constitutes the most suitable way to obtain the structural response. Unfortunately, the computational effort required to perform a full analysis is high (a sequence of linear complementarity problems must be solved for discrete structures) and not always justified during the initial phase of the structure design. Actually, in this phase, it is enough to obtain approximate information about the structural response, keeping the computational effort down.

A quantitative rough evaluation of suitable measures of the real plastic deformation may be obtained by applying some appropriate methods (see, e.g., Zarka and Casier, 1981; Polizzotto, 1989) or applying the so-called bounding techniques (see, e.g., Ponter, 1972; Capurso et al., 1979; König, 1979; Polizzotto, 1982, 1989; Giambanco et al., 1990, 1992) which require, in general, the solution to a linear programming problem.

In the present paper we deal with the shakedown problem for a continuous solid body constituted of material having a temperature-dependent elastic hardening (constitutive) behavior described by means of internal variables.

At first, in order to obtain upper bounds on suitably chosen measures of the real plastic deformation produced in the body during the transient phase, a proper deformation bounding theorem is proved; this theorem represents a generalization of analogous theorems (see, e.g., Polizzotto, 1991) to the case of bodies constituted of material having a temperature-dependent plastic potential. One recognizes that the relevant bounding quantity so obtained is susceptible of optimization, with the aim of making the bound most stringent. The bound minimization problem is formulated and the related Euler-Lagrange equations are de-

Contributed by the Applied Mechanics Division of THE AMERICAN SOCIETY OF MECHANICAL ENGINEERS for publication in the ASME JOURNAL OF APPLIED MECHANICS.

Discussion on this paper should be addressed to the Technical Editor, Professor Lewis T. Wheeler, Department of Mechancial Engineering, University of Houston, Houston, TX 77204-4792, and will be accepted until four months after final publication of the paper itself in the ASME JOURNAL OF APPLIED MECHANICS.

Manuscript received by the ASME Applied Mechanics Division, Apr. 15, 1996; final revision, Jan. 13, 1997. Associate Technical Editor: W. J. Drugan.

duced. These last equations provide useful information on the bound features in optimality conditions. A numerical application concludes the paper.

2 The Elastic Hardening Solid Body

Let us consider a continuous solid body, occupying the open domain V surrounded by the surface S and constrained on $S_u \subset S$ to prevent rigid motions, referred to a cartesian orthogonal coordinate system $\mathbf{x} = (x_1, x_2, x_3)$. The body is subjected to an assigned history of quasi-static external actions described by the scalar $\vartheta = \vartheta(\mathbf{x}, t)$ and the vector $\mathbf{P} = \mathbf{P}(\mathbf{x}, t)$. ϑ is the thermal load (temperature increment with respect to the initial state temperature T_i), while $\mathbf{P}$ collects external actions as body forces $\mathbf{b} = \mathbf{b}(\mathbf{x}, t)$ in V, surface forces $\mathbf{f} = \mathbf{f}(\mathbf{x}, t)$ on $S_f = S - S_u$, and imposed displacements $\mathbf{u}_u = \mathbf{u}_u(\mathbf{x}, t)$ on S_u. The time variable t is not the physical time, but just some monotonically increasing variable to specify the loading sequence $(0 \le t \le \bar{t})$.

The compatibility and equilibrium equations read as follows:

$$\left.\begin{aligned} \boldsymbol{\epsilon} &= \boldsymbol{\epsilon}^e + \boldsymbol{\epsilon}^\vartheta + \boldsymbol{\epsilon}^p, \text{ in } V, \forall t \in (0, \bar{t}), && (1)\\ \boldsymbol{\epsilon} &= \mathbf{C}\mathbf{u}, \text{ in } V, \forall t \in (0, \bar{t}), && (2)\\ \mathbf{u} &= \mathbf{u}_u, \text{ on } S_u, \forall t \in (0, \bar{t}), && (3) \end{aligned}\right\} \text{compatibility}$$

$$\left.\begin{aligned} \mathbf{C}^T\boldsymbol{\sigma} + \mathbf{b} &= \mathbf{0}, \text{ in } V, \forall t \in (0, \bar{t}), && (4)\\ \mathbf{C}_n^T\boldsymbol{\sigma} &= \mathbf{f}, \text{ on } S_f, \forall t \in (0, \bar{t}), && (5) \end{aligned}\right\} \text{equilibrium}$$

where $\mathbf{u} = \mathbf{u}(\mathbf{x}, t)$ is the displacement vector, $\boldsymbol{\epsilon} = \boldsymbol{\epsilon}(\mathbf{x}, t)$ is the (total) strain vector sum of the elastic $[\boldsymbol{\epsilon}^e = \boldsymbol{\epsilon}^e(\mathbf{x}, t)]$, thermal $[\boldsymbol{\epsilon}^\vartheta = \boldsymbol{\epsilon}^\vartheta(\mathbf{x}, t)]$ and plastic $[\boldsymbol{\epsilon}^p = \boldsymbol{\epsilon}^p(\mathbf{x}, t)]$ part, $\boldsymbol{\sigma} = \boldsymbol{\sigma}(\mathbf{x}, t)$ is the stress vector, $\mathbf{C}$ is the well-known compatibility differential operator matrix, $\mathbf{C}^T$ is the equilibrium matrix (adjoint of $\mathbf{C}$), and $\mathbf{C}_n^T$ is an algebraical operator which applied to the stress vector $\boldsymbol{\sigma}$ provides the surface force vector $\mathbf{f}$.

A temperature-dependent elastic hardening material model is assumed as described by the following equations:

$$\boldsymbol{\epsilon}^e = \mathbf{A}\boldsymbol{\sigma}, \quad \boldsymbol{\epsilon}^\vartheta = \boldsymbol{\alpha}\vartheta, \tag{6a}$$

$$\varphi(\boldsymbol{\sigma}, \boldsymbol{\chi}, \vartheta) \le 0, \quad \dot{\lambda} \ge 0, \quad \dot{\lambda}\varphi(\boldsymbol{\sigma}, \boldsymbol{\chi}, \vartheta) = 0, \tag{6b}$$

$$\dot{\boldsymbol{\epsilon}}^p = \dot{\lambda}\frac{\partial\varphi}{\partial\boldsymbol{\sigma}}, \quad \dot{\boldsymbol{\xi}} = -\dot{\lambda}\frac{\partial\varphi}{\partial\boldsymbol{\chi}}, \tag{6c}$$

to be satisfied in V and at all instants of the loading process. Here $\mathbf{A}$ is the elastic compliance matrix, $\boldsymbol{\alpha}$ is the vector collecting the material thermal expansion coefficients, $\varphi = \varphi(\boldsymbol{\sigma}, \boldsymbol{\chi}, \vartheta)$ is the yield function (having also the role of plastic potential), by hypothesis smooth in the $(\boldsymbol{\sigma}, \boldsymbol{\chi}, \vartheta)$-space and convex in the $(\boldsymbol{\sigma}, \boldsymbol{\chi})$-space; for simplicity, we assume that the shape of the yield condition function does not vary with temperature and only the yield stress depends on it; $\dot{\lambda}$ is the plastic activation coefficient; vectors $\boldsymbol{\chi}$ and $\boldsymbol{\xi}$ are internal variables dual of each other, with $\boldsymbol{\xi}$ describing the material microstructure state of slip and $\boldsymbol{\chi}$ being local thermodynamic forces in one-to-one correspondence with $\boldsymbol{\xi}$:

$$\boldsymbol{\chi} = \frac{\partial\Psi}{\partial\xi}, \quad \boldsymbol{\xi} = \frac{\partial\Omega}{\partial\boldsymbol{\chi}}, \tag{7}$$

where $\Psi = \Psi(\boldsymbol{\xi})$ and $\Omega = \Omega(\boldsymbol{\chi})$ are the primal and dual (convex, differentiable) internal variable thermodynamic potentials, respectively. The following relation holds:

$$\Omega(\boldsymbol{\chi}) = \boldsymbol{\chi}^T\boldsymbol{\xi} - \Psi(\boldsymbol{\xi}). \tag{8}$$

The intrinsic dissipation function $\dot{D}$ depends not only on the plastic strain rate and on the kinematic internal variable rate but also on the instantaneous temperature variation value, i.e.,

$$\begin{aligned} \dot{D} = \dot{D}(\dot{\boldsymbol{\epsilon}}^p, \dot{\boldsymbol{\xi}}, \vartheta) &= \dot{D}^p(\dot{\boldsymbol{\epsilon}}^p, \vartheta) - \dot{D}^h(\dot{\boldsymbol{\xi}}) \\ &= \boldsymbol{\sigma}^T\dot{\boldsymbol{\epsilon}}^p - \boldsymbol{\chi}^T\dot{\boldsymbol{\xi}}. \end{aligned} \tag{9}$$

The part $\dot{D}^p$ of function $\dot{D}$ depending on plastic deformation is proportional to the increase in the yield stress σ_y, i.e.,

$$\dot{D}^p(\dot{\boldsymbol{\epsilon}}^p, \vartheta) = \dot{D}_0^p(\dot{\boldsymbol{\epsilon}}^p)\cdot\zeta(\vartheta), \tag{10}$$

where $\dot{D}_0^p(\dot{\boldsymbol{\epsilon}}^p)$ is the energy rate appropriate to $\vartheta = 0$ and $\zeta(\vartheta)$ defines the temperature dependence of σ_y on ϑ:

$$\sigma_y(\vartheta) = \sigma_{y_0}\cdot\zeta(\vartheta), \quad \sigma_{y_0} = \sigma_y(0), \quad \zeta(0) = 1. \tag{11}$$

Most metals exhibit properties which are such that $(\partial\zeta/\partial\vartheta) < 0$.

The partial derivatives of $\dot{D}$ with respect to $\dot{\boldsymbol{\epsilon}}^p$ and $\dot{\boldsymbol{\xi}}$ provide the stress vector $\boldsymbol{\sigma}$ and the static internal variable vector $\boldsymbol{\chi}$, respectively, i.e.,

$$\boldsymbol{\sigma} = \frac{\partial\dot{D}}{\partial\dot{\boldsymbol{\epsilon}}^p} = \frac{\partial\dot{D}^p}{\partial\dot{\boldsymbol{\epsilon}}^p}, \quad \boldsymbol{\chi} = -\frac{\partial\dot{D}}{\partial\dot{\boldsymbol{\xi}}} = \frac{\partial\dot{D}^h}{\partial\dot{\boldsymbol{\xi}}}. \tag{12}$$

At any state $(\boldsymbol{\sigma}, \boldsymbol{\chi}, \vartheta)$ such that $\varphi(\boldsymbol{\sigma}, \boldsymbol{\chi}, \vartheta) = 0$ (plastic state), where there is not elastic return, the following relations hold:

$$\dot{\lambda} > 0, \quad \dot{\varphi}\dot{\lambda} = 0, \tag{13}$$

i.e.,

$$\dot{\varphi} = \left(\frac{\partial\varphi}{\partial\boldsymbol{\sigma}}\right)^T\dot{\boldsymbol{\sigma}} + \left(\frac{\partial\varphi}{\partial\boldsymbol{\chi}}\right)^T\dot{\boldsymbol{\chi}} + \frac{\partial\varphi}{\partial\vartheta}\dot{\vartheta} = 0. \tag{14}$$

Using Eqs. (6) and (7), Eq. (14) provides

$$\dot{\lambda} = \frac{1}{h}\left\langle\left(\frac{\partial\varphi}{\partial\boldsymbol{\sigma}}\right)^T\dot{\boldsymbol{\sigma}} + \frac{\partial\varphi}{\partial\vartheta}\dot{\vartheta}\right\rangle, \tag{15}$$

where $h = h(\boldsymbol{\sigma}, \boldsymbol{\chi}) > 0$ is the hardening modulus (Martin, 1975) given by

$$h = \left(\frac{\partial\varphi}{\partial\boldsymbol{\chi}}\right)^T\frac{\partial^2\Psi}{\partial\boldsymbol{\xi}\partial\boldsymbol{\xi}}\frac{\partial\varphi}{\partial\boldsymbol{\chi}}. \tag{16}$$

As a consequence of Eq. (15):

(i) if $(\partial\varphi/\partial\boldsymbol{\sigma})^T\dot{\boldsymbol{\sigma}} + (\partial\varphi/\partial\vartheta)\dot{\vartheta} < 0$ (elastic return), then $\dot{\lambda} = 0$,

(ii) if $(\partial\varphi/\partial\boldsymbol{\sigma})^T\dot{\boldsymbol{\sigma}} + (\partial\varphi/\partial\vartheta)\dot{\vartheta} = 0$ (neutral loading), then $\dot{\lambda} = 0$,

(iii) if $(\partial\varphi/\partial\boldsymbol{\sigma})^T\dot{\boldsymbol{\sigma}} + (\partial\varphi/\partial\vartheta)\dot{\vartheta} > 0$ (plastic activation), then $\dot{\lambda} > 0$.

It is worth noting that, since $(\partial\varphi/\partial\vartheta)$ is always positive, when $\dot{\vartheta} > 0$ the quantity in brackets on the right-hand side of Eq. (15), and as a consequence $\dot{\lambda}$, may be positive even if the loading index is negative, i.e., even if $(\partial\varphi/\partial\boldsymbol{\sigma})^T\dot{\boldsymbol{\sigma}} < 0$, (Fig. 1).

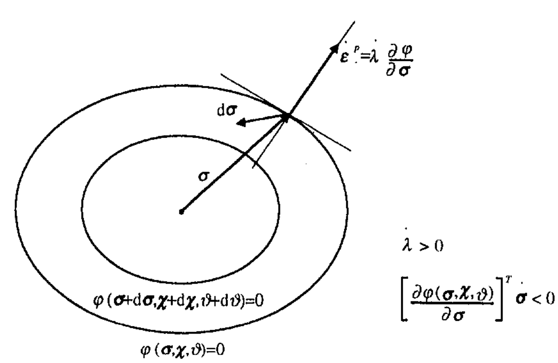

Fig. 1 Temperature-dependent yield surfaces: plastic deformation may occur also in the presence of negative loading index

A typical example of linearly hardening material showing a mixed kinematic-isotropic hardening behavior with a Mises yield function and a quadratic thermodynamic potential (Lemaitre and Chaboche, 1985) is obtained by the choices

$$\varphi(\boldsymbol{\sigma}, \boldsymbol{\chi}, \chi_0, \vartheta) \equiv \tfrac{3}{2}[(\boldsymbol{\sigma}' - \boldsymbol{\chi}')^T(\boldsymbol{\sigma}' - \boldsymbol{\chi}')]^{1/2} - \chi_0 - \sigma_y(\vartheta), \quad (17a)$$

$$(\boldsymbol{\sigma}')^T = |\sigma_x - \sigma_m \quad \sigma_y - \sigma_m \quad \sigma_z - \sigma_m \quad \sqrt{2}\tau_x \quad \sqrt{2}\tau_y \quad \sqrt{2}\tau_z|, \quad (17b)$$

$$\sigma_m = (\sigma_x + \sigma_y + \sigma_z)/3, \quad (17c)$$

$$\Psi(\boldsymbol{\xi}, \xi_0) \equiv \tfrac{1}{2}(\boldsymbol{\xi}^T\mathbf{B}\boldsymbol{\xi} + b\xi_0^2), \quad (17d)$$

where vector $\boldsymbol{\chi}'$ has analogous definition as $\boldsymbol{\sigma}'$, $(\boldsymbol{\chi}, \chi_0)$ and $(\boldsymbol{\xi}, \xi_0)$ are sets of dual vector and scalar internal variables, $\mathbf{B}$ is a constant positive definite matrix and b a constant positive scalar. A usual piecewise form for the yield stress function $\sigma_y = \sigma_y(\vartheta)$ is the following one (König, 1987):

$$\sigma_y = \sigma_{y_0}, \text{ for } T \le T_0, \quad (18a)$$

$$\sigma_y = \sigma_{y_0}[1 - \mu(T - T_0)], \text{ for } T_0 \le T \le T_1, \quad (18b)$$

where

$$T = T_i + \vartheta \quad (19)$$

is the actual temperature, sum of the initial state temperature T_i and of the temperature variation ϑ, T_0 and T_1 are two reference temperatures and μ is a dimensional positive scalar.

3 Shakedown Criteria

We assume that ϑ and $\mathbf{P}$, as functions of t, can be identified with cyclic temperature variation and loading, respectively, such that

$$\vartheta(t + \Delta t) = \vartheta(t), \quad \mathbf{P}(t + \Delta t) = \mathbf{P}(t), \quad \forall t > 0, \quad (20)$$

Δt being the time period. In addition we assume that the reference loads ϑ and $\mathbf{P}$ are affected by a load multiplier $\beta > 0$; in such a way an homothetic load family $\pi(\beta)$ can be identified (Fig. 2), where $\pi(1)$ is the reference cyclic load.

The conditions under which the solid body has the ability to eventually shake down in the elastic regime (or to adapt to the loads) when subjected to loads $\beta\vartheta(t)$ and $\beta\mathbf{P}(t)$ as previously defined can be established through the statical shakedown theorem (Melan, 1938a, b) and the kinematical shakedown theorem (Koiter, 1960). These theorems are here recalled in the form of lower bound and upper bound theorem, because these are more appropriate for the purpose of the present paper.

Lower Bound Theorem. A number $\beta^s > 0$ is a statical load multiplier if, correspondingly, a time-independent self-stress vector $\boldsymbol{\rho}^s(\mathbf{x})$ and a time-independent vector $\boldsymbol{\chi}^s(\mathbf{x})$ exist such that

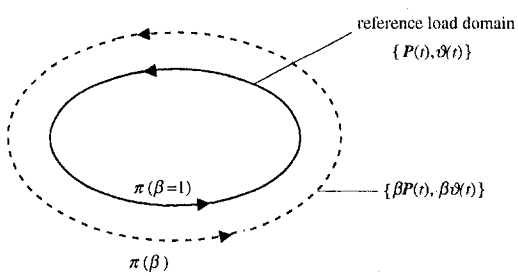

Fig. 2 Load domain dependency on the load multiplier β

$$\varphi(\beta^s\boldsymbol{\sigma}^E + \boldsymbol{\rho}^s, \boldsymbol{\chi}^s, \beta^s\vartheta) \le 0, \quad \text{in } V \times (0, \Delta t), \quad (21a)$$

$$\mathbf{C}^T\boldsymbol{\rho}^s = \mathbf{0}, \quad \text{in } V, \quad \mathbf{C}_n^T\boldsymbol{\rho}^s = \mathbf{0}, \quad \text{on } S_f, \quad (21b)$$

where $\boldsymbol{\sigma}^E = \boldsymbol{\sigma}^E(\mathbf{x}, t)$ is the purely thermoelastic stress response to the reference loads.

A statical load multiplier does not exceed the shakedown limit load multiplier β^*, i.e., $\beta^s \le \beta^*$.

Upper Bound Theorem. A number $\beta^c > 0$ is a kinematical load multiplier if it identifies with the total intrinsic dissipation promoted in the body by a plastic accumulation mechanism, that is a kinematic internal variable rate distribution $\dot{\boldsymbol{\xi}}^c = \dot{\boldsymbol{\xi}}^c(\mathbf{x}, t)$ $t \in (0, \Delta t)$ resulting in a vanishing kinematic internal variable distribution $\boldsymbol{\xi}^c$ and a strain rate distribution $\dot{\boldsymbol{\epsilon}}^{p^c} = \dot{\boldsymbol{\epsilon}}^{p^c}(\mathbf{x}, t)$ $t \in (0, \Delta t)$ resulting in a compatible strain distribution $\boldsymbol{\epsilon}^{p^c}$ and such that the external loads do unit work, i.e.,

$$\beta^c = \int_0^{\Delta t}\int_V \dot{D}(\dot{\boldsymbol{\epsilon}}^{p^c}, \dot{\boldsymbol{\xi}}^c, \vartheta)dVdt, \quad (22a)$$

$$\boldsymbol{\epsilon}^{p^c} = \int_0^{\Delta t} \dot{\boldsymbol{\epsilon}}^{p^c}dt = \mathbf{C}\mathbf{u}^c, \text{ in } V, \quad (22b)$$

$$\boldsymbol{\xi}^c = \int_0^{\Delta t} \dot{\boldsymbol{\xi}}^c dt = \mathbf{0}, \text{ in } V, \quad (22c)$$

$$\int_0^{\Delta t}\int_V \boldsymbol{\sigma}^{E^T}\dot{\boldsymbol{\epsilon}}^{p^c}dVdt = 1. \quad (22d)$$

A kinematical load multiplier is not smaller than β^*, i.e., $\beta^c \ge \beta^*$.

Shakedown Limit Load Multiplier Assessment. The shakedown limit load multiplier β^* can be obtained either as the maximum statical load multiplier or as the minimum kinematical load multiplier:

$$\max \beta^s = \beta^* = \min \beta^c, \quad (23)$$

i.e., solving the problem:

$$\beta^* = \max_{(\beta^s, \boldsymbol{\rho}^s, \boldsymbol{\chi}^s)} \beta^s \quad (24a)$$

subject to

$$\varphi(\beta^s\boldsymbol{\sigma}^E + \boldsymbol{\rho}^s, \boldsymbol{\chi}^s, \beta^s\vartheta) \le 0, \quad \text{in} \quad V \times (0, \Delta t), \quad (24b)$$

$$\mathbf{C}^T\boldsymbol{\rho}^s = \mathbf{0} \quad \text{in} \quad V, \quad \mathbf{C}_n^T\boldsymbol{\rho}^s = \mathbf{0}, \quad \text{on } S_f, \quad (24c)$$

or solving the problem:

$$\beta^* = \min_{(\boldsymbol{\epsilon}^{p^c}, \dot{\boldsymbol{\xi}}^c, \mathbf{u}^c)} \beta^c \quad (25a)$$

subject to

$$\boldsymbol{\epsilon}^{p^c} = \int_0^{\Delta t} \dot{\boldsymbol{\epsilon}}^{p^c}dt = \mathbf{C}\mathbf{u}^c, \text{ in } V, \quad (25b)$$

$$\boldsymbol{\xi}^c = \int_0^{\Delta t} \dot{\boldsymbol{\xi}}^c dt = \mathbf{0}, \text{ in } V, \quad (25c)$$

$$\int_0^{\Delta t}\int_V \boldsymbol{\sigma}^{E^T}\dot{\boldsymbol{\epsilon}}^{p^c}dVdt = 1. \quad (25d)$$

Making reference to the load program $\beta\vartheta$, $\beta\mathbf{P}$ (as previously defined) we can state that when $\beta^E \le \beta \le \beta^*$, β^E being the elastic limit load multiplier, the relevant body surely shakes down, i.e., after a certain number of load cycles during which it behaves elastoplastically and a finite amount of plastic strain is produced (transient phase), the response becomes purely elastic (stationary phase). Although finite, the amount of plastic strain produced during the transient phase may exceed the ductility limits of the material and/or some servibility limits and, thus, the computation of suitably chosen measures of this plastic deformation may be useful. The exact computation of chosen measures of the real plastic deformation related to the transient phase may be effected by a step-by-step analysis worked out for a suitable number of cycles, but often it just suffices to evaluate bounds on the chosen relevant measures, at the computational low cost of appropriate bounding techniques.

4 A Deformation Bounding Theorem

Let $(\boldsymbol{\sigma}, \boldsymbol{\chi}, \beta\vartheta)$ and $(\dot{\boldsymbol{\epsilon}}^p, \dot{\boldsymbol{\xi}}, \dot{\lambda})$ be real mechanical, thermal, and kinematical quantities (corresponding to each other through the plastic flow laws). Furthermore, let $(\boldsymbol{\sigma}_1, \boldsymbol{\chi}_1, \vartheta_1)$ be any plastically admissible set, i.e.,

$$\varphi(\boldsymbol{\sigma}_1, \boldsymbol{\chi}_1, \vartheta_1) \leq 0, \quad \text{in} \quad V \times (0, \Delta t). \tag{26}$$

Because φ is convex in the $(\boldsymbol{\sigma}, \boldsymbol{\chi})$-space, we can write

$$\varphi(\boldsymbol{\sigma}_1, \boldsymbol{\chi}_1, \beta\vartheta) - \varphi(\boldsymbol{\sigma}, \boldsymbol{\chi}, \beta\vartheta) \geq \left(\frac{\partial\varphi}{\partial\boldsymbol{\sigma}}\right)^T (\boldsymbol{\sigma}_1 - \boldsymbol{\sigma}) + \left(\frac{\partial\varphi}{\partial\boldsymbol{\chi}}\right)^T (\boldsymbol{\chi}_1 - \boldsymbol{\chi}), \text{ in } V \times (0, \Delta t). \tag{27}$$

Multiplying Eq. (27) by $\dot{\lambda} > 0$, since $\dot{\lambda}\varphi(\boldsymbol{\sigma}, \boldsymbol{\chi}, \beta\vartheta) = 0$, we obtain the central inequality

$$(\boldsymbol{\sigma} - \boldsymbol{\sigma}_1)^T\dot{\boldsymbol{\epsilon}}^p - (\boldsymbol{\chi} - \boldsymbol{\chi}_1)^T\dot{\boldsymbol{\xi}} + \dot{\lambda}\varphi(\boldsymbol{\sigma}_1, \boldsymbol{\chi}_1, \beta\vartheta) \geq 0, \quad \text{in} \quad V \times (0, \Delta t), \tag{28}$$

which holds for any arbitrary set $(\boldsymbol{\sigma}_1, \boldsymbol{\chi}_1, \vartheta_1)$ fulfilling Eq. (26). It is worth noting that in the central inequality the sign of term $\varphi(\boldsymbol{\sigma}_1, \boldsymbol{\chi}_1, \beta\vartheta)$ is not known.

The central inequality (28) constitute a new result valid for bodies constituted of temperature-dependent elastic-plastic material. If $\vartheta_1 = \beta\vartheta$, since $\dot{\lambda}\varphi(\boldsymbol{\sigma}_1, \boldsymbol{\chi}_1, \beta\vartheta) \leq 0$ results, Eq. (28) assumes the form usually related to bodies constituted of elastic-plastic material (see, e.g., Polizzotto et al., 1991)

$$(\boldsymbol{\sigma} - \boldsymbol{\sigma}_1)^T\dot{\epsilon}^p - (\boldsymbol{\chi} - \boldsymbol{\chi}_1)^T\dot{\boldsymbol{\xi}} \geq 0, \quad \text{in} \quad V \times (0, \Delta t), \tag{29}$$

but also valid in the present more general context provided that $(\boldsymbol{\sigma}, \boldsymbol{\chi})$ and $(\boldsymbol{\sigma}_1, \boldsymbol{\chi}_1)$ are related to the same temperature variation $\beta\vartheta$.

Let $g(\mathbf{x})$ and $\mathbf{s}(\mathbf{x})$ be scalar and vector fields (perturbation functions), defined in V as

$$g = 1 + \omega\overline{\gamma}(\mathbf{x}), \quad 0 \leq \overline{\gamma}(\mathbf{x}) \leq 1, \tag{30a}$$

$$\mathbf{s} = \omega\overline{\mathbf{s}}(\mathbf{x}), \tag{30b}$$

where ω is a positive scalar parameter (perturbation multiplier). The set $\overline{\gamma}(\mathbf{x}), \overline{\mathbf{s}}(\mathbf{x})$ specifies a yield function perturbation mode. We assume that $\overline{\gamma}$ and $\overline{\mathbf{s}}$ are exclusive of each other, i.e., $\overline{\mathbf{s}} = \mathbf{0}$ if $\overline{\gamma} \neq 0$ and vice versa. Taking into account Eqs. (30), the perturbed yield function φ^* can be defined as

$$\varphi^*(\boldsymbol{\sigma}, \boldsymbol{\chi}, \beta\vartheta) = \varphi(g\boldsymbol{\sigma} + \mathbf{s}, \boldsymbol{\chi}, \beta\vartheta), \text{ in } V \times (0, \Delta t). \tag{31}$$

Let us define the test stresses $\hat{\boldsymbol{\sigma}}, \hat{\boldsymbol{\chi}}$ and the test temperature variation $\hat{\vartheta}$:

$$\hat{\boldsymbol{\sigma}}(\mathbf{x}, t) = \beta\boldsymbol{\sigma}^E(\mathbf{x}, t) + \hat{\boldsymbol{\sigma}}^r(\mathbf{x}), \ \hat{\boldsymbol{\chi}} = \hat{\boldsymbol{\chi}}(\mathbf{x}), \quad \text{in } V \times (0, \Delta t), \tag{32a}$$

$$\hat{\vartheta} = \hat{\vartheta}(\mathbf{x}, t) \geq \vartheta(\mathbf{x}, t), \text{ in } V \times (0, \Delta t), \tag{32b}$$

where $\hat{\boldsymbol{\sigma}}^r(\mathbf{x})$ and $\hat{\boldsymbol{\chi}}(\mathbf{x})$ are a residual stress field and a static internal variable field, respectively, both time independent, and let us define a kinematic time-independent internal variable field $\hat{\boldsymbol{\xi}}(\mathbf{x})$ corresponding to $\hat{\boldsymbol{\chi}}(\mathbf{x})$, i.e.,

$$\hat{\boldsymbol{\xi}}(\mathbf{x}) = \left.\frac{\partial\Omega(\boldsymbol{\chi})}{\partial\boldsymbol{\chi}}\right|_{\boldsymbol{\chi}=\hat{\boldsymbol{\chi}}}. \tag{33}$$

We assume that the test stresses and temperature variation $(32a, b)$ are plastically admissible with respect to the perturbed yield function, i.e., they fulfill the following test condition:

$$\varphi^*(\hat{\boldsymbol{\sigma}}, \hat{\boldsymbol{\chi}}, \beta\hat{\vartheta}) = \varphi(g\hat{\boldsymbol{\sigma}} + \mathbf{s}, \hat{\boldsymbol{\chi}}, \beta\hat{\vartheta}) \leq 0, \quad \text{in} \quad V \times (0, \Delta t). \tag{34}$$

Applying the central inequality (28) with

$$\boldsymbol{\sigma}_1 = g\hat{\boldsymbol{\sigma}} + \mathbf{s}, \quad \boldsymbol{\chi}_1 = \hat{\boldsymbol{\chi}}, \quad \vartheta_1 = \beta\hat{\vartheta}, \tag{35}$$

we have

$$(\boldsymbol{\sigma} - g\hat{\boldsymbol{\sigma}} - \mathbf{s})^T\dot{\boldsymbol{\epsilon}}^p - (\boldsymbol{\chi} - \hat{\boldsymbol{\chi}})^T\dot{\boldsymbol{\xi}} + \dot{\lambda}\varphi(g\hat{\boldsymbol{\sigma}} + \mathbf{s}, \hat{\boldsymbol{\chi}}, \beta\vartheta) \geq 0, \quad \text{in} \quad V \times (0, \Delta t), \tag{36}$$

where $\boldsymbol{\sigma}, \boldsymbol{\chi}, \dot{\lambda}, \dot{\boldsymbol{\epsilon}}^p, \dot{\boldsymbol{\xi}}$, and $\beta\vartheta$ refer to the actual elastic-plastic process. Summing up and subtracting the product $g\boldsymbol{\sigma}^T\dot{\boldsymbol{\epsilon}}^p$ and taking into account Eq. (9) the inequality (36) can be easily transformed as

$$\frac{\omega}{g}\overline{\gamma}\dot{D}^p(\dot{\boldsymbol{\epsilon}}^p) + \frac{\omega}{g}\overline{\mathbf{s}}^T\dot{\boldsymbol{\epsilon}}^p \leq (\boldsymbol{\sigma} - \hat{\boldsymbol{\sigma}})^T\dot{\boldsymbol{\epsilon}}^p - \frac{1}{g}(\boldsymbol{\chi} - \hat{\boldsymbol{\chi}})^T\dot{\boldsymbol{\xi}} + \frac{1}{g}\dot{\lambda}\varphi(g\hat{\boldsymbol{\sigma}} + \mathbf{s}, \hat{\boldsymbol{\chi}}, \beta\vartheta), \quad \text{in} \quad V \times (0, \Delta t). \tag{37}$$

Since $\dot{\lambda} \geq 0$ and since $\varphi(\boldsymbol{\sigma}, \boldsymbol{\chi}, \beta\vartheta)$ is an increasing function of ϑ, by virtue of Eqs. $(30a)$, $(32b)$, and (34) we can write

$$\frac{1}{g}\dot{\lambda}\varphi(g\hat{\boldsymbol{\sigma}} + \mathbf{s}, \hat{\boldsymbol{\chi}}, \beta\vartheta) \leq \frac{1}{g}\dot{\lambda}\varphi(g\hat{\boldsymbol{\sigma}} + \mathbf{s}, \hat{\boldsymbol{\chi}}, \beta\hat{\vartheta}) \leq 0, \quad \text{in} \quad V \times (0, \Delta t) \tag{38}$$

and, thus, the last addend on the right-hand side of (37) can be disregarded.

Remembering that the two perturbation modes are exclusive of each other, and thus $g = 1$ can be set in the denominator of the second addend on the left-hand side of (37), and taking into account that $(1 + \omega) \geq g$, and thus g in the denominator of the first addend of the left-hand side of (37) can be replaced by $(1 + \omega)$, an integration over V of this last inequality gives

$$\frac{1}{1+\omega}\int_V \overline{\gamma}\dot{D}^p(\dot{\boldsymbol{\epsilon}}^p)dV + \int_V \overline{\mathbf{s}}^T\dot{\boldsymbol{\epsilon}}^p dV \leq \frac{1}{\omega}\left(\int_V (\boldsymbol{\sigma} - \hat{\boldsymbol{\sigma}})^T\dot{\boldsymbol{\epsilon}}^p dV - \int_V \frac{1}{g}(\boldsymbol{\chi} - \hat{\boldsymbol{\chi}})^T\dot{\boldsymbol{\xi}} dV\right), \quad \text{in} \quad (0, \Delta t). \tag{39}$$

Making use of the identity

$$\dot{\boldsymbol{\epsilon}}^p = \dot{\boldsymbol{\epsilon}} - \beta\dot{\boldsymbol{\epsilon}}^E - \mathbf{A}(\dot{\boldsymbol{\sigma}} - \dot{\hat{\boldsymbol{\sigma}}}), \quad \text{in} \quad V \times (0, \Delta t) \tag{40}$$

and by virtue of the virtual work principle one obtains

$$\int_V (\boldsymbol{\sigma} - \hat{\boldsymbol{\sigma}})^T\dot{\boldsymbol{\epsilon}}^p dV = -\frac{d}{dt}\left(\frac{1}{2}\int_V (\boldsymbol{\sigma} - \hat{\boldsymbol{\sigma}})^T\mathbf{A}(\boldsymbol{\sigma} - \hat{\boldsymbol{\sigma}})dV\right), \quad \text{in} \quad (0, \Delta t). \tag{41}$$

The second addend in brackets on the right hand side of (39) can be transformed by utilizing eqs. (7) and (8):

$$\int_V \frac{1}{g}(\chi - \hat{\chi})^T\dot{\xi}dV = \int_V \frac{1}{g}\left[\left(\frac{\partial\Psi}{\partial\xi}\right)^T\dot{\xi} - \hat{\chi}^T\dot{\xi}\right]dV$$

$$= \frac{d}{dt}\int_V \frac{1}{g}[\Psi(\xi) - \Psi(\hat{\xi}) - \hat{\chi}^T(\xi - \hat{\xi})]dV$$

$$= \frac{d}{dt}\int_V \frac{1}{g}[\Omega(\hat{\chi}) - \Omega(\chi) - \xi^T(\hat{\chi} - \chi)]dV. \quad (42)$$

Setting

$$L^*(t) = \frac{1}{2}\int_V (\sigma - \hat{\sigma})^T\mathbf{A}(\sigma - \hat{\sigma})dV + \int_V \frac{1}{g}[\Psi(\xi) - \Psi(\hat{\xi}) - \hat{\chi}^T(\xi - \hat{\xi})]dV$$

$$= \frac{1}{2}\int_V (\sigma - \hat{\sigma})^T\mathbf{A}(\sigma - \hat{\sigma})dV + \int_V \frac{1}{g}[\Omega(\hat{\chi}) - \Omega(\chi) - \xi^T(\hat{\chi} - \chi)]dV, \quad (43)$$

the inequality (39) can be rewritten as:

$$\frac{1}{1+\omega}\int_V \bar{\gamma}\dot{D}^p(\dot{\epsilon}^p)dV + \int_V \bar{\mathbf{s}}^T\dot{\epsilon}^p dV \le -\frac{1}{\omega}\frac{d}{dt}L^*(t). \quad (44)$$

We recognize that $L^*(t)$ ($\forall t \ge 0$) is a non-negative scalar quantity: actually the first addend is a quadratic form and the second is non-negative in V due to the convexity of functions $\Psi(\xi)$ and $\Omega(\chi)$.

An integration of (44) over $(0, t_1)$, with $0 \le t_1 \le \infty$, taking into account that $\sigma^E(0) = \mathbf{0}$ in V, provides

$$\frac{1}{1+\omega}\int_V \bar{\gamma}\left[\int_0^{t_1}\dot{D}^p(\dot{\epsilon}^p)dt\right]dV + \int_V \bar{\mathbf{s}}^T\left(\int_0^{t_1}\dot{\epsilon}^p dt\right)dV$$

$$\le \frac{1}{\omega}[L^*(0) - L^*(t_1)] \le \frac{1}{\omega}L^*(0) \le \frac{1}{\omega}L_0$$

$$= \frac{1}{\omega}\left\{\frac{1}{2}\int_V (\hat{\sigma}^r)^T\mathbf{A}\hat{\sigma}^r dV + \int_V [\hat{\chi}^T\hat{\xi} - \Psi(\hat{\xi})]dV\right\}$$

$$= \frac{1}{\omega}\left[\frac{1}{2}\int_V (\hat{\sigma}^r)^T\mathbf{A}\hat{\sigma}^r dV + \int_V \Omega(\hat{\chi})dV\right], \quad (45)$$

where L_0 is deduced by $L^*(0)$ setting $g = 1$, so that $L_0 \ge L^*(0)$ results. The scalar quantity L_0/ω is an upper bound to the peak value of the left-hand side quantity in (45).

Since the two perturbation modes are exclusive of each other, inequality (45) provides

$$\max_{0\le t\le\infty}\int_V \bar{\mathbf{s}}(\mathbf{x})^T\epsilon^p(\mathbf{x}, t)dV \le \frac{1}{\omega}L_0 \equiv U_1, \quad (46a)$$

$$\int_V \bar{\gamma}(\mathbf{x})\left[\int_0^\infty \dot{D}^p(\dot{\epsilon}^p)dt\right]dV \le \frac{1+\omega}{\omega}L_0 \equiv U_2. \quad (46b)$$

The scalar quantities on the right-hand side of (46) are upper bounds on plastic deformations produced in some region of the body during the transient phase: the quantity U_2 in (46b) is an upper bound to the whole plastic dissipation produced in the region where $\bar{\gamma} \ne 0$; the quantity U_1 in (46a) is an upper bound to the peak value of any other chosen measure of the plastic deformation in the region where $\bar{\mathbf{s}} \ne 0$ is suitably defined.

The bounding theorem (45) (and the consequent inequalities (46)) represents a generalization of analogous previous bounding theorems (see, e.g., Polizzotto, 1991) to the case of bodies constituted of material having a temperature-dependent plastic potential.

As previously described the test temperature variation $\hat{\vartheta}$ may be any function satisfying (32b). Anyway, in order to calculate upper bounds (46a, b) some special choices of $\hat{\vartheta}$ can be advisable, as, for example, the following provided ones.

(i) If the loading history is smooth with respect to time t, then the test temperature variation can be chosen as

$$\hat{\vartheta} = \hat{\vartheta}(\mathbf{x}) = \max_{0\le t\le\Delta t}\vartheta(\mathbf{x}, t), \quad \text{in } V. \quad (47)$$

The choice (47) guarantees that deformation bounds (46a, b) hold for any mechanical loading history inside the convex hull generated by the amplified cyclic mechanical load $\beta\mathbf{P}$ associated with arbitrary temperature variations ϑ^a within the range $0 \le \vartheta^a \le \beta\hat{\vartheta}$.

(ii) If the mechanical loading history is a piecewise linear path with m sides and m vertices $\mathbf{P}_k$ ($k \in I(m) = \{1, 2, \ldots, m\}$), the test condition can be written as

$$\varphi[g(\beta\sigma_k^E + \hat{\sigma}^r) + \mathbf{s}, \hat{\chi}, \beta\hat{\vartheta}_k] \le 0, \quad \text{in } V, \forall k \in I(m), \quad (48)$$

where σ_k^E is the thermoelastic stress response to the kth reference basic load $(\mathbf{P}_k, \hat{\vartheta}_k)$, being $\hat{\vartheta}_k$ the maximum value that $\vartheta(\mathbf{x}, t)$ reaches in $t_{k-1} \le t \le t_{k+1}$ (by definition $\vartheta_0 \equiv \vartheta_m$ and $\vartheta_{m+1} = \vartheta_1$).

(iii) If the mechanical loading history is a piecewise linear path with m sides and m vertices $\mathbf{P}_k(k \in I(m))$ and the test temperature variation is chosen as

$$\hat{\vartheta} = \hat{\vartheta}(\mathbf{x}) = \max_{0\le t\le\Delta t}\vartheta(\mathbf{x}, t) = \max_k \vartheta_k(\mathbf{x}), \quad \text{in } V \quad (49)$$

then the test condition reads

$$\varphi[g(\beta\sigma_k^E + \hat{\sigma}^r) + \mathbf{s}, \hat{\chi}, \beta\hat{\vartheta}(\mathbf{x})] \le 0, \quad \text{in } V, \forall k \in I(m). \quad (50)$$

The choice (49) guarantees that deformation bounds (46a, b) hold for any mechanical loading history inside the convex hull generated by the amplified basic mechanical loads $\beta\mathbf{P}_k$ associated with arbitrary temperature variations ϑ^a within the range $0 \le \vartheta^a \le \beta\hat{\vartheta}$.

For a selected test temperature variation history $\hat{\vartheta}(\mathbf{x}, t)$ in $V \times (0, \Delta t)$, the mechanical quantities $\hat{\sigma}^r$ and $\hat{\chi}$, necessary to calculate U_1 and U_2 in (46a, b), can be obtained, for example, solving the following problem:

$$\hat{\beta}^* = \max_{(\beta, \hat{\sigma}^r, \hat{\chi})}\beta \quad (51a)$$

subject to

$$\varphi(g\hat{\sigma} + \mathbf{s}, \hat{\chi}, \beta\hat{\vartheta}) \le 0, \quad \text{in } V \times (0, \Delta t) \quad (51b)$$

$$\mathbf{C}^T\hat{\sigma}^r = \mathbf{0}, \quad \text{in } V, \quad \mathbf{C}_n^T\hat{\sigma}^r = \mathbf{0}, \quad \text{on } S_f. \quad (51c)$$

Problem (51) is a shakedown limit load multiplier one, analogous to (24) but with a perturbed yield function. It can be proved that, due to the introduced yield function perturbations, the objective function $\hat{\beta}^*$ turns out to be just a lower bound on the shakedown limit load multiplier β^*, i.e., $\hat{\beta}^* \le \beta^*$.

After all, with the low computational effort required by the solution to the linear maximum problem (51) and by the subsequent computation of U_1 and U_2 in (46), it is possible to obtain approximate evaluations of the shakedown limit load multiplier β^* and of the chosen measures of the real plastic deformation. Even if approximate, these evaluations can be usefully utilized during the initial stage of the structural design.

5 Bound Optimization

The simplificative hypotheses introduced in the bounding theorem mathematics (e.g., in (37) and (45)) and the choices (47) or (48) or (49) may produce even large differences between the values of the real process variables and the values of the related bounding quantities. Consequently, it can be advisable to sustain a further computational effort (but always lower than the one required by a full analysis) in order to obtain more stringent bounds.

With this aim, the authors recognize that the scalar quantities on the right-hand side of (46) are susceptible to optimization with respect to its arguments and propose the following procedure in order to make the bounds as stringent as possible.

If we are interested to the optimization of U_1 in (46a), the following minimum problem must be solved:

$$U_1^{\text{opt}} = \min U_1 = \min_{(\hat{\boldsymbol{\sigma}}^r, \hat{\boldsymbol{\chi}}, \omega)} \frac{1}{\omega}\left(\frac{1}{2}\int_V \hat{\boldsymbol{\sigma}}^{r^T}\mathbf{A}\hat{\boldsymbol{\sigma}}^r dV + \int_V \Omega(\hat{\boldsymbol{\chi}})dV\right) \quad (52a)$$

subject to

$$\varphi(\boldsymbol{\sigma}^*, \hat{\boldsymbol{\chi}}, \beta\hat{\vartheta}) \le 0, \quad \text{in } V \times (0, \Delta t), \quad (52b)$$

$$\mathbf{C}^T\hat{\boldsymbol{\sigma}}^r = \mathbf{0}, \quad \text{in } V, \quad \mathbf{C}_n^T\hat{\boldsymbol{\sigma}}^r = \mathbf{0}, \text{ on } S_t, \quad (52c)$$

where, as previously defined, variables $\hat{\boldsymbol{\sigma}}^r$, $\hat{\boldsymbol{\chi}}$, ω are a time independent self stress field, a time independent mechanical internal variables field and the perturbation multiplier, respectively, $\Omega(\hat{\boldsymbol{\chi}})$ is the thermodynamic potential expressed in terms of mechanical internal variables, (52c) are the self-stress equilibrium equations, $\varphi(\boldsymbol{\sigma}^*, \hat{\boldsymbol{\chi}}, \beta\hat{\vartheta})$ is the perturbed yield function, being

$$\boldsymbol{\sigma}^* \equiv \beta\boldsymbol{\sigma}^E + \hat{\boldsymbol{\sigma}}^r + \omega\overline{\mathbf{s}}. \quad (53)$$

Let us define the augmented functional

$$U_1^L = \frac{1}{\omega}\left\{\frac{1}{2}\int_V \hat{\boldsymbol{\sigma}}^{r^T}\mathbf{A}\hat{\boldsymbol{\sigma}}^r dV + \int_V \Omega(\hat{\boldsymbol{\chi}})dV + \int_0^{\Delta t}\int_V \dot{\lambda}^*\varphi(\boldsymbol{\sigma}^*, \hat{\boldsymbol{\chi}}, \beta\hat{\vartheta})dVdt + \int_V \mathbf{u}^{*T}\mathbf{C}^T\hat{\boldsymbol{\sigma}}^r dV - \int_{S_t} \mathbf{u}^{*T}\mathbf{C}_n^T\hat{\boldsymbol{\sigma}}^r dS\right\} \quad (54)$$

where $\dot{\lambda}^*/\omega$ and $\mathbf{u}^*/\omega$ are suitable Lagrange multipliers, with ω just a scaling factor not subjected to variations. Taking the first variation of functional (54) with respect to all the variables, taking into account that U_1^L must have a minimum with respect to the variables of problem (52) and a maximum with respect to the Lagrange multipliers, the relevant Euler-Lagrange equations related to problem (52) turn out to be

$$\varphi(\boldsymbol{\sigma}^*, \hat{\boldsymbol{\chi}}, \beta\hat{\vartheta}) \le 0, \quad \dot{\lambda}^* \ge 0,$$

$$\dot{\lambda}^*\varphi(\boldsymbol{\sigma}^*, \hat{\boldsymbol{\chi}}, \beta\hat{\vartheta}) = 0, \quad \text{in} \quad V \times (0, \Delta t), \quad (55a)$$

$$\dot{\boldsymbol{\epsilon}}^{p^*} = \dot{\lambda}^*\frac{\partial\varphi}{\partial\boldsymbol{\sigma}^*}, \quad \dot{\boldsymbol{\xi}}^* = -\dot{\lambda}^*\frac{\partial\varphi}{\partial\hat{\boldsymbol{\chi}}}, \quad \text{in } V \times (0, \Delta t), \quad (55b)$$

$$\Delta\boldsymbol{\epsilon}^{p^*} = \int_0^{\Delta t} \dot{\boldsymbol{\epsilon}}^{p^*}dt, \quad \Delta\boldsymbol{\xi}^* = \int_0^{\Delta t} \dot{\boldsymbol{\xi}}^* dt, \quad \text{in } V, \quad (55c)$$

$$\mathbf{C}\mathbf{u}^* = \mathbf{A}\hat{\boldsymbol{\sigma}}^r + \Delta\boldsymbol{\epsilon}^{p^*}, \quad \text{in } V, \quad \mathbf{u}^* = \mathbf{0}, \quad \text{on } S_u, \quad (55d)$$

$$\mathbf{C}^T\hat{\boldsymbol{\sigma}}^r = \mathbf{0} \quad \text{in } V, \quad \mathbf{C}_n^T\hat{\boldsymbol{\sigma}}^r = \mathbf{0}, \quad \text{on } S_t, \quad (55e)$$

$$\frac{\partial\Omega}{\partial\hat{\boldsymbol{\chi}}} = \hat{\boldsymbol{\xi}} = \Delta\boldsymbol{\xi}^*, \quad \text{in } V, \quad (55f)$$

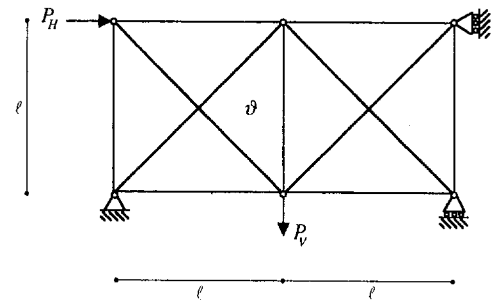

Fig. 3 The structure: geometry, mechanical load P_V, P_H, and thermal load ϑ applied in all the elements

$$\frac{1}{\omega}\left[\frac{1}{2}\int_V \hat{\boldsymbol{\sigma}}^{r^T}\mathbf{A}\hat{\boldsymbol{\sigma}}^r dV + \int_V \Omega(\hat{\boldsymbol{\chi}})dV\right] = U_1^{\text{opt}} = \int_V \overline{\mathbf{s}}\Delta\boldsymbol{\epsilon}^{p^*}dV. \quad (55g)$$

Euler-Lagrange Eqs. (55) allow us to deduce the meaning of the introduced Lagrange multipliers. Actually, $\dot{\lambda}^*$ is the fictitious plastic activation coefficient and $\mathbf{u}^*$ is the displacement field produced by the fictitious plastic deformation $\Delta\boldsymbol{\epsilon}^{p^*}$. Equation (55$g$) provides the optimal bound U_1^{opt}; comparing this last relation with Eq. (46a) we deduce

$$\max_{0\le t\le\infty} \int_V \overline{\mathbf{s}}^T(\mathbf{x})\boldsymbol{\epsilon}^p(\mathbf{x}, t)dV \le \int_V \overline{\mathbf{s}}^T(\mathbf{x})\Delta\boldsymbol{\epsilon}^{p^*}(\mathbf{x})dV. \quad (56)$$

Equation (56) shows that the optimal bound depends just on the fictitious plastic deformation produced in the same region of the body where we want to compute the peak value of the real plastic deformation (that is the region where $\overline{\mathbf{s}}(\mathbf{x}) \neq \mathbf{0}$ is assumed), i.e., the optimal bound has a local character.

The optimization process utilized to obtain U_1^{opt} can be analogously applied to Eq. (46b) in order to evaluate the optimal bound U_2^{opt}, but this point is here omitted for brevity.

6 Application

As an application the truss structure of Fig. 3 has been studied. The structure is subjected to the mechanical loads P_V, P_H and to the uniform thermal load ϑ, all cyclically variable in time. We assume that the reference mechanical loading path is piecewise linear and that along each side the temperature variation changes linearly (Fig. 4). According to Eqs. (18a, b) the yield stress is assumed as a piecewise linear function of ϑ, i.e.,

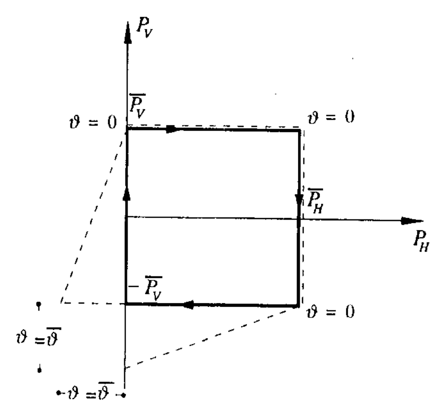

Fig. 4 Reference piecewise linear mechanical loading path (solid line) and temperature variation along the sides (dashed line)

$$\sigma_y = 40 \text{ kN/cm}^2 \quad \text{for } T \le 200°\text{C}, \tag{57a}$$

$$\sigma_y = 40[1 - 0.0004(T - 200)] \text{ kN/cm}^2 \quad \text{for } 200°\text{C} \le T \le 600°\text{C}. \tag{57b}$$

The other data of the problem are:

l = 200 cm; A = element cross-section areas = 10 cm^2;
α = thermal expansion coefficient = 0.000012(°C)$^{-1}$;
E^e = Young modulus = 21,000 kN/cm^2; E^h = hardening modulus = 500 kN/cm^2;
T_i = initial state temperature = 200°C;
$\bar{\vartheta}$ = reference temperature variation = 0 ÷ 100°C;
$\bar{P}_H$ = reference horizontal load = 200 kN;
$\bar{P}_V$ = reference vertical load = 100 kN.

As advisable measure of the real plastic deformation the vertical residual displacement u_1 of the hinge H has been chosen (Fig. 5(a)). According to this choice the perturbation mode $\bar{\mathbf{s}}$ identifies with the elastic stress response of the truss subjected to a unit load F_1 as represented in Fig. 5(b).

In order to specify suitable ranges of the load multiplier β within which to compute the chosen residual displacement and its optimal bound, the following problem has been solved:

$$\beta^* = \max_{(\beta, \mathbf{Q}^r, \mathbf{X})} \beta \tag{58a}$$

subject to:

$$\mathbf{N}^T\mathbf{Q}_m^E\beta + \mathbf{N}^T\mathbf{Q}^r - \mathbf{N}^T\mathbf{X} - \mathbf{Q}_y \le \mathbf{0}, \quad (m = 1, 2, 3, 4) \tag{58b}$$

$$\mathbf{C}^T\mathbf{Q}^r = \mathbf{0}, \tag{58c}$$

obtaining the shakedown limit load multiplier β^* in the hypothesis of kinematic hargening (as it is well known, in the case of isotropic hardening $\beta^* = \infty$). Symbols utilized in problem (58) have the usual meaning, i.e.:

$\mathbf{Q}^r$ = residual axial force vector;
$\mathbf{X}$ = mechanical internal variable vector;
$\mathbf{N}$ = matrix of unit external normals to the yield surface;
$\mathbf{Q}_y$ = plastic resistance vector;
m = index of the typical basic load condition (m = 1, 2, 3, 4);
$\mathbf{Q}_m^E$ = purely thermoelastic stress response to the mth basic load;

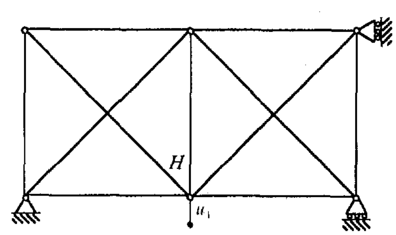

Fig. 5(a)

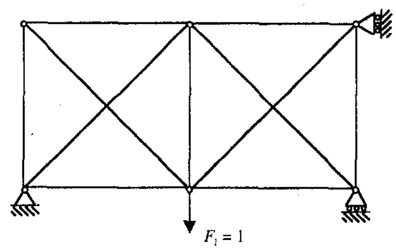

Fig. 5(b)

Fig. 5 Choice of the advisable measure of the real plastic deformation: (a) vertical residual displacement u_1 of the hinge H; (b) auxiliary load condition for the evaluation of the perturbation mode $\bar{\mathbf{s}}$

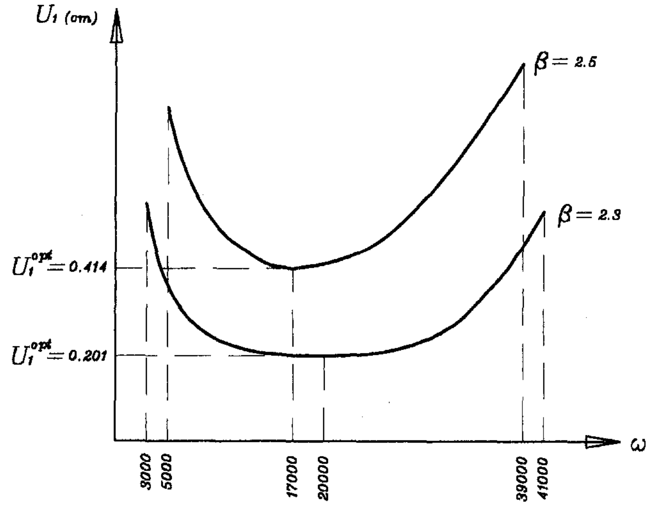

Fig. 6 Bound U_1 as function of the parameter ω for two different values of the load multiplier β, with ϑ = 0°C, in the case of kinematic hardening

$\mathbf{C}^T$ = equilibrium matrix of the relevant structure.

By imposing $\mathbf{Q}^r = \mathbf{0}$ and $\mathbf{X} = \mathbf{0}$ the solution to problem (58) provided the elastic limit load multiplier β^E. By imposing just $\mathbf{X} = \mathbf{0}$ the solution to problem (58) provided the shakedown limit load multiplier β^p of the relevant structure but constituted by elastic perfectly plastic material.

Subsequently, different ranges of β have been chosen to represent the relevant strain quantities in Figs. 7 and 8. Actually, in Figs. 7(a) and 8(a) (kinematic hardening) the significant range $\beta^E \le \beta \le \beta^*$ has been taken into account, while in Figs. 7(b) and 8(b) (isotropic hardening) just a convenient one.

For a selected value of the multiplier β, the optimal bound U_1^{opt} on the chosen residual displacement u_1 can be obtained by solving the minimum problem (52), that in this special case transforms into a mathematical programming problem, i.e.,

$$U_1^{\text{opt}} = \min_{(\omega, \hat{\mathbf{Q}}^r, \hat{\mathbf{X}}^{\text{kin}}, \hat{\mathbf{X}}^{\text{iso}})} \frac{1}{2\omega} (\hat{\mathbf{Q}}^{r^T}\mathbf{A}\hat{\mathbf{Q}}^r + \hat{\mathbf{X}}^{\text{kin}^T}\mathbf{B}\hat{\mathbf{X}}^{\text{kin}} + \hat{\mathbf{X}}^{\text{iso}^T}\mathbf{B}\hat{\mathbf{X}}^{\text{iso}}), \tag{59a}$$

subject to

$$\mathbf{N}^T(\beta\mathbf{Q}_m^E + \omega\bar{\mathbf{s}}) + \mathbf{N}^T\hat{\mathbf{Q}}^r - \mathbf{N}^T\hat{\mathbf{X}}^{\text{kin}} - \mathbf{N}_+^T\hat{\mathbf{X}}^{\text{iso}} - \mathbf{Q}_y \le \mathbf{0}, \quad (m = 1, 2, 3, 4) \tag{59b}$$

$$\mathbf{C}^T\hat{\mathbf{Q}}^r = \mathbf{0}, \tag{59c}$$

where $\mathbf{N}$, $\mathbf{Q}_y$, m, $\mathbf{Q}_m^E$, and $\mathbf{C}^T$ have the same meaning as before, $\mathbf{N}_+$ is deduced by $\mathbf{N}$ imposing $N_+^{ij} = |N^{ij}|$ for all i and j, and

$\hat{\mathbf{Q}}^r$ = fictitious residual axial force vector;
$\hat{\mathbf{X}}^{\text{kin}}$ = fictitious mechanical internal variable vector in the case of kinematic hardening;
$\hat{\mathbf{X}}^{\text{iso}}$ = fictitious mechanical internal variable vector in the case of isotropic hardening;
ω = perturbation multiplier;
$\mathbf{A}$ = diag (l_j/E^eA_j) $\quad (j = 1, 2, \ldots, 11)$;
$\mathbf{B}$ = diag (l_j/E^hA_j) $\quad (j = 1, 2, \ldots, 11)$.

By imposing, alternatively, $\hat{\mathbf{X}}^{\text{iso}} = \mathbf{0}$ or $\hat{\mathbf{X}}^{\text{kin}} = \mathbf{0}$, the solution to problem (59) provides the optimal bound in the case of kinematic hardening or in the case of isotropic hardening, respectively.

The mathematical programming problem (59) has been solved as a parametric quadratic programming problem. With this aim a suitable discrete set of selected values ω_k (k = 1, 2, 3, ...) has been assigned to variable ω, the corresponding values

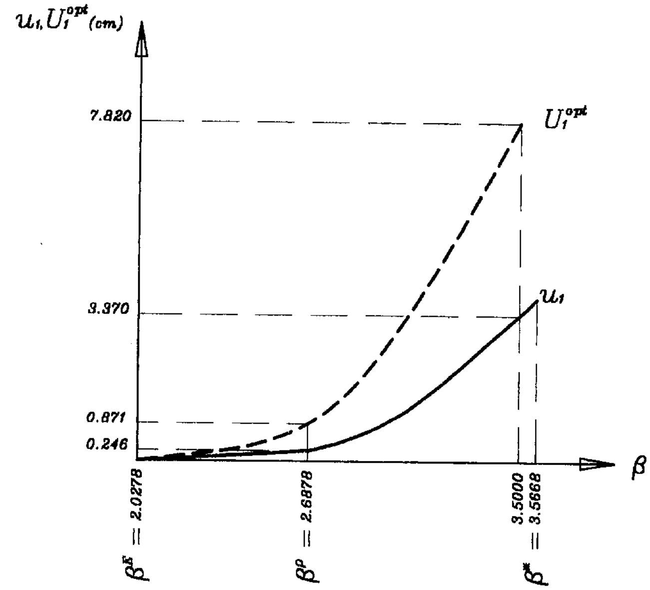

Fig. 7(*a*)

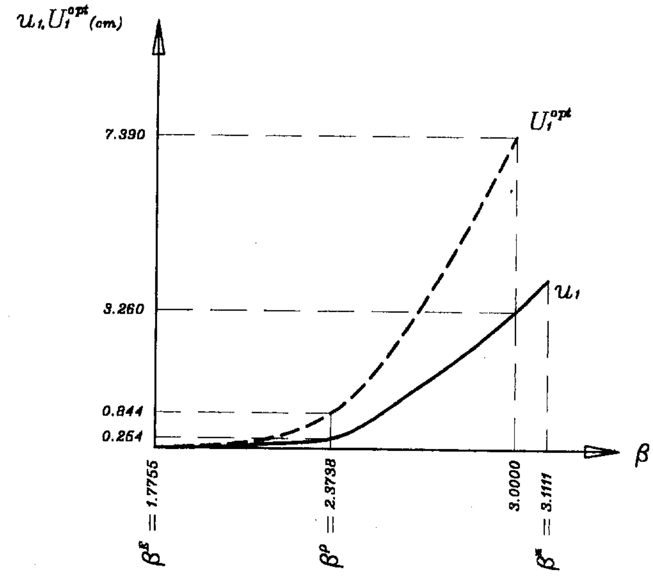

Fig. 8(*a*)

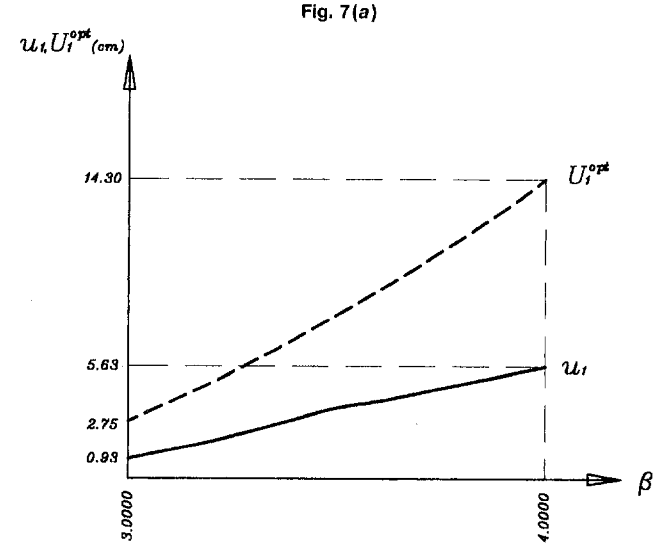

Fig. 7(*b*)

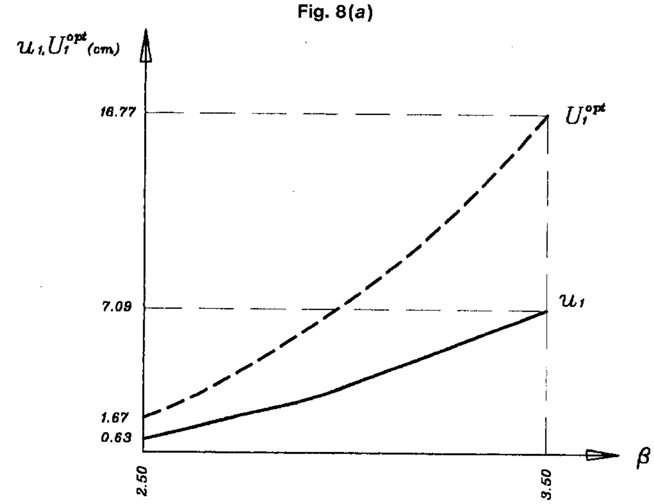

Fig. 8(*b*)

Fig. 7 Real residual displacement u_1 (solid line) and its optimal bound U_1^{opt} (dashed line) as functions of the load multiplier β, with $\vartheta = 0°C$: (*a*) in the case of kinematic hardening; (*b*) in the case of isotropic hardening

Fig. 8 Real residual displacement u_1 (solid line) and its optimal bound U_1^{opt} (dashed line) as functions of the load multiplier β, with $\vartheta = 100°C$: (*a*) in the case of kinematic hardening; (*b*) in the case of isotropic hardening

U_{1k} of the bounding quantity has been computed and the optimal bound

$$U_1^{opt} = \min_{(k)} U_{1k} \tag{60}$$

has been obtained. In Fig. 6 functions $U_1(\omega)$ for two different values of the load multiplier β and for $\vartheta = 0$, in the case of kinematic hardening, are plotted.

For different values of the load multiplier β, for the two assigned values of $\bar{\vartheta}$, in the case of kinematic hardening and in the case of isotropic hardening the real residual displacement u_1 has been computed by means of a step-by-step analysis effected for a convenient number of cycles, till to reach eventually an elastic behavior of the structure. In Figs. 7 and 8 the real residual displacement u_1 and its optimal bound U_1^{opt} are compared in the case of $\bar{\vartheta} = 0°C$ and $\bar{\vartheta} = 100°C$, respectively. In Figs. 7(*a*) and 8(*a*) the relevant quantities evaluated in the case of kinematic hardening are compared, in Figs. 7(*b*) and 8(*b*) the relevant quantities evaluated in the case of isotropic hardening are compared.

Except that for β values very close to β^* (actually $U_1^{opt} \to \infty$ for $\beta \to \beta^*$), the proposed technique provided good bounds, satisfactorily close to the bounded real displacement.

It is worth noting that, in all the effected computation, for values of β such that $\beta^E \leq \beta \leq \beta^{\hat{p}} < \beta^p$ (with $\beta^{\hat{p}}$ analogous of β^p and close enough to it, but related with a perturbed yield function) the real displacement u_1 is very small and (obviously) the structure shakes down for the simultaneous presence of self stresses $\mathbf{Q}^r$ and static internal variables $\mathbf{X}$, while the bound U_1^{opt} is connected with a fictitious process characterized by vanishing values of $\hat{\mathbf{X}}^{kin}$ and/or $\hat{\mathbf{X}}^{iso}$. Anyway, in this range of β, U_1^{opt} is very close to u_1.

7 Conclusions

The present paper concerned the study of a continuous solid body subjected to cyclic loads not exceeding the shakedown limit. We assumed that the relevant body is constituted by elastic hardening material described by means of an internal variable constitutive model. The dependency of the yield function on the temperature variations has also been taken into account.

The shakedown limit load multiplier problem related to the relevant solid body has been formulated according to both the lower and the upper bound theorems.

In order to obtain upper bounds on suitably chosen measures of the real plastic deformation produced in the body during the initial transient phase, a deformation bounding theorem, based on a yield function perturbation technique and specialized to the assumed constitutive behavior of the material, has been proved. The bounding quantity expression is a function of some fictitious (time-independent) self-stresses and static internal variables produced in the whole body, as well as of the perturbation multiplier. As a consequence, in general, a measure of the real plastic deformation produced in a selected region of the body is bounded by a quantity depending on variables which must be evaluated in the whole body.

In order to make the upper bound most stringent an optimization problem has been formulated. In particular, we searched for the minimum upper bound according to the plastic admissibility of the mechanical quantities related to the fictitious process and the equilibrium of the self-stresses. The Euler-Lagrange equations related to the optimization problem have been deduced. They showed that, in optimality conditions, the optimal bound on the real plastic deformation produced in a selected region of the body depends just on some fictitious plastic deformations evalued in the same region of it, i.e., the optimal bound has a local character.

A special choice of the temperature variation fictitious process allowed us to generalize the proposed technique to the case of loads arbitrarily varying in a given domain.

The effected numerical experiences showed the good features of the utilized bounding technique.

References

Capurso, M., Corradi, L., and Maier, G., 1979, "Bounds on deformations and displacements in shakedown theory," *Matériaux et structures sous chargement cyclique,* Ass. amicale des ingénieurs anciens eléves de l'E.N.P.C., Paris, pp. 231–244.

Cohn, M. Z., and Maier, G., 1977, *Engineering Plasticity by Mathematical Programming,* Pergamon Press, Oxford, UK.

Corradi, L., and Zavelani Rossi, A., 1974, "A linear programming approach to shakedown analysis of structures," *Comp. Meth. Appl. Mech. Eng.,* Vol. 3, pp. 37–53.

Giambanco, F., Lo Bianco, M., and Palizzolo, L., 1990, "A bilateral convergent bounding technique for plastic deformations," *Meccanica,* Vol. 25, pp. 181–188.

Giambanco, F., Palizzolo, L., and Panzeca, T., 1992, "A bounding technique for plastic deformations," *Computational Mechanics,* Vol. 9, pp. 153–171.

Gokhfeld, D. A., and Cherniavsky, O. F., 1980, *Limit Analysis of Structure at Thermal Cycling,* Sijthoff & Noordhoff, Alphen aan den Rijn, The Netherlands.

Koiter, W. T., 1960, "General theorems for elastic-plastic solids," *Progress in Solid Mechanics,* I. N. Sneddon and R. Hill, eds., North Holland, Amsterdam, pp. 165–219.

König, J. A., 1979, "On upper bounds to shakedown loads," *Z. Angew. Math.,* Vol. 59, pp. 349–354.

König, J. A., 1987, *Shakedown of Elastic Plastic Structures,* Warsaw, PWN-Polish Scientific Publishiers, Elsevier, Amsterdam.

Lemaitre, J., and Chaboche, J. L., 1985, *Mécanique des matériaux solides,* Dunod, Paris.

Maier, G., 1987, "A generalization to nonlinear hardening of the first shakedown theorem for discrete elastic-plastic models," *Atti Acc. Lincei Rend. Fis.,* Vol. 8, No. 81, pp. 161–174.

Maier, G., and Novati, G., 1987, "Deformation bounds for elastic-plastic discrete structures with piecewise linear yield locus and nonlinear hardening," *Computational Plasticity,* D. R. J. Owen, E. Hinton, and E. Oñate, eds., Pineridge Press, Swansea, U.K., pp. 17–31.

Maier, G., and Novati, G., 1990, "Dynamic shakedown and bounding theory for a class of nonlinear hardening discrete structural models," *Int. J. Plasticity,* Vol. 6, pp. 551–572.

Martin, J. B., 1975, *Plasticity: Fundamentals and General Results,* The MIT Press, Cambridge, MA.

Melan, E., 1938a, "Der Spannungszustand eines Hencky-Mises'shen Kontinuum bei veränderlicher Belastung," *Sitz. Ber. AK. Wiss Wien,* Vol. IIa, No. 147, p. 73

Melan, E., 1938b, "Zur Plastizität des räumlichen Kontinuum," *Ing. Arch.,* Vol. 9, p. 116.

Polizzotto, C., 1982, "A unified treatment of shakedown theory and related bounding techniques," *S.M. Archives,* Vol. 7, pp. 19–75.

Polizzotto, C., 1989, "Simplified methods of structural analysis for cyclic plasticity," Commission of the European Communities, Nuclear Science and Technology, Final Report, Contract N. RD1-0116(N).

Polizzotto, C., Borino, G., Caddemi, S., and Fuschi, P., 1991, "Shakedown problems for material models with internal variables," *Eur. Journal Mech., A/Solids,* Vol. 10, No. 6, pp. 621–639.

Ponter, A. R. S., 1972, "An Upper Bound on the Displacement of Elastic Perfectly Plastic Structures," ASME JOURNAL OF APPLIED MECHANICS, Vol. 39, pp. 959–963.

Zarka, J., and Casier, J., 1981, "Elastic plastic response of a structure to cyclic loading: practical rules," *Mechanics Today,* S. Nemat-Nasser, ed., Vol. 6, Pergamon Press, pp. 93–198.

E. Nakamachi
Professor,
Department of Mechanical Engineering,
Osaka Institute of Technology,
5-16-1 Omiya, Asahiku,
Osaka 535, Japan
Mem. ASME.

X. Dong
Department of Plastic Forming Engineering,
Huazhong University of Science and Technology,
Wuhan, Hubei, China

Study of Texture Effect on Sheet Failure in a Limit Dome Height Test by Using Elastic/Crystalline Viscoplastic Finite Element Analysis

By combining the crystalline orientation distribution with a hardening evolution equation, a new elastic/crystalline viscoplastic material model is established. We focus our discussion on looking primarily at the texture effects on the strain localization of limit dome height (LDH) tests which are simulated using our Dynamic-Explicit finite element code. Three crystalline models in addition to the classical plastic potential and associated flow law model (J_2F) are employed. The results demonstrate that, according to our failure criterion, the random orientation model shows the earliest indication of failure. The better formability is obtained for aluminum alloy 6111-T4 and cube texture models than the random crystalline orientation model. The J_2F model shows no signs of strain localization. A comparison between numerical results also confirms that the strain localization region and crystalline rotation are different, due to the crystalline orientation distribution, which is initially set.

1 Introduction

The plastic deformation behavior of sheet metal is greatly affected by its initial and deformation induced plastic anisotropy. To describe this plastic anisotropy evolution, classical potential theory, such as the associated flow law and the nonassociated flow law, require many parameters to be determined using an enormous amount of experimental data. On the other hand, by employing the fundamental process of sliding in crystalline slip systems, the meso-scale constitutive equation—nonclassical theory—has been developed to avoid the complexity of parameter fitting. Originating from the pioneering work of Taylor and Elam, many crystalline plasticity models have been proposed. A rate-dependent model has been proposed by Peirce et al. (1983). Their model was later modified by Zhou et al. (1993) through the investigation of the interaction differences between glide dislocations and forests. Bassani and Wu (1991) proposed the hardening moduli evaluation in the deformation stage I and II based on their experimental observations. Due to the presence of selected orientations it is possible that the easy glide stage I may appear during a sheet forming process. We proposed the hardening evolution model, which is available for the whole stages, I, II, III, and IV (Nakamachi and Dong, 1996). In general, the crystalline plasticity model requires a great extent of the microstructural parameters as well as the hardening evolution description. The great progress in the microstructure measurement technology offers precise information for modeling the crystal aggregate. Through combining this experiment technology with FE analysis, we have developed highly accurate simulation models. The crystalline orientation distribution of the sheet metal, obtained by X-ray diffraction analysis, is introduced to the elastic/crystalline viscoplastic model, which is embedded in our Dynamic-Explicit finite element code. Two kinds of failure criteria, the critical thickness strain and the critical gradient of thickness strain—punch height curve, are proposed to evaluate the forming limit of the sheet metal in the LDH test analyses.

Contributed by the Applied Mechanics Division of THE AMERICAN SOCIETY OF MECHANICAL ENGINEERS for publication in the ASME JOURNAL OF APPLIED MECHANICS.

Discussion on the paper should be addressed to the Technical Editor, Professor Lewis T. Wheeler, Department of Mechanical Engineering, University of Houston, Houston, TX 77204-4792, and will be accepted until four months after final publication of the paper itself in the ASME JOURNAL OF APPLIED MECHANICS.

Manuscript received by the ASME Applied Mechanics Division, Apr. 22, 1996; final revision, Oct. 24, 1996. Associate Technical Editor: R. Becker.

2 Crystalline Structure Characterization

Crystalline structure are characterized by their geometrical properties. The geometrical features include:

(1) Lattice structure, e.g., f.c.c. or b.c.c., and multiphases.
(2) Orientation distribution, or texture of polycrystal.
(3) Grain shape, size, and boundary description.

The slip system is determined by the lattice structure, which is unchanged when no phase transformation has taken place. For polycrystal, texture is the main factor to cause plastic anisotropy, and it plays an important role for the sheet metal formability. Crystalline plasticity introduces corners on yield loci, the radius of which are affected by the textures of the material, as discussed by Zhou et al. (1995). Grain shape and boundary are also important for the plastic straining and hardening evolution, because of the boundary constraint for the crystalline deformation and the interaction phenomena between the matrix and second-phase particles. In this paper, we concentrate on the texture features. This means that the lattice structure and orientation distribution obtained by X-ray diffraction analysis are considered to establish the finite element modeling.

2.1 Determination of Euler Angles. The orientation distribution of f.c.c. sheet metal can be described by Euler angles obtained from a crystalline pole figures. Three coordinate systems for f.c.c. sheet metals are introduced as shown in Fig. 1(a), (b), and (c). The X, Y, and Z-axes of the specimen global coordinate system are chosen as the TD, RD, and ND directions of the sheet metal, respectively. The x, y, and z-

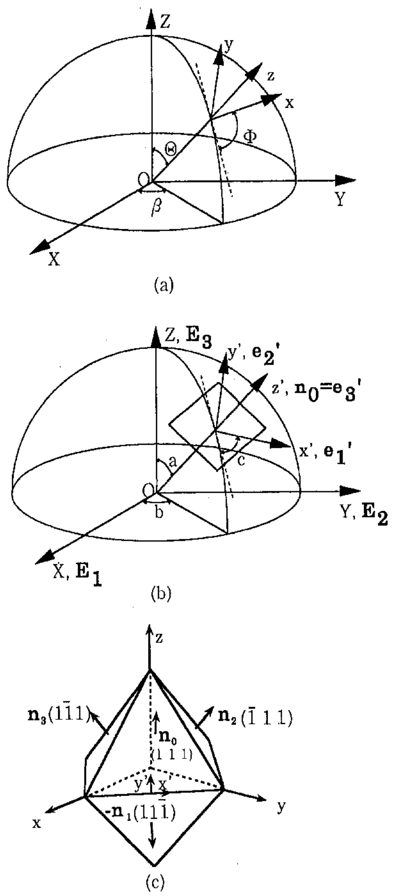

Fig. 1 Definition of the specimen global coordinate system, the lattice local coordinate system and the slip plane coordinate system

axes of the lattice local coordinate system are defined as the crystallographic [100], [010], and [001] directions. Further, a coordinate system defined on the slip plane is introduced, denoted by $x'y'z'$, as shown in Fig. 1(*b*). Here the unit normal to (111) plane is chosen as the base vector $\mathbf{e}_3'$ along z'-axis. The other three independent unit normals of the {111} family, $\mathbf{n}_1$, $\mathbf{n}_2$, and $\mathbf{n}_3$ are introduced.

The procedure of the approximation method to determine Euler angle can be indicated as follows:

1st Process: {111} pole figure, obtained by X-ray diffraction analysis, are divided into 640 sections—those have almost the same area. The intensity factor of each section by referring contours of {111} pole figure is defined. By accounting the intensity factor, the corresponding number of points are generated in the section. These "generated points," which have coordinate (X, Y) in the {111} pole figure plane, are randomly distributed in the section. Total number of these generated points is 160.

2nd Process: By selecting the coordinate (X, Y) of generated point in the first quadrant of {111} pole figure, two direction angles, such as a and b as shown in Fig. 1(*b*), are determined as follows;

$$a = 2 \arctan (X^2 + Y^2)^{1/2}$$
$$b = \arctan \left(\frac{Y}{X}\right). \tag{1}$$

3rd Process: The algorithm to find the direction angle c, as shown in Fig. 1, can be described as follows: The 480 equidivided "candidate angles" of c ($0 \le c \le \frac{2}{3}\pi$) are defined in the first quadrant of {111} pole figure. By arbitrarily choosing the candidate angle c, three alternative slip planes $(\bar{1}\bar{1}1)$, $(\bar{1}11)$, $(1\bar{1}1)$, can be defined. Those slip planes have unit normals, $\mathbf{n}_1$, $\mathbf{n}_2$, and $\mathbf{n}_3$, as shown Fig. 1(*c*).

$$\mathbf{n}_1 = (-2\sqrt{2}\mathbf{e}_2' + \mathbf{e}_3')/3$$
$$\mathbf{n}_2 = (\sqrt{6}\mathbf{e}_1' + \sqrt{2}\mathbf{e}_2' + \mathbf{e}_3')/3$$
$$\mathbf{n}_3 = (-\sqrt{6}\mathbf{e}_1' + \sqrt{2}\mathbf{e}_2' + \mathbf{e}_3')/3 \tag{2}$$

where

$$\mathbf{e}_1' = (\cos a \cos b \cos c - \sin b \sin c)\mathbf{E}_1 + (\sin a \sin b \cos c + \cos b \sin c)\mathbf{E}_2$$
$$\mathbf{e}_3' = \sin a \cos b\mathbf{E}_1 + \sin a \sin b\mathbf{E}_2 + \cos a\mathbf{E}_3$$
$$\mathbf{e}_2' = \mathbf{e}_3' \times \mathbf{e}_1'. \tag{3}$$

Those normals $\mathbf{n}_1$, $\mathbf{n}_2$, and $\mathbf{n}_3$, have three "projection points" in three quadrants, such as the second, third, and fourth quadrants of {111} pole figure.

4th Process: The distances between these three projection points and three points, selected from generated points in three quadrants are calculated, and the minimum distance between each three points can be evaluated. It means that each candidate angle c has the minimum distance. By comparison of these 480 minimum distances, the angle c, which has smallest "minimum distance," can be selected as the correct angle c. Next, the selected four generated points are eliminated.

5th Process: Repeat 2nd, 3rd, and 4th processes, until the "generated points" in the {111} pole figure are eliminated completely. Finally 160 "direction angle" sets are determined.

6th Process: By using the direction angles, Euler angles Θ, β, and ϕ can be obtained as follows:

$$\cos \Theta = \frac{1}{\sqrt{3}} (\sqrt{2} \sin a \sin c + \cos a)$$
$$\tan \beta = [\sqrt{2} (\cos b \cos c - \cos a \sin b \sin c) + \sin a \sin b]/[-\sqrt{2} (\sin b \cos c + \cos a \cos b \sin c) + \sin a \cos b]$$
$$\tan \phi = \frac{-(\sqrt{3} \cos c + \sin c) \sin a + \sqrt{2} \cos a}{-[(\sqrt{3} \cos c - \sin c) \sin a + \sqrt{2} \cos a]} \tag{4}$$

Figure 2 shows {111} pole figure of aluminum alloy 6111-T4 obtained by X-ray diffraction analysis. By using 160 Euler angle sets determined by the approximation method, {111} pole figure can be reproduced, as shown in Fig. 7(*b*-1). Many duplicated points are observed around brass texture.

2.2 Polycrystalline Modeling. We introduce the orientation distribution of polycrystals to represent the inhomogeneous material properties. We propose the following finite element

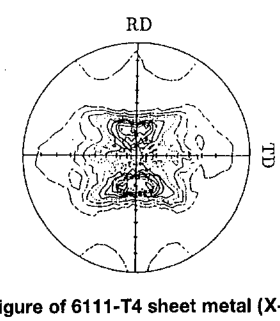

Fig. 2 {111} pole figure of 6111-T4 sheet metal (X-ray diffraction analysis)

modeling: first, Euler angle sets are determined by the approximation method, as discussed in the Section 2.1. This population has P Euler angle sets. Next, Q sets are randomly selected from the population and assigned to the integration point of each finite element. Using a Taylor assumption, compatibility at each integration point is enforced. In case of $P = Q$, a homogeneous material modeling can be established. On the other hand, for $Q < P$, an inhomogeneous one might be. In this paper, each finite element is assigned to have one Euler angle set. It means that each finite element represents a grain having the same crystalline orientation. This finite element modeling can be understood as the inhomogeneous material modeling.

3 Crystalline Hardening Evolution

Strain hardening in each slip system is an intrinsic property, it is caused by internal multiplication and interaction of dislocations in a grain. Other extrinsic hardening phenomena are caused by solution, second-phase particles, and grain boundaries. In our study, only strain hardening determined by a macroscale uni-axial stress-strain relationship is considered. It has been confirmed how the hardening evolution affects plastic instability of a single crystal tension test (Nakamachi and Dong, 1996).

We adopt the rate-dependent model proposed by Peirce et al. (1983), the shear strain in slip system (a) is obtained by the following equation:

$$\dot{\gamma}^{(a)} = \dot{a}^{(a)} \left[\frac{\tau^{(a)}}{g^{(a)}} \right] \left[\left| \frac{\tau^{(a)}}{g^{(a)}} \right| \right]^{(1/m)-1}. \quad (5)$$

Here $\tau^{(a)}$ means the resolved shear stress on the slip system (a). $g^{(a)}$ represents the reference shear stress, $\dot{a}^{(a)}$ the reference shear strain rate, and m the strain rate sensitivity. The hardening evolution law is introduced to define the evolution of $g^{(a)}$ and is written as

$$\dot{g}^{(a)} = \sum_{b=1}^{N} h_{ab} |\dot{\gamma}^{(b)}|, \quad (6)$$

where N is the number of slip systems. h_{ab}, the hardening moduli, is expressed as follows:

$$h_{ab} = h(\gamma) q_{ab} \quad (7)$$

where a matrix q_{ab} is introduced to describe the self and latent hardening. The parameter q_{ab} proposed by Zhou et al. (1993) are employed for the coplanar or colinear slip systems, $q_c = 1$. For the slip systems which have mutually perpendicular Burgers vectors, $q_v = 1.2$. For the others, $q_l = 1.3$. γ is the accumulated slip summation over all the slip systems, $h(\gamma)$ is determined by the following inverse method. Previous attempts at determining the hardening evolution parameters of sheet metals adopted Taylor's isotropic hardening assumption (see, e.g., Beaudoin (1994)). The inverse iterative procedure to find the parameters is introduced to fit the experimental uni-axial tension test. In this procedure, we assume a uniform initial hardening state and account for latent hardening.

$\bar{\sigma}$, $\dot{\bar{\epsilon}}^p$, g, and $\dot{\gamma}$ denote the effective stress, effective strain rate, the critical shear stress, and the summation of shear strain rate over all slip systems, respectively. Employing the Taylor factor

$$M \equiv \bar{\sigma}/g = \dot{\gamma}/\dot{\bar{\epsilon}}^p = \begin{cases} 3.06, & f.c.c \\ 2.83, & b.c.c. \end{cases}$$

A first trial of the evolution of g can be obtained from the experimental effective stress - effective strain relationship

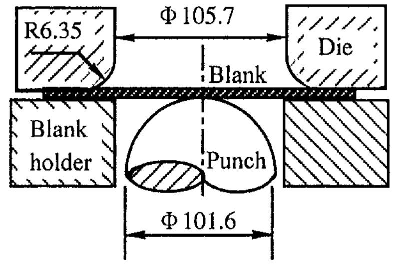

Fig. 3 Tool geometry of LDH test (180 mm × 100 mm rectangular sheet with 0.92 mm thickness)

$$\bar{\sigma} = f(a_i, \bar{\epsilon}^p), \quad (8)$$

by replacing $\bar{\sigma}$ and $\bar{\epsilon}^p$ with g and γ as follows:

$$g = \frac{1}{M} f\left(a_i, \frac{\gamma}{M}\right). \quad (9)$$

Due to the presence of an initial texture and the latent hardening effects, parameters a_i should be adjusted to fit the experimental results.

The effective stress - effective strain relation of 6111-T4 sheet metal obtained by simple tension experiment is

$$\bar{\sigma} = 488(0.00713 + \bar{\epsilon}^p)^{0.232}(\text{MPa}). \quad (10)$$

By fitting the finite element simulation results of rectangular block tension test using $2 \times 2 \times 2 = 8$ solid elements, we determined the following $h(\gamma)$ function:

$$h(\gamma) = 18.228[0.372(0.002 + \gamma)]^{-0.65}(\text{MPa}) \quad (11)$$

which corresponds to

$$g = 140[0.372(0.002 + \gamma)]^{0.35}(\text{MPa}). \quad (12)$$

In the simulation a cube orientation is assumed and the strain rate is maintained at $\dot{\epsilon}_0 = 100\ \text{s}^{-1}$. The stress-strain curve obtained by simulation agrees reasonably with the experimental results. Other parameters in this crystalline plasticity model include $g_0 = 50$ MPa, $m = 0.03$ and $\dot{a} = 0.5\ \text{s}^{-1}$.

4 Numerical Simulation of LDH Test

The NUMISHEET'96 LDH benchmark test problem (Lee et al., 1996), was adopted to investigate the effects of textures on strain localization and formability of the sheet metal. The geometry of the tools are shown in Fig. 3. Only a quarter of the sheet is analyzed because of symmetry. For the draw bead condition, the maximum draw-in through the draw bead along the X-axis is assumed to be 0.25 mm. A detail description of the draw bead model can be found in the reference Wang (1994). In our simulation, 1125 eight-node SRI (selected reduced integration) solid elements are used. The punch is linearly accelerated to a maximum speed 20 m/s within 10 mm punch travel, and this speed is maintained throughout the remaining simulation steps. The material properties are assumed as Young's modulus $E = 69$ GPa and Poisson's ratio $\nu = 0.33$. The cubic elastic constants for the crystal are $c_{11} = 10{,}8200$ MPa, $c_{12} = 61{,}300$ MPa and $c_{44} = 28{,}500$ MPa. Coulomb's coefficient of friction is set as $\mu = 0.1$. The hardening law is given by Eqs. (7), (8), and (12). Three texture models are introduced:

Model 1: Single crystal with the cube orientation (cube).
Model 2: Aluminum alloy 6111-T4, as shown in Fig. 7 (b-1) (6111-T4).
Model 3: Polycrystal with random orientation distribution (random).

In addition, two models of J_2 flow rule (J_2F) and the cube texture single crystal with thermal softening effect (cube texture with thermal effect) are also employed for the comparison. It is assumed in the thermal softening model, the plastic deformation energy is transformed into the heat energy. The inhomogeneous modeling in case of 6111-T4 and the random models are employed, where the different initial orientations are assigned by randomly sampling from their corresponding population of Euler angle sets.

The deformed shapes with the major principal strain distribution are shown in Fig. 4. For all the models, the deformation and wrinkle pattern are identical, but the strain distribution is very different. Since the simulations are executed under the same conditions, with the exception of the material models, it is possible to isolate the texture effect on the straining.

These effects are shown more clearly in Fig. 5. Top view of major principal strains at punch height (PH) 30 mm (25 mm for cube-thermal) are shown in Fig. 5(a)-(e), respectively. The J_2F model has features of homogeneous and isotropic elasticity and plasticity. The effect of friction is particularly evident for this model, giving rise to strain localization region far away from center of the hemispherical punch, as shown in Fig. 5(a).

The single crystal with cube texture has also a homogeneous nature but includes both anisotropic elasticity and plasticity. This leads to the material possessing its own characteristic deformation direction in which strain localizes very easily. As shown in Fig. 5(b). The rather narrow strain localization region occurs at about 55 deg inclined to the X coordinate, it implies that only favorable slip systems, which generate the extreme thinning along this direction, are dominant. The figure shows that both the friction and the material anisotropy induces localization conflict one another, with the latter being the more dominant.

The random orientation model would produce the isotropic yield surface, if the model comprises infinite number of orienta-

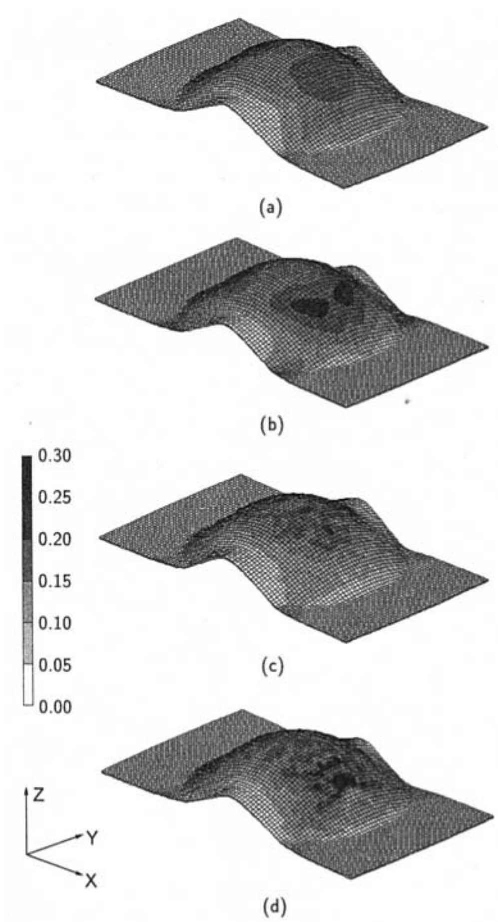

Fig. 4 Distribution of major principal strain on the upper surface when punch travels 30 mm. (a) J_2F model, (b) cube model, (c) 6111-T4 model, and (d) random model.

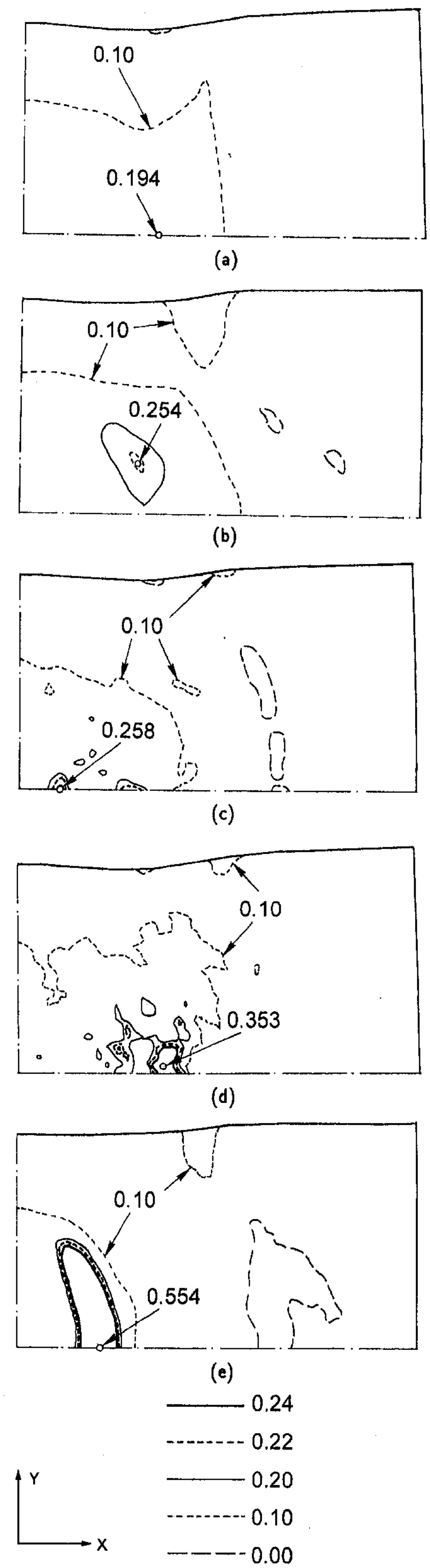

Fig. 5 Top view of major principal strain distribution at punch travel = 30 mm. (a) J_2F model, (b) cube model, (c) 6111-T4 model, (d) random model, and (e) cube-thermal model.

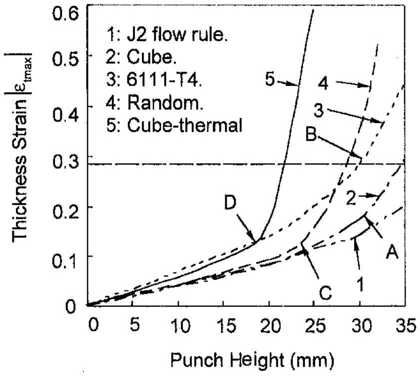

Fig. 6 The thickness strain versus punch height curves

tion and finite element. However, for this case where only 160 orientation sets and 1125 elements are employed, this does not represent fully the homogeneous and isotropy material characteristics. In this random model, the orientation randomness introduces an initial material imperfection. As shown in Fig. 5(*d*), the extreme localization, with a maximum strain of 0.353, occurs rather far away from the center. It means that the combined effect with friction and initial material imperfection promotes the strain localization, earlier and more far away from the center.

Aluminum alloy 6111-T4, which has a typical brass texture, shows material characteristics between those of the cube and random models. This is clearly manifested in Fig. 5(*c*), where the area of extreme strain localization moves from the preferred orientated narrow region to the region on the X coordinate. Again, because of friction, this occurs a small distance away from the center.

Figure 5(*e*) shows the thermal softening effect on the cube model's strain localization very clearly, where a more pronounced favorable orientated localization region and excessive thinning are observed.

The relationship between the maximum thickness strain $|\epsilon_{t\max}|$ and the punch height $\hat{Z}$ is shown in Fig. 6. To predict the forming limit of the sheet, two criteria are introduced: (1) the limit thickness strain $|\epsilon_{t\max}|_c = 0.28$ and (2) the limit slope $(d|\epsilon_{t\max}|/d\hat{Z}) \approx 0.02$ (1/mm). The limit punch height in the case of criterion (1) gives 35 mm, 30 mm, and 28 mm, respectively, for the cube, 6111-T4, and random models. Whereas criterion (2) gives 31 mm, 30 mm, and 24 mm, respectively. In the case of J_2F, no failure was observed. When the thermal softening effect is introduced to the cube model, lower limit punch heights are obtained, viz: 22 mm for criterion (1), and 19 mm for criterion (2). These results demonstrate that the inhomogeneous and initial imperfection material model, such as the random case and the 6111-T4 case, generate earlier strain localization.

The crystalline orientation distribution, represented by {111} pole figures, at the initial, 30 mm and 28 mm punch heights are shown in Figs. 7(*a*), (*b*), and (*c*), respectively. Figures 7(*a*-1) and (*a*-2) predict clearly the large rotation from the cube orientation at the extreme localization regions. When thermal softening is introduced, a greater rotation is observed as shown in Fig. 7(*a*-3). The 6111-T4 and random cases also exhibit this rotation induces scattering effect, though it is not as pronounced as the cube model, as shown in Figs. 7(*b*) and (*c*). For the 6111-T4 case, the crystals, which have {111} directions and directions close to RD, show larger rotations than other directions. The random model shows the least amount of rotation of the four models for the same prescribed deformation conditions. The deformation compatibility of the finite element boundaries imposes rotation constraints, which prevents an increase in the slip system activity and as a consequence it limits the localization area. This produces the combined phenomena of small rotations with larger shear strains on fewer slip systems. On the other hand, the cube case offers the least number of rotation constraints, which allows the crystal rotation to induce a strain localization expansion along the preferred orientation.

5 Conclusions

An elastic/crystalline viscoplastic finite element code has been applied to analyze the LDH test problem. In modeling, the crystalline material, an inverse iterative method has been introduced to determine the Euler angles of crystal from a {111} pole figure of 6111-T4 aluminum alloy, obtained from X-ray diffraction analysis. A new approximation algorithm was also proposed to assign the crystalline orientation to each finite element. We adopt five material models, viz: cube texture (single crystal), aluminum alloy 6111-T4, random orientation polycrystal, cube texture with thermal softening, and J_2F (classical plastic potential theory). Numerical results show evidence of

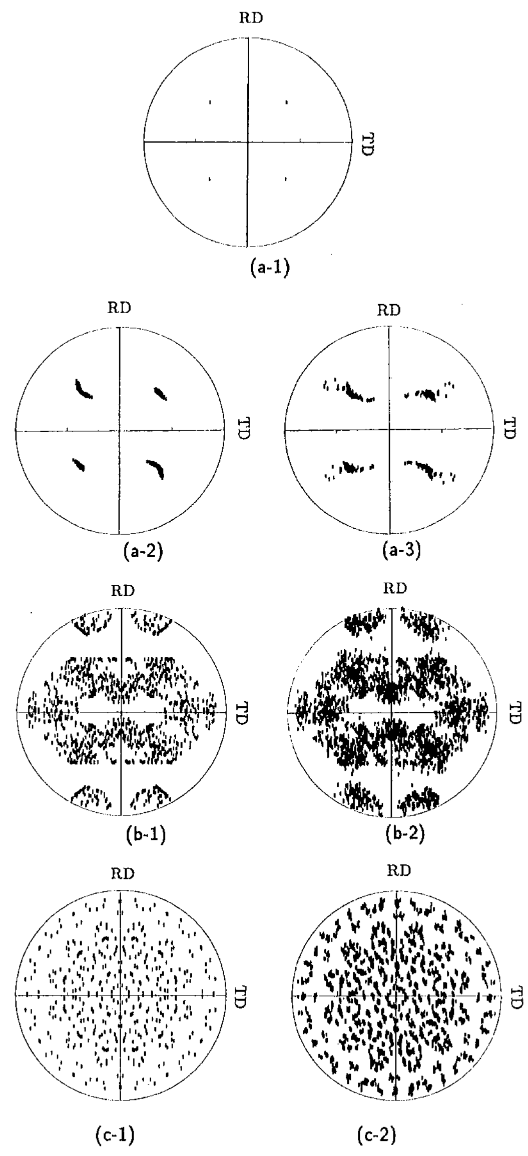

Fig. 7 {111} pole figures obtained by simulation. (*a*-1) Initial pole figure of the cube model. (*a*-2) The pole figure of the cube single crystal model when punch height = 30 mm. (*a*-3) The pole figure of cube single crystal with thermal softening effect model when punch height = 28 mm. (*b*-1) Initial pole figure of the 6111-T4 model. (*b*-2) The pole figure of the 6111-T4 model when punch height = 30 mm. (*c*-1) Initial pole figure of the random model. (*c*-2) The pole figure of the random model when punch height = 30 mm.

texture effects on the strain localization. A strong cube texture, i.e., single crystal, is found to postpone strain localization and leads to higher formability, while a random orientation distribution of polycrystal triggers localization earlier and leads to a lower formability. The random nature of this latter model introduces an initial material imperfection. The results for the aluminum alloy 6111-T4 show a formability between the above two extreme texture cases. The crystalline rotation induced by the deformation is not affected very much from the texture, whereas the formability is. Thermal softening is shown to reduce formability. No failure is observed in the J_2F model because of the homogeneous material characteristics and consistently smooth yield surface.

Acknowledgments

X. Dong would like to take the opportunity to thank the Sheet Forming Simulation Research Group (Japan) for financial support, and Dr. S. P. Wang for fruitful discussion on draw bead modeling. In addition, the authors would like to thank Mr. B. Hildebrand for proof reading.

References

Bassani, J. L., and Wu, T. Y., 1991, "Latent hardening in single crystals, II. Analytical characterization and predictions," *Proc. R. Soc. Lond.*, Vol. A435, pp. 21–41.

Beaudoin, A. J., Dawson, P. R., Mathur, K. K., Kocks, U. F., and Korzekwa, D. A., 1994, "Application of polycrystal plasticity to sheet forming," *Comput. Methods Appl. Mech. Engrg.*, Vol. 117, pp. 49–70.

Lee, J. K., Kinzel, G. L., and Wagoner, R. H., 1996, *NUMISHEET'96*, Proceedings of The 3rd Int. Conf. Numerical Simulation of 3D Sheet Metal Forming Processes, The Ohio State University.

Nakamachi, E., and Dong, X., 1996, "Elastic/crystalline-viscoplastic finite element analysis of dynamic deformation of sheet metal," *Int. J. Computer-Aided Engrg. Software*, Vol. 13, pp. 308–326.

Peirce, D., Asaro, R. J., and Needleman, A., 1983, "Material rate dependent and localized deformation in crystalline solids," *Acta Metall. Mater.* Vol. 31, pp. 1951–1976.

Takahashi, H., Mashiko, M., Motohashi, H., and Tsuchida, S., 1994, "Prediction of plastic anisotropy in aluminum sheet by finite-element polycrystal model (2nd Report)," *Trans. Japan Soc. Mech. Engineers, A*, Vol. 60, pp. 1210–1215.

Wang, S. P., and Makinouchi, A., 1994, "On the implementation of a new draw bead model to the elasto-plastic sheet metal forming simulation FE code," *Proc. 45th Japanese Joint Conf. Tech. Plasticity*, pp. 295–298.

Zhou, Y., Neale, K. W., and Toth, L. S., 1993, "A modified model for simulating latent hardening during the plastic deformation of rate-dependent FCC polycrystals," *International Journal of Plasticity*, Vol. 9, pp. 961–978.

Zhou, Y., and Neale, K. W., 1995, "Predictions of forming limit diagrams using a rate-sensitive crystal plasticity model," *International Journal of Mechanics Science*, Vol. 37, pp. 1–20.

Stress Singularity of Edge Delamination in Angle-Ply and Cross-Ply Laminates

Wen-Hwa Chen
Professor and Dean,
Mem. ASME.

Tain-Fu Huang[1]
Graduate Student.

Department of Power Mechanical Engineering,
College of Engineering,
National Tsing Hua University,
Hsinchu, Taiwan 30043,
Republic of China

By utilizing the general solutions derived for the plies with arbitrary fiber orientations under uniform axial strain (Huang and Chen, 1994), the explicit solutions of the edge-delamination stress singularities for the angle-ply and cross-ply laminates are obtained. The dominant edge-delamination stress singularities for the angle-ply laminates are found to be a real constant, $-\frac{1}{2}$, and a pair of complex conjugates, $-\frac{1}{2} \pm i/2\pi \ln \{(b + \sqrt{b^2 - a^2})/a\}$. For the cross-ply laminates, the significant effect of transverse shear stresses of the laminate is considered and the dominant edge-delamination stress singularities are shown as $-\frac{1}{2}$ and $-\frac{1}{2} \pm i/2\pi \ln \{(c_2 + \sqrt{c_2^2 - 4c_1c_3})/2c_1\}$. a, b, c_1, c_2, and c_3 are the corresponding combined complex constants. In addition, two elementary forms of edge-delamination stress singularity, say, $r^{-1/2}$ and $r^{\delta_r}(\ln r)^n(\delta_r = n - \frac{3}{2}, n = 1, 2 \ldots)$ exist for both the angle-ply and cross-ply laminates. Excellent correlations between the present results and available solutions show the validity of the approach. The deficiencies of the solutions available in the literature are compensated. New results for other angle-ply and cross-ply laminates are also provided.

1 Introduction

A composite laminate often involves geometric/material discontinuities or structural defects which may reduce load carrying capability of the structure and will be a source of laminate failure. The edge-delamination problem has become of great concern in laminate failure analysis recently. Basically, edge delamination is a fracture problem involving an interfacial crack between two anisotropic materials. The stress field of such a problem is very complex and is attributed to the singular nature which generally occurs at the crack tip. Hence, a rigorous investigation on the edge-delamination stress singularity is imperative.

The problem of an interfacial crack between two dissimilar isotropic materials has received much attention. For an interfacial crack between two anisotropic materials, however, only limited research has been done. Assuming an r^δ stress field, Wang and Yuan (1983) employed Lekhnitskii's approach (Lekhnitskii, 1963) together with a hybrid finite element model to deal with the edge-delamination problem of angle-ply laminates. r is the radial distance from the crack tip and δ is a complex constant. Due to the drawbacks of the numerical techniques, an analytical approach for the edge-delamination stress singularity in angle-ply and cross-ply laminates was made by Wang (1984). However, the explicit expression for the edge-delamination stress singularity δ was not presented for angle-ply laminates. Moreover, only the stretching and bending of the laminate were analyzed in cross-ply laminates and thus four stress components σ_{xx}, σ_{yy}, σ_{zz}, and τ_{xy} were considered. For completeness, the significant role of the transverse shear stresses τ_{xz} and τ_{yz} in the cross-ply laminates is worthy of further investigation. Ting (1986) employed Stroh's formalism (Stroh, 1962) to study the special geometry of composite wedges with singularity. Although the research also can be used to study the edge-delamination stress singularity, the explicit solution for anisotropic materials was too complicated to solve and only the case for isotropic materials was illustrated. To compensate for these deficiencies in the previous research studies (Wang and Yuan, 1983; Wang, 1984; Ting, 1986), a complete and explicit analysis on the edge-delamination stress singularity for angle-ply and cross-ply laminates under uniform axial strain is carried out in this work.

Recently, some general solutions for the plies with 0 deg, 90 deg and arbitrary fiber orientations under uniform axial strain have been successfully derived and employed to study the free-edge stress singularities of general composite laminates (Huang and Chen, 1994). In this work, to determine the edge-delamination stress singularities, those general solutions are adopted and first expressed into appropriate polar forms. Based on those, the transcendental characteristic equations $|\mathbf{K}(\delta)| = 0$ satisfying the traction-free conditions on crack surfaces and the continuity conditions along the ply interface are then established. For angle-ply laminates, $\mathbf{K}(\delta)$ is a 12×12 matrix of the complex constant δ. For the cross-ply laminates, assuming the transverse shear stresses τ_{xz} and τ_{yz} to be proportional to a r^γ form, $\mathbf{K}(\delta)$ can be further categorized as $\mathbf{K_d}(\delta)$ and $\mathbf{K}(\gamma)$, where $\mathbf{K_d}(\delta)$ and $\mathbf{K}(\gamma)$ are 8×8 and 4×4 matrices for the complex constants δ and γ, respectively. After tricky and tedious manipulations, the transcendental characteristic equations can be expanded with the aid of a symbolic operation technique (Pavelle and Wang, 1985). After solving the transcendental characteristic equations, the detailed characters and simple explicit forms of the edge-delamination stress singularities for any angle-ply and cross-ply laminates under uniform axial strain are derived analytically and the lack of explicit expression for edge-delamination stress singularities in the literature (Wang, 1984; Ting, 1986) is compensated. As a result, once the material properties of specific composite laminates are provided, the researcher can compute the edge-delamination stress singularities directly in a simple way.

[1] Presently Associate Research Scientist of Industrial Technology Research Institute/Materials Research Laboratories.

Contributed by the Applied Mechanics Division of The American Society of Mechanical Engineers for publication in the ASME Journal of Applied Mechanics.

Discussion on the paper should be addressed to the Technical Editor, Professor Lewis T. Wheeler, Department of Mechanical Engineering, University of Houston, Houston, TX 77204-4792, and will be accepted until four months after final publication of the paper itself in the ASME Journal of Applied Mechanics.

Manuscript received by the ASME Applied Mechanics Division, July 13, 1993; final revision, Dec. 9, 1996. Associate Technical Editor: M. Taya.

To demonstrate the singular nature of the edge-delamination stress field, the graphite-epoxy laminates under uniform axial strain are selected as test examples. Comparisons of the present calculated results with limited available solutions of angle-ply laminates show the validity of the approach. The cases for other commonly used angle-ply and cross-ply laminates are also studied.

2 General Solutions of Composite Laminates

Consider a long composite laminate subjected to the uniform axial strain $\epsilon_{zz} = e$, as depicted in Fig. 1, and the edge delamination occurs along the interface of dissimilar plies with fiber orientations θ_1 and θ_2. Perfect bonding is assumed in the composite laminate everywhere except in the region of delamination. Since the composite laminate is sufficiently long, the end effect can be negligible due to the Saint Venant's principle. Under these conditions, the displacements (except the displacement in the z direction, w), strains and stresses in the composite laminate can be thus viewed as independent of the z-coordinate. For further study, the general solutions of various types of ply (Huang and Chen, 1994) are quoted and discussed briefly below.

2.1 Arbitrary Fiber Orientations Other than 0 Deg and 90 Deg. By assuming the stress field near the crack tip as a r^{δ} form and separating the order of singularity δ into real and imaginary parts, say, δ_r and δ_i, the general solutions of stresses and displacements for an arbitrary orientation ply other than 0 deg and 90 deg can be derived by Lekhnitskii's approach as (Huang and Chen, 1994)

$$\sigma_{xx} = \sum_{k=1}^{3} \{ C_k\mu_k^2 Z_{k\mu}^{\delta_r}[\cos(\delta_i \ln Z_{k\mu}) + i\sin(\delta_i \ln Z_{k\mu})] + \bar{C}_k\bar{\mu}_k^2 \bar{Z}_{k\mu}^{\delta_r}[\cos(\delta_i \ln \bar{Z}_{k\mu}) - i\sin(\delta_i \ln \bar{Z}_{k\mu})]\}$$

$$\sigma_{yy} = \sum_{k=1}^{3} \{ C_k Z_{k\mu}^{\delta_r}[\cos(\delta_i \ln Z_{k\mu}) + i\sin(\delta_i \ln Z_{k\mu})] + \bar{C}_k \bar{Z}_{k\mu}^{\delta_r}[\cos(\delta_i \ln \bar{Z}_{k\mu}) - i\sin(\delta_i \ln \bar{Z}_{k\mu})]\}$$

$$\tau_{yz} = -\sum_{k=1}^{3} \{ C_k\eta_k Z_{k\mu}^{\delta_r}[\cos(\delta_i \ln Z_{k\mu}) + i\sin(\delta_i \ln Z_{k\mu})] + \bar{C}_k\bar{\eta}_k \bar{Z}_{k\mu}^{\delta_r}[\cos(\delta_i \ln \bar{Z}_{k\mu}) - i\sin(\delta_i \ln \bar{Z}_{k\mu})]\}$$

$$\tau_{xz} = \sum_{k=1}^{3} \{ C_k\eta_k\mu_k Z_{k\mu}^{\delta_r}[\cos(\delta_i \ln Z_{k\mu}) + i\sin(\delta_i \ln Z_{k\mu})] + \bar{C}_k\bar{\eta}_k\bar{\mu}_k \bar{Z}_{k\mu}^{\delta_r}[\cos(\delta_i \ln \bar{Z}_{k\mu}) - i\sin(\delta_i \ln \bar{Z}_{k\mu})]\}$$

$$\tau_{xy} = -\sum_{k=1}^{3} \{ C_k\mu_k Z_{k\mu}^{\delta_r}[\cos(\delta_i \ln Z_{k\mu}) + i\sin(\delta_i \ln Z_{k\mu})] + \bar{C}_k\bar{\mu}_k \bar{Z}_{k\mu}^{\delta_r}[\cos(\delta_i \ln \bar{Z}_{k\mu}) - i\sin(\delta_i \ln \bar{Z}_{k\mu})]\}$$

$$\sigma_{zz} = (e - S_{13}\sigma_{xx} - S_{23}\sigma_{yy} - S_{35}\tau_{xz})\frac{1}{S_{33}} \quad (1)$$

and

$$u = \sum_{k=1}^{3} \left\{ \frac{C_k p_{k\mu} Z_{k\mu}^{\delta_r+1}}{[(\delta_r+1)+i\delta_i]}[\cos(\delta_i \ln Z_{k\mu}) + i\sin(\delta_i \ln Z_{k\mu})] + \frac{\bar{C}_k \bar{p}_{k\mu} \bar{Z}_{k\mu}^{\delta_r+1}}{[(\delta_r+1)-i\delta_i]}[\cos(\delta_i \ln \bar{Z}_{k\mu}) - i\sin(\delta_i \ln \bar{Z}_{k\mu})] \right\} + \frac{S_{13}}{S_{33}} ex - \omega_3 y + u_0$$

$$v = \sum_{k=1}^{3} \left\{ \frac{C_k q_{k\mu} Z_{k\mu}^{\delta_r+1}}{[(\delta_r+1)+i\delta_i]}[\cos(\delta_i \ln Z_{k\mu}) + i\sin(\delta_i \ln Z_{k\mu})] + \frac{\bar{C}_k \bar{q}_{k\mu} \bar{Z}_{k\mu}^{\delta_r+1}}{[(\delta_r+1)-i\delta_i]}[\cos(\delta_i \ln \bar{Z}_{k\mu}) - i\sin(\delta_i \ln \bar{Z}_{k\mu})] \right\} + \omega_3 x + \frac{S_{23}}{S_{33}} ey + v_0$$

$$w = \sum_{k=1}^{3} \left\{ \frac{C_k t_{k\mu} Z_{k\mu}^{\delta_r+1}}{[(\delta_r+1)+i\delta_i]}[\cos(\delta_i \ln Z_{k\mu}) + i\sin(\delta_i \ln Z_{k\mu})] + \frac{\bar{C}_k \bar{t}_{k\mu} \bar{Z}_{k\mu}^{\delta_r+1}}{[(\delta_r+1)-i\delta_i]} \times [\cos(\delta_i \ln \bar{Z}_{k\mu}) - i\sin(\delta_i \ln \bar{Z}_{k\mu})] \right\} + \left(\frac{S_{35}}{S_{33}} e - \omega_2\right)x + \omega_1 y + ez + w_0. \quad (2)$$

All the notations of each variable are referred to Huang and Chen (1994). It is noted that the stresses and displacements as expressed in Eqs. (1) and (2) are real and the unknown coefficients C_k, $\bar{C}_k$, δ_r, and δ_i for a specific composite laminate with arbitrary orientation plies other than 0 deg and 90 deg can be determined by given boundary conditions.

To understand the singularity nature of the stresses and displacements further, the trigonometric functions as seen in Eqs. (1) and (2) can be expanded into infinite series

$$\cos(\delta_i \ln Z_{k\mu}) = 1 - \frac{\delta_i^2}{2!}(\ln Z_{k\mu})^2 + \frac{\delta_i^4}{4!}(\ln Z_{k\mu})^4 - \frac{\delta_i^6}{6!}(\ln Z_{k\mu})^6 + \frac{\delta_i^8}{8!}(\ln Z_{k\mu})^8 \ldots$$

and

$$\sin(\delta_i \ln Z_{k\mu}) = \delta_i \ln Z_{k\mu} - \frac{\delta_i^3}{3!}(\ln Z_{k\mu})^3 + \frac{\delta_i^5}{5!}(\ln Z_{k\mu})^5 - \frac{\delta_i^7}{7!}(\ln Z_{k\mu})^7 \ldots$$

Although the functions $\cos(\delta_i \ln Z_{k\mu})$ and $\sin(\delta_i \ln Z_{k\mu})$ are divergent, their sum $[\cos(\delta_i \ln Z_{k\mu}) + i\sin(\delta_i \ln Z_{k\mu})]$ remains bounded. Similarly, the complex conjugate of the associated quantity $[\cos(\delta_i \ln \bar{Z}_{k\mu}) - i\sin(\delta_i \ln \bar{Z}_{k\mu})]$ is also bounded. Thus, as discussed in Huang and Chen (1994), the stress singu-

$E_{11} = E_{22} = 14.5$ (GPa),

$E_{33} = 138$ (GPa),

$G_{12} = G_{23} = G_{31} = 5.9$ (GPa),

$\nu_{21} = \nu_{31} = \nu_{32} = 0.21$.

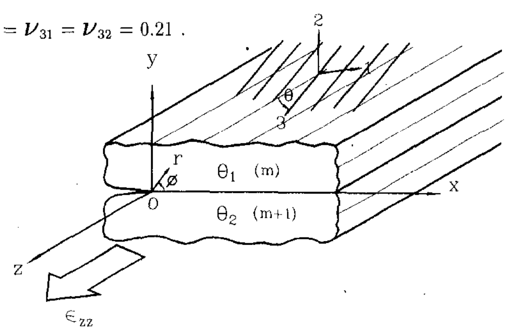

Fig. 1 Edge delamination of a composite laminate

larity of the arbitrary orientation ply other than 0 deg and 90 deg in the composite laminate may include three elementary forms: r^{δ_r}; $(\ln r)^n$; and $r^{\delta_r}(\ln r)^n$ ($n = 1, 2 \ldots$), depending on the magnitudes of δ_r and δ_i. The occurrence of those three elementary stress singularities, as seen from Eq. (1), can be listed as follows: (*i*) the r^{δ_r} singularity appears as $\delta_i = 0$ and $-1 < \delta_r < 0$, (*ii*) the $(\ln r)^n$ singularity happens as $\delta_i \neq 0$ and $\delta_r = 0$, and (*iii*) the $r^{\delta_r}(\ln r)^n$ singularity ($n = 1, 2, \ldots$) exists as $\delta_i \neq 0$ and $\delta_r > -1$.

2.2 The 0 Deg and 90 Deg Fiber Orientations. Similarly, the general solutions of 0 deg and 90 deg fiber orientation plies are presented as (Huang and Chen, 1994)

$$\sigma_{xx} = \sum_{k=1}^{2} \{ C_k\zeta_k^2 Z_{k\zeta}^{\delta_r}[\cos(\delta_i \ln Z_{k\zeta}) + i \sin(\delta_i \ln Z_{k\zeta})] + \bar{C}_k\bar{\zeta}_k^2 \bar{Z}_{k\zeta}^{\delta_r}[\cos(\delta_i \ln \bar{Z}_{k\zeta}) - i \sin(\delta_i \ln \bar{Z}_{k\zeta})]\}$$

$$\sigma_{yy} = \sum_{k=1}^{2} \{ C_k Z_{k\zeta}^{\delta_r}[\cos(\delta_i \ln Z_{k\zeta}) + i \sin(\delta_i \ln Z_{k\zeta})] + \bar{C}_k \bar{Z}_{k\zeta}^{\delta_r}[\cos(\delta_i \ln \bar{Z}_{k\zeta}) - i \sin(\delta_i \ln \bar{Z}_{k\zeta})]\}$$

$$\tau_{yz} = -\{ C_3 Z_{1\xi}^{\gamma_r}[\cos(\gamma_i \ln Z_{1\xi}) + i \sin(\gamma_i \ln Z_{1\xi})] + \bar{C}_3 \bar{Z}_{1\xi}^{\gamma_r}[\cos(\gamma_i \ln \bar{Z}_{1\xi}) - i \sin(\gamma_i \ln \bar{Z}_{1\xi})]\}$$

$$\tau_{xz} = \{ C_3\xi_1 Z_{1\xi}^{\gamma_r}[\cos(\gamma_i \ln Z_{1\xi}) + i \sin(\gamma_i \ln Z_{1\xi})] + \bar{C}_3\bar{\xi}_1 \bar{Z}_{1\xi}^{\gamma_r}[\cos(\gamma_i \ln \bar{Z}_{1\xi}) - i \sin(\gamma_i \ln \bar{Z}_{1\xi})]\}$$

$$\tau_{xy} = \sum_{k=1}^{2} \{ C_k\zeta_k Z_{k\zeta}^{\delta_r}[\cos(\delta_i \ln Z_{k\zeta}) + i \sin(\delta_i \ln Z_{k\zeta})] + \bar{C}_k\bar{\zeta}_k \bar{Z}_{k\zeta}^{\delta_r}[\cos(\delta_i \ln \bar{Z}_{k\zeta}) - i \sin(\delta_i \ln \bar{Z}_{k\zeta})]\}$$

$$\sigma_{zz} = (e - S_{13}\sigma_{xx} - S_{23}\sigma_{yy}) \frac{1}{S_{33}} \tag{3}$$

and

$$u = \sum_{k=1}^{2} \left\{ \frac{C_k p_{k\zeta} Z_{k\zeta}^{\delta_r+1}}{[(\delta_r + 1) + i\delta_i]} [\cos(\delta_i \ln Z_{k\zeta}) + i \sin(\delta_i \ln Z_{k\zeta})] + \frac{\bar{C}_k \bar{p}_{k\zeta} \bar{Z}_{k\zeta}^{\delta_r+1}}{[(\delta_r + 1) - i\delta_i]} [\cos(\delta_i \ln \bar{Z}_{k\zeta}) - i \sin(\delta_i \ln \bar{Z}_{k\zeta})] \right\} + \frac{S_{13}}{S_{33}} ex - \omega_3 y + u_0$$

$$v = \sum_{k=1}^{2} \left\{ \frac{C_k q_{k\zeta} Z_{k\zeta}^{\delta_r+1}}{[(\delta_r + 1) + i\delta_i]} [\cos(\delta_i \ln Z_{k\zeta}) + i \sin(\delta_i \ln Z_{k\zeta})] + \frac{\bar{C}_k \bar{q}_{k\zeta} \bar{Z}_{k\zeta}^{\delta_r+1}}{[(\delta_r + 1) - i\delta_i]} [\cos(\delta_i \ln \bar{Z}_{k\zeta}) - i \sin(\delta_i \ln \bar{Z}_{k\zeta})] \right\} + \omega_3 x + \frac{S_{23}}{S_{33}} ey + v_0$$

$$w = \left\{ \frac{C_3 t_{1\xi} Z_{1\xi}^{\gamma_r+1}}{[(\gamma_r + 1) + i\gamma_i]} [\cos(\gamma_i \ln Z_{1\xi}) + i \sin(\gamma_i \ln Z_{1\xi})] + \frac{\bar{C}_3 \bar{t}_{1\xi} \bar{Z}_{1\xi}^{\gamma_r+1}}{[(\gamma_r + 1) - i\gamma_i]} \times [\cos(\gamma_i \ln \bar{Z}_{1\xi}) - i \sin(\gamma_i \ln \bar{Z}_{1\xi})] \right\} - \omega_2 x + \omega_1 y + ez + w_0. \tag{4}$$

The stress singularity of the 0 deg or 90 deg ply in the composite laminate also may contain three elementary forms: $(r^{\delta_r}, r^{\gamma_r})$; $(\ln r)^n$; and $(r^{\delta_r}(\ln r)^n, r^{\gamma_r}(\ln r)^n)$ ($n = 1, 2 \ldots$), depending on the magnitudes of (δ_r, γ_r) and (δ_i, γ_i). As seen from Eq. (3), the occurrence of those three elementary stress singularities may be stated as the similar conditions of the previous case.

3 Edge-Delamination Stress Singularity

Assume the edge delamination between two plies, say, the (m)th and $(m + 1)$th plies, as shown in Fig. 1. The polar stresses $(\sigma_{rr}, \sigma_{\phi\phi}, \sigma_{zz}, \tau_{r\phi}, \tau_{\phi z}, \tau_{rz})$ and displacements (u_r, u_ϕ, u_z) can be expressed in terms of $(\sigma_{xx}, \sigma_{yy}, \sigma_{zz}, \tau_{xy}, \tau_{yz}, \tau_{xz})$ and (u, v, w), as indicated earlier, by the relations

$$\sigma_{rr} = \sigma_{xx} \cos^2 \phi + \sigma_{yy} \sin^2 \phi + 2\tau_{xy} \sin \phi \cos \phi$$

$$\sigma_{\phi\phi} = \sigma_{xx} \sin^2 \phi + \sigma_{yy} \cos^2 \phi - 2\tau_{xy} \sin \phi \cos \phi$$

$$\tau_{r\phi} = (\sigma_{yy} - \sigma_{xx}) \sin \phi \cos \phi + \tau_{xy}(\cos^2 \phi - \sin^2 \phi))$$

$$\tau_{\phi z} = \tau_{yz} \cos \phi - \tau_{xz} \sin \phi$$

$$\tau_{rz} = \tau_{yz} \sin \phi + \tau_{xz} \cos \phi$$

$$\sigma_{zz} = \sigma_{zz}$$

and

$$u_r = u \cos \phi + v \sin \phi$$

$$u_\phi = -u \sin \phi + v \cos \phi$$

$$u_z = w.$$

To evaluate the edge-delamination stress singularity, the complex constants $\delta = \delta_r + i\delta_i$ and $\gamma = \gamma_r + i\gamma_i$ which appeared in the general solutions of Eqs. (1) ~ (4) need to be determined by satisfying the near-field boundary conditions of the corresponding composite laminate. This leads to solving an eigenvalue problem. The near-field boundary conditions include the traction-free conditions at the crack surfaces and the continuity conditions along the ply interface. The traction-free conditions at the crack surfaces of the (m)th and $(m + 1)$th plies in the polar coordinates are (see Fig. 1)

$$\sigma_{\phi\phi}^{(m+1)} = \tau_{\phi z}^{(m+1)} = \tau_{r\phi}^{(m+1)} = 0 \quad \text{on} \quad \phi = -\pi$$

and

$$\sigma_{\phi\phi}^{(m)} = \tau_{\phi z}^{(m)} = \tau_{r\phi}^{(m)} = 0 \quad \text{on} \quad \phi = \pi, \tag{5}$$

where the superscripts (m) and $(m + 1)$ denote the (m)th and $(m + 1)$th plies of the composite laminate, respectively. The continuity conditions along the ply interface give

$$\{\sigma_{\phi\phi}^{(m+1)}, \tau_{\phi z}^{(m+1)}, \tau_{r\phi}^{(m+1)}, u_r^{(m+1)}, u_\phi^{(m+1)}, u_z^{(m+1)}\} = \{\sigma_{\phi\phi}^{(m)}, \tau_{\phi z}^{(m)}, \tau_{r\phi}^{(m)}, u_r^{(m)}, u_\phi^{(m)}, u_z^{(m)}\} \quad \text{on} \quad \phi = 0. \tag{6}$$

Since the angle-ply and cross-ply laminates are often adopted in the practical structural component, the edge-delamination stress singularity of the two laminates is examined in the following analysis, respectively.

3.1 Angle-Ply Laminates. After expressing the general solutions of Eqs. (1) and (2) in polar forms, the system of algebraic equation satisfying the traction-free conditions (Eq. (5)) and the continuity conditions (Eq. (6)) for angle-ply laminates is derived as

$$\mathbf{K}(\delta)\mathbf{C} = 0,$$

where $\mathbf{K}(\delta)$ is a 12×12 matrix of the complex constant δ and $\mathbf{C}$ is a 12×1 column vector made of the complex constants $C_k^{(m)}$ and $C_k^{(m+1)}$ ($k = 1 \sim 6$). To have nontrivial $\mathbf{C}$, the determinant of $\mathbf{K}(\delta)$, say $|\mathbf{K}(\delta)|$, vanishes. This is

$$
|\mathbf{K}(\delta)| = e^{-6i\pi\delta}
\begin{vmatrix}
1 & 1 & 1 & 1 & 1 & 1 & 1 & 1 & 1 & 1 & 1 & 1 \\
\mu_1 & \bar{\mu}_1 & \mu_2 & \bar{\mu}_2 & \mu_3 & \bar{\mu}_3 & \mu_1 & \bar{\mu}_1 & \mu_2 & \bar{\mu}_2 & \mu_3 & \bar{\mu}_3 \\
\eta_1 & \bar{\eta}_1 & \eta_2 & \bar{\eta}_2 & \eta_3 & \bar{\eta}_3 & -\eta_1 & -\bar{\eta}_1 & -\eta_2 & -\bar{\eta}_2 & -\eta_3 & -\bar{\eta}_3 \\
p_{1\mu} & \bar{p}_{1\mu} & p_{2\mu} & \bar{p}_{2\mu} & p_{3\mu} & \bar{p}_{3\mu} & p_{1\mu} & \bar{p}_{1\mu} & p_{2\mu} & \bar{p}_{2\mu} & p_{3\mu} & \bar{p}_{3\mu} \\
q_{1\mu} & \bar{q}_{1\mu} & q_{2\mu} & \bar{q}_{2\mu} & q_{3\mu} & \bar{q}_{3\mu} & q_{1\mu} & \bar{q}_{1\mu} & q_{2\mu} & \bar{q}_{2\mu} & q_{3\mu} & \bar{q}_{3\mu} \\
t_{1\mu} & \bar{t}_{1\mu} & t_{2\mu} & \bar{t}_{2\mu} & t_{3\mu} & \bar{t}_{3\mu} & -t_{1\mu} & -\bar{t}_{1\mu} & -t_{2\mu} & -\bar{t}_{2\mu} & -t_{3\mu} & -\bar{t}_{3\mu} \\
A & 1 & A & 1 & A & 1 & 0 & 0 & 0 & 0 & 0 & 0 \\
0 & 0 & 0 & 0 & 0 & 0 & 1 & A & 1 & A & 1 & A \\
\mu_1 A & \bar{\mu}_1 & \mu_2 A & \bar{\mu}_2 & \mu_3 A & \bar{\mu}_3 & 0 & 0 & 0 & 0 & 0 & 0 \\
0 & 0 & 0 & 0 & 0 & 0 & \mu_1 & \bar{\mu}_1 A & \mu_2 & \bar{\mu}_2 A & \mu_3 & \bar{\mu}_3 A \\
\eta_1 A & \bar{\eta}_1 & \eta_2 A & \bar{\eta}_2 & \eta_3 A & \bar{\eta}_3 & 0 & 0 & 0 & 0 & 0 & 0 \\
0 & 0 & 0 & 0 & 0 & 0 & \eta_1 & \bar{\eta}_1 A & \eta_2 & \bar{\eta}_2 A & \eta_3 & \bar{\eta}_3 A
\end{vmatrix} = 0,
$$

where $A = e^{2i\pi\delta}$. The material constants μ_k, η_k, $p_{k\mu}$, $q_{k\mu}$ and $t_{k\mu}$ in the adjacent plies of the angle-ply laminates are known as $\mu_k^{(m)} = \mu_k^{(m+1)} = \mu_k$, $\eta_k^{(m)} = -\eta_k^{(m+1)} = \eta_k$, $p_{k\mu}^{(m)} = p_{k\mu}^{(m+1)} = p_{k\mu}$, $q_{k\mu}^{(m)} = q_{k\mu}^{(m+1)} = q_{k\mu}$ and $t_{k\mu}^{(m)} = -t_{k\mu}^{(m+1)} = t_{k\mu}$. To avoid numerical errors in computing δ, after tricky and tedious manipulations, the transcendental characteristic equation $|\mathbf{K}(\delta)| = 0$ for the angle-ply laminates is expanded by the aid of the symbolic operation technique (Pavelle and Wang, 1985) analytically instead of using the numerical Muller method (Wang and Yuan, 1983), say,

$$|\mathbf{K}(\delta)| = A^{-3}(1-A)^3(A+1)[aA^2+2bA+a] = 0, \quad (7)$$

where the complex coefficients a and b are related to material constants of adjacent plies and given in Appendix A. When Eq. (7) is solved, the eigenvalues δ_n are found as

$$\delta_n = n, \left(n - \frac{1}{2}\right) \text{ and } \left(n - \frac{1}{2}\right) \pm \frac{i}{2\pi} \ln\left\{\frac{b + \sqrt{b^2 - a^2}}{a}\right\}$$

$$(n = 0, 1, 2, \ldots\ldots). \quad (8)$$

As seen from Eqs. (1) and (8), the explicit solutions of the edge-delamination stress singularity for the angle-ply laminates are concluded as $\delta_n = -\frac{1}{2}$ and $(n - \frac{1}{2}) \pm i/2\pi \ln\{(b + \sqrt{b^2 - a^2})/a\}$ $(n = 0, 1, 2, \ldots\ldots)$. Hence, the edge-delamination stress singularity of the angle-ply laminates only contains the $r^{-1/2}$ and $r^{\delta_r}(\ln r)^n$ $(n = 1, 2 \ldots)$ forms. This finding can clarify the abstruse solution derived by Ting (1986) and the lack of explicit expression for δ (Wang, 1984; Ting, 1986) is thus compensated.

3.2 Cross-Ply Laminates. Since the edge-delamination stress singularity of the cross-ply laminates cannot be induced from angle-ply laminates, the transcendental characteristic equation for cross-ply laminates needs to be rederived. Again, after substituting the polar form of the general solutions of Eqs. (3) and (4) into the traction-free conditions (Eq. (5)) and the continuity conditions (Eq. (6)), the system of algebraic equations for the cross-ply laminates can be categorized as

$$\mathbf{K}_d(\delta)\mathbf{C} = 0$$

and

$$\mathbf{K}(\gamma)\mathbf{D} = 0,$$

where $\mathbf{K}_d(\delta)$ and $\mathbf{K}(\gamma)$ are 8×8 and 4×4 matrices for the complex constants δ and γ, respectively. $\mathbf{C}$ and $\mathbf{D}$ are 8×1 and 4×1 column vectors made of the complex constants $(C_k^{(m)}, C_k^{(m+1)})$ $(k = 1 \sim 4)$ and $(k = 5 \sim 6)$. The nontrivial conditions of $\mathbf{C}$ and $\mathbf{D}$ are $|\mathbf{K}_d(\delta)| = 0$ and $|\mathbf{K}(\gamma)| = 0$. The transcendental characteristic equations can thus be easily derived as follows:

$$
|\mathbf{K}_d(\delta)| = e^{-4i\pi\delta}
\begin{vmatrix}
1 & 1 & 1 & 1 & 1 & 1 & 1 & 1 \\
\zeta_1^{(m)} & \bar{\zeta}_1^{(m)} & \zeta_2^{(m)} & \bar{\zeta}_2^{(m)} & \zeta_1^{(m+1)} & \bar{\zeta}_1^{(m+1)} & \zeta_2^{(m+1)} & \bar{\zeta}_2^{(m+1)} \\
p_{1\zeta}^{(m)} & \bar{p}_{1\zeta}^{(m)} & p_{2\zeta}^{(m)} & \bar{p}_{2\zeta}^{(m)} & p_{1\zeta}^{(m+1)} & \bar{p}_{1\zeta}^{(m+1)} & p_{2\zeta}^{(m+1)} & \bar{p}_{2\zeta}^{(m+1)} \\
q_{1\zeta}^{(m)} & \bar{q}_{1\zeta}^{(m)} & q_{2\zeta}^{(m)} & \bar{q}_{2\zeta}^{(m)} & q_{1\zeta}^{(m+1)} & \bar{q}_{1\zeta}^{(m+1)} & q_{2\zeta}^{(m+1)} & \bar{q}_{2\zeta}^{(m+1)} \\
A & 1 & A & 1 & 0 & 0 & 0 & 0 \\
0 & 0 & 0 & 0 & 1 & A & 1 & A \\
A\zeta_1^{(m)} & \bar{\zeta}_1^{(m)} & A\zeta_2^{(m)} & \bar{\zeta}_2^{(m)} & 0 & 0 & 0 & 0 \\
0 & 0 & 0 & 0 & \zeta_1^{(m+1)} & A\bar{\zeta}_1^{(m+1)} & \zeta_2^{(m+1)} & A\bar{\zeta}_2^{(m+1)}
\end{vmatrix} = 0
$$

and

$$
|\mathbf{K}(\gamma)| = e^{-2i\pi\gamma}
\begin{vmatrix}
1 & 1 & 1 & 1 \\
t_{1\zeta}^{(m)} & \bar{t}_{1\zeta}^{(m)} & t_{1\zeta}^{(m+1)} & \bar{t}_{1\zeta}^{(m+1)} \\
B & 1 & 0 & 0 \\
0 & 0 & 1 & B
\end{vmatrix}
$$

$$= (t_{1\zeta}^{(m+1)} - \bar{t}_{1\zeta}^{(m)})B^{-1}(B-1)(B+1) = 0, \quad (9)$$

where $B = e^{2i\pi\gamma}$. The transcendental characteristic equation $|\mathbf{K}_d(\delta)| = 0$ governing the stresses (σ_{xx}, σ_{yy}, σ_{zz}, and τ_{xy}) and displacements (u and v) of the cross-ply laminates can be also expanded as

$$|\mathbf{K}_d(\delta)| = A^{-2}(1-A)^2[c_1A^2 + c_2A + c_3] = 0, \quad (10)$$

where the complex coefficients c_1, c_2, and c_3 are the related material constants computed from adjacent 0 deg and 90 deg plies and given in Appendix B. The eigenvalues δ_n are determined as

$$\delta_n = n \quad \text{and} \quad \left(n - \frac{1}{2}\right) \pm \frac{i}{2\pi} \ln\left\{\frac{c_2 + \sqrt{c_2^2 - 4c_1c_3}}{2c_1}\right\}$$

$$(n = 0, 1, 2, \ldots\ldots). \quad (11)$$

Hence, as seen from Eqs. (3) and (11), the explicit solutions of the edge-delamination stress singularity for the stresses (σ_{xx}, σ_{yy}, σ_{zz}, and τ_{xy}) in the cross-ply laminates are denoted as $\delta_n = (n - \frac{1}{2}) \pm i/2\pi \ln \{(c_2 + \sqrt{c_2^2 - 4c_1c_3})/2c_1\}$ ($n = 0, 1, 2, \ldots$). In other words, the edge-delamination stress singularity of the stresses (σ_{xx}, σ_{yy}, σ_{zz}, and τ_{xy}) only contains the $r^{\delta_r}(\ln r)^n$ singularity ($n = 1, 2, \ldots$) in the cross-ply laminates. As for the eigenvalue γ_n of the transcendental characteristic Eq. (9), the solutions can be obtained as

$$\gamma_n = n \quad \text{and} \quad (n - \tfrac{1}{2}) \quad (n = 0, 1, 2, \ldots\ldots). \tag{12}$$

As seen from Eqs. (3) and (12), the transverse shear stresses τ_{xz} and τ_{yz} in the cross-ply laminates with edge delamination have a $r^{-1/2}$ singularity, which is the same as that of linear elastic crack problems. This makes up for the deficiency of the previous research (Wang, 1984).

Therefore, for the cross-ply laminates, the explicit solutions of the edge-delamination stress singularities are concluded as $\gamma = -\frac{1}{2}$ and $\delta_n = (n - \frac{1}{2}) \pm i/2\pi \ln \{(c_2 + \sqrt{c_2^2 - 4c_1c_3})/2c_1\}$ ($n = 0, 1, 2, \ldots\ldots$). Thus, the edge-delamination stress singularity of the cross-ply laminates also contains the $r^{-1/2}$ and $r^{\delta_r}(\ln r)^n$ ($n = 1, 2 \ldots$) forms. In addition, γ_n is associated with the deformations due to antiplane displacements and δ_n is associated with that due to in-plane displacements in the cross-ply laminates. In the case of dissimilar isotropic materials, the eigenvalue δ_n of Eq. (11) can be simplified as

$$\delta_n = \left(n - \frac{1}{2}\right) \pm \frac{i}{2\pi} \ln \left\{ \frac{G^{(m)} + G^{(m+1)}(3 - 4\nu^{(m)})}{G^{(m+1)} + G^{(m)}(3 - 4\nu^{(m+1)})} \right\}$$

$$(n = 0, 1, 2, \ldots\ldots), \tag{13}$$

which agrees with the result obtained by Williams (1959) (the result obtained by Wang (1984) can't be simplified to Eq. (13)). G and ν denote the shear modulus and Poisson's ratio, respectively.

3.3 Dominant Edge-Delamination Stress Singularity. Since the stress distribution in the interior region can be adequately described by the general solution for the corresponding $\delta = 0$ and the singular terms of the near-field solutions should have a weak effect on the stress field far away from the crack tip, other nonsingular terms of the general solutions ($\delta_i = 0$ and $\delta_r > 0$) are negligible in the analysis. In addition, although the $r^{\delta_r}(\ln r)^n$ stress singularity also exists as $\delta_i \neq 0$ and $\delta_r > 0$, the strength in this range is much smaller than other singularities. Hence, even though the eigenvalues have infinite numbers, only the ones with δ_r in the range of $-1 < \delta_r \leq 0$ are the main concern. The dominant edge-delamination stress singularities for the angle-ply laminates contain a pair of complex conjugates, $-\frac{1}{2} \pm i/2\pi \ln \{(b + \sqrt{b^2 - a^2})/a\}$, and a real constant, $-\frac{1}{2}$. For the cross-ply laminates, the dominant edge-delamination stress singularities are denoted as $-\frac{1}{2} \pm i/2\pi \ln \{(c_2 + \sqrt{c_2^2 - 4c_1c_3})/2c_1\}$ and $-\frac{1}{2}$.

Although the expressions of a, b, c_1, c_2, and c_3 as presented in the Appendices are slightly complicated (but explicit), they can compensate the lack of explicit expression for δ (Wang, 1984; Ting, 1986) and provide the researcher a simple way to compute the edge-delamination stress singularities for arbitrary angle-ply and cross-ply laminates directly by substituting appropriate elastic material constants into Eqs. (8) and (11). To comprehend the edge-delamination effects near the crack tip, however, the eigenvalues δ_n of the transcendental characteristic equation are worthy of further thorough examination.

4 Results and Discussions

To evaluate the edge-delamination stress singularity quantitatively, without loss of generality, the graphite-epoxy laminates with a delamination lying between θ_1 and θ_2 plies (Fig. 1) under uniform axial strain are examined. The Young's moduli $\mathbf{E}_{ii}$, shear moduli $\mathbf{G}_{ij}$ and Poisson's ratios $\boldsymbol{\nu}_{ij}$ in the transverse (1), thickness (2) and fiber directions (3) of each graphite-epoxy ply are shown in Fig. 1. The material constants μ_k, η_k, $q_{k\mu}$, ζ_k, ξ_k, $q_{k\zeta}$, and $t_{k\xi}$ are shown to be imaginary and $p_{k\mu}$, $t_{k\mu}$, and $p_{k\zeta}$ are real (Wang and Choi, 1982; Zwiers et al., 1982; Huang and Chen, 1994).

4.1 Angle-Ply Graphite-Epoxy Laminates. Based on the previous findings, the asymptotic stress field of the angle-ply laminates in the vicinity of the crack tip is governed by the singular terms as $\delta = -\frac{1}{2} \pm i/2\pi \ln \{(b + \sqrt{b^2 - a^2})/a\}$ and $-\frac{1}{2}$. For the composite laminates having imaginary terms of μ_k, η_k, and $q_{k\mu}$, and real $p_{k\mu}$ and $t_{k\mu}$ terms, the transcendental characteristic Eq. (7) can be simplified as

$$\begin{aligned} |\mathbf{K}(\delta)| = 8A^{-3}(1 - A)^3(1 + A)[p_{1\mu}(\eta_2 - \eta_3) \\ + p_{2\mu}(\eta_3 - \eta_1) + p_{3\mu}(\eta_1 - \eta_2)] \\ \times [\mu_1(\eta_2 - \eta_3) + \mu_2(\eta_3 - \eta_1) + \mu_3(\eta_1 - \eta_2)] \\ \times [a^*A^2 + 2b^*A + a^*] = 0 \end{aligned}$$

where

$$\begin{aligned} a^* = [\mu_1(\eta_2 - \eta_3) + \mu_2(\eta_3 - \eta_1) + \mu_3(\eta_1 - \eta_2)] \\ \times [\mu_1(q_{2\mu}t_3 - q_{3\mu}t_2) + \mu_2(q_{3\mu}t_1 - q_{1\mu}t_3) \\ + \mu_3(q_{1\mu}t_2 - q_{2\mu}t_1)], \end{aligned}$$

and

$$\begin{aligned} b^* = a^* + 2[\mu_1(q_{2\mu} - q_{3\mu}) + \mu_2(q_{3\mu} - q_{1\mu}) \\ + \mu_3(q_{1\mu} - q_{2\mu})] \times [\mu_1(t_{2\mu}\eta_3 - t_{3\mu}\eta_2) \\ + \mu_2(t_{3\mu}\eta_1 - t_{1\mu}\eta_3) + \mu_3(t_{1\mu}\eta_2 - t_{2\mu}\eta_1)]. \end{aligned}$$

The explicit solution of the edge-delamination stress singularity for the angle-ply graphite-epoxy composites is thus derived as $\delta = -\frac{1}{2}$ and $\delta = (n - \frac{1}{2}) \pm i/2\pi \ln \{[b^* + \sqrt{(b^*)^2 - (a^*)^2}]/a^*\}$ ($n = 0, 1, 2, \ldots\ldots$). The dominant edge-delamination stress singularities computed by the present analysis for the angle-ply graphite-epoxy laminates with various fiber orientations are shown in Table 1. Excellent correlations between the present results and available solutions (Wang and Yuan, 1983; Wang, 1984) are noted. The results for several commonly used fiber orientations are also provided. For $\theta = 0$ deg and 90 deg, the composite laminates become unidirectional and the $r^{-1/2}$ singularity for orthotropic elastic crack problems is also noted.

4.2 Cross-Ply Graphite-Epoxy Laminate. Although the edge-delamination stress singularity of the transverse shear stresses τ_{xz} and τ_{yz} in the cross-ply laminates is known as $r^{-1/2}$, that of the stresses (σ_{xx}, σ_{yy}, σ_{zz}, and τ_{xy}) needs to be further investigated. From the material analysis of the graphite-epoxy laminates, the characteristic Eq. (10) for the stresses (σ_{xx}, σ_{yy}, σ_{zz}, and τ_{xy}) and displacements (u and v) of the cross-ply laminates can be rewritten as

$$\begin{aligned} |\mathbf{K}_d(\delta)| = A^{-2}(1 - A)^2 \frac{(\zeta_1^{(m)} - \zeta_2^{(m)})^2(\zeta_1^{(m+1)} - \zeta_2^{(m+1)})^2}{\zeta_1^{(m)}\zeta_2^{(m)}\zeta_1^{(m+1)}\zeta_2^{(m+1)}} \\ \times [c_1^*A^2 + 2c_2^*A + c_1^*] = 0 \end{aligned}$$

where

$$\begin{aligned} c_2^* - c_1^* = 2\{[\zeta_1^{(m)}\zeta_2^{(m)}(\beta_{12}^{(m+1)} - \beta_{12}^{(m)}) - 2\beta_{22}^{(m)}] \\ \times [\zeta_1^{(m+1)}\zeta_2^{(m+1)}(\beta_{12}^{(m+1)} - \beta_{12}^{(m)}) + 2\beta_{22}^{(m+1)}] \end{aligned}$$

Table 1 Dominant edge-delamination stress singularity for the graphite-epoxy laminates with various fiber orientations

$\pm\theta$	δ_1		$\delta_{2,3}$	
	Present	Wang (1983,1984)	Present	Wang (1983,1984)
0°	−0.5	−0.5	−0.5	−0.5
5°	−0.5		$-0.5\pm0.0010698378i$	
10°	−0.5		$-0.5\pm0.0029365319i$	
15°	−0.5	−0.5	$-0.5\pm0.0064447201i$	$-0.5\pm0.00642i$
20°	−0.5		$-0.5\pm0.0116593204i$	
25°	−0.5		$-0.5\pm0.0178610378i$	
30°	−0.5	−0.5	$-0.5\pm0.0240083815i$	$-0.5\pm0.02399i$
35°	−0.5		$-0.5\pm0.0291530300i$	
40°	−0.5		$-0.5\pm0.0326769565i$	
45°	−0.5	−0.5	$-0.5\pm0.0343365146i$	$-0.5\pm0.03434i$
50°	−0.5		$-0.5\pm0.0341812663i$	
55°	−0.5		$-0.5\pm0.0324380924i$	
60°	−0.5	−0.5	$-0.5\pm0.0294152218i$	$-0.5\pm0.02942i$
65°	−0.5		$-0.5\pm0.0254388209i$	
70°	−0.5		$-0.5\pm0.0208139569i$	
75°	−0.5	−0.5	$-0.5\pm0.0157990021i$	$-0.5\pm0.01579i$
80°	−0.5		$-0.5\pm0.0105880264i$	
85°	−0.5		$-0.5\pm0.0053027852i$	
90°	−0.5	−0.5	−0.5	−0.5

$$+ \zeta_1^{(m)}\zeta_2^{(m)}\zeta_1^{(m+1)}\zeta_2^{(m+1)}(\beta_{11}^{(m+1)}\beta_{22}^{(m+1)} + \beta_{11}^{(m)}\beta_{22}^{(m)}) + 2\beta_{22}^{(m+1)}\beta_{22}^{(m)}\},$$

and

$$c_2^* + c_1^* = 2[\beta_{11}^{(m)}(\zeta_1^{(m)} + \zeta_2^{(m)}) + \beta_{11}^{(m+1)}(\zeta_1^{(m+1)} + \zeta_2^{(m+1)})] \times [\beta_{22}^{(m)}\zeta_1^{(m+1)}\zeta_2^{(m+1)}(\zeta_1^{(m)} + \zeta_2^{(m)}) + \beta_{22}^{(m+1)}\zeta_1^{(m)}\zeta_2^{(m)}(\zeta_1^{(m+1)} + \zeta_2^{(m+1)})].$$

Thus, for the composite laminates having imaginary ζ_k, $q_{k\zeta}$, and $t_{k\xi}$ and real $p_{k\zeta}$, the explicit solution of the edge-delamination stress singularity for the stresses (σ_{xx}, σ_{yy}, σ_{zz}, and τ_{xy}) in the [0°/90°] graphite-epoxy laminates can be found as $\delta = (n - \frac{1}{2}) \pm i/2\pi \ln \{[c_2^* + \sqrt{(c_2^*)^2 - (c_1^*)^2}]/c_1^*\}$ ($n = 0, 1, 2, \ldots\ldots$). For the present cross-ply graphite-epoxy laminate, the dominant edge-delamination stress singularity of the stresses (σ_{xx}, σ_{yy}, σ_{zz}, and τ_{xy}) is computed as $\delta = -0.5 \pm 0.0511803090i$. Obviously, the magnitude of the imaginary part of δ in the [0°/90°] graphite-epoxy laminate is larger than those of the angle-ply laminates.

5 Conclusions

A rigorous investigation on the edge-delamination stress singularities for angle-ply and cross-ply laminates has been successfully achieved. Based on the results obtained, the edge-delamination stress singularities for angle-ply and cross-ply laminates with two different orthotropic plies can be evaluated directly by substituting appropriate elastic material constants into Eqs. (8) and (11). The deficiency found in the literature also has been modified. The present approach developed can be further extended to deal with various types of singularity problems, for example, the transverse crack and delamination crack originating from transverse crack in the composite laminates.

Acknowledgments

The authors are grateful to the National Science Council of the Republic of China for financial support through grant NSC82-0401-E007-083.

References

Huang, T. F., and Chen, W. H., 1994, "On the Free-Edge Stress Singularity of General Composite Laminates Under Uniform Axial Strain," *International Journal of Solids and Structures,* Vol. 31, pp. 3139–3151.

Lekhnitskii, S. G., 1963, *Theory of Elasticity of an Anisotropic Body,* Holden-Day, San Francisco.

Muller, D. E., 1956, "A Method for Solving Algebraic Equations Using an Automatic Computer," *Mathematical Tables and Computations,* Vol. 10, pp. 208–215.

Pavelle, R., and Wang, P. S., 1985, "Macsyma from F to G," *Journal of Symbolic Computations,* Vol. 1, pp. 69–100.

Stroh, A. N., 1962, "Steady State Problems in Anisotropic Elasticity," *Journal of Mathematics and Physics,* Vol. 41, pp. 77–103.

Ting, T. C. T., 1986, "Explicit Solution and Invariance of the Singularities at an Interface Crack in Anisotropic Composites," *International Journal of Solids and Structures,* Vol. 22, pp. 965–983.

Wang, S. S., and Yuan, F. G., 1983, "A Hybrid Finite Element Approach to Composite Laminate Elasticity Problems With Singularities," ASME JOURNAL OF APPLIED MECHANICS, Vol. 50, pp. 835–844.

Wang, S. S., 1984, "Edge Delamination in Angle-Ply Composite Laminates" *AIAA Journal,* Vol. 22, pp. 256–264.

Williams, M. L., 1959, "The Stresses Around a Fault or Crack in Dissimilar Media," *Bulletin of the Seismological Society of America,* Vol. 49, pp. 199–204.

APPENDIX A

The Determinant $|K(\delta)|$ for Angle-Ply Laminates

$$|\mathbf{K}(\delta)| = A^{-3}(1 - A)^3(A + 1)[aA^2 + 2bA + a],$$

where

$$a = -[(\mu_2 - \mu_1)(\eta_3 - \eta_1) - (\mu_3 - \mu_1)(\eta_2 - \eta_1)] \times [(\bar{\mu}_2 - \bar{\mu}_1)(\bar{\eta}_3 - \bar{\eta}_1) - (\bar{\mu}_3 - \bar{\mu}_1)(\bar{\eta}_2 - \bar{\eta}_1)]$$

$$\times \begin{vmatrix} (\bar{t}_{2\mu} - \bar{t}_{1\mu}) & (\bar{t}_{3\mu} - \bar{t}_{1\mu}) & -(t_{1\mu} + \bar{t}_{1\mu}) & -(t_{2\mu} - t_{1\mu}) & -(t_{3\mu} - t_{1\mu}) \\ (\bar{p}_{2\mu} - \bar{p}_{1\mu}) & (\bar{p}_{3\mu} - \bar{p}_{1\mu}) & (p_{1\mu} - \bar{p}_{1\mu}) & (p_{2\mu} - p_{1\mu}) & (p_{3\mu} - p_{1\mu}) \\ (\bar{q}_{2\mu} - \bar{q}_{1\mu}) & (\bar{q}_{3\mu} - \bar{q}_{1\mu}) & (q_{1\mu} - \bar{q}_{1\mu}) & (q_{2\mu} - q_{1\mu}) & (q_{3\mu} - q_{1\mu}) \\ (\bar{\mu}_2 - \bar{\mu}_1) & (\bar{\mu}_3 - \bar{\mu}_1) & (\mu_1 - \bar{\mu}_1) & (\mu_2 - \mu_1) & (\mu_3 - \mu_1) \\ (\bar{\eta}_2 - \bar{\eta}_1) & (\bar{\eta}_3 - \bar{\eta}_1) & -(\eta_1 + \bar{\eta}_1) & -(\eta_2 - \eta_1) & -(\eta_3 - \eta_1) \end{vmatrix}$$

and

$$
\begin{aligned}
b = {} & \begin{vmatrix}
(\mu_2-\mu_1) & (\mu_3-\mu_1) & -\mu_1 & 0 & 0 \\
(\eta_2-\eta_1) & (\eta_3-\eta_1) & -\eta_1 & 0 & 0 \\
(t_{2\mu}-t_{1\mu}) & (t_{3\mu}-t_{1\mu}) & -(\bar{t}_{1\mu}+t_{1\mu}) & -(\bar{t}_{2\mu}-\bar{t}_{1\mu}) & -(\bar{t}_{3\mu}-\bar{t}_{1\mu}) \\
0 & 0 & \bar{\mu}_1 & (\bar{\mu}_2-\bar{\mu}_1) & (\bar{\mu}_3-\bar{\mu}_1) \\
0 & 0 & \bar{\eta}_1 & (\bar{\eta}_2-\bar{\eta}_1) & (\bar{\eta}_3-\bar{\eta}_1)
\end{vmatrix} \\
& \times \begin{vmatrix}
(\bar{p}_{2\mu}-\bar{p}_{1\mu}) & (\bar{p}_{3\mu}-\bar{p}_{1\mu}) & (p_{2\mu}-p_{1\mu}) & (p_{3\mu}-p_{1\mu}) \\
(\bar{q}_{2\mu}-\bar{q}_{1\mu}) & (\bar{q}_{3\mu}-\bar{q}_{1\mu}) & (q_{2\mu}-q_{1\mu}) & (q_{3\mu}-q_{1\mu}) \\
(\bar{\mu}_2-\bar{\mu}_1) & (\bar{\mu}_3-\bar{\mu}_1) & (\mu_2-\mu_1) & (\mu_3-\mu_1) \\
(\bar{\eta}_2-\bar{\eta}_1) & (\bar{\eta}_3-\bar{\eta}_1) & -(\eta_2-\eta_1) & -(\eta_3-\eta_1)
\end{vmatrix}
- \begin{vmatrix}
(\mu_2-\mu_1) & (\mu_3-\mu_1) & 0 & 0 \\
(\eta_2-\eta_1) & (\eta_3-\eta_1) & -(\bar{\eta}_2-\bar{\eta}_1) & -(\bar{\eta}_3-\bar{\eta}_1) \\
(t_{2\mu}-t_{1\mu}) & (t_{3\mu}-t_{1\mu}) & -(\bar{t}_{2\mu}-\bar{t}_{1\mu}) & -(\bar{t}_{3\mu}-\bar{t}_{1\mu}) \\
0 & 0 & (\bar{\mu}_2-\bar{\mu}_1) & (\bar{\mu}_3-\bar{\mu}_1)
\end{vmatrix} \\
& \times \begin{vmatrix}
0 & 0 & \eta_1 & (\eta_2-\eta_1) & (\eta_3-\eta_1) \\
(\bar{p}_{2\mu}-\bar{p}_{1\mu}) & (\bar{p}_{3\mu}-\bar{p}_{1\mu}) & (p_{1\mu}-\bar{p}_{1\mu}) & (p_{2\mu}-p_{1\mu}) & (p_{3\mu}-p_{1\mu}) \\
(\bar{q}_{2\mu}-\bar{q}_{1\mu}) & (\bar{q}_{3\mu}-\bar{q}_{1\mu}) & (q_{1\mu}-\bar{q}_{1\mu}) & (q_{2\mu}-q_{1\mu}) & (q_{3\mu}-q_{1\mu}) \\
(\bar{\mu}_2-\bar{\mu}_1) & (\bar{\mu}_3-\bar{\mu}_1) & (\mu_1-\bar{\mu}_1) & (\mu_2-\mu_1) & (\mu_3-\mu_1) \\
(\bar{\eta}_2-\bar{\eta}_1) & (\bar{\eta}_3-\bar{\eta}_1) & -\bar{\eta}_1 & 0 & 0
\end{vmatrix} \\
& + \begin{vmatrix}
(\mu_2-\mu_1) & (\mu_3-\mu_1) & (\bar{\mu}_2-\bar{\mu}_1) & (\bar{\mu}_3-\bar{\mu}_1) \\
(\eta_2-\eta_1) & (\eta_3-\eta_1) & 0 & 0 \\
(t_{2\mu}-t_{1\mu}) & (t_{3\mu}-t_{1\mu}) & -(\bar{t}_{2\mu}-\bar{t}_{1\mu}) & -(\bar{t}_{3\mu}-\bar{t}_{1\mu}) \\
0 & 0 & (\bar{\eta}_2-\bar{\eta}_1) & (\bar{\eta}_3-\bar{\eta}_1)
\end{vmatrix} \\
& \times \begin{vmatrix}
0 & 0 & \mu_1 & (\mu_2-\mu_1) & (\mu_3-\mu_1) \\
(\bar{p}_{2\mu}-\bar{p}_{1\mu}) & (\bar{p}_{3\mu}-\bar{p}_{1\mu}) & (p_{1\mu}-\bar{p}_{1\mu}) & (p_{2\mu}-p_{1\mu}) & (p_{3\mu}-p_{1\mu}) \\
(\bar{q}_{2\mu}-\bar{q}_{1\mu}) & (\bar{q}_{3\mu}-\bar{q}_{1\mu}) & (q_{1\mu}-\bar{q}_{1\mu}) & (q_{2\mu}-q_{1\mu}) & (q_{3\mu}-q_{1\mu}) \\
(\bar{\mu}_2-\bar{\mu}_1) & (\bar{\mu}_3-\bar{\mu}_1) & -\bar{\mu}_1 & 0 & 0 \\
(\bar{\eta}_2-\bar{\eta}_1) & (\bar{\eta}_3-\bar{\eta}_1) & -(\eta_1+\bar{\eta}_1) & -(\eta_2-\eta_1) & -(\eta_3-\eta_1)
\end{vmatrix} .
\end{aligned}
$$

APPENDIX B

The Determinant $|\mathbf{K}_d(\delta)|$ for Cross-Ply Laminates

$$|\mathbf{K}_d(\delta)| = A^{-2}(1-A)^2[c_1A^2 + c_2A + c_3],$$

where

$$
\begin{aligned}
c_1 = {} & (\zeta_1^{(m)} - \zeta_2^{(m)})(\bar{\zeta}_1^{(m+1)} - \bar{\zeta}_2^{(m+1)}) \times \{ -\bar{\zeta}_1^{(m)}[\bar{q}_{2\zeta}^{(m)}(p_{1\zeta}^{(m+1)} \\
& - p_{2\zeta}^{(m+1)}) + q_{1\zeta}^{(m+1)}(p_{2\zeta}^{(m+1)} - \bar{p}_{2\zeta}^{(m)}) \\
& + q_{2\zeta}^{(m+1)}(\bar{p}_{2\zeta}^{(m)} - p_{1\zeta}^{(m+1)})] + \bar{\zeta}_2^{(m)}[\bar{q}_{1\zeta}^{(m)}(p_{1\zeta}^{(m+1)} - p_{2\zeta}^{(m+1)}) \\
& + q_{1\zeta}^{(m+1)}(p_{2\zeta}^{(m+1)} - \bar{p}_{1\zeta}^{(m)}) + q_{2\zeta}^{(m+1)}(\bar{p}_{1\zeta}^{(m)} - p_{1\zeta}^{(m+1)})] \\
& - \zeta_1^{(m+1)}[\bar{q}_{1\zeta}^{(m)}(\bar{p}_{2\zeta}^{(m)} - p_{2\zeta}^{(m+1)}) + \bar{q}_{2\zeta}^{(m)}(p_{2\zeta}^{(m+1)} - \bar{p}_{1\zeta}^{(m)}) \\
& + q_{2\zeta}^{(m+1)}(\bar{p}_{1\zeta}^{(m)} - \bar{p}_{2\zeta}^{(m)})] + \zeta_2^{(m+1)}[\bar{q}_{1\zeta}^{(m)}(\bar{p}_{2\zeta}^{(m)} - p_{1\zeta}^{(m+1)}) \\
& \qquad + \bar{q}_{2\zeta}^{(m)}(p_{1\zeta}^{(m+1)} - \bar{p}_{1\zeta}^{(m)}) + q_{1\zeta}^{(m+1)}(\bar{p}_{1\zeta}^{(m)} - \bar{p}_{2\zeta}^{(m)})]\},
\end{aligned}
$$

$$
\begin{aligned}
c_2 = {} & (\bar{\zeta}_1^{(m)} - \bar{\zeta}_2^{(m)}) \times \{ \zeta_1^{(m)}\bar{\zeta}_1^{(m+1)}[(q_{2\zeta}^{(m)} - \bar{q}_{2\zeta}^{(m+1)})(p_{1\zeta}^{(m+1)} \\
& - p_{2\zeta}^{(m+1)}) - (q_{1\zeta}^{(m+1)} - q_{2\zeta}^{(m+1)})(p_{2\zeta}^{(m)} - \bar{p}_{2\zeta}^{(m+1)})] \\
& - \zeta_1^{(m)}\bar{\zeta}_2^{(m+1)}[(q_{2\zeta}^{(m)} - \bar{q}_{1\zeta}^{(m+1)})(p_{1\zeta}^{(m+1)} - p_{2\zeta}^{(m+1)}) \\
& - (q_{1\zeta}^{(m+1)} - q_{2\zeta}^{(m+1)})(p_{2\zeta}^{(m)} - \bar{p}_{1\zeta}^{(m+1)})] + \zeta_2^{(m)}\bar{\zeta}_2^{(m+1)}[(q_{1\zeta}^{(m)} \\
& - \bar{q}_{1\zeta}^{(m+1)})(p_{1\zeta}^{(m+1)} - p_{2\zeta}^{(m+1)}) - (q_{1\zeta}^{(m+1)} - q_{2\zeta}^{(m+1)}) \\
& \times (p_{1\zeta}^{(m)} - \bar{p}_{1\zeta}^{(m+1)})] - \zeta_2^{(m)}\bar{\zeta}_1^{(m+1)}[(q_{1\zeta}^{(m)} - \bar{q}_{2\zeta}^{(m+1)})(p_{1\zeta}^{(m+1)} \\
& - p_{2\zeta}^{(m+1)}) - (q_{1\zeta}^{(m+1)} - q_{2\zeta}^{(m+1)})(p_{1\zeta}^{(m)} - \bar{p}_{2\zeta}^{(m+1)})]\} \\
& + (\zeta_1^{(m+1)} - \zeta_2^{(m+1)}) \times \{ \zeta_1^{(m)}\bar{\zeta}_1^{(m+1)}[(\bar{q}_{1\zeta}^{(m)} - \bar{q}_{2\zeta}^{(m)}) \\
& \times (p_{2\zeta}^{(m)} - \bar{p}_{2\zeta}^{(m+1)}) - (q_{2\zeta}^{(m)} - \bar{q}_{2\zeta}^{(m+1)})(\bar{p}_{1\zeta}^{(m)} - \bar{p}_{2\zeta}^{(m)})] \\
& - \zeta_1^{(m)}\bar{\zeta}_2^{(m+1)}[(\bar{q}_{1\zeta}^{(m)} - \bar{q}_{2\zeta}^{(m)})(p_{2\zeta}^{(m)} - \bar{p}_{1\zeta}^{(m+1)}) \\
& - (q_{2\zeta}^{(m)} - \bar{q}_{1\zeta}^{(m+1)})(\bar{p}_{1\zeta}^{(m)} - \bar{p}_{2\zeta}^{(m)})] + \zeta_2^{(m)}\bar{\zeta}_2^{(m+1)}[(\bar{q}_{1\zeta}^{(m)} \\
& - \bar{q}_{2\zeta}^{(m)})(p_{1\zeta}^{(m)} - \bar{p}_{1\zeta}^{(m+1)}) - (q_{1\zeta}^{(m)} - \bar{q}_{1\zeta}^{(m+1)})(\bar{p}_{1\zeta}^{(m)} - \bar{p}_{2\zeta}^{(m)})] \\
& - \zeta_2^{(m)}\bar{\zeta}_1^{(m+1)}[(\bar{q}_{1\zeta}^{(m)} - \bar{q}_{2\zeta}^{(m)})(p_{1\zeta}^{(m)} - \bar{p}_{2\zeta}^{(m+1)}) \\
& - (q_{1\zeta}^{(m)} - \bar{q}_{2\zeta}^{(m+1)})(\bar{p}_{1\zeta}^{(m)} - \bar{p}_{2\zeta}^{(m)})]\} + (\zeta_1^{(m)} - \zeta_2^{(m)}) \\
& \times \{ \bar{\zeta}_1^{(m)}\zeta_1^{(m+1)}[(\bar{q}_{2\zeta}^{(m)} - q_{2\zeta}^{(m+1)})(\bar{p}_{1\zeta}^{(m+1)} - \bar{p}_{2\zeta}^{(m+1)}) \\
& - (\bar{q}_{1\zeta}^{(m+1)} - \bar{q}_{2\zeta}^{(m+1)})(\bar{p}_{2\zeta}^{(m)} - p_{2\zeta}^{(m+1)})] \\
& - \bar{\zeta}_1^{(m)}\zeta_2^{(m+1)}[(\bar{q}_{2\zeta}^{(m)} - q_{1\zeta}^{(m+1)})(\bar{p}_{1\zeta}^{(m+1)} - \bar{p}_{2\zeta}^{(m+1)}) \\
& - (\bar{q}_{1\zeta}^{(m+1)} - \bar{q}_{2\zeta}^{(m+1)})(\bar{p}_{2\zeta}^{(m)} - p_{1\zeta}^{(m+1)})] \\
& + \bar{\zeta}_2^{(m)}\zeta_2^{(m+1)}[(\bar{q}_{1\zeta}^{(m)} - q_{1\zeta}^{(m+1)})(\bar{p}_{1\zeta}^{(m+1)} - \bar{p}_{2\zeta}^{(m+1)}) \\
& - (\bar{q}_{1\zeta}^{(m+1)} - \bar{q}_{2\zeta}^{(m+1)})(\bar{p}_{1\zeta}^{(m)} - p_{1\zeta}^{(m+1)})] \\
& - \bar{\zeta}_2^{(m)}\zeta_1^{(m+1)}[(\bar{q}_{1\zeta}^{(m)} - q_{2\zeta}^{(m+1)})(\bar{p}_{1\zeta}^{(m+1)} - \bar{p}_{2\zeta}^{(m+1)}) \\
& - (\bar{q}_{1\zeta}^{(m+1)} - \bar{q}_{2\zeta}^{(m+1)})(\bar{p}_{1\zeta}^{(m)} - p_{2\zeta}^{(m+1)})]\} + (\bar{\zeta}_1^{(m+1)} \\
& - \bar{\zeta}_2^{(m+1)}) \times \{ \bar{\zeta}_1^{(m)}\zeta_1^{(m+1)}[(q_{1\zeta}^{(m)} - q_{2\zeta}^{(m)})(\bar{p}_{2\zeta}^{(m)} - p_{2\zeta}^{(m+1)}) \\
& - (\bar{q}_{2\zeta}^{(m)} - q_{2\zeta}^{(m+1)})(p_{1\zeta}^{(m)} - p_{2\zeta}^{(m)})] - \bar{\zeta}_1^{(m)}\zeta_2^{(m+1)}[(q_{1\zeta}^{(m)} \\
& - q_{2\zeta}^{(m)})(\bar{p}_{2\zeta}^{(m)} - p_{1\zeta}^{(m+1)}) - (\bar{q}_{2\zeta}^{(m)} - q_{1\zeta}^{(m+1)}) \\
& \times (p_{1\zeta}^{(m)} - p_{2\zeta}^{(m)})] + \bar{\zeta}_2^{(m)}\zeta_2^{(m+1)}[(q_{1\zeta}^{(m)} - q_{2\zeta}^{(m)})(\bar{p}_{1\zeta}^{(m)} \\
& - p_{1\zeta}^{(m+1)}) - (\bar{q}_{1\zeta}^{(m)} - q_{1\zeta}^{(m+1)})(p_{1\zeta}^{(m)} - p_{2\zeta}^{(m)})] \\
& - \bar{\zeta}_2^{(m)}\zeta_1^{(m+1)}[(q_{1\zeta}^{(m)} - q_{2\zeta}^{(m)})(\bar{p}_{1\zeta}^{(m)} - p_{2\zeta}^{(m+1)}) \\
& \qquad - (\bar{q}_{1\zeta}^{(m)} - q_{2\zeta}^{(m+1)})(p_{1\zeta}^{(m)} - p_{2\zeta}^{(m)})]\}
\end{aligned}
$$

and

$$
\begin{aligned}
c_3 = {} & (\bar{\zeta}_1^{(m)} - \bar{\zeta}_2^{(m)})(\zeta_1^{(m+1)} - \zeta_2^{(m+1)}) \\
& \times \{ -\zeta_1^{(m)}[q_{2\zeta}^{(m)}(\bar{p}_{1\zeta}^{(m+1)} - \bar{p}_{2\zeta}^{(m+1)}) + \bar{q}_{1\zeta}^{(m+1)}(\bar{p}_{2\zeta}^{(m+1)} - p_{2\zeta}^{(m)}) \\
& + \bar{q}_{2\zeta}^{(m+1)}(p_{2\zeta}^{(m)} - \bar{p}_{1\zeta}^{(m+1)})] + \zeta_2^{(m)}[q_{1\zeta}^{(m)}(\bar{p}_{1\zeta}^{(m+1)} - \bar{p}_{2\zeta}^{(m+1)}) \\
& + \bar{q}_{1\zeta}^{(m+1)}(\bar{p}_{2\zeta}^{(m+1)} - p_{1\zeta}^{(m)}) + \bar{q}_{2\zeta}^{(m+1)}(p_{1\zeta}^{(m)} - \bar{p}_{1\zeta}^{(m+1)})] \\
& - \bar{\zeta}_1^{(m+1)}[q_{1\zeta}^{(m)}(p_{2\zeta}^{(m)} - \bar{p}_{2\zeta}^{(m+1)}) + q_{2\zeta}^{(m)}(\bar{p}_{2\zeta}^{(m+1)} - p_{1\zeta}^{(m)}) \\
& + \bar{q}_{2\zeta}^{(m+1)}(p_{1\zeta}^{(m)} - p_{2\zeta}^{(m)})] + \bar{\zeta}_2^{(m+1)}[q_{1\zeta}^{(m)}(p_{2\zeta}^{(m)} - \bar{p}_{1\zeta}^{(m+1)}) \\
& \qquad + q_{2\zeta}^{(m)}(\bar{p}_{1\zeta}^{(m+1)} - p_{1\zeta}^{(m)}) + \bar{q}_{1\zeta}^{(m+1)}(p_{1\zeta}^{(m)} - p_{2\zeta}^{(m)})]\}.
\end{aligned}
$$

Q. Wang[1]
Department of Mechanics,
Peking University,
Beijing, People's Republic of China

K. M. Liew
Division of Engineering Mechanics,
School of Mechanical and
Production Engineering,
Nanyang Technological University,
Singapore 639798
Mem. ASME

A Theory for Reduced Order Control Design of Plate Systems

This paper describes the theory of wave domain control for the reduced control design of plate systems. A transformation, which changes the original system into an image system in which the control force is designed in wave domain control and wave control, is proposed such that the number of degrees-of-freedom of the undisturbed state in its image system is reduced. The control design in the original system is then derived by an inverse transformation. This work focuses on, first, proposing a new wave control theory and, second, applying the theory for structural control design.

1 Introduction

Structural analysis using numerical techniques, such as the finite element method, involves the use of many degrees-of-freedom. It is generally advantageous to reduce the number of degrees-of-freedom in control design (Hughes, 1981; Balas, 1986; Wang and Wang, 1994a, 1994b, 1994c; Wang et al., 1995a, 1995b). From the higher-order Ricatti equation, it is evident that the complexities in computation increase exponentially with the number of degrees-of-freedom. Also computation of higher-order matrix may result in an increase of round-off errors in the higher modes. In experimental evaluation of space structures (when many degrees-of-freedom are considered), many actuators and sensors are used when control design methods are employed, for example in the IMSC (Independent Modal Space Control), only n number of modes can be controlled for n actuators and sensors. This makes the whole evaluation process very costly. Also the hardware, sometime, may not be compatible to study structures under a large number of degrees-of-freedom, for example, the capacity of an on orbit computer.

There exists two kinds of approaches for the design of the reduced order control. The open-loop reduced order in which the order of the mathematical model of the original system is directly reduced and the usual design of system is obtained based on the reduced order model, and the close-loop reduced order in which the order of the controller is derived based on direct reduction of the original system. In contrast to the conventional approaches, a theory of wave domain control in structural design was proposed and a reduced order control design was developed (Wang et al., 1994a). This is aimed to establish a transformation in which the original system is changed to an image system. The initial disturbance in the image system, which is transformed from the initial displacements or other state variables, is defined in a spatial domain so that the theory on structural wave domain control can be used to design the control force, that enables some states of the image system remain undisturbed and reducible. Using the reduced order control design in the image system, the control design and the state response in the original system can be derived by an inverse transformation. If the transformation is nonunique, the problem becomes "how to find a *better* image system for the control design." Following this, a new research path or further study into this important topic is needed.

The aim of this paper is to present a reduced order design of a plate system by using the wave control theory. We will highlight and discuss *how* to apply the theory into practical applications. A numerical example which simulates a simply supported rectangular plate is given to illustrate the details of the theory.

2 Theoretical Formulations

The state equation of a system can be expressed as

$$\dot{x} = \mathbf{A}x + \mathbf{B}u \tag{1}$$

where $\mathbf{A}$ and $\mathbf{B}$ are the matrices of the system and control, and x and u are the vectors of state and control, respectively, namely

$$\mathbf{A} \in R^{n\times n}, \quad \mathbf{B} \in R^{n\times r}, \quad x \in R^n, \quad u \in R^r. \tag{2}$$

Before we go into further analyses, we first introduce the following symbols: $\mathbf{A}(i, j)$ and $\mathbf{B}(i, j)$ are the matrices with their entries consisting of the first i rows and the first j columns, $\mathbf{A}(\mathbf{i}, j)$ and $\mathbf{B}(\mathbf{i}, j)$ are those with the last i rows and the first j columns of the matrices. Also, $x(t, i)$ is a vector with the first i elements of vector x and $x(t, \mathbf{i})$ is that with the last i elements of x. $\mathbf{P}_{n\times j}$ is a matrix, whose column vectors are that of the j column vectors of unit matrix $\mathbf{I}_{n\times n}$. On the other hand, $\bar{\mathbf{P}}_{n\times j}$ is a matrix, whose column vectors are that of the $n - j$ column vectors of $\mathbf{I}_{n\times n}$. And the following notations are defined:

$$\mathbf{B}_{11} = \mathbf{B}(n - i, r)\mathbf{P}, \quad \mathbf{B}_{21} = \mathbf{B}(n - i, r)\bar{\mathbf{P}} \tag{3a}$$

$$\mathbf{B}_{21} = \mathbf{B}(\mathbf{i}, r)\mathbf{P}, \quad \mathbf{B}_{22} = \mathbf{B}(\mathbf{i}, r)\bar{\mathbf{P}} \tag{3b}$$

$$\mathbf{A}_{11} = \mathbf{A}(n - i, n - i), \quad \mathbf{A}_{21} = \mathbf{A}(i, n - i). \tag{3c}$$

All the definitions to be discussed are tenable only if the matrix $\mathbf{P}$ satisfies the following equation:

$$R(\mathbf{B}(\mathbf{i}, r)\mathbf{P}) = R(\mathbf{B}(\mathbf{i}, r)) \tag{4}$$

where $R(.)$ is the spanning space of the corresponding matrix, and $\mathbf{B}_{21}^{+}$ is the pseudo-inverse of $\mathbf{B}_{21}$. Let

$$\bar{\mathbf{B}} = \mathbf{B}_{12} - \mathbf{B}_{11}\mathbf{B}_{21}^{+}\mathbf{B}_{22}, \quad \bar{\mathbf{A}} = \mathbf{A}_{11} - \mathbf{B}_{11}\mathbf{B}_{21}^{+}\mathbf{A}_{21}. \tag{5}$$

The following definitions and criteria in view of structural wave dynamics are defined (Wang et al., 1995b):

- *Definition* 1: Equation (1) is wave domain controllable, if $\exists i$ (i is an integer smaller than n), $\forall x(0, n - i)$, $\exists u(\tau)$ ($\tau > 0$), which results in $x(t, \mathbf{i}) = 0$ for all $t > 0$.
- *Definition* 2: The degree of controllability of Eq. (1) is defined as the integer i in *Definition* 1.

[1] Current Address: School of Mechanical and Production Engineering, Nanyang Technological University, Singapore.

Contributed by the Applied Mechanics Division of THE AMERICAN SOCIETY OF MECHANICAL ENGINEERS for publication in the ASME JOURNAL OF APPLIED MECHANICS.

Discussion on the paper should be addressed to the Technical Editor, Professor Lewis T. Wheeler, Department of Mechanical Engineering, University of Houston, Houston, TX 77204-4792, and will be accepted until four months after final publication of the paper itself in the ASME JOURNAL OF APPLIED MECHANICS.

Manuscript received by the ASME Applied Mechanics Division, Oct. 13, 1995; final revision, Oct. 11, 1996. Associate Technical Editor: M. Shinozuka.

- *Definition* 3: A structure is wave controllable which means, $\exists i(i < n)$, $\forall x(0, n - i)$, $\forall t > 0$, $\exists u(\tau)(\tau \in (0, t))$ which results in $x(t', \mathbf{i}) = 0$ $(t' \geq 0)$ and $x(t, n - i) = 0$.
- *Criterion* 1: The degree of controllability of Eq. (1) is i, iff $R(\mathbf{B}(\mathbf{i}, r)) \supset R(\mathbf{A}(\mathbf{i}, n - i))$, i.e., rank $(\mathbf{B}(i, r))$ = rank $(\mathbf{B}(\mathbf{i}, r), \mathbf{A}(\mathbf{i}, n - i))$.
- *Criterion* 2: A structure is wave controllable, if
  (a) $\exists i(i < n)$, $R(\mathbf{B}(\mathbf{i}, r)) \supset R(\underline{\mathbf{A}}(\mathbf{i}, n - i))$.
  (b) $\exists P$, which makes rank $(\bar{B}, \overline{AB}, \ldots, \bar{A}^{(n-i-l)}\bar{B}) = n - i$.

The physical significance of *Definitions* 1 and 2, and *Criterion* 1 is that they testify whether a given spatial domain is undisturbed by an applied control force. A simple proof of the criterion and numerical simulation with the model of spring-mass system is given in Wang et al. (1995b). However, *Definition* 3 and *Criterion* 2 are used to testify whether the structure can be controlled to zero state, when (i) a given spatial domain is undisturbed by an applied control force, and (ii) a disturbance in a spatial domain is given. The *proof* of *Criterion* 2 and some numerical simulations with the models of spring-mass system is given in Wang et al. (1995b).

3 Reduced Order Control Design

We define the transformation of system (1) as follows:

$$\{x\} = \begin{bmatrix} \varphi_{11} & \varphi_{12} \\ \varphi_{21} & \varphi_{22} \end{bmatrix} \begin{Bmatrix} v_1 \\ v_2 \end{Bmatrix} = [\varphi]\{v\} \tag{6}$$

where

$$v_1 \in R^l, \quad v_2 \in R^{n-l} \tag{7a}$$

$$\varphi_{11} \in R^{l\times l}, \quad \varphi_{12} \in R^{l\times(n-l)},$$

$$\varphi_{21} \in R^{(n-l)\times l}, \quad \varphi_{22} \in R^{(n-l)\times(n-l)}. \tag{7b}$$

The transformation relies on the following conditions:

(a) φ can be inverted.
(b) $\{x\}_0 = [\varphi]\{v\}_0$.
(c) $\{v_2\}_0 = [0, 0, \ldots, 0]^T$, x_0 and v_0 are the initial conditions in different systems, respectively.

Substituting Eq. (6) into Eq. (1) leads to

$$[\varphi]\{\dot{v}\} = \mathbf{A}[\varphi]\{v\} + \mathbf{B}u. \tag{8}$$

Multiplying φ^{-1} on both sides of the above equation, we obtain

$$\dot{v} = \varphi^{-1}\mathbf{A}\varphi v + \varphi^{-1}\mathbf{B}u = \bar{\mathbf{A}}v + \bar{\mathbf{B}}u \tag{9}$$

which is called the image system, and vector v is a generalized coordinate.

Now, the control force is designed in the image system by the theory of wave control, which makes the disturbance be absorbed on the determined spatial domains, so that they are undisturbed and are reduced. Then the control design of the original system can be derived by the transformation in Eq. (6). Since the degree of controllability of Eq. (9) is i, according to *Criterion* 1, Eq. (9) can be rewritten as

$$\begin{Bmatrix} \dot{v}_3 \\ \dot{v}_4 \end{Bmatrix} = \begin{bmatrix} A_{11} & A_{12} \\ A_{21} & A_{22} \end{bmatrix} \begin{Bmatrix} v_3 \\ v_4 \end{Bmatrix} + \begin{bmatrix} B_{11} & B_{12} \\ B_{21} & B_{22} \end{bmatrix} \begin{Bmatrix} u_1 \\ u_2 \end{Bmatrix} \tag{10a}$$

where

$$v_3 \in R^{(n-i)}, \quad v_4 \in R^i, \quad u_1 \in R^{(r-i)}, \quad u_2 \in R^i \tag{10b}$$

in which A_{mj} and B_{mj} $(m = 1, 2; j = 1, 2)$ are the corresponding matrices. Assuming Eq. (10a) to be wave controllable, that is, *Criterion* 2 is satisfied. State v_4 is reduced, and Eq. (10a) becomes

$$A_{21}v_3 + B_{21}u_1 + B_{22}u_2 = 0 \tag{11}$$

$$\dot{v}_3 = A_{11}v_3 + B_{11}u_1 + B_{12}u_2 \tag{12}$$

which is the reduced order model on which the control force is designed. From the transformation in Eq. (6), we have

$$\{x\} = [\varphi]\{v\} = \begin{bmatrix} \varphi_{11} & \varphi_{12} \\ \varphi_{21} & \varphi_{22} \end{bmatrix} \begin{Bmatrix} v_3 \\ v_4 \end{Bmatrix}. \tag{13}$$

So the following expression is satisfied:

$$\{x\} = \begin{Bmatrix} x_3 \\ x_4 \end{Bmatrix} = \begin{Bmatrix} \varphi_{11}v_3 \\ \varphi_{21}v_3 \end{Bmatrix}, \tag{14}$$

which is the state response of the original system.

Through the above procedures, it shows that the theory studied is based on the general state (Eq. (1)) and the transformation (Eq. (6)). It is expected that a general engineering system can be designed according to the theory introduced. A simple example applying the above design procedures is given in Wang et al. (1996) using a spring-mass system model. A reduced control design of a plate system will be presented in next section according to the above theory.

4 Reduced Control Design of Plate

Consider a rectangular plate with simply supported boundary conditions, its dynamic equation and initial conditions are written as

$$\ddot{w}(x, y, t) + D\nabla^2\nabla^2 w(x, y, t) = 0 \tag{15a}$$

$$w(x, 0, t) = \frac{\partial^2 w}{\partial x^2} = 0 \tag{15b}$$

$$w(0, y, t) = \frac{\partial^2 w}{\partial y^2} = 0 \tag{15c}$$

$$w(x, y, 0) = A(x, y), \quad 0 \leq x \leq a, \quad 0 \leq y \leq b \tag{15d}$$

where the operator $\nabla^2\nabla^2 = \partial^4/\partial x^4 + 2(\partial^2\partial^2/\partial x^2\partial y^2) + \partial^4/\partial y^4$, a and b are the length and width of the plate, and $D = \sqrt{Eh^3/12(1 - \gamma^2)}$ is the plate material parameter.

Let

$$w(x, y, t) = \sum_{m=1}^{\infty} \sum_{n=1}^{\infty} \varphi_m(x)\psi_n(y)\eta_{mn}(t). \tag{16}$$

Substituting Eq. (16) into Eq. (15a–d), the eigenvalue solution is given as

$$\ddot{\eta}_{mn}(t) + \omega_{mn}^2\eta_{mn}(t) = 0 \tag{17a}$$

$$\omega_{mn} = \pi^2\left[\left(\frac{m}{a}\right)^2 + \left(\frac{n}{b}\right)^2\right]\sqrt{D} \tag{17b}$$

$$\varphi_{mn}(x) = \sin\frac{m\pi x}{a}, \quad \psi_{mn}(y) = \sin\frac{n\pi y}{b} \tag{17c}$$

$$\eta_{mn}(0) = \int_0^a\int_0^b w(x, y, 0)\varphi_m(x)\psi_n(y)dxdy \tag{17d}$$

where $m, n = 1, 2, \ldots, \infty$.

Rewriting Eq. (15a–d) in its discretized form, it leads to a lumped parameter free vibration system with an initial condition vector:

$$[\mathbf{M}]\{\ddot{w}\} + [\mathbf{K}]\{w\} = 0 \tag{18a}$$

$$\{w\}_0 = \{z\}_0 \tag{18b}$$

where $\mathbf{M}$ and $\mathbf{K}$ are the mass and stiffness matrices $\mathbf{M} \in R^{n\times n}$, and $\mathbf{K} \in R^{n\times n}$, and w is the discretized vector of the plate $w \in R^n$.

Assuming

$$\{w\} = [\phi]\{\eta\}, \tag{19}$$

substituting Eq. (19) into Eq. (18*a*) leads to

$$\ddot{\eta}_i + \omega_i^2 \eta_i = 0, \quad i = 1, 2, \dots n \tag{20}$$

and the modal matrix has the following orthogonal characteristics:

$$[\phi]^T[\mathbf{M}][\phi] = [I] \tag{21}$$

$$[\phi]^T[\mathbf{K}][\phi] = \begin{bmatrix} w_1^2 & & & \\ & w_2^2 & & \\ & & \ddots & \\ & & & w_n^2 \end{bmatrix}. \tag{22}$$

The control equation of the plate is given by

$$[\mathbf{M}]\{\ddot{w}\} + [\mathbf{K}]\{w\} = [\mathbf{B}]\{u\} \tag{23a}$$

$$\{w\}_0 = \{z\}_0 \tag{23b}$$

where u is the control vector $u \in R^m$, and $\mathbf{B}$ is the control matrix $\mathbf{B} \in R^{n\times m}$, whose function is to distribute the control vector of the structure. The reduced control design based on the wave domain control theory can be achieved as follows.

According to the method introduced above, the transformation is written as

$$\{w\} = [\mathbf{P}]\{w'\} \tag{24}$$

i.e.,

$$\begin{Bmatrix} w_1 \\ w_2 \end{Bmatrix} = \begin{bmatrix} p_{11} & P_{12} \\ P_{21} & P_{22} \end{bmatrix} \begin{Bmatrix} w_1' \\ w_2' \end{Bmatrix} \tag{25}$$

and the initial form is

$$\begin{Bmatrix} w_1 \\ w_2 \end{Bmatrix}_0 = \begin{bmatrix} P_{11} & P_{12} \\ P_{21} & P_{22} \end{bmatrix} \begin{Bmatrix} w_1' \\ w_2' \end{Bmatrix}_0 \tag{26}$$

where $\mathbf{P}$ is the transformation matrix whose inverse is $\mathbf{P}^{-1}$, and $w_1' \in R^{n-l}$, which expresses the initial disturbance of the image system.

Thus Eq. (23*a*) takes the form

$$[\mathbf{M}][\mathbf{P}]\{\ddot{w}'\} + [\mathbf{K}][\mathbf{P}]\{w'\} = [\mathbf{B}]\{u\}. \tag{27}$$

Multiplying $\mathbf{P}^{-1}\mathbf{M}^{-1}$ to Eq. (27) leads to

$$[\ddot{w}'] + [\mathbf{P}]^{-1}[\mathbf{M}]^{-1}[\mathbf{K}][\mathbf{P}]\{w'\} = [\mathbf{P}]^{-1}[\mathbf{M}]^{-1}[\mathbf{B}]\{u\} \tag{28}$$

i.e.,

$$\{\ddot{w}'\} + [\mathbf{K}']\{w'\} = [\mathbf{B}']\{u\} \tag{29}$$

where

$$[\mathbf{K}'] = [\mathbf{P}]^{-1}[\mathbf{M}]^{-1}[\mathbf{K}][\mathbf{P}],$$
$$[\mathbf{B}'] = [\mathbf{P}]^{-1}[\mathbf{M}]^{-1}[\mathbf{B}]. \tag{30}$$

The following condition must be satisfied before we can begin the reduced control design according to the wave domain control theory introduced in *Criterion* 1 expressed in the previous sections,

$$R(\mathbf{B}'(\mathbf{l}, m)) \supset R(\mathbf{K}'(\mathbf{l}, n - l)) \tag{31}$$

which means the spanning space of the matrix $R(\mathbf{B}'(\mathbf{l}, m))$ must include that of the matrix $R(\mathbf{K}'(\mathbf{l}, n - l))$. The physical interpretation of Eq. (31) is emphasized to assure the existence of the control vector u which makes the system (Eq. (29)) be wave domain controlled.

With the existence of control vector u, Eq. (28) becomes

$$\{\ddot{w}_1'\} + [K_{11}']\{w_1'\} = \mathbf{B}'(n - l, m)\{u\} = \{\tilde{u}_1\} \tag{32}$$

$$[\mathbf{K}_{21}']\{w_1'\} = \mathbf{B}'(\mathbf{l}, m)\{u\} = \{\tilde{u}_2\}. \tag{33}$$

The transformation matrix $\mathbf{P}$ can be expressed as

$$[\mathbf{P}] = \begin{bmatrix} P_{11} & 0 \\ P_{21} & I \end{bmatrix} \tag{34}$$

where $P_{11} \in R^{(n-l)\times(n-l)}$, $0 \in R^{(n-l)\times l}$, $P_{21} \in R^{l\times(n-l)}$, $I \in R^{l\times l}$, and

$$[P_{11}] = \text{diag}\left(\frac{w_{1i}}{w_{1i}'}\right), \quad i = 1, 2, \dots, n - l. \tag{35}$$

Therefore we can obtain

$$[\mathbf{P}]^{-1} = \begin{bmatrix} P_{11}^{-1} & 0 \\ -P_{21}P_{11}^{-1} & I \end{bmatrix} \tag{36}$$

where

$$[P_{11}]^{-1} = \text{diag}\left(\frac{w_{1i}'}{w_{1i}}\right), \quad i = 1, 2, \dots, n - 1. \tag{37}$$

In order to make $P_{21}(i, j)$, $(i = 1, 2, \dots, l; j = 1, 2, \dots, n - l)$ physical meaningful, we suggest that $P_{21}(i, j)$ should be formed based on the following principle. Let $P_{21}(i, j)$ be the displacement of point i when a unit force acts on point j. Back to Eq. (32) and Eq. (33), we now can investigate how to solve the image system.

From Eq. (32), we find that

$$[\mathbf{K}_{11}'] = [\mathbf{P}_{11}]^{-1}([\mathbf{M}]^{-1}[\mathbf{K}])_{11}[\mathbf{P}_{11}]. \tag{38}$$

According to eigenvalue problem, the matrix $\mathbf{K}_{11}'$ has the same eigenvalue with that of matrix $(\mathbf{M}^{-1}\mathbf{K})_{11}$, and the eigenmatrix of $\mathbf{K}_{11}'$ becomes

$$[x'] = [P_{11}]^{-1}[x] \tag{39}$$

where $[x]$ is the eigenmatrix of $(\mathbf{M}^{-1}\mathbf{K})_{11}$.

After the control vector $\tilde{u}$ is designed, the reduced order vector w' in its image system is controlled by the theories of wave domain control and wave control. Using the inverse transformation, we obtain

$$\begin{Bmatrix} w_1 \\ w_2 \end{Bmatrix} = \begin{bmatrix} P_{11} & 0 \\ P_{21} & I \end{bmatrix} \begin{Bmatrix} w_1' \\ 0 \end{Bmatrix} \tag{40}$$

i.e.,

$$w_1 = P_{11}w_1', \quad w_2 = P_{21}w_1', \tag{41}$$

and the control force in the original system is

$$\{u\} = [\mathbf{P}]\{\tilde{u}\}. \tag{42}$$

5 Results and Discussion

We provide a numerical simulation of a rectangular plate to illustrate the above design procedures. Consider a simply supported rectangular plate, whose material parameter $D = 6 \times 10^8$ GPa, and the length to width ratio $a/b = 2/3$.

The transformation is

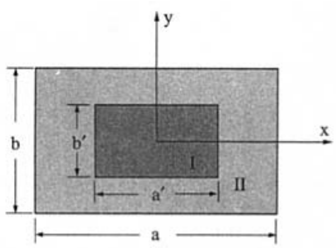

Fig. 1 General diagram of the example plate problem

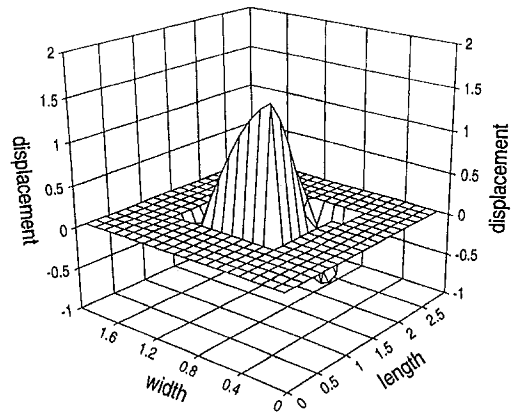

Fig. 2 Initial condition in the image system

$$\{w\} = [\mathbf{P}]\{w'\} \tag{43}$$

which makes

$$\begin{Bmatrix} w_1 \\ w_2 \end{Bmatrix} = \begin{bmatrix} P_{11} & 0 \\ P_{21} & I \end{bmatrix} \begin{Bmatrix} w_1' \\ 0 \end{Bmatrix}. \tag{44}$$

Actually, condition in Eq. (31) should be tested with a given distribution of control force. We let B' be a square matrix which satisfies condition in Eq. (31). We now investigate this problem.

In Fig. 1, a new model of an image system is given (Section I). The length-to-width ratio of the new model (in the center of the plate) is $a'/b' = 2/3$. The initial disturbances for the two models (the original and image systems) are shown in Figs. 2 and 3, respectively. The difference method is used in discretizing the original system. In the analysis, we use $(\mathbf{M}^{-1}\mathbf{K})_{11}$ to express the stiffness matrix of the model shown in Section I in Fig. 1. Its eigenvalue problem was stated in Eqs. (38) and (39).

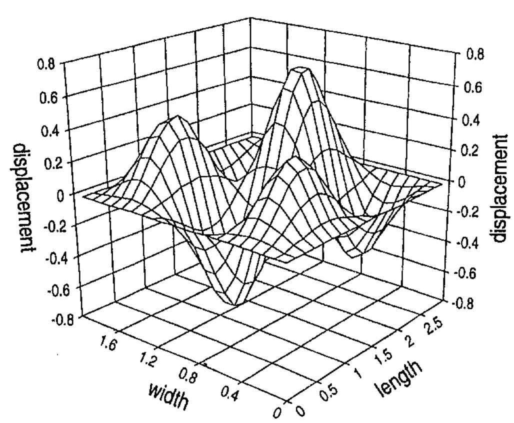

Fig. 3 Initial displacement in the original system

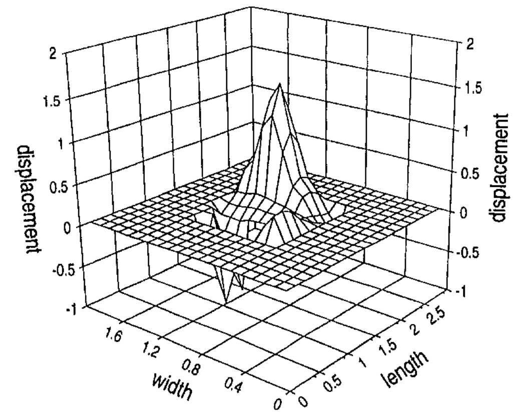

Fig. 4 Displacement at 1st time-step

Figures 4–9 show the control process of the displacement in the image system. The time-step used for these calculations is $\Delta t = 0.2$ s.

The feedback modal control method is used in the present design. The degree-of-freedom of the image system is 10×10. From the simulation, we observe that the displacement in the image system is well controlled after $t = 1.2$ s (after six time-steps). By using the inverse transformation (Eq. 6), we derive the control process of the displacement w in the original system shown in Figs. 10–15. The degree-of-freedom in the original plate system is 20×20. The inverse transformation is straight-

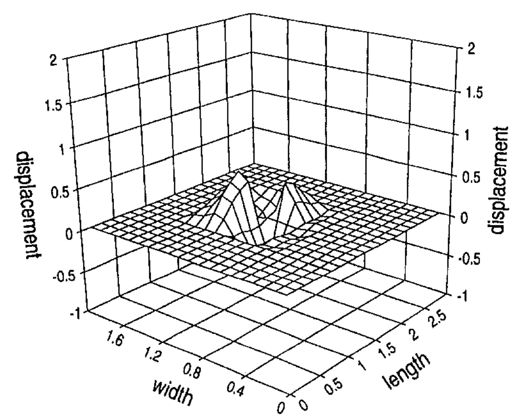

Fig. 5 Displacement at 2nd time-step

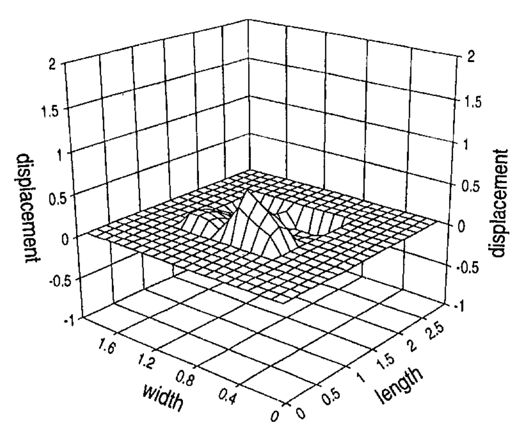

Fig. 6 Displacement at 3rd time-step

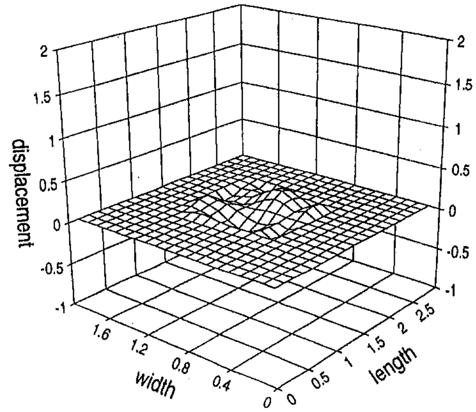

Fig. 7 Displacement at 4th time-step

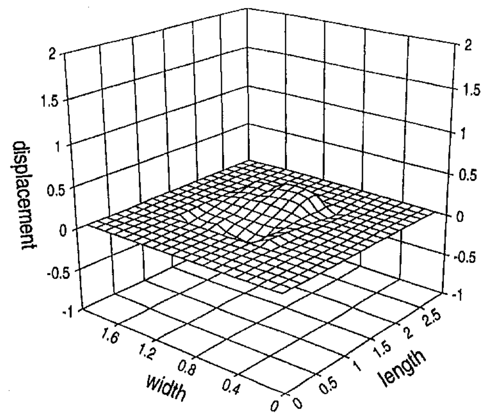

Fig. 8 Displacement at 5th time-step

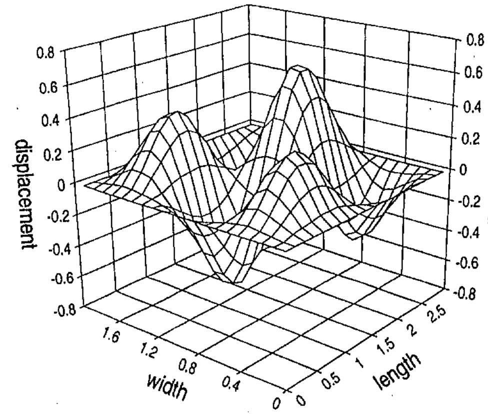

Fig. 10 Displacement at 1st time-step

By comparing the existing works on the design of structural reduced order with our present work, the following characteristics are concluded (1) all the design of control is derived based on one system *the image system* and with this image system, the theory of wave domain control and wave control can be applied; (2) the numbers of the reduced order of the proposed method can be very large depending on the selection of the image systems; (3) it is realized from the procedures of this method that the reduced state in the image system is undisturbed by the applied control force, unlike the other existing methods in which the state is reduced according to some indexes, for example, the degree of state controllability; and (4) since this new design is obtained based on the general state (Eq. (1)) and forward which involves only a single algebraic computation. From Figs. 10–15, it is seen that the original plate system is well controlled. The computation time has been tremendously reduced (by comparing the degree-of-freedom in the two systems which results in four times less) by using the reduced order control design.

6 Concluding Remarks

A new design of structural reduced order control is introduced in this paper, which is based on the concepts and criteria of structural wave domain control and wave control.

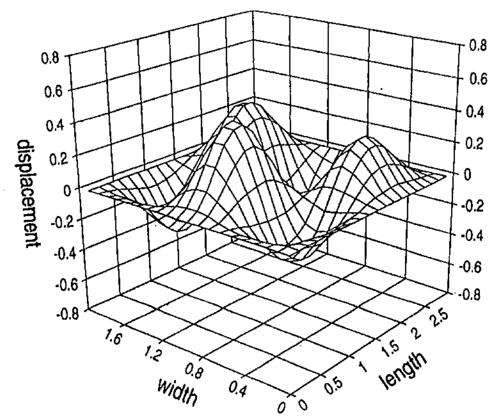

Fig. 11 Displacement at 2nd time-step

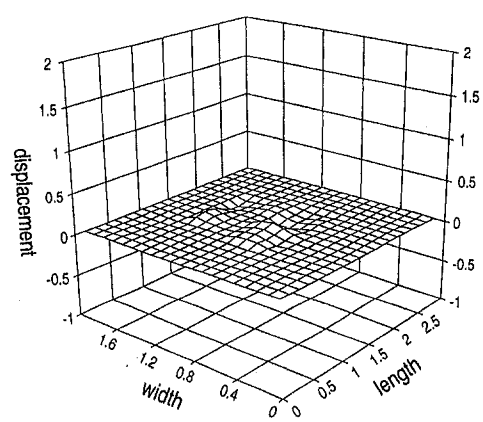

Fig. 9 Displacement at 6th time-step

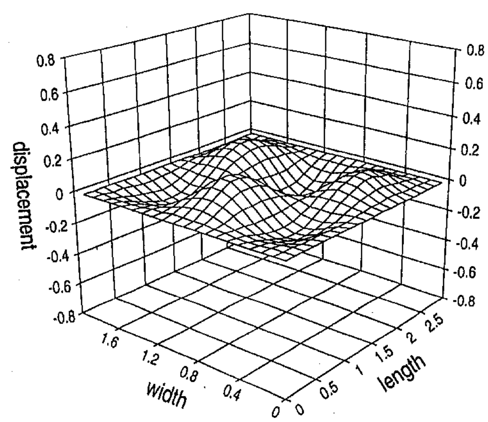

Fig. 12 Displacement at 3rd time-step

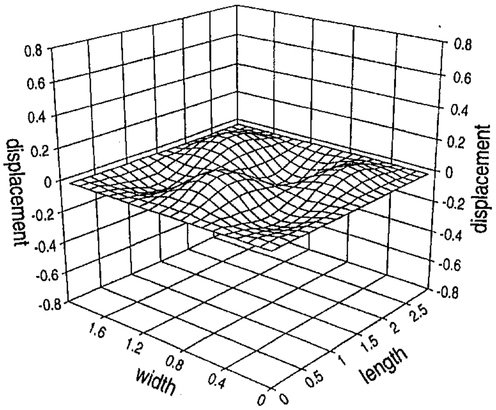

Fig. 13 Displacement at 4th time-step

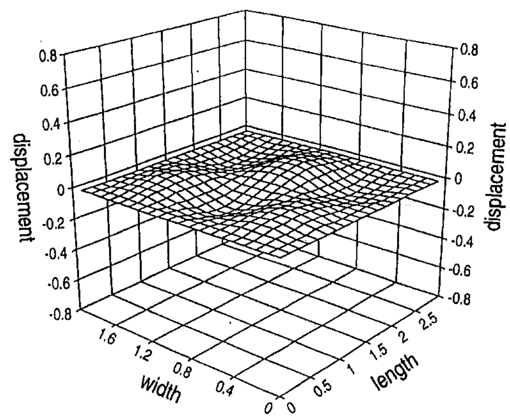

Fig. 14 Displacement at 5th time-step

the transformation (Eq. (6)), it provides us a large space for applying the theory of structural wave control design into a general engineering system, such as the special space domain control of a solar panel in space station.

The research on reduced order control design is only in its infant stage. Further research is needed, for example, which image system is "better" is still unsolved due to the large possible selections of image system with the initial state of the original system and the initial disturbance given in the image

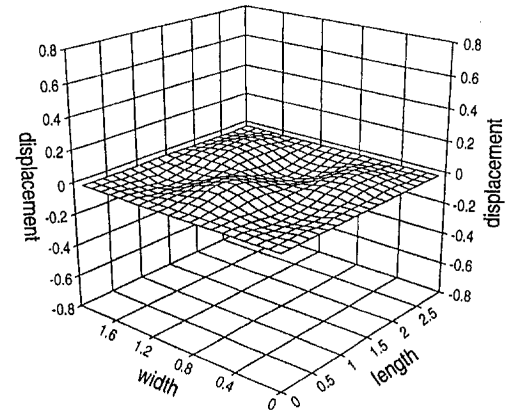

Fig. 15 Displacement at 6th time-step

system. From our earlier example, the image system used is a rectangular plate, which is only a special case. In actual applications, the image system may be of some irregular forms, so that the design will encounter some other difficulties.

References

Balas, M. J., 1986, "Finite-dimensional control of distributed parameter systems by Galerkin approximation of infinite dimensional controllers," *Journal of Mathematical Analysis and Applications*, Vol. 114, pp. 17–36.

Gibson, J. S., 1986, "A note on stabilization of infinite dimensional linear oscillators by compact linear feedback," *SIAM Journal of Control and Optimization*, Vol. 18, pp. 311–316.

Hughes, P. C., and Skelton, R. E., 1981, "Modal truncation for flexible spacecraft," *Journal of Guidance and Control*, Vol. 4, pp. 291–297.

Wang, Q., and Wang, D. J., 1994a, "A reduced order model about structural wave control based upon the concept of degree of controllability," *IEEE Transaction on Automatic Control*, Vol. 39, pp. 1711–1713.

Wang, Q., and Wang, D. J., 1994b, "Some researches and new concepts about the controllability of structural wave control," ISTS'94-S-10, International Symposium on Space Technology and Science, Yokoham, May 15–24.

Wang, Q., and Wang, D. J., 1994c, "Some methods and problems in structural wave control," Asia and pacific Conference on Aerospace Technology and Science, Hangzhou, China.

Wang, Q., Leung, A. Y. T., and Wang, D. J., 1995a, "A new reduced control design based on the theory of wave domain control." 1995 IEEE International Conference on Systems, Man and Cybernetics, Vancouver, British Columbia, Canada, Oct. 22–25.

Wang, D. J., Wang, Q., and Leung, A. Y. T., 1995b, "Successive decrease and concept of harmonic wave filter in structure wave control," *Proceedings of ASME Design Engineering Technology Conference*, Boston, MA, Sept. 17.

Wang, Q., Liew, K. M., and Wang, D. J., 1996, "Space domain control in flexible structures—Its concepts, results and problems," *Journal of Sound and Vibration*, submitted for publication.

A Layer-Wise Laminate Theory Rationally Deduced From the Three-Dimensional Elasticity

P. Bisegna
Department of Civil Engineering,
University of Rome "Tor Vergata",
00133 Rome, Italy

E. Sacco
Department of Industrial Engineering,
University of Cassino,
03043 Cassino, Italy

A layer-wise theory of laminated plates, which accounts for piecewise constant shear strain in the thickness, is derived from the three-dimensional elasticity theory by imposing suitable constraints on the strain and stress fields. At this aim, the Hu-Washizu functional of the three-dimensional elasticity is modified according to the Lagrange multipliers theory. In fact, a nonstandard application of the Lagrange theory is presented, because of the simultaneous presence of constraints on dual spaces. The imposed constraints make reactive strain and stress fields arise. Thus, it is necessary to distinguish between elastic and total strain and stress fields. The difference between them is emphasized in a numerical application.

1 Introduction

A composite laminate is made up of several layers of thin laminae bonded together to act as an integral structural element. Because of its specific geometry, i.e. one dimension is fairly smaller than the other two, the analysis of a composite laminate is usually carried out by means of approximate two-dimensional models. The reduction of the three-dimensional elastostatic problem to a two-dimensional approximate one is performed by considering opportune assumptions on the strain or stress fields. Thus, several laminate, as well as plate, theories have been presented in the specialized literature, depending on the particular hypotheses considered. Two different approaches have been proposed to investigate the response of a laminated composite plate. They lead to two classes of laminate theories: the single-layer theories and the multilayer (or layer-wise) theories.

Single-layer theories are direct extensions to laminates of plate theories. They can be regarded as degenerated laminate models, since global assumptions on the strain or stress fields in the whole thickness of the laminate are adopted. Thus, the laminate is reduced to a single-layer plate with equivalent anisotropic material properties. This is the case of the classical laminate theory (Reissner and Stavsky, 1961; Stavsky, 1961; Lekhnitskii, 1968; Ambartsumyan, 1970), which is an extension of the classical plate theory based on Kirchhoff-Love's assumptions. It neglects the shear deformation in the thickness of the laminate. This fact represents a severe limitation to the use of the classical laminate theory, since composite laminates usually have low shear moduli with respect to the longitudinal moduli and hence are subjected to non-negligible shear deformations. Furthermore, the transverse stresses (i.e., the shear stress and the normal stress in the thickness direction) computed by the classical laminate theory are not very accurate. It can be pointed out that the interlaminar stresses (i.e., the transverse stresses at the interface between two adjacent laminae) play a very important role in the damage of composite laminates, since they may lead to delamination. A justification of the classical laminate theory has been presented by Lembo and Podio-Guidugli (1991), on the basis of a procedure proposed by Podio-Guidugli (1989) for the analysis of homogeneous plates.

The first-order shear deformation laminate theory (Yang et al., 1966; Whitney and Pagano, 1970) is based on the Reissner (1945), Hencky (1947), and Mindlin (1951) plate theories, and accounts for the shear deformation in a very simple way. Then, several higher-order laminate theories have been proposed (Lo et al., 1977; Reddy, 1984; Murthy and Vellaichamy, 1987). It can be emphasized that the transverse stresses obtained by using the constitutive equations are discontinuous in the thickness coordinate. Thus, many authors (e.g., Lo et al., 1978) suggested to use the local, i.e., three-dimensional, equilibrium equations to carry out the stresses in the thickness of the laminate, but did not justify that procedure.

The multilayer (or layer-wise) theories are obtained by introducing hypotheses on the behavior of each layer of the laminate. One of the first layer-wise theories has been proposed by Seide (1980). He assumed that the shear deformation is constant in each layer of the laminate, but differs from layer to layer. The continuity of the transverse stresses was enforced, and the equilibrium equations of the laminate were deduced from the equilibrium equations of each lamina. Reddy (1987) proposed a general approach to the multilayer theories, deducing the equilibrium equations by using the Hamilton principle. Barbero and Reddy (1989) and Barbero et al. (1990) developed and applied to several technical problems a layer-wise theory based on piecewice linear displacements in the thickness of the laminate. Then, Di Sciuva (1987) and Di Sciuva and Icardi (1993) enforced the continuity of the stresses in the thickness direction, and so obtained a model which requires only five generalized displacements to describe the kinematics of the laminate deformation. It is worth to note that also for the multilayer theories, the transverse stresses are computed by using the local equilibrium equations, also when the stress continuity at the interface has been imposed. Xianquiang and Dahsin (1992) presented a refined multilayer theory, by considering piecewise nonlinear displacement distribution in the thickness direction. Furthermore, they imposed the continuity of the transverse stresses at the interface of the layers, and computed those stresses by the constitutive equations. Fraternali and Reddy (1993) used the penalty method to enforce the perfect bonding of adjacent layers, and to evaluate the interlaminar stresses.

Among the several multilayer theories proposed in the literature, in this paper the layer-wise theory by Barbero and Reddy (1989), which assumes constant transverse shear strains in each layer, is deduced in the framework of constrained three-dimensional elasticity, by using a general procedure presented by

Contributed by the Applied Mechanics Division of The American Society of Mechanical Engineers for publication in the ASME Journal of Applied Mechanics.

Discussion on this paper should be addressed to the Technical Editor, Professor Lewis T. Wheeler, Department of Mechanical Engineering, University of Houston, Houston, TX 77204-4792, and will be accepted until four months after final publication of the paper itself in the ASME Journal of Applied Mechanics.

Manuscript received by the ASME Applied Mechanics Division, Jan. 26, 1996; final revision, Oct. 20, 1996. Associate Technical Editor: J. N. Reddy.

Bisegna and Sacco (1995, 1997). In fact, that procedure is based on the conjecture that plate theories, as well as laminate theories, can be derived from the three-dimensional elasticity theory when suitable frictionless constraints on the spaces of strain and stress fields are enforced. In other words, the specific approximations introduced to define a plate or laminate theory are regarded as internal constraints to be imposed on the three-dimensional body.

The constrained elasticity problem is treated by using the Lagrange multipliers theory, as suggested also by Antman and Marlow (1991).

The proposed procedure allows to obtain a rational justification of known plate or laminate theories from the three-dimensional elasticity. Such a justification is not a speculative issue, but leads to a safer technical use of those theories.

The paper is organized as follows. In Section 2 the elastic equilibrium problem is formulated in the framework of the constrained elasticity. Special attention is paid to the case of a simultaneous presence of constraints acting on both the dual spaces of strain fields and stress fields. Those constraints make a reactive stress field and a reactive strain field arise, respectively. As a consequence, it is necessary to distinguish between elastic and total strain or stress fields.

In Section 3 the problem of laminated plates is introduced. The main section of the paper is Section 4. There, the hypotheses on which the layer-wise theory by Barbero and Reddy (1989) relies are recalled and interpreted as constraints acting on both the stress and strain fields. On the basis of the results reported in Section 2, a Lagrangian functional, derived by the Hu-Washizu functional, is built up. Its stationary conditions are given, and the classical potential energy formulation of the layer-wise theory by Barbero and Reddy is obtained. In particular, the use of the so-called reduced constitutive law (Cauchy, 1829) is clearly justified.

A numerical application is developed in Section 5. The problem of the simply supported laminated plate is considered. Elastic and total strain and stress fields supplied by the procedure presented in this paper are compared with the results given by the exact three-dimensional solution (Pagano, 1970; Srinivas and Rao, 1970).

2 Constrained Elasticity

Let a body Ω, i.e., a regular region of the three-dimensional Euclidean point space, be given. A Cartesian frame (O, x_1, x_2, x_3) is fixed. Cartesian components are denoted by subscript indices: latin indices imply the values $\{1, 2, 3\}$, while greek indices imply the values $\{1, 2\}$. The Einstein summation convention is adopted. A comma followed by an index denotes partial differentiation with respect to the relevant coordinate (i.e., $f_{,i} = \partial f/\partial x_i$). The material comprising Ω is assumed to be linearly elastic, and its elasticity tensor is C_{ijhk}: It has the major and minor symmetries. The body Ω is subjected to volume forces b_i, and surface forces p_i on the part $\partial_f\Omega$ of its boundary $\partial\Omega$. In addition, an assigned displacement field s_{0i} is imposed on $\partial_s\Omega := \partial\Omega/\partial_f\Omega$.

In the framework of the infinitesimal deformation theory, the unique solution of the elastostatic problem is given by the displacement vector field s_i, the symmetric strain tensor field ϵ_{ij}, and the symmetric stress tensor field σ_{ij} over Ω which satisfy the compatibility, equilibrium, and constitutive equations (e.g., Gurtin, 1972).

The elastic equilibrium problem can be recast by adopting several variational formulations (Reissner, 1950; Washizu, 1968; Oden and Reddy, 1976). Here the Hu-Washizu formulation is briefly recalled: "find the displacement, strain and stress fields which make stationary the Hu-Washizu functional:

$$\begin{aligned} H(s_i, \epsilon_{ij}, \sigma_{ij}) := & \int_\Omega \tfrac{1}{2} C_{ijhk}\epsilon_{ij}\epsilon_{hk} dv - \int_\Omega \sigma_{ij}\epsilon_{ij} dv \\ & + \int_\Omega \sigma_{ij}(s_{i,j} + s_{j,i})/2 dv - \int_\Omega b_i s_i dv \\ & - \int_{\partial_f\Omega} p_i s_i da - \int_{\partial_s\Omega} \sigma_{ij} n_j (s_i - s_{0i}) da," \end{aligned} \quad (1)$$

where n_i is the outward normal unit vector to $\partial\Omega$, and dv, da denote the volume element in Ω and the surface element on $\partial\Omega$, respectively.

Laminate theories, as well as plate theories, can be regarded as very special elastostatic problems. They can be derived from the three-dimensional elasticity, by imposing suitable constraints on the strain and stress fields.

The Lagrange multipliers theory (Lyusternik, 1934; Luenberger, 1969) can be adopted in order to formulate a general three-dimensional constrained elastic equilibrium problem involving constraints on both the strain field and the stress field. This is a quite subtle situation, since both a reactive stress field and a reactive strain field arise as a consequence of the imposed constraints.

As a matter of fact, it is shown that two different mechanical situations may take place, corresponding to two different Lagrangian functionals, both derived by the Hu-Washizu functional. The stationary conditions of those Lagrangian functionals are obtained and the reactive fields which arise as a consequence of the enforced constraints are determined. It is worth noting that the representation form of such reactive fields is not postulated, but is obtained as a consequence of the machinery adopted.

Let the strain and stress fields be constrained to belong to the kernel of the linear (possibly differential) operators G_{ijhk} and H_{ijhk}, both satisfying the minor symmetries. Two different Lagrangian functionals may be adopted, leading to different ways of enforcing the constraints (Bisegna and Sacco, 1996):

$$\begin{aligned} & L_{\mathrm{I}}(s_i, \epsilon_{ij}, \sigma_{ij}, \chi_{ij}, \omega_{ij}) \\ & := H(s_i, \epsilon_{ij}, \sigma_{ij}) - \int_\Omega \chi_{ij} G_{ijhk}\epsilon_{hk} dv - \int_\Omega \omega_{ij} H_{ijhk}\sigma_{hk} dv, \end{aligned} \quad (2)$$

or

$$\begin{aligned} & L_{\mathrm{II}}(s_i, \epsilon_{ij}, \sigma_{ij}, \chi_{ij}, \omega_{ij}) \\ & := H(s_i, \epsilon_{ij}, \sigma_{ij}) - \int_\Omega \chi_{ij} G_{ijhk}\epsilon_{hk} dv - \int_\Omega \omega_{ij} H_{ijhk}\sigma_{hk} dv \\ & \qquad - \int_\Omega G^*_{ijhk}\chi_{hk} H^*_{ijpq}\omega_{pq} dv, \end{aligned} \quad (3)$$

where the symmetric tensors χ_{ij}, ω_{ij} are Lagrange multipliers and G^*_{ijhk}, H^*_{ijhk} denote the adjoint operators of G_{ijhk}, H_{ijhk}, respectively. Note that G^*_{ijhk}, H^*_{ijhk} are linear operators which may contain field and boundary terms. The stationary condition of both the functionals (2) and (3) with respect to s_i yields the equilibrium equations

$$\begin{cases} \sigma_{ij,j} + b_i = 0 & \text{in} \quad \Omega \\ \sigma_{ij} n_j = p_i & \text{on} \quad \partial_f\Omega; \end{cases} \quad (4)$$

that one with respect to ϵ_{ij} yields the constitutive equations

$$\sigma_{ij} + G^*_{ijhk}\chi_{hk} = C_{ijhk}\epsilon_{hk} \quad \text{in} \quad \Omega; \quad (5)$$

that one with respect to σ_{ij} yields the compatibility equations

$$\begin{cases} \epsilon_{ij} + H^*_{ijhk}\omega_{hk} = (s_{i,j} + s_{j,i})/2 & \text{in} \quad \Omega \\ s_i = s_{0i} & \text{on} \quad \partial_s\Omega. \end{cases} \quad (6)$$

For the sake of brevity, let the following definitions be introduced: the *total* strain field is the symmetric part of the gradient of the displacement field; the *total* stress field satisfies the equilibrium equations; the *elastic* stress and strain fields are related to each other by the linear elastic constitutive relationships. Hence, by Eq. (4), (5), and (6), it turns out that σ_{ij} and $\epsilon_{ij} + H^{*}_{ijhk}\omega_{hk}$ are the total stress and strain fields, respectively, while $\sigma_{ij} + G^{*}_{ijhk}\chi_{hk}$ and ϵ_{ij} are the elastic stress and strain fields, respectively. As a consequence, the reactive stress and strain fields, defined as the difference between the total and elastic fields, turn out to be $-G^{*}_{ijhk}\chi_{hk}$ and $H^{*}_{ijhk}\omega_{hk}$, respectively.

The stationary conditions of the functional (2) with respect to χ_{ij} and ω_{ij} yield, respectively, the constraint equations

$$G_{ijhk}\epsilon_{hk} = 0 \quad \text{and} \quad H_{ijhk}\sigma_{hk} = 0. \tag{7}$$

On the other hand, the stationary conditions of the functional (3) with respect to χ_{ij} and ω_{ij} yield, respectively, the constraint equations

$$G_{ijhk}(\epsilon_{hk} + H^{*}_{hkpq}\omega_{pq}) = 0 \quad \text{and}$$
$$H_{ijhk}(\sigma_{hk} + G^{*}_{hkpq}\chi_{pq}) = 0. \tag{8}$$

As a consequence, the following conclusion can be drawn: if the constraints (7), acting on the elastic strain field and on the total stress field, have to be enforced, then the Lagrangian functional (2) must be adopted; on the other hand, if the constraints (8), acting on the total strain field and on the elastic stress field, have to be enforced, then the Lagrangian functional (3) must be considered.

Both those ways of imposing constraints are of interest in mechanics. In particular, the latter one is used in the following to deduce a layer-wise theory of laminated plates in the framework of three-dimensional constrained elasticity.

3 The Problem of the Laminated Plate

It is supposed that Ω is a plate-like body, with middle cross section $\mathcal{P}$. The Cartesian frame (O, x_1, x_2, x_3) is chosen with the x_1 and x_2-axes parallel to $\mathcal{P}$. The laminate Ω is made by N perfectly bonded layers. In the following any quantity relevant to the lth layer is discriminated by a superscript index$^{(l)}$, and the summation over a repeated layer index (l or m) is excluded. The lth layer occupies the region $\mathcal{P} \times]\zeta_-^{(l)}, \zeta_+^{(l)}[= \Omega^{(l)}$, where the scalars $\zeta_\pm^{(l)}$ are such that $\zeta_+^{(l)} = \zeta_-^{(l+1)}$. Hence, the thickness of the lth layer is $h^{(l)} = \zeta_+^{(l)} - \zeta_-^{(l)}$.

The laminate is acted upon by volume forces b_i. The boundary $\partial\mathcal{P}$ of $\mathcal{P}$ is subdivided into two complementary parts, say $\partial_s\mathcal{P}$ and $\partial_f\mathcal{P}$. Such a subdivision subordinates a partition of the lateral boundary of $\Omega^{(l)}$ into $\partial_s\mathcal{P} \times]\zeta_-^{(l)}, \zeta_+^{(l)}[= \partial_s\Omega^{(l)}$ and $\partial_f\mathcal{P} \times]\zeta_-^{(l)}, \zeta_+^{(l)}[= \partial_f\Omega^{(l)}$, where the displacement s_{0i} and the surface tractions $\hat{p}_i$ are assigned, respectively. On the upper (+) and lower (−) faces of Ω the surface tractions $p_i^{\pm}$ are assigned.

Each layer of the laminate is composed by a linearly elastic homogeneous material, having at least a monoclinic symmetry, with the symmetry plane parallel to $\mathcal{P}$. As a consequence, $C_{\alpha\beta\gamma3} = C_{33\gamma3} = 0$.

The Hu-Washizu functional (1), specialized to the case of a laminate, can be written as

$$H = \sum_{l=1}^{N} \frac{1}{2}\int_{\Omega^{(l)}} C^{(l)}_{ijhk}\epsilon^{(l)}_{ij}\epsilon^{(l)}_{hk}dv + \sum_{l=1}^{N}\int_{\Omega^{(l)}} \sigma^{(l)}_{ij}[(s^{(l)}_{i,j} + s^{(l)}_{j,i})/2 - \epsilon^{(l)}_{ij}]dv - \sum_{l=1}^{N}\int_{\Omega^{(l)}} b^{(l)}_i s^{(l)}_i dv - \sum_{l=1}^{N}\int_{\partial_f\Omega^{(l)}} \hat{p}^{(l)}_i s^{(l)}_i dl dx_3 - \sum_{l=1}^{N}\int_{\partial_s\Omega^{(l)}} \sigma^{(l)}_{i\alpha}n_\alpha(s^{(l)}_i - s^{(l)}_{0i})dl dx_3 - \int_{\mathcal{P}} p^-_i s^{(1)}_i|_{\zeta^{(1)}_-} da + \sum_{l=1}^{N-1}\int_{\mathcal{P}} \sigma^{(l+1)}_{i3}(s^{(l+1)}_i - s^{(l)}_i)|_{\zeta^{(l)}_+} da - \int_{\mathcal{P}} p^+_i s^{(N)}_i|_{\zeta^{(N)}_+} da, \tag{9}$$

where $\cdot\,|_{\zeta^{(l)}_\pm}$ is the value of $(\cdot)$ at $x_3 = \zeta^{(l)}_\pm$, and dl, dx_3 denote the arc element along $\partial\mathcal{P}$, and the line element along x_3, respectively.

The stationary conditions of the functional H with respect to $s^{(l)}_i$, $\sigma^{(l)}_{ij}$, $\epsilon^{(l)}_{ij}$ yield the equilibrium, compatibility, and constitutive equations governing the elastic equilibrium problem for the laminate Ω, regarded as a three-dimensional body.

4 A Layer-Wise Theory

The layer-wise theory by Barbero and Reddy (1989) is based on the following hypotheses:

(i) the normal stress in the thickness direction is assumed to vanish;
(ii) the normal strain in the thickness direction is assumed to vanish;
(iii) the transverse shear strain is assumed to be constant in each layer (the constant value may be different in different layers).

The hypotheses (i), (ii), and (iii), which of course introduce approximations in the equilibrium problem for the laminate, are regarded here as constraints for the three-dimensional body Ω. In particular, the operators G_{ijhk} and H_{ijhk} in the lth layer are such that

$$G^{(l)}_{ijhk}\epsilon^{(l)}_{hk} = \begin{pmatrix} 0 & 0 & \epsilon^{(l)}_{13,3} \\ 0 & 0 & \epsilon^{(l)}_{23,3} \\ \epsilon^{(l)}_{13,3} & \epsilon^{(l)}_{23,3} & \epsilon^{(l)}_{33} \end{pmatrix}_{ij},$$

$$\text{and} \quad H^{(l)}_{ijhk}\sigma^{(l)}_{hk} = \begin{pmatrix} 0 & 0 & 0 \\ 0 & 0 & 0 \\ 0 & 0 & \sigma^{(l)}_{33} \end{pmatrix}_{ij}. \tag{10}$$

It can be emphasized that the hypotheses (ii) and (iii) are used by Barbero and Reddy (1989) to represent the displacement field: hence, they are constraints on the total strain field. On the contrary, the hypothesis (i) is introduced into the constitutive equations; hence, it is a constraint on the elastic stress field.

As a consequence, the Lagrangian functional (3) must be used to deduce the layer-wise theory from the three-dimensional elasticity. To this end, starting from the Hu-Washizu functional reported in Eq. (9), the Lagrangian functional for the laminated plate, leading to the layer-wise theory, is

$$L = H - \sum_{l=1}^{N}\int_{\Omega^{(l)}} (\omega^{(l)}_{33}\sigma^{(l)}_{33} + \chi^{(l)}_{33}\epsilon^{(l)}_{33} + 2\chi^{(l)}_{\alpha3}\epsilon^{(l)}_{\alpha3,3})dv - \sum_{l=1}^{N}\int_{\Omega^{(l)}} \omega^{(l)}_{33}\chi^{(l)}_{33}dv. \tag{11}$$

The stationary conditions of this Lagrangian functional with respect to $s^{(l)}_i$, $\sigma^{(l)}_{ij}$, $\epsilon^{(l)}_{ij}$, $\omega^{(l)}_{ij}$, and $\chi^{(l)}_{ij}$ yield the equilibrium, compatibility, constitutive, and constraint equations governing the elastic equilibrium problem for the laminate Ω, regarded as a three-dimensional *constrained* body. They are reported in Table 1.

In particular, it turns out that the total and elastic stress fields are, respectively,

$$\begin{pmatrix} \sigma_{11}^{(l)} & \sigma_{12}^{(l)} & \sigma_{13}^{(l)} \\ \sigma_{12}^{(l)} & \sigma_{22}^{(l)} & \sigma_{23}^{(l)} \\ \sigma_{13}^{(l)} & \sigma_{23}^{(l)} & \sigma_{33}^{(l)} \end{pmatrix} \quad \text{and}$$

$$\begin{pmatrix} \sigma_{11}^{(l)} & \sigma_{12}^{(l)} & \sigma_{13}^{(l)} - \chi_{13,3}^{(l)} \\ \sigma_{12}^{(l)} & \sigma_{22}^{(l)} & \sigma_{23}^{(l)} - \chi_{23,3}^{(l)} \\ \sigma_{13}^{(l)} - \chi_{13,3}^{(l)} & \sigma_{23}^{(l)} - \chi_{23,3}^{(l)} & \sigma_{33}^{(l)} + \chi_{33}^{(l)} \end{pmatrix}, \tag{12}$$

while the total and elastic strain fields are, respectively,

$$\begin{pmatrix} \epsilon_{11}^{(l)} & \epsilon_{12}^{(l)} & \epsilon_{13}^{(l)} \\ \epsilon_{12}^{(l)} & \epsilon_{22}^{(l)} & \epsilon_{23}^{(l)} \\ \epsilon_{13}^{(l)} & \epsilon_{23}^{(l)} & \epsilon_{33}^{(l)} + \omega_{33}^{(l)} \end{pmatrix} \quad \text{and} \quad \begin{pmatrix} \epsilon_{11}^{(l)} & \epsilon_{12}^{(l)} & \epsilon_{13}^{(l)} \\ \epsilon_{12}^{(l)} & \epsilon_{22}^{(l)} & \epsilon_{23}^{(l)} \\ \epsilon_{13}^{(l)} & \epsilon_{23}^{(l)} & \epsilon_{33}^{(l)} \end{pmatrix}. \tag{13}$$

When the stationary conditions with respect to $\sigma_{ij}^{(l)}$ and $\epsilon_{ij}^{(l)}$ are a priori satisfied and substituted into the Lagrangian functional L, a potential energy functional Ψ is obtained:

$$\begin{aligned}
\Psi = \sum_{l=1}^{N} \frac{1}{2} \int_{\Omega^{(l)}} & [C_{\alpha\beta\gamma\delta}^{(l)}(s_{\alpha,\beta}^{(l)} + s_{\beta,\alpha}^{(l)})/2(s_{\gamma,\delta}^{(l)} + s_{\delta,\gamma}^{(l)})/2 \\
& + C_{\alpha\beta 33}^{(l)}(s_{\alpha,\beta}^{(l)} + s_{\beta,\alpha}^{(l)})(s_{3,3}^{(l)} - \omega_{33}^{(l)}) + C_{3333}^{(l)}(s_{3,3}^{(l)} - \omega_{33}^{(l)})^2 \\
& + C_{\alpha 3\beta 3}^{(l)}(s_{3,\alpha}^{(l)} + s_{\alpha,3}^{(l)})(s_{3,\beta}^{(l)} + s_{\beta,3}^{(l)})]dv \\
& - \sum_{l=1}^{N} \int_{\Omega^{(l)}} b_i^{(l)} s_i^{(l)} dv - \sum_{l=1}^{N} \int_{\partial_f \Omega^{(l)}} \hat{p}_i^{(l)} s_i^{(l)} dl dx_3 \\
& - \int_{\mathcal{P}} (p_i^- s_i^{(1)}|_{\zeta_-^{(1)}} + p_i^+ s_i^{(N)}|_{\zeta_+^{(N)}}) da \\
& + \sum_{l=1}^{N} \int_{\Omega^{(l)}} [\chi_{\alpha 3,3}^{(l)}(s_{3,\alpha}^{(l)} + s_{\alpha,3}^{(l)}) - \chi_{33}^{(l)} s_{3,3}^{(l)}] dv.
\end{aligned} \tag{14}$$

It should be noted, however, that Ψ depends upon the reactive fields and is defined on the manifold:

$$\begin{aligned}
s_i^{(l)} = s_{0i}^{(l)} \quad & \text{on} \quad \partial_s \Omega^{(l)}, \quad l = 1 \,.\,. N \\
s_i^{(l+1)} = s_i^{(l)} \quad & \text{on} \quad \mathcal{P} \times \{\zeta_+^{(l)}\}, \quad l = 1 \,.\,. N-1 \\
\chi_{\alpha 3}^{(l)} = 0 \quad & \text{on} \quad \mathcal{P} \times \{\zeta_\pm^{(l)}\}, \quad l = 1 \,.\,. N.
\end{aligned} \tag{15}$$

In order to obtain a potential-energy functional which does not depend upon the Lagrangian multipliers, it is sufficient to make the stationary conditions of Ψ with respect to the Lagrangian multipliers a-priori satisfied. The stationary condition of Ψ with respect to $\omega_{33}^{(l)}$ is

$$C_{33\alpha\beta}^{(l)}(s_{\alpha,\beta}^{(l)} + s_{\beta,\alpha}^{(l)})/2 + C_{3333}^{(l)} s_{3,3}^{(l)} = C_{3333}^{(l)} \omega_{33}^{(l)}. \tag{16}$$

The stationary conditions of Ψ with respect to $\chi_{33}^{(l)}$ and $\chi_{\alpha 3}^{(l)}$ are, respectively,

$$s_{3,3}^{(l)} = 0 \quad \text{and} \quad (s_{3,\alpha}^{(l)} + s_{\alpha,3}^{(l)})_{,3} = 0. \tag{17}$$

Equations (16) and (17) hold in $\Omega^{(l)}$, for $l = 1 \,.\,. N$.

From Eqs. (17), the following representation formulas for the displacement field can be deduced:

$$\begin{aligned}
s_\alpha^{(l)}(x_1, x_2, x_3) &= u_\alpha^{(l)}(x_1, x_2) + x_3 \varphi_\alpha^{(l)}(x_1, x_2) \\
s_3^{(l)}(x_1, x_2, x_3) &= w^{(l)}(x_1, x_2),
\end{aligned} \tag{18}$$

where $u_\alpha^{(l)}$, $\varphi_\alpha^{(l)}$, and $w^{(l)}$ are unknown functions. The scalar function $w^{(l)}$ is the deflection of the lth layer. The functions $u_\alpha^{(l)}$ and $\varphi_\alpha^{(l)}$ are the in-plane dispacement and rotation of the fibers parallel to x_3 of the lth layer, respectively. As a consequence of Eqs. (15), it follows that the unknown functions $w^{(l)}$, $u_\alpha^{(l)}$, and $\varphi_\alpha^{(l)}$ must satisfy the following continuity conditions in $\mathcal{P}$, for $l = 1 \,.\,. N-1$:

$$w^{(l+1)} = w^{(l)}, \quad u_\alpha^{(l+1)} + \zeta_-^{(l+1)} \varphi_\alpha^{(l+1)} = u_\alpha^{(l)} + \zeta_+^{(l)} \varphi_\alpha^{(l)}, \tag{19}$$

and the following constraint equations on $\partial_s \mathcal{P}$, for $l = 1 \,.\,. N$:

$$\begin{aligned}
w^{(l)} &= s_{03}^{(l)}, \\
u_\alpha^{(l)} + x_3 \varphi_\alpha^{(l)} &= s_{0\alpha}^{(l)}, \quad \text{for} \quad x_3 \in \,]\zeta_-^{(l)}, \zeta_+^{(l)}[.
\end{aligned} \tag{20}$$

From Eqs. (19) and (20) some compatibility conditions on the data $s_{0i}^{(l)}$ can be easily deduced. In fact, the prescribed transversal dispacement must be constant in the thickness, while the prescribed in-plane displacement must be continuous and piecewise linear.

In order to make the continuity conditions (19) a priori satisfied, the following representation for the functions $w^{(l)}$, $u_\alpha^{(l)}$, and $\varphi_\alpha^{(l)}$ is introduced, for $l = 1 \,.\,. N$:

$$\begin{aligned}
w^{(l)} = w, \quad u_\alpha^{(l)} &= \bar{u}_\alpha^{(l)} - \frac{\bar{u}_\alpha^{(l)} - \bar{u}_\alpha^{(l-1)}}{h^{(l)}} \zeta_+^{(l)} \quad \text{and} \\
\varphi_\alpha^{(l)} &= \frac{\bar{u}_\alpha^{(l)} - \bar{u}_\alpha^{(l-1)}}{h^{(l)}},
\end{aligned} \tag{21}$$

where w and $\bar{u}_\alpha^{(l)}$, $l = 0 \,.\,. N$, are unknown functions of x_1 and x_2. The former one is the out-of-plane deflection of the laminate, while the latter ones are the in-plane displacements of the upper and lower faces and of the interlaminar surfaces.

By substituting $\omega_{33}^{(l)}$ from Eq. (16) and $s_i^{(l)}$ from Eqs. (18) into Eq. (14), and then performing an integration in the thickness variable x_3, the potential energy functional Ψ is transformed into

$$\begin{aligned}
\Phi = & \sum_{l=1}^{N} \frac{\Delta\zeta^{(l)}}{2} \int_{\mathcal{P}} \bar{C}_{\alpha\beta\gamma\delta}^{(l)}(u_{\alpha,\beta}^{(l)} + u_{\beta,\alpha}^{(l)})/2(u_{\gamma,\delta}^{(l)} + u_{\delta,\gamma}^{(l)})/2 da \\
& + \sum_{l=1}^{N} \frac{\Delta(\zeta^{(l)^2})}{2} \int_{\mathcal{P}} \bar{C}_{\alpha\beta\gamma\delta}^{(l)}(u_{\alpha,\beta}^{(l)} + u_{\beta,\alpha}^{(l)})/2(\varphi_{\gamma,\delta}^{(l)} + \varphi_{\delta,\gamma}^{(l)})/2 da \\
& + \sum_{l=1}^{N} \frac{\Delta(\zeta^{(l)^3})}{6} \int_{\mathcal{P}} \bar{C}_{\alpha\beta\gamma\delta}^{(l)}(\varphi_{\alpha,\beta}^{(l)} + \varphi_{\beta,\alpha}^{(l)})/2(\varphi_{\gamma,\delta}^{(l)} + \varphi_{\delta,\gamma}^{(l)})/2 da \\
& + \sum_{l=1}^{N} \frac{\Delta\zeta^{(l)}}{2} \int_{\mathcal{P}} C_{\alpha 3\beta 3}^{(l)}(\varphi_\alpha^{(l)} + w_{,\alpha}^{(l)})(\varphi_\beta^{(l)} + w_{,\beta}^{(l)}) da \\
& - \sum_{l=1}^{N} \int_{\mathcal{P}} (r_\alpha^{(l)} u_\alpha^{(l)} + m_\alpha^{(l)} \varphi_\alpha^{(l)} + r_3^{(l)} w^{(l)}) da \\
& - \sum_{l=1}^{N} \int_{\partial_f \mathcal{P}} (\hat{r}_\alpha^{(l)} u_\alpha^{(l)} + \hat{m}_\alpha^{(l)} \varphi_\alpha^{(l)} + \hat{r}_3^{(l)} w^{(l)}) dl \\
& - \int_{\mathcal{P}} [p_\alpha^-(u_\alpha^{(1)} + \zeta_-^{(1)} \varphi_\alpha^{(1)}) + p_\alpha^+(u_\alpha^{(N)} + \zeta_+^{(N)} \varphi_\alpha^{(N)}) \\
& \qquad + p_3^- w^{(1)} + p_3^+ w^{(N)}] da,
\end{aligned} \tag{22}$$

where the functions $w^{(l)}$, $u_\alpha^{(l)}$, and $\varphi_\alpha^{(l)}$ have to be substituted from Eqs. (21), and

$$\begin{aligned}
\Delta\zeta^{(l)} = h^{(l)} = \zeta_+^{(l)} - \zeta_-^{(l)}, \quad & \Delta(\zeta^{(l)^2}) = \zeta_+^{(l)^2} - \zeta_-^{(l)^2}, \\
\Delta(\zeta^{(l)^3}) &= \zeta_+^{(l)^3} - \zeta_-^{(l)^3}, \\
r_\alpha^{(l)} = \int_{\zeta_-^{(l)}}^{\zeta_+^{(l)}} b_\alpha^{(l)} dx_3, \quad & m_\alpha^{(l)} = \int_{\zeta_-^{(l)}}^{\zeta_+^{(l)}} x_3 b_\alpha^{(l)} dx_3, \\
r_3^{(l)} = \int_{\zeta_-^{(l)}}^{\zeta_+^{(l)}} b_3^{(l)} dx_3, \quad & \hat{r}_\alpha^{(l)} = \int_{\zeta_-^{(l)}}^{\zeta_+^{(l)}} \hat{p}_\alpha^{(l)} dx_3, \\
\hat{m}_\alpha^{(l)} = \int_{\zeta_-^{(l)}}^{\zeta_+^{(l)}} x_3 \hat{p}_\alpha^{(l)} dx_3, \quad & \hat{r}_3^{(l)} = \int_{\zeta_-^{(l)}}^{\zeta_+^{(l)}} \hat{p}_3^{(l)} dx_3.
\end{aligned} \tag{23}$$

Table 1 Equations of the layer-wise theory obtained as stationary conditions of Lagrangian functional L (11) for the laminate

Dual variable	Equations			
$s_\alpha^{(l)}$	$\sigma_{\alpha\beta,\beta}^{(l)} + \sigma_{\alpha 3,3}^{(l)} + b_\alpha^{(l)} = 0$ $\sigma_{\alpha\beta}^{(l)} n_\beta = \hat{p}_\alpha^{(l)}$ $\sigma_{\alpha 3}^{(1)} = -p_\alpha^-$ $\sigma_{\alpha 3}^{(l+1)} = \sigma_{\alpha 3}^{(l)}$ $\sigma_{\alpha 3}^{(N)} = p_\alpha^+$	in on on on on	$\Omega^{(l)}$, $\partial_f \Omega^{(l)}$, $\mathcal{P} \times \{\zeta_-^{(1)}\}$ $\mathcal{P} \times \{\zeta_+^{(l)}\}$, $\mathcal{P} \times \{\zeta_+^{(N)}\}$	$l = 1..N$ $l = 1..N$ $l = 1..N-1$
$s_3^{(l)}$	$\sigma_{3\alpha,\alpha}^{(l)} + \sigma_{33,3}^{(l)} + b_3^{(l)} = 0$ $\sigma_{3\alpha}^{(l)} n_\alpha = \hat{p}_3^{(l)}$ $\sigma_{33}^{(1)} = -p_3^-$ $\sigma_{33}^{(l+1)} = \sigma_{33}^{(l)}$ $\sigma_{33}^{(N)} = p_3^+$	in on on on on	$\Omega^{(l)}$, $\partial_f \Omega^{(l)}$, $\mathcal{P} \times \{\zeta_-^{(1)}\}$ $\mathcal{P} \times \{\zeta_+^{(l)}\}$, $\mathcal{P} \times \{\zeta_+^{(N)}\}$	$l = 1..N$ $l = 1..N$ $l = 1..N-1$
$\sigma_{\alpha\beta}^{(l)}$	$\varepsilon_{\alpha\beta}^{(l)} = (s_{\alpha,\beta}^{(l)} + s_{\beta,\alpha}^{(l)})/2$ $s_\alpha^{(l)} = s_{0\alpha}^{(l)}$	in on	$\Omega^{(l)}$, $\partial_s \Omega^{(l)}$,	$l = 1..N$ $l = 1..N$
$\sigma_{\alpha 3}^{(l)}$	$\varepsilon_{\alpha 3}^{(l)} = (s_{\alpha,3}^{(l)} + s_{3,\alpha}^{(l)})/2$ $s_3^{(l)} = s_{03}^{(l)}$ $s_\alpha^{(l+1)} = s_\alpha^{(l)}$	in on on	$\Omega^{(l)}$, $\partial_s \Omega^{(l)}$, $\mathcal{P} \times \{\zeta_+^{(l)}\}$,	$l = 1..N$ $l = 1..N$ $l = 1..N-1$
$\sigma_{33}^{(l)}$	$\varepsilon_{33}^{(l)} + \omega_{33}^{(l)} = s_{3,3}^{(l)}$ $s_3^{(l+1)} = s_3^{(l)}$	in on	$\Omega^{(l)}$, $\mathcal{P} \times \{\zeta_+^{(l)}\}$,	$l = 1..N$ $l = 1..N-1$
$\varepsilon_{\alpha\beta}^{(l)}$	$C_{\alpha\beta\gamma\delta}^{(l)} \varepsilon_{\gamma\delta}^{(l)} + C_{\alpha\beta 33}^{(l)} \varepsilon_{33}^{(l)} = \sigma_{\alpha\beta}^{(l)}$	in	$\Omega^{(l)}$,	$l = 1..N$
$\varepsilon_{\alpha 3}^{(l)}$	$2C_{\alpha 3\beta 3}^{(l)} \varepsilon_{\beta 3}^{(l)} = \sigma_{\alpha 3}^{(l)} - \chi_{\alpha 3,3}^{(l)}$ $\chi_{\alpha 3}^{(l)} = 0$	in on	$\Omega^{(l)}$, $\mathcal{P} \times \{\zeta_\pm^{(l)}\}$,	$l = 1..N$ $l = 1..N$
$\varepsilon_{33}^{(l)}$	$C_{33\alpha\beta}^{(l)} \varepsilon_{\alpha\beta}^{(l)} + C_{3333}^{(l)} \varepsilon_{33}^{(l)} = \sigma_{33}^{(l)} + \chi_{33}^{(l)}$	in	$\Omega^{(l)}$,	$l = 1..N$
$\chi_{33}^{(l)}$	$\varepsilon_{33}^{(l)} + \omega_{33}^{(l)} = 0$	in	$\Omega^{(l)}$,	$l = 1..N$
$\chi_{\alpha 3}^{(l)}$	$\varepsilon_{\alpha 3,3}^{(l)} = 0$	in	$\Omega^{(l)}$,	$l = 1..N$
$\omega_{33}^{(l)}$	$\sigma_{33}^{(l)} + \chi_{33}^{(l)} = 0$	in	$\Omega^{(l)}$,	$l = 1..N$

The functional Φ, depending on w and $\bar{u}_\alpha^{(l)}$, is the classical potential energy functional of the layer-wise theory (Barbero and Reddy, 1989). It is emphasized that the so-called *reduced constitutive law* enters the expression of Φ:

$$\bar{C}_{\alpha\beta\gamma\delta}^{(l)} = C_{\alpha\beta\gamma\delta}^{(l)} - \frac{1}{C_{3333}^{(l)}} C_{\alpha\beta 33}^{(l)} C_{\gamma\delta 33}^{(l)}. \tag{24}$$

The present derivation clearly shows that the appearance of $\bar{C}_{\alpha\beta\gamma\delta}^{(l)}$ is a straightforward and rational consequence of the constraint (i) acting on the elastic stress field and leading to the constraint Eq. (16). In other words, the reduced constitutive tensor $\bar{C}_{\alpha\beta\gamma\delta}^{(l)}$ comes out from the machinery adopted and is not a priori enforced. This is an important difference between the present approach and Podio-Guidugli's (1989), where an ad hoc constitutive law was used. In addition, it can be pointed out that by using the proposed technique no contradiction arises between the constraints (i) and (ii), since the latter one acts on the total strain field.

The stationary conditions of the functional Φ supply the well-known equations of the layer-wise theory, which, for the sake of brevity, are not reported herein. They allow to compute the unknown functions w and $\bar{u}_\alpha^{(l)}$, and thus the displacement field $s^{(l)}$.

In many technical problems the item of interest is the total stress field, i.e., the stress field which is in equilibrium with the applied loads. Indeed, just that stress field should be compared against the strength of the constituent materials, in order to prevent a failure of the structure.

According to (12), the total stresses $\sigma_{\alpha\beta}^{(l)}$ are equal to the corresponding elastic stresses and hence they can be computed by using the constitutive equations:

$$\sigma_{\alpha\beta}^{(l)} = C_{\alpha\beta\gamma\delta}^{(l)} \epsilon_{\gamma\delta}^{(l)} + C_{\alpha\beta 33}^{(l)} \epsilon_{33}^{(l)} = \bar{C}_{\alpha\beta\gamma\delta}^{(l)} \epsilon_{\gamma\delta}^{(l)}$$
$$= \bar{C}_{\alpha\beta\gamma\delta}^{(l)} [(u_{\gamma,\delta}^{(l)} + u_{\delta,\gamma}^{(l)})/2 + x_3(\varphi_{\gamma,\delta}^{(l)} + \varphi_{\delta,\gamma}^{(l)})/2]. \tag{25}$$

On the other hand, the constitutive equations cannot be used to compute the transverse total shear stresses $\sigma_{\alpha 3}^{(l)}$ or the trans-

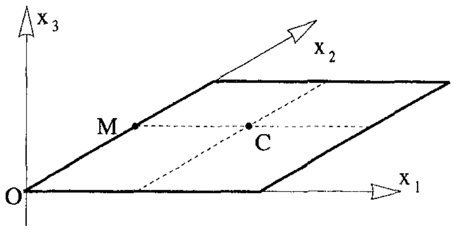

Fig. 1 Scheme of the middle plane of the laminate

verse total normal stress $\sigma^{(l)}_{33}$. In order to compute those stresses, the equilibrium equations, given by the stationary conditions of the Lagrangian functional L with respect to $s^{(l)}_\alpha$ and $s^{(l)}_3$, and reported in Table 1, must be used. Hence, this procedure for the computation of the stresses, proposed by many researchers for single-layer as well as multilayer laminate theories (e.g., Lo et al., 1978; Barbero and Reddy, 1989), is completely justified herein in the framework of constrained elasticity.

According to this procedure, the interlaminar stresses, i.e., the interaction between two adjacent layers, are carried out. It is emphasized that those interlaminar stresses are defined without any ambiguity, when the total stress field, instead of the elastic one, is considered. Thus, at the interface between the layer l and the layer $l+1$, a tangential stress $\tilde\sigma^{(l)}_{\alpha3}$ and a normal stress $\tilde\sigma^{(l)}_{33}$ are computed by the equilibrium equations, and have the following expressions:

$$\begin{aligned}
\tilde\sigma^{(l)}_{\alpha3} &= C^{(l)}_{\alpha3\beta3}(\varphi^{(l)}_\beta + w^{(l)}_{,\beta}) + \chi^{(l)}_{\alpha3,3}|_{\zeta^{(l)}_+} \\
&= -p^-_\alpha - \sum_{m=1}^{l} r^{(m)}_\alpha - \sum_{m=1}^{l} \Delta\zeta^{(m)}\bar C^{(m)}_{\alpha\beta\gamma\delta}(u^{(m)}_{\gamma,\delta} + u^{(m)}_{\delta,\gamma})_{,\beta}/2 \\
&\quad - \sum_{m=1}^{l} \Delta(\zeta^{(m)^2})\bar C^{(m)}_{\alpha\beta\gamma\delta}(\varphi^{(m)}_{\gamma,\delta} + \varphi^{(m)}_{\delta,\gamma})_{,\beta}/4 \\
\tilde\sigma^{(l)}_{33} &= -\chi^{(l)}_{33} = -p^-_3 - \sum_{m=1}^{l} r^{(m)}_3 \\
&\quad - \sum_{m=1}^{l} \Delta\zeta^{(m)} C^{(m)}_{\alpha3\beta3}(\varphi^{(m)}_\beta + w^{(m)}_{,\beta})_{,\alpha}. \qquad (26)
\end{aligned}$$

Then, it is easy to compute $\sigma^{(l)}_{\alpha3}$ and $\sigma^{(l)}_{33}$ in the lth layer:

$$\begin{aligned}
\sigma^{(l)}_{\alpha3} &= \tilde\sigma^{(l)}_{\alpha3} + \int_{x_3}^{\zeta^{(l)}_+} b^{(l)}_\alpha dx_3 + (\zeta^{(l)}_+ - x_3)\bar C^{(l)}_{\alpha\beta\gamma\delta}(u^{(l)}_{\gamma,\delta} + u^{(l)}_{\delta,\gamma})_{,\beta}/2 \\
&\quad + [(\zeta^{(l)}_+)^2 - x_3^2]\bar C^{(l)}_{\alpha\beta\gamma\delta}(\varphi^{(l)}_{\gamma,\delta} + \varphi^{(l)}_{\delta,\gamma})_{,\beta}/4
\end{aligned}$$

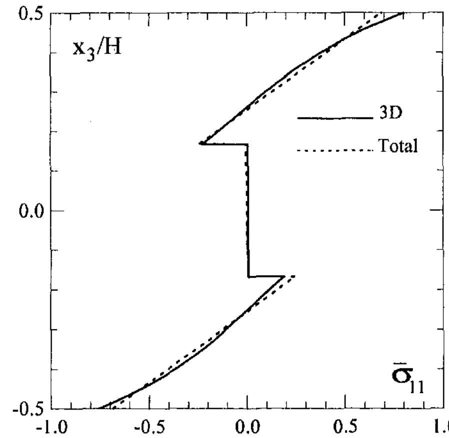

Fig. 3 Dimensionless in-plane normal stress $\bar\sigma_{11}$ versus the dimensionless thickness variable x_3/H

$$\sigma^{(l)}_{33} = \tilde\sigma^{(l)}_{33} + \int_{x_3}^{\zeta^{(l)}_+} b^{(l)}_3 dx_3 + \int_{x_3}^{\zeta^{(l)}_+} \sigma^{(l)}_{3\alpha,\alpha} dx_3. \qquad (27)$$

5 Applications

A numerical application is presented, in order to emphasize the difference between the elastic, reactive, and total strain and stress fields. A square cross-ply 0°/90°/0° laminated plate with side A and thickness H is considered. The Cartesian frame is chosen such that the axes x_1 and x_2 coincide with two edges of the plate, as shown in Fig. 1. The material is orthotropic tetragonal, with $E_L/E_T = 25$, $G_{LT}/E_T = 0.5$, $G_{TT}/E_T = 0.2$, $\nu_{LT} = \nu_{TT} = 0.25$, where L represents the fibers direction and T the orthogonal direction. The plate is simply supported along its boundary, has a side/thickness ratio $R = A/H = 4$ and is loaded on the upper face by a transversal load $p^+_3 = q_0 \sin(\pi x_1/A) \sin(\pi x_2/A)$.

Elastic and total strain and stress fields computed by means of the procedure presented in this paper are compared with the results given by the exact three-dimensional solution (Pagano, 1970; Srinivas and Rao, 1970). In particular, the following quantities are plotted versus the dimensionless thickness variable x_3/H:

(a) dimensionless in-plane normal strain and stress in the x_1 direction at the point C (Figs. 2 and 3):

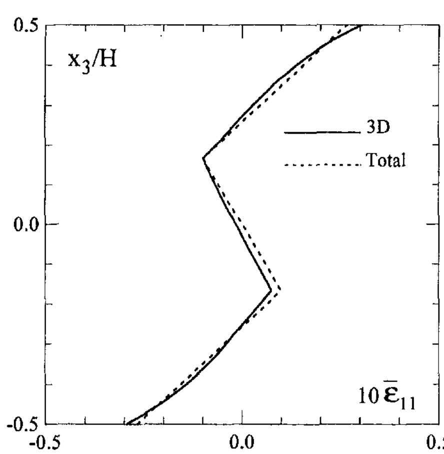

Fig. 2 Dimensionless in-plane normal strain $\bar\varepsilon_{11}$ versus the dimensionless thickness variable x_3/H

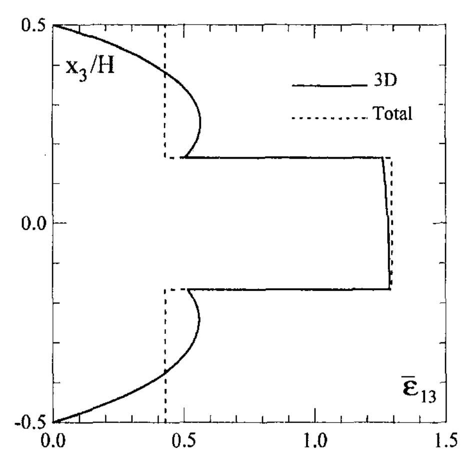

Fig. 4 Dimensionless transverse shear strain $\bar\varepsilon_{13}$ versus the dimensionless thickness variable x_3/H

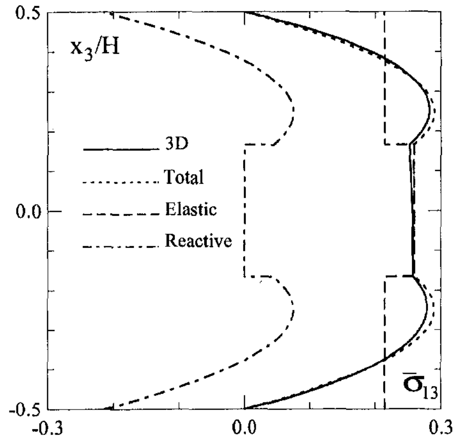

Fig. 5 Dimensionless transverse shear stress $\bar{\sigma}_{13}$ versus the dimensionless thickness variable x_3/H

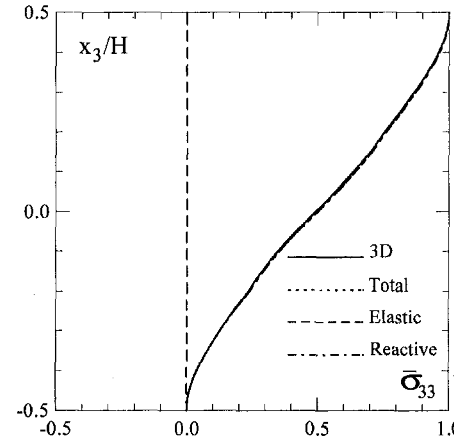

Fig. 7 Dimensionless transverse normal stress $\bar{\sigma}_{33}$ versus the dimensionless thickness variable x_3/H. The total field and the reactive field coincide, since the elastic field vanishes.

$$\bar{\epsilon}_{11} = \frac{E_T \epsilon_{11}}{q_0 R^2}, \quad \bar{\sigma}_{11} = \frac{\sigma_{11}}{q_0 R^2}; \tag{28}$$

(b) dimensionless transverse shear strain and stress in the x_1 direction at the point M (Figs. 4 and 5):

$$\bar{\epsilon}_{13} = \frac{E_T \epsilon_{13}}{q_0 R}, \quad \bar{\sigma}_{13} = \frac{\sigma_{13}}{q_0 R}; \tag{29}$$

(c) dimensionless transverse normal strain and stress at the point C (Figs. 6 and 7):

$$\bar{\epsilon}_{33} = \frac{E_T \epsilon_{33}}{q_0 R^2}, \quad \bar{\sigma}_{33} = \frac{\sigma_{33}}{q_0}. \tag{30}$$

The numerical results show that the stress solutions are very satisfactory. Moreover, as far as total stress fields are considered, the transverse shear stress and the transverse normal stress are continuous functions along the thickness of the laminate and satisfy the equilibrium boundary conditions on the upper and lower faces.

6 Conclusions

The layer-wise theory of laminated plates proposed by Barbero and Reddy (1989) was framed in the context of constrained elasticity. In fact, the governing equations of the layer-wise theory were rationally deduced from the three-dimensional elasticity theory, by enforcing suitable constraints on both the strain field and the stress field. To this end, a nonstandard application of the Lagrange multipliers theory, which takes into account the simultaneous presence of constraints on the dual spaces of strain and stress fields, was adopted.

The reactive fields, arising as a consequence of the imposed constraints, were computed. As a matter of fact, they can be regarded as an error estimate between the layer-wise solution, i.e., the constrained elasticity solution, and the exact three-dimensional unconstrained solution.

A justification for computing the transverse shear stress and the transverse normal stress by using the equilibrium equations, instead of the constitutive equations, was supplied. According to this procedure, no ambiguity arises in the computation of the interlaminar stresses.

Finally, it is emphasized that the technique presented clarified the role played by the various hypotheses on which the layer-wise theory relies. In particular, the adopted machinery allowed to rationally obtain the correct reduced constitutive law.

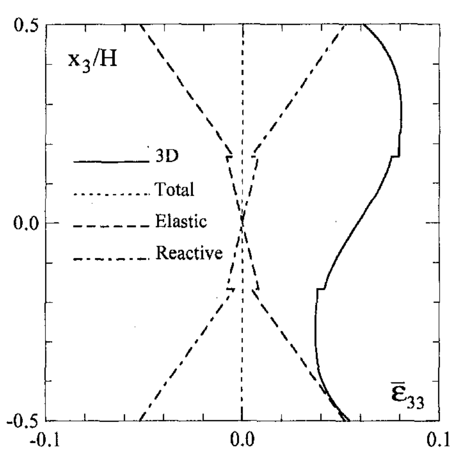

Fig. 6 Dimensionless transverse normal strain $\bar{\epsilon}_{33}$ versus the dimensionless thickness variable x_3/H

Acknowledgments

The financial supports of the Italian National Research Council (CNR), of the Italian Ministry of University and Research (MURST), and of the Italian Space Agency (ASI) are gratefully acknowledged.

References

Ambartsumyan, S. A., 1970, *Theory of Anisotropic Plates,* J. E. Ashton, ed. (T. Cheron, translator), Technomic, Stamford, pp. 73–80.

Antman, S. S., and Marlow, R. S., 1991, "Material Constraints, Lagrange Multiplier, and Compatibility. Applications to Rod and Shell Theories," *Arch. Rat. Mech. Anal.,* Vol. 116, pp. 257–299.

Barbero, E. J., and Reddy, J. N., 1989, "On a Generalized Laminate Plate Theory with Application to Bending, Vibration and Delamination Buckling in Composite Laminates," Virginia Polytechnic Institute and State University Report CCMS-89-20, Blacksburg, VA.

Barbero, E. J., Reddy, J. N., and Teply, J. L., 1990, "An Accurate Determination of Stresses in Thick Laminates Using a Generalized Plate Theory," *Int. J. Numer. Meth. Engng.,* Vol. 29, pp. 1–14.

Bisegna, P., and Sacco, E., 1995, "Deduzione di Teorie di Piastre Laminate dalla Elasticità Tridimensionale," *Proceedings XII AIMETA National Conference,* L. Nunziante, ed., Francesco Giannini & Figli, Napoli, pp. 257–262.

Bisegna, P., and Sacco, E., 1997, "A Rational Deduction of Plate Theories from the Three-Dimensional Linear Elasticity," *Zeit. Angew. Math. Mech.,* Vol. 77, pp. 349–366.

Cauchy, A. L., 1829, "Sur l'Équilibre et le Mouvement d'une Plaque Élastique dont l'Élasticité n'est pas la Même dans Tous les Sens," *Exercises Math.,* Vol. 4, pp. 1–14.

Di Sciuva, M., 1987, "An Improved Shear Deformation Theory for Moderately Thick Multilayered Anisotropic Shells and Plates," ASME JOURNAL OF APPLIED MECHANICS, Vol. 54, pp. 589–596.

Di Sciuva, M., and Icardi, U., 1993, "Discrete-Layer Models for Multilayered Shells Accounting for Interlayer Continuity," *Meccanica,* Vol. 28, pp. 281–291.

Fraternali, F., and Reddy, J. N., 1993, "A Penalty Model for the Analysis of Laminated Composite Shells," *Int. J. Solids Struct.,* Vol. 30, pp. 3337–3355.
Gurtin, M. E., 1972, "The Linear Theory of Elasticity," *Handbuch der Physik,* S. Flügge, ed., Band VIa/2, Spinger-Verlag, Berlin, pp. 129–131.
Hencky, H., 1947, "Über die Berücksichtigung der Schubverzerrung in ebenen Platten," *Ing. Arch.,* Vol. 16, pp. 72–76.
Lekhnitskii, S. G., 1968, *Anisotropic Plates,* S. W. Tsai, and T. Cheron, (translators) Gordon and Breach, New York, pp. 295–299.
Lembo, M., and Podio Guidugli, P., 1991, "Plate Theory as an Exact Consequence of Three-Dimensional Linear Elasticity," *European J. Mech. A/Solids,* Vol. 10, pp. 485–516.
Lo, K. H., Christensen, R. M., and Wu, E. M., 1977, "A High-Order Theory of Plate Deformation. Part II: Laminated Plates," ASME JOURNAL OF APPLIED MECHANICS, Vol. 44, pp. 669–676.
Lo, K. H., Christensen, R. M., and Wu, E. M., 1978, "Stress Solution Determination for High-Order Plate Theory," *Int. J. Solids Struct.,* Vol. 14, pp. 655–662.
Luenberger, D. G., 1969, *Optimization by Vector Space Methods,* John Wiley and Sons, New York, pp. 240–253.
Lyusternik, L. A., 1934, "On Constrained Extrema of Functionals," *Mat. Sb.,* Vol. 41, pp. 390–401.
Mindlin, R. D., 1951, "Influence of Rotatory Inertia and Shear on Flexural Motions of Isotropic, Elastic Plates," ASME JOURNAL OF APPLIED MECHANICS, Vol. 38, pp. 31–38.
Murthy, A. V. K., and Vellaichamy, S., 1987, "On Higher-Order Shear Deformation Theory of Laminated Composite Panels," *Composite Structures,* Vol. 8, pp. 247–270.
Oden, J. T., and Reddy, J. N., 1976, *Variational Methods in Theoretical Mechanics,* Springer-Verlag, Berlin, pp. 104–114.
Pagano, N. J., 1970, "Exact Solutions for Rectangular Bidirectional Composites and Sandwich Plates," *J. Composite Materials,* Vol. 4, pp. 20–34.
Podio-Guidugli, P., 1989, "An Exact Derivation of Thin Plates Equations," *J. Elasticity,* Vol. 22, pp. 121–133.
Reddy, J. N., 1984, "A Simple Higher-Order Theory for Laminated Composite Plates," ASME JOURNAL OF APPLIED MECHANICS, Vol. 51, pp. 745–752.
Reddy, J. N., 1987, "A Generalization of Two-Dimensional Theories of Laminated Plates," *Commun. Appl. Numer. Meth.,* Vol. 3, pp. 173–180.
Reissner, E., 1945, "The Effect of Transverse Shear Deformation on the Bending of Elastic Plates," ASME JOURNAL OF APPLIED MECHANICS, Vol. 12, pp. 69–77.
Reissner, E., 1950, "On a Variational Theorem in Elasticity," *J. Math. and Phys.,* Vol. 29, pp. 90–95.
Reissner, E., and Stavsky, Y., 1961, "Bending and Streching of Certain Types of Heterogeneous Aelotropic Elastic Plates," ASME JOURNAL OF APPLIED MECHANICS, Vol. 28, pp. 402–412.
Seide, P., 1980, "An Improved Approximate Theory for Bending of Laminated Plates," *Mech. Today,* Vol. 5, pp. 451–466.
Srinivas, S., and Rao, A. K., 1970, "Bending, Vibration and Buckling of Simply Supported Thick Orthotropic Rectangular Plates and Laminates," *Int. J. Solids Structures,* Vol. 6, pp. 1463–1481.
Stavsky, Y., 1961, "Bending and Streching of Laminated Aelotropic Plates," *Proc. Am. Soc. Civil Engrs.: J. Engr. Mech. Div.,* Vol. 87, pp. 31–42.
Washizu, K., 1968, *Variational Methods in Elasticity and Plasticity,* Pergamon Press, Oxford, UK, pp. 98–104.
Whitney, J. M., and Pagano, N. J., 1970, "Shear Deformation in Heterogeneous Anisotropic Plates," ASME JOURNAL OF APPLIED MECHANICS, Vol. 37, pp. 1031–1036.
Xianquiang, L., and Dahsin, L., 1992, "An Interlaminar Shear Stress Continuity Theory for both Thin and Thick Composite Laminate," ASME JOURNAL OF APPLIED MECHANICS, Vol. 59, pp. 502–509.
Yang, P. C., Norris, C. H., and Stavsky, Y., 1966, "Elastic Wave Propagation in Heterogeneous Plates," *Int. J. Solids Struct.,* Vol. 2, pp. 665–684.

Transient Analysis of a Subsonic Propagating Interface Crack Subjected to Antiplane Dynamic Loading in Dissimilar Isotropic Materials

Yi-Shyong Ing
Graduate Student.

Chien-Ching Ma[1]
Professor.

Department of Mechanical Engineering,
National Taiwan University,
Taipei, Taiwan 10617
Republic of China

In this study, the transient stress fields and the dynamic stress intensity factor of a semi-infinite antiplane crack propagating along the interface between two different media are analyzed in detail. The crack is initially at rest and, at a certain instant, is subjected to an antiplane uniformly distributed loading on the stationary crack faces. After some delay time, the crack begins to move along the interface with a constant velocity, which is less than the smaller of the shear wave speed of these two materials. A new fundamental solution is proposed in this study, and the solution is determined by superposition of the fundamental solution in the Laplace transform domain. The proposed fundamental problem is the problem of applying exponentially distributed traction (in the Laplace transform domain) on the propagating crack faces. The exact full-field solutions and the stress intensity factor are found in the time domain by using the Cagniard-de Hoop method (de Hoop, 1958) of Laplace inversion. The near-tip fields are also obtained from the reduction of the full-field solutions. Numerical results for the dynamically extending crack are evaluated in detail. The region of the stress singular field dominated in the transient process is also discussed.

1 Introduction

For the last two decades, the importance of composite materials has increased very rapidly in engineering applications because of their high strength and light weight. However, flaws contained at the interfaces of composite bodies due to improper adhesion may lead to serious danger, and a better understanding of interface fracture mechanics is needed. The interface crack problem is also important in engineering and seismology applications. Since the inherent time dependence of a dynamic fracture process results in mathematical models that are more complex than equivalent quasi-static models, most of the analyses done regarding cracked composite bodies are quasi-static. However, there is still substantial interest in the dynamic fracture problem due to its importance in many engineering applications. The problem is encountered in impact damage to fan blades, and automotive and aircraft windshields. There is also considerable interest in the problem of arrest of a fast running crack, especially in large structures like pipelines, ships, and nuclear reactors.

Problems of crack propagation in a homogeneous medium have been studied by many authors. A stationary crack lying along the interface between dissimilar isotropic materials subjected to static loading was first considered by Williams (1959) for plane-strain conditions. Further investigations of the problem were conducted by England (1965), Erdogan (1965), and Rice and Sih (1965). They derived the expression of the stress fields near the crack tip and discussed the singularities given by Williams (1959). In the field of propagating interface cracks, Willis (1971) investigated the energy release rate of a steadily extending interface crack by means of the local form of the Griffith virtual work argument. He also derived an explicit fracture criterion which involves a suitably defined "stress concentration vector." In recent years, Wu (1991) treated the similar but anisotropic problem and derived the crack-tip fields and energy release rate successfully by employing the Stroh formalism for anisotropic elasticity. Deng (1992) used the Radok complex function formulation with a two-term complex eigenexpansion technique to analyze the near-tip fields for steadily growing interface cracks in dissimilar isotropic materials. Yang, Suo, and Shih (1991) have analyzed the problems of steadily propagating interface cracks in dissimilar isotropic and orthotropic bimaterials. They solved the crack-tip fields by the Stroh formulation and discussed the singularities for antiplane and in-plane deformations carefully. The stress singularities and the angular stress distributions near a propagating interface crack in different transonic regimes for both antiplane and in-plane cases were determined by Yu and Yang (1994, 1995). Because of mathematical complexity and difficulty, many of the investigators mentioned above have investigated only the near-tip fields. However, transient full-field solutions for the problem of a propagating crack in a homogeneous material or in a bimaterial are rare.

Brock and Achenbach (1973) analyzed the extension of an interface crack under the influence of a transient horizontally polarized shear wave. It is assumed that the adhesive behaves as a perfectly plastic material, so that the stress in the zone of interface yielding is uniform and equal to the yield stress. Analytic solutions for the time of rupture and for the interface stress ahead of yield zone are obtained by applying integral transform methods. Brock (1974) followed the approach of Freund

[1] To whom all correspondence should be addressed.

Contributed by the Applied Mechanics Division of The American Society of Mechanical Engineers for publication in the ASME Journal of Applied Mechanics.

Discussion on the paper should be addressed to the Technical Editor, Professor Lewis T. Wheeler, Department of Mechanical Engineering, University of Houston, Houston, TX 77204-4792, and will be accepted until four months after final publication of the paper itself in the ASME Journal of Applied Mechanics.

Manuscript received by the ASME Applied Mechanics Division, Apr. 15, 1996; final revision, Nov. 11, 1996. Associate Technical Editor: W. J. Drugan.

(1972b) and solved the problem of a partially loaded interface flaw which extends at a nonuniform rate. The external load was assumed to be a time-independent antiplane shear traction and was applied over the newly created surfaces. He derived the stress intensity factor and the difference in the particle velocities at the edge of the nonuniformly extending flaw. Recently, Chung and Robinson (1992) solved the transient problem of a mode-III crack propagating along the interface between two different media. In their study, the compound body is loaded by a constant shear traction at infinity such that the problem becomes "self-similar." This self-similar problem can be solved effectively by the method of self-similar potentials (SSP). In a series of papers, Freund (1972a, 1972b, 1973, 1974) developed important analytical methods for evaluation of the transient stress field of a propagating crack in a homogeneous material under quite general dynamic loading situations. These particular cases analyzed by Freund are also self-similar, but they are solved by means of integral transform methods rather than by direct application of similarity arguments. An indirect analytical approach proposed by Freund is based on a superposition over a fundamental solution. Based on the superposition method proposed by Freund, a series of problems for nonplanar crack propagation in an infinite domain was solved by Ma and Burgers (1986, 1987, 1988) and Ma (1988, 1990). A thorough summary of analysis for transient problems under antiplane loading in dynamic fracture has been given by Coussy (1984). For the aforementioned problems (except for the SSP method), either the direct application of the well-known Wiener-Hopf technique (Noble, 1958) is used or the superposition method proposed by Freund is performed to solve the problem. However, if a crack is subjected to incident nonplanar waves, none of the known methods can be used directly to obtain the transient solutions.

In this paper, the transient problem of an interface crack propagating with a subsonic speed in an infinite medium is considered. At time $t = 0$, the crack is at rest and a uniformly distributed antiplane loading acts on the stationary crack faces. After some delay time t_f, the crack begins to run along the interface with a constant velocity v as shown in Fig. 1. A new fundamental solution is proposed and it is successfully applied towards solving the problem. The fundamental problem is the problem of applying an exponentially distributed traction on the propagating crack faces in the Laplace transform domain and is demonstrated as an efficient methodology to solve similar problems. The alternative superposition scheme has been used to solve many transient problems for a homogeneous medium successfully, e.g., Tsai and Ma (1992) for a stationary crack and Ma and Ing (1995) for a propagating crack. The transient full-field stresses and the stress intensity factor for the problem considered are obtained and expressed in a closed form. The stress singular solutions are obtained from the reduction of the full-field solutions and the region of the stress singular field dominance is also investigated in detail.

2 Required Fundamental Solutions

Consider a fundamental problem of antiplane deformation for an extending interface crack in dissimilar materials. The crack propagates with a constant velocity v, which is less than the minimum of the shear wave speed of these two materials.

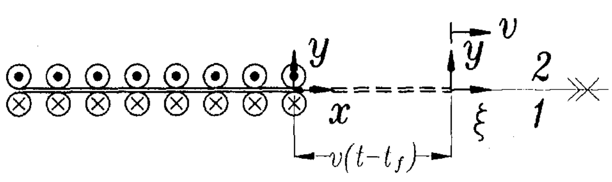

Fig. 1 Configuration and coordinate system of a propagating interface crack in bimaterial medium

Figure 1 shows the interface crack geometry and the coordinate systems. Materials 1 and 2 occupy the two half-spaces. The coordinate ξ defined by $\xi = x - vt$ is fixed with respect to the moving crack tip. In analyzing this problem, it is convenient to express the governing equations of wave motions in the moving coordinates $\xi - y$ as follows:

$$(1 - b_j^2 v^2)\frac{\partial^2 w_j}{\partial \xi^2} + \frac{\partial^2 w_j}{\partial y^2} + 2b_j^2 v\frac{\partial^2 w_j}{\partial \xi \partial t} - b_j^2\frac{\partial^2 w_j}{\partial t^2} = 0, \quad j = 1, 2 \quad (1)$$

where the subscript j ($j = 1, 2$) refers to the lower and upper media, respectively; w_j are the out-of-plane displacements, and b_j are the slownesses of the shear waves given by

$$b_j = \frac{1}{c_{sj}} = \sqrt{\frac{\rho_j}{\mu_j}},$$

in which c_{sj} are the shear wave speeds, and μ_j and ρ_j are the respective shear moduli and the mass densities of two materials. Without loss of generality, we assume $b_1 > b_2$; that is, the shear wave speed in the lower material is less than that in the upper material. The nonvanishing shear stresses are

$$\tau_{yzj} = \mu_j \frac{\partial w_j}{\partial y}, \quad \tau_{xzj} = \mu_j \frac{\partial w_j}{\partial x}. \quad (2)$$

The solution for an exponentially distributed loading applied at the crack faces in the Laplace transform domain will be referred to as the fundamental solution. Then the boundary conditions on the crack surfaces expressed in the Laplace transform domain can be described as follows:

$$\bar{\tau}_{yz1}(\xi, 0, s) = \bar{\tau}_{yz2}(\xi, 0, s) = e^{s\eta\xi}, \quad -\infty < \xi < 0 \quad (3)$$

where s is the Laplace transform parameter and η is a constant. The overbar symbol is used for denoting the transform on time t. The one-sided Laplace transform with respect to time and the two-sided Laplace transform with respect to ξ are defined by

$$\bar{w}(\xi, y, s) = \int_0^\infty w(\xi, y, t)e^{-st}dt,$$

$$\bar{w}^*(\lambda, y, s) = \int_{-\infty}^\infty \bar{w}(\xi, y, s)e^{-s\lambda\xi}d\xi.$$

The displacements and shear stresses must be continuous on the interface, which gives the following conditions on the interface:

$$\bar{\tau}_{yz1}(\xi, 0, s) = \bar{\tau}_{yz2}(\xi, 0, s) = \bar{\tau}_{yz+}, \quad 0 < \xi < \infty \quad (4)$$

$$\bar{w}_1(\xi, 0, s) = \bar{w}_2(\xi, 0, s). \quad 0 < \xi < \infty. \quad (5)$$

The solution of the proposed fundamental problem can be obtained in the usual way by making use of integral transform methods. Apply a one-sided Laplace transform with respect to t and a two-sided Laplace transform with respect to ξ on (1). General solutions in the transform domain, which are bounded as $y \to -\infty$ (and $+\infty$, respectively), can be expressed as

$$\bar{w}_1^*(\lambda, y, s) = A_1(s, \lambda)e^{s\alpha_1^*(\lambda)y}, \quad (6)$$

$$\bar{w}_2^*(\lambda, y, s) = A_2(s, \lambda)e^{-s\alpha_2^*(\lambda)y}, \quad (7)$$

where

$$\alpha_j^*(\lambda) = \sqrt{b_j + \lambda(1 - b_j v)}\sqrt{b_j - \lambda(1 + b_j v)} = \alpha_{j+}^*(\lambda)\alpha_{j-}^*(\lambda), \quad j = 1, 2 \quad (8)$$

and A_1, A_2 are unknown functions. We define $b_{j,1} = b_j/(1 + b_j v)$ and $b_{j,2} = b_j/(1 - b_j v)$. The branch cuts of α_j^* are introduced to ensure $\mathrm{Re}(\alpha_j^*) \geq 0$ in the entire cut complex λ-plane, where "Re" denotes the real part.

Application of the Laplace transforms to the boundary conditions (3) to (5) yields

$$\bar{\tau}^*_{yz1}(\lambda, 0, s) = \bar{\tau}^*_{yz2}(\lambda, 0, s) = \frac{1}{s(\eta - \lambda)} + \bar{\tau}^*_{yz+}, \quad (9)$$

$$\bar{w}^*_1(\lambda, 0, s) = \bar{w}^*_2(\lambda, 0, s) = A_+, \quad (10)$$

where $\bar{\tau}^*_{yz+}$ and A_+ are unknown functions that are analytic in $\mathrm{Re}(\lambda) > -b_{2,2}$.

From Eqs. (6), (7), (9), and (10), the transformed displacements and shear stresses along the crack line $y = 0$ are

$$\bar{w}^*_1(\lambda, 0, s) = A_1 = A_+ + A_{1-}, \quad (11)$$

$$\bar{w}^*_2(\lambda, 0, s) = A_2 = A_+ + A_{2-}, \quad (12)$$

$$\mu_1 s \alpha^*_1(\lambda) A_1 = -\mu_2 s \alpha^*_2(\lambda) A_2 = \frac{1}{s(\eta - \lambda)} + \bar{\tau}^*_{yz+}. \quad (13)$$

In Eqs. (11) and (12), A_{1-} and A_{2-} are unknown functions analytic in $\mathrm{Re}(\lambda) < b_{j,1}$, respectively. Eliminating A_+ through (11) to (13), we have

$$A_- = \frac{\mu_1\alpha^*_1(\lambda) + \mu_2\alpha^*_2(\lambda)}{s\mu_1\mu_2\alpha^*_1(\lambda)\alpha^*_2(\lambda)}\left[\frac{1}{s(\eta - \lambda)} + \bar{\tau}^*_{yz+}\right], \quad (14)$$

where $A_- \equiv A_{1-} - A_{2-}$ is the transformed crack-opening displacement. At this point it is convenient to introduce a new function $Q^*(\lambda)$ by defining

$$Q^*(\lambda) = \frac{\mu_1\alpha^*_1(\lambda) + \mu_2\alpha^*_2(\lambda)}{\mu_1\mu_2 k\alpha^*_1(\lambda)}, \quad (15)$$

where

$$k = \frac{\mu_1\sqrt{1 - b_1^2 v^2} + \mu_2\sqrt{1 - b_2^2 v^2}}{\mu_1\mu_2\sqrt{1 - b_1^2 v^2}}.$$

The function $Q^*(\lambda)$ has the properties that $Q^*(\lambda) \to 1$ as $|\lambda| \to \infty$, and that $Q^*(\lambda)$ has neither zeros nor poles in the λ-plane by cuts along $b_{2,1} < \lambda < b_{1,1}$ and $-b_{1,2} < \lambda < -b_{2,2}$. From the general product factorization method, $Q^*(\lambda)$ can be written as the product of two regular functions $Q^*_+(\lambda)$ and $Q^*_-(\lambda)$, where

$$Q^*_+(\lambda) = \exp\left\{\frac{-1}{\pi}\int_{b_{2,2}}^{b_{1,2}} \tan^{-1}\left[\frac{\mu_2|\alpha^*_2(-z)|}{\mu_1\alpha^*_1(-z)}\right]\frac{dz}{z + \lambda}\right\} \quad (16)$$

and

$$Q^*_-(\lambda) = \exp\left\{\frac{-1}{\pi}\int_{b_{2,1}}^{b_{1,1}} \tan^{-1}\left[\frac{\mu_2|\alpha^*_2(z)|}{\mu_1\alpha^*_1(z)}\right]\frac{dz}{z - \lambda}\right\}. \quad (17)$$

In view of the previous discussion, Eq. (14) may be rewritten as

$$\frac{s\alpha^*_{2-}(\lambda)A_-}{Q^*_-(\lambda)} - \frac{kQ^*_+(\eta)}{s(\eta - \lambda)\alpha^*_{2+}(\eta)} = \frac{k}{s(\eta - \lambda)}\left[\frac{Q^*_+(\lambda)}{\alpha^*_{2+}(\lambda)} - \frac{Q^*_+(\eta)}{\alpha^*_{2+}(\eta)}\right] + \frac{kQ^*_+(\lambda)}{\alpha^*_{2+}(\lambda)}\bar{\tau}^*_{yz+}. \quad (18)$$

The left-hand side of this equation is regular for $\mathrm{Re}(\lambda) < b_{2,1}$, while the right-hand side is regular for $\mathrm{Re}(\lambda) > -b_{2,2}$. Applying the analytic continuation argument, therefore, each side of Eq. (18) represents one and the same entire function, say $E(\lambda)$. By Liouville's theorem, the bounded entire function $E(\lambda)$ is a constant. The magnitude of the constant can be obtained from order conditions on $E(\lambda)$ as $|\lambda| \to \infty$, which in turn are obtained from order conditions on the dependent field variables in the vicinity of $\xi = 0$. Furthermore, $\bar{w}_{1-}(\xi, 0, s) - \bar{w}_{2-}(\xi, 0, s)$ is expected to vanish as $\xi \to 0^-$ to ensure continuity of displacement, and $\bar{\tau}_{yz+}(\xi, 0, s)$ is expected to be square root singular as $\xi \to 0^+$ for the subsonic case. Consequently, from the Abel theorem, $E(\lambda)$ vanishes completely, and then from Eq. (18), we find

$$A_- \equiv A_{1-} - A_{2-} = \frac{kQ^*_+(\eta)Q^*_-(\lambda)}{s^2(\eta - \lambda)\alpha^*_{2+}(\eta)\alpha^*_{2-}(\lambda)}. \quad (19)$$

Making use of Eqs. (11) to (13) and eliminating $\bar{\tau}^*_{yz+}$, we obtain

$$A_+ = -\frac{\mu_1\alpha^*_1(\lambda)A_{1-} + \mu_2\alpha^*_2(\lambda)A_{2-}}{\mu_1\alpha^*_1(\lambda) + \mu_2\alpha^*_2(\lambda)}. \quad (20)$$

Substituting A_{2-} from (19) into (20), the amplitude of $\bar{w}^*_1$ in the transform domain can be found as

$$A_1 = \frac{Q^*_+(\eta)\alpha^*_{2+}(\lambda)}{s^2\mu_1\alpha^*_{2+}(\eta)(\eta - \lambda)\alpha^*_1(\lambda)Q^*_+(\lambda)}. \quad (21)$$

Similarly substituting A_{1-} from (19) into (20), we have

$$A_2 = \frac{-Q^*_+(\eta)}{s^2\mu_2\alpha^*_{2+}(\eta)(\eta - \lambda)\alpha^*_{2-}(\lambda)Q^*_+(\lambda)}. \quad (22)$$

In view of Eqs. (21), (22), (6), and (7), inverting the two-sided Laplace transform, we obtain the solutions of stresses and displacements for the fundamental problem in the Laplace transform domain as follows:

$$\bar{\tau}_{yz1}(\xi, y, s) = \frac{1}{2\pi i}\int \frac{Q^*_+(\eta)\alpha^*_{2+}(\lambda)}{\alpha^*_{2+}(\eta)(\eta - \lambda)Q^*_+(\lambda)} \times e^{s\alpha^*_1(\lambda)y + s\lambda\xi}d\lambda, \quad (23)$$

$$\bar{\tau}_{xz1}(\xi, y, s) = \frac{1}{2\pi i}\int \frac{\lambda Q^*_+(\eta)\alpha^*_{2+}(\lambda)}{\alpha^*_{2+}(\eta)(\eta - \lambda)\alpha^*_1(\lambda)Q^*_+(\lambda)} \times e^{s\alpha^*_1(\lambda)y + s\lambda\xi}d\lambda, \quad (24)$$

$$\bar{w}_1(\xi, y, s) = \frac{1}{2\pi i}\int \frac{Q^*_+(\eta)\alpha^*_{2+}(\lambda)}{s\mu_1\alpha^*_{2+}(\eta)(\eta - \lambda)\alpha^*_1(\lambda)Q^*_+(\lambda)} \times e^{s\alpha^*_1(\lambda)y + s\lambda\xi}d\lambda, \quad (25)$$

$$\bar{\tau}_{yz2}(\xi, y, s) = \frac{1}{2\pi i}\int \frac{Q^*_+(\eta)\alpha^*_{2+}(\lambda)}{\alpha^*_{2+}(\eta)(\eta - \lambda)Q^*_+(\lambda)} \times e^{-s\alpha^*_2(\lambda)y + s\lambda\xi}d\lambda, \quad (26)$$

$$\bar{\tau}_{xz2}(\xi, y, s) = \frac{1}{2\pi i}\int \frac{-\lambda Q^*_+(\eta)}{\alpha^*_{2+}(\eta)(\eta - \lambda)\alpha^*_{2-}(\lambda)Q^*_+(\lambda)} \times e^{-s\alpha^*_2(\lambda)y + s\lambda\xi}d\lambda, \quad (27)$$

$$\bar{w}_2(\xi, y, s) = \frac{1}{2\pi i}\int \frac{-Q^*_+(\eta)}{s\mu_2\alpha^*_{2+}(\eta)(\eta - \lambda)\alpha^*_{2-}(\lambda)Q^*_+(\lambda)} \times e^{-s\alpha^*_2(\lambda)y + s\lambda\xi}d\lambda. \quad (28)$$

The corresponding result of the dynamic stress intensity factor in the Laplace transform domain is

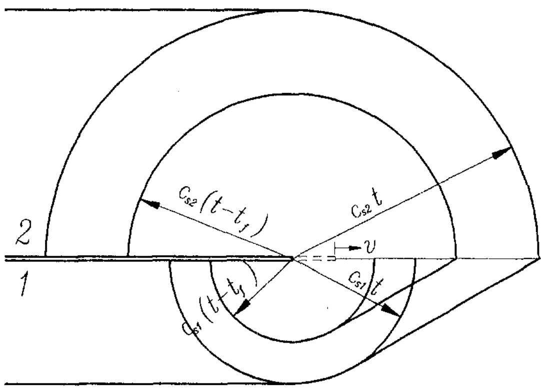

Fig. 2 Wave fronts of the incident and diffracted waves for $t > t_f$

$$\bar{K}(s) = \lim_{\xi\to 0} \sqrt{2\pi\xi}\,\bar{\tau}_{yz1}(\xi, 0, s) = \lim_{\xi\to 0} \sqrt{2\pi\xi}\,\bar{\tau}_{yz2}(\xi, 0, s)$$
$$= \frac{-\sqrt{2(1 - b_2 v)}\,Q_{+}^{*}(\eta)}{\sqrt{s}\,\alpha_{2+}^{*}(\eta)}. \quad (29)$$

3 Transient Analysis for a Propagating Crack Subjected to Antiplane Loadings

Consider a bimaterial medium composed of two homogeneous, isotropic, and linearly elastic solids. Materials 1 and 2 occupy the lower and upper half-planes, respectively. A semi-infinite crack lying along the interface of the bimaterial is initially stress-free and at rest. At time $t = 0$, an antiplane uniformly distributed dynamic loading with magnitude τ_0 is applied at the crack faces of the stationary semi-infinite crack. The time dependence of the loading is represented by the Heaviside step function $H(t)$. At time $t = t_f$, the crack suddenly propagates along the interface of these two materials with a constant velocity v as shown in Fig. 1. The loading does not expand over the newly created crack faces, but it continues to act on the original crack faces. For the subsonic case considered here, we assume $v < b_1^{-1} < b_2^{-1}$. The pattern of wave fronts for $t > t_f$ is indicated in Fig. 2. The transient elastodynamic problem is solved by superposition of the fundamental solutions obtained in the previous section in the Laplace transform domain. The transient solutions are composed of incident and diffracted fields, which are denoted by superscripts of i and d (or g), respectively. The incident waves are presented by two propagating plane waves that are induced by applying a uniformly distributed loading on crack faces. The diffracted waves include two parts, the first one is induced from the stationary crack tip by the application of a uniformly distributed traction on the crack faces and the second one is generated from the propagating crack tip as the crack starts to move. We now focus the analysis on the diffracted field generated by the stationary crack due to the incident plane wave (i.e., $t < t_f$). The incident field of the plane wave expressed in the Laplace transform domain can be expressed as follows:

$$\bar{\tau}_{yz}^{i}(x, 0, s) = \frac{1}{2\pi i}\int \frac{\tau_0}{s\lambda} e^{s\lambda x} d\lambda. \quad (30)$$

The applied traction on the crack faces, as indicated in (30), has the functional form $e^{s\lambda x}$. Since the solutions of applying traction $e^{s\eta x}$ on crack faces have been obtained in Section 2 (by setting $v = 0$), the diffracted field generated from the stationary semi-infinite crack can be constructed by superimposing the incident wave traction that is equal to (30). When we combine (23), (24), (26), and (27) by setting $v = 0$ and (30), the stress fields for the lower and upper planes in the Laplace transform domain can be obtained as follows:

$$\bar{\tau}_{yz1}^{d}(x, y, s) = \frac{1}{2\pi i}\int \frac{\tau_0}{s\eta_1}\left\{\frac{1}{2\pi i}\right.$$
$$\times \left.\int \frac{Q_{+}(\eta_1)\alpha_{2+}(\eta_2)}{\alpha_{2+}(\eta_1)(\eta_1 - \eta_2)Q_{+}(\eta_2)} e^{s\alpha_1 y + s\eta_2 x} d\eta_2\right\} d\eta_1$$
$$= \frac{1}{2\pi i}\int \frac{\tau_0 Q_{+}(0)\alpha_{2+}(\lambda)}{\sqrt{b_2}\, s\lambda Q_{+}(\lambda)} e^{s\alpha_1 y + s\lambda x} d\lambda, \quad (31)$$

$$\bar{\tau}_{xz1}^{d}(x, y, s) = \frac{1}{2\pi i}\int \frac{\tau_0 Q_{+}(0)\alpha_{2+}(\lambda)}{\sqrt{b_2}\, s\alpha_1(\lambda) Q_{+}(\lambda)} e^{s\alpha_1 y + s\lambda x} d\lambda, \quad (32)$$

$$\bar{\tau}_{yz2}^{d}(x, y, s) = \frac{1}{2\pi i}\int \frac{\tau_0 Q_{+}(0)\alpha_{2+}(\lambda)}{\sqrt{b_2}\, s\lambda Q_{+}(\lambda)} e^{-s\alpha_2 y + s\lambda x} d\lambda, \quad (33)$$

$$\bar{\tau}_{xz2}^{d}(x, y, s) = \frac{-1}{2\pi i}\int \frac{\tau_0 Q_{+}(0)}{\sqrt{b_2}\, s\alpha_{2-}(\lambda) Q_{+}(\lambda)} e^{-s\alpha_2 y + s\lambda x} d\lambda, \quad (34)$$

in which

$$Q(\lambda) = Q_{+}(\lambda)Q_{-}(\lambda) = Q_{+}^{*}(\lambda)|_{v=0}\, Q_{-}^{*}(\lambda)|_{v=0},$$
$$Q_{+}(0) = Q_{-}(0) = \sqrt{\frac{(\mu_1 b_1 + \mu_2 b_2)}{(u_1 + \mu_2) b_1}},$$
$$\alpha_j(\lambda) = \alpha_{j+}(\lambda)\alpha_{j-}(\lambda) = \alpha_{j+}^{*}(\lambda)|_{v=0}\,\alpha_{j-}^{*}(\lambda)|_{v=0}$$
$$= \sqrt{b_j + \lambda}\,\sqrt{b_j - \lambda}\,.$$

Applying the Cagniard-de Hoop method of Laplace inversion (see Appendix), the solutions of the stress field for the stationary crack in a time domain are obtained as follows:

$$\tau_{yz1}^{d}(x, y, t) = \frac{\tau_0 Q_{+}(0)}{\pi\sqrt{b_2}}\int_{b_1 R}^{t} \mathrm{Im}\left[\frac{\alpha_{2+}(\lambda_1^{+})\,\dfrac{\partial \lambda_1^{+}}{\partial t}}{\lambda_1^{+} Q_{+}(\lambda_1^{+})}\right]_{t=\tau} d\tau$$
$$- \tau_0 H(t + b_1 y) H(-x)$$
$$+ \frac{\tau_0 Q_{+}(0)}{\pi\sqrt{b_2}}\int_{0}^{t} \mathrm{Im}\left[\frac{\alpha_{2+}(\lambda_h)\,\dfrac{\partial \lambda_h}{\partial t}}{\lambda_h Q_{+}(\lambda_h)}\right]_{t=\tau} d\tau [H(t - t_h)$$
$$- H(t - b_1 R)] H\left(\cos\varphi - \frac{b_2}{b_1}\right), \quad (35)$$

$$\tau_{xz1}^{d}(x, y, t) = \frac{\tau_0 Q_{+}(0)}{\pi\sqrt{b_2}}\int_{b_1 R}^{t} \mathrm{Im}\left[\frac{\alpha_{2+}(\lambda_1^{+})\,\dfrac{\partial \lambda_1^{+}}{\partial t}}{\alpha_1(\lambda_1^{+}) Q_{+}(\lambda_1^{+})}\right]_{t=\tau} d\tau$$
$$+ \frac{\tau_0 Q_{+}(0)}{\pi\sqrt{b_2}}\int_{0}^{t} \mathrm{Im}\left[\frac{\alpha_{2+}(\lambda_h)\,\dfrac{\partial \lambda_h}{\partial t}}{\alpha_1(\lambda_h) Q_{+}(\lambda_h)}\right]_{t=\tau} d\tau [H(t - t_h)$$
$$- H(t - b_1 R)] H\left(\cos\varphi - \frac{b_2}{b_1}\right), \quad (36)$$

$$\tau_{yz2}^{d}(x, y, t) = \frac{\tau_0 Q_{+}(0)}{\pi\sqrt{b_2}}\int_{b_2 R}^{t} \mathrm{Im}\left[\frac{\alpha_{2+}(\lambda_2^{+})\,\dfrac{\partial \lambda_2^{+}}{\partial t}}{\lambda_2^{+} Q_{+}(\lambda_2^{+})}\right]_{t=\tau} d\tau$$
$$- \tau_0 H(t - b_2 y) H(-x), \quad (37)$$

$$\tau^d_{xz2}(x, y, t) = \frac{-\tau_0 Q_+(0)}{\pi\sqrt{b_2}} \int_{b_2R}^{t} \mathrm{Im}\left[\frac{\dfrac{\partial \lambda_2^+}{\partial t}}{\alpha_{2-}(\lambda_2^+)Q_+(\lambda_2^+)}\right]_{t=\tau} d\tau, \quad (38)$$

where

$$\lambda_j^+ = \frac{-t}{R}\cos\varphi + \frac{i\sin\varphi}{R}(t^2 - b_j^2R^2)^{1/2}, \quad j = 1, 2,$$

$$\lambda_h = \frac{-t}{R}\cos\varphi + \frac{\sin\varphi}{R}(b_1^2R^2 - t^2)^{1/2} + i\epsilon,$$

$$t_h = b_2R|\cos\varphi| - R\sin\varphi\sqrt{b_1^2 - b_2^2},$$

$$R = (x^2 + y^2)^{1/2}, \quad \varphi = \cos^{-1}\left(\frac{x}{R}\right).$$

The corresponding stress intensity factor expressed in the Laplace transform domain is

$$\bar{K}^d(s) = \frac{1}{2\pi i}\int \frac{\tau_0}{s\lambda}\left\{\frac{-\sqrt{2}Q_+(\lambda)}{\sqrt{s}\alpha_{2+}(\lambda)}\right\}d\lambda = \frac{\sqrt{2}\tau_0 Q_+(0)}{s^{3/2}\sqrt{b_2}}. \quad (39)$$

The dynamic stress intensity factor of the stationary interface crack induced by a diffracted d wave expressed in a time domain will be

$$K^d(t) = 2\tau_0 Q_+(0)\sqrt{\frac{2t}{\pi b_2}} = 2\tau_0\sqrt{\frac{2t(\mu_1 b_1 + \mu_2 b_2)}{\pi b_1 b_2(\mu_1 + \mu_2)}}. \quad (40)$$

The first terms in Eqs. (35)–(38) represent cylindrical waves which are radiated from the stationary crack tip due to the applied loading. The second terms in Eqs. (35) and (37) represent the corresponding plane waves in two half-planes. The last terms shown in (35) and (36) describe head waves generated by the mismatch bimaterial. The stress intensity factor expressed in (40) is equal to the one for a homogeneous medium multiplies a material-dependent function $Q_+(0)$. If $\mu_1 = \mu_2$, $b_1 = b_2$, in a homogeneous material, we have $Q_+(0) = 1$. The stress singular fields can be obtained by letting $R \to 0$ in Eqs. (35)–(38) and finally yield

$$\tau^{d,s}_{yz1}(x, y, t) = \tau^{d,s}_{yz2}(x, y, t) = \frac{2\tau_0 Q_+(0)}{\pi}\cos\left(\frac{\varphi}{2}\right)\sqrt{\frac{t}{b_2R}}, \quad (41)$$

$$\tau^{d,s}_{xz1}(x, y, t) = -\tau^{d,s}_{xz2}(x, y, t) = \frac{2\tau_0 Q_+(0)}{\pi}\sin\left(\frac{\varphi}{2}\right)\sqrt{\frac{t}{b_2R}}. \quad (42)$$

At time $t = t_f$, the dynamic stress intensity factor is assumed to reach its critical value and the interface crack starts to propagate with a constant subsonic speed v along the interface with uniformly distributed loading applied only on the original crack faces $-\infty < x < 0$. The applied uniformly distributed stress τ_0 on the original crack faces written in the Laplace transform domain for the moving coordinate system will have the following form:

$$\bar{\tau}^i_{yz}(\xi, 0, s) = \frac{1}{2\pi i}\int \frac{-\tau_0 d}{s\lambda(\lambda - d)} e^{s\lambda(\xi - vt_f)} d\lambda, \quad (43)$$

in which $d = 1/v$ is the slowness of the crack velocity and $\xi = x - v(t - t_f)$. The applied traction on the crack faces, as expressed in (43), has the functional form $e^{s\lambda\xi}$. Since the Laplace transform solutions of applying traction $e^{s\eta\xi}$ on the crack faces have been solved in the previous section, the stress fields generated from the propagating crack tip can be constructed by superimposing the fundamental solutions and the stress distribution in (43). The results of shear stresses expressed in the Laplace transform domain will be

$$\bar{\tau}^g_{yz1}(\xi, y, s) = \frac{1}{2\pi i}\int \frac{-\tau_0 d}{s\eta_1(\eta_1 - d)} e^{-s\eta_1 vt_f} \times \left\{\frac{1}{2\pi i}\int \frac{Q^*_+(\eta_1)\alpha^*_{2+}(\eta_2)}{\alpha^*_{2+}(\eta_1)(\eta_1 - \eta_2)Q^*_+(\eta_2)} \times e^{s\alpha^*_1 y + s\eta_2\xi} d\eta_2\right\} d\eta_1$$

$$= \frac{1}{2\pi i}\int \frac{\tau_0\alpha^*_{2+}(\lambda)}{sQ^*_+(\lambda)}\left[\frac{Q^*_+(0)}{\sqrt{b_2}\lambda} - \frac{Q^*_+(d)e^{-st_f}}{\sqrt{d}(\lambda - d)}\right] \times e^{s\alpha^*_1 y + s\lambda\xi} d\lambda, \quad (44)$$

$$\bar{\tau}^g_{xz1}(\xi, y, s) = \frac{1}{2\pi i}\int \frac{\tau_0\lambda\alpha^*_{2+}(\lambda)}{s\alpha^*_1(\lambda)Q^*_+(\lambda)} \times \left[\frac{Q^*_+(0)}{\sqrt{b_2}\lambda} - \frac{Q^*_+(d)e^{-st_f}}{\sqrt{d}(\lambda - d)}\right] e^{s\alpha^*_1 y + s\lambda\xi} d\lambda, \quad (45)$$

$$\bar{\tau}^g_{yz2}(\xi, y, s) = \frac{1}{2\pi i}\int \frac{\tau_0\alpha^*_{2+}(\lambda)}{sQ^*_+(\lambda)} \times \left[\frac{Q^*_+(0)}{\sqrt{b_2}\lambda} - \frac{Q^*_+(d)e^{-st_f}}{\sqrt{d}(\lambda - d)}\right] e^{-s\alpha^*_2 y + s\lambda\xi} d\lambda, \quad (46)$$

$$\bar{\tau}^g_{xz2}(\xi, y, s) = \frac{-1}{2\pi i}\int \frac{\tau_0\lambda}{s\alpha^*_{2-}(\lambda)Q^*_+(\lambda)} \times \left[\frac{Q^*_+(0)}{\sqrt{b_2}\lambda} - \frac{Q^*_+(d)e^{-st_f}}{\sqrt{d}(\lambda - d)}\right] e^{-s\alpha^*_2 y + s\lambda\xi} d\lambda. \quad (47)$$

Inverting the Laplace transform of (44)–(47), the exact transient solutions for a propagating interface crack at an unbounded bimaterial medium in time domain can be obtained as follows:

$$\tau^g_{yz1}(\xi, y, t) = \frac{\tau_0 Q^*_+(0)}{\pi\sqrt{b_2}}\int_{t_{d1}}^{t} \mathrm{Im}\left[\frac{\alpha^*_{2+}(\lambda_3^+)\dfrac{\partial\lambda_3^+}{\partial t}}{\lambda_3^+ Q^*_+(\lambda_3^+)}\right]_{t=\tau} d\tau$$

$$- \frac{\tau_0 Q^*_+(d)}{\pi\sqrt{d}}\int_{t_{d1}}^{t-t_f} \mathrm{Im}\left[\frac{\alpha^*_{2+}(\lambda_3^+)\dfrac{\partial\lambda_3^+}{\partial t}}{(\lambda_3^+ - d)Q^*_+(\lambda_3^+)}\right]_{t=\tau} d\tau$$

$$+ \left\{\frac{\tau_0 Q^*_+(0)}{\pi\sqrt{b_2}}\int_0^t \mathrm{Im}\left[\frac{\alpha^*_{2+}(\lambda_H)\dfrac{\partial\lambda_H}{\partial t}}{\lambda_H Q^*_+(\lambda_H)}\right]_{t=\tau} d\tau\right.$$

$$-\frac{\tau_0 Q_{\ddagger}^*(d)}{\pi\sqrt{d}}\int_0^{t-t_f}\mathrm{Im}\left[\frac{\alpha_{2+}^*(\lambda_H)\dfrac{\partial\lambda_H}{\partial t}}{(\lambda_H-d)Q_{\ddagger}^*(\lambda_H)}\right]_{t=\tau}d\tau\Bigg\}$$

$$\times[H(t-t_H)-H(t-t_{d1})]H\left(\cos\varphi-\frac{b_2}{b_1}\right),\quad (48)$$

$$\tau_{xz1}^g(\xi,y,t)=\frac{-\tau_0 Q_{\ddagger}^*(0)}{\pi\sqrt{b_2}}\int_{t_{d1}}^{t}\mathrm{Im}\left[\frac{\alpha_{2+}^*(\lambda_3^+)\dfrac{\partial\lambda_3^+}{\partial t}}{\alpha_1^*(\lambda_3^+)Q_{\ddagger}^*(\lambda_3^+)}\right]_{t=\tau}d\tau$$

$$+\frac{\tau_0 Q_{\ddagger}^*(d)}{\pi\sqrt{d}}\int_{t_{d1}}^{t-t_f}\mathrm{Im}\left[\frac{\lambda_3^+\alpha_{2+}^*(\lambda_3^+)\dfrac{\partial\lambda_3^+}{\partial t}}{\alpha_1^*(\lambda_3^+)(\lambda_3^+-d)Q_{\ddagger}^*(\lambda_3^+)}\right]_{t=\tau}d\tau$$

$$\times\Bigg\{\frac{-\tau_0 Q_{\ddagger}^*(0)}{\pi\sqrt{b_2}}\int_0^{t}\mathrm{Im}\left[\frac{\alpha_{2+}^*(\lambda_H)\dfrac{\partial\lambda_H}{\partial t}}{\alpha_1^*(\lambda_H)Q_{\ddagger}^*(\lambda_H)}\right]_{t=\tau}d\tau$$

$$+\frac{\tau_0 Q_{\ddagger}^*(d)}{\pi\sqrt{d}}\int_0^{t-t_f}\mathrm{Im}\left[\frac{\lambda_H\alpha_{2+}^*(\lambda_H)\dfrac{\partial\lambda_3^+}{\partial t}}{\alpha_1^*(\lambda_H)(\lambda_H-d)Q_{\ddagger}^*(\lambda_H)}\right]_{t=\tau}d\tau\Bigg\}$$

$$\times[H(t-t_H)-H(t-t_{d1})]H\left(\cos\varphi-\frac{b_2}{b_1}\right),\quad (49)$$

$$\tau_{yz2}^g(\xi,y,t)=\frac{\tau_0 Q_{\ddagger}^*(0)}{\pi\sqrt{b_2}}\int_{t_{d2}}^{t}\mathrm{Im}\left[\frac{\alpha_{2+}^*(\lambda_4^+)\dfrac{\partial\lambda_4^+}{\partial t}}{\lambda_4^+Q_{\ddagger}^*(\lambda_4^+)}\right]_{t=\tau}d\tau$$

$$-\frac{\tau_0 Q_{\ddagger}^*(d)}{\pi\sqrt{d}}\int_{t_{d2}}^{t-t_f}\mathrm{Im}\left[\frac{\alpha_{2+}^*(\lambda_4^+)\dfrac{\partial\lambda_4^+}{\partial t}}{(\lambda_4^+-d)Q_{\ddagger}^*(\lambda_4^+)}\right]_{t=\tau}d\tau,\quad (50)$$

$$\tau_{xz2}^g(\xi,y,t)=\frac{-\tau_0 Q_{\ddagger}^*(0)}{\pi\sqrt{b_2}}\int_{t_{d2}}^{t}\mathrm{Im}\left[\frac{\dfrac{\partial\lambda_4^+}{\partial t}}{\alpha_{2-}^*(\lambda_4^+)Q_{\ddagger}^*(\lambda_4^+)}\right]_{t=\tau}d\tau$$

$$+\frac{\tau_0 Q_{\ddagger}^*(d)}{\pi\sqrt{d}}\int_{t_{d2}}^{t-t_f}\mathrm{Im}\left[\frac{\lambda_4^+\dfrac{\partial\lambda_4^+}{\partial t}}{\alpha_{2-}^*(\lambda_4^+)(\lambda_4^+-d)Q_{\ddagger}^*(\lambda_4^+)}\right]_{t=\tau}d\tau,$$

$$(51)$$

where

$$\lambda_j^+=\frac{-(\xi t+b_{j-2}^2 vy^2)+i|y|\sqrt{t^2-b_{j-2}^2[y^2+(\xi+tv)^2]}}{\xi^2+(1-b_{j-2}^2v^2)y^2},\quad j=3,4,$$

$$\lambda_H=\frac{-(\xi t+b_1^2 vy^2)+|y|\sqrt{b_1^2[y^2+(\xi+tv)^2]-t^2}}{\xi^2+(1-b_1^2v^2)y^2},$$

$$t_{dj}=\frac{b_j\{b_jv\xi+[\xi^2+(1-b_j^2v^2)y^2]^{1/2}\}}{1-b_j^2v^2},\quad j=1,2,$$

$$t_H=\frac{b_2\xi-y\sqrt{b_1^2-b_2^2}}{1-b_2v}.$$

The results expressed in (48)–(51) reveal a very interesting phenomenon. The full-field solutions of an interfacial crack propagating with constant speed subjected to loads applied on the original crack faces can be expressed by two parts, each one having its own physical meaning. The odd terms represent the first part due to applying the uniform loading on the original and new crack faces for a crack which begins to grow at constant speed at time t_f after the loading is applied. The functional form of the first part is the same as the solution of the problem with a uniform loading applied on the original and new crack faces with no delay time. The only dependence on delay time is through the definition of ξ. The even terms represent the second part for a crack which starts to propagate at time t_f with loading applied uniformly on the new crack faces only.

The dynamic stress intensity factor for a propagating interface crack can also be constructed in a similar manner. The result in the Laplace transform domain can be obtained from (29) and (43) and is expressed as follows:

$$\bar{K}^g(s)=\frac{1}{2\pi i}\int\frac{-\tau_0 d}{s\lambda(\lambda-d)}e^{-s\lambda vt_f}\times\left\{\frac{-\sqrt{2(1-b_2v)}Q_{\ddagger}^*(\lambda)}{\sqrt{s}\alpha_{2+}^*(\lambda)}\right\}d\lambda.\quad (52)$$

The inversion of the Laplace transform (52) to the time domain will have the following form:

$$K^g(t)=\frac{2\sqrt{2(1-b_2v)}\tau_0}{\sqrt{\pi}}\times\left[Q_{\ddagger}^*(0)\sqrt{\frac{t}{b_2}}-Q_{\ddagger}^*(d)\sqrt{\frac{t-t_f}{d}}\right].\quad (53)$$

For the limit case $b_1=b_2$, the solutions of (48)–(51) and (53) for the propagating interface crack in a bimaterial can be reduced to that obtained by Ma and Burgers (1988) and Ma and Ing (1995) in a homogeneous material. If the propagating speed v approaches the lowest shear wave speed c_{s1}, then the dynamic stress intensity factor approaches zero.

The singular stresses near the propagating crack tip can be deduced from the full-field solutions expressed in (48)–(51), and the results are

$$\tau_{yz1}^{g,s}(\xi,y,t)=\frac{2\sqrt{1-b_2v}\tau_0}{\pi\sqrt{r_1}}\times\cos\frac{\theta_1}{2}\left[Q_{\ddagger}^*(0)\sqrt{\frac{t}{b_2}}-Q_{\ddagger}^*(d)\sqrt{\frac{t-t_f}{d}}\right],\quad (54)$$

$$\tau_{xz1}^{g,s}(\xi,y,t)=\frac{2\sqrt{1-b_2v}\tau_0}{\sqrt{1-b_1^2v^2}\pi\sqrt{r_1}}\times\sin\frac{\theta_1}{2}\left[Q_{\ddagger}^*(0)\sqrt{\frac{t}{b_2}}-Q_{\ddagger}^*(d)\sqrt{\frac{t-t_f}{d}}\right],\quad (55)$$

$$\tau_{yz2}^{g,s}(\xi,y,t)=\frac{2\sqrt{1-b_2v}\tau_0}{\pi\sqrt{r_2}}\times\cos\frac{\theta_2}{2}\left[Q_{\ddagger}^*(0)\sqrt{\frac{t}{b_2}}-Q_{\ddagger}^*(d)\sqrt{\frac{t-t_f}{d}}\right],\quad (56)$$

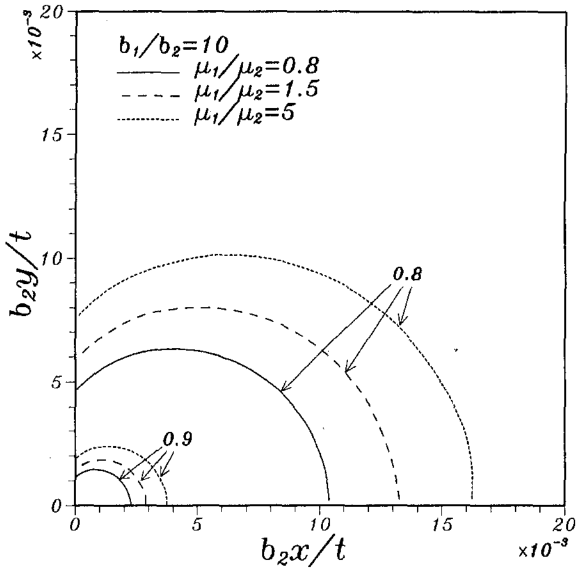

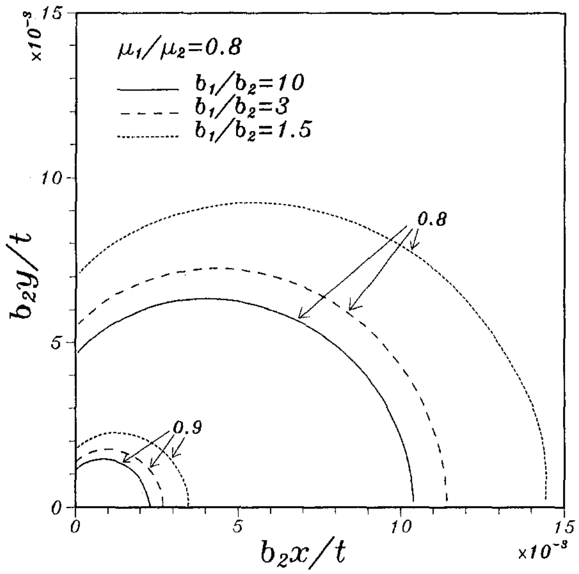

Fig. 3 The ratios of the transient solution τ^d_{yz2} to the stress singular field $\tau^{d,s}_{yz2}$ for different values of μ_1/μ_2 for the stationary crack

Fig. 4 The ratios of the transient solution τ^d_{yz2} to the stress singular field $\tau^{d,s}_{yz2}$ for different values of b_1/b_2 for the stationary crack

$$\tau^{g,s}_{xz2}(\xi, y, t) = \frac{-2\tau_0}{\sqrt{1 + b_2 v}\,\pi\sqrt{r_2}} \times \sin\frac{\theta_2}{2}\left[Q^*_+(0)\sqrt{\frac{t}{b_2}} - Q^*_+(d)\sqrt{\frac{t-t_f}{d}}\right], \quad (57)$$

where

$$r_1 = [\xi^2 + (1 - b_1^2 v^2)y^2]^{1/2},$$
$$\theta_1 = \tan^{-1}(\sqrt{1 - b_1^2 v^2}\, y/\xi), \quad -\pi/2 < \theta_1 < 0,$$
$$r_2 = [\xi^2 + (1 - b_2^2 v^2)y^2]^{1/2},$$
$$\theta_2 = \tan^{-1}(\sqrt{1 - b_2^2 v^2}\, y/\xi), \quad 0 < \theta_2 < \pi/2.$$

4 Numerical Results

In the previous section, the transient full-field solutions and the stress intensity factors for the problem of an interface crack subjected to antiplane uniform loading in a bimaterial are derived. For time $t < t_f$, the stress intensity factor of the stationary crack is given by (40). It can be seen from the solution that the material-dependent function $Q_+(0)$ is the only influence factor on the stress intensity factor for different material combinations. For the case we have studied, namely $b_1 > b_2$, $Q_+(0)$ is always less than one for any combination of two material constants. This means that the dynamic stress intensity factor of a bimaterial is always less than that of a homogeneous material. For the special case of $\mu_1/\mu_2 \to \infty$, then $Q_+(0) \to 1$, and for $\mu_1/\mu_2 \to 0$, then $Q_+(0) \to \sqrt{b_2/b_1}$.

The ratios of the full-field stress τ^d_{yz2} evaluated from (37) to the stress singular field (41) have been computed numerically for different values of μ_1/μ_2 and b_1/b_2, and the results are shown in Figs. 3 and 4. Assume that for a ratio of 0.9, the actual stress is accurately described by the stress singular field. Then the region of the stress singular field will be valid only for material points very close to the stationary crack tip, within a distance from the tip of 0.2 percent ~ 0.4 percent of the distance to the cylindrical shear wave front of material 2. The region of validity of the stress singular field is time-dependent in the highly transient process. Hence, the use of the singular field to approximate the actual stress field should be carefully considered, especially in the early stages of the dynamic transient field. The transient stress field along the interface normalized by the singular field for different material combinations is shown in Fig. 5, which indicates that the homogeneous case has the largest region of a singular field for the stationary crack.

Figures 6 and 7 show the dimensionless stress intensity factors of a propagating crack versus dimensionless time t/t_f for various values of μ_1/μ_2 and b_1/b_2, respectively. It is shown in Fig. 6 that the smaller μ_1/μ_2 is, the smaller the stress intensity factor for constant v and b_1/b_2. In addition, Fig. 7 indicates that the smaller b_1/b_2 is, the smaller the stress intensity factor for constant v and μ_1/μ_2. Figure 8 plots the dimensionless stress intensity factors versus dimensionless time t/t_f for different values of crack velocity v for $b_1/b_2 = 10$ and $\mu_1/\mu_2 = 0.8$. It is also noted that the stress intensity factor decreases as the crack running velocity increases; that is, the stationary crack ($v = 0$) will induce the maximum dynamic stress intensity factor among those different running cases. Because the crack-tip speed changes discontinuously at $t = t_f$, the stress intensity factor also

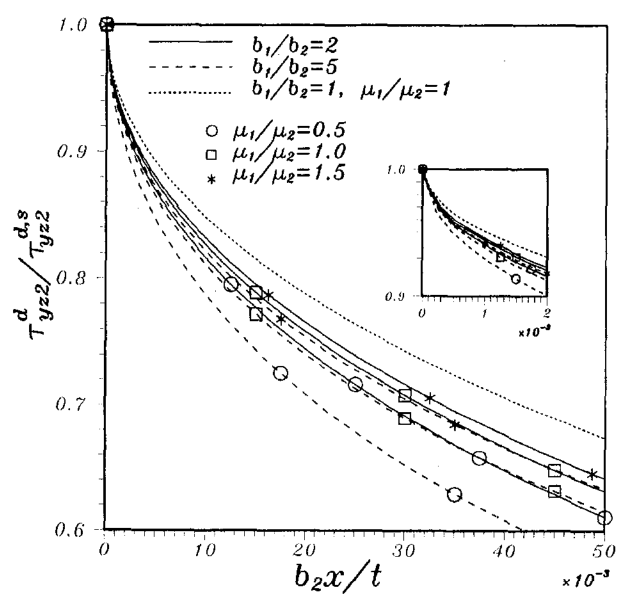

Fig. 5 The transient stress field along the interface for different material combinations for the stationary crack

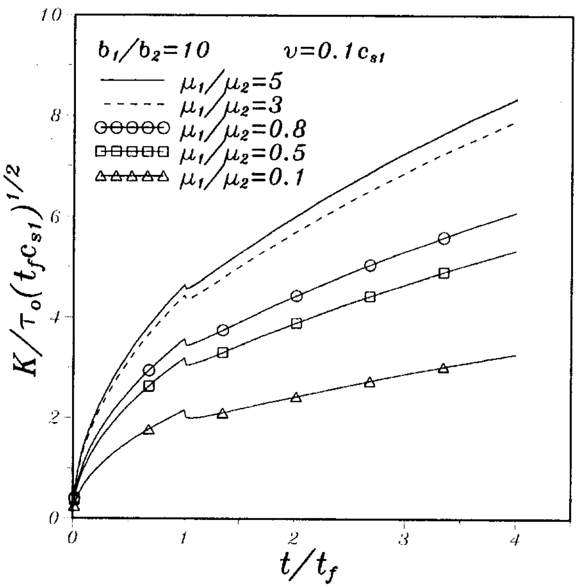

Fig. 6 Stress intensity factors of a propagating interface crack for different values of μ_1/μ_2

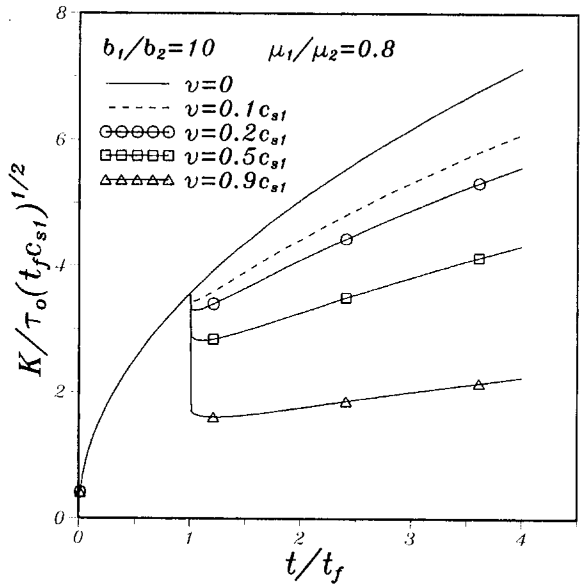

Fig. 8 Stress intensity factors of a propagating interface crack for different values of crack velocity v

changes abruptly at the same time. In all cases, the magnitude of the stress intensity factor immediately after the jump is

$$\frac{Q_+^*(0)\sqrt{1-b_2 v}\sqrt{(\mu_1+\mu_2)b_1}}{\sqrt{\mu_1 b_1+\mu_2 b_2}}$$

times the magnitude just before the jump.

In order to investigate the effect of the crack propagation speed on the stress singular field, we have also calculated the ratio of the exact stress (50) around the propagating crack tip and the singular part of the stress field (56). In Fig. 9 the position of the fixed ratios 0.9 and 0.8 for the full field and the singular field is plotted for applied uniformly distributed loading on the original crack faces only (i.e., along $-\infty < x \le 0$). If we compare the results for the propagating crack case (Fig. 9) with the results of the stationary crack case (Fig. 3 and Fig. 4), it is very surprising to find that there is a large difference in the area around the crack tip dominated by the singular field for the slow crack-tip speed ($b_1/d = 0.1$) and the stationary crack case. Moreover, we found that the region for the singular field is large for higher crack speed. The stress along the interface for the propagating crack is shown in Fig. 10 and it also indicates that the stationary crack has the smallest region of stress singular field. We try to find out what is the significant reason that influences the region of the singular field, i.e., the mismatch of the material properties or the loading condition. We plot the transient stress field along the interface normalized by the singular field for a homogeneous crack case (i.e., $b_1/b_2 = 1$, $\mu_1/\mu_2 = 1$) and the result is shown in Fig. 11. A similar result as for the bimaterial interface crack is also obtained, that is the singular field is large for higher crack speed. Finally, the contour of fixed ratios for the full field and singular field for applied uniformly distributed loading on the original and propagating crack face (i.e., along $-\infty < \xi \le 0$) is shown in Fig. 12. An interesting result is obtained: the size of the region for

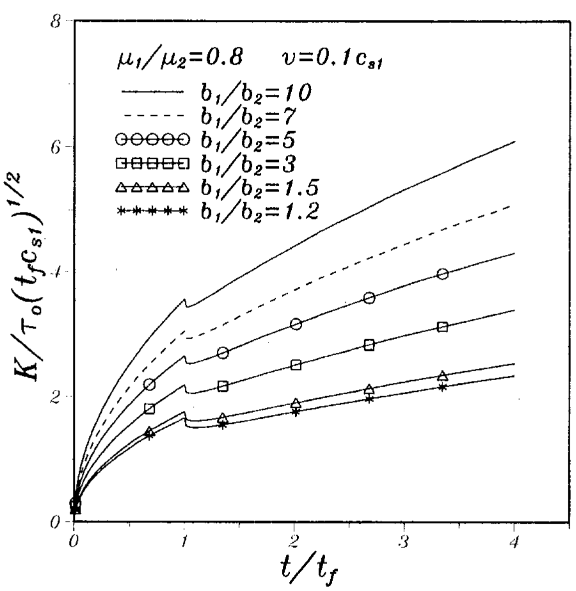

Fig. 7 Stress intensity factors of a propagating interface crack for different values of b_1/b_2

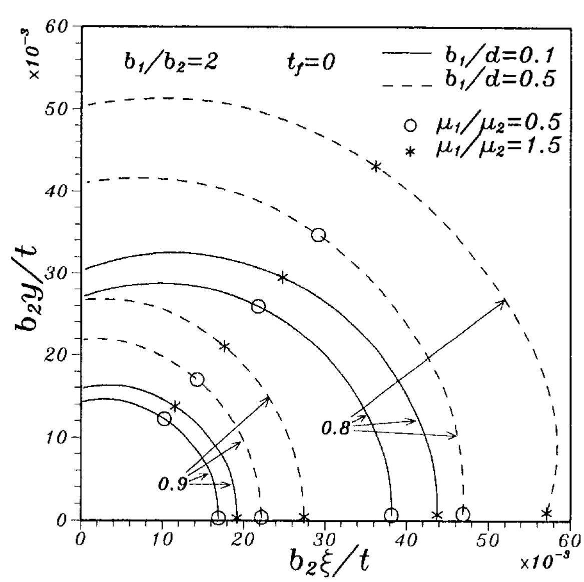

Fig. 9 The ratios of the transient solution τ_{yz2}^{g} to the stress singular field $\tau_{yz2}^{g,s}$ for the propagating interface crack with loading applied on the original crack faces only

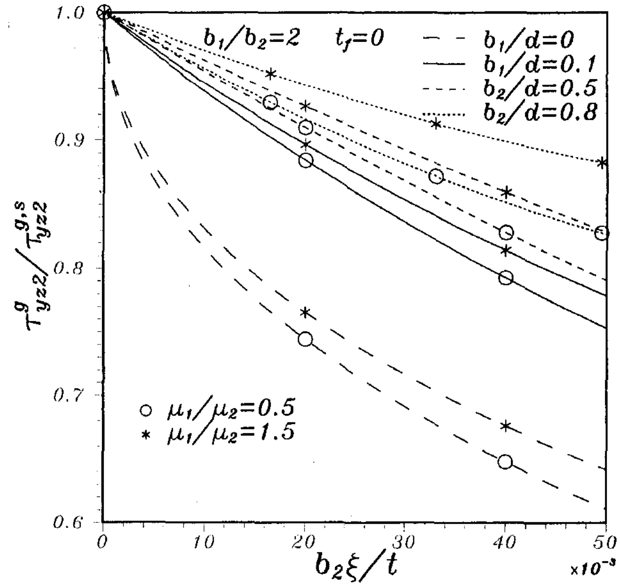

Fig. 10 The transient stress field along the interface for the propagating crack

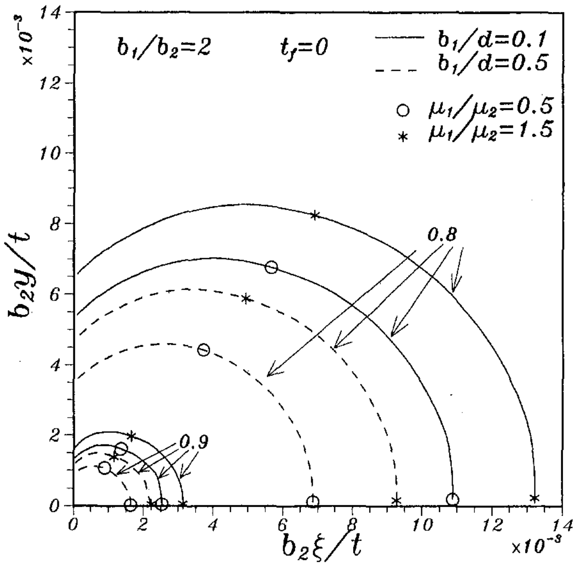

Fig. 12 The ratios of the transient solution τ^{g}_{yz2} to the stress singular field $\tau^{g,s}_{yz2}$ for the propagating interface crack with loading applied on the original and newly created crack faces

the singular field is large for lower crack speed. Hence we can conclude that the region of the singular field is strongly dependent on the loading condition applied on the crack faces.

For in-plane homogeneous crack propagation, Ma and Freund (1986) and Ma and Chen (1992) also indicated that the region of the stress singular field will be valid only for points very close to the crack tip. They found that the extent of the stress singular field during dynamic crack growth is more limited than a steady-state analysis would indicate. In the case of dynamic loading on a stationary crack, the ability to find a stress singular field over a region of some minimal size near the crack tip may hinge only on waiting for the wavefronts to pass and the transients to die away. In the case of dynamic crack propagation, however, the transients are being continuously refreshed. Freund and Rosakis (1992) used a higher order asymptotic expansion of crack-tip fields for transient in-plane crack growth. They found that the transient nature of the stress field during the early phase of crack growth prevents a complete stress singular field to be established, which suggests that higher order transient terms should be included in the analysis.

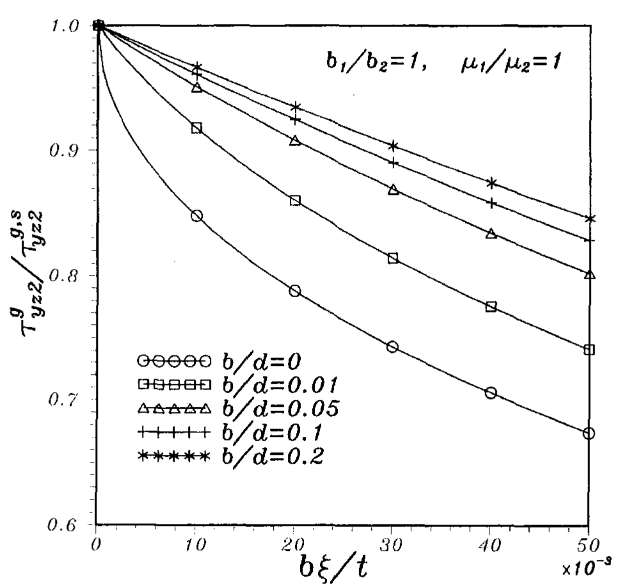

Fig. 11 The transient stress field along the interface for the homogeneous case

5 Conclusions

The mechanical behavior of many newly developed multiphase materials are mainly controlled by the response of the interface. Many researchers have devoted effort to investigating the field of dynamic debonding along a bimaterial interface. The transient problem of a propagating interface crack in an infinite bimaterial is considered in this study. The equivalent steady-state problem has been studied by many investigators in the past twenty years, but the transient solution was not found. In this paper, the transient full-field solutions and the stress intensity factor are obtained by superposition of a useful fundamental solution in the Laplace transform domain. The proposed fundamental solution is an exponentially distributed traction applied on the propagating crack faces. This fundamental solution is successfully applied towards solving this transient problem and is demonstrated as an efficient methodology to solve other similar problems.

In the study of dynamic crack propagation phenomena, it is very important to have available as complete a description of the prevailing mechanical fields as possible. Interest in the stress intensity factor in considering dynamic crack growth stems from its potential as a driving force for the fracture process. From the experimental point of view, measurements of the field quantities near the crack tip are used to obtain the stress intensity factor. Interpretation of the stress field near the edge of a crack in terms of a stress intensity factor magnitude is usually based on the assumption that a stress singular field does indeed exist. Whether or not the data obtained from the experimental observations are within the stress singular field is important in the determination of the correct stress intensity factor. In order to investigate the region where the stress singular field is valid for the propagating crack, a detailed investigation is made in this study between the singular part of the stress field and the complete transient stress field near the propagating interface crack. It is found that the region of the stress singular field will be valid only for material points very close to the crack tip, within a distance from the crack tip of 0.2 to 2 percent of the distance to the largest value of the shear wave front. It is also indicated in this study that the size of the stress singular field is strongly dependent on the loading condition applied on the crack faces.

The stress singular field will propagate out from the crack tip. If we fix a material point near the moving crack tip, the ratio of actual stress and stress calculated from the stress singular field will increase as time increases and this material point will eventually be inside the stress singular field. Hence, the stress singular field needs time to build up over a region of given size near the propagating tip in the highly transient process.

Acknowledgments

The authors gratefully acknowledge the financial support of this research by the National Science Council (Republic of China) under Grant NSC 84-2212-E001-062.

References

Brock, L. M., 1974, "Dynamic Intensity Factors for an Interface Flaw Extending at a Non-Uniform Rate," *Journal of Elasticity*, Vol. 4, pp. 51–63.

Brock, L. M., and Achenbach, J. D., 1973, "Extension of an Interface Flaw under the Influence of Transient Waves," *International Journal of Solids and Structures*, Vol. 9, pp. 53–68.

Cagniard, L., 1962, *Reflection and Refraction of Progressive Seismic Waves* (translation by E. A. Flinn and C. H. Dix), McGraw-Hill, New York.

Chung, Y. L., and Robinson, A. R., 1992, "The Transient Problem of a Mode-III Interface Crack," *Engineering Fracture Mechanics*, Vol. 41, pp. 321–330.

Coussy, O., 1984, "Rupture Dynamique Fragile d'une Interface en Mouvement Transitoire Antiplane," *C. R. Acad. Sc., Paris*, t. 299, Serie II, No. 16.

de Hoop, A. T., 1958, "Representation Theorems for the Displacement in an Elastic Solid and Their Application to Elastodynamic Diffraction Theory," Doctoral dissertation, Technische hoegschool, Delft, The Netherlands.

de Hoop, A. T., 1961, "A Modification of Cagniard's Method for Solving Seismic Pulse Problems," *Applied Scientific Research*, Vol. B8, pp. 349–356.

Deng, X., 1992, "Complete Complex Series Expansions of Near-tip Fields for Steadily Growing Interface Cracks in Dissimilar Isotropic Materials," *Engineering Fracture Mechanics*, Vol. 2, pp. 237–242.

England, A. H., 1965, "A Crack Between Dissimilar Media," ASME Journal of Applied Mechanics, Vol. 32, pp. 400–402.

Erdogan, F., 1965, "Stress Distribution in Bonded Dissimilar Material With Cracks," ASME Journal of Applied Mechanics, Vol. 32, pp. 403–410.

Freund, L. B., 1972a, "Crack Propagation in an Elastic Solid Subjected to General Loading—I. Constant Rate of Extension," *J. Mech. Phys. Solids*, Vol. 20, pp. 129–140.

Freund, L. B., 1972b, "Crack Propagation in an Elastic Solid Subjected to General Loading—II. Non-uniform Rate of Extension," *J. Mech. Phys. Solids*, Vol. 20, pp. 141–152.

Freund, L. B., 1973, "Crack Propagation in an Elastic Solid Subjected to General Loading—III. Stress Wave Loading," *J. Mech. Phys. Solids*, Vol. 21, pp. 47–61.

Freund, L. B., 1974, "Crack Propagation in an Elastic Solid Subjected to General Loading—IV. Obliquely Incident Stress Pulse," *J. Mech. Phys. Solids*, Vol. 22, pp. 137–146.

Freund, L. B., and Rosakis, A. J., 1992, "The Structure of the Near-Tip Field during Transient Elastodynamic Crack Growth," *J. Mech. Phys. Solids*, Vol. 40, pp. 699–719.

Ma, C. C., and Freund, L. B., 1986, "The Extent of the Stress Intensity Factor Field during Crack Growth under Dynamic Loading Conditions," ASME Journal of Applied Mechanics, Vol. 53, pp. 303–310.

Ma, C. C., and Burgers, P., 1986, "Mode III Kinking With Delay Time: An Analytical Approximation," *International Journal of Solids and Structures*, Vol. 22, pp. 883–899.

Ma, C. C., and Burgers, P., 1987, "Dynamic Mode I and Mode II Crack Kinking Including Delay Time Effects," *International Journal of Solids and Structures*, Vol. 23, pp. 897–918.

Ma, C. C., and Burgers, P., 1988, "Initiation, Propagation, and Kinking of an Antiplane Crack," ASME Journal of Applied Mechanics, Vol. 55, pp. 111–119.

Ma, C. C., 1988, "Initiation, Propagation, and Kinking of an In-Plane Crack," ASME Journal of Applied Mechanics, Vol. 55, pp. 587–595.

Ma, C. C., 1990, "Dynamic Mixed Mode I–II Crack Kinking Under Oblique Stress Wave Loading in Brittle Solids," ASME Journal of Applied Mechanics, Vol. 57, pp. 117–127.

Ma, C. C., and Chen, S. K., 1992, "Investigations on the Stress Intensity Factor Field for Unstable Dynamic Crack Growth," *International Journal of Fracture*, Vol. 58, pp. 345–359.

Ma, C. C., and Ing, Y. S., 1995, "Transient Analysis of Dynamic Crack Propagation with Boundary Effect," ASME Journal of Applied Mechanics, Vol. 62, pp. 1029–1038.

Noble, B., 1958, "The Wiener-Hopf Technique," Pergamon Press, New York.

Rice, J. R., and Sih, G. C., 1965, "Plane Problems of Cracks in Dissimilar Media," ASME Journal of Applied Mechanics, Vol. 32, pp. 418–423.

Tsai, C. H., and Ma, C. C., 1992, "Transient Analysis of a Semi-Infinite Crack Subjected to a Dynamic Concentrated Forces," ASME Journal of Applied Mechanics, Vol. 59, pp. 804–811.

Williams, M. L., 1959, "The Stress Around a Fault or Crack in Dissimilar Media," *Bull. Seism. Soc. America*, Vol. 49, pp. 199–204.

Willis, J. R., 1971, "Fracture Mechanics of Interfacial Cracks," *J. Mech. Phys. Solids*, Vol. 19, pp. 353–368.

Wu, K. C., 1991, "Explicit Crack-Tip Fields of an Extending Interface Crack in an Anisotropic Bimaterial," *International Journal of Solids and Structures*, Vol. 27, pp. 455–466.

Yang, W., Suo, Z., and Shih, C. F., 1991, "Mechanics of Dynamic Debonding," *Proc. of the Royal Society London*, Vol. A433, pp. 679–697.

Yu, H., and Yang, W., 1994, "Mechanics of Transonic Debonding of a Bimaterial Interface: The Anti-plane Shear Case," *J. Mech. Phys. Solids*, Vol. 42, pp. 1789–1802.

Yu, H., and Yang, W., 1995, "Mechanics of Transonic Debonding of a Bimaterial Interface: The In-plane Shear Case," *J. Mech. Phys. Solids*, Vol. 43, pp. 207–232.

APPENDIX

By inspecting Eqs. (31)–(34), one must evaluate two inversion integrals to obtain solutions in the physical (time) domain. To execute this step, de Hoop (1961) proposed a powerful technique introduced earlier by Cagniard (1962) to invert two transforms in one operation. In this study, we used the so-called Cagniard-de Hoop method for the inversion of the Laplace transform to obtain the transient results of shear stresses and stress intensity factor. Here we would like to perform the Laplace transform inversion for $\bar{\tau}^d_{yz1}$ in some detail. We rewrite Eq. (31) as

$$\bar{\tau}^d_{yz1}(x, y, s) = \frac{1}{2\pi i}\int \frac{\tau_0 Q_+(0)\alpha_{2+}(\lambda_1)}{\sqrt{b_2} s\lambda_1 Q_+(\lambda_1)} e^{s\alpha_1 y + s\lambda_1 x} d\lambda_1, \quad \text{(A1)}$$

and then the change of variable is used by letting

$$\alpha_1 y + \lambda_1 x = -t. \quad \text{(A2)}$$

Equation (A2) can be solved for λ_1 to yield

$$\lambda_1^{\pm} = \frac{-t}{R}\cos\varphi \pm \frac{i\sin\varphi}{R}(t^2 - b_1^2 R^2)^{1/2}, \quad \text{(A3)}$$

where

$$R = (x^2 + y^2)^{1/2}, \quad \varphi = \cos^{-1}\left(\frac{x}{R}\right).$$

The path of integration for λ_1 in Eq. (A1) is initially parallel to the imaginary axis and satisfies $-b_2 < \mathrm{Re}[\lambda_1] < 0$ in the complex λ_1-plane. The branch cuts and the only pole at the origin for the kernel of the integration are shown in Fig. 13. The idea of the Cagniard-de Hoop method is to deform the path of integration in the complex λ_1-plane. In view of Eq. (A3), the change of path for λ_1 can be classified into three various cases for different observed positions.

(a) $-\pi < \varphi < -\pi/2$**:** In this case, the path of integration will be changed to the right half-plane and a simple pole at $\lambda_1 = 0$ will be enclosed as shown in Fig. 13. Then Eq. (A1) can be written as

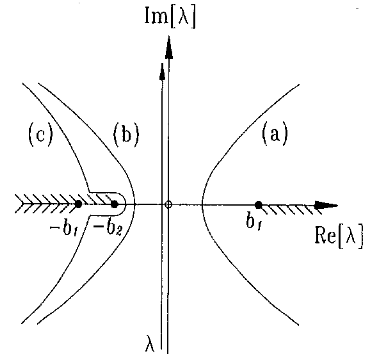

Fig. 13 Cagniard-de Hoop contours in the complex λ_1-plane

$$\bar{\tau}^d_{yz1}(x, y, s) = \frac{\tau_0 Q_+(0)}{2\pi i s\sqrt{b_2}} \left[\int_\infty^{b_1 R} \frac{\alpha_{2+}(\lambda_1^-)}{\lambda_1^- Q_+(\lambda_1^-)} \frac{\partial \lambda_1^-}{\partial t} e^{-st} dt + \int_{b_1 R}^\infty \frac{\alpha_{2+}(\lambda_1^+)}{\lambda_1^+ Q_+(\lambda_1^+)} \frac{\partial \lambda_1^+}{\partial t} e^{-st} dt \right], \quad (A4)$$

plus the contribution of the pole at $\lambda_1 = 0$. Using Eq. (A3), Eq. (A4) may thus be written as

$$\bar{\tau}^d_{yz1}(x, y, s) = \frac{\tau_0 Q_+(0)}{\pi s\sqrt{b_2}} \times \int_0^\infty \mathrm{Im}\left[\frac{\alpha_{2+}(\lambda_1^+)}{\lambda_1^+ Q_+(\lambda_1^+)} \frac{\partial \lambda_1^+}{\partial t} \right] H(t - b_1 R) e^{-st} dt. \quad (A5)$$

Since the inverse Laplace transform of the integral part in Eq. (A5) can be obtained by inspection

$$L^{-1}\left\{ \int_0^\infty \mathrm{Im}\left[\frac{\alpha_{2+}(\lambda_1^+)}{\lambda_1^+ Q_+(\lambda_1^+)} \frac{\partial \lambda_1^+}{\partial t} \right] H(t - b_1 R) e^{-st} dt \right\} = \mathrm{Im}\left[\frac{\alpha_{2+}(\lambda_1^+)}{\lambda_1^+ Q_+(\lambda_1^+)} \frac{\partial \lambda_1^+}{\partial t} \right] H(t - b_1 R), \quad (A6)$$

the inverse transform of Eq. (A5) may be carried out by the convolution theorem and the result is expressed as

$$\tau^d_{yz1}(x, y, t) = \frac{\tau_0 Q_+(0)}{\pi\sqrt{b_2}} \int_{b_1 R}^t \mathrm{Im}\left[\frac{\alpha_{2+}(\lambda_1^+) \dfrac{\partial \lambda_1^+}{\partial t}}{\lambda_1^+ Q_+(\lambda_1^+)} \right]_{t=\tau} d\tau. \quad (A7)$$

On the other hand, the contribution of the pole $\lambda_1 = 0$ must be taken into account for this case and the contribution from the pole is

$$\bar{\tau}^d_{yz1}(x, y, s) = -\frac{\tau_0 e^{s b_1 y}}{s}. \quad (A8)$$

The inverse Laplace transform of the corresponding wave in Eq. (A8) is

$$\tau^d_{yz1}(x, y, t) = -\tau_0 H(t + b_1 y) H(-x). \quad (A9)$$

(b) $-\pi/2 < \varphi < -\cos^{-1}(b_2/b_1)$: The path of integration will change to the left half-plane and the new path does not cross the branch cuts in the complex λ_1-plane. No pole should be taken into account in this case. Following the same procedure mentioned above, the final result of inversion can be obtained and the solution has the same form as Eq. (A7).

(c) $-\cos^{-1}(b_2/b_1) < \varphi < 0$: In this case, the path of integration will change to path (c) in the left half-plane as shown in Fig. 13. The new path consists of a hyperbola plus an indentation between the branch points $\lambda_1 = -b_2$ and $\lambda_1 = -b_1$. The contribution from the path of hyperbola has the same formulation as Eq. (A7). Furthermore, the integral of a straight line around the branch cut can be inverted and the result is

$$\tau^d_{yz1}(x, y, t) = \frac{\tau_0 Q_+(0)}{\pi\sqrt{b_2}} \int_0^t \mathrm{Im}\left[\frac{\alpha_{2+}(\lambda_h) \dfrac{\partial \lambda_h}{\partial t}}{\lambda_h Q_+(\lambda_h)} \right]_{t=\tau} d\tau \times [H(t - t_h) - H(t - b_1 R)] H\left(\cos\varphi - \frac{b_2}{b_1} \right). \quad (A10)$$

Combining the results obtained in (A7), (A9), and (A10), the transient full-field solution for $\tau^d_{yz1}(x, y, t)$ is expressed in Eq. (35).

In-Plane and Out-of-Plane Free Vibration Analysis of Archimedes-Type Spiral Springs

V. Yıldırım
Associate Professor,
Department of Mechanical Engineering,
Çukurova University,
01330 Balcalı, Adana, Turkey

The in-plane and out-of-plane free vibration frequencies of Archimedes-type spiral springs are computed by the transfer matrix method. Taking into account the effects of the axial and the shear deformations and the rotary inertia, the overall dynamic transfer matrix is computed up to any desired numerical accuracy by the complementary functions method. Since there are no restrictions for the number of coils and for the form of the spring (close-coiled or open-coiled), the presented method is general. After having verified the soundness of the computer program devised, the effects of the number of coils, of the axial and shear deformations, of rotary inertia and of the boundary conditions on the frequencies are also investigated.

1 Introduction

The problem of the free vibration of bars whose axes are in the form of a curve in-plane has been investigated by many researchers. Using the Bernoulli-Euler beam theory, Volterra and Morrell (1960, 1961a, b), have obtained the fundamental frequencies of both the in-plane and the out-of-plane free vibrations of curved bars having the center line in the forms of a cycloid, a catenary, or a parabola. Suzuki et al. (1978) have also worked out the out-of-plane free vibration of curved bars with clamped ends having the center lines in the form of ellipses, sines, catenaries, hyperbolas, parabolas, and cycloids by the classical beam theory. Lee and Wilson (1989) have investigated parabolic, sinusoidal, and elliptic arches, both theoretically and experimentally. The axial deformations and the rotary inertia have been considered in their paper. Neglecting the shear deformations they have reported the effect of rotary inertia on the in-plane natural frequencies.

As is known, the spiral springs are used in many practical applications in the area of mechanical engineering. Wahl (1963) has summarized the basic analysis of the spiral springs. The fundamental analytical formula used in the statical analysis is based on the assumption that the spring has many close coils. However, this assumption restricts many practical applications. In addition to this disadvantage, the problem of buckling arises when the spring has many coils.

Although there is considerable research on the free-vibration analysis of bars whose central lines are any plane curves such as parabolas, cycloids, etc., papers about the free vibrational problem of the spiral springs exist scarcely in the literature (Naraikin, 1976; Haktanır, 1993, 1994a). It is believed that the gap in the field of the free-vibration analysis of the spiral springs can be filled up a little by the present work.

In this study, first all the geometrical properties of the Archimedes-type spiral springs have been determined. The free-vibration equations, which are in the form of differential equations of first order with variable coefficients, have been obtained using Timoshenko's beam theory. The transfer matrix method has been employed in the free-vibration analysis. The standard solution of the transfer matrix by series expansion cannot be achieved because the elements of the differential matrix, which can be determined from the governing differential equations of the spiral springs, are variables and not constants. Thus, the overall transfer matrix has been obtained by the numerical integration of the set of equations using the complementary functions method. Since there is no sufficient numerical data in the literature, the free vibration frequencies obtained by the computer program devised in the present study have been compared with the finite element's results computed by the software ANSYS. The effects of some parameters on the free-vibration frequencies have also been investigated.

2 Geometrical Properties of Archimedes-Type Spiral Springs

Figure 1(a) represents a spring whose central line is a plane Archimedes spiral curve. The parametric equation of the spiral in polar coordinates is

$$r(\theta) = a\theta \tag{1}$$

where a is the radial distance between the centroids of the two adjacent sections (Fig. 1(b)), and is obtained from

$$r(\theta + 2\pi) - r(\theta) = a = h + \delta. \tag{2}$$

In Eq. (2), δ and h stand for the radial clearance between two adjacent sections and width of a rectangular section, respectively. Denoting the beginning and the end radial coordinates of the spiral by r_1 and r_2, for the number of coils of spring, the following can be written

$$n = (r_2 - r_1)/2\pi a \tag{3}$$

where n needs not be an integer. The total length of the wire is

$$L = (r_2^2 - r_1^2)/2a. \tag{4}$$

Using the parametric equation of the spiral given in Eq. (1), the infinitesimal length of the curve is obtained as

$$ds = a(1 + \theta^2)^{(1/2)} d\theta = z(\theta) d\theta. \tag{5}$$

The curvature of the spiral, which varies along the axis, as given by Haktanır (1993, 1994a) as

$$\chi(\theta) = \frac{2 + \theta^2}{a(1 + \theta^2)^{(3/2)}}. \tag{6}$$

3 Free-Vibrational Equations

The free vibrational equations of a spatial bar made of an elastic, isotropic, and homogeneous material having a double

Contributed by the Applied Mechanics Division of The American Society of Mechanical Engineers for publication in the ASME Journal of Applied Mechanics.

Discussion on the paper should be addressed to the Technical Editor, Professor Lewis T. Wheeler, Department of Mechanical Engineering, University of Houston, Houston, TX 77204-4792, and will be accepted until four months after final publication of the paper itself in the ASME Journal of Applied Mechanics.

Manuscript received by the ASME Applied Mechanics Division, July 17, 1996; final revision, Jan. 9, 1997. Associate Technical Editor: V. K. Kinra.

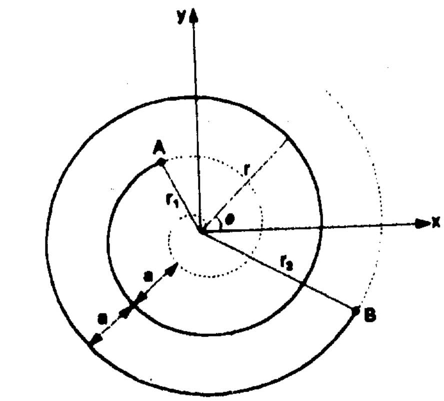

Fig. 1(*a*)

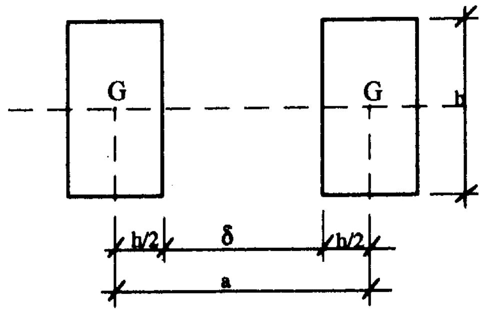

Fig. 1(*b*)

Fig. 1 Geometrical properties of an Archimedes-type spiral spring

symmetrical section in the vectorial form are as follows (Haktanır, 1993; Yıldırım, 1996):

$$\frac{d\mathbf{\Omega}}{ds} - \mathbf{D}^{-1}.\mathbf{M} = 0 \quad \frac{d\mathbf{U}}{ds} + \mathbf{t}\times\mathbf{\Omega} - \mathbf{C}^{-1}\mathbf{T} = 0 \quad (7a)$$

$$\frac{d\mathbf{T}}{ds} + \omega^2\rho A\mathbf{U} = 0 \quad \frac{d\mathbf{M}}{ds} + \mathbf{t}\times\mathbf{T} + \omega^2\mathbf{H}.\mathbf{\Omega} = 0 \quad (7b)$$

where the displacement, rotation, internal force, internal moment, and the tangential unit vectors are denoted by the $\mathbf{U}$, $\mathbf{\Omega}$, $\mathbf{T}$, $\mathbf{M}$, and $\mathbf{t}$, respectively. ω designates the angular frequency, A stands for the cross-sectional area, and ρ is the mass density. The elements of the rigidity tensors $\mathbf{C}$ and $\mathbf{D}$ are

$$\mathbf{D} = \begin{bmatrix} GI_t & 0 & 0 \\ 0 & EI_n & 0 \\ 0 & 0 & EI_b \end{bmatrix} \quad \mathbf{C} = \begin{bmatrix} EA & 0 & 0 \\ 0 & GA/\alpha_n & 0 \\ 0 & 0 & GA/\alpha_b \end{bmatrix} \quad (8)$$

and $\mathbf{H}$ is

$$\mathbf{H} = \begin{bmatrix} \rho I_t & 0 & 0 \\ 0 & \rho I_n & 0 \\ 0 & 0 & \rho I_b \end{bmatrix}. \quad (9)$$

In (8) and (9), E is the Young's modulus, G is the shear modulus, α_n and α_b are the Timoshenko's coefficients, I_t is the torsional moment of inertia, and I_n and I_b are the moment of inertias of cross section about the principal axes.

The Frenet formulae for any planar curves are given by Sokolnikoff and Redeffer (1958) as

$$\frac{d\mathbf{t}}{ds} = \chi\mathbf{n} \quad \frac{d\mathbf{n}}{ds} = -\chi\mathbf{t} \quad \frac{d\mathbf{b}}{ds} = 0 \quad (10)$$

and the Frenet components of the vectorial quantities in Eq. (7) are defined as below,

Table 1 The in-plane natural frequencies (rad/s) of the spiral spring (r_1 = 0, r_2 = 10 mm, n = 5.305, L = 0.167 m, a = 0.3 mm)

Modes	1	2	3	4	5	6
Present Study	741.1	1111.4	1265.9	1615.0	2096.4	2646.6
ANSYS (212 elements)	703.6	1093.7	1263.7	1581.7	2030.2	2624.0

$$\mathbf{T} = T_t\mathbf{t} + T_n\mathbf{n} + T_b\mathbf{b} \quad \mathbf{M} = M_t\mathbf{t} + M_n\mathbf{n} + M_b\mathbf{b} \quad (11a)$$

$$\mathbf{U} = U_t\mathbf{t} + U_n\mathbf{n} + U_b\mathbf{b} \quad \mathbf{\Omega} = \Omega_t\mathbf{t} + \Omega_n\mathbf{n} + \Omega_b\mathbf{b}, \quad (11b)$$

where $\mathbf{n}$ and $\mathbf{b}$ are the normal and bi-normal unit vectors, respectively.

The free-vibration equations of any planar bar can be obtained from Eqs. (7) with the help of the Frenet formulae, Eq. (10), as follows:

$$dU_t/ds = \chi U_n + (1/EA)T_t \quad (12a)$$

$$dU_n/ds = -\chi U_t + \Omega_b + (\alpha_n/GA)T_n \quad (12b)$$

$$dU_b/ds = -\Omega_n + (\alpha_b/GA)T_b \quad (12c)$$

$$d\Omega_t/ds = \chi\Omega_n + (1/GI_t)M_t \quad (12d)$$

$$d\Omega_n/ds = -\chi\Omega_t + (1/EI_n)M_n \quad (12e)$$

$$d\Omega_b/ds = (1/EI_b)M_b \quad (12f)$$

$$dT_t/ds = \chi T_n - \omega^2\rho AU_t \quad (12g)$$

$$dT_n/ds = -\chi T_t - \omega^2\rho AU_n \quad (12h)$$

$$dT_b/ds = -\omega^2\rho AU_b \quad (12i)$$

$$dM_t/ds = \chi M_n - \omega^2\rho I_t\Omega_t \quad (12j)$$

$$dM_n/ds = T_b - \chi M_t - \omega^2\rho I_n\Omega_n \quad (12k)$$

$$dM_b/ds = -T_n - \omega^2\rho I_b\Omega_b \quad (12l)$$

As can be seen from the above equations, they can be divided into two equations set governing the in-plane and out-of-plane free vibration of a planar bar, respectively.

Substituting the curvature and the infinitesimal length of the spiral into Eqs. (12), the free-vibration equations are found in the in-plane case as

$$\frac{dU_t}{d\theta} = \chi(\theta)z(\theta)U_n + \frac{z(\theta)}{EA}T_t = \chi(\theta)z(\theta)U_n + AD \quad (13a)$$

$$\frac{dU_n}{d\theta} = -\chi(\theta)z(\theta)U_t + z(\theta)\Omega_b + \frac{z(\theta)\alpha_n}{GA}T_n$$
$$= -\chi(\theta)z(\theta)U_t + z(\theta)\Omega_b + SD \quad (13b)$$

$$\frac{d\Omega_b}{d\theta} = \frac{z(\theta)}{EI_b}M_b \quad (13c)$$

$$\frac{dT_t}{d\theta} = \chi(\theta)z(\theta)T_n - z(\theta)\rho A\omega^2U_t \quad (13d)$$

$$\frac{dT_n}{d\theta} = -\chi(\theta)z(\theta)T_t - z(\theta)\rho A\omega^2U_n \quad (13e)$$

Table 2 The in-plane natural frequencies (rad/s) of the spiral spring (r_1 = 5 mm, r_2 = 15 mm, n = 5.305, L = 0.333 m, a = 0.3 mm)

Modes	1	2	3	4	5	6
Present Study	240.9	358.3	383.3	481.4	601.4	681.0
ANSYS (212 elements)	241.9	359.4	384.7	483.4	603.6	683.8

Table 3 The out-of-plane natural frequencies (rad/s) of the spiral spring (r_1 = 5 mm, r_2 = 15 mm, n = 5.305, L = 0.333 m, a = 0.3 mm)

Modes	1	2	3	4	5	6
Present Study	313.2	506.4	547.3	634.4	806.7	952.2
ANSYS (212 elements)	315.0	508.6	549.5	637.9	810.8	957.2

$$\frac{dM_b}{d\theta} = -z(\theta)T_n - z(\theta)\rho I_b\omega^2\Omega_b = -z(\theta)T_n - DI \quad (13f)$$

and the out-of-plane case as

$$\frac{dU_b}{d\theta} = -z(\theta)\Omega_n + \frac{z(\theta)\alpha_b}{GA}T_b = -z(\theta)\Omega_n + SD \quad (14a)$$

$$\frac{d\Omega_t}{d\theta} = \chi(\theta)z(\theta)\Omega_n + \frac{z(\theta)}{GI}M_t \quad (14b)$$

$$\frac{d\Omega_n}{d\theta} = -\chi(\theta)z(\theta)\Omega_t + \frac{z(\theta)}{EI_n}M_n \quad (14c)$$

$$\frac{dT_b}{d\theta} = -z(\theta)\rho A\omega^2 U_b \quad (14d)$$

$$\frac{dM_t}{d\theta} = \chi(\theta)z(\theta)M_n - z(\theta)\rho A\omega^2 I_t\Omega_t = \chi(\theta)z(\theta)M_n - DI \quad (14e)$$

$$\frac{dM_n}{d\theta} = -\chi(\theta)z(\theta)M_t + z(\theta)T_b - z(\theta)\rho\omega^2 I_n\Omega_n = -\chi(\theta)z(\theta)M_t + z(\theta)T_b - DI \quad (14f)$$

The terms AD, SD, and RI in Eqs. (13) and (14) represent the axial deformation, shear deformation and rotary inertia effects, respectively. If all AD, SD, and RI terms are neglected, then the analysis is the Bernoulli-Euler analysis.

Equation (13) or (14) can be written in matrix notation as

$$\frac{d\{S(\theta)\}}{d\theta} = [A]\{S(\theta)\} \quad (15)$$

where $[A]$ is the dynamic differential matrix and $\{S\}$ is the state vector. The solution of Eq. (15) associated with the dynamic transfer matrix, $[F]$, is given as follows (İnan, 1964):

$$\{S(\theta)\} = [F(\theta)]\{S(0)\}. \quad (16)$$

Since the curvature of the spiral spring varies along the axis, the overall transfer matrix cannot be numerically obtained from the standard solution which is in the form

$$[F(\theta)] = e^{[A]\theta} = [I] + \theta[A] + \frac{\theta^2[A]^2}{2!} + \frac{\theta^3[A]^3}{3!} + \frac{\theta^4[A]^4}{4!} + \ldots \quad (17)$$

Table 4 The in-plane natural frequencies (rad/s) of the spiral spring (r_1 = 5 mm, a = 0.3 mm, RI = rotary inertia, AD = axial deformation, SD = shear deformation)

		Modes					
r_2 (mm)	neglect	1	2	3	4	5	6
fixed - fixed							
7	—	3988.9	11042.9	23778.0	40949.9	62266.1	87343.6
	RI	3989.0	11043.2	23779.7	40955.9	62281.8	87376.7
	RI+AD+SD	3990.0	11052.1	23810.3	41030.0	62429.0	87640.7
20	—	99.9	153.5	161.3	201.7	263.1	287.1
	RI+AD+SD	99.9	153.5	161.3	201.7	263.1	287.1
fixed - hinged							
7	—	2395.1	8619.9	20363.8	36683.8	57107.1	81340.3
	RI	2395.2	8620.1	20365.2	36688.9	57121.0	81370.2
	RI+AD+SD	2395.6	8625.1	20385.3	36741.2	57230.1	81571.8
20	—	66.2	121.2	157.2	187.3	234.8	275.0
	RI+AD+SD	66.2	121.2	157.2	187.3	234.8	275.0
fixed - free							
7	—	1505.2	2465.9	4814.0	12975.2	25809.2	43087.8
	RI	1505.2	2465.9	4814.1	12976.0	25812.6	43097.6
	RI+AD+SD	1505.3	2466.2	4815.7	12984.0	25838.2	43157.9
20	—	43.8	88.5	88.7	149.8	220.3	226.7
	RI+AD+SD	43.8	88.5	88.7	149.8	220.3	226.7

In this study, the overall transfer matrix has been obtained by the numerical integration of Eqs. (13) and (14), employing the complementary functions method. As known, the complementary functions method is the method of initial value problems. In this method, the homogeneous solution of Eqs. (13) and (14) is given as (Lance, 1960; Aktaş, 1972; Haktanır, 1993, 1994a, b, 1995)

$$\{S(\theta)\} = \sum_{m=1}^{6} C_m\{U^{(m)}(\theta)\} = [U(\theta)]\{C\} = [\{U^{(1)}\}, \{U^{(2)}\}, \ldots, \{U^{(6)}\}]\{C\} \quad (18)$$

where the matrix $[U(\theta)]$ is composed of the six homogeneous solutions of the following differential equations

$$\frac{d\{U^m(\theta)\}}{d\theta} = [A]\{U^m(\theta)\} \quad (19)$$

with the boundary conditions: mth element of the state vector equals 1 as its other elements are all zero. In the solution (18), the matrix $\{C\}$ has constant elements which are obtained from the given boundary conditions at both ends of spiral.

It can be shown without difficulty that the overall transfer matrix is identical to the matrix $[U]$, and elements of both the state vector at $\theta = 0$ and $\{C\}$ are also the same.

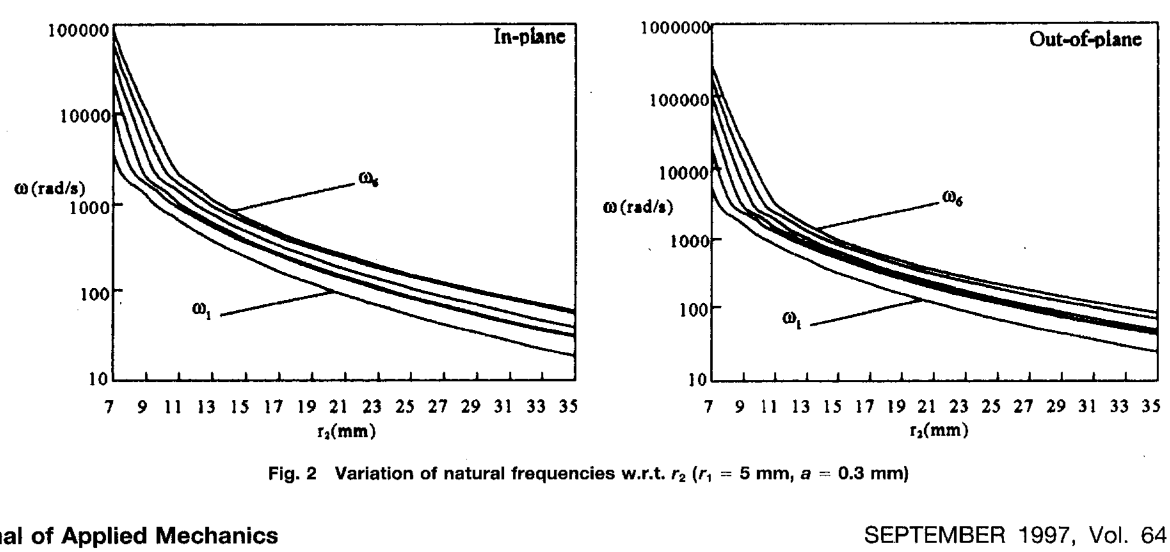

Fig. 2 Variation of natural frequencies w.r.t. r_2 (r_1 = 5 mm, a = 0.3 mm)

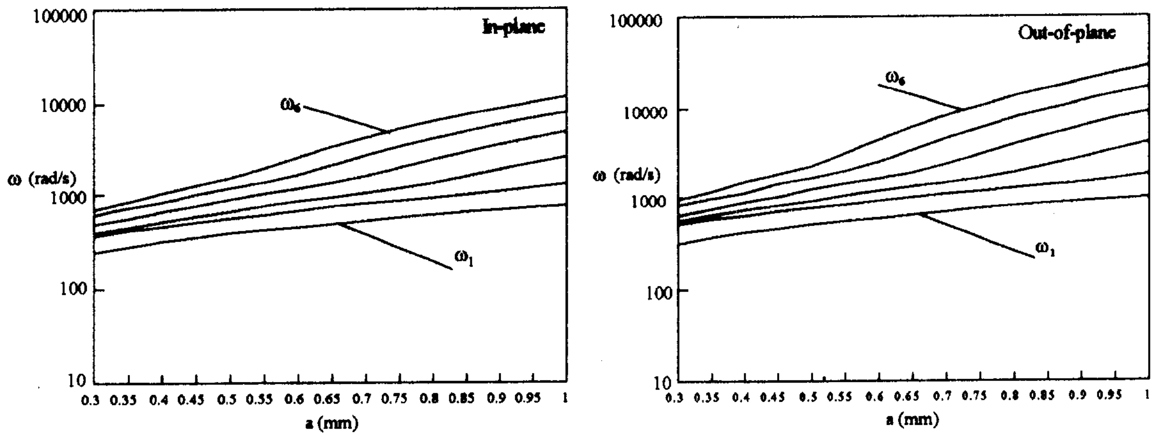

Fig. 3 Variation of natural frequencies w.r.t. the radial distance (r_1 = 5 mm, r_2 = 15 mm)

After computing the overall transfer matrix, the frequency equation can be obtained from the boundary conditions given at both ends using Eq. (16). Boundary conditions are determined for a fixed end as

$$U_t = U_n = \Omega_b = 0 \text{ (in plane)}$$
$$U_b = \Omega_t = \Omega_n = 0 \text{ (out-of-plane)} \tag{20}$$

for a hinged end as

$$U_t = U_n = M_b = 0 \text{ (in plane)}$$
$$U_b = M_t = M_n = 0 \text{ (out-of-plane)} \tag{21}$$

and for a free end as

$$T_t = T_n = M_b = 0 \text{ (in plane)}$$
$$T_b = M_t = M_n = 0 \text{ (out-of-plane).} \tag{22}$$

The natural frequency is determined by setting the determinant of the coefficient matrix equal to zero.

4 Test Examples

In order to illustrate the efficiency of the present method, consider an Archimedes-type spiral spring fixed at both ends as an example with the following fixed properties:

$$\rho = 7850 \text{ kg/m}^3 \quad E = 2.1\ 10^{11} \text{ N/m}^2 \quad \nu = 0.3$$
$$b = 2 \text{ mm} \quad h = 0.2 \text{ mm} \quad \alpha_n = \alpha_b = 1.2$$

where ν is the Poisson's ratio and b is the height of section (Fig. 1(*b*)).

4.1 In-Plane Case. As a first in-plane problem, a spiral spring whose first end is placed at the origin is considered. The results are presented in Table 1 in a comparative manner.

As a second example, the spiral spring whose first end is not placed at the origin is chosen as in practice. In this example the number of coils is the same as in the previous problem. The results are tabulated in Table 2.

Table 1 and Table 2 show that the reliable solutions are obtained by the program devised in this study. Although the number of coils is chosen as the same in the two examples, the frequencies are different. The reason for this is the difference between the values of the total length of the spring.

As can be seen obviously from the Eq. (6), the curvature decreases with increasing θ (a = constant). That is, for small θs the curvature is great and the radius of the curvature is small. The length of the inner coil is also less than the others. If inner coils have been constructed by few straight beams which have the same length, then the real geometry of inner coil cannot be represented actually. Consequently, since the approximation to the construction of the inner curve is not a sufficient value for the representation of real geometry of curve, the ANSYS results obtained in Table 1 are different from the exact frequencies obtained in this study. The fundamental frequency, especially, is affected from this condition.

4.2 Out-of-Plane Case. In this example, the out-of-plane free-vibrational frequencies of the spiral having the same properties given in the previous problem are computed and presented in Table 3. There is a very good agreement between the results of the present study and ANSYS.

5 Effects of the Number of Coils, the Shear and Axial Deformations, the Rotary Inertia, and the Boundary Conditions on the Natural Frequencies

In order to illustrate the variation of the natural frequencies with the number of coils, first, the number of coils is determined by attributing different values to the radial coordinate r_2 under the condition that all the other properties are the same. The number of coils is computed using Eq. (3). In this way the range of $7 \le r_2 \le 35$ corresponds to the range of $1.061 \le n \le 15.915$. The results are presented in Fig. 2 for both the in-plane and the out-of-plane case. As can be expected, when the number of coils is increased, the frequencies decrease. For the small values of r_2, a fast decline is observed. Increasing of the number of coils causes an extension of the total length of the spring.

As seen in Eq. (3), the different number of coils can also be obtained using various values of the radial distance. The increment of the values of the radial distance between the centroids of two adjacent sections means a decrement of the number of

Table 5 The out-of-plane natural frequencies (rad/s) of the spiral spring (r_1 = 5 mm, a = 0.3 mm, *RI* = rotary inertia, *SD* = shear deformation)

		Modes					
r_2 (mm)	neglect	1	2	3	4	5	6
fixed - fixed							
7	—	5373.2	18793.3	48516.2	98394.0	170410.9	265294.0
	RI	5383.0	18912.1	49141.4	100553.6	176113.1	277767.5
	RI+SD	5384.4	18933.3	49324.2	101427.1	179070.7	285741.8
20	—	132.0	218.1	231.0	259.3	347.1	401.9
	RI+SD	132.0	218.2	231.2	259.3	347.2	402.1
fixed - hinged							
7	—	2420.8	6824.8	25558.3	62706.1	121392.0	203483.3
	RI	2424.5	6862.9	25853.0	64004.1	125372.6	213171.5
	RI+SD	2424.7	6864.2	25880.6	64216.3	126341.9	216389.1
20	—	82.5	102.4	165.0	242.8	306.4	336.8
	RI+SD	82.5	102.5	165.0	242.8	306.5	337.0
fixed - free							
7	—	1966.5	3488.6	9795.7	31296.7	71374.4	133067.6
	RI	1967.6	3500.9	9902.5	31920.0	73662.2	139316.5
	RI+SD	1967.9	3501.0	9905.3	31960.5	73935.8	140487.4
20	—	72.7	100.3	104.6	193.8	292.5	325.2
	RI+SD	72.7	100.3	104.6	193.8	292.6	325.4

coils provided that all the other properties of the spring are the same. The variation of the natural frequencies versus to the value a is shown in Fig. 3. The natural frequencies become smaller with a decrease of the values of a, and with an increase of the number of coils.

The effects of changes of the boundary conditions, the axial and shear deformations, and the rotary inertia on the natural frequencies are given in Tables 4 and 5.

Since the effects of the axial and shear deformations seem to be more pronounced from the Table 4, the effect of rotary inertia (maximum relative error = 0.04 percent) may be neglected in the case of the in-plane vibration.

For the out-of-plane vibration, the effects of both the rotary inertia and the shear deformations should be taken into account. If the rotary inertia only is neglected, a maximum relative error of 4.7 percent results. For the case where both the shear deformations and the rotary inertia are neglected, maximum relative error of 7.7 percent for fixed-fixed ends of 6.3 percent for fixed-hinged ends and of 5.6 percent for fixed-free ends is observed.

For small values of the number of coils, generally, the rotary inertia and the shear and axial deformations are of importance at higher frequencies.

6 Conclusions

In this study, the analysis of free vibration of uniform spiral springs is numerically treated with the help of the transfer matrix method. The real geometry of the spring is considered in the formulation. The complementary functions method is employed for the accurate computation of the overall transfer matrix for a large number of coils which is changeable with respect to the value of the radial distance, a. All the effects of shear and axial deformations and rotary inertia have been taken into account. Calculation of the mode shapes associated with the natural frequencies is not considered. The solution method can be applied to any planar bar.

References

Aktaş, Z., 1972, "Numerical solutions of two-point boundary value problems with initial value problems," Habilitation thesis, Middle East Technical University.

Haktanır, V., 1993, "In-plane free vibration of Archimedes spiral springs," *Proc. 6th National Symp. on Machinery Theory,* Trabzon, pp. 411–420 (in Turkish).

Haktanır, V., 1994a, "Free vibration vertical to its plane of Archimedes type spiral springs," *15th Anniversary Symposium of Fac. of Eng. and Arch. of Çukurova University,* Vol. 1, pp. 301–311 (in Turkish).

Haktanır, V., 1994b, "A new method for the element stiffness matrix of arbitrary planar bars," *Compt. & Struct.,* Vol. 52, No. 4, pp. 679–691.

Haktanır, V., 1995, "The complementary functions method for the element stiffness matrix of arbitrary spatial bars of helicoidal axis," *Int. J. Numer. Meth. Engng.,* Vol. 38, No. 6, pp. 1031–1056.

İnan, M., 1964, *Transfer Matrix Methods in Elastomechanics,* Tech. Univ. of Istanbul, Faculty of Civil Engineering, No. 585 (in Turkish).

Lance, G. N., 1960, *Numerical Methods for High Speed Computers,* Iliffe and Sons, London, pp. 64–68.

Lee, B. K., and Wilson, J. F., 1989, "Free vibrations of arches with variable curvature," *J. Sound and Vibration,* Vol. 136, No. 1, pp. 75–89.

Naraikin, O. S., 1976, "Natural vibrations of spiral springs," *Izvestiya Vysshikh Uchebnykh Zavedenii, Mashinostroenie,* Vol. 8, pp. 21–29 (in Russian).

Sokolnikoff, I. S., and Redeffer, R. M., 1958, *Mathematics of Physics and Modern Engineering,* McGraw-Hill, Tokyo.

Suzuki, K., Aida, H., and Takahashi, S., 1978, "Vibrations of curved bars perpendicular to their planes," *Bulletin of the JSME,* Vol. 21, No. 162, pp. 1685–1695.

Volterra, E., and Morell, J. D., 1960, "A note on the lowest frequency of elastic arcs," ASME Journal of Applied Mechanics, Vol. 27, pp. 744–746.

Volterra, E., and Morell, J. D., 1961a, "Lowest natural frequency of elastic arc for vibrations outside the plane of initial curvature," ASME Journal of Applied Mechanics, Vol. 28, pp. 624–627.

Volterra, E., and Morell, J. D., 1961b, "Lowest natural frequency of elastic hinged arcs," *The Journal of the Acoustical Society of America,* Vol. 33, No. 12, pp. 1787–1790.

Wahl, A. M., 1963, *Mechanical Springs,* McGraw-Hill, New York.

Yildirim, V., 1996, "Investigation of parameters affecting free vibration frequency of helical springs," *Int. Numer. Meth. Engng.,* Vol. 39, No. 1, pp. 99–114.

Steady-State Motion of a Line Mechanical/Heat Source Over a Half-Space: A Thermoelastodynamic Solution

L. M. Brock
Department of Engineering Mechanics,
University of Kentucky,
Lexington, KY 40506-0046
Fellow ASME

H. G. Georgiadis
Mechanics Division,
NTUA,
1 Konitsis Street,
Zographou 15773, Greece
Mem. ASME

An asymptotic solution within the bounds of steady-state coupled thermoelastodynamic theory is given for the surface displacement and temperature due to a line mechanical/heat source that moves at a constant velocity over the surface of a half-space. This problem is of basic interest in the fields of contact mechanics and tribology, and an exact formulation is considered. The results may serve as a Green's function for more general thermoelastodynamic contact problems. The problem may also be viewed as a generalization of the classical Cole-Huth problem and the associated Georgiadis-Barber correction. Asymptotic expressions are obtained by means of the two-sided Laplace transform, and by performing the inversions exactly. The range of validity of these expressions is actually quite broad, because of the small value of the thermoelastic characteristic length appearing in the governing equations.

Introduction

An important problem concerning such diverse fields as wave propagation, contact mechanics and tribology is the rapid motion of a line mechanical and/or thermal load over the surface of a half-space. Indeed, this is the case when (a) ground motion and stresses are produced by surface blast waves due to explosives or by supersonic aircraft, (b) high-velocity rocket sleds moving on guide rails, or (c) mating systems in brakes or bearing seals (e.g., those used in submarines) are pressed against each other and undergo relative sliding motion accompanied by dry friction. Such dynamical mechanical/heat loading may produce severe deformation and temperature rises in a thin zone near the half-space surface, and thereby cause excessive wear and even cracking near the contact zone. It is therefore useful to analyze this class of problems by using a formulation that is as exact as possible, and to provide results for surface and/or near-surface field quantities (displacements, tangential stresses, temperature) that may be required for design purposes.

In many cases, the above-described problem can be modeled as a plane-strain steady-state situation involving an elastic half-plane under a concentrated line mechanical/heat loading which moves over the half-plane surface at constant speed. This is the problem examined here and, in order to fully incorporate thermal aspects, its solution is obtained by considering a material response governed by coupled thermoelastodynamics (Biot, 1956; Lessen, 1956; Chadwick, 1960; Francis, 1972).

To relate the present study and previous work, we first note that, in the absence of thermal effects, our study degenerates into the well-known problem of steady-state elastodynamic motion of a line force along a half-plane surface considered by Cole and Huth (1958) and Georgiadis and Barber (1993a). When thermal effects are included, one can find in the literature several approaches which commonly use uncoupled thermoelasticity and exclude inertial (dynamic) effects. Also, many of these studies do not address the case of a *mechanical* loading, but only that of a heat source moving at constant speed over the half-plane surface. Important examples of this type of investigation are due to Ling and Mow (1965), Mow and Cheng (1967), Kilaparti and Burton (1978), Ju and Huang (1982), Barber (1984), Huang and Ju (1985), and Bryant (1988). In particular, Barber (1984) introduced an interesting superposition scheme that employed transient results based on uncoupled thermoelasticity (Barber and Martin-Moran, 1982) and was thus able to obtain exact results for surface displacements, stresses, and temperature. In addition, useful comparisons were made with earlier results (Barber, 1984). Also, it should be noted that Bryant (1988) provided results for subsurface quantities as well, while Kennedy (1984) presented in a review paper interesting discussions of the associated heat checking problem (brake and face seal surface cracking due to both mechanical and thermal effects caused by moving asperities).

At this point, it must be emphasized that direct comparison between the aforementioned work dealing with moving heat sources and the present one is difficult because of the different assumptions employed. Under the steady-state assumption, however, the present formulation more completely accounts for both inertial and thermal-coupling effects. The corresponding transient coupled-thermoelastodynamic problem, which involves, of course, the most general formulation, has also been considered by the present authors, and its solution will appear soon in a separate paper. Nevertheless, the steady-state assumption employed here has its own justification in the dynamic analysis of moving sources (see, e.g., Fung, 1965; Eringen and Suhubi, 1975; Georgiadis and Theocaris, 1985; Brock, 1994, 1995) and may yield reliable results when the mechanical/thermal load in question has, as here, been applied and moving for a long time.

The results reported in this study for surface displacements, stresses, and temperature are derived from a rather robust asymptotic solution of the title problem obtained through use of the two-sided Laplace transform and exact inversions. Subsurface results can also be obtained from general expressions presented here through a more elaborate scheme.

Contributed by the Applied Mechanics Division of THE AMERICAN SOCIETY OF MECHANICAL ENGINEERS for publication in the ASME JOURNAL OF APPLIED MECHANICS.

Discussion on the paper should be addressed to the Technical Editor, Professor Lewis T. Wheeler, Department of Mechanical Engineering, University of Houston, Houston, TX 77204-4792, and will be accepted until four months after final publication of the paper itself in the ASME JOURNAL OF APPLIED MECHANICS.

Manuscript received by the ASME Applied Mechanics Division, Sept. 1, 1995; final revision, Dec. 2, 1996. Associate Technical Editor: D. M. Barnett.

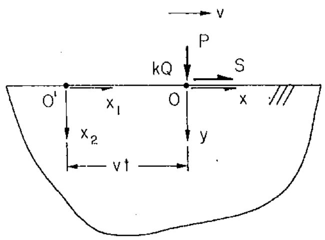

Fig. 1 A line mechanical/heat source moving a constant velocity v over the surface of a half-plane (P and S are the mechanical loading components and kQ is the thermal loading intensity)

Problem Statement

Consider a thermally conducting linearly elastic body in the form of a half-space $x_2 \geq 0$ under plane-strain conditions. This otherwise unloaded body is at rest at a uniform temperature $T_o(K)$, but is then disturbed by the motion of a mechanical/thermal source over the half-space surface (see Fig. 1). The concentrated line load depicted has components P and S, whereas the line heat source has intensity kQ per unit length per unit time, with k denoting the thermal conductivity and Q being a multiplier expressed in degrees of temperature. Then, with respect to a fixed Cartesian coordinate system $(O'x_1, O'x_2)$, the governing equations according to coupled thermoelastic theory are written as

$$\sigma_{ij} = \lambda\delta_{ij}u_{l,l} + \mu(u_{i,j} + u_{j,i}) - (3\lambda + 2\mu)\delta_{ij}\beta_o\theta, \qquad (1)$$

$$\mu u_{i,jj} + (\lambda + \mu)u_{j,ji} - (3\lambda + 2\mu)\beta_o\theta_{,i} = \rho \frac{\partial^2 u_i}{\partial t^2}, \qquad (2)$$

$$k\theta_{,ii} - \rho c_v \frac{\partial \theta}{\partial t} - (3\lambda + 2\mu)\beta_o T_o \frac{\partial u_{i,i}}{\partial t} = 0, \qquad (3)$$

where indicial notation is employed, with $(\ )_{,i}$ denoting x_i-differentiation, the indices (i, j) take on the values 1 and 2 only, δ_{ij} is the Kronecker delta, $\sigma_{ij}\ (=\sigma_{ji})$ is the stress tensor, u_i is the displacement vector, (λ, μ) are the Lamé constants, β_o is the coefficient of linear expansion, $\theta\ (=T - T_o)$ is the change in temperature, ρ is the mass density, t is the time and c_v is the specific heat at constant deformation.

Equation (1) is the thermoelastic Hooke's law, whereas (2) and (3) can be regarded as, respectively, the generalized Navier-Cauchy equations and generalized heat conduction equation. It is also noted that the third term in the l.h.s. of both Eqs. (2) and (3) arises from the interaction of elastic deformation with heat conduction. The presence of the dilatational time rate in (3) indicates that only mechanical energy expended in volume change is converted into heat (see, e.g., Chadwick, 1960) and, consequently, that dilatational and not shear waves are modified by thermal straining.

Now, if the mechanical/heat source has been applied for some time, and is moving at a constant speed v, then a steady-state can be assumed to prevail in the neighborhood of the load as seen by an observer using the moving load as a frame of reference. It is this steady-state response that will be the object of the analysis, and we shall not be concerned with initial behavior, a course of action followed in similar problems by, for instance, Cole and Huth (1958), Fung (1965), Eringen and Suhubi (1975), Georgiadis and Barber (1993a), and Brock (1994, 1995).

Under this assumption, considerable simplification can be gained in analyzing the problem at hand. Specifically, the Galilean transformation $x = x_1 - vt$, $y = x_2$ can be introduced, so that the time derivative in the fixed Cartesian system becomes

$$\frac{\partial}{\partial t} - v\frac{\partial}{\partial x}. \qquad (4)$$

In the steady-state, an observer in the moving frame sees no variation with time, so that the partial derivative w.r.t t in (4) can be neglected and then (1)–(3) can be written as

$$\frac{1}{\mu}\sigma_x = m^2 \frac{\partial u_x}{\partial x} + (m^2 - 2)\frac{\partial u_y}{\partial y} + \beta\theta, \qquad (5a)$$

$$\frac{1}{\mu}\sigma_y = (m^2 - 2)\frac{\partial u_x}{\partial x} + m^2 \frac{\partial u_y}{\partial y} + \beta\theta, \qquad (5b)$$

$$\frac{1}{\mu}\tau_{xy} = \frac{\partial u_x}{\partial y} + \frac{\partial u_y}{\partial x}, \qquad (5c)$$

$$\nabla^2 u_x + \frac{\partial[(m^2 - 1)\Delta + \beta\theta]}{\partial x} - m^2c^2 \frac{\partial^2 u_x}{\partial x^2} = 0, \qquad (6a)$$

$$\nabla^2 u_y + \frac{\partial[(m^2 - 1)\Delta + \beta\theta]}{\partial y} - m^2c^2 \frac{\partial^2 u_y}{\partial x^2} = 0, \qquad (6b)$$

$$\frac{k}{\mu}\nabla^2\theta + c_v \frac{mc}{v_2}\frac{\partial \theta}{\partial x} - \beta T_o c v_1 \frac{\partial \Delta}{\partial x} = 0, \qquad (7)$$

where $(\sigma_x, \sigma_y, \tau_{xy})$ and (u_x, u_y) are the components of the stress tensor and displacement vector, respectively, $m = v_1/v_2 > 1$ with $v_1 = \sqrt{(\lambda + 2\mu)/\rho}$ being the dilatational wave speed in the *absence* of thermal effects and $v_2 = \sqrt{\mu/\rho}$ being the shear-wave speed, $\beta = \beta_o(4 - 3m^2) < 0$, while $c \equiv M_1 = v/v_1$ and $mc \equiv M_2 = v/v_2$ are the Mach numbers, $\Delta = (\partial u_x/\partial x) + (\partial u_y/\partial y)$ is the dilatation, and $\nabla^2 = (\partial^2/\partial x^2) + (\partial^2/\partial y^2)$ is the two-dimensional Laplacian operator.

In addition, the boundary conditions of the problem can be written as (see Fig. 1)

$$\sigma_y(x, y = 0) = -P\delta(x), \qquad (8a)$$

$$\tau_{xy}(x, y = 0) = -S\delta(x), \qquad (8b)$$

$$\frac{\partial\theta(x, y = 0)}{\partial y} = -Q\delta(x), \qquad (8c)$$

for all $-\infty < x < \infty$, where $\delta(\ )$ is the Dirac delta distribution. Note that (8c) implies that no heat flows across the half-space surface except under the load; this insulated surface condition is a situation often (see, e.g., Barber, 1984; Bryant, 1988) assumed in contact problems. We now proceed to attack the system of equations (4)–(8).

Integral Transform Analysis

The problem formulated in the previous section will be addressed by means of the two-sided Laplace transform pair (van der Pol and Bremmer, 1950)

$$f^*(q, y) = \int_{-\infty}^{+\infty} f(x, y)e^{-qx}dx, \qquad (9a)$$

$$f(x, y) = \frac{1}{2\pi i}\int_{\mathrm{Br}} f^*(q, y)e^{qx}dq, \qquad (9b)$$

where Br denotes the Bromwich path in the complex q-plane. Application of (9a) to the field equations (6) and (7) results in a coupled set of ordinary differential equations having the following general solutions that are bounded for $y > 0$:

$$u_x^* = -q\bar{A}_+ - q\bar{A}_- + \bar{B}, \qquad (10)$$

$$u_y^* = \alpha_+\bar{A}_+ + \alpha_-\bar{A}_- + \frac{q}{b}\bar{B}, \qquad (11)$$

$$\theta^* = \frac{m^2}{b}(M_+\bar{A}_+ + M_-\bar{A}_-), \qquad (12)$$

where

$$\bar{A}_\pm = A_\pm e^{-\alpha_\pm y}, \quad \bar{B} = Be^{-by}, \qquad (13a, b)$$

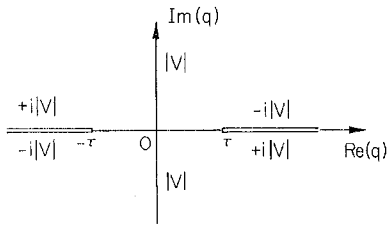

Fig. 2 The cut complex q-plane for the function $V(q) = \sqrt{\tau^2 - q^2}$, where τ is a positive real constant

with (A_+, A_-, B) being arbitrary functions of q and

$$\alpha_\pm = \sqrt{c(r_+ \pm r_-)^2 + q}\,\sqrt{\tau - q}, \tag{14}$$

$$b = \sqrt{1 - m^2c^2}\,\sqrt{\tau^2 - q^2}, \tag{15}$$

$$2r_\pm = \sqrt{(\sqrt{c}\,\sqrt{\tau - q} \pm 1/\sqrt{h})^2 + (\epsilon/h)}, \tag{16}$$

$$M_\pm = -cq[(r_+ \pm r_-)^2 + cq], \tag{17}$$

when the source speed is subsonic ($v < v_2$). In (14)–(16), τ is a real positive vanishingly small number that is introduced merely to clarify the definition of the pertinent branch cuts for $(\alpha_\pm, b)$. Once the transforms are inverted by use of (9b), τ will be allowed to vanish. This procedure is a standard one in solution by transform methods, e.g., Carrier, Krook and Pearson (1966). The necessary restriction (in view of the forms chosen as being bounded for $y > 0$) that Re $(\alpha_\pm, b) \geq 0$ in the cut q-plane leads to the conclusion that both functions $\alpha_-(q)$ and $b(q)$ should have branch cuts along $|\mathrm{Re}(q)| > \tau$ for $\mathrm{Im}(q) = 0$ (see Fig. 2), while $\alpha_+(q)$ should exhibit branch cuts along $\mathrm{Re}(q) > \tau$, $\mathrm{Re}(q) < -[1 + \epsilon/(1 - c^2)](c/h)$ for $\mathrm{Im}(q) = 0$. It should be noted that two important quantities have been introduced in (14) and (16): the thermoelastic characteristic length h and the dimensionless coupling constant ϵ. These are defined by

$$h = \frac{kv_2}{\mu mc_v}, \quad \epsilon = \frac{T_o}{c_v}\left(\frac{\beta v_2}{m}\right)^2. \tag{18a, b}$$

For typical conducting materials of engineering interest (e.g., aluminum, copper, lead, titanium, 4340 steel) the orders of magnitude of these two constants are

$$h = O(10^{-10})m, \quad \epsilon = O(10^{-2}). \tag{19a, b}$$

Finally, $(\alpha_\pm, M_\pm)$ can also be written in the alternative forms

$$\alpha_\pm = \sqrt{M_\pm - (1 - c^2)q^2}, \quad M_\pm = -cq(\rho_+ \pm \rho_-)^2 \tag{20a, b}$$

$$2\rho_\pm = \sqrt{(\sqrt{c}\,\sqrt{\tau + q} \pm \sqrt{\epsilon/h})^2 + 1/h}. \tag{21}$$

We complete the general transform solution of the governing equations by obtaining from (5), (9a), and (10)–(12) the stress transforms

$$\frac{1}{\mu}\sigma_x^* = T_+\bar{A}_+ + T_-\bar{A}_- + 2q\bar{B}, \tag{22a}$$

$$\frac{1}{\mu}\sigma_y^* = -T\bar{A}_+ - T\bar{A}_- - 2q\bar{B}, \tag{22b}$$

$$\frac{1}{\mu}\tau_{xy}^* = -2q\alpha_+\bar{A}_+ - 2q\alpha_-\bar{A}_- + \frac{T}{b}\bar{B}, \tag{22c}$$

where $T = (m^2c^2 - 2)q^2 = Kq^2$, $T_\pm = 2\alpha_\pm^2 - m^2c^2q^2$.

However, before passing to the transformed boundary conditions that will yield expressions for A_+, A_-, and B, we note that the general solution (10)–(12) and (22) will need to be modified for regimes other than the subsonic ($v < v_2$). Some of these modifications must await discussion of the asymptotic forms mentioned at the outset, but that involving the function $b(q)$ can be introduced now: when the source speed $v > v_2$ ($mc > 1$), (15) must be replaced with $b = q\sqrt{m^2c^2 - 1}$, where it is understood that evaluation is along the Bromwich contour $\mathrm{Re}(q) = 0$, $-\infty < \mathrm{Im}(q) < \infty$. This new form is compatible with the pertinent radiation condition that states that the solution field should not exhibit disturbances that originate at infinity and converge toward the source. Indeed, one can observe that multiplying the term $B\exp(qy\sqrt{m^2c^2 - 1})$ by the term $\exp(qx)$ appearing in the inversion operation (9b) gives the solution form $B\exp[i\mathrm{Im}(q)(x + y\sqrt{m^2c^2 - 1})]$ which, of course, is consistent with the physical condition that for $v_2 < v$ the material in front of the moving source is not disturbed by shear stresses and, therefore, that only backward shear waves should exist, the term containing $x - y\sqrt{m^2c^2 - 1}$ being rejected from the solution.

Now, by operating with (9a) on the boundary conditions (8) and employing (12) and (22), a system of three equations results that can be solved to give

$$A_+ = -P\frac{K\alpha_-M_-}{\mu G} - S\frac{2\alpha_-bM_-}{\mu qG} + Q\frac{\beta(K^2q^2 + 4\alpha_-b)}{m^2G}, \tag{23a}$$

$$A_- = P\frac{K\alpha_+M_+}{\mu G} + S\frac{2\alpha_+bM_+}{\mu qG} - Q\frac{\beta(K^2q^2 + 4\alpha_+b)}{m^2G} \tag{23b}$$

$$B = P\frac{2\alpha_+\alpha_-b(M_+ - M_-)}{\mu qG} - S\frac{Kb(\alpha_+M_+ - \alpha_-M_-)}{\mu G} + Q\frac{2\beta Kbq(\alpha_+ - \alpha_-)}{m^2G}, \tag{23c}$$

where the thermoelastic Rayleigh function G is given by

$$G = K^2q^2(\alpha_+M_+ - \alpha_-M_-) + 4\alpha_+\alpha_-b(M_+ - M_-). \tag{24}$$

Combining (10)–(12) and (22) with (23) provides transforms for the displacements, stresses, and temperature. These will be inverted according to the operation (9b) in the next section for some interesting particular cases.

Transform Inversion and Results

Equations (23) and (24) show that the transforms (10)–(12) and (22) are analytic when $\mathrm{Re}(q) = 0$. Therefore, the contour Br in the LaPlace transform (LT) inversion operation (9b) can be taken as the entire $\mathrm{Im}(q)$-axis. However, Cauchy theory can be used to replace this path in the expressions resulting from Eqs. (10)–(12), (22), and (23) by integrals along a real axis that can be performed numerically. Alternatively, if analytical forms are of no interest, then one can resort to a direct numerical inversion using (9b) (see, e.g., the method of Dubner-Abate, 1968; Crump, 1976; Georgiadis, 1993; Georgiadis et al., 1994, 1995). In this first-step study, however, we are interested in analytical forms, and so obtain exact inversions for the surface ($y = 0$) displacements and temperature by first extracting pertinent asymptotic expressions for $\alpha_\pm$ and $M_\pm$ and then employ contour integration and LT inversion tables. The surface field itself is useful in this type of problem because any related experimental measurements are likely to be made on the surface and, in practical situations, wear and cracking occur near the surface.

By asymptotic results, we mean those that are valid when either $|x/h| \gg 1$ or $|x/h| \ll 1$. Because the thermoelastic characteristic length is so small (see (19a)), the first case is not very restrictive and, indeed, we will here take the interval $O(10^{-6})m < |x| < \infty$ to be range of validity. This choice, which easily satisfies the asymptotic inequality above, follows from Brock's (1994, 1995) study of the similar problem of steady-state crack growth using, respectively, full expressions and results valid for $|x/h| \gg 1$. The second case is admittedly not as useful, unless solution behavior very near the moving sources is of major interest. Some rather representative results for this case are given here mainly for purposes of completeness.

The expressions for $M_\pm$, $\alpha_\pm$, and b arising from asymptotic considerations are first recorded, and then some aspects of the resulting inversion operations are outlined. It will be seen that the very form of the asymptotic expressions depends somewhat on the value of the source speed, v. Specifically, by considering the case of small $|q|$ ($|x/h| \gg 1$) and large $|q|$ ($|x/h| \ll 1$), we obtain the following results:

(1a) $|x/h| \gg 1$ and $v < v_2$ (subsonic range)

$$M_+ \cong -c[(1+\epsilon)/h]q, \quad M_- \cong -c^2[\epsilon/(1+\epsilon)]q^2, \quad (25a,b)$$

$$\alpha_+ \cong \sqrt{c(1+\epsilon)/h}\,\sqrt{\tau - q},$$

$$\alpha_- \cong \sqrt{1 - c^2/(1+\epsilon)}\,\sqrt{\tau^2 - q^2}, \quad (26a,b)$$

$$b = \sqrt{1 - m^2c^2}\,\sqrt{\tau^2 - q^2}. \quad (27)$$

(1b) $|x/h| \gg 1$ and $v_2 < v < v_1\sqrt{1+\epsilon}$ (transonic range)

$M_\pm$, $\alpha_\pm$ given by (25) and (26), respectively, and

$$b = q\sqrt{m^2c^2 - 1}. \quad (28)$$

(1c) $|x/h| \gg 1$ and $v > v_1\sqrt{1+\epsilon}$ (supersonic range)

$M_\pm$, α_+, b given by (25), (26a), and (28), respectively, and

$$\alpha_- \cong q\sqrt{c^2/(1+\epsilon) - 1}. \quad (29)$$

(2a) $|x/h| \ll 1$ and $v < v_2$ (subsonic range)

b given by (27) and

$$M_+ \cong -(1+\epsilon)c^2q^2, \quad M_- \cong -cq\epsilon/(1+\epsilon)h, \quad (30a,b)$$

$$\alpha_+ \cong \sqrt{1 + \epsilon c}\,\sqrt{\tau^2 - q^2},$$

$$\alpha_- \cong \sqrt{1 - c^2}\,\sqrt{\tau^2 - q^2}. \quad (31a,b)$$

(2b) $|x/h| \ll 1$ and $v_2 < v < v_1$ (transonic range)

$M_\pm$, $\alpha_\pm$, b given by (30), (31), and (28), respectively.

(2c) $|x/h| \ll 1$ and $v > v_1$ (supersonic range)

$M_\pm$, α_+, b given by (30), (31a), and (28), respectively, and

$$\alpha_- \cong q\sqrt{c^2 - 1}. \quad (32)$$

Inserting now the above asymptotic expressions in Eqs. (10)–(12), (22), and (23) results in forms for the transformed surface field which in most cases can readily be inverted. Because displacements in a steady-state analysis can be determined only to within an arbitrary rigid-body motion, the quantities ($\partial u_x/\partial x$, $\partial u_y/\partial x$) for $y = 0$ will be obtained by operating on the expressions (qu_x^*, qu_y^*) with (9b). These quantities will then be integrated indefinitely w.r.t. x. Because no rigid-body motion is involved, the inversion of θ^* for $y = 0$ can be performed directly. Typical forms of the surface field in the q-plane contain terms of the type 1, $1/q$, $1/\sqrt{\tau - q}$, $1/(\tau^2 - q^2)$, $\sqrt{\tau^2 - q^2}/\sqrt{q^2 - \tau^2}$ and $q/\sqrt{\tau^2 - q^2}$. Indeed, the first four terms yield upon use of LT tables (see, e.g., van der Pol and Bremmer, 1950; Bracewell, 1965) the functions $\delta(x)$, $(1/2)\,\mathrm{sgn}\,(x)$, $\sqrt{-\pi x}H(-x)$ and $(1/2\tau)\exp(-\tau|x|)$, respectively, where sgn ( ) is the signum function, $H(\ )$ is the Heaviside step function and τ is of course a real number such that $\tau > 0$, $\tau \to 0$. The last two of the typical q-forms can be inverted by contour integration. For instance, LT inversion of the term $q/\sqrt{\tau^2 - q^2}$ that appears in (qu_x^*, qu_y^*) for $y = 0$ involves the integral

$$I(x) = \frac{1}{2\pi i}\int_{-i\infty}^{i\infty} \frac{qe^{qx}}{\sqrt{\tau^2 - q^2}}\,dq, \quad (33)$$

where the branch cuts run along ($-\infty < \mathrm{Re}(q) < -\tau$, $\mathrm{Im}(q) = 0$) and ($\tau < \mathrm{Re}(q) < \infty$, $\mathrm{Im}(q) = 0$). Then, by deforming the original Bromwich path onto one that includes the large quarter-circular paths at infinity in the $\mathrm{Re}(q) < 0$ half-plane connecting the point pairs ($\mathrm{Re}(q) = 0$, $\mathrm{Im}(q) = +\infty$), ($\mathrm{Re}(q) = -\infty$, $\mathrm{Im}(q) = 0^+$) and ($\mathrm{Re}(q) = -\infty$, $\mathrm{Im}(q) = 0^-$), ($\mathrm{Re}(q) = 0$, $\mathrm{Im}(q) = -\infty$) and also the straight paths ($-\infty < \mathrm{Re}(q) < -\tau$, $\mathrm{Im}(q) = 0^+$), ($-\tau > \mathrm{Re}(q) > -\infty$, $\mathrm{Im}(q) = 0^-$) along the pertinent branch cut, and by using Cauchy's integral theorem, we conclude that $I(x)$ can be expressed as

$$I(x) = -\frac{1}{\pi}\int_{\tau}^{\infty} \frac{qe^{-qx}}{\sqrt{q^2 - \tau^2}}\,dq, \; x > 0. \quad (34)$$

An analogous expression for $x < 0$ can be obtained by deforming the contour in (33) into the right half-plane $\mathrm{Re}(q) > 0$. The integral in (34) can be obtained directly from the entry 3.387-6 in the table by Gradshteyn and Ryzhik (1980) as $-(\tau/\pi)K_1(\tau x)$. Here K_1 is the modified Bessel function of order unity, and behaves as $K_1(z) \to 1/\pi z$, $z \to 0$. Therefore, (34) becomes

$$I(x) = \frac{-1}{\pi x} \quad (35)$$

and it is noted that the parameter τ in this case has dropped out. The indefinite integral of (35) w.r.t x is $-(1/\pi)\ln(|x|)$. By a similar procedure, the inversion of $\sqrt{\tau^2 - q^2}/\sqrt{q^2 - \tau^2}$ is found to give $1/\pi x$.

Some representative expressions for the surface temperature, displacement and stress are now given, with the interesting case $|x/h| \gg 1$ presented first for all speed ranges:

(a) subsonic range ($v < v_2$)

$$\theta(|x| \gg h, y = 0) = \frac{Pm^2c^2\epsilon K}{\mu\beta(1+\epsilon)R_\epsilon}\delta(x) + \frac{2Sm^2c^2\epsilon\beta_2}{\pi\mu\beta(1+\epsilon)R_\epsilon}\frac{1}{x} + \frac{Q\sqrt{h}}{\sqrt{\pi c}(1+\epsilon)}\frac{H(-x)}{\sqrt{-x}}, \quad (36)$$

$$u_x(|x| \gg h, y = 0) = \frac{P(2\beta_{1\epsilon}\beta_2 + K)}{2\mu R_\epsilon}\,\mathrm{sgn}\,(x) - \frac{Sm^2c^2\beta_2}{\pi\mu R_\epsilon}\ln(|x|) + \frac{2Q\beta hc\beta_2}{\pi(1+\epsilon)R_\epsilon}\ln(|x|), \quad (37)$$

$$u_y(|x| \gg h, y = 0) = -\frac{Pm^2c^2\beta_{1\epsilon}}{\pi\mu R_\epsilon}\ln(|x|) + \frac{S(2\beta_{1\epsilon}\beta_2 + K)}{2\mu R_\epsilon}\,\mathrm{sgn}\,(x) + \frac{Q\beta hcK}{2(1+\epsilon)R_\epsilon}\,\mathrm{sgn}\,(x), \quad (38)$$

$$\sigma_x(|x| \gg h, y = 0) = -\frac{2Q\mu\beta\sqrt{h}}{m^2\sqrt{\pi c}(1+\epsilon)}\frac{H(-x)}{\sqrt{-x}}. \quad (39)$$

Here $\beta_{1\epsilon} = \sqrt{1 - c^2/(1+\epsilon)}$, $\beta_2 = \sqrt{1 - m^2c^2}$ and $R_\epsilon(v) = 4\beta_{1\epsilon}\beta_2 - K^2$ is the steady-state thermoelastic Rayleigh function (Chadwick, 1960). This function has the properties $R_\epsilon > 0$, $v < v_{R\epsilon}$ and $R_\epsilon < 0$, $v_2 > v > v_{R\epsilon}$, with $v_{R\epsilon}$ being the thermoelastic Rayleigh-wave speed defined by the equation $R_\epsilon(v_{R\epsilon}) = 0$, which can be solved to yield (Brock, 1994)

$$m^2v_{R\epsilon} = \sqrt{2(m^2 - 1)}G_o, \quad (40a)$$

$$\ln G_o = -\frac{1}{\pi}\int_{1/\sqrt{1+\epsilon}}^{m}\frac{dt}{t} \times \tan^{-1}\frac{4t^2\sqrt{m^2 - t^2}\,\sqrt{t^2 - 1/(1+\epsilon)}}{(m^2 - 2t^2)^2}. \quad (40b)$$

In Eq. (39), only the results for a moving heat source are given because they are of particular interest in the type of problems we discuss (Barber, 1984).

(b) transonic range ($v_2 < v < v_1\sqrt{1+\epsilon}$)

$$\theta(|x| \gg h, y=0) = -\frac{Pm^2c^2\epsilon K}{\mu\beta(1+\epsilon)\chi_\epsilon}\left[K^2\delta(x) - \frac{4\beta_{1\epsilon}\gamma_2}{\pi x}\right]$$

$$-\frac{2Sm^2c^2\epsilon\gamma_2}{\mu\beta(1+\epsilon)\chi_\epsilon}\left[K^2\delta(x) - \frac{4\beta_{1\epsilon}\gamma_2}{\pi x}\right]$$

$$+\frac{Q\sqrt{h}}{\sqrt{\pi c(1+\epsilon)}}\frac{H(-x)}{\sqrt{-x}}, \quad (41)$$

$$u_y(|x| \gg h, y=0)$$

$$= \frac{Pm^2c^2\beta_{1\epsilon}}{\mu\chi_\epsilon}\left[\frac{K^2}{\pi}\ln(|x|) - 2\beta_{1\epsilon}\gamma_2 \operatorname{sgn}(x)\right]$$

$$+\frac{S}{\mu\chi_\epsilon}\left[\frac{2m^2c^2K\beta_{1\epsilon}\gamma_2}{\pi}\ln(|x|) + \frac{8\beta_{1\epsilon}^2\gamma_2^2 - K^3}{2}\operatorname{sgn}(x)\right]$$

$$+\frac{Q\beta hcK}{(1+\epsilon)\chi_\epsilon}\left[\frac{4\beta_{1\epsilon}\gamma_2}{\pi}\ln(|x|) - \frac{K^2}{2}\operatorname{sgn}(x)\right]. \quad (42)$$

Here $\gamma_2 = \sqrt{m^2c^2 - 1}$ and $\chi_\epsilon = K^4 + 16\beta_{1\epsilon}^2\gamma_2^2$. The stress $\sigma_x(|x| \gg h, y=0)$ due to a heat source only ($P, S = 0$) would again be given by (39).

(c) supersonic range ($v > v_1\sqrt{1+\epsilon}$)

$$\theta(|x| \gg h, y=0) = \frac{Pm^2c^2\epsilon K}{\mu\beta(1+\epsilon)R_\epsilon}\delta(x) + \frac{2Sm^2c^2\epsilon\gamma_2}{\mu\beta(1+\epsilon)R_\epsilon}\delta(x)$$

$$+\frac{Q\sqrt{h}}{\sqrt{\pi c(1+\epsilon)}}\frac{H(-x)}{\sqrt{-x}}, \quad (43)$$

$$u_y(|x| \gg h, y=0) = \left[-\frac{Pm^2c^2\gamma_{1\epsilon}}{2\mu R_\epsilon} + \frac{S(K - 2\gamma_{1\epsilon}\gamma_2)}{2\mu R_\epsilon}\right.$$

$$\left.+\frac{Q\beta hcK}{2(1+\epsilon)R_\epsilon}\right]\operatorname{sgn}(x). \quad (44)$$

Here $\gamma_{1\epsilon} = \sqrt{c^2/(1+\epsilon) - 1}$ and now $R_\epsilon = -4\gamma_{1\epsilon}\gamma_2 - K^2$ and, again, the stress $\sigma_x(|x| \gg h, y=0)$ for ($P = S = 0, Q \neq 0$) remains the same as in the subsonic case.

It should be noted for the displacements that the relation $\operatorname{sgn}(x) = 1 - 2H(-x)$ can be introduced by removing rigid-body displacements, a procedure used by Eringen and Suhubi (1975) in analogous problems.

As one check on these results, we allow $\beta \to 0$ in the governing equations (5)–(7) and $Q \to 0$ in the boundary condition (8c), thereby approaching the nonthermal (purely mechanical) limit problem. Appropriately, the present results are found to become identical to the Cole-Huth (1958) solution in the subsonic regime (see also Eringen and Suhubi, 1975) and the Georgiadis-Barber (1993a) solution in the transonic regime.

Finally, the following observations on Eqs. (37)–(44) can also be made: (a) the term multiplying Q in the expressions for $\theta(|x| \gg h, y=0)$ remains unaltered in the three different speed ranges, (b) the $\ln(|x|)$-term multiplying P in the expressions for $u_y(|x| \gg h, y=0)$ in the subsonic and transonic ranges disappears in the supersonic range, (c) the $\ln(|x|)$-term appearing with both S and Q in the expression for this displacement in the transonic range disappears in the subsonic and supersonic ranges, (d) some field quantities exhibit "resonance phenomena" when $v \to v_{R\epsilon}$ (see, e.g., Georgiadis and Barber (1993b) for a discussion of this phenomenon in the nonthermal case).

We close this presentation by recording without comment some expressions for the perhaps less useful case $|x/h| \ll 1$ in the subsonic speed range:

$$\theta(|x| \ll h, y=0)$$

$$= -\frac{Pm^2Kc\epsilon(\sqrt{1+\epsilon c} - \sqrt{1-c^2})}{2\mu\beta(1+\epsilon)h(K^2 - 4\sqrt{1+\epsilon c}\sqrt{1-c^2}\sqrt{1-m^2c^2})}$$

$$\times \operatorname{sgn}(x) - \frac{Q}{\pi\sqrt{1+\epsilon c}}\ln(|x|), \quad (45)$$

$$\sigma_x(|x| \ll h, y=0) = -\frac{2Q\mu\beta(\sqrt{1+\epsilon c} - \sqrt{1-c^2})}{\pi m^2c^2(1+\epsilon)R}$$

$$\times\left[\frac{(K\beta_1 + 2\beta_2)K}{\sqrt{1+\epsilon c}} - R\right]\ln(|x|). \quad (46)$$

Here $R(v) = 4\beta_1\beta_2 - K^2$ is the classical steady-state Rayleigh function, with properties $R > 0$, $v < v_R$ and $R < 0$, $v > v_R$, here v_R being the nonthermal Rayleigh wave speed. This speed satisfies the equation $R(v_R) = 0$ (see, e.g., Eringen and Suhubi, 1975), and can, therefore, be obtained from Eq. (40) merely by setting $\epsilon = 0$. It should also be noted that (45) presented the special case $S = 0$, while $P = S = 0$ in (46).

Conclusion

In this work, the problem of a line mechanical/heat source moving over the surface of a half-space was analyzed. This problem has applications in contact mechanics and tribology. The steady-state coupled thermoelastodynamic theory was employed, and the two-sided Laplace transform along with exact asymptotic inversions provided expressions for the surface temperature, displacement, and stress. These expressions showed generally that a significant rise in the magnitudes of the field quantities occurs in the vicinity of the moving source. Also, the behavior of the various field quantities changes radically when the source velocity crosses a characteristic wave speed ($v_{R\epsilon}$, v_2, $v_1\sqrt{1+\epsilon}$) and passes into a different range. The use of asymptotics was justified because of the extremely small magnitude of a thermoelastic characteristic length, h, yet the resulting expressions showed clearly the influence of thermal parameters.

Acknowledgment

The authors acknowledge the support of NSF Grant DMS 9121700 to L. M. Brock and NATO Grant CRG 931330 to H. G. Georgiadis and L. M. Brock. The work was carried out while H. G. Georgiadis was a Visiting Faculty Member in the Department of Engineering Mechanics at the University of Kentucky.

References

Barber, J. R., 1984, "Thermoelastic Displacements and Stresses due to a Heat Source Moving Over the Surface of a Half Plane," ASME JOURNAL OF APPLIED MECHANICS, Vol. 51, pp. 636–640.

Barber, J. R., and Martin-Moran, C. J., 1982, "Green's functions for transient thermoelastic contact problems for the half-plane," *Wear*, Vol. 79, pp. 11–19.

Biot, M. A., 1956, "Thermoelasticity and Irreversible Thermodynamics," *Journal of Applied Physics*, Vol. 27, pp. 240–253.

Bracewell, R., 1965, *The Fourier Transform and Its Application*, McGraw-Hill, New York.

Brock, L. M., 1994, "Coupled thermoelastic effects in rapid steady-state quasi-brittle fracture," *International Journal of Solids and Structures*, Vol. 31, pp. 1537–1548.

Brock, L. M., 1995, "Rapid quasi-brittle tearing of a thermoelastic strip," *Acta Mechanica*, Vol. 112, pp. 95–106.

Bryant, M. D., 1988, "Thermoelastic Solutions for Thermal Distributions Moving Over Half Space Surfaces and Application to the Moving Heat Source," ASME JOURNAL OF APPLIED MECHANICS, Vol. 55, pp. 87–92.

Carrier, G. A., Krook, M., and Pearson, C. E., 1966, *Functions of a Complex Variable,* McGraw-Hill, New York, pp. 336–344, 380–400.

Chadwick, P., 1960, "Thermoelasticity: the dynamical theory," *Progress in Solid Mechanics,* Vol. 1, I. N. Sneddon and R. Hill, eds., North-Holland, Amsterdam, pp. 263–328.

Cole, J., and Huth, J., 1958, "Stresses Produced in a Half Plane by Moving Loads," ASME Journal of Applied Mechanics, Vol. 25, pp. 433–436.

Crump, K. J., 1976, "Numerical inversion of Laplace transforms using a Fourier series approximation," *Journal of the Association of Computing Machinery,* Vol. 23, pp. 89–96.

Dubner, H., and Abate, J., 1968, "Numerical inversion of Laplace transforms by relating them to the finite Fourier cosine transform," *Journal of the Association of Computing Machinery,* Vol. 15, pp. 115–123.

Eringen, A. C., and Suhubi, E. S., 1975, *Elastodynamics,* Vol. 2, Academic Press, New York.

Francis, P. H., 1972, "Thermomechanical effects in elastic wave propagation: a survey," *Journal of Sound and Vibration,* Vol. 21, pp. 181–192.

Fung, Y. C., 1965, *Foundations of Solid Mechanics,* Prentice-Hall, Englewood Cliffs, NJ.

Georgiadis, H. G., 1993, "Shear and torsional impact of cracked viscoelastic bodies—A numerical integral equation/transform approach," *International Journal of Solids and Structures,* Vol. 30, pp. 1891–1906.

Georgiadis, H. G., and Barber, J. R., 1993a, "Steady-state transonic motion of a line load over an elastic half-space: the corrected Cole-Huth solution," ASME Journal of Applied Mechanics, Vol. 60, pp. 772–774.

Georgiadis, H. G., and Barber, J. R., 1993b, "On the super-Rayleigh/subseismic elastodynamic indentation problem," *Journal of Elasticity,* Vol. 31, pp. 141–161.

Georgiadis, H. G., and Charalambakis, N., 1994, "An analytical/numerical approach for cracked elastic strips under concentrated loads—transient response," *International Journal of Fracture,* Vol. 65, pp. 49–61.

Georgiadis, H. G., Rigatos, A. P., and Charalambakis, N. C., 1995, "Dynamic stress concentration around a hole in a viscoelastic plate," *Acta Mechanica,* Vol. 111, pp. 1–12.

Georgiadis, H. G., and Theocaris, P. S., 1985, "On the solution of steady-state elastodynamic crack problems by using complex variable methods," *Journal of Applied Mathematics and Physics (ZAMP),* Vol. 36, pp. 141–165.

Gradshteyn, I. S., and Ryzhik, I. M., 1980, *Tables of Integrals, Series and Products,* Academic Press, New York.

Huang, J. H., and Ju, F. D., 1985, "Thermomechanical cracking due to moving frictional loads," *Wear,* Vol. 102, pp. 81–104.

Ju, F. D., and Huang, J. H., 1982, "Heat checking in the contact zone of a bearing seal: A two-dimensional model of a single moving asperity," *Wear,* Vol. 79, pp. 107–118.

Kennedy, F. D., 1984, "Thermal and thermomechanical effects in dry sliding," *Wear,* Vol. 100, pp. 453–476.

Kilaparti, S. R., and Burton, R. A., 1978, "The thermoelastic patch contact problem for large Peclet number," ASME *Journal of Lubrication Technology,* Vol. 100, pp. 65–69.

Lessen, M., 1956, "Thermoelasticity and thermal shock," *Journal of the Mechanics and Physics of Solids,* Vol. 5, pp. 57–61.

Ling, F. F., and Mow, V. C., 1965, "Surface displacements of a convective elastic half-space under an arbitrarily distributed fast-moving heat source," ASME *Journal of Basic Engineering,* Vol. 87, pp. 729–734.

Mow, V. C., and Cheng, H. S., 1967, "Thermal stresses in an elastic half space associated with an arbitrarily distributed moving heat source," *Journal of Applied Mathematics and Physics (ZAMP),* Vol. 18, pp. 500–507.

van der Pol, B., and Bremmer, H., 1950, *Operational Calculus Based on the Two-Sided Laplace Integral,* Cambridge University Press, Cambridge, UK.

Diffraction of SH-Wave by Interacting Matrix Crack and an Inhomogeneity

X. D. Wang
Mem. ASME.

S. A. Meguid
Mem. ASME.

Engineering Mechanics and Design Laboratory, Department of Mechanical and Industrial Engineering, University of Toronto, 5 King's College Road, Toronto, Ontario M5S 3G8, Canada

This article presents an analytical treatment of the dynamic interaction between a crack and an arbitrarily located circular inhomogeneity under antiplane incident wave. The method is based upon the use of a pseudo-incident wave technique which reduces the interaction problem into a coupled solution of a single crack and a single inhomogeneity problems. The newly proposed pseudo-incident wave technique avoids the numerical integration commonly used in the boundary element and volume integral methods and thus provides reliable and accurate analytical solutions. The resulting dynamic stress intensity factor of the crack is verified by comparison with existing results and numerical examples are provided to show the dependence of dynamic shielding and amplification upon the frequency of the incident wave, the material combination and the location of the inhomogeneity. The results show that the toughening associated with special geometric configurations under quasi-static loading may provide undesirable weakening effect upon the crack under dynamic loading in a certain frequency region.

1 Introduction

Composite materials are generally characterized by heterogeneity, anisotropy, load sharing, and interfaces. Indeed, increasing evidence suggests that the presence of inhomogeneities such as precipitates, transformed particles, fibers, inclusions, and microcracks often control the overall failure mechanism of these solids; see, e.g., the reviews by Mura (1987) and Evans (1990) on the subject. Accordingly, an accurate assessment of the toughness of advanced composite materials would necessitate the determination of the influence of these inhomogeneities.

The quasi-static behavior of interacting cracks in a homogeneous medium under plane and antiplane deformations has been extensively investigated (see, Rose, 1986; Hutchinson, 1987; Kachanov, 1987; Gong and Meguid, 1991, and others). An important result of crack interaction is the existence of shielding and amplification phenomenon which forms one of the basic toughening mechanisms of ceramic composites (Evans, 1990). The static interaction between cracks and inhomogeneities has also been the subject of various publications. Except for the simplified case in which only thermal mismatch is considered (Muller, 1994), the general interaction between a crack(s) and an inhomogeneity is treated numerically using the integral equation method (Erdogan et al., 1974, 1975; Muller and Schmauder, 1993).

In spite of the fact that most advanced composite material are considered for use in situations involving dynamic loading, dynamic problems of interacting cracks and inhomogeneities have received much less attention. Existing solutions which account for the dynamic interaction between defects deal mainly with crack configurations using the integral transform method (Jain and Kanwal, 1972; Itou, 1980), the superposition technique (Meguid and Wang, 1994, 1995), and the boundary integral equation method (Gross, et al., 1988; Zhang and Achenbach, 1989; Zhang, 1992). In addition, results concerning the dynamic interaction between inhomogeneities are mainly based upon boundary integral method (Schafbuch et al., 1990) or volume integral method (Lee and Mal, 1994).

The objective of the present paper is to develop a generalized theoretical method to describe the dynamic interaction between a crack and an *arbitrarily* located circular inhomogeneity subjected to an incident antiplane shear wave. The governing formulations are based upon the use of a pseudo-incident wave technique, which reduces the multiple interaction problem into a coupled solution of a single crack and a single inhomogeneity problems. As the result of such a reduction, the present method avoids the complex numerical integration commonly used in the boundary element and volume integral methods and thus provides more reliable and accurate analytical solutions. The analysis of the crack problem is based upon the use of Fourier transform and the solution of the resulting singular integral equations, while the stress field due to the inhomogeneity is given by making use of the Fourier expansion of the displacement field. The singular stress field of the crack in the presence of the inhomogeneity is then obtained by solving these coupled problems.

2 Description and Decomposition of the Problem

2.1 Description of the Problem. Consider an elastic infinitely extended isotropic solid containing a matrix crack of length $2a$ and an arbitrarily located circular inhomogeneity of radius R, as shown in Fig. 1. The shear moduli of the matrix and the inhomogeneity are assumed to be μ_M and μ_F, and the corresponding shear wave speeds c_M and c_F, respectively. A cartesian (x, y) and a polar (r, ϕ) coordinate systems are used to characterize the crack and the inhomogeneity. The distance between the right tip of the crack and the center of the inhomogeneity is denoted d and the inclination angle of the inhomogeneity center with respect to the x-axis is denoted θ. The solid is subjected to a steady-state antiplane wave and the boundary conditions at the surfaces of the crack are assumed traction-free.

The elastodynamic behaviour of the current medium under steady-state antiplane deformation is governed by the following Helmholtz equations (Achenbach, 1973),

Contributed by the Applied Mechanics Division of THE AMERICAN SOCIETY OF MECHANICAL ENGINEERS for publication in the ASME JOURNAL OF APPLIED MECHANICS.

Discussion on this paper should be addressed to the Technical Editor, Professor Lewis T. Wheeler, Department of Mechanical Engineering, University of Houston, Houston, TX 77204-4792, and will be accepted until four months after final publication of the paper itself in the ASME JOURNAL OF APPLIED MECHANICS.

Manuscript received by the ASME Applied Mechanics Division, Oct. 18, 1995; final revision, Apr. 17, 1997. Associate Technical Editor: V. K. Kinra.

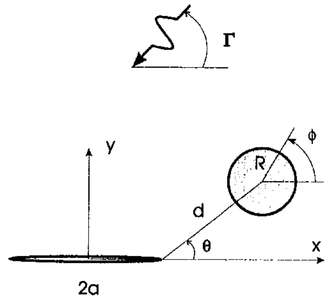

Fig. 1 Arbitrarily located inhomogeneity near the tip of a matrix crack

$$(\nabla^2 + k_M^2)w = 0 \quad \text{in the matrix} \tag{1}$$

$$(\nabla^2 + k_F^2)w = 0 \quad \text{in the inhomogeneity} \tag{2}$$

in which w is the antiplane displacement, ∇^2 is the Laplacian operator, $k_M = \omega/c_M$, and $k_F = \omega/c_F$ are the shear wave numbers with ω being the circular frequency of the incident wave. It should be noted that, for the sake of convenience, the time factor $\exp(-i\omega t)$ which applies to all the field parameters has been suppressed. The nonvanishing stress components can be expressed as

$$\tau_{xz} = \frac{\partial w}{\partial x}\begin{cases}\mu_M & \text{in the matrix}\\ \mu_F & \text{in the inhomogeneity}\end{cases} \tag{3}$$

$$\tau_{yz} = \frac{\partial w}{\partial y}\begin{cases}\mu_M & \text{in the matrix}\\ \mu_F & \text{in the inhomogeneity.}\end{cases} \tag{4}$$

2.2 Pseudo-Incident Wave Method. The current dynamic interaction problem involves complex boundary and interfacial conditions which result in multiple scattering of elastic waves between the crack and the inhomogeneity. As a result, it is difficult to solve the original problem directly using the traditional Fourier transform method. To overcome these difficulties, let us focus our attention to two simpler problems which involve either the crack or the inhomogeneity, as shown in Figs. 2(a) and 2(b).

In the crack problem (Fig. 2(a)), the cracked medium is subjected to a pseudo-incident wave w_i^c which is the superposition of the real incident wave w^0 and the unknown scattering wave of the inhomogeneity problem w^f, such that

$$w_i^c = w^0 + w^f. \tag{5}$$

The corresponding pseudo-incident stress field can then be expressed as

$$\tau_{jz}(w_i^c) = \tau_{jz}(w^0) + \tau_{jz}(w^f), \quad j = x, y. \tag{6}$$

As a result of this incident wave, a scattering wave w^c is formed due to the reflection of the crack surface. To ensure that the traction-free condition along the crack surface is satisfied, the superposition of the Pseudo incident wave and the scattering wave should give zero shear stress at the crack surface, i.e.,

$$\tau_{yz}(w_i^c)|_{\text{crack}} + \tau_{yz}(w^c)|_{\text{crack}} = 0 \tag{7}$$

which provides the boundary condition for the solution of the scattering field.

In the inhomogeneity problem (Fig. 2(b)), the medium is subjected to a pseudo-incident wave w_i^f which is the superposition of the real incident wave w^0 and the scattering wave of the crack problem w^c, i.e.,

$$w_i^f = w^0 + w^c. \tag{8}$$

The corresponding pseudo-incident stress can be expressed as

$$\tau_{jz}(w_i^f) = \tau_{jz}(w^0) + \tau_{jz}(w^c), \quad j = x, y. \tag{9}$$

In this case, in addition to the resulting scattering wave w^f in the matrix, a displacement field w^F is also induced in the inhomogeneity. The continuity of the displacement and stress fields along the interface between the inhomogeneity and the matrix indicate the existence of the following relations:

$$w_i^f|_{\text{inter}} + w^f|_{\text{inter}} = w^F|_{\text{inter}},$$
$$\tau_n(w_i^f)|_{\text{inter}} + \tau_n(w^f)|_{\text{inter}} = \tau_n(w^F)|_{\text{inter}} \tag{10}$$

where τ_n is the shear stress along the interface.

Upon the solution of these two problems, we can build up the following superimposed displacement field:

$$w = \begin{cases} w^0 + w^c + w^f & \text{in the matrix}\\ w^F & \text{in the inhomogeneity}\end{cases} \tag{11}$$

and the corresponding stress field

$$\tau_{jz} = \begin{cases}\tau_{jz}(w^0) + \tau_{jz}(w^c) + \tau_{jz}(w^f) & \text{in the matrix}\\ \tau_{jz}(w^F) & \text{in the inhomogeneity}\end{cases}$$

$$j = x, y. \tag{12}$$

The solution given by Eq. (11) satisfies the governing wave Eqs. (1) and (2).

Let us now consider the boundary condition at the crack surface and the continuity conditions along the interface. According to Eq. (12), the shear stress at the crack surface can be expressed as

$$\tau_{yz}|_{\text{crack}} = \tau_{yz}(w^0)|_{\text{crack}} + \tau_{yz}(w^c)|_{\text{crack}} + \tau_{yz}(w^f)|_{\text{crack}}. \tag{13}$$

By making use of Eq. (6), the stress given by Eq. (13) can be rewritten as

$$\tau_{yz}|_{\text{crack}} = \tau_{yz}(w_i^c)|_{\text{crack}} + \tau_{yz}(w^c)|_{\text{crack}} = 0, \tag{14}$$

which means that the traction-free condition at the crack surface is satisfied.

Now consider the continuity condition along the interface between the matrix and the inhomogeneity. In the matrix, the displacement and the shear stress near the interface can be expressed as

$$w^M|_{\text{inter}} = w^0 + w^c + w^f \tag{15}$$

$$\tau_n(w^M)|_{\text{inter}} = \tau_n(w^0) + \tau_n(w^c) + \tau_n(w^f). \tag{16}$$

Equations (15) and (16) can be further rewritten, by making use of Eqs. (8), (9) and (12), as

$$w^M|_{\text{inter}} = w_i^f|_{\text{inter}} + w^f|_{\text{inter}} = w^F|_{\text{inter}} \tag{17}$$

$$\tau_n(w^M)|_{\text{inter}} = \tau_n(w_i^f)|_{\text{inter}} + \tau_n(w^f)|_{\text{inter}} = \tau_n(w^F)|_{\text{inter}} \tag{18}$$

which indicate the imposition of the continuity conditions along the interface.

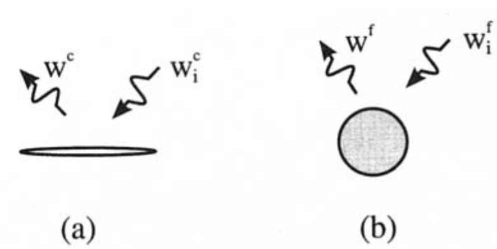

Fig. 2 Pseudo-incident wave method

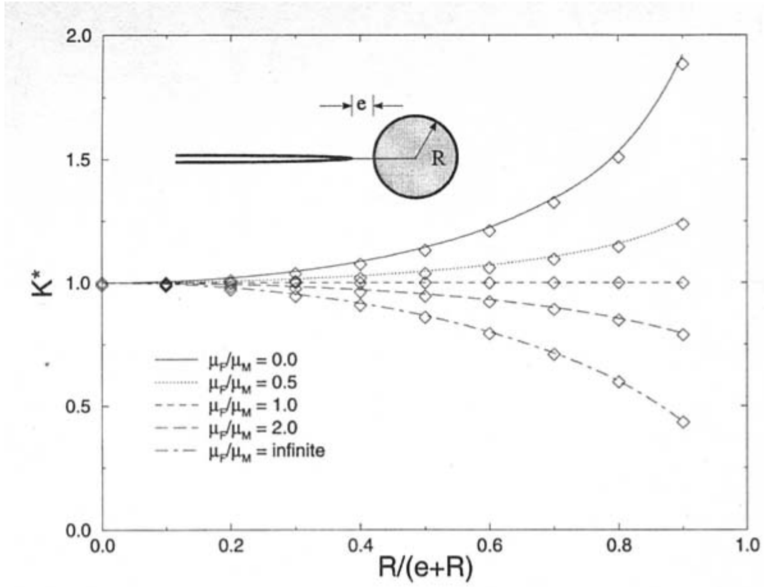

Fig. 3 Quasi-static interaction between a crack and an inhomogeneity

To sum up, both the boundary condition at the crack surface and the continuity condition along the interface are satisfied by the general solution given by Eqs. (11) and (12). In addition, the radiation condition at infinity is also satisfied, since the scattering fields (w^c and w^f) vanish at points far from the crack and the inhomogeneity and the displacement and stresses given by Eqs. (11) and (12) tend to the results of the incident wave.

3 Solution of Dynamic Interaction Problem

According to the pseudo-incident wave method described in the previous section, the solution of the present dynamic interaction problem consists of two solutions involving either a crack or an inhomogeneity. The pseudo-incident waves that they are subjected to are unknown and need to be determined in the solution procedure.

Let us consider the solution of the crack problem first. The scattering field of the crack problem is governed by the deformation of the crack surface, which can be described in terms of the following dislocation density function

$$\psi(x) = \frac{\partial w^c(x, 0^+)}{\partial x}, \quad |x| \le a. \tag{19}$$

This function includes the well-known square-root singularity and can be generally expressed in terms of Chebyshev polynomials as

$$\psi(x) = \sum_{n=0}^{\infty} \frac{A_n}{\sqrt{1 - \dfrac{x^2}{a^2}}} T_n\left(\frac{x}{a}\right). \tag{20}$$

To maintain the traction-free condition of the crack surface (Fig. 2(a)) in the scattering problem, the crack surface boundary is assumed to be subjected to a shear stress due to the pseudo incident wave w_i^c but in an opposite direction, i.e., $\tau_{yz}|_{\text{crack}} = -\tau_{yz}(w_i^c)|_{\text{crack}}$. The imposition of this boundary condition results in a singular integral equation for $\psi(x)$ from which the solution of A_n can be obtained. By truncating the Chebyshev polynomials to the Nth term, the solution can be expressed as

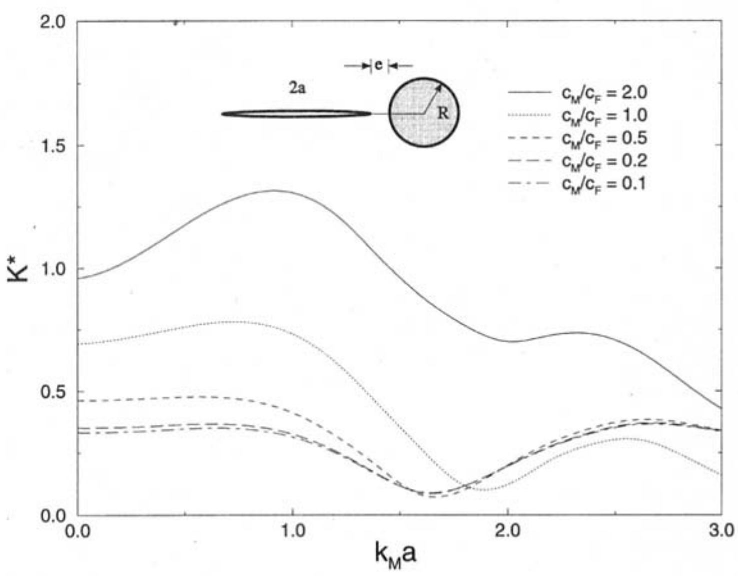

Fig. 4 Effect of the frequency upon the normalized dynamic stress intensity factor K^* for an oblique incident wave Γ = 45 deg

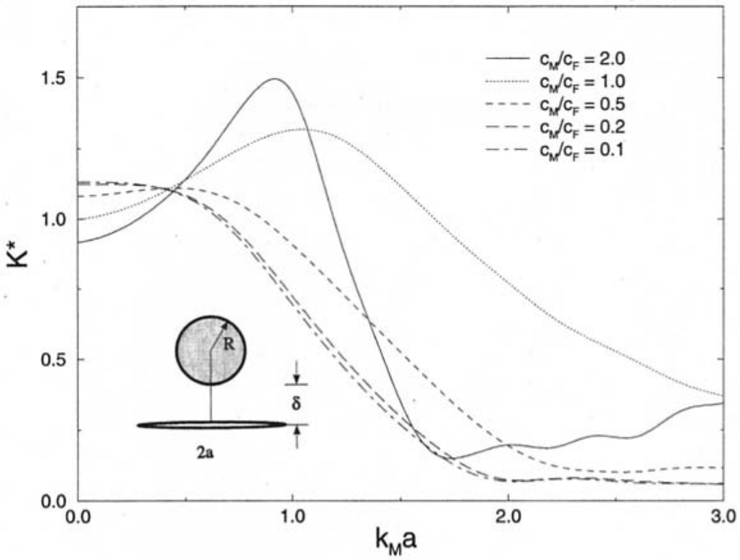

Fig. 5 Effect of an inhomogeneity above the crack upon the normalized dynamic stress intensity factor K^*

$$\{A\} = [S_1]\{\tau_i^c\} \tag{21}$$

where $\{A\} = \{A_1, A_2 \ldots A_N\}^T$, $\{S_1\}$ is a known matrix and

$$\{\tau_i^c\} = \{\tau_1, \tau_2, \ldots \tau_N\}^T, \tag{22}$$

being the boundary stress due to the pseudo-incident wave at the collocation points of the crack surface (refer to Appendix A for details). According to Eq. (6), this boundary stress can be expressed as

$$\{\tau_i^c\} = \{\tau^0\} + \{\tau^f\} \tag{23}$$

with $\{\tau^0\}$ and $\{\tau^f\}$ being the shear stress at the collocation points along the crack surface due to the initial incident wave and the scattering wave of the inhomogeneity problem, respectively. According to this solution, the scattering displacement of the crack problem along the interface site can be described in term of $\{A\}$; as being

$$w^c(\phi) = w^c(\bar{x}, \bar{y}) = [F_1(\phi)]\{A\} \tag{24}$$

where

$$[F_1(\phi)] = \{p_1(\bar{x}, \bar{y}), p_2(\bar{x}, \bar{y}), \ldots, p_N(\bar{x}, \bar{y})\} \tag{25}$$

and

$$\bar{x} = a + d\cos\theta + R\cos\phi \quad \text{and}$$
$$\bar{y} = d\sin\theta + R\sin\phi \tag{26}$$

with $p_1, p_2, \ldots, p_N$ being known functions given in Appendix A. The corresponding shear stress distribution along the interface site can be expressed as

$$\tau_{rz}^c(\phi) = \tau_{xz}^c(\bar{x}, \bar{y})\cos\phi + \tau_{yz}^c(\bar{x}, \bar{y})\sin\phi = [F_2(\phi)]\{A\} \tag{27}$$

where

$$[F_2(\phi)] = \{\bar{p}_1(\bar{x}, \bar{y}), \bar{p}_2(\bar{x}, \bar{y}), \ldots, \bar{p}_N(\bar{x}, \bar{y})\} \tag{28}$$

with $\bar{p}_1, \bar{p}_2, \ldots, \bar{p}_N$ being known functions, given in Appendix A.

Let us now consider the displacement and stress fields due to a single inhomogeneity subjected to a pseudo incident wave w_i^f. The governing equations ((1) and (2)) of the present problem can be expressed in a polar coordinate system (r, ϕ) and the displacement field can be generally expressed as

$$w^f(r, \phi) = \begin{cases} \sum_{n=0}^{\infty} H_n^{(1)}(k_M r)[a_n e^{in\phi} + b_n e^{-in\phi}] & \text{in the matrix} \\ \sum_{n=0}^{\infty} J_n(k_F r)[c_n e^{in\phi} + d_n e^{-in\phi}] & \text{in the inhomogeneity} \end{cases} \tag{29}$$

where $H_n^{(1)}$ and J_n are Hankel function and Bessel function of the first kind, respectively. The solution of a_n, b_n, c_n, and d_n corresponding to an incident wave w_i^f can be obtained by making use of the continuity condition along the interface, such that

$$\begin{Bmatrix} a_n \\ c_n \end{Bmatrix} = [H_n]\int_0^{2\pi} \begin{Bmatrix} w_i^f|_{\text{inter}} \\ \tau_{rz}(w_i^f)|_{\text{inter}} \end{Bmatrix} e^{-in\phi} d\phi \tag{30}$$

$$\begin{Bmatrix} b_n \\ d_n \end{Bmatrix} = [H_n]\int_0^{2\pi} \begin{Bmatrix} w_i^f|_{\text{inter}} \\ \tau_{rz}(w_i^f)|_{\text{inter}} \end{Bmatrix} e^{in\phi} d\phi \tag{31}$$

where

$$[H_n] = -\frac{1}{2\pi}\begin{bmatrix} H_n^{(1)}(k_M R) & -J_n(k_F R) \\ \mu_M k_M H_n^{(1)\prime}(k_M R) & -\mu_f k_F J_n'(k_F R) \end{bmatrix}^{-1} \tag{32}$$

with the prime (′) representing the derivative. Since the pseudo-incident wave of the inhomogeneity problem consists of the original incident wave and the scattering wave of the crack problem (Eqs. (8) and (9)), then by making use of Eqs. (24) and (27), this solution can be rewritten in term of $\{A\}$ as follows:

$$\begin{Bmatrix} a_n \\ c_n \end{Bmatrix} = [H_n]\int_0^{2\pi} \left(\begin{bmatrix} F_1(\phi) \\ F_2(\phi) \end{bmatrix} \{A\} + \begin{bmatrix} w^0(\phi) \\ \tau_{rz}^0(\phi) \end{bmatrix} \right) e^{-in\phi} d\phi \tag{33}$$

$$\begin{Bmatrix} b_n \\ d_n \end{Bmatrix} = [H_n]\int_0^{2\pi} \left(\begin{bmatrix} F_1(\phi) \\ F_2(\phi) \end{bmatrix} \{A\} + \begin{bmatrix} w^0(\phi) \\ \tau_{rz}^0(\phi) \end{bmatrix} \right) e^{in\phi} d\phi \tag{34}$$

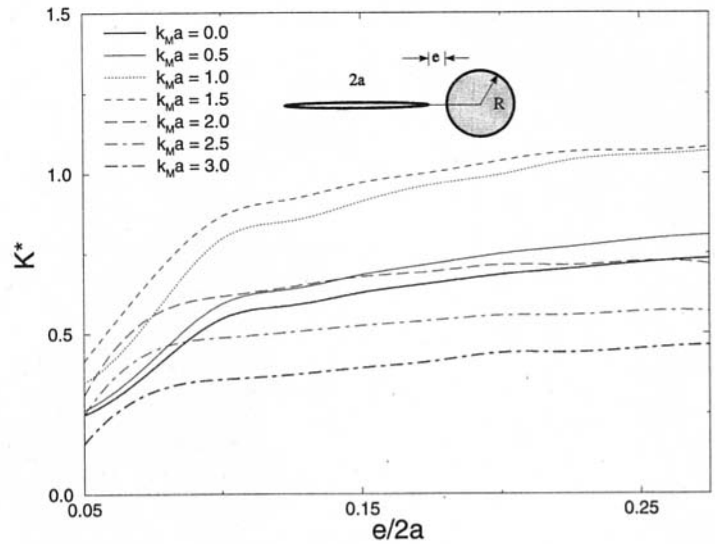

Fig. 6 Effect of the position of the inhomogeneity ($e/2a$) upon the normalized dynamic stress intensity factor K^* for $\mu_M/\mu_F = 0.1$

where $w^0(\phi)$ and $\tau_{rz}^0(\phi)$ are the displacement and stress fields corresponding to the initial incident wave along the inhomogeneity boundary. According to this solution, the resulting shear stress at the crack site can be obtained as

$$\tau_{yz}^f(x) = \tau_{rz}(\bar{r}, \bar{\phi}) \sin \phi + \tau_{\phi z}(\bar{r}, \bar{\phi}) \cos \phi$$
$$= [F_3(x)]\{A\} + \{F_4(x)\} \tag{35}$$

where $[F_3(x)]$ and $[F_4(x)]$ are two known matrices given in Appendix B and

$$\bar{r} = \sqrt{d^2 + (x-a)^2 - 2d(x-a)\cos\theta},$$
$$\bar{\phi} = -\frac{\pi}{2} - \tan^{-1}\frac{d\cos\theta - (x-a)}{d\sin\theta}. \tag{36}$$

Therefore, the stress at the collocation points of the crack surface can be expressed as

$$\{\tau^f\} = [S_2]\{A\} + \{S_3\} \tag{37}$$

where

$$[S_2] = \begin{bmatrix} F_3(x_1) \\ F_3(x_2) \\ \cdots \\ F_3(x_N) \end{bmatrix}, \quad [S_3] = \begin{bmatrix} F_4(x_1) \\ F_4(x_2) \\ \cdots \\ F_4(x_N) \end{bmatrix}. \tag{38}$$

Substituting Eqs. (23) and (37) into Eq. (21) gives

$$\{A\} = [S_1](\{\tau^0\} + [S_2]\{A\} + \{S_3\}) \tag{39}$$

from which $\{A\}$ can be obtained as being

$$\{A\} = (I - [S_1][S_2])^{-1}([S_1]\{\tau^0\} + [S_1]\{S_3\}). \tag{40}$$

According to Eq. (40), the dynamic stress intensity factor at the right tip of the crack in the presence of the inhomogeneity can be expressed in terms of A_n ($n = 1, 2, \ldots, N$) as

$$K_{III} = \mu_M\sqrt{\pi a}\sum_{n=1}^{N} A_n. \tag{41}$$

4 Results and Discussions

The theoretical analysis described in the previous sections is used to investigate the dynamic effect of a circular inhomogeneity upon the dynamic stress intensity factor of a matrix crack under an incident antiplane harmonic wave. The wave is directed at an angle Γ with the x-axis (Fig. 1) and can be expressed as

$$\tau_{xz}^0 = \tau \cos \Gamma e^{-ik_M(x\cos\Gamma + y\sin\Gamma)},$$
$$\tau_{yz}^0 = \tau \sin \Gamma e^{-ik_M(x\cos\Gamma + y\sin\Gamma)}$$

and

$$w^0(x, y) = \frac{i\tau}{k_M\mu_M} e^{-ik_M(x\cos\Gamma + y\sin\Gamma)}$$

in which τ is the maximum value of the shear stress corresponding to the wave front.

To verify the validity of the current method, consider first the quasi-static antiplane interaction between a circular inhomogeneity and a collinear crack with an initial stress intensity factor (K_0) for which the solution has been found by Turska-Klebek and Sokolowski (1984) using the complex variable method. This solution can be predicted by the current method for a relatively large crack length ($a/R > 3$). The normalized stress intensity factor ($K^* = K_{III}/K_0$) predicted by Turska-Klebek and Sokolowski (lines) is compared with that calculated by the current method (diamonds) in Fig. 3 for different material combinations using 20 terms in Chebyshev polynomial expansion and 40 terms in the Bessel function expansion. In view of the excellent agreement observed between the two, even for the case where the inhomogeneity is very close to the crack tip ($e = d - R = 0.1R$), the number of terms used in this example was retained for the remainder of this study.

Consider now the general dynamic interaction between an arbitrarily located inhomogeneity and a crack. The present formulations predict the dependence of the normalized stress intensity factors ($K^* = K_{III}/\tau\sqrt{\pi a}$) upon the location and size (d/a, θ and R/a) of the inhomogeneity, the material combination, the frequency (ω) and the incident angle (Γ) of the incident wave. It should be recognized that the dynamic stress intensity factor produced by a time-harmonic wave is in general a complex quantity. For convenience, only the amplitude of the normalized complex dynamic stress intensity factor is considered in the following figures. Furthermore, only the stress intensity factor at the right tip of the crack is considered.

Figure 4 shows the variation of the normalized stress intensity factor K^* versus the normalized wave number k_Ma for different material combinations resulting from an oblique ($\Gamma = 45$ deg) incident wave, for cases where $e/a = 0.2$, $R = a$ and $\rho_M =$

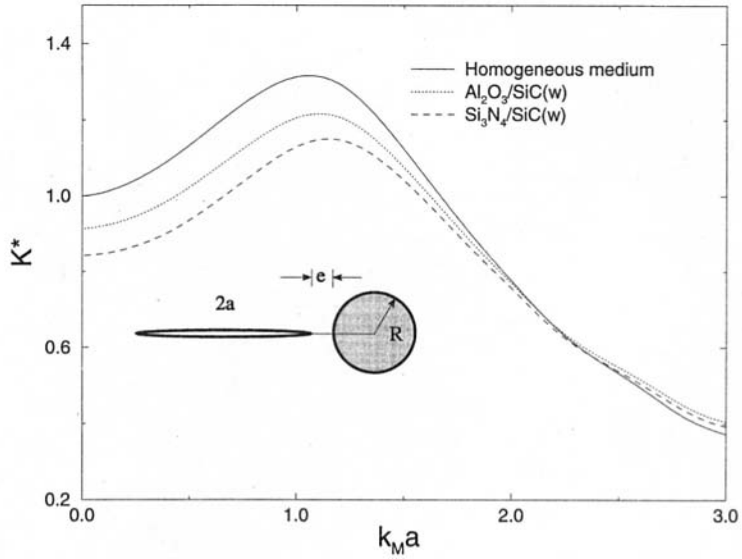

Fig. 7 Effect of a SiC fiber (whisker) upon a matrix crack in Al_2O_3 and Si_3N_4 matrices

ρ_F with ρ being the mass density. The well-known overshoot phenomenon for crack problems is observed for all the cases examined. In most of the frequency range considered, the effect of the inhomogeneity is governed by the relative modulus c_M/c_F. The inhomogeneity exhibits an amplification effect when $c_M/c_F > 1$ and a shielding effect when $c_M/c_F < 1$, although a weak amplification effect is observed for $k_M a > 1.8$.

Figure 5 shows the variation of K^* with $k_M a$ for the case where the inhomogeneity is directly above the crack, with $d^2 = a^2 + (\delta + R)^2$, $\delta = 0.5a$, $R = a$, and $\rho_M = \rho_F$, subjected to a normal incident wave ($\Gamma = 90$ deg). A totally different result is observed for low frequencies ($k_M a < 0.5$); softer inhomogeneity ($c_M/c_F > 1$) exhibits a shielding effect, while stiffer inhomogeneity ($c_M/c_F < 1$) exhibits an amplification effect. It is interesting to note that for high frequencies ($k_M a > 1.2$), the inhomogeneity provides a shielding effect for all the material combinations considered.

Figure 6 shows the variation of the stress intensity factors K^* with the distance between the crack and the inhomogeneity (e) for different frequencies under normal incident wave ($\Gamma = 90$ deg) for the collinear configuration with $R = a$, $\mu_M/\mu_F = 0.1$ and $\rho_M = \rho_F$. These results indicate obvious shielding effect of the inhomogeneity upon the crack, when $e/2a$ is small. For all the frequencies considered, K^* increases monotonically with increasing e and then tends to the corresponding single crack solution.

The comparison between Figs. 4–6 indicates that the shielding effect of the inhomogeneity under static loading condition is inverted into amplification in a special frequency range. However, it is interesting to note that for most of the geometric configurations and the frequencies considered, a stiffer inhomogeneity ($c_M/c_F < 1$) will provide a beneficial shielding effect upon the matrix crack.

Let us now consider real material coefficients to demonstrate the effect of reinforcing fibers upon matrix cracks. Figure 7 shows the effect of a SiC fiber (whisker) upon a matrix crack in Al_2O_3 and Si_3N_4 matrices, respectively, for the case where the fiber is ahead of the crack. The material constants considered for SiC(w) were: $E = 490$ (Gpa), $\rho = 3.18$ (g/cm^3); for Al_2O_3: $E = 390$ (Gpa), $\rho = 3.99$ (g/cm^3), and for Si_3N_4: $E = 300$ (Gpa), $\rho = 3.2$ (g/cm^3). The results reveal that significant shielding effect of the fiber can be observed for $k_M a < 2$.

According to the present solution, the dynamic response of the crack in some useful limiting cases can be obtained directly. When $c_M/c_F \to 0$ and $\rho_M/\rho_F =$ constant, the inhomogeneity reduces to a rigid inclusion with a finite mass density; while when $c_M/c_F \to \infty$ and $\rho_M/\rho_F =$ constant, the inhomogeneity can be regarded as a damage zone with zero elastic modulus and finite mass density. In addition, when $\mu_M/\mu_F \to \infty$ and $\rho_M/\rho_F \to \infty$, the inhomogeneity reduces to a hole which corresponds to a fully debonded inhomogeneity.

5 Concluding Remarks

A general solution is provided to the dynamic interaction problem of a matrix crack with an arbitrarily located inhomogeneity under antiplane loading. The analysis is based upon the use of a newly developed pseudo-incident wave method. This method can be generalized to treat more complex interaction problems involving multiple cracks and inhomogeneities.

The validity and versatility of the present solution have been demonstrated by application to specific examples. Furthermore, the effect of the location of the inhomogeneity, the material combination and the frequency of the incident wave upon the dynamic stress intensity factor of the matrix crack and the resulting shielding and amplification effects are examined and discussed.

Acknowledgments

This work was supported in part by the Natural Sciences and Engineering Research Council of Canada (CRD program) and in part by ALCOA Foundation of the USA.

References

Achenbach, J. D., 1973, *Wave propagation in elastic solids*, North-Holland, Amsterdam.

Evans, A. G., 1990, "Perspective on the Development of High-Toughness Ceramics," *J. Am. Ceram. Soc.*, Vol. 73, pp. 187–206.

Erdogan, F., Gupta, G. D., and Ratwani, M., 1974, "Interaction between a Circular Inclusion and an Arbitrarily Oriented Crack," ASME JOURNAL OF APPLIED MECHANICS, Vol. 41, pp. 1007–1013.

Erdogan, F., and Gupta, G. D., 1975, "The Inclusion Problem with a Crack Crossing the Boundary," *Int. J. Frac.*, Vol. 11, pp. 13–27.

Gross, D., and Zhang, Ch., 1988, "Diffraction of SH Waves by a System of Cracks: Solution by an Integral Equation Method," *Int. J. Solids Structures*, Vol. 24, pp. 41–49.

Gong, S. X., and Meguid, S. A., 1991, "A General Solution to the Antiplane Problem of an Arbitrarily Located Elliptical Hole near the Tip of a Main Crack," *Int. J. Solids Structures*, Vol. 28, pp. 249–263.

Hutchinson, J. W., 1987, "Crack Tip Shielding by Micro-Cracking in Brittle Solids," *Acta Metall.* Vol. 35, pp. 1605–1619.

Itou, S., 1980, "Diffraction of an Antiplane Shear Wave by Two Coplanar Griffith Cracks in an Infinite Elastic Medium," *Int. J. Solids Structures*, Vol. 16, pp. 1147–1153.

Jain, D. L., and Kanwal, R. P., 1972, "Diffraction of Elastic Waves by Two Coplanar Griffith Cracks in an Infinite Elastic Medium," *Int. J. Solids Structures*, Vol. 8, pp. 961–975.

Kachanov, M., 1987, "Elastic Solids with Many Cracks: A Simple Method of Analysis," *Int. J. Solids Structures*, Vol. 23, pp. 23–44.

Lee, J. K., and Mal, A. K., 1994, "A Volume Integral Equation Technique for Multiple Scattering Problems in Elastodynamics," *Appl. Math. and Comp.*, Vol. 67, pp. 135–159.

Muller, W. H., Harris, D. O., and Dedhia, D. D., 1994, "Stress Intensity Factor of Two-Dimensional and Three-Dimensional Cracks next to a Thermally Mismatched Inclusion, ASME JOURNAL OF APPLIED MECHANICS, Vol. 61, pp. 731–735.

Muller, W. H., and Schmauder, S., 1993, "Stress-Intensity Factors of r-Cracks in Fiber-Reinforced Composites under Thermal and Mechanical Loading," *Int. J. Frac.*, Vol. 59, pp. 307–343.

Meguid, S. A., and Wang, X. D., 1994, "The Dynamic Interaction of a Microcrack with a Main Crack under Antiplane Loading," *Int. J. Solids Structures*, Vol. 31, pp. 1085–1097.

Meguid, S. A., and Wang, X. D., 1995, "On the Dynamic Interaction Between a Microdefect and a Main Crack," *Proc. R. Soc., Lond.*, Vol. A409, pp. 449–464.

Mura, T., 1987, *Micromechanics of Defects in Solids*, 2nd ed., Martinus Nijhoff, Boston.

Rose, L. K. F., 1986, "Microcrack Interaction with a Main Crack," *Int. J. Frac.*, Vol. 31, pp. 233–242.

Schafbuch, P., Thompson, R. B., and Rizzo, F., 1990, "Application of Boundary Element Method to Elastic Wave Scattering by Irregular Defects," *J. Nondest. Eval.*, Vol. 9, pp. 113–127.

Zhang, Ch., and Achenbach, J. D., 1989, "Time-Domain Boundary Element Analysis of Dynamic Near-Tip Fields for Impact-Loaded Collinear Cracks," *Engng Fracure Mech.*, Vol. 32, pp. 899–909.

Zhang, Ch., 1992, "Elastodynamic Analysis of a Periodic Array of Mode III Cracks in Transversely Isotropic Solids," ASME JOURNAL OF APPLIED MECHANICS, Vol. 59, pp. 366–371.

APPENDIX A

The matrix $[S_1]$ used in Eq. (21) is given by

$$[S_1]^{-1} = [s_{lj}], \quad s_{lj} = \frac{\sin\left(\dfrac{jl\pi}{N+1}\right)}{\sin\left(\dfrac{j\pi}{N+1}\right)} + g_j(x_l),$$

$$j, l = 1, 2, \ldots, N$$

where

$$g_j(x) = \begin{cases} (-1)^n a \displaystyle\int_0^\infty \left(\frac{\alpha}{s} - 1\right) J_j(sc)\cos(sx)\,ds & j = 2n+1 \\ (-1)^{(n+1)} a \displaystyle\int_0^\infty \left(\frac{\alpha}{s} - 1\right) J_j(sc)\sin(sx)\,ds & j = 2n \end{cases}$$

$$\alpha = \begin{cases} \sqrt{s^2 - k_M^2} & |s| \geq k_M \\ -i\sqrt{k_M^2 - s^2} & |s| < k_M \end{cases}$$

in which J_j is the first kind Bessel function of order j, and

$$x_l = a\cos\left(\frac{l}{N+1}\pi\right), \quad l = 1, 2, \ldots N$$

being the collocation points along the crack surface.

In addition, the functions p_j and $\overline{p_j}$ in Eqs. (25) and (28) are given by

$$p_j(x, y) = -a \begin{cases} (-1)^n \displaystyle\int_0^\infty \frac{1}{s} J_j(sc)\cos(sx) e^{-\alpha|y|}\,ds & j = 2n+1 \\ (-1)^{(n+1)} \displaystyle\int_0^\infty \frac{1}{s} J_j(sc)\sin(sx) e^{-\alpha|y|}\,ds & j = 2n \end{cases}$$

$$\overline{p_j}(x, y) = X_j(x, y)\cos\phi + Y_j(x, y)\sin\phi$$

where

$$X_j(x, y) = \mu_M a \begin{cases} (-1)^n \displaystyle\int_0^\infty \frac{\alpha}{s} J_j(sc)\cos(sx) e^{-\alpha|y|}\,ds & j = 2n+1 \\ (-1)^{(n+1)} \displaystyle\int_0^\infty \frac{\alpha}{s} J_j(sc)\sin(sx) e^{-\alpha|y|}\,ds & j = 2n \end{cases}$$

and

$$Y_j(x, y) = \mu_M a \operatorname{sgn}(y) \times \begin{cases} (-1)^n \displaystyle\int_0^\infty J_j(sc)\sin(sx) e^{-\alpha|y|}\,ds & j = 2n+1 \\ (-1)^n \displaystyle\int_0^\infty J_j(sc)\cos(sx) e^{-\alpha|y|}\,ds & j = 2n. \end{cases}$$

The following results are used in calculating the above integrals involving Bessel functions:

$$\int_0^\infty J_k(as)\cos(s|x|) e^{-s|y|}\,ds = \frac{a^k \cos\left(Ak - \dfrac{|B|}{2}\right)}{R\left[\left(R\cos\dfrac{|B|}{2} + |y|\right)^2 + \left(R\sin\dfrac{|B|}{2} + |x|\right)^2\right]^{k/2}}$$

$$\int_0^\infty J_k(as)\sin(s|x|) e^{-s|y|}\,ds = \frac{-a^k \sin\left(Ak - \dfrac{|B|}{2}\right)}{R\left[\left(R\cos\dfrac{|B|}{2} + |y|\right)^2 + \left(R\sin\dfrac{|B|}{2} + |x|\right)^2\right]^{k/2}}$$

where

$$R = 4\sqrt{(y^2 - x^2 + a^2)^2 + 4x^2y^2}$$

$$B = -\left|\arccos\frac{y^2 - x^2 + a^2}{R^2}\right|$$

$$A = -\operatorname{arc} tg \frac{R\sin\dfrac{|B|}{2} + |x|}{R\cos\dfrac{|B|}{2} + |y|}.$$

APPENDIX B

The matrices in Eq. (35) are given by

$$[F_3(x)] = [W_1(\bar{r}, \bar{\theta})]\sin\phi + [W_3(\bar{r}, \bar{\theta})]\cos\phi,$$

$$[F_4(x)] = [W_2(\bar{r}, \bar{\theta})]\sin\phi + [W_4(\bar{r}, \bar{\theta})]\cos\phi$$

where

$$[W_1(r,\theta)] = \mu_M k_M \sum_{n=0}^{\infty} H_n^{(1)\prime}(k_M r)\{1, 0\}[H_n] \times \int_0^{2\pi} \begin{Bmatrix} F_1(\xi) \\ F_2(\xi) \end{Bmatrix} (e^{-in(\xi-\phi)} + e^{in(\xi-\phi)}) d\xi$$

$$[W_2(r,\theta)] = \mu_M k_M \sum_{n=0}^{\infty} H_n^{(1)\prime}(k_M r)\{1, 0\}[H_n] \times \int_0^{2\pi} \begin{Bmatrix} w^0(\xi) \\ \tau_{rz}^0(\xi) \end{Bmatrix} (e^{-in(\xi-\phi)} + e^{in(\xi-\phi)}) d\xi$$

$$[W_3(r,\theta)] = i\mu_M \sum_{n=0}^{\infty} n H_n^{(1)}(k_M r)\{1, 0\}[H_n] \times \int_0^{2\pi} \begin{Bmatrix} F_1(\xi) \\ F_2(\xi) \end{Bmatrix} (e^{-in(\xi-\phi)} - e^{in(\xi-\phi)}) d\xi$$

$$[W_4(r,\theta)] = i\mu_M \sum_{n=0}^{\infty} n H_n^{(1)}(k_M r)\{1, 0\}[H_n] \times \int_0^{2\pi} \begin{Bmatrix} w^0(\xi) \\ \tau_{rz}^0(\xi) \end{Bmatrix} (e^{-in(\xi-\phi)} - e^{in(\xi-\phi)}) d\xi.$$

J. F. Cardenas-Garcia
Mem. ASME.

Y. L. Tian
Assoc. Mem. ASME.

J. Hashemi
Assoc. Mem. ASME.

Department of Mechanical Engineering,
Texas Tech University,
Lubbock, TX 79409-1021

A. J. Durelli

Department of Civil Engineering,
The Catholic University of America,
Washington, DC 20064

A Least-Squares Approach to the Practical Use of the Hole Method in Photoelasticity

The use of a small circular hole in elastostatic photoelasticity to determine the stress tensor for any two-dimensional general loading situation is well known. The original application required fringe-order information at four points on the boundary, on opposite sides, along the axes of symmetry or principal stress directions. Later, to obtain greater precision, it was adapted so that fringe information inside the field could be used. This led to the also limited use of fringe-order information from four points at 1.4 and two times the radius of the hole, along the principal axes of symmetry. More recent work has even allowed the use of fringe-order information, at a fixed radius, anywhere along the two principal axes of symmetry. The greatest limitation of all of these approaches is that the majority of the fringe-order information that is available, away from the axes of symmetry, is not utilized at all. The current work presents a least-squares approach to the hole method that allows the simultaneous use of information anywhere and at any radial distance from the center of the hole inside the stress field. The objectives of this paper are: to apply the use of the least-squares approach to the hole method in photoelasticity; and, to show the consistent and practical application of this least-squares approach to the hole method. The achievement of this last objective permits the use of the values of specimen birefringence at a large number of points, taken from anywhere in the field around the hole.

Introduction

The photoelastic method permits the full-field visualization of maximum shear stresses (isochromatics) in two-dimensional problems. The maximum shear stress $\tau_{\max}$ at a point is equal to one-half the difference between the two principal stresses, σ_1 and σ_2 in the plane. Though the isochromatics might be well characterized, the "separation of stresses," i.e., the determination of the individual principal stresses is usually needed, but difficult to obtain. The "hole" method, an approach suggested by Tesar (1932), is useful to determine the two-dimensional stress tensor in photoelasticity. Tesar suggested that an artificially created free boundary, a hole in the field, could solve the problem of the separation of stresses. Since on free boundaries the stress perpendicular to the boundary is zero, and it is one of the principals, the value of $\tau_{\max}$ obtained from the isochromatic at that point gives directly the value of the other principal stress. The direction of the principal stresses is given by the direction of the two axes of symmetry of the fringe pattern around the hole. The values of the far-field principal stresses are given by

$$\sigma_1 = \tfrac{1}{8}(\sigma_A + 3\sigma_B)$$

$$\sigma_2 = \tfrac{1}{8}(3\sigma_A + \sigma_B) \qquad (1)$$

where σ_A and σ_B are the normal stresses tangential to the edge of the hole at the intersection of the edge with the axis of symmetry of the fringe pattern (see Fig. 1).

Contributed by the Applied Mechanics Division of THE AMERICAN SOCIETY OF MECHANICAL ENGINEERS for publication in the ASME JOURNAL OF APPLIED MECHANICS.

Discussion on this paper should be addressed to the Technical Editor, Professor Lewis T. Wheeler, Department of Mechanical Engineering, University of Houston, Houston, TX 77204-4792, and will be accepted until four months after final publication of the paper itself in the ASME JOURNAL OF APPLIED MECHANICS.

Manuscript received by the ASME Applied Mechanics Division, Feb. 14, 1996; final revision, Aug. 13, 1996. Associate Technical Editor: I. M. Daniel.

In almost all cases the precision of the measurements using the hole method has been unfavorably influenced by the fact that readings of birefringence at the edge of small holes are less precise than similar readings in the field because of thickness effects, shadows and machining effects on the edge. Also, the visibility of fringes is usually poorer at the edge of the hole as a consequence of the high gradient of stresses. For applications related to photoelastic coatings, the precision of measurement at the edge may be lower as a consequence of (1) the mismatch of the mechanical properties of the coating and of the material under it, and (2) the size of the hole that must be small with respect to the gradient of the stresses in the field, and big with respect to the thickness of the coating. These experimental factors introduce errors related to the differences in stresses, for the cases of plane stress and plane strain.

Durelli and Murray (1941) pursued the same objective by drilling a hole in plastic models and using a new set of equations obtained for points that instead of being located at the boundary of the hole are located at a distance from the center of the hole equal to twice the radius of the hole, i.e., $r = 2a$ (see Fig. 1). The equations used to obtain the far-field principal stresses are

$$\sigma_1 = \tfrac{1}{11}(7\sigma_C + 15\sigma_E)$$

$$\sigma_2 = \tfrac{1}{11}(15\sigma_C + 7\sigma_E) \qquad (2)$$

where σ_C and σ_E are the fringe order values at points C and E, respectively. σ_C and σ_E are actually the difference between the local principal stresses at points C and E, i.e., if p and q are labeled as the local principal stresses we can write

$$(p - q)|_{\phi=0} = 2\tau_{\max}|_{\phi=0} = \frac{n_C f_\sigma}{h} = \sigma_C \qquad (3)$$

$$(p - q)|_{\phi=(\pi/2)} = 2\tau_{\max}|_{\phi=(\pi/2)} = \frac{n_E f_\sigma}{h} = \sigma_E \qquad (4)$$

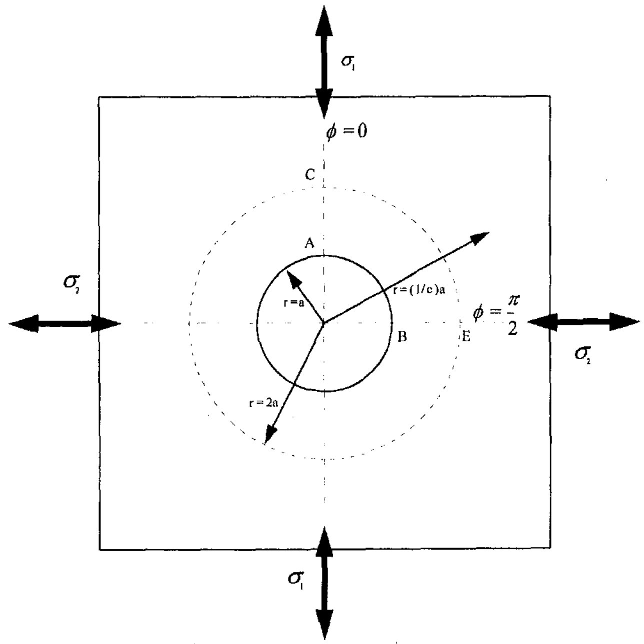

Fig. 1 Schematic diagram of a bi-axially loaded infinite plate with a hole

and these equations are valid only at $r = 2a$. In the context of this paper, for simplicity, the values for the various σ's are defined to be equivalent to the fringe orders. The suggestion was also made for using points located at a distance 1.4 times the radius of the hole, i.e., $r = 1.4a$ (Durelli and Rajaiah, 1980).

Another recently proposed approach (Cárdenas-García et al., 1995) uses the geometry for a bi-axially loaded infinite plate with a central hole of radius a shown in Fig. 1. The proposed equations are

$$\sigma_1 = k_1\sigma|_{\phi=0} + k_2\sigma|_{\phi=(\pi/2)}$$
$$\sigma_2 = k_2\sigma|_{\phi=0} + k_1\sigma|_{\phi=(\pi/2)} \tag{5}$$

in which

$$k_1 = \frac{a_2}{a_3}, \quad \text{and} \quad k_2 = \frac{a_1}{a_3}, \tag{6}$$

where

$$a_1 = 3c^4 - c^2 + 1, \quad a_2 = 3c^4 - 3c^2 + 1,$$
$$a_3 = a_1^2 - a_2^2, \tag{7}$$

and $c = a/r$, for any value of r. For most practical applications the range of r is $a \le r \le 2a$.

Note that the application of Eqs. (5)–(7) permits the use of any distance r corresponding to the precisely located axis of a fringe within the region of practical interest $a \le r \le 2a$. The constants k_1 and k_2 may be plotted as functions of $1/c = r/a$, and may be used instead of Eqs. (6) and (7). It is also easily shown that at values of $r = a$ and $r = 2a$ Eqs. (5)–(7) reduce to Eqs. (1) and (2), respectively. These new equations have been presented and evaluated with reference to an experimental result and found to be in good agreement (Cárdenas-García et al., 1995). The validity of all of the above equations for plates of finite width is something that should also be considered. Durelli and Murray (1941), based on work by Nadai, Baud, and Wahl (1930), state that: ". . . the results of photoelastic tests agree with the theory to within 5 per cent when the ratio $B/2a$, width of plate to diameter of hole, is greater than 6.25." So we can state with some degree of confidence that if the distance from the edge of the hole to the nearest boundary is of the order of five to six times the radius of the hole we are dealing, for all practical purposes, with a hole in an infinite plate.

The greatest limitation of all of these approaches is that much of the available fringe-order information, i.e., that away from the axes of symmetry, is not utilized at all. Thus, the objective of this paper is to present a least-squares approach to the hole method, that allows the simultaneous use of information anywhere and at any radial distance from the center of the hole.

The Nonlinear Least-Squares Approach Applied to the Hole Method

The least-squares method is used in regression analysis to obtain regression coefficients. Sanford and Dally (1979) and Sanford (1980) have pioneered the application of a least-squares approach, in conjunction with photoelastic field data, to obtain material and other parameters. An excellent summary of the use of linear and nonlinear least-squares as it applies in experimental solid mechanics is presented in Dally and Riley (1991). The basic assumption that underlies this approach is that there are always differences between experimental results and theoretical values. This general relationship between experimental results and theoretical values may be expressed for the hole method as

$$F_i = f(\sigma_1, \sigma_2) + e_i, \tag{8}$$

where F_i represents the experimental data at some point (r_i, ϕ_i) in the specimen; $f(\sigma_1, \sigma_2)$ represents the nonlinear theoretical equation evaluated at (r_i, ϕ_i), with undetermined coefficients σ_1 and σ_2; and e_i is the random error. The objective in applying least-squares is to fit the experimentally obtained data to the theoretical solution, and doing it so as to minimize the errors. The fact that the undetermined coefficients (σ_1, σ_2) in the governing equations involve expressions made up of nonlinear terms requires that a nonlinear least-squares approach be adopted in the solution of this problem. The present work faithfully follows previous pioneering nonlinear least-squares approaches but applies the technique to the hole method in photoelasticity.

Let us then consider the more specific relationships of applying nonlinear least-squares to the hole method in photoelasticity. Kirsch (1898) developed equations for the case of a circular hole in a uni-axially loaded infinite plate. These equations defined the displacement and stress fields around the circular hole as a function of location (r, ϕ) and uni-axial far-field stress, σ_1. The Kirsch results were later modified by Durelli and Murray (1941) to obtain displacement and stress field equations for a circular hole in a bi-axially loaded infinite plate. The difference between local principal stresses, p and q, is coupled to the stress-optic law (see, for example, Durelli and Riley, 1965) by the expression

$$(p - q) = 2\tau_{\max} = \frac{nf_\sigma}{h} \tag{9}$$

where $\tau_{\max}$ is the maximum shear stress, f_σ is the fringe value, and h is the plate thickness. Substituting for p and q, taken

Table 1 Idealized calculation of far-field principal stresses from exact fringe data around a hole in a bi-axially loaded plate

Exact Data	Largest Principal Stress	Smallest Principal Stress
Assumed Values	-2.00	1.00
Calculated Values	-2.0000	1.0003

from Durelli and Murray (1941), the expression in Eq. (9) becomes

$$(p-q) = 2\tau_{\max} = \frac{nf_\sigma}{h}$$
$$= \sigma_2\Bigg[\left(\frac{\sigma_1}{\sigma_2}-1\right)^2 A\sin^2 2\phi + \left(1-\frac{\sigma_1}{\sigma_2}\right)^2 B\cos^2 2\phi$$
$$+ C\left(1+\frac{\sigma_1}{\sigma_2}\right)^2 + \left[1-\left(\frac{\sigma_1}{\sigma_2}\right)^2\right]D\cos 2\phi\Bigg]^{1/2} \quad (10)$$

where σ_1 and σ_2 are the far-field principal stresses and the dimensionless coefficients A, B, C, and D are defined in terms of the nondimensionalized radius c,

$$A = 9c^8 - 12c^6 - 2c^4 + 4c^2 + 1 \quad (11a)$$

$$B = 9c^8 - 12c^6 + 10c^4 - 4c^2 + 1 \quad (11b)$$

$$C = c^4 \quad (11c)$$

$$D = c^2(2 + 6c^4 - 4c^2) \quad (11d)$$

where $c = a/r$, where a is the radius of the circle and r is the distance to the point of interest.

In this problem there are two unknowns, σ_1 and σ_2 which are related to the experimentally obtained fringe orders n_i at positions (r_i, ϕ_i). The governing equation for the hole method problem then becomes

$$F_i = (p-q)_i^2 = (2\tau_{\max})^2 = \left(\frac{nf_\sigma}{h}\right)^2 = f(\sigma_1, \sigma_2) + e_i \quad (12)$$

or

$$(2\tau_{\max})^2 = \left(\frac{nf_\sigma}{h}\right)^2$$
$$= \sigma_2^2\Bigg[\left(\frac{\sigma_1}{\sigma_2}-1\right)^2 A\sin^2 2\phi + \left(1-\frac{\sigma_1}{\sigma_2}\right)^2 B\cos^2 2\phi$$
$$+ C\left(1+\frac{\sigma_1}{\sigma_2}\right)^2 + \left[1-\left(\frac{\sigma_1}{\sigma_2}\right)^2\right]D\cos 2\phi\Bigg]. \quad (13)$$

To solve this equation in an overdeterministic sense it is rewritten in the form of a function

$$f_k(\sigma_1, \sigma_2)$$
$$= \sigma_2^2\Bigg[\left(\frac{\sigma_1}{\sigma_2}-1\right)^2 A_k\sin^2 2\phi_k + \left(1-\frac{\sigma_1}{\sigma_2}\right)^2 B_k\cos^2 2\phi_k$$
$$+ C_k\left(1+\frac{\sigma_1}{\sigma_2}\right)^2 + \left[1-\left(\frac{\sigma_1}{\sigma_2}\right)^2\right]D_k\cos 2\phi_k\Bigg]$$
$$-\left(\frac{n_k f_\sigma}{h}\right)^2 = 0 \quad (14)$$

where $k = 1, 2, 3, \ldots, m$ and (r_k, ϕ_k) are coordinates defining a point on an isochromatic fringe of order n_k, which influence the values of (A_k, B_k, C_k, D_k). A Taylor series expansion of Equation (14) yields

$$(f_k)_{i+1} = (f_k)_i + \left(\frac{\partial f_k}{\partial\sigma_1}\right)_i \Delta\sigma_1 + \left(\frac{\partial f_k}{\partial\sigma_2}\right)_i \Delta\sigma_2 \quad (15)$$

where i refers to the ith iteration step and $\Delta\sigma_1$ and $\Delta\sigma_2$ are corrections to the previous estimates of σ_1 and σ_2, i.e.,

$$\Delta\sigma_1 = (\sigma_1)_{i+1} - (\sigma_1)_i \quad \Delta\sigma_2 = (\sigma_2)_{i+1} - (\sigma_2)_i. \quad (16)$$

Therefore, the corrected estimates of σ_1 and σ_2 are

$$(\sigma_1)_{i+1} = (\sigma_1)_i + \Delta\sigma_1 \quad (\sigma_2)_{i+1} = (\sigma_2)_i + \Delta\sigma_2. \quad (17)$$

If we are very close to the least-squares solution it is clear from Eq. (15) that $(f_k)_{i+1} = 0$, and we can write

$$-(f_k)_i = \left(\frac{\partial f_k}{\partial\sigma_1}\right)_i \Delta\sigma_1 + \left(\frac{\partial f_k}{\partial\sigma_2}\right)_i \Delta\sigma_2 \quad (18)$$

which may be represented in matrix form as

$$\{f\} = [a]\{\Delta\sigma\} \quad (19)$$

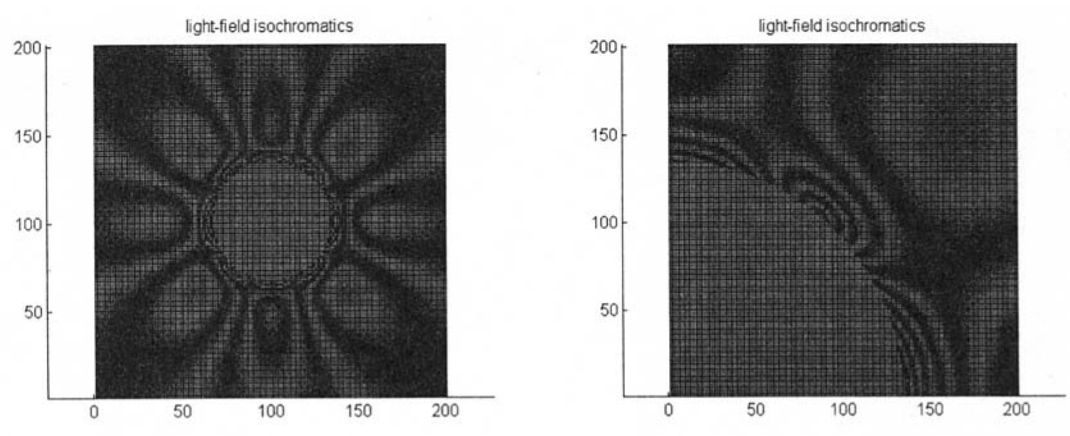

(a) (b)

Fig. 2 Theoretical light-field photoelastic fringes associated with the bi-axial loading of a plate with a hole; (*a*) full circle image, (*b*) quarter circle image

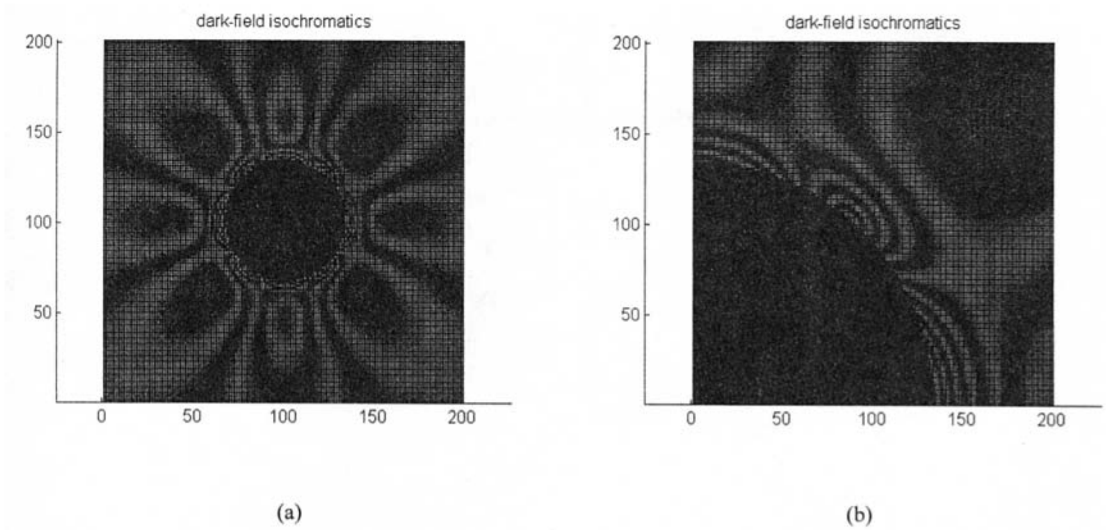

Fig. 3 Theoretical dark-field photoelastic fringes associated with the bi-axial loading of a plate with a hole; (*a*) full-circle image (*b*) quarter-circle image

where

$$\{f\} = \begin{Bmatrix} f_1 \\ f_2 \\ \vdots \\ f_m \end{Bmatrix} \quad [a] = \begin{bmatrix} \dfrac{\partial f_1}{\partial \sigma_1} & \dfrac{\partial f_1}{\partial \sigma_2} \\ \dfrac{\partial f_2}{\partial \sigma_1} & \dfrac{\partial f_2}{\partial \sigma_2} \\ \vdots & \vdots \\ \dfrac{\partial f_m}{\partial \sigma_1} & \dfrac{\partial f_m}{\partial \sigma_2} \end{bmatrix}$$

$$\{\Delta\sigma\} = \begin{Bmatrix} \Delta\sigma_1 \\ \Delta\sigma_2 \end{Bmatrix} \tag{20}$$

and, for $i = 1, 2, 3, \ldots, m$

$$f_i = \left(\frac{n_i f_\sigma}{h}\right)^2 - [A_i(\sigma_1 - \sigma_2)^2 \sin^2 2\phi_i + B_i(\sigma_2 - \sigma_1)^2 \cos^2 2\phi_i + c_k^4(\sigma_1 + \sigma_2)^2 + D_i(\sigma_2^2 - \sigma_1^2)\cos 2\phi_i] \tag{21}$$

$$\frac{\partial f_i}{\partial \sigma_1} = [2A_i(\sigma_1 - \sigma_2)\sin^2 2\phi_i + 2B_i(\sigma_1 - \sigma_2)\cos^2 2\phi_i + 2c_k^4(\sigma_1 + \sigma_2) - 2D_i\sigma_1 \cos 2\phi_i] \tag{22}$$

$$\frac{\partial f_i}{\partial \sigma_2} = [2A_i(\sigma_2 - \sigma_1)\sin^2 2\phi_i + 2B_i(\sigma_2 - \sigma_1)\cos^2 2\phi_i + 2c_k^4(\sigma_1 + \sigma_2) + 2D_i\sigma_2 \cos 2\phi_i]. \tag{23}$$

The correction factors $\{\Delta\sigma\}$ may be obtained by the following matrix manipulations, starting with Eq. (19),

$$[a]^T\{f\} = [a]^T[a]\{\Delta\sigma\} = [c]\{\Delta\sigma\} \tag{24}$$

where we have let

$$[c] = [a]^T[a]. \tag{25}$$

Multiplying Eq. (17) through by the inverse of $[c]$ we finally obtain

$$\{\Delta\sigma\} = [c]^{-1}[a]^T\{f\}. \tag{26}$$

This solution gives the correction factor required to modify the previously used values of σ_1 and σ_2 so as to get new estimates to iterate to a better fit of the function $\{f\}$ to m data points. This iteration process is repeated until "acceptable" convergence is obtained, e.g., solution convergence can be made dependent on parameters $|\epsilon_{\sigma_1}|$ and $|\epsilon_{\sigma_2}|$ such that,

$$|\epsilon_{\sigma_1}| = \left|\frac{(\sigma_1)_{i+1} - (\sigma_1)_i}{(\sigma_1)_{i+1}}\right| \ll 1;$$

$$|\epsilon_{\sigma_2}| = \left|\frac{(\sigma_2)_{i+1} - (\sigma_2)_i}{(\sigma_2)_{i+1}}\right| \ll 1 \tag{27}$$

fall below an acceptable stopping criterion.

Verification of the Least-Squares Hole Method Approach

To verify the least-squares hole method a three step approach is followed. First, the least-squares approach is verified for the hole method using exact numerical data taken from the calculated values of the fringe orders for a set of assumed far-field

Table 2 Results of the calculation of far-field principal stresses from light-field isochromatic data around a hole in a bi-axially loaded plate

Obtained From Light-Field Isochromatics			
Exact Data	Number of Data Points	Largest Principal Stress	Smallest Principal Stress
Assumed Values		-2.60	1.30
Calc. Values - Set A	60	-2.5713 (1.10%)	1.3139 (1.07%)
Calc. Values - Set B	50	-2.5988 (0.05%)	1.3046 (0.35%)
Calc. Values - Set C	20	-2.5971 (0.11%)	1.3164 (1.26%)

Table 3 Results of the calculation of far-field principal stresses from dark-field isochromatic data around a hole in a bi-axially loaded plate

Obtained From Dark-Field Isochromatics			
Exact Data	Number f Data Points	Largest Principal Stress	Smallest Principal Stress
Assumed Values		-2.60	1.30
Calc. Values - Set A	60	-2.6127 (0.49%)	1.3002 (0.02%)
Calc. Values - Set B	60	-2.6060 (0.23%)	1.2942 (0.45%)
Calc. Values - Set C	30	-2.5853 (0.57%)	1.2812 (1.45%)

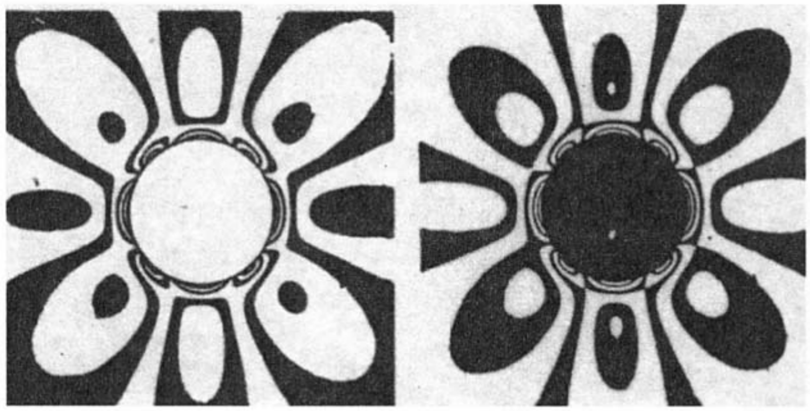

(a) (b)

Fig. 4 The photoelastic fringes associated with the bi-axial loading of a plate with a hole adapted from (Durelli and Murray, 1941); (*a*) light-field image (*b*) dark-field image

principal stress values. These calculated results are shown in Table 1 for a set of 20 points: ten each along the horizontal and vertical axes of symmetry, with (r/a) values varying from 1.0 to 1.45 in increments of 0.05. The data show that the predicted values are essentially the same as the assumed values of far-field stresses.

Next, full-field isochromatic data around a hole are generated from the theory and plotted as digital images for far-field stress values of $\sigma_1 = -2.60$ and $\sigma_2 = 1.30$, with a principal stress ratio of $k = -2$. The resulting digital images showing light and dark-field isochromatics are shown, respectively, in Figs. 2 and 3. The quarter-circle representations have been added to show the isochromatic fringe detail which is not identifiable in the full-circle representations. These digital images were then analyzed using SigmaScan/Image™ software (1993) to facilitate the data gathering process. The data sets generated were then organized and put in an appropriate format for use by a computer program, written in FORTRAN, to finalize the nonlinear least-squares data analysis. The idea is to attempt to duplicate the exact procedures that would be followed were actual experimental images of isochromatic patterns around a circular hole in an experimental specimen available, and to gauge the exactness of the data gathering process. The results are shown in Tables 2 and 3, for light-field and dark-field isochromatics, respectively, with the resulting discrepancy from the actual results shown in parenthesis. In the case of light-field isochromatics, 100 points are chosen for a basic data set, from which three data subsets (labeled A, B, and C) are used as input data. Subsets A and B contain fringe data from regions 0 to 4 deg, 29 to 42 deg, and 84 to 90 deg from the vertical axis of symmetry, while subset C contains fringe data from a region 29 to 42 deg from the vertical axis of symmetry. In the case of dark-field isochromatics 120 points are chosen for a second basic data set, from which three data subsets (labeled A, B, and C) are also used as input data. Subsets A and B contain fringe data from regions 0 to 6 deg, 37 to 46 deg, and 85 to 90 deg from the vertical axis of symmetry, while subset C contains fringe data from a region 37 to 46 deg from the vertical axis of symmetry. No attempt is made to correlate the exactness of results from the location of the values shown in Tables 2 and 3, nor from the number of data points used. The objective is to simply show that even for exact, calculated isochromatic data it is very possible to generate errors from the data gathering process, as would also be the case if the data gathering is from actual experimental results. Notice that the largest calculated errors are of the order of one percent.

Lastly, light and dark-field photoelasticity results taken from Durelli and Murray (1941) are used to perform the same analysis. These are shown in Fig. 4. They were obtained by scanning photocopies of these images at a resolution level of 600 dots per inch. The experimentally known far-field stress values for these photographs are: $\sigma_1 = -2$ and $\sigma_2 = 1$, which also have a stress ratio $k = -2$. The results of applying Eqs. (5)–(7) to calculate the far-field stresses yield calculated average values for σ_1 and σ_2 of -2.13 (6.5 percent error) and 1.19 (19 percent error), respectively (Cárdenas-García et al., 1995). For the present least-squares analysis, these photographs yield the light

Table 4 Typical values for light and dark-field photoelastic fringe data around a hole in a bi-axially loaded plate

LIGHT-FIELD DATA		
Normalized Radius	Angle	Fringe Order
1.08	300.50	3.50
1.19	305.62	3.50
1.21	311.61	3.50
1.24	318.56	3.50
1.28	325.59	3.50
1.56	334.15	3.50
1.66	290.18	3.50
1.48	289.41	3.50
1.30	280.56	3.50
1.30	261.96	3.50
1.59	250.82	3.50
1.06	238.37	3.50
1.18	233.48	3.50
1.22	225.72	3.50
1.29	215.84	3.50
1.41	208.54	3.50
1.63	206.11	3.50
1.67	24.67	3.50
1.38	28.18	3.50
1.24	40.97	3.50
1.21	50.86	3.50
1.23	130.24	3.50
1.26	139.65	3.50
1.37	149.77	3.50
1.68	154.65	3.50
1.54	12.79	2.50
1.32	12.36	2.50
1.25	6.01	2.50
1.24	353.62	2.50
1.50	346.63	2.50
1.57	166.67	2.50
1.33	167.71	2.50
1.25	174.69	2.50
1.26	187.29	2.50
1.58	193.53	2.50
1.08	332.40	2.50
1.12	326.62	2.50
1.12	319.20	2.50
1.10	312.60	2.50
1.12	222.90	2.50
1.14	214.90	2.50
1.06	207.80	2.50
1.09	48.49	2.50
1.11	33.59	2.50
1.14	147.22	2.50
1.12	134.74	2.50

DARK-FIELD DATA		
Normalized Radius	Angle	Fringe Order
1.91	340.95	3.00
1.57	340.57	3.00
1.15	317.01	3.00
1.10	307.32	3.00
1.18	339.69	3.00
1.19	31.49	3.00
1.17	41.28	3.00
1.47	158.92	3.00
1.19	145.06	3.00
1.11	190.37	3.00
1.06	232.98	3.00
1.05	12.23	4.00
1.07	5.37	4.00
1.07	353.07	4.00
1.02	188.47	4.00
1.03	172.04	4.00
1.34	312.40	4.00
1.76	326.96	4.00
1.31	223.89	4.00
1.75	213.50	4.00
1.18	255.96	4.00
1.21	102.31	4.00
1.08	62.42	4.00
1.57	60.29	4.00
1.03	251.82	5.00
1.06	258.31	5.00
1.08	266.21	5.00
1.07	283.20	5.00
1.03	290.32	5.00
1.07	71.20	5.00
1.09	75.60	5.00
1.11	83.70	5.00
1.11	95.93	5.00
1.07	105.05	5.00
1.01	281.07	6.00
1.02	276.87	6.00
1.02	272.80	6.00
1.02	267.60	6.00
1.02	264.77	6.00
1.05	84.13	6.00
1.05	93.12	6.00

Table 5 Results of calculation of σ_1 and σ_2 from photoelastic fringe data around a hole in a bi-axially loaded plate for various data sets

Field	Radius	Largest Principal Stress	% Difference from Ideal	Smallest Principal Stress	% Difference from Ideal
Light	138.0	-2.18	9	1.15	15
Dark	139.75	-1.95	2.5	1.07	7
Combination	138.875	-1.99	0.5	1.15	15
Combination	138.0 & 139.75	-1.95	2.5	1.14	14

and dark-field photoelastic data shown in Table 4. These data sets are also obtained using SigmaScan/Image™ software. After organizing these data sets in an appropriate format they were processed using the same computer program, mentioned above, to finalize the nonlinear least-squares data analysis. All of these data points are taken away from the principal axes of symmetry. A summary of the results for four separate data sets is shown in Table 5: (1) light-field data using a radius of 138 pixels or picture elements; (2) dark-field data using a radius of 139.75 pixels; (3) combination of light and dark-field data using an average radius of 138.875 pixels; and (4) combination of light and dark-field data using normalized radius values according to whether its light or dark-field data. The results show that in general the calculated values for σ_1 and σ_2 are closer to the experimental values than those calculated using Eqs. (5)–(7).

Some sources of error for these calculations may be ascribed to the use of an experimental result from a secondary source and also to the method of gathering data. The experimental result was obtained from a photocopy of the article cited above (Durelli and Murray, 1941). The photocopy was then digitized with a scanner at an image density level of 600 dots per inch, and then analyzed using SigmaScan/Image™ with all the difficulties inherent to identifying the precise center and edges of the hole, and the center of the isochromatic fringes. A further source of error which is difficult to characterize is that related to the original experiment, i.e., how close is the actual experiment to the stress values given to characterize it? The only assertion that can be made is that nominally the far-field stresses are $\sigma_1 = -2$ and $\sigma_2 = 1$. The exactness of these values impacts the comparison that is made once a calculation utilizing the original data is done.

Discussion, Summary of Results, and Conclusions

A short review of the use of a small circular hole in plane elastostatic photoelasticity to determine the stress tensor for any general loading situation has been presented. Originally the determination of the stress at four points at the free boundary of the hole ($r = a$) allowed the far-field stress tensor to be obtained. One can increase precision if the measurements are taken at points located at a distance from the center of the hole equal to 1.4 and even twice its radius ($r = 2a$). Additionally, measurements may also be made at any radial distance along the principal axes of symmetry, enhancing the possibility of accurately obtaining and comparing stress tensor values from several measurements of the same photoelastic image. The employment of a least-squares approach to the hole method presented here also shows that acceptable results may be obtained, using data away from the principal axes of symmetry.

It should also be noted that the application of the hole method described above is for situations where a pre-existing hole is used for the determination of the far-field stresses. This means that the holes are drilled on the specimen of interest before any loads are applied to the specimen. Loading the specimen then reveals the direction and magnitude of the principal stresses, e.g., if we apply Tesar's approach, at the points on the specimen where the pre-existing holes are present. There are also situations, such as those encountered in the measurement of residual stresses, where the hole is drilled after the external loads have been applied or after residual stresses have been impressed on the specimen of interest. This situation is one which can be found in many practical situations, and which could easily be addressed by an extension of the method presented in this paper using a photoelastic approach. This would require changing the governing equation to solve the residual stresses problem. An excellent summary of the practical application of this type of hole-drilling method using strain gages is presented in Technical Note 503-1 (1985) put out by Measurements Group, Inc. This technical note details the background to this residual measurement approach, which also relies on Kirsch's solution (Kirsch, 1898). Thus, the present approach can be applied, with some slight modifications, to the measurement of residual stresses as well. This will be the emphasis of a future paper that is in preparation by the authors.

Thus, several objectives have been realized in this paper: (1) a brief review of previous developments in the use of the hole method, showing that previous approaches are limited in their use of available photoelastic data; (2) the development of the use of the least-squares approach to the hole method in photoelasticity, showing another application where the least-squares approach may also be used; and, (3) showing the consistent and practical application of this least-squares approach, using the values of the birefringence at any number, large or small, of points taken from anywhere in the field, to the hole method. It is anticipated that similar "least-squares hole method" approaches may be used to assess the two-dimensional stress tensor using other optical techniques such as moiré and holographic interferometry.

References

Cárdenas-Garcia, J. F., Hashemi, J., and Durelli, A. J., 1995, "The Practical Use of the Hole Method in Photoelasticity," *Mechanics Research Communications*, Vol. 22, No. 3, pp. 239–244.

Dally, J. W., and Riley, W. F., 1991, *Experimental Stress Analysis*, 3rd ed., McGraw-Hill, New York, pp. 616–619.

Durelli, A. J., and Riley, W. F., 1965, *Introduction to Photomechanics*, Prentice-Hall, Englewood Cliffs, NJ, pp. 52–81.

Durelli, A. J., and Murray, W. M., 1941, "Stress Distribution Around a Circular Discontinuity in Any Two-Dimensional System of Combined Stress," *Proceedings of the 14th Semi-Annual Eastern Photoelasticity Conference*, Yale University, pp. 21–36.

Durelli, A. J., and Rajaiah, K., 1980, "Determination of Strains in Photoelastic Coatings," *Experimental Mechanics*, Vol. 20, No. 2, pp. 57–64.

Kirsch, G., 1898, "Die Theorie d. Elastizitat u. d. Bedurinisse d. Festigkeitslehre," *V. D. J.*, m. 42, No. 29, S.799.

Measurements Group Technical Note, 1985, "Measurement of Residual Stresses by the Hole-Drilling Strain-Gage Method," TN-503-1, Measurements Group, Raleigh, NC.

Nadai, A., Baud, R., and Wahl, A., 1930, *Mechanical Engineering*, Mar., p. 187; as cited in Durelli and Murray, 1941.

Sanford, R. J., 1980, "Application of the Least Squares Method to Photoelastic Analysis," *Experimental Mechanics*, Vol. 20, pp. 192–197.

Sanford, R. J., and Dally, J. W., 1979, "A General Method for Determining Mixed-Mode Stress Intensity Factors from Isochromatic Fringe Patterns," *Engineering Fracture Mechanics*, Vol. 11, pp. 621–633.

SigmaScan/Image™, 1993, *Image Analysis Software*, Version 1.20.09, Jandel Scientific Corporation, San Rafael, CA.

Tesar, V., 1932, "La Photoelasticimetrie et ses Applications dans les Constructions Aeronautiques," *La Science Aerienne*, Paris, p. 372.

Determination of Noncontributing Forces and Noncontributing Impulses in Three-Phase Motions

S. Djerassi
Rafael,
P. O. Box 2250,
Haifa 31021, Israel

Numerous dynamical systems undergo, while in motion, imposition and/or removal of constraints. Three phases of motion are involved: a phase during which the motion is defined as unconstrained, a phase during which the motion is defined as constrained, and an intermediate, transition phase, when constraints are imposed or removed. Noncontributing forces (sometimes called nonworking, reaction forces), and noncontributing impulses, namely, impulses associated with noncontributing forces in the transition phase, play a central role in the mechanics of systems undergoing such motions, and are the subject matter of the present paper. Specifically, a six-step procedure is introduced for the determination of noncontributing forces and of noncontributing impulses throughout three phase motions.

1 Introduction

Robotic arms performing pick and place tasks, satellites undergoing docking, drones deploying lift surfaces, and helicopters releasing cargo provide examples of mechanical systems undergoing, while in motion, a change in their number of degrees-of-freedom. This type of motion can be described with greater precision with the aid of the system shown in Fig. 1. Here, a cone A undergoes a motion in N, a Newtonian reference frame, defined as unconstrained. That is, no particles of A are in contact with particles of N. Suppose that at time $t = T$ a particle R of A hits a particle $\hat{R}$ lying on line L fixed in N; and that when $t > T$, A undergoes a constrained motion in which R slides along L. Alternatively, suppose that A moves such that R slides along L, that at $t = T$ R is released, and that when $t > T$ the motion of A in N is unconstrained.

One may conclude that the motions mentioned consist of a first phase, during which the motion is defined as unconstrained, a second, transition phase, when constraints are imposed on the motion, and a third phase, throughout which the motion is defined as constrained; or, alternatively, of a first phase, during which the motion is defined as constrained, a second, transition phase, when constraints are removed, and a third phase, throughout which the motion is defined as unconstrained.

The present paper deals with the determination of *noncontributing forces* (sometimes called nonworking, reaction forces) and of *noncontributing impulses* (namely, impulses associated with such forces) throughout three-phase motions. Such forces and impulses can be pointed out in connection with the motion of the cone in Fig. 1. For that purpose, let $\bar{R}$ be a particle of L, momentarily in contact with R in the constrained phase. Moreover, let P be a plane fixed in A, passing through A^*, the mass center of A, dividing A into two rigid bodies B and C, the former containing R, and both having mass centers which lie on the line connecting R with A^*. Lastly, let $\bar{B}$ and $\hat{C}$ be particles of B and of C, respectively, coinciding with A^*. Examples of noncontributing forces are those exerted by $\bar{R}$ on R and by $\bar{B}$ on $\hat{C}$, and a couple (i.e., a set of forces whose resultant is zero) exerted by B on C during the first and third phases; and examples of noncontributing impulses are those associated with the indicated forces during the transition phase.

Traditionally, the determination of these forces and impulses involves the application of three distinct procedures: one for the determination of noncontributing forces in the constrained phase, one for the determination of noncontributing forces in the unconstrained phase, and one for the determination of noncontributing impulses in the transition phase. For example, Huston (1990, Chapter 10) discusses noncontributing forces in connection with constrained systems. Kane (1985, Section 4.9) introduces the idea of auxiliary generalized speed used to identify noncontributing forces. Finally, Levinson and Kane (1983), Fitz-Coy and Cochran (1986), and Rhody et al. (1993) solve imposition of constraints problems, introducing sets of equations involving *both* changes in the generalized speeds *and* impulses as unknowns. Noting that these works represent the state of the art in the subject matter, one may conclude that no work has been dedicated to date to the exploration of interrelations between noncontributing forces and impulses in three-phase motions, a task undertaken in the present work.

It will be shown that expressions for noncontributing forces in the constrained phase are also valid in the unconstrained phase. It will further be shown that the determination of nonworking impulses can be decoupled from the determination of changes in the generalized speeds. Finally, it will be shown that it is sufficient to generate expressions for noncontributing forces in the constrained phase; that these expressions can be used to determine the associated noncontributing forces and noncontributing impulses in the unconstrained phase and in the transition phase, respectively; and a six-step procedure leading to the requisite expressions will be established. This procedure incorporates the indicated observations, and constitute one, unified approach for the determination of noncontributing forces and impulses in three-phase motions.

This paper is organized as follows. First, the main results of the theory of imposition and removal of constraints (Djerassi, 1994), which plays a central role in describing the type of motion in question, namely, a three-phase motion, are reported in Section 2. Next, a six-step procedure for the determination

Contributed by the Applied Mechanics Division of The American Society of Mechanical Engineers for publication in the ASME Journal of Applied Mechanics.

Discussion on the paper should be addressed to the Technical Editor, Professor Lewis T. Wheeler, Department of Mechanical Engineering, University of Houston, Houston, TX 77204-4792, and will be accepted until four months after final publication of the paper itself in the ASME Journal of Applied Mechanics.

Manuscript received by the ASME Applied Mechanics Division, Mar. 26, 1996; final revision, Oct. 11, 1996. Associate Technical Editor: N. C. Perkins.

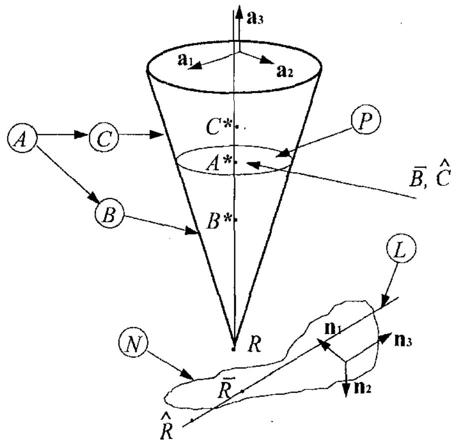

Fig. 1 A cone undergoing three-phase motion

of noncontributing forces for simple, nonholonomic systems is reported, proved and illustrated in Sections 3, 4, and 5, respectively. The procedure in then extended to a three-phase motion in Section 6, and its use is illustrated in Section 7. A few comments in Section 8 conclude the present work.

2 The Theory of Imposition-Removal of Constraints: Main Results

Let S be a simple, nonholonomic system of υ particles P_i ($i = 1, \ldots, \upsilon$) of mass m_i possessing $\bar{n}$ generalized coordinates $q_1, \ldots, q_{\bar{n}}$ and n (where $n \le \bar{n}$) generalized speeds $u_1, \ldots, u_n$ in N, a Newtonian reference frame. Let S undergo three phases of motion as follows. Phase (a) occurs in the time interval $0 \le t \le t_1$. The motion of S in N is *defined* as unconstrained, and is governed by n dynamical equations, namely,

$$F_r + F_r^* = 0 \quad (r = 1, \ldots, n) \tag{1}$$

where F_r and F_r^* are the rth generalized active force and the rth generalized inertia force, respectively (Kane, 1985). Phase (b), a transition phase, occurs in the time interval $t_1 \le t \le t_2$ where $t_2 - t_1$ is "infinitely small," e.g., as compared with time constants associated with the motion of S. Then m constraints of the form

$$u_k = \sum_{r=1}^{p} C_{kr} u_r + D_k \quad (k = p + 1, \ldots, n) \tag{2}$$

are imposed on S, where

$$p \triangleq n - m \tag{3}$$

and C_{kr} and D_k are functions of $q_1, \ldots, q_{\bar{n}}$ and time t. In this phase, the configuration of S in N remains unaltered, that is,

$$q_r(t_2) = q_r(t_1) \quad (r = 1, \ldots, \bar{n}), \tag{4}$$

and the number of independent generalized speeds reduces from n to p. The relations between $u_k(t_2)$ ($r = p + 1, \ldots, n$), the values of the dependent generalized speeds at $t = t_2$, and $u_r(t_2)$ ($r = 1, \ldots, p$), the values of the independent generalized speeds at $t = t_2$, is given by

$$u_k(t_2) = \sum_{r=1}^{p} C_{kr} u_r(t_2) + D_k \quad (k = p + 1, \ldots, n). \tag{5}$$

Additionally, if the magnitudes of the active forces contributing to Eqs. (1) are all bounded, and if particles of S exert contact forces on one another, and, possibly, on members of R_B, a set of particles whose motion is not affected by the forces exerted on them by particles of S, then relations between $u_s(t_2)$ ($s = 1, \ldots, n$) and $u_s(t_1)$ ($s = 1, \ldots, n$) are given by

$$\sum_{s=1}^{n} \left(m_{rs} + \sum_{k=p+1}^{n} C_{kr} m_{ks}\right)[u_s(t_2) - u_s(t_1)] = 0 \quad (r = 1, \ldots, p). \tag{6}$$

Here, m_{rs} the element in row r, column s of the mass matrix associated with Eqs. (1), is defined

$$m_{rs} \triangleq -\sum_{i=1}^{\upsilon} m_i \frac{\partial \mathbf{v}^{P_i}}{\partial u_r} \cdot \frac{\partial \mathbf{v}^{P_i}}{\partial u_s} \quad (r, s = 1, \ldots, n) \tag{7}$$

where $\mathbf{v}^{P_i}$ is the velocity of P_i in N. Equations (5) and (6) furnish $m + p$ relations between $u_r(t_2)$ and $u_r(t_1)$ ($r = 1, \ldots, n$) that enable one to evaluate the former, given the latter, with C_{kr}, D_k, and m_{rs} ($k = p + 1, \ldots, n$; $r, s = 1, \ldots, n$) calculated at $t = t_1$. Phase (c) occurs when $t \ge t_2$. Then the motion of S in N is *defined* as constrained, and is governed by p dynamical equations, namely,

$$F_r + F_r^* + \sum_{k=p+1}^{n} C_{kr}(F_k + F_k^*) = 0 \quad (r = 1, \ldots, p). \tag{8}$$

Removal of constraints is said to take place when Phases (a), (b), and (c) occur in reverse order. The constrained phase (now called Phase (a)), the transition, removal phase (Phase (b)), and the unconstrained phase (now called Phase (c)) occur when $0 \le t \le t_1$, $t_1 \le t \le t_2$ and $t \ge t_2$, and are governed by Eqs. (8) and (2), (4)–(6) and (1), respectively, with t_1 replacing t_2 in Eqs. (5). If Eqs. (2) are satisfied both at t_1 and at t_2, then

$$u_r(t_2) = u_r(t_1) \quad (r = 1, \ldots, n). \tag{9}$$

3 Determination of Noncontributing Forces

Consider a simple, nonholonomic system S of υ particles P_i ($i = 1, \ldots, \upsilon$) possessing n generalized speeds, whose motion in N is governed by Eqs. (1). Let M be a number such that $0 < M \le 3\upsilon - n$, and let $P_{n+1}, \ldots, P_{n+M}$ be a set S_M of M particles of S coinciding (momentarily or continually), respectively, with $\bar{P}_{n+1}, \ldots, \bar{P}_{n+M}$, a set $\bar{S}_M$ of M particles each of which belong either to S or to R_B (the indices of $P_{n+1}, \ldots, P_{n+M}$ and $\bar{P}_{n+1}, \ldots, \bar{P}_{n+M}$ are chosen so as to match those of variables introduced shortly). Let $\bar{P}_j$ exert a contact force $\mathbf{R}_j$ on P_j ($j = n + 1, \ldots, n + M$), and let R_j be defined

$$R_j \triangleq \mathbf{R}_j \cdot \hat{\mathbf{a}}_j \quad (j = n + 1, \ldots, n + M), \tag{10}$$

where $\hat{\mathbf{a}}_j$ is a unit vector parallel to the line of action of $\mathbf{R}_j$. Note that, in accordance with the law of action and reaction, P_j exerts on $\bar{P}_j$ a contact force $\bar{\mathbf{R}}_j$ which equals $-\mathbf{R}_j$, namely,

$$\mathbf{R}_j = R_j \hat{\mathbf{a}}_j, \quad \bar{\mathbf{R}}_j = -R_j \hat{\mathbf{a}}_j \quad (j = n + 1, \ldots, n + M); \tag{11}$$

and that $\mathbf{R}_{n+1}, \ldots, \mathbf{R}_{n+M}$ and $\bar{\mathbf{R}}_{n+1}, \ldots, \bar{\mathbf{R}}_{n+M}$, called *noncontributing forces,* contribute nothing to Eqs. (1); that is, $R_{n+1}, \ldots, R_{n+M}$ do not appear in Eqs. (1). With Eqs. (1) in hand, however, $R_{n+1}, \ldots, R_{n+M}$ can be determined with the aid the following six-step procedure.

Step 1. Obtain expressions for $\mathbf{v}^{P_j}$ and $\mathbf{v}^{\bar{P}_j}$, the velocities in N of P_j and $\bar{P}_j$ ($j = n + 1, \ldots, n + M$), particles belonging to S_M and $\bar{S}_M$, respectively.

Step 2. Introduce M new variables $\bar{u}_{n+1}, \ldots, \bar{u}_{n+M}$ called *auxiliary generalized speeds,* and construct M equations called *auxiliary constraint equations,* defining $\bar{u}_{n+1}, \ldots, \bar{u}_{n+M}$ as linear combinations of $u_1, \ldots, u_n$, that is,

$$\bar{u}_k = \sum_{r=1}^{n} \bar{C}_{kr} u_r + \bar{D}_k \quad (k = n + 1, \ldots, n + M), \tag{12}$$

where overbars are used as a reminder to the special nature of $\bar{u}_{n+1}, \ldots, \bar{u}_{n+M}$. Regard these as constraints being removed from the motion of S and $u_1, \ldots, u_n, \bar{u}_{n+1}, \ldots, \bar{u}_{n+M}$ as independent. Accordingly, redefine $\mathbf{v}^{P_j}$ ($j = n + 1, \ldots, n + M$) and $\mathbf{v}^{\bar{P}_j}$ (j

$= n+1, \ldots, n+M$) as functions of $u_1, \ldots, u_n, \bar{u}_{n+1}, \ldots, \bar{u}_{n+M}$ such that (a) when $\bar{u}_{n+1}, \ldots, \bar{u}_{n+M}$ are eliminated with the aid of Eqs. (12) (which means that the constraint in Eqs. (12) are imposed), the expressions for $\mathbf{v}^{P_j}$ ($j = n+1, \ldots, n+M$) and $\mathbf{v}^{\bar{P}_j}$ ($j = n+1, \ldots, n+M$) obtained in Step 1 are restored; and (b) the $M \times M$ matrix having $\hat{a}_{jr}$ ($j, r = n+1, \ldots, n+M$), defined

$$\hat{a}_{jr} \triangleq \left(\frac{\partial \mathbf{v}^{P_j}}{\partial \bar{u}_r} - \frac{\partial \mathbf{v}^{\bar{P}_j}}{\partial \bar{u}_r}\right) \cdot \hat{\mathbf{a}}_j \quad (j, r = n+1, \ldots, n+M), \quad (13)$$

as its element in row $(j-n)$, column $(r-n)$ is of rank M. If $\hat{a}_{jr} = \pm\delta_{jr}$ ($r = n+1, \ldots, n+M$), where δ_{jr} is the Kronecker delta, then $\mathbf{R}_j$ and $\bar{\mathbf{R}}_j$ are said to be forces associated with the jth constraint.

Step 3. Redefine, in terms of $u_1, \ldots, u_n, \bar{u}_{n+1}, \ldots, \bar{u}_{n+M}$, the velocities of those particles of S not included in S_M and $\bar{S}_M$ (so that when the constraint in Eqs. (12) are imposed, the original expressions for the indicated velocities are restored).

Step 4. Assuming that the constraints in Eqs. (12) have been removed, formulate equations governing the motion of the system, including contributions form $\mathbf{R}_{n+1}, \ldots, \mathbf{R}_{n+M}, \bar{\mathbf{R}}_{n+1}, \ldots, \bar{\mathbf{R}}_{n+M}$, so that now

$$\bar{F}_r + \bar{F}_r^* = -\sum_{j=n+1}^{n+M} \hat{a}_{jr} R_j \quad (r = 1, \ldots, n+M) \quad (14)$$

where $\bar{F}_r + \bar{F}_r^*$ ($r = 1, \ldots, n+M$) are sums of the generalized active forces and generalized inertia forces associated with $u_1, \ldots, u_n, \bar{u}_{n+1}, \ldots, \bar{u}_{n+M}$, respectively. (In fact, only the M last of Eqs. (14), namely, those associated with $\bar{u}_{n+1}, \ldots, \bar{u}_{n+M}$, have to be formulated; hence, no extension of the definition of $\hat{a}_{jr}$ is required.)

Step 5. Solve Eqs. (1) for $\dot{u}_r$ ($r = 1, \ldots, n$).

Step 6. Use Eqs. (12) to eliminate $\bar{u}_{n+1}, \ldots, \bar{u}_{n+M}$ and $\dot{\bar{u}}_{n+1}, \ldots, \dot{\bar{u}}_{n+M}$ from the M last of Eqs. (14) and solve these for $R_{n+1}, \ldots, R_{n+M}$.

Next, let $P_{n+1}, \ldots, P_{n+M}$ (comprising S_M) be M rigid bodies of S, each possessing a surface which coincides (momentarily or continually), respectively, with surfaces of $\bar{P}_{n+1}, \ldots, \bar{P}_{n+M}$ (comprising $\bar{S}_M$), M rigid bodies each of which may belong either to S or to R_B (a rigid body belonging to S is one whose particles constitute a subset of $P_1, \ldots, P_\nu$). Let $\bar{P}_j$ exert a couple of torque $\mathbf{R}_j$ on P_j ($j = n+1, \ldots, n+M$) across the coinciding surfaces of $\bar{P}_j$ and P_j, let R_j be defined as in Eqs. (10), and, noting that P_j exerts on $\bar{P}_j$ a couple of torque $\bar{\mathbf{R}}_j$ which equals $-\mathbf{R}_j$, let $\mathbf{R}_j$ and $\bar{\mathbf{R}}_j$ be given by Eqs. (11). Then the six-step procedure for the determination of $R_{n+1}, \ldots, R_{n+M}$ applies if $\mathbf{v}^{P_j}$ and $\mathbf{v}^{\bar{P}_j}$ are replaced with $\boldsymbol{\omega}^{P_j}$ and $\boldsymbol{\omega}^{\bar{P}_j}$, the angular velocities of P_j and $\bar{P}_j$ ($j = n+1, \ldots, n+M$), respectively, in N. Finally, the procedure applies if $P_{n+1}, \ldots, P_{n+M}$ and $\bar{P}_{n+1}, \ldots, \bar{P}_{n+M}$ are mixed sets of particles and rigid bodies, and if $\mathbf{R}_{n+1}, \ldots, \mathbf{R}_{n+M}, \bar{\mathbf{R}}_{n+1}, \ldots, \bar{\mathbf{R}}_{n+M}$ and $R_{n+1}, \ldots, R_{n+M}$ are interpreted accordingly.

One may find it helpful to read Section 5 before reading Section 4.

4 Rationale

Let a system of $n + M$ linear equations in M unknowns be represented by the matrix equation

$$\mathbf{B} = \mathbf{AR} \quad (15)$$

where $\mathbf{B}$ and $\mathbf{A}$ are $(n+M) \times 1$ and $(n+M) \times M$ matrices with $R_{n+1}, \ldots, R_{n+M}$, the M elements of $\mathbf{R}$, as unknowns. This matrix equation has a unique solution if, and only if, $\mathbf{A}$ is of rank M and $\mathbf{B}$ is in the column space of $\mathbf{A}$ (Strang, 1980). Now, let $\mathbf{A}$ in Eq. (15) be an $(n+M) \times M$ matrix of rank M, and let the elements in the n first rows be equal to zero. Then Eq. (15) has a unique solution if, and only if, the n first elements of $\mathbf{B}$ equal zero.

To show this, define an $M \times M$ matrix $\hat{\mathbf{A}}$ consisting of the M last rows of $\mathbf{A}$; and partition $\mathbf{B}$ into an $n \times 1$ and $M \times 1$ matrices $\bar{\mathbf{B}}$ and $\hat{\mathbf{B}}$, respectively. Then Eq. (15) can be replaced with

$$\begin{vmatrix} \bar{\mathbf{B}} \\ \hat{\mathbf{B}} \end{vmatrix} = \begin{vmatrix} \mathbf{0} \\ \hat{\mathbf{A}} \end{vmatrix} \mathbf{R} \quad (16)$$

or

$$\bar{\mathbf{B}} = \mathbf{0R} \quad (17)$$

and

$$\hat{\mathbf{B}} = \hat{\mathbf{A}}\mathbf{R}, \quad (18)$$

where $\mathbf{0}$ is the $n \times M$ null matrix. Because $\hat{\mathbf{A}}$, like $\mathbf{A}$, is of rank M, Eq. (18) has a unique solution, namely,

$$\mathbf{R} = \hat{\mathbf{A}}^{-1}\hat{\mathbf{B}} \quad (19)$$

and, if $\bar{\mathbf{B}} = \mathbf{0}$, $\mathbf{R}$ is also the solution for Eq. (16). If, on the other hand, $\bar{\mathbf{B}} \neq \mathbf{0}$, then Eq. (17) is not satisfied and Eq. (16) has no solution. Now, Eqs. (1), on the one hand, and Eqs. (14) (obtained with the aid of Steps 1–4 and the first part of Step 6), on the other, are two valid sets of equations governing the motion of S in N. However, Eqs. (14) contain both $\dot{u}_1, \ldots, \dot{u}_n$ and $R_{n+1}, \ldots, R_{n+M}$ as unknowns, whereas the unknowns in Eqs. (1) are $\dot{u}_1, \ldots, \dot{u}_n$. Therefore, Eqs. (1) are solved for $\dot{u}_1, \ldots, \dot{u}_n$, as in Step 5. Furthermore, with reference to Eqs. (14) and (15), let $\mathbf{B}$ play the role of the $(n+M) \times 1$ matrix $|\bar{F}_1 + \bar{F}_1^*, \ldots, \bar{F}_{n+M} + \bar{F}_{n+M}^*|^T$. Then Eqs. (14) can be brought to the form represented by Eqs. (16) if the n first of Eqs. (14) are replaced with Eqs. (1). Such a replacement is valid, because Eqs. (1) comprise linear combinations of Eqs. (14) exposed when, in conjunction with the removal of Eqs. (12), Eqs. (14), (1), and (12) are regarded as playing the roles of Eqs. (1), (8), and (2) in Section 2, respectively. Notably, the right-hand sides of Eqs. (1) are zero (due to the fact that $\mathbf{R}_{n+1}, \ldots, \mathbf{R}_{n+M}$ and $\bar{\mathbf{R}}_{n+1}, \ldots, \bar{\mathbf{R}}_{n+M}$ contribute nothing to Eqs. (1) (Kane, 1985, Section 4.5)). Thus, the n first of Eqs. (14) are represented by Eqs. (17), and the M last of Eqs. (14) are represented by Eqs. (18); and, since $\hat{\mathbf{A}}$, here an $M \times M$ matrix having $\hat{a}_{jr}$ in Eq. (13) as element in row $(j-n)$, column $(r-n)$, is of rank M, a fact established in Step 2, Step 6 can be completed in accordance with Eqs. (19), yielding a unique solution for $R_{n+1}, \ldots, R_{n+M}$.

The following comments are in order.

(a) Regarding $\dot{u}_1, \ldots, \dot{u}_n$ in Eqs. (14) as unknown, substituting $R_{n+1}, \ldots, R_{n+M}$ just obtained in the n first of Eqs. (14), and solving for $\dot{u}_1, \ldots, \dot{u}_n$, one arrives at precisely the same $\dot{u}_1, \ldots, \dot{u}_n$ resulting from Eqs. (1). Hence, $\mathbf{R}_{n+1}, \ldots, \mathbf{R}_{n+M}$ and those of $\bar{\mathbf{R}}_{n+1}, \ldots, \bar{\mathbf{R}}_{n+M}$ exerted on particles of S can be regarded as forces compelling the unconstrained system to perform a motion characterized by the same generalized speeds as those characterizing the constrained system; and therefore are interpreted as constraint forces.

(b) $R_{n+1}, \ldots, R_{n+M}$ do not depend on the choice of auxiliary generalized speeds. This can be shown formally if a choice of M auxiliary generalized speeds other than that defined in Eqs. (12) is made, say, $\tilde{u}_s$ ($s = n+1, \ldots, n+M$); and if note is taken of the fact that the latter can be expressed as linear combinations of $\bar{u}_k$ ($s = n+1, \ldots, n+M$), with G_{sk} ($s, k = n+1, \ldots, n+M$), functions of $q_1, \ldots, q_n$ and t, as weighting factors. Consequently, the M last of Eqs. (14) give way to an alternative set of M equations, each of which is a linear combination of the M last of Eqs. (14), with G_{sk} ($s, k = n+1, \ldots,$

$n + M$) as weighting factors; and it is immaterial which of these two sets of M equations is solved for $R_{n+1}, \ldots, R_{n+M}$.

(c) No auxiliary generalized coordinates have been introduced along with the auxiliary generalized speeds in Step 2. For, if each instant t is regarded as a point in time t_1 at which removal of auxiliary constraints represented by Eqs. (12) starts, and if $q_{\bar{n}+1}, \ldots, q_{\bar{n}+M}$ are M auxiliary generalized coordinates, then $q_{\bar{n}+j}(t_1) = 0$ ($j = 1, \ldots, M$); and, since during removal of constraints the configuration of S in N remains unaltered, $q_{\bar{n}+j}(t_2) = q_{\bar{n}+j}(t_1)$ ($j = 1, \ldots, M$). Thus, the auxiliary generalized coordinates at t_2 always equal zero, and hence need not be introduced.

(d) Particles and bodies of S may appear in S_M and $\bar{S}_M$ more than once, and be denoted with different indices, as, for instance, R, denoted P_5 and P_6, and $\bar{R}$, denoted $\bar{P}_5$ and $\bar{P}_6$ in the following example. It is convenient to denote particles and bodies of S not included in S_M or in $\bar{S}_M$ with indices other than $n+1, \ldots, n+M$.

5 Example

Let the cone A shown in Fig. 1 move so that R slides without friction along L, which is assumed to be parallel to $\mathbf{n}_3$, a unit vector fixed in N. Let $\mathbf{n}_i$ (1, 2, 3) be a set of three dextral, mutually perpendicular unit vectors fixed in N, and let $\mathbf{a}_i$ (1, 2, 3) be a similar set fixed in A, so that $\mathbf{a}_1$, $\mathbf{a}_2$, and $\mathbf{a}_3$ are parallel to central principal axes of A; and let A_{ij} be defined

$$A_{ij} \triangleq \mathbf{n}_i \cdot \mathbf{a}_j \quad (i, j = 1, 2, 3). \tag{20}$$

Let M_A be the mass of A, and I_{A1}, I_{A2}, and I_{A3} the central principal moments of inertia of A for $\mathbf{a}_1$, $\mathbf{a}_2$, and $\mathbf{a}_3$, and define, with the aid of $\boldsymbol{\omega}^A$, the angular velocity of A in N, and $\mathbf{v}^{A^*}$, the velocity of A^* in N, the following generalized speeds:

$$u_r \triangleq \boldsymbol{\omega}^A \cdot \mathbf{a}_r \quad (r = 1, 2, 3), \quad u_4 \triangleq \mathbf{v}^{A^*} \cdot \mathbf{n}_3 \tag{21}$$

so that

$$\boldsymbol{\omega}^A = u_1\mathbf{a}_1 + u_2\mathbf{a}_2 + u_3\mathbf{a}_3, \quad \mathbf{v}^{A^*} = u_4\mathbf{n}_3 + \mathbf{v} \tag{21a}$$

where

$$\mathbf{v} \triangleq r(-A_{12}u_1 + A_{11}u_2)\mathbf{n}_1 + r(-A_{22}u_1 + A_{21}u_2)\mathbf{n}_2. \tag{21b}$$

Then, with $\mathbf{p}^{A^*/R}$ as the position vector from A^* to R, and with

$$r \triangleq -\mathbf{p}^{A^*/R} \cdot \mathbf{a}_3 \tag{22}$$

so that

$$\mathbf{p}^{A^*/R} = -r\mathbf{a}_3, \tag{22a}$$

the equations playing the role of Eqs. (1) and governing the motion of S in N read

$$\begin{aligned} &-I_{A1}\dot{u}_1 - u_3u_2(I_{A3} - I_{A2}) \\ &\quad - M_Ar^2A_{12}(\dot{u}_1A_{12} - \dot{u}_2A_{11} + u_1\dot{A}_{12} - u_2\dot{A}_{11}) \\ &\qquad - M_Ar^2A_{22}(\dot{u}_1A_{22} - \dot{u}_2A_{21} + u_1\dot{A}_{22} - u_2\dot{A}_{21}) = 0 \end{aligned} \tag{23}$$

$$\begin{aligned} &-I_{A2}\dot{u}_2 - u_1u_3(I_{A1} - I_{A3}) \\ &\quad + M_Ar^2A_{11}(\dot{u}_1A_{12} - \dot{u}_2A_{11} + u_1\dot{A}_{12} - u_2\dot{A}_{11}) \\ &\qquad + M_Ar^2A_{21}(\dot{u}_1A_{22} - \dot{u}_2A_{21} + u_1\dot{A}_{22} - u_2\dot{A}_{21}) = 0 \end{aligned} \tag{24}$$

$$-I_{A3}\dot{u}_3 - u_2u_1(I_{A2} - I_{A1}) = 0 \tag{25}$$

$$-M_A\dot{u}_4 = 0, \tag{26}$$

where $\dot{A}_{ij}$ ($i, j = 1, 2, 3$) are functions of u_r ($r = 1, 2, 3$) and of A_{ij} ($i, j = 1, 2, 3$) given by Poisson's kinematical equations.

Now, in connection with particles $\bar{R}$, R, $\bar{B}$ and $\hat{C}$, and bodies B and C, let $\mathbf{R}_5$ and $\mathbf{R}_6$ be forces exerted by $\bar{R}$ on R in the $\mathbf{n}_1$ and $\mathbf{n}_2$ directions; respectively, so that both P_5 and P_6 play the role of R, and both $\bar{P}_5$ and $\bar{P}_6$ play the role of $\bar{R}$. Moreover, let P be perpendicular to $\mathbf{a}_3$, let $\mathbf{R}_7$ be the torque of a couple exerted by B on C in the $\mathbf{a}_3$ direction. Lastly, let $\mathbf{R}_8$ be the force exerted by $\bar{B}$ on $\hat{C}$ in the $\mathbf{a}_3$ direction. Thus, P_7, P_8, $\bar{P}_7$, and $\bar{P}_8$ play the roles of B, $\bar{B}$, C, and $\hat{C}$, respectively. With $\mathbf{R}_i$ ($i = 5, 6, 7, 8$) expressed as

$$\mathbf{R}_5 = R_5\mathbf{n}_1, \quad \mathbf{R}_6 = R_6\mathbf{n}_2, \quad \mathbf{R}_7 = R_7\mathbf{a}_3, \quad \mathbf{R}_8 = R_8\mathbf{a}_3, \tag{27}$$

so that

$$\begin{aligned} \bar{\mathbf{R}}_5 &= -R_5\mathbf{n}_1, \quad \bar{\mathbf{R}}_6 = -R_6\mathbf{n}_2, \\ \bar{\mathbf{R}}_7 &= -R_7\mathbf{a}_3, \quad \bar{\mathbf{R}}_8 = -R_8\mathbf{a}_3, \end{aligned} \tag{28}$$

(where $\bar{\mathbf{R}}_5$ and $\bar{\mathbf{R}}_6$ are forces exerted by R on $\bar{R}$ in the $\mathbf{n}_1$ and $\mathbf{n}_2$ directions, respectively, $\bar{\mathbf{R}}_7$ is the torque of a couple exerted by C on B in the $\mathbf{a}_3$ direction, and $\bar{\mathbf{R}}_8$ is the force exerted by $\hat{C}$ on $\bar{B}$ in the $\mathbf{a}_3$ direction), it is required to determine R_5, R_6, R_7, and R_8. Using the six-step procedure, one has the following:

Step 1. In view of Eqs. (21a) and (22a)

$$\mathbf{v}^{P_5} = \mathbf{v}^R = [u_4 + r(A_{32}u_1 - A_{31}u_2)]\mathbf{n}_3, \quad \mathbf{v}^{\bar{P}_5} = \mathbf{v}^{\bar{R}} = 0 \tag{29}$$

$$\mathbf{v}^{P_6} = \mathbf{v}^R = [u_4 + r(A_{32}u_1 - A_{31}u_2)]\mathbf{n}_3, \quad \mathbf{v}^{\bar{P}_6} = \mathbf{v}^{\bar{R}} = 0 \tag{30}$$

$$\begin{aligned} \boldsymbol{\omega}^{P_7} &= \boldsymbol{\omega}^C = u_1\mathbf{a}_1 + u_2\mathbf{a}_2 + u_3\mathbf{a}_3, \\ \boldsymbol{\omega}^{\bar{P}_7} &= \boldsymbol{\omega}^B = u_1\mathbf{a}_1 + u_2\mathbf{a}_2 + u_3\mathbf{a}_3 \end{aligned} \tag{31}$$

$$\mathbf{v}^{P_8} = \mathbf{v}^{\bar{B}} = u_4\mathbf{n}_3 + \mathbf{v}, \quad \mathbf{v}^{\bar{P}_8} = \mathbf{v}^{\hat{C}} = u_4\mathbf{n}_3 + \mathbf{v}. \tag{32}$$

Step 2. Here, $n = 4$ and $M = 4$. In accordance with Eqs. (12), the auxiliary generalized speeds are defined

$$\bar{u}_5 = 0, \quad \bar{u}_6 = 0, \quad \bar{u}_7 = 0, \quad \bar{u}_8 = 0, \tag{33}$$

with which $\mathbf{v}^{P_5}$, $\mathbf{v}^{P_6}$, $\boldsymbol{\omega}^{P_7}$ and $\mathbf{v}^{P_8}$, on the one hand, and $\mathbf{v}^{\bar{P}_5}$, $\mathbf{v}^{\bar{P}_6}$, $\boldsymbol{\omega}^{\bar{P}_7}$ and $\mathbf{v}^{\bar{P}_8}$, on the other, are redefined as follows:

$$\begin{aligned} \mathbf{v}^{P_5} &= [u_4 + r(A_{32}u_1 - A_{31}u_2)]\mathbf{n}_3 + \bar{u}_5\mathbf{n}_1 + \bar{u}_6\mathbf{n}_2, \\ \mathbf{v}^{\bar{P}_5} &= 0 \end{aligned} \tag{34}$$

$$\begin{aligned} \mathbf{v}^{P_6} &= [u_4 + r(A_{32}u_1 - A_{31}u_2)]\mathbf{n}_3 + \bar{u}_5\mathbf{n}_1 + \bar{u}_6\mathbf{n}_2 \\ \mathbf{v}^{\bar{P}_6} &= 0 \end{aligned} \tag{35}$$

$$\begin{aligned} \boldsymbol{\omega}^{P_7} &= u_1\mathbf{a}_1 + u_2\mathbf{a}_2 + u_3\mathbf{a}_3 + \bar{u}_7\mathbf{a}_3, \\ \boldsymbol{\omega}^{\bar{P}_7} &= u_1\mathbf{a}_1 + u_2\mathbf{a}_2 + u_3\mathbf{a}_3 \end{aligned} \tag{36}$$

$$\begin{aligned} \mathbf{v}^{P_8} &= u_4\mathbf{n}_3 + \mathbf{v} + \bar{u}_5\mathbf{n}_1 + \bar{u}_6\mathbf{n}_2, \\ \mathbf{v}^{\bar{P}_8} &= u_4\mathbf{n}_3 + \mathbf{v} + \bar{u}_5\mathbf{n}_1 + \bar{u}_6\mathbf{n}_2 - \bar{u}_8\mathbf{a}_3. \end{aligned} \tag{37}$$

Hence, substitutions from Eqs. (33) in Eqs. (34)–(37) restore Eqs. (29)–(32). Moreover, noting that $\mathbf{v}^{P_7}$ and $\mathbf{v}^{\bar{P}_7}$ are replaced with $\boldsymbol{\omega}^{P_7}$ and $\boldsymbol{\omega}^{\bar{P}_7}$ (see Eqs. (31)), and that, in view of Eqs. (27), $\hat{\mathbf{a}}_5 = \mathbf{n}_1$, $\hat{\mathbf{a}}_6 = \mathbf{n}_2$, $\hat{\mathbf{a}}_7 = \mathbf{a}_3$ and $\hat{\mathbf{a}}_8 = \mathbf{a}_3$, one has

$$\left(\frac{\partial \mathbf{v}^{P_j}}{\partial \bar{u}_r} - \frac{\partial \mathbf{v}^{\bar{P}_j}}{\partial \bar{u}_r}\right) \cdot \hat{\mathbf{a}}_j = \delta_{rj} \quad (j, r = 5, 6, 7, 8) \tag{38}$$

and

$$\text{rank} \begin{vmatrix} 1 & 0 & 0 & 0 \\ 0 & 1 & 0 & 0 \\ 0 & 0 & 1 & 0 \\ 0 & 0 & 0 & 1 \end{vmatrix} = 4 = M. \tag{39}$$

Step 3. $\mathbf{v}^{A^*}$, used in the generation of Eqs. (23)–(26), is redefined as

$$\mathbf{v}^{A^*} = u_4\mathbf{n}_3 + \mathbf{v} + \bar{u}_5\mathbf{n}_1 + \bar{u}_6\mathbf{n}_2, \tag{40}$$

and reduces to the second of Eqs. (21a) when Eqs. (33) are used to eliminate $\bar{u}_5$ and $\bar{u}_6$.

Step 4. Substitutions in the four last of Eqs. (14) leads, with simplifications, to

$$-M_A r(-\dot{u}_1 A_{12} + \dot{u}_2 A_{11} - u_1 \dot{A}_{12} + u_2 \dot{A}_{11} + \dot{\bar{u}}_5/r) = -R_5 \quad (41)$$

$$-M_A r(-\dot{u}_1 A_{22} + \dot{u}_2 A_{21} - u_1 \dot{A}_{22} + u_2 \dot{A}_{21} + \dot{\bar{u}}_6/r) = -R_6 \quad (42)$$

$$-I_{C3}(\dot{\bar{u}}_7 + \dot{u}_3) - u_2 u_1 (I_{C2} - I_{C1}) = -R_7 \quad (43)$$

$$M_C \left[\frac{M_B s}{M_A}(u_1^2 + u_2^2) - \dot{\bar{u}}_8 - A_{13} r(-\dot{u}_1 A_{12} + \dot{u}_2 A_{11} - u_1 \dot{A}_{12} + u_2 \dot{A}_{11}) - A_{23} r(-\dot{u}_1 A_{22} + \dot{u}_2 A_{21} - u_1 \dot{A}_{22} + u_2 \dot{A}_{21}) - A_{33}\dot{u}_4 \right] = -R_8 \quad (44)$$

where I_{C1}, I_{C2}, and I_{C3} are central principal moments of inertia of C, the associated axes having been assumed to be parallel to $\mathbf{a}_1$, $\mathbf{a}_2$, and $\mathbf{a}_3$, respectively; M_B and M_C are the masses of B and C, respectively, and s is the distance between B^* and C^*, the mass centers of B and C.

Step 5. Equations (23)–(26) are solved for $\dot{u}_1, \ldots, \dot{u}_4$.

Step 6. Equations (41)–(44), together with

$$\dot{\bar{u}}_5 = 0, \quad \dot{\bar{u}}_6 = 0, \quad \dot{\bar{u}}_7 = 0, \quad \dot{\bar{u}}_8 = 0 \quad (45)$$

resulting from Eqs. (33), yield

$$R_5 = M_A r(-\dot{u}_1 A_{12} + \dot{u}_2 A_{11} - u_1 \dot{A}_{12} + u_2 \dot{A}_{11}) \quad (46)$$

$$R_6 = M_A r(-\dot{u}_1 A_{22} + \dot{u}_2 A_{21} - u_1 \dot{A}_{22} + u_2 \dot{A}_{21}) \quad (47)$$

$$R_7 = I_{C3}\dot{u}_3 + u_2 u_1 (I_{C2} - I_{C1}) \quad (48)$$

$$R_8 = M_C \left[-\frac{M_B s}{M_A}(u_1^2 + u_2^2) + A_{13} r(-\dot{u}_1 A_{12} + \dot{u}_2 A_{11} - u_1 \dot{A}_{12} + u_2 \dot{A}_{11}) + A_{23} r(-\dot{u}_1 A_{22} + \dot{u}_2 A_{21} - u_1 \dot{A}_{22} + u_2 \dot{A}_{21}) + A_{33}\dot{u}_4 \right]. \quad (49)$$

A different choice of auxiliary generalized speeds, denoted here with tilde, is

$$\tilde{u}_5 = r(-A_{12}u_1 + A_{11}u_2), \quad \tilde{u}_6 = r(-A_{22}u_1 + A_{21}u_2), \quad \tilde{u}_7 = 0, \quad \tilde{u}_8 = 0 \quad (50)$$

with which the six-step procedure leads to the following results. Equations (29)–(32) remain unaltered. Moreover, if $\bar{u}_5, \ldots, \bar{u}_8$ are replaced with $\tilde{u}_5, \ldots, \tilde{u}_8$, respectively, and $u_4\mathbf{n}_3$ is replaced with $u_4\mathbf{n}_3 - \mathbf{v}$ in Eqs. (34)–(37), then these equations remain valid, as are Eqs. (38) and (39). Finally, Eqs. (41)–(44) give way to

$$-M_A \dot{\tilde{u}}_5 = -R_5 \quad (51)$$

$$-M_A \dot{\tilde{u}}_6 = -R_6 \quad (52)$$

$$-I_{C3}(\dot{\tilde{u}}_7 + \dot{u}_3) - u_2 u_1 (I_{C2} - I_{C1}) = -R_7 \quad (53)$$

$$M_C \left[\frac{M_B s}{M_A}(u_1^2 + u_2^2) - \dot{\tilde{u}}_8 - A_{13}\dot{\tilde{u}}_5 - A_{23}\dot{\tilde{u}}_6 - A_{33}\dot{u}_4 \right] = -R_8 \quad (54)$$

and, using the time derivatives of $\tilde{u}_5$, $\tilde{u}_6$, $\tilde{u}_7$, and $\tilde{u}_8$ in Eqs. (50) to eliminate $\dot{\tilde{u}}_5, \ldots, \dot{\tilde{u}}_8$ from Eqs. (51)–(54), one arrives at Eqs. (46)–(49).

6 Three-Phase Motions, Noncontributing Forces, and Noncontributing Impulses

Let S be a simple, nonholonomic system of n degrees-of-freedom, undergoing a three-phase motion involving imposition of constraints, as described in Section 1. Let $\mathbf{R}_{n+1}, \ldots, \mathbf{R}_{n+M}$ be M noncontributing forces (and/or torques) of interest, and suppose it is required to determine $R_{n+1}, \ldots, R_{n+M}$ *throughout* the motion.

The six-step procedure can be used to determine $R_{n+1}, \ldots, R_{n+M}$ during Phase (a). Moreover, one can define, in connection with Phase (b), $\mathbf{S}_j$ and $\bar{\mathbf{S}}_j$, the impulses associated with $\mathbf{R}_j$ and $\bar{\mathbf{R}}_j$, respectively, and S_j, as

$$\mathbf{S}_j \triangleq \int_{t_1}^{t_2} \mathbf{R}_j dt, \quad \bar{\mathbf{S}}_j \triangleq \int_{t_1}^{t_2} \bar{\mathbf{R}}_j dt, \quad S_j \triangleq \mathbf{S}_j \cdot \hat{\mathbf{a}}_j \quad (j = n+1, \ldots, n+M).$$

Then, in view of Eqs. (10), S_j $(j = n+1, \ldots, n+M)$ become

$$S_j = \int_{t_1}^{t_2} R_j dt \quad (j = n+1, \ldots, n+M), \quad (55)$$

and can be obtained if the M last of Eqs. (14) are integrated from t_1 to t_2, yielding (Djerassi, 1994, Eqs. (20) and (23))

$$\sum_{s=1}^{n} m_{rs}[u_s(t_2) - u_s(t_1)] + \sum_{s=n+1}^{n+M} m_{rs}[\bar{u}_s(t_2) - \bar{u}_s(t_1)] = -\sum_{j=n+1}^{n+M} \hat{a}_{jr} S_j \quad (r = n+1, \ldots, n+M), \quad (56)$$

where an extension of the indices range of m_{rs} in Eq. (7) is implied. If, in addition, Eqs. (12) are similarly integrated, the result is

$$\bar{u}_k(t_2) - \bar{u}_k(t_1) = \sum_{r=1}^{n} \bar{C}_{kr}[u_r(t_2) - u_r(t_1)] \quad (k = n+1, \ldots, n+M). \quad (57)$$

Eliminating $\bar{u}_k(t_2) - \bar{u}_k(t_1)$ $(k = n+1, \ldots, n+M)$ from Eqs. (56) with the aid of Eqs. (57), one has

$$\sum_{s=1}^{n} \left(m_{rs} + \sum_{k=n+1}^{n+M} \bar{C}_{ks} m_{rk}\right)[u_s(t_2) - u_s(t_1)] = -\sum_{j=n+1}^{n+M} \hat{a}_{jr} S_j \quad (r = n+1, \ldots, n+M), \quad (58)$$

M equations possessing a unique solution for $S_{n+1}, \ldots, S_{n+M}$ (the coefficients of $S_{n+1}, \ldots, S_{n+M}$ are identical with those of $R_{n+1}, \ldots, R_{n+M}$ in Eqs. (14)). Note that $\bar{u}_k(t_1)$ and $\bar{u}_k(t_2)$ $(k = n+1, \ldots, n+M)$ do not appear in Eqs. (58), and that $u_s(t_2)$ $(s = 1, \ldots, n)$ are, by virtue of Eqs. (5) and (6), known quantities. Furthermore, note that, with expressions for $R_{n+1}, \ldots, R_{n+M}$ in hand, $S_{n+1}, \ldots, S_{n+M}$ can be found (more expeditiously) by direct substitutions in Eqs. (55). Finally, the same role played by Eqs. (14) in Phase (a), is played in Phase (c) by the following equations:

$$\bar{F}_r + \bar{F}_r^* + \sum_{k=p+1}^{n} C_{kr}(\bar{F}_k + \bar{F}_k^*) = -\sum_{j=n+1}^{n+M} \hat{a}_{jr} R_j - \sum_{k=n+1}^{n} C_{kr} \sum_{j=n+1}^{n+M} \hat{a}_{jk} R_j \quad (r = 1, \ldots, p)$$

$$\bar{F}_r + \bar{F}_r^* = -\sum_{j=n+1}^{n+M} \hat{a}_{jr} R_j \quad (r = n+1, \ldots, n+M) \quad (59)$$

obtained when the constraints in Eqs. (2) are imposed on the system, whose motion is regarded as being governed by Eqs. (14). Clearly, the M last of Eqs. (59) are identical with the M last of Eqs. (14), an observation indicating that the same expressions for $R_{n+1}, \ldots, R_{n+M}$ in Phase (a) are valid in Phase (c).

Now, it is implied by Eqs. (14) and (59) that none of $\mathbf{R}_{n+1}, \ldots, \mathbf{R}_{n+M}$ is associated with the constraints in Eqs. (2). However, if, in connection with Phase (c), one wishes to determine, in addition to $\mathbf{R}_{n+1}, \ldots, \mathbf{R}_{n+M}$, m forces $\mathbf{R}_{p+1}, \ldots, \mathbf{R}_n$ associated with Eqs. (2), one can proceed as follows. Regard $u_{p+1}, \ldots, u_n$ as *additional* auxiliary generalized speeds (i.e., additional to $\bar{u}_{n+1}, \ldots, \bar{u}_{n+M}$) and Eqs. (2) as *additional* auxiliary constraint equation (i.e., additional to Eqs. (12)). Remove these constraints in additions to those defined in Eqs. (12), introducing contributions from the associated forces (and/or torques) $\mathbf{R}_{p+1}, \ldots, \mathbf{R}_n$ and $\bar{\mathbf{R}}_{p+1}, \ldots, \bar{\mathbf{R}}_n$ (in addition to contributions from $\mathbf{R}_{n+1}, \ldots, \mathbf{R}_{n+M}$ and $\bar{\mathbf{R}}_{n+1}, \ldots, \bar{\mathbf{R}}_{n+M}$), and obtain a set of equations governing the motion in Phase (c). Similarly to Eqs. (14), these equations read

$$\bar{F}_r + \bar{F}_r^* = -\sum_{j=p+1}^{n+M} \hat{a}_{jr} R_j \quad (r = 1, \ldots, n + M) \quad (60)$$

where the range of j has been extended from $j = n + 1, \ldots, n + M$ to $j = p + 1, \ldots, n + M$, and where the associated extension of the definitions of $\hat{a}_{jr}$ in Eqs. (13) will be reported presently and of R_j in Eqs. (10) is implied. Moreover, Eqs. (55) and (58) are replaced with the following equations:

$$S_j = \int_{t_1}^{t_2} R_j dt \quad (j = p + 1, \ldots, n + M) \quad (61)$$

$$\sum_{s=1}^{n} (m_{rs} + \sum_{k=n+1}^{n+M} \bar{C}_{ks} m_{rk})[u_s(t_2) - u_s(t_1)] = -\sum_{j=p+1}^{n+M} \hat{a}_{jr} S_j$$

$$(r = p + 1, \ldots, n + M), \quad (62)$$

where the extended range of j comes into evidence. Now, $\mathbf{R}_{p+1}, \ldots, \mathbf{R}_{n+M}$ and $\bar{\mathbf{R}}_{p+1}, \ldots, \bar{\mathbf{R}}_{n+M}$, called *noncontributing forces,* contribute nothing to Eqs. (1) and (8); that is, $R_{p+1}, \ldots, R_{n+M}$ do not appear in Eqs. (1) and (8). Similarly, $\mathbf{S}_{p+1}, \ldots, \mathbf{S}_{n+M}$ and $\bar{\mathbf{S}}_{p+1}, \ldots, \bar{\mathbf{S}}_{n+M}$, called *noncontributing impulses,* contribute nothing to Eqs. (6), that is, $S_{p+1}, \ldots, S_{n+M}$ do not appear in Eqs. (6). With Eqs. (1), (8), and (6) in hand, however, $R_{p+1}, \ldots, R_{n+M}$ and $S_{p+1}, \ldots, S_{n+M}$ in three-phase motions can be determined with the aid of the following (extended) six-step procedure.

Step 1. Obtain expressions for $\mathbf{v}^{P_j}$ and $\mathbf{v}^{\bar{P}_j}$ $(j = p + 1, \ldots, n + M)$ in the unconstrained phase.

Step 2. Introduce M new variables $\bar{u}_{n+1}, \ldots, \bar{u}_{n+M}$ and construct M equations defining $\bar{u}_{n+1}, \ldots, \bar{u}_{n+M}$ as linear combinations of $u_1, \ldots, u_n$, that is,

$$\bar{u}_k = \sum_{r=1}^{n} \bar{C}_{kr} u_r + \bar{D}_k$$

$$(k = n + 1, \ldots, n + M) \quad \text{(repeated)}. \quad (12)$$

Regard these as constraints being removed and $u_1, \ldots, u_n, \bar{u}_{n+1}, \ldots, \bar{u}_{n+M}$ as independent. Redefine $\mathbf{v}^{P_j}$ $(j = p + 1, \ldots, n + M)$ and $\mathbf{v}^{\bar{P}_j}$ $(j = p + 1, \ldots, n + M)$ as functions of $u_1, \ldots, u_n, \bar{u}_{n+1}, \ldots, \bar{u}_{n-M}$ such that (a) when $\bar{u}_{n+1}, \ldots, \bar{u}_{n+M}$ are eliminated with the aid of Eqs. (12), the expressions for $\mathbf{v}^{P_j}$ $(j = p + 1, \ldots, n + M)$ and $\mathbf{v}^{\bar{P}_j}$ $(j = p + 1, \ldots, n + M)$ obtained in Step 1 are restored; and (b) the $(m + M) \times (m + M)$ matrix having $\hat{a}_{jr}$ $(j, r = p + 1, \ldots, n + M)$, defined as

$$\hat{a}_{jr} \triangleq \left(\frac{\partial \mathbf{v}^{P_j}}{\partial \tilde{u}_r} - \frac{\partial \mathbf{v}^{\bar{P}_j}}{\partial \tilde{u}_r} \right) \cdot \hat{\mathbf{a}}_j \quad (j, r = p + 1, \ldots, n + M), \quad (63)$$

where $\tilde{u}_r = u_r (r = p + 1, \ldots, n)$, as its element in row $(j - p)$, column $(r - p)$, is of rank $m + M$.

Step 3. Redefine, in terms of $u_1, \ldots, u_n, \bar{u}_{n+1}, \ldots, \bar{u}_{n+M}$, the velocities of those particles of S not included in S_M and $\bar{S}_M$.

Step 4. Assuming that the constraints in Eqs. (2) and (12) have been removed, formulate equations governing the motion of the system, including contributions form $\mathbf{R}_{p+1}, \ldots, \mathbf{R}_{n+M}$ and $\bar{\mathbf{R}}_{p+1}, \ldots, \bar{\mathbf{R}}_{n+M}$, so that now

$$\bar{F}_r + \bar{F}_r^* = -\sum_{j=p+1}^{n+M} \hat{a}_{jr} R_j$$

$$(r = 1, \ldots, n + M) \quad \text{(repeated)} \quad (60)$$

(in fact, only the $m + M$ last of Eqs. (60), namely, those associated with $u_{p+1}, \ldots, u_n, \bar{u}_{n+1}, \ldots, \bar{u}_{n+M}$, have to be formulated).

Step 5. Solve Eqs. (1) for $\dot{u}_r$ $(r = 1, \ldots, n)$ in Phase (a), Eqs. (5) and (6) for $u_1(t_2), \ldots, u_n(t_2)$ in Phase (b), and Eqs. (8) for $\dot{u}_r$ $(r = 1, \ldots, p)$ in Phase (c).

Step 6. Use Eqs. (12) to eliminate $\bar{u}_{n+1}, \ldots, \bar{u}_{n+M}$ and $\dot{\bar{u}}_{n+1}, \ldots, \dot{\bar{u}}_{n+M}$ from the $m + M$ last of Eqs. (60) and solve these for $R_{p+1}, \ldots, R_{n+M}$. In connection with Phase (a), disregard expressions for $R_{p+1}, \ldots, R_n$ (which equal zero in this phase). In connection with Phase (c), eliminate $u_{p+1}, \ldots, u_n$ and $\dot{u}_{p+1}, \ldots, \dot{u}_n$ form $R_{p+1}, \ldots, R_{n+M}$ with the aid of Eqs. (2). In connection with Phase (b), substitute $R_{p+1}, \ldots, R_{n+M}$ in Eqs. (61) and integrate to obtain $S_{p+1}, \ldots, S_{n+M}$.

If removal of constrains is under consideration, then Eqs. (62), in conjunction with Eqs. (9), decree

$$S_j = 0 \quad (j = p + 1, \ldots, n + M), \quad (64)$$

which means that removal of constraints (when governed by Eqs. (9)) is an event free of impulses. Then the six-step procedure apply if Phases (a) and (c) exchange roles, and if those parts of Steps 5 and 6 concerning Phase (b) are disregarded.

7 Example (continued)

With reference to the example discussed earlier, suppose S undergoes a three-phase motion, as described in Section 4, such that the unconstrained phase (Phase (a)) is one in which no point of A is in contact with points of N. Then, with u_5 and u_6 defined as

$$u_5 \triangleq \mathbf{v}^{A^*} \cdot \mathbf{n}_1, \quad u_6 \triangleq \mathbf{v}^{A^*} \cdot \mathbf{n}_2 \quad (65)$$

and with the same definitions for $u_1, \ldots, u_4$ as in Eqs. (21), $\boldsymbol{\omega}^A$ and $\mathbf{v}^{A^*}$ can be written

$$\boldsymbol{\omega}^A = u_1\mathbf{a}_1 + u_2\mathbf{a}_2 + u_3\mathbf{a}_3, \quad \mathbf{v}^{A^*} = u_4\mathbf{n}_3 + u_5\mathbf{n}_1 + u_6\mathbf{n}_2; \quad (65a)$$

and the equations governing the motion of A in the unconstrained phase become

$$-I_{A1}\dot{u}_1 - (I_{A3} - I_{A2})u_3u_2 = 0 \quad (66)$$

$$-I_{A2}\dot{u}_2 - (I_{A1} - I_{A3})u_1u_3 = 0 \quad (67)$$

$$-I_{A3}\dot{u}_3 - (I_{A2} - I_{A1})u_2u_1 = 0 \quad (68)$$

$$-M\dot{u}_4 = 0 \quad (69)$$

$$-M\dot{u}_5 = 0 \quad (70)$$

$$-M\dot{u}_6 = 0, \quad (71)$$

playing the role of Eqs. (1). With

$$\mathbf{v}^R = \mathbf{v}^{A^*} + \omega^A \times \mathbf{p}^{A^*/R} = u_4\mathbf{n}_3 + u_5\mathbf{n}_1 + u_6\mathbf{n}_2$$

$$+ (u_1\mathbf{a}_1 + u_2\mathbf{a}_2 + u_3\mathbf{a}_3) \times (-r\mathbf{a}_3) \quad (72)$$

the constraints are

$$\mathbf{v}^R \cdot \mathbf{n}_1 = 0, \quad \mathbf{v}^R \cdot \mathbf{n}_2 = 0 \tag{73}$$

or

$$u_5 = -rA_{12}u_1 + rA_{11}u_2, \quad u_6 = -rA_{22}u_1 + rA_{21}u_2, \tag{74}$$

equations playing the role of Eqs. (2). Hence, the constrained phase (Phase (c)) is the one described in Section 4, and the equations of motion are Eqs. (23)–(26), playing the role of Eqs. (8). The transition phase (Phase (b)) is one in which contact between R and $\hat{R}$ is established. That is, the constraints in Eqs. (74) are imposed, a process resulting in a change in the generalized speeds, which, in accordance with Eqs. (5) and (6), can be evaluated if the following matrix equation is solved for $u_1(t_2), \ldots, u_6(t_2)$:

$$\begin{vmatrix} -I_{A1} & 0 & 0 & 0 & rA_{12}M & rA_{22}M \\ 0 & -I_{A2} & 0 & 0 & -rA_{11}M & -rA_{21}M \\ 0 & 0 & -I_{A3} & 0 & 0 & 0 \\ 0 & 0 & 0 & -M & 0 & 0 \\ -rA_{12} & rA_{11} & 0 & 0 & -1 & 0 \\ -rA_{22} & rA_{21} & 0 & 0 & 0 & -1 \end{vmatrix} \begin{vmatrix} u_1(t_2) \\ u_2(t_2) \\ u_3(t_2) \\ u_4(t_2) \\ u_5(t_2) \\ u_6(t_2) \end{vmatrix} = \begin{vmatrix} -I_{A1} & 0 & 0 & 0 & rA_{12}M & rA_{22}M \\ 0 & -I_{A2} & 0 & 0 & -rA_{11}M & -rA_{21}M \\ 0 & 0 & -I_{A3} & 0 & 0 & 0 \\ 0 & 0 & 0 & -M & 0 & 0 \\ 0 & 0 & 0 & 0 & 0 & 0 \\ 0 & 0 & 0 & 0 & 0 & 0 \end{vmatrix} \begin{vmatrix} u_1(t_1) \\ u_2(t_1) \\ u_3(t_1) \\ u_4(t_1) \\ u_5(t_1) \\ u_6(t_1) \end{vmatrix}. \tag{75}$$

Under these circumstances, it is required to determine R_5, R_6, R_7, and R_8 (see Eqs. (27)–(28)) throughout the motion.

Step 1. In view of Eqs. (65a) and (22a)

$$\mathbf{v}^{P_5} = u_4\mathbf{n}_3 + r(u_1\mathbf{a}_2 - u_2\mathbf{a}_1) + u_5\mathbf{n}_1 + u_6\mathbf{n}_2, \quad \mathbf{v}^{\bar{P}_5} = 0 \tag{76}$$

$$\mathbf{v}^{P_6} = u_4\mathbf{n}_3 + r(u_1\mathbf{a}_2 - u_2\mathbf{a}_1) + u_5\mathbf{n}_1 + u_6\mathbf{n}_2, \quad \mathbf{v}^{\bar{P}_6} = 0 \tag{77}$$

$$\boldsymbol{\omega}^{P_7} = u_1\mathbf{a}_1 + u_2\mathbf{a}_2 + u_3\mathbf{a}_3, \quad \boldsymbol{\omega}^{\bar{P}_7} = u_1\mathbf{a}_1 + u_2\mathbf{a}_2 + u_3\mathbf{a}_3 \tag{78}$$

$$\mathbf{v}^{P_8} = u_4\mathbf{n}_3 + u_5\mathbf{n}_1 + u_6\mathbf{n}_2, \quad \mathbf{v}^{\bar{P}_8} = u_4\mathbf{n}_3 + u_5\mathbf{n}_1 + u_6\mathbf{n}_2. \tag{79}$$

Step 2. Here $n = 6$, $p = 4$, $m = 2$, and $M = 2$. The auxiliary generalized speeds are defined

$$\bar{u}_7 = 0, \quad \bar{u}_8 = 0, \tag{80}$$

and the constraint equations are Eqs. (74). $\mathbf{v}^{P_5}$, $\mathbf{v}^{P_6}$, $\boldsymbol{\omega}^{P_7}$ and $\mathbf{v}^{P_8}$, on the one hand, and $\mathbf{v}^{\bar{P}_5}$, $\mathbf{v}^{\bar{P}_6}$, $\boldsymbol{\omega}^{\bar{P}_7}$ and $\mathbf{v}^{\bar{P}_8}$, on the other, are redefined as

$$\mathbf{v}^{P_5} = u_4\mathbf{n}_3 + r(u_1\mathbf{a}_2 - u_2\mathbf{a}_1) + u_5\mathbf{n}_1 + u_6\mathbf{n}_2, \quad \mathbf{v}^{\bar{P}_5} = 0 \tag{81}$$

$$\mathbf{v}^{P_6} = u_4\mathbf{n}_3 + r(u_1\mathbf{a}_2 - u_2\mathbf{a}_1) + u_5\mathbf{n}_1 + u_6\mathbf{n}_2, \quad \mathbf{v}^{\bar{P}_6} = 0 \tag{82}$$

$$\boldsymbol{\omega}^{P_7} = u_1\mathbf{a}_1 + u_2\mathbf{a}_2 + u_3\mathbf{a}_3 + \bar{u}_7\mathbf{a}_3,$$
$$\boldsymbol{\omega}^{\bar{P}_7} = u_1\mathbf{a}_1 + u_2\mathbf{a}_2 + u_3\mathbf{a}_3 \tag{83}$$

$$\mathbf{v}^{P_8} = u_4\mathbf{n}_3 + u_5\mathbf{n}_1 + u_6\mathbf{n}_2,$$
$$\mathbf{v}^{\bar{P}_8} = u_4\mathbf{n}_3 + u_5\mathbf{n}_1 + u_6\mathbf{n}_2 - \bar{u}_8\mathbf{a}_3. \tag{84}$$

Equation (38) and (39) remain valid.

Step 3. Here, redefinitions are not required.

Step 4. Substitutions in the four last of Eqs. (60) lead to

$$-M\dot{u}_5 = -R_5 \tag{85}$$

$$-M\dot{u}_6 = -R_6 \tag{86}$$

$$-I_{C3}(\dot{\bar{u}}_7 + \dot{u}_3) - u_2u_1(I_{C2} - I_{C1}) = -R_7 \tag{87}$$

$$M_C\left[\frac{M_B s}{M_A}(u_1^2 + u_2^2) - \dot{\bar{u}}_8 - A_{13}\dot{u}_5 - A_{23}\dot{u}_6 - A_{33}\dot{u}_4\right] = -R_8. \tag{88}$$

Step 5. Equations (66)–(71) are solved for $\dot{u}_1, \ldots, \dot{u}_6$ in Phase (a); Eqs. (75) are solved for $u_1(t_2), \ldots, u_6(t_2)$ in Phase (b); and Eqs. (23)–(26) are solved for $\dot{u}_1, \ldots, \dot{u}_4$ in Phase (c).

Step 6. Equations (85)–(88) together with $\dot{\bar{u}}_7 = 0$ and $\dot{\bar{u}}_8 = 0$ (Eqs. (80)) yield

$$R_5 = M\dot{u}_5 \tag{89}$$

$$R_6 = M\dot{u}_6 \tag{90}$$

$$R_7 = I_{C3}\dot{u}_3 + u_2u_1(I_{C2} - I_{C1}) \tag{91}$$

$$R_8 = M_C\left[-\frac{M_B s}{M_A}(u_1^2 + u_2^2) + A_{13}\dot{u}_5 + A_{23}\dot{u}_6 + A_{33}\dot{u}_4\right]. \tag{92}$$

As concerns Phase (a), $R_5 = R_6 = 0$, and Eqs. (89) and (90) should be disregarded. As concerns Phase (c), R_5, R_6, R_7, and R_8 are given by Eqs. (89)–(92) after u_5 and u_6 have been eliminated with the aid of Eqs. (74), a procedure leading to equations identical with Eqs. (46)–(49). Lastly, S_5, S_6, S_7, and S_8 can be obtained by substitutions in Eqs. (62). However, with Eqs. (46)–(49) in hand, one can obtain S_5, S_6, S_7, and S_8 more expeditiously by direct substitutions in Eqs. (61). Thus, if both sides of Eqs. (46)–(49) are multiplied with dt and integrated from t_1 to t_2, one has, noting that R_5, R_6, R_7 and R_8 are linear functions of $\dot{u}_1$, $\dot{u}_2$, $\dot{u}_3$, and $\dot{u}_4$, and that the functions of $u_1, \ldots, u_4, A_{ij}$, and $\dot{A}_{ij}$ $(i, j = 1, 2, 3)$ appearing in Eqs. (46)–(49) are all bounded (hence become zero when integrated from t_1 to t_2),

$$S_5 = M_A r\{-A_{12}[u_1(t_2) - u_1(t_1)] + A_{11}[u_2(t_2) - u_2(t_1)]\} \tag{93}$$

$$S_6 = M_A r\{-A_{22}[u_1(t_2) - u_1(t_1)] + A_{21}[u_2(t_2) - u_2(t_1)]\} \tag{94}$$

$$S_7 = I_{C3}[u_3(t_2) - u_3(t_1)] \tag{95}$$

$$S_8 = M_C\{A_{33}[u_4(t_2) - u_4(t_1)] + r(-A_{12}A_{13} - A_{22}A_{23})[u_1(t_2) - u_1(t_1)] + r(A_{11}A_{13} + A_{21}A_{23})[u_2(t_2) - u_2(t_1)]\}. \tag{96}$$

8 Summary

Noncontributing forces and noncontributing impulses were discussed in connection with dynamical systems undergoing three-phase motions, and an efficient procedure for their determination has been proposed. Accordingly, it has been shown that the noncontributing forces $\mathbf{R}_{p+1}, \ldots, \mathbf{R}_{n+M}$ need to be determined only in connection with the *constrained* phase, and that, with these in hand, noncontributing forces and noncontributing impulses throughout the motion can be obtained straightforwardly. Thus, the m first of these equal zero in the unconstrained phase and the associated expressions should be disregarded. Moreover, being functions of $u_1, \ldots, u_n$ and $\dot{u}_1, \ldots, \dot{u}_n$, $\mathbf{R}_{p+1}, \ldots, \mathbf{R}_{n+M}$ are valid in the constrained phase, provided $u_{p+1}, \ldots, u_n$ and $\dot{u}_{p+1}, \ldots, \dot{u}_n$ have been eliminated. Finally, (simple) integration of $\mathbf{R}_{p+1}, \ldots, \mathbf{R}_{n+M}$ leads to $\mathbf{S}_{p+1}, \ldots, \mathbf{S}_{n+M}$ in the transition phase, impulses which are zero if constraints are removed.

The preceding discussion of noncontributing impulses emphasizes one central feature of the theory of imposition of constraints, reported briefly in the Introduction, namely, the evaluation of $u_k(t_2)$ ($k = 1, \ldots, n$) with Eqs. (5) and (6), without impulses having been brought into the analysis. This may lead to significant simplifications in the formulation of problems where systems undergo a change in their number of degrees-of-freedom, as in the works by and Levinson and Kane (1983), Fitz-Coy and Cochran (1986), and Rhody et al. (1993).

References

Djerassi, S., 1994, "Imposition of Constraints," ASME Journal of Applied Mechanics, Vol. 61, pp. 434–439.

Fitz-Coy, N. G., and Cochran, J. E., 1986, "Space Station/Shuttle Orbiter Dynamics During Docking," *Structural Dynamics and Control Interaction of Flexible Structure Conference*, Huntsville, AL, NASA Conference Publication 2467 Part 1, pp. 133–174.

Huston, R. L., 1990, *Multibody Dynamics*, Butterworth-Heinmann, Boston.

Kane, T. R., and Levinson, D. A., 1985, *Dynamics, Theory and Application*, McGraw-Hill, New York.

Levinson, D. A., and Kane, T. R., 1983, "Docking of a Spacecraft with an Unrestrained Orbiting Structure," *The Journal of the Astronautical Sciences*, Vol. 31, No. 1, pp. 23–48.

Rhody, B. J., Heppler, G. R., and Golnaraghi, M. F., 1993, "Modeling the Dynamics of Mass Captured by a Single Flexible Link," *Proceedings of the 2nd International Conference on Dynamics and Control of Structures in Space*, Cranfield, England, pp. 121–137.

Strang, G., 1980, *Linear Algebra and its Application*, Academic Press, New York.

M. W. Hilburger
Ph.D. Candidate.

A. M. Waas[1]
Associate Professor.

Department of Aerospace Engineering,
University of Michigan,
Ann Arbor, MI 48109-2118

J. H. Starnes, Jr.
Head, Structural Mechanics Branch,
NASA Langley Research Center,
Hampton, VA

Modeling the Dynamic Response and Establishing Post-buckling/Post Snap-thru Equilibrium of Discrete Structures via a Transient Analysis

Results of a transient analysis developed to model the dynamic response and establish post-buckling/post snap-thru equilibrium of discrete structures are presented. Three systems that exhibit unstable buckling characteristics are analyzed. The analysis consisted of first statically loading the structures up to there respective static limit loads. The structure is then perturbed from their critical state and a transient analysis is used to model the ensuing dynamic response. The transient formulation is first applied to two simple one-degree-of-freedom systems consisting of rigid links, springs, dampers, and lumped masses. The first of these systems was an arch with a point load applied at its vertex. This structure admits dynamic snap-thru response when loaded beyond its limit load. The second system was a model of a curved panel under an applied axial end-shortening. This system exhibited dynamic buckling behavior consisting of a large decrease in the resultant axial load when loaded beyond its limit load. The transient analysis was then applied to a finite element model of a cylindrical shell with a cutout under an applied axial compression load to model the dynamics of the global buckling response upon reaching its limit load. The results from this study illustrate the usefulness of the transient analysis in modeling the dynamics of an unstable structural response and establishing equilibrium beyond any points of instability.

Introduction

The analysis of structures that admit an unstable buckling or snap-thru response can be a difficult task. Many of these structures have the added complication of clustered bifurcation points. A transient analysis, i.e., one that incorporates dynamic effects during the transition from one equilibrium state to another, offers a novel approach to solving problems associated with unstable equilibrium points. Throughout this text, the terminology used is similar to that described in standard texts on Elastic Stability Theory, such as Brush and Almroth (1974). Many structures are designed to operate in the post-buckled state such as the skin of aircraft wings or fuselage. Often during flight, these structures experience compressive loads, and thus their buckling response characteristics must be considered in the design process. Current methods of numerical nonlinear static analysis are sufficient in modeling the response of many structures, even some that exhibit unstable buckling, despite the fact that when the structure undergoes unstable buckling a significant amount of kinetic energy is associated with the transition from one equilibrium state to another. By unstable buckling, we mean situations that correspond to an unstable equilibrium path immediately beyond buckling, or a maximum load point. Thus, bifurcation buckling with a corresponding negative slope in the initial post-buckling response as well as limit load instabilities fall into this category. In some cases of unstable buckling, difficulties can arise when a purely static approach is adopted. In these instances, a transient analysis can be used to supplement the inherent static approach. When such a combination is adopted, it becomes a convenient and useful tool for the determination of the load carrying capacity of the structure, a task that may be prohibitive if only a static approach is adopted.

The recent focus on the development of a transient analysis as described in Riks and Rankin (1994) and Rankin et al. (1996) was driven by the need for an analysis technique that could locate the post-buckled equilibrium solutions of complex structures that have clustered bifurcation points. Their work was motivated by the fact that the standard "arc length" method (Riks, 1972) used in many finite element routines failed to converge to any equilibrium solutions beyond the limit load of these structures. This failure is due to the degenerative nature of the solution beyond the limit load since, in the post-buckled regime, several closely spaced bifurcation equilibrium paths are encountered. In some cases, the finite element routine may provide solutions beyond the limit load, but this does not guarantee convergence onto the correct equilibrium path. The response of a cylindrical shell subjected to an axial compression load is a good example of a structure that has these characteristics. Thus, the essence of the solution technique proposed and demonstrated herein, consists of first carrying out a static analysis of a particular structure up to an unstable equilibrium point. Then, a perturbation is applied to the structure at this point. The damped equations of motion associated with the dynamic response triggered by the perturbations are next solved and the large time response of the structure is sought. Over time the structural damping dissipates the kinetic energy in the system and a new stable equilibrium position is obtained. The analysis

[1] To whom all correspondence should be addressed.

Contributed by the Applied Mechanics Division of THE AMERICAN SOCIETY OF MECHANICAL ENGINEERS for publication in the ASME JOURNAL OF APPLIED MECHANICS.

Discussion on the paper should be addressed to the Technical Editor, Professor Lewis T. Wheeler, Department of Mechanical Engineering, University of Houston, Houston, TX 77204-4792, and will be accepted until four months after final publication of the paper itself in the ASME JOURNAL OF APPLIED MECHANICS.

Manuscript received by the ASME Applied Mechanics Division, Dec. 12, 1995; final revision, March 10, 1997. Associate Technical Editor: S. Kyriakides.

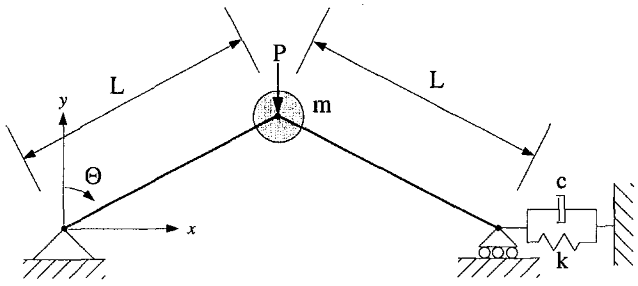

Fig. 1 Model 1: simple arch

associated with the motion of the structure from one equilibrium position to another is referred to as a *transient analysis.*

The present paper focuses on the details of such a transient analysis that has been developed to aid in establishing post-buckled/post snap-thru equilibrium of structures that exhibit unstable response characteristics when loaded beyond there limit loads. The transient analysis alleviates solution problems associated with structures that have clustered bifurcation points. This paper utilizes two simple one-degree-of-freedom systems made up of rigid links, springs, dampers, and lumped masses to illustrate the transient analysis and is then extended to a finite element format to model the dynamic collapse of a cylindrical shell.

Model and Analysis Description

One-Degree-of-Freedom Systems.

Snap-thru of an Arch. The first system modeled the dynamic snap-thru response of an arch with a vertically aligned point load applied at its vertex. The arch was modeled with a simple one-degree-of-freedom system made up of two rigid links, a lumped mass, a spring and a damper (see Fig. 1). The lumped mass represents the mass of the structure while the spring provides stiffness to the system and the damper provides structural damping during the dynamic response. The equations of motion were developed using the modified form of Lagrange's equations to include damping. Let $\mathcal{L}$ denote the *Lagrangian* for a discrete system defined by

$$\mathcal{L} \triangleq \mathcal{C} - \mathcal{V}, \tag{1}$$

where $\mathcal{C}$ and $\mathcal{V}$ denote the *kinetic* and *potential energy* of the system, respectively. Let $\mathbf{y}$ denote the *solution vector,* ϕ_i and λ_i denote the ith *constraint equation* and the ith *Lagrange Multiplier,* respectively. Let $\mathcal{F}$ denote *Rayleigh's Dissipation Function* defined as follows:

$$\mathcal{F} \triangleq \frac{1}{2} \sum_{i=1}^{n} \sum_{j=1}^{n} c_{ij} \dot{y}_i \dot{y}_j, \tag{2}$$

where c_{ij} denotes the *damping matrix* and $\dot{y}_i$ and $\dot{y}_j$ denote the *velocity components* associated with the respective degrees of

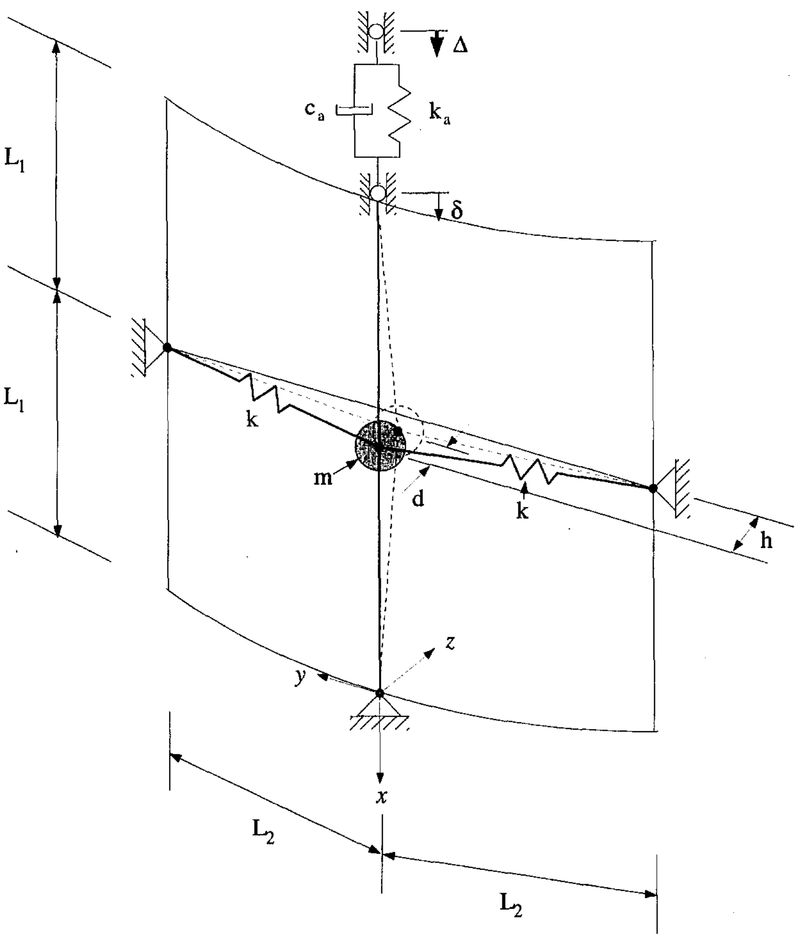

Note: 1) ----- denotes deformed configuration
2) some elements left out for clarity

Fig. 2 Model 2: curved panel

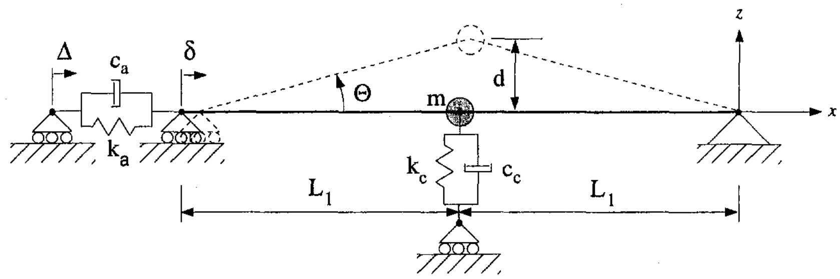

Note: ---- denotes deformed configuration

Fig. 3 Modified version of model 2

freedom. Then the *modified form of Lagrange's equations of motion* are given by Greenwood (1988)

$$\frac{\partial}{\partial t}\left(\frac{\partial \mathcal{L}}{\partial \dot{\mathbf{y}}}\right) - \frac{\partial \mathcal{L}}{\partial \mathbf{y}} + \frac{\partial \mathcal{F}}{\partial \dot{\mathbf{y}}} + \sum_{i=1}^{n} \lambda_i \frac{\partial \phi_i}{\partial \mathbf{y}} = \mathbf{0}. \tag{3}$$

The first step of the analysis consists of solving for the static, pre snap-thru response of the structure by neglecting the acceleration and velocity components in Eq. (3). The static equilibrium equations for a discrete system under load control where the *load P* is prescribed can be represented by

$$\mathbf{R}_s(P, \mathbf{y}) = 0. \tag{4}$$

The subscript s signifies the static state. For a simple one-degree-of-freedom system it is sufficient to use an incremental solution technique in which P is increased and the static equilibrium equations, (4), are solved iteratively at each step. To do this in the present study, a nontrivial, kinematically admissible initial guess of the solution was made and then a Newton-Raphson method was used to correct the solution until a suitable convergence was met. When possible, the algorithm used the previous step's solution as the initial guess to the current solution. The Hessian (stability) matrix and the load versus end-shortening (Δ) response was monitored at each step to identify the critical load (P_{cr}) of the structure. That is, P_{cr} is obtained when the condition $H(y, P_{cr}) = 0$ where H denotes the determinant of the Hessian, associated with the system of static equations. Let the solution of (4) at $P = P_{cr-}$ be denoted by $\mathbf{y}^*$, then by definition

$$\mathbf{R}_s(P_{cr-}, \mathbf{y}^*) = 0 \tag{5}$$

where P_{cr-} is the value of P just below P_{cr}. To initiate the transient analysis, the system is perturbed from a state as defined in (5). In the case of a load control problem, the perturbation is in the form of an incremental increase in the load P. Let $P = P_{cr-} + dP$, where dP is a perturbation to the load parameter as seen in Fig. 5. Note that, $P_{cr-} + dP > P_{cr}$. Due to the perturbation, the solution vector $\mathbf{y}$ becomes $\mathbf{y}(t) = \mathbf{y}^* + \mathbf{w}(t)$, where $\mathbf{w}(t)$ is the perturbation to $\mathbf{y}(t)$ as a result of dP. Then (3) can be represented by

$$\mathbf{R}_d(P_{cr-} + dP, \mathbf{y}(t)) = 0 \tag{6}$$

where the subscript d signifies a dynamic state and the solution vector $\mathbf{y}$ is now a function of time. To model the dynamic response, (6) is cast as an equivalent first-order system (Brenan et al., 1975) and solved using a standard time integration scheme. Note that, with the addition of the incremental load, the system is no longer in equilibrium for $\mathbf{y}(t) = \mathbf{y}^*$. Thus, for the system to regain equilibrium at the prescribed load ($P_{cr-} + dP$), it moves via a dynamic jump path (signified by $\mathbf{w}(t)$) to a new stable equilibrium configuration (see Fig. 5).

Buckling of a Curved Panel. The second system is representative of the buckling of a curved panel under an applied axial end shortening. A simple one-degree-of-freedom representation of the curved panel consisted of a lumped mass, rigid links, springs, and dampers as seen in Fig. 2. The curvature of the panel is changed by varying the height h. At an h of zero, the representation reduces to that of a flat plate. Let k_a and k denote the *axial* and *circumferential stiffness* of the system, respectively, and let Δ denote the *applied end-shortening* of the system, as indicated in Fig. 2.

Although this system appears more complicated than the arch model, it is still a one-degree-of-freedom system. The circumferential springs in Fig. 2 can be collapsed down into one spring of stiffness k_c as shown in Fig. 3 where

$$k_c = k\,\frac{L_2 - \sqrt{L_2^2 + hL_1 \sin a_1 + (L_1 \sin \Theta_1)^2}}{(L_1 \sin \Theta_1)^2}. \tag{7}$$

The analysis of the curved panel model followed a similar routine used for the arch model. The first step was to solve for the

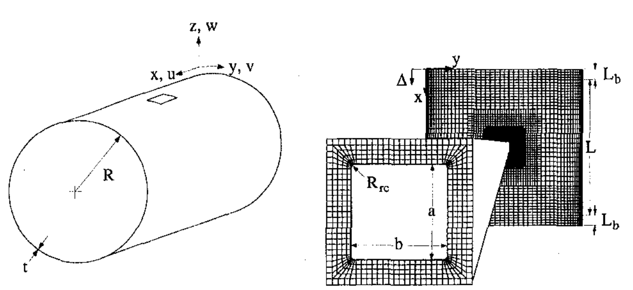

Fig. 4 Geometry and mesh for the finite element model of a cylinder with a cutout

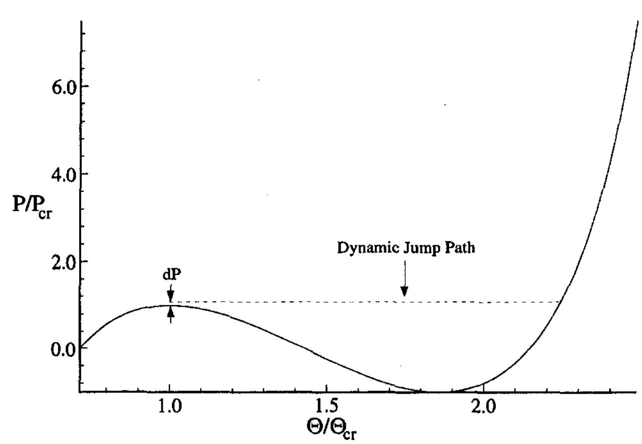

Fig. 5 Load versus theta curve for model 1 illustrating the dynamic jump path

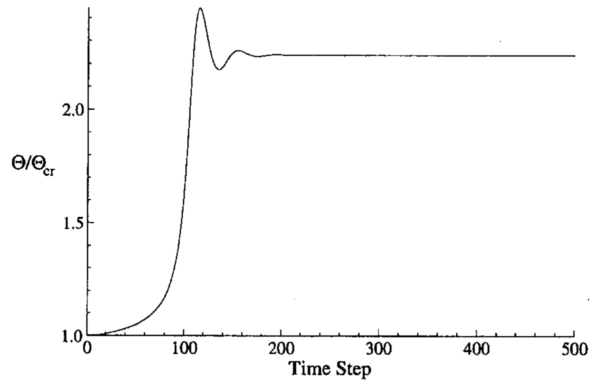

Fig. 6 Theta versus time step for model 1 during snap-thru

static pre-buckling response of the system by neglecting all acceleration and velocity terms in Eq. (3). The static equilibrium equations for a system under displacement control can be represented by

$$\mathbf{R}_s(\Delta, \mathbf{y}) = 0 \tag{8}$$

where Δ is the applied end-shortening and the subscript s denotes the static state. A similar iterative solution technique as for the arch problem is used where Δ is increased and the static equilibrium Eq. (8) is solved at each step. The Hessian (stability) matrix was monitored to determine at what critical displacement Δ_{cr} the structure loses stability. That is, Δ_{cr} is obtained when the condition $H(y, \Delta_{cr}) = 0$, where H denotes the determinant of the Hessian, associated with the system of static equations and P denotes the resultant axial load on the panel. Let the solution of (8) at $\Delta = \Delta_{cr-}$ be denoted by $\mathbf{y}^*$, then by definition,

$$\mathbf{R}_s(\Delta_{cr-}, \mathbf{y}^*) = 0 \tag{9}$$

where Δ_{cr-} is the value of the end shortening Δ just below the critical end-shortening Δ_{cr}. The transient analysis is initiated by applying a perturbation to the system at a state defined by (9). For the displacement control problem, the perturbation is in the form of an incremental increase in the end shortening Δ. Let $\Delta = \Delta_{cr-} + d\Delta$, where $d\Delta$ is a perturbation to the end-shortening as seen in Fig. 7. Note that $\Delta_{cr-} + d\Delta > \Delta_{cr}$. The perturbation is applied to the system at $\mathbf{y} = \mathbf{y}^*$. Due to the perturbation, $\mathbf{y}$ becomes $\mathbf{y}(t) = \mathbf{y}^* + \mathbf{w}(t)$, where $\mathbf{w}(t)$ is the perturbation to $\mathbf{y}(t)$ as a result of $d\Delta$. Then Eq. (3) can be written

$$\mathbf{R}_d(\Delta_{cr-} + d\Delta, \mathbf{y(t)}) = 0 \tag{10}$$

where the subscript d signifies the dynamic state of the system and $\mathbf{y}$ is a function of time. To model the dynamic response, (10) is cast as an equivalent first-order system (Brenan et al., 1995) and is solved using a standard time integration scheme. With the addition of the perturbation $d\Delta$, the system is no longer in equilibrium for $\mathbf{y}(t) = \mathbf{y}^*$. Thus, for the system to regain equilibrium at the prescribed end-shortening ($\Delta_{cr-} + d\Delta$), it moves via a dynamic jump path (signified by $\mathbf{w}(t)$) to a new stable equilibrium configuration (see Fig. 7).

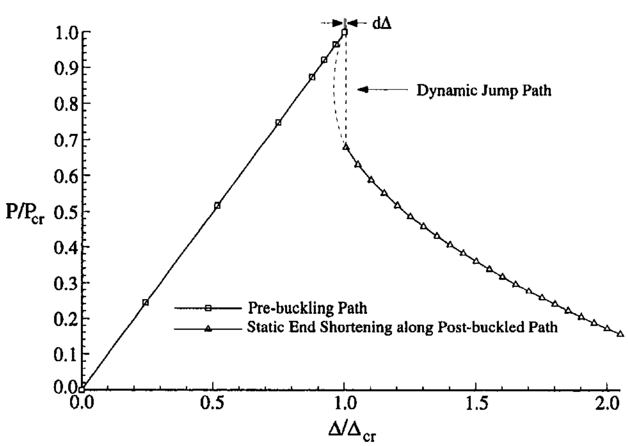

Fig. 7 Load end-shortening response curve for model 2 illustrating the dynamic jump

Finite Element Model. A circular cylinder with a rectangular cutout under an applied axial compressive load was modeled using the STAGS finite element code. More details about STAGS can be found in Brogan et al. (1994). The finite element mesh was created via a user written subroutine that worked in conjunction with the STAGS code (see Fig. 4). The cylindrical shell analyzed in this paper has a circular cross section with a radius R = 20.32 cm (8.0 in.) and length L = 35.56 cm (14.0 in.) as seen in Fig. 4. The centrally located cutout is 2.54 cm by 2.54 cm (1.0 in. by 1.0 in.) with re-entrant corners of radius R_{rc} = 0.127 cm (0.05 in.) as seen in Fig. 4. Clamped boundary conditions were used for the cylinder model. In the model, the v and w degrees-of-freedom were set to zero in a region extending a length L_p = 2.54 cm (1.0 in.) on each end. These conditions were imposed in an attempt to model similar clamped boundary conditions proposed for experimental testing. The bottom of the cylinders were then held fixed while the axial compressive load was applied via a prescribed end shortening Δ as shown in Fig. 4. The cylinder wall is an eight-ply laminate with a stacking sequence of $[\pm 45/0/90]_s$. The thickness of each ply is nominally 0.0127 cm (0.005 in.) giving the laminate a total thickness of t = 0.1016 cm (0.04 in.). The lamina properties were as follows: longitudinal modulus E_1 = 127.8 GPa (18.5 Mpsi), transverse modulus E_2 = 11.0 GPa (1.6 Mpsi), in-plane shear modulus G_{12} = 5.7 GPa (0.832 Mpsi), and a major Poisson's ratio ν_{12} = 0.35. Here we have adopted commonly used notation for continuous fiber laminates as discussed in Jones (1975).

The general form of the equations for a discretized structure in a finite element code is

$$[M]\{\ddot{u}(t)\} + [C]\{\dot{u}(t)\} + \{f(\lambda, u(t))\} = 0 \tag{11}$$

where M is the mass matrix, C is the damping matrix, $u(t)$ is the matrix of nodal displacements, and $f(\lambda, u(t))$ is a set of nonlinear functions of the nodal degrees-of-freedom and load parameter, λ, that describe the internal stiffness and external loads. Thus, it follows that the tangent stiffness matrix, K =

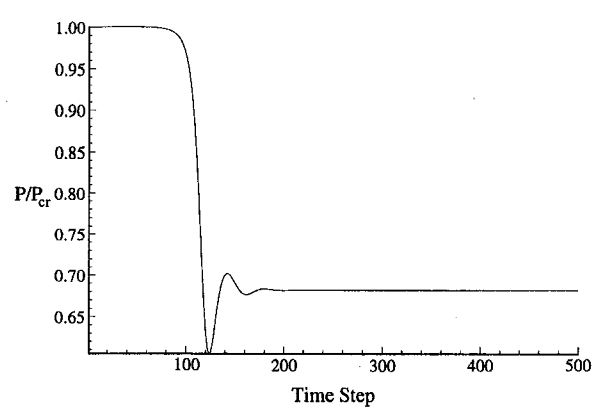

Fig. 8 Load versus time step for model 2 during buckling

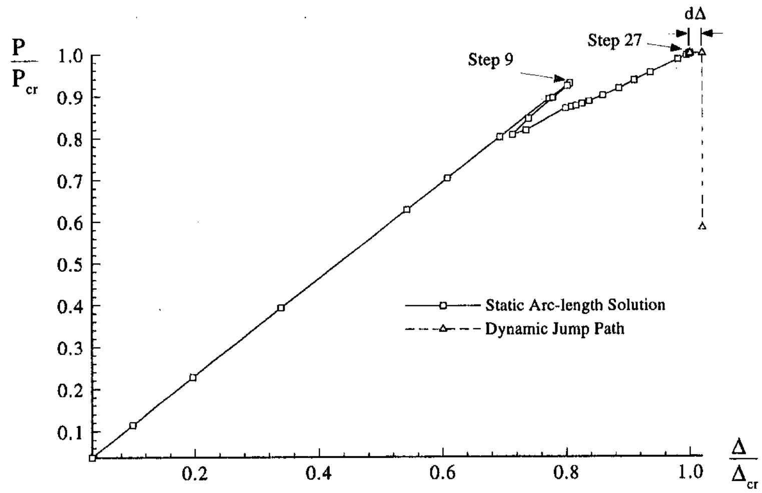

Fig. 9 Load versus end-shortening response of cylinder model

$(\partial f / \partial u)$. A dot above a variable denotes a derivative with respect to time. In the context of this displacement control problem, λ is the applied end-shortening as seen in Fig. 4. A similar analysis format used in the one-degree-of-freedom systems is extended to the finite element model. The static, prebuckling response of the cylinder was sought by neglecting the acceleration and velocity terms found in (11) producing the equilibrium equations

$$f(\Delta, u) = 0. \tag{12}$$

Equation (12) is solved using a standard arc length method under displacement control. This is carried out until an unstable equilibrium point is identified. STAGS identifies an unstable equilibrium point when a negative root appears in the tangent stiffness matrix. Let Δ_{cr-} denote a value of end-shortening at the last solution step before the step that admits the first negative root in the tangent stiffness matrix. At this point the static solution is stopped and the transient analysis begins where the static solution left off. The transient analysis is initiated by applying a perturbation in the form of an incremental increase in the applied end shortening $d\Delta$ to the cylinder while holding the resultant load state in the cylinder constant. Equation (11) then becomes

$$[M]\{\ddot{u}(t)\} + [C]\{\dot{u}(t)\} + \{f(\Delta_{cr-} + d\Delta, u(t))\} = 0. \tag{13}$$

Once perturbed, the cylinder will dynamically move towards its new equilibrium configuration. To model the dynamic collapse of the cylinder, Eq. (13) is solved using a time-step integrater provided in STAGS. Rayleigh's proportional damping of the form

$$[C] = \alpha[M] + \beta[K] \tag{14}$$

is used in STAGS where α and β are mass and stiffness damping factors, respectively. Assuming the response will be dominated by one frequency, α and β can be calculated from the following:

$$\alpha = 2\pi\nu\zeta$$
$$\beta = \frac{\zeta}{2\pi\nu} \tag{15}$$

where ν is the lowest frequency obtained from a linear vibration analysis and ζ is the fraction of critical damping with values ranging from 0.05 to 0.2. It was found that for the initial stages of the transient analysis setting $\zeta = 0.05$ and setting $\beta = 0$ in Eq. (15) allowed for rapid growth in the kinetic energy of the system. Once it was determined that the motion was well developed, $\zeta = 0.15$ was used in Eq. 15 for α and β. The kinetic energy of the system was monitored throughout the analysis. Once the kinetic energy dissipated, the transient analysis was terminated and the new equilibrium configuration obtained.

Results

The first model studied successfully produced the dynamic snap-thru response of an arch under load control, and demonstrated the ability to establish post snap-thru equilibrium via a transient analysis. As seen in Fig. 5, with the onset of a perturbation of the form dP with the system at its critical configuration, the structure moved dynamically towards a new equilibrium position. With the aid of structural damping, the kinetic energy was removed from the system over time and the new post snap-thru equilibrium configuration was established as seen in Fig. 6.

The second model studied successfully produced the dynamic buckling response similar to that of a curved panel under displacement control, and demonstrated the ability to establish a stable post-buckling equilibrium configuration via a transient analysis. A seen in Fig. 7, when a perturbation of the form $d\Delta$

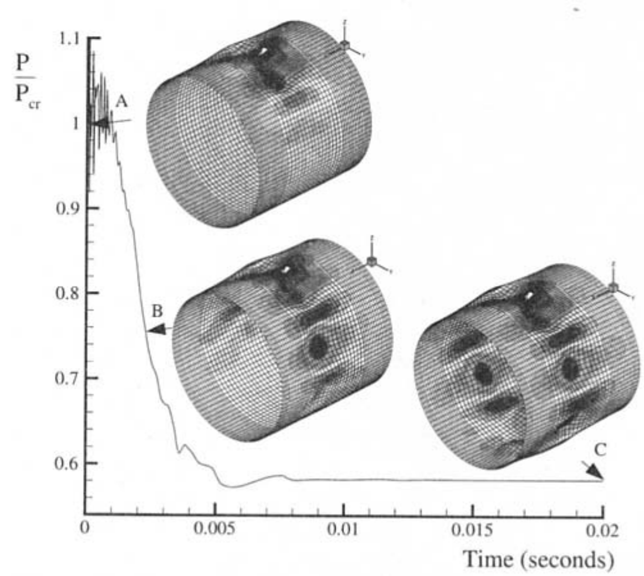

Fig. 10 Load versus time for the global collapse of the cylinder model

was added to the system at an unstable equilibrium point, the structure moved dynamically towards a new stable equilibrium position. As before, structural damping was used to remove the kinetic energy in the system and establish the new post-buckled equilibrium configuration as seen in Fig. 8. Once post-buckling equilibrium was established, the structure was then loaded statically in order to obtain additional results corresponding to the post-buckled equilibrium response as seen in Fig. 7.

The cylinder model (STAGS analysis) was loaded statically producing a load-shortening response curve as seen in Fig. 9. The first unstable equilibrium point identified in the solution (point 9 in Fig. 9) corresponded to a local buckling phenomena as evident by the distinct cusp in the load end-shortening curve. The local buckling response is due to the existence of the cutout. In this case the arc-length method was able to map out the unstable local response of the cylinder. It must be noted that if the end-shortening is increased beyond the value corresponding to step 9, then the cylinder will dynamically jump to the post-buckled equilibrium path below. While this possibility exists, and was investigated, it is not included in the discussion since the numerical static solver was able to proceed without any numerical difficulty beyond this point. Our focus was confined to those situations where the static approach failed to yield a converged solution, as was the case when the cylinder approached the collapse load (point 27 in Fig. 9). Thus, the static loading continued until the global collapse load was reached and the transient analysis was implemented. The axial load history during the collapse of the cylinder is shown in Fig. 10. For the first 0.002 seconds the load oscillates rapidly with large amplitude. The high-frequency oscillations are expected for such a structure, but the large amplitude of the oscillations is mainly due to the fact that there was no damping applied in the initial stages of the transient analysis. Once damping was applied at around 0.001 seconds, the amplitude of the oscillations decreased. At point A on the load history curve, the deformation of the cylinder is local to the cutout. During the collapse of the cylinder the deformations become more wide spread as seen at point B. Once the kinetic energy of the cylinder has completely dissipated, the global collapse mode is obtained as seen at point C on the load history.

Concluding Remarks

The details of a transient analysis has been presented and then used to establish post-buckling/post snap-thru equilibrium of three selected discrete structural systems. The results obtained have shown that the transient analysis is effective in establishing the correct post-buckling or post-snap through equilibrium path for the systems studied under either load control or displacement control loading. In the current paper, via some simple one-degree-of-freedom systems, the effectiveness and the methodology of the transient analysis has been demonstrated. The extension of the transient analysis was then made to the STAGS finite element code to demonstrate the effectiveness of this method on the analysis of a composite laminated cylinder, containing a rectangular cutout and subjected to an axial compression load. In addition to being a useful technique in solving problems of the type discussed here, the transient analysis models the true dynamic nature of the response of a structure at an unstable equilibrium point and follows the evolution of the response as a function of time as seen in the collapse of the cylinder.

Acknowledgments

The authors are grateful for the financial support from Graduate Student Researchers Program at NASA Langley, Grant NGT-51256. The authors are also grateful for the constructive criticism of one of the reviewers.

References

Brenan, K. E., Campbell, S. L., and Petzold, L. R., 1996, "Numerical Solution of Initial-Value Problems in DAE's," *SIAM.*

Brogan, F. A., Rankin, C. C., and Cabiness, H. D., 1994, "STAGS User Manual," Lockheed Palo Alto Research Laboratory, Report LMSC P032594.

Brush, D., and Almroth, B., 1974, *Buckling of Bars, Plates, and Shells,* McGraw-Hill, New York.

Greenwood, D. T., 1988, *Principles of Dynamics,* Prentice-Hall, Englewood Cliffs, NJ.

Jones, R. M., 1975, *Mechanics of Composite Materials,* McGraw-Hill, New York.

Rankin, C. C., Riks, E., and Brogan, F. A., 1996, "On the solution of mode jumping phenomena in the thin-walled shell structures," *Computer Methods in Applied Mechanics and Engineering,* Vol. 136, pp. 59–92.

Riks, E., 1972, "The Application of Newton's Method to the Problem of Elastic Stability," ASME Journal of Applied Mechanics, Vol. 39, pp. 1060–1066.

Riks, E., and Rankin, C. C., 1974, "Computer Simulation of Dynamic Buckling Phenomena Under Quasi static Loads," in final program and abstracts, Euromech Colloquium 317, Mar. 21–23, Liverpool, UK.

Critical Velocities of a Harmonic Load Moving Uniformly Along an Elastic Layer

H. A. Dieterman
Delft University of Technology,
Faculty of Civil Engineering,
Stevinweg 1,
2628 CN Delft, Holland

A. Metrikine[1]
Mechanical Engineering Institute,
Russian Academy of Sciences,
Nizhny Novgorod, Russia

The critical (resonance) velocities of a harmonically varying point load moving uniformly along an elastic layer are determined as a function of the load frequency. It is shown that resonance occurs when the velocity of the load is equal to the group velocity of the waves generated by the load. The critical depths of the layer are determined as function of the load velocity in the case the load frequency is proportional to the load velocity. This is of importance for high-speed trains where the loading frequency of the train wheel excitations is mainly determined by the ratio between the train velocity and the distance between the sleepers (ties). It is shown that the critical depths are decreasing with increasing train velocity. It is concluded that the higher the train velocity, the more important are the properties of the ballast and the border between the ballast and the substrate.

1 Introduction

With the development of high-speed trains it is necessary to take into account the wave processes in the railroad track and the supporting soil due to the train. Important for practice are so-called critical regimes of the train motion when the amplitude of the track vibrations increases significantly. If the vibrations of the train wheels are negligible, the critical regime is determined by the velocities of the train near the Rayleigh wave velocity in the subsoil (Cole and Huth, 1958; Lansing, 1965; Payton, 1967; Miklowitz, 1978; Dieterman and Metrikine, 1996). But as measurements show (Kjorling, 1993), the excitations at the sleepers become significant for high-speed trains and to predict the critical velocities it is necessary to investigate the motion of a harmonic load along the track. There are many investigations devoted to this problem (Fryba, 1972; Bogacz et al., 1989; Dean, 1990; Vesnitsky and Metrikine, 1993; Knothe and Grassie, 1993; Metrikine, 1994); however, most of them are dealing with one-dimensional models for the track.

In the present paper we model the track-supporting ballast as an elastic layer and the train-sleeper excitation as a uniformly moving harmonically varying point load. The choice of an elastic layer model for the ballast is given by the following reasoning. Despite the wave guide nature of the ballast, the resonance will be mainly in the vertical direction due to the reflections at the transition of the ballast and the supporting soil.

We define the critical velocities as the load velocities at which a steady-state amplitude of the layer vibrations is infinite. The resonance is not only derived at the point of loading, so it is not related to the point character of the load. It is shown that resonance occurs when the velocity of the load is equal to the group velocity of the waves generated by the load. The critical velocities are determined as a function of the load frequency for a Poisson's ratio of the layer $\nu = 0.3$. Since the main frequency of a train wheel excitation is determined as the ratio of the train velocity and the distance between the centers of the sleepers (Kjorling, 1993), the critical depths of the layer can be determined as a function of the train velocity. From the analysis it is concluded that the higher the train velocity, the more important are the properties of the ballast and the character of the border between ballast and the substrate.

2 Model and Governing Equations

Let a harmonically varying concentrated load of amplitude P and frequency Ω be applied normally to the surface of an elastic layer and be moved along a straight line at a constant velocity V as shown in Fig. 1. The equations of the layer motion read as

$$\mu\nabla^2\mathbf{u} + (\lambda + \mu)\nabla(\nabla\mathbf{u}) = \rho\frac{\partial^2\mathbf{u}}{\partial t^2}, \tag{1}$$

where $\mathbf{u}(x, y, z, t) = (U_1(x, y, z, t), U_2(x, y, z, t), U_3(x, y, z, t))$ is the vectorial displacement, λ and μ are Lamés constants for the elastic layer, and ρ its mass density.

Assuming that the layer is fixed at the bottom and free at the top, regardless the loading point, we have the following boundary conditions at $z = 0$ (the bottom) and at $z = -H$ (the top)

$$\mathbf{u}(x, y, 0, t) = 0, \tag{2}$$

$$\tau_{xz}(x, y, -H, t) = \tau_{yz}(x, y, -H, t) = 0, \tag{3a}$$

$$\sigma_{zz}(x, y, -H, t) = -\mathrm{P}e^{-i\Omega t}\delta(y)\delta(x - Vt), \tag{3b}$$

where $\sigma_{zz}(x, y, z, t)$ is the normal stress, $\tau_{xz}(x, y, z, t)$ and $\tau_{yz}(x, y, z, t)$ are the shear stresses, H is the depth of the layer, and $\delta(\ldots)$ is the delta function. As shown by Lamb (1904), the equations of motion for the layer (1) are satisfied by letting

$$U_1 = \frac{\partial\varphi}{\partial x} + \frac{\partial^2\psi}{\partial x\partial z}$$

$$U_2 = \frac{\partial\varphi}{\partial y} + \frac{\partial^2\psi}{\partial y\partial z}$$

$$U_3 = \frac{\partial\varphi}{\partial z} + \frac{\partial^2\psi}{\partial z^2} - \frac{1}{c_t^2}\frac{\partial^2\psi}{\partial t^2}, \tag{4}$$

provided that two so-called stress functions $\varphi(x, y, z, t)$ and $\psi(x, y, z, t)$ are solutions of the three-dimensional wave equations

[1] On post-doctoral leave at the Faculty of Civil Engineering, Delft University of Technology.

Contributed by the Applied Mechanics Division of THE AMERICAN SOCIETY OF MECHANICAL ENGINEERS for publication in the ASME JOURNAL OF APPLIED MECHANICS.

Discussion on the paper should be addressed to the Technical Editor, Professor Lewis T. Wheeler, Department of Mechanical Engineering, University of Houston, Houston, TX 77204-4792, and will be accepted until four months after final publication of the paper itself in the ASME JOURNAL OF APPLIED MECHANICS.

Manuscript received by the ASME Applied Mechanics Division, Mar. 10, 1995; final revision, Dec. 27, 1996. Associate Technical Editor: D. M. Barnett.

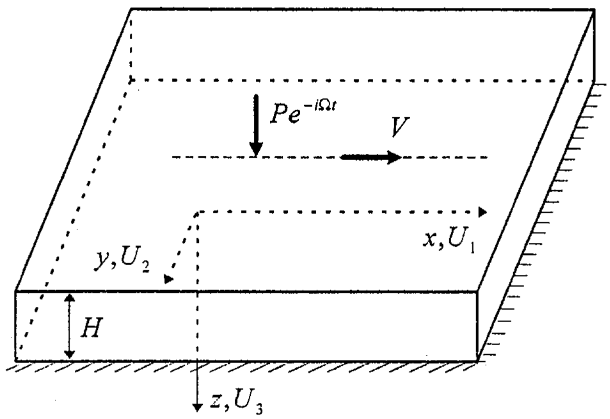

Fig. 1 Reference system and loading

$$\nabla^2\varphi = \frac{1}{c_l^2}\frac{\partial^2\varphi}{\partial t^2} \quad (5)$$

$$\nabla^2\psi = \frac{1}{c_t^2}\frac{\partial^2\varphi}{\partial t^2} \quad (6)$$

in which $c_l = \sqrt{(\lambda + 2\mu)/\rho}$ is the velocity of the compressional waves (P-waves) and $c_t = \sqrt{\mu/\rho}$ is the velocity of the shear waves (S-waves). In terms of these stress functions the normal stress σ_{zz} becomes

$$\sigma_{zz} = \frac{\lambda}{c_l^2}\frac{\partial^2\varphi}{\partial t^2} + 2\mu\left(\frac{\partial^2\varphi}{\partial z^2} + \frac{\partial^3\psi}{\partial z^3}\right) - 2\rho\frac{\partial^3\psi}{\partial z\partial t^2} \quad (7)$$

and the shear stresses τ_{xz} and τ_{yz} become

$$\tau_{xz} = 2\mu\left(\frac{\partial^2\varphi}{\partial x\partial z} + \frac{\partial^3\psi}{\partial x\partial z^2}\right) - \rho\frac{\partial^3\psi}{\partial x\partial t^2} \quad (8)$$

$$\tau_{yz} = 2\mu\left(\frac{\partial^2\varphi}{\partial y\partial z} + \frac{\partial^3\psi}{\partial y\partial z^2}\right) - \rho\frac{\partial^3\psi}{\partial y\partial t^2}. \quad (9)$$

3 Steady-State Displacements

The general expression for the steady-state displacements of the layer can be derived by applying exponential Fourier transforms over time and spatial coordinates x and y. We define these transforms as follows:

$$f(k_1, k_2, z, \omega) = \int_{-\infty}^{\infty}\int_{-\infty}^{\infty}\int_{-\infty}^{\infty}\varphi(x, y, z, t) \times \exp\{i(\omega t - k_1x - k_2y)\}dtdxdy$$

$$g(k_1, k_2, z, \omega) = \int_{-\infty}^{\infty}\int_{-\infty}^{\infty}\int_{-\infty}^{\infty}\psi(x, y, z, t) \times \exp\{i(\omega t - k_1x - k_2y)\}dtdxdy. \quad (10)$$

Application of the integral transforms (10) on the governing Eqs. (1)–(3), using the expressions (4)–(9), the following system of equations results:

- For the equations of the layer motion,

$$\frac{\partial^2 f}{\partial z^2} + \left(\frac{\omega^2}{c_l^2} - k_1^2 - k_2^2\right)f = 0$$

$$\frac{\partial^2 g}{\partial z^2} + \left(\frac{\omega^2}{c_t^2} - k_1^2 - k_2^2\right)g = 0. \quad (11)$$

- For the boundary conditions at $z = 0$,

$$f + \frac{\partial g}{\partial z} = 0$$

$$\frac{\partial f}{\partial z} + \frac{\partial^2 g}{\partial z^2} + \frac{\omega^2}{c_t^2}g = 0 \quad (12)$$

- For the boundary conditions at $z = -H$,

$$2\mu\left(\frac{\partial f}{\partial z} + \frac{\partial^2 g}{\partial z^2}\right) + \rho\omega^2 g = 0 \quad -\frac{\omega^2\lambda}{c_l^2}f + 2\mu\left(\frac{\partial^2 f}{\partial z^2} + \frac{\partial^3 g}{\partial z^3}\right) + 2\rho\omega^2\frac{\partial g}{\partial z} = -2\pi P\delta(\omega - \Omega - k_1V). \quad (13)$$

The general solutions of the Eqs. (11) are

$$f = B_1(k_1, k_2, \omega)\sinh(zR_l) + B_2(k_1, k_2, \omega)\cosh(zR_l),$$
$$g = B_3(k_1, k_2, \omega)\sinh(zR_t) + B_4(k_1, k_2, \omega)\cosh(zR_t),$$
$$R_{l,t} = \sqrt{k_1^2 + k_2^2 - \omega^2/c_{l,t}^2}. \quad (14)$$

Substituting (14) into the boundary conditions (12)–(13) yields

$$B_2 + R_tB_3 = 0$$

$$R_lB_1 + R_t^2B_4 + \frac{\omega^2}{c_t^2}B_4 = 0$$

$$2\mu(R_lB_1\cosh(R_lH) - R_lB_2\sinh(R_lH) - R_t^2B_3\sinh(R_tH) + R_t^2B_4\cosh(R_tH)) + \rho\omega^2(-B_3\sinh(R_tH) + B_4\cosh(R_tH)) = 0$$

$$-\frac{\omega^2\lambda}{c_l^2}(-B_1\sinh(R_lH) + B_2\cosh(R_lH)) + 2\mu(-R_l^2B_1\sinh(R_lH) + R_l^2B_2\cosh(R_lH) + R_t^3B_3\cosh(R_tH) - R_t^3B_4\sinh(R_tH)) + 2\rho\omega^2(R_tB_3\cosh(R_tH) - R_tB_4\sinh(R_tH)) = -2\pi P\delta(\omega - \Omega - k_1V). \quad (15)$$

When solved for $B_i (i = 1 \,..\, 4)$ system (15) gives

$$B_i = \Delta_i/\Delta, \quad (16a)$$

where

$$\Delta = 4x^2R_lR_t\gamma + x^2(4R_l^2R_t^2 + \gamma^2)\sinh(R_lH)\sinh(R_tH) - R_lR_t(4x^4 + \gamma^2)\cosh(R_lH)\cosh(R_tH),$$
$$\Delta_1 = Tx^2(\gamma\sinh(R_tH) - 2R_lR_t\sinh(R_lH))\delta(\omega - \Omega - k_1V) = \Delta_{11}\delta(\omega - \Omega - k_1V),$$
$$\Delta_2 = TR_lR_t(\gamma\cosh(R_tH) - 2x^2\cosh(R_lH))\delta(\omega - \Omega - k_1V) = \Delta_{22}\delta(\omega - \Omega - k_1V),$$
$$\Delta_3 = TR_l(2x^2\cosh(R_lH) - \gamma\cosh(R_tH))\delta(\omega - \Omega - k_1V) = \Delta_{33}\delta(\omega - \Omega - k_1V),$$
$$\Delta_4 = TR_l(2R_lR_t\sinh(R_lH) - \gamma\sinh(R_tH))\delta(\omega - \Omega - k_1V) = \Delta_{44}\delta(\omega - \Omega - k_1V),$$
$$x^2 = k_1^2 + k_2^2, \quad \gamma = 2x^2 - \omega^2/c_t^2, \quad T = 2\pi P/\mu. \quad (16b)$$

In accordance with the representation (4), expressions (14), and solution (16a), the Fourier-images $\tilde{U}_n(k_1, k_2, z, \omega)$ of the layer displacements $U_n(x, y, z, t)$ are given as

$$\tilde{U}_1 = ik_1Q(k_1, k_2, z, \omega), \quad \tilde{U}_2 = ik_2Q(k_1, k_2, z, \omega), \quad (17a)$$

in which

$$Q = \frac{1}{\Delta}(\Delta_1 \sinh(zR_l) + \Delta_2 \cosh(zR_l) + R_t\Delta_3 \cosh(zR_t) + R_t\Delta_4 \sinh(zR_t))$$

and

$$\tilde{U}_3 = \frac{1}{\Delta}(R_l(\Delta_1 \cosh(zR_l) + \Delta_2 \sinh(zR_l)) + x^2(\Delta_3 \sinh(zR_t) + \Delta_4 \cosh(zR_t))). \quad (17b)$$

4 Critical Velocities of the Load

The critical velocities of the load as a function of the load frequency will now be determined. These velocities are defined as the load velocities at which a steady-state amplitude of the layer vibrations is infinite in all points of the layer (excluding the fixed plane $z = 0$). Thus the resonance is not related to the point character of the load.

We will prove that resonance occurs when the velocity of the load is equal to the group velocity of the waves generated by the load, i.e., the necessary condition for resonance can be mathematically formulated as

$$\left.\frac{d\omega}{d\mathbf{k}}\right|_{\mathbf{k}=\mathbf{k}^*} = \mathbf{V}, \quad (18)$$

where $\omega = \omega(k)$ is the dispersion relation for the layer (this relation is the solution of dispersion equation $\Delta(\omega, \mathbf{k}) = 0$ and Δ is determined by (16b)), $\mathbf{k} = (k_1, k_2)$, $\mathbf{V} = (V, 0)$, $\mathbf{k}^*$ is a wave vector of the radiated wave. Indeed, in accordance with (17), the expression for the amplitude of the layer vibrations in z-direction (for x and y-directions all arguments are the same) can be rewritten as

$$U_3(x, y, z, t) = \int_{-\infty}^{\infty}\int_{-\infty}^{\infty}\int_{-\infty}^{\infty} \frac{F(\omega, k_1, k_2, z)}{\Delta(\omega, k_1, k_2)} \exp\{-i(\omega t - k_1x - k_2y)\}\delta(\omega - \Omega - k_1V)d\omega dk_1dk_2$$
$$= \int_{-\infty}^{\infty}\int_{-\infty}^{\infty} \frac{F(\Omega + k_1V, k_1, k_2, z)}{\Delta(\Omega + k_1V, k_1, k_2)} \exp\{-i((\Omega + k_1V)t - k_1x - k_2y)\}dk_1dk_2, \quad (19)$$

where

$$F(\omega, k_1, k_2, z) = R_l(\Delta_{11} \cosh(zR_l) + \Delta_{22} \sinh(zR_l)) + x^2(\Delta_{33} \sinh(zR_t) + \Delta_{44} \cosh(zR_t)).$$

Now we will formulate a theorem for the determination of the critical velocities of the load.

Theorem. Consider the double-integral $I = \int_{-\infty}^{\infty}\int_{-\infty}^{\infty}(dxdy/D(x, y))$, where $D(x, y)$ is an analytical function and $(1/(D(x, y)))$ is integrable at infinity. The integral I diverges if there exists a real isolated root (x^*, y^*) of the equation $D(x, y) = 0$ for which $(\partial D/\partial x) = (\partial D/\partial y) = 0$ at $(x, y) = (x^*, y^*)$.

The proof of this theorem is given in the Appendix. The integrand in Eq. (19) satisfies all the conditions of the theorem. Its zeros are related to the zeros of R_l and R_t. The order of the zeros of the numerator and denominator of the integrand are of the same order as is easily shown by a Taylor series expansion. So, the integral (19) will be infinite when equation $\Delta(\Omega + k_1V, k_1, k_2) = 0$ has an isolated real pair of roots (k_1^*, k_2^*) for which

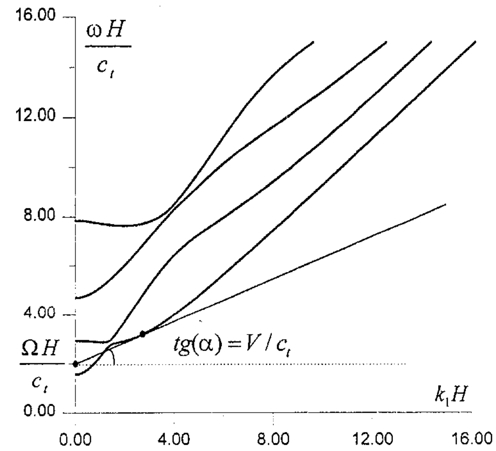

Fig. 2 Dispersion relations for four lowest modes

$$F(\Omega + k_1^*V, k_1^*, k_2^*, z) \neq 0 \quad \text{and} \quad \left.\frac{\partial\Delta}{\partial k_1}\right|_{\substack{k_1=k_1^*\\k_2=k_2^*}} = \left.\frac{\partial\Delta}{\partial k_2}\right|_{\substack{k_1=k_1^*\\k_2=k_2^*}} = 0.$$

The equation $\Delta = 0$ can be formulated as $\omega = \omega(\mathbf{k})$ and, consequently (expression Eq. $(a) \Leftrightarrow$ Eq. (b) means that Eq. (a) is equivalent to Eq. (b)):

$$\Delta(\Omega + k_1V, k_1, k_2) = 0 \Leftrightarrow \Omega + k_1V = \omega(\mathbf{k})$$
$$\frac{\partial\Delta}{\partial k_1} = 0 \Leftrightarrow V = \frac{\partial\omega}{\partial k_1}$$
$$\frac{\partial\Delta}{\partial k_2} = 0 \Leftrightarrow 0 = \frac{\partial\omega}{\partial k_2}.$$

Thus, the criterion of resonance is

$$\left.\frac{\partial\omega}{\partial k_1}\right|_{\substack{k_1=k_1^*\\k_2=k_2^*}} = V, \quad \left.\frac{\partial\omega}{\partial k_2}\right|_{\substack{k_1=k_1^*\\k_2=k_2^*}} = 0,$$

which is the same as Eq. (18).

Therefore we can use the criterion (18) to determine the critical velocities of the load. Due to the isotropy of the layer in the horizontal plane, $(\partial\omega/\partial k_2) = 0$ when $k_2 = 0$ and only for this value of k_2. Thus, to determine the critical velocities it is sufficient to solve the following set of equations:

$$\Delta(\omega, k_1, 0) = 0$$
$$\omega = \Omega + k_1V$$
$$\frac{\partial\omega}{\partial k_1} = V \quad (20)$$

where the first equation is the dispersion relation for the plane waves in the layer, travelling along the x-axis, the second equation reflects the equality of the phase of the vibrations of the moving load and the phase of the radiated waves at the point of loading and the third equation is the condition of the equality of the group velocity of the radiated waves and the load velocity.

The graphical solution of the system (20) is depicted in Fig. 2. The family of curves $\omega = \omega(k_1)$ shown, represent the dispersion relations for the four lowest modes of the layer vibrations and the straight line $\omega = \Omega + k_1V$ is the so-called "kinematic invariant," see Vesnitsky (1991) (in this paper this concept has been elaborated). Actually the kinematic invariant represents the Doppler effect of the moving harmonic load, i.e., the phase shift k_1V between the load frequency Ω and the radiated wave frequency ω. When this straight line is tangential to one of the dispersion curves, the group velocity $d\omega/dk_1$ of one of the radiated waves is equal to the velocity of the load V (the

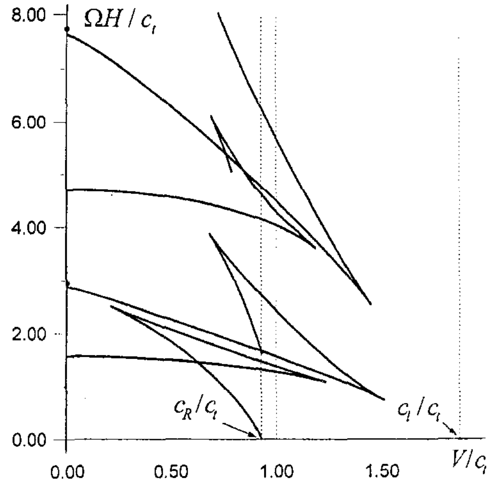

Fig. 3 Critical velocities

tangent of the angle between the kinematic invariant and k_1H-axis).

The frequencies and wave numbers of the radiated waves are determined by the coordinates of the cross points between the kinematic invariant and the dispersion curves. Thus, to obtain the critical velocities of the load as a function of the load frequency, we have to analyze the relation between the slope of the kinematic invariant at its tangential behavior with the dispersion curves and the coordinate of the cross point of the kinematic invariant and $\omega H/c_t$-axis.

The result of this analysis is shown in Fig. 3 for the Poisson's ratio of the layer $\nu = 0.3$. Each curve is related to a mode of the layer vibrations (we considered the four lowest modes). For example, the lowest curve is related to the first shear mode and at zero load velocity it gives the lowest layer eigenfrequency ($\pi/(2\tau_c)$, with $\tau_c = H/c_t$) for shear excitations, as is easily verified. Further we have the curves related to the first compressional, second shear, and third shear mode, respectively. The coupling of the modes in the layer (see Fig. 2 and Ewing et al. (1957)) leads to a nonmonotonous dependence of the group velocity on the wave number. For instance, for the first and third mode, the group velocity is increasing, than decreasing and increasing again with increasing wave number. It results in the self-crossings of the curves in Fig. 3 because a critical regime occurs as the load velocity is equal to the group velocity of radiated waves. For the second and the fourth modes additionally $d\omega/dk_1$ is smaller then zero for small wave numbers. This interval of wave numbers is bounded by the points with zero group velocity. It results in two critical frequencies for zero load velocity for each mode. The first one is equal to the layer eigenfrequency (the lowest eigenfrequency for compressional excitations for the second mode and the third eigenfrequency for shear excitations for the fourth mode) and depicted as dots on the vertical axes in Fig. 3. The last ones are slightly smaller and related to the minimum of the dispersion curves for the second and fourth modes shown in Fig. 2. Note that for a given layer depth and a given load velocity an infinite number of critical frequencies of the load exist due to the infinite number of modes. For the constant load case ($\Omega = 0$) the critical velocity is equal to c_R, confirming the result found in Dieterman and Metrikine (1996), assuming the layer thickness is large. The figure further shows that the critical velocities are bounded to some value which is about $1.5c_R$, above which no critical velocities exist for any loading frequency. For the higher modes the asymptotic behavior for $\Omega \to 0$ or $H \to 0$ results in a critical velocity c_R.

5 Critical Depths of the Layer

The critical depths of the layer are determined now under the assumption that the frequency of the load is the ratio between the train (load) velocity and the distance between the centres of the sleepers.

Experimental investigations show (Kjorling, 1993) that the main frequency of a train wheel excitation can be determined as

$$\Omega = 2\pi \frac{V}{d}, \tag{21}$$

where V is the velocity of the train and d is the period of the sleepers. This expression and the dependency of the critical load velocities on the load frequency (see Fig. 3) give the critical depths of the layer as a function of the train velocity. Indeed, the dependency, depicted in Fig. 3, can be written down as

$$\Omega = \frac{c_t}{H} f\left(\frac{V}{c_t}\right).$$

Substitution of (21) in this relation results in

$$2\pi \frac{V}{d} = \frac{c_t}{H} f\left(\frac{V}{c_t}\right) \quad \text{or} \quad \frac{H}{d} = \frac{1}{2\pi}\frac{c_t}{V} f\left(\frac{V}{c_t}\right). \tag{22}$$

The dependency (22) is depicted in Fig. 4. For the interpretation of the figure we have to keep in mind that only the critical depths due to the harmonically varying load have been given. An additional constant part in the loading will give the critical velocity c_R for an arbitrary depth. For a given load velocity, resulting in a specific loading frequency, Fig. 4 shows that an infinite number of critical depths exist which are increasing with higher modes. Looking at the lowest mode the figure shows that one critical depth exist for low velocities, three critical depths for velocities between $0.25c_R$ and c_R and two for velocities between c_R and $1.5c_R$. A similar kind of reasoning applies for the higher modes. It can be seen further that for load velocities higher than $1.5c_R$ no critical depths exist anymore. Note, that Fig. 4 shows increasing critical depths for each mode as the load velocity tends to zero. In the limit this will not result in a transition to a half-space model. The reflections of the waves from the fixed substrate will in all cases determine the system behavior.

The figure shows further, that the critical depths of the layer decrease with increasing load velocity. The curves of all modes tend to the critical velocity c_R for $H \to 0$ for a harmonically varying load. Normally the period of the sleepers d is in the order 0.6 m. When the velocity of the train is near the velocity of Rayleigh waves c_R, the critical depths are located in the

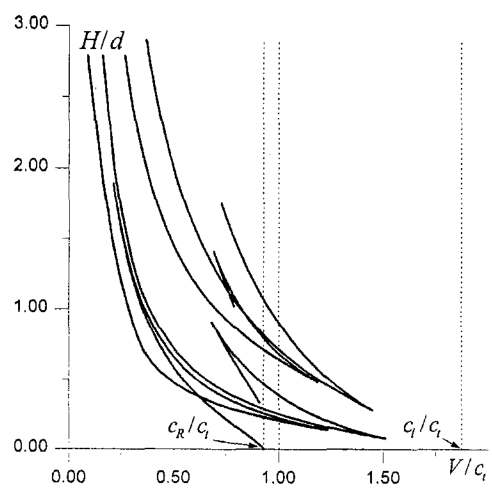

Fig. 4 Critical depths as function of load velocity

interval $0 < H \leq 1.5$ m. This depth is in the order of normal ballast depths. So to avoid resonance phenomena in the ballast due to high speed trains it is important to increase internal friction losses in the ballast and/or to avoid differences in the impedances of the ballast and the substrate.

6 Conclusions

The critical velocities of a harmonically varying load moving uniformly along an elastic layer have been derived as a function of the load velocity. The critical velocities exist both for velocities higher and lower than the Rayleigh wave velocity in the layer. However, there is a certain velocity of the load, located between the velocities of the compressional and shear waves in the layer, beyond which resonance does not occur for any frequencies of the load. The critical depths of the layer have been determined as a function of the load velocity. These depths decrease with increasing load velocity. It is concluded that the higher the train velocity, the more important are the properties of the ballast and the character of the border between the ballast and the substrate.

References

Bogacz, R., Krzyzinsky, T., and Popp, K., 1989, "On the Generalisation of Mathewss Problem of the Vibrations of a Beam on Elastic Foundation," *ZAMM*, Vol. 69, pp. 243–252.

Cole, J., and Huth, J., 1958, "Stresses Produced in a Half Plane by Moving Loads," ASME JOURNAL OF APPLIED MECHANICS, Vol. 25, pp. 433–436.

Dean, G. D., 1990, "The Response of an Infinite Railroad Track to a Moving, Vibrating Mass," ASME JOURNAL OF APPLIED MECHANICS, Vol. 57, pp. 66–73.

Dieterman, H. A., and Metrikine, A. V., 1996, "The Equivalent Stiffness of a Half-Space Interacting With a Beam. Critical Velocities of a Moving Load Along the Beam," *European Journal of Mechanics Solids/A*, Vol. 15, No. 1, pp. 67–90.

Ewing, W. M., Jardetsky, W. S., and Press, F., 1957, *Elastic Waves in Layered Media*, McGraw-Hill, New York.

Fryba, L., 1972, *Vibrations of Solids and Structures Under Moving Loads*, Noordhoff International Publishing, Groningen.

Kjorling, M., 1993, "Measurements on the Track at Algaras, Between Laxa and Toreboda, Sweden," Royal Institute of Technology Report TRITA-BST-0161, Stockholm, Sweden.

Knothe, Kl., and Grassie, S. L., 1993, "Modelling of Railway Track and Vehicle/Track Interaction at High Frequencies," *Vehicle System Dynamics*, Vol. 22, pp. 209–262.

Lamb, H., 1904, "On the Propagation of Tremors Over the Surface of an Elastic Solid," *Phil. Trans. Roy. Soc. London*, Vol. A203, No. 1, pp. 1–42.

Lansing, D. L., 1966, "The Displacements in an Elastic Half-Space Due to a Moving Concentrated Normal Load," NASA Technical Report TR R-238, Washington, DC.

Metrikine, A. V., 1994, "Unstable Lateral Oscillations of an Object Moving Uniformly Along an Elastic Guide as a Result of an Anomalous Doppler Effect," *Soviet Physics. Acoustics*, Vol. 40, pp. 85–89 (translated from Russian).

Miklowitz, J., 1978, *The Theory of Elastic Waves and Waveguides*, NHPC, Amsterdam.

Payton, R. J., 1967, "Transient Motion of an Elastic Half-Space Due to a Moving Surface Line Load," *Int. J. Engng. Sci.*, Vol. 5, pp. 49–79.

Vesnitskii, A. I., 1991, "Wave Effects in Elastic Systems," *Wave Dynamics of Machines*, Nauka, Moscow, pp. 15–30 (in Russian).

Vesnitskii, A. I., and Metrikine A. V., 1993, "Parametric Instability in the Oscillations of a Body Moving Uniformly in a Periodically Inhomogeneous Elastic System," *Journal of Applied Mechanics and Technical Physics*, Vol. 34, pp. 226–271 (translated from Russian).

APPENDIX

Theorem. Consider the double integral $I = \int_{-\infty}^{\infty}\int_{-\infty}^{\infty}(dxdy/D(x, y))$, where $D(x, y)$ is an analytical function and $(1/(D(x, y)))$ is integrable at infinity. The integral I diverges if there exists a real isolated root (x^*, y^*) of the equation $D(x, y) = 0$ for which $(\partial D/\partial x) = (\partial D/\partial y) = 0$ at $(x, y) = (x^*, y^*)$.

Proof. We represent the integral as

$$I = \int_{-\infty}^{\infty}\int_{-\infty}^{\infty}\frac{dxdy}{D(x, y)} = \iint_S \frac{dxdy}{D(x, y)} + \iint_{S_\epsilon}\frac{dxdy}{D(x, y)}$$

where

$$S = \{(x, y): (x - x^*)^2 + (y - y^*)^2 > \rho_0^2\};$$
$$S_\epsilon = \{(x, y): (x - x^*)^2 + (y - y^*)^2 \leq \rho_0^2\}$$

ρ_0 is a positive constant.

The integral $\int\int_S (dxdy/(D(x, y))$ converges since the integrand has no singular points in the S-area and $(1/(D(x, y)))$ is integrable at infinity. Therefore, convergence of I depends on the integral $\int\int_{S_\epsilon}(dxdy/(D(x, y))$. In the classical sense this integral is equal to

$$\iint_{S_\epsilon}\frac{dxdy}{D(x, y)} = \lim_{\epsilon\to 0}\iint_{\epsilon^2 \leq (x-x^*)^2+(y-y^*)^2 \leq \rho_0^2}\frac{dxdy}{D(x, y)} \quad (1a)$$

As ρ_0 is an arbitrary constant, we consider it small and expand $D(x, y)$ into a Taylor series around the point (x^*, y^*):

$$D(x, y) = D(x^*, y^*) + \sum_{n=1}^{\infty}\frac{1}{n!}d^nD(x^*, y^*) \quad (2a)$$

where $d^nD(x^*, y^*)$ is the differential of $D(x, y)$ of the order n at the point (x^*, y^*).

In accordance with the theorem conditions, $D(x^*, y^*) = dD(x^*, y^*) = 0$. Moreover, since (x^*, y^*) is the real isolated zero of $D(x, y)$, there exists a natural number m, $m = 2k (k \geq 1)$, that $d^mD(x^*, y^*) \neq 0$ and $d^iD(x^*, y^*) = 0$ if $1 \leq i < m$. Therefore, introducing the polar system of coordinates $x - x^* = \rho\cos(\varphi)$, $y - y^* = \rho\sin(\varphi)$, we rewrite Eq. $(2a)$ as

$$D(\rho, \varphi) = \frac{1}{(2k)!}\rho^{2k}f(\varphi) + o(\rho^{2k}) \quad (3a)$$

where $f(\varphi) \neq 0$ (since (x^*, y^*) is the isolated zero and, consequently, $D(\rho, \varphi) \neq 0$ if $\rho \neq 0$).

Substituting Eq. $(3a)$ into Eq. $(1a)$ and taking into account the Jacobian ρ, we obtain

$$\iint_{S_\epsilon}\frac{dxdy}{D(x, y)} = \lim_{\epsilon\to 0}\int_{\epsilon}^{\rho_0}\int_0^{2\pi}\frac{(2k)!\rho}{f(\varphi)\rho^{2k}}d\rho d\varphi \quad (4a)$$

The member $o(\rho^{2k})$ in Eq. $(3a)$ is dropped as ρ_0 is an arbitrary small value. The integral with respect to φ in Eq. $(4a)$ will result in a finite constant A since $f(\varphi) \neq 0$ and k is a finite number. Then

$$\iint_{S_\epsilon}\frac{dxdy}{D(x, y)} = A\lim_{\epsilon\to 0}\int_{\epsilon}^{\rho_0}\frac{d\rho}{\rho^{2k-1}}$$
$$= A\lim_{\epsilon\to 0}\left\{\begin{array}{ll} \ln\rho_0 - \ln\epsilon & \text{if} \quad k = 1 \\ \frac{1}{2-2k}\left(\frac{1}{\rho_0^{2-2k}} - \frac{1}{\epsilon^{2-2k}}\right) & \text{if} \quad k > 1\end{array}\right\} = \infty.$$

Thus, the integral I diverges.

A Symmetric Inverse Vibration Problem for Nonproportional Underdamped Systems

L. Starek
Faculty of Mechanical Engineering,
Slovak Technical University of Bratislava,
812 31 Bratislava, Slovakia

D. J. Inman
Department of Engineering Science and Mechanics,
Virginia Polytechnic Institute and State University,
Blacksburg, VA 24061-0219
Fellow ASME

This paper considers a symmetric inverse vibration problem for linear vibrating systems described by a vector differential equation with constant coefficient matrices and nonproportional damping. The inverse problem of interest here is that of determining real symmetric, coefficient matrices assumed to represent the mass normalized velocity and position coefficient matrices, given a set of specified complex eigenvalues and eigenvectors. The approach presented here gives an alternative solution to a symmetric inverse vibration problem presented by Starek and Inman (1992) and extends these results to include noncommuting (or commuting) coefficient matrices which preserve eigenvalues, eigenvectors, and definiteness. Furthermore, if the eigenvalues are all complex conjugate pairs (underdamped case) with negative real parts, the inverse procedure described here results in symmetric positive definite coefficient matrices. The new results give conditions which allow the construction of mass normalized damping and stiffness matrices based on given eigenvalues and eigenvectors for the case that each mode of the system is underdamped. The result provides an algorithm for determining a nonproportional (or proportional) damped system which will have symmetric coefficient matrices and the specified spectral and modal data.

1 Introduction

Here we consider linear lumped parameter systems which can be modeled by a vector differential equation in the second order form given by

$$M\ddot{q}(t) + D\dot{q}(t) + Kq(t) = 0 \tag{1.1}$$

where $q(t)$ is an n vector of time-varying elements representing the displacement of the masses in a lumped mass model of some structure or device. The vectors $\dot{q}(t)$ and $\ddot{q}(t)$ represent the velocities and accelerations, respectively. The coefficients M, D, and K are $n \times n$ matrices of constant real elements representing the various physical parameters of mass, damping, and stiffness. The matrices M, D, and K could in general be asymmetric; however, here we are concerned with the symmetric case and the case in which M is positive definite.

Since M is positive definite and symmetric it has a matrix square root, with a symmetric, positive definite inverse denoted by $M^{-1/2}$. Let us then consider the transformation $q(t) = M^{-1/2}u(t)$. Substitution of this change of coordinates into Eq. (1.1) yields

$$\ddot{u}(t) + \tilde{D}\dot{u}(t) + \tilde{K}u(t) = 0 \tag{1.2}$$

where $\tilde{K} = M^{-1/2}KM^{-1/2}$ and $\tilde{D} = M^{-1/2}DM^{-1/2}$ are necessarily symmetric. The matrices $\tilde{D}$ and $\tilde{K}$ are referred to here as the mass normalized damping and stiffness matrices.

The eigenvalue problem of the system described by (1.2) is defined by

$$(\lambda^2 I + \lambda\tilde{D} + \tilde{K})x = 0 \tag{1.3}$$

where x is a nonzero vector of constants, called the eigenvector, and λ is a scalar, called the eigenvalue. From the spectral theory of matrix polynomials it is well known that the solutions of the system (1.2) are intimately connected with the algebraic properties of the matrix polynomials (Gohberg et al., 1982) of the form

$$L(\lambda) = \lambda^2 I + \lambda\tilde{D} + \tilde{K}. \tag{1.4}$$

Here a scalar λ and a nonzero vector x are again called an eigenvalue and associated (right) eigenvector of $L(\lambda)$ if det $L(\lambda) = 0$ and $L(\lambda)x = 0$, respectively. This forms an obvious connection between (1.3) and (1.4).

Previously, inverse spectral problems in vibration of lumped nonconservative systems have been solved by Danek (1982), Gladwell (1986), Lancaster and Maroulas (1987), and Starek and Inman (1991, 1992). Gladwell (1986) has solved the inverse spectral problem in vibration of lumped conservative systems ($\tilde{D} = 0$) modeled by tridiagonal matrices. Danek (1982) has solved this problem for the case of real nonsingular coefficient matrices and he has defined the inverse formulas which determine the coefficient matrices M, D, and K of the above-mentioned systems with given spectral and modal data. Starek and Inman (1991) have solved the inverse problem in the state space form and they have determined the inverse formulas which directly determine real coefficient matrices $M^{-1}K$ and $M^{-1}D$ for the case that D and K are singular coefficient matrices (i.e., there exist rigid-body modes). The symmetric inverse problem with overdamped modes has been discussed by Starek and Inman (1995).

The results presented here build on those of Lancaster and Maroulas (1987) and those of Starek and Inman (1992). Lancaster and Maroulas have solved the inverse problem in vibration by means of the spectral theory of matrix polynomials. They defined Jordan pairs that determine a self-adjoint matrix polynomial. Starek and Inman (1992) have solved the inverse spectral problems in the state-space form. They have defined the conditions for given spectral and modal data under which the inverse formulas determine real symmetric coefficient matrices $\tilde{K}$ and $\tilde{D}$, but their solution requires that the given eigenvalues must all be complex valued and does not preserve given

Contributed by the Applied Mechanics Division of The American Society of Mechanical Engineers for publication in the ASME Journal of Applied Mechanics.

Discussion on this paper should be addressed to the Technical Editor, Professor Lewis T. Wheeler, Department of Mechanical Engineering, University of Houston, Houston, TX 77204-4792, and will be accepted until four months after final publication of the paper itself in the ASME Journal of Applied Mechanics.

Manuscript received by the ASME Applied Mechanics Division, Oct. 14, 1995; final revision, Oct. 1, 1996. Associate Technical Editor: S. W. Shaw.

eigenvectors. Lancaster (1961) provides a direct formula, but unfortunately requires prior knowledge of M and D for normalization of the eigenvectors.

The goal of this paper is to give an alternative solution to the inverse problem solved in Starek and Inman (1992) and to extend these results to include the preservation of eigenvectors. In the earlier result an algorithm is given for a symmetric inverse vibration problem for underdamped systems which determine real symmetric coefficient matrices given desired natural frequencies and damping ratios. The goal of this paper is to derive conditions under which spectral and modal data determine real, symmetric coefficient matrices $\tilde{D}$ and $\tilde{K}$ which do not necessarily commute. The method will be outlined which allows the synthesis of a symmetric, underdamped linear system having desired eigenvalues and eigenvectors. Symmetric systems are of particular interest in the eigenstructure assignment method from control theory (Inman and Kress 1995), in the model updating problem of structural dynamics (Inman, 1993) and in fault detection problems for machine and structure diagnostics (Kaouk and Zimmerman, 1994). Such inverse methods have been adapted for use in determining the condition of the bonding of the protective tiles to the space shuttle (Mueller and Moslehy, 1996).

2 Non-negative Matrix Polynomial Conditions

From the theory of matrix polynomials it is well known that since $\tilde{D}$ and $\tilde{K}$ are Hermitian, $L(\lambda)$ is a self-adjoint matrix polynomial and thus can be decomposed into a product of two linear factors, i.e., there are $n \times n$ complex valued matrices Z and T, such that $L(\lambda) = (I\lambda - T)(I\lambda - Z)$. The eigenvalues of Z and of T make up the eigenvalues of $L(\lambda)$. The eigenvectors of Z are also eigenvectors of $L(\lambda)$. The first of the abovementioned results gives the relation between the eigenvectors of T and $L(\lambda)$ as follows. Let $[A, B]$ denote the matrix A augmented by a dimensionally compatible matrix B. Let diag $[\Lambda_A, \Lambda_B]$ denote the diagonal matrix Λ_A extended by the diagonal matrix Λ_B.

Theorem 1 (Lancaster and Maroulas). Let $L(\lambda) = (I\lambda - T)(I\lambda - Z)$, and assume that the set of eigenvalues of matrices T and Z make up disjoint parts of the spectrum of $L(\lambda)$, and let $Z = X_Z J_Z X_Z^{-1}$ where J_Z is the Jordan normal form of the matrix Z. Let $V = [X_Z, Y]$ and $\Lambda = \text{diag}\,[J_Z, J_T]$ be a Jordan pair for $L(\lambda)$. Then there is a nonsingular matrix X_T such that $T = X_T J_T X_T^{-1}$ where

$$X_T = YJ_T - ZY. \tag{2.1}$$

Conversely, if we are given $T = X_T J_T X_T^{-1}$ and Y is the unique solution of (2.1), then $[X_T, Y]$, $\Lambda = \text{diag}\,[J_Z, J_T]$ is a Jordan pair for $L(\lambda)$. The concepts of Jordan pairs is reviewed in the Appendix.

Gohberg et al., give the following result concerning a monic nonnegative matrix polynomial of degree two (see Theorem 12.8 of Gohberg et al., 1982).

Theorem 2 (Gohberg et al.). Let $L(\lambda)$ be an $n \times n$ monic, self-adjoint, matrix polynomial of degree two. Then the following statements are equivalent:

(i) $L(\lambda)$ is a non-negative monic matrix polynomial.
(ii) There is a matrix $Z \in C^{n\times n}$ such that $L(\lambda) = (I\lambda - Z^*)(I\lambda - Z)$.
(iii) The partial multiplicities of all real eigenvalues of $L(\lambda)$ are all even and the sign characteristic of $L(\lambda)$ consists entirely of plus ones.

In Theorem 1 we may set $T = Z^* = (X_Z^{-1})^* \bar{J}_Z X_Z^*$ and it is easily seen that $X_T = (X_Z^{-1})^* P$. Substitution of $Z = X_Z J_Z X_Z^{-1}$ we get the following result given by Lancaster and Maroulas (1987).

Corollary 1. Let $L(\lambda) = (I\lambda - Z^*)(I\lambda - Z)$. The set of eigenvalues of matrices Z^* and Z make up disjoint parts of the spectrum of $L(\lambda)$, and $Z = X_Z J_Z X_Z^{-1}$, where J_Z is a Jordan normal form. Let $\hat{Y}$ be the unique solution of

$$\hat{Y} J_Z^* - J_Z \hat{Y} = (X_Z^* X_Z)^{-1} \tag{2.2}$$

and $Y = X_Z \hat{Y} P$ (where P is the permutation matrix for which $J_Z^T = P J_Z P$). Then $[X_Z, Y]$, diag $[J_Z, \bar{J}_Z]$ is a Jordan pair for $L(\lambda)$ where the entries of $\bar{J}_Z$ are the complex conjugate of those in J_Z.

3 Solution of the Real Symmetric Inverse Problem

The goal here is to derive the conditions under which spectral and modal data determine real symmetric coefficient matrices $\tilde{D}$ and $\tilde{K}$ of Eq. (1.2) for the case where all eigenvalues are complex. At first we note an important property of spectral and modal data of lumped linear systems described by real coefficient matrices. The eigenvalues (and their multiplicities) of such a system are symmetric with respect to the real axis of the complex plane. This implies that there is a Jordan matrix Λ such that (the case when all eigenvalues are complex)

$$\Lambda = \text{diag}\,[J_Z, J_T] = \text{diag}\,[J_Z, \bar{J}_Z] \tag{3.1}$$

where J_Z is the matrix with all its eigenvalues in the upper half of the complex plane. The modal matrix V is partitioned in a compatible way as (3.1), i.e.,

$$V = [X_Z, Y] = [X_Z, \bar{X}_Z] \tag{3.2}$$

where X_Z is complex valued.

From the Theorem 2 and Corollary 1 it follows that spectral and modal data will determine non-negative, self-adjoint matrix polynomials if they fulfill condition (2.2). In addition the coefficients of this matrix polynomial will be real if in the Jordan pair for this matrix polynomial, given by $V = [X_Z, Y]$ and $\Lambda = \text{diag}\,[J_Z, J_T]$, we substitute $Y = \bar{X}_Z U$ for some $U \in \mathcal{A}_T(J_Z)$. Note that for any square matrix J_Z, $\mathcal{A}_I(J_Z)$ denotes sub algebra of invertible matrices that commute with J_Z (see Theorem 1 of Lancaster and Maroulas (1987)).

Now we shall define our goal more precisely. Our concern here is: how to choose the matrices X_Z and J_Z (and hence the matrix Z) such that the rewritten condition (2.2) for the case of $Y = \bar{X}_Z U$ will be satisfied. To this end substitute $Y = \bar{X}_Z U$ into $\hat{Y} = X_Z^{-1} Y P$ and then substitute $\hat{Y}$ into (2.2). This yields

$$X_Z^{-1} \bar{X}_Z U P J_Z^* - J_Z X_Z^{-1} \bar{X}_Z U P = (X_Z^* X_Z)^{-1}. \tag{3.3}$$

Because $PJP = J^T$ or $PJ^* = \bar{J}P$ and we assume the system to be of simple structure (Λ is a diagonal matrix and so $J_Z^* = \bar{J}_Z$ and $P = I$) we have

$$X_Z^{-1} \bar{X}_Z \bar{J}_Z U - J_Z X_Z^{-1} \bar{X}_Z U = X_Z^{-1} (X_Z^{-1})^*. \tag{3.4}$$

After some manipulation this results in

$$X_Z^* (\bar{Z} - Z) \bar{X}_Z U = I. \tag{3.5}$$

From Eq. (3.5) the following conclusion results.

Theorem 3. Specific spectral and modal data, consisting of only complex eigenvalues and possibly complex eigenvectors, will generate real symmetric matrices $\tilde{D}$ and $\tilde{K}$ if the eigenvalues and eigenvectors of the matrix Z satisfy the condition (3.5).

The question remains of how to choose eigenvalues and eigenvectors of a matrix Z such that (3.5) will be valid. To this end rewrite Eq. (3.5) as follows: Since $Z = Z_r + iZ_i$ then $\bar{Z} - Z = -2iZ_i$, where Z_r is the real and Z_i the imaginary part of the matrix Z. Let

$$X_Z = X_{Zr} + iX_{Zi} \quad \text{and} \quad J_Z = J_{Zr} + iJ_{Zi},$$

where X_{Zr}, J_{Zr} are the real parts and X_{Zi}, J_{Zi} are the imaginary parts of X_Z and J_Z, respectively. Substituting Z, X_Z, and J_Z into $ZX_Z = X_Z J_Z$ yields

$$Z_i = (X_{Zr}J_{Zi} + X_{Zi}J_{Zr} - X_{Zr}J_{Zr}X_{Zr}^{-1}X_{Zi} + X_{Zi}J_{Zi}X_{Zr}^{-1}X_{Zi}) \times (X_{Zr} + X_{Zi}X_{Zr}^{-1}X_{Zi})^{-1}. \quad (3.6)$$

This assumes the X_{Zr}^{*} is nonsingular, a reasonable assumption because its columns are required eigenvectors of a simple matrix polynomial. Substituting $\bar{Z} - Z = -2iZ_i$, $X_Z^* = X_{Zr}^T - iX_{Zr}^T$ and $\bar{X}_Z = X_{Zr} - iX_{Zi}$ into Eq. (3.5) and manipulating results in

$$-2[X_{Zi}^TZ_iX_{Zr} + X_{Zr}^TZ_iX_{Zi} + i(X_{Zr}^TZ_iX_{Zr} - X_{Zi}^TZ_iX_{Zi})]U = I. \quad (3.7)$$

From the theory of self-adjoint matrix polynomials (Gohberg et al., 1982) it is known that if the matrix of left eigenvector, Y, and the matrix of right eigenvectors are related by a standard involuntary permutation matrix (see the Appendix) by $Y_{ij} = \epsilon_{ij}P_{ij}X_{ij}$, $\epsilon_{ij} = \pm 1$, then the associated matrix polynomial is self-adjoint. This motivates us to look for a matrix C such that

$$X_{Zi} = X_{Zr}C \quad (3.8)$$

where C is yet to be determined. Substitution of Eq. (3.8) into (3.6) yields

$$Z_i = X_{Zr}AX_{Zr}^{-1} \quad (3.9)$$

where

$$A = (J_{Zi} + CJ_{Zr} - J_{Zr}C + CJ_{Zi}C)(I + C^2)^{-1}. \quad (3.10)$$

Substituting (3.8) and (3.9) into (3.7) yields

$$-2[C^TX_{Zr}^TX_{Zr}A + X_{Zr}^TX_{Zr}AC + i(X_{Zr}^TX_{Zr}A - C^TX_{Zr}^TX_{Zr}AC)]U = I. \quad (3.11)$$

If the required spectral and modal data are to generate real symmetric matrices $\tilde{D}$ and $\tilde{K}$, the eigenvalues and eigenvectors of a matrix Z must now satisfy Eq. (3.11).

Rewrite Eq. (3.11) as follows:

$$-2(C^TX_{Zr}^TX_{Zr}A + X_{Zr}^TX_{Zr}AC)U = I \quad (3.12)$$

$$(X_{Zr}^TX_{Zr}A - C^TX_{Zr}^TX_{Zr}AC)U = 0. \quad (3.13)$$

Because the matrix U is nonsingular it follows from Eq. (3.13) that

$$X_{Zr}^TX_{Zr}A = C^TX_{Zr}^TX_{Zr}AC. \quad (3.14)$$

From Eq. (3.12) and knowledge that U is nonsingular and diagonal it follows

$$(C^TX_{Zr}^TX_{Zr}A + X_{Zr}^TX_{Zr}AC)^T = C^TX_{Zr}^TX_{Zr}A + X_{Zr}^TX_{Zr}AC.$$

After some manipulation the following condition results:

$$A^TX = XA \quad (3.15)$$

where $X = X^T = X_{Zr}^TX_{Zr}$.

Now we rewrite Eq. (3.12) as follows:

$$C^TXA + XAC = -\tfrac{1}{2}U^{-1}. \quad (3.16)$$

If the matrix C is of full rank, then after substitution of Eq. (3.14) into Eq. (3.16) we obtain

$$(C^2)^TXAC + C^TXAC^2 = \tfrac{1}{2}U^{-1}$$

or

$$C^TXA + XAC = -\tfrac{1}{2}(CUC^T)^{-1}. \quad (3.17)$$

Because the left sides of Eqs. (3.16) and (3.17) are the same, we have

$$U = CUC^T \quad \text{or} \quad C^{-1}U = UC^T. \quad (3.18)$$

In the case when U is the identity matrix, $U = I$, the condition for the matrix C becomes

$$C^TC = CC^T = I \quad (3.19)$$

so that the matrix C must be *orthoganal.*

By using the conditions (3.15) and (3.19), Eq. (3.17) becomes

$$C^TA^TX + XAC = -\tfrac{1}{2}I. \quad (3.20)$$

If we put $E = C^TA^T$ or $E^T = AC$ and $F = \frac{1}{2}I$ into Eq. (3.20) the Lyapunov equation

$$EX + XE^T = -F \quad (3.21)$$

results. For the solution of the Lyapunov Eq. (3.21) we use the MATLAB subroutine (code) X = lyap (E, F). The result of lyap (E, F) is a symmetric matrix $X = X_{Zr}^TX_{Zr}$. The problem which arises, is to choose the matrix C in such a way that the matrix X will be a positive definite matrix. To this end we use the Cholesky factorization of X for computing X_{Zr}.

The procedure for determining real symmetric matrices $\tilde{D}$ and $\tilde{K}$ is summarized as follows (using MATLAB, but other software could be used here as well):

(*a*) Select the required eigenvalues of the system described by Eq. (1.2) (they are given by the matrix J_Z).

(*b*) Choose the orthonormal matrix C.

(*c*) Use the MATLAB code X = lyap (E, F) for computing the matrix X which must be a positive definite matrix.

(*d*) Use the MATLAB code X_{Zr} = chol (X) which produces an upper triangular X_{Zr} so that $X = X_{Zr}^TX_{Zr}$.

(*e*) Determine the coefficient matrices $\tilde{D}$ and $\tilde{K}$ either by inverse formulas (see Starek and Inman (1992))

$$[-\tilde{K} \;\; -\tilde{D}] = V\Lambda^2X^{-1} \quad (3.22)$$

where the modal matrix V and the spectral matrix Λ are given by the Eq. (3.2) and (3.1) and the matrix X is given by

$$X = \begin{bmatrix} V \\ V\Lambda \end{bmatrix} \quad (3.23)$$

or from the formulas that follows from the definition of a non-negative matrix polynomial $L(\lambda) = (I\lambda - Z^*)(I\lambda - Z)$ which is given by the Theorem 2, i.e.,

$$\tilde{D} = -Z - Z^* \quad (3.24)$$

$$\tilde{K} = Z^*Z. \quad (3.25)$$

This represents only one possible solution of the condition given by Eq. (3.5).

Example. Consider the inverse problem with three eigenvalues given by

$$Jz = \begin{bmatrix} -0.5000 + 1.0000i & 0 & 0 \\ 0 & -1.0000 + 2.0000i & 0 \\ 0 & 0 & -2.0000 + 3.0000i \end{bmatrix}$$

Choose the orthoganal matrix C to be

$$C = \begin{bmatrix} 0.8507 & 0.5257 & 0 \\ -0.5257 & 0.8507 & 0 \\ 0 & 0 & 1.0000 \end{bmatrix}$$

and note that $CC^T = I$ as it should. Then compute

$$A = [J_i + CJ_r - J_rC + CJ_iC][1 + C^2]^{-1} = \begin{bmatrix} 0.9188 & 0.1776 & 0 \\ 0.1776 & 2.0812 & 0 \\ 0 & 0 & 3.0000 \end{bmatrix}.$$

Then using $E = C^TA^T$ and $F = -.5I$ the Lyapunov equation can be solved (MATLAB command lyap (E, F)) to yield

$$X = \begin{bmatrix} 0.3252 & -0.0278 & 0 \\ -0.0278 & 0.1436 & 0 \\ 0 & 0 & 0.0833 \end{bmatrix}.$$

which has Cholesky factorization

$$X_{Zr} = \begin{bmatrix} 0.5703 & -0.0487 & 0 \\ 0 & 0.3758 & 0 \\ 0 & 0 & 0.2887 \end{bmatrix}$$

so that $X_Z = X_{Zr}(I + iC)$ becomes

$$X_Z = \begin{bmatrix} 0.5703 + 0.5107i & -0.0487 + 0.2584i & 0 \\ 0 - 0.1976i & 0.3758 + 0.3197i & 0 \\ 0 & 0 & 0.2887 + 0.2887i \end{bmatrix}.$$

The matrix $Z = X_ZJ_ZX_Z^{-1}$ becomes

$$Z = \begin{bmatrix} -0.6268 + 0.9036i & -0.6061 + 0.1170i & 0 \\ -0.2750 + 0.1170i & -0.8732 + 2.0964i & 0 \\ 0 & 0 & -2.0000 + 3.0000i \end{bmatrix}$$

so that

$$\tilde{D} = -Z - Z^* = \begin{bmatrix} 1.2537 & 0.8812 & 0 \\ 0.8812 & 1.7463 & 0 \\ 0 & 0 & 4.0000 \end{bmatrix}$$

and

$$\tilde{K} = Z^*Z = \begin{bmatrix} 1.2988 & 0.9711 & 0 \\ 0.9711 & 5.5383 & 0 \\ 0 & 0 & 13.0000 \end{bmatrix}.$$

Note that $\tilde{K}$ and $\tilde{D}$ are both symmetric and positive definite (because $\text{Re}\lambda_i < 0$ for all i). Also note that the matrix product $\tilde{K}\tilde{D}$ is not symmetric, so that the system is not proportionally damped. The system also has the desired eigenstructure.

4 Positive Definite Solution

Once the symmetry of the coefficient matrices resulting from an inverse procedure is guaranteed, the definiteness of the matrices follows from simple considerations. In the above example note that our solution produced symmetric, positive-definite coefficient matrices. This follows from the assumption that the modes are all underdamped (i.e., λ_i appear in complex conjugate pairs) and that $\tilde{D}$ and $\tilde{K}$ are symmetric. If the real part of each λ_i are further restricted to be negative, both $\tilde{D}$ and $\tilde{K}$ will necessarily be positive definite.

To see this note that for each eigenvector x_i and eigenvalue λ_i (1.3) must hold when multiplied from the left by x_i^*. This yields that λ_i must satisfy

$$\lambda_i = -\frac{x_i^*\tilde{D}x_i}{2x_i^*x_i} \pm \frac{1}{2x_i^*x_i}\sqrt{(x_i^*\tilde{D}x_i)^2 - 4x_i^*x_ix_i^*\tilde{K}x_i} \quad (3.26)$$

From Inman and Andry (1980) it is known that for underdamped systems (λ_i complex) the radical is purely imaginary so that $\text{Re}\lambda_i = -(x_i^*\tilde{D}x_i/x_i^*x_i)$. Under the assumption that $\text{Re}\lambda_i < 0$ for all i we have

$$-x_i^*\tilde{D}x_i < 0 \quad \text{or} \quad x_i^*\tilde{D}x_i > 0$$

for all eigenvectors x_i. Next let $x \in R^n$ (i.e., x is a real valued vector of appropriate dimensions), then since x_i are complete in R^n there exists scalars a_i not all zero such that $x = \Sigma_{i=1}^n a_ix_i$. Thus, for any $x \neq 0$, $x^T\tilde{D}x = \Sigma_{i=1}^n a_i^2(x_i^T\tilde{D}x_i)$ which is the sum of all positive numbers, hence $x^T\tilde{D}x > 0$ for all $x \neq 0$ and $\tilde{D}$ must be positive definite. Next since the system is underdamped, the matrix $4\tilde{K} - \tilde{D}^2$ is positive definite (Inman and Andry, 1980) and $4x^T\tilde{K}x > x^T\tilde{D}^2x > 0$ for all $x \neq 0$, so $\tilde{K}$ must also be positive definite (i.e., if $\tilde{D}$ is positive definite so is $\tilde{D}^2$).

Thus, if the set of desired eigenvalues are chosen to be complex with negative real parts, and the eigenvectors are complex valued the inverse algorithm presented here will produce symmetric and positive definite mass normalized damping and stiffness matrices.

5 Proportional Damping

It is obvious that the condition for given spectral and modal data, Eq. (3.11) is always fulfilled if the matrix X_{Zr} is made up of orthogonal vectors and the matrix C is diagonal. After substituting into (3.11) all the matrices in this equation become diagonal and if U is any invertible matrix that commutes with J_Z then Eq. (3.11) is satisfied.

If the matrix C is diagonal then the complex eigenvector can be normalized to produce real vectors in the following way. Multiply each real part of eigenvector given by the matrix X_{Zr} by the appropriate complex number given by the matrix $(I + iC)$. From this matrix of complex eigenvectors we can generate a matrix of real eigenvectors by multiplying the matrix X_Z by a complex conjugate matrix to the matrix $(I + iC)$. This is consistent with the idea presented by Caughey and O'Kelly (1965) that proportionally damped systems have eigenvectors which can be represented by real mode shapes.

The procedure for determining real symmetric matrices $\tilde{D}$ and $\tilde{K}$ in the simplifying case of diagonal C results in proportional damping and this is summarized in the following:

(*a*) Select the required eigenvalues of the system described by the Eq. (1.2), given by the matrix J_Z.

(*b*) Select the required eigenvectors of the system described by Eq. (1.2), given by the matrix X_{Zr} in such a way that they will be orthogonal.

(*c*) Choose the nonsingular diagonal matrix C.

(*d*) Determine the coefficient matrices $\tilde{D}$ and $\tilde{K}$ either by the inverse formulas (see Starek and Inman, 1992).

$$[-\tilde{K} - \tilde{D}] = V\Lambda^2X^{-1}.$$

Where the modal matrix V and the spectral matrix are given by the Eqs. (3.2) and (3.1) and the matrix X is given by

$$X = \begin{bmatrix} V \\ V\Lambda \end{bmatrix}$$

or from the formulas that follows from the definition of a nonnegative matrix polynomial $L(\lambda) = (I\lambda - Z^*)(I\lambda - Z)$ which is given by the Theorem 2, i.e.,

$$\tilde{D} = -Z - Z^*$$

$$\tilde{K} = Z^*Z.$$

Note that in the case of a diagonal matrix C the system (1.2) determined by matrices $\tilde{D}$ and $\tilde{K}$ will have proportional damping, and the eigenvectors have a real valued representation. If C is not diagonal, the matrices $\hat{D}$ and $\hat{K}$ constructed by Eq. (3.24) and (3.25) will not commute and the system eigenvectors, will necessarily be complex valued.

6 Conclusion

This manuscript presents a solution to the inverse vibration problem for the case that the desired coefficient matrices be symmetric and the resulting system contains the desired or specified eigenvalues and eigenvectors. This is an improvement over symmetric inverse problem solutions which do not preserve the eigenvectors. This is useful for vibrating systems where it is known in advance that the system described by the equations of motion should be symmetric. Furthermore, if the real part of the eigenvalues are all negative, the resulting inverse solution produces positive definite matrices. In this paper the condition (3.5) for given spectral and modal properties is defined. When this condition is fulfilled then inverse formula (3.22) or alternately Eqs. (3.24) and (3.25) determine real symmetric matrices for linear lumped parameter nonconservative systems. The synthesized system must be of simple structure (i.e., diagonal spectral matrix) and each mode of the system is underdamped. The system identified by this inverse vibration problem will have proportional damping if the eigenvectors are chosen to all be real. In general, however, nonproportional damping results.

The weak point of the proposed method is clearly the choice of the orthoganal matrix C in step b. This choice is somewhat arbitrary and little guidance is provided by the theory. The numerical methods work well for any size problem, except that as the order becomes larger the choice of C becomes more illusive. Our approach is to choose a simple form of C, such as the identity matrix, keeping in mind that diagonal C will produce a proportionally damped system. Likewise, a nondiagonal C will produce a nonproportionally damped system with complex mode shapes. A sparse matrix is used in the example simply because it is the first level of complexity past a diagonal matrix. The nature of the matrix C, and precise methods for constructing C form the topics of future research.

Acknowledgments

This publication is based on work sponsored by the U.S.-Slovak Science and Technology Joint Fund in cooperation with the Slovakian Ministry of Education and Science and the U.S. National Institute of Standards and Technology under project number 93014. The second author was supported in part by U.S. Army Research Office grant number DAAL03-92-G-01880. The comments and suggestions of the anonymous reviewers are also greatly appreciated.

References

Caughey, T. K., and O'Kelly, M. E. J., 1965, "Classical Normal Modes in Damped Linear Dynamic Systems," ASME JOURNAL OF APPLIED MECHANICS, Vol. 132, pp. 583–588.

Danek, I., 1982, "Nonconservative Dynamic Systems," *Strojnicky casopis 33*, c. 6, pp. 667–680 (in Czech).

Gladwell, G. M. L., 1986, *Inverse Problem in Vibration*, Martinus Nijhoff Publishers, Dordrecht, The Netherlands.

Gohberg, I., Lancaster, P., and Rodman, L., 1982, *Matrix Polynomials*, Academic Press, New York.

Inman, D. J., 1993, "Model Correction Using Frequency Data," *Proceedings International Conference on Structural Dynamics Modeling, Test, Analysis and Correlation*," NAFEMS, pp. 349–358.

Inman, D. J., and Andry, A. N., Jr., 1980, "Some Results on the Nature of Eigenvalues of Discrete Damped Linear Systems," ASME JOURNAL OF APPLIED MECHANICS, Vol. 47, pp. 927–930.

Inman, D. J., and Kress, A., 1995, "Eigenstructure Assignment Using Inverse Eigenvalue Methods," *AIAA Journal of Guidance, Control and Dynamics*, to appear.

Kaouk, M., and Zimmerman, D. C., 1994, "Structural Damage Detection Using Measured Modal Data and No Original Analytical Model," *Proceedings of the 12th International Modal Analysis Conference*, pp. 474–480.

Lancaster, P., 1961, "Expressions for Damping Matrices in Linear Vibration Problems," *Journal of the Aerospace Sciences*, Vol. 28, p. 256.

Lancaster, P., and Maroulas, J., 1987, "Inverse Eigenvalue Problems for Damped Vibrating Systems," *Journal of Mathematical Analysis and Applications*, Vol. 123, No. 1, pp. 238–261.

Mueller, S. A., and Moslehy, F. A., 1996, "An Inverse Vibration Method Applied to Bond Evaluation of Space Shuttle Tiles," ASME *Journal of Vibration and Acoustics*, Vol. 118, pp. 454–462.

Starek, L., and Inman, D. J., 1991, "On Inverse Problems With Rigid Body Modes," ASME JOURNAL OF APPLIED MECHANICS, Vol. 58, pp. 1101–1104.

Starek, L., and Inman, D. J., 1992, "A Symmetric Inverse Vibration Problem," ASME *Journal of Vibration and Acoustics*, Vol. 114, pp. 564–568.

Starek, L., and Inman, D. J., 1995, "A Symmetric Inverse Vibration Problem with Over-damped Modes," *Journal of Sound and Vibration*, Vol. 181, No. 5, pp. 893–903.

APPENDIX

A few concepts from the theory of matrix polynomials are reviewed here. More precise details can be found in Gohberg et al. (1982).

Let M, D, and K be of size $n \times n$. A pair of matrices, X and J, are called a Jordan pair of the matrix polynomials given in Eq. (1.3) if $X = [X_1 \ldots X_r]$, $J = \text{diag}\,[J_1, J_2 \ldots J_r]$ where X_i and J_i, $i = 1, 2 \ldots r$ are a Jordan pair for the eigenvalue λ_i. Here X is $n \times 2n$, J is $2n \times 2n$ and r is the number of distinct eigenvalues. Note that if all the λ_i are distinct then $r = 2n$ and X_i is a right eigenvector of (1.3) and $J_i = \lambda_i$, a simple eigenvalue. In this case, X becomes the usual matrix of right eigenvectors and J becomes the diagonal matrix of eigenvalues. The matrix Y, referred to in the text, then becomes the matrix of left eigenvectors.

Roughly speaking, the *sign characteristics* of a matrix polynomial are an ordered set of numbers consisting of plus ones or minus ones (ordered according to the related eigenvalue index). These numbers are not explicitly used here, but are key to matrix polynomial analysis. These numbers denoted by ϵ_{ij} are used with the *standard involuntary permutation* matrix, denoted P_{ij}, to relate the left eigenvector and right eigenvector by

$$Y_{ij} = \epsilon_{ij} P_{ij} X_{ij}^*$$

where the index reflects the multiplicity of a given eigenvalue and the nature of its corresponding Jordan block (i.e., is there an off diagonal 1 or not), P_{ij} is a matrix of ones and zeros.

On the Existence of Mayer's Potential

V. M. Čović

M. M. Lukačević

Faculty of Mechanical Engineering,
University of Belgrade,
27. marta 80,
11000 Belgrade, Yugoslavia

A complete solution of the well-known Mayer's problem, which is concerned with the possibility of extending Hamilton's principle expressed in the form valid for conservative dynamical systems to one special case of nonconservative systems (Appell, 1911), is obtained. Namely, the necessary and sufficient conditions which have to be satisfied by the coefficients of the given nonconservative generalized forces so that the Mayer's potential (and, as a consequence, the descriptive function of the system) can be constructed, are established. This result is illustrated by an example.

1 Introduction

We consider a holonomic nonconservative dynamical system with n degrees-of-freedom, whose position at any moment t is determined by n Lagrangian coordinates $q^1, q^2, \ldots, q^n$ and whose Lagrangian function we denote by L. It is well known (see, e.g., Pars, 1965) that the integral variational principle of the Hamiltonian type, as a true variational problem,[1] can be established for such a system if the work done by the given nonconservative forces, which we denote by Q_α, in an arbitrary virtual displacement can be expressed in the form

$$Q_\alpha \delta q^\alpha = \left[\frac{d}{dt}\left(\frac{\partial V}{\partial \dot{q}^\alpha}\right) - \frac{\partial V}{\partial q^\alpha}\right]\delta q^\alpha \tag{1}$$

where $\dot{q}^\alpha$ are the generalized velocities of the system, and where

$$V(q^\alpha, \dot{q}^\alpha, t) = -A_\beta(q^\alpha, t)\dot{q}^\beta - A_{n+1}(q^\alpha, t). \tag{2}$$

The functions $A_\beta(q^\alpha, t)$, $A_{n+1}(q^\alpha, t)$, as well as their first and second partial derivatives, are assumed to be defined and continuous in some domain of $q^1, q^2, \ldots, q^n, t$.

In this case the descriptive function

$$L_1 = L - V \tag{3}$$

may be constructed, and the differential equations of motion of the system can be obtained from the integral principle of the Hamiltonian type, given by

$$\delta \int_{t_0}^{t_1} L_1(q^\alpha, \dot{q}^\alpha, t)dt = 0. \tag{4}$$

The indices α and β, as well as γ, which will be used throughout the paper, take the values $1, 2, \ldots, n$, with summation over this range of values in the case of repeated indices. For the sake of brevity, functions depending on $q^1, q^2, \ldots, q^n; \dot{q}^1, \dot{q}^2, \ldots, \dot{q}^n; t$ e.g., the function $V(q^1, \ldots, q^n; \dot{q}^1, \ldots, \dot{q}^n; t)$, we write simply as $V(q^\alpha, \dot{q}^\alpha, t)$, and similarly $A_\beta(q^1, \ldots, q^n; t)$, $A_{n+1}(q^1, \ldots, q^n; t)$ as $A_\beta(q^\alpha, t)$, $A_{n+1}(q^\alpha, t)$.

We note that the problem of constructing the descriptive function in the case when the generalized forces of the system satisfy the condition (1) was first considered by Mayer, who, remaining in the context of a free dynamical system, viewed the function (2) as a "potential" function corresponding to the given nonconservative forces, as was pointed out by Appell (1911). For that reason, this problem is known as a problem of determining Mayer's potential.

Using (1) and (2), we easily obtain

$$Q_\alpha = b^{(0)}_{\alpha\beta}\dot{q}^\beta + b^{(0)}_{\alpha n+1}, \tag{5}$$

where

$$b^{(0)}_{\alpha\beta}(q^\gamma, t) = \frac{\partial A_\beta}{\partial q^\alpha} - \frac{\partial A_\alpha}{\partial q^\beta} \tag{6}$$

and

$$b^{(0)}_{\alpha n+1}(q^\gamma, t) = \frac{\partial A_{n+1}}{\partial q^\alpha} - \frac{\partial A_\alpha}{\partial t}. \tag{7}$$

From (6) it is obvious that the coefficients $b^{(0)}_{\alpha\beta}$ are skew symmetric:

$$b^{(0)}_{\alpha\beta} = -b^{(0)}_{\beta\alpha}. \tag{8}$$

We note that (6), by virtue of (8), reduces to the $n(n-1)/2$ relations

$$\frac{\partial A_b}{\partial q^a} - \frac{\partial A_a}{\partial q^b} = b^{(0)}_{ab}, \tag{6'}$$

where $a = 1, 2, \ldots, n-1$, and $b = a+1, a+2, \ldots, n$.

So, the forces $Q_\alpha(q^\beta, \dot{q}^\beta, t)$ are linear in the generalized velocities, i.e., they must have the form

$$Q_\alpha = b^{(0)}_{\alpha\beta}(q^\gamma, t)\dot{q}^\beta + b^{(0)}_{\alpha n+1}(q^\gamma, t) \tag{9}$$

in order to allow their virtual work to be written in the form (1), and this follows from the considerations presented by Pars (1965). We shall now search for the conditions which have to be satisfied by the coefficients from the given forces (9), in order for them to be derivable from the Mayer's potential. To establish these conditions we start with the fact that the Mayer's potential, if it exists for the *given* forces, ought to have the form (2). So, supposing that the Mayer's potential exists and has the form (2), we easily obtain, having in mind (6), the conditions (8), as a part of the necessary conditions for the forces (9) to be derivable from the potential (2). The remaining necessary conditions which have to be satisfied by the coefficients in (9), as well as the sufficiency of all the established conditions, and the procedure which results in the potential (2), will be considered in the following.

2 The Case of Gyroscopic Forces

Let us consider, to begin with, the case $b^{(0)}_{\alpha n+1} = 0$. The forces (9), assuming that (8) holds, are gyroscopic then, as the work

[1] A variational problem results from the stationarity of an integral. So, one speaks of Hamilton's principle as a true variational problem when it expresses stationarity of the Hamiltonian action, given by the integral $W = \int_{t_0}^{t_1} L dt$.

Contributed by the Applied Mechanics Division of The American Society of Mechanical Engineers for publication in the ASME Journal of Applied Mechanics.

Discussion on the paper should be addressed to the Technical Editor, Professor Lewis T. Wheeler, Department of Mechanical Engineering, University of Houston, Houston, TX 77204-4792, and will be accepted until four months after final publication of the paper itself in the ASME Journal of Applied Mechanics.

Manuscript received by the ASME Applied Mechanics Division, Nov. 28, 1995; final revision, Dec. 22, 1996. Associate Technical Editor: N. C. Perkins.

done by them on the elementary actual displacement of the system vanishes.

As $b^{(0)}_{\alpha n+1} = 0$, using (7) one obtains

$$A_\alpha = \int_{c_0}^{t} \frac{\partial A_{n+1}}{\partial q^\alpha} dt + \Phi_\alpha(q^\beta), \tag{10}$$

where $\Phi_\alpha(q^\beta)$ are arbitrary functions of q^β, of class C_1 in some domain of $q^1, \ldots, q^n$, and where c_0 is an arbitrary constant value for t. Combining now (6) and (10), we obtain

$$b^{(0)}_{\alpha\beta} = \frac{\partial \Phi_\beta}{\partial q^\alpha} - \frac{\partial \Phi_\alpha}{\partial q^\beta},$$

which leads to

$$\frac{\partial b^{(0)}_{\alpha\beta}}{\partial t} = 0,$$

and the forces (9) take the form

$$Q_\alpha = b^{(0)}_{\alpha\beta}(q^\gamma)\dot{q}^\beta, \quad b^{(0)}_{\alpha\beta} = -b^{(0)}_{\beta\alpha}. \tag{11}$$

In order to determine the function (2) in this case, let us first examine a system with two degrees-of-freedom. Then (6′) becomes

$$\frac{\partial A_2}{\partial q^1} - \frac{\partial A_1}{\partial q^2} = b^{(0)}_{12}. \tag{12}$$

It can be easily verified that the function

$$V = -A_1(q^1, q^2, t)\dot{q}^1 - A_2(q^1, q^2, t)\dot{q}^2 - A_3(q^1, q^2, t) \tag{13}$$

can always be determined without any further restriction on the forces Q_1 and Q_2, i.e., on the coefficient $b^{(0)}_{12}(q^1, q^2)$. Namely, taking

$$A_3 = \Phi_3(q^1, q^2, t), \tag{14}$$

where $\Phi_3(q^1, q^2, t)$ is an arbitrary function of class C_1 in some domain $D_0(q^1, q^2, t)$, and taking, in accordance with (10),

$$A_1 = \int_{c_0}^{t} \frac{\partial \Phi_3}{\partial q^1} dt + \Phi^{(0)}_1(q^1, q^2), \tag{15}$$

where $\Phi^{(0)}_1(q^1, q^2)$ is an arbitrary function of class C_1 in a domain $D_1(q^1, q^2)$, we obtain from (12)

$$A_2 = \int_{c_1}^{q^1} b^{(0)}_{12} dq^1 + \int_{c_1}^{q^1} \frac{\partial \Phi^{(0)}_1}{\partial q^2} dq^1 + \int_{c_0}^{t} \frac{\partial \Phi_3}{\partial q^2} dt - \int_{c_0}^{t} \left[\frac{\partial \Phi_3}{\partial q^2}\right]_{q^1=c_1} dt + F^{(1)}_2(q^2, t), \tag{16}$$

where c_1 is any constant value of q^1 belonging to $D_1(q^1, q^2)$, and where $F^{(1)}_2$ denotes an arbitrary function of q^2, t, of class C_1 in a certain domain of q^2, t. Keeping in mind that, in the case considered, the relation (7) gives

$$\frac{\partial A_2}{\partial t} = \frac{\partial \Phi_3}{\partial q^2}$$

and finding from (16)

$$\frac{\partial A_2}{\partial t} = \frac{\partial \Phi_3}{\partial q^2} - \left[\frac{\partial \Phi_3}{\partial q^2}\right]_{q^1=c_1} + \frac{\partial F^{(1)}_2}{\partial t},$$

we obtain

$$\left[\frac{\partial \Phi_3}{\partial q^2}\right]_{q^1=c_1} = \frac{\partial F^{(1)}_2}{\partial t}, \tag{17}$$

so that (16) reduces to

$$A_2 = \int_{c_1}^{q^1} b^{(0)}_{12} dq^1 + \int_{c_1}^{q^1} \frac{\partial \Phi^{(0)}_1}{\partial q^2} dq^1 + \int_{c_0}^{t} \frac{\partial \Phi_3}{\partial q^2} dt + \Phi^{(1)}_2, \tag{16′}$$

where

$$\Phi^{(1)}_2(q^2) = F^{(1)}_2(q^2, t = c_0),$$

i.e., $\Phi^{(1)}_2$ is an arbitrary function of q^2, of class C_1 in the relevant domain of q^2. Now (4) takes the form

$$\delta \int_{t_0}^{t_1} \Bigg[L + \left(\Phi^{(0)}_1 + \int_{c_0}^{t} \frac{\partial \Phi_3}{\partial q^1} dt\right)\dot{q}^1 + \left(\int_{c_1}^{q^1} b^{(0)}_{12} dq^1 + \int_{c_0}^{t} \frac{\partial \Phi^{(0)}_1}{\partial q^2} dq^1 + \int_{c_0}^{t} \frac{\partial \Phi_3}{\partial q^2} dt + \Phi^{(1)}_2\right)\dot{q}^2 + \Phi_3 \Bigg] dt = 0, \tag{18}$$

which leads to the differential equations of motion for our system of two degrees-of-freedom.

It is noteworthy that when we form the descriptive function L_1, the expression

$$\left(\Phi^{(0)}_1 + \int_{c_0}^{t} \frac{\partial \Phi_3}{\partial q^1} dt\right)\dot{q}^1 + \left(\Phi^{(1)}_2 + \int_{c_1}^{q^1} \frac{\partial \Phi^{(0)}_1}{\partial q^2} dq^1 + \int_{c_0}^{t} \frac{\partial \Phi_3}{\partial q^2} dt\right)\dot{q}^2 + \Phi_3,$$

being a total derivative with respect to time of the function

$$F(q^1, q^2, t) = \int_{c_1}^{q^1} \Phi^{(0)}_1 dq^1 + \int_{c_2}^{q^2} \Phi^{(1)}_2 dq^2 + \int_{c_0}^{t} \Phi_3 dt,$$

may simply be omitted, and (18) reduces to

$$\delta \int_{t_0}^{t_1} \left(L + \dot{q}^2 \int_{c_1}^{q^1} b^{(0)}_{12} dq^1\right) dt = 0. \tag{18′}$$

We now turn to the case $n > 2$, assuming still that $b^{(0)}_{\alpha n+1} = 0$, i.e., that the force Q_α have the form (11). In contrast to the case when $n = 2$, in this case the coefficients A_α can be found from (6′) if, and only if, the independent conditions

$$\frac{\partial b^{(0)}_{ab}}{\partial q^c} + \frac{\partial b^{(0)}_{bc}}{\partial q^a} = \frac{\partial b^{(0)}_{ac}}{\partial q^b} \tag{19}$$

$$a = 1, 2, \ldots, n-2;$$

$$b = a+1, a+2, \ldots, n-1;$$

$$c = b+1, b+2, \ldots, n;$$

hold. To prove the necessity of the conditions (19) for finding A_α, and consequently the function (2), we first determine, using (6), the partial derivatives

$$\frac{\partial b^{(0)}_{\alpha\beta}}{\partial q^\gamma} = \frac{\partial^2 A_\beta}{\partial q^\alpha \partial q^\gamma} - \frac{\partial^2 A_\alpha}{\partial q^\beta \partial q^\gamma} \tag{20}$$

wherefrom, by the appropriate substitution of indices, we have

$$\frac{\partial b^{(0)}_{\beta\gamma}}{\partial q^\alpha} = \frac{\partial^2 A_\gamma}{\partial q^\beta \partial q^\alpha} - \frac{\partial^2 A_\beta}{\partial q^\gamma \partial q^\alpha}, \tag{21}$$

$$\frac{\partial b^{(0)}_{\alpha\gamma}}{\partial q^\beta} = \frac{\partial^2 A_\gamma}{\partial q^\alpha \partial q^\beta} - \frac{\partial^2 A_\alpha}{\partial q^\gamma \partial q^\beta}. \tag{22}$$

Using (20), (21), and (22), we easily obtain

$$\frac{\partial b^{(0)}_{\alpha\beta}}{\partial q^{\gamma}} + \frac{\partial b^{(0)}_{\beta\gamma}}{\partial q^{\alpha}} = \frac{\partial b^{(0)}_{\alpha\gamma}}{\partial q^{\beta}}. \quad (23)$$

Having now in mind that, since $b^{(0)}_{\alpha\beta} = -b^{(0)}_{\beta\alpha}$, the relations (23) refer to the case $\alpha < \beta < \gamma$, we write them in the form (19), and the necessity of (19) follows.

To demonstrate the sufficiency of the conditions (8) and (19) for determining the Mayer's potential (2), we shall find this potential assuming that the coefficients of the given forces (9) satisfy these conditions.

We start taking

$$A_{n+1}(q^{\alpha}, t) = \Phi_{n+1}(q^{\alpha}, t),$$

where $\Phi_{n+1}(q^{\alpha}, t)$ is an arbitrary function of $q^1, q^2, \ldots, q^n$, t, of class C_1 in some domain $D_0(q^1, \ldots, q^n, t)$, so that, in accordance with (10), we can write

$$A_1 = \Phi^{(0)}_1(q^{\gamma}) + \int_{c_0}^{t} \frac{\partial \Phi_{n+1}}{\partial q^1} dt, \quad (24)$$

where $\Phi^{(0)}_1(q^{\gamma})$ is an arbitrary function of $q^1, q^2, \ldots, q^n$, of class C_1 in some domain $D_1(q^1, \ldots, q^n)$, and where c_0 is a constant value for t from D_0.

Now, integrating $n - 1$ relations

$$\frac{\partial A_b}{\partial q^1} - \frac{\partial A_1}{\partial q^b} = b^{(0)}_{1b}, \quad b = 2, 3, \ldots, n \quad (25)$$

which we obtain from (6′) using $a = 1$, we find

$$A_b = \int_{c_1}^{q^1} b^{(0)}_{1b} dq^1 + \int_{c_1}^{q^1} \frac{\partial \Phi^{(0)}_1}{\partial q^b} dq^1 + \int_{c_0}^{t} \frac{\partial \Phi_{n+1}}{\partial q^b} dt - \int_{c_0}^{t} \left[\frac{\partial \Phi_{n+1}}{\partial q^b}\right]_{q^1=c_1} dt + F^{(1)}_b(q^2, q^3, \ldots, t), \quad (26)$$

where c_1 is any constant value for q^1 from D_1, and $F^{(1)}_b$ are functions of $q^2, q^3, \ldots, t$, of class C_1 in a domain $D_2(q^2, q^3, \ldots, q^n, t)$.

Further, using the relation

$$\left[\frac{\partial \Phi_{n+1}}{\partial q^b}\right]_{q^1=c_1} = \frac{\partial F^{(1)}_b}{\partial t},$$

which is easy to prove combining (7) and (26), with (26) we obtain

$$A_b = \int_{c_1}^{q^1} b^{(0)}_{1b} dq^1 + \int_{c_1}^{q^1} \frac{\partial \Phi^{(0)}_1}{\partial q^b} dq^1 + \int_{c_0}^{t} \frac{\partial \Phi_{n+1}}{\partial q^b} dt + \Phi^{(1)}_b, \quad (27)$$

$$b = 2, 3, \ldots, n$$

where

$$\Phi^{(1)}_b(q^2, q^3, \ldots, q^n) = F^{(1)}_b(q^2, q^3, \ldots, q^n, t = c_0)$$

are functions which do not depend on t explicitly. We notice that $\Phi^{(1)}_2$ is an arbitrary function of $q^2, q^3, \ldots, q^n$, while $\Phi^{(1)}_3, \ldots, \Phi^{(1)}_n$ can be expressed through $\Phi^{(1)}_2$. To prove this, we use again (6′), wherefrom, taking $a = 2$, we obtain

$$\frac{\partial A_c}{\partial q^2} - \frac{\partial A_2}{\partial q^c} = b^{(0)}_{2c}, \quad c = 3, 4, \ldots, n. \quad (28)$$

From (27) and (28) we further find

$$\int_{c_1}^{q^1} \left(\frac{\partial b^{(0)}_{1c}}{\partial q^2} - \frac{\partial b^{(0)}_{12}}{\partial q^c}\right) dq^1 + \frac{\partial \Phi^{(1)}_c}{\partial q^2} - \frac{\partial \Phi^{(1)}_2}{\partial q^c} = b^{(0)}_{2c}, \quad (29)$$

$$c = 3, 4, \ldots, n$$

wherefrom, keeping in mind that, if we take $a = 1$ and $b = 2$, (19) leads to

$$\frac{\partial b^{(0)}_{1c}}{\partial q^2} - \frac{\partial b^{(0)}_{12}}{\partial q^c} = \frac{\partial b^{(0)}_{2c}}{\partial q^1}, \quad c = 3, 4, \ldots, n.$$

We obtain

$$\frac{\partial \Phi^{(1)}_c}{\partial q^2} - \frac{\partial \Phi^{(1)}_2}{\partial q^c} = b^{(1)}_{2c}, \quad c = 3, 4, \ldots, n \quad (30)$$

where

$$b^{(1)}_{2c}(q^2, q^3, \ldots, q^n) = b^{(0)}_{2c}(q^1 = c_1, q^2, \ldots, q^n). \quad (31)$$

Integrating (30), we have

$$\Phi^{(1)}_c = \int_{c_2}^{q^2} b^{(1)}_{2c} dq^2 + \int_{c_2}^{q^2} \frac{\partial \Phi^{(1)}_2}{\partial q^c} dq^2 + \Phi^{(2)}_c, \quad (32)$$

$$c = 3, 4, \ldots, n$$

where c_2 denotes any constant value for q^2 from D_2, and $\Phi^{(2)}_c$ are functions of $q^3, q^4, \ldots, q^n$, of class C_1 in a relevant domain of coordinates $q^3, q^4, \ldots, q^n$, provided that $\Phi^{(2)}_3$ is an arbitrary function, while $\Phi^{(2)}_4, \ldots, \Phi^{(2)}_n$ can be expressed by $\Phi^{(2)}_3$. Namely, using the notations

$$b^{(a)}_{bc} = b^{(a)}_{bc}(q^{a+1}, q^{a+2}, \ldots, q^n) = b^{(0)}_{bc}(q^1 = c_1, \ldots, q^a = c_a, q^{a+1}, q^{a+2}, \ldots, q^n) \quad (33)$$

$$a = 1, 2, \ldots, n-2$$

$$b = a+1, a+2, \ldots, n-1$$

$$c = b+1, b+2, \ldots, n$$

where $c_1, c_2, \ldots, c_n$ are constants, and introducing the functions

$$\Phi^{(a)}_b = \Phi^{(a)}_b(q^{a+1}, q^{a+2}, \ldots, q^n)$$

$$a = 1, 2, \ldots, n-1$$

$$b = a+1, a+2, \ldots, n$$

we obtain, by the same procedure used in arriving at the relations (19) and (32), the analogous relations

$$\frac{\partial b^{(i)}_{ab}}{\partial q^c} + \frac{\partial b^{(i)}_{bc}}{\partial q^a} = \frac{\partial b^{(i)}_{ac}}{\partial q^b} \quad (19')$$

$$i = 1, 2, \ldots, n-3$$

$$a = i+1, i+2, \ldots, n-2$$

$$b = a+1, \ldots, n-1$$

$$c = b+1, \ldots, n$$

and

$$\Phi^{(a)}_b = \int_{c_{a+1}}^{q^{a+1}} b^{(a)}_{a+1\,b} dq^{a+1} + \int_{c_{a+1}}^{q^{a+1}} \frac{\partial \Phi^{(a)}_{a+1}}{\partial q^b} dq^{a+1} + \Phi^{(a+1)}_b, \quad (32')$$

$$a = 1, 2, \ldots, n-2$$

$$b = a+2, \ldots, n$$

where the repeated index here does not imply summation. We notice that (32′) includes (32), for $a = 1$, and that $\Phi^{(a)}_{a+1}$, where $a = 1, 2, \ldots, n-1$, are arbitrary functions of $q^{a+1}, q^{a+2}, \ldots, q^n$, of class C_1 in a relevant domain of q's.

Finally, using (32′), (27) gives

$$A_b = \int_{c_1}^{q^1} b_{1b}^{(0)} dq^1 + \int_{c_2}^{q^2} b_{2b}^{(1)} dq^2 + \ldots + \int_{c_{b-1}}^{q^{b-1}} b_{b-1b}^{(b-2)} dq^{b-1}$$
$$+ \int_{c_1}^{q^1} \frac{\partial \Phi_1^{(0)}}{\partial q^b} dq^1 + \int_{c_2}^{q^2} \frac{\partial \Phi_2^{(1)}}{\partial q^b} dq^2 + \ldots$$
$$+ \int_{c_{b-1}}^{q^{b-1}} \frac{\partial \Phi_{b-1}^{(b-2)}}{\partial q^b} dq^{b-1} + \int_{c_0}^{t} \frac{\partial \Phi_{n+1}}{\partial q^b} dt + \Phi_b^{(b-1)} \quad (34)$$
$$b = 2, 3, \ldots, n.$$

So, if the coefficients of the gyroscopic forces (11) satisfy the conditions (19), the generalized Hamilton's principle (4), with the descriptive function

$$L_1 = L + \left(\Phi_1^{(0)} + \int_{c_0}^{t} \frac{\partial \Phi_{n+1}}{\partial q^1} dt \right) \dot{q}^1 + \sum_{b=2}^{n} A_b \dot{q}^b + \Phi_{n+1}, \quad (35)$$

where A_b are given by (34), holds for the system considered. We notice that the descriptive function (35) can be reduced to the form

$$L_1 = L + \sum_{b=2}^{n} \left(\int_{c_1}^{q^1} b_{1b}^{(0)} dq^1 + \int_{c_2}^{q^2} b_{2b}^{(1)} dq^2 + \ldots \right.$$
$$\left. + \int_{c_{b-1}}^{q^{b-1}} b_{b-1b}^{(b-2)} dq^{b-1} \right) \dot{q}^b \quad (36)$$

since the expression

$$\left(\Phi_1^{(0)} + \int_{c_0}^{t} \frac{\partial \Phi_{n+1}}{\partial q^1} dt \right) \dot{q}^1 + \sum_{b=2}^{n} \left(\int_{c_1}^{q^1} \frac{\partial \Phi_1^{(0)}}{\partial q^b} dq^2 + \ldots \right.$$
$$\left. + \int_{c_{b-1}}^{q^{b-1}} \frac{\partial \Phi_{b-1}^{(b-2)}}{\partial q^b} dq^{b-1} + \int_{c_0}^{t} \frac{\partial \Phi_{n+1}}{\partial q^b} dt + \Phi_b^{(b-1)} \right) \dot{q}^b + \Phi_{n+1}$$

can be written as a total derivative

$$\frac{d}{dt} \left(\int_{c_1}^{q^1} \Phi_1^{(0)} dq^1 + \int_{c_2}^{q^2} \Phi_2^{(1)} dq^2 + \ldots \right.$$
$$\left. + \int_{c_n}^{q^n} \Phi_n^{(n-1)} dq^n + \int_{c_0}^{t} \Phi_{n+1} dt + \text{const.} \right),$$

and consequently can be omitted in (35). This is, of course, in accordance with the fact that, since the functions $\Phi_1^{(0)}$, $\Phi_2^{(1)}$, $\ldots$, $\Phi_n^{(n-1)}$, Φ_{n+1} are arbitrary, we may choose

$$\Phi_1^{(0)} = \Phi_2^{(1)} = \ldots = \Phi_n^{(n-1)} = \Phi_{n+1} = 0.$$

3 The Case of Nongyroscopic Forces

Let us now move to the nongyroscopic case, assuming that $b_{\alpha n+1}^{(0)} \neq 0$, i.e., that Q_α (see (9), (8)) have the form

$$Q_\alpha = b_{\alpha\beta}^{(0)} \dot{q}^\beta + b_{\alpha n+1}^{(0)}, \quad b_{\alpha\beta}^{(0)} = -b_{\beta\alpha}^{(0)}. \quad (37)$$

Introducing the new coordinate

$$q^{n+1} = t,$$

and having in mind that $\dot{q}^{n+1} = 1$, we can write the function (2) in the form

$$V(q^i, \dot{q}^i) = -A_i \dot{q}^i, \quad i = 1, 2, \ldots, n + 1 \quad (38)$$

with $A_i = A_i(q^1, q^2, \ldots, q^{n+1})$, while the forces (37) become

$$Q_\alpha = b_{\alpha i}^{(0)} \dot{q}^i, \quad (37')$$

where $i = 1, 2, \ldots, n + 1$, $b_{\alpha i}^{(0)}(q^1, q^2, \ldots, q^{n+1}) = -b_{i\alpha}^{(0)}(q^1, q^2, \ldots, q^{n+1})$, and where repeated indices imply summation.

In order to make the results obtained for gyroscopic forces applicable to this case, we further introduce the new "generalized force" (which does not appear in (1)):

$$Q_{n+1} = b_{n+1i}^{(0)} \dot{q}^i \quad (39)$$

where $b_{n+1\alpha}^{(0)} = -b_{\alpha n+1}^{(0)}$ and $b_{n+1n+1}^{(0)} = 0$, so that combining (37′) and (39) we can write

$$Q_i = b_{ij} \dot{q}^j, \quad i, j = 1, 2, \ldots, n + 1 \quad (40)$$

where

$$b_{ij}^{(0)}(q^1, q^2, \ldots, q^{n+1}) = -b_{ji}^{(0)}(q^1, q^2, \ldots, q^{n+1}). \quad (41)$$

Now, keeping in mind (19) and (36), it is obvious that the conditions

$$\frac{\partial b_{ij}^{(0)}}{\partial q^k} + \frac{\partial b_{jk}^{(0)}}{\partial q^i} = \frac{\partial b_{ik}^{(0)}}{\partial q^j} \quad (42)$$
$$i = 1, 2, \ldots, n - 1$$
$$j = i + 1, i + 2, \ldots, n$$
$$k = j + 1, j + 2, \ldots, n + 1$$

have to be satisfied by the coefficients (41), to ensure that the descriptive function

$$L_1 = L + \sum_{i=2}^{n+1} \left(\int_{c_1}^{q^1} b_{1i}^{(0)} dq^1 + \int_{c_2}^{q^2} b_{2i}^{(1)} dq^2 + \ldots \right.$$
$$\left. + \int_{c_{i-1}}^{q^{i-1}} b_{i-1i}^{(i-2)} dq^{i-1} \right) \dot{q}^i \quad (43)$$

can be constructed.

Finally, replacing the coordinate q^{n+1} with t, (42) and (43) read

$$\frac{\partial b_{ij}^{(0)}}{\partial q^k} + \frac{\partial b_{jk}^{(0)}}{\partial q^i} = \frac{\partial b_{ik}^{(0)}}{\partial q^j}, \quad (42'a)$$
$$i = 1, 2, \ldots, n - 2$$
$$j = i + 1, i + 2, \ldots, n - 1$$
$$k = j + 1, j + 2, \ldots, n$$
$$\frac{\partial b_{ij}^{(0)}}{\partial t} + \frac{\partial b_{jn+1}^{(0)}}{\partial q^i} = \frac{\partial b_{in+1}^{(0)}}{\partial q^j} \quad (42'b)$$
$$i = 1, 2, \ldots, n - 1$$
$$j = i + 1, i + 2, \ldots, n$$

and

$$L_1 = L + \sum_{i=2}^{n} \left(\int_{c_1}^{q^1} b_{1i}^{(0)} dq^1 + \int_{c_2}^{q^2} b_{2i}^{(1)} dq^2 + \ldots \right.$$
$$\left. + \int_{c_{i-1}}^{q^{i-1}} b_{i-1i}^{(i-2)} dq^{i-1} \right) \dot{q}^i + \sum_{i=1}^{n} \int_{c_i}^{q^i} b_{in+1}^{(i-1)} dq^i \quad (43')$$

where, analogous to (33),

$$b_{i+1j}^{(i)} = b_{i+1j}^{(i)}(q^{i+1}, q^{i+2}, \ldots, q^n, t) = b_{i+1j}^{(i)}(q^1 = c_1,$$
$$q^2 = c_2, \ldots, q^i = c_i, q^{i+1}, q^{i+2}, \ldots, q^n, t) \quad (44)$$
$$i = 1, 2, \ldots, n - 2$$
$$j = i + 2, i + 3, \ldots, n.$$

Thus the necessary and sufficient conditions which ensure the given generalized forces (9) are derivable from a Mayer's potential are given by the relations (8) and (42'a), (42'b).

4 Relation Between Mayer's Potential and the Potential Considered by Santilli

Santilli (1983) presented the necessary and sufficient conditions for a local class C^1 Newtonian force $\mathbf{F}(t, \mathbf{r}, \dot{\mathbf{r}})$ to be derivable from a potential $U(t, \mathbf{r}, \dot{\mathbf{r}})$, which we further call Santilli's potential. These conditions are summarized presently.

The projections Y_1, Y_2, Y_3 of the Newtonian force $\mathbf{F} = \mathbf{F}(t, \mathbf{r}, \dot{\mathbf{r}})$ on the axes of a rectangular Cartesian coordinate system $Oy_1y_2y_3$ have to be of the form

$$Y_a = \rho_{ab}(t, y^1, y^2, y^3)\dot{y}^b + \rho_{at}(t, y^1, y^2, y^3), \quad (46)$$

$$a, b = 1, 2, 3$$

and the following conditions

$$\rho_{ab} + \rho_{ba} = 0$$

$$\frac{\partial \rho_{ab}}{\partial y^c} + \frac{\partial \rho_{bc}}{\partial y^a} + \frac{\partial \rho_{ca}}{\partial y^b} = 0$$

$$\frac{\partial \rho_{ab}}{\partial t} + \frac{\partial \rho_{bt}}{\partial y^a} - \frac{\partial \rho_{at}}{\partial y^b} = 0 \quad (47)$$

$$a, b, c = 1, 2, 3$$

have to be identically satisfied in a star-shaped neighborhood of a point (t, y^1, y^2, y^3).

It is obvious that the Santilli's potential coincides with Mayer's potential if the latter corresponds to the motion of a free particle under the action of a force which satisfies the conditions for the existence of Santilli's potential. Namely, in this case Y_a is the generalized force corresponding to the Cartesian coordinate y^a, and the existence conditions of a Mayer's potential reduce to (46), (47).

Let us now consider the system of particles $M_1, \ldots, M_N$, acted on by the system of forces

$$\mathbf{F}_1, \mathbf{F}_2, \ldots, \mathbf{F}_N, \quad (48)$$

where $\mathbf{F}_i$ denotes the force applied to M_i, $i = 1, 2, \ldots, N$. The motion of the system is assumed to be constrained by the holonomic constraints

$$f^\nu(y^1_{(1)}, y^2_{(1)}, y^3_{(1)}, y^1_{(2)}, y^2_{(2)}, y^3_{(2)}, \ldots, y^1_{(N)}, y^2_{(N)}, y^3_{(N)}, t) = 0, \quad (49)$$

$$\nu = 1, 2, \ldots, l; \quad l < 3N$$

where $y^1_{(i)}$, $y^2_{(i)}$, $y^3_{(i)}$ are Cartesian coordinates of M_i.

Let us further suppose that the conditions ensuring the existence of Santilli's potential (i.e., conditions of the form (46), (47), satisfied by the functions $\rho_{ab(i)}$, $\rho_{at(i)}$ corresponding to the force $\mathbf{F}_i$) are fulfilled for each force in (48). The consequence of that fact is that the conditions for the existence of Mayer's potential are also fulfilled. However, the inverse statement does not hold. This will be proved below.

Let each force from the system (48) satisfy conditions (46) and (47) for the existence of Santilli's potential. In this case the expression for the generalized force Q_α will have the form required for the existence of Mayer's potential:

$$Q_\alpha = b^{(0)}_{\alpha\beta}(q^\gamma, t)\dot{q}^\beta + b^{(0)}_{\alpha n+1}(q^\gamma, t), \quad b^{(0)}_{\alpha\beta} = -b^{(0)}_{\beta\alpha}.$$

Here the coefficients $b^{(0)}_{\alpha\beta}$, $b^{(0)}_{\alpha n+1}$ are given by

$$b^{(0)}_{\alpha\beta} = \sum_{i=1}^{N} \rho_{ab(i)} \frac{\partial y^a_{(i)}}{\partial q^\alpha} \frac{\partial y^b_{(i)}}{\partial q^\beta},$$

$$b^{(0)}_{\alpha n+1} = \sum_{i=1}^{N} \left(\rho_{ab(i)} \frac{\partial y^a_{(i)}}{\partial q^\alpha} \frac{\partial y^b_{(i)}}{\partial t} + \rho_{at(i)} \frac{\partial y^a_{(i)}}{\partial q^\alpha} \right). \quad (50)$$

The remaining conditions for the existence of Mayer's potential, given by (42'a) and (42'b), take the form

$$\frac{\partial b^{(0)}_{\alpha\beta}}{\partial q^\gamma} + \frac{\partial b^{(0)}_{\beta\gamma}}{\partial q^\alpha} + \frac{\partial b^{(0)}_{\gamma\alpha}}{\partial q^\beta} = \sum_{i=1}^{N} \left(\frac{\partial \rho_{ab(i)}}{\partial y^c_{(i)}} + \frac{\partial \rho_{bc(i)}}{\partial y^a_{(i)}} + \frac{\partial \rho_{ca(i)}}{\partial y^b_{(i)}} \right) \times \frac{\partial y^a_{(i)}}{\partial q^\alpha} \frac{\partial y^b_{(i)}}{\partial q^\beta} \frac{\partial y^c_{(i)}}{\partial q^\gamma} = 0 \quad (51a)$$

$$\frac{\partial b^{(0)}_{\alpha\beta}}{\partial t} + \frac{\partial b^{(0)}_{\beta\gamma}}{\partial q^\alpha} - \frac{\partial b^{(0)}_{\alpha n+1}}{\partial q^\beta} = \sum_{i=1}^{N} \left(\frac{\partial \rho_{ab(i)}}{\partial y^c_{(i)}} + \frac{\partial \rho_{bc(i)}}{\partial y^a_{(i)}} + \frac{\partial \rho_{ca(i)}}{\partial y^b_{(i)}} \right) \times \frac{\partial y^a_{(i)}}{\partial q^\alpha} \frac{\partial y^b_{(i)}}{\partial q^\beta} \frac{\partial y^c_{(i)}}{\partial t} + \sum_{i=1}^{N} \left(\frac{\partial \rho_{ab(i)}}{\partial t} + \frac{\partial \rho_{bt(i)}}{\partial y^a_{(i)}} - \frac{\partial \rho_{at(i)}}{\partial y^b_{(i)}} \right) \times \frac{\partial y^a_{(i)}}{\partial q^\alpha} \frac{\partial y^b_{(i)}}{\partial q^\beta} = 0, \quad (51b)$$

where the fulfillment of the conditions (46), (47) for the existence of Santilli's potential for each force from (48) has as a consequence that the conditions for the existence of Mayer's potential are also fulfilled. To prove that the inverse statement does not hold, we shall analyze the following case. Let the forces from the system (48) have the form (46), and let

$$\frac{\partial \rho_{ab(i)}}{\partial t} = 0, \quad \rho_{at(i)} = 0, \quad (52)$$

$$\rho_{ab(i)} + \rho_{ba(i)} = 0, \quad (53)$$

$$\frac{\partial \rho_{ab(i)}}{\partial y^c_{(i)}} + \frac{\partial \rho_{bc(i)}}{\partial y^a_{(i)}} + \frac{\partial \rho_{ca(i)}}{\partial y^b_{(i)}} \neq 0. \quad (54)$$

$$i = 1, 2, \ldots, N$$

$$a, b, c = 1, 2, 3.$$

The relations (54) indicate that not one of the forces of the system (48) has Santilli's potential. If the constraints (49) satisfy the condition

$$\frac{\partial f^\nu}{\partial t} = 0,$$

the relations

$$\frac{\partial y^a_{(i)}}{\partial t} = 0$$

will also be valid. These relations, together with (52) and (50), lead to the trivial fulfillment of the relations (51b). In the case $n = 2$ the conditions (51a) will also be satisfied, in spite of (54), what is easy to verify having in mind the skew symmetry of the tensor

$$\frac{\partial b^{(0)}_{\alpha\beta}}{\partial q^\gamma} + \frac{\partial b^{(0)}_{\beta\gamma}}{\partial q^\alpha} + \frac{\partial b^{(0)}_{\gamma\alpha}}{\partial q^\beta}$$

with respect to any pair of indices. This is in accordance with our conclusion referring to the case $n = 2$, obtained in Section 2 of this paper.

5 An Example

Let us consider, as an example, the system of particles $M_1, M_2, \ldots, M_N$, with masses $m_1, m_2, \ldots, m_N$ respectively, moving with respect to the frame of reference $O\xi\eta\zeta$ whose angular velocity $\boldsymbol{\omega} = \boldsymbol{\omega}(t)$ relative to a Newtonian base is prescribed. The system is subject to the constraints

$$f^{\nu}(\xi_1, \eta_1, \zeta_1, \ldots, \xi_N, \eta_N, \zeta_N, t) = 0, \quad (55)$$

$$\nu = 1, 2, \ldots, l; \quad l < 3N$$

where ξ_i, η_i, ζ_i are the coordinates of M_i, $i = 1, 2, \ldots, N$, with respect to the system $O\xi\eta\zeta$. Find the conditions for which the generalized Coriolis forces are derivable from a Mayer's potential,[2] and then determine this potential.

Solution. The Coriolis force applied to the particle M_i is given by

$$\mathbf{F}_{(i)\mathrm{cor}} = -2m_i\boldsymbol{\omega} \times \frac{d_r\boldsymbol{\rho}_i}{dt}$$

where $\boldsymbol{\rho}_i$ is the radius vector from O to M_i, and where d_r/dt denotes the relative derivative with respect to t.

As a consequence of (55) we may write

$$\boldsymbol{\rho}_i = \boldsymbol{\rho}_i(q^1, q^2, \ldots, q^n, t), \quad n = 3N - l$$

where $q^1, q^2, \ldots, q^n$ are the Lagrangian coordinates of the system. The generalized Coriolis force corresponding to the coordinate q^α reads

$$Q_{\alpha\mathrm{cor}} = -2\boldsymbol{\omega} \cdot \sum_{i=1}^{N} m_i \frac{d_r\boldsymbol{\rho}_i}{dt} \times \frac{\partial\boldsymbol{\rho}_i}{\partial q^\alpha}, \quad (56)$$

i.e.,

$$Q_{\alpha\mathrm{cor}} = -2\boldsymbol{\omega} \cdot \sum_{i=1}^{N} m_i \left(\frac{\partial\boldsymbol{\rho}_i}{\partial q^\beta} \times \frac{\partial\boldsymbol{\rho}_i}{\partial q^\alpha} \right) \dot{q}^\beta - 2\boldsymbol{\omega} \cdot \sum_{i=1}^{N} m_i \left(\frac{\partial_r\boldsymbol{\rho}_i}{\partial t} \times \frac{\partial\boldsymbol{\rho}_i}{\partial q^\alpha} \right), \quad (56')$$

$$\alpha, \beta = 1, 2, \ldots, n$$

wherefrom it is evident that it has the form (37), with the coefficients

$$b^{(0)}_{\alpha\beta} = -2\boldsymbol{\omega} \cdot \sum_{i=1}^{N} m_i \left(\frac{\partial\boldsymbol{\rho}_i}{\partial q^\beta} \times \frac{\partial\boldsymbol{\rho}_i}{\partial q^\alpha} \right), \quad b^{(0)}_{\alpha\beta} = -b^{(0)}_{\beta\alpha}$$

$$b^{(0)}_{\alpha n+1} = -2\boldsymbol{\omega} \cdot \sum_{i=1}^{N} m_i \left(\frac{\partial_r\boldsymbol{\rho}_i}{\partial t} \times \frac{\partial\boldsymbol{\rho}_i}{\partial q^\alpha} \right) \quad (57)$$

$$\alpha, \beta = 1, 2, \ldots, n.$$

The forces (56) have Mayer's potential if, and only if, the coefficients (57) satisfy the conditions $(42'a)$, $(42'b)$.

Having in mind that

$$\frac{\partial b^{(0)}_{\alpha\beta}}{\partial q^\gamma} = -2\boldsymbol{\omega} \cdot \sum_{i=1}^{N} m_i \left(\frac{\partial^2\boldsymbol{\rho}_i}{\partial q^\beta \partial q^\gamma} \times \frac{\partial\boldsymbol{\rho}_i}{\partial q^\alpha} + \frac{\partial\boldsymbol{\rho}_i}{\partial q^\beta} \times \frac{\partial^2\boldsymbol{\rho}_i}{\partial q^\alpha \partial q^\gamma} \right),$$

it is easy to verify that the conditions $(42'a)$ are always satisfied. Further, as

$$\frac{\partial b^{(0)}_{\alpha\beta}}{\partial t} = -2\dot{\boldsymbol{\omega}} \cdot \sum_{i=1}^{N} m_i \left(\frac{\partial\boldsymbol{\rho}_i}{\partial q^\beta} \times \frac{\partial\boldsymbol{\rho}_i}{\partial q^\alpha} \right) - 2\boldsymbol{\omega} \cdot \sum_{i=1}^{N} m_i \left\{ \left[\frac{\partial_r}{\partial t} \left(\frac{\partial\boldsymbol{\rho}_i}{\partial q^\beta} \right) \right] \times \frac{\partial\boldsymbol{\rho}_i}{\partial q^\alpha} + \frac{\partial\boldsymbol{\rho}_i}{\partial q^\beta} \times \left[\frac{\partial_r}{\partial t} \left(\frac{\partial\boldsymbol{\rho}_i}{\partial q^\alpha} \right) \right] \right\}$$

and

$$\frac{\partial b^{(0)}_{\alpha n+1}}{\partial q^\beta} = -2\boldsymbol{\omega} \cdot \sum_{i=1}^{N} m_i \left\{ \left[\frac{\partial}{\partial q^\beta} \left(\frac{\partial_r\boldsymbol{\rho}_i}{\partial t} \right) \right] \times \frac{\partial\boldsymbol{\rho}_i}{\partial q^\alpha} + \frac{\partial_r\boldsymbol{\rho}_i}{\partial t} \times \frac{\partial^2\boldsymbol{\rho}_i}{\partial q^\alpha \partial q^\beta} \right\},$$

we find that the conditions $(42'b)$ are fulfilled if and only if the relations

$$\boldsymbol{\epsilon} \cdot \sum_{i=1}^{N} m_i \left(\frac{\partial\boldsymbol{\rho}_i}{\partial q^\alpha} \times \frac{\partial\boldsymbol{\rho}_i}{\partial q^\beta} \right) = 0, \quad (\boldsymbol{\epsilon} = \boldsymbol{\epsilon}(t) = \dot{\boldsymbol{\omega}}(t)) \quad (58)$$

hold. These relations lead to the following conditions:

$$\boldsymbol{\omega} = \text{const.}, \quad (59)$$

$$\sum_{i=1}^{N} m_i \left(\frac{\partial\boldsymbol{\rho}_i}{\partial q^\alpha} \times \frac{\partial\boldsymbol{\rho}_i}{\partial q^\beta} \right) = 0, \quad (60)$$

$$\boldsymbol{\epsilon} \perp \sum_{i=1}^{N} m_i \left(\frac{\partial\boldsymbol{\rho}_i}{\partial q^\alpha} \times \frac{\partial\boldsymbol{\rho}_i}{\partial q^\beta} \right), \quad (61)$$

each of which ensures $(42'b)$.

In the case (60) the forces $(56')$ do not depend on the generalized velocities of the system and the conditions $(42'a)$ are trivially satisfied, while $(42'b)$ reduces to the well-known conditions providing the existence of a potential for the given forces which depend on the position of the system and on time.

In cases (59) and (61) Mayer's potential is given by (see (38))

$$V = -\sum_{j=1}^{n+1} A_j \dot{q}^j, \quad (q^{n+1} = t, \dot{q}^{n+1} = 1) \quad (62)$$

where A_j, after omitting terms which are irrelevant in the case considered, have the form (see (24) and (34))

$$A_1 = 0, \quad A_j = \sum_{k=1}^{j-1} \int_{c_k}^{q^k} b^{(k-1)}_{kj} dq^k, \quad (63)$$

$$j = 2, 3, \ldots, n+1$$

or, by virtue of (57), the form

$$A_1 = 0, \quad A_j = -2\boldsymbol{\omega} \cdot \sum_{i=1}^{N} m_i \sum_{k=1}^{j-1} \left[\left(\frac{\partial\boldsymbol{\rho}_i^{(k-1)}}{\partial q^j} \times \boldsymbol{\rho}_i^{(k-1)} \right) \Bigg|_{c_k}^{q^k} - \int_{c_k}^{q^k} \left(\frac{\partial^2\boldsymbol{\rho}_i}{\partial q^k \partial q^j} \times \boldsymbol{\rho}_i^{(k-1)} \right) dq^j \right] \quad (63')$$

$$j = 2, 3, \ldots, n+1$$

where the notations

$$\boldsymbol{\rho}_i^{(0)} = \boldsymbol{\rho}_i, \quad \boldsymbol{\rho}_i^{(k)} = \boldsymbol{\rho}_i(q^1 = c_1, q^2 = c_2, \ldots, q^k = c_k, q^{k+1}, q^{k+2}, \ldots, q^n, t),$$

$$k = 1, 2, \ldots, n$$

are introduced.

Now using $(63')$, after rather lengthy calculations whose details we omit, and neglecting the terms which are total derivatives with respect to time of the functions depending on coordinates and time, (62) becomes

[2] Lagrange's equations describing the motion of a system of particles relative to a moving the base involve, as it is known, generalized Coriolis forces (see, e.g., Merkin, 1956). The question of the existence of Mayer's potential for these forces is of fundamental importance.

$$V = \boldsymbol{\omega} \cdot \sum_{i=1}^{N} m_i \sum_{j=1}^{n+1} \left(\frac{\partial \boldsymbol{\rho}_i^{(0)}}{\partial q^j} \times \boldsymbol{\rho}_i^{(0)} \right) \dot{q}^j$$

$$+ \boldsymbol{\epsilon} \cdot \sum_{i=1}^{N} m_i \sum_{j=1}^{n} \int_{c_j}^{q^j} \left(\frac{\partial \boldsymbol{\rho}_i^{(j-1)}}{\partial q^j} \times \boldsymbol{\rho}_i^{(j-1)} \right) dq^j, \quad (64)$$

where, in the case (59), $\boldsymbol{\epsilon} = 0$.

Finally, as a concrete example, let us consider a system consisting of two particles M_1, M_2, with masses $m_1 = m_2 = 1$, moving on the surface given with respect to the Cartesian frame $O\xi\eta\zeta$ by

$$\xi + t(\eta + \zeta) - 2t = 0. \quad (65)$$

The frame $O\xi\eta\zeta$ rotates about a fixed point O, having the absolute angular velocity

$$\boldsymbol{\omega}(t) = 2\boldsymbol{\lambda} - t^2\boldsymbol{\mu} + (2 + t^2)\boldsymbol{\nu}, \quad (66)$$

where $\boldsymbol{\lambda}$, $\boldsymbol{\mu}$, $\boldsymbol{\nu}$ are the unit vectors of the system $O\xi\eta\zeta$.

The radius vectors $\boldsymbol{\rho}_1^{(0)}$, $\boldsymbol{\rho}_2^{(0)}$ of the points $M_1(\xi_1, \eta_1, \zeta_1)$, $M_2(\xi_2, \eta_2, \zeta_2)$ respectively, can be written, keeping in mind (65), in the form

$$\boldsymbol{\rho}_1^{(0)} = (2t - tq^1 - tq^2)\boldsymbol{\lambda} + q^1\boldsymbol{\mu} + q^2\boldsymbol{\nu},$$

$$\boldsymbol{\rho}_2^{(0)} = (2t - tq^3 - tq^4)\boldsymbol{\lambda} + q^3\boldsymbol{\mu} + q^4\boldsymbol{\nu},$$

where

$$q^1 = \eta_1, \quad q^2 = \zeta_1, \quad q^3 = \eta_2, \quad q^4 = \zeta_2.$$

Now, using (56), we find

$$Q_{1\mathrm{cor}} = 4(1 + t)\dot{q}^2 - 2(2 - q^1 - q^2)(2 + t^2),$$

$$Q_{2\mathrm{cor}} = -4(1 + t)\dot{q}^1 - 2(2 - q^1 - q^2)t^2,$$

$$Q_{3\mathrm{cor}} = 4(1 + t)\dot{q}^4 - 2(2 - q^3 - q^4)(2 + t^2),$$

$$Q_{4\mathrm{cor}} = -4(1 + t)\dot{q}^3 - 2(2 - q^3 - q^4)t^2,$$

from where

$$b_{12}^{(0)} = -b_{21}^{(0)} = 4(1 + t), \quad b_{13}^{(0)} = -b_{31}^{(0)} = 0,$$

$$b_{14}^{(0)} = -b_{41}^{(0)} = 0, \quad b_{15}^{(0)} = -2(2 - q^1 - q^2)(2 + t^2),$$

$$b_{23}^{(0)} = -b_{32}^{(0)} = 0, \quad b_{24}^{(0)} = -b_{42}^{(0)} = 0,$$

$$b_{25}^{(0)} = -2(2 - q^1 - q^2)t^2,$$

$$b_{34}^{(0)} = -b_{43}^{(0)} = 4(1 + t), \quad b_{35}^{(0)} = -2(2 - q^3 - q^4)(2 + t^2),$$

$$b_{45}^{(0)} = -2(2 - q^3 - q^4)t^2. \quad (68)$$

It is not difficult to verify that the conditions (58), ensuring the existence of the Mayer's potential

$$V = \sum_{j=2}^{4} A_j\dot{q}^j + A_5,$$

are satisfied. Using (68) and (44), and taking $c_1 = c_2 = c_3 = 0$, we further find

$$b_{23}^{(1)} = b_{24}^{(1)} = 0, \quad b_{25}^{(1)} = -2(2 - q^2)t^2,$$

$$b_{34}^{(2)} = 4(1 + t), \quad b_{35}^{(2)} = -2(2 - q^3 - q^4)(2 + t^2),$$

$$b_{45}^{(3)} = -2(2 - q^4)t^2,$$

so that (63) leads to

$$A_2 = 4(1 + t)q^1, \quad A_3 = 0, \quad A_4 = 4(1 + t)q^3,$$

$$A_5 = -(2 + t^2)[q^1(4 - q^1 - 2q^2) + q^3(4 - q^3 - 2q^4)] - t^2[q^2(4 - q^2) + q^4(4 - q^4)]$$

and the Mayer's potential from which the Coriolis forces (67) are derivable reads

$$V = 4(1 + t)(q^1\dot{q}^2 + q^3\dot{q}^4) - (2 - t^2)[q^1(4 - q^1 - 2q^2) + q^3(4 - q^3 - 2q^4)] - t^2[q^2(4 - q^2) + q^4(4 - q^4)].$$

6 Conclusion

As a conclusion, we summarize the following theorem: Hamilton's principle, expressed in the form valid for conservative dynamical systems, can be extended so as to include the case of a nonconservative system if the generalized nonconservative forces have the form (9), with coefficients which satisfy the conditions (8), (42′*a*) and (42′*b*). In the special case of a system with two degrees-of-freedom acted on by gyroscopic forces, the extension of Hamilton's principle is possible without additional conditions.

References

Appell, P., 1911, *Traité de mécanique rationnelle,* T. II, Gauthier-Villars, Paris, pp. 440–441.

Merkin, D. R., 1956, *Gyroscopic Systems,* Gostechizdat, Moscow, pp. 17–20; 52–54.

Pars, L. A., 1965, *A Treatise on Analytical Dynamics,* Heinemann, London, pp. 81–82.

Santilli, R. M., 1978, *Foundations of Theoretical Mechanics, I,* Springer-Verlag, New York.

Santilli, R. M., 1983, *Foundations of Theoretical Mechanics, II,* Springer-Verlag, New York, p. 3.

W. D. Zhu
Assistant Professor,
Department of Mechanical and Automation Engineering,
The Chinese University of Hong Kong,
Shatin, N.T., Hong Kong
Assoc. Mem. ASME

C. D. Mote, Jr.
FANUC Chair in Mechanical Systems and Vice Chancellor,
Department of Mechanical Engineering,
University of California,
Berkeley, CA 94720

B. Z. Guo
Department of Applied Mathematics,
Beijing Institute of Technology,
Beijing, China

Asymptotic Distribution of Eigenvalues of a Constrained Translating String

A new spectral analysis for the asymptotic locations of eigenvalues of a constrained translating string is presented. The constraint modeled by a spring-mass-dashpot is located at any position along the string. Asymptotic solutions for the eigenvalues are determined from the characteristic equation of the coupled system of contraint and string for all constraint parameters. Damping in the constraint dissipates vibration energy in all modes whenever its dimensionless location along the string is an irrational number. It is shown that although all eigenvalues have strictly negative real parts, an infinite number of them approach the imaginary axis. The analytical predictions for the distribution of eigenvalues are validated by numerical analyses.

1 Introduction

A class of flexible translating elements including textile fibers, magnetic tapes, transmission belts, band saws, and tramway cables is commonly modeled as an axially moving string (Wickert and Mote, 1988). The model of a constrained translating string can also describe a bandsaw passing over a guide bearing and a magnetic tape traveling over a read-write head. Perkins (1990) analyzed the natural frequencies and modes of a string translating across a discrete, and uniform, elastic foundation. By transfer function formulation, Yang (1992) presented an eigenvalue inclusion principle for the translating string under nondissipative, pointwise constraints. Characterized by multiple wave scattering, the transient response of constrained translating strings under arbitrary disturbances was determined by Zhu and Mote (1995).

Control of vibration of the translating string by a point force applied in the domain requires the dimensionless location of it to be an irrational number (Yang and Mote, 1991b). A criterion for design of a stabilizing controller that ensures that all closed-loop eigenvalues lie in the left half-plane was given by Yang and Mote (1991a). The distances of the eigenvalues of the controlled continuous system from the imaginary axis, especially the infinite number of high modes, have not been investigated.

In the present study, a new spectral analysis for the constrained translating string is developed. The constraint, represented by mass m, stiffness k, and damping c, is located at an arbitrary position d along the span. The asymptotic locations of all eigenvalues are determined from the characteristic Eq. (23) through the use of the Rouché's Theorem. When $m \neq 0$ all eigenvalues of large modulus approach the imaginary axis. When $m = 0$ and $c \neq 0$, all eigenvalues remain in the left half-plane if d is irrational. However, an infinite number of eigenvalues approach the imaginary axis. Hence the system is not exponentially stable in any case. The methodology is applicable to predicting the closed-loop eigenvalues for the controller designs in Yang and Mote (1991a).

2 Model and Eigenvalue Problem

As shown schematically in Fig. 1, a string of tension P and mass per unit length ρ is traveling at a subcritical speed V ($V < \sqrt{P/\rho}$) between two supports separated by L. A flexible constraint with mass M, stiffness K, and damping constant C is located at a distance D ($0 < D < L$) from the left end. The interaction force between the string and constraint is $R(T)$. The string is subjected to gravitational force ρg and a distributed external force $F(X, T)$. The transverse displacements of the string and the mass M, relative to the horizontal X-axis, are $U(X, T)$ and $Z(T)$, respectively.

The string transverse displacement $U(X, T)$ is small and planar. The friction force between the string and the constraint is negligible compared to the tension. Introduce the following dimensionless variables:

$$x = X/L \quad u = U/L \quad z = Z/L \quad d = D/L$$
$$v = V(\rho/P)^{1/2} \quad t = T(P/\rho L^2)^{1/2}$$
$$m = M/\rho L \quad k = KL/P \quad c = C/(P\rho)^{1/2}$$
$$w = \rho g L/P \quad f = FL/P \quad r = R/P. \tag{1}$$

The equation governing transverse motion of the translating string is

$$u_{tt}(x, t) + 2vu_{xt}(x, t) + (v^2 - 1)u_{xx}(x, t) = r(t)\delta(x - d) + f(x, t) - w \tag{2}$$

with the boundary conditions

$$u(0, t) = u(1, t) = 0. \tag{3}$$

The equation of motion for the flexible constraint is

$$-r(t) + k[z_0 + z^* - z(t)] - c\dot{z}(t) - mw = m\ddot{z}(t) \tag{4}$$

where $z(t) = u(d, t)$, z^* is the equilibrium displacement of the constraint mass to be determined, and z_0 is the compression of the spring at equilibrium.

The equilibrium displacement of the string $u^*(x)$ and static preload r^* are derived from the equilibrium balance following (2)–(4):

Contributed by the Applied Mechanics Division of THE AMERICAN SOCIETY OF MECHANICAL ENGINEERS for publication in the ASME JOURNAL OF APPLIED MECHANICS.

Discussion on the paper should be addressed to the Technical Editor, Professor Lewis T. Wheeler, Department of Mechanical Engineering, University of Houston, Houston, TX 77204-4792, and will be accepted until four months after final publication of the paper itself in the ASME JOURNAL OF APPLIED MECHANICS.

Manuscript received by the ASME Applied Mechanics Division, Nov. 20, 1995; final revision, Sept. 9, 1996. Associate Technical Editor: N. C. Perkins.

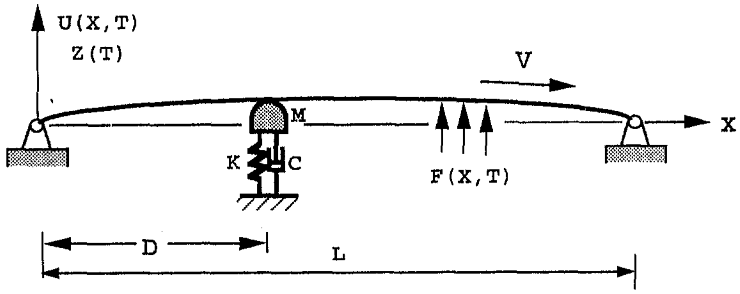

Fig. 1 Schematic of a constrained translating string

$$(v^2 - 1)u^*_{xx}(x) = r^*\delta(x - d) + f^*(x) - w \quad (5)$$

$$u^*(0) = u^*(1) = 0 \quad (6)$$

$$r^* = kz_0 - mw \quad z^* = u^*(d) \quad (7)$$

where $f^*(x)$ is the equilibrium component of $f(x, t)$. Substitution of $u(x, t) = u^*(x) + \tilde{u}(x, t)$, $z(t) = z^* + \tilde{z}(t)$, $r(t) = r^* + \tilde{r}(t)$, and $f(x, t) = f^*(x) + \tilde{f}(x, t)$ into (2)–(4), and use of (5)–(6), yield the equations describing small amplitude motions of the string and constraint around the equilibrium:

$$\tilde{u}_{tt}(x, t) + 2v\tilde{u}_{xt}(x, t) + (v^2 - 1)\tilde{u}_{xx}(x, t) = \tilde{r}(t)\delta(x - d) + \tilde{f}(x, t) \quad (8)$$

$$\tilde{u}(0, t) = \tilde{u}(1, t) = 0 \quad (9)$$

$$\tilde{r}(t) = -k\tilde{z}(t) - c\dot{\tilde{z}}(t) - m\ddot{\tilde{z}}(t), \quad \tilde{z}(t) = \tilde{u}(d, t). \quad (10)$$

The natural frequencies and vibration modes of the constrained translating string around its equilibrium are derived from (8)–(10). By setting $\tilde{f}(x, t) = 0$ in (8), assuming a separable solution

$$\tilde{u}(x, t) = U(x)e^{\lambda t} = \begin{cases} U_1(x)e^{\lambda t}, & 0 < x < d \\ U_2(x)e^{\lambda t}, & d < x < 1 \end{cases} \quad (11)$$

where $U(x)$ and λ are, in general, complex, and substituting (11) into (8)–(10), yields

$$\lambda^2 U_1(x) + 2v\lambda U_1'(x) + (v^2 - 1)U_1''(x) = 0, \quad 0 < x < d \quad (12a)$$

$$\lambda^2 U_2(x) + 2v\lambda U_2'(x) + (v^2 - 1)U_2''(x) = 0, \quad d < x < 1 \quad (12b)$$

$$U_1(0) = 0 \quad U_2(1) = 0. \quad (13)$$

Because $u(x, t)$ is continuous at $x = d$, we have

$$U_1(d) = U_2(d) \quad (14)$$

By (11) $u_t(x, t)$ and $u_{tt}(x, t)$ are also continuous at $x = d$. Integration of (8) from $x = d^-$ to $x = d^+$ and use of (10)–(11) gives

$$(v^2 - 1)[U_2'(d) - U_1'(d)] + [m\lambda^2 + c\lambda + k]U_1(d) = 0. \quad (15)$$

The eigenvalue problem (12a)–(15) leads to the characteristic equation

$$(m\lambda^2 + c\lambda + k)\sinh\frac{\lambda d}{1 - v^2}\sinh\frac{\lambda(1 - d)}{1 - v^2} + \lambda\sinh\frac{\lambda}{1 - v^2} = 0 \quad (16)$$

whose roots are the complex eigenvalues $\lambda = \mu + \omega i$, where μ and ω are real and $i = \sqrt{-1}$. They appear in complex conjugate pairs, $\lambda_{\pm n} = \mu_n \pm \omega_n i$ ($n = 1, 2, 3, \ldots$), where the positive ω_n, arranged in ascending order of magnitude, gives the sequence of the dimensionless natural frequencies of the system. Temporal variation of the vibration amplitude for mode n is described by μ_n, whose positive and negative values indicate the rate of amplitude growth and decay, respectively. For $c = 0$, eigenvalues are imaginary and (16) reduces to

$$(k - m\omega^2)\sin\frac{\omega d}{1 - v^2}\sin\frac{\omega(1 - d)}{1 - v^2} + \omega\sin\frac{\omega}{1 - v^2} = 0. \quad (17)$$

The special case of $m = 0$ in (17) returns the characteristic equation for a translating string guided by a single spring (Perkins, 1990). If in addition, $k = 0$ in (17), the positive roots of (17) recover the natural frequencies of the classical moving threadline, $\omega_n = n\pi(1 - v^2)$ ($n = 1, 2, 3, \ldots$) (Sack, 1954).

The complex eigenfunction $U_n(x)$ corresponding to the complex eigenvalue λ_n is obtained from (12a)–(15) as follows:

$$U_n(x) = e^{\lambda_n x/(1-v)} - e^{-\lambda_n/(1+v)}, \quad 0 < x < d \quad (18a)$$

$$U_n(x) = -e^{-\lambda_n/(1-v^2)}\frac{\sinh\dfrac{\lambda_n d}{1 - v^2}}{\sinh\dfrac{\lambda_n(1 - d)}{1 - v^2}} \times (e^{\lambda_n x/(1-v)} - e^{2\lambda_n/(1-v^2)}e^{-\lambda_n x/(1+v)}), \quad d < x < 1. \quad (18b)$$

Hence, the general solution $\tilde{u}(x, t)$ describing free response can be obtained by superposition of the separable form (11) for each eigensolution $\{\lambda_n, U_n(x)\}$ so determined:

$$\tilde{u}(x, t) = \sum_{n=1}^{\infty}(A_n U_n(x)e^{\lambda_n t} + A_{-n}U_{-n}(x)e^{\lambda_{-n}t}) \quad (19)$$

where the eigenfunction associated with the eigenvalue $\lambda_{-n} = \bar{\lambda}_n$ is $U_{-n}(x) = \bar{U}_n(x)$ by (18a, b), with the overbar denoting complex conjugation. Because $\tilde{u}(x, t)$ is real, $A_{-n} = \bar{A}_n$ with A_n determined from initial conditions.

3 Spectral Analysis

The solutions to (16) are symmetric with respect to the center of the string $d = \frac{1}{2}$. For $c \neq 0$ and subcritical transport speed $v < 1$, $\mathrm{Re}\,\lambda = \mu \leq 0$. The system is asymptotically stable, i.e., $\mu_n < 0$ for all $n \in \mathbf{N}$, only when d is irrational. This can be shown by substituting $\lambda = \omega i$ into (16) to give

$$(k - m\omega^2)\sin\frac{\omega d}{1 - v^2}\sin\frac{\omega(1 - d)}{1 - v^2} + \omega\sin\frac{\omega}{1 - v^2} + ic\,\omega\sin\frac{\omega d}{1 - v^2}\sin\frac{\omega(1 - d)}{1 - v^2} = 0. \quad (20)$$

Separating the real and imaginary parts, we obtain for $c \neq 0$:

$$\sin \frac{\omega}{1-v^2} = \sin \frac{\omega d}{1-v^2} = 0 \quad \text{or}$$

$$\sin \frac{\omega}{1-v^2} = \sin \frac{\omega(1-d)}{1-v^2} = 0. \qquad (21)$$

Hence $\mu = 0$ if and only if $d = p/q$, where $p, q \in \mathbf{N}$ and $0 \le p \le q$. For $p = 0$ and $p = q$ the constraint location coincides with one or the other support. The other discrete locations $d = p/q$ with $p = 1, 2, \ldots, q-1$ give the $q-1$ nodal points of mode q of the classical moving threadline. To provide damping to all the vibration modes, $d \neq p/q$ for all q and $0 < p < q$ in agreement with Yang and Mote (1991b). For a rational $d = p/q$ with p and q co-prime, the imaginary eigenvalues are $nq\pi(1-v^2)i$ $(n = 1, 2, 3, \ldots)$ by (21).

Introduction of the new variables

$$\lambda^* = \frac{\lambda}{1-v^2} \quad m^* = m\frac{1-v^2}{2} \quad c^* = \frac{c}{2}$$

$$k^* = \frac{k}{2(1-v^2)} \qquad (22)$$

into (16) and deletion of the asterisks in the notation yields

$$(m\lambda^2 + c\lambda + k)[e^{\lambda} - e^{(1-2d)\lambda} - e^{-(1-2d)\lambda} + e^{-\lambda}] + \lambda[e^{\lambda} - e^{-\lambda}] = 0. \qquad (23)$$

3.1 Spectrum for $d = \frac{1}{2}$. When $d = \frac{1}{2}$ two branches of the solution to (23) result:

$$e^{\lambda} = 1; \quad e^{\lambda} = \frac{m\lambda^2 + c\lambda + k - \lambda}{m\lambda^2 + c\lambda + k + \lambda}. \qquad (24a, b)$$

The eigenvalues of the first branch, $\lambda_n = 2n(1-v^2)i$ $(n = 1, 2, 3, \ldots)$ by (22) and (24a), are the even-numbered modes of a classical moving threadline. The eigenvalues of the second branch are obtained from (24b) for the following cases:

Case I: $m \neq 0$. Equation (24b) is written in the form

$$e^{\lambda} - 1 + \frac{2}{m}\frac{1}{\lambda} + O(|\lambda|^{-2}) = 0. \qquad (25)$$

The zeros of $e^{\lambda} = 1$ are $\sigma_n = 2n\pi i$ $(n = 1, 2, 3, \ldots)$. The zeros of (25) for λ of large modulus are asymptotic to σ_n following the theorem of Rouché (Carrier et al., 1983):

Rouché's Theorem: Let $f(z)$ and $g(z)$ be analytic inside and on C, with $|g(z)| < |f(z)|$ on C. Then $f(z)$ and $f(z) + g(z)$ have the same number of zeros inside C.

In the present case, let $f(\lambda) = e^{\lambda} - 1$ and $g(\lambda) = (2/m)(1/\lambda) + O(|\lambda|^{-2})$. A disk C_n centered at σ_n is defined: $\lambda = \sigma_n + (\epsilon/|\sigma_n|)e^{i\theta}$, where $0 \le \theta \le 2\pi$. On C_n, we have

$$|f(\lambda)| = |e^{(\epsilon/|\sigma_n|)e^{i\theta}} - 1| = \left|\frac{\epsilon}{|\sigma_n|}e^{i\theta} + O(|\sigma_n|^{-2})\right|$$

$$= \frac{\epsilon}{|\sigma_n|} + O(|\sigma_n|^{-2}) \qquad (26)$$

where the Taylor expansion has been used in (26). Because $|\lambda| \ge |\sigma_n| - (\epsilon/|\sigma_n|)$, we have

$$\frac{1}{|\lambda|} \le \frac{1}{|\sigma_n| - \dfrac{\epsilon}{|\sigma_n|}}. \qquad (27)$$

Take $\epsilon > 0$, such that

$$\frac{2}{m}\frac{1}{|\sigma_n| - \dfrac{\epsilon}{|\sigma_n|}} < \frac{\epsilon}{|\sigma_n|}. \qquad (28)$$

That is, $(2/m)|\sigma_n| < \epsilon|\sigma_n| - \epsilon^2/|\sigma_n|$. So if $\epsilon > 2/m$, there exists $N > 0$, such that for $n \ge N$, (28) is satisfied. Hence by (27), $(2/m)/(1/|\lambda|) < \epsilon/|\sigma_n|$. Take $N_0 \ge N$, such that for $n \ge N_0$,

$$|g(\lambda)| = \left|\frac{2}{m}\frac{1}{\lambda} + O(|\lambda|^{-2})\right|$$

$$= \frac{2}{m}\frac{1}{|\lambda|} + O(|\lambda|^{-2}) < |f(\lambda)| \qquad (29)$$

on C_n. By Rouché's Theorem, there exists one solution λ_n to (25) inside C_n for $n \ge N_0$, i.e., $|\lambda_n - \sigma_n| < \epsilon/|\sigma_n|$. Hence by returning to the former variables in (22), the eigenvalues of the second branch are

$$\lambda_n = (1-v^2)\sigma_n + O\left(\frac{1}{n}\right) = 2n\pi(1-v^2)i + O\left(\frac{1}{n}\right). \qquad (30)$$

Each eigenvalue λ_n of the second branch in (30) is asymptotic to one on the first branch, $2n\pi(1-v^2)i$. Hence eigenvalues of high modes exist in closely located pairs near the imaginary axis. They are independent of the constraint parameters, m, c, and k, to the first order.

Case II: $m = 0$ and $c \neq 1$. Equation (24b) becomes

$$e^{\lambda} = \frac{c-1}{c+1} + \frac{2k}{1+c}\frac{1}{(1+c)\lambda + k}. \qquad (31)$$

The solutions to $e^{\lambda} = (c-1)/(c+1)$ are

$$\sigma_n = \ln\frac{c-1}{c+1} + 2n\pi i, \quad \text{for} \quad c > 1 \qquad (32a)$$

$$\sigma_n = \ln\frac{1-c}{1+c} + (2n-1)\pi i, \quad \text{for} \quad c < 1 \qquad (32b)$$

for $n = 1, 2, 3, \ldots$. Hence by (22) the exact eigenvalues of the second branch for $k = 0$ are $\lambda_n = (1-v^2)\sigma_n$. By use of the Rouché's Theorem and (22) similar to Case I, the eigenvalues of the second branch for $k \neq 0$ are

$$\lambda_n = (1-v^2)\ln\frac{c-2}{c+2} + 2n\pi(1-v^2)i + O\left(\frac{1}{n}\right),$$

$$\text{for} \quad c > 2, \qquad (33a)$$

$$\lambda_n = (1-v^2)\ln\frac{2-c}{2+c} + (2n-1)\pi(1-v^2)i + O\left(\frac{1}{n}\right),$$

$$\text{for} \quad c < 2. \qquad (33b)$$

They are independent of k to the first order. In either case $\mu_n = \mathrm{Re}\lambda_n = (1-v^2)\ln|(2-c)/(2+c)| + O(1/n)$. Hence the decay rates for high modes are nearly constant.

Case III: $m = 0$ and $c = 1$. Equation (24b) reduces to

$$(2\lambda + k)e^{\lambda} = k \qquad (34)$$

and $k \neq 0$, $e^{\mathrm{Re}\lambda} = k/|2\lambda + k|$. Hence $\mathrm{Re}\lambda = \ln(k/|2\lambda + k|)$, and $\mu = \mathrm{Re}\lambda \to -\infty$ as $|\lambda| \to \infty$. Reducing k increases the damping rates for all the modes on the second branch. $\mathrm{Re}\lambda \to -\infty$ in (34) yields $2\lambda e^{\lambda} = k$. Hence (34) is asymptotic to

$$\mathrm{Re}\lambda + \ln|\lambda| = \ln\frac{k}{2}. \tag{35}$$

The asymptotic locations of the eigenvalues of (35) can be obtained. Let $\lambda = |\lambda| e^{i\theta}$,

$$\cos\theta = \frac{\mathrm{Re}\lambda}{|\lambda|} = \frac{1}{|\lambda|}\ln\frac{k}{2} - \frac{\ln|\lambda|}{|\lambda|} \to 0, \quad \text{as} \quad |\lambda| \to \infty. \tag{36}$$

Hence $\theta \to (\pi/2)$ as $|\lambda| \to \infty$. Also,

$$e^{i\,\mathrm{Im}\lambda} = \frac{k}{2\lambda} e^{-\mathrm{Re}\lambda} = \frac{|\lambda|}{\lambda} = e^{-i\theta}. \tag{37}$$

Hence by (22), (35), and (37) the asymptotic eigenvalues of the second branch are given by

$$\omega_n = \mathrm{Im}\lambda_n = (1 - v^2)\left(2n\pi - \frac{\pi}{2}\right) \tag{38a}$$

$$\mu_n = \mathrm{Re}\lambda_n = (1 - v^2)\ln\frac{k}{4(1 - v^2)} - (1 - v^2)\ln\left(2n\pi - \frac{\pi}{2}\right). \tag{38b}$$

By (38a) ω_n is independent of k to the first order.

For $k = 0$ there are no finite solutions to $e^{\lambda} = 0$. Hence there are no eigenvalues corresponding to (34). $\mathrm{Re}\lambda = -\infty$ in this case implies that all the modes of the second branch are completely dissipated by damping after a finite time.

3.2 Spectrum for $m \neq 0$ and arbitrary d. Equation (23) is written in the form

$$e^{2\lambda} - e^{2d\lambda} - e^{2(1-d)\lambda} + 1 = -\frac{\lambda(e^{2\lambda} - 1)}{m\lambda^2 + c\lambda + k}. \tag{39}$$

If $\mathrm{Re}\lambda \to -\infty$ as $|\lambda| \to \infty$, (39) yields a contradiction, $1 = 0$. Hence there exists $A > 0$, such that $-A < \mathrm{Re}\lambda \leq 0$. Therefore e^{λ} and $e^{-\lambda}$ are bounded. As $|\lambda| \to \infty$, we have from (23):

$$(e^{d\lambda} - e^{-d\lambda})(e^{(1-d)\lambda} - e^{-(1-d)\lambda}) = -\frac{\lambda(e^{\lambda} - e^{-\lambda})}{m\lambda^2 + c\lambda + k} \to 0. \tag{40}$$

Hence either $e^{2d\lambda} \to 1$ or $e^{2(1-d)\lambda} \to 1$ as $|\lambda| \to \infty$. In either case $\mathrm{Re}\lambda \to 0$ as $|\lambda| \to \infty$. For irrational d, though $\mathrm{Re}\lambda_n < 0$ for all n, all eigenvalues approach the imaginary axis as $|\lambda| \to \infty$. Hence the system is asymptotically, but not exponentially, stable.

Determination of Eigenvalues. By (23) we have

$$(e^{2d\lambda} - 1)(e^{2(1-d)\lambda} - 1) + \frac{1}{m\lambda}(e^{2\lambda} - 1) + O(|\lambda|^{-2}) = 0. \tag{41}$$

Let $f(\lambda) = (e^{2d\lambda} - 1)(e^{2(1-d)\lambda} - 1)$ and $g(\lambda) = (1/m\lambda)(e^{2\lambda} - 1) + O(|\lambda|^{-2})$. The roots of $e^{2d\lambda} = 1$ are $\sigma_n = n\pi i/d$. Define C_n around σ_n: $\lambda = \sigma_n + (\epsilon/|\sigma_n|)e^{i\theta}$, where $0 \leq \theta \leq 2\pi$. For any λ on C_n, using the Taylor expansion we have

$$|e^{2d\lambda} - 1| = |e^{2d(\epsilon/|\sigma_n|)e^{i\theta}} - 1| = 2d\frac{\epsilon}{|\sigma_n|} + O(|\sigma_n|^{-2}) \tag{42}$$

$$|e^{2(1-d)\lambda} - 1| = |e^{(2n\pi/d)i}e^{2(1-d)(\epsilon/|\sigma_n|)e^{i\theta}} - 1| = |e^{(2n\pi/d)i} - 1| + O(|\sigma_n|^{-1})$$

$$|e^{2\lambda} - 1| = |e^{(2n\pi/d)i} - 1| + O(|\sigma_n|^{-1}). \tag{43}$$

Hence on C_n,

$$|f(\lambda)| = |e^{2d\lambda} - 1||e^{2(1-d)\lambda} - 1| = 2d\frac{\epsilon}{|\sigma_n|}|e^{(2n\pi/d)i} - 1| + O(|\sigma_n|^{-2})$$

$$|g(\lambda)| = \frac{1}{m}\frac{1}{|\sigma_n|}|e^{(2n\pi/d)i} - 1| + O(|\sigma_n|^{-2}). \tag{44}$$

For irrational d, $|e^{(2n\pi/d)i} - 1| \neq 0$. For rational $d = p/q$, with p and q co-prime, $|e^{(2n\pi/d)i} - 1| = 0$ only when p divides n. In this case (43) and (44) become

$$|e^{2(1-d)\lambda} - 1| = \frac{2(1 - d)\epsilon}{|\sigma_n|} + O(|\sigma_n|^{-2})$$

$$|e^{2\lambda} - 1| = \frac{2\epsilon}{|\sigma_n|} + O(|\sigma_n|^{-2}) \tag{45}$$

$$|f(\lambda)| = \frac{4d(1 - d)\epsilon^2}{|\sigma_n|^2} + O(|\sigma_n|^{-3})$$

$$|g(\lambda)| = \frac{2\epsilon}{m|\sigma_n|^2} + O(|\sigma_n|^{-3}). \tag{46}$$

Choose $\epsilon > 1/[2d(1 - d)m]$, then for either (44) or (46) there exists $N > 0$ such that when $n \geq N$, $|g(\lambda)| < |f(\lambda)|$ on C_n. By Rouché's Theorem, there is one solution λ_n to (41) inside C_n for $n \geq N$, i.e., $|\lambda_n - \sigma_n| < \epsilon/|\sigma_n|$. Hence by (22) one branch of eigenvalues is

$$\lambda_n = \frac{n\pi}{d}(1 - v^2)i + O\left(\frac{1}{n}\right). \tag{47a}$$

Similarly the roots of $e^{2(1-d)\lambda} - 1 = 0$ are $\sigma_n = n\pi i/(1 - d)$. Following the same analysis, the other branch of eigenvalues is

$$\lambda_n = \frac{n\pi}{1 - d}(1 - v^2)i + O\left(\frac{1}{n}\right). \tag{47b}$$

For $d = \frac{1}{2}$ the two branches of eigenvalues are both of the form $2n\pi(1 - v^2)i + O(1/n)$, consistent with Section 3.1.

3.3 Spectrum for $m = 0$ and Arbitrary d. Because of symmetry of the spectrum with respect to $d = \frac{1}{2}$, we consider $d < \frac{1}{2}$. Because $\lambda = 0$ is not an eigenvalue, (23) becomes

$$\left(c + 1 + \frac{k}{\lambda}\right)e^{2\lambda} - \left(c + \frac{k}{\lambda}\right)e^{2(1-d)\lambda} - \left(c + \frac{k}{\lambda}\right)e^{2d\lambda} + c - 1 + \frac{k}{\lambda} = 0. \tag{48}$$

For $c \neq 1$ the roots of (48) of large modulus are asymptotic to those of the characteristic equation corresponding to $k = 0$ (Bellman and Cooke, 1963):

$$(c + 1)e^{2\lambda} - ce^{2(1-d)\lambda} - ce^{2d\lambda} + c - 1 = 0. \tag{49}$$

For $c = 1$ and $k \neq 0$ (48) is written as

$$2e^{2(1-d)\lambda} - e^{2(1-2d)\lambda} - 1 + \frac{k}{\lambda}[e^{-2d\lambda} + e^{2(1-d)\lambda} - e^{2(1-2d)\lambda} - 1] = 0. \tag{50}$$

For $c = 1$ and $k = 0$ (48) becomes

$$2e^{2\lambda} = e^{2(1-d)\lambda} + e^{2d\lambda}. \quad (51)$$

If $\mathrm{Re}\lambda \to -\infty$ as $|\lambda| \to \infty$, (48) implies $c = 1$. For $c = 1$ and $k = 0$, we have by (51)

$$2 = e^{2(d-1)\lambda}(1 + e^{2(1-2d)\lambda}) \quad (52)$$

$\mathrm{Re}\lambda \to -\infty$ in (52) leads to a contradiction, $2 = \infty$. Hence there exists $A > 0$, such that $-A < \mathrm{Re}\lambda \le 0$. For $c = 1$ and $k \ne 0$, $\mathrm{Re}\lambda \to -\infty$ in (50) yields $1 = ke^{-2d\lambda}/\lambda$. Hence, $e^{-2d\mathrm{Re}\lambda} = |\lambda|/k$. A branch of eigenvalues of (50) of large modulus is asymptotic to

$$\mathrm{Re}\lambda + \frac{1}{2d}\ln|\lambda| = \frac{1}{2d}\ln k, \quad (53)$$

which is similar in form to (35) for the case $d = \frac{1}{2}$. Let $\lambda = |\lambda|e^{i\theta}$, we have

$$\cos\theta = \frac{\mathrm{Re}\lambda}{|\lambda|} = -\frac{1}{2d}\frac{\ln|\lambda|}{|\lambda|} + \frac{1}{2d}\frac{\ln k}{|\lambda|} \to 0, \quad \text{as } |\lambda| \to \infty. \quad (54)$$

Hence $\theta \to \pi/2$ as $|\lambda| \to \infty$. Further,

$$e^{-i2d\mathrm{Im}\lambda} = \frac{\lambda}{k}e^{2d\mathrm{Re}\lambda} = \frac{\lambda}{|\lambda|} = e^{i\theta}. \quad (55)$$

Hence by (22) and (53)–(55) the asymptotic locations of the eigenvalues on (53) are

$$\omega_n = \mathrm{Im}\lambda_n = \frac{1-v^2}{2d}\left(2n\pi - \frac{\pi}{2}\right) \quad (56a)$$

$$\mu_n = \mathrm{Re}\lambda_n = \frac{1-v^2}{2d}\left[\ln\frac{k}{2(1-v^2)} - \ln\frac{1}{2d}\left|2n\pi - \frac{\pi}{2}\right|\right]. \quad (56b)$$

All other branches of eigenvalues of (50) must satisfy $-A < \mathrm{Re}\lambda \le 0$ for some constant $A > 0$. They are determined next.

Case I: Rational d. Let $d = p/q$ with p and q co-prime, and $2p < q$. Equations (49) and (51) reduce, respectively, to the polynomial equations

$$(c+1)z^q - cz^{q-p} - cz^p + c - 1 = 0 \quad (57)$$

$$2z^q - z^{q-p} - z^p = 0 \quad (58)$$

where $z = e^{(2/q)\lambda}$. Because there are no finite solutions for λ corresponding to the root $z = 0$, (58) reduces to

$$2z^{q-p} - z^{q-2p} - 1 = 0. \quad (59)$$

There are at most q and $q - p$ distinct roots for (57) and (59) respectively. By (22) the branch of eigenvalues corresponding to the root z_l of (57) or (59) is

$$\lambda_n = \frac{q}{2}(1-v^2)[\ln|z_l| + i(\arg z_l + 2\pi n)], \quad n = 1, 2, 3, \ldots. \quad (60)$$

Each branch of eigenvalues in (60) lies on a straight line parallel to the imaginary axis and hence represents a constant rate of damping. Because $z = 1$ is a root of (57) or (59), the corresponding branch of eigenvalues is imaginary: $nq\pi(1-v^2)i$ ($n = 1, 2, 3, \ldots$) by (22), in agreement with (21). Note that (60) is the exact solution to (48) when $k = 0$.

In addition to the branch of eigenvalues given by (56a, b), we show that all other eigenvalues of (50) are asymptotic to those of (51) determined by (59) and (60). Let

$$f(\lambda) = 2e^{2(1-d)\lambda} - e^{2(1-2d)\lambda} - 1$$

$$g(\lambda) = \frac{k}{\lambda}[e^{-2d\lambda} + e^{-2(1-d)\lambda} - e^{2(1-2d)\lambda} - 1]. \quad (61)$$

Equation (50) becomes $f(\lambda) + g(\lambda) = 0$. Each branch of zeros, σ_n, of $f(\lambda) = 0$ satisfies

$$e^{2\sigma_n/q} = z_n \quad 2z_n^{q-p} = z_n^{q-2p} + 1. \quad (62)$$

Define C_n around σ_n by $\lambda = \sigma_n + (1/\sqrt{|\sigma_n|})e^{i\theta}$, where $0 \le \theta \le 2\pi$. For any λ on C_n, by using the Taylor expansion and (62) we obtain

$$|f(\lambda)| = \left|2z_n^{q-p}\left[1 + \frac{2(1-d)}{\sqrt{|\sigma_n|}}e^{i\theta}\right] - z_n^{q-2p}\left[1 + \frac{2(1-2d)}{\sqrt{|\sigma_n|}}e^{i\theta}\right] - 1 + O(|\sigma_n|)^{-1})\right|$$

$$= \frac{1}{\sqrt{|\sigma_n|}}|2dz_n^{q-2p} + 2(1-d)| + O(|\sigma_n|^{-1}) \quad (63)$$

$$|g(\lambda)| = \left|\frac{k}{\lambda}\left[z_n^{-p} + z_n^{q-p} - z_n^{q-2p} - 1 + O(|\sigma_n|^{-1/2})\right]\right|$$

$$= \frac{k}{|\sigma_n|}|z_n^{-p} - z_n^{q-p}| + O(|\sigma_n|^{-3/2}). \quad (64)$$

Because there are only a finite number of zeros z_n, $|2dz_n^{q-2p} + 2(1-d)|$ and $|z_n^{-p} - z_n^{q-p}|$ are bounded. It can be further shown that $|2dz_n^{q-2p} + 2(1-d)| \ne 0$ in (63). Hence $|g(\lambda)| < |f(\lambda)|$ on C_n for sufficiently large $|\sigma_n|$. By Rouché's Theorem there is one solution λ_n to (50) inside C_n such that $|\lambda_n - \sigma_n| < 1/\sqrt{|\sigma_n|}$. On the other hand, if (50) has a branch of zeros λ_l other than those of λ_n, let $F(\lambda) = f(\lambda) + g(\lambda)$ and $G(\lambda) = -g(\lambda)$. Because $-A < \mathrm{Re}\lambda \le 0$, $e^{-2d\mathrm{Re}\lambda}$ is bounded. Following the same approach we can show that $|G(\lambda)| < |F(\lambda)|$ on a disk C_l around λ_l for sufficiently large $|\lambda_l|$. Hence $F(\lambda) + G(\lambda) = f(\lambda)$ also has another branch of zeros around λ_l, which is impossible. Therefore eigenvalues of (50) of large modulus are asymptotic to those given by (59), (60) and (56a, b). Note that (56a, b) apply for both rational and irrational d.

Case II: Irrational d. For irrational d all eigenvalues lie strictly within the left half-plane and the system is asymptotically stable. We will show that there are an infinite number of eigenvalues arbitrarily close to the imaginary axis, hence the system is not exponentially stable.

By Theorem 185 of Hardy and Wright (1979), every irrational number $0 < d < 1$ can be approximated by an infinite number of rational fractions p/q such that $|p/q - d| < 1/q^2$. Hence we assume $d = p_n/q_n + b_n/q_n^2$ ($n = 1, 2, 3, \ldots$), where p_n and q_n are co-prime positive integers arranged in the ascending order of magnitude of q_n, and $|b_n| < 1$. Let

$$f(\lambda) = (c+1)e^{2\lambda} - ce^{2[1-(p_n/q_n)\lambda]} - ce^{2(p_n/q_n)\lambda} + c - 1 \quad (65)$$

$$g(\lambda) = \frac{k}{\lambda}e^{2\lambda} - \frac{k}{\lambda}e^{2(1-d)\lambda} - \frac{k}{\lambda}e^{2d\lambda} + \frac{k}{\lambda} + ce^{2(1-p_n/q_n)\lambda}(1 - e^{-2(b_n/q_n^2)\lambda}) + ce^{2(p_n/q_n)\lambda}(1 - e^{2(b_n/q_n^2)\lambda}). \quad (66)$$

Equation (48) becomes $f(\lambda) + g(\lambda) = 0$. Because $f(\lambda) = 0$ has zeros $\sigma_n = lq_n\pi i$, where l is any positive integer, we define C_n around σ_n by $\lambda = \sigma_n + (1/|\sigma_n|)e^{i\theta}$, where $0 \le \theta \le 2\pi$. For any λ on C_n, using the Taylor expansion we have

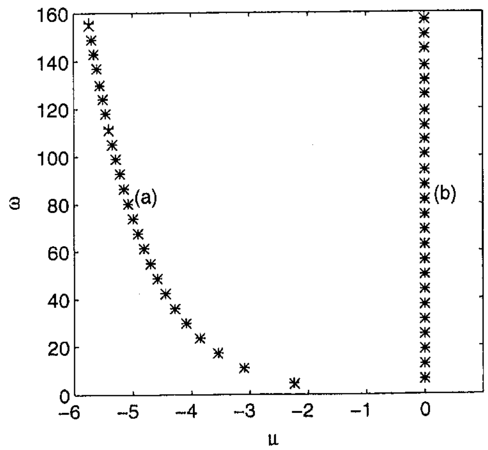

Fig. 2 Distribution of the first 50 eigenvalues for $m = 0$, $d = \frac{1}{2}$, $v = 0.1$, and $c = 2$. (a) Numerical ("+") and asymptotic ("×") solutions for $k = 2$; (b) numerical solutions for $k = 2$ ("+") and $k = 0$ ("×").

$$|f(\lambda)| = |(c+1)e^{(2/|\sigma_n|)e^{i\theta}} - ce^{(1-p_n/q_n)(2/|\sigma_n|)e^{i\theta}} - ce^{(p_n/q_n)(2/|\sigma_n|)e^{i\theta}} + c - 1|$$

$$= \left|\frac{2}{|\sigma_n|}e^{i\theta} + O(|\sigma_n|^{-2})\right|$$

$$= \frac{2}{|\sigma_n|} + O(|\sigma_n|^{-2}) \tag{67}$$

$$\frac{k}{\lambda}[e^{2\lambda} - e^{2(1-d)\lambda} - e^{2d\lambda} + 1]$$

$$= \frac{k}{\lambda}[e^{(2/|\sigma_n|)e^{i\theta}} - e^{[1-(p_n/q_n)](2/|\sigma_n|)e^{i\theta}} \times e^{-2(b_n/q_n^2)[\sigma_n+(1/|\sigma_n|)e^{i\theta}]} - e^{(p_n/q_n)(2/|\sigma_n|)e^{i\theta}}e^{2(b_n/q_n^2)[\sigma_n+(1/|\sigma_n|)e^{i\theta}]} + 1]$$

$$= \frac{k}{\lambda}\left[\frac{4b_n\pi^2l^2i}{|\sigma_n|^2}\left(1 - 2\frac{p_n}{q_n}\right)e^{i\theta} + \frac{4}{|\sigma_n|^2}e^{2i\theta} + O(|\sigma_n|^{-3})\right]$$

$$= O(|\sigma_n|^{-3}) \tag{68}$$

$$ce^{2[1-(p_n/q_n)]\lambda}(1 - e^{-2(b_n/q_n^2)\lambda}) + ce^{2(p_n/q_n)\lambda}(1 - e^{2(b_n/q_n^2)\lambda})$$

$$= c\left[-2\pi^2\frac{b_nl^2}{\sigma_n} + O(|\sigma_n|^{-2})\right] + c\left[2\pi^2\frac{b_nl^2}{\sigma_n} + O(|\sigma_n|^{-2})\right] = O(|\sigma_n|^{-2}). \tag{69}$$

Hence $|g(\lambda)| = O(|\sigma_n|^{-2}) < |f(\lambda)|$ on C_n. By Rouché's Theorem, there exists one solution λ_n to (48) inside C_n, that is $|\lambda_n - \sigma_n| < 1/|\sigma_n| = 1/lq_n\pi$. Because there are an infinite number of distinct q_n, $q_n \to \infty$ as $n \to \infty$. Therefore $\text{Re}\lambda_n \to \text{Re}\sigma_n = 0$ as $n \to \infty$. As noted, $\sigma_n = lq_n\pi i$ ($l = 1, 2, 3, \ldots$) correspond to the infinite number of eigenvalues on the imaginary axis when d is approximated by the rational fraction p_n/q_n. As $n \to \infty$, $p_n/q_n \to d$ and σ_n ($l = 1, 2, 3, \ldots$) approach those corresponding to the irrational d.

4 Examples and Discussions

Eigenvalues for different cases are calculated numerically from (16) and compared with the analytical solutions in Section 3.

In the first example $m = 0$, $d = \frac{1}{2}$, $v = 0.1$, and $c = 1$. When $k = 0$ the locations of the first 50 eigenvalues agree with the exact solutions in (24a) and (32b). One branch of eigenvalues lies on the imaginary axis: $2n\pi(1 - v^2)i = 6.22ni$ ($n = 1, 2, 3, \ldots$). They correspond to the even-numbered modes with nodal points at $d = \frac{1}{2}$. The other branch of eigenvalues given by $(1 - v^2)[\ln(2 - c)/(2 + c) + (2n - 1)\pi i] = -1.09 + 3.11(2n - 1)i$ ($n = 1, 2, 3, \ldots$) corresponds to the odd-numbered modes. These eigenvalues have a constant real part $\mu = -1.09$. When $k = 2$ the branch of eigenvalues on the imaginary axis remains unchanged, while the other branch is quickly asymptotic to that for $k = 0$ (not shown here), in agreement with (33b).

In the example shown in Fig. 2, $c = 2$ and all other parameters remain the same as those in the previous example. The first 50 eigenvalues for $k = 2$ separate along two branches. The first branch lies on the imaginary axis as in the previous case. Locations of the eigenvalues on the second branch agree with the asymptotic solution in (38a, b). Unlike any other damping constant c which would yield a nearly constant decay rate, rates of decay of the eigenvalues on the second branch increase monotonically. Hence $c = 2$ is optimal damping in this sense. When $k = 0$ as shown in Fig. 2, the second branch disappears and all eigenvalues lie on the imaginary axis, as predicted in Case III of Section 3.1.

The distribution of the first 50 eigenvalues for $m = v = d = 0.1$, $k = 2$, and $c = 1$ is shown in Fig. 3. The eigenvalues on the imaginary axis are $10n\pi(1 - v^2)i = 31.1ni$ ($n = 1, 2, \ldots, 5$), as predicted by (21). In addition there is a sequence of eigenvalues asymptotic to each eigenvalue on the imaginary axis, in agreement with (47a). Hence introduction of a small inertia m alters the behavior of the spectrum significantly. For $m = 0.5$ and other parameters unchanged (not shown here), the eigenvalues approach the imaginary axis faster and all λ_n for $n > 10$ are located close to the imaginary axis.

For $m = k = 0$, $d = \frac{1}{4}$, $v = 0.1$, and $c = 1$, the first 50 eigenvalues shown in Fig. 4 are in agreement with the exact solutions in (57) and (60). The roots of (57) are 1, −5.523, and $-0.0572 \pm 0.7748i$. By (60) the resulting four branches of eigenvalues are: $12.44ni$, $-1.18 + 6.22(2n + 1)i$, $-0.50 + (3.26 + 12.44n)i$, and $-0.50 + (9.18 + 12.44n)i$ ($n = 1, 2, \ldots$). They are distributed along three μ = constant lines because the last two branches are both located on $\mu = -0.50$. When $k = 2$ with other parameters unchanged, eigenvalues of high modes are asymptotic to those corresponding to $k = 0$, as predicted by (49).

In Fig. 5 are shown the first 50 eigenvalues for $c = 2$ and other parameters same as those in Fig. 4. The roots of (58) are 1 and $-0.25 \pm 0.6614i$. The corresponding branches of eigenvalues for $k = 0$: $12.44ni$, $-0.686 + (3.83 + 12.44n)i$, and $-0.686 + (8.61 + 12.44n)i$ ($n = 1, 2, 3, \ldots$) by (60) are distributed along two lines $\mu = 0$ and $\mu = -0.686$, as shown

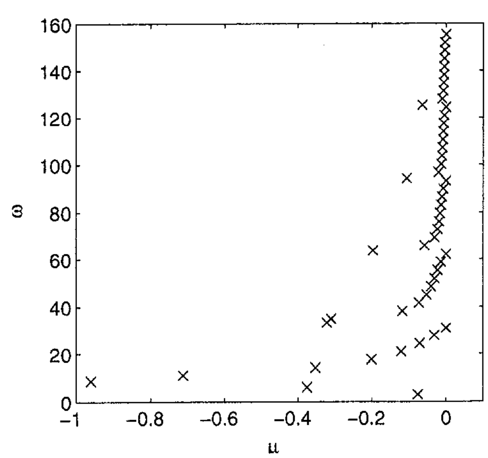

Fig. 3 Distribution of the first 50 eigenvalues for $m = v = d = 0.1$, $k = 2$, and $c = 1$

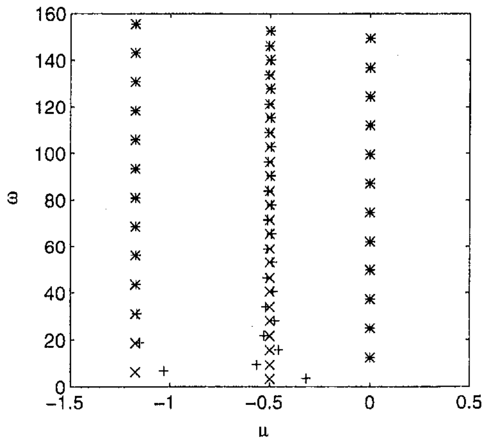

Fig. 4 Distribution of the first 50 eigenvalues for $m = 0$, $d = \frac{1}{4}$, $v = 0.1$, and $c = 1$. (1) $k = 0$ ("×"); (2) $k = 2$ ("+").

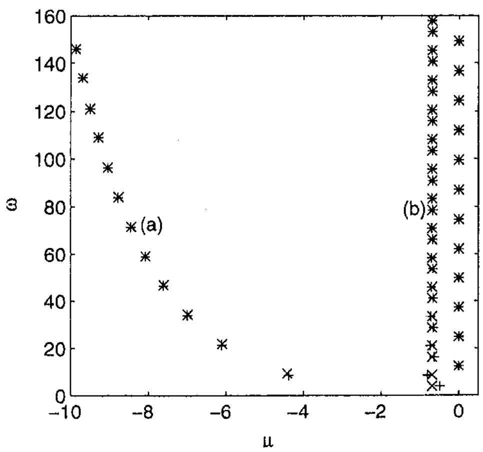

Fig. 5 Distribution of the first 50 eigenvalues for $c = 2$ and other parameters same as those in Fig. 4. (a) Numerical ("+") and asymptotic ("×") solutions for $k = 2$; (b) numerical solutions for $k = 2$ ("+") and $k = 0$ ("×").

in Fig. 5. When $k = 2$, the branch of eigenvalues on the imaginary axis is unchanged, and the other branch is asymptotic to that corresponding to $k = 0$, as expected. In addition to those two branches, there is a branch of eigenvalues shown in Fig. 5(a) with increasing rates of decay $|\mu|$, as predicted by (56a, b).

5 Conclusions

1 When $c \neq 0$ the constrained translating string is asymptotically stable if and only if d is irrational. However, even for irrational d, there are an infinite number of eigenvalues approaching the imaginary axis. Hence the system is not exponentially stable. If $d = p/q$ is rational, where p and q are co-prime, the branch of eigenvalues on the imaginary axis is given by $nq\pi(1 - v^2)i$ ($n = 1, 2, \ldots$).

2 When $m \neq 0$ and c and k are arbitrary, eigenvalues of the high modes are asymptotic to $(n\pi/d)(1 - v^2)i$ and $[n\pi/(1 - d)](1 - v^2)i$ ($n = 1, 2, \ldots$). The asymptotic behavior of the eigenvalues for sufficiently high modes is independent of m, c, and k.

3 For $d = p/q$, $m = k = 0$, and $c \neq 2$, the exact solutions for the eigenvalues are given by (57) and (60). All eigenvalues are distributed along the imaginary axis and along at most $q - 1$ lines of constant $\mu = \text{Re}\lambda$ in the left half-plane. The distribution of the eigenvalues for nonzero k is asymptotic to that corresponding to $k = 0$. Hence the asymptotic locations of the eigenvalues are independent of k.

4 $c = 2$ is a special damping constant when $m = 0$. If d is rational, the exact eigenvalues for $k = 0$ are given by (58) and (60). They are distributed along the imaginary axis and along a maximum number of $q - p - 1$ lines of constant $\mu = \text{Re}\lambda$ in the left half-plane. The vibration corresponding to the other p branches of eigenvalues is dissipated by damping in finite time. When $k \neq 0$, in addition to the branch of eigenvalues in (56a, b) which has monotonically increasing decay rates, all other eigenvalues are asymptotic to those corresponding to $k = 0$.

Acknowledgments

This work was supported by the Engineering Direct Grant and the Summer Research Grant of the Chinese University of Hong Kong.

References

Bellman, R., and Cooke, K., 1963, *Differential-Difference Equations*, Academic Press, New York.

Carrier, G. F., Krook, M., and Pearson, C. E., 1983, *Functions of a Complex Variable: Theory and Technique*, Hod Books, Ithaca, NY.

Hardy, G. H., and Wright, E. M., 1979, *An Introduction to the Theory of Numbers*, 5th ed, Oxford University Press, Oxford, UK.

Perkins, N. C., 1990, "Linear Dynamics of a Translating String on an Elastic Foundation," *Journal of Vibration and Acoustics*, Vol. 112, No. 5, pp. 2–7.

Sack, R. A., 1954, "Transverse Oscillations in Travelling Strings," *British Journal of Applied Physics*, Vol. 5, pp. 224–226.

Wickert, J. A., and Mote, C. D. Jr., 1988, "Current Research on the Vibration and Stability of Axially Moving Materials," *Shock and Vibration Digest*, Vol. 20, No. 5, pp. 3–13.

Yang, B., 1992, "Eigenvalue Inclusion Principles for Distributed Gyroscopic Systems," ASME Journal of Applied Mechanics, Vol. 59, pp. 425–443.

Yang, B., and Mote, C. D., Jr., 1991a, "Active Vibration Control of the Axially Moving String in the *s* Domain," ASME Journal of Applied Mechanics, Vol. 58, pp. 189–196.

Yang, B., and Mote, C. D., Jr., 1991b, "Controllability and Observability of Distributed Gyroscopic Systems," ASME *Journal of Dynamic Systems, Measurement and Control*, Vol. 113, pp. 11–17.

Zhu, W. D., and Mote, C. D., Jr., 1995, "Propagation of Boundary Disturbances in an Axially Moving Strip in Contact with Rigid and Flexible Constraints," ASME Journal of Applied Mechanics, Vol. 62, pp. 873–879.

Transient Analysis of a Propagating In-Plane Crack in a Finite Geometry Body Subjected to Static Loadings

Chwan-Huei Tsai[1]
Associate Professor,
Department of Mechanical Engineering,
Huafan College of Humanities and Technology,
Taipei Hsien, Taiwan 223,
Republic of China

Chien-Ching Ma
Professor,
Department of Mechanical Engineering,
National Taiwan University,
Taipei, Taiwan 10617, Republic of China

In this study, a cracked body with finite boundaries subjected to static loading and the crack propagating with a constant speed are analyzed. The interaction of the propagating crack with reflected waves generated from traction-free boundaries is investigated in detail. The methodology for constructing the scattered field by superimposing the fundamental solution in the Laplace transform domain is proposed. The fundamental solutions represent the responses of applying exponentially distributed loadings in the Laplace transform domain on the surface of a half-plane or a crack. The dynamic stress intensity factors of a propagating crack induced from the interaction with the first few reflected waves generated from the traction-free boundary are obtained in an explicit closed form. The analytical solutions of dynamic stress intensity factors are compared with available numerical and experimental results and the agreement is quite good. We find one thing very interesting: the dynamic stress intensity factor for a long time period is a universal function of the instantaneous extending rate of a crack tip times the static stress intensity factor for an equivalent stationary crack for the finite strip problem. It was also found that the reflected waves generated from free boundaries always increase the stress intensity factor, and the influence from reflected waves generated from the boundary, which is perpendicular to the crack, are weaker than those generated from the boundary, which is parallel to the crack.

1 Introduction

When a static loading is applied to a cracked body and is increased to a sufficiently large magnitude, the crack will begin to extend. The most frequently observed phenomenon in the experiments shows that the crack growth rate is constant during the extending history except in the final unstable or arresting stage. The crack propagating velocity measured experimentally by Kalthoff, Beinert, and Winkler (1977) shows that the assumption of a constant extending rate is acceptable. If the extending rate is high, the inertial effect must be taken into consideration in the analysis. The inherent time dependence of a crack propagation process makes the mathematical models more complex than the equivalent quasi-static models.

The effect of reflected waves interaction with a moving crack had only been discussed in numerical calculation and experimental observations. Kobayashi and Wade (1972) studied the problem of crack propagation and arrest in a tensile plate made of Homalite-100 by using the dynamic photoelastic method. The significant influence of the reflected stress waves generated from the plate boundary was investigated. Experimental results indicated that the reflected waves dominate the stability of crack propagation. The possibility of crack arrest, acceleration, or branching depends on the responses of reflected waves generated from the specimen boundary. Some significant numerical results were obtained by using the finite element method (see Kishimoto, Aoki, and Sakata, 1980). At the same time, Nishioka and Atluri (1980a, b) developed a moving singular element of the finite element method to calculate the dynamic stress intensity factor.

The theoretical analysis of crack propagation, due to general static loading in an unbounded medium, was first addressed by Freund (1972a, b). Freund proposed a superposition method in the time domain to study the dynamic effect of crack propagation in which a fundamental solution is proposed and is used to develop the solution for the negation of the stress distribution on the prospective fracture plane. But this method is valid only for the semi-infinite crack embedded in an infinite medium. Analytical solution for a crack in a finite geometry body is rare. The only available results are provided by Nilsson (1973) and Ma and Ing (1995) for a mode III crack propagating in a finite strip and subjected to static and dynamic loading, respectively.

An interesting conclusion obtained in Freund's paper (1972b) is that the dynamic stress intensity factor has the form of a universal function of an instantaneous extending rate of a crack tip multiplied by the stress intensity factor of an equivalent stationary crack for the unbounded medium problem. The equivalent stationary crack is subjected to the same static loadings and the crack length is equal to the instantaneous length of the actual crack. Whether the above-mentioned result can be generalized in the case of finite boundaries and how the dynamic solutions converge to the corresponding static solution will be discussed in this paper.

A powerful and efficient methodology for constructing the scattered field by superimposing the fundamental solution in the Laplace transform domain has been proposed in recent years by the authors. The Cagniard's method for Laplace inversion is used to obtain the transient solution in a time domain. This methodology was first addressed by Tsai and Ma (1991, 1992)

[1] To whom all correspondence should be addressed.

Contributed by the Applied Mechanics Division of THE AMERICAN SOCIETY OF MECHANICAL ENGINEERS for publication in the ASME JOURNAL OF APPLIED MECHANICS.

Discussion on this paper should be addressed to the Technical Editor, Professor Lewis T. Wheeler, Department of Mechanical Engineering, University of Houston, Houston, TX 77204-4792, and will be accepted until four months after final publication of the paper itself in the ASME JOURNAL OF APPLIED MECHANICS.

Manuscript received by the ASME Applied Mechanics Division, Feb. 14, 1996; final revision, Nov. 20, 1996. Associate Technical Editor: J. W. Ju.

in solving the problems of applying a buried dynamic point body force in a half-plane and a dynamic point body force interaction with a semi-infinite stationary crack. The solution of applying exponentially distributed traction at the surface of a half-plane or a stationary crack face in the Laplace transform domain is considered as the fundamental solution. The reflected and diffracted fields generated from a half-plane and crack tip can be obtained by superimposing the fundamental solutions.

In this paper, the above-mentioned methodology will be generalized and applied in the research of an extending crack. The transient response for a propagating crack with constant velocity in a finite geometry body is obtained by using the generalized method. The orientations of a crack face considered in this study are parallel or perpendicular to the boundary. The main purpose in solving problems concerned with dynamic crack propagation is to determine the dependence of characterizing parameters of the crack-tip field on the applied loading and on the configuration of the body. Since the stress intensity factor is the key parameter in characterizing dynamic crack growth, we will focus our attention mainly on the determination of the dynamic stress intensity factor.

When the stress intensity factor for a stationary crack subjected to static loading reaches its fracture toughness, the crack starts to extend with constant velocity. The diffracted longitudinal wave (denoted by P) and shear wave (denoted by S) will be emitted from the propagating crack tip. The P wave will be reflected from the traction-free-boundary of a half-plane and will generate reflected longitudinal waves and shear waves, which are denoted as PP and PS waves, respectively. Similarly, the S wave will be reflected from the boundary of a half-plane and generate reflected longitudinal (SP) and shear waves (SS). All these reflected waves will arrive at the moving crack tip at a later time and interact with the moving crack. The diffraction, for the second time, will repeat the forward reflection phenomena. In this study, we will neglect the reflected effect on the crack tip of the second time, the third time, etc., because the first reflected waves are much stronger than the reflected waves of later times.

Finally, the analytical solution of a finite cracked body of a rectangular specimen subjected to static loading is obtained without considering the effect of the reflected waves generated from the boundaries perpendicular to the crack and the diffracted waves generated from the corners of the plate. The experimental results obtained by Kalthoff, Beinert, and Winkler (1977), and Hodulak, Kobayashi, and Emery (1990) are discussed and compared with the analytical prediction in light of the present theoretical analysis.

2 Proposed Fundamental Solutions

The solutions of the problem considered in this study can be determined by superposition of the following problems. Problem A treats a static loading applied to a cracked body in an unbounded medium, at time $t = 0$. The crack starts to grow and a new crack propagates out of the original crack with a constant velocity, which will induce a traction on the plane that will eventually define the traction-free boundary of a half-plane. In problem B, a half-plane is considered in which the boundary is subjected to tractions which are equal and opposite to those on the corresponding planes in problem A. Problem C considers an infinite body containing a propagating crack in which the crack face is subjected to the reflected waves which are generated by the half-plane boundary in problem B. The above-mentioned problems A, B, and C are superimposed to construct the solution for propagating crack interaction with stress waves generated from the boundaries.

From physical consideration, the reflected and diffracted waves are generated to eliminate the stress induced by incident waves on the traction-free boundaries. For most of the dynamic problems the stress induced by incident waves can be represented in an integral form of which the kernel is usually an exponential function in the Laplace transform domain of time, so that the solutions of applying exponentially distributed traction at the boundary (surface of half-plane or crack faces) in the Laplace transform domain are considered as the fundamental solutions. The reflected and diffracted waves can be constructed by superimposing the predetermined fundamental solutions in the Laplace transform domain. Some symbols are defined as follows for convenience in the following derivation:

$$\alpha_\pm = \alpha_\pm(\lambda) = [a \pm \lambda(1 \mp av)]^{1/2},$$

$$\alpha_\pm^0 = \alpha_\pm^0(\lambda) = (a \mp \lambda)^{1/2},$$

$$\alpha = \alpha(\lambda) = \alpha_+(\lambda)\alpha_-(\lambda), \quad \alpha^0 = \alpha^0(\lambda) = \alpha_+^0(\lambda)\alpha_-^0(\lambda),$$

$$\beta_\pm = \beta_\pm(\lambda) = [b \pm \lambda(1 \mp bv)]^{1/2},$$

$$\beta_\pm = \beta_\pm^0(\lambda) = (b \mp \lambda)^{1/2},$$

$$\beta = \beta(\lambda) = \beta_+(\lambda)\beta_-(\lambda), \quad \beta^0 = \beta^0(\lambda) = \beta_+^0(\lambda)\beta_-^0(\lambda),$$

$$R = R(\lambda) = (b^2(1 - \lambda v)^2 - 2\lambda^2)^2 + 4\lambda^2\alpha\beta$$
$$= \kappa(d - \lambda)^2(c_1 - \lambda)(c_2 + \lambda)S_+(\lambda)S_-(\lambda),$$

$$\kappa = 4(1 - a^2v^2)^{1/2}(1 - b^2v^2)^{1/2} - (2 - b^2v^2)^2, \quad d = 1/v,$$

$$a_1 = a/(1 + av), \quad b_1 = b/(1 + bv), \quad c_1 = c/(1 + cv),$$

$$a_2 = a/(1 - av), \quad b_2 = b/(1 - bv), \quad c_2 = c/(1 - cv),$$

$$S_\pm = S_\pm(\lambda)$$
$$= \exp\left(\frac{-1}{\pi}\int_{a_{2,1}}^{b_{2,1}} \tan^{-1}\left[\frac{4\xi^2|\alpha||\beta|}{(b^2(1 \mp \xi v)^2 - 2\xi^2)^2}\right]\frac{d\xi}{\xi \pm \lambda}\right),$$

$$R^0 = R^0(\lambda) = R(\lambda)|_{v=0}, \quad S_\pm^0 = S_\pm^0(\lambda) = S_\pm(\lambda)|_{v=0} \quad (1)$$

where a $(=1/v_l)$, b $(=1/v_s)$, and c $(=1/v_r)$ are the slowness of the longitudinal wave, the shear wave and the Rayleigh wave, respectively. Here v_l, v_s, v_r, and v are the propagating speed of the longitudinal wave, shear wave, Rayleigh wave, and the moving crack tip, respectively.

2.1 Fundamental Solution of a Half-Plane. The solution of applying an exponentially distributed loading in the Laplace transform domain at the surface of a half-plane is denoted as the fundamental solution of a half-plane. Consider a half-plane as shown in Fig. 1. An exponentially distributed normal traction in the Laplace transform domain is applied on the surface of the half-plane. The relation between the fixed and moving coordinates is $x_1 = \xi + vt$. The boundary conditions on the half-plane can be written as

$$\bar{\sigma}_{22}(\xi, 0, p) = e^{p\eta\xi} \quad \text{for} \quad -\infty < \xi < \infty, \quad (2)$$

$$\bar{\sigma}_{12}(\xi, 0, p) = 0 \quad \text{for} \quad -\infty < \xi < \infty, \quad (3)$$

where p is the Laplace transform parameter and is assumed to be real and positive, and η is an arbitrary imaginary number. The overbar symbol is used for denoting the transform on time

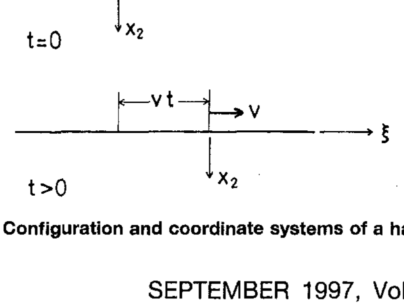

Fig. 1 Configuration and coordinate systems of a half-plane

t. The solutions of stresses that satisfy boundary conditions (2) and (3) can be expressed in the Laplace transform domain as

$$\bar{\sigma}_{11} = \frac{((b^2 - 2a^2)(1 - \eta v)^2 + 2\eta^2)(b^2(1 - \eta v)^2 - 2\eta^2)}{R} \times e^{-p\alpha x_2 + p\eta\xi} + \frac{4\eta^2\alpha\beta}{R} e^{-p\beta x_2 + p\eta\xi}, \quad (4)$$

$$\bar{\sigma}_{12} = \frac{-2\eta\alpha(b^2(1 - \eta v)^2 - 2\eta^2)}{R} e^{-p\alpha x_2 + p\eta\xi} + \frac{2\eta\alpha(b^2(1 - \eta v)^2 - 2\eta^2)}{R} e^{-p\beta x_2 + p\eta\xi}, \quad (5)$$

$$\bar{\sigma}_{22} = \frac{(b^2(1 - \eta v)^2 - 2\eta^2)^2}{R} e^{-p\alpha x_2 + p\eta\xi} + \frac{4\alpha\beta\eta^2}{R} e^{-p\beta x_2 + p\eta\xi}. \quad (6)$$

If the surface traction is applied in the tangential direction, the corresponding boundary conditions are

$$\bar{\sigma}_{22}(\xi, 0, p) = 0 \quad \text{for} \quad -\infty < \xi < \infty, \quad (7)$$

$$\bar{\sigma}_{12}(\xi, 0, p) = e^{p\eta\xi} \quad \text{for} \quad -\infty < \xi < \infty. \quad (8)$$

The solutions of the stresses which satisfy boundary conditions (7) and (8) are expressed in the Laplace transform domain as follows:

$$\bar{\sigma}_{11} = \frac{-2\eta\beta((b^2 - 2a^2)(1 - \eta v)^2 + 2\eta^2)}{R} e^{-p\alpha x_2 + p\eta\xi} + \frac{-2\eta\beta((b^2(1 - \eta v)^2 - 2\eta^2)}{R} e^{-p\beta x_2 + p\eta\xi}, \quad (9)$$

$$\bar{\sigma}_{12} = \frac{4\eta^2\alpha\beta}{R} e^{-p\alpha x_2 + p\eta\xi} + \frac{(b^2(1 - \eta v)^2 - 2\eta^2)^2}{R} e^{-p\beta x_2 + p\eta\xi}, \quad (10)$$

$$\bar{\sigma}_{22} = \frac{-2\eta\beta(b^2(1 - \eta v)^2 - 2\eta^2)}{R} e^{-p\alpha x_2 + p\eta\xi} + \frac{2\eta\beta(b^2(1 - \eta v)^2 - 2\eta^2)}{R} e^{-p\beta x_2 + p\eta\xi}. \quad (11)$$

2.2 Fundamental Solution of a Propagating Crack. The solution of applying an exponentially distributed load in the Laplace transform domain on the propagating crack faces is denoted as the fundamental solution of a propagating crack. Consider a semi-infinite crack propagating with constant speed $v = 1/d$ in an unbounded medium as shown in Fig. 2. The coordinate system (ξ, x_2) is fixed with respect to the moving crack tip and moves with a constant speed v. The upper and lower crack faces are acted by opposite distributed normal tractions which yields the boundary condition in the Laplace transform domain as follows:

$$\bar{\sigma}_{22}(\xi, 0, p) = e^{p\eta\xi} \quad \text{for} \quad -\infty < \xi < 0, \quad (12)$$

$$\bar{\sigma}_{12}(\xi, 0, p) = 0 \quad \text{for} \quad -\infty < \xi < \infty, \quad (13)$$

$$\bar{u}_2(\xi, 0, p) = 0 \quad \text{for} \quad 0 < \xi < \infty, \quad (14)$$

where η is a complex number. Applying the two-sided Laplace transform with respect to ξ and using the Wiener-Hopf technique, the full-field solutions can be obtained as follows:

$$\bar{\sigma}_{ij} = \frac{1}{2\pi i} \int [S_{ij}^1(\lambda) e^{-p\alpha x_2 + p\lambda\xi} + S_{ij}^2(\lambda) e^{-p\beta x_2 + p\lambda\xi}] d\lambda, \quad (15)$$

where

$$S_{11}^1(\lambda) = -((b^2 - 2a^2)(1 - \lambda v)^2 + 2\lambda^2) \times (b^2(1 - \lambda v)^2 - 2\lambda^2)\alpha_+(\eta) G(\eta, \lambda)/\alpha_+(\lambda),$$

$$S_{11}^2(\lambda) = 4\lambda^2\beta(\lambda)\alpha_-(\lambda)\alpha_+(\eta) G(\eta, \lambda),$$

$$S_{12}^1(\lambda) = 2\lambda(b^2(1 - \lambda v)^2 - 2\lambda^2)\alpha_-(\lambda)\alpha_+(\eta) G(\eta, \lambda),$$

$$S_{12}^2(\lambda) = -2\lambda(b^2(1 - \lambda v)^2 - 2\lambda^2)\alpha_-(\lambda)\alpha_+(\eta) G(\eta, \lambda),$$

$$S_{22}^1(\lambda) = -(b^2(1 - \lambda v)^2 - 2\lambda^2)^2\alpha_+(\eta) G(\eta, \lambda)/\alpha_+(\lambda),$$

$$S_{22}^2(\lambda) = -4\lambda^2\beta(\lambda)\alpha_-(\lambda)\alpha_+(\eta) G(\eta, \lambda),$$

$$G(\eta, \lambda) = 1/(\kappa(d - \lambda)^2(c_1 - \lambda) \times (c_2 + \eta) S_-(\lambda) S_+(\eta)(\lambda - \eta)). \quad (16)$$

The associated mode I stress intensity factor expressed in the Laplace transform domain is

$$\bar{K}_I = \frac{-\sqrt{2}}{\sqrt{p}} \frac{\alpha_+(\eta)}{\sqrt{1 - av}\,(c_2 + \eta) S_+(\eta)}. \quad (17)$$

3 Transient Analysis for a Propagating Crack Interaction With Boundaries

Consider a stationary semi-infinite crack subjected to a general static loading, the crack tip is located at $x_1 = 0$ for $t < 0$. Let the resulting normal stress σ_{22} along the crack-tip line $x_1 > 0$, $x_2 = 0$ be $-p(x_1)$, when the loading is increased to a sufficiently large magnitude, the crack will begin to extend at a constant speed and the normal stress $-p(x_1)$ will be released from the growing traction-free surface of the crack along $0 < x_1 < vt$, $x_2 = 0$. The released stress will induce diffracted waves radiating from the moving crack tip. According to the result provided by Freund (1972a), the radiated stress fields σ_{ij}^* and the correspondence stress intensity factor K_I^* can be obtained from the following superposition integral:

$$\sigma_{ij}^*(\xi, x_2, t) = \int_0^{vt} \sigma_{ij}(\xi - x_0, x_2, t - x_0/v) p(x_0) dx_0, \quad (18)$$

$$K_I^*(t) = \int_0^{vt} K_I(t - x_0/v) p(x_0) dx_0 \quad (19)$$

where $\sigma_{ij}(\xi - x_0, x_2, t - x_0/v)$ and $K_I(t - x_0/v)$ are the transient solutions of a crack extending at a constant rate v and subjected to the dynamic concentrated forces of unit magnitude appearing at the crack tip at time $t = x_0/v$.

The diffracted waves emitted from the moving crack tip will be reflected from the boundaries of the finite cracked body. In order to extend Freund's method to apply in the analysis of a finite cracked body, the preliminarily required solutions $\sigma_{ij}(\xi - x_0, x_2, t - x_0/v)$ and $K_I(t - x_0/v)$ with the reflected effect are derived in detail in the following Sections 3.1 to 3.3. Then the stress intensity factor of a crack

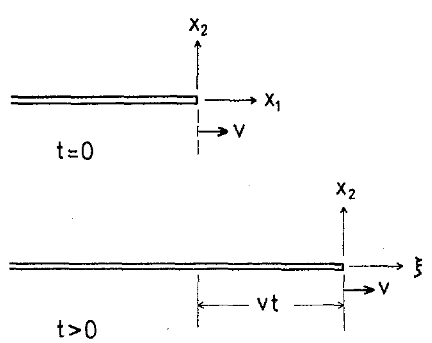

Fig. 2 Configuration and coordinate systems of a propagating crack

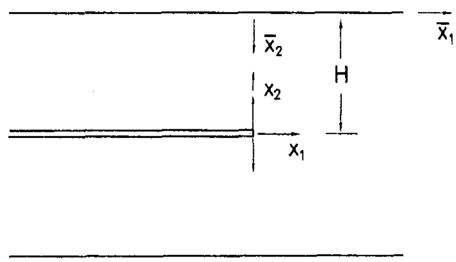

Fig. 3 Configuration and coordinate systems of a semi-infinite crack embedded in a strip

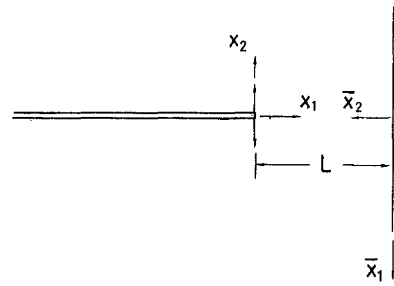

Fig. 4 Configuration and coordinate systems of a semi-infinite crack embedded in a half-plane

in the finite body subjected to a general static loading and extending at a constant speed can be obtained by the superposition integral (19).

3.1 Diffracted Waves in Infinite Medium. A semi-infinite crack moving in a strip and moving in a half-plane is considered in Fig. 3 and Fig. 4, respectively. The distance from the crack tip to the boundary parallel to the crack is denoted as H and to the boundary perpendicular to the crack is denoted as L. The coordinate system (ξ, x_2) is attached at the moving crack tip and the extending rate is v. A concentrated force of unit magnitude is applied at the crack tip at time $t = 0$. Before the diffracted wave generated from the moving crack tip reaches the boundary, the problem can be considered as a semi-infinite crack propagating in an unbounded medium and the boundary conditions can be expressed as follows:

$$\sigma_{22}(\xi, 0, t) = -\delta(\xi + vt)H(t) \quad \text{for} \quad -\infty < \xi < 0, \quad (20)$$

$$\sigma_{12}(\xi, 0, t) = 0 \quad \text{for} \quad -\infty < \xi < \infty, \quad (21)$$

$$u_2(\xi, 0, t) = 0 \quad \text{for} \quad 0 < \xi < \infty. \quad (22)$$

The boundary conditions represented in the Laplace transform domain are

$$\bar{\sigma}_{22}(\xi, 0, t) = -de^{pd\xi} \quad \text{for} \quad -\infty < \xi < 0, \quad (23)$$

$$\bar{\sigma}_{12}(\xi, 0, p) = 0 \quad \text{for} \quad -\infty < \xi < \infty, \quad (24)$$

$$\bar{u}_2(\xi, 0, p) = 0 \quad \text{for} \quad 0 < \xi < \infty. \quad (25)$$

The fundamental solutions for applying the exponentially distributed traction $\bar{\sigma}_{22}(\xi, o, p) = e^{p\eta\xi}$ at crack faces have been obtained in Section 2, so that the radiated diffracted stress fields from the moving crack tip can be obtained by taking $\eta = d$ and multiplying the magnitude $-d$ to (15). The stresses expressed in the Laplace transform domain are

$$\bar{\sigma}_{11}^D = \frac{1}{2\pi i}\int \frac{((b^2 - 2a^2)(1 - \lambda v)^2 + 2\lambda^2)(b^2(1 - \lambda v)^2 - 2\lambda^2))}{\kappa d^2\alpha_+(1 - \lambda v)^2(c_1 - \lambda)S_-(\lambda)} F(\lambda)e^{-p\alpha x_2 + p\lambda\xi} - \frac{4\lambda^2\alpha_-\beta}{\kappa d^2(1 - \lambda v)^2(c_1 - \lambda)S_-(\lambda)} F(\lambda)e^{-p\beta x_2 + p\lambda\xi}d\lambda, \quad (26)$$

$$\bar{\sigma}_{22}^D = \frac{1}{2\pi i}\int \frac{(b^2(1 - \lambda v)^2 - 2\lambda^2)^2}{\kappa d^2\alpha_+(1 - \lambda v)^2(c_1 - \lambda)S_-(\lambda)} F(\lambda)e^{-p\alpha x_2 + p\lambda\xi} + \frac{4\lambda^2\alpha_-\beta}{\kappa d^2(1 - \lambda v)^2(c_1 - \lambda)S_-(\lambda)} F(\lambda)e^{-p\beta x_2 + p\lambda\xi}d\lambda, \quad (27)$$

$$\bar{\sigma}_{12}^D = \frac{1}{2\pi i}\int \frac{-2\lambda\alpha_-(b^2(1 - \lambda v)^2 - 2\lambda^2)}{\kappa d^2(1 - \lambda v)^2(c_1 - \lambda)S_-(\lambda)} F(\lambda)e^{-p\alpha x_2 + p\lambda\xi} + \frac{2\lambda\alpha_-(b^2(1 - \lambda v)^2 - 2\lambda^2)}{\kappa d^2(1 - \lambda v)^2(c_1 - \lambda)S_-(\lambda)} F(\lambda)e^{-p\beta x_2 + p\lambda\xi}d\lambda, \quad (28)$$

where

$$F(\lambda) = \frac{d\alpha_+(d)}{(d - \lambda)(c_2 + d)S_+(d)}. \quad (29)$$

The associated stress intensity factor expressed in the Laplace transform domain can also be obtained by taking $\eta = d$ and multiplying $-d$ to (17) as follows:

$$\bar{K}_I = \frac{d\sqrt{2}\alpha_+(d)}{\sqrt{p}\sqrt{1 - av}\,(c_2 + d)S_+(d)}. \quad (30)$$

The stress intensity factor in the time domain is

$$K_I = \sqrt{\frac{2}{\pi v t}}\,\kappa(d), \quad (31)$$

where

$$\kappa(d) = \frac{d}{\sqrt{1 - a/d}\,(c_2 + d)S_+(d)}.$$

3.2 Dynamic Stress Intensity Factors due to Reflected Waves Generated From the Boundary Parallel to the Crack. The diffracted waves emitted from the propagating crack tip will be reflected from the boundary which is parallel to the crack at $x_2 = H$. From Eqs. (27) and (28), it is obvious that the traction, which must be applied at $x_2 = H$ to eliminate the stresses $\bar{\sigma}_{22}^D$ and $\bar{\sigma}_{12}^D$ induced at the boundary, can be represented by the exponential function $e^{p\lambda\xi}$. The fundamental solutions for applying the normal traction $e^{p\eta\xi}$ and tangential traction $e^{p\eta\xi}$ at the surface of the half-plane have already been obtained in (6) and (11).

The reflected waves generated from the boundary can be obtained by superimposing the fundamental solutions as follows:

$$\bar{\sigma}_{22}^{R} = \frac{1}{2\pi i}\int \frac{-(b^2(1-\lambda v)^2 - 2\lambda^2)^2((b^2(1-\lambda v)^2 - 2\lambda^2)^2 - 4\lambda^2\alpha\beta)}{\kappa d^2\alpha_+(1-\lambda v)^2(c_1-\lambda)S_-(\lambda)R} F(\lambda)e^{-pH\alpha - p\alpha\bar{x}_2 + p\lambda\xi} d\lambda$$
$$+ \frac{1}{2\pi i}\int \frac{-8\lambda^2\alpha_-\beta(b^2(1-\lambda v)^2 - 2\lambda^2)^2}{\kappa d^2(1-\lambda v)^2(c_1-\lambda)S_-(\lambda)R} F(\lambda)e^{-p\alpha H - p\beta\bar{x}_2 + p\lambda\xi} d\lambda$$
$$+ \frac{1}{2\pi i}\int \frac{-8\lambda^2\alpha_-\beta(b^2(1-\lambda v)^2 - 2\lambda^2)^2}{\kappa d^2(1-\lambda v)^2(c_1-\lambda)S_-(\lambda)R} F(\lambda)e^{-p\beta H - p\alpha\bar{x}_2 + p\lambda\xi} d\lambda,$$
$$+ \frac{1}{2\pi i}\int \frac{4\lambda^2\alpha_-\beta((b^2(1-\lambda v)^2 - 2\lambda^2)^2 - 4\lambda^2\alpha\beta)}{\kappa d^2(1-\lambda v)^2(c_1-\lambda)S_-(\lambda)R} F(\lambda)e^{-p\beta H - p\beta\bar{x}_2 + p\lambda\xi} d\lambda. \quad (32)$$

It is noted that the traction, which should be applied at $\bar{x}_2 = H$ to eliminate the stress $\bar{\sigma}_{22}^{R}$ at the propagating crack face, is represented by the function $e^{p\lambda\xi}$. The fundamental solution for applying the normal traction $e^{p\eta\xi}$ at the crack surfaces has been expressed in (17), so that the stress intensity factor induced by the reflected waves generated from the boundary can be obtained by superimposing the fundamental solution as follows:

$$\bar{K}_I = \frac{1}{2\pi i p^{1/2}}\int \frac{-2(b^2(1-\lambda v)^2 - 2\lambda^2)^2((b^2(1-\lambda v)^2 - 2\lambda^2)^2 - 4\alpha\beta\lambda^2)}{\sqrt{1-av}\,R^2} F(\lambda)e^{-2p\alpha H} d\lambda$$
$$+ \frac{1}{2\pi i p^{1/2}}\int \frac{-32\lambda^2\alpha\beta(b^2(1-\lambda v)^2 - 2\lambda^2)^2}{\sqrt{1-av}\,R^2} F(\lambda)e^{-p\alpha H - p\beta H} d\lambda$$
$$+ \frac{1}{2\pi i p^{1/2}}\int \frac{8\alpha\beta\lambda^2((b^2(1-\lambda v)^2 - 2\lambda^2)^2 - 4\alpha\beta\lambda^2)}{\sqrt{1-av}\,R^2} F(\lambda)e^{-2p\beta H} d\lambda. \quad (33)$$

By using the Cagniard-de Hoop method for Laplace inversion, the stress intensity factors in time domain can be obtained, and the results are

$$K_I = \frac{1}{\pi^{3/2}}\int_{T_{PP}}^{t} \frac{1}{\sqrt{t-\tau}} \operatorname{Im}\left[\frac{-(b^2(1-\lambda_1 v)^2 - 2\lambda_1^2)^2((b^2(1-\lambda_1 v)^2 - 2\lambda_1^2)^2 - 4\alpha\beta\lambda_1^2)F(\lambda_1)}{\sqrt{1-av}\,R^2}\frac{\partial\lambda_1}{\partial\tau}\right] d\tau$$
$$+ \frac{1}{\pi^{3/2}}\int_{T_{PS}}^{t} \frac{1}{\sqrt{t-\tau}} \operatorname{Im}\left[\frac{-16\lambda_2^2\alpha\beta(b^2(1-\lambda_2 v)^2 - 2\lambda_2^2)^2F(\lambda_2)}{\sqrt{1-av}\,R^2}\frac{\partial\lambda_2}{\partial\tau}\right] d\tau$$
$$+ \frac{1}{2\pi^{3/2}}\int_{T_{SS}}^{t} \frac{1}{\sqrt{t-\tau}} \operatorname{Im}\left[\frac{4\alpha\beta\lambda_3^2((b^2(1-\lambda_3 v)^2 - 2\lambda_3^2)^2 - 4\alpha\beta\lambda_3^2)F(\lambda_3)}{\sqrt{1-av}\,R^2}\frac{\partial\lambda_3}{\partial\tau}\right] d\tau, \quad (34)$$

where

$$\lambda_1 = \frac{-2va^2H + i\sqrt{\tau^2 - a^2v^2\tau^2 - 4a^2H^2}}{2H(1-a^2v^2)},$$
$$\lambda_3 = \frac{-2vb^2H + i\sqrt{\tau^2 - b^2v^2\tau^2 - 4b^2H^2}}{2H(1-b^2v^2)},$$

and λ_2 is the root of $\alpha(\lambda)H + \beta(\lambda)H - \tau = 0$. The arrival times are $T_{PP} = 2\sqrt{a_1a_2}\,H$, $T_{SS} = 2\sqrt{b_1b_2}\,H$, $T_{PS} = T_{SP}$, where T_{PS} is the corresponding value of τ at which the imaginary part of λ_2 begins to vanish.

3.3 Dynamic Stress Intensity Factors due to Reflected Waves Generated From the Boundary Perpendicular to the Crack. Now, we consider the case that a propagating crack interaction with the boundary which is perpendicular to the crack as shown in Fig. 4. The diffracted waves expressed by the moving coordinate system (ξ, x_2) can be rewritten in the stationary coordinate system (x_1, x_2) in Laplace transform domain as

$$\bar{\sigma}_{11}^{D} = \frac{1}{2\pi i}\int \frac{((b^2-2a^2)(1-\bar{\lambda}v)^2 + 2\bar{\lambda}^2)(b^2(1-\bar{\lambda}v)^2 - 2\bar{\lambda}^2)}{\alpha_+(\bar{\lambda})\kappa d^2(1-\bar{\lambda}v)^2(c_1-\bar{\lambda})S_-^*(\bar{\lambda})(1+\lambda v)} \times F(\bar{\lambda})e^{-p\alpha^0|x_2| + p\lambda x_1}$$
$$- \frac{4\bar{\lambda}^2\alpha_-(\bar{\lambda})\beta(\bar{\lambda})}{\kappa d^2(1-\bar{\lambda}v)^2(c_1-\bar{\lambda})^2(c_1-\bar{\lambda})S_-(\bar{\lambda})(1+\lambda v)} \times F(\bar{\lambda})e^{-p\beta^0|x_2| + p\lambda x_1} d\lambda, \quad (35)$$

$$\bar{\sigma}_{12}^{D} = \frac{\operatorname{sgn}(x_2)}{2\pi i}\int \frac{-2\bar{\lambda}\alpha_-(\bar{\lambda})(b^2(1-\bar{\lambda}v)^2) - 2\bar{\lambda}^2)}{\kappa d^2(1-\bar{\lambda}v)^2(c_1-\bar{\lambda})S_-(\bar{\lambda})(1+\lambda v)} \times F(\bar{\lambda})e^{-p\alpha^0|x_2| + p\lambda x_1}$$
$$+ \frac{2\bar{\lambda}\alpha_-(\bar{\lambda})(b^2(1-\bar{\lambda}v)^2 - 2\bar{\lambda}^2)}{\kappa d^2(1-\bar{\lambda}v)^2(c_1-\bar{\lambda})S_-(\bar{\lambda})(1+\lambda v)} \times F(\bar{\lambda})e^{-p\beta^0|x_2| + p\lambda x_1} d\lambda, \quad (36)$$

where

$$\bar{\lambda} = \frac{\lambda}{1+\lambda v},$$

and $\operatorname{sgn}(x_2) = 1$ for $x_2 > 0$, $\operatorname{sgn}(x_2) = -1$ for $x_2 < 0$. The diffracted waves emitted from the crack tip will be reflected from the boundary at some later time. It is obvious to see that the traction, which must be applied at $x_1 = L$ to eliminate the stress $\bar{\sigma}_{11}^{D}$ and $\bar{\sigma}_{12}^{D}$, can be represented by the exponential function $e^{-p\alpha^0|x_2|}$, $e^{-p\beta^0|x_2|}$. The fundamental solutions for applying normal traction and tangential traction $e^{-p\alpha^0|x_2|}$ or $e^{-p\beta^0|x_2|}$ at the surface of a half-plane were proposed by Tsai and Ma (1991). So that the reflected waves can be obtained by superimposing the fundamental solutions as follows:

$$\bar{\sigma}_{22}^R = \frac{1}{2\pi i}\int\left[\frac{-((b^2-2a^2)(1-\bar{\lambda}v)^2+2\bar{\lambda}^2)(b^2(1-\bar{\lambda}v)^2-2\bar{\lambda}^2)(b^2-2\alpha^{02})(b^2-2\lambda^2)F(\bar{\lambda})}{\alpha_+(\bar{\lambda})\kappa d^2(1-\bar{\lambda}v)^2(c_1-\bar{\lambda})S_-(\bar{\lambda})(1-\lambda v)R^0(\alpha^0)}\right.$$
$$\left.-\frac{4g\bar{\lambda}(b^2(1-\bar{\lambda}v)^2-2\bar{\lambda}^2)\alpha_-(\bar{\lambda})\alpha^0\beta^0(\alpha^0)(b^2-2\lambda^2)F(\bar{\lambda})}{\kappa d^2(1-\bar{\lambda}v)^2(c_1-\bar{\lambda})S_-(\bar{\lambda})(1-\lambda v)R^0(\alpha^0)}\right]e^{-2p\lambda L+p\lambda x_1}d\lambda$$
$$+\frac{1}{2\pi i}\int\frac{8((b^2-2a^2)(1-\bar{\lambda}v)^2+2\bar{\lambda}^2)(b^2(1-\bar{\lambda}v)^2-2\lambda^2)\alpha_-(\bar{\lambda})\lambda^2\beta^{02}F(\bar{\lambda})}{\alpha_+(\bar{\lambda})\kappa d^2(1-\bar{\lambda}v)^2(c_1-\bar{\lambda})S_-(\bar{\lambda})(1-\alpha^0(\beta^0)v)R^0(\beta^0)}e^{-p\alpha^0(\beta^0)L-p\lambda L+p\lambda x_1}d\lambda$$
$$+\frac{1}{2\pi i}\int\frac{-8\bar{\lambda}^2\beta(\bar{\lambda})\alpha_-(\bar{\lambda})(b^2-2\beta^0(\alpha^0)^2)(b^2-2\lambda^2)\lambda F(\bar{\lambda})}{\kappa d^2(1-\bar{\lambda}v)^2(c_1-\bar{\lambda})S_-(\bar{\lambda})(1-\beta^0(\alpha^0)v)R^0(\bar{\alpha}^0)}e^{-p\beta^0(\alpha^0)L-p\lambda L+p\lambda x_1}d\lambda$$
$$+\frac{1}{2\pi i}\int\frac{-16\bar{\lambda}^2\beta(\bar{\lambda})\alpha_-(\bar{\lambda})\lambda\beta^{02}\alpha^0(\beta^0)-4\bar{\lambda}\lambda(b^2(1-\bar{\lambda}v)^2-2\bar{\lambda}^2)\alpha_-(\bar{\lambda})\beta^0(b^2-2\lambda^2)F(\bar{\lambda})}{\kappa d^2(1-\bar{\lambda}v)^2(c_1-\bar{\lambda})S_-(\bar{\lambda})(1-\lambda v)R^0(\beta^0)}e^{-2p\lambda L+p\lambda x_1}d\lambda \quad (37)$$

where

$$\bar{\lambda} = \frac{-\lambda}{1-\lambda v}$$

for the first and fourth terms, and

$$\bar{\lambda} = \frac{-\alpha^0(\beta^0)}{1-\alpha^0(\beta^0)v},\quad \bar{\lambda} = \frac{-\beta^0(\alpha^0)}{1-\beta^0(\alpha^0)v}$$

for the second and third terms.

In order to obtain the stress intensity factor attributed to the reflected waves, the reflected waves must be transformed to the moving coordinate system (ξ, x_2) by using the transformation principle. The stress intensity factor induced by reflected waves generated from the boundary can be expressed as follows:

$$\bar{K}_I = \frac{\sqrt{2}}{2\pi i p^{1/2}}\int G_1(\lambda)e^{-2p\lambda L}d\lambda$$
$$+\frac{\sqrt{2}}{2\pi i p^{1/2}}\int G_2(\lambda)e^{-p\lambda L-p\alpha^0(\bar{\beta}^0)(1-\lambda v)L}d\lambda$$
$$+\frac{\sqrt{2}}{2\pi i p^{1/2}}\int G_3(\lambda)e^{-p\lambda L-p\beta^0(\bar{\alpha}^0)(1-\lambda v)L}d\lambda$$
$$+\frac{\sqrt{2}}{2\pi i p^{1/2}}\int G_4(\lambda)e^{-2p\lambda L}d\lambda, \quad (38)$$

where

$$G_1(\lambda) = \frac{((b^2-2a^2)(1-\tilde{\lambda}v)^2+2\tilde{\lambda}^2)(b^2(1-\tilde{\lambda}v)^2-2\tilde{\lambda}^2)\tilde{\alpha}_-(b^2-2\bar{\alpha}^{02})(b^2-2\lambda^2)F'(\tilde{\lambda})}{\kappa d^2(1-\tilde{\lambda}v)^2\tilde{\alpha}(c_1-\tilde{\lambda})S_-(\tilde{\lambda})(1-\bar{\lambda}v)(1-\lambda v)R^0(\bar{\alpha}^0)}$$
$$+\frac{4\tilde{\lambda}(b^2(1-\tilde{\lambda}v)^2-2\tilde{\lambda}^2)\tilde{\alpha}_-\bar{\alpha}^0\beta^0(\bar{\alpha}^0)(b^2-2\bar{\lambda}^2)F'(\tilde{\lambda})}{\kappa d^2(1-\tilde{\lambda}v)^2(c_1-\tilde{\lambda})S_-(\tilde{\lambda})(1-\bar{\lambda}v)(1-\lambda v)R^0(\bar{\alpha}^0)}$$

$$G_2(\lambda) = \frac{-8\bar{\lambda}^2\bar{\beta}^2((b^2-2a^2)(1-\tilde{\lambda}v)^2+2\tilde{\lambda}^2)(b^2(1-\tilde{\lambda}v)^2-2\tilde{\lambda}^2)F'(\tilde{\lambda})}{\kappa d^2(1-\tilde{\lambda}v)^2\tilde{\alpha}_+(c_1-\tilde{\lambda})S_-(\tilde{\lambda})(1-\alpha^0(\bar{\beta}^0)v)R^0(\bar{\beta}^0)(1-\lambda v)}$$

$$G_3(\lambda) = \frac{8\tilde{\lambda}^2\tilde{\beta}\tilde{\alpha}_+(b^2-2\beta^0(\bar{\alpha}^0)^2)(b^2-2\bar{\lambda}^2)\bar{\lambda}F'(\tilde{\lambda})}{\kappa d^2(1-\tilde{\lambda}v)^2(c_1-\tilde{\lambda})S_-(\tilde{\lambda})(1-\beta^0(\bar{\alpha}^0)v)R^0(\bar{\alpha}^0)(1-\lambda v)}$$

$$G_4(\lambda) = \frac{16\tilde{\lambda}^2\tilde{\beta}\tilde{\alpha}_-\bar{\beta}^{02}\alpha^0(\bar{\beta}^0)\bar{\lambda}+4\tilde{\lambda}(b^2(1-\tilde{\lambda}v)^2-2\tilde{\lambda}^2)\tilde{\alpha}_-\bar{\lambda}\bar{\beta}^0(b^2-2\bar{\lambda}^2)F'(\tilde{\lambda})}{\kappa d^2(1-\tilde{\lambda}v)^2(c_1-\tilde{\lambda})S_-(\tilde{\lambda})(1-\bar{\lambda}v)(1-\lambda v)R^0(\bar{\beta}^0)}, \quad (39)$$

and

$$\tilde{\alpha} = \alpha(\tilde{\lambda}),\quad \bar{\alpha} = \alpha(\bar{\lambda}),\quad \bar{\alpha}^0 = \alpha^0(\bar{\lambda}),$$
$$\tilde{\beta} = \beta(\tilde{\lambda}),\quad \bar{\beta} = \beta(\bar{\lambda}),\quad \bar{\beta}^0 = \beta^0(\bar{\lambda}),$$

$$\bar{\lambda} = \frac{\lambda}{1-\lambda v},\quad F'(\tilde{\lambda}) = \frac{\alpha_+(\lambda)}{\sqrt{1-av}\,(c_2+\lambda)S_+(\lambda)}F(\tilde{\lambda}), \quad (40)$$

and

$$\tilde{\lambda} = \frac{-\lambda}{1-2\lambda v},$$

for the first and fourth terms of (38),

$$\tilde{\lambda} = \frac{-\alpha^0(\bar{\beta}^0)}{1-\alpha^0(\bar{\beta}^0)v},\quad \tilde{\lambda} = \frac{-\beta^0(\bar{\alpha}^0)}{1-\beta^0(\bar{\alpha}^0)v},$$

for the second and third terms of (38). By using the Cagniard-de Hoop method, the stress intensity factors can be obtained in the time domain as follows:

$$K_I = \frac{1}{\pi^{3/2}}\int_{T_{PP}}^{t}\frac{1}{\sqrt{t-\tau}}\,\mathrm{Im}\left[G_1(\lambda_1)\frac{\partial\lambda_1}{\partial\tau}\right]d\tau$$
$$+\frac{1}{\pi^{3/2}}\int_{T_{PS}}^{t}\frac{1}{\sqrt{t-\tau}}\,\mathrm{Im}\left[G_2(\lambda_2)\frac{\partial\lambda_2}{\partial\tau}\right]d\tau$$
$$+\frac{1}{\pi^{3/2}}\int_{T_{SP}}^{t}\frac{1}{\sqrt{t-\tau}}\,\mathrm{Im}\left[G_3(\lambda_3)\frac{\partial\lambda_3}{\partial\tau}\right]d\tau$$

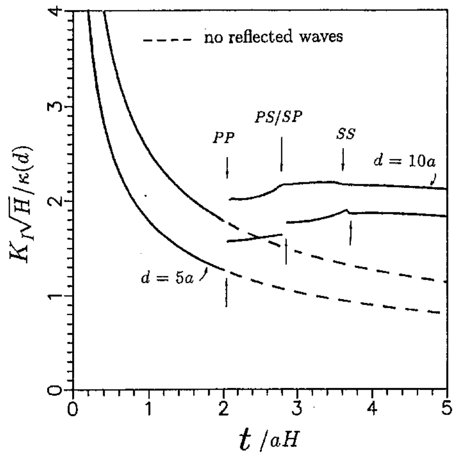

Fig. 5 Stress intensity factors of an embedded crack in a strip subjected to a pair of concentrated forces applied at $x_1 = 0$

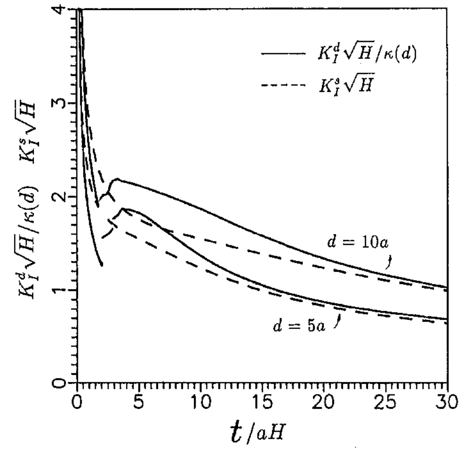

Fig. 6 Dynamic and static stress intensity factors (K_I^d, K_I^s) of a crack embedded in a strip subjected to a pair of concentrated forces applied at $x_1 = 0$

$$+ \frac{1}{\pi^{3/2}} \int_{T_{SS}}^{t} \frac{1}{\sqrt{t-\tau}} \operatorname{Im}\left[G_4(\lambda_4) \frac{\partial \lambda_4}{\partial \tau} \right] d\tau, \quad (41)$$

where $\lambda_1 = \lambda_4 = (\tau/2L)$ and λ_2 and λ_3 are the roots of

$$\lambda L + \alpha^0(\bar{\beta}^0)(1 - \lambda v)L - \tau = 0,$$

and

$$\lambda L + \beta^0(\bar{\alpha}^0)(1 - \lambda v)L - \tau = 0,$$

respectively. The correspondent arrival times are

$$T_{PP} = 2a_1L, \quad T_{PS} = \frac{aL}{1 + bv} + b_1L,$$

$$T_{SP} = \frac{bL}{1 + av} + a_1L, \quad T_{SS} = 2b_1L. \quad (42)$$

4 Numerical Results

With the analytic solution constructed in the previous section, we now perform the numerical investigation of the dynamic stress intensity factor for a propagating crack interaction with stress waves reflected from boundaries. In this study, Poisson's ratio ν is assumed to be equal to 0.25 which gives ratios of the slowness of $b = \sqrt{3}\, a$ and $c = 1.884a$. First, the results of an embedded semi-infinite crack contained in a finite strip and in a half-plane, as shown in Figs. 3 and 4, are investigated. At time $t = 0$, a concentrated force of unit magnitude is applied at the crack tip, and the crack begins to propagate along the crack tip line with constant speed v. The extending rates $v = 0.1v_l$, $0.2v_l$ (i.e., slowness ratios $d/a = 10, 5$) are chosen for numerical investigation.

For the case of a semi-infinite crack which is embedded parallel to the boundaries of the strip (i.e. Fig. 3), the diffracted waves will be emitted from the propagating crack tip and will be reflected from the two boundaries of the strip. The transient results for the dynamic stress intensity factors are shown in Fig. 5. At the time $t = 2.04aH$ (=$2.01aH$), the reflected PP wave for the extending slownesses $d/a = 5$ (=10) arrives at the propagating crack tip. The reflected waves from the boundaries will enlarge the stress intensity factor. The dash line represents the stress intensity factor without considering the reflected waves from the boundaries, i.e., a semi-infinite crack propagates in an unbounded medium.

In order to understand how dynamic transient response approaches the corresponding static value the long-time behavior, which accounts only the first few reflected waves, is calculated and shown in Fig. 6. The dynamic stress intensity factors K_I^d divided by the universal function $\kappa(d)$ are presented by solid lines that are evaluated without considering the reflected waves of the second time, the third time, etc., from the horizontal boundary. The dash lines represent the equivalent static solution K_I^s at which the point loading is applied at a distance vt from the crack tip. It is shown that these two lines will approach each other as time is large. Even though the reflected waves of the second time, the third time, etc, are neglected in the numerical calculation, it is reasonable to concluded that the long-time behavior of a stress intensity factor of a propagating crack in a strip has the form of a universal function $\kappa(d)$ of an instantaneous extending rate of crack tip multiplied by the stress intensity factor for a stationary crack with the instantaneous length of the actual crack subjected to the same static loadings. Hence, Freund's result (1972b) is shown to be valid for the finite strip problem also. It is also concluded that the result is accurate enough to evaluate the dynamic stress intensity factor without considering the reflected waves of the second time, the third time, etc., and only when taking the first reflected waves into consideration. The result will cause only a small tolerance (about six percent) in the calculation of dynamic stress intensity factor.

For the case of a semi-infinite crack which is embedded perpendicularly to the boundaries of a half-plane (i.e., Fig. 4), the numerical results of transient stress intensity factors are shown in Fig. 7. The dashed line represents the value without

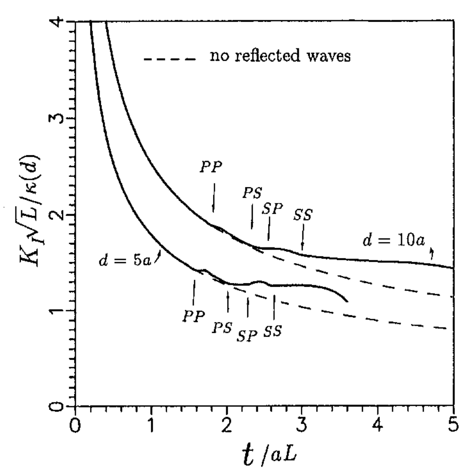

Fig. 7 Stress intensity factors of an embedded crack in a half-plane subjected to a pair of concentrated forces applied at $x_1 = 0$

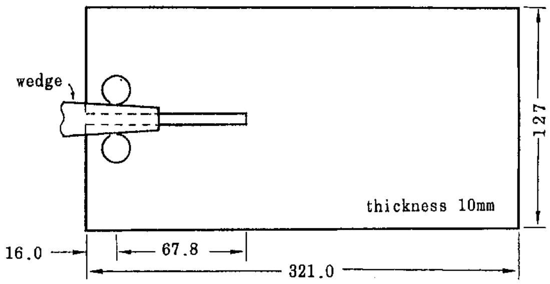

Fig. 8 Specimen configuration of rectangular double cantilever specimen investigated by Kalthoff et al. (1977) and Atluri et al. (1985)

considering the contribution from reflected waves. At time $t = 1.67aL$ ($=1.82aL$), the reflected PP wave generated from the boundary for the extending slownesses $d/a = 5$ ($=10$) arrives at the propagating crack tip. Unlike the case of an embedded crack in a strip as discussed in Fig. 5, the reflected effect for this case is relatively small.

Next, experimental results reported by Kalthoff, Beinert, and Winkler (1977) and the numerical results reported by Atluri and Nishioka (1985) are discussed, and both results will be compared with the present analytical solutions. A rectangular double-cantilever specimen made by photoelastic material Araldite B, as shown in Fig. 8, is considered. The material properties of Araldite B are density $\rho = 1047$ kg/m^3, Poisson's ratio $\nu = 0.33$, Young's modulus $E = 3.38$ GPa, which yield the longitudinal wave speed $v_l = 1903$ m/s, shear wave speed $v_s = 1102$ m/s, and Rayleigh wave speed $v_R = 1081$ m/s. When a static loading is applied and is increased to the the fracture toughness $K_C = 2.32$ MPa $\sqrt{m}$, the crack begins to extend at a constant speed $v = 295$ m/s during the early 300 μs.

The function $p(x_1)$ as shown in (18), which is the resulting negation of the stress σ_{22} ahead of the crack tip before extension occurred, is calculated by the finite element method. Then substitute the numerical result of $p(x_1)$ into (18), the stress intensity factor can be obtained based on the analysis in the previous section and the result is shown in Fig. 9. Since the reflected effect generated from boundaries perpendicular to a crack and reflected waves of the second time, the third time, etc., are small enough, only the first few reflected waves generated from the boundaries parallel to the crack are considered in the analysis. The results based on the theoretical solution are consistent with the finite element results of Atluri and Nishioka (1985) and experimental results of Kalthoff, Beinert, and Winkler (1977).

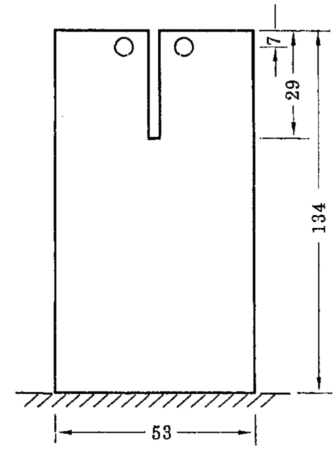

Fig. 10 Specimen configuration of rectangular double cantilever specimen investigated by Hodulak et al. (1980)

The equivalent static stress intensity factor for the given crack growing length referred to in Kalthoff (1985) is also presented in Fig. 9.

At the instant of crack propagation, the stress intensity factor jumps from 2.32 MPa $\sqrt{m}$ to 2.07 MPa $\sqrt{m}$ with the decreasing ratio $\kappa(d)$, where $d = (v_l/v)a = 6.45a$. Because the kinetic energy is radiated into the specimen, the dynamic stress intensity factor is smaller than the equivalent static stress intensity factor for the given crack growing length (i.e., $K_I^d < K_I^s$). As the crack continuously propagates, the distance between the loading point and crack tip will increase, and the stress intensity factor will decrease. After the first reflected PP wave arrives at the crack tip (i.e., at time $t = 67.55$ μs), the tensile effect of the reflected waves will slow down the decay effect of the stress intensity factor and make $K_I^d > K_I^s$.

Finally, a similar photoelastic specimen of material Araldite B, as shown in Fig. 10, which is studied by Hodulak, Kobayashi and Emery (1980), is considered. When the loading is increased up to the the fracture toughness $K_C = 2.0$ MPa $\sqrt{m}$, the crack begins to extend at a constant speed $v = 240$ m/s. By using the same procedure as mentioned in the foregoing problem, the finite element method is applied to obtain the stress distribution function $p(x_1)$ along the crack-tip line, and the dynamic stress intensity factors are shown in Fig. 11. The theoretical results presented in this study are consistent with the finite element results and experimental results by Hodulak, Kobayashi, and

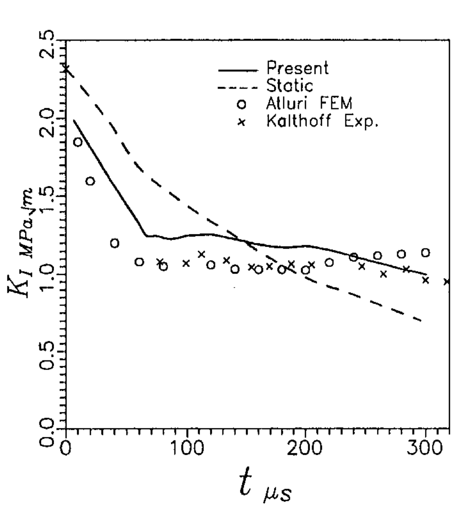

Fig. 9 Dynamic stress intensity factor of a propagating crack as shown in Fig. 8

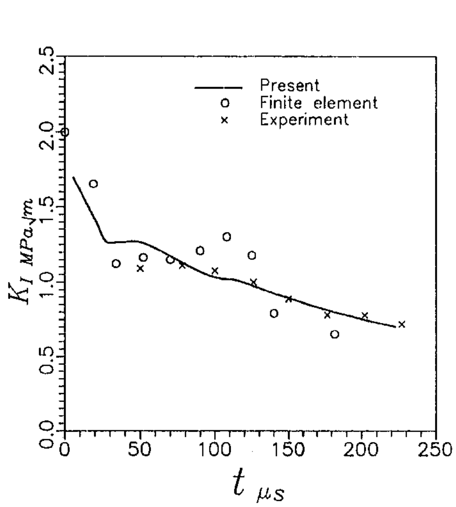

Fig. 11 Dynamic stress intensity factor of a propagating crack as shown in Fig. 10

Emery (1980). At the instant of crack propagation, the stress intensity factor jumps from 2.0 MPa $\sqrt{m}$ to 1.81 MPa $\sqrt{m}$ with the decreasing ratio $\kappa(d)$, where $d = (v_l/v)a = 7.93a$. At time $t = 28.07$ μs, the reflected PP wave returns to the crack tip and induces a tensile effect for the crack which will slow down the decay behavior of the stress intensity factor.

5 Conclusion

A powerful method for the theoretical formulation of a crack propagating in finite boundaries and subjected to general static loading is proposed in this study. The effects of reflected waves generated from boundaries and their interaction with a propagating crack have been successfully obtained and are shown to be in good agreement with the existing experimental and numerical results.

Freund's remarkable result (1972b) for crack propagating in an unbounded medium is shown to be valid for the finite strip problem also. For the finite boundary problem, we have shown that the long-time behavior of the stress intensity factor possesses the form of a universal function $\kappa(d)$ of an instantaneous extending rate of a crack tip multiplied by the stress intensity factor of an equivalent stationary crack. The equivalent stationary crack is subjected to the same static loading and the crack length is equal to the instantaneous length of the actual crack. It is also concluded that the result is accurate enough to evaluate the dynamic stress intensity factor without considering the contribution for reflected waves of the second time, the third time, etc., and only when taking the first reflected waves into consideration, which will result only in a small tolerance (about six percent) in the calculation of the long-time behavior.

The reflected waves generated from the boundary, which is parallel to a crack, have a stronger influence on the stress intensity factor of crack propagation than that generated from the boundary perpendicular to a crack. The reflected waves usually behave as a tensile effect, the dynamic stress intensity factor will generally increase after the reflected waves generated from a free boundary arrive at the crack tip.

There still are many unanswered questions in dynamic fracture and this work may provide a useful technique for further investigation in more complicated dynamic fracture problems, especially on the crack propagation event. The proposed method in this study has already been extended to solve more difficult problems of crack propagation in a finite geometry body subjected to dynamic impact loadings, and the results will be shown in a future paper.

Acknowledgment

The authors gratefully acknowledge the financial support of this research by the National Science Council (Republic of China) under Grant NSC 81-0401-E002-18 to National Taiwan University.

References

Atluri, S. N., and Nishioka, T., 1985, "Numerical Studies in Dynamic Fracture Mechanics," *International Journal of Fracture*, Vol. 27, pp. 245–261.

Freund, L. B., 1972a, "Crack Propagation in an Elastic Solid Subjected to General Loading–I. Constant Rate of Extension," *Journal of the Mechanics and Physics of Solids*, Vol. 20, pp. 129–140.

Freund, L. B., 1972b, "Crack Propagation in an Elastic Solid Subjected to General Loading–II. Non-uniform Rate of Extension," *Journal of the Mechanics and Physics of Solids*, Vol. 20, pp. 141–152.

Hodulak, L., Kobayashi, A. S., and Emery, A. F., 1980, "Influence of Dynamic Fracture Toughness on Dynamic Crack Propagation," *Engineering Fracture Mechanics*, Vol. 13, pp. 85–93.

Kalthoff, J. F., Beinert, J., and Winkler, S., 1977, *Fast Fracture and Crack Arrest*, G. T. Hahn et al., eds., ASTM STP 627 pp. 161–176.

Kalthoff, J. F., 1985, "On the Measurement of Dynamic Fracture Toughnesses," *International Journal of Fracture*, Vol. 27, pp. 277–298.

Kishimoto, S. Aoki, and Sakata M., 1980, "Computer Simulation of Fast Crack Propagation in Brittle Material," *International Journal of Fracture*, Vol. 16, pp. 3–13.

Kobayashi, A. S., and Wade, B. G., 1972, "Crack Propagation and Arrest in Impact Plates," *Proceeding of an International Conference on Dynamic Crack Propagation*, G. C. Sih, ed., Lehigh University, Lehigh, PA, pp. 663–678.

Ma, C. C., and Ing, Y. S., 1995, "Transient Analysis of Dynamic Crack Propagation with Boundary Effect," ASME JOURNAL OF APPLIED MECHANICS, Vol. 62, pp. 1029–1038.

Nilsson, F., 1973, "A Transient Crack Problem for an Infinite Strip under Antiplane Shear," *Dynamic Crack Propagation*, G. C. Sih, ed., Nordhoff, Dordrecht, The Netherlands, pp. 543–551.

Nishioka, T., and Atluri, S. N., 1980, "Numerical Modeling of Dynamic Crack Propagation in Finite Bodies, by Moving Singular Elements Part 1: Formulation," ASME JOURNAL OF APPLIED MECHANICS, Vol. 47, pp. 570–576.

Nishioka, T., and Atluri, S. N., 1980, "Numerical Modeling of Dynamic Crack Propagation in Finite Bodies, by Moving Singular Elements Part 2: Results," ASME JOURNAL OF APPLIED MECHANICS, Vol. 47, pp. 577–582.

Ravi-Chandar, K., and Knauss, W. G., 1982, "Dynamic Crack-tip Stresses Under Stress Wave Loading: A Comparison of Theory and Experiment," *International Journal of Fracture*, Vol. 20, pp. 209–222.

Ravi-Chandar, K., and Knauss, W. G., 1984, "An Experimental Investigation into Dynamic Fracture: II. Microstructural Aspects," *International Journal of Fracture*, Vol. 26, pp. 65–80.

Tsai, C. H., and Ma, C. C., 1991, "Exact Transient Solutions of Buried Dynamic Point Forces and Displacement Jumps for an Elastic Half Space," *International Journal of Solids and Structures*, Vol. 28, pp. 955–974.

Tsai, C. H., and Ma, C. C., 1992, "Transient Analysis of a Semi-infinite Crack Subjected to Dynamic Concentrated Forces," ASME JOURNAL OF APPLIED MECHANICS, Vol. 59, pp. 804–811.

An Eigenvector Expansion Method for the Solution of Motion Containing Fractional Derivatives

L. E. Suarez
Department of Civil Engineering,
Mem. ASME.

A. Shokooh
Department of General Engineering.

University of Puerto Rico,
Mayaguez, PR 00681-5000

The use of fractional derivatives has proved to be very successful in describing the behavior of damping materials, in particular, the frequency dependence of their parameters. In this article the three-parameter model with fractional derivatives of order $\frac{1}{2}$ is applied to single-degree-of-freedom systems. This model leads to second-order semidifferential equations of motion for which previously there were no closed-form solutions available. A new procedure that permits to obtain simple closed-form solutions of these equations is introduced. The method is based on the transformation of the equations of motions into a set of first-order semidifferential equations. The closed-form expression of the eigenvalues and eigenvectors of an associated eigenproblem are used to uncouple the equations. Using the Laplace transform method, closed-form expressions to calculate the impulse response function, the step response function and the response to initial conditions are derived.

1 Introduction

The use of passive damping treatment in structures subjected to excessive vibrations levels is a well accepted and established technique to attenuate the vibratory motion (Nashif et al., 1985; Rogers, 1986). All the materials used for damping applications are known to have a strong dependency of their parameters on the frequency of vibration and temperature (Lazan, 1968; Nashif et al., 1985). In the search for analytical models that describe the frequency variation of the commonly used viscoelastic materials in damping treatments, the model based on fractional derivatives has been shown to be one of the most effective approaches. Although fractional derivatives are rarely used in other engineering areas, the concept of fractional calculus is nearly as old as the conventional derivatives of integer orders (Ross, 1977). There are several definitions of a derivative of fractional order; for our purpose we will adopt the definition based on the Riemann-Liouville integral: for $0 < \alpha < 1$, the derivative of order α of a function $x(t)$ is (Oldham and Spanier, 1974)

$$D^\alpha x(t) = \frac{1}{\Gamma(1-\alpha)} \frac{d}{dt} \int_0^t \frac{x(t-u)}{u^\alpha} du. \qquad (1)$$

The fractional calculus model of viscoelastic behavior employs these derivatives of fractional order to relate the stress fields to the strain fields in viscoelastic materials. In a one-dimensional state of stress, the simplest form of the constitutive equation of the fractional calculus model can be expressed as

$$\sigma_{xx} = E_0\epsilon_{xx} + E_1 D^\alpha \epsilon_{xx} \qquad (2)$$

or

$$\tau_{xy} = G_0\gamma_{xy} + G_1 D^\alpha \gamma_{xy}. \qquad (3)$$

This model is known as the three-parameter model. Although they will not be discussed in this paper, there are more elaborate models in which the single fractional operator D^α is replaced by linear fractional differential operators of the form $\sum_{n=0}^{\infty} p_n D^{\alpha_n}$ acting on the strains and stresses (Bagley, 1979; Bagley and Torvik, 1983, 1986; Rogers, 1983).

When the viscoelastic behavior of a single-degree-of-freedom oscillator is described by either Eq. (2) or (3), the equation of motion assumes the form

$$mD^2x(t) + cD^\alpha x(t) + kx(t) = f(t) \qquad (4)$$

where, as usual, m, c, and k represents the mass, damping, and stiffness coefficients, respectively. The meaning of c and k depends on the constitutive equation, the mathematical model and the discretization method used to obtain Eq. (4). Although the coefficient α, known as the memory parameter, can take any value between 0 and 1, the value $\frac{1}{2}$ was adopted for this study because it has been shown that it describes the frequency dependence of the damping materials quite satisfactorily (Bagley, 1979; Bagley and Torvik, 1983; Torvik and Bagley, 1984).

We will presently introduce an analytical method, which we will use to obtain the response of an oscillator whose equation of motion can be written in the form of Eq. (4). The method is based on a transformation of the equation of motion from the configuration space to another space akin to the state space. The expanded equations of motion are then solved using an eigenvector expansion and Laplace transforms. It is shown that it is possible to obtain closed-form solutions which will enable us to predict the response to several types of excitations. The method presented can also be implemented to obtain the response to a load with arbitrary time variation.

The problem of calculating the response of oscillators in which the damping is described by a fractional calculus model was previously studied by several authors. The methods proposed for this purpose include Laplace transforms (Bagley and Torvik, 1979, 1983, 1985; Shokooh and Suarez, 1994; Suarez and Shokooh, 1995; Suarez et al., 1995), Fourier transforms (Gaul et al., 1989, 1991; Shokooh and Suarez, 1994), numerical methods (Koh and Kelly, 1990; Padovan, 1987; Shokooh and Suarez, 1994), and power series expansions (Shokooh and

Contributed by the Applied Mechanics Division of THE AMERICAN SOCIETY OF MECHANICAL ENGINEERS for publication in the ASME JOURNAL OF APPLIED MECHANICS.

Discussion on the paper should be addressed to the Technical Editor, Professor Lewis T. Wheeler, Department of Mechanical Engineering, University of Houston, Houston, TX 77204-4792, and will be accepted until four months after final publication of the paper itself in the ASME JOURNAL OF APPLIED MECHANICS.

Manuscript received by the ASME Applied Mechanics Division, Apr. 10, 1996; final revision, Oct. 1, 1996. Associate Technical Editor: M. Ortiz.

Suarez, 1994, 1996). None of these methods, however, is able to provide full closed-form solutions. For instance, the Laplace transform methods require the numerical evaluation of an improper integral. The Fourier transform methods also require a numerical implementation, either via an FFT or numerical integration. The power series expansion, although theoretically interesting, cannot be used in its present form for response calculations because of its slow convergence rate.

2 State-Space Formulation of the Equation of Motion

The equation of motion (4) can be written in the form

$$D^2x(t) + 2\eta\omega^{3/2}D^{1/2}x(t) + \omega_n^2 x(t) = f^*(t) \tag{5}$$

where

$$2\eta\omega_n^{3/2} = \frac{c}{m}, \quad \omega_n^2 = \frac{k}{m}, \quad f^*(t) = \frac{f(t)}{m}. \tag{6}$$

The coefficient η is the damping ratio of an oscillator with fractional damping of order $\frac{1}{2}$. The reason for defining η in this way is to use an expression similar to that for the damping ratio of oscillators with viscous damping. The exponent $\frac{3}{2}$ was introduced for consistency of dimensions.

Introducing the following variables

$$\begin{aligned} z_1 &= D^{3/2}x(t), \quad z_2 = Dx(t), \\ z_3 &= D^{1/2}x(t), \quad z_4 = x(t), \end{aligned} \tag{7}$$

and letting

$$a = 2\eta\omega_n^{3/2}, \quad b = \omega_n^2,$$

the equation of motion (5) can be transformed into the following system in a state space:

$$\begin{bmatrix} 0 & 0 & 0 & 1 \\ 0 & 0 & 1 & 0 \\ 0 & 1 & 0 & 0 \\ 1 & 0 & 0 & a \end{bmatrix} D^{1/2} \begin{Bmatrix} z_1 \\ z_2 \\ z_3 \\ z_4 \end{Bmatrix} - \begin{bmatrix} 0 & 0 & 1 & 0 \\ 0 & 1 & 0 & 0 \\ 1 & 0 & 0 & 0 \\ 0 & 0 & 0 & -b \end{bmatrix} \begin{Bmatrix} z_1 \\ z_2 \\ z_3 \\ z_4 \end{Bmatrix} = \begin{Bmatrix} 0 \\ 0 \\ 0 \\ f^*(t) \end{Bmatrix}. \tag{8}$$

To solve the system of differential Eqs. (8) we will consider the following eigenvalue problem:

$$[\mathbf{A}]\{\Psi\}_j = \lambda_j[\mathbf{B}]\{\Psi\}_j \tag{9}$$

where the matrices $[\mathbf{A}]$ and $[\mathbf{B}]$ are

$$[\mathbf{B}] = \begin{bmatrix} 0 & 0 & 0 & 1 \\ 0 & 0 & 1 & 0 \\ 0 & 1 & 0 & 0 \\ 1 & 0 & 0 & a \end{bmatrix}; \quad [\mathbf{A}] = \begin{bmatrix} 0 & 0 & 1 & 0 \\ 0 & 1 & 0 & 0 \\ 1 & 0 & 0 & 0 \\ 0 & 0 & 0 & -b \end{bmatrix}. \tag{10}$$

Note that the eigenvalue problem (9) cannot be obtained in the usual way, namely by considering the free vibration case of Eq. (8) and assuming a solution of the form $e^{\lambda t}\{\Psi\}$. The reason is that the application of the operator $D^{1/2}$ to the exponential term $e^{\lambda t}$ does not produce $\lambda e^{\lambda t}$. Therefore, Eq. (9) is an eigenvalue problem, associated with Eq. (8), which will permit us to obtain the solution in a relatively simple way.

The matrices $[\mathbf{A}]$ and $[\mathbf{B}]$ are symmetric and hence, if the eigenvectors are normalized with respect to $[\mathbf{B}]$, they have the following orthogonality properties:

$$\{\Psi\}_i^T[\mathbf{B}]\{\Psi\}_i = \delta_{ij} \tag{11}$$

$$\{\Psi\}_i^T[\mathbf{A}]\{\Psi\}_i^T = \lambda_j\delta_{ij}. \tag{12}$$

It is shown in Appendix A that it is possible to obtain closed-form solutions for the eigenvalues λ_j and the normalized eigenvectors $\{\Psi\}_i$. Letting

$$\{\mathbf{z}\} = [\Psi]\{\mathbf{y}\} \tag{13}$$

where

$$\{\mathbf{z}\} = [z_1, z_2, z_3, z_4]^T, \quad \{\mathbf{y}\} = [y_1, y_2, y_3, y_4]^T \tag{14}$$

premultiplying Eq. (8) by $\{\Psi\}_i^T$, we are led, in view of Eqs. (11) and (12), to a set of four decoupled differential equations

$$D^{1/2}y_j(t) - \lambda_j y_j(t) = \Psi_{4j}f(t); \quad j = 1, 2, 3, 4 \tag{15}$$

where, as shown in Appendix A,

$$\Psi_{4j} = \frac{1}{\sqrt{4\lambda_j^3 + 2\eta\omega_n^{3/2}}}. \tag{16}$$

Differential equations of the form of Eq. (15), involving fractional derivatives of order $\frac{1}{2}$, are referred to as "semi-differential equations" (Oldham and Spanier, 1974). In certain cases it is possible to obtain closed-form solutions of these equations by means of the Laplace transform, which is based on the following property: the Laplace transform $L[\ldots]$ of a fractional derivative of order α of a function $x(t)$ is

$$L[D^\alpha x(t)] = s^\alpha X(s) - C \tag{17}$$

where $X(s)$ is the Laplace transform of $x(t)$ and C is a constant defined as

$$C = D^{\alpha-1}x(t)|_{t=0}. \tag{18}$$

It is important to note that the value of C is as yet undetermined, and cannot be set C equal to zero arbitrarily. Taking the Laplace transform of Eq. (15) and using the result in Eq. (17) for $\alpha = \frac{1}{2}$, we obtain

$$Y_j(s) = \frac{\Psi_{4j}F(s) + R_j}{\sqrt{s} - \lambda_j}; \quad j = 1, 2, 3, 4 \tag{19}$$

where $Y_j(s)$ and $F(s)$ are the Laplace transforms of $y_j(t)$ and $f(t)$, respectively. The coefficient R_j is defined as

$$R_j = D^{-1/2}y_j(t)|_{t=0}. \tag{20}$$

To obtain the response in the time domain, we need to calculate the inverse Laplace transform of $Y_j(s)$ and substitute it in Eq. (13). If we are interested in the displacement $x(t)$, from Eqs. (7) and (14) it follows that

$$x(t) = \sum_{j=1}^{4} \Psi_{4j}y_j(t) = \sum_{j=1}^{4} \Psi_{4j}L^{-1}[Y_j(s)] \tag{21}$$

where $L^{-1}[\ldots]$ is the inverse Laplace transform of the function in brackets. We will apply this formulation to calculate the response to three types of input: free vibrations with initial displacements and velocities, step function load, and impulsive load.

3 Response to Initial Conditions

We will assume that at time $t = 0$ the oscillator has initial displacement $x(0) = x_0$ and initial velocity $\dot{x}(0) = \dot{x}_0$. To obtain the free-vibration response, we set $F(s) = 0$ in Eq. (19) and calculate the inverse Laplace transform of the remaining terms. Using residue theory and contour integration, it can be shown (Suarez et al., 1995) that

$$L^{-1}\left[\frac{1}{\sqrt{s} - \lambda_j}\right] = \frac{1}{\sqrt{\pi t}} + \lambda_j e^{\lambda_j^2 t}[1 + Erf(\lambda_j\sqrt{t})]. \tag{22}$$

Using this result in Eq. (21), the response $x(t)$ becomes

$$x(t) = \frac{1}{\sqrt{\pi t}} \sum_{j=1}^{4} \Psi_{4j} R_j + \sum_{j=1}^{4} \Psi_{4j} \lambda_j R_j g_j(t) \tag{23}$$

where we introduced the notation

$$g_j(t) = e^{\lambda_j^2 t}[1 + Erf(\lambda_j \sqrt{t})]. \tag{24}$$

Note that the first term in Eq. (23) becomes unbounded as $t \to 0$. Therefore, the constants R_j must be such that

$$\sum_{j=1}^{4} \Psi_{4j} R_j = 0. \tag{25}$$

Moreover, at time $t = 0$, $g_j(0) = 1$ and Eq. (23) yields an additional condition

$$x_0 = \sum_{j=1}^{4n} \Psi_{4j} \lambda_j R_j. \tag{26}$$

In addition to Eqs. (25) and (26), we need two more equations in order to solve for the four constants R_j. These can be obtained by examining the velocity $\dot{x}(t)$. Considering Eqs. (7), (13), and (14), the velocity can be obtained as

$$\dot{x}(t) = \sum_{j=1}^{4} \Psi_{2j} L^{-1}[Y_j(s)] \tag{27}$$

and with Eqs. (19) and (22), the velocity can be written as

$$\dot{x}(t) = \frac{1}{\sqrt{\pi t}} \sum_{j=1}^{4} \Psi_{2j} R_j + \sum_{j=1}^{4} \Psi_{2j} \lambda_j R_j g_j(t). \tag{28}$$

For the response to be bounded, the denominator in the first term must be zero:

$$\sum_{j=1}^{4} \Psi_{2j} R_j = 0. \tag{29}$$

Evaluating Eq. (28) at $t = 0$ yields the fourth condition

$$\dot{x}_0 = \sum_{j=1}^{4} \Psi_{2j} \lambda_j R_j. \tag{30}$$

Equations (25), (26), (29), and (30) can now be written as

$$\begin{bmatrix} \lambda_1\Psi_{21} & \lambda_2\Psi_{22} & \lambda_3\Psi_{23} & \lambda_4\Psi_{44} \\ \Psi_{21} & \Psi_{22} & \Psi_{23} & \Psi_{24} \\ \lambda_1\Psi_{41} & \lambda_2\Psi_{42} & \lambda_3\Psi_{43} & \lambda_4\Psi_{44} \\ \Psi_{41} & \Psi_{42} & \Psi_{43} & \Psi_{44} \end{bmatrix} \begin{Bmatrix} R_1 \\ R_2 \\ R_3 \\ R_4 \end{Bmatrix} = \begin{Bmatrix} \dot{x}_0 \\ 0 \\ x_0 \\ 0 \end{Bmatrix}. \tag{31}$$

Before attempting to solve the system of equations, it is convenient to note the following. From the eigenproblem in Eq. (9), it is easy to conclude that

$$\Psi_{3j} = \lambda_j \Psi_{4j}$$
$$\Psi_{2j} = \lambda_j \Psi_{3j} = \lambda_j^2 \Psi_{4j}$$
$$\Psi_{1j} = \lambda_j \Psi_{2j} = \lambda_j^3 \Psi_{4j}, \quad j = 1, 2, 3, 4 \tag{32}$$

in view of which the system of Eqs. (31) can be written as

$$[\boldsymbol{\Psi}] \begin{Bmatrix} R_1 \\ R_2 \\ R_3 \\ R_4 \end{Bmatrix} = \begin{Bmatrix} \dot{x}_0 \\ 0 \\ x_0 \\ 0 \end{Bmatrix}. \tag{33}$$

Using the orthonormality condition of the eigenvector matrix $[\boldsymbol{\Psi}]$, the constants R_i are now easily calculated:

$$\begin{Bmatrix} R_1 \\ R_2 \\ R_3 \\ R_4 \end{Bmatrix} = [\boldsymbol{\Psi}]^T[\mathbf{B}] \begin{Bmatrix} \dot{x}_0 \\ 0 \\ x_0 \\ 0 \end{Bmatrix} = \begin{Bmatrix} \Psi_{41}(\dot{x}_0 + \lambda_1^2 x_0) \\ \Psi_{42}(\dot{x}_0 + \lambda_2^2 x_0) \\ \Psi_{43}(\dot{x}_0 + \lambda_3^2 x_0) \\ \Psi_{44}(\dot{x}_0 + \lambda_4^2 x_0) \end{Bmatrix} \tag{34}$$

The displacement of the oscillator is then obtained substituting the constants R_j in Eq. (23) and taking into account Eq. (25):

$$x(t) = \sum_{j=1}^{4} \Psi_{4j} \lambda_j R_j g_j(t)$$
$$= (\sum_{j=1}^{4} \Psi_{4j}^2 \lambda_j g_j)\dot{x}_0 + (\sum_{j=1}^{4} \Psi_{4j}^2 \lambda_j^3 g_j) x_0. \tag{35}$$

As it is explained in Appendix A, two eigenvalues, say λ_1 and λ_2, always occur in complex conjugate pairs. The remaining eigenvalues can be real or complex conjugates depending on the value of the damping ratio η. Therefore, the response can be written as

$$x(t) = \{2\,\mathrm{Re}[\Psi_{41}^2 \lambda_1 g_1(t)] + \Psi_{43}^2 \lambda_3 g_3(t) + \Psi_{44}^2 \lambda_4 g_4(t)\}\dot{x}_0 + \{2\,\mathrm{Re}[\Psi_{41}^2 \lambda_1^3 g_1(t)] + \Psi_{43}^2 \lambda_3^3 g_3(t) + \Psi_{44}^2 \lambda_4^3 g_4(t)\} x_0. \tag{36}$$

4 Step Function Response

We will now consider an initially stationary oscillator subjected to an excitation of the form

$$f(t) = f_0 u(t) \tag{37}$$

where $u(t)$ is the Heaviside function. Substituting the Laplace transform of the excitation, $F(s) = F_0/s$, in Eq. (19), the time domain solution of the decoupled equation is

$$y_j(t) = F_0 \Psi_{4j} L^{-1}\left[\frac{1}{s(\sqrt{s} - \lambda_j)}\right] + R_j L^{-1}\left[\frac{1}{\sqrt{s} - \lambda_j}\right]. \tag{38}$$

It can be shown that the inverse Laplace transform of the first term in Eq. (38) is (Suarez et al., 1995)

$$L^{-1}\left[\frac{1}{s(\sqrt{s} - \lambda_j)}\right] = \frac{g_j(t) - 1}{\lambda_j} \tag{39}$$

where $g_j(t)$ is defined in Eq. (24). The total solution is obtained via modal combination

$$x(t) = F_0 \sum_{j=1}^{4} \frac{\Psi_{4j}^2}{\lambda_j}[g_j(t) - 1] + \sum_{j=1}^{4} \Psi_{4j} R_j \left[\frac{1}{\sqrt{\pi t}} + \lambda_j g_j(t)\right]. \tag{40}$$

Note that since $g_j(0) = 1$, the first term vanishes at $t = 0$. Therefore, the constants R_j can be obtained as explained in the free vibration case and the second term is identical to $x(t)$ in Eq. (36). Since we assumed that the initial conditions x_0 and $\dot{x}_0$ are zero, the response to the step function loading is

$$x(t) = 2F_0\,\mathrm{Re}\left\{\frac{\Psi_{41}^2}{\lambda_1}[g_1(t) - 1]\right\} + \frac{F_0\Psi_{43}^2}{\lambda_3}[g_3(t) - 1] + \frac{F_0\Psi_{44}^2}{\lambda_4}[g_4(t) - 1]. \tag{41}$$

5 Impulse Response

The third case to be studied is the response to a unit impulsive load $F(t) = \delta(t)$ and zero initial conditions. Taking $F(s) = 1$ in Eq. (19), the time response of the decoupled semidifferential equations is

$$y_j(t) = (\Psi_{4j} + R_j) L^{-1}\left(\frac{1}{\sqrt{s} - \lambda_j}\right). \tag{42}$$

Recalling Eq. (22) and Eq. (21), the impulsive response is

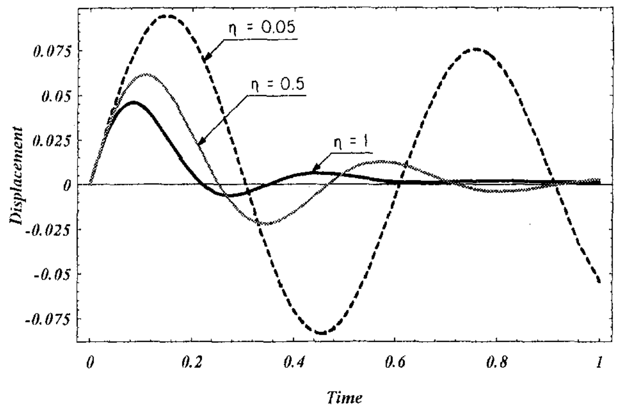

Fig. 1 Impulse response function for oscillators with damping ratios η = 0.05, 0.5, and 1

$$x(t) = \frac{1}{\sqrt{\pi t}} \sum_{j=1}^{4} (\Psi_{4j}^2 + \Psi_{4j} R_j) + \sum_{j=1}^{4} (\lambda_j \Psi_{4j}^2 g_j(t) + \lambda_j \Psi_{4j} g_j(t) R_j). \quad (43)$$

It is shown in Appendix B that the eigenvalues λ_j and the eigenvectors $\{\Psi\}_i$ of Eq. (9) satisfy the following relationships:

$$\sum_{j=1}^{4} \Psi_{4j}^2 = 0 \quad (44)$$

$$\sum_{j=1}^{4} \lambda_j \Psi_{4j}^2 = 0. \quad (45)$$

Therefore, evaluating expression (43) at time $t = 0$, and recalling that $g_j(0) = 1$, the constants R_j must satisfy the condition in Eq. (25) for bounded response. Moreover, since we are considering zero initial conditions, the remaining terms yield

$$0 = \sum_{j=1}^{4} \lambda_j \Psi_{4j} R_j. \quad (46)$$

If we calculate the velocity $\dot{x}(t)$ by substituting Ψ_{4j} by Ψ_{2j}, and study the resulting expression at $t = 0$, we obtain again the condition in Eq. (29) and one additional condition

$$0 = \sum_{j=1}^{4} \lambda_j \Psi_{2j} R_j. \quad (47)$$

The above results mean that the constants R_j are obtained from the solution of the system in Eq. (31) with $x_0 = \dot{x}_0 = 0$. Therefore, the constants are zero, and Eq. (43) reduces to

$$x(t) = \sum_{j=1}^{4} \lambda_j \Psi_{4j}^2 g_j(t) \quad (48)$$

which, using the usual notation for the unit impulse response, can be written as

$$h(t) = 2\,\mathrm{Re}\{\lambda_1 \Psi_{41}^2 g_1(t)\} + \lambda_3 \Psi_{43}^2 g_3(t) + \lambda_4 \Psi_{44}^2 g_4(t). \quad (49)$$

Finally, replacing the eigenvector elements Ψ_{4j} from Eq. (16) the impulse response function of the oscillator with fractional damping:

$$h(t) = \mathrm{Re}\left\{\frac{\lambda_1}{2\lambda_1^3 + \eta\omega_n^{3/2}} g_1(t)\right\} + \frac{\lambda_3/2}{2\lambda_3^3 + \eta\omega_n^{3/2}} g_3(t) + \frac{\lambda_3/2}{2\lambda_4^3 + \eta\omega_n^{3/2}} g_4(t) \quad (50)$$

6 Numerical Results

The analytical expressions previously obtained to calculate the response to the three loading conditions were implemented in the program MATHEMATICA (Wolfram Research, 1993). The procedure is quite simple. First, the eigenvalues λ_1, λ_3, and λ_4 are calculated using Eqs. (A.6)–(A.7) of Appendix A. Next, the eigenvector elements $\Psi_{4,1}$, $\Psi_{4,3}$, and $\Psi_{4,4}$ are calculated using Eq. (16). The auxiliary functions $g_1(t)$, $g_3(t)$ and $g_4(t)$ are defined as in Eq. (24). Equations (36), (41), and (50) are then used to obtain the response to initial conditions, the step response, or the impulse response, respectively.

Equation (50) was used to calculate the impulse response functions shown in Fig. 1 for oscillators with natural frequency $\omega_n = 10$ rad/s and damping ratios $\eta = 0.05$, 0.5, and 1. Note that the impulse response for $\eta = 1$ has an oscillatory character. In fact, fractional model predicts that the system will experience oscillations with sign change even for value greater than 1. More precisely, the fractional damping models does not present an overdamped behavior in the sense of the standard viscous model. When the damping ratio is equal to $\sqrt{\pi}$, the curves are tangent to the axis of zero displacement, regardless of the value of ω_n. For values greater than $\sqrt{\pi}$, the curves tend to zero without crossing the zero axis. In this regard, the value $\eta = \sqrt{\pi}$ can be considered as a "critical" damping ratio, in the sense that it separates two different behaviors of the impulse response function. Figure 2 shows the impulse response functions for an oscillator with $\omega_n = 10$ rad/s and damping ratios equal $\sqrt{\pi}$, 3 and 5. Note that the first curve touches once the zero axis whereas the impulse functions for $\eta > \sqrt{\pi}$ show oscillations above the equilibrium position.

In the next numerical example, three oscillators with undamped natural frequency $\omega_n = 10$ rad/s and damping ratios equal 0.05, 0.5, and 1 are given a unit initial displacement. The subsequent displacements as a function of time are plotted in Fig. 3. Here again, the damping ratio $\eta = 1$ is not associated with any special situation. Note that, as expected, if an oscillator is given a unit initial velocity, the response obtained with Eq. (36) coincides with the impulse response function. This can be clearly seen by comparing Eq. (36) and Eq. (49) with $x_0 = 0$.

In the next numerical example, three oscillators with natural frequency of 5 rad/s and damping ratios 0.05, 0.5, and 1 are subjected to a step load of magnitude $F_0 = 1$. Figure 4 shows

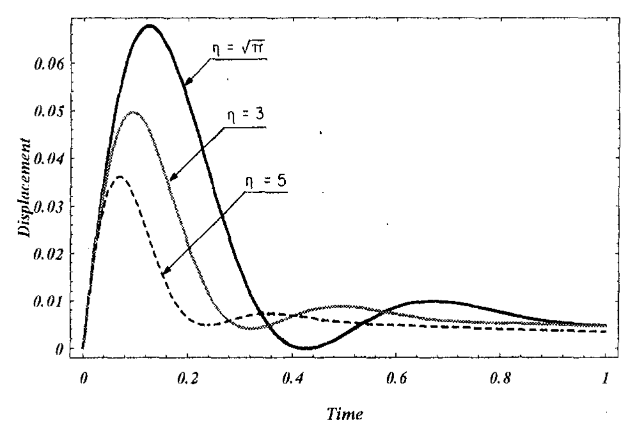

Fig. 2 Impulse response function for oscillators with damping ratios η = sqrt(π), 3 and 5

the displacement response of the oscillators. Note that the curves for $\eta = 0.5$ and 1 do not show oscillations around the static equilibrium response $F_0/\omega_n^2 = 0.04$. However, all the curves approach the equilibrium position as time grows.

Finally, although it was not presented in this paper, we must point out that all the responses presented here were compared with results obtained using other available techniques, (such as the semi-analytical expressions obtained by the authors based on the Laplace transform (Suarez and Shokooh, 1994) and the direct integration of the equations of motion using numerical algorithms (Shokooh and Suarez, 1994, 1996)). The results match perfectly in all cases, except for the cases where the numerical algorithms fail to converge to the correct answer.

7 Conclusions

This paper presents a methodology to calculate the response of damped oscillators in which the damping is described by the fractional calculus model of viscoelasticity. In the model used for the present study, the viscous damping term in the equation of motion is replaced by a term proportional to the derivative of order $\frac{1}{2}$ of the displacement. The equations of motion of the oscillators with fractional damping become second-order semidifferential equations. To solve these equations, they are first transformed into a set of four first-order semidifferential equations. The transformed equations are decoupled using an eigenvector expansion. Closed-form solutions of these eigenproperties are provided. The decoupled semidifferential equations are solved using the Laplace transform technique.

Some of the unique features of the fractional model are revealed in the numerical examples presented. It should be pointed out, however, that it is not the object of this paper to discuss the phenomenological aspects of the model, but to present tools for the time response analysis of these systems. If the fractional calculus model is to become a strong and convincing competitor of the classical damping models, it is imperative to have available simple closed-form solutions.

It is possible to extend the methodology presented to calculate the response of multi-degree-of-freedom systems. Moreover, it is also possible to generalize the method to treat models with more elaborate constitutive equations than the Eqs. (2) and (3) used in this paper. The response to loads with arbitrary time variations can also be calculated with the proposed methodology. For this, the loading function must be first sampled and assumed to be constant within small time intervals. The response at the end of each time interval is then calculated by adding the response to the initial displacement and velocity at the beginning of the interval and the response to the step load.

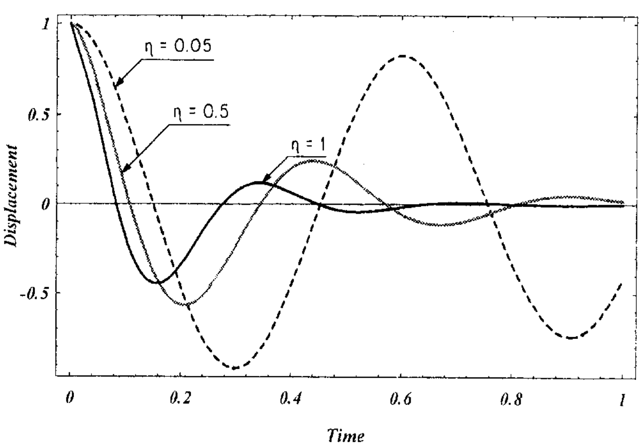

Fig. 3 Response of oscillators with damping ratios η = 0.05, 0.5 and 1 to a unit initial displacement

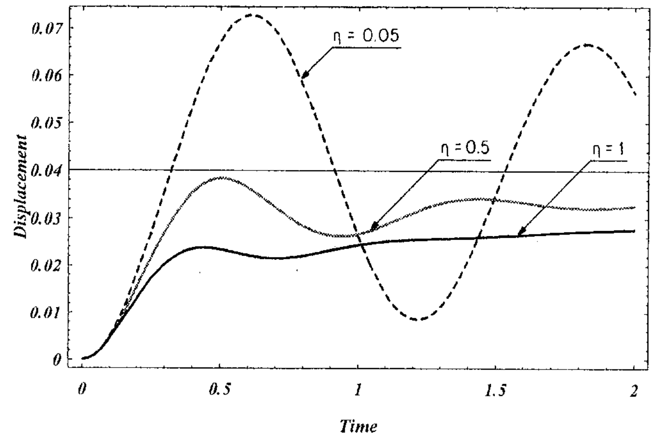

Fig. 4 Unit step response function for oscillators with damping ratios η = 0.05, 0.5, and 1

Acknowledgments

This work presented in this paper was made possible by a grant (NAG-1-1496) from NASA Langley Research Center with Dr. Lucas Horta serving as Technical Monitor. The support of Dr. Michael Card, former Chief Scientist of Langley, and Mr. Edwin Prior, Deputy Director of University Affairs, is also gratefully acknowledged.

References

Bagley, R. L., 1979, "Applications of Generalized Derivatives to Viscoelasticity," Technical Report AFML-TR-79-4103, Air Force Materials Laboratory, Wright-Patterson Air Force Base, OH.

Bagley, R. L., and Torvik, P. J., 1979, "A Generalized Derivative Model for an Elastomer Damper," *The Shock and Vibration Bulletin*, Vol. 49, Part 2, pp. 135–143.

Bagley, R. L., and Torvik, P. J., 1983, "A Theoretical Basis for the Application of Fractional Calculus to Viscoelasticity," *Journal of Rheology*, Vol. 27, No. 3, pp. 201–210.

Bagley, R. L., and Torvik, P. J., 1983, "Fractional Calculus—A Different Approach to the Analysis of Viscoelastically Damped Structures," *AIAA Journal*, Vol. 21, No. 5, pp. 741–748.

Bagley, R. L., and Torvik, P. J., 1985, "Fractional Calculus in the Transient Analysis of Viscoellastically Damped Structures," *AIAA Journal*, Vol. 23, No. 6, pp. 918–925.

Bagley, R. L., and Torvik, P. J., 1986, "On the Fractional Calculus Model of Viscoelastic Behavior," *Journal of Rheology*, Vol. 3, No. 1, pp. 133–155.

Gaul, L., Klein, P., and Kemple, S., 1989, "Impulse Response Function of an Oscillator with Fractional Derivative in Damping Description," *Mechanics Research Communications*, Vol. 16, No. 5, pp. 297–305.

Gaul, L., Klein, P., and Kemple, S., 1991, "Damping Description Involving Fractional Operators," *Mechanical Systems and Signal Processing*, Vol. 5, No. 2, pp. 8–88.

Koh, C. G., and Kelly, J. M., 1990, "Application of Fractional Derivatives M. Seismic Analysis of Base-Isolated Models," *Earthquake Engineering and Structural Dynamics*, Vol. 19, pp. 229–241.

Lazan, B. J., 1968, *Damping of Materials and Members in Structural Mechanics*, Pergamon Press, New York.

Nashif, A. D., Jones, D. I. G., and Henderson, J. P., 1985, *Vibration Damping*, John Wiley and Sons, New York.

Oldham, K. B., and Spanier, J., 1974, *The Fractional Calculus*, Academic Press, New York.

Padovan, J., 1987, "Computational Algorithms for Finite Element Formulation Involving Fractional Operators," *Computational Mechanics*, Vol. 2, pp. 271–287.

Rogers, L., 1983, "Operators and Fractional Derivatives for Viscoelastic Constitutive Equations," *Journal of Rheology*, Vol. 27, No. 4, pp. 351–372.

Rogers, L., 1986, "Damping as a Design Parameter," *Mechanical Engineering Magazine*, ASME, New York.

Ross, B., 1977, "Fractional Calculus," *Mathematics Magazine*, Vol. 50, No. 3, pp. 115–122.

Shokooh, A., and Suarez, L., 1994, "On the Fractional Derivative Modeling of Damping Materials," Technical Report prepared for NASA Langley, College of Engineering, University of Puerto Rico, Mayaguez, PR.

Shokooh, A., and Suarez, L., 1996, "A Comparison of Numerical Methods Applied to Fractional Model of Damping Materials," *Journal of Vibration and Control*, submitted for publication.

Suarez, L., and Shokooh, A., 1995, "Response of Systems with Damping Materials Modeled Using Fractional Calculus," ASME *Applied Mechanics Review*, Vol. 48, No. 11, Part 2, pp. S118–S127.

Suarez, L., Shokooh, A., and Arroyo, J., 1995, "Finite Element Analysis of Damping Materials Modeled by the Fractional Derivative Method," Technical Report prepared for NASA Langley, College of Engineering, University of Puerto Rico, Mayaguez, PR.

Torvik, P. J., and Bagley, R. L., 1984, "On the Appearance of the Fractional Derivative in the Behavior of Real Materials," ASME JOURNAL OF APPLIED MECHANICS, Vol. 51, pp. 294–298.

Wolfram Research, Inc., 1993, *Mathematica: A System for Doing Mathematics by Computer*, Champaign, IL.

APPENDIX A

Eigenvalues and Eigenvectors of the (4 × 4) Problem for the Single-Degree-of-Freedom Oscillator

To solve the eigenproblem in Eq. (9), it is convenient to write it in the standard form:

$$[\mathbf{B}]^{-1}[\mathbf{A}]\{\mathbf{\Psi}\}_j = \lambda_j\{\mathbf{\Psi}\}_j \tag{A.1}$$

where

$$[\mathbf{B}]^{-1}[\mathbf{A}] = \begin{bmatrix} 0 & 0 & -a & -b \\ 1 & 0 & 0 & 0 \\ 0 & 1 & 0 & 0 \\ 0 & 0 & 1 & 0 \end{bmatrix}. \tag{A.2}$$

Expanding the characteristic determinant one obtains

$$\lambda^4 + a\lambda + b = 0. \tag{A.3}$$

This is the same equation obtained in the Laplace transform solution of the equation of motion by Shokooh and Suarez (1994). The authors have shown that the roots or eigenvalues are

$$\lambda_1 = \bar{\lambda}_2 = p + iq$$
$$\lambda_3 = -p + is$$
$$\lambda_4 = -p - is \tag{A.4}$$

where

$$p = \sqrt{\omega_n \kappa}$$
$$q = \sqrt{\omega_n\left(\kappa + \frac{\eta}{2\sqrt{\kappa}}\right)}$$
$$s = \sqrt{\omega_n\left(\kappa - \frac{\eta}{2\sqrt{\kappa}}\right)} \tag{A.5}$$

and κ is a function of the damping ratio defined as

$$\kappa = \frac{2^{1/3}}{4}\left[\left(\eta^2 + \sqrt{\eta^4 - \frac{16}{27}}\right)^{1/3} + \left(\eta^2 - \sqrt{\eta^4 - \frac{16}{27}}\right)^{1/3}\right]. \tag{A.6}$$

The function κ is a nondecreasing function of η and therefore the coefficients p and q are always positive which in turn implies that λ_1 and λ_2 are always a complex conjugate pair. The coefficient s, however, can become imaginary when $\kappa < (\eta/2)^{2/3}$. It can be shown that this occurs for $\eta > 2/3^{3/4} = 0.877$. In this case the eigenvalues λ_3 and λ_4 become real and equal to $-(p + s)$ and $-(p - s)$, respectively. In any case, Eqs. (A.4)–(A.6) can always be used to define the eigenvalues λ_i.

From the eigenvalue problem in Eq. (A.1), the elements of the jth eigenvector are related as

$$\Psi_{1j} = \lambda_j \Psi_{2j}; \quad \Psi_{2j} = \lambda_j \Psi_{3j}; \quad \Psi_{3j} = \lambda_j \Psi_{4j}. \tag{A.7}$$

Selecting the last element of the eigenvector equal to an arbitrary constant,

$$\Psi_{4j} = \alpha_j \tag{A.8}$$

the eigenvector becomes

$$\{\mathbf{\Psi}\}_j = [\lambda_j^3 \quad \lambda_j^2 \quad \lambda_j \quad 1]^T \alpha_j. \tag{A.9}$$

The constant αj can be selected such that the eigenvectors are normalized with respect to matrix $[\mathbf{B}]$:

$$\{\mathbf{\Psi}\}_j^T[\mathbf{B}]\{\mathbf{\Psi}\}_j = 1. \tag{A.10}$$

Sustituting $\{\mathbf{\Psi}\}_j$ from Eq. (A.8) in Eq. (A.9) one obtains

$$\alpha_j = \frac{1}{\sqrt{4\lambda_j^3 + a}} \tag{A.11}$$

and the fourth element of the eigenvectors is given by Eq. (16).

APPENDIX B

Orthogonality Relationships

From the orthogonality properties of the eigenvectors $\{\mathbf{\Psi}_j\}$ in Eqs. (11) and (12) written in matrix form

$$[\mathbf{\Psi}]^T[\mathbf{B}][\mathbf{\Psi}] = [\mathbf{I}] \tag{B.1}$$

$$[\mathbf{\Psi}]^T[\mathbf{A}][\mathbf{\Psi}] = [\mathbf{\Lambda}] \tag{B.2}$$

it is straightforward to obtain that

$$[\mathbf{B}]^{-1}[\mathbf{A}][\mathbf{B}]^{-1} = [\mathbf{\Psi}][\mathbf{\Lambda}][\mathbf{\Psi}]^T \tag{B.3}$$

where $[\Lambda]$ is a (4 × 4) diagonal matrix with the eigenvalues λ_i. Using the matrices $[\mathbf{B}]$ and $[\mathbf{A}]$ defined in Eq. (10), the left-hand side of the above equation becomes

$$[\mathbf{B}]^{-1}[\mathbf{A}][\mathbf{B}]^{-1} = \begin{bmatrix} -b & -a & 0 & 0 \\ -a & 0 & 0 & 1 \\ 0 & 0 & 1 & 0 \\ 0 & 1 & 0 & 0 \end{bmatrix}. \tag{B.4}$$

Recalling from Eq. (A.7) that the elements of the eigenvectors $\{\mathbf{\Psi}_j\}$ are related through the eigenvalues, the matrix of eigenvectors $[\mathbf{\Psi}]$ can be written as

$$[\mathbf{\Psi}] = \begin{bmatrix} \Phi_1 \\ \Phi_2 \\ \Phi_3 \\ \Phi_4 \end{bmatrix} = \begin{bmatrix} \Phi_4\Lambda^3 \\ \Phi_4\Lambda^2 \\ \Phi_4\Lambda \\ \Phi_4 \end{bmatrix} \tag{B.5}$$

where $[\mathbf{\Phi}_i]$ are (1 × 4) matrices with the elements Ψ_{ik}:

$$[\mathbf{\Phi}_i] = [\mathbf{\Psi}_{i1}, \mathbf{\Psi}_{i2}, \mathbf{\Psi}_{i3}, \mathbf{\Psi}_{i4}]. \tag{B.6}$$

Substituting $[\mathbf{\Psi}]$ from Eq. (B.5) in the right hand side of Eq. (B.3), carrying out the triple products leads to

$$[\mathbf{\Psi}][\mathbf{\Lambda}][\mathbf{\Psi}]^T = \begin{bmatrix} \Phi_4\Lambda^7\Phi_4^T & \Phi_4\Lambda^6\Phi_4^T & \Phi_4\Lambda^5\Phi_4^T & \Phi_4\Lambda^4\Phi_4^T \\ & \Phi_4\Lambda^5\Phi_4^T & \Phi_4\Lambda^4\Phi_4^T & \Phi_4\Lambda^3\Phi_4^T \\ & & \Phi_4\Lambda^3\Phi_4^T & \Phi_4\Lambda^2\Phi_4^T \\ \text{SYMM.} & & & \Phi_4\Lambda\Phi_4^T \end{bmatrix} \tag{B.7}$$

Equating Eqs. (B.4) and (B.7) one obtains the following relationships:

$$[\mathbf{\Phi}_4][\mathbf{\Lambda}^7][\mathbf{\Phi}_4]^T = -b \tag{B.8}$$

$$[\mathbf{\Phi}_4][\mathbf{\Lambda}^6][\mathbf{\Phi}_4]^T = -a \tag{B.9}$$

$$[\mathbf{\Phi}_4][\mathbf{\Lambda}^3][\mathbf{\Phi}_4]^T = 1 \tag{B.10}$$

$$[\mathbf{\Phi}_4][\mathbf{\Lambda}^k][\mathbf{\Phi}_4]^T = 0; \quad k = 1, 2, 4, 5 \qquad \text{(B.11)}$$

Taking $k = 1$ in Eq. (B.11) we verify Eq. (45):

$$[\mathbf{\Phi}_4][\mathbf{\Lambda}][\mathbf{\Phi}_4]^T = \sum_{j=1}^{4} \lambda_j \Psi_{4j}^2 = 0. \qquad \text{(B.12)}$$

The proof of Eq. (44) requires further work. Substituting $[\mathbf{\Psi}]$ from Eq. (B.5) and $[\mathbf{A}]$ from Eq. (10) in the orthogonality property in Eq. (B.2), leads to

$$[\mathbf{\Lambda}^2][\mathbf{\Phi}_4]^T[\mathbf{\Phi}_4][\mathbf{\Lambda}^2] + [\mathbf{\Lambda}^3][\mathbf{\Phi}_4]^T[\mathbf{\Phi}_4][\mathbf{\Lambda}] + [\mathbf{\Lambda}][\mathbf{\Phi}_4]^T[\mathbf{\Phi}_4][\mathbf{\Lambda}^3] - b[\mathbf{\Phi}_4][\mathbf{\Phi}_4]^T = [\mathbf{\Lambda}]. \qquad \text{(B.13)}$$

Pre and post-multiplying by $[\mathbf{\Phi}_4]$ and $[\mathbf{\Phi}_4]^T$, respectively, and making use of Eq. (B.11), Eq. (B.13) reduces to

$$-b[\mathbf{\Phi}_4][\mathbf{\Phi}_4]^T[\mathbf{\Phi}_4][\mathbf{\Phi}_4]^T = 0 \qquad \text{(B.14)}$$

which verifies Eq. (44),

$$[\mathbf{\Phi}_4][\mathbf{\Phi}_4]^T = \sum_{j=1}^{4} \Psi_{4j}^2 = 0. \qquad \text{(B.15)}$$

C. M. Leech
FASME,
Department of Mechanical Engineering,
UMIST,
Manchester M60 1QD, UK
Fellow ASME

B. Tabarrok
Department of Mechanical Engineering,
University of Victoria,
Victoria, Canada

Nonseparable Solutions to the Hamilton-Jacobi Equation

The Hamilton-Jacobi partial differential equation is solved for potential energy functionals of constant, linear, and quadratic form using a class of nonseparable solutions; these solutions give a geometric property to the generating solution, embedding it into the class of conics. These solutions have two basic components, that designated as a kernel component which belongs to the system regardless of the specific dynamics of the system and the primary and secondary system functions that are dependent on the specific initial conditions. Solutions are obtained for the linear oscillator, a rheonomic oscillator and a two-degree-of-freedom system, the latter suggesting an approach for general multidegree-of-freedom systems.

Introduction

The Hamilton-Jacobi theory has been developed from Hamilton's principle and the use of ignorable variables via Jacobi (canonical) transformations; this theory is not repeated here since it is fully developed in many texts on classical dynamics (Lanczos, 1966; Goldstein, 1980; Pars, 1965; Landau and Lifshitz, 1969; Leech, 1965; Synge, 1960; Saletan and Cromer, 1971; Sanz-Serna and Calvo, 1994). In this article, nonseparable solutions for the principal function are developed; separable solutions, developed for example in Pars (1965), Saletan and Cromer (1971), Benton (1977), and Denman and Buch (1973), are those whose forms are the sum or the repeated product of functions, each of these a function of only one generalized coordinate or time. There is also a geometrical aspect to these solutions, in the form of multidimensional ellipsoids or hyperboloids for a specific class of Lagrangians.

Background

The Hamilton-Jacobi theory is summarised in outline so that there is a starting point for the present development. Consider a dynamic system with n generalized coordinates $q_1, q_2 \ldots q_n$. The system has inertia and this is represented by the kinetic energy T which is a function of the generalized velocities $v_1, v_2, \ldots v_n$ where $v_i = dq_i/dt$, the generalized coordinates $q_1, q_2 \ldots q_n$ and possibly time t. The system also has stiffness represented by a work function U, a function of the generalized coordinates and time.

The terms scleronomic[1] and rheonomic are usually applied to constraints; however, the explicit resolution of the constraints into a reduced set of unconstrained generalized coordinates will usually result in the time explicitness being transferred to the kinetic and/or potential energy functions; the classification "autonomous" is usually applied to equations and this excludes the explicit appearance of time in the equations of motion. In this paper, Lagrangians that contain time explicitly will be referred to as rheonomic as there does not appear to be an alternate appropriate label. Monogenic[2] systems are considered in this development as the Hamilton-Jacobi theory is applicable to those systems where all the noninertial forces are derivable from a work function, Lanczos (1966). For systems in which the work function is not explicit in time the system is conservative, and there exists a potential (energy) function $V(= -U)$. The kinetic energy T and work function U or the potential energy V are then combined to form the Lagrangian, $L = T + U = T - V$; the Hamiltonian H is then defined by the following:

$$H = \sum_{i=1}^{i=n} p_i v_i - L \tag{1}$$

where the generalized momenta p_i are

$$p_i = \frac{\partial L}{\partial v_i}, \quad i = 1, 2 \ldots n. \tag{2}$$

This latter equation can usually be inverted to present the generalized velocities in terms of the generalized momenta and generalized coordinates

$$v_i = v_i(p_1, p_2, \ldots p_n, q_1, q_2, \ldots q_n, t) \tag{3}$$

so that the Lagrangian, and more importantly the Hamiltonian, can be expressed in terms of the generalized momenta and generalized coordinates

$$H = H(p_1, p_2, \ldots p_n, q_1, q_2, \ldots q_n, t). \tag{4}$$

The generalized momenta are then transformed to ignorable coordinates $\alpha_1, \alpha_2 \ldots \alpha_n$. This leads to the Hamilton-Jacobi equation

$$\frac{\partial S}{\partial t} + H\left\{\frac{\partial S}{\partial q_1}, \frac{\partial S}{\partial q_2}, \ldots \frac{\partial S}{\partial q_n}, q_1, q_2, \ldots q_n, t\right\} = 0 \tag{5}$$

where S is the Hamilton principal function (or the generating function); this is a function of $q_1, q_2 \ldots q_n$ and t and can be thought of as a surface moving in $q_1, q_2 \ldots q_n$ space. This is a partial differential equation with one dependent, the principal function S, and $n + 1$ independents, the generalized coordinates, $q_1, q_2 \ldots, q_n$ and time, t. There are thus $n + 1$ constants of integration and if the system is conservative, one of these can be and usually is the total energy of the system E and the others are ignorable constants, $\alpha_1, \alpha_2 \ldots \alpha_n$. Since these are ignorable, there are constants of motion β_i where

Contributed by the Applied Mechanics Division of THE AMERICAN SOCIETY OF MECHANICAL ENGINEERS for publication in the ASME JOURNAL OF APPLIED MECHANICS.

Discussion on the paper should be addressed to the Technical Editor, Professor Lewis T. Wheeler, Department of Mechanical Engineering, University of Houston, Houston, TX 77204-4792, and will be accepted until four months after final publication of the paper itself in the ASME JOURNAL OF APPLIED MECHANICS.

Manuscript received by the ASME Applied Mechanics Division, Jan. 7, 1995; final revision, Jan. 4, 1997. Associate Technical Editor: S. W. Shaw.

[1] Lanczos (1966) states "If both the kinetic energy and work function are scleronomic, i.e., time-independent. . . . If either kinetic energy or work function or both are rheonomic, i.e. time-dependent . . .".

[2] The term monogenic has been introduced by Lanczos (1966) and is applied to systems where there exists a work function, a scalar function from which the generalized forces are derivable. If this function is not explicit in time the system is conservative.

$$\beta_i = \frac{\partial S}{\partial \alpha_i}, \quad i = 1, 2, \ldots n. \tag{6}$$

However, there is a development that starts with the first-order partial differential equation, with the generalized coordinates and time as the independent coordinates; since the Hamilton-Jacobi equation when derived for dynamic systems is in this category, the development continues with the search for specific Lagrangians and Hamiltonians that lead to any of the class of Hamilton-Jacobi equations. This is the inverse problem and this has been examined by Havas (1956) who considered the question: given the following system of equations of motion

$$G_i(q_1, q_2, \ldots q_n, \dot{q}_1, \dot{q}_2, \ldots \dot{q}_n, \ddot{q}_1, \ddot{q}_2, \ldots \ddot{q}_n, t) = 0 \quad \text{for} \quad i = 1, 2 \ldots n$$

find the Lagrangian(s) $L(q_1, q_2, \ldots q_n, \dot{q}_1, \dot{q}_2, \ldots \dot{q}_n, t)$ such that

$$\frac{d}{dt}\frac{\partial L}{\partial \dot{q}_i} - \frac{\partial L}{\partial q_i} = G_i = 0 \quad \text{for} \quad i = 1, 2 \ldots n;$$

he then investigated the introduction of suitable integrating factors, linear combinations of the equations of motion, and transformations of the generalized coordinates in order to generate a Lagrangian. The Lagrangian thus found is not unique and indeed given a form for G_i there are a multiplicity of candidate Lagrangians.

Currie and Saletan (1966) and Kobussen (1979) established procedures for retreiving these Lagrangians through "fouling" and "gauge transformations," respectively; they labelled the candidate Lagrangians introduced above as "equivalent Lagrangians." A comprehensive survey of the inverse problem appears in the text by Santilli (1978). Denman (1966) and Denman and Buch (1973) examined the inverse problem for dissipative systems, namely linearily damped systems and showed the existence of a constant "Hamiltonian" even though the total energy of the systems considered is not conserved. In fact what they show is the existence of parallel systems where the governing equations of motions produce similar solutions even though the systems are quite different. For example, the system shown in Denman and Buch (1973), the motion of a particle, mass m_0 in a one-dimensional viscous medium given by the following equation of motion:

$$m_0\ddot{x} + m_0\gamma\dot{x} = 0$$

is exactly that for the free motion of a mass accruing system $(m(t) = m_0 e^{\gamma t})$,

$$\frac{d}{dt}(m_0 e^{\gamma t}\dot{x}) = 0.$$

These are two different systems with the same equation of motion, and the Lagrangian of the second could be assumed to be a candidate Lagrangian for the first system; however, although the free motion of the two systems is the same, the forced motion, due to the action of an external force, of the two systems is quite different. Also the kinetic energy in the two systems decreases by different (multiplying) rates, $e^{-2\gamma t}$ in the first system and $e^{-\gamma t}$ in the second.

The solution for S has been achieved classically by considering separable functions (Benton, 1977) and this is illustrated in the following; consider a linear oscillator with constant mass m, and constant stiffness, k. The Hamiltonian is

$$H = \frac{1}{2m}P^2 + \frac{1}{2}kq^2 \tag{11}$$

and the Hamilton-Jacobi equation is

$$\frac{\partial S}{\partial t} + \frac{1}{2m}\left(\frac{\partial S}{\partial q}\right)^2 + \frac{1}{2}kq^2 = 0. \tag{12}$$

The conventional additive separable solution for S is taken as

$$S(q, t) = S_q(q) + S_t(t) \tag{13}$$

and substituting in the above Hamilton-Jacobi equation yields

$$S_t = -\alpha t \quad \text{and}$$

$$S_q = \int_{q_n}^{q} \sqrt{m(2\alpha - kq^2)}\, dq \tag{14}$$

Although the latter can be integrated to give the following,

$$S_q = \sqrt{m}\left(\frac{q}{2}\sqrt{2\alpha - kq^2} + \frac{\alpha}{k}\sin^{-1}\sqrt{\frac{k}{2\alpha}}\, q\right), \tag{15}$$

this is not a necessary step; instead the constant of motion β is immediately obtained from the following:

$$\beta = \frac{\partial S}{\partial \alpha} = \sqrt{\frac{m}{k}}\cos^{-1}\left(q\sqrt{\frac{k}{2\alpha}}\right) - t$$

$$\text{or} \quad q = \sqrt{\frac{2\alpha}{k}}\cos\sqrt{\frac{k}{m}}(t + \beta) \tag{16}$$

where α and β are the constants of motion determined by the initial configuration $q(t = 0)$ and the energy of motion $E\,(=\alpha)$.

This separable form for S has been used for a variety of conservative systems; other separable forms for S invoke the separation into a function of time times a function of q (Denman and Buch, 1973), that is

$$S(q, t) = S_q(q)S_t(t). \tag{17}$$

Other forms for S have been used, for example, Saletan and Cromer (1971) and Benton (1977); however, there does not appear to be a unified solution for rheonomic and multidegree-of-freedom systems.

Nonseparable Solutions

These are demonstrated using the above linear oscillator and are then generalized for multidegree-of-freedom systems; the systems are restricted to quadratic forms of potential but are not necessarily scleronomic.

The solution form is based on the polynomial expansion in the generalized coordinates

$$S(q, t) = a(t)q^2 + b(t)q + c(t) \tag{18}$$

where a, b, and c are functions to be determined. Using the above,

$$\frac{da}{dt} = -\frac{2a^2}{m} - \frac{k}{2}$$

$$\frac{db}{dt} = -\frac{2ab}{m} \quad \text{and}$$

$$\frac{dc}{dt} = -\frac{b^2}{2m}. \tag{19}$$

The function $a(t)$ will be labeled the kernel function as it will be seen to be independent of the initial conditions or constants of integration and is a function that is core to the system. The solution to this set of equations is not unique; a candidate solution is

$$a(t) = -\frac{\sqrt{km}}{2}\tan\omega t \tag{20}$$

where the system frequency $\omega = (k/m)^{1/2}$. It is observed that this solution approaches infinity for many times, $t = (2i-1)\pi/(2\omega)$, i being any integer; this presents a problem if the kernel solution were to be determined numerically.[3] The primary system function $b(t)$ is then

$$b(t) = \alpha e^{-\int_0^t (2a/m)dt} = \frac{\alpha}{\cos\omega t} \tag{21}$$

where the initial condition is $b = \alpha$ when $t = 0$. The final (secondary) system function is

$$c(t) = -\frac{\alpha^2}{2\sqrt{km}}\tan\omega t \tag{22}$$

and the principal function can be assembled; finally the constant of motion β is determined since

$$\beta = \frac{\partial S}{\partial\alpha} = \frac{\partial b}{\partial\alpha}q + \frac{\partial c}{\partial\alpha} = \frac{q}{\cos\omega t} - \frac{\alpha}{\sqrt{km}}\tan\omega t \tag{23}$$

or

$$q = \beta\cos\omega t + \frac{\alpha}{\sqrt{km}}\sin\omega t. \tag{24}$$

Note that the constant of motion β depends explicitly on the primary and secondary system functions $b(t)$ and $c(t)$ and not the kernel function $a(t)$; thus the kernel function has to be determined only once for a given system whereas the system functions are configuration dependent.

A second type of solution belonging to scleronomic systems is $a = j(mk/4)^{1/2}$ where $j = \sqrt{(-1)}$; the associated system functions are

$$b = \alpha e^{-j\omega t} \quad \text{and}$$

$$c = -\frac{j\alpha^2}{4\sqrt{km}}e^{-2j\omega t} \tag{25}$$

and the solution follows

$$q = \beta e^{j\omega t} + \frac{j\alpha}{2\sqrt{km}}e^{-j\omega t}, \tag{26}$$

which is the same as the previous solution with different values for α and β. This exercise has been pursued to demonstrate the alternate principal function S for the Hamilton-Jacobi equation; there is no advantage to using this specific solution for the single-degree-of-freedom system considered. However, for multidegree-of-freedom and/or for rheonomic systems there may be benefits in the form of the solution obtained.

Nonseparable Solutions, Rheonomic Systems

A rheonomic system was defined as one in which the Lagrangian L is explicitly dependent on time t. An example from Havas (1956), Denman (1966), Denman and Buch (1973), and Logan (1977) is introduced:

$$L = \tfrac{1}{2}(mv^2 - kq^2)e^{\mu t}. \tag{27}$$

This[4] exhibits the characteristics of a linear damped system even though there exists a work function $(\tfrac{1}{2}kq^2e^{\mu t})$; the free response of this system can be shown to be

$$q(t) = \beta_1 e^{s_1 t} + \beta_2 e^{s_2 t} \tag{28}$$

where β_1 and β_2 are the constants of the motion and s_1 and s_2 are the roots,

$$s_{1,2} = -\frac{\mu}{2}\left(1 \pm \sqrt{1 - \frac{4k}{m\mu^2}}\right), \tag{29}$$

and hence the solution can be written as (for $k/m > \mu^2/4$)

$$q(t) = e^{-(\mu t/2)}(\beta_1\sin\omega t + \beta_2\cos\omega t) \tag{30}$$

where

$$\omega = \sqrt{\frac{k}{m} - \frac{\mu^2}{4}}. \tag{31}$$

The generalized momentum is

$$p = \frac{\partial L}{\partial v} = mve^{\mu t} \tag{32}$$

and the Hamiltonian becomes

$$H = pv - L = \frac{p^2}{2m}e^{-\mu t} + \frac{kq^2}{2}e^{\mu t}. \tag{33}$$

Using the Hamilton-Jacobi equation and introducing the nonseparable solution

$$S(q, t) = a(t)q^2 + b(t)q + c(t) \tag{34}$$

gives the following coefficients of q^2, q, and q^0,

$$\frac{da}{dt} + \frac{2a^2}{m}e^{-\mu t} + \frac{k}{2}e^{\mu t} = 0$$

$$\frac{db}{dt} + \frac{2ab}{m}e^{-\mu t} = 0$$

$$\text{and} \quad \frac{dc}{dt} + \frac{b^2}{2m}e^{-\mu t} = 0. \tag{35}$$

The first equation admits a kernel solution

$$a(t) = Ae^{\mu t} \tag{36}$$

where the constant A is determined by substitution, to be

$$A = -\frac{m}{2}\left(\frac{\mu}{2} \pm j\omega\right). \tag{37}$$

The primary system function is

$$b(t) = \alpha e^{-(2At/m)} = \alpha\exp\left[\left(\frac{\mu}{2} \pm j\omega\right)t\right] \tag{38}$$

[3] Although it is not necessary to compute S or its components, $a(t)$, $b(t)$, and $c(t)$ numerically, this option is useful if these components cannot be established analytically; their numerical evaluation can then be used to find the system dynamics since only b and c are dependent on the constant of integration and both can be explicitly differentiated with respect to this constant.

[4] The linearily damped oscillator and the associated equivalent Lagrangians have been considered by other investigators. Havas (1956) used a different equivalent Lagrangian which is also considered by Kobussen (1979); this Lagrangian is not reproduced here as it is complex and would not contribute to the following development.

where α is the constant of integration. The secondary system function is

$$c(t) = \frac{\alpha^2}{2(4A + m\mu)} e^{-[(4A/m)+\mu]t}$$
$$= \frac{\mp\alpha^2}{2m\mu\sqrt{1 - \frac{4k}{m\mu^2}}} e^{\pm 2j\omega t}. \quad (39)$$

Finally, the constant of motion β is given

$$\beta = \frac{\partial S}{\partial \alpha} = q\frac{\partial b}{\partial \alpha} + \frac{\partial c}{\partial \alpha}$$
$$= qe^{-(2A/m)t} + \frac{\alpha}{(4A + m\mu)} e^{-[(4A/m)+\mu]t}. \quad (40)$$

This can be simplified so that

$$q = e^{-(\mu t/2)}\left(\beta e^{j\omega t} - \frac{\alpha}{(4A + m\mu)} e^{-j\omega t}\right)$$

$$\text{or} \quad = e^{-(\mu t/2)}(\beta_1 \sin \omega t + \beta_2 \cos \omega t), \quad (41)$$

which is the solution initially quoted; the constants β_1 and β_2 are determined from the initial conditions and may be related to the constants of motion α and β.

Multidegree-of-Freedom Systems

The generalised coordinates are q_i written in vector form as $\mathbf{q}$, a column vector; the velocity $\mathbf{v}$ is $d\mathbf{q}/dt$. The Lagrangian L is given generally for quadratic potential energy functions as

$$L = \tfrac{1}{2}\mathbf{v}'M\mathbf{v} + \mathbf{q}'D\mathbf{v} - \tfrac{1}{2}\mathbf{q}'K\mathbf{q} - \mathbf{G}'\mathbf{q} \quad (42)$$

where M, D, and K are square matrices; M and K are symmetric, and M is positive definite ($\|M\| > 0$, where the $\| \quad \|$ denotes a matrix norm). The last term in the Lagrangian, $G'q$, allows for a uniform gravitational-type potential. The generalised momenta $\mathbf{p}$ are thus

$$\mathbf{p} = \nabla_v L = M\mathbf{v} + D'\mathbf{q}. \quad (43)$$

Then

$$\mathbf{v} = M^{-1}(\mathbf{p} - D'\mathbf{q}) \quad (44)$$

and the Hamiltonian H is

$$H = \mathbf{p}'\mathbf{v} - L = \tfrac{1}{2}\mathbf{p}'M^{-1}\mathbf{p} - \tfrac{1}{2}(\mathbf{p}'M^{-1}D'\mathbf{q} + \mathbf{q}'DM^{-1}\mathbf{p})$$
$$+ \tfrac{1}{2}\mathbf{q}'(DM^{-1}D' + K)\mathbf{q} + \mathbf{G}'\mathbf{g}. \quad (45)$$

The principal function S is now posed as

$$S = \tfrac{1}{2}\mathbf{q}'A\mathbf{q} + B'\mathbf{q} + C \quad (46)$$

where A is a square symmetric matrix, the kernel function matrix, $\mathbf{B}$ is the primary system function (vector) and C, the secondary system function is scalar; these functions can be time dependent.

The Hamilton-Jacobi equation is

$$\frac{\partial S}{\partial t} + H(\nabla_{\mathbf{q}} S\mathbf{q}, t) = 0 \quad (47)$$

and substituting the above principal function and comparing coefficients of the multiplied combinations of q_i leads to the following:

$$\frac{dA}{dt} + A'M^{-1}A - A'M^{-1}D' - DM^{-1}A + DM^{-1}D' + K = 0$$
$$\frac{d\mathbf{B}}{dt} + (A - D)M^{-1}\mathbf{B} + \mathbf{G} = 0$$
$$\frac{dC}{dt} + \frac{1}{2}\mathbf{B}'M^{-1}\mathbf{B} = 0. \quad (48)$$

The first of these equations may be integrated (even numerically) to find the kernel function matrix A; the system functions could then be determined with the initial conditions for B_i ($=\alpha_i$ at $t = 0$). The constants of motion β_i are then used in the following:

$$\beta_i = \frac{\partial S}{\partial \alpha_i} = \sum_{j=0}^{n} \frac{\partial B_j}{\partial \alpha_i} q_j + \frac{\partial C}{\partial \alpha_i}, \quad i = 1, 2 \ldots n. \quad (49)$$

Using the above formulation, $\mathbf{B}$ is linear in the initial conditions $\boldsymbol{\alpha}$ and the partial differentiation of $\mathbf{B}$ and C is explicit; it is thus possible to determine the vector function $\mathbf{B}$ due to unit initial conditions and then to rewrite the last equation in terms of the initial conditions. In this way the vector function $\mathbf{B}$ and the scalar function C can be determined.

Example

To demonstrate the above solution, consider a two-degree-of-freedom system shown in Fig. 1.

There are two masses, m_1 and m_2 connected to the three springs k_1, k_2, and k_3. The kinetic and potential energies are as follows:

$$T = \frac{1}{2} m_1 \frac{dq_1^2}{dt} + \frac{1}{2} m_2 \frac{dq_2^2}{dt}$$
$$V = \tfrac{1}{2}k_1 q_1^2 + \tfrac{1}{2}k_2(q_2 - q_1)^2 + \tfrac{1}{2}k_3 q_2^2 \quad (50)$$

and the mass and stiffness matrices are

$$M = \begin{bmatrix} m_1 & 0 \\ 0 & m_2 \end{bmatrix}$$

$$K = \begin{bmatrix} k_1 + k_2 & -k_2 \\ -k_2 & k_2 + k_3 \end{bmatrix}. \quad (51)$$

The substitution of these matrices into the Hamiltonian results in the following:

$$\frac{dA}{dt} + A'M^{-1}A + K = 0$$
$$\frac{d\mathbf{B}}{dt} + A'M^{-1}\mathbf{B} = 0$$
$$\frac{dC}{dt} + \tfrac{1}{2}\mathbf{B}'M^{-1}\mathbf{B} = 0. \quad (52)$$

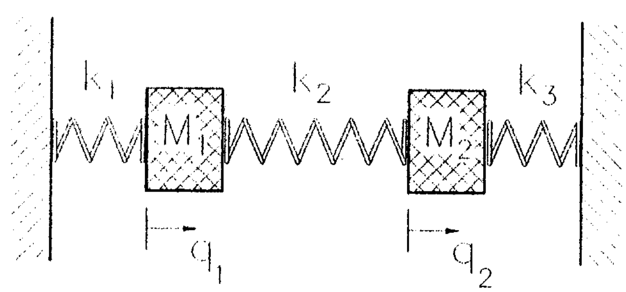

Fig. 1 Two-degree-of-freedom system

Since the system is scleronomic the kernel function can be written as

$$A'M^{-1}A + K = 0$$

$$\text{or} \quad A = j\phi'\mu\phi\psi'\lambda\psi \tag{53}$$

where ϕ is the modal matrix for the mass matrix, ψ is the modal matrix for K, and μ and λ are diagonal matrices derived from the eigenvalues of M and K as detailed in the following:

$$M = \phi' M \phi$$

$$\text{and} \quad K = \psi'\Lambda\psi. \tag{54}$$

The masses and stiffness in the following will be assumed equal ($m_1 = m_2 = m$, and $k_1 = k_2 = k_3 = k$) to simplify the arithmetic; in this case the modal and diagonal eigenvalue matrices are

$$\phi = \begin{bmatrix} 1 & 0 \\ 0 & 1 \end{bmatrix}$$

$$M = \begin{bmatrix} m & 0 \\ 0 & m \end{bmatrix} \tag{55}$$

and

$$\psi = \frac{1}{\sqrt{2}} \begin{bmatrix} 1 & 1 \\ 1 & -1 \end{bmatrix}$$

$$\Lambda = \begin{bmatrix} k & 0 \\ 0 & 3k \end{bmatrix}. \tag{56}$$

The μ and λ matrices are thus

$$\lambda = \begin{bmatrix} \sqrt{k} & 0 \\ 0 & \sqrt{3k} \end{bmatrix}$$

$$\mu = \begin{bmatrix} \sqrt{m} & 0 \\ 0 & \sqrt{m} \end{bmatrix} \tag{57}$$

so that the kernel matrix A is

$$A = \frac{j\sqrt{km}}{2} \begin{bmatrix} 1+\sqrt{3} & 1-\sqrt{3} \\ 1-\sqrt{3} & 1+\sqrt{3} \end{bmatrix}. \tag{58}$$

The primary system vector $\mathbf{B}$ can be determined by solving the second equation

$$\frac{d\mathbf{B}}{dt} + A'M^{-1}\mathbf{B} = 0 \tag{59}$$

and since this is integrable,

$$B = e^{-j\sqrt{1/m}\int_0^t \psi'\lambda\psi dt}\boldsymbol{\alpha}$$

$$= \psi' \upsilon \psi \boldsymbol{\alpha}, \tag{60}$$

where the matrix υ is again a diagonal matrix developed from the eigenvalues, and for scleronomic systems is as follows:

$$\upsilon = \begin{bmatrix} e^{-j\sqrt{k/m}t} & 0 \\ 0 & e^{-j\sqrt{3k/m}t} \end{bmatrix}. \tag{61}$$

Finally $\mathbf{B}$ becomes

$$\mathbf{B} = \frac{1}{2} \begin{bmatrix} e^{-j\gamma_1 t} + e^{-j\gamma_2 t} & e^{-j\gamma_1 t} - e^{-j\gamma_2 t} \\ e^{-j\gamma_1 t} - e^{-j\gamma_2 t} & e^{-j\gamma_1 t} + e^{-j\gamma_2 t} \end{bmatrix} \mathbf{B}_0 \tag{62}$$

where

$$\gamma_1 = \sqrt{\frac{k}{m}} \quad \text{and} \quad \gamma_2 = \sqrt{\frac{3k}{m}}. \tag{63}$$

The constant vector $\mathbf{B}_0$, arising as a constant of the motion is rewritten in terms of the constant vector $\boldsymbol{\alpha}$, resulting in $\mathbf{B}$ as follows:

$$\mathbf{B} = \begin{bmatrix} e^{-j\gamma_1 t} & e^{-j\gamma_2 t} \\ e^{-j\gamma_1 t} & -e^{-j\gamma_2 t} \end{bmatrix} \boldsymbol{\alpha}. \tag{64}$$

The secondary system function C results from the solution of

$$\frac{dC}{dt} + \frac{1}{2}\mathbf{B}'M^{-1}\mathbf{B} = 0 \tag{65}$$

yielding

$$C = \frac{1}{2jm}\left(\frac{\alpha_1^2}{\gamma_1}e^{-2j\gamma_1 t} + \frac{\alpha_2^2}{\gamma_2}e^{-2j\gamma_2 t}\right). \tag{66}$$

Finally the constants of motion β_1 and β_2 are determined by

$$\beta_i = \sum_{j=1}^{2} \frac{\partial B_j}{\partial \alpha_i} q_j + \frac{\partial C}{\partial \alpha_i}; \quad i = 1, 2. \tag{67}$$

Thus

$$\beta_1 = e^{-j\gamma_1 t}(q_1 + q_2) + \frac{\alpha_1}{jm\gamma_1} e^{-2j\gamma_1 t}$$

$$\beta_2 = e^{-j\gamma_2 t}(q_1 - q_2) + \frac{\alpha_2}{jm\gamma_2} e^{-2j\gamma_2 t} \tag{68}$$

or

$$q_1 + q_2 = \beta_1 e^{j\gamma_1 t} + \frac{j\alpha_1}{m\gamma_1} e^{-j\gamma_1 t}$$

$$q_1 - q_2 = \beta_2 e^{j\gamma_2 t} + \frac{j\alpha_2}{m\gamma_2} e^{-j\gamma_2 t}. \tag{69}$$

These are the equations for the normal modes, the two frequencies $(k/m)^{1/2}$ and $(3k/m)^{1/2}$ being the oscillation of the decoupled modes, first when the masses move together and the connecting spring (k_2) is unstretched and second the asymmetric mode when the two masses move in opposite directions.

Conclusions

The theory of the Hamilton-Jacobi equation is briefly reviewed and a form of solution is proposed. This form, which does not require separability is first illustrated by considering a single-degree-of-freedom system; its application to the analysis of multidegree-of-freedom systems is then demonstrated by considering the motion of a two-degree-of-freedom system. This approach opens the way for other forms of nonseparable solutions, that is sequence functions other than polynomial; it also offers other solutions to the inverse problem where the Hamilton-Jacobi equation is developed from the equations of motion.

References

Benton, S. H., Jr., *The Hamilton-Jacobi Equation: A Global Approach* (Mathematics in Science and Engineering) Vol. 131, Academic Press, pp. 8–13.

Currie, D. G., and Saletan, E. J., 1966, "q-Equivalent Particle Hamiltonians, I. The Classical One-Dimensional Case," *J. Math. Physics,* Vol. 7, No. 6, pp. 967–974.

Denman, H. H., 1966, "On Linear Friction in Lagrange's Equation," *Am. J. Physics,* Vol. 34, pp. 1147–1149.

Denman, H. H., and Buch, L. H., 1973, "Solution of the Hamilton-Jacobi Equation for Certain Dissipative Mechanical Systems," *J. Math. Phys.*, Vol. 14, No. 3, pp. 326–329.

Goldstein, H., 1980, "Classical Mechanics," 2nd ed., Addison-Wesley, Reading, MA, pp. 438–457.

Havas, P., 1956, *The Range of Application of the Lagrange Formalism*, Nuovo Cimento Supplemento, Volume V, Serie X, pp. 363–388.

Kobussen, J. A., 1979, "Some Comments on the Lagrangian Formalism for Systems with General Velocity-Dependent Forces," *Acta Physica Austriaca*, Vol. 51, pp. 293–309.

Lanczos, C., 1966, Variational Principles of Mechanics 3rd ed., University of Toronto Press, Toronto, Canada, pp. 229–243.

Landau, L. D., and Lifshitz, E. M., 1969, *Mechanics, Course of Theoretical Physics*, Vol. 1, 2nd ed., Pergamon Press, London, pp. 147–154.

Leech, J. W., 1965, *Classical Mechanics*, 2nd ed., Methuen, London, pp. 76–81.

Logan, J. D., 1977, *Invariant Variational Principles*, Academic Press, San Diego, CA, pp. 56–58.

Pars, L. A., 1965, *A Treatise on Analytical Dynamics*, Heinemann, London, pp. 268–286.

Saletan, E. J., and Cromer, A. H., 1971, *Theoretical Mechanics*, John Wiley and Sons, New York, pp. 225–258.

Santilli, R. M., 1978, *Foundations of Theoretical Mechanics I; The Inverse Problem in Newtonian Mechanics*, Springer-Verlag, New York, pp. 140–166, 182.

Sanz-Serna, J. M., and Calvo, M. P., 1994, *Numerical Hamiltonian Problems* (Applied Mathematics and Mathematical Computation 7), Chapman and Hall, London, pp. 129–153.

Synge, J. L., 1960, *Classical Dynamics in Encyclopedia of Physics, 3/1* S. Flugge, ed. Springer, Berlin, pp. 125–130.

Nonlinear System Response for Impulsive Parametric Input

S. Caddemi

M. Di Paola

Dipartimento di Ingegneria
Strutturale e Geotecnica,
Università degli Studi di Palermo,
Viale delle Scienze,
I 90128 Palermo, Italy

In engineering applications when the intensity of external forces depends on the response of the system, the input is called parametric. In this paper dynamical systems subjected to a parametric deterministic impulse are dealt with. Particular attention has been devoted to the evaluation of the discontinuity of the response when the parametric impulse occurs. The usual forward difference and trapezoidal integration schemes have been shown to provide only approximated solutions of the jump of the response; hence, the exact solution has been pursued and presented under the form of a numerical series. The impulse is represented throughout the paper by means of a classical Dirac's delta function; however, a new model of Dirac's delta is presented and adopted in order to validate the results provided by the numerical series.

1 Introduction

In many cases of engineering interest, such as the case of follower-type forces, the equations of motion are such that the intensity of the forcing function depends on the state variable itself. These systems are usually referred to as parametric excited ones. An example is wind-exposed suspended bridges (Lin and Li, 1993). In view of the random nature of the loads, such systems have been considered within the framework of the stochastic analysis and studied by means of the stochastic differential calculus. However, this paper is essentially devoted to deterministic analysis of nonlinear systems excited by a parametric deterministic impulse; in fact, in the authors' opinion, the tools of the stochastic analysis are strongly based on the deterministic analysis.

As far as the stochastic analysis is concerned, many books (Arnold, 1973; Soong and Grigoriu, 1993; Jazwinski, 1973; Gardiner, 1990; Ibrahim, 1985) have been devoted to the subject of nonlinear systems under parametric white noise stochastic input, increasing the interest of scientists and engineers in this area. The white noise can be thought of as a particular case of delta-correlated process, which is in general composed of a sequence of impulses uncorrelated to each other; when the impulse occurrences tend to infinity and, at the same time, the mean square of such impulses remains constant, then we obtain a white noise. In view of the irregularity of such a stochastic process, the Riemann integrals of the differential equations does not converge to a unique value; this is due to the fact that the Wiener process, whose derivative is the white noise, exhibits unbounded variations in infinitesimal intervals. In order to integrate differential equations involving so irregular kind of input, the stochastic differential calculus has to be adopted. Two main integrals can be used for the integration of such differential equations: the Itô stochastic integral (Itô, 1951) and the Stratonovich stochastic integral (Stratonovich, 1966). These two integrals are mainly related to the choice of the value of the response at each impulse occurrence. Itô selected the initial value, hence fully representing a forward difference integration scheme, while Stratonovich considered the average of the initial value and the final value corresponding to a trapezoidal integration scheme.

Contributed by the Applied Mechanics Division of THE AMERICAN SOCIETY OF MECHANICAL ENGINEERS for publication in the ASME JOURNAL OF APPLIED MECHANICS.

Discussion on this paper should be addressed to the Technical Editor, Professor Lewis T. Wheeler, Department of Mechanical Engineering, University of Houston, Houston, TX 77204-4792, and will be accepted until four months after final publication of the paper itself in the ASME JOURNAL OF APPLIED MECHANICS.

Manuscript received by the ASME Applied Mechanics Division, Jan. 26, 1995; final revision, June 10, 1996. Associate Technical Editor: M. Shinozuka.

From the above discussion researchers not working in the random vibration area are disconcerted since so irregular input, showing "*unbounded variations in infinitesimal intervals*" is quite different from the usual kind of deterministic input. As a consequence, such a sophisticated calculus seems to be an exclusive background of scientists working on random vibration theory. However, a particular effort is devoted in this paper to provide an easy deterministic background to the stochastic differential calculus. More precisely, since a white noise can be thought of as a sequence of impulses, the case of a single parametric impulse (where no "*unbounded variations*" occur) is important and should be studied.

Nonlinear systems excited by a parametric impulse are considered in this paper, where the impulse is represented by means of a classical Dirac's delta function. In correspondence with the impulse occurrence, the response exhibits a discontinuity whose evaluation can be obtained by means of the classical forward difference or trapezoidal integration schemes. However, it will be shown how these integration rules provide only approximate solutions and represent the first few terms of the exact solution, which is here presented under the form of a numerical series.

On this basis it can be recognized that a forward difference integration scheme is the deterministic counterpart of the Itô integral, while a trapezoidal integration rule is the counterpart of the Stratonovich integral.

For better understanding, a quasi-linear system is treated first, then more general nonlinear cases are treated.

A further insight into the performance of the proposed numerical series is provided in this paper by introducing a new model of the Dirac's delta representing a physical deterministic impulse.

2 Quasi-Linear Systems

In this section a very simple case of parametric input will be dealt with in order to show the meaning of Itô and Stratonovich integrals in deterministic analysis.

We will evaluate the response of a dynamical system whose equation is written in the form

$$\dot{Z}(t) = b + \gamma Z(t)\delta(t - t_0); \quad Z(0) = Z_0 \tag{1}$$

where b and γ are constants, $\delta(\cdot)$ is the Dirac's delta. Since the impulsive external force $\gamma\delta(t - t_0)$ multiplies the response Z, this kind of input is called "*parametric*" or "*multiplicative*," and the particular system under study in this section is called "*quasi-linear*" or "*bilinear*." The initial condition Z_0 is here assumed to be zero.

Integration of Eq. (1) can be performed in the time interval $[0, t_0^-]$, where t_0^- is the instant immediately before the Dirac's delta occurrence, and in this interval we obtain

$$Z(t) = bt \quad \forall\ 0 \le t < t_0 \tag{2}$$

and, immediately before the impulse, the response is $Z(t_0^-) = bt_0$.

The impulse can be thought of having some finite duration Δ, and in the time interval $[t_0, t_0 + \Delta]$ the intensity of the load is $1/\Delta$ so that Eq. (1) writes

$$\dot{Z}(t) = b + \frac{\gamma}{\Delta} Z(t) \quad \forall\ t_0 \le t < t_0 + \Delta \tag{3}$$

and the response can be immediately found in the form

$$Z(t) = \left(bt_0 + \frac{b\Delta}{\gamma}\right) \exp\left[\frac{\gamma}{\Delta}(t - t_0)\right] - \frac{b\Delta}{\gamma} \qquad \forall\ t_0 \le t < t_0 + \Delta \tag{4}$$

and, at the limit, as the duration Δ tends to zero and the intensity of the load tends to infinity, the correct response at the time instant immediately after the Dirac's delta occurrence, in the following denoted as t_0^+, simply writes

$$Z(t_0^+) = bt_0 \exp(\gamma). \tag{5}$$

So, as the response at t_0^- was $Z(t_0^-) = bt_0$ and at t_0^+ is given by Eq. (5), the response Z exhibits a jump given as

$$J = Z(t_0^+) - Z(t_0^-) = bt_0(\exp(\gamma) - 1). \tag{6}$$

From Eq. (6) we recognize that the jump depends on the value of the response immediately before the Dirac's delta occurrence and on the intensity of the impulse. At last, for $t > t_0$ the second term in Eq. (1) vanishes and the response is

$$Z(t) = bt + bt_0 \exp(\gamma) \quad \forall\ t > t_0. \tag{7}$$

In order to achieve this result we have only used the rules of classical differential calculus.

Now we will deal with the same problem but working in integral form; in order to do this we rewrite Eq. (1) in the form

$$dZ = bdt + g(Z)dH(t - t_0); \quad Z(0) = Z_0 \tag{8}$$

where $H(t)$ is the unit step function and

$$g(Z) = \gamma Z. \tag{9}$$

By performing integration of both members of Eq. (8) we can write

$$Z(t) - Z_0 = \int_0^t bdt + \gamma \int_0^t Z(\tau)dH(\tau - t_0). \tag{10}$$

The first integral in Eq. (10) is a classical Riemann integral, while the last is not a Riemann-Stiljies integral. In fact, the Riemann-Stiljies integral over the time interval $[t_0 - \epsilon, t_0 + \epsilon]$, with ϵ arbitrary small, can be written by selecting any partition $t_1, t_2, \ldots, t_k, \ldots, t_n$ of the time interval $[t_0 - \epsilon, t_0 + \epsilon]$, as follows:

$$Z(t_0 + \epsilon) - Z(t_0 - \epsilon) = \gamma \int_{t_0-\epsilon}^{t_0+\epsilon} Z(\tau)dH(\tau - t_0)$$
$$= \gamma \lim_{\substack{n\to\infty \\ \Delta t_{\max}\to 0}} \sum_{k=1}^{n} Z(\bar{t}_k)[H(t_k - t_0) - H(t_{k-1} - t_0)] \tag{11}$$

where $Z(\bar{t}_k)$ is the response at an intermediate point $\bar{t}_k$ between $[t_{k-1}, t_k]$ and $\Delta t_{\max}$ is the maximum amplitude of the intervals $[t_{k-1}, t_k]$ $(k = 1, 2, \ldots, n)$. Now $Z(t)$ exhibits a jump in the interval $[t_0 - \epsilon, t_0 + \epsilon]$ and the summation appearing in Eq. (11) depends on the choice of the intermediate point selected. It has to be noted that in Eq. (11), since the interval ϵ is arbitrarily small, the first term appearing in Eq. (10) is infinitesimal and it has been neglected; then Eq. (11) gives the total jump due to the Dirac's delta. If we assume $\bar{t}_k = t_{k-1}$, we obtain a "*forward integral*" that is the deterministic counterpart of the Itô integral (Itô, 1951). In this case the jump is

$$J(I_d) = \gamma bt_0 \tag{12}$$

where $J(I_d)$ stands for jump evaluated in Itô deterministic sense. By comparing Eqs. (6) and (12) we recognise that $J(I_d)$ is the approximation of the exact jump obtained by truncating the Taylor series of $\exp(\gamma)$ to the second term, it follows that the lesser the intensity of the Dirac's delta the better the prediction of the jump in Itô sense.

Now we perform the summation appearing in Eq. (11) by selecting $Z(\bar{t}_k)$ as the average of the initial value $Z(t_{k-1})$ and the final value $Z(t_k)$ at each interval $[t_{k-1}, t_k]$ hence adopting a "*trapezoidal integration scheme*" which represents the counterpart of the Stratonovich integral concept (Stratonovich, 1951) in the deterministic case, hence we obtain

$$Z(t_0 + \epsilon) - Z(t_0 - \epsilon) = \gamma \int_{t_0-\epsilon}^{t_0+\epsilon} Z(\tau)dH(\tau - t_0)$$
$$= \gamma \lim_{\substack{n\to\infty \\ \Delta t_{\max}\to 0}} \sum_{k=1}^{n} \frac{Z(t_k) + Z(t_{k-1})}{2}[H(t_k - t_0) - H(t_{k-1} - t_0)]. \tag{13}$$

The jump of the response evaluated according to Eq. (13) is

$$Z(t_0^+) - Z(t_0^-) = \gamma \frac{Z(t_0^+) + Z(t_0^-)}{2}. \tag{14}$$

From Eq. (14) we obtain

$$J(S_d) = \frac{\gamma}{1 - \gamma/2} bt_0 \simeq \left(\gamma + \frac{\gamma^2}{2}\right) bt_0, \tag{15}$$

where $J(S_d)$ stands for jump evaluated in Stratonovich deterministic sense. That is the jump evaluated in this form corresponds to the approximation of the exact jump obtained by retaining the first three terms of the Taylor expansion of $\exp(\gamma)$. The problem now is concerned with the possibility of capturing the effect of all terms of the Taylor expansion of $\exp(\gamma)$ in order to have the exact jump. The problem is very important since, although we possess the exact solution for the jump of quasi-linear systems, at this stage no exact prediction for the jump of the response can be provided when nonlinear parametric systems (any non linear function $g(Z)$ in Eq. (8)) are dealt with.

3 Nonlinear Parametric Dirac's Delta Input

This section will be devoted to the general case of nonlinear systems excited by parametric Dirac's delta occurrence and it will be shown how the exact response can be identified as the counterpart in the nonlinear case of the Taylor expansion of $\exp(\gamma)$.

Let now the differential equation be written in more general form,

$$\dot{Z} = f(Z, t) + g(Z, t)\delta(t - t_0); \quad Z(0) = Z_0, \tag{16}$$

where f and g are nonlinear functions of Z and t. In order to evaluate the exact expression of the jump we can use a different approach to this problem. In a book by Picone and Fichera (1975) we read that the more general expression for the Taylor expansion of an increment of a real-valued function $\phi(Z, t)$, continuously differentiable on t, and infinite times differentiable on Z, is given in the form

$$\Delta\phi(Z,t) = d\phi(Z,t) + \frac{1}{2!}d^2\phi(Z,t) + \frac{1}{3!}d^3\phi(Z,t) + \ldots \quad (17)$$

Using the common rules of differentiation of composite functions we can write (with arguments omitted)

$$d\phi = \frac{\partial\phi}{\partial t}dt + \frac{\partial\phi}{\partial Z}dZ$$

$$d^2\phi = \frac{\partial^2\phi}{\partial Z^2}(dZ)^2 + \frac{\partial\phi}{\partial Z}d^2Z$$

$$d^3\phi = \frac{\partial^3\phi}{\partial Z^3}(dZ)^3 + 3\frac{\partial^2\phi}{\partial Z^2}d^2ZdZ + \frac{\partial\phi}{\partial Z}d^3Z. \quad (18)$$

Selecting $\phi(Z, t) = Z$ we obtain, according to Eq. (17), for an increment of Z

$$\Delta Z = dZ + \frac{1}{2!}d^2Z + \frac{1}{3!}d^3Z + \ldots = \sum_{j=1}^{\infty}\frac{d^jZ}{j!} \quad (19)$$

now, before the impulse and after the impulse, we have that $\Delta Z = dZ$, since higher order differentials are infinitesimals of order greater than dt, while at $t = t_0$, as Z exhibits a jump, the higher order differentials appearing in Eq. (19) cannot be neglected. Writing Eq. (16) in the differential form

$$dZ = f(Z,t)dt + g(Z,t)dH(t-t_0); \quad Z(0) = Z_0 \quad (20)$$

the jump ΔZ, by accounting for all terms of Eq. (19), proves to be

$$\Delta Z = \sum_{j=1}^{\infty}\frac{g^{(j)}(Z,t)}{j!}(dH(t-t_0))^j \quad (21)$$

where

$$g^{(j)}(Z,t) = \frac{\partial g^{(j-1)}(Z,t)}{\partial Z}g^{(1)}(Z,t);$$

$$g^{(1)}(Z,t) = g(Z,t). \quad (22)$$

The coefficients $g^{(j)}(Z, t)$ given by Eq. (22) have to be evaluated at t_0^-. Remembering that dH is the increment of the unit step function, that is $H(t_0^+ - t_0) - H(t_0^- - t_0) = 1$, the increment of Z in correspondence of the impulse, that is the jump, is given in the form

$$J = \sum_{j=1}^{\infty}\frac{g^{(j)}(Z(t_0^-),t_0)}{j!} \quad (23)$$

For the quasi-linear case $g^{(1)}(Z) = \gamma Z$, $g^{(j)}(Z) = \gamma^jZ$ and the jump of Z is hence given by

$$J = \left(\sum_{j=1}^{\infty}\frac{\gamma^j}{j!}\right)Z(t_0^-) = (\exp(\gamma)-1)bt_0. \quad (24)$$

That is the Taylor expansion given by Eq. (19) allows to capture the whole effect of the parametric Dirac's delta.

As an example we will deal with the nonlinear system given in the form

$$\dot{Z} = b + \gamma Z^2\delta(t-t_0); \quad Z(0) = 0. \quad (25)$$

The solution of Eq. (25) at t_0^- is bt_0; in order to evaluate the jump we need the coefficients $g^{(j)}(Z(t_0^-))$, they are given, in view of Eq. (22), by

$$g^{(j)}(Z) = j!\gamma^jZ^{j+1}. \quad (26)$$

By means of Eq. (23), we obtain the exact jump of the response Z, which is otherwise unknown, as

$$J = \sum_{j=1}^{\infty}\gamma^jZ(t_0^-) = \sum_{j=1}^{\infty}\gamma^j(bt_0)^{j+1}. \quad (27)$$

From this simple example one immediately realizes that, depending on the various parameters γ, b, t_0, the jump could become a divergent quantity. People can be disconcerted for this result, since for a physical impulse the jump is obviously a finite quantity. But this simply means that, if the duration of a constant amplitude impulse decreases one has to expect a different quantity whatever the physical duration of the impulse; as a result, the system is very sensitive to the input.

On behalf of the reader who possesses a deep knowledge of stochastic analysis in Appendix A, a discussion concerning the stochastic differential calculus is presented on the base of the study of the single deterministic impulse.

Furthermore, the study of n-degree-of-freedom nonlinear systems excited by a parametric impulsive input is reported in Appendix B.

4 A Dirac's Delta Model

A further insight into the performance of Itô and Stratonovich integrals, in order to evaluate the jump of the response of nonlinear systems, can be provided by means of a suitable local interpretation of the impulsive input (represented by the Dirac's delta). To this purpose in this section a new model of Dirac's delta is presented.

The Dirac's delta occuring at time t_0, represented in Fig. 1(a), is commonly defined as a discontinuous function attaining an infinite value at t_0 and zero otherwise, and whose integral is one. The Dirac's delta is usually adopted to represent an impulse of unit intensity delivering its power in an infinitesimal time interval $dt = t_0^+ - t_0^-$. We state that, if we shape the Dirac's delta in some way within the infinitesimal time interval $dt = t_0^+ - t_0^-$ but leaving unchanged the total area, the total jump of the response is always that provided by the numerical series (Eq. (23)) for both quasi-linear and nonlinear parametric impulses, how it will be shown in the following.

Keeping this in mind, the Dirac's delta occurring at time t_0 can be thought of as an arbitrary noise composed of individual spikes whose sum is deterministically one. A sample of such a model of Dirac's delta is provided in Fig. 1(b) where the infinitesimal time interval $dt = t_0^+ - t_0^-$ has been fictitiously stretched. In this way the numerical integration of Eq. (16) can be performed over the pseudo-time interval $dt = t_0^+ - t_0^-$ without taking into account of the term $f(Z, t)$, hence simply evaluating the jump of the response due to each single spike composing the Dirac's delta and neglecting the evolution of the response between two subsequent spikes. The jump due to each spike is evaluated by means of Eq. (23). The smaller the intensity of each spike, the lesser the number of terms to be included in the summation appearing in Eq. (23).

As an example let us consider in the pseudo-time interval $dt = t_0^+ - t_0^-$ a sequence of n spikes of identical intensity. Since the summation of the intensities of these spikes is one, the intensity of each single spike is $A_r = 1/n$. In this way the number of terms in the summation appearing in Eq. (23) can be reduced since it depends on the intensity of the spikes. The jump of a quasi-linear system given by Eq. (24) can now be written as

$$J = \sum_{r=1}^{n}\left[\sum_{j=1}^{p}\frac{(\gamma A_r)^j}{j!}\right]Z(t_{0,r}^-)$$

$$= \sum_{r=1}^{n}\left[\sum_{j=1}^{p}\frac{1}{j!}\left(\frac{\gamma}{n}\right)^j\right]Z(t_{0,r}^-) \quad (28)$$

where $Z(t_{0,r}^-)$ is the value of $Z(t_0^-)$ before the rth spike within the pseudo-time interval $dt = t_0^+ - t_0^-$. The inner summation

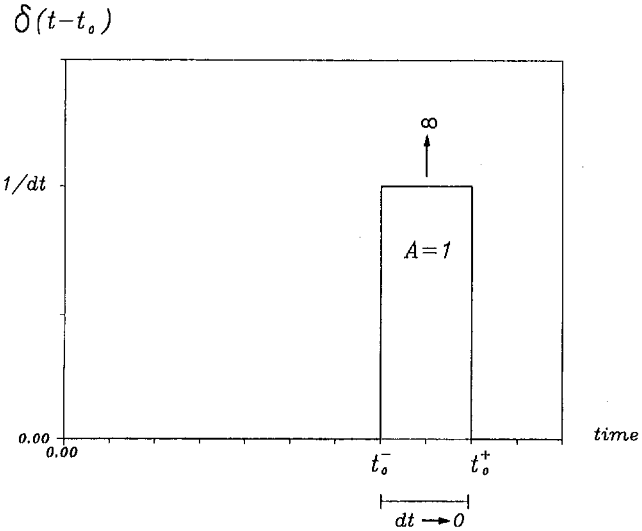

Fig. 1(*a*)

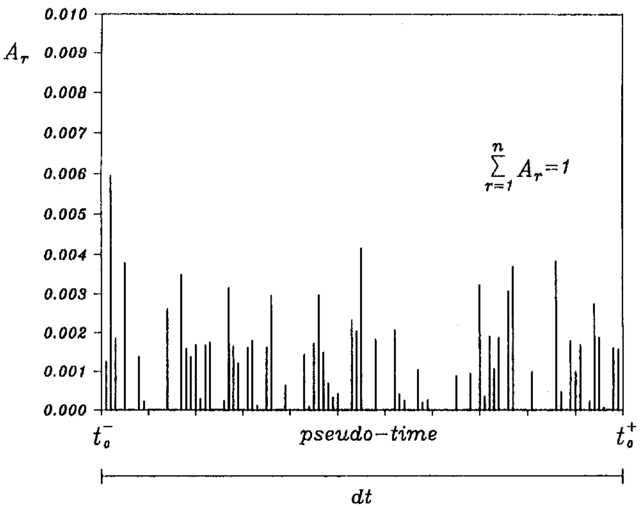

Fig. 1(*b*)

Fig. 1 Dirac's delta occurrence at real time t_0 (*a*), and a Dirac's delta sample inside the pseudo-time interval $dt = [t_0^-, t_0^+]$ (*b*)

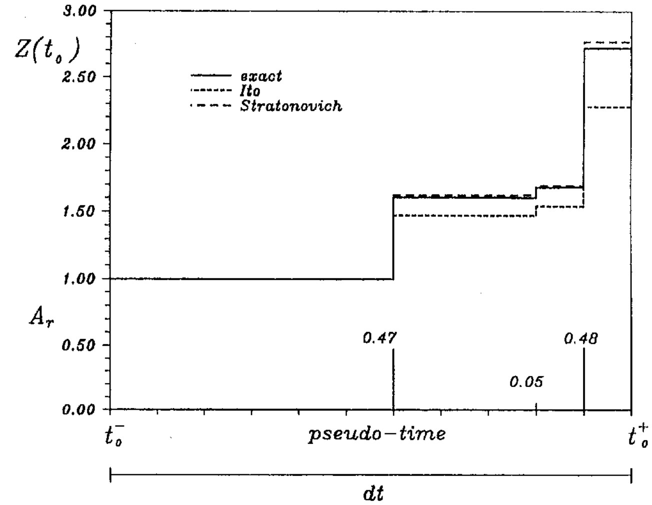

Fig. 2(*a*)

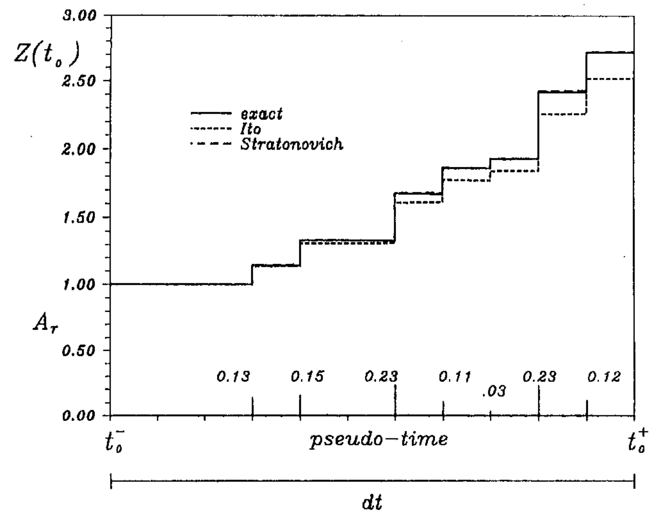

Fig. 2(*b*)

Fig. 2 Evolution of the response $Z(t_0)$ of a quasi-linear system inside the pseudo-time interval $dt = [t_0^-, t_0^+]$ for samples of Dirac's delta composed of $n = 3$ spikes (*a*), and $n = 7$ spikes (*b*)

appearing in Eq. (28) has been evaluated up to p terms but it can be further reduced by increasing the number n of spikes considered for modelling the Dirac's delta.

At the limit, as n diverges, one can retain only the first term of the inner summation which corresponds to evaluating the jump due to a single spike in the Itô sense. As a consequence, as n diverges, repeated evaluations of the Itô approximated jump due to a single spike, as well as Stratonovich approximated jump, converge to the exact total jump caused by the parametric Dirac's delta provided by Eq. (23).

Moreover, it will be shown in the following section that whatever casual sequence of n spikes of intensity A_r ($r = 1, 2, \ldots, n$), occurring within the Dirac's delta, is adopted under the constraint that $\sum_{r=1}^{n} A_r = 1$, the jump of the response attains always the same value provided by the numerical series reported in Eq. (23).

5 Numerical Aspects

5.1 Quasi-Linear System. The quasi-linear system represented by Eq. (1) has been considered first. The aim is evaluating the jump of the system at time t_0 where the Dirac's delta occurs.

Let us perform hence the integration of Eq. (1) at time t_0 by assuming $\gamma = 1$ and $Z(t_0^-) = bt_0 = 1$. According to Eq. (6) the exact jump is given by $J = Z(t_0^+) - Z(t_0^-) = \exp(1) - 1 = 1.718$, hence $Z(t_0^+) = 2.718$.

On the other hand, evaluation of J in the Itô sense (Eq. (12)) and Stratonovich sense (Eq. (15)) leads to approximate values of the jump J given by $J(I_d) = 1$ and $J(S_d) = 2$, respectively.

As previously stated, integration of Eq. (1) at time t_0 can also be performed by modeling the Dirac's delta as a sequence of n spikes occurring inside the pseudo-time interval $dt = t_0^+ - t_0^-$. In Fig. 2(a) the evolution of the exact Itô and Stratonovich response $Z(t_0)$ of the quasi-linear system between t_0^- and t_0^+ is represented, where the Dirac's delta has been considered as composed of $n = 3$ spikes of random intensity $A_r > 0$ (s.t. $\sum_{r=1}^{n} A_r = 1$). In Fig. 2(b) the path followed by the response is then plotted for the case $n = 7$ spikes.

Analysis of Figs. 2(a, b) confirms that, as the number n of spikes increases the exact response $Z(t_0^+)$ does not change, while the Itô response and the Stratonovich response tend to the exact one.

5.2 Nonlinear System. A system excited by a parametric Dirac's delta of the form given by Eq. (25) has been considered.

The exact jump due to a single spike Dirac's delta occurring at time t_0 has been evaluated by means of Eq. (27), where it has been assumed $\gamma = 0.5$ and $Z(t_0^-) = 1$, by truncating the summation at the 10th term: It takes the value $J = 1$. Approximated values of J have been evaluated in the Itô and Stratonovich sense as follows: $J(I_d) = 0.5$ and $J(S_d) = 2$, respectively, and the response $Z(t_0)$, so evaluated, at time t_0 is plotted in Fig. 3(a).

When the Dirac's delta is modeled by means of an increasing number n of spikes, as previously mentioned, it is possible to retain a decreasing number of terms in the summation appearing in Eq. (27).

Figures 3(b, c) show the path followed by the exact Itô and Stratonovich response between t_0^- and t_0^+ if the Dirac's delta is composed of $n = 3$ and $n = 7$ spikes, respectively. The exact response has been evaluated by retaining eight terms and five terms in the summation of Eq. (27) for the case $n = 3$ and $n = 7$, respectively.

In Figs. 3(b, c) the path followed by the exact response, if the number of spikes tends to infinity and their intensity is uniformly distributed, is also plotted.

Analysis of Figs. 3(a, b, c) proves that, as n increases, the Itô and Stratonovich jumps tend to the exact one and the path followed by the response inside the pseudo-time interval tends to follow the exact one.

The evolution of the exact response inside the pseudo-time interval has been also evaluated for linear distributions of the intensity of the spikes composing the Dirac's delta. In particular, both linearly increasing and decreasing distributions of intensities of a number $n \rightarrow \infty$ of spikes have been considered. The results are plotted in Fig. 4 together with that of uniformly distributed intensities of spikes. Since the same response $Z(t_0^+)$ at time t_0^+ is reached anyway, whatever the path followed by the exact response inside the pseudo-time interval, it can be stated that the governing differential equation is not sensitive to the sample chosen to represent the Dirac's delta.

6 Closure

An initial effort conducted by several scientists in the past aimed at integrating differential equations subjected to parametric normal white noise giving rise to a branch of stochastic analysis called ''*stochastic differential calculus.*'' Further studies extended the stochastic differential calculus to the case of non-normal delta correlated processes.

The strong feeling of the authors that the stochastic differential calculus relies on a deterministic base has been the source of this paper.

Particular attention has been devoted, in fact, to the case of parametric impulsive input without any stochastic characteristic, hence usually called deterministic. It has been proposed the correct numerical series that provides the exact response otherwise unknown (except in very simple cases). The concepts introduced by Itô and Stratonovich for stochastic integrals have been adopted in the paper for deterministic integrals and they have been shown to rely on different integration rules, forward difference and trapezoidal integration rules, respectively. Evaluations of the jump of the response by means of forward difference or trapezoidal integration rule represent only approximate solutions.

An interpretation of the Dirac's delta, as an arbitrary sequence of spikes whose total intensity is one, has also been presented. On the base of this model of the Dirac's delta, it has been proved that a reiterated application of the Itô or Stratonovich approximated response leads to the exact solution.

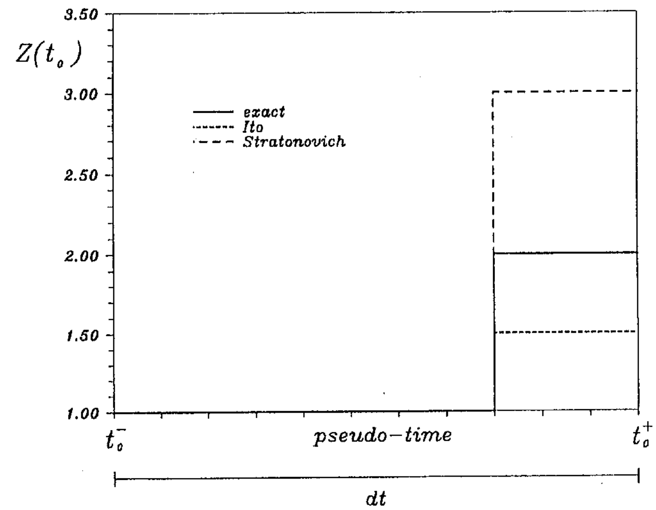

Fig. 3(a)

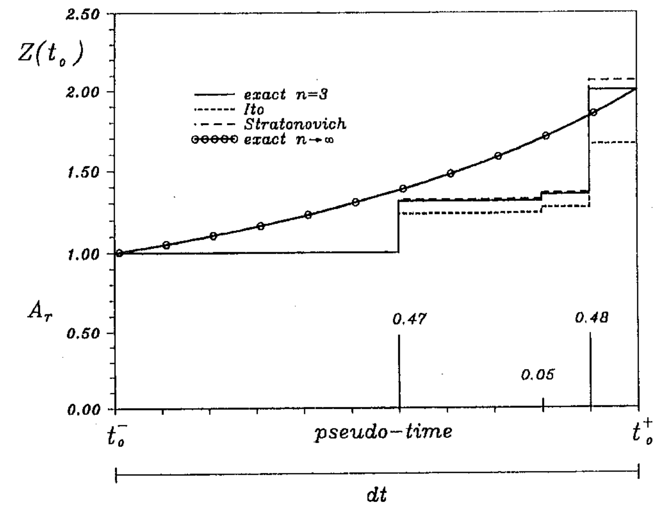

Fig. 3(b)

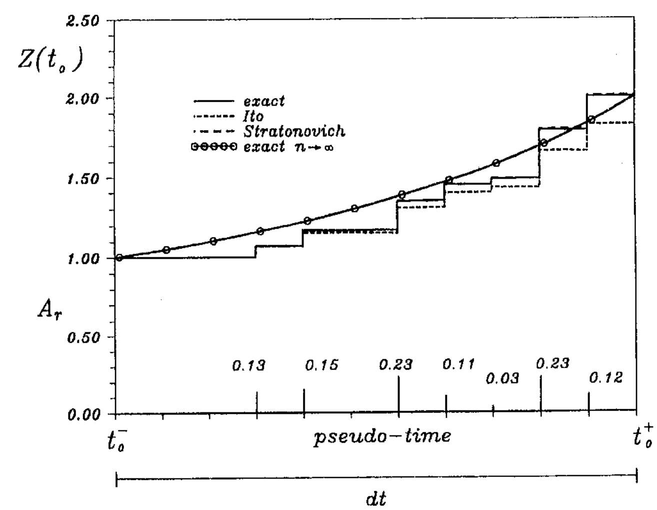

Fig. 3(c)

Fig. 3 Evolution of the response $Z(t_0)$ of a nonlinear system inside the pseudo-time interval $dt = [t_0^-, t_0^+]$ for samples of Dirac's delta composed of $n = 1$ spike (a), $n = 3$ spikes (b), and $n = 7$ spikes (c)

Finally it has been shown how this model of Dirac's delta provides the exact solution regardless of the distribution of the spike intensities composing the Dirac's delta itself, hence the validity of Eq. (23) is confirmed.

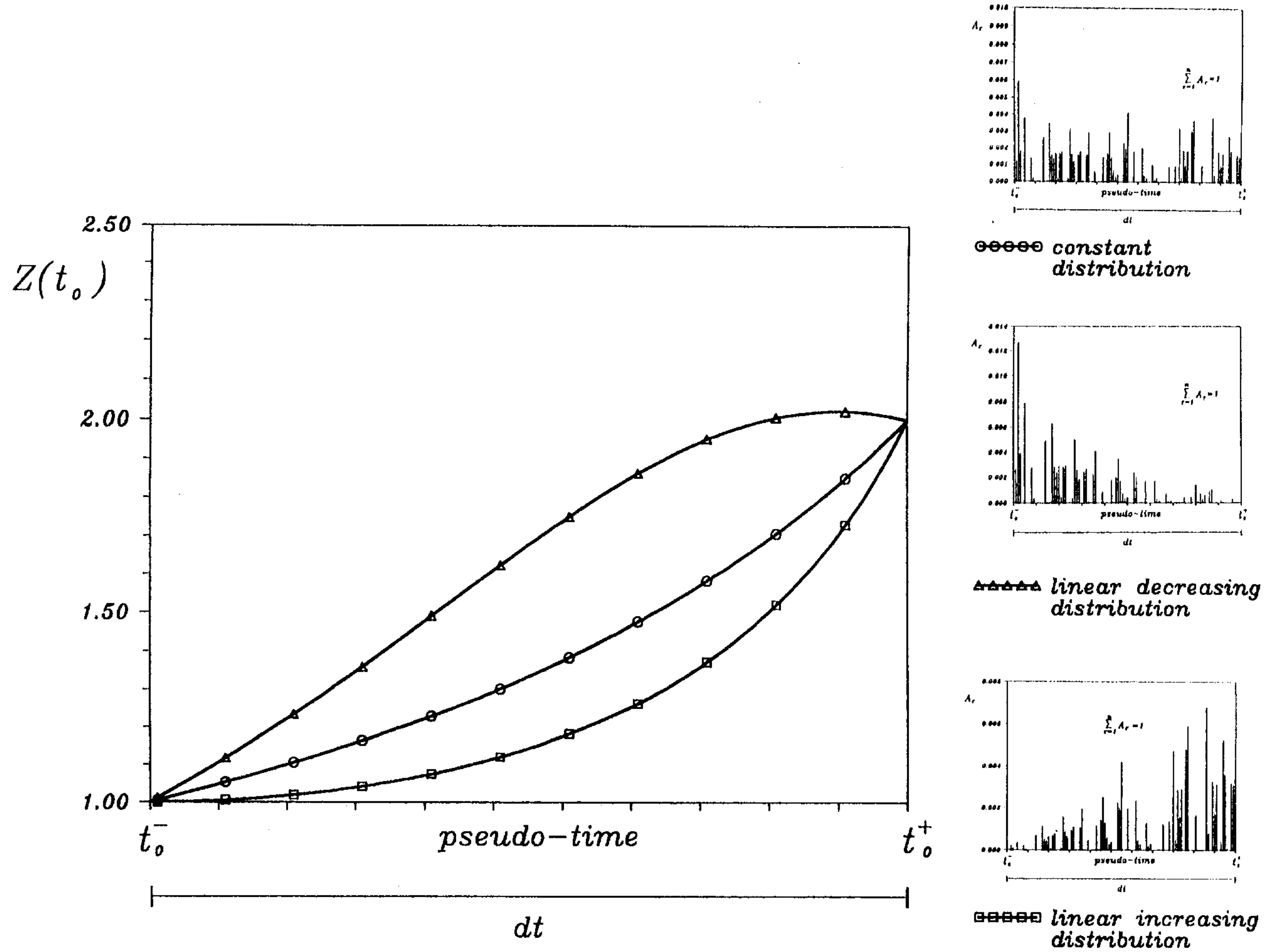

Fig. 4 Evolution of the exact response $Z(t_0)$ of a nonlinear system inside the pseudo-time interval $dt = [t_0^-, t_0^+]$ for three samples of Dirac's delta composed of $n \to \infty$ spikes

References

Arnold, L., 1973, *Stochastic Differential Equations: Theory and Applications,* John Wiley and Sons, New York.

Di Paola, M., and Falsone, G., 1993a, "Stochastic Dynamics of Nonlinear Systems Driven by Non-Normal Delta-Correlated Processes," ASME JOURNAL OF APPLIED MECHANICS, Vol. 60, pp. 141–148.

Di Paola, M., and Falsone, G., 1993b, "Itô and Stratonovich Integrals for Delta-Correlated Processes," *Probabilistic Engineering Mechanics,* Vol. 8, pp. 197–208.

Gardiner, C. W., 1990, *Handbook of Stochastic Methods,* Springer-Verlag, Berlin.

Ibrahim, R. A., 1985, *Parametric Random Vibration,* Research Studies Press, Letchworth, UK.

Itô, K., 1951, "On a Formula Concerning Stochastic Differential," *Nagoya Mathematical Journal,* Vol. 3, pp. 55–65.

Jazwinski, A. H., 1973, *Stochastic Processes and Filtering Theory,* Academic Press, New York.

Lin, Y. K., and Li, Q. C., 1993, "New Stochastic Theory for Bridge Stability in Turbulent Flow," *ASCE Journal of Engineering Mechanics,* Vol. 119, pp. 113–127.

Picone, M., and Fichera, G., 1975, *Corso di Analisi Matematica,* Libreria eredi Virgilio Veschi, Roma (in Italian).

Soong, T. T., and Grigoriu, M., 1993, *Random Vibration of Mechanical and Structural Systems,* Prentice-Hall, Englewood Cliffs, NJ.

Stratonovich, R. L., 1966, "A New Form of Representing Stochastic Integrals and Equations," *Journal SIAM Control,* Vol. 4, pp. 362–371.

Wong, E., and Zakai, M., 1965, "On the Relation Between Ordinary and Stochastic Differential Equations," *International Journal of Engineering Sciences,* Vol. 3, pp. 213–229.

APPENDIX A

Normal White Noise and Response

In this Appendix a few remarks concerning the stochastic differential calculus are proposed and framed in the deterministic context outlined in the paper.

The equation of motion of a system subjected to a stochastic input $W(t)$ can be written as

$$\dot{Z} = f(Z, t) + g(Z, t)W(t); \quad Z(0) = Z_0. \qquad \text{(A1)}$$

Let the time axis be subdivided into small intervals of length Δt_j, and let $t_0, t_1, \ldots, t_n$ be the subdivision time instants. Let $Y_0, Y_1, \ldots, Y_n$ be a realisation of a zero-mean normal random variable Y with unit variance. If we define at each time instant t_j an impulse of amplitude $Y_j\sqrt{\Delta t_j}$, the stochastic process $W(t)$ so constructed, appearing in Eq. (A1), is a delta correlated process and at the limit, as $\Delta t_{\max} = \max_j(\Delta t_j) \to 0$, the stochastic process tends to a normal white noise. As a consequence the cumulants K_r with $r > 2$ are of order $(\Delta t_{\max})^{r/2}$ hence are infinitesimals with respect to the second-order cumulant K_2 which is of order $\Delta t_{\max}$.

For the integration of Eq. (A1), it should be considered that the solution $Z(t_j^-)$ before the impulse occurrence $Y_j\sqrt{\Delta t_j}$ is known and the solution $Z(t_{j+1}^-)$ has to be evaluated. In order to do this the following two-step procedure can be adopted:

$$Z(t_j^+) = Z(t_j^-) + \sum_{s=1}^{\infty} \frac{Y_j^s}{s!} g^{(s)}(Z(t_j^-), t_j))(\Delta t_j)^{s/2} \qquad \text{(A2)}$$

$$Z(t_{j+1}^-) = Z(t_j^+) + f(Z(t_j), t_j)\Delta t_j. \qquad \text{(A3)}$$

Equation (A2), on the base of the jump evaluation provided by Eq. (23), leads to the response at time t_j^+ after the impulse occurrence; while Eq. (A3), on the base of a forward difference integration scheme, provides the solution at time t_{j+1}^- before the subsequent impulse occurrence.

Equation (A2), as $\Delta t_{\max} \to 0$, can be written as

$$Z(t_j^+) = Z(t_j^-) + Y_{jg}^{(1)}(Z(t_j^-), t_j)(\Delta t_j)^{1/2} + \frac{Y_j^2}{2!} g^{(2)}(Z(t_j^-), t_j)\,\Delta t_j + \sum_{s=3}^{\infty} [O(\Delta t_j^{s/2})]. \quad \text{(A4)}$$

The contributions included in the last summation appearing in Eq. (A4) can be neglected, hence Eqs. (A3) and (A4) represent the integration scheme for the Monte-Carlo simulation of stochastic differential equations under parametric white noise processes.

Equations (A3) and (A4) can now be written together in differential form, as $\Delta t_{\max} \to 0$, as follows:

$$dZ(t) = f(Z(t), t)\,dt + g^{(1)}(Z(t), t))\,dB(t) + \frac{1}{2!} g^{(2)}(Z(t), t))\,(dB(t))^2 \quad \text{(A5)}$$

where $B(t)$ is a Wiener process, hence Eq. (A5) represents an Itô-type stochastic differential equation. The extra term 1/2! $g^{(2)}(Z(t), t))\,(dB(t))^2$, appearing in Eq. (A5), is the so-called Wong-Zakai or Stratonovich correction term.

APPENDIX B

Multidimensional Case

In this Appendix the case of n-degree-of-freedom mechanical systems excited by a parametric impulsive input will be dealt with.

The study of n-degree-of-freedom mechanical systems including the structural ones, can be reconduced to a set of first-order differential equations in the form

$$\dot{\mathbf{Z}} = \mathbf{f}(\mathbf{Z}, t) + \mathbf{G}(\mathbf{Z}, t)\mathbf{F}(t); \quad \mathbf{Z}(0) = \mathbf{Z}_0, \quad \text{(B1)}$$

where $\mathbf{Z}$ is the n-state-space variable vector, $\mathbf{f}(\mathbf{Z}, t)$ is the nonlinear n-vector function of $\mathbf{Z}$ and t, $\mathbf{G}(\mathbf{Z}, t)$ is a matrix of order $n \times m$ of functions of $\mathbf{Z}$, and $\mathbf{F}(t)$ is an m-vector of (known) forcing functions, $\mathbf{Z}_0$ is the n-vector of initial conditions. Let $\mathbf{F}(t)$ be a vector of Dirac's deltas occuring at time $t = t_0$, then one can write

$$\mathbf{F}(t) = \mathbf{r}\delta(t - t_0) \quad \text{(B2)}$$

where $\mathbf{r}$ is an n-vector whose components represent the intensity of the impulses. Then Eq. (B1) can be written in the form

$$d\mathbf{Z} = \mathbf{f}(\mathbf{Z}, t)\,dt + \mathbf{g}(\mathbf{Z}, t)dH(t - t_0); \quad \mathbf{Z}(0) = \mathbf{Z}_0 \quad \text{(B3)}$$

where $\mathbf{g}(\mathbf{Z}, t)$ is the n-vector defined as

$$\mathbf{g}(\mathbf{Z}, t) = \mathbf{G}(\mathbf{Z}, t)\mathbf{r}. \quad \text{(B4)}$$

Let the solution vector at time t_0^-, denoted as $\mathbf{Z}(t_0^-)$, be known. In order to evaluate the jump vector we can apply the expansion given by Eq. (19) extended to the case of vector function $\mathbf{Z}$ in the form

$$\Delta\mathbf{Z} = d\mathbf{Z} + \frac{1}{2!} d^2\mathbf{Z} + \frac{1}{3!} d^3\mathbf{Z} + \ldots = \sum_{j=1}^{\infty} \frac{1}{j!} d^j\mathbf{Z} \quad \text{(B5)}$$

where only at time t_0, at which the Dirac's delta occurs, we have accounted for the term $\mathbf{g}(\mathbf{Z}, t)dH(t - t_0)$, then, keeping this in mind, the jump $\Delta\mathbf{Z}$ in correspondence of the δ occurrence writes

$$\Delta\mathbf{Z} = \sum_{j=1}^{\infty} \frac{\mathbf{g}^{(j)}(\mathbf{Z}(t_0^-), t)}{j!} \quad \text{(B6)}$$

where $\mathbf{g}^{(j)}(\mathbf{Z}, t)$ can be evaluated in the recurrence form

$$\mathbf{g}^{(j)}(\mathbf{Z}(t), t) = (\nabla_z \mathbf{g}^{(j-1)}(\mathbf{Z}(t), t))\mathbf{g}^{(1)}(\mathbf{Z}(t), t)$$
$$\mathbf{g}^{(1)}(\mathbf{Z}(t), t) = \mathbf{g}(\mathbf{Z}(t), t) \quad \text{(B7)}$$

and $\nabla_z \mathbf{g}^{(j-1)}(\mathbf{Z}(t), t)$ is the gradient operator of the vector $\mathbf{g}^{(j-1)}(\mathbf{Z}(t), t)$, that is

$$\nabla_z \mathbf{g}^{(j)}(\mathbf{Z}(t), t) = \begin{bmatrix} \frac{\partial g_1^{(j)}}{\partial Z_1} & \frac{\partial g_1^{(j)}}{\partial Z_2} & \cdots & \frac{\partial g_1^{(j)}}{\partial Z_n} \\ \frac{\partial g_2^{(j)}}{\partial Z_1} & \frac{\partial g_2^{(j)}}{\partial Z_2} & \cdots & \frac{\partial g_2^{(j)}}{\partial Z_n} \\ \cdots & \cdots & \cdots & \cdots \\ \frac{\partial g_n^{(j)}}{\partial Z_1} & \frac{\partial g_n^{(j)}}{\partial Z_2} & \cdots & \frac{\partial g_n^{(j)}}{\partial Z_n} \end{bmatrix}. \quad \text{(B8)}$$

As an example, let the equation of motion of a single-degree-of-freedom system be given in the form

$$\ddot{x} + 2\xi\omega_0\dot{x} + \omega_0^2 x + (\rho x + \gamma\dot{x})\delta(t - t_0) = 0. \quad \text{(B9)}$$

By means of the state variable approach we set $Z_1 = x$, $Z_2 = \dot{x}$ and Eq. (B9) can be written in the standard form

$$\dot{\mathbf{Z}} = \mathbf{D}\mathbf{Z} + \mathbf{g}(\mathbf{Z})\delta(t - t_0) \quad \text{(B10)}$$

where $\mathbf{Z}^T = [Z_1, Z_2]$ and

$$\mathbf{D} = \begin{bmatrix} 0 & 1 \\ -\omega_0^2 & -2\xi\omega_0 \end{bmatrix} \mathbf{g}(\mathbf{Z}) = \begin{bmatrix} 0 \\ -\rho Z_1 - \gamma Z_2 \end{bmatrix} \quad \text{(B11)}$$

by evaluating $\mathbf{g}^{(j)}(\mathbf{Z})$ we can write

$$\mathbf{g}^{(j)}(\mathbf{Z}) = (-\gamma)^{j-1}\mathbf{g}(\mathbf{Z}) \quad \text{(B12)}$$

and the jump, evaluated by means of Eq. (B6) is simply written as

$$\Delta\mathbf{Z} = \mathbf{Z}(t_0^+) - \mathbf{Z}(t_0^-) = \exp(-\gamma)[-\rho Z_1(t_0^-) - \gamma Z_2(t_0^-)] \begin{bmatrix} 0 \\ 1 \end{bmatrix} \quad \text{(B13)}$$

that is, how we expected, for a single oscillator no jump is present for the displacement x, while the velocity exhibits a jump depending on the values of displacement and velocity evaluated at time t_0^- and on the coefficients γ and ρ.

S. P. Vaze
Assoc. Mem. ASME.

E. Corona
Assoc. Mem. ASME.

Department of Aerospace and Mechanical Engineering, University of Notre Dame, Notre Dame, IN 46556

Response and Stability of Square Tubes Under Bending

This paper addresses the response and stability of elastic-plastic steel tubes with square cross section under pure bending. An analytical model with sufficiently nonlinear kinematics to capture the development of ripples in the compression flange was developed. The results indicate that collapse of such tubes is imperfection sensitive for tubes with "high" height-to-thickness ratio (h/t), but the sensitivity decreases as h/t decreases. Experimentally, the tubes collapse due to a limit moment instability which is followed by the formation of a kink on the compression flange of the tubes. The limit moment and the development of the kink are captured well by the analytical model.

Introduction

Thin-walled tubes are commonly used as structural members in many engineering applications to resist axial and bending loads. It was realized by researchers in the 1920s that the deformation of the cross section which accompanies bending could influence the response, strength, and stability of such tubes. See, for example, the work of Timoshenko (1923) and Brazier (1927). The work of Brazier, in particular, demonstrated that bending-induced ovalization of tubes of circular cross section leads to a limit moment instability. It is also well known that shell-type instabilities can precede the limit moment and induce collapse of the tubes at lower curvatures. Kyriakides and Ju (1992) discuss the various instabilities which can occur in tubes of circular cross section under bending with emphasis on the elastic-plastic case. Tubes of rectangular and square cross section exhibit some instabilities similar to those identified in circular tubes, although some clear differences are also apparent.

Studies of the bending response of tubes with rectangular cross section have been conducted by Hasan and Hancock (1989). They found that, as bending proceeded, the bending moment of the tubes suddenly dropped when a kink formed in the compression flange. Corona and Vaze (1996) presented an experimental investigation of the pure bending response of elastic-plastic tubes of square cross section. This paper identified that the response and collapse of tubes with height-to-thickness ratios (h/t) in the range $15.4 \leq h/t \leq 28.6$ are influenced by the development of axial ripples in the compression flange. These ripples arise from a shell-type bifurcation at a critical value of curvature. This study also considered the numerical modeling of the pre-bifurcation response of the tubes and developed a bifurcation test to determine the critical curvature at which these ripples appear. The limitations of the kinematics used, however, precluded numerical studies of the collapse of the tubes.

The present paper removes the limitations in the pre-bifurcation analysis and concentrates on the numerical prediction of the response and collapse of tubes of square cross section. The effects of initial imperfections are reviewed in detail for the h/t range mentioned above. The salient aspects of the problem, which need to be modeled, can be identified by a careful look at one set of experimental results.

Contributed by the Applied Mechanics Division of THE AMERICAN SOCIETY OF MECHANICAL ENGINEERS for publication in the ASME JOURNAL OF APPLIED MECHANICS.

Discussion on this paper should be addressed to the Technical Editor, Professor Lewis T. Wheeler, Department of Mechancial Engineering, University of Houston, Houston, TX 77204-4792, and will be accepted until four months after final publication of the paper itself in the ASME JOURNAL OF APPLIED MECHANICS.

Manuscript received by the ASME Applied Mechanics Division, July 11, 1996; final revision, Oct. 15, 1996. Associate Technical Editor: S. Kyriakides.

Review of Experimental Results

Figure 1 shows a set of experimental results for curvature controlled pure bending of a steel 4130 seamless square tube with $h/t = 20.4$. The nominal height of the cross section was $h = 25.4$ mm (1 in.) and the length of the specimen was 0.76 m (30 in.). The experimental set-up and procedure are described in detail in Corona and Vaze (1996). Figure 1(*a*) shows the moment-curvature response (M-κ) of the specimen. The moment and the curvature have been nondimensionalized by $M_o = \frac{3}{2}\sigma_o th^2$ and $\kappa_1 = \frac{3}{2}(\pi^2 t^2/(h^3(1-\nu^2)))$ respectively, where σ_o is the 0.2 percent offset yield stress and ν is the Poisson ratio. The response was initially linear but became nonlinear as the material yielded. The bending process was stopped at predetermined values of curvature to make the measurements presented in Fig. 1(*b*). The dips in moment were caused by material relaxation while the curvature was held at a constant value. Upon continued bending, the M-κ response achieved a limit moment at $\kappa/\kappa_1 = 2.52$ after which a kink similar to the one shown in Fig. 2 developed in the compression flange causing the moment to drop suddenly and the specimen to collapse.

Figure 1(*b*) shows measurements of the decrease in height of the cross section in the plane of bending (denoted by Δ in the insert) as a function of axial position s for several values of curvature. Both Δ and s have been normalized by h. The circled numbers in Fig. 1(*a*) correspond to those in Fig. 1(*b*). Measurement 1 was taken prior to the beginning of the bending process, when the specimen was still unloaded. It revealed a periodic variation of Δ/h with wavelength of approximately 8.2 and an amplitude of 0.002. This is an initial geometric imperfection introduced during manufacturing of the tube. As the curvature was increased to point 3, Δ increased in a fairly uniform manner along the specimen. Measurement 3 revealed the beginnings of short wavelength ripples of normalized wavelength 1.1. These ripples became clearly defined by measurement 5. From this point onwards, the growth of Δ had two components, one was uniform along the specimen and the other was periodic with wavelength $\lambda/h = 1.1$. Both components grew reasonably uniformly along the specimen up to point 8. Note that the M-κ response has a positive slope up until the vicinity of point 12. Measurement 12, taken just before collapse, indicates that the amplitude of one ripple had increased significantly in comparison with the others. This ripple gave rise to the kink which appeared on the compression flange of the tube at collapse. It is obvious that in this case the localization process, which led to the formation of the kink, was highly unstable.

Clearly, the growth and localization of the ripples play an important role in the collapse of the tubes. The prediction of these events requires an analytical formulation that can capture axial variations in the deflections of the flanges and webs of

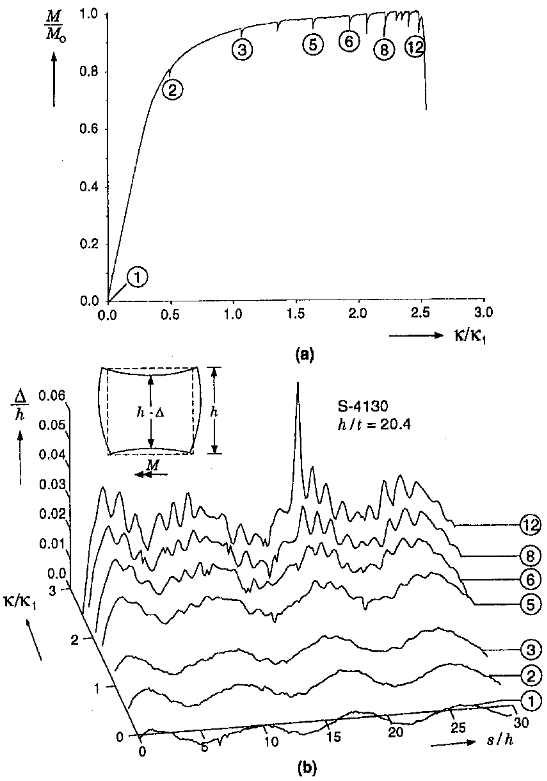

Fig. 1 Response of a square tube with $h/t = 20.4$ under pure bending; (*a*) moment-curvature, (*b*) Δ as function of axial location and curvature

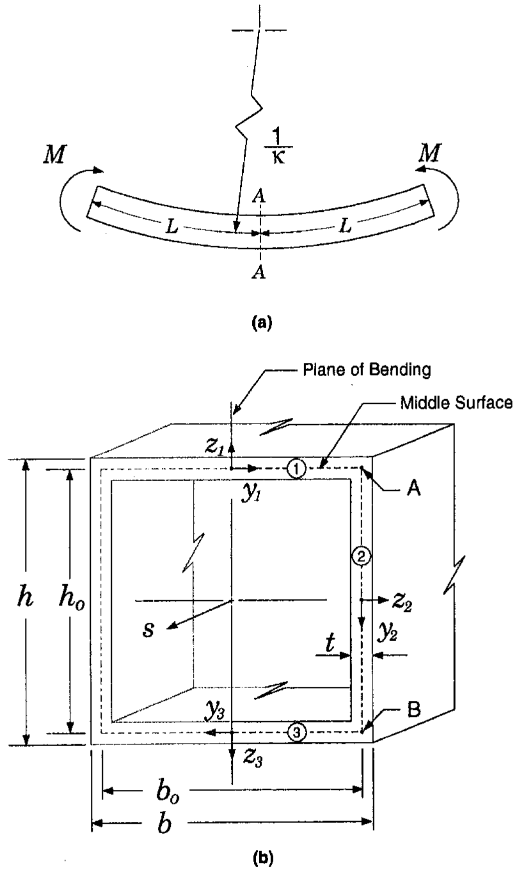

Fig. 3 Problem geometry

the tube. The objective of the present paper is to develop such formulation and use it to study the phenomena observed experimentally.

Formulation

The formulation considers a tube with rectangular cross section of length $2L$. The tube develops a bending moment M upon being bent to a curvature κ as shown in Fig. 3(a). The cross section has wall thickness t, flange width b and web height h as shown in Fig. 3(b) to accommodate for slight variations from the nominally square cross section of the tubes as observed in the experiments. The curvature is assumed to remain constant along the tube. Furthermore, deformations are assumed to be symmetric about plane A-A in Fig. 3(a) and the plane of bending in Fig. 3(b). The domain consists of the three regions shown in Fig. 3(b): half of the upper flange, one web, and half of the lower flange, which are denoted by ①, ②, and ③ respectively.

The coordinates used are also shown in Fig. 3(b). The coordinate along the tube axis is denoted by s. The y_i coordinates[1] run along the midsurface of each region and the z_i coordinates point in the respective through-thickness directions. The common assumption that plane sections originally perpendicular to the s and y_i-axes remain plane during loading is adopted for all three regions.

[1] i denotes the region under consideration and will appear as a subscript of coordinates and displacements but as a superscript of all other quantities.

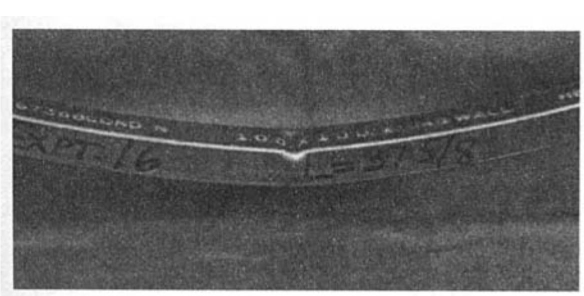

Fig. 2 Tube with nominal $b/t = 20.4$ after collapse

Kinematics. The kinematics employed are based on thin shell theory. In order to derive the strain-displacement relationships, we employ the deformation composition scheme shown schematically in Fig. 4, which is based on the work of Fabian (1981) and Ju and Kyriakides (1992) for circular tubes under bending. The objective of the scheme is to derive the expressions for the strain in a deformed tube shown schematically in Fig. 4(d) referred to the imperfect straight configuration of Fig. 4(b). The displacement components in each region are shown in the insert Ⓐ in Fig. 4.

The first and second fundamental forms for the imperfect straight tube, $\mathbf{a}^{0^{(i)}}$ and $\mathbf{b}^{0^{(i)}}$, can be found from the respective forms of a perfect straight tube (Fig. 4(a)) which are given by

$$\mathbf{a}^{p^{(i)}} = \begin{bmatrix} 1 & 0 \\ 0 & 1 \end{bmatrix} \quad \mathbf{b}^{p^{(i)}} = \begin{bmatrix} 0 & 0 \\ 0 & 0 \end{bmatrix}. \tag{1}$$

As an example, a geometric imperfection with displacement fields $u_1^0 = 0$, $v_1^0 = 0$ and $w_1^0 = w_1^0(s, y_1)$ has been shown in Fig. 4(b) in region ①. Similar imperfections can be prescribed in the other regions. Both $\mathbf{a}^{0^{(i)}}$ and $\mathbf{b}^{0^{(i)}}$ can be obtained using the relationships

$$a_{\alpha\beta}^{0(i)} = a_{\alpha\beta}^{p(i)} + 2E_{\alpha\beta}^{0(i)} \quad b_{\alpha\beta}^{0(i)} = b_{\alpha\beta}^{p(i)} + K_{\alpha\beta}^{0(i)} \tag{2}$$

where α and β can be s or y_i. The quantities $E_{\alpha\beta}^{0(i)}$ and $K_{\alpha\beta}^{0(i)}$ are the membrane and bending strains in the imperfect, straight

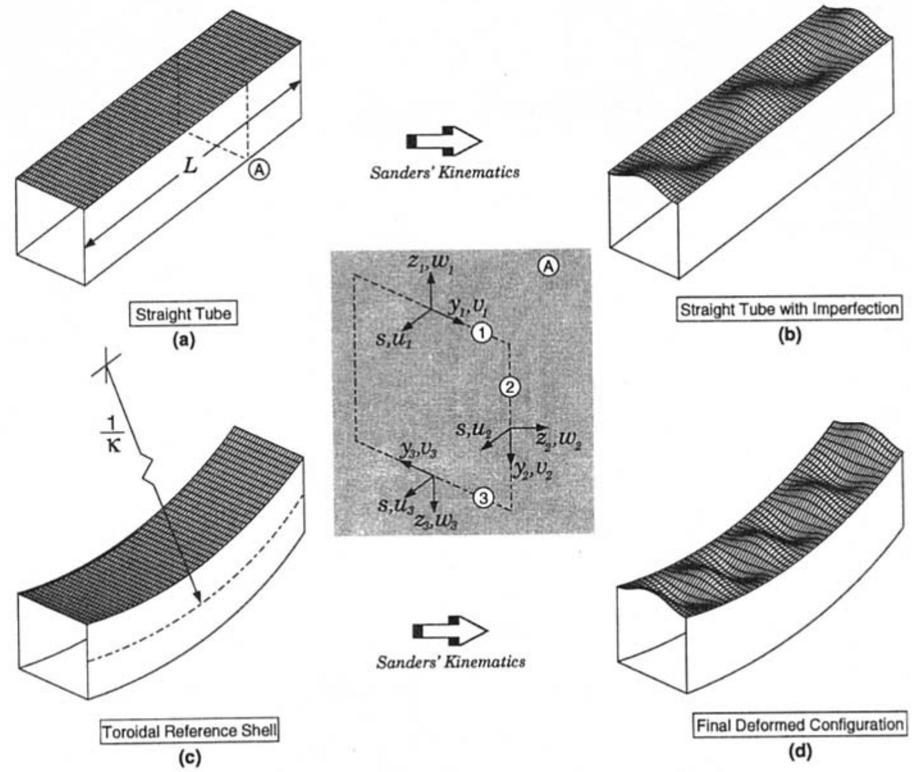

Fig. 4 Deformation composition scheme

tube with respect to the perfect configuration. For any region on the tube cross section, we can write

$$\mathbf{a}^{0(i)} = \begin{bmatrix} 1 + w_{i,s}^{0^2} & w_{i,s}^0 w_{i,y_i}^0 \\ w_{i,y_i}^0 w_{i,s}^0 & 1 + w_{i,y_i}^{0^2} \end{bmatrix}$$

$$\mathbf{b}^{0(i)} = \begin{bmatrix} -w_{i,ss}^0 & -w_{i,sy_i}^0 \\ -w_{i,y_is}^0 & -w_{i,y_iy_i}^0 \end{bmatrix}. \quad (3)$$

For algebraic convenience and ease of interpretation of results we refer the displacement components (u_i, v_i and w_i) of the deformed tube in Fig. 4(d) to a perfect toroid of curvature κ shown in Fig. 4(c). The toroid has the following fundamental forms:

$$\mathbf{a}^{t(1)} = \begin{bmatrix} (1 - h_o\kappa/2)^2 & 0 \\ 0 & 1 \end{bmatrix} \quad \mathbf{b}^{t(1)} = \begin{bmatrix} -\kappa/(1 - h_o\kappa/2) & 0 \\ 0 & 0 \end{bmatrix}$$

$$\mathbf{a}^{t(2)} = \begin{bmatrix} (1 + y_2\kappa)^2 & 0 \\ 0 & 1 \end{bmatrix} \quad \mathbf{b}^{t(2)} = \begin{bmatrix} 0 & 0 \\ 0 & 0 \end{bmatrix}$$

$$\mathbf{a}^{t(3)} = \begin{bmatrix} (1 + h_o\kappa/2)^2 & 0 \\ 0 & 1 \end{bmatrix}$$

$$\mathbf{b}^{t(3)} = \begin{bmatrix} \kappa/(1 + h_o\kappa/2) & 0 \\ 0 & 0 \end{bmatrix}. \quad (4)$$

The fundamental forms for the final deformed tube configuration in Fig. 4(d) can be obtained using

$$a_{\alpha\beta}^{f(i)} = a_{\alpha\beta}^{t(i)} + 2\bar{E}_{\alpha\beta}^{(i)} \quad b_{\alpha\beta}^{f(i)} = b_{\alpha\beta}^{t(i)} + \bar{K}_{\alpha\beta}^{(i)} \quad (5)$$

where $\bar{E}_{\alpha\beta}^{(i)}$ and $\bar{K}_{\alpha\beta}^{(i)}$ are the small strain, moderate rotation Sanders' (1963) membrane, and bending strain components of the deformed configuration with respect to the perfect toroid. They are presented for convenience in the Appendix. The expressions for the total strain components in the final deformed configuration can be obtained as follows:

$$E_{\alpha\beta}^{(i)} = \tfrac{1}{2}(a_{\alpha\beta}^{f(i)} - a_{\alpha\beta}^{0(i)}) \quad K_{\alpha\beta}^{(i)} = (b_{\alpha\beta}^{f(i)} - b_{\alpha\beta}^{0(i)}). \quad (6)$$

For the range of curvature considered, the total strain at any point in the shell can be expressed by

$$\epsilon_{\alpha\beta}^{(i)} = E_{\alpha\beta}^{(i)} + z_i K_{\alpha\beta}^{(i)}. \quad (7)$$

In order to satisfy compatibility of displacements and rotations at the junctions of the three regions, we introduce eight constraint equations, four each at corners **A** and **B** in Fig. 3(b).

At the junction of regions 1 and 2 ($y_1 = b_o/2$, $y_2 = -h_o/2$, s),

$$C_1 = v_2 + w_1 = 0, \quad C_2 = w_2 - v_1 = 0,$$

$$C_3 = \phi_{y_2}^{(2)} - \phi_{y_1}^{(1)} = 0, \quad C_4 = u_2 - u_1 = 0. \quad (8)$$

At the junction of regions 2 and 3 ($y_3 = -b_o/2$, $y_2 = h_o/2$, s),

$$C_5 = v_2 - w_3 = 0, \quad C_6 = w_2 + v_3 = 0,$$

$$C_7 = \phi_{y_2}^{(2)} - \phi_{y_3}^{(3)} = 0, \quad C_8 = u_3 - u_2 = 0. \quad (9)$$

Here, $\phi_{y_i}^{(i)}$ is the rotation of the outward normal of region i about the s-axis (see the Appendix).

Constitutive Model. The geometric and material properties of the tubes considered were such that the material was in the elastic-plastic range during most of the loading process. Consequently, we adopt the J_2 incremental theory of plasticity with isotropic hardening to model the material behavior. The through-thickness stress components are neglected as it is customary in thin shell theory. The total strain increment is assumed to be given by the sum of elastic and plastic components. The elastic components $\{d\epsilon_{ss}^e, d\epsilon_{yy}^e, d\gamma_{sy}^e\}$ are related to the stress increments $\{d\sigma_{ss}, d\sigma_{yy}, d\tau_{sy}\}$ through

$$\begin{bmatrix} d\epsilon_{ss}^e \\ d\epsilon_{yy}^e \\ d\gamma_{sy}^e \end{bmatrix} = \frac{1}{E} \begin{bmatrix} 1 & -\nu & 0 \\ -\nu & 1 & 0 \\ 0 & 0 & 2(1+\nu) \end{bmatrix} \begin{bmatrix} d\sigma_{ss} \\ d\sigma_{yy} \\ d\tau_{sy} \end{bmatrix} \quad (10)$$

where E is Young's modulus and ν is Poisson's ratio. The plastic strain components are given by

$$\begin{bmatrix} d\epsilon_{ss}^P \\ d\epsilon_{yy}^P \\ d\gamma_{sy}^P \end{bmatrix} = \frac{9}{4\sigma_e^2}\left(\frac{1}{E_t} - \frac{1}{E}\right) \times \begin{bmatrix} S_{ss}S_{ss} & S_{ss}S_{yy} & 2S_{ss}S_{sy} \\ S_{yy}S_{ss} & S_{yy}S_{yy} & 2S_{yy}S_{sy} \\ 2S_{sy}S_{ss} & 2S_{sy}S_{yy} & 4S_{sy}S_{sy} \end{bmatrix} \begin{bmatrix} d\sigma_{ss} \\ d\sigma_{yy} \\ d\tau_{sy} \end{bmatrix} \quad (11)$$

where S_{ss}, S_{yy}, and S_{sy} are components of the deviatoric stress and σ_e is the equivalent stress, given by

$$\sigma_e = \sqrt{\sigma_{ss}^2 - \sigma_{ss}\sigma_{yy} + \sigma_{yy}^2 + 3\tau_{sy}^2}. \quad (12)$$

E_t is the tangent modulus of the stress-strain curve. The uniaxial stress-strain curves of the materials were measured experimentally as described in Corona and Vaze (1996) and represented with the three-parameter Ramberg-Osgood fit

$$\epsilon = \frac{\sigma}{E}\left[1 + \frac{3}{7}\left(\frac{\sigma}{\sigma_Y}\right)^{n-1}\right]. \quad (13)$$

The initial yield surface is given by

$$\sigma_e - \sigma_o = 0 \quad (14)$$

where σ_o is the stress at the proportional limit of the uniaxial stress-strain curve. Subsequent yield surfaces are given by

$$\sigma_e - \sigma_{e_{\max}} = 0 \quad (15)$$

where $\sigma_{e_{\max}}$ represents the largest equivalent stress achieved during the loading history.

Principle of Virtual Work. Equilibrium is satisfied by invoking the principle of virtual work. For this problem it can be stated as follows:

$$\int_{-L}^{L} \sum_{i=1}^{3} \int_{A^{(i)}} [\sigma_{ss}^{(i)}\delta\epsilon_{ss}^{(i)} + \sigma_{y_iy_i}^{(i)}\delta\epsilon_{y_iy_i}^{(i)} + \tau_{sy_i}^{(i)}\delta\gamma_{sy_i}^{(i)}]dA^{(i)}ds + \int_{-L}^{L} \sum_{j=1}^{8} [\lambda_j\delta C_j + C_j\delta\lambda_j]ds = 0 \quad (16)$$

where $dA^{(i)} = dy_i dz_i$ and λ_js are Lagrange multiplier functions[2] used to introduce the eight constraints C_j into the principle of virtual work. The right-hand side of the equation is zero since loading is accomplished by prescribing the axial curvature of the tube.

Numerical Solution. The displacement components u_i, v_i, and w_i are discretized using the trigonometric series shown below.

$$u_1 = \epsilon_{ss}^0 s + \sum_{m=1}^{N_a}\left(a_{0m}^u + \sum_{l=1}^{N_f} a_{lm}^u \cos\left(\frac{l\pi y_1}{b_o}\right)\right)\sin(m\hat{p}s),$$

$$v_1 = \sum_{m=0}^{N_a}\left(a_{0m}^v y_1 + \sum_{l=1}^{N_f} a_{lm}^v \sin\left(\frac{l\pi y_1}{b_o}\right)\right)\cos(m\hat{p}s),$$

$$w_1 = \sum_{m=0}^{N_a}\left(a_{0m}^w + \sum_{l=1}^{N_f} a_{lm}^w \cos\left(\frac{l\pi y_1}{b_o}\right)\right)\cos(m\hat{p}s),$$

$$u_2 = \epsilon_{ss}^0 s + \sum_{m=1}^{N_a}\left(b_{0m}^u + \sum_{l=1}^{N_w}\left[b_{lm}^u \cos\left(\frac{l\pi y_2}{h_o}\right) + c_{lm}^u \sin\left(\frac{l\pi y_2}{h_o}\right)\right]\right)\sin(m\hat{p}s),$$

$$v_2 = \sum_{m=0}^{N_a}\left(b_{0m}^v + c_{0m}^v y_2^2 + \sum_{l=1}^{N_w}\left[b_{lm}^v \cos\left(\frac{l\pi y_2}{h_o}\right) + c_{lm}^v \sin\left(\frac{l\pi y_2}{h_o}\right)\right]\right)\cos(m\hat{p}s),$$

$$w_2 = \sum_{m=0}^{N_a}\left(b_{0m}^w + \sum_{l=1}^{N_w}\left[b_{lm}^w \cos\left(\frac{l\pi y_2}{h_o}\right) + c_{lm}^w \sin\left(\frac{l\pi y_2}{h_o}\right)\right]\right)\cos(m\hat{p}s),$$

$$u_3 = \epsilon_{ss}^0 s + \sum_{m=1}^{N_a}\left(d_{0m}^u + \sum_{l=1}^{N_f} d_{lm}^u \cos\left(\frac{l\pi y_3}{b_o}\right)\right)\sin(m\hat{p}s),$$

$$v_3 = \sum_{m=0}^{N_a}\left(d_{0m}^v y_3 + \sum_{l=1}^{N_f} d_{lm}^v \sin\left(\frac{l\pi y_3}{b_o}\right)\right)\cos(m\hat{p}s),$$

$$w_3 = \sum_{m=0}^{N_a}\left(d_{0m}^w + \sum_{l=1}^{N_f} d_{lm}^w \cos\left(\frac{l\pi y_3}{b_o}\right)\right)\cos(m\hat{p}s), \quad (17)$$

where $\hat{p} = \pi/L$. The coefficient d_{00}^w is set to zero to suppress rigid-body motion. The Lagrange multiplier functions are also expressed as trigonometric series expansions of the form

$$\lambda_j = \sum_{m=0}^{N_a} \lambda_{jm}\cos(m\hat{p}s) \quad \text{for} \quad j = 1\text{–}3,\ 5\text{–}7,$$

$$\lambda_j = \sum_{m=1}^{N_a} \lambda_{jm}\sin(m\hat{p}s) \quad \text{for} \quad j = 4 \quad \text{or} \quad 8. \quad (18)$$

Substituting Eqs. (17) and (18) into Eqs. (A1)–(A2), (5)–(9) and into (16) yields a system of $(18N_a + 2(N_f + N_w)(2 + 3N_a) + 13)$ nonlinear algebraic equations in terms of the coefficients of the series expansions of the displacements and the coefficients of the Lagrange multiplier series. The system of equations is solved using the Newton-Raphson method. The nonlinearity in the constitutive relations is handled using the same iterative method. The integrations in (16) are carried out using Gaussian quadrature. In view of the size of the problem, it was important to limit the number of unknown coefficients and integration points. Accurate solutions were obtained with $N_f = N_w = 4$, five integration points along y_1 and y_3, 12 points along y_2 and three points through the thickness. The value of N_a as well as the number of integration points in the axial direction depend on the nature of the case considered and will be indicated for each case in the Results section.

Loading of the structure is achieved by prescribing the curvature κ incrementally. Following convergence of the iterative scheme, the strains and stresses are updated and the resulting bending moment evaluated from

$$M = 2\sum_{i=1}^{3}\int_{A^{(i)}} \sigma_{ss}^{(i)}\zeta^{(i)}dA^{(i)} \quad (19)$$

at any value of s, where $\zeta^{(i)}$ is the correct distance from any point in region i to the line $y_2 = 0$.

[2] Since C_js are functions of the axial coordinate s, the corresponding λ_js are functions of s as well.

Table 1 Geometric and material parameters used in the calculations. ($\nu = 0.3$)

h/t	b, mm (in)	h, mm (in)	t, mm (in)	E, GPa (Msi)	n	σ_Y, MPa (ksi)	σ_p, MPa (ksi)	σ_o, MPa (ksi)
28.6	25.25 (0.9942)	25.49 (1.0035)	0.886 (0.0349)	208 (30.1)	13.4	534 (77.5)	296 (43.0)	564 (81.8)
20.4	25.23 (0.9932)	25.52 (1.0047)	1.21 (0.0476)	210 (30.5)	15.2	610 (88.5)	402 (58.3)	642 (93.1)
15.4	25.15 (0.9901)	25.29 (0.9956)	1.61 (0.0633)	206 (29.9)	15.5	642 (93.1)	475 (68.9)	659 (95.6)

Results

The results presented in this paper were obtained by introducing a geometric imperfection in the initial configuration of the tube. The bending process was then simulated until a limit moment curvature was exceeded. The general response and stability characteristics of a given tube were deduced from the observed responses for various different types of initial imperfection.

In the case of pure bending of tubes with circular cross section, Ju and Kyriakides (1992) demonstrated that prediction of the curvature at which a limit moment instability occurs requires a formulation which includes axial variations in the displacement of the shell if it has sufficiently high diameter-to-thickness ratio. Corona and Vaze (1996) demonstrated that accurate prediction of the limit moment instabilities which lead to collapse in the case of square tubes with sufficiently high h/t also may require a model which can take the development and growth of ripples into account, similar to that presented by Ju and Kyriakides (1992). Predictions obtained by neglecting the development of ripples yielded limit moments which were entirely due to uniform deformation of the cross section along the specimen. The difference between experimentally measured and predicted limit moment curvatures ranged from 8.7 percent for tubes with $h/t = 15.4$ to 187 percent for tubes with $h/t = 28.6$.

The first imperfection considered is harmonic in s with wavelength λ and is given by

$$\frac{w_1^{0(I)}}{h} = \frac{a_\Delta}{2}\left\{1 + \cos\left(\frac{2\pi y_1}{b_o}\right)\right\}\cos\left(\frac{2\pi s}{\lambda}\right). \quad (20)$$

This imperfection was introduced in the compression flange of the tube only. As it is customary in imperfection sensitivity studies, λ was chosen to be $\lambda_{cr} = 1.12h$, which is the axial wavelength of the bifurcation buckling mode calculated in Corona and Vaze (1996) for the tubes considered. This value also agrees with the experimental value given in the Introduction and is the same for all the h/t values considered. In view of the harmonic nature of this imperfection, the length of the domain L need only be $\lambda_{cr}/2$. A parametric study indicated that $N_a = 3$ and 16 Gauss integration points in the axial direction provided excellent accuracy.

Measurements by Vaze (1996) indicated that the initial imperfection of the tubes tested had short wavelength components with amplitudes $a_\Delta \approx 0.0002$, so values of a_Δ in this vicinity will be considered. The geometric and material parameters used in all cases considered are shown in Table 1. Figure 5(a) shows the predicted M-κ response of a tube with $h/t = 20.4$ for various values of a_Δ. The case $a_\Delta = 0$ was conducted with $m = 0$ in (17) and is presented for comparison. It is clear that the four M-κ responses are virtually indistinguishable for $\kappa/\kappa_1 < 1.5$ but diverge from the perfect case as they approach their limit moment curvatures (κ_L, identified by ↑). Notice that κ_L steadily decreases with increasing amplitude of the imperfection.

Figure 5(b) shows the predicted growth of Δ for the case $a_\Delta = -0.0005$ at regular increments in curvature $\delta\kappa/\kappa_1 = 0.186$. The initial imperfection has been shown in dashed line. As demonstrated experimentally, the growth of Δ with curvature has two components. A uniform axial component, which is dominant for lower values of curvature and a component which corresponds to an increase in the amplitude of the axial variation. This component becomes more dominant as the curvature increases. The seventh line in Fig. 5(b) nearly corresponds to the bifurcation curvature for this tube ($\kappa_{cr}/\kappa_1 = 1.24$). Indeed, it is after this juncture that the second component seems to become more noticeable with Δ increasing faster at $s = 0$. The next to the highest trace nearly corresponds to the value of curvature at which the limit moment developed.

Results similar to the ones in Fig. 5 are given in Figs. 6 and 7 for cases with $h/t = 28.6$ and $h/t = 15.4$, respectively. They qualitatively resemble the results in Fig. 5, but exhibit some important quantitative differences. Figure 6(a) shows that for a tube with $h/t = 28.6$, the reduction in κ_L with increasing a_Δ is more drastic than that for $h/t = 20.4$ (the limit moment curvature for the case $a_\Delta = 0$, not shown in the figure, occurs at $\kappa/\kappa_1 = 5.40$). Also, Fig. 6(b) shows that the increase in the amplitude of the axial variation is even more pronounced, compared to the uniform component, than in the case with $h/t = 20.4$. In fact, the growth of the cross-sectional parameter Δ

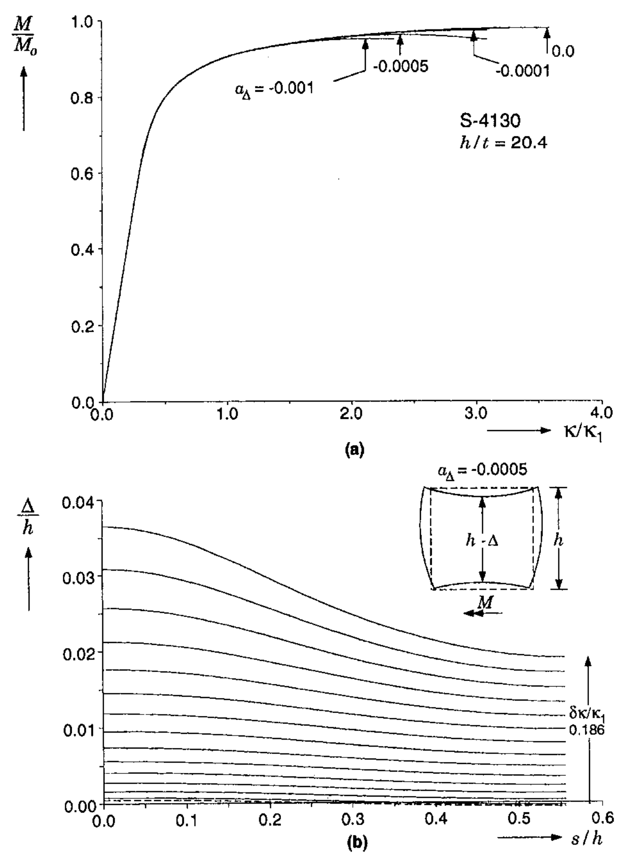

Fig. 5 Response of a tube with $h/t = 20.4$; (a) sensitivity of the moment-curvature response to the severity of initial imperfection $w_1^{0(I)}$, (b) predicted growth of Δ for $a_\Delta = -0.0005$

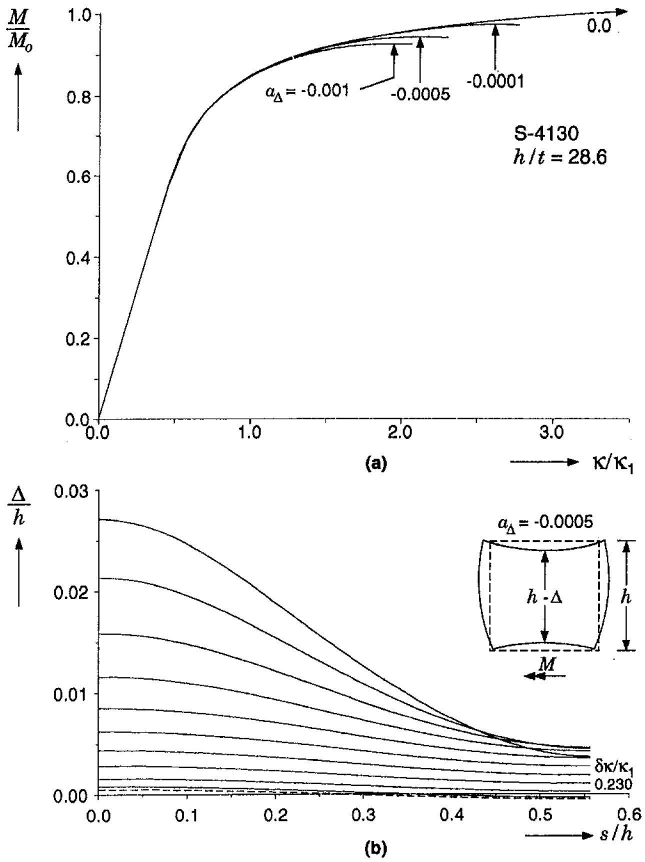

Fig. 6 Response of a tube with $h/t = 28.6$; (a) sensitivity of the moment-curvature response to the severity of initial imperfection $w_1^{0(i)}$, (b) predicted growth of Δ for $a_\Delta = -0.0005$

reverses at points close to $s = \lambda_{cr}/2$ as κ_L is approached. Predictions for curvatures higher than κ_L are not accurate since the use of the present imperfection cannot simulate the localization process which gives rise to the kink which appears at collapse.

On the other hand, the reduction in κ_L for increasing values of a_Δ is mild for tubes with $h/t = 15.4$ as shown in Fig. 7(a). Notice that even the case $a_\Delta = 0$ predicts a value of κ_L which falls in the vicinity of the imperfect cases considered. The reason for this is apparent in Fig. 7(b) where the uniform component of Δ is found to be dominant throughout the loading history.

Figure 8 compares predictions of the growth of Δ at $s = 0$ and $s = \lambda_{cr}/2$ with experimental measurements. The measurements were conducted at the midspan of the specimens but the position of the measuring device with respect to the ripples is unknown, that is, it can not be correlated to a specific value of s. It can be expected, however, that the predicted responses will bound the experimental measurements. This is indeed the case in Figs. 8(a) and (b). The measured growth of Δ in Fig. 8(c) exceeds the predicted one beyond $\kappa/\kappa_1 = 1.0$. This can be attributed to the fact that Δ was monitored in the region where localization occurred (see Fig. 9(b) in Corona and Vaze, 1996) and near the point where the kink developed. The agreement between experiment and analysis is very good in all cases. The somewhat abrupt changes in the curvature of the experimental curves in Figs. 8(a) ($\kappa/\kappa_1 = 0.8$) and (b) ($\kappa/\kappa_1 = 0.5$) are due to the presence of residual stresses as discussed in Corona and Vaze (1996). This was not taken into account in the present analysis.

The values of κ_L found in all cases discussed above have been tabulated in Table 2. The experimentally determined values have also been given in the table. As observed previously, the values of κ_L for $a_\Delta = 0$ are consistently higher than the experimental ones. However, introducing the imperfection results in a reduction in κ_L to the range observed in the experiments. The exception was the case with $h/t = 28.6$ which has an experimentally determined value of κ_L which is lower than predicted. These tubes, however, exhibited significant residual stresses, which may be responsible for the disagreement. Notice that the higher the h/t ratio, the more imperfection sensitive the structure.

In order to verify the assumption that setting $\lambda = \lambda_{cr}$ represents the most critical imperfection, a study was conducted to quantify the influence of λ on the response. This study was conducted by varying λ/h between 0.8 and 1.3 with $a_\Delta = -0.0005$. The external work (W) required to bend a unit length of tube up to a curvature κ_L was then determined by integrating the moment-curvature response,

$$W = \int_0^{\kappa_l} M d\kappa. \tag{21}$$

The results are shown in Fig. 9 for tubes with $h/t = 20.4$. The work done when $\lambda = \lambda_{cr}$ is denoted by W_{cr} and is used to normalize W. The graph indicates that the least amount of work required to reach κ_L indeed occurs when λ/h is in the vicinity of 1.12.

The experimental results presented in the introduction show that the tubes tested had a ''long'' wavelength imperfection with significantly higher amplitude than imperfection features with shorter wavelengths. In order to investigate the effect of the long wavelength component of the imperfection, results were also generated using an imperfection which superimposes short and long wavelength features as follows:

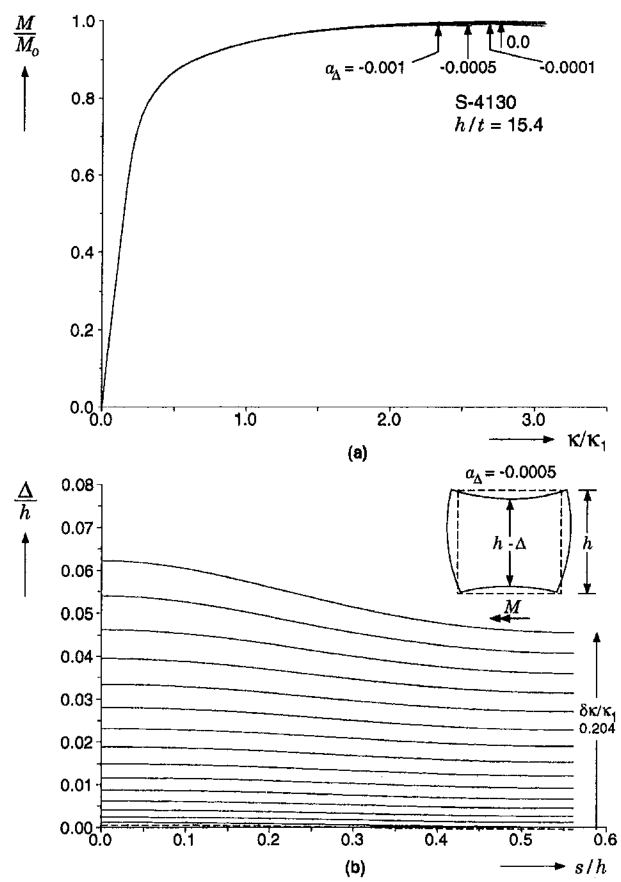

Fig. 7 Response of a tube with $h/t = 15.4$; (a) sensitivity of the moment-curvature response to the severity of initial imperfection $w_1^{0(i)}$, (b) predicted growth of Δ for $a_\Delta = -0.0005$

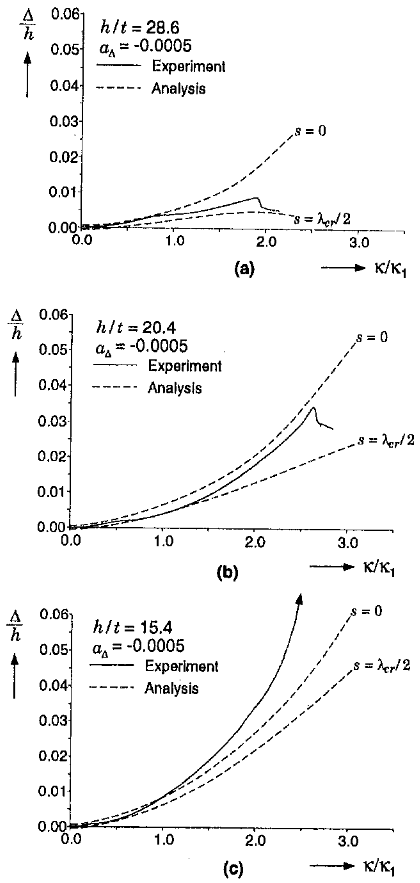

Fig. 8 Comparison of the measured growth of Δ with predictions at $s/h = 0$ and $s/h = \lambda_{cr}/2h$; (*a*) $h/t = 28.6$, (*b*) 20.4, and (*c*) 15.4

$$\frac{w_1^{0(II)}}{h} = \left\{1 + \cos\left(\frac{2\pi y_1}{b_o}\right)\right\} \times \left[\frac{a_\Delta}{2}\cos\left(\frac{2\pi s}{\lambda}\right) + \frac{b_\Delta}{2}\cos\left(\frac{2\pi s}{7\lambda}\right)\right]. \quad (22)$$

The domain of the region analyzed had a length of $7\lambda_{cr}/2$, which nearly corresponds to one-half long wavelength in the initial imperfection shown in Fig. 1. $N_a = 14$ and 56 axial Gauss integration points were used in this case. Results obtained for $a_\Delta = -0.0001$, $b_\Delta = -0.001$ (this value was chosen from actual measurement of the specimen), are shown in Fig. 10. Moment-curvature responses obtained with an initially perfect geometry and with $a_\Delta = -0.0001$, $b_\Delta = 0$ are also shown in Fig. 10 for comparison. The results indicate that the long wavelength feature of the initial imperfection had a negligible effect on the predicted value of κ_L. The evolution of Δ along the domain is shown in Fig. 10(*b*). The dashed line represents the initial imperfection. It is clear that both components of the imperfection and the uniform component of Δ grow during bending, but the long wavelength component grows the slowest. The limit moment occurred at $\kappa/\kappa_1 = 2.99$, between the last and next-to-the-last lines in Fig. 10(*b*). Also note that the short waves located in the crests of the long waves grow somewhat faster, especially near the limit moment. This trend is also clear in the experimental results presented in Fig. 1(*b*). In fact, the kink which formed in the compression flange at collapse in the experiments occurred preferably at locations where the long wavelength imperfection produced a maximum in Δ.

Table 2 Limit moment curvatures κ_l/κ_1 for imperfection $w_1^{0(I)}$

a_Δ	κ_l/κ_1 $h/t = 15.4$	$h/t = 20.4$	$h/t = 28.6$
0.0	2.76	3.59	5.40
−0.0001	2.68	2.98	2.61
−0.0005	2.53	2.40	2.12
−0.0010	2.32	2.12	1.94
Experiment	2.54	2.50	1.88

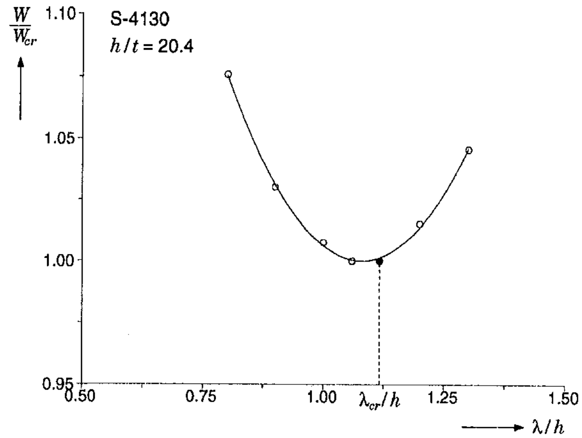

Fig. 9 Effect of λ on the work done (W) prior to the limit moment

In order to simulate the localization process which leads to the formation of a kink in circular tubes with intermediate diameter-to-thickness ratios, Ju and Kyriakides (1992) used an imperfection with a domain spanning several short-wave ripples

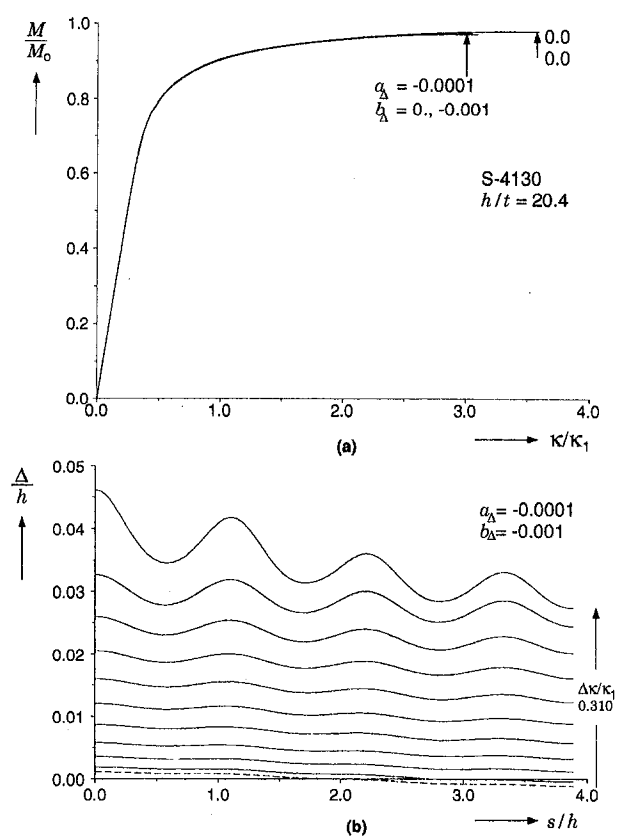

Fig. 10 Response of a tube with $h/t = 20.4$ to an imperfection of the form $w_1^{0(II)}$; (*a*) moment-curvature, (*b*) predicted growth of Δ for $a_\Delta = -0.0001$, $b_\Delta = 0.001$

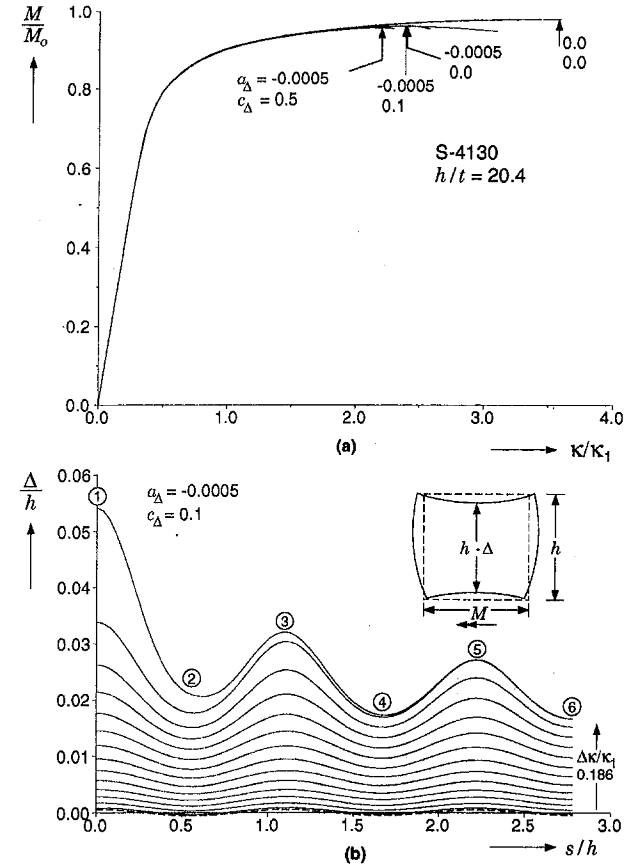

Fig. 11 Response of a tube with h/t = 20.4 to an imperfection of the form $w_1^{0(III)}$; (a) moment-curvature, (b) predicted growth of Δ for a_Δ = −0.0005, c_Δ = 0.1

in which one of the ripples is "biased," that is, it has larger amplitude than the rest. In the problem at hand, such an imperfection can be expressed as

$$\frac{w_1^{0(III)}}{h} = \frac{a_\Delta}{2}\left\{1 + \cos\left(\frac{2\pi y_1}{b_o}\right)\right\} \times \left[1 + c_\Delta \cos\left(\frac{2\pi s}{5\lambda}\right)\right] \cos\left(\frac{2\pi s}{\lambda}\right). \quad (23)$$

For negative values of a_Δ and positive values of c_Δ, this imperfection gives the ripple at $s = 0$ slightly higher amplitude than the others. The value of c_Δ dictates the extent of the bias. The length of the domain in this case is $L = 2.5\lambda$. Again, the wavelength λ is chosen to be λ_{cr}. The axial direction was discretized by setting $N_a = 12$ and using 56 Gauss integration points.

Figure 11 shows a set of results obtained for a tube with $h/t = 20.4$. The moment-curvature response has been plotted in Fig. 11(a) for cases with $a_\Delta = -0.0005$ and three values of c_Δ. Results from the perfect case are also shown for comparison. The data demonstrates that increasing the bias causes a reduction in the limit moment curvature since the imperfection at $s = 0$ becomes more severe. Figure 11(b) shows the growth of the parameter Δ along the tube at regular curvature increments $\delta\kappa/\kappa_1 = 0.186$ for the case $a_\Delta = -0.0005$ with $c_\Delta = 0.1$. Note that the effect of c_Δ is small and hardly noticeable in the initial imperfection shown by the dashed line. As the curvature increases, all ripples grow as expected but, as κ_L is approached, the biased ripple grows faster. The limit moment occurs at $\kappa/\kappa_1 = 2.38$, just prior to the next to the last line in Fig. 11(b).

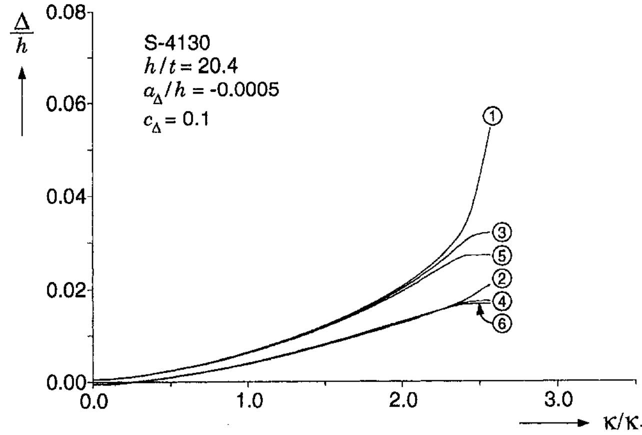

Fig. 12 Growth of Δ at six axial locations for h/t = 20.4 with an initial imperfection of the form $w_1^{0(III)}$. Plot based on Fig. 11(b)

Once the limit moment is exceeded, the ripple at $s = 0$ grows much more rapidly while Δ stops growing for $s/h > 2$. This behavior closely resembles the experimental observations. By comparing the M-κ response in the cases with $c_\Delta = 0$ and 0.1 note that, although $c_\Delta = 0.1$ produces a negligible change in κ_L, the post limit moment response displays a more precipitous drop in bending moment. Ju and Kyriakides pointed out that the post limit moment response is also highly dependent on the length of the tubes considered.

Figure 12 illustrates the growth of Δ as function of curvature at the six points identified by the circled numbers in Fig. 11(b). It is clear that, at low curvature, the traces of Δ at the three peaks and the three troughs are indistinguishable, but Δ grows somewhat faster at the peaks. For high curvature the traces spread and once the limit moment is reached, the trace at 1 rises rapidly but those at 3 and 5 slow down considerably. Similarly, Δ at 2 continues to rise but Δ at 4 stops growing and Δ at 6 reverses its growth as the moment drops.

In order to compare experimental and analytical results, the case presented in Fig. 1 was simulated using an initial imperfection of the form $w_1^{0(III)}$ with $a_\Delta = -0.0002$ (as determined from measurements) and $c_\Delta = 0.1$. Measurements of Δ at the location of the ripple which eventually localized and formed a kink as function of curvature are shown by "•" in Fig. 13. The scatter appears because the data were obtained from measurements taken with a moving instrument. Naturally, this instrument is less accurate than the stationary instruments used to measure Δ in Fig. 8. The predicted growth of Δ at $s = 0$ is shown as a solid line. The agreement between experiment and analysis is

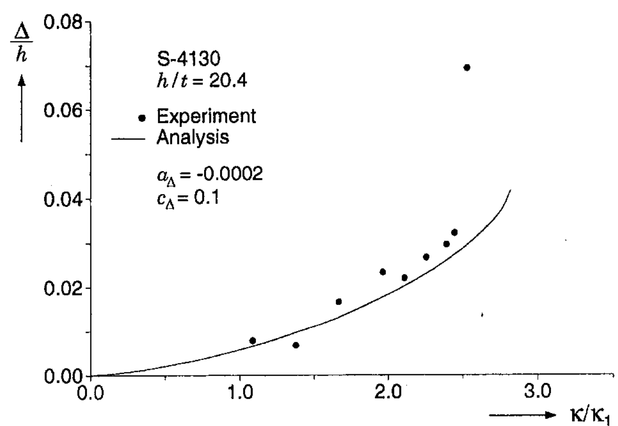

Fig. 13 Comparison of measured and predicted development of Δ at the fastest growing crest in Fig. 1

very good. The predicted value of κ_L was ten percent higher than the measured value. This difference is likely to be due to the inhomogeneity of the material properties and the presence of residual stresses in the actual specimens (see Corona and Vaze, 1996).

Summary and Conclusions

This paper addressed the response and stability of steel tubes of square cross section under pure bending. An analytical model with sufficiently nonlinear kinematics to accommodate axial variations of the deformation of the cross section was developed. The material behavior was modeled using J_2 incremental plasticity with isotropic hardening. The objective of the investigation was to enable accurate prediction of the limit moment instability which characterizes collapse of such tubes.

The results obtained agree well with experimental data and suggest that collapse of the tubes is imperfection sensitive. The degree of imperfection sensitivity is particularly high for tubes in the high end of the range of h/t considered ($h/t > 18$, approximately, from observation of the experimental results), while collapse of tubes with low h/t is relatively imperfection insensitive. In fact, in the case with $h/t = 15.4$, the axial variation in cross section deformation is not very significant in the determination of the limit moment curvature and can be neglected.

The tubes used in the experiments had long wavelength imperfection components of amplitude five times larger than that of components with wavelengths in the order of that of the buckling mode. The results obtained here, however, indicate that the effect of such long wavelength component in the imperfection can be neglected in the calculation of the limit moment curvature. The phenomenon of ripple localization and formation of the kink which appears on the compression flange of the tubes upon collapse was successfully simulated by introducing an imperfection in which the amplitude of the ripples is biased, similar to the one used by Ju and Kyriakides (1992) for circular tubes. Again, comparison with experiment was very good.

Acknowledgments

The work reported was carried out with the financial support of the National Science Foundation under Grant No. MSS92-10894. The support of the University of Notre Dame is also greatly appreciated.

References

Brazier, L. G., 1927, "On the Flexure of Thin Cylindrical Shells and Other 'Thin' Sections," *Royal Society Proceedings, Mathematics and Physics*, Vol. A116, pp. 104–114.

Corona, E., and Vaze, S. P., 1996, "Buckling of Elastic-Plastic Square Tubes Under Bending," *International Journal of Mechanical Sciences*, Vol. 38, pp. 753–775.

Fabian, O., 1981, "Elastic-Plastic Collapse of Long Tubes Under Combined Bending and Pressure Load," *Ocean Engineering*, Vol. 8, pp. 295–330.

Hasan, S. W., and Hancock, G. J., 1989, "Plastic Bending Test of Cold-Formed Rectangular Hollow Sections," *Journal of the Australian Institute of Steel Construction*, Vol. 23, pp. 2–19.

Kyriakides, S., and Ju, G. T., 1992, "Bifurcation and Localization Instabilities in Cylindrical Shells Under Bending. Part I: Experiments," *International Journal of Solids and Structures*, Vol. 29, pp. 1117–1142.

Ju, G. T., and Kyriakides, S., 1992, "Bifurcation and Localization Instabilities in Cylindrical Shells Under Bending. Part II: Predictions," *International Journal of Solids and Structures*, Vol. 29, pp. 1143–1171.

Sanders, J. L., 1963, "Nonlinear Theories for Thin Shells," *Quarterly of Applied Mathematics*, Vol. 21, pp. 21–36.

Timoshenko, S. P., 1923, "Bending Stresses in Curved Tubes of Rectangular Cross-Section," *Transactions of the ASME*, Vol. 45, pp. 135–140.

Vaze, S. P., 1996, "Response and Buckling of Elastic-Plastic Square Tubes Under Cyclic Bending," Structural and Solid Mechanics Laboratory Report 96/2, Department of Aerospace and Mechanical Engineering, University of Notre Dame, Notre Dame, IN.

APPENDIX

Sanders' Kinematics

$$\bar{E}_{ss}^{(i)} = \frac{u_{i,s}}{\alpha_s^{(i)}} + \frac{\alpha_{s,y_i}^{(i)} v_i}{\alpha_s^{(i)}\alpha_{y_i}^{(i)}} + \frac{w_i}{R_s^{(i)}} + \frac{1}{2}\phi_s^{(i)^2} + \frac{1}{2}\phi^{(i)^2}$$

$$\bar{E}_{y_iy_i}^{(i)} = \frac{v_{i,y_i}}{\alpha_{y_i}^{(i)}} + \frac{\alpha_{y_i,s}^{(i)} u_i}{\alpha_s^{(i)}\alpha_{y_i}^{(i)}} + \frac{w_i}{R_{y_i}^{(i)}} + \frac{1}{2}\phi_{y_i}^{(i)^2} + \frac{1}{2}\phi^{(i)^2}$$

$$\bar{E}_{sy_i}^{(i)} = \frac{1}{2}\left[\frac{v_{i,s}}{\alpha_s^{(i)}} + \frac{u_{i,y_i}}{\alpha_{y_i}^{(i)}} - \frac{\alpha_{s,y_i}^{(i)} u_i}{\alpha_s^{(i)}\alpha_{y_i}^{(i)}} - \frac{\alpha_{y_i,s}^{(i)} v_i}{\alpha_s^{(i)}\alpha_{y_i}^{(i)}} + \phi_s^{(i)}\phi_{y_i}^{(i)}\right] = \bar{E}_{y_is}^{(i)}$$

$$\bar{K}_{ss}^{(i)} = \frac{\phi_{s,s}^{(i)}}{\alpha_s^{(i)}} + \frac{\alpha_{s,y_i}^{(i)}\phi_{y_i}^{(i)}}{\alpha_s^{(i)}\alpha_{y_i}^{(i)}}$$

$$\bar{K}_{y_iy_i}^{(i)} = \frac{\phi_{y_i,y_i}^{(i)}}{\alpha_{y_i}^{(i)}} + \frac{\alpha_{y_i,s}^{(i)}\phi_s^{(i)}}{\alpha_s^{(i)}\alpha_{y_i}^{(i)}}$$

$$\bar{K}_{sy_i}^{(i)} = \frac{1}{2}\left[\frac{\phi_{y_i,s}^{(i)}}{\alpha_s^{(i)}} + \frac{\phi_{s,y_i}^{(i)}}{\alpha_{y_i}^{(i)}} - \frac{\alpha_{s,y_i}^{(i)}\phi_s^{(i)}}{\alpha_s^{(i)}\alpha_{y_i}^{(i)}} - \frac{\alpha_{y_i,s}^{(i)}\phi_{y_i}^{(i)}}{\alpha_s^{(i)}\alpha_{y_i}^{(i)}} + \left(\frac{1}{R_{y_i}^{(i)}} - \frac{1}{R_s^{(i)}}\right)\phi^{(i)}\right] = \bar{K}_{sy_i}^{(i)} \quad \text{(A1)}$$

where

$$\phi_s^{(i)} = \frac{-w_{i,s}}{\alpha_s^{(i)}} + \frac{u_i}{R_s^{(i)}}$$

$$\phi_{y_i}^{(i)} = \frac{-w_{i,y_i}}{\alpha_{y_i}^{(i)}} + \frac{v_i}{R_{y_i}^{(i)}}$$

$$\phi^{(i)} = \tfrac{1}{2}\left[(\alpha_{y_i}^{(i)} v_i)_{,s} - (\alpha_s^{(i)} u_i)_{,yi}\right] \quad \text{(A2)}$$

and, for a toroid of rectangular cross section,

$$\alpha_s^{(1)} = 1 - h_o\kappa/2 \quad \alpha_{y1}^{(1)} = 1 \quad 1/R_s^{(1)} = -1/(1/\kappa - h_o/2) \quad 1/R_{y1}^{(1)} = 0$$

$$\alpha_s^{(2)} = 1 + \kappa y_2 \quad \alpha_{y2}^{(2)} = 1 \quad 1/R_s^{(2)} = 0 \quad 1/R_{y2}^{(2)} = 0$$

$$\alpha_s^{(3)} = 1 + h_o\kappa/2 \quad \alpha_{y2}^{(3)} = 1 \quad 1/R_s^{(3)} = 1/(1/\kappa + h_o/2) \quad 1/R_{y2}^{(3)} = 0.$$

The Hamilton-Jacobi Equation Applied to Continuum

C. M. Leech
Department of Mechanical Engineering,
UMIST,
Manchester M60 1QD, U.K.
Fellow ASME

The Hamilton-Jacobi partial differential equation is established for continuum systems; to do this a new concept in material distributions is introduced. The Lagrangian and Hamiltonian are developed, so that the Hamilton-Jacobi equation can be formulated and the principal function defined. Finally the principal function is constructed for the dynamics of a one-dimensional linear elastic bar; the solution for its' vibrations is then established following the differentiation of the principal function.

Introduction

The Hamilton-Jacobi theory applied to discrete systems has been well established (Lanczos, 1966; Goldstein, 1980; Pars, 1965; Landau and Lifshitz, 1969; Leech, 1965; Synge, 1960) and is indeed a major topic in classical mechanics. The principal function S is the dependent variable and the generalized coordinates are the independent variables; for discrete systems these are q_i, $i = 1 \ldots n$ for an n-degree-of-freedom system. The dynamics of the system is given by the gradient with respect to the constants of integration, of the principal function being constant, this consequent to the theory of ignorable coordinates.

The exploitation of Hamilton-Jacobi theory for the solution of the dynamics of mechanical systems is the subject of some discussion; it may be that a unification of dynamics is possible and the theory will be commonplace in the way that Hamiltons principle and the Lagrange equations are common features of many dynamic problems. It is with this in mind that the following development is pursued.

The principal function S has often been constructed as a summation of separable functions and this restricted form is useful for many classical systems. Leech and Tabarrok (1996) showed the existence of nonseparable forms for the principal function and the inclusion of these increase the number of known solutions to the Hamilton-Jacobi partial differential equation. These nonseparable functions are useful for rheonomic systems, but at this time they are restricted to quadratic and linear forms of the potential/strain energy of the system; the separable forms are useful for scleronomic systems and are not restricted to quadratic potential energy forms.

The analysis of continuous systems by variational mechanics has been well considered; the establishment of the kinetic, potential, and strain energies is widely used to generate partial differential equations whose solutions model the behavior of the relevant system. The approaches of Konopinski (1969) and Saletan and Cromer (1971) are typical. However, it will be seen that the representations of the energies are not properly consistent with variational field mechanics, and have been useful solely because most fields are diagonal or the result of Local Action (Truesdell, 1965, 1977); this will be discussed later. In this paper the Lagrangian for a general continuum, albeit one-dimensional, will be posed and from this the generalized momentum, the Hamiltonian, and finally the Hamilton-Jacobi partial differential equation.

Contributed by the Applied Mechanics Division of THE AMERICAN SOCIETY OF MECHANICAL ENGINEERS for publication in the ASME JOURNAL OF APPLIED MECHANICS.

Discussion on this paper should be addressed to the Technical Editor, Professor Lewis T. Wheeler, Department of Mechanical Engineering, University of Houston, Houston, TX 77204-4792, and will be accepted until four months after final publication of the paper itself in the ASME JOURNAL OF APPLIED MECHANICS.

Manuscript received by the ASME Applied Mechanics Division, June 29, 1995; final revision, Aug. 29, 1996. Associate Technical Editor: S. W. Shaw.

Nonseparable solutions for the principal function are then suggested following the approach of Leech and Tabarrok (1996) and the whole is applied to a real problem, the axial vibrations of a shaft, the resulting solution being recognizable as a form of solution obtainable by classical methods.

Hamilton-Jacobi for Continuous Systems

Assume a one-dimension domain 0-L, a coordinate ξ over that domain and a dependent variable $w(\xi, t)$; then generally the Lagrangian can be written

$$\mathcal{L} = \frac{1}{2}\int_0^L \int_0^L \left[M(\xi, \zeta)\frac{\partial w(\xi, t)}{\partial t}\frac{\partial w(\zeta, t)}{\partial t} - K(\xi, \zeta) D_\xi w(\xi, t) D_\zeta w(\zeta, t)\right] d\xi d\zeta$$

where $M(\xi, \zeta)$ is mass distribution and $K(\xi, \zeta)$ is stiffness distribution over the domain $0 \le \xi, \zeta \le L$; D_ξ and D_ζ are differential operators. The M and K shown above are not usual and will be discussed later.

The next step is to manipulate the integrand so that the differentials D_ξ and D_ζ operate on the stiffness distribution and not on the dependent variable; this is done by integrating by parts and assuming that the edges of the domain are fixed, the following results:

$$\mathcal{L} = \frac{1}{2}\int_0^L \int_0^L \left[M(\xi, \zeta)\frac{\partial w(\xi, t)}{\partial t}\frac{\partial w(\zeta, t)}{\partial t} - w(\xi, t)\, w(\zeta, t) D_\xi D_\zeta K(\xi, \zeta)\right] d\xi d\zeta.$$

The generalized momentum $p(\xi, t)$ is given by

$$p(\xi, t) = \frac{\partial \mathcal{L}}{\partial \dfrac{\partial w(\xi, t)}{\partial t}} = \int_0^L M(\xi, \zeta)\frac{\partial w(\zeta, t)}{\partial t} d\zeta$$

and this can be inverted to give

$$\frac{\partial w(\zeta, t)}{\partial t} = \int_0^L M^{-1}(\zeta, \xi) p(\xi, t) d\xi$$

where $M^{-1}(\xi, \zeta)$ is the inverse of $M(\xi, \zeta)$ such that

$$\int_0^L M(\xi, \eta)\, M^{-1}(\eta, \zeta) d\eta = \delta(\xi - \zeta)$$

and where $\delta(\xi - \zeta)$ is the Dirac delta function.

The Hamiltonian H is

$$H = \int_0^L p(\xi, t) \frac{\partial w(\xi, t)}{\partial t} d\xi - \mathcal{L}$$

$$= \frac{1}{2} \int_0^L \int_0^L [M^{-1}(\xi, \zeta) p(\xi, t)\, p(\zeta, t) + w(\xi, t)\, w(\zeta, t) D_\zeta D_\xi K(\xi, \zeta)] d\xi d\zeta.$$

The Hamilton-Jacobi equation is

$$\frac{\partial S}{\partial t} + H\left(\frac{\partial S}{\partial w(\xi, t)}, w(\xi, t), t\right) = 0$$

where S is the Hamilton principal function, a function of the generalized coordinates $w(\xi, t)$ and time t; this is a first-order partial differential equation in time and the generalized coordinate space $w(\xi)$. The generalized momenta $p(\xi)$ have been replaced by the gradient of the principal function S in the generalized coordinate space $w(\xi)$,

$$\frac{\partial S}{\partial w(\xi, t)} = p(\xi, t).$$

Finally the constant equation of motion is obtained by differentiating with respect to the constants of integration

$$\Phi(\xi) = \frac{\partial S}{\partial w(\xi, t=0)} \text{ for all } \xi \text{ in } \langle 0, L \rangle$$

and the application of this equation gives the equation of motion of the system.

Nonseparable Solutions for the Principal Function S

A nonseparable form for S is

$$S = \frac{1}{2} \int_0^L \int_0^L a(\xi, \zeta, t)\, w(\xi, t)\, w(\zeta, t) d\xi d\zeta + \int_0^L b(\xi, t)\, w(\xi, t) d\xi + c(t).$$

An equivalent form for the principal function for discrete systems has been discussed by Leech and Tabarrok (1996); there the function $a(t)$ has been designated the kernel function and is dependent only on the system configuration. $b(t)$ and $c(t)$ are called the primary and secondary system functions and these are dependent on the system initial conditions, that is the point in configuration space. Because of the quadratic form associated with $a(\xi, \zeta, t)$, it is symmetric, that is $a(\xi, \zeta, t) = a(\zeta, \xi, t)$; it then follows that

$$\frac{\partial S}{\partial w(\xi, t)} = \int_0^L a(\xi, \zeta, t)\, w(\zeta, t) d\zeta + b(\xi, t)$$

and that

$$\frac{\partial S}{\partial t} = \frac{1}{2} \int_0^L \int_0^L \frac{\partial a(\xi, \zeta, t)}{\partial t} w(\xi, t)\, w(\zeta, t) d\xi d\zeta + \int_0^L \frac{\partial b(\xi, t)}{\partial t} w(\xi, t) d\xi + \frac{\partial c(t)}{\partial t}.$$

The next stage is to substitute for the above in the Hamilton-Jacobi equation; the result of these substitutions is a lengthy multiple integration equation as follows:

$$\frac{1}{2} \int_0^L \int_0^L \frac{\partial a(\xi, \zeta, t)}{\partial t} w(\xi, t)\, w(\zeta, t) d\xi d\zeta + \int_0^L \frac{\partial b(\xi, t)}{\partial t} w(\xi, t) d\xi + \frac{\partial c(t)}{\partial t}$$
$$+ \frac{1}{2} \int_0^L \int_0^L M^{-1}(\xi, \zeta) \left[\int_0^L a(\xi, \mu, t)\, w(\mu, t) d\mu + b(\xi, t)\right] \times \left[\int_0^L a(\zeta, \nu, t)\, w(\nu, t) d\nu + b(\zeta, t)\right] d\xi d\zeta$$
$$+ \frac{1}{2} \int_0^L \int_0^L D_\xi D_\zeta K w(\xi, t)\, w(\zeta, t) d\xi d\zeta = 0.$$

This can be rewritten as an integral, the integrand having terms that are multiplied by $w(\xi, t)\, w(\zeta, t)$, by $w(\xi, t)$, and finally those that are independent of $w(\xi, t)$. The integrand is arranged in these groups and the coefficient multipliers are then put to zero and the following integro-differential equations result:

$$\frac{\partial a(\xi, \zeta, t)}{\partial t} + \int_0^L \int_0^L M^{-1}(\mu, \nu)\, a(\mu, \xi, t)\, a(\nu, \zeta, t) d\nu d\mu + D_\xi D_\zeta K(\xi, \zeta) = 0$$

and

$$\frac{\partial b(\xi, t)}{\partial t} + \int_0^L \int_0^L M^{-1}(\mu, \nu)\, a(\mu, \xi, t)\, b(\nu, t) d\mu d\nu = 0$$

and finally

$$\frac{\partial c(t)}{\partial t} + \frac{1}{2} \int_0^L \int_0^L M^{-1}(\xi, \zeta)\, b(\xi, t)\, b(\zeta, t) d\xi d\zeta = 0.$$

These three integro-differential equations can be solved in the following way; the first is solved for $a(\xi, \zeta, t)$ by integration in time given the initial condition, $a(\xi, \zeta, 0) = 0$. The second is then solved for $b(\xi, t)$, again as integration in time; since this equation is linear, the solution is of the following form:

$$b(\xi, t) = b_0(\xi)\, \mathcal{F}(\xi, t)$$

where $\mathcal{F}(\xi, 0) = 1$. The final equation is solved for $c(t)$, this being quadratic in $b(\xi, t)$ and hence in the initial conditions $b_0(\xi)$; the initial condition for $c(0)$ is assumed arbitrarily zero as its value will not influence the solution.

Finally the constant of motion is obtained by differentiating with respect to the constants of integration,

$$\Phi(\xi) = \frac{\partial S}{\partial b_0(\xi)} \text{ for all } \xi \text{ in } \langle 0, L \rangle,$$

and the application of this equation gives the equation of motion of the system.

The One-dimensional Axial Vibrations of an Elastic Rod

To illustrate the previous theory and subsequent development, a typical elastic system is considered; this is a one-dimensional elastic rod that can vibrate along its length. The area distribution is assumed uniform; the ends of the rod are firmly fixed so that the displacement at these points is zero. The axial motion of any point in the rod is $w(\xi, t)$, the density is ρ, the elastic modulus is E, the cross-section area is A, and the length of the rod is L. This is a well-considered system and the solution for $w(\xi, t)$ is well documented.

The Lagrangian $\mathcal{L}$ is

$$\mathcal{L} = \frac{1}{2}\int_0^L \int_0^L \left[\rho A(\xi, \zeta) \frac{\partial w(\xi, t)}{\partial t} \frac{\partial w(\zeta, t)}{\partial t} - EA(\xi, \zeta) \frac{\partial w(\xi, t)}{\partial \xi} \frac{\partial w(\zeta, t)}{\partial \zeta} \right] d\xi d\zeta.$$

Considering the last term and integration by parts gives

$$\int_0^L \int_0^L EA(\xi, \zeta) \frac{\partial w(\xi, t)}{\partial \xi} \frac{\partial w(\zeta, t)}{\partial \zeta} d\xi d\zeta = \int_0^L EA(\xi, \zeta) \frac{\partial w(\zeta, t)}{\partial \zeta} w(\xi, t) \Big]_{\xi=0}^{\xi=L} d\zeta - \int_0^L \int_0^L \frac{\partial EA(\xi, \zeta)}{\partial \xi} w(\xi, t) \frac{\partial w(\zeta, t)}{\partial \zeta} d\zeta d\xi$$

which can be further developed:

$$\int_0^L \int_0^L EA(\xi, \zeta) \frac{\partial w(\xi, t)}{\partial \xi} \frac{\partial w(\zeta, t)}{\partial \zeta} d\xi d\zeta = EA(\xi, \zeta) w(\xi, t) \Big]_{\xi=0}^{\xi=L} w(\zeta, t) \Big]_{\zeta=0}^{\zeta=L} - \int_0^L \frac{\partial EA(\xi, \zeta)}{\partial \zeta} w(\xi, t) \Big]_{\xi=0}^{\xi=L} w(\zeta, t) d\zeta - \int_0^L \frac{\partial EA(\xi, \zeta)}{\partial \xi} w(\zeta, t) \Big]_{\zeta=0}^{\zeta=L} w(\xi, t) d\xi + \int_0^L \int_0^L \frac{\partial^2 EA(\xi, \zeta)}{\partial \xi \partial \zeta} w(\xi, t) w(\zeta, t) d\zeta d\xi.$$

Since the end points are fixed, $w(0, t) = w(L, t) = 0$, the Lagrangian becomes

$$\mathcal{L} = \frac{1}{2}\int_0^L \int_0^L \left[\rho A(\xi, \zeta) \frac{\partial w(\xi, t)}{\partial t} \frac{\partial w(\zeta, t)}{\partial t} - \frac{\partial^2 EA(\xi, \zeta)}{\partial \xi \partial \zeta} w(\xi, t) w(\zeta, t) \right] d\xi d\zeta.$$

The generalized momentum $p(\xi, t)$ is given as follows:

$$p(\xi, t) = \frac{\partial \mathcal{L}}{\partial \dfrac{\partial w(\xi, t)}{\partial t}} = \int_0^L \rho A(\xi, \zeta) \frac{\partial w(\zeta, t)}{\partial t} d\zeta;$$

the inverse relation is introduced,

$$\frac{\partial w(\xi, t)}{\partial t} = \int_0^L m_i(\xi, \zeta) p(\zeta, t) d\zeta$$

where

$$\int_0^L \rho A(\xi, \eta) m_i(\eta, \zeta) d\eta = \delta(\xi - \zeta)$$

and the Hamiltonian H is then given by

$$H = \int_0^L p(\xi, t) \frac{\partial w(\xi, t)}{\partial t} d\xi - \mathcal{L} = \frac{1}{2}\int_0^L \int_0^L \left[m_i(\xi, \zeta) p(\xi, t) p(\zeta, t) + \frac{\partial^2 EA(\xi, \zeta)}{\partial \xi \partial \zeta} w(\xi, t) w(\zeta, t) \right] d\xi d\zeta.$$

The Hamilton-Jacobi equation

$$\frac{\partial S}{\partial t} + H\left(\frac{\partial S}{\partial w(\xi, t)}, w(\xi, t), t \right) = 0$$

thus becomes

$$\frac{\partial S}{\partial t} + \frac{1}{2}\int_0^L \int_0^L \left(m_i(\xi, \zeta) \frac{\partial S}{\partial w(\xi, t)} \frac{\partial S}{\partial w(\zeta, t)} + \frac{\partial^2 EA(\xi, \zeta)}{\partial \xi \partial \zeta} w(\xi, t) w(\zeta, t) \right) d\xi d\zeta = 0.$$

Using the nonseparable form for the Hamilton principal function

$$S = \frac{1}{2}\int_0^L \int_0^L a(\xi, \zeta, t) w(\xi, t) w(\zeta, t) d\xi d\zeta + \int_0^L b(\xi, t) w(\xi, t) d\xi + c(t)$$

in the Hamilton-Jacobi equation and considering the resulting integral, the integrand is grouped by into terms that are multiplied by $w(\xi, t) w(\zeta, t)$, by $w(\xi, t)$, and those independent of $w(\xi, t)$. These groups are isolated and the coefficient multipliers are then put to zero yielding the following integro-differential equations:

$$\frac{\partial a(\xi, \zeta, t)}{\partial t} + \int_0^L \int_0^L m_i(\mu, \nu) a(\mu, \xi, t) a(\nu, \zeta, t) d\nu d\mu + \frac{\partial^2 EA}{\partial \xi \partial \zeta} = 0$$

and

$$\frac{\partial b(\xi, t)}{\partial t} + \int_0^L \int_0^L m_i(\mu, \nu) a(\mu, \xi, t) b(\nu, t) d\mu d\nu = 0$$

and finally

$$\frac{\partial c(t)}{\partial t} + \frac{1}{2}\int_0^L \int_0^L m_i(\xi, \zeta) b(\xi, t) b(\zeta, t) d\xi d\zeta = 0.$$

For scleronomic systems, the system coefficients ρA and EA are time independent, and the first of the above equations has a solution of the form $a(\xi, \zeta, t) = a_0(\xi, \zeta)$, where

$$\int_0^L \int_0^L m_i(\mu, \nu) a_0(\mu, \xi) a_0(\nu, \zeta) d\nu d\mu + \frac{\partial^2 EA}{\partial \xi \partial \zeta} = 0.$$

This solution can be employed since any solution to the Hamilton-Jacobi will suffice.

Basis Functions (Lighthill, 1964; Friedman, 1956)

In order to solve the above equations for a, b and c, linear-independent (and complete) basis functions are introduced; this is just one of the solution procedures available and is chosen since the solution obtained is readily compared with the classic solution. These basis functions $\phi_i(\xi)$ must be complete and independent functions so that any function $\psi(\xi)$ can be written as a linear combination of the basis functions

$$\psi(\xi) = \sum_{i=1}^{i=\infty} f_i \phi_i(\xi).$$

If the functions are orthonormal then

$$\int_0^L \phi_i(\xi)\, \phi_j(\xi) d\xi = \delta_{ij}$$

where δ_{ij} is the Kroneker delta, that is

$$\begin{aligned} \delta_{ij} &= 1 \quad \text{if} \quad i = j \text{ and} \\ &= 0 \quad \text{if} \quad i \neq j. \end{aligned}$$

The above function $\psi(\xi)$ can be expressed as a projection on this basis where the projections f_i are

$$f_i = \int_0^L \psi(\xi)\, \phi_i(\xi) d\xi \text{ for } i = 1, 2 \ldots \infty.$$

The basis functions must span the space so that only a null function, that is $\psi(\xi) = 0$ for all ξ, $0 < \xi < L$ has zero projections ($f_i = 0$ for all i) on the basis functions.

The Dirac delta function $\delta(\xi - \zeta)$, which will be used in the following section, is similarly represented:

$$\delta(\xi - \zeta) = \sum_{i=1}^{i=\infty} \phi_i(\xi)\, \phi_i(\zeta)$$

so that

$$\phi_i(\xi) = \int_0^L \delta(\xi - \zeta)\, \phi_i(\zeta) d\zeta.$$

These orthonormal functions will be used extensively throughout the remainder of this paper to generate the solution for the generating function S and the final equation of motion.

Two orthonormal basis functions that will be used in this paper are

$$\phi_i(\xi) = \sqrt{\frac{1}{L}}, \sqrt{\frac{2}{L}} \cos\left(\frac{\pi\xi}{L}\right), \ldots \sqrt{\frac{2}{L}} \cos\left(\frac{(i-1)\pi\xi}{L}\right) \ldots$$

and

$$\phi_i(\xi) = \sqrt{\frac{2}{L}} \sin\left(\frac{\pi\xi}{L}\right),$$

$$\sqrt{\frac{2}{L}} \sin\left(\frac{2\pi\xi}{L}\right), \ldots \sqrt{\frac{2}{L}} \sin\left(\frac{i\pi\xi}{L}\right) \ldots.$$

Material Distribution

The functions $EA(\xi, \zeta)$ and $\rho A(\xi, \zeta)$ have been introduced through the Lagrangian; these functions are the distributions of stiffness and inertia through the system; they show the possibility of the motion of material at one location ζ having a quantifiable effect on the energy at another point.

Consider first the stiffness disposition $EA(\xi, \zeta)$; this could be represented by the linear independent orthonormal basis functions above by

$$EA(\xi, \zeta) = \sum_{i=1}^{i=\infty} \sum_{j=1}^{j=\infty} [EA]_{ij}\, \phi_i(\xi)\, \phi_j(\zeta)$$

where

$$[EA]_{ij} = \int_0^L \int_0^L EA(\xi, \zeta)\, \phi_i(\xi)\, \phi_j(\zeta) d\xi d\zeta.$$

At this point the form of $EA(\xi, \zeta)$ is examined by recalling the Principle of Local Action (Truesdell, 1965, 1977) which states that the motion of body points at a finite distance from X of some shape B may be disregarded in calculating the stress at X; this restricts $EA(\xi, \zeta)$ to the following:

$$\begin{aligned} EA(\xi, \zeta) &= EA(\xi)\, \delta(\xi - \zeta) \\ &= \sum_{i=1}^{i=\infty} \sum_{j=1}^{j=\infty} [EA]_i \phi_i(\xi) \phi_j(\xi) \phi_j(\zeta). \end{aligned}$$

Finally for a uniform distribution, the stiffness distribution becomes

$$\begin{aligned} EA(\xi, \zeta) &= EA(\xi)\, \delta(\xi - \zeta) \\ &= EA \sum_{i=1}^{i=\infty} \phi_i(\xi) \phi_i(\zeta). \end{aligned}$$

The other material disposition $\rho A(\xi, \zeta)$ is not apparently restricted by the Principle of Local Action; however, it would seem that this principle ought to be applied as say a principle of localized inertia. For the purpose of this, the following is assumed:

$$\begin{aligned} \rho A(\xi, \zeta) &= \rho A(\xi)\, \delta(\xi - \zeta) \\ &= \sum_{i=1}^{i=\infty} \sum_{j=1}^{j=\infty} [\rho A]_i \phi_i(\xi) \phi_j(\xi) \phi_j(\zeta) \end{aligned}$$

and for a uniform structure, the mass distribution becomes

$$\begin{aligned} \rho A(\xi, \zeta) &= \rho A\ \delta(\xi - \zeta) \\ &= \rho A \sum_{i=1}^{i=\infty} \phi_i(\xi) \phi_i(\zeta). \end{aligned}$$

It is noted here that Principle of Local Action does not apply to discrete systems, it being very common for nondiagonal stiffness and mass matrices to exist.

Selection of Basis Functions

The solution for the principle function S in the Hamilton-Jacobi equation is not unique; any solution (Greenwood, 1977) to this equation can be used as a primary generating function. Using the above cosine functions as linear independent basis functions, $EA\delta(\xi - \zeta)$ can be expanded as an infinite summation

$$EA\delta(\xi - \zeta) = \frac{EA}{L} + \frac{2EA}{L} \sum_{i=1}^{\infty} \cos\left(\frac{i\pi\xi}{L}\right) \cos\left(\frac{i\pi\zeta}{L}\right)$$

then

$$\frac{\partial^2 EA(\xi, \zeta)}{\partial\xi\partial\zeta} = \frac{2EA}{L} \sum_{i=1}^{\infty} \left(\frac{i\pi}{L}\right)^2 \sin\left(\frac{i\pi\xi}{L}\right) \sin\left(\frac{i\pi\zeta}{L}\right).$$

Similarly the mass distribution $\rho A\delta(\xi - \zeta)$ can be represented by the basis functions, but in this case the sine functions are used,

$$\rho A(\xi, \zeta) = \frac{2\rho A}{L} \sum_{i=1}^{\infty} \sin\left(\frac{i\pi\xi}{L}\right) \sin\left(\frac{i\pi\zeta}{L}\right);$$

the inverse is

$$m_i(\xi, \zeta) = \frac{2}{\rho AL} \sum_{i=1}^{\infty} \sin\left(\frac{i\pi\xi}{L}\right) \sin\left(\frac{i\pi\zeta}{L}\right)$$

Determination of $a_o(\mu, \xi)$

An expansion of the following form

$$a_0(\mu, \xi) = \frac{2}{L} \sum_{i=1}^{\infty} a_i \sin\left(\frac{i\pi\mu}{L}\right) \sin\left(\frac{i\pi\xi}{L}\right)$$

will satisfy the Hamilton-Jacobi equation; substituting this expansion in the equation to solve for $a_0(\mu, \nu)$ gives

$$\frac{2}{\rho AL} \int_0^L \int_0^L \sum_{i=1}^{\infty} \sin\left(\frac{i\pi\mu}{L}\right) \sin\left(\frac{i\pi\nu}{L}\right)$$

$$\frac{4}{L^2} \sum_{m=1}^{\infty} a_m \sin\left(\frac{m\pi\mu}{L}\right) \sin\left(\frac{m\pi\xi}{L}\right)$$

$$\times \sum_{n=1}^{\infty} a_n \sin\left(\frac{n\pi\nu}{L}\right) \sin\left(\frac{n\pi\zeta}{L}\right) d\nu d\mu$$

$$= -\frac{2EA}{L} \sum_{i=1}^{\infty} \left(\frac{i\pi}{L}\right)^2 \sin\left(\frac{i\pi\xi}{L}\right) \sin\left(\frac{i\pi\zeta}{L}\right).$$

Performing the integrations and noting the orthogonality of the sine functions, that is

$$\int_0^L \frac{2}{L} \sin\left(\frac{i\pi\mu}{L}\right) \sin\left(\frac{j\pi\mu}{L}\right) d\mu = 1 \text{ if } i = j$$

$$= 0 \text{ if } i \neq j,$$

then

$$\sum_{i=1}^{\infty} \left[\frac{a_i^2}{\rho A} + \left(\frac{i\pi}{L}\right)^2 EA\right] = 0.$$

Since any solution (Greenwood, 1977) is required, then the solution

$$a_i = \frac{i\pi}{L} J A \sqrt{E\rho} \quad \text{where} \quad J = \sqrt{-1}$$

will suffice.

Determination of $b(\xi, t)$

Recalling the expression for $b(\xi, t)$

$$\frac{\partial b(\xi, t)}{\partial t} + \int_0^L \int_0^L m_i(\mu, \nu)\, a(\mu, \xi)\, b(\nu, t) d\mu d\nu = 0$$

and assuming the following

$$b(\xi, t) = \sqrt{\frac{2}{L}} \sum_{i=1}^{\infty} b_i e^{\lambda_i t} \sin\frac{i\pi\xi}{L},$$

then substituting in the equation above

$$\sqrt{\frac{2}{L}} \sum_{i=1}^{\infty} \lambda_i b_i e^{\lambda_i t} \sin\frac{i\pi\xi}{L} + \int_0^L \int_0^L \frac{2}{\rho AL} \sum_{i=1}^{\infty} \sin\frac{i\pi\mu}{L} \sin\frac{i\pi\nu}{L}$$

$$\times \frac{2}{L} \sum_{j=1}^{\infty} a_j \sin\frac{j\pi\mu}{L} \sin\frac{j\pi\xi}{L} \sqrt{\frac{2}{L}} \sum_{k=1}^{\infty} b_k e^{\lambda_k t} \sin\frac{k\pi\nu}{L} d\mu d\nu = 0,$$

integrating with respect to μ and ν, and noting the orthogonality of the sines results in

$$\sum_{i=1}^{\infty} \left(\lambda_i + \frac{a_i}{\rho A}\right) b_i e^{\lambda_i t} \sin\frac{i\pi\nu}{L} = 0.$$

Thus

$$\lambda_i = -\frac{a_i}{\rho A} = -J\frac{i\pi}{L}\sqrt{\frac{E}{\rho}}.$$

Determination of $c(t)$

Using the above series representations of $m_i(\xi, \zeta)$ and $b(\xi, t)$ and substituting in the equation for $c(t)$ leads to the following:

$$\frac{\partial c(t)}{\partial t} = -\frac{1}{2} \int_0^L \int_0^L m_i(\xi, \zeta) b(\xi, t) b(\zeta, t) d\xi d\zeta$$

$$= -\frac{1}{2} \sqrt{\frac{L}{2}} \sum_{i=1}^{\infty} \frac{b_i^2}{\rho A} e^{2\lambda_i t}$$

and finally

$$c(t) = -\frac{1}{4} \sqrt{\frac{L}{2}} \sum_{i=1}^{\infty} \frac{b_i^2}{\rho A \lambda_i} e^{2\lambda_i t}.$$

The General Solution

The above has yielded expressions for a (the kernel function), b (the primary system function), and c (the secondary system function); the last two are the result of an integration process and include constants of integration b_i.

The constants of motion ϕ_i result from the differentiation of the principal function S with respect to the ignorable constants, the above constants of integration; recalling the expression for S

$$S = \frac{1}{2} \int_0^L \int_0^L a(\xi, \zeta, t)\, w(\xi, t)\, w(\zeta, t) d\xi d\zeta$$

$$+ \int_0^L b(\xi, t)\, w(\xi, t) d\xi + c(t)$$

and noting that the constants of integration occur within $b(\xi, t)$ and $c(t)$, then

$$\Phi_i = \frac{\partial S}{\partial b_i}, \; i = 1, 2 \ldots \infty.$$

Thus

$$\Phi_i = \frac{\partial S}{\partial b_i}$$

$$= \int_0^L \sqrt{\frac{2}{L}} e^{\lambda_i t} \sin\frac{i\pi\xi}{L} w(\xi, t) d\xi - \frac{1}{2} \sqrt{\frac{L}{2}} \frac{b_i}{\rho A \lambda_i} e^{2\lambda_i t}.$$

Finally solving for $w(\xi, t)$ gives the following equation:

$$\int_0^L \sin\frac{i\pi\xi}{L} w(\xi, t) d\xi = \sqrt{\frac{L}{2}} \Phi_i e^{-\lambda_i t} + \frac{L}{4} \frac{b_i}{\rho A \lambda_i} e^{\lambda_i t},$$

that is

$$w(\xi, t) = \sum_{i=1}^{\infty} \left(\sqrt{\frac{2}{L}} \Phi_i e^{-\lambda_i t} + \frac{b_i}{2\rho A \lambda_i} e^{\lambda_i t}\right) \sin\frac{i\pi\xi}{L}.$$

This is the general solution for the dynamics of the axial motion and the constants of motion associated with the initial conditions are the constants b_i and ϕ_i in the equation above.

Conclusions

The Hamilton-Jacobi partial differential equation has been applied to continuum systems; the application has necessitated the formulation of the Lagrangian, generalized momentum, and Hamiltonian, and ultimately the Hamilton principal function. A solution procedure for quadratic energy functionals is proposed and the theory is applied to a one-dimensional continuum, extracting the classical solution for the axial motion of an elastic rod.

The use of the Hamilton-Jacobi partial differential equation and the Hamilton principal function may lead to alternative considerations in continuum mechanics although this work really represents a cautious step in this direction.

References

Friedman, B., 1956, *Principles and Techniques of Applied Mathematics* (Applied Mathematics Series), John Wiley and Sons, New York, pp. 136–137, 259–263.

Goldstein, H., 1980, *Classical Mechanics*, 2nd ed., Addison-Wesley, pp. 438–457.

Greenwood, D. T., 1977, *Classical Dynamics* (Prentice-Hall International Series in Dynamics), Prentice-Hall, Englewood Cliffs, NJ, pp. 195–197.

Konopinski, E. J., 1969, *Classical Descriptions of Motion*, W. H. Freeman, pp. 461–468.

Landau, L. D., and Lifshitz, E. M., 1969, *Mechanics: Course of Theoretical Physics*, Vol. 2, 2nd ed., Pergamon Press, London, pp. 147–154.

Lanczos, C., 1966, *Variational Principles of Mechanics*, 3rd ed., University of Toronto Press, Toronto, Canada, pp. 229–243.

Leech, C. M., and Tabarrok, B., 1996, "Nonseparable Solutions to the Hamilton-Jacobi Equation," ASME Journal of Applied Mechanics, Vol. 63 (in press).

Leech, J. W., 1965, *Classic Mechanics*, 2nd ed., Methuen, London, pp. 76–81.

Lighthill, M., 1964, *Introduction to Fourier Series and Generalised Functions*, Cambridge University Press, Cambridge, W. K., pp. 15–26, 58–75.

Pars, L. A. 1965, *A Treatise on Analytical Dynamics*, Heinemann Educational Books, pp. 268–286.

Saletan, E. J., and Cromer, A. H., *Theoretical Mechanics*, John Wiley and Sons, New York, pp. 267–276.

Synge, J. L., 1960, *Dynamics in Encyclopedia of Physics*, 3/1, S. Flugge, ed., Springer, Berlin, pp. 125–130.

Truesdell, C., 1965, *The Elements of Continuum Mechanics*, Springer-Verlag, New York, p. 34.

Truesdell, C., 1977, *A First Course in Rational Continuum Mechanics*, Vol. 1, Academic Press, New York, pp. 161–162.

Y.-J. Ren
Mem. ASME.

I. Elishakoff
Mem. ASME.

Department of Mechanical Engineering,
Florida Atlantic University,
Glades Road 777
Boca Raton, FL 33431-0991

M. Shinozuka
Department of Civil Engineering,
University of Southern California,
University Park,
Los Angeles, CA 90089-0242
Fellow ASME

Finite Element Method for Stochastic Beams Based on Variational Principles

This paper proposes a new version (fundamentally different from the existing ones) of finite element method for the mean and covariance functions of the displacement for bending beams with spatially random stiffness. Apart from the conventional finite element method for stochastic problems, which utilizes either perturbation or series expansion technique or the Monte Carlo simulation, the present method is based on the newly established variational principles. The finite element scheme is formulated directly with respect to the mean function and covariance function, rather than perturbed components of the displacement. It takes into account an information on joint probability distribution function of the random stiffness to obtain the covariance function of the displacement. Therefore, the accurate solution can be obtained even if the coefficient of variation of the random stiffness is large, in contrast to conventional technique. Several examples are given to illustrate the advantage of the proposed method, compared with the conventional ones.

Introduction

Structures involving spatially random material and/or geometrical parameters are dubbed as *stochastic structures*. The analysis of stochastic structures has attracted significant interest of many researchers in the recent decade. However, difficulties arise in obtaining exact solutions for these structures since their governing equations constitute random differential equations with random coefficient functions, and possibly with random boundary conditions. Therefore, several approximate analytical and numerical methods have been developed to address this problem. Among these methods, the finite element method developed recently for stochastic problems is one example of perturbation-based numerical methods (Nakagiri and Hisada, 1985; Ghanem and Spanos, 1991; Kleiber and Hien, 1993).

Actually, the existing finite element method for stochastic structures is basically a combination of deterministic finite element method and perturbation technique. It obtains zeroth, first, and/or second perturbed components of displacements by recursively solving the finite element equilibrium equation. Due to computational cost, and the fact that higher-order probabilistic information of spatially random parameters is generally not available for practical problems, only first-order (and second or third-order in some cases) conventional finite element method for stochastic structures were suggested in the existing literature.

For the beam bending, both spatially random material parameter (Young's modulus) or geometrical parameters (dimension of the cross section) can be combined into a single random parameter—the bending stiffness. In this paper, we formulate a new kind of finite element method for the statically determinate bending of beams with spatially random stiffness, based on the newly established variational principles for the mean and covariance function of the displacement. The variational principles, for the mean and covariance functions of the displacement, respectively, are derived from the governing equations themselves. The new finite element method is *fundamentally* different from the finite element method for stochastic structures based on conventional variational approaches. The latters were obtained just by perturbing the deterministic variational principles with respect to deviations of the random parameters and therefore basically constitute a perturbation method; one should stress that the use of variational principles was a definitive contribution to the subject (Hien and Kleiber, 1990; Kleiber and Hien, 1993; Liu, Besterfield, and Belytschko, 1988).

In this study the new finite element method for stochastic beams is directly established for the mean and covariance functions of the displacement. Moreover, the perturbation technique is no longer adopted. The new method can be applied to any probabilistic distribution of the random stiffness, especially for the large correlation coefficients where the perturbation-based finite element method fails. Some examples are illustrated to show the accuracy and effectiveness of the proposed method. A detailed comparison of the results obtained by the present method with the conventional first-order finite element method and analytical solution is performed.

Basic Equations and Variational Principles

1 Basic Equations. The beam-bending problem with spatially stochastic stiffness $D(x) = E(x)I(x)$ subjected to deterministic loads is governed by

$$\frac{d^2}{dx^2}\left[D(x)\frac{d^2w}{dx^2}\right] = q(x) \tag{1}$$

where $w(x)$ = displacement, $q(x)$ = transverse distributed force, $D(x)$ = the bending stiffness which is assumed to be a spatially random field, $E(x)$ = Young's modulus, and $I(x)$ = moment of inertia. For statically determinate beams, it has been shown that the mean displacement $\bar{w}(x) = E[w(x)]$ is governed by the following equation (Elishakoff, Ren, and Shinozuka, 1995):

$$\frac{d^2}{dx^2}\left[D_0(x)\frac{d^2\bar{w}}{dx^2}\right] = q(x) \tag{2}$$

with the attendant boundary conditions

Contributed by the Applied Mechanics Division of THE AMERICAN SOCIETY OF MECHANICAL ENGINEERS for publication in the ASME JOURNAL OF APPLIED MECHANICS.

Discussion on the paper should be addressed to the Technical Editor, Professor Lewis T. Wheeler, Department of Mechanical Engineering, University of Houston, Houston, TX 77204-4792, and will be accepted until four months after final publication of the paper itself in the ASME JOURNAL OF APPLIED MECHANICS.

Manuscript received by the ASME Applied Mechanics Division, May 25, 1995; final revision, Sept. 30, 1996. Associate Technical Editor: L. T. Wheeler.

$$\bar{w} = 0 \quad \text{or} \quad \frac{d\bar{w}}{dx} = 0$$

$$\frac{d}{dx}\left[D_0(x)\frac{d^2\bar{w}}{dx^2}\right] = \bar{Q} \quad \text{or} \quad D_0\frac{d^2\bar{w}}{dx^2} = \bar{M} \tag{3}$$

where $\bar{M}$ and $\bar{Q}$ are prescribed moment and shear force, respectively, and

$$f_0(x) = \frac{1}{D_0(x)} = E\left[\frac{1}{D(x)}\right]. \tag{4}$$

The governing Eq. (2) and boundary conditions in Eq. (3) are identical in its form with those of a bending beam with equivalent deterministic stiffness $D_0(x)$ or equivalent deterministic flexibility $f_0(x)$. The covariance function $C(x, y) = E\{[w(x) - \bar{w}(x)][w(y) - \bar{w}(y)]\}$ for the displacement $w(x)$ is governed by

$$\frac{\partial^4 C(x, y)}{\partial x^2 \partial y^2} = \frac{m(x)m(y)}{D_1(x, y)} = f_1(x, y)m(x)m(y) \tag{5}$$

where $m(x)$ is the moment distribution in the beam, and

$$f_1(x, y) = \frac{1}{D_1(x, y)} = \mathrm{Cov}\left[\frac{1}{EI(x)}, \frac{1}{EI(y)}\right] \tag{6}$$

is the covariance function of the beam flexibility. By partially differentiating Eq. (5) twice with respect to x and twice with respect to y, an alternative form of the governing equation for covariance function $C(x, y)$ can be obtained as

$$\frac{\partial^4}{\partial x^2 \partial y^2}\left[D_1(x, y)\frac{\partial^4 C(x, y)}{\partial x^2 \partial y^2}\right] = q(x)q(y). \tag{7}$$

The boundary conditions for the covariance function $C(x, y)$ are as follows:
At $x = 0$ and $x = L$,

$$\frac{\partial C}{\partial x} = 0 \quad \text{or} \quad C = 0$$

$$D_1\frac{\partial^4 C}{\partial x^2 \partial y^2} = \bar{M}m(y) \quad \text{or} \quad \frac{\partial}{\partial x}\left[D_1\frac{\partial^4 C}{\partial x^2 \partial y^2}\right] = \bar{Q}m(y). \tag{8}$$

At $y = 0$ and $y = L$,

$$\frac{\partial C}{\partial y} = 0 \quad \text{or} \quad C = 0$$

$$D_1\frac{\partial^4 C}{\partial x^2 \partial y^2} = \bar{M}m(x) \quad \text{or} \quad \frac{\partial}{\partial y}\left[D_1\frac{\partial^4 C}{\partial x^2 \partial y^2}\right] = \bar{Q}m(x). \tag{9}$$

2 Variational Principles. The variational principle for the mean displacement $\bar{w}(x)$ corresponding to the governing Eq. (2) and boundary conditions in Eq. (3) requires the minimizing of the following functional:

$$\pi_1 = \int_0^L \left[\frac{1}{2}D_0(x)\left(\frac{d^2\bar{w}}{dx^2}\right)^2 - q(x)\bar{w}\right]dx - \left[M\frac{d\bar{w}}{dx} - Q\bar{w}\right]\Bigg|_0^L. \tag{10}$$

The above functional is identical to that of a deterministic beam (Hu, 1981), which has an equivalent deterministic stiffness $D_0(x)$. The variational principle for the covariance function $C(x, y)$ corresponding to the governing Eq. (7) and boundary conditions in Eqs. (8), (9) requires the minimizing of the following functional:

$$\begin{aligned}\pi_2 = &\int_0^L\int_0^L \left[\frac{1}{2}D_1(x, y)\left(\frac{\partial^4 C}{\partial x^2 \partial y^2}\right)^2 - q(x)q(y)C\right]dxdy \\ &- \left[\int_0^L \left(\bar{M}\frac{\partial C}{\partial x} - \bar{Q}C\right)q(y)dy\right]\Bigg|_{x=0}^{x=L} \\ &- \left[\int_0^L \left(\bar{M}\frac{\partial C}{\partial y} - \bar{Q}C\right)q(x)dx\right]\Bigg|_{y=0}^{y=L} \\ &- \left[\bar{M}\bar{M}\frac{\partial^2 C}{\partial x \partial y} - \bar{M}\bar{Q}\frac{\partial C}{\partial x} - \bar{M}\bar{Q}\frac{\partial C}{\partial y} + \bar{Q}\bar{Q}C\right]\Bigg|_{y=0}^{y=L}\Bigg|_{x=0}^{x=L}.\end{aligned} \tag{11}$$

The proof of this variational principle has been given in the study by Elishakoff, Ren, and Shinozuka (1996). The functional π_2 was derived by first guessing the double integration term in the right side of the Eq. (11), from the Eq. (7), and then carrying out the variation of the term with respect to $C(x, y)$ to construct appropriate boundary terms. The physical implication of π_2 is not addressed here. The proof that the functional π_2 reaches its minimum value when the covariance function $C(x, y)$ is the exact one has been given in Appendix A.

It is seen that the function to be integrated in the first integral in the functional π_2 consists of mixed fourth-order derivative of correlation function $C(x, y)$ with respect to x and y. Hence, at least C^1-continuous interpolating functions are required to guarantee the convergence of the finite element formulation based on the variational principle in Eq. (11). Furthermore, the very fact that only terms with at least x^2 and y^2 in interpolating polynomials contribute the stiffness matrix, implies that higher-order interpolating functions are required. Due to these two shortcomings, we propose an alternative form of the variational principle for the covariance function $C(x, y)$, which corresponds to the governing Eq. (5) and geometry boundary conditions in Eqs. (8), (9). The functional to be minimized reads

$$\begin{aligned}\pi_3 = &\int_0^L\int_0^L \left[\frac{1}{2}\left(\frac{\partial^2 C}{\partial x \partial y}\right)^2 - f_1(x, y)m(x)m(y)C\right]dxdy \\ &+ \int_0^L m(x)H_1(x)C|_{y=L}dx \\ &+ \int_0^L m(y)H_2(y)C|_{x=L}dy - GC|_{x=L,y=L}\end{aligned} \tag{12}$$

where

$$H_1(x) = \int_0^L f_1(x, y)m(y)dy, \quad H_2(y) = \int_0^L f(x, y)m(x)dx$$

$$G = \int_0^L\int_0^L f_1(x, y)m(x)m(y)dxdy. \tag{13}$$

The variational principle in Eq. (12) is applicable to the beams simply supported at both ends $x = 0$ and $x = L$ or clamped at left end $x = 0$, namely either $w = dw/dx = 0$ at $x = 0$ or $w = 0$ at $x = 0, L$. The functional π_3 requires C^0-continuous only and comparatively lower interpolating functions. Its proof is given in Appendix B.

Finite Element Formulation

1 Formulation for the Mean Displacement. The mean displacement $\bar{w}(x)$ is actually the response of a bending beam with varying bending stiffness $D_0(x)$, as we have mentioned in previous section. Therefore, the conventional finite element formulas for deterministic beams can be used. In this paper, the two-node cubic Hermitian beam element (Hinton and Owen, 1972) is adopted. The interpolation of the mean displacement in the element $x_1 \le x \le x_2$ is given by

$$\bar{w} = \sum_{i=1}^{4} \bar{N}_i d_i = \bar{\mathbf{N}}\mathbf{d} \tag{14}$$

where

$$\mathbf{d} = [d_1, d_2, d_3, d_4]^T = \left[\bar{w}_1, \left(\frac{d\bar{w}}{dx}\right)_1, \bar{w}_2, \left(\frac{d\bar{w}}{dx}\right)_2\right]^T \tag{15}$$

is the nodal displacement vector, and

$$\bar{\mathbf{N}} = [\bar{N}_1, \bar{N}_2, \bar{N}_3, \bar{N}_4]^T$$

$$\bar{N}_1 = (2+\xi)\left(\frac{\xi-1}{2}\right)^2, \quad \bar{N}_2 = a(\xi+1)\left(\frac{\xi-1}{2}\right)^2$$

$$\bar{N}_3 = (2-\xi)\left(\frac{\xi+1}{2}\right)^2, \quad \bar{N}_4 = a(\xi-1)\left(\frac{\xi+1}{2}\right)^2 \tag{16}$$

are shape functions, $\xi = (x - x_1)/(x_2 - x_1) - (x_2 - x)/(x_2 - x_1)$ is the local coordinate, $a = (x_2 - x_1)/2$.

Discretizing the beam into n elements, substituting Eq. (14) into Eq. (10) and then minimizing the potential π_1, we get

$$\sum_{e=1}^{n} \mathbf{K}_1^e \mathbf{d} = \sum_{e=1}^{n} \mathbf{F}_1^e \tag{17}$$

where the element stiffness matrix $\mathbf{K}_1^e$ and the element equivalent nodal force vector $\mathbf{F}_1^e$ are given, respectively, as follows:

$$\mathbf{K}_1^e = \int_{x_1}^{x_2} D_0(x) \frac{d^2\bar{N}^T}{dx^2}\frac{d^2\bar{N}}{dx^2} dx \tag{18}$$

$$\mathbf{F}_1^e = \int_{x_1}^{x_2} \bar{\mathbf{N}}^T q(x) dx - \left[M\frac{d\bar{N}}{dx} - Q\bar{N}\right]\Big|_0^l. \tag{19}$$

2 Formulation for the Covariance Function. To construct finite element formulas for the covariance function, we can apply either the variational principle in Eq. (11) or the variational principle in Eq. (12). Since the functional π_2 contains mixed fourth-order derivative of the covariance function with respect to x and y, C^1-continuous interpolating functions should be used to guarantee the convergence of the solution and higher-order interpolating polymonials must be assumed to contribute the stiffness matrix. On the other hand, the functional π_3 consists of only mixed second-order derivative of the covariance function $C(x, y)$ with respect to x and y, C^0-continuous interpolating functions can be used to reach the convergence requirement and lower-order interpolating polynomials can be adopted to satisfy the accuracy. Therefore, the functional π_3 is utilized hereby to construct the finite element equilibrium equations for the covariance function $C(x, y)$.

Due to the fact that the functional π_3 possesses symmetry in x and y, a four-node rectangular element, which is commonly used in plate-bending problems, is adopted here. The covariance function $C(x, y)$ in the element $x_1 \le x \le x_2$ and $y_1 \le y \le y_2$ is interpolated as follows:

$$C = \sum_{i=1}^{4} \mathbf{N}_i \delta_i = \mathbf{N}\delta \tag{20}$$

where δ is the vector of nodal degrees-of-freedom

$$\delta = [\delta_1, \delta_2, \delta_3, \delta_4]^T$$

$$\delta_i = \left[C_i, \left(\frac{\partial C}{\partial x}\right)_i, \left(\frac{\partial C}{\partial y}\right)_i\right]^T \tag{21}$$

and $\mathbf{N}$ is vector of shape functions

$$\mathbf{N} = [\mathbf{N}_1, \mathbf{N}_2, \mathbf{N}_3], \quad \mathbf{N}_i = [N_{i1}, N_{i2}, N_{i3}]$$

$$N_{i1} = \frac{\xi_i\eta_i}{8}(2 + \xi_i\xi + \eta_i\eta - \xi^2 - \eta^2)(\xi + \xi_i)(\eta + \eta_i)$$

$$N_{i2} = \frac{\eta_i a}{8}(\xi^2 - 1)(\xi + \xi_i)(\eta + \eta_i)$$

$$N_{i3} = \frac{\xi_i b}{8}(\eta^2 - 1)(\xi + \xi_i)(\eta + \eta_i) \tag{22}$$

where $\xi = (x - x_1)/(x_2 - x_1) - (x_2 - x)/(x_2 - x_1)$ and $\eta = (y - y_1)/(y_2 - y_1) - (y_2 - y)/(y_2 - y_1)$ are local coordinates, $a = (x_2 - x_1)/2$ and $b = (y_2 - y_1)/2$ are side lengths of the rectangular element. Discretizing the domain into $n \times n$ elements, then substituting Eq. (20) into Eq. (12) and minimizing π_3, we get

$$\sum_{e=1}^{n\times n} \mathbf{K}_2^e \delta = \sum_{e=1}^{n\times n} \mathbf{F}_2^e \tag{23}$$

where the element stiffness matrix $\mathbf{K}_2^e$ and the equivalent nodal force vector $\mathbf{F}_2^e$ are given, respectively, as follows:

$$\mathbf{K}_2^e = \int_{x_1}^{x_2}\int_{y_1}^{y_2} \frac{\partial^2\mathbf{N}^T}{\partial x\partial y}\frac{\partial^2\mathbf{N}}{\partial x\partial y} dxdy \tag{24}$$

$$\mathbf{F}_2^e = \int_{x_1}^{x_2}\int_{y_1}^{y_2} f_1(x, y)m(x)m(y)\mathbf{N}^T dxdy. \tag{25}$$

Numerical Example

Consider a simply supported beam with length L and subjected to uniform load q. The stiffness $D(x)$ of the beam is assumed to be a spacially homogeneous random field $D(x) = D_0[1 + k\alpha(x)]$, where k = constant and $\alpha(x)$ is a normalized random field. It is assumed that $\alpha(x)$ possesses a uniform two-dimensional Pearson Type II probability distribution (Johnson, 1987)

$$p_{\alpha(x)\alpha(y)}(u, v) = \begin{cases} \dfrac{1}{\pi\sqrt{1-\rho^2(x, y)}}, \\ \quad \text{for } (u, v) \in \Omega: u^2 - 2\rho uv + v^2 \le 1 - \rho^2 \\ 0, \quad \text{elsewhere} \end{cases} \tag{26}$$

where $\rho(x, y)$ is the function characterizing the correlation between $\alpha(x)$ and $\alpha(y)$, and is assumed to be exponential, namely

$$\rho(x, y) = \exp\left(-\frac{|x - y|}{d}\right), \quad |x - y| \le L \tag{27}$$

where d = scale of fluctuation. The normalized random field $\alpha(x)$ has zero mean and correlation function of $\rho(x, y)/4$. Its one-dimensional marginal distribution reads

$$p_{\alpha(x)}(u) = \frac{2}{\pi}\sqrt{(1 - u^2)}, \quad u \in [-1, 1]. \tag{28}$$

Therefore, the mean and correlation function of the flexibility $f(x) = 1/D(x)$ can be obtained, respectively, as

$$f_0 = E[f] = \int_{-1}^{1} \frac{1}{D_0(1 + ku)} p_{\alpha(x)}(u)du$$

$$= \frac{2}{\pi D_0}\int_{-1}^{1} \frac{\sqrt{1 - u^2}}{1 + ku} du \tag{29}$$

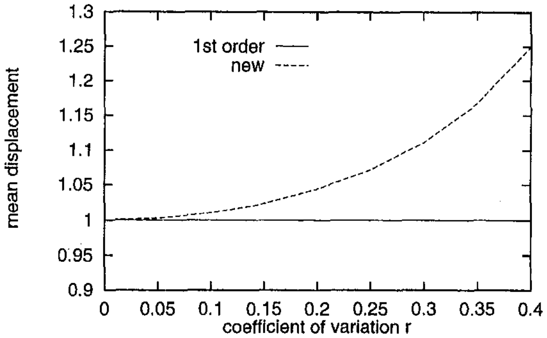

Fig. 1 The mean displacement at the middle of the simply supported beam versus coefficient of variation of random stiffness *r*

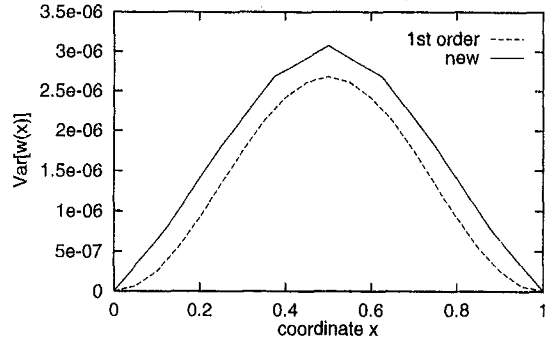

Fig. 3 The variances of the displacement along the beam's axis (coefficient of variation of random stiffness $r = 0.15$)

and

$$R(x, y) = \mathrm{Cov}\,[f(x), f(y)]$$
$$= \iint_\Omega \frac{1}{D_0^2(1+ku)(1+kv)}\, p_{\alpha(x)\alpha(y)}(u, v)\,du\,dv$$
$$= \frac{1}{\pi D_0^2}\int_{-1}^{1} \frac{1}{C_1 C_2} \ln \frac{C_1 + C_2\sqrt{1-u^2}}{C_1 - C_2\sqrt{1-u^2}}\,du \tag{30}$$

where

$$C_1 = 1 + \frac{k\sqrt{1+\rho}}{2}\,u$$
$$C_2 = \frac{k\sqrt{1+\rho}}{2}\,u. \tag{31}$$

The covariance function between the flexibilities $f(x)$ and $f(y)$ is $\mathrm{Cov}\,[f(x), f(y)] = R[f(x), f(y)] - E[f(x)]E[f(y)]$.

To illustrate the accuracy and efficiency of the variational principle based finite element method presented in this study, we calculate the mean and covariance functions of the displacement of the simply supported beam by both the first-order perturbation finite element method and the present finite element method. The scale of fluctuation in Eq. (27) is taken to be $d = 0.5$. The results are depicted in Figs. 1–4. Figure 1 portrays the mean displacements at midspan of the simply supported beam for different values of the coefficient of variation of the stochastic bending stiffness. The results have been normalized by the perturbation solution $w_c = 0.01302/D_0$. The exact solution of the mid-displacement of the simply supported beam is obtainable to be

$$\bar{w}(x = L/2) = \frac{5qL^4\bar{f}}{384}. \tag{32}$$

The variation of the exact mid-displacement with respect to the coefficient of variation r of the random stiffness can be plotted in Fig. 1 and coincides with that of the new finite element result. Thus we reach a remarkable conclusion that the present solution coincides with the exact solution for any value of coefficient of variation of the stiffness. For small values of coefficient of variation of the bending stiffness, the solution obtained by the first-order perturbation method also agrees with the exact solution or the new finite element solution. However, the difference between two solutions increases when the coefficient of variation of the bending stiffness increases, as expected. This observation clearly demonstrates the superiority of the proposed method.

Figure 2 portrays the variances of the mid-displacement, obtained by the present finite element method and the first-order perturbative finite element method, for different values of coefficient of variation of the stochastic bending stiffness. Again, it is seen that the result obtained by the present method agrees with the results obtained by the first-order perturbative finite element method for small values of coefficient of variation of the stiffness. However, for larger values of the coefficient of variation of the stiffness, the difference between the perturbation solution and the new variational principle based solution increases. For example, the differences are about four percent, eight percent, and 35 percent, respectively, for the coefficient of variation $r = 0.1$, 0.15, and 0.3.

Figures 3 and 4 compare more illustratively the results obtained by the first-order perturbation method and the present variational principle based finite element method. Figure 3 shows the changes of the variance of the displacement along the beam cross section for the coefficient of variation of the stiffness $r = 0.15$. Figure 4 shows the changes of the variance of the displacement for the coefficient of variation of the stiffness $r = 0.3$. It is seen that in the case of the small value of the coefficient of variation of the stiffness ($r = 0.15$), two solutions are close to each other. For the case of $r = 0.3$, however, the first-order perturbation solution is much less those by the

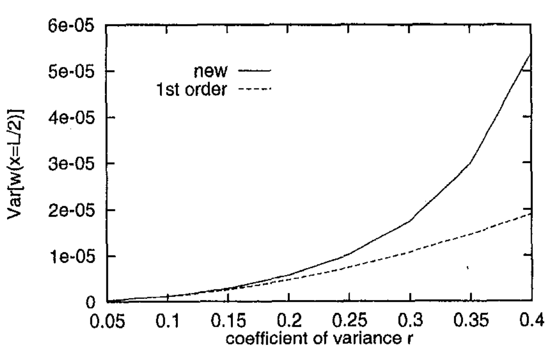

Fig. 2 The variance of the mid-displacement of simply supported beam versus coefficient of variation of random stiffness *r*

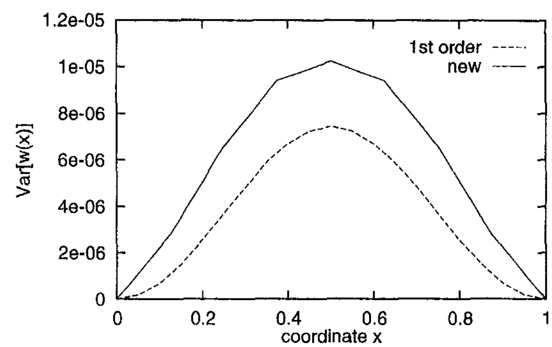

Fig. 4 The variances of the displacement along the beam's axis (coefficient of variation of random stiffness $r = 0.3$)

variational principle based finite element method. This confirms the conclusion that the perturbation-based solutions are acceptable only for the small values of the coefficient of variation. This conclusion is well known and understandable; yet the present work appears to be the first one which develops a simulation-free finite element method for arbitrary value of the coefficient of variation.

Note that in this study the finite element method based on the variational principles has been developed only for statically determinate beams. The generalization of the principles to more general systems of high dimension is under study.

Acknowledgment

This work has been supported by the National Center for Earthquake Engineering Research (NCEER).

References

Elishakoff, I., Ren, Y., and Shinozuka, M., 1995, "Some exact solutions for bending of beams with spatially stochastic stiffness," *International Journal of Solid and Structures*, Vol. 32, No. 16, pp. 2315–2327.

Elishakoff, I., Ren, Y., and Shinozuka, M., 1996, "Variational principles developed for and applied to analysis of stochastic beams," *Journal of Engineering Mechanics*, Vol. 126, No. 6, pp. 559–565.

Ghanem, R. G., and Spanos, P. D., 1991, *Stochastic Finite Elements: A Spectral Approach*, Springer-Verlag, New York.

Johnson, M. E., 1987, *Multivariate Statistical Simulation*, John Wiley and Sons, New York.

Hien, T. D., and Kleiber, M., 1990, "Finite element analysis based on stochastic Hamilton variational principle," *Computer & Structures*, Vol. 37, No. 6, pp. 893–902.

Hu, H. C., 1981, *Variational Principles of Theory of Elasticity with Applications*, Science Press, Beijing, China.

Kleiber, M., and Hien, T. D., 1993, *Stochastic Finite Element Method*. John Wiley and Sons, New York.

Liu, W. K., Mani, A., and Besterfield, G., and Belytschko, T., 1988, "Variational Approach to Probabilistic Finite Elements," *Journal of Engineering Mechanics*, Vol. 114, pp. 2115–2133.

Nakagiri, S., and Hisada, T., 1985, *An Introduction to Stochastic Finite Element Method: Analysis of Uncertain Structures*, BaiFuKan, Tokyo, Japan (in Japanese).

APPENDIX A

Proof of Minimum Property of Functional π_2 in Eq. (11)

Assume that C_0 is the exact solution of Eq. (7) pertinent to boundary conditions in Eqs. (8), (9). Denoting $C = C_0 + C_1$ and substituting it into Eq. (11), we have

$$
\begin{aligned}
\pi_2(C) &= \pi_2(C_0 + C_1) \\
&= \int_0^L \int_0^L \left\{ \frac{1}{2} D_1(x, y) \left[\frac{\partial^4 (C_0 + C_1)}{\partial x^2 \partial y^2} \right]^2 - q(x) q(y) (C_0 + C_1) \right\} dxdy \\
&\quad - \left\{ \int_0^L \left[\bar{M} \frac{\partial (C_0 + C_1)}{\partial x} - \bar{Q}(C_0 + C_1) \right] q(y) dy \right\} \Bigg|_{x=0}^{x=L} \\
&\quad - \left\{ \int_0^L \left[\bar{M} \frac{\partial (C_0 + C_1)}{\partial y} - \bar{Q}(C_0 + C_1) \right] q(x) dx \right\} \Bigg|_{y=0}^{y=L} \\
&\quad - \left[\bar{M}\bar{M} \frac{\partial^2 (C_0 + C_1)}{\partial x \partial y} - \bar{M}\bar{Q} \frac{\partial (C_0 + C_1)}{\partial x} - \bar{M}\bar{Q} \frac{\partial (C_0 + C_1)}{\partial y} + \bar{Q}\bar{Q}(C_0 + C_1) \right] \Bigg|_{y=0}^{y=L} \Bigg|_{x=0}^{x=L} \\
&= \pi_2(C_0) + \pi_2(C_1) + \int_0^L \int_0^L D_1(x, y) \frac{\partial^4 C_0}{\partial x^2 \partial y^2} \frac{\partial^4 C_1}{\partial x^2 \partial y^2} dxdy. \quad (33)
\end{aligned}
$$

Let us consider the integral term:

$$
\begin{aligned}
I &= \int_0^L \int_0^L D_1(x, y) \frac{\partial^4 C_0}{\partial x^2 \partial y^2} \frac{\partial^4 C_1}{\partial x^2 \partial y^2} dxdy \\
&= \int_0^L \frac{\partial^3 C_1}{\partial x \partial y^2} \left[D_1(x, y) \frac{\partial^4 C_0}{\partial x^2 \partial y^2} \right] dy \Bigg|_{x=0}^{x=L} - \int_0^L \int_0^L \frac{\partial}{\partial x} \left[D_1(x, y) \frac{\partial^4 C_0}{\partial x^2 \partial y^2} \right] \frac{\partial^3 C_1}{\partial x \partial y^2} dxdy \\
&= \frac{\partial^2 C_1}{\partial x \partial y} \left[D_1(x, y) \frac{\partial^4 C_0}{\partial x^2 \partial y^2} \right] \Bigg|_{x=0}^{x=L} \Bigg|_{y=0}^{y=L} - \int_0^L \frac{\partial}{\partial y} \left[D_1(x, y) \frac{\partial^4 C_0}{\partial x^2 \partial y^2} \right] \frac{\partial^2 C_1}{\partial x \partial y} dy \Bigg|_{x=0}^{x=L} \\
&\quad - \int_0^L \frac{\partial}{\partial x} \left[D_1(x, y) \frac{\partial^4 C_0}{\partial x^2 \partial y^2} \right] \frac{\partial^2 C_1}{\partial x \partial y} dx \Bigg|_{y=0}^{y=L} + \int_0^L \int_0^L \frac{\partial^2}{\partial x \partial y} \left[D_1(x, y) \frac{\partial^4 C_0}{\partial x^2 \partial y^2} \right] \frac{\partial^2 C_1}{\partial x \partial y} dxdy. \quad (34)
\end{aligned}
$$

Note that C_0 satisfies the Eq. (7) and boundary conditions in Eqs. (8), (9), therefore

$$
\begin{aligned}
I &= \bar{M}\bar{M} \frac{\partial^2 C_1}{\partial x \partial y} \Bigg|_{x=0}^{x=L} \Bigg|_{y=0}^{y=L} - \int_0^L \frac{\partial}{\partial y} \left[D_1(x, y) \frac{\partial^4 C_0}{\partial x^2 \partial y^2} \right] \frac{\partial^2 C_1}{\partial x \partial y} dy \Bigg|_{x=0}^{x=L} \\
&\quad - \int_0^L \frac{\partial}{\partial x} \left[D_1(x, y) \frac{\partial^4 C_0}{\partial x^2 \partial y^2} \right] \frac{\partial^2 C_1}{\partial x \partial y} dx \Bigg|_{y=0}^{y=L} + \int_0^L \int_0^L \frac{\partial^2}{\partial x \partial y} \left[D_1(x, y) \frac{\partial^4 C_0}{\partial x^2 \partial y^2} \right] \frac{\partial^2 C_1}{\partial x \partial y} dxdy \\
&= \left[\bar{M}\bar{M} \frac{\partial^2 C_1}{\partial x \partial y} - \bar{M}\bar{Q} \frac{\partial C_1}{\partial x} - \bar{M}\bar{Q} \frac{\partial C_1}{\partial y} \right] \Bigg|_{x=0}^{x=L} \Bigg|_{y=0}^{y=L} + \int_0^L \frac{\partial^2}{\partial y^2} \left[D_1(x, y) \frac{\partial^4 C_0}{\partial x^2 \partial y^2} \right] \frac{\partial C_1}{\partial x} dy \Bigg|_{x=0}^{x=L} \\
&\quad + \int_0^L \frac{\partial^2}{\partial x^2} \left[D_1(x, y) \frac{\partial^4 C_0}{\partial x^2 \partial y^2} \right] \frac{\partial C_1}{\partial y} dx \Bigg|_{y=0}^{y=L} + \int_0^L \int_0^L \frac{\partial^2}{\partial x \partial y} \left[D_1(x, y) \frac{\partial^4 C_0}{\partial x^2 \partial y^2} \right] \frac{\partial^2 C_1}{\partial x \partial y} dxdy \\
&= \left[\bar{M}\bar{M} \frac{\partial^2 C_1}{\partial x \partial y} - \bar{M}\bar{Q} \frac{\partial C_1}{\partial x} - \bar{M}\bar{Q} \frac{\partial C_1}{\partial y} \right] \Bigg|_{x=0}^{x=L} \Bigg|_{y=0}^{y=L} + \int_0^L \bar{M} q(y) \frac{\partial C_1}{\partial x} dy \Bigg|_{x=0}^{x=L} + \int_0^L \bar{M} q(x) \frac{\partial C_1}{\partial y} dx \Bigg|_{y=0}^{y=L} \\
&\quad + \int_0^L \frac{\partial^2}{\partial x \partial y} \left[D_1(x, y) \frac{\partial^4 C_0}{\partial x^2 \partial y^2} \right] \frac{\partial C_1}{\partial y} dy \Bigg|_{x=0}^{x=L} - \int_0^L \int_0^L \frac{\partial^3}{\partial x^2 \partial y} \left[D_1(x, y) \frac{\partial^4 C_0}{\partial x^2 \partial y^2} \right] \frac{\partial C_1}{\partial y} dxdy
\end{aligned}
$$

$$= \left[\bar{M}\bar{M} \frac{\partial^2 C_1}{\partial x \partial y} - \bar{M}\bar{Q} \frac{\partial C_1}{\partial x} - \bar{M}\bar{Q} \frac{\partial C_1}{\partial y} + \bar{Q}\bar{Q}C_1 \right] \Bigg|_{x=0}^{x=L} \Bigg|_{y=0}^{y=L}$$

$$+ \int_0^L \left[\bar{M} \frac{\partial C_1}{\partial x} - \bar{Q}C_1 \right] q(y)dy \Bigg|_{x=0}^{x=L}$$

$$+ \int_0^L \left[\bar{M} \frac{\partial C_1}{\partial y} - \bar{Q}C_1 \right] q(x)dx \Bigg|_{y=0}^{y=L}$$

$$+ \int_0^L \int_0^L \frac{\partial^4}{\partial x^2 \partial y^2} \left[D_1(x, y) \frac{\partial^4 C_0}{\partial x^2 \partial y^2} \right] C_1 dxdy$$

$$= \int_0^L \int_0^L \frac{1}{2} D_1(x, y) \left(\frac{\partial^4 C_1}{\partial x^2 \partial y^2} \right)^2 dxdy - \pi_2(C_1). \quad (35)$$

Substituting it back into Eq. (33), we obtain

$$\pi_2(C_0 + C_1) = \pi_2(C_0) + \int_0^L \int_0^L \frac{1}{2} D_1(x, y) \left(\frac{\partial^4 C_1}{\partial x^2 \partial y^2} \right)^2 dxdy$$

$$\geq \pi_2(C_0). \quad (36)$$

Q.E.D.

APPENDIX B

Proof of Variational Principle in Eq. (12)

The variation of the first integral in the functional π_3 of Eq. (12) reads

$$\delta J = \int_0^L \int_0^L \frac{\partial^2 C}{\partial x d \partial} \frac{\partial^2 \delta C}{\partial x \partial y} dxdy$$

$$= \int_0^L \frac{\partial^2}{\partial x \partial y} \frac{\partial \delta C}{\partial y} \Bigg|_{x=0}^{x=L} dy - \int_0^L \int_0^L \frac{\partial^3 C}{\partial x^2 \partial y} \frac{\partial \delta C}{\partial y} dxdy$$

$$= \int_0^L \frac{\partial^2 C}{\partial x \partial y} \frac{\partial \delta C}{\partial y} \Bigg|_{x=0}^{x=L} dy - \int_0^L \frac{\partial^3 C}{\partial x^2 \partial y} \Bigg) \delta C|_{y=0}^{y=L} dx$$

$$+ \int_0^L \int_0^L \frac{\partial^4 C}{\partial x^2 \partial y^2} \delta C dxdy$$

$$= \frac{\partial^2 C}{\partial x \partial y} \delta C|_{x=0, y=0}^{x=L, y=L} - \int_0^L \frac{\partial^3 C}{\partial x \partial y^2} \delta C|_{x=0}^{x=L} dy$$

$$- \int_0^L \frac{\partial^3 C}{\partial x^2 \partial y} \delta C|_{y=0}^{y=L} dx + \int_0^L \int_0^L \frac{\partial^4 C}{\partial x^2 \partial y^2} \delta C dxdy. \quad (37)$$

The variation of the functional π_3 is then

$$\delta \pi_3 = \int_0^L \int_0^L \left[\frac{\partial^4 C}{\partial x^2 \partial y^2} - f_1(x, y)m(x)m(y)\delta C \right] dxdy$$

$$- \int_0^L \frac{\partial^3 C}{\partial x^2 \partial y} \delta C|_{y=0}^{y=L} dx + \int_0^L m(x)H_1(x)\delta C|^{y=L} dx$$

$$- \int_0^L \frac{\partial^3 C}{\partial x \partial y^2} \delta C|_{x=0}^{x=L} dy + \int_0^L m(y)H_2(y)\delta C|^{x=L} dy$$

$$+ \frac{\partial^2 C}{\partial x \partial y} \delta C|_{x=0, y=0}^{x=L, y=L} - G\delta C|^{x=L, y=L}. \quad (38)$$

The stationarity condition of π_3 leads to
(i) the governing equation

$$\frac{\partial^4 C}{\partial x^2 \partial y^2} = f_1(x, y)m(x)m(y), \quad \forall x, y, \quad (39)$$

(ii) boundary conditions at sides

$$\left[\frac{\partial^3 C}{\partial x \partial y^2} - m(y)H_2(y) \right] \delta C = 0, \quad \forall y \quad \text{at} \quad x = L$$

$$\frac{\partial^3 C}{dxdy^2} \delta C = 0, \quad \forall y \quad \text{at} \quad x = 0$$

$$\left[\frac{\partial^3 C}{\partial x^2 \partial y} - m(x)H_1(x) \right] \delta C = 0, \quad \forall x \quad \text{at} \quad y = L$$

$$\frac{\partial^3 C}{\partial x^2 \partial y} \delta C = 0, \quad \forall x \quad \text{at} \quad y = 0, \quad (40)$$

(iii) and boundary conditions at corners

$$\left[\frac{\partial^2 C}{\partial x \partial y} - G \right] \delta C = 0, \quad \text{at} \quad x = L; \quad y = L$$

$$\frac{\partial^2 C}{\partial x \partial y} \delta C = 0, \quad \text{at} \quad x = 0; \quad y = 0, L \quad \text{or}$$

$$x = L; \quad y = 0. \quad (41)$$

It can be shown that it is sufficient that the function $C(x, y)$ satisfy the following conditions in order for the above boundary conditions to be specified, in some specific cases:

$$C = 0, \quad \text{at} \quad x = 0, L; \quad \text{or} \quad y = 0, L \quad (42)$$

$$C = \frac{\partial C}{\partial x} = 0 \quad \text{at} \quad x = 0; \quad C = \frac{\partial C}{\partial y} = 0 \quad \text{at} \quad y = 0. \quad (43)$$

The boundary conditions in Eq. (42) are referred to simply supported beams, whereas the boundary conditions in Eq. (43) are referred to as the left-side clamped beams.

Stochastic Vibration of a Mobile Manipulator

U. O. Akpan

M. R. Kujath

Department of Mechanical Engineering,
Technical University of Nova Scotia,
Halifax, Nova Scotia B3J 2X4, Canada

The stochastic vibration of a flexible, articulated, and mobile manipulator is studied. The manipulator is mounted on a vehicle which is supported by a suspension system. Stochastic excitation of the manipulator is induced by the uniform horizontal motion of the vehicle on a traction surface. The power spectral density representation and the state-space representation are used to derive expressions for the covariance matrices of the manipulator tip motions. Sensitivity of the variance of the tip motion to the manipulator configuration, length, vehicle velocity, surface roughness coefficient, and structural damping and stiffness are explored. Suggestions for mobile manipulator design to minimize the influence of the stochastic base vibration on the manipulator tip motion are proposed.

1 Introduction

In many future applications such as space explorations, toxic waste clean up, fire fighting, logging, and planting—in unstructured environments outside the factories—mobile manipulators will be required instead of the conventional industrial manipulators which are mounted on fixed bases. The motion of the vehicle on a rough terrain will induce stochastic vibration in the manipulator structure. An understanding of the stochastic vibration of a mobile manipulator and its sensitivity to the system parameters is important for the structural design and control strategy development.

Most studies on mobile manipulators treat them as simple vehicles without dynamics. These reports focus on the map building of the unknown environments (Yun-Hui and Suguru, 1991) and on the motion planning algorithm (Jacobs and Canny, 1989). The limited studies on the dynamics of mobile manipulators treat the manipulator as chains of rigid links mounted on a vehicle (Hootsman and Dubowsky, 1991). In addition, the reported studies do not consider the base excitation as stochastic. Since in practical application, the motion of the tip of a manipulator is very important the study is concerned with the stochastic vibration of the tip of a mobile manipulator.

To study the tip vibration two representations are used: the state-space representation and the power spectral density representation. Figure 1 shows a model of a planar manipulator mounted on a vehicle which is supported by a suspension. The suspension is connected to the vehicle body by a linear joint.

It is assumed that the flexibility of the manipulator and the suspension is concentrated at the joints; the kinematic configuration of the links of the mobile manipulator can be represented using Denavit Hartenberg homogenous transformation matrix (Spong and Vidyasagar, 1989) and is assumed invariant when the stochastic vibration is studied; the motion vector $\mathbf{r} = [r_1, r_2, \ldots, r_n]^T$ represents the small elastic motion about a kinematic configuration; the vehicle suspension motion vector $\mathbf{r}_v = [s, r_0]^T$ is known; the total motion of the system can be expressed as $\mathbf{r} + \mathbf{r}_v$; the system damping is viscous, below critical value, concentrated at the joints, and invariant with respect to changes of the kinematic configuration; Kelvin-Voigt spring damping system is used; the random excitation—due to the uniform motion of the vehicle on a traction surface is small and produces small responses; the vehicle suspension maintains constant contact with the ground and there is no deformation of the surface during motion; the effect of gravity is neglected.

Contributed by the Applied Mechanics Division of THE AMERICAN SOCIETY OF MECHANICAL ENGINEERS for publication in the ASME JOURNAL OF APPLIED MECHANICS.

Discussion on this paper should be addressed to the Technical Editor, Professor Lewis T. Wheeler, Department of Mechanical Engineering, University of Houston, Houston, TX 77204-4792, and will be accepted until four months after final publication of the paper itself in the ASME JOURNAL OF APPLIED MECHANICS.

Manuscript received by the ASME Applied Mechanics Division, July 26, 1995; final revision, Feb. 11, 1996. Associate Technical Editor: M. Shinozuka.

2 Mathematical Formulation

2.1 Surface Profile. A mobile manipulator can move on diverse surfaces. For a large class of problems, the excitation produced by the surface $r_0(t)$ can be modeled as output of a shaping filter to a white noise expressed by (Narayanan and Raju, 1990)

$$\dot{r}_0(t) = \mathbf{F}_s(t)\mathbf{r}_0(t) + \dot{s}(t)\mathbf{B}_s(t)\mathbf{w}(t) \quad \text{for} \quad \dot{s}(t) \geq 0 \quad (1)$$

where $\mathbf{w}(s(t))$ is a vector of white noise consider as a function of the space coordinate s (which in turn is a function of time) with covariance matrix

$$E\{\mathbf{w}(s(t_1))\mathbf{w}^T(s(t_2))\} = \mathbf{Q}\delta(s(t_1) - s(t_2)). \quad (2)$$

Equation (1) gives the state space representation of the excitation $r_0(t)$ and is also the time domain description. Since the vehicle velocity $\dot{s}(t)$ is constant, the system excitation $r_0(t)$ is stationary and has power spectral density

$$\mathbf{S}_{r_0r_0} = \mathbf{S}(\omega, \dot{s}). \quad (3)$$

Equation (3) is the frequency domain representation of the excitation.

2.2 System Equation of Motion. Application of the Lagrangian principle leads to the equation of motion

$$\mathbf{D}\ddot{\mathbf{r}}(t) + \mathbf{C}\dot{\mathbf{r}}(t) + \mathbf{K}\mathbf{r}(t) = \mathbf{F}_1 r_0(t) + \mathbf{F}_2\dot{r}_0(t) \quad (4)$$

where $\mathbf{D}$, $\mathbf{C}$, $\mathbf{K}$, $\mathbf{F}_1$, and $\mathbf{F}_2$ are the inertia matrix, damping matrix, stiffness matrix, coefficient vector involving the excitation $r_0(t)$ and coefficient vector involving the excitation $\dot{r}_0(t)$, respectively. Two representations—the power spectral density representation and the state-space representation—are used to solve Eq. (4) for the joint vibration.

2.3 Power Spectral Density Representation. The vector $\mathbf{r}$ can be expressed in terms of the mass normalized modal matrix $\mathbf{U}$ and the normal coordinate $\mathbf{e}$ as

$$\mathbf{r}(t) = \mathbf{U}\mathbf{e}(t). \quad (5)$$

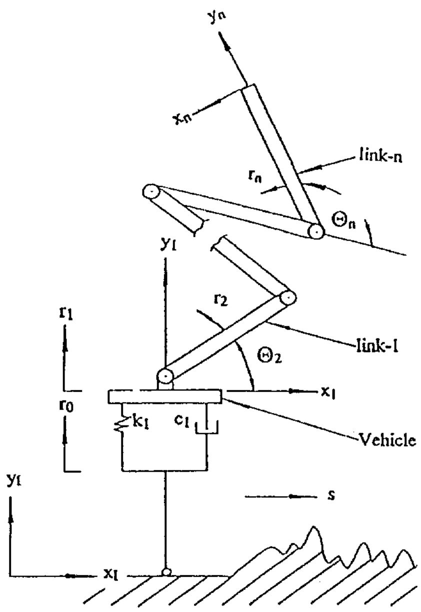

Fig. 1 Definition of the manipulator coordinates: $\Theta_2 \ldots \Theta_n$—system configuration coordinates, s—vehicle horizontal motion, r_0—forced motion of the suspension, r_1—vehicle vertical motion, $r_1, \ldots, r_n$ joint elastic motion, $x_1 = [x_1, y_1]^T$—vehicle frame, $x_n = [x_n, y_n]^T$—tip frame, $x_I = [x_I, y_I]^T$—inertia frame

Equation (4) can be expressed in the decoupled form

$$\ddot{e}_v(t) + 2\xi_v\omega_v\dot{e}_v(t) + \omega_v^2 e_v(t) = \mathbf{u}_v^T(\mathbf{F}_1 r_0 + \mathbf{F}_2\dot{r}_0(t)),$$
$$v = 1, 2, \ldots, n \quad (6)$$

where $\mathbf{u}_v^T$ represents the transpose of the vth column of $\mathbf{U}$, ω_v is the natural frequency of mode v and ξ_v is the damping factor. Using the Duhamel integral the displacement response of mode v is obtained as

$$e_v(t) = \int_{-\infty}^{\infty} h_v(t-\tau)\mathbf{u}_v^T(\mathbf{F}_1 r_0 + \mathbf{F}_2\dot{r}_0(t))d\tau \quad (7)$$

$$h_v(t) = u(t)\frac{1}{\omega_{dv}}e^{-\xi_v\omega_v t}\sin(\omega_{dv}t), \quad \omega_{dv} = \omega_v\sqrt{1-\xi_v^2}, \quad (8)$$

τ is the time lag, $h_v(t)$ is the impulse response function of mode v, and $u(t)$ is the unit step function. The crosscorrelation of the displacements of joint v and joint-m $R_{r_v r_m}(\tau)$ is obtained as

$$R_{r_v r_m}(\tau) = E\{r_v(t)r_m(t+\tau)\}$$
$$= \sum_{j=1}^{n}\sum_{k=1}^{n} U_{vj}U_{mk}E\{e_j(t)e_k(t+\tau)\}. \quad (9)$$

The power spectral density of r_v and r_m can be obtained by the Wiener Khinchine relation (Yang, 1986) using Eqs. (3), (6), (7), and (8) as

$$S_{r_v r_m}(\omega) = (\mathbf{U}_v^T\mathbf{F}_1\mathbf{S}_{r_0 r_0}(\omega)\mathbf{U}_m^T\mathbf{F}_1$$
$$+ \omega^2\mathbf{U}_v^T\mathbf{F}_2\mathbf{S}_{r_0 r_0}(\omega)\mathbf{U}_m^T\mathbf{F}_2)\sum_{j=1}^{n}\sum_{k=1}^{n} U_{vj}U_{mk}H_j H_k^* \quad (10)$$

where $H_j = (\omega_j^2 - \omega^2 + 2i\xi_j\omega\omega_j)^{-1}$, $i = \sqrt{-1}$. The covariance matrix of the joint displacements can be obtained as

$$\mathbf{R}_{\mathbf{rr}}(0) = E\{\mathbf{rr}^T\} = \int_{-\infty}^{\infty}\mathbf{S}_{\mathbf{rr}}(\omega)d\omega. \quad (11)$$

The residue theorem can be used to solve Eq. (11).

2.4 State-Space Representation. The joint motion variables $\mathbf{r}$, $\dot{\mathbf{r}}$ and the excitation vector r_0 can be transformed to a state variable $\mathbf{y}$ define as

$$\mathbf{y} = [\mathbf{r}^T, \dot{\mathbf{r}}^T, r_0]^T. \quad (12)$$

Application of Eq. (12) to Eqs. (1) and (4) transform them to

$$\dot{\mathbf{y}} = \mathbf{A}\mathbf{y} + \dot{s}(t)\mathbf{B}\mathbf{w}(s(t))$$
$$\mathbf{A} = \begin{bmatrix} \mathbf{A}_z & \mathbf{D}^{-1}(\mathbf{F}_1 + \mathbf{F}_2\mathbf{F}_s(t)) \\ \mathbf{0} & \mathbf{F}_s \end{bmatrix},$$
$$\mathbf{A}_z = \begin{bmatrix} \mathbf{0} & \mathbf{I} \\ -\mathbf{D}^{-1}\mathbf{K} & -\mathbf{D}^{-1}\mathbf{C} \end{bmatrix}, \quad \mathbf{B} = \begin{bmatrix} \mathbf{D}^{-1}\mathbf{B}_s \\ \mathbf{B}_s \end{bmatrix} \quad (13)$$

The covariance matrix $\mathbf{P}$ of the state vector $\mathbf{y}$ can be define as

$$\mathbf{P} = E\{\mathbf{y}\mathbf{y}^T\} \quad (14)$$

where $E\{\cdot\}$ is the expectation operator. Since the vehicle horizontal velocity $\dot{s}(t)$ is constant, it can be shown (Akpan, 1996) that for a stochastic dynamic system modeled by Eq. (3), the covariance matrix $\mathbf{P}$ satisfies the Liapunov matrix algebraic equation

$$\mathbf{AP} + \mathbf{PA}^T = -\dot{s}(t)\mathbf{BQB}^T. \quad (15)$$

The components of the state covariance matrix $\mathbf{P}$ can be reassembled into the displacement vector $\mathbf{r}$, and the velocity vector $\dot{\mathbf{r}}$ covariance matrices defined as $\mathbf{R}_{\mathbf{rr}}(0) = E\{\mathbf{rr}^T\}$ and $\mathbf{R}_{\dot{\mathbf{r}}\dot{\mathbf{r}}}(0) = E\{\dot{\mathbf{r}}\dot{\mathbf{r}}^T\}$, respectively.

2.5 Tip Covariance. The covariance matrix of the tip motion can be computed in any moving coordinate frame attached either to the vehicle or any of the links. A Jacobian $\mathbf{J}$ relating the joint motion $\mathbf{r}$ (obtained using any of the two representations) to the tip motion vector $\mathbf{x}$ can be applied to compute the later, i.e.,

$$\mathbf{x} = \mathbf{J}\mathbf{r}. \quad (16)$$

Using for example $\mathbf{x}_1$ frame which is attached to the vehicle then the covariance matrix of the tip motion is

$$\mathbf{R}_{\mathbf{x}_1\mathbf{x}_1}(0) = E\{\mathbf{x}_1\mathbf{x}_1^T\} = E\{\mathbf{J}_1\mathbf{r}(\mathbf{J}_1\mathbf{r})^T\}$$
$$= \mathbf{J}_1 E\{\mathbf{rr}^T\}\mathbf{J}_1^T = \mathbf{J}_1\mathbf{R}_{\mathbf{rr}}(0)\mathbf{J}_1^T \quad (17)$$

where $\mathbf{J}_1$ is the Jacobian associated with the frame. A rotated frame $\mathbf{x}_*$ in which the covariance matrix of the tip motion is diagonal can be used to compute the covariance matrix of the tip response. This frame will be referred to as the principal variance frame. The principal Jacobian $\mathbf{J}_*$ can be defined as the Jacobian associated with the principal variance frame, i.e.,

$$\mathbf{R}_{\mathbf{x}_*\mathbf{x}_*}(0) = \mathbf{J}_*\mathbf{R}_{\mathbf{rr}}(0)\mathbf{J}_*^T. \quad (18)$$

To compute the principal variance matrix $\mathbf{R}_{\mathbf{x}_*\mathbf{x}_*}(0)$ singular value decomposition of the tip motion covariance matrix in a

Table 1 Parameter values used for simulation

Parameter	Value	Unit
m_1	10	kg
m_2	2	kg
m_3	2	kg
k_1	4000	N/m
k_2	4000	N/rad
k_3	4000	N/rad
c_1	10	Ns/m
c_2	10	Ns/rad
c_3	10	Ns/rad

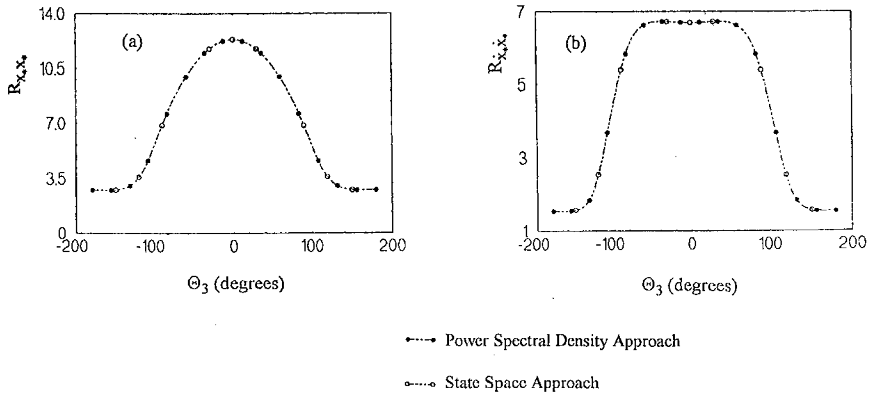

Fig. 2 Comparison of results from state-space representation (SS) and power spectral density representation (PSD) for $\Theta_3 = 0$ deg, $\dot{s}(\bar{t}) = 5$. $\alpha = .45$: (*a*) displacement variance $R_{x_*x_*}(0)$, (*b*) velocity variance $R_{\dot{x}_*\dot{x}_*}(0)$

known frame, for example $\mathbf{R}_{x_1x_1}(0)$, is employed and this process leads to

$$\mathbf{R}_{x_1x_1}(0) = \mathbf{U}_{x_1}\Sigma_{x_1}\mathbf{U}_{x_1}^T \tag{19}$$

where $\mathbf{U}_{x_1}$ is an orthornomal matrix. The diagonal matrix Σ_{x_1} contains the eigenvalues of $\mathbf{R}_{x_1x_1}(0)$ and its elements represents the principal variance of the tip displacements $\mathbf{R}_{x_*x_*}(0)$, i.e.,

$$\mathbf{R}_{x_*x_*}(0) = \Sigma_{x_1}(0). \tag{20}$$

Similar representation can be made for the tip velocity.

3 Examples

To illustrate the principles discussed in the preceding sections, two examples are considered. A zero-mean homogenous surface model with spatial autocorrelation function in the vehicle motion coordinate s of the form $R_{r_0r_0}(s_1 - s_2) = \sigma^2 e^{-\alpha|s_1-s_2|}$ where the term $s_1 - s_2$ stands for the spatial lag $s(t_1) - s(t_2)$ is employed. This model employed by Hac (1985) represents the surface of a road. The parameter $\alpha = .15$/m represents an asphalt road and $\alpha = .45$/m represents a paved road (Hac, 1985), σ is the variance of the surface irregularity. The first-order autoregressive model of the autocorrelation function is represented in the time domain t as

$$\dot{r}_0(t) = -\dot{s}(t)\alpha r_0(t) + \dot{s}(t)\sigma\sqrt{2\alpha}w(s(t)). \tag{21}$$

Equation (21) is the state-space representation of the excitation that is used in the examples. The double-sided power spectral density of the excitation r_0 is

$$S_{r_0r_0} = \frac{\sigma^2\alpha\dot{s}}{\pi(\omega^2 + \alpha^2\dot{s}^2)}. \tag{22}$$

To generalize the results, a dimensionless time $\bar{t}$ defined as

$$t = \sqrt{\frac{D_{11}}{K_{11}}}\,\bar{t}, \quad \frac{d}{dt} = \sqrt{\frac{K_{11}}{D_{11}}}\frac{d}{d\bar{t}}, \quad \frac{d^2}{dt^2} = \frac{K_{11}}{D_{11}}\frac{d^2}{d\bar{t}^2},$$

where D_{11} and K_{11} are the (1, 1) elements of the inertia and stiffness matrices, respectively, can be introduced. Further, all responses are normalized by the standard deviation of the surface profile σ. In this study, the Smith algorithm (1971) was used to solve Eq. (15).

Example 1: Single Link Manipulator on a Vehicle. The Lagrangian L and the Rayleigh dissipation function R for the system are

$$L = \tfrac{1}{2}b_1(\dot{r}_1^2 + \dot{s}^2) + \tfrac{1}{2}b_2\dot{r}_2^2 + b_3\dot{r}_1\dot{r}_2\cos(\Theta_1) + \tfrac{1}{2}k_1(r_1 - r_0)^2 + \tfrac{1}{2}k_2r_2^2$$

$$R = \tfrac{1}{2}c_1(\dot{r}_1 - \dot{r}_0)^2 + \tfrac{1}{2}c_2\dot{r}_2^2$$

$$b_1 = m_1 + m_2, \quad b_2 = I_2 + m_2(l_{c2})^2, \quad b_3 = m_2l_{c2}.$$

The elements of the resulting system matrices can be obtained. Using the representations discussed in Section 2.3 the variance of the vehicle displacement, manipulator joint displacement, and the covariance of the vehicle/manipulator joint displace-

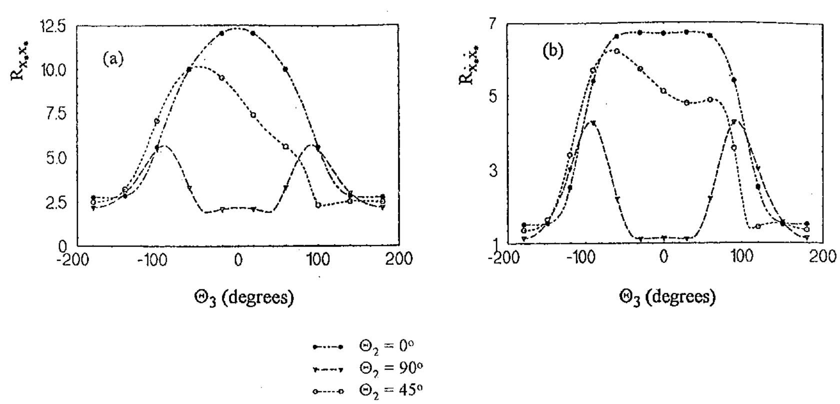

Fig. 3 Sensitivity of normalized responses to manipulator configuration for $\dot{s}(\bar{t}) = 5$, $\alpha = .45$: (*a*) displacement variance $R_{x_*x_*}(0)$, (*b*) velocity variance $R_{\dot{x}_*\dot{x}_*}(0)$

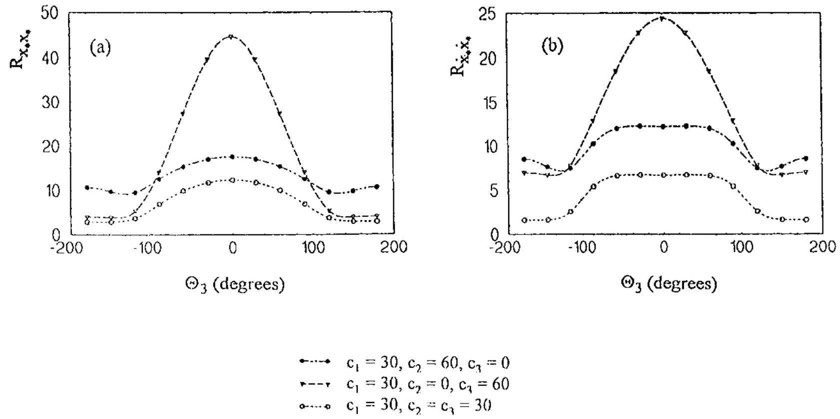

Fig. 4 Sensitivity of normalized responses to system damping for $\Theta_2 = 0$ deg, $\dot{s}(\bar{t}) = 5$, $\alpha = .45$: (a) displacement variance $R_{x_*x_*}(0)$, (b) velocity variance $R_{\dot{x}_*\dot{x}_*}(0)$

ment can be obtained as $R_{r_1r_1}(0)$, $R_{r_2r_2}(0)$ and $R_{r_1r_2}(0)$, respectively. It can be shown that the covariance matrix of the tip response in the vehicle frame $\mathbf{x}_1$ is given as

$$\mathbf{R}_{\mathbf{x}_1\mathbf{x}_1}(0) = \begin{bmatrix} R_{11} & R_{12} \\ R_{21} & R_{22} \end{bmatrix},$$

$$R_{11} = R_{r_2r_2}(0)l^2 \sin^2(\Theta_1),$$

$$R_{21} = R_{12}$$
$$= -R_{r_2r_2}(0)l^2 \cos(\Theta_1)\sin(\Theta_1) - R_{r_1r_2}(0)l \sin(\Theta_1),$$

$$R_{22} = R_{r_2r_2}(0)l^2\cos^2(\Theta_1) + 2R_{r_1r_2}(0)l\cos(\Theta_1) + R_{r_1r_1}(0).$$

Further, using the principles developed in Section 2.4, it can be shown that the maximum variance of the tip response occurs at the configuration $\Theta_1 = 0$ deg $\pm$ 180 deg and has the value

$$\mathbf{R}_{\mathbf{x}_*\mathbf{x}_*}(0) = (R_{r_2r_2}(0)l^2 + R_{r_1r_1}(0) + 2R_{r_1r_2}(0)l)\begin{bmatrix} 0 & 0 \\ 0 & 1 \end{bmatrix}. \quad (23)$$

Example 2: Two Links Manipulator on a Vehicle. The Lagrangian L of the two-link flexible manipulator with the vehicle motion and the elements of the resulting system matrices are given in the Appendix.

4 Simulation Results and Discussions

Numerical simulations to determine the principal variance of the tip motion were performed. The main focus of the discussion are the results for the two-link mobile manipulator. Table 1 gives the values of the parameters used for simulation. In the following discussion the term displacement refers to the major principal variance of the tip displacement, while the term velocity refers to the major principal variance of the tip velocity.

Figures 2 and 3 are made for the specified values of Θ_2, and for ± 180 deg range of Θ_3; $\alpha = .45$; $\dot{s} = 5$. Figure 2 shows the displacements and velocities obtained using the power spectral density and the state-space representations. Both representations yield the same displacements and velocities. The state-space representation, however, has some advantages over the power spectral density representation since it can accommodate nonproportional damping. Also, unlike the power spectral density, the state-space representation yields the displacements and the velocities simultaneously (see Eq. (15)). Further, it avoids the contour integrals required for the power spectral density representation (Eq. (11)) and it can be used for very large degree-of-freedom systems.

Figure 3 shows the sensitivities of the displacements and velocities to changes in the manipulator configuration Θ_2. It is observed that the more perpendicular the manipulator structure to the excitation, the higher the response. Thus, the highest responses occur at $\Theta_2 = \Theta_3 = 0$ deg. At this configuration the links of the manipulator are perpendicular to the stochastic base excitations $\dot{r}_0(t)$ and $r_0(t)$. The displacement and velocity at $\Theta_2 = 90$ deg and for $\Theta_3 = 0$ deg are that of the vehicle since the dynamic coupling terms between the vehicle and the links are zero ($D_{12} = D_{21} = D_{13} = D_{31} = 0$) therefore the vehicle moves with the link as a rigid body.

The influence of the manipulator damping on displacement and velocity is shown in Fig. 4. The displacement and the

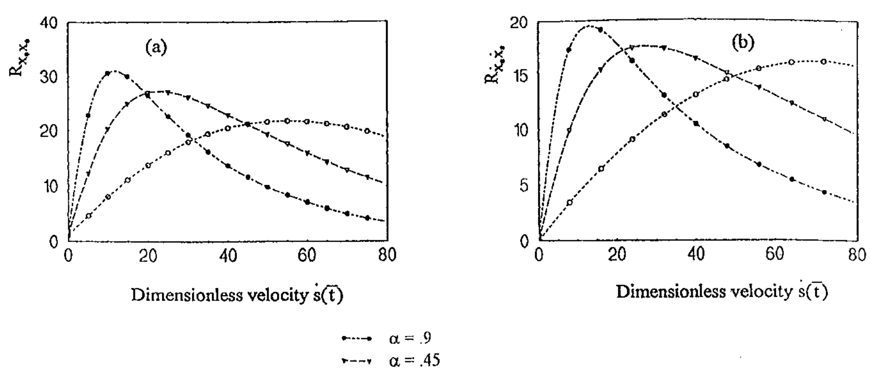

Fig. 5 Effect of surface roughness coefficient on normalized major principal variances for $\Theta_2 = \Theta_3 = 0$ deg; (a) displacement variance $R_{x_*x_*}(0)$, (b) velocity variance $R_{\dot{x}_*\dot{x}_*}(0)$

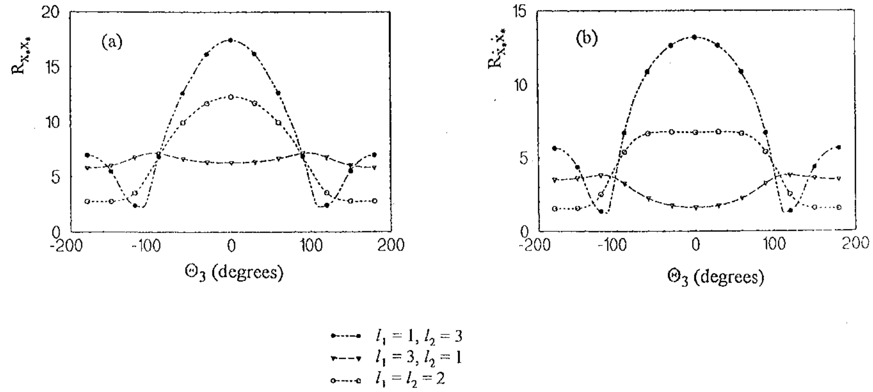

Fig. 6 Sensitivity of normalized response to manipulator links lengths for, $\Theta_2 = 0$ deg, $\dot{s}(t) = 5$, $\alpha = .45$: (a) displacement variance $R_{x_*x_*}(0)$, (b) velocity variance $R_{\dot{x}_*\dot{x}_*}(0)$

velocity responses can be reduced with the presence of damping. But if only the upper link (link 2) and the suspension are damped, the responses have low sensitivity to damping. On the other hand, if only the lower link (link 1) and the suspension are damped are damped the responses are very sensitive to damping.

Figure 5 shows the effect of the surface roughness coefficient α on the responses for the configuration $\Theta_2 = \Theta_3 = 0$. The surface with high roughness coefficient $\alpha = .9$ results in quick rise and very high responses. The influence of the relative lengths of the lower link (link 1) to the upper link (link 2) on the displacements and velocities is shown in Fig. 6. It is noted that the longer the terminal link (link 2) compared to link 1, the higher the responses. Figure 7 shows the computed orientations and the scaled values of the principal variances of the tip motion for six configurations $[\Theta_2, \Theta_3] = [0°, 0°]$, $[0°, 90°]$, $[45°, 0°]$, $[45°, 90°]$, $[90°, 90°]$, $[90°, 0°]$. The principal variances are illustrated by the crossed line segments located at the manipulator tip. The major variance is very high compared to the minor variance, i.e., the stochastic motion of the manipulator tip is almost unidirectional though the direction is different for different configurations.

5 Conclusions

The stochastic vibration of a mobile manipulator subjected to a random base excitation has been studied. The manipulator was mounted on a vehicle with wheels. Uniform motion of the vehicle on a rough traction surface induces stochastic excitation on the manipulator. Two representations—the Power Spectral Density and the State-Space—have been used to develop expressions for the covariance matrices of the manipulator joint and tip responses. Further, by using the singular value decomposition technique expressions for the direction and magnitude of the principal variance of the tip motion have been derived.

A single-link and a two-link flexible mobile manipulators have been used to illustrate the ideas. Numerical studies of the principal variance show that the responses obtained from the power spectral density and the state-space representations are the same. The state-space representation is, however, recommended for practical applications, because it gives the velocity and the displacement covariance simultaneously. Also, the state-space representation can accommodate nonproportional damping without computational complications and it avoids complex contour integration. The direction and the magnitude of the principal variance has been found to vary significantly for different configurations and to be almost unidirectional along the major principal variance axis. From the sensitivity analysis it can be concluded that to minimize the stochastic vibration of the manipulator tip: in addition to the suspension damping the damping efforts should be concentrated in the lower links and joints; the lower links should be stiffer than the upper links; the lower links should be longer than the upper links. Therefore, it is suggested that for minimal tip vibration most of the design and control efforts should be focused on the vehicle suspension and the manipulator lower links and joints.

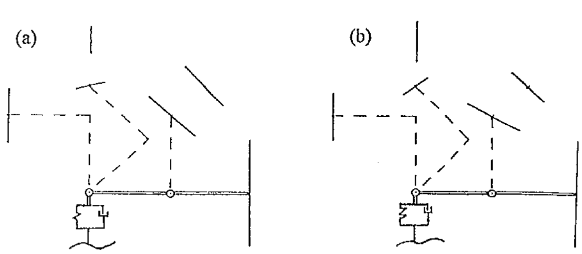

Fig. 7 Major and minor principal variances of the tip motion illustrated by the line segments located at the manipulator tip ($\dot{s}(t) = 5$, $\alpha = .45$): (a) displacement variance $R_{x_*x_*}(0)$, (b) velocity variance $R_{\dot{x}_*\dot{x}_*}(0)$

References

Akpan, U. O., 1996, "Dynamics of Mobile Manipulator Structures," Ph.D. thesis, Technical University of Nova Scotia, Nova Scotia, Canada.

Hac, A., 1985, "Suspension Optimization of a 2 DOF Vehicle Model Using 'Stochastic Optimal Control Technique,' " *Journal of Sound and Vibration*, Vol. 100, No. 3, pp. 343–357.

Hootsmans, N. A. M., and Dubowsky, S., 1991, "Large motion Control of mobile Manipulators Including Vehicle Suspension Characteristics," *Proceedings IEEE International Conference on Robotics and Automation*, Sacramento, CA, pp. 2336–2341.

Jacobs, P., and Canny, J., 1989, "Planning Smooth Paths for Mobile Robots," *Proceedings IEEE International Conference on Robotics and Automation*, Scottsdale, Az.

Narayanan, S., and Raju, G. V., 1990, "Stochastic Optimal Control of Non-Stationary Response of a Single-Degree-of-Freedom Vehicle Model," *Journal of Sound and Vibration*, Vol. 141, No. 3, pp. 449–463.

Smith, P. G., 1971, "Numerical Solution of the Matrix Equation $\mathbf{AX} + \mathbf{XA}^T + \mathbf{B} = \mathbf{0}$" *IEEE Transaction on Automatic Control*, Vol. AC-16, pp. 278–279.

Spong, M. W., and Vidyasagar, M., 1989, *Robot Dynamics and Control*, John Wiley and Sons, New York.

Yang, C. Y., 1986, *Random Vibration of Structures*, John Wiley and Sons, New York.

Yun-Hui, L., and Suguru, A., 1991, "Proposal Tangent Graph and Extended Tangent Graph for Path Planning of Mobile Robots," *Proceedings IEEE International Conference on Robotics and Automation*, Sacramento, CA, pp. 312–317.

APPENDIX

Derivation of Equation of Motion

The Lagrangian L for a two-link flexible manipulator structure with revolute joints including the vehicle motion and the Rayleigh dissipation function R are given as

$$L = \tfrac{1}{2}a_1(\dot{r}_1^2 + \dot{s}^2) + \tfrac{1}{2}a_2\dot{r}_2^2 + \tfrac{1}{2}a_3(\dot{r}_2 + \dot{r}_3)^2 + a_4\dot{r}_2(\dot{r}_3 + \dot{r}_2)$$

$$\times \cos(\Theta_3 + r_3) + a_5\dot{r}_1\dot{r}_2 \cos(\Theta_2 + r_2)$$

$$+ a_6\dot{r}_1(\dot{r}_2 + \dot{r}_3)\cos(\Theta_2 + r_2 + \Theta_3 + r_3)$$

$$- a_5\dot{s}\dot{r}_2 \sin(\Theta_2 + r_2) - a_6\dot{s}(\dot{r}_2 + \dot{r}_3)\sin(\Theta_2 + r_2$$

$$+ \Theta_3 + r_3) + \tfrac{1}{2}k_1(r_1 - r_0)^2 + \tfrac{1}{2}k_2 r_2^2 + \tfrac{1}{2}k_3 r_3^2 \quad \text{(A1)}$$

$$R = \tfrac{1}{2}c_1(\dot{r}_1 - \dot{r}_0)^2 + \tfrac{1}{2}c_2\dot{r}_2^2 + \tfrac{1}{2}c_3\dot{r}_3^2. \quad \text{(A2)}$$

The elements of the system matrices are given below.

Inertia Matrix D

$$D_{11} = a_1 \quad D_{12} = D_{21} = a_5\cos(\Theta_2) + a_6\cos(\Theta_2 + \Theta_3)$$

$$D_{13} = D_{31} = a_6\cos(\Theta_2 + \Theta_3)$$

$$D_{22} = a_2 + a_3 + 2.0a_4\cos(\Theta_3)$$

$$D_{23} = D_{32} = a_3 + a_4\cos(\Theta_3) \quad D_{33} = a_3$$

$$a_1 = m_1 + m_2 + m_3, \quad a_2 = I_2 + m_2(l_{c2})^2 + m_3(l_2)^2,$$

$$a_3 = I_3 + m_3(l_{c3})^2$$

$$a_4 = m_3 l_{c3} l_2, \quad a_5 = m_2 l_{c2} + m_3 l_2, \quad a_6 = m_3 l_{c3}$$

Stiffness Matrix K

$$K_{11} = k_1, \quad K_{22} = k_2, \quad K_{33} = k_3, \quad K_{nm} = 0 \quad \text{for} \quad n \neq m$$

Damping Matrix C

$$C_{11} = c_1, \quad C_{22} = c_2, \quad C_{33} = c_3, \quad C_{nm} = 0 \quad \text{for} \quad n \neq m$$

Excitation Vectors $\mathbf{F}_1$, and $\mathbf{F}_2$

$$\mathbf{F}_1 = \begin{bmatrix} k_1 \\ 0 \\ 0 \end{bmatrix}, \quad \mathbf{F}_2 = \begin{bmatrix} c_1 \\ 0 \\ 0 \end{bmatrix}$$

$$F_s(t) = -\dot{s}(t)\alpha \quad \mathbf{B}_s = \sigma\sqrt{2\alpha}$$

Jacobian Matrix $\mathbf{J}_1$

$$J_{11} = 0 \quad J_{12} = -l_2\sin(\Theta_2) - l_3\sin(\Theta_2 + \Theta_3)$$

$$J_{13} = -l_3\sin(\Theta_2 + \Theta_3)$$

$$J_{21} = 1 \quad J_{22} = l_2\cos(\Theta_2) + l_3\cos(\Theta_2 + \Theta_3)$$

$$J_{23} = l_3\cos(\Theta_2 + \Theta_3)$$

F. Zhu
Graduate Student.

R. Sharma
Graduate Student.

C. D. Rahn[1]
Assistant Professor,
Assoc. Mem. ASME.

Department of Mechanical Engineering,
Clemson University,
Clemson, SC 29634-0921

Vibrations of Ballooning Elastic Strings

This paper investigates the nonlinear dynamic response of a linearly elastic string fixed at one boundary and undergoing constant speed circular motion at the other boundary. The response divides into nonlinear steady-state ballooning that is fixed relative to a rotating coordinate system and linearized vibration about the steady state. Single-loop balloons have high tension and purely imaginary eigenvalues. The single-loop vibration frequencies generally decrease with increasing balloon length. Highly extensible strings whirl in first and higher modes with forward whirling modes having lower frequencies. Axially stiff strings exhibit whirling only in higher modes. If the nondimensional string stiffness is larger than 1000, then the inextensible steady-state solutions and the lowest six vibration frequencies match the extensible results to within three percent. One-and-a-half loop balloons are divergently unstable. Long and/or sufficiently extensible strings form low-tension double-loop balloons. Inextensible double balloons are coupled mode flutter unstable. The steady-state balloons, steady-state eyelet tension, and balloon stability are experimentally verified.

1 Introduction

Manufacture and transport of fibers, filaments, wire, and yarn often requires material rotation. Low tension and/or highly extensible material undergoes a variety of complex motions during rotation. Motion that appears fixed relative to a rotating coordinate frame is called ballooning (Ames et al., 1968). Buckling instability can cause a rapid change in the balloon shape commonly called "balloon collapse" in the textile industry. Flutter instability can induce material oscillation about the nominal balloon shape (Stump and Fraser, 1996). These dynamic behaviors cause tension variations that can lead to material failure and reduced productivity of the associated process.

Textile applications such as high-speed spinning and unwinding motivated early research on the formation and behavior of ballooning strings (De Barr and Catling, 1965). Batra et al. (1989a, 1989b) summarized early contributions and introduced numerical predictions of the balloon shapes and tension in textile processes. Fraser et al. (1992) developed and solved the yarn path on the package and in the balloon for over-end unwinding. Fraser (1993) formulated the ring spinning balloon equations of motion and boundary conditions. The effects of traveller mass on the guide eye tension and shape of free and controlled balloons were investigated. Stump and Fraser (1996) numerically simulated the dynamics of the ring spinning balloon for inextensible yarns.

Kolodner (1955) initiated mathematical research on rotating strings. He discussed the effect of rotating speed on the steady motions of a fixed-free inelastic string. Stuart (1975) applied a global bifurcation theory to extend Kolodner's work to different boundary conditions. Ames et al. (1968) analytically and experimentally investigated the ballooning motion of an axially moving string under a periodic planar boundary excitation. Shih (1975) further analyzed the elliptic ballooning of these systems. Soedel and Soedel (1989) investigated the dynamics of a straight string rotating about a parallel axis. Antman (1995) developed general equations of motion for elastic strings including both whirling and drawing effects. O'Reilly (1996) studied the steady motion of a drawn string.

In related work, Healey (1990a) investigated the stability of rotating elastic and inextensible closed loops. Yang and Hutton (1995) included the interaction between the rotating string and stationary constraints. Healey (1990b) used group theoretic methods to study the large-amplitude, steadily rotating solutions of a conducting elastic wire stretched between fixed supports in a magnetic field.

This paper extends and complements the cited prior research by studying the dynamics of the linearly elastic balloon that forms between a fixed eyelet and a rotating eyelet. The equations of motion derive from Antman (1995) with a rotating boundary condition similar to Ames et al. (1968). Unlike previous researchers, however, the equations are solved in a two-step process. First, following Fraser (1993), shooting techniques solve the nonlinear equations governing the steady-state balloons. Second, modal analysis of the linearized equations of motion determines balloon stability, vibration frequencies, and mode shapes. The balloon shapes, steady-state tension, and balloon stability are experimentally verified.

2 Equations of Motion

Figure 1 shows a schematic diagram of the ballooning string system. The string is modeled as a perfectly flexible one-dimensional continuum pinned at the left boundary and attached to an eyelet rotating with constant angular velocity Ω at the right boundary. The unstressed, κ^0, steady state, κ^1, and final, κ^2, configurations of the string are shown. The coordinate system axes $\mathbf{e}_1$, $\mathbf{e}_2$, and $\mathbf{e}_3$ rotate about $\mathbf{e}_3$ with speed Ω. In this coordinate system, the steady-state κ^1 is stationary.

In the absence of air drag and gravity forces, the steady-state configuration lies in the $\mathbf{e}_1$–$\mathbf{e}_3$ plane. The vector $\mathbf{R}_1(S_0, T) = X(S_0)\mathbf{e}_1 + Z(S_0)\mathbf{e}_3$ locates κ^1 where S_0 is the arc length coordinate measured along κ^0 and T is time. The final configuration κ^2 is located by $\mathbf{R}_2(S_0, T)$. The relative displacement of the string between κ^1 and κ^2 is

$$\mathbf{U}(S_0, T) = \mathbf{R}_2 - \mathbf{R}_1 = U_1\mathbf{e}_1 + U_2\mathbf{e}_2 + U_3\mathbf{e}_3. \quad (1)$$

From Antman (1995), the balance of linear momentum in the absence of surface tractions and body forces is

[1] To whom all correspondence should be addressed.

Contributed by the Applied Mechanics Division of THE AMERICAN SOCIETY OF MECHANICAL ENGINEERS for publication in the ASME JOURNAL OF APPLIED MECHANICS.

Discussion on this paper should be addressed to the Technical Editor, Professor Lewis T. Wheeler, Department of Mechanical Engineering, University of Houston, Houston, TX 77204-4792, and will be accepted until four months after final publication of the paper itself in the ASME JOURNAL OF APPLIED MECHANICS.

Manuscript received by the ASME Applied Mechanics Division, July 29, 1996; final revision, Jan. 8, 1997. Associate Technical Editor: S. W. Shaw.

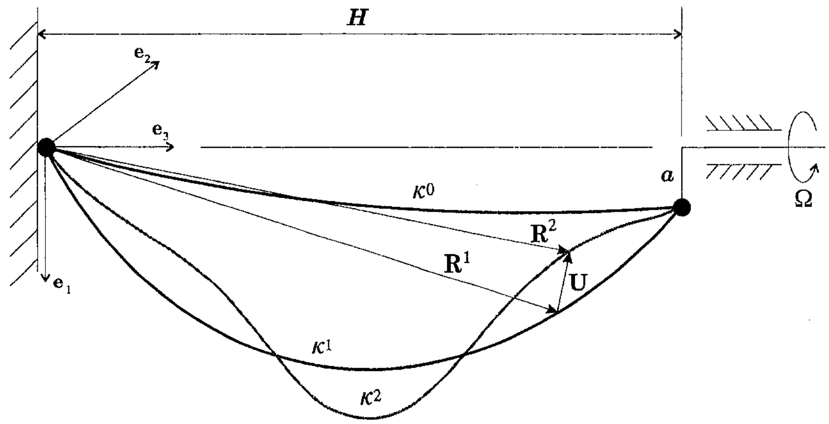

Fig. 1 Schematic diagram of a ballooning string

$$\frac{\partial \mathbf{P}_2}{\partial S_0} = \rho A_0 \frac{\partial^2 \mathbf{R}_2}{\partial T^2}, \tag{2}$$

where ρ and A_0 are the constant mass density and cross-sectional area of the unstressed string, respectively. The string tension vectors are defined by

$$\mathbf{P}_i = P_i \frac{\partial \mathbf{R}_i}{\partial S_0} \Big/ \frac{\partial S_i}{\partial S_0}, \tag{3}$$

where $i = 1$ and 2 for the steady-state and final configurations, respectively. For a linearly elastic material

$$P_i = EA_0\epsilon_i, \tag{4}$$

where E is Young's modulus. The strains of the string are

$$\epsilon_i = \frac{\partial S_i}{\partial S_0} - 1, \tag{5}$$

where S_1 and S_2 are the arc length coordinates measured along κ^1 and κ^2, respectively. For small strains, Eq. (5) approximates to

$$\epsilon_i = \frac{1}{2}\left(\frac{\partial \mathbf{R}_i}{\partial S_0}\cdot\frac{\partial \mathbf{R}_i}{\partial S_0} - 1\right). \tag{6}$$

Substitution of Eqs. (4) and (5) into Eq. (3) gives

$$\mathbf{P}_2 = \frac{P_1\epsilon_2}{\epsilon_1(1+\epsilon_2)}\frac{\partial \mathbf{R}_2}{\partial S_0}. \tag{7}$$

Substitution of Eqs. (1) and (7) into Eq. (2) with $\partial \mathbf{R}_1/\partial T = 0$ yields

$$\frac{\partial}{\partial S_0}\left(\frac{P_1\epsilon_2}{\epsilon_1(1+\epsilon_2)}\left(\frac{\partial \mathbf{R}_1}{\partial S_0} + \frac{\partial \mathbf{U}}{\partial S_0}\right)\right) = \rho A_0 \left\{ \Omega^2 \mathbf{e}_3 \times (\mathbf{e}_3 \times \mathbf{R}_1) + \Omega^2 \mathbf{e}_3 \times (\mathbf{e}_3 \times \mathbf{U}) + 2\Omega \mathbf{e}_3 \times \frac{\partial \mathbf{U}}{\partial T} + \frac{\partial^2 \mathbf{U}}{\partial T^2}\right\}, \tag{8}$$

or, nondimensionalized,

$$\frac{\partial}{\partial s}\left(\frac{p\epsilon_2}{\epsilon_1(1+\epsilon_2)}\left(\frac{\partial \mathbf{r}}{\partial s} + \frac{\partial \mathbf{u}}{\partial s}\right)\right) = \mathbf{e}_3 \times (\mathbf{e}_3 \times \mathbf{r}) + \mathbf{e}_3 \times (\mathbf{e}_3 \times \mathbf{u}) + 2\mathbf{e}_3 \times \frac{\partial \mathbf{u}}{\partial t} + \frac{\partial^2 \mathbf{u}}{\partial t^2}, \tag{9}$$

where

$$\mathbf{r} = x\mathbf{e}_1 + z\mathbf{e}_3 = \frac{\mathbf{R}_1}{a}, \quad s = \frac{S_0}{a}, \quad \mathbf{u} = \frac{\mathbf{U}}{a}, \tag{10}$$

$$p = \frac{P_1}{\rho A_0 a^2 \Omega^2}, \quad \gamma = \frac{E}{\rho a^2 \Omega^2}, \quad t = \Omega T, \quad \epsilon_1 = \frac{p}{\gamma}, \tag{11}$$

and a is the length of the rotating eyelet. From Eq. (6)

$$\epsilon_2 = \epsilon_1 + \frac{\partial \mathbf{r}}{\partial s}\cdot\frac{\partial \mathbf{u}}{\partial s} + \frac{1}{2}\frac{\partial \mathbf{u}}{\partial s}\cdot\frac{\partial \mathbf{u}}{\partial s}. \tag{12}$$

The corresponding boundary conditions are

$$\mathbf{r}(0) = 0, \quad \mathbf{r}(l_0) = \mathbf{e}_1 + h\mathbf{e}_3, \tag{13}$$

$$\mathbf{u}(0, t) = \mathbf{u}(l_0, t) = 0, \tag{14}$$

where $l_0 = L_0/a$ and $h = H/a$ are the nondimensional unstretched string length and balloon height, respectively.

3 Steady-State Balloon Shapes

Substitution of $\mathbf{u} = \mathbf{0}$ into Eq. (9) yields

$$\frac{d}{ds}\left(\frac{p}{1+p/\gamma}\frac{d\mathbf{r}}{ds}\right) = \mathbf{e}_3 \times (\mathbf{e}_3 \times \mathbf{r}), \tag{15}$$

or, in scalar form,

$$\frac{d}{ds}\left(\frac{p}{1+p/\gamma}\frac{dx}{ds}\right) = -x \tag{16}$$

$$\frac{d}{ds}\left(\frac{p}{1+p/\gamma}\frac{dz}{ds}\right) = 0. \tag{17}$$

Dot multiplication of Eq. (15) by $d\mathbf{r}/ds$ and use of Eq. (5) gives

$$\frac{d}{ds}\left(p + \frac{p^2}{2\gamma}\right) = \frac{d}{ds}\left(-\frac{1}{2}x^2\right). \tag{18}$$

Integration of Eq. (18) yields

$$p = \gamma\sqrt{(1+p_e/\gamma)^2 - x^2/\gamma} - \gamma, \tag{19}$$

where $p_e = p(0)$ is the nondimensional left eyelet tension.

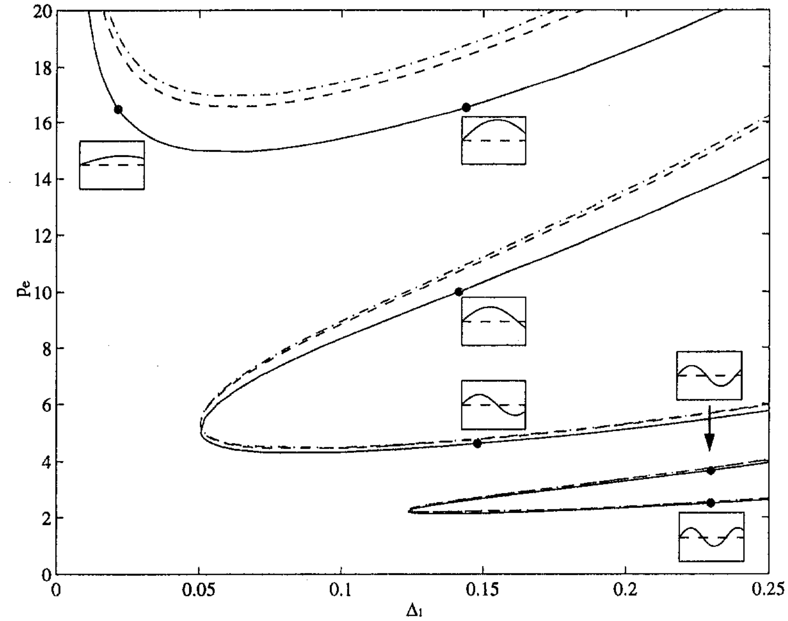

Fig. 2 Nondimensional eyelet tension versus string length: $h = 10$, $\gamma = 100$ (solid), $\gamma = 1000$ (dashed), and inextensible (dash-dotted). Subplots of balloon shapes correspond to the nearest marked points on the solid curve.

For an inextensible string, Eqs. (15) and (19) simplify to

$$\frac{d}{ds}\left(p\,\frac{d\mathbf{r}}{ds}\right) = \mathbf{e}_3 \times (\mathbf{e}_3 \times \mathbf{r}) \tag{20}$$

and

$$p = p_e - \tfrac{1}{2}x^2. \tag{21}$$

These equations can be solved analytically via Jacobi's elliptic sine functions (Hall et al., 1995).

Equations (16), (17), and (19) are solved using a shooting technique for the unknown functions $x(s)$, $z(s)$, and $p(s)$. Following Fraser (1993), the equations are integrated from $s = 0$ to $z(l_0) = h$ for given p_e using a Runge-Kutta fourth-order integrator. The initial conditions for the integration are

$$x(0) = z(0) = \frac{dz}{ds} = 0, \quad \frac{dx}{ds} = x_0',$$

The initial values x_0' that provide $x(l_0)^2 = 1$ are determined using an optimization algorithm in MATLAB.

The numerical results for p_e versus the steady-state length parameter $\Delta_1 = (l_1 - h)/l_1$ are shown in Fig. 2 for $\gamma = 100$ (solid curve), $\gamma = 1000$ (dashed curve), and inextensible (dash-dotted curve). The balloon shapes corresponding to the

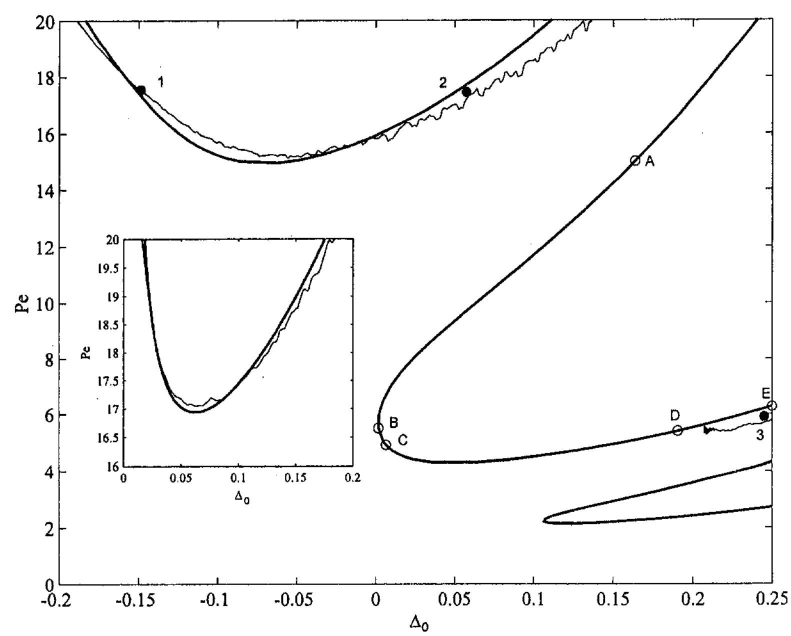

Fig. 3 Theoretical (thick smooth curves) and experimental (thin jagged curves) nondimensional eyelet tension versus string length: $h = 10$, $\gamma = 100$ (main plot), and inextensible (inset plot). Solid circles (●) correspond to the balloons in Fig. 8.

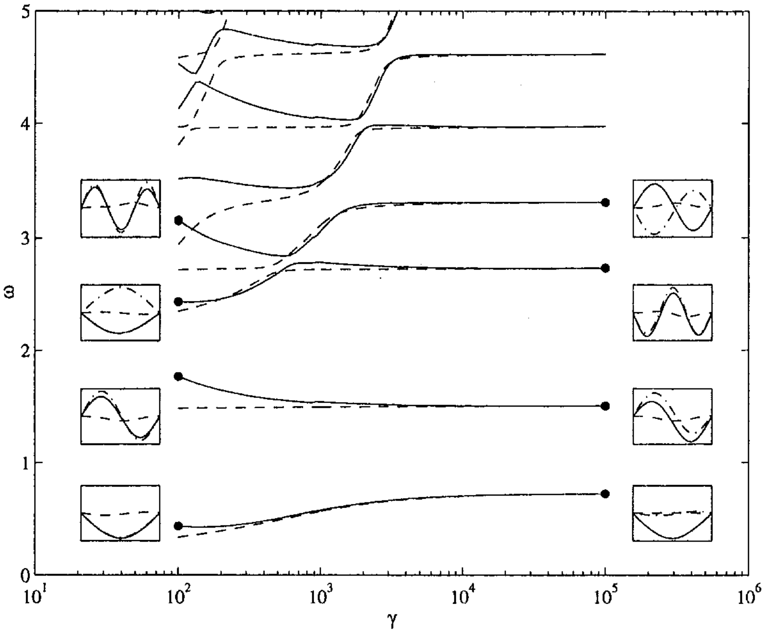

Fig. 4 Frequencies versus string stiffness of a single loop balloon based on the extensible (solid) and inextensible (dashed) steady-state solutions at $p_e = 17.5$ (left solution). Inset plots show the first four modes at $\gamma = 10^2$ and $\gamma = 10^5$. The modal displacements are: tangential (– –), binormal (——), normal (– · –).

marked points on the $\gamma = 100$ curve are also shown. The height of the balloon is fixed at $h = 10$, so increasing Δ_1 indicates increasing l_1 or increasing balloon length. All balloons start at the left eyelet with $x = z = 0$ and end at the right, rotating eyelet with $|x| = 1$ and $z = h$. The top curves in Fig. 2 correspond to single-loop balloons. Taut balloons with small Δ_1 have high tension. With increasing Δ_1, the eyelet tension reduces to a minimum near $\Delta_1 = 0.06$ and then increases.

As the tension decreases, the balloons acquire more loops. The balloons corresponding to the next lower curves change shape from one-and-a-half loop to double loop at the turning point near $p_e = 5.5$. The tension increases with increasing Δ_1 for these balloons except for a small region near the turning point. The balloons on the bottom curves have two-and-a-half loops and triple loops.

For all balloons, the tension decreases with decreasing γ for the same Δ_1. The difference is largest in single-loop balloons. The maximum difference between the $\gamma = 1000$ and inextensible cases, however, is less than 0.5 percent, so the inextensible assumption appears reasonable for strings with $\gamma > 1000$.

The smooth, thick curves in Fig. 3 show p_e versus the unstressed length parameter $\Delta_0 = (l_0 - h)/l_0$ for $\gamma = 100$ and inextensible cases. The top curves in the main plot and the curves in the inset plot correspond to single loop balloons. The curves from A to B, and B to E correspond to one-and-a-half loop and double loop balloons, respectively. The curves for $\gamma = 100$, especially the top curves, shift left relative to Fig. 2 due to string stretch.

4 Linearized Equation of Vibration

Substitution of Eq. (12) into Eq. (9), elimination of the nonlinear $\mathbf{u}(s, t)$ terms, and cancellation of the steady-state terms from Eq. (15) produce the linearized equation of motion

$$\frac{\partial}{\partial s}\left[\bar{\gamma}\left(\frac{\partial \mathbf{r}}{\partial s}\cdot\frac{\partial \mathbf{u}}{\partial s}\right)\frac{\partial \mathbf{r}}{\partial s} + \bar{p}\frac{\partial \mathbf{u}}{\partial s}\right] = \mathbf{e}_3 \times (\mathbf{e}_3 \times \mathbf{u}) + 2\mathbf{e}_3 \times \frac{\partial \mathbf{u}}{\partial t} + \frac{\partial^2 \mathbf{u}}{\partial t^2} \quad (22)$$

with boundary conditions (14) and

$$\bar{p} = \frac{p}{1 + p/\gamma}, \quad \bar{\gamma} = \frac{\gamma}{(1 + p/\gamma)^2}. \quad (23)$$

Equation (22) in operator form is

$$\ddot{\boldsymbol{u}} + \mathbf{G}\dot{\boldsymbol{u}} + \mathbf{K}\boldsymbol{u} = \mathbf{0}, \quad (24)$$

where the displacement vector $\boldsymbol{u}(s, t) = [u_1, u_2, u_3]^T$ and $(\dot{\ }) = \partial(\cdot)/\partial t$. The gyroscopic and stiffness operators are

$$\mathbf{G} = \begin{bmatrix} 0 & -2 & 0 \\ 2 & 0 & 0 \\ 0 & 0 & 0 \end{bmatrix}, \quad \mathbf{K} = \begin{bmatrix} K_{11} & 0 & K_{13} \\ 0 & K_{22} & 0 \\ K_{13} & 0 & K_{33} \end{bmatrix}, \quad (25)$$

respectively, with

$$K_{11} = -1 - (\bar{p} + \bar{\gamma}x^2{}_{,s})\partial^2 - (\bar{p}_{,s} + 2\bar{\gamma}x_{,s}x_{,ss})\partial$$

$$K_{13} = -\bar{\gamma}(z_{,s}x_{,s}\partial^2 + [z_{,s}x_{,s}]_{,s}\partial)$$

$$K_{22} = -1 - \bar{p}\partial^2 - \bar{p}_{,s}\partial$$

$$K_{33} = -(\bar{p} + \bar{\gamma}z_{,s}^2)\partial^2 - (\bar{p}_{,s} + 2\bar{\gamma}z_{,s}z_{,ss})\partial,$$

where $(\cdot)_{,s}$ and ∂ indicate partial differentiation with respect to s. The in-plane vibrations u_1 and u_3 are coupled through the stiffness operator. The out-of-plane vibration u_2 is coupled to in-plane vibration u_1 through the gyroscopic operator. With the inner product

$$\langle \boldsymbol{u}, \boldsymbol{v} \rangle = \int_0^{l_0} \boldsymbol{u}^T \boldsymbol{v}\, ds \quad (26)$$

the gyroscopic operator is skew symmetric and the stiffness operator is symmetric, i.e.,

$$\langle \mathbf{G}\boldsymbol{u}, \boldsymbol{v} \rangle = -\langle \boldsymbol{u}, \mathbf{G}\boldsymbol{v} \rangle$$

$$\langle \mathbf{K}\boldsymbol{u}, \boldsymbol{v} \rangle = \langle \boldsymbol{u}, \mathbf{K}\boldsymbol{v} \rangle. \quad (27)$$

Thus the eigenvalues of the system are real and stable if the

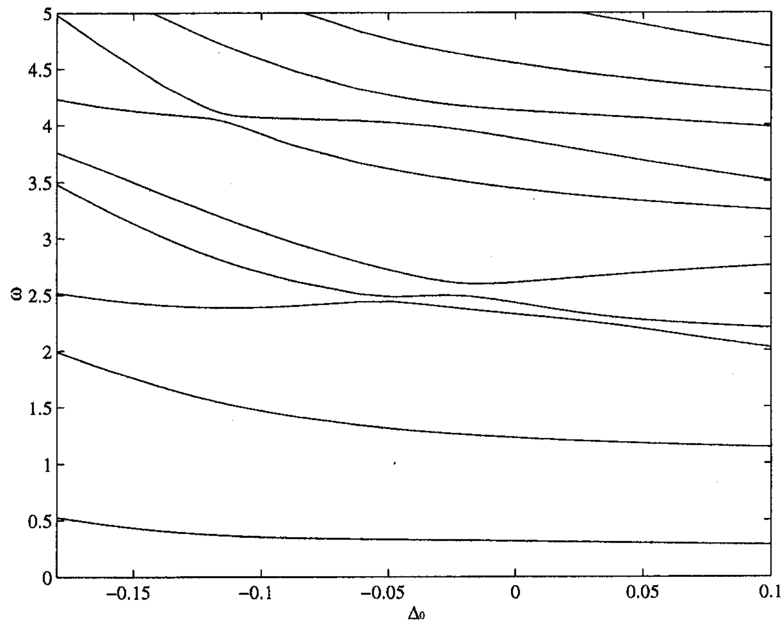

Fig. 5 Frequencies versus string length for single loop balloons with $\gamma = 100$

stiffness operator is positive definite. The stiffness operator is positive definite if

$$\int_0^l (\boldsymbol{u},_s^T \mathbf{Q} \boldsymbol{u},_s - u_1^2 - u_2^2) ds > 0, \tag{28}$$

where

$$\mathbf{Q}(s) = \begin{bmatrix} \bar{p} + \bar{\gamma} x,_s^2 & 0 & \bar{\gamma} x,_s z,_s \\ 0 & \bar{p} & 0 \\ \bar{\gamma} x,_s z,_s & 0 & \bar{p} + \bar{\gamma} z,_s^2 \end{bmatrix} \tag{29}$$

is a symmetric positive definite matrix. Equation (28) is difficult to verify because the integral includes both positive and negative terms. In addition, the system may be gyroscopically stabilized if the stiffness operator is negative definite (Wickert and Mote, 1990). Therefore, a Galerkin method is used for numerical balloon stability analysis.

The displacement field is represented by an N-term separable series of the form

$$\boldsymbol{u}(s, t) = \sum_{j=1}^{N} \sum_{k=1}^{3} \eta_{jk}(t) \theta_j(s) \boldsymbol{e}_k, \tag{30}$$

where $\boldsymbol{e}_1 = [1, 0, 0]^T$, $\boldsymbol{e}_2 = [0, 1, 0]^T$, $\boldsymbol{e}_3 = [0, 0, 1]^T$, and the comparison functions

$$\theta_j(s) = \sqrt{2} \sin (j\pi s / l_0) \tag{31}$$

satisfy the pinned boundary conditions. Substitution of Eq. (30)

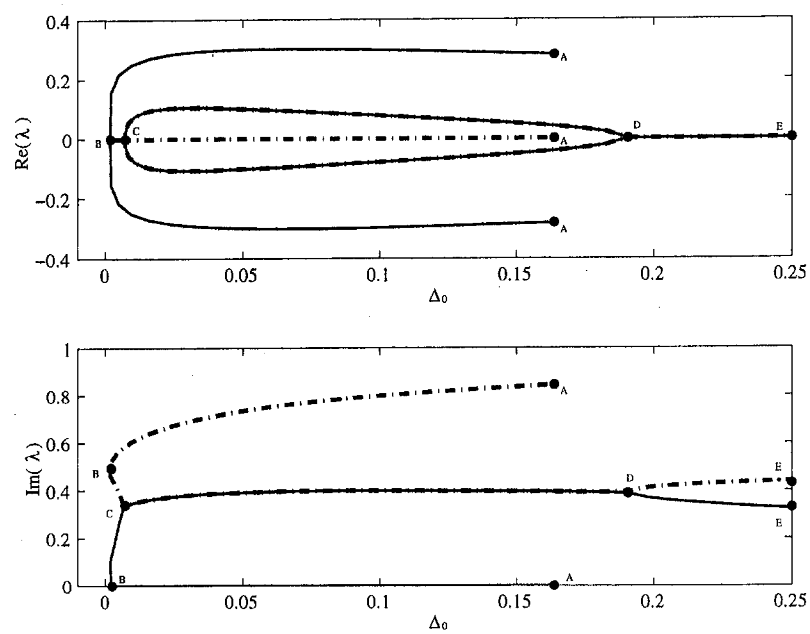

Fig. 6 Root-locus for one-and-a-half loop (A to B) and double loop (B to E) balloons corresponding to Fig. 2 ($\gamma = 100$): first eigenvalues (solid) and second eigenvalues (dash-dotted). Complex conjugate eigenvalues are not shown.

into Eq. (24) and application of Galerkin's method provides the discretized equations of motion

$$\ddot{\boldsymbol{\eta}} + \boldsymbol{G}\dot{\boldsymbol{\eta}} + \boldsymbol{K}\boldsymbol{\eta} = \boldsymbol{0}, \tag{32}$$

where $\boldsymbol{\eta} = [\eta_{11}, \eta_{12}, \eta_{13}, \eta_{21}, \ldots, \eta_{N3}]^T$.

5 Natural Frequencies, Modes, and Stability

The eigenvalues λ_n of the state matrix associated with Eq. (32)

$$\boldsymbol{A} = \begin{bmatrix} \boldsymbol{0} & \boldsymbol{I} \\ -\boldsymbol{K} & -\boldsymbol{G} \end{bmatrix} \tag{33}$$

are determined using MATLAB. The imaginary parts of the eigenvalues correspond to the nondimensional natural vibration frequencies of the ballooning string. The lowest ten natural frequencies converge to within 0.5 percent of their final values at $N = 10$, so this value is used for all calculations. Stable balloons have eigenvalues with nonpositive real parts. Eigenvalues with positive real parts and nonzero imaginary parts correspond to flutter instability. A single, real, positive eigenvalue signifies divergence instability. This analysis bases on the linear Eq. (22) so only linear stability results are obtained.

The numerical results show that all single-loop balloons are stable with purely imaginary eigenvalues $\lambda = \pm j\omega$. The single-loop balloon natural frequencies ω with $p_e = 17.5$ (left solution) versus the string stiffness are shown as solid lines in Fig. 4. The range $10^2 \le \gamma \le 10^5$ maintains small strains ($\epsilon_1 < 0.2$). The dashed lines indicate frequencies calculated using the inextensible steady state solution. For small γ, the dashed lines differ significantly from the corresponding solid lines. For $\gamma > 1000$, however, the first six frequencies obtained from the two approaches match to within three percent.

The lowest four normalized modes at $\gamma = 10^2$ and $\gamma = 10^5$ are shown on the left and right of Fig. 4, respectively. The dashed, solid, and dash-dotted curves represent displacements from the steady-state balloon shape in the tangential v_1, binormal v_2, and normal v_3 directions, respectively. These displacements are calculated as follows:

$$v_1 = u_1 \sin\theta + u_3 \cos\theta, \quad v_2 = u_2, \quad v_3 = u_1 \cos\theta - u_3 \sin\theta,$$

where θ is the angle between the balloon tangent and the z-axis. The modes show very little tangential displacement, even at small γ. The lowest mode contains half-sine out-of-plane and in-plane normal displacements for small values of γ. As γ increases, the in-plane amplitude decreases until only out-of-plane displacement remains. At $\gamma = 100$, the first mode whirls in the same direction as Ω. The third mode whirls in the opposite direction with almost the same mode shape. Soedel and Soedel (1989) observed this phenomena in an eccentrically rotating string. As γ increases, however, first mode whirling disappears and third mode whirling veers upward in frequency. Second and fourth whirling modes veer downward in frequency and exist at $\gamma = 10^5$. The first four modes involve little string stretch for $\gamma = 10^5$.

Figure 5 shows the effect of balloon length on the natural frequencies of single-loop balloons with $\gamma = 100$. The frequencies generally decrease with increasing Δ_0. Taut (small Δ_0) balloons have modes similar to the $\gamma = 100$ modes in Fig. 4, while the long-length balloons have more complicated mode shapes.

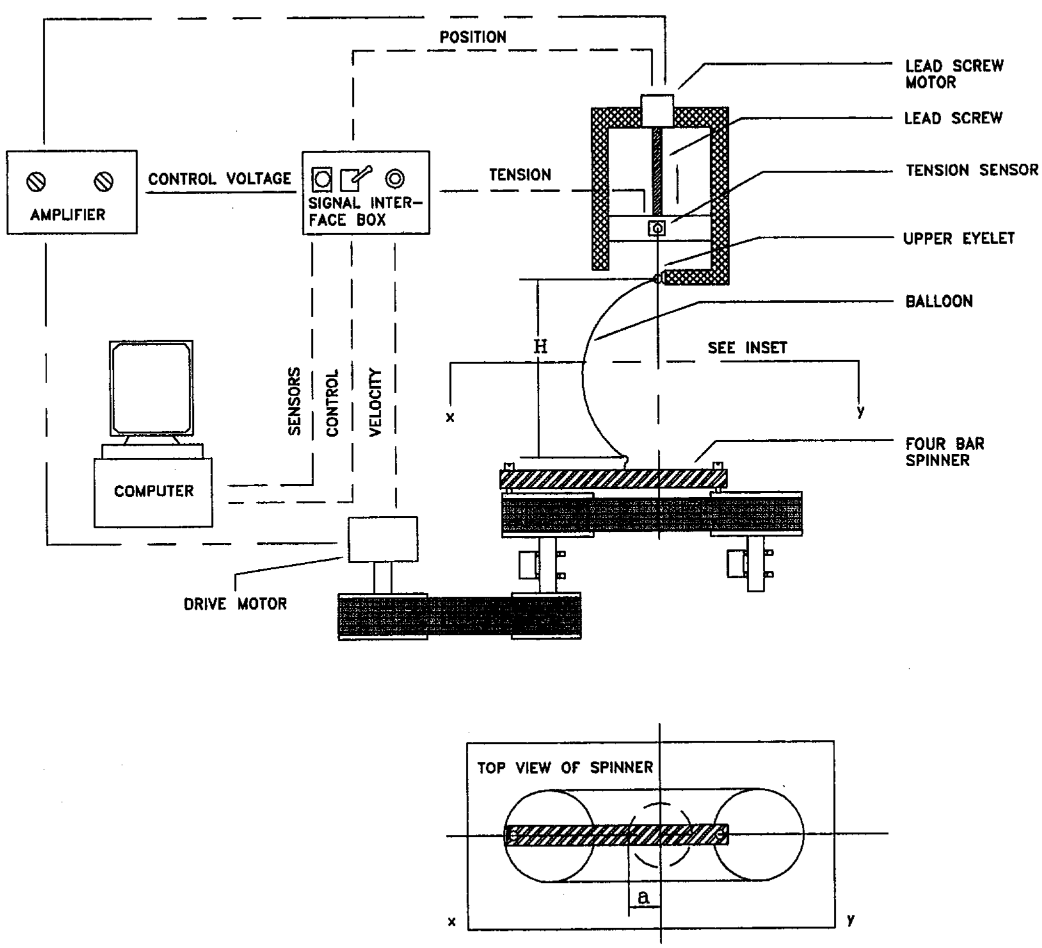

Fig. 7 Balloon test system: signal (– –) and power (– · · · –) flow

Figure 6 plots the one-and-a-half loop and double-loop balloon eigenvalue loci versus Δ_0 using dash-dotted and solid lines for pairs of eigenvalues. Capital letters A to E correlate to the circled positions in Fig. 3. The top and bottom plots show the real and imaginary parts of the eigenvalues, respectively. The loci are symmetric with respect to the real axis, as expected from the symmetry properties of **G** and **K**.

From A to B, the one-and-a-half loop balloons are divergent unstable with two real eigenvalues with opposite sign (solid lines) and two purely imaginary eigenvalues (dash-dotted lines). At the turning point B, the two real eigenvalues merge at the origin and the other two remain purely imaginary. Between B and C the eigenvalues have zero real part with nonzero imaginary part, indicating stable double-loop balloons. At C, two pairs of repeated imaginary eigenvalues form. From C to D, the system is coupled mode flutter unstable with two pairs of complex poles with opposite sign real parts. At D the eigenvalues coalesce and from D to E double loop balloons are stable. The eigenvalues of two-and-a-half loop and triple-loop balloons behave similarly to those of the one-and-a-half loop and double-loop balloons except that B and C merge together and the stable region D-E does not exist. Hence, stable triple loop balloons do not exist in the length range of Fig. 3.

As string stiffness increases, the B-C and D-E regions decrease. Thus, the coupled mode flutter region increases and fewer stable double-loop balloons exist. For inextensible strings, no stable double-loop balloons exist for $\Delta < 0.25$.

6 Experimental Results

The balloon test system (BTS) shown in Fig. 7 experimentally verifies the steady-state solutions and stability. The BTS has four components: the test stand, signal interface box, PC, and power amplifier. A four-bar linkage driven by a DC motor rotates the string between the lower eyelet and the upper eyelet. The lower eyelet, which is attached to the rotating link, undergoes circular motion at a constant speed set by the PC based data acquisition and control system. A balloon forms between the rotating eyelet and the fixed eyelet. The string terminates at the tension sensor above the fixed eyelet. Vertical motion of the tension sensor on a motorized lead screw feeds string into the system at a negligibly slow speed (1 cm/s). The data acquisition system records the speed of the rotating link, the tension signal produced by the tension sensor, and the string length. Heavy, approximately cylindrical strings are used in the experiments to reduce the effect of air drag. The balloon height and rotating eyelet length are fixed at 25.4 cm and 2.54 cm, respectively.

The first set of experiments verifies the theoretical curves corresponding to stable single and double-loop balloons. The eyelet tension is measured for Δ_0 ranging from -0.2 to 0.25 with the spinning speed set at 1220 rpm. An approximately linearly elastic rubber string with $EA_0 = 1.702$ N and $\rho A_0 = 1.54$ gms/m gives $\gamma = 100$. The tension and length data are collected, nondimensionalized, and plotted in Fig. 3. The thick smooth curves correspond to theoretical data and the thin jagged curves correspond to experimental data.

The experimental data for a single loop balloon matches the theoretical results to within four percent. The tension decreases with increasing Δ_0, reaching a minimum at $\Delta_0 = -0.025$. As Δ_0 increases from this minimum value, the tension increases. As predicted by the theory, no stable one-and-a-half loop balloons are observed. In the region C-D, the experimental balloon flutters or jumps up to a stable single loop balloon. Double loop balloons can be formed in the region B-C but they are extremely sensitive to external disturbances. Consequently, the balloon stays stable only for a very short time and then jumps to a single-loop balloon. The experimentally stable double-loop balloon region is slightly smaller than the D-E theoretical region. The experimentally measured tension for stable double loop balloons deviates from the theoretical curve by about eight percent. No stable triple loop balloons are observed.

The inset plot in Fig. 3 shows the theoretical and experimental p_e versus Δ_0 curves for inextensible single loop balloons. A nylon string with $\rho A_0 = 1.63$ gms/m, $\Omega = 1070$ rpm, and immeasurably small extension is used for the experiment. The smooth curve corresponds to the theoretical data and the jagged curve corresponds to the experimental data. The experimental curve matches the theoretical curve to within three percent. As predicted by the theory, no stable double or triple loop balloons are observed for $\Delta_0 < 0.25$.

The second set of experiments compares theoretical and experimental balloon shapes for $\gamma = 100$. A strobe and a video

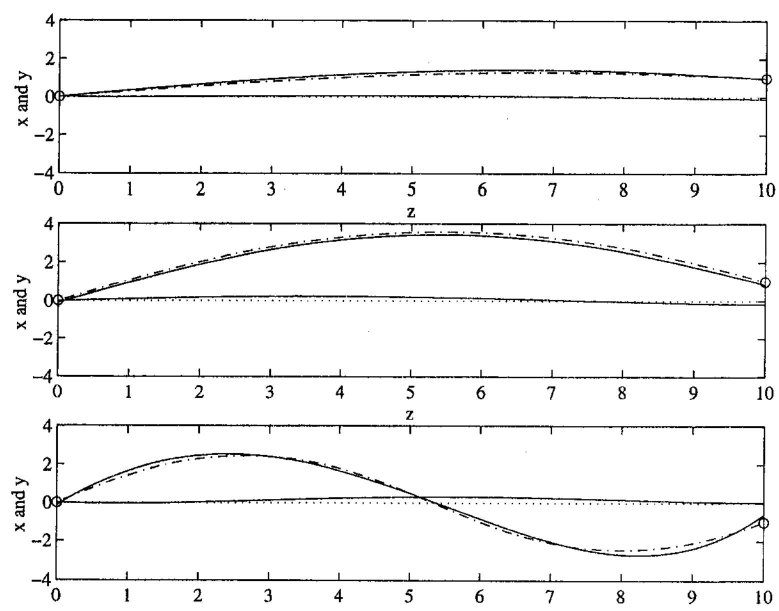

Fig. 8 Experimental (solid) and Theoretical (dashed) balloon shapes corresponding to the solid circles (●) in Fig. 3. ($\gamma = 100$). The variable y represents the nondimensional steady-state string displacement in e_2 direction.

camera acquire digitized balloon images. Two orthogonal pictures generate the three-dimensional balloon shapes. The string path is computer traced and converted to numerical coordinates. Figure 8 shows the theoretical and experimental balloon shapes corresponding to the three marked points in Fig. 3. The dashed-dotted and solid lines represent the theoretical and the experimental balloon shapes, respectively. Air drag causes negligible out-of-plane displacement (y, in the $\mathbf{e}_2$ direction) in the experimental balloons. The experimental in-plane balloon shapes match the theory to within three percent.

7 Conclusions

Single-loop balloons have high tension and stable, purely imaginary eigenvalues that generally decrease with increasing balloon length. Highly extensible strings whirl about these steady-state balloons in first and higher modes with forward whirling modes having lower frequencies. Axially stiff strings exhibit single loop balloon whirling only in higher modes. One-and-a-half loop and two-and-a-half loop balloons are divergent unstable. Short length and high stiffness double loop balloons are coupled mode flutter unstable. With long string length, stable double loop balloons exist for $\gamma = 100$. If $\gamma > 1000$ then the inextensible steady-state solutions and lowest six frequencies match the extensible results to within three percent. Experimental data closely matches the theoretical steady state tension (eight percent), balloon shapes (three percent), and balloon stability.

Acknowledgment

The authors would like to thank an anonymous reviewer for comments that greatly improved this paper. This research was supported by the National Textile Center.

References

Ames, W. F., Lee, S. Y., and Zaiser, J. N., 1968, "Non-Linear Vibration of a Traveling Threadline," *Int. J. Non-Linear Mechanics*, Vol. 3, pp. 449–469.

Antman, S. S., 1995, *Nonlinear problems of elasticity*, Springer-Verlag, New York.

Batra, S., Ghosh, T., and Zeidman, M., 1989a, "An Integrated Approach to Dynamic Analysis of the Ring Spinning Process—I," *Textile Research Journal*, Vol. 59, pp. 309–317.

Batra, S., Ghosh, T., and Zeidman, M., 1989b, "An Integrated Approach to Dynamic Analysis of the Ring Spinning Process—II," *Textile Research Journal*, Vol. 59, pp. 416–424.

De Barr, A., and Catling, H. M., 1965, *The principles and theory of ring spinning. Manual of cotton spinning*, Vol. 5, F. Charnley and P. Harrison, eds. Butterworths, London.

Fraser, W., Ghosh, T., and Batra, S., 1992, "On Unwinding Yarn From a Cylindrical Package," *Proc. R. Soc. Lond.*, Vol. A436, pp. 479–498.

Fraser, W., 1993, "On the Theory of Ring Spinning," *Phil. Trans. R. Soc. Lond.*, Vol. A342, pp. 439–468.

Hall, K. J., Zhu, F., and Rahn, C., 1995, "Three Dimensional Vibration of a Ballooning String," ASME *Design Engineering Technical Conferences*, Vol. 3, Part B, pp. 1411–1418.

Healey, T. J., 1990, "Stability and Bifurcation of Rotating Nonlinear Elastic Loops," *Quarterly of Applied Mathematics*, Vol. 48, pp. 679–698.

Healey, T. J., 1990, "Large Rotating States of a Conducting Elastic Wire in a Magnetic Field: Subtle Symmetry and Multiparameter Bifurcation," *Journal of Elasticity*, Vol. 24, pp. 211–227.

Kolodner, I. I., 1955, "Heavy Rotating String—A Nonlinear Eigenvalue Problem," *Comm. Pure Appl. Math.*, Vol. 8, pp. 394–408.

O'Reilly, O. M., 1996, "Steady Motions of a Drawn Cable," ASME JOURNAL OF APPLIED MECHANICS, Vol. 63, pp. 180–189.

Soedel, S. M., and Soedel, W., 1989, "Free and Forced Vibrations of an Eccentrically Rotating String on a Viscoelastic Foundation," *Journal of Sound and Vibration*, Vol. 135, pp. 197–212.

Shih, L. Y., 1975, "Motion of Elliptic Ballooning for a Traveling String," *Int. J. Non-Linear Mechanics*, Vol. 10, pp. 183–191.

Stuart, C. A., 1975, "Spectral Theory of Rotating Chains," *Proc. Roy. Soc. Edinburgh, Sect. A*, Vol. 73, pp. 199–214.

Stump, M., and Fraser, W., 1996, "Transient Solutions of the Ring-Spinning Balloon Equations," ASME JOURNAL OF APPLIED MECHANICS, Vol. 63, pp. 523–528.

Wickert, J., and Mote, C., 1990, "Classical Vibration Analysis of Axially-Moving Continua," ASME JOURNAL OF APPLIED MECHANICS, Vol. 57, pp. 738–744.

Yang, L., and Hutton, S. G., 1995, "Interactions Between an Idealized Rotating String and Stationary Constraints," *Journal of Sound and Vibration*, Vol. 185, pp. 139–154.

Closed-Form Solutions and the Eigenvalue Problem for Vibration of Discrete Viscoelastic Systems

A. Muravyov
Research Fellow,
Doctoral Candidate.

S. G. Hutton
Professor,
Mem. ASME.

Department of Mechanical Engineering,
University of British Columbia,
Vancouver, BC V6T 1W5, Canada

A procedure for obtaining closed-form homogeneous solutions for the problem of vibration of a discrete viscoelastic system is developed for the case where the relaxation kernel characterizing the constitutive relation of the material is expressible as a sum of exponentials. The developed procedure involves the formulation of an eigenvalue problem and avoids difficulties encountered with the application of the Laplace transform approach to multi-degree-of-freedom viscoelastic systems. Analytical results computed by using the developed method are demonstrated on an example of a viscoelastic beam.

1 Introduction

In this study the equation of motion will include an integral term in which the history of strain is required for its formulation. Materials yielding such a constitutive relation (requiring history) are called as viscoelastic, but the term "hereditary material" will be used in this study as well. Hereditary properties are present, e.g., in elastomeric materials such as chloroprene rubber, acrylonitrile-butadiene rubber and many others.

Isotropic homogeneous hereditary materials are considered and it is assumed that material is in isothermal state. The viscoelastic system (or structure), which is under consideration, is also assumed homogeneous. The case when different isotropic materials are involved is a straightforward extension of all formulae presented in this paper and for the sake of brevity is omitted here.

The principal equations to be used are (*i*) the constitutive relation between stress and strain tensors of the deformable body, and (*ii*) the equation of motion.

In the theory of linear viscoelasticity, one of hereditary models (Rabotnov, 1969, 1980; Flugge, 1967) is a constitutive law of the form (a one-dimensional element is taken as an illustration):

$$\sigma = E\left(e - \int_0^t \Gamma(t-\tau)e(\tau)d\tau\right) \tag{1}$$

where the scalar function $\Gamma(t-\tau)$ is called the relaxation kernel and E is the instantaneous Young's modulus. An alternative form of representing (1), which was used by Christensen, (1982), Carini and Donato (1992), Ferry (1970), and Creus, (1986) is as follows:

$$\sigma = \int_0^t G(t-\tau)\dot{e}(\tau)d\tau \tag{2}$$

which can be reduced to (1) by integration by parts. $G(t-\tau)$ is called the relaxation function. Note that $G'_\tau(t-\tau) = E\Gamma(t-\tau)$. Thus the forms (1) and (2) are equivalent. In this study form (1) will be used.

Contributed by the Applied Mechanics Division of THE AMERICAN SOCIETY OF MECHANICAL ENGINEERS for publication in the ASME JOURNAL OF APPLIED MECHANICS.

Discussion on the paper should be addressed to the Technical Editor, Professor Lewis T. Wheeler, Department of Mechanical Engineering, University of Houston, Houston, TX 77204-4792, and will be accepted until four months after final publication of the paper itself in the ASME JOURNAL OF APPLIED MECHANICS.

Manuscript received by the ASME Applied Mechanics Division, Sept. 16, 1996; final revision, Feb. 4, 1997. Associate Technical Editor: N. C. Perkins.

Note that this model of the hereditary material has a so-called difference type relaxation kernel, i.e.,

$$\Gamma(t, \tau) = \Gamma(t-\tau),$$

which is an appropriate assumption for many elastomeric materials.

Application of the finite element method to elastic systems allows the formulation of dynamic problems in terms of mass and stiffness matrices; and vector of displacement (response) and force (excitation). For viscoelastic systems E (Young's modulus) and ν (Poisson's ratio) should be replaced by their hereditary analogs (operators). In the case of the finite element method this implies the replacement of material constants E, ν in the stiffness matrix by their viscoelastic analogs (operators) $\tilde{E}$, $\tilde{\nu}$.

Finite element method applications for dynamic viscoelastic systems are usually described in the literature in the context of step-by-step numerical integration (in time) schemes ("ABAQUS," 1993; Day and Minster, 1984), or based on numerical inversion algorithms of the Laplace transformed solution. Description of these numerical methods can be found, e.g., in Brunner et al. (1986) and Linz (1985). It may be noted that the use of numerical integration for the boundary value problem (when conditions are prescribed at different points in time) is much more complicated than for the initial value problem.

In practice one of the widely used models of the constitutive viscoelastic law is when the relaxation kernel is represented by the sum of exponentials. The existence of homogeneous analytical solutions to the free vibration problem for this case has been shown (Muravyov, 1996) using the Laplace transform method. In this paper a different approach is developed to determine the unknown parameters which are involved in the analytical solution. This approach also yields the formulation of an eigenvalue problem.

It is also shown that a closed-form solution can be determined not only for initial conditions, but also for the boundary value problem. This is a distinct advantage in having the solution in analytical form.

2 The Initial Value Problem for Discrete Viscoelastic Systems

2.1 Single-Degree-of-Freedom System. Consider a mass m connected to the base by a one-dimensional massless element which combines the properties of hereditary and viscosity in parallel. The equation of unforced motion is as follows:

$$m\ddot{x}(t) + c\dot{x} + k\left[x(t) - \int_0^t \Gamma(t-\tau)x(\tau)d\tau\right] = 0 \quad (3)$$

where the relaxation kernel is assumed to be of the form

$$\Gamma(t-\tau) = \sum_{i=1}^{n} a_i e^{-\alpha_i(t-\tau)}.$$

The initial conditions are

$$x(0) = x_0 \quad \dot{x}(0) = \dot{x}_0.$$

The presence of the term $c\dot{x}$ arises from placing a viscous dashpot in parallel with a viscoelastic element. It should be noted that for some elastomeric materials the term $c\dot{x}$ can be introduced into the constitutive law of the material. Here the integral term plus the instantaneous part $kx(t)$ will be referred as a viscoelastic element, and term $c\dot{x}$ as a viscous element.

2.1.1 Application of the Laplace Transform. Applying the Laplace transform to (3), one obtains

$$m(p^2\bar{x} - \dot{x}(0) - px(0)) + c(p\bar{x} - x(0)) + k\bar{x} - k\bar{x}\sum_{i=1}^{n}\frac{a_i}{p+\alpha_i} = 0.$$

Thus

$$\bar{x} = \frac{m(\dot{x}(0) + px(0)) + cx(0)}{p^2m + pc + k\left(1 - \sum_{i=1}^{n}\frac{a_i}{p+\alpha_i}\right)} = \frac{R(p)}{T(p)}.$$

Knowing the roots p_i (in general complex) of denominator $T(p)$, and assuming they are simple (multiplicity of 1), one can obtain a solution in the form (see the theorem in Bugrov, 1989)

$$x(t) = \sum_{i=1}^{n+2}\frac{R(p_i)}{T'(p_i)}e^{p_it}. \quad (4)$$

Thus the free vibration solution in complex form is given by (4). If the initial conditions x_0 and $\dot{x}_0$ are assumed real, then the solution (4) will be real, because the roots p_i are either complex conjugate or real. In general one can assume that x_0 and $\dot{x}_0$ are complex, then the real part of the complex solution (4) will be a solution for the real parts of x_0, $\dot{x}_0$, and imaginary part of (4) will be a solution for the imaginary parts of x_0, $\dot{x}_0$.

2.1.2 The Substitution Method. The solution of (3) will be sought in the following form (Muravyov and Hutton, 1996):

$$x(t) = \sum_{j=1}^{n+2} c_j e^{p_jt} \quad (5)$$

where c_j, p_j are complex. It may be noted that the number of terms comprising the solution is dependent upon n, which is the number of terms in the relaxation kernel. Substituting (5) in (3) one obtains

$$\sum_{j=1}^{n+2}\left[mp_j^2 + cp_j + k - k\sum_{i=1}^{n}\frac{a_i}{p_j+\alpha_i}\right]c_je^{p_jt} + k\sum_{i=1}^{n}\left[\sum_{j=1}^{n+2}\frac{a_i}{p_j+\alpha_i}c_j\right]e^{-\alpha_it} = 0. \quad (6)$$

In this equation there is a sum of exponential functions. To satisfy this equation one can set all the coefficients of these functions to zero, namely

$$mp_j^2 + cp_j + k\left(1 - \sum_{i=1}^{n}\frac{a_i}{p_j+\alpha_i}\right) = 0 \quad j = 1, n+2 \quad (7)$$

and

$$\sum_{j=1}^{n+2}\frac{a_i}{p_j+\alpha_i}c_j = 0 \quad i = 1, n. \quad (8)$$

The initial conditions

$$\sum_{j=1}^{n+2} c_j = x_0 \quad \sum_{j=1}^{n+2} c_jp_j = \dot{x}_0 \quad (9)$$

provide two more equations.

Equation (7) can be called as the characteristic equation with respect to $n + 2$ complex (in general) roots p_j. They can be determined, for example, by using Newton's method, or by reduction to an eigenvalue problem (see the REMARK below).

Equations (8), (9) yield a linear system of $n + 2$ equations with $n + 2$ unknown complex constants c_j. In matrix form one obtains

$$\begin{bmatrix} \frac{a_1}{p_1+\alpha_1} & \frac{a_1}{p_2+\alpha_1} & \cdots & \frac{a_1}{p_{n+2}+\alpha_1} \\ \cdots & \cdots & \cdots & \cdots \\ \frac{a_n}{p_1+\alpha_n} & \frac{a_n}{p_2+\alpha_n} & \cdots & \frac{a_n}{p_{n+2}+\alpha_n} \\ 1 & 1 & \cdots & 1 \\ p_1 & p_2 & \cdots & p_{n+2} \end{bmatrix} \begin{bmatrix} c_1 \\ \cdots \\ c_{n+2} \end{bmatrix} = \begin{bmatrix} 0 \\ \cdots \\ 0 \\ x_0 \\ \dot{x}_0 \end{bmatrix}. \quad (10)$$

Note that $a_i \neq 0$ for $i = 1, n$, otherwise it does not make sense to introduce a term in the constitutive law which is a priori 0. It is interesting to note that the requirement that roots p_j are simple (multiplicity of 1) is necessary here to provide the nonsingularity of the matrix in (10). It may be noted that if there is a repeated root then the corresponding columns in (10) will be identical and the determinant of the matrix vanishes. This simple roots requirement is not a restriction imposed on a system, it is just an indicator which can be used to determine if a given viscoelastic system (3) assumes a solution in the form (5), or not. If it assumes, then according to the theorem of uniqueness (Linz, 1985) this solution is unique. The satisfaction of this requirement is expected for most viscoelastic systems, although if this requirement is not satisfied, then the analytical homogeneous solution may differ from (5), and this requires additional investigation.

REMARK. The reduction of characteristic Eq. (7) to an eigenvalue problem is as follows. Equation (7) can be rewritten as

$$\frac{p^{n+2}b_{n+2} + p^{n+1}b_{n+1} + \ldots + pb_1 + b_0}{\prod_{i=1}^{n}(p+\alpha_i)} = 0$$

or

$$p^{n+2}b_{n+2} + p^{n+1}b_{n+1} + \ldots + pb_1 + b_0 = 0 \quad (11)$$

where coefficient $b_{n+2} = m$ and the other coefficients can be readily evaluated (expressions for them are omitted here).

Introducing the state-space vector $Q = q_0[1\ p\ p^2 \ldots p^{n+1}]^T$, the following eigenproblem will correspond to the characteristic Eq. (11):

$$\left(p \begin{bmatrix} b_1 & b_2 & b_3 & \cdots & b_{n+2} \\ 1 & 0 & 0 & \cdots & 0 \\ 0 & 1 & 0 & \cdots & 0 \\ 0 & 0 & 1 & \cdots & 0 \\ \cdots & \cdots & \cdots & \cdots & \cdots \\ 0 & 0 & \cdots & 1 & 0 \end{bmatrix} + \begin{bmatrix} b_0 & 0 & 0 & \cdots & 0 \\ 0 & -1 & 0 & \cdots & 0 \\ 0 & 0 & -1 & \cdots & 0 \\ \cdots & \cdots & \cdots & \cdots & \cdots \\ 0 & 0 & 0 & \cdots & -1 \end{bmatrix} \right) Q = \begin{bmatrix} 0 \\ 0 \\ \cdots \\ 0 \end{bmatrix}$$

or in abbreviated form

$$(pA + B)Q = 0. \tag{12}$$

The eigenvalues of (12) will be the characteristic roots of (7). Equation (12) can be interpreted as a generalization of the state-space form eigenvalue problem for a nonclassically damped system.

EXAMPLE. For the purpose of illustration, consider the equation

$$\ddot{x} + x - \int_0^t \tfrac{1}{2} e^{-(t-\tau)} x(\tau) d\tau = 0$$

with initial conditions: $x(0) = 1 + i0$, $\dot{x}(0) = 0 + i0$. The complex solutions obtained by application of the Laplace transform (4) and by using the substitution method (12), (10), (5) are identical:

$$x(t) = (0.6184 - i0.03739)e^{p_1 t} + (0.6184 + i0.03739)e^{p_2 t} - 0.2368 e^{p_3 t}$$

where the roots of the characteristic equation are

$$p_1 = -0.1761 + i0.86071 \quad p_2 = -0.1761 - i0.86071$$
$$p_3 = -0.64779.$$

In this example the free vibration response comprises a combination of a decaying oscillatory mode and one overdamped mode.

2.2 Multi-Degree-of-Freedom System. Application of the finite element method to an elastic system yields the mass matrix M and the stiffness matrix K. Represent the stiffness matrix as

$$K = EK_0. \tag{13}$$

For viscoelastic systems it is necessary to replace Young's modulus by the viscoelastic operator $\tilde{E}$. Although the assumption that Poisson's ratio is constant for viscoelastic material is not supported by experiment, for the sake of brevity it is assumed here that the Poisson operator is elastic (i.e., constant) $\tilde{\nu} = \nu$ = const. The approach when the Poisson operator is not constant will be presented in a subsequent paper.

The hereditary Young's modulus operator $\tilde{E}$ has form

$$\tilde{E}(.) = E\left[1(.) - \int_0^t \Gamma(t-\tau)(.)d\tau \right] \tag{14}$$

where the relaxation kernel is assumed as a sum of exponentials

$$\Gamma(t-\tau) = \sum_{i=1}^{n} a_i e^{-\alpha_i(t-\tau)}. \tag{15}$$

The equation of free motion can be written as

$$M\ddot{X} + C\dot{X} + \tilde{E}K_0 X = 0 \tag{16}$$

where X is a vector of displacements.

The term $C\dot{X}$, as was mentioned before, takes into account the presence of viscous damping arbitrary distributed over the system.

2.2.1 Laplace Transform Method. Applying the Laplace transform to (16) and taking into account (14), (13), (15) one obtains

$$\left[p^2 M + pC + K\left(1 - \sum_{i=1}^{n} \frac{a_i}{p + \alpha_i}\right)\right]\bar{X} = M(\dot{X}(0) + pX(0)) + CX(0).$$

In abbreviated form, denoting the matrix coefficient of $\bar{X}$ as S,

$$S(p)\bar{X} = M(\dot{X}(0) + pX(0)) + CX(0), \tag{17}$$

where the matrix $S(p)$ can be written as

$$S(p) = \frac{1}{\prod_{i=1}^{n}(p+\alpha_i)} D(p).$$

The elements of matrix $D(p)$ are polynomials of degree $n + 2$. Inverting the matrix $S(p)$

$$S^{-1}(p) = \prod_{i=1}^{n}(p+\alpha_i) D^{-1}(p)$$

and introducing the adjoint matrix $A(p) = D^{-1}(p)\det(D(p))$, Eq. (17) can be written as follows:

$$\bar{X} = \prod_{i=1}^{n}(p+\alpha_i)\frac{A(p)}{\det(D(p))} \times [M(\dot{X}(0) + pX(0)) + CX(0)].$$

Denoting the roots of the polynomial $\det(D(p))$ as p_k, the determinant of $D(p)$ will be

$$\det(D(p)) = g\prod_{k=1}^{N}(p - p_k)$$

where $N = m(n+2)$, m is the number of degrees-of-freedom and g = constant complex coefficient. Now one can express the solution of the free vibration problem in a form analogous to (4):

$$X(t) = \sum_{i=1}^{N}\prod_{j=1}^{n}(p_i + \alpha_j)\frac{A(p_i)}{g\prod_{k=1,k\neq i}^{N}(p_i - p_k)} \times [M(\dot{X}(0) + p_i X(0)) + CX(0)]e^{p_i t}. \tag{18}$$

This is the extension of the theorem from Bugrov (1989) (the scalar case was considered there) to the matrix case. It should be noted that a formula similar to (18), but for the case of an elastic undamped system, is mentioned in Meirovitch (1967).

REMARK. Note that in the use of formula (18), it is not an easy task to derive the analytical expressions for $D^{-1}(p)$, and consequently for $A(p)$. Also the computation of $A(p_i)$ by $A(p_i) = D^{-1}(p_i)\det(D(p_i))$ requires the calculation of the limit

$$A(p_i) = \lim_{p\to p_i}[D^{-1}(p)\det(D(p))]$$

where $\lim_{p\to p_i}\det(D(p)) = 0$, and $\lim_{p\to p_i}\|D^{-1}(p)\| = \infty$. Therefore the numerical calculation of $A(p_i)$ is not well-posed.

The substitution method described below yields a better way to obtain the closed-form solution, and moreover it provides the formulation of the eigenvalue problem.

2.2.2 The Substitution Method. The solution of (16) is sought in the form (Muravyov and Hutton, 1996):

$$X(t) = \sum_{j=1}^{m(n+2)} c_j X_j e^{p_j t} \tag{19}$$

where X_j = a complex vector ($m \times 1$), c_j, p_j are complex, m

= number of degrees-of-freedom (size of matrices, M, C, K), and n is the number of terms in the relaxation kernel.

Substituting (19) into (16) and taking into account (14), (13), (15), one obtains

$$\sum_{j=1}^{m(n+2)} \left[p_j^2 M + p_j C + K\left(1 - \sum_{i=1}^{n} \frac{a_i}{p_j + \alpha_i}\right)\right] c_j X_j e^{p_j t} + K \sum_{i=1}^{n} \left[\sum_{j=1}^{m(n+2)} \frac{a_i}{p_j + \alpha_i} c_j X_j \right] e^{-\alpha_i t} = 0.$$

In this equation there is a sum of exponential functions. To satisfy this equation one can set all the coefficients of these functions to zero, namely

$$\left[p_j^2 M + p_j C + K\left(1 - \sum_{i=1}^{n} \frac{a_i}{p_j + \alpha_i}\right)\right] X_j = 0 \qquad j = 1, m(n+2) \quad (20)$$

and (with nonsingular matrix K)

$$\sum_{j=1}^{m(n+2)} \frac{a_i}{p_j + \alpha_i} c_j X_j = 0 \quad i = 1, n. \qquad (21)$$

Equation (20) can be called as the characteristic equation, which can be reduced to the eigenvalue problem (see the REMARK below) and the characteristic roots (eigenvalues) p_j along with vectors X_j can be determined.

The initial conditions of the problem are

$$\sum_{j=1}^{m(n+2)} c_j X_j = X_0 \quad \sum_{j=1}^{m(n+2)} c_j p_j X_j = \dot{X}_0. \qquad (22)$$

Note that initial conditions (22) could be replaced by other conditions, for example,

$$\sum_{j=1}^{m(n+2)} c_j X_j = X_0 \quad \sum_{j=1}^{m(n+2)} c_j X_j e^{p_j T} = X(T), \qquad (23)$$

where T represents some given instant of time ($T > 0$). Thus instead of the initial value problem, the boundary value problem (23) (or its modifications) can be posed, and it will only require the change in the two last matrix rows in the system (24).

We will proceed with conditions (22). Relations (21), (22) constitute a system of linear $m(n+2)$ equations with respect to $m(n+2)$ unknowns c_j. In matrix form this system can be written as

$$\begin{bmatrix} \frac{a_1}{p_1+\alpha_1} X_1 & \frac{a_1}{p_2+\alpha_1} X_2 & \cdots & \frac{a_1}{p_{m(n+2)}+\alpha_1} X_{m(n+2)} \\ \cdots & \cdots & \cdots & \cdots \\ \frac{a_n}{p_1+\alpha_n} X_1 & \frac{a_n}{p_2+\alpha_n} X_2 & \cdots & \frac{a_n}{p_{m(n+2)}+\alpha_n} X_{m(n+2)} \\ X_1 & X_2 & \cdots & X_{m(n+2)} \\ p_1 X_1 & p_2 X_2 & \cdots & p_{m(n+2)} X_{m(n+2)} \end{bmatrix} \times \begin{bmatrix} c_1 \\ \cdots \\ c_{m(n+2)} \end{bmatrix} = \begin{bmatrix} 0 \\ \cdots \\ 0 \\ X_0 \\ \dot{X}_0 \end{bmatrix}. \qquad (24)$$

REMARK. Introducing a common denominator for all terms, Eq. (20) can be rewritten as follows:

$$\left[(p_j^2 M + p_j C + K) \prod_{i=1}^{n} (p_j + \alpha_i) - K \sum_{i=1}^{n} a_i \prod_{k=1, k\neq i}^{n} (p_j + \alpha_k) \right] X_j = 0.$$

Collecting the matrix coefficients of $p_j^{n+2}, p_j^{n+1}, \ldots, p_j^0$ and denoting them as $B_{n+2}, B_{n+1}, \ldots, B_0$, respectively, Eq. (20) is equivalent to

$$\left(p \begin{bmatrix} B_1 & B_2 & B_3 & \cdots & B_{n+2} \\ I & 0 & 0 & \cdots & 0 \\ 0 & I & 0 & \cdots & 0 \\ \cdots & \cdots & \cdots & \cdots & \cdots \\ 0 & 0 & \cdots & I & 0 \end{bmatrix} + \begin{bmatrix} B_0 & 0 & 0 & \cdots & 0 \\ 0 & -I & 0 & \cdots & 0 \\ 0 & 0 & -I & \cdots & 0 \\ \cdots & \cdots & \cdots & \cdots & \cdots \\ 0 & 0 & 0 & \cdots & -I \end{bmatrix} \right) \hat{Q} = \begin{bmatrix} 0 \\ 0 \\ \cdots \\ 0 \end{bmatrix} \qquad (25)$$

or, in abbreviated form,

$$(p\hat{A} + \hat{B})\hat{Q} = 0, \qquad (26)$$

where the jth eigenvector will be

$$\hat{Q}_j = \begin{bmatrix} X_j \\ p_j X_j \\ p_j^2 X_j \\ \cdots \\ p_j^{n+1} X_j \end{bmatrix} \quad j = 1, m(n+2).$$

The matrix coefficient $B_{n+2} = M$, and other coefficients can be readily evaluated (the expressions for them are omitted here). In the next section the expressions for matrices B_k will be shown for one example of a viscoelastic system.

The eigenvalues of (26) will be the characteristic roots of (20). The basic part X_j of eigenvector $\hat{Q}_j$ is used in (24), (19).

As far as the eigenvalues p_j are concerned, they are allowed to be multiple (for the multi-degree-of-freedom system case). However, they must have linearly independent corresponding eigenvectors, to provide nonsingularity of the matrix in (24). It is easy to note that if there is a root, for example of multiplicity 2, which has only one eigenvector (the second one is linear dependent), then the two corresponding columns in (24) will be linearly dependent and the determinant of the matrix vanishes. In other words, in order to have a solution of (16) in the form (19), it is required that the eigenproblem (25) yields $N = m(n+2)$ linearly independent eigenvectors. This requirement is not a restriction imposed on a system, it is just an indicator which can be used to determine if a given viscoelastic system (14)–(16) assumes a solution in the form (19) or not. If it assumes, then according to the theorem of uniqueness (Linz, 1985), this solution is unique. The satisfaction of this requirement is expected for most viscoelastic systems, although if this requirement is not satisfied, then the analytical homogeneous solution may differ from (19).

It should be noted that the size of eigenvalue problem (25) can be quite large, so it is necessary to have an effective eigensolver for matrices of the type in (25).

2.2.3 Periodic Loading Case. Application of the Substitution Method. The general case of periodic loading with a period $T = 2\pi/\omega$ is treated by using a complex Fourier series. The forcing function is represented as

$$F(t) = \sum_{k=0}^{L} F_k e^{i\omega_k t} \quad \omega_k = k\omega$$

where F_k are vectors of size m.

The equation of motion is written as follows:

$$M\ddot{X} + C\dot{X} + \tilde{E}K_0X = \sum_{k=0}^{L} F_k e^{i\omega_k t} \tag{27}$$

with initial conditions

$$X(0) = X_0 \quad \dot{X}(0) = \dot{X}_0.$$

The general solution is now sought as a sum of homogeneous and particular solutions, namely

$$X(t) = \sum_{j=1}^{m(n+2)} c_j X_j e^{p_j t} + \sum_{k=0}^{L} Z_k e^{i\omega_k t}. \tag{28}$$

Substituting (28) in (27) and taking into account (14), (13), (15) one obtains

$$\sum_{j=1}^{m(n+2)} \left[p_j^2 M + p_j C + K\left(1 - \sum_{i=1}^{n} \frac{a_i}{p_j + \alpha_i}\right)\right] X_j e^{p_j t}$$

$$+ \sum_{k=0}^{L} \left[-\omega_k^2 M + i\omega_k C + K\left(1 - \sum_{i=1}^{n} \frac{a_i}{i\omega_k + \alpha_i}\right)\right] Z_k e^{i\omega_k t}$$

$$+ K \sum_{i=1}^{n} \left[\sum_{j=1}^{m(n+2)} \frac{a_i}{p_j + \alpha_i} c_j X_j + \sum_{k=0}^{L} \frac{a_i}{i\omega_k + \alpha_i} Z_k \right] e^{-\alpha_i t}$$

$$= \sum_{k=0}^{L} F_k e^{i\omega_k t}.$$

From this the characteristic Eq. (20) and subsequently the eigenproblem (25) follows yielding values for p_j and X_j.

The quantities Z_k are determined as follows:

$$Z_k = \left[-\omega_k^2 M + i\omega_k C + K\left(1 - \sum_{i=1}^{n} \frac{a_i}{i\omega_k + \alpha_i}\right)\right]^{-1} F_k$$

$$k = 0, L.$$

The linear system of Eq. (24) with respect to unknowns c_j in this case will have the modified right-hand side:

$$\begin{bmatrix} \frac{a_1}{p_1 + \alpha_1} X_1 & \frac{a_1}{p_2 + \alpha_1} X_2 & \cdots & \frac{a_1}{p_{m(n+2)} + \alpha_1} X_{m(n+2)} \\ \cdots & \cdots & \cdots & \cdots \\ \frac{a_n}{p_1 + \alpha_n} X_1 & \frac{a_n}{p_2 + \alpha_n} X_2 & \cdots & \frac{a_n}{p_{m(n+2)} + \alpha_n} X_{m(n+2)} \\ X_1 & X_2 & \cdots & X_{m(n+2)} \\ p_1 X_1 & p_2 X_2 & \cdots & p_{m(n+2)} X_{m(n+2)} \end{bmatrix}$$

$$\times \begin{bmatrix} c_1 \\ \cdots \\ c_{m(n+2)} \end{bmatrix} = \begin{bmatrix} -\sum_{k=0}^{L} \frac{a_1}{i\omega_k + \alpha_1} Z_k \\ \cdots \\ -\sum_{k=0}^{L} \frac{a_n}{i\omega_k + \alpha_n} Z_k \\ X_0 - \sum_{k=0}^{L} Z_k \\ \dot{X}_0 - \sum_{k=0}^{L} i\omega_k Z_k \end{bmatrix}.$$

3 Numerical Results

A program was written which calculates analytical solutions according to the substitution method and was used for the examples below.

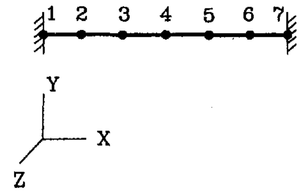

Fig. 1 Viscoelastic beam with fixed ends

Numerical results are presented for a viscoelastic beam with fixed ends (Fig. 1). The parameters of the beam's cross section were 0.01×0.01 m, the length $= 0.12$ m, the instantaneous Young's modulus E was 0.15e+08 Pa, $\nu = 0.3$, $\rho = 0.141\text{e+}04$ kg/m^3. The beam was meshed by six general beam elements. Each node of a beam element had six degrees-of-freedom (three linear and three rotational). Thus the size of the problem (number of degrees-of-freedom) was $m = 30$.

The relaxation kernel in (15) was taken as

$$\Gamma(t - \tau) = a_1 e^{-\alpha_1(t-\tau)} \tag{29}$$

where $a_1 = 150\ s^{-1}$, $\alpha_1 = 200\ s^{-1}$ $(n = 1)$. Thus the size of eigenvalue problem (25) and of linear system (24) was $m(n + 2) = 90$.

The matrix coefficients in (25) for this case are computed as follows:

$$B_0 = K(\alpha_1 - a_1) \quad B_1 = C\alpha_1 + K \quad B_2 = M\alpha_1 + C \quad B_3 = M.$$

One can see that if a_1 is negligible ($a_1 \approx 0$), then the characteristic matrix Eq. (20) is reduced to the usual complex eigenvalue problem of a viscously damped system. To investigate the effect of the hereditary part (term $\tilde{E}K_0X$) in (16), and not it's combined effect along with the viscous damping term $C\dot{X}$, it was assumed that the damping matrix $C = 0$.

Standard subroutine "DREIGN" (Nicol, 1982) was used for the eigenproblem (25) and the subroutine "CDSOLN" for (24).

Consider the eigenvalue problem (25) in more detail. For the system in Fig. 1 the computed eigenvalues are presented in Fig. 2 (imaginary parts) and in Fig. 3 (real parts). Numeration of the eigenvalues was done on the basis of their absolute values.

It is found that for the model (29) defined by only one exponential term there are 30 (note this number is equal to the number of degrees of freedom times number of exponential terms in the relaxation kernel) real eigenvalues which correspond to "overdamped" eigenvectors (also real). The other 30 pairs of complex conjugate eigenvalues, which have a nonzero

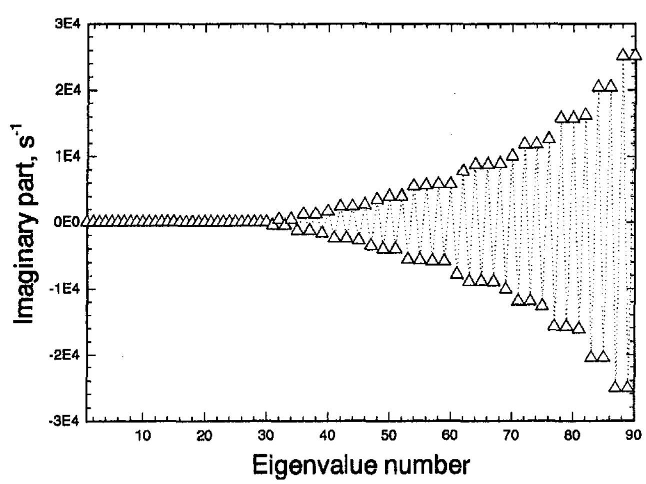

Fig. 2 Imaginary part of eigenvalues

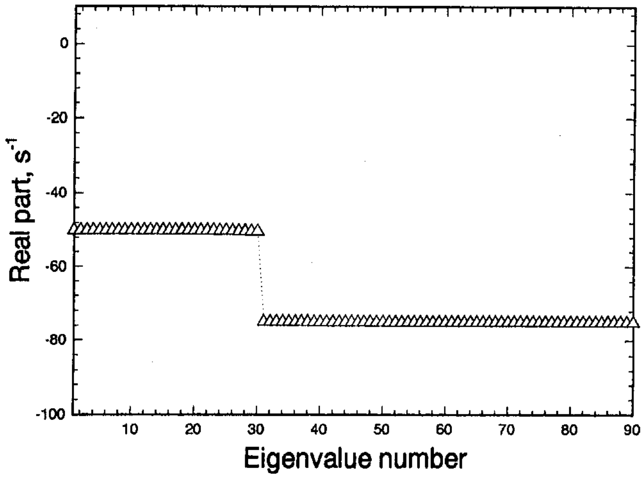

Fig. 3 Real part of eigenvalues

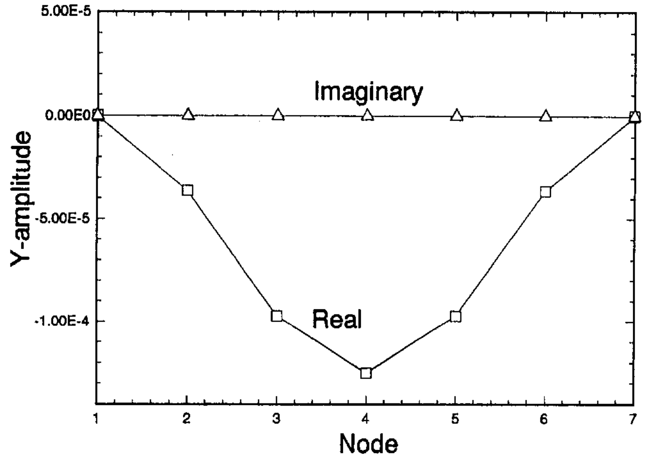

Fig. 5 The 29th real eigenvector (analog to the 31st one)

imaginary part, correspond to "underdamped" eigenvectors. Although the terms overdamped and underdamped are usually used in the context of viscously damped system, their use in the case of a viscoelastic (hereditary) system may be adopted as well.

For the purpose of illustration, some of the eigenvectors are presented below in Figs. 4 and 5. The first of the underdamped eigenvectors (corresponding to eigenvalue No. 31) has a shape of vibration in plane $X - Y$ shown in Fig. 4. For eigenvalue No. 29 the real eigenvector has the same shape (Fig. 5) as the complex eigenvector corresponding to eigenvalue No. 31.

The numerical results in terms of displacements are presented in Figs. 6 and 7. The vertical displacements and velocities were imparted to the middle node 4 at $t = 0$. The following variations of initial conditions were considered for node 4: case (1) $y(0) = 0.005$ m, $\dot{y}(0) = 0$; case (2) $y(0) = 0$, $\dot{y}(0) = 10$ m/s. All the other degrees-of-freedom had zero initial conditions. The Y displacements of node No. 4 (Fig. 1) were chosen to illustrate the response. The results of free vibration response are presented in Fig. 6 for the case (1), Fig. 7 (case (2)). The response of the elastic beam ($a_1 = 0$) is shown by a dashed line for comparison purposes.

The contribution of vectors $c_j X_j$ to the solution, namely, their norms $\|c_j X_j\|$ are presented in Figs. 8 and 9 for the initial conditions (1) and (2), respectively. As would be expected the contribution of eigenvectors to the free vibration response depends on initial conditions. Note that the complex conjugate eigenvectors contribute equally, for example, pairs of eigenvectors No. 31 and 32, 43 and 44, 59 and 60, 71 and 72, and 85 and 86 in Fig. 8. It is clear that relative contribution of the underdamped eigenvectors (with respect to each other) will not change in time, because the real parts of their eigenvalues are the same (Fig. 3). One can see that the contribution of the overdamped eigenvectors No. 24 and 29 is quite noticeable for the case of initial conditions (2) (Fig. 9). Note that their relative contribu-

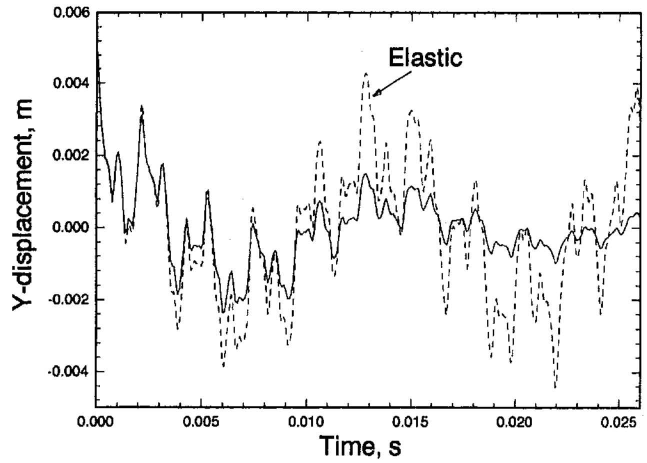

Fig. 6 Free vibration response, case (1)

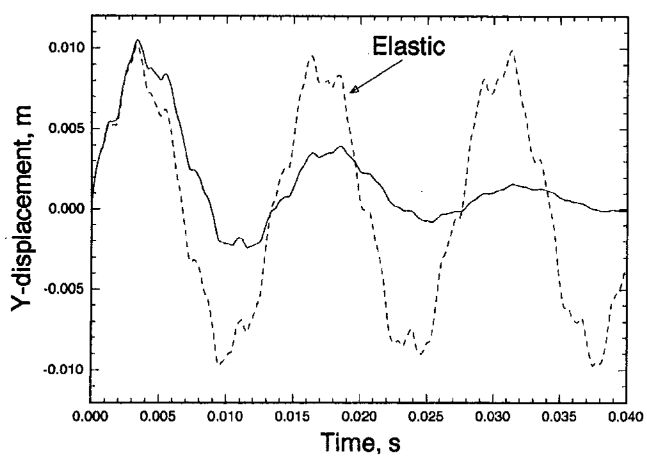

Fig. 7 Free vibration response, case (2)

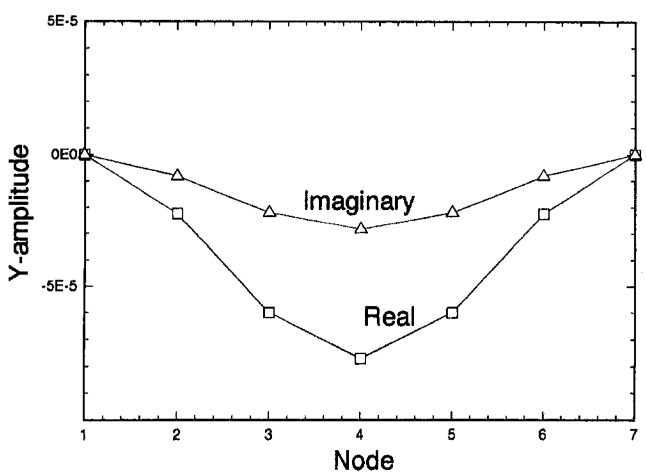

Fig. 4 The 31st complex eigenvector

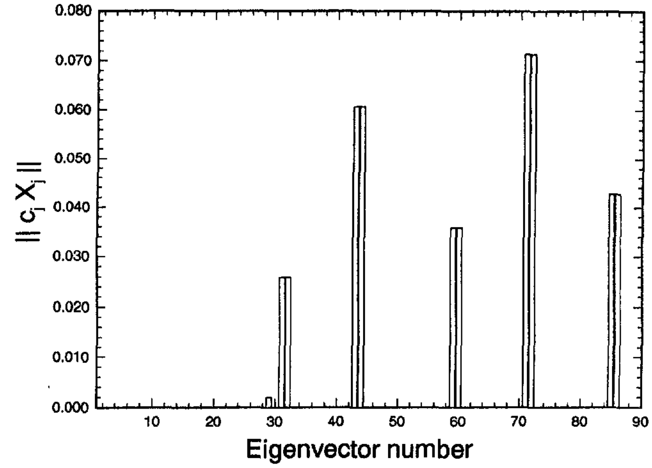

Fig. 8 Contribution of eigenvectors, case (1)

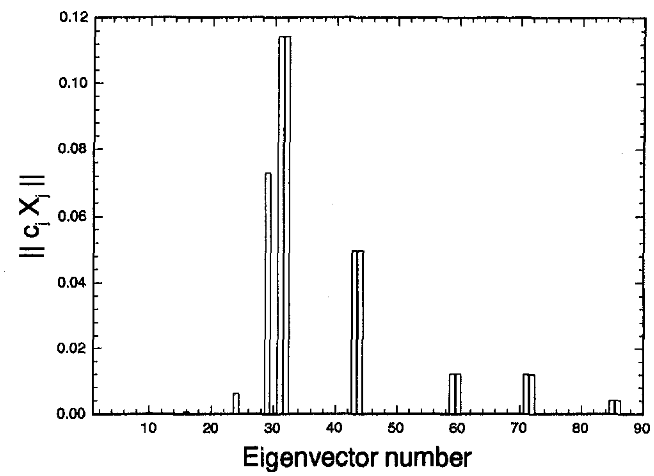

Fig. 9 Contribution of eigenvectors, case (2)

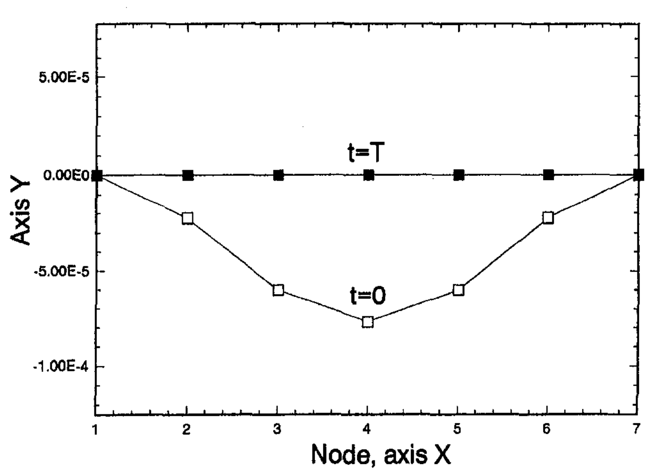

Fig. 10 Initial and terminal shapes

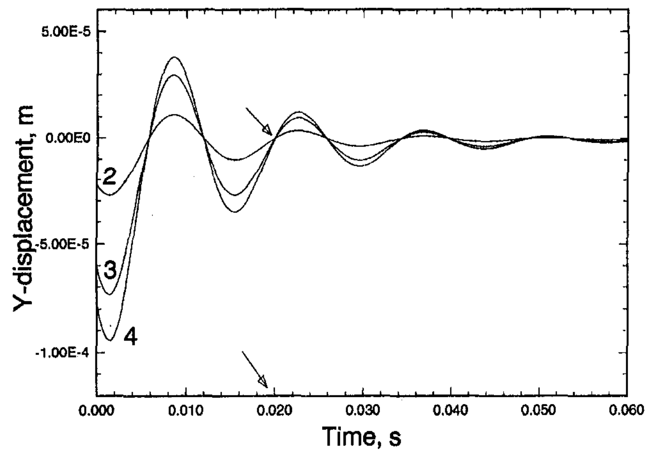

Fig. 11 Solution for conditions (23), T = 0.02 s

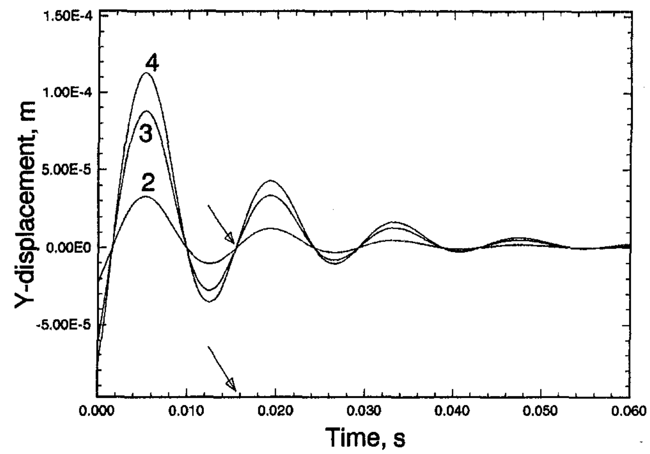

Fig. 12 Solution for conditions (23), T = 0.016 s

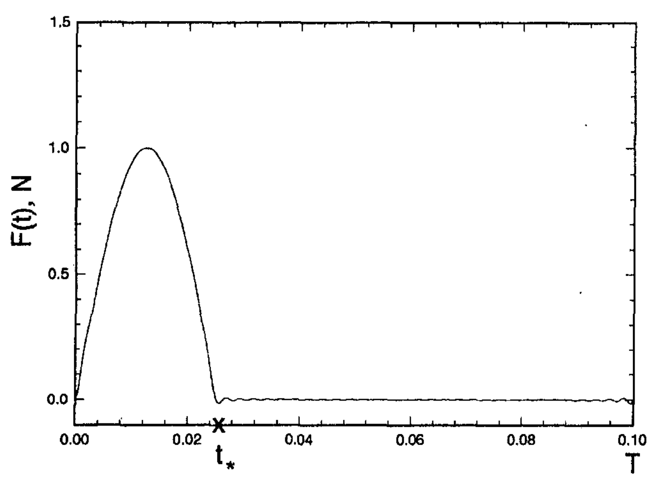

Fig. 13 Forcing function

tion with respect to the underdamped terms will increase in time, because real parts of their eigenvectors are greater (less negative) (Fig. 3).

A boundary value problem (23) was then considered. The conditions shown in Fig. 10 were assumed, where for a chosen instant of time $T = 0.02$ s, all the displacements were prescribed to be zero. The solution (the vertical displacements of nodes 2, 3, 4) for this case is shown in Fig. 11. Then an instant T = 0.016 s was chosen, and the response is shown in Fig. 12. One can observe the difference in the initial velocities which are not prescribed, but computed.

For forced vibration a vertical periodic force $F(t)$ (Fig. 13) was applied at the node 4. It is supposed that $F(t) = 0$ for $t \subset [t_*, T]$.

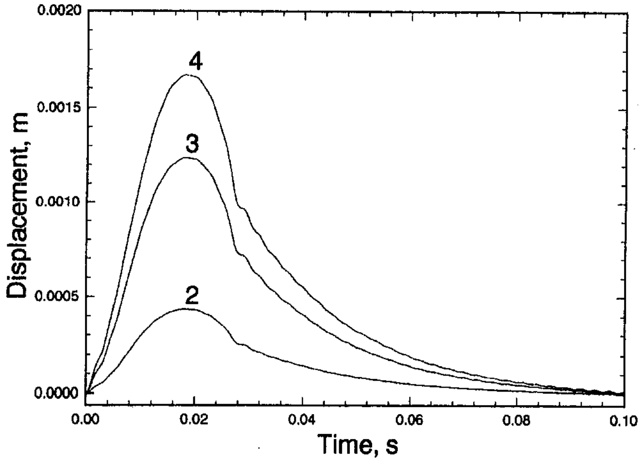

Fig. 14 Forced response with zero initial conditions

This case of loading has a period of $T = 0.1$ s and Fourier series (40 harmonics) was used to represent the forcing function $F(t)$. The high-frequency harmonic contribution is slightly noticeable after $t = t_*$ due to the limited number of terms in the Fourier series.

The vertical displacements of the nodes 2, 3, 4 (Fig. 1) were chosen to illustrate the response. The solution with zero initial conditions (for all degrees-of-freedom) is presented in Fig. 14 for $t \subset [0, T]$.

Summary

In this study the two methods of obtaining analytical solutions in the time domain for discrete viscoelastic systems (in which the relaxation kernel is represented as a series of exponentials) have been shown.

A new method (substitution method) has been proposed that avoids the difficulty encountered in the use of the Laplace transform approach for multi-degree-of-freedom systems and which involves formulation of an eigenvalue problem.

The analysis of eigenvalues and eigenvectors has shown that there will be a significant number of overdamped eigenvectors, which correspond to real negative eigenvalues.

Finite element formulations for viscoelastic systems have traditionally been described in the literature in the context of step-by-step numerical integration (in time) schemes. The substitution method yields an alternative independent solution tool for an important class of viscoelastic systems for which the relaxation kernel is represented as a series of exponentials.

It has been shown that a closed-form solution can be determined not only for initial conditions, but also for the boundary value problem. This is a distinct advantage in having the solution in analytical form. It may be noted that the use of numerical integration for the boundary value problem is much more complicated than for the initial value problem.

Acknowledgment

Funds for this work were provided by the Defense Research Establishment Atlantic, Canadian Department of National Defense.

References

ABAQUS: user's manual, 1993, Version 5.3, Hibbit, Earlsson and Sorensen.

Brunner, H., and Von der Houwen, P. J., 1986, *The numerical solution of Volterra equations*, North-Holland, Amsterdam.

Bugrov, Ya.S., and Nikolski, S. M., 1989, *Differential equations, Multiple integrals, Series, Functions of a complex variable*, Moscow (in Russian).

Carini, A., and De Donato, O., 1992, "Fundamental solutions for linear viscoelastic continua," *Journal of Solids and Structures*, Vol. 29, No. 23, pp. 2989–3009.

Christensen R. M., 1982, *Theory of viscoelasticity*, Academic Press, San Diego, CA.

Creus, G. J., 1986, *Viscoelasticity—Basic Theory and Applications to concrete structures*, Springer-Verlag, New York.

Day, S. M., and Minster, J. B., 1984, "Numerical simulation of attenuated wavefields using a Pade approximant method," *Geophys. J. R. astr. Soc*, Vol. 78, pp. 105–118.

Ferry, J. D., 1970, *Viscoelastic properties of polymers*, John Wiley and Sons, New York.

Flugge, W., 1967, *Viscoelasticity*, Blaisdell, Waltham, MA.

Linz, P., 1985, *Analytical and numerical methods for Volterra equations*, SIAM, Philadelphia, PA.

Meirovitch, L., 1967, *Analytical methods in vibrations*, The Macmillan Company, London.

Muravyov, A., 1996, "Analytical solutions in the time domain for vibration problems of discrete viscoelastic systems," *Journal of Sound and Vibration*, to appear.

Muravyov, A., and Hutton, S. G., 1996, "Free vibration of discrete viscoelastic systems and the eigenvalue problem," *Proceedings of the 1st South African Conference on Applied Mechanics*, Eskom Midrand, South Africa, July, pp. 215–222.

Nicol, T., ed., 1982, *UBC Matrix book (A Guide to Solving Matrix Problems)*, Computing Centre, UBC, Vancouver, BC, March.

Rabotnov, Yu., N., 1980, *Elements of hereditary solid mechanics*, Mir Publishers, Moscow.

Rabotnov, Yu., N., 1969, *Creep problems in structural members*, North-Holland, Amsterdam.

Journal of Applied Mechanics

Brief Notes

A Brief Note is a short paper that presents a specific solution of technical interest in mechanics but which does not necessarily contain new general methods or results. A Brief Note should not exceed 1500 words *or equivalent* (a typical one-column figure or table is equivalent to 250 words; a one line equation to 30 words). Brief Notes will be subject to the usual review procedures prior to publication. After approval such Notes will be published as soon as possible. The Notes should be submitted to the Technical Editor of the JOURNAL OF APPLIED MECHANICS. Discussions on the Brief Notes should be addressed to the Editorial Department, ASME, United Engineering Center, 345 East 47th Street, New York, N. Y. 10017, or to the Technical Editor of the JOURNAL OF APPLIED MECHANICS. Discussions on Brief Notes appearing in this issue will be accepted until two months after publication. Readers who need more time to prepare a Discussion should request an extension of the deadline from the Editorial Department.

The Reissner-Sagoci Problem for the Transversely Isotropic Half-Space

M. T. Hanson[1,2] **and I. W. Puja**[1]

This paper evaluates the elastic field in a transversely isotropic half-space caused by a circular flat bonded punch under torsion loading. The elastic field is found by integrating the point force potential functions. For the case of isotropy the present results agree with previous analysis.

1 Introduction

In isotropic elasticity a class of mixed boundary value problems for the elastic half-space can be classified as axisymmetric torsion. In this case the elastic field in cylindrical components takes a particularly simple form consisting of only one nonzero displacement and two nonzero stress components. For this loading case Reissner and Sagoci (1944) were possibly the first to examine a mixed boundary value problem between the tangential displacement and stress on the half-space surface. They considered the problem of a circular flat disk bonded to a half-space under the action of a torsional couple. Their analysis provided the contact shear stress under the disk and the tangential displacement on the surface outside the disk. The elastic field was soon thereafter given by Sneddon (1947) illustrating the use of Hankel transforms in developing complete solutions to mixed boundary value problems.

In the present study the Reissner-Sagoci problem is revisited for the transversely isotropic half-space. The reasons for this are twofold. The first is to display how the elastic field can be obtained by a direct integration of the point force potentials. The first reason leads directly to the second which is to put the elastic field in a form consistent with other mixed boundary value problems which have recently been solved for the transversely isotropic half-space. Fabrikant (1988) evaluated the elastic field caused by a rigid flat punch acted upon by a concentric force or tilting moment. Hanson (1994) included the effect of shear traction. Also Hanson (1992a, b; 1993) evaluated the elastic field for the additional cases of a spherical and conical punch under normal and shear loading. In all of these solutions the elastic fields are given in a consistent fashion in terms of two length parameters. The present analysis puts the elastic field for the Reissner-Sagoci problem in this same form.

2 Potential Functions for Transverse Isotropy

The transversely isotropic half-space is taken as the region $z > 0$ where the surface $z = 0$ is parallel to the planes of isotropy, Fig. 1. A potential function formulation was first given by Elliot (1948). The notation of Fabrikant (1989) is presently adopted. The displacements are taken as u, v, and w in the x, y, and z directions. Here A_{11}, A_{13}, A_{33}, A_{44}, and A_{66} are the five elastic constants. The solution of the equilibrium equations in terms of three potential functions F_1, F_2, and F_3 is given by Fabrikant (1989) in the form

$$u^c = \Lambda(F_1 + F_2 + iF_3), \quad w = m_1 \frac{\partial F_1}{\partial z} + m_2 \frac{\partial F_2}{\partial z}, \quad (1)$$

with i being the complex number, $i = \sqrt{(-1)}$, m_1 and m_2 are constants defined below, and u^c is the complex displacement

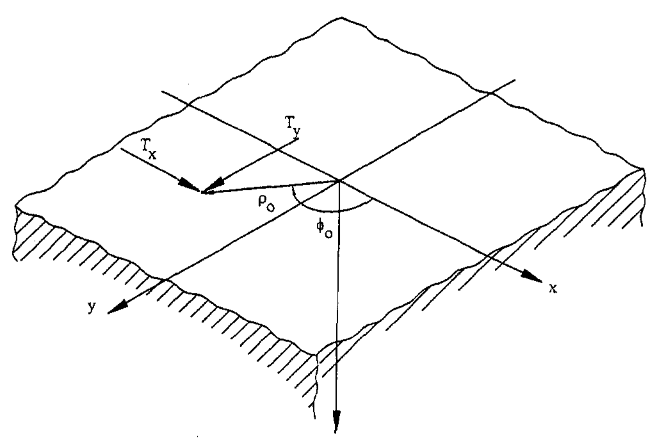

Fig. 1 Geometry and coordinate system for point loading

[1] Department of Engineering Mechanics, University of Kentucky, Lexington, KY 40506-0046.

[2] Mem. ASME.

Contributed by the Applied Mechanics Division of THE AMERICAN SOCIETY OF MECHANICAL ENGINEERS for publication in the ASME JOURNAL OF APPLIED MECHANICS. Manuscript received by the ASME Applied Mechanics Division, Nov. 14, 1995; final revision, Dec. 11, 1996. Associate Technical Editor: R. Abeyaratne.

$u^c = u + iv$. The operator Λ and the operator Δ used subsequently are given as

$$\Lambda = \frac{\partial}{\partial x} + i\frac{\partial}{\partial y}, \quad \Delta = \frac{\partial^2}{\partial x^2} + \frac{\partial^2}{\partial y^2}. \tag{2}$$

The functions F_j satisfy the relations

$$\Delta F_j + \gamma_j^2 \frac{\partial^2 F_j}{\partial z^2} = 0, \quad j = 1, 2, 3, \tag{3}$$

where γ_j are also constants. The constant γ_3 is given as $\gamma_3^2 = A_{44}/A_{66}$ while $\gamma_j^2 = n_j$, $j = 1, 2$ and n_j are the two (real or complex conjugate) roots of the quadratic equation

$$A_{11}A_{44}n_j^2 + [A_{13}(A_{13} + 2A_{44}) - A_{11}A_{33}]n_j + A_{33}A_{44} = 0. \tag{4}$$

The constants m_j are related to γ_j as

$$m_j = \frac{A_{11}\gamma_j^2 - A_{44}}{A_{13} + A_{44}} = \frac{(A_{13} + A_{44})\gamma_j^2}{A_{33} - \gamma_j^2 A_{44}}, \quad j = 1, 2. \tag{5}$$

Using the following stress combinations in Cartesian (x, y, z) or cylindrical (ρ, ϕ, z) components $\sigma_1 = \sigma_{xx} + \sigma_{yy} = \sigma_{\rho\rho} + \sigma_{\phi\phi}$, $\sigma_2 = \sigma_{xx} - \sigma_{yy} + 2i\tau_{xy} = e^{2i\phi}(\sigma_{\rho\rho} - \sigma_{\phi\phi} + 2i\tau_{\rho\phi})$ and $\tau_z = \tau_{xz} + i\tau_{yz} = e^{i\phi}(\tau_{\rho z} + i\tau_{\phi z})$, the stress field can be written in the following form:

$$\sigma_1 = 2A_{66}\frac{\partial^2}{\partial z^2}\{[\gamma_1^2 - (1 + m_1)\gamma_3^2]F_1 + [\gamma_2^2 - (1 + m_2)\gamma_3^2]F_2\},$$

$$\sigma_2 = 2A_{66}\Lambda^2[F_1 + F_2 + iF_3],$$

$$\sigma_{zz} = A_{44}\frac{\partial^2}{\partial z^2}[\gamma_1^2(1 + m_1)F_1 + \gamma_2^2(1 + m_2)F_2],$$

$$\tau_z = A_{44}\Lambda\frac{\partial}{\partial z}[(1 + m_1)F_1 + (1 + m_2)F_2 + iF_3]. \tag{6}$$

3 Point Shear Force Green's Functions

The geometry and coordinate system are shown in Fig. 1. Using cylindrical coordinates (ρ, ϕ, z), a point force is applied on the surface at ρ_o, ϕ_o with components T_x and T_y in the x and y directions, respectively. The potential functions for these fundamental point force solutions were put in a very convenient form by Fabrikant (1989) as

$$F_1(\rho, \phi, z; \rho_o, \phi_o) = \frac{H\gamma_1}{(m_1 - 1)}\frac{\gamma_2}{2}(T\bar{\Lambda} + \bar{T}\Lambda)\chi(z_1)$$

$$F_2(\rho, \phi, z; \rho_o, \phi_o) = \frac{H\gamma_2}{(m_2 - 1)}\frac{\gamma_1}{2}(T\bar{\Lambda} + \bar{T}\Lambda)\chi(z_2)$$

$$F_3(\rho, \phi, z; \rho_o, \phi_o) = i\frac{\gamma_3}{4\pi A_{44}}(T\bar{\Lambda} - \bar{T}\Lambda)\chi(z_3) \tag{7}$$

where $T = T_x + iT_y$, an overbar indicates complex conjugation and the function $\chi(z_j)$ is

$$\chi(z_j) = z_j \ln[R_j + z_j] - R_j, \quad j = 1, 2, 3, \tag{8}$$

with

$$R_j^2 = \rho^2 + \rho_o^2 - 2\rho\rho_o\cos(\phi - \phi_o) + z_j^2,$$

$$z_j = \frac{z}{\gamma_j}, \quad j = 1, 2, 3, \tag{9}$$

and the constant H is defined as

$$H = \frac{(\gamma_1 + \gamma_2)A_{11}}{2\pi(A_{11}A_{33} - A_{13}^2)}. \tag{10}$$

4 Potentials for the Reissner-Sagoci Problem

Consider now the boundary conditions for the Reissner-Sagoci problem. The physical interpretation is that of a rigid flat punch of circular geometry perfectly bonded to a half-space under the action of a torsional couple which causes a rotation parallel to the surface. Using the cylindrical displacements u_ρ, u_ϕ and stress components $\tau_{\rho z}$, $\tau_{\phi z}$ the mixed boundary conditions on $z = 0$ become

$$u_\rho = w = 0, \quad u_\phi = \lambda\rho, \quad \rho < a;$$

$$\tau_{\rho z} = \tau_{\phi z} = \sigma_{zz} = 0, \quad \rho > a, \tag{11}$$

where λ is a constant. The special case of transverse isotropy considered presently results in this problem being one of axisymmetric torsion, analogous to the isotropic solution. Hence the stresses in the contact region are similar to the isotropic form and can be taken as (Reissner and Sagoci, 1944)

$$\tau_{\rho z} = \sigma_{zz} = 0, \quad \tau_{\phi z}(\rho) = -\frac{A\rho}{(a^2 - \rho^2)^{1/2}}, \quad \rho < a, \tag{12}$$

where A is a constant related to λ above.

The potential functions for this problem can now be found by direct integration. The complex force $T = T_x + iT_y$ in Eq. (7) is replaced with $-ie^{i\phi_o}\tau_{\phi z}(\rho_o)\rho_o d\rho_o d\phi_o$ and the result is integrated over $0 < \rho_o < a$, $0 < \phi_o < 2\pi$. The potentials then have the form

$$F_j(\rho, \phi, z) = \frac{iAH\gamma_1\gamma_2}{2(m_j - 1)}\{\bar{\Lambda}[z_j\psi(\rho, \phi, z_j) - \Phi(\rho, \phi, z_j)] - \Lambda[z_j\bar{\psi}(\rho, \phi, z_j) - \bar{\Phi}(\rho, \phi, z_j)]\}, \quad j = 1, 2,$$

$$F_3(\rho, \phi, z) = -\frac{A\gamma_3}{4\pi A_{44}}\{\bar{\Lambda}[z_3\psi(\rho, \phi, z_3) - \Phi(\rho, \phi, z_3)] + \Lambda[z_3\bar{\psi}(\rho, \phi, z_3) - \bar{\Phi}(\rho, \phi, z_3)]\}, \tag{13}$$

where the functions $\psi(\rho, \phi, z_j)$ and $\Phi(\rho, \phi, z_j)$ are defined as

$$\psi(\rho, \phi, z_j) = \int_0^{2\pi}\int_0^a \frac{\rho_o e^{i\phi_o}}{(a^2 - \rho_o^2)^{1/2}}\ln[R_j + z_j]\rho_o d\rho_o d\phi_o,$$

$$\Phi(\rho, \phi, z_j) = \int_0^{2\pi}\int_0^a \frac{\rho_o e^{i\phi_o}}{(a^2 - \rho_o^2)^{1/2}} R_j \rho_o d\rho_o d\phi_o, \tag{14}$$

and $\bar{\psi}(\rho, \phi, z_j)$, $\bar{\Phi}(\rho, \phi, z_j)$ can be obtained from above by replacing $e^{i\phi_o}$ with $e^{-i\phi_o}$.

The above integrals can be extracted from the results in Fabrikant (1988) and Hanson (1994) as

$$\psi(\rho, \phi, z_j) = \pi\rho e^{i\phi}\left\{z_j \sin^{-1}\frac{l_{1j}(a)}{\rho} - [a^2 - l_{1j}^2(a)]^{1/2} \times \left[1 - \frac{2a^2 + l_{1j}^2(a)}{3\rho^2}\right] - \frac{2a^3}{3\rho^2}\right\},$$

$$\Phi(\rho, \phi, z_j) = \pi\rho e^{i\phi}\left\{\frac{1}{8}[\rho^2 + 4z_j^2 - 4a^2]\sin^{-1}\frac{l_{1j}(a)}{\rho} - \left[l_{1j}^2(a) + 2l_{2j}^2(a) - \frac{3\rho^2}{2}\right]\frac{l_{1j}(a)[\rho^2 - l_{1j}^2(a)]^{1/2}}{4\rho^2}\right\}, \tag{15}$$

where

$$l_1(a) = \tfrac{1}{2}\{[(\rho + a)^2 + z^2]^{1/2} - [(\rho - a)^2 + z^2]^{1/2}\},$$

$$l_2(a) = \tfrac{1}{2}\{[(\rho + a)^2 + z^2]^{1/2} + [(\rho - a)^2 + z^2]^{1/2}\}, \quad (16)$$

and $l_{1j}(a)$, $l_{2j}(a)$ are found from the above equation by replacing z with z_j. The functions $\bar{\psi}(\rho, \phi, z_j)$, $\bar{\Phi}(\rho, \phi, z_j)$ can be obtained from above by replacing $e^{i\phi}$ with $e^{-i\phi}$.

To find the potentials the following results can be used:

$$\Lambda\bar{\psi}(\rho, \phi, z_j) = \bar{\Lambda}\psi(\rho, \phi, z_j) = 2\pi\left\{ z_j \sin^{-1}\frac{l_{1j}(a)}{\rho} - [a^2 - l_{1j}^2(a)]^{1/2} \right\},$$

$$\Lambda\bar{\Phi}(\rho, \phi, z_j) = \bar{\Lambda}\Phi(\rho, \phi, z_j) = 2\pi\left\{ \frac{1}{4}[\rho^2 + 2z_j^2 - 2a^2] \times \sin^{-1}\frac{l_{1j}(a)}{\rho} + \frac{[l_{1j}^2(a) - 2a^2][\rho^2 - l_{1j}^2(a)]^{1/2}}{4l_{1j}(a)} \right\}. \quad (17)$$

From these results the potentials become

$$F_j(\rho, \phi, z) = 0, \quad j = 1, 2,$$

$$F_3(\rho, \phi, z) = -\frac{A\gamma_3}{2\pi A_{44}}\{z_3\bar{\Lambda}\psi(\rho, \phi, z_3) - \bar{\Lambda}\Phi(\rho, \phi, z_3)\}. \quad (18)$$

5 The Elastic Field

The elastic field can now be found by direct differentiation. In Cartesian coordinates the results are

$$u^c = -\frac{A\gamma_3 i\rho e^{i\phi}}{A_{44}}\left\{ -\frac{1}{2}\sin^{-1}\frac{l_{13}(a)}{\rho} + \frac{l_{13}(a)[\rho^2 - l_{13}^2(a)]^{1/2}}{2\rho^2} \right\}, \quad (19)$$

$$\sigma_2 = -\frac{2iA\rho e^{i2\phi}}{\gamma_3}\frac{l_{13}^3(a)[\rho^2 - l_{13}^2(a)]^{1/2}}{\rho^3[l_{23}^2(a) - l_{13}^2(a)]}, \quad (20)$$

$$\tau_z = -iA\rho e^{i\phi}\frac{l_{13}^2(a)[a^2 - l_{13}^2(a)]^{1/2}}{\rho^2[l_{23}^2(a) - l_{13}^2(a)]}, \quad (21)$$

where $w = \sigma_1 = \sigma_{zz} = 0$. In cylindrical coordinates the nonzero displacement and stress components are

$$u_\phi = -\frac{A\gamma_3\rho}{A_{44}}\left\{ -\frac{1}{2}\sin^{-1}\frac{l_{13}(a)}{\rho} + \frac{l_{13}(a)[\rho^2 - l_{13}^2(a)]^{1/2}}{2\rho^2} \right\}, \quad (22)$$

$$\tau_{\phi z} = -A\frac{l_{13}^2(a)[a^2 - l_{13}^2(a)]^{1/2}}{\rho[l_{23}^2(a) - l_{13}^2(a)]}, \quad (23)$$

$$\tau_{\phi\rho} = -\frac{A}{\gamma_3}\frac{l_{13}^3(a)[\rho^2 - l_{13}^2(a)]^{1/2}}{\rho^2[l_{23}^2(a) - l_{13}^2(a)]}. \quad (24)$$

Now the relation between the constants A and λ can be easily obtained. On the surface as $z \to 0$ it is easy to verify

$$\lim_{z\to 0} l_{13}(a) = \min(a, \rho), \quad \lim_{z\to 0} l_{23}(a) = \max(a, \rho), \quad (25)$$

where min is the minimum of the two values and max is the maximum. Thus for $z = 0$, $\rho < a$ Eqs. (11), (22) provide

$$u_\phi = \frac{A\pi\gamma_3}{4A_{44}}\rho, \quad \lambda = \frac{A\pi\gamma_3}{4A_{44}}, \quad A = \frac{4A_{44}\lambda}{\pi\gamma_3}. \quad (26)$$

For an isotropic material $\gamma_3 \to 1$, $z_3 \to z$ and $l_{13}(a)$, $l_{23}(a)$ become $l_1(a)$, $l_2(a)$ as defined in Eq. (16). Furthermore $A_{44} \to \mu$ where μ is the shear modulus. In this case Eq. (26) provides $A = 4\mu\lambda/\pi$. Applying these results in Eqs. (19)–(24) provides the elastic field for isotropy.

6 Discussion

It is noted that Reissner and Sagoci (1944) did not give the elastic field. However, they did give the expression for u_ϕ on the surface when $\rho > a$. The present result is found from Eqs. (22), (26) above for isotropy as

$$u_\phi = -\frac{4\lambda\rho}{\pi}\left\{ -\frac{1}{2}\sin^{-1}\frac{a}{\rho} + \frac{a[\rho^2 - a^2]^{1/2}}{2\rho^2} \right\}. \quad (27)$$

Using the identity

$$\sin^{-1}\frac{a}{\rho} = \tan^{-1}\frac{a}{[\rho^2 - a^2]^{1/2}} = \frac{\pi}{2} - \tan^{-1}\frac{[\rho^2 - a^2]^{1/2}}{a}, \quad (28)$$

allows the Eq. (23) in Reissner and Sagoci (1944) to be obtained apart from a misprint in their formula (the $\pi/2$ should be $2/\pi$). It is also noted that this result also agrees with a similar expression derived by Sneddon (1947) if one corrects the misprints by replacing the symbol a with r_o and adds ρ in the denominator of the last term.

Sneddon (1947) derived the elastic field for the case of isotropy. His solution is given in terms of four parameters λ, θ, R, and ϕ. The present solution is written in terms of the two parameters $l_1(a)$ and $l_2(a)$ defined in Eq. (16). In fact the solution can be written in terms of only one parameter since $l_1(a)l_2(a) = a\rho$. Although Sneddon's expressions for u_ϕ and $\tau_{\phi z}$ are in a quite different form, a numerical analysis showed them to be equivalent. In this regard one should note that in the expression for $\tau_{\phi z}$ the term λ/R should be λ/R^2. In making a numerical calculation using Sneddon's expressions, the angle ϕ should be chosen as pointed out in Eq. (70) of Hanson (1992b).

References

Elliot, H. A., 1948, "Three-Dimensional Stress Distributions in Hexagonal Aeolotropic Crystals," *Proceedings of the Cambridge Philosophical Society*, Vol. 44, pp. 522–533.

Fabrikant, V. I., 1988, "Elastic Field Around a Circular Punch," ASME JOURNAL OF APPLIED MECHANICS, Vol. 55, pp. 604–610.

Fabrikant, V. I., 1989, *Applications of Potential Theory in Mechanics: A Selection of New Results*, Kluwer Academic Publishers, The Netherlands, pp. 71–79.

Hanson, M. T., 1994, "The Elastic Field for an Upright or Tilted Sliding Circular Flat Punch on a Transversely Isotropic Half Space," *International Journal of Solids and Structures*, Vol. 31, pp. 567–586.

Hanson, M. T., 1993, "The Elastic Field for a Sliding Conical Punch on an Isotropic Half Space," ASME JOURNAL OF APPLIED MECHANICS, Vol. 60, pp. 557–559.

Hanson, M. T., 1992a, "The Elastic Field for Spherical Hertzian Contact Including Sliding Friction for Transverse Isotropy," ASME *Journal of Tribology*, Vol. 114, pp. 606–611.

Hanson, M. T., 1992b, "The Elastic Field for Conical Indentation Including Sliding Friction for Transverse Isotropy," ASME JOURNAL OF APPLIED MECHANICS, Vol. 59, pp. S123–S130.

Reissner, E., and Sagoci, H. F., 1944, "Forced Torsional Oscillations of an Elastic Half Space. I," *Journal of Applied Physics*, Vol. 15, pp. 652–654.

Sneddon, I. N., 1947, "Note on a Boundary Value Problem of Reissner and Sagoci," *Journal of Applied Physics*, Vol. 18, pp. 130–132.

An Approximate Analysis of Notch-Tip Deformation Under Mixed-Mode Loading in Ductile Solids

A. K. Ghosal[3,5] and R. Narasimhan[4,5]

Introduction

In practical situations, the loading experienced at the tip of a crack or notch in a structural component could be very complex resulting in mixed-mode fracture. In recent years, several investigators (Tohgo et al., 1988; Aoki et al., 1990; Maccagno and Knott, 1992; Ghosal and Narasimhan, 1994) have studied mixed-mode ductile fracture initiation (involving modes I and II) using experimental and computational methods. Ghosal and Narasimhan (1994) concluded, based on numerical simulations which modeled the micromechanics of ductile fracture, that the notch-tip deformation length (see definition given below) at fracture initiation is reasonably independent of mode-mixity (except for loadings very close to Mode II). This contention is supported by the experimental results for the notch-tip displacements at fracture initiation presented by Tohgo et al. (1988) for a structural steel SM41A. Thus, the notch-tip deformation length may be viewed as a *local* fracture characterizing parameter under mixed-mode loading in ductile solids.

However, an analytical expression connecting this quantity with the J-integral is not available in the literature. Such an expression can facilitate interpretation of experimentally measured notch-tip displacements under mixed-mode loading. Further, since at present there is no method for determining the near-tip plastic mode-mixity, experimental results (see, for example, Tohgo et al., 1988) are being reported using the ratio of the elastic stress intensity factors (K_I/K_{II}). This may be meaningless because large plastic yielding can take place prior to fracture initiation in low strength alloys. It is proposed here that a measurement of the notch-tip opening and sliding displacements (as in Tohgo et al. (1988) and Maccagno and Knott (1992)) can be used to deduce the near-tip plastic mode-mixity.

Approximate Expression for Notch-Tip Deformation Length Under Mixed-mode Loading

In this note, an approximate method for calculating the notch-tip deformation length using the asymptotic mixed-mode crack-tip fields in a power-law-hardening solid of Shih (1974) and Symington et al. (1988) will be presented. For a power-law hardening solid obeying an uniaxial relation of the type given by

$$\epsilon/\epsilon_0 = \alpha(\sigma/\sigma_0)^n, \qquad (1)$$

Shih (1974) has derived the asymptotic mixed-mode (involving modes I and II) displacement field as

$$u_i = \alpha\epsilon_0 r\left(\frac{J}{\alpha\sigma_0\epsilon_0 I_n(M^p)r}\right)^{n/(n+1)}\tilde{u}_i(\theta, n, M^p). \qquad (2)$$

Here, (r, θ) are polar coordinates centered at the crack tip.

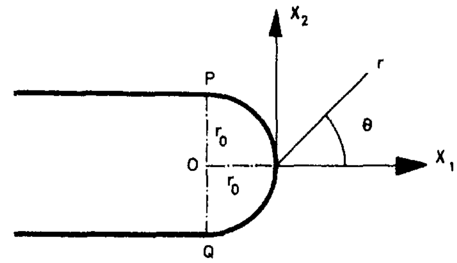

Fig. 1 Schematic illustration of a semi-circular notch tip in the undeformed configuration

Also, σ_0 is the initial yield stress of the material, $\epsilon_0 = \sigma_0/E$ is the initial yield strain, n is the power-hardening exponent, α is a material constant, and J is the J-integral. Further, M^p is a near-tip plastic mode-mixity parameter which is defined by Shih (1974) as

$$M^p = \frac{2}{\pi}\tan^{-1}\left|\lim_{r\to 0}\frac{\sigma_{\theta\theta}(r,0)}{\sigma_{r\theta}(r,0)}\right|, \qquad (3)$$

and I_n is a dimensionless constant which is dependent on M^p and n. The value of I_n for different M^p and n have been tabulated by Symington et al. (1988) for the case of plane strain. The dimensionless angular functions $\tilde{u}_i$ are also given in tabular form by Symington et al. (1988) for different n and M^p.

Under conditions of small-scale yielding, Shih (1974) has obtained (through full-field finite element analyses) the relationship between the near-tip plastic mode-mixity M^p and the far-field (remote) elastic mode-mixity M^e which is given by

$$M^e = (2/\pi)\tan^{-1}(K_I/K_{II}) = (2/\pi)\psi. \qquad (4)$$

For example, from his results for the plane-strain case, it is found that for $\psi = \pi/3$ and $\pi/6$ and corresponding to $n = 10$, the values of M^p are approximately 0.8 and 0.5, respectively.

Now, consider a semi-circular notch of radius r_0 (see Fig. 1) and assume that the asymptotic mixed-mode displacement field (Eq. (2)) can be applied to obtain the displacements of points P and Q on the notch flanks which are above and below the center of curvature O of the notch in the undeformed configuration. Thus, it is assumed that

$$u_i^P/r_0 \simeq A(J/(\sigma_0 r_0))^{n/(n+1)}\tilde{u}_i(\pi, n, M^p), \qquad (5)$$

and

$$u_i^Q/r_0 \simeq A(J/(\sigma_0 r_0))^{n/(n+1)}\tilde{u}_i(-\pi, n, M^p). \qquad (6)$$

Here, the factor A is given by

$$A = \alpha\epsilon_0(1/(\alpha\epsilon_0 I_n))^{n/(n+1)}. \qquad (7)$$

It must be noted that Eqs. (5) and (6) apply strictly for a sharp crack (under the assumption of small geometry changes and validity of the deformation theory of plasticity) in the limit as $r_0 \to 0$. However, it will be seen to hold reasonably well for a notch taking into account finite deformations, when comparisons are made later with finite element results.

Now, the notch-tip deformation length d is defined as the linear distance between points P and Q after deformation under mixed-mode loading. On determining the location of points P and Q in the deformed configuration using the displacements given by Eq. (5) and (6), and computing the distance between them, the normalized notch tip deformation length is found to be

[3] Graduate Research Student.
[4] Associate Professor.
[5] Department of Mechanical Engineering, Indian Institute of Science, Bangalore 560012, India.
Contributed by the Applied Mechanics Division of THE AMERICAN SOCIETY OF MECHANICAL ENGINEERS for publication in the ASME JOURNAL OF APPLIED MECHANICS. Manuscript received by the ASME Applied Mechanics Division, Jan. 22, 1996; final revision, July 6, 1996. Associate Technical Editor: M. Ortiz.

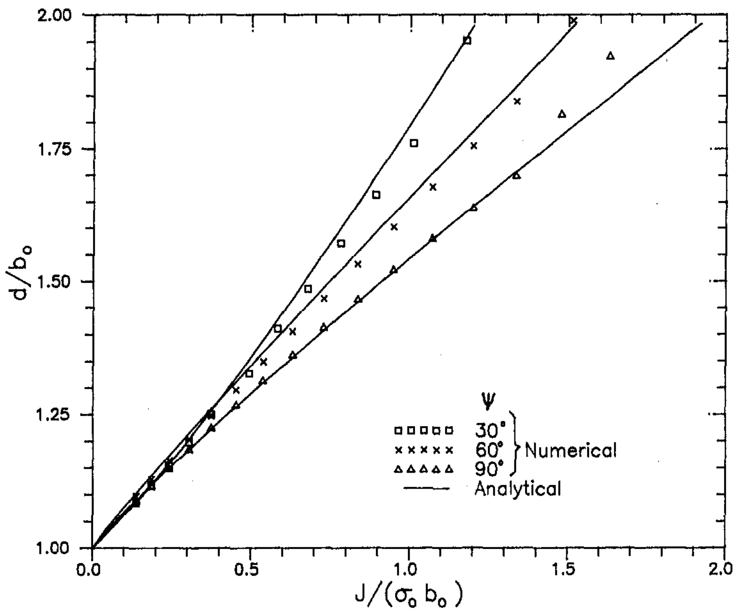

Fig. 2 Variation of the normalized notch-tip deformation length d/b_0 with the loading parameter $J/(\sigma_0 b_0)$. Comparison between the approximate analytical and numerical solutions.

$$\frac{d}{b_0} \simeq \frac{1}{2} \times \sqrt{\left[A\left(\frac{2J}{\sigma_0 b_0}\right)^{n/(n+1)} \Delta\tilde{u}_1\right]^2 + \left[2 + A\left(\frac{2J}{\sigma_0 b_0}\right)^{n/(n+1)} \Delta\tilde{u}_2\right]^2} . \tag{8}$$

Here, $b_0 = 2r_0$ is the initial notch diameter and $\Delta\tilde{u}_i = \tilde{u}_i(\pi, n, M^p) - \tilde{u}_i(-\pi, n, M^p)$.

In order to check the validity of the above equation, the notch-tip deformation length as a function of $J/(\sigma_0 b_0)$, computed from Eq. (8), is compared in Fig. 2 with the finite element results of Ghosal and Narasimhan (1994). This finite element analysis was based on a finite deformation formulation under small-scale yielding and the values of ϵ_0, n, and α were taken as 1/500, 10, and 1, respectively. The values of M^p, I_n, A, and $\Delta\tilde{u}_i$ for different far-field elastic mode-mixities ψ were obtained from Shih (1974) and Symington et al. (1988) corresponding to the above material constants and used in Eq. (8) to generate the approximate analytical variations. It can be seen from Fig. 2 that the approximate analytical variations match quite well with the numerical (finite element) results.

The near-tip plastic mode-mixity M^p can also be deduced from measurements of the notch-tip opening displacement δ_I and sliding displacement δ_{II} (as in Tohgo et al. (1988) and Maccagno and Knott (1992)). Indeed, from the tables of Symington et al. (1988), it is possible to obtain the ratio of $\Delta\tilde{u}_1/\Delta\tilde{u}_2$ for a given M^p. Thus, the value of M^p corresponding to a particular mixed-mode specimen (and load) can be determined by matching the ratio of (the experimentally measured) δ_{II}/δ_I with a corresponding ratio $\Delta\tilde{u}_1/\Delta\tilde{u}_2$ from the tables of Symington et al. (1988).

On making use of the above approach, it will be possible to obtain the values of both J and M^p from experimental measurements of crack-tip opening and sliding displacements at fracture initiation. This will enable organization of experimental data on mixed-mode fracture toughness in low strength alloys using a physically acceptable J_c versus M^p locus rather than the presently used $K_I - K_{II}$ locus.

References

Aoki, S., Kishimoto, K., Yoshida, T., Sakata, M., and Richard, H. A., 1990, "Elastic-plastic fracture behavior of an aluminium alloy under mixed-mode loading," *Journal of Mechanics and Physics of Solids*, Vol. 38, pp. 195–213.

Ghosal, A. K., and Narasimhan, R., 1994, "A finite element analysis of mixed-mode fracture initiation by ductile failure mechanisms," *Journal of Mechanics and Physics of Solids*, Vol. 42, pp. 953–978.

Maccagno, T. M., and Knott, J. F., 1992, "The mixed mode I/II fracture behaviour of lightly tempered HY130 steel at room temperature," *Engineering Fracture Mechanics*, Vo. 41, pp. 805–820.

Shih, C. F., 1974, "Small-scale yielding analysis of mixed mode plane strain crack problems," *Fracture Analysis*, ASTM STP 560, pp. 187–210.

Symington, M., Shih, C. F., and Ortiz, M., 1988, "Tables of Plane Strain Mixed-Mode Plastic Crack Tip Fields," Brown University Report, Providence, RI.

Tohgo, K., Otsuka, A., and Gao, H. W., 1988, "The behavior of ductile crack initiation from a notch under mixed-mode loading," M. Sakata, ed., *Proc. Far East Fracture Group Workshop*, Tokyo Inst. of Tech., Tokyo, Japan, pp. 101–108.

An Axisymmetric Inclusion in One of Two Perfectly Bonded Dissimilar Elastic Half-Spaces

A. M. Korsunsky[6]

This paper introduces an effective method for the solution of axisymmetric elastic inclusions in bonded dissimilar half-spaces. The method leads to new concise expressions for the elastic fields in terms of only two scalar Papkovich potential functions. A host of earlier solutions, which were obtained using a range of alternative techniques, involving surface stress relaxation and Hankel transforms, are shown to be subsumed in the present result.

1 Introduction

Ellipsoidal inclusions and inhomogeneities play an important role in elastostatics. Eshelby (1957, 1959) was the first to demonstrate that any inhomogeneity of ellipsoidal shape may be modeled by an inclusion of the same shape with uniform stress-free strains (eigenstrains) (Mura, 1982). Earlier findings, such as Goodier's solution for ellipsoidal inclusions with thermal expansion eigenstrains (Goodier, 1937) represent specific cases of the general Eshelby result.

Elastic solutions such as Eshelby inclusions are closely related to the family of fundamental singular solutions in the theory elasticity, such as point forces, force doublets, centers of dilatation, infinitesimal dislocation loops, etc., which Mindlin and Cheng (1950) termed *nuclei of strain.* Specific relationships exist between various strain nuclei. For example, force doublet solutions are derived from the Kelvin's solution for a concentrated force in an infinite space by differentiation with respect to the coordinate of the point of application. If now $\mathbf{F}_{kl}$ denotes some set of functions describing the elastic field of a force doublet, and $\mathbf{D}_{ij}$ denotes the corresponding set of functions for an infinitesimal dislocation loop, then for an isotropic solid

$$\mathbf{D}_{ij} = \mu\left[\mathbf{F}_{ij} + \mathbf{F}_{ji} + \frac{(3-\kappa)}{(\kappa-1)}\delta_{ij}\mathbf{F}_{kk}\right], \qquad (1)$$

where μ is the modulus of rigidity, and the Kolosov's constant $\kappa = 3 - 4\nu$, where ν is the Poisson's ratio.

Distributions of the strain nuclei may be used to model other objects, which give rise to singular or regular elastic fields. For example, it is easy to show that the solution for an Eshelby inclusion with purely dilatational (thermal expansion) eigenstrain can be obtained by the superposition of centers of dilatation uniformly distributed over the inclusion volume. Uniform surface distributions of infinitesimal displacement discontinuities produce finite Volterra dislocation loops (Dundurs and Salamon, 1972; Salamon and Dundurs, 1971), while distributions of unknown density may be used to obtain integral equation formulations of crack problems.

Mindlin (1936) was the first to address the problem of finding the analog of Kelvin's point force solution for the case of an elastic half space. Mindlin presented his solution in terms of the Galerkin vector, and later extended his results to include other strain nuclei (Mindlin and Cheng, 1958), such as force doublets, centers of dilatation and rotation, etc. Rongved (1955) developed the solutions for a concentrated force in one of two perfectly bonded dissimilar elastic half-spaces.

From the above discussion, two patterns emerge which are used in the derivation. On the one hand, the solutions are developed for progressively complex strain nuclei in an infinite elastic medium. This is generally done using the method of superposition, which may lead to integral or differential relationships, e.g., such as Eq. (1). On the other hand, fundamental solutions for strain nuclei such as the point force are found for progressively complex problem geometries, such as an elastic half-space or two perfectly bonded dissimilar elastic half-spaces.

The interrelationship between various solutions is illustrated in Fig. 1. Taking the solution A for a point force in an infinite space as the starting point, the step can be made to solution B for a general strain nucleus. Also, solution C for a point force in a complex problem geometry can be found. In order to obtain solution D for a general strain nucleus in a complex problem geometry, two routes, ABD or ACD, can be taken. Both involve the transformation of an infinite space solution into that for a complex geometry. If this transformation can be formalized into a recipe for an arbitrary strain nucleus, solution D can be readily obtained using any of the two routes.

For the particular case of an axisymmetric Eshelby inclusion in an elastic half-space, the derivation of the solution (which corresponds to a specific case of solution D in the above scheme) was given by Yu and Sanday (1990). In the derivation, the relaxation of surface stresses and the method of Hankel transforms were used. However, the final solution does not contain any integrals of Bessel functions, which suggests that greater economy could be achieved in the derivation if more effective techniques were to be applied. A general transformation recipe allowing the solutions for complex problem geometries to be obtained by formal application of specific rules provides such a technique.

An example of such recipe for the case of problem geometry given by two perfectly bonded dissimilar elastic half-spaces was given by Aderogba (1977). In his paper, Aderogba formulated a theorem which relates the Papkovich potentials for an arbitrary strain nucleus in the two geometries.

2 Axisymmetric Strain Nuclei

The set of Papkovich potentials (Papkovich, 1932) consists of a harmonic scalar potential Ψ and a harmonic vector potential $\mathbf{\Phi}$. Displacements and stresses due to these potentials are given by

$$2\mu u_i = (\kappa + 1)\Phi_i - (x_j\Phi_j + \Psi)_{,i} \qquad (2)$$

$$\sigma_{ij} = \tfrac{1}{2}(\kappa - 1)(\Phi_{j,i} + \Phi_{i,j}) + \tfrac{1}{2}(3-\kappa)\Phi_{k,k}\delta_{ij} - x_k\Phi_{k,ij} - \Psi_{,ij}, \qquad (3)$$

where a comma preceding an index denotes differentiation with respect to the relevant Cartesian coordinate.

In this paper we will focus our attention on the axisymmetric strain nuclei. In this particular case the number of Papkovich potentials required to describe the elastic fields can be reduced to two, namely, the scalar potential Ψ and the axial component of the vector potential Φ. Of course, these two functions are

A: Point force solution in an infinite space	C: Point force solution in a complex problem geometry
B: General strain nucleus solution in an infinite space	D: General strain nucleus solution in a complex problem geometry

Fig. 1 Derivation of elasticity solutions

[6] Department of Materials Science and Metallurgy, University of Cambridge, Pembroke Street, Cambridge CB2 3QZ, UK. Present address: Materials Division, Department of Mechanical, Materials and Manufacturing Engineering, University of Newcastle, Newcastle-upon-Tyne NE1 7RU, UK.

Contributed by the Applied Mechanics Division of THE AMERICAN SOCIETY OF MECHANICAL ENGINEERS for publication in the ASME JOURNAL OF APPLIED MECHANICS. Manuscript received by the ASME Applied Mechanics Division, May 28, 1996; final revision, Sept. 26, 1996. Associate Technical Editor: X. Markenscoff.

not independent. In fact, the solution may be described using a single biharmonic function, such as the Love's stress function. However, the Papkovich potential formulation is more convenient for the present analysis.

For an arbitrary axisymmetric nucleus of strain, the stresses are given in terms of the pair of axisymmetric Papkovich potentials by (Korsunsky, 1995)

$$\sigma_{rr} = \frac{1}{2}(3-\kappa)\Phi_{,z} + z\Phi_{,zz} + \frac{z}{r}\Phi_{,r} + \Psi_{,zz} + \frac{1}{r}\Psi_{,r}, \quad (4)$$

$$\sigma_{\theta\theta} = \frac{1}{2}(3-\kappa)\Phi_{,z} - \frac{z}{r}\Phi_{,r} - \frac{1}{r}\Psi_{,r}, \quad (5)$$

$$\sigma_{zz} = \tfrac{1}{2}(\kappa+1)\Phi_{,z} - z\Phi_{,zz} - \Psi_{,zz}, \quad (6)$$

$$\sigma_{rz} = \tfrac{1}{2}(\kappa-1)\Phi_{,r} - z\Phi_{,rz} - \Psi_{,rz}. \quad (7)$$

We now quote Aderogba's result for the particular case of axisymmetric strain nuclei.

Let us call the half-space containing the inclusion half-space 1, and the half-space free from inclusions half-space 2, and introduce the following parameters:

$$\Gamma = \frac{\mu_2}{\mu_1}, \quad (8)$$

$$A = \frac{(\Gamma-1)}{(\Gamma\kappa_1+1)} = \frac{\alpha-\beta}{1+\beta}, \quad (9)$$

$$B = \frac{(\Gamma\kappa_1-\kappa_2)}{(\Gamma+\kappa_2)} = \frac{\alpha+\beta}{1-\beta}, \quad (10)$$

where $\kappa_i = 3-4\nu_i$, ν_i is the Poisson's ratio in half space i, μ_i is the shear modulus in half space i, and α and β are the Dundurs bimaterial parameters.

According to Aderogba's theorem (Aderogba, 1977) for the strain nuclei which in an infinite space give rise to elastic fields described by only two functions, the scalar potential Ψ and the axial component of the vector potential Φ, the potentials for two bonded dissimilar half-spaces are given by

$$\Psi^{(1)} = \Psi_0(r,z) - A\kappa_1\Psi_0(r,-z) - \frac{(A\kappa_1^2-B)}{2}\int\Phi_0(r,-z)dz, \quad (11)$$

$$\Phi^{(1)} = \Phi_0(r,z) - A\kappa_1\Phi_0(r,-z) - 2A\frac{\partial}{\partial z}\Psi_0(r,-z), \quad (12)$$

$$\Psi^{(2)} = (A+1)\Psi_0(r,-y) - \frac{(A\kappa_1^2-B)}{2}\Gamma\int\Phi_0(r,-y)dy, \quad (13)$$

$$\Phi^{(2)} = -(B+1)\Phi_0(r,-y), \quad (14)$$

where $\Psi^{(i)}$, $\Phi^{(i)}$ are potentials in material i, and $y=-z$.

An example of the application of this corollary of Aderogba's theorem to the case of an axisymmetric Eshelby inclusion is given below.

3 Infinite Space Solutions

Consider eigenstrain

$$e_{ij}^* = \delta_{ij}(\epsilon + \beta\delta_{i3}), \quad i,j = 1,2,3, \quad (15)$$

being defined within a spheroidal domain Ω which is symmetric with respect to the axis x_3, with semi-axes $a_1 = a_2$ and a_3, centered at the origin. Using the cylindrical coordinates (r, θ, z), the stresses due to this inclusion are given by (Yu and Sanday, 1990)

$$\sigma_{rr} = \frac{\mu\epsilon(\kappa+1)}{\pi(\kappa+1)}\left[\phi_{,zz} + \frac{\phi_{,r}}{r}\right] - \frac{\mu\beta}{\pi(\kappa+1)}\left[\phi_{,zz} + z\phi_{,zzz} + \frac{(\kappa-1)}{2r}\phi_{,r} + \frac{z}{r}\phi_{,rz} + f\left(2\phi_{,zz} + \frac{1}{r}\phi_{,r} + r\phi_{,rzz} + z\phi_{,zzz} + \frac{z}{r}\phi_{,rz}\right)\right], \quad (16)$$

$$\sigma_{\theta\theta} = -\frac{\mu\epsilon(\kappa+1)}{\pi(\kappa+1)}\frac{\phi_{,r}}{r} - \frac{\mu\beta}{\pi(\kappa+1)}\left[\frac{(3-\kappa)}{2}\phi_{,zz} - \frac{(k-1)}{2r}\phi_{,r} - \frac{z}{r}\phi_{,rz} + f\left(\phi_{,zz} - \frac{1}{r}\phi_{,r} - \frac{z}{r}\phi_{,rz}\right)\right], \quad (17)$$

$$\sigma_{zz} = -\frac{\mu\epsilon(\kappa+1)}{\pi(\kappa+1)}\phi_{,zz} - \frac{\mu\beta}{\pi(\kappa+1)}[\phi_{,zz} - z\phi_{,zzz} - f(3\phi_{,zz} + z\phi_{,zzz} + r\phi_{,rzz})], \quad (18)$$

$$\sigma_{rz} = -\frac{\mu\epsilon(\kappa+1)}{\pi(\kappa+1)}\phi_{,rz} + \frac{\mu\beta}{\pi(\kappa+1)}[z\phi_{,rzz} + f(2\phi_{,rz} + z\phi_{,rzz} - r\phi_{,zzz})], \quad (19)$$

$$\sigma_{r\theta} = \sigma_{z\theta} = 0, \quad (20)$$

where $\kappa = 3-4\nu$, ν is the Poisson's ratio, μ is the shear modulus, $f = a_3^2/(a_1^2 - a_3^2)$, and ϕ denotes the harmonic gravitational potential of matter of unit density filling the volume Ω.

The form of the stresses around an axisymmetric inclusion can be matched to the Papkovich potentials by the suitable choice of functions Ψ and Φ.

Consider the following cases:

$-\beta = 0$. It may be verified by substitution that the required Papkovich potentials are

$$\Psi = \frac{\mu\epsilon}{\pi(\kappa+1)}(\kappa-1)\phi, \quad (21)$$

$$\Phi = 0. \quad (22)$$

For an infinitesimal inclusion, these potentials give a center of dilatation (Korsunsky, 1994).

$-\epsilon = 0$, $f = 0$. The required Papkovich potentials are

$$\Psi = -\frac{\mu\beta}{\pi(\kappa+1)}\frac{(\kappa-1)}{2}\phi, \quad (23)$$

$$\Phi = -\frac{\mu\beta}{\pi(\kappa+1)}\phi_{,z}. \quad (24)$$

For an infinitesimal inclusion, these potentials give an infinitesimal prismatic dislocation loop.

$-\epsilon = 0$, $\beta = 0$, but $\beta f \neq 0$. The required Papkovich potentials are

$$\Psi = -\frac{\mu\beta f}{\pi(\kappa+1)}[\phi + z\phi_{,z} + r\phi_{,r}], \quad (25)$$

$$\Phi = 0. \quad (26)$$

By combining the above results the complete Papkovich potentials for an axisymmetric inclusion in an infinite space are found in the form

$$\Psi = \frac{\mu}{\pi(\kappa+1)}\left\{\epsilon(\kappa-1)\,\phi - \beta\left[\frac{(\kappa-1)}{2}\phi + f(\phi + z\phi_{,z} + r\phi_{,r})\right]\right\}, \quad (27)$$

$$\Phi = \frac{\mu}{\pi(\kappa+1)}\{-\beta\phi_{,z}\}. \quad (28)$$

An obvious advantage achieved by recording the solution in terms of the Papkovich potentials over the form given by Yu and Sanday (1990) is a great reduction in the complexity of expression. However, the benefits of recasting the solution are not confined to shorter lengths of expressions. A straightforward application of a well-established theorem will now provide general results for dissimilar bonded half-spaces.

4 Bonded Half-Spaces Solutions

The first step in the solution involves the derivation of the Papkovich potentials for the spheroidal inclusion Ω centred at $(0, 0, c)$ from the potentials found in the previous section for the inclusion centred at the origin. This is done by applying the lemma about translation of the origin (Korsunsky, 1996). In the present case, the lemma states that the new Papkovich potentials Ψ_0, Φ_0 are related to the old potentials Ψ, Φ according to

$$\Psi_0 = \Psi - c\Phi, \quad (29)$$

$$\Phi_0 = \Phi. \quad (30)$$

Therefore, Ψ_0 and Φ_0 for an inclusion Ω in an infinite space are given by

$$\Psi_0 = \frac{\mu}{\pi(\kappa+1)}\left\{\epsilon(\kappa-1)\phi - \beta\left[\frac{(\kappa-1)}{2}\phi + f(\phi + (z-c)\phi_{,z} + r\phi_{,r})\right]\right\}, \quad (31)$$

$$\Phi_0 = \frac{\mu}{\pi(\kappa+1)}\{-\beta\phi_{,z}\}. \quad (32)$$

The next step now requires the application of the corollary to Aderogba's theorem which is applicable to axisymmetric strain nuclei. This result has been introduced in the preceding sections.

Note that the transformation formulae involve differentiation and integration of the infinite space potentials Ψ_0 and Φ_0. The fact that integration of the potential Φ_0 may not be carried out explicitly in all cases restricts the number of problems for which fully analytical treatment is possible using this method.

In the present case, however, the integration may be carried out in full, since Φ_0 is given by the *derivative* of the gravitational potential ϕ. Let us use an overbar, $\bar{\phi}$, to denote the "conjugate" function, which is obtained from ϕ by substituting $-z$ instead of z, $\bar{\phi} = \phi(r, -z)$. It is important to distinguish the order of differentiation (integration) and conjugation, since, for example

$$\overline{(\phi_{,z})} = -(\bar{\phi})_{,z}. \quad (33)$$

Therefore

$$\int \Phi_0(r, -z)dz = \int \bar{\Phi}_0 dz = -\overline{\int \Phi_0 dz} = \frac{\mu\beta}{\pi(\kappa+1)}\bar{\phi}, \quad (34)$$

$$\frac{\partial}{\partial z}\Psi_0(r, -z) = (\bar{\Psi}_0)_{,z} = -\overline{(\Psi_0)_{,z}}, \quad (35)$$

and also

$$\int \Phi_0(r, -y)dy = -\int \Phi_0 dz = \frac{\mu\beta}{\pi(\kappa+1)}\phi. \quad (36)$$

As a result, the potentials are given by

$$\Psi^{(1)} = \frac{\mu_1}{\pi(\kappa_1+1)}\left\{\epsilon(\kappa_1-1)(\phi - A\kappa_1\bar{\phi}) - \beta\left[\frac{\kappa_1-1}{2}\phi + \frac{A\kappa_1 - B}{2}\bar{\phi} + f(\phi + (z-c)\phi_{,z} + r\phi_{,r} - A\kappa_1\bar{\phi} - A\kappa_1(z+c)\bar{\phi}_{,z} - A\kappa_1 r\bar{\phi}_{,r})\right]\right\}, \quad (37)$$

$$\Phi^{(1)} = \frac{\mu_1}{\pi(\kappa_1+1)}\{-2\epsilon A(\kappa_1-1)\bar{\phi}_{,z} - \beta[\phi_{,z} + A\bar{\phi}_{,z} - 2Af(\bar{\phi} + (z+c)\bar{\phi}_{,z} + r\bar{\phi}_{,r})]\}, \quad (38)$$

$$\Psi^{(2)} = \frac{\mu_1}{\pi(\kappa_1+1)}\left\{\epsilon(A+1)(\kappa_1-1)\phi - \beta\left[\frac{(A+1)(\kappa_1-1) + (A\kappa_1^2 - B)\Gamma}{2}\phi + f(A+1)(\phi + (z-c)\phi_{,z} + r\phi_{,r})\right]\right\} \quad (39)$$

$$\Phi^{(2)} = \frac{\mu_1}{\pi(\kappa_1+1)}(B+1)\beta\phi_{,z}. \quad (40)$$

In the particular case of the second half-space being void, the parameters assume the values $A = B = -1$, $\Gamma = 0$. The potentials $\Psi^{(2)}$ and $\Phi^{(2)}$ vanish, while the potentials for half-space 1 assume the form

$$\Psi^{(1)} = \frac{\mu_1}{\pi(\kappa_1+1)}\left\{\epsilon(\kappa_1-1)(\phi + \kappa_1\bar{\phi}) - \beta\left[\frac{\kappa_1-1}{2}(\phi - \bar{\phi}) + f(\phi + (z-c)\,\phi_{,z} + r\phi_{,r} + \kappa_1\bar{\phi} + \kappa_1(z+c)\bar{\phi}_{,z} + \kappa_1 r\bar{\phi}_{,r})\right]\right\}, \quad (41)$$

$$\Phi^{(1)} = \frac{\mu_1}{\pi(\kappa_1+1)}\{2\epsilon(\kappa_1-1)\bar{\phi}_{,z} - \beta[\phi_{,z} - \bar{\phi}_{,z} + 2f(\bar{\phi} + (z+c)\bar{\phi}_{,z} + r\bar{\phi}_{,r})]\}. \quad (42)$$

The stresses and displacements associated with these potential functions may be written down using Eqs. (4)–(7), and show agreement with the results of Yu and Sanday (1990). The separation of the elastic fields into the infinite space terms and "image" terms is apparent in the form of the Papkovich potentials.

5 Summary

An effective and concise method of derivation for the elastic fields of an axisymmetric ellipsoidal inclusion in one of two dissimilar perfectly bonded elastic half-spaces has been presented. The method which has been effectively used previously for dislocation loops (Korsunsky, 1996) and ring dislocation dipoles (Korsunsky, 1995) was applied here to Eshelby inclusions, which shows its wide range of applicability. No direct application of Hankel transform or cancelling of surface stresses (Yu and Sanday, 1990) was required. The final results apply to arbitrary pairs of elastic materials occupying the two bonded half-spaces, including the case when the second material has vanishing elastic moduli, i.e., inclusion in a half-space. The results obtained in the paper by Yu and Sanday (1990) form a subset of the present solution.

The advantage of the Papkovich potential notation for the representation of elastic fields is not confined to the ease of derivation of new solutions. The final results for axisymmetric inclusions in one of two dissimilar elastic half-spaces were kept in this form in the previous section quite deliberately. From the practical viewpoint, the application of the solutions presented in this paper is likely to involve computer coding of the formulae. The concise potential form of the solutions allows the final stress and displacement formulae to be rederived and verified as many times as necessary using well established recipes, which in this case are given by Eqs. (4)–(7).

References

Aderogba, K., 1977, "On Eigenstresses in Dissimilar Media," *Philosophical Magazine,* Vol. 35, pp. 281–292.

Dundurs, J., and Salamon, N. J., 1972, "Circular Prismatic Dislocation Loop in a Two-Phase Material," *Physica Status Solidi (b),* Vol. 50, pp. 125–133.

Eshelby, J. D., 1957, "The Determination of the Elastic Field of an Ellipsoidal Inclusion and Related Problems," *Proceedings of the Royal Society of London,* Vol. A241, pp. 376–396.

Eshelby, J. D., 1959, "The Elastic Field Outside an Ellipsoidal Inclusion," *Proceedings of the Royal Society of London,* Vol. A252, pp. 561–569.

Goodier, J. N., 1937, "On the Integration of the Thermo-Elastic Equations," *Philosophical Magazine,* Vol. 23, pp. 1017–1032.

Korsunsky, A. M., 1994, "The solution of axisymmetric crack problems in inhomogeneous media," D.Phil. thesis, University of Oxford, Oxford, UK.

Korsunsky, A. M., 1995, "Fundamental eigenstrain solutions for axisymmetric crack problems," *Journal of Mechanics and Physics of Solids,* Vol. 43, pp. 1221–1241.

Korsunsky, A. M., 1996, "The Somigliana ring dislocation revisited, 2: Solutions for dislocations in a half space and in one of two perfectly bonded dissimilar half spaces," to appear in *Journal of Elasticity.*

Mindlin, R. D., 1936, "Force at a Point in the Interior of a Semi-Infinite Solid," *Physics,* Vol. 7, pp. 195–202.

Mindlin, R. D., and Cheng, D. H., 1950, "Nuclei of strain in the semi-infinite solid," *Journal of Applied Physics,* Vol. 21, pp. 926–930.

Mura, T., 1982, *Micromechanics of defects in solids,* Martinus Nijhoff, Dordrecht, Netherlands.

Papkovich, P. F., 1932, "Solution générale des équations différentieles fondamentales d'élasticité, exprimée par trois fonctions harmoniques," *Comptes Rendus Academie des Sciences,* Vol. 193, pp. 513–515.

Rongved, L., 1955, "Force Interior to One of Two Joined Semi-Infinite Solids," *Proceedings of the Second Midwestern Conference on Solid Mechanics,* pp. 1–13.

Salamon, N. J., and Dundurs, J., 1971, "Elastic Fields of a Dislocation Loop in a Two-Phase Material," *Journal of Elasticity,* Vol. 1, pp. 153–164.

Yu, H. Y., and Sanday, S. C., 1990, "Axisymmetric Inclusion in a Half Space," ASME Journal of Applied Mechanics, Vol. 57, pp. 74–77.

Thermal Post-buckling Analysis of Imperfect Laminated Plates on Two-Parameter Elastic Foundations

Hui-Shen Shen[7] and F. W. Williams[8]

1 Introduction

Composite laminated structures are being increasingly used in aeronautical and aerospace construction. Their components are subjected to severe aerothermal loads due to kinetic heating. Component plates may be supported by an elastic medium and have significant and unavoidable initial geometrical imperfections. Moreover, because of the boundary constraints the thermal loads induce compressive stresses which may cause buckling, particularly for thin-walled members. Therefore, there is a need to understand the thermal buckling and post-buckling behavior of imperfect composite laminated plates resting on elastic foundations. Such solutions have important potential applications in analyzing the face behavior of certain types of foam-filled sandwich panels. The simplest model for elastic foundations is the Winkler one, but for many practical foundations it is not sufficiently accurate. This has led to the development of more accurate foundation models, including the so-called two-parameter, i.e., Pasternak-type, model.

Raju and Rao (1988) calculated the thermal post-buckling response of isotropic square plates resting on Winkler elastic foundations by the finite element method. In contrast, Dumir (1988) used the Galerkin method to analyze the thermal post-buckling of isotropic rectangular plates resting on Pasternak-type elastic foundations, but he only gave numerical results for the Winkler elastic foundation case. Also recently, Shen (1995a, 1995b) analyzed the post-buckling of uniaxially compressed, perfect and imperfect, isotropic and anisotropic plates resting on two-parameter elastic foundations, from which results for Winkler elastic foundations follow as a limiting case. However, the authors are not aware of any published information on the thermal post-buckling behavior of imperfect composite laminated plates resting on two-parameter elastic foundations.

Therefore, this study deals with simply supported, perfect and imperfect, composite laminated plates subjected to uniform or parabolically nonuniform thermal loading and resting on two-parameter elastic foundations. The analysis uses a mixed Galerkin-perturbation technique to determine the required thermal buckling loads and the post-buckling equilibrium paths, with the material properties assumed to be independent of temperature. The initial geometrical imperfection of the plate is taken into account but, for simplicity, its form is taken as the buckling mode of the plate. The theory presented is for plate thermal post-buckling response and accounts for the combined effects of an initial geometrical imperfection and of plate-foundation interaction.

2 Analysis

Consider a thin rectangular plate of length a, width b, and thickness t which consists of N plies of any kind, is subjected to thermal loading and rests on a two-parameter elastic foundation. This type of foundation yields the load-displacement relation $p = \bar{K}_1\bar{W} - \bar{K}_2\nabla^2\bar{W}$, where ∇^2 is the Laplace operator in X and Y, p is the force per unit area, $\bar{K}_1$ is the elastic spring constant, and $\bar{K}_2$ is a constant showing the effect of the shear interactions of the vertical elements. $\bar{U}$, $\bar{V}$, and $\bar{W}$ are the plate displacements parallel to a right-hand set of axes (X, Y, Z), where X is longitudinal and Z is perpendicular to the plate. Denoting the initial deflection by $\bar{W}^*(X, Y)$, let $\bar{W}(X, Y)$ be the additional deflection and $\bar{F}(X, Y)$ be the stress function for the stress resultants, so that $N_x = \bar{F}_{,yy}$, $N_y = \bar{F}_{,xx}$ and $N_{xy} = -\bar{F}_{,xy}$.

The in-plane temperature variation is assumed as

$$T(X, Y, Z) = T_0 + T_1\left[1 - \left(\frac{2Y - b}{b}\right)^2\right] \tag{1}$$

and the thermal forces and moments are defined by

$$\begin{bmatrix} N_x^T, & M_x^T \\ N_y^T, & M_y^T \\ N_{xy}^T, & M_{xy}^T \end{bmatrix} = \sum_{k=1} \int_{t_{k-1}}^{t_k} (1, Z) \begin{bmatrix} A_x \\ A_y \\ A_{xy} \end{bmatrix}_k T(X, Y, Z)dZ. \tag{2}$$

[7] Professor of Civil Engineering, Shanghai Jiao Tong University, Shanghai 200030, China.

[8] Professor of Structural Engineering, University of Wales Cardiff, Cardiff CF2 1XH, UK.

Contributed by the Applied Mechanics Division of The American Society of Mechanical Engineers for publication in the ASME Journal of Applied Mechanics. Manuscript received by the ASME Applied Mechanics Division, July 8, 1996; final revision, Oct. 8, 1996. Associate Technical Editor: S. Kyriakides.

to arbitrary pairs of elastic materials occupying the two bonded half-spaces, including the case when the second material has vanishing elastic moduli, i.e., inclusion in a half-space. The results obtained in the paper by Yu and Sanday (1990) form a subset of the present solution.

The advantage of the Papkovich potential notation for the representation of elastic fields is not confined to the ease of derivation of new solutions. The final results for axisymmetric inclusions in one of two dissimilar elastic half-spaces were kept in this form in the previous section quite deliberately. From the practical viewpoint, the application of the solutions presented in this paper is likely to involve computer coding of the formulae. The concise potential form of the solutions allows the final stress and displacement formulae to be rederived and verified as many times as necessary using well established recipes, which in this case are given by Eqs. (4)–(7).

References

Aderogba, K., 1977, "On Eigenstresses in Dissimilar Media," *Philosophical Magazine,* Vol. 35, pp. 281–292.

Dundurs, J., and Salamon, N. J., 1972, "Circular Prismatic Dislocation Loop in a Two-Phase Material," *Physica Status Solidi (b),* Vol. 50, pp. 125–133.

Eshelby, J. D., 1957, "The Determination of the Elastic Field of an Ellipsoidal Inclusion and Related Problems," *Proceedings of the Royal Society of London,* Vol. A241, pp. 376–396.

Eshelby, J. D., 1959, "The Elastic Field Outside an Ellipsoidal Inclusion," *Proceedings of the Royal Society of London,* Vol. A252, pp. 561–569.

Goodier, J. N., 1937, "On the Integration of the Thermo-Elastic Equations," *Philosophical Magazine,* Vol. 23, pp. 1017–1032.

Korsunsky, A. M., 1994, "The solution of axisymmetric crack problems in inhomogeneous media," D.Phil. thesis, University of Oxford, Oxford, UK.

Korsunsky, A. M., 1995, "Fundamental eigenstrain solutions for axisymmetric crack problems," *Journal of Mechanics and Physics of Solids,* Vol. 43, pp. 1221–1241.

Korsunsky, A. M., 1996, "The Somigliana ring dislocation revisited, 2: Solutions for dislocations in a half space and in one of two perfectly bonded dissimilar half spaces," to appear in *Journal of Elasticity.*

Mindlin, R. D., 1936, "Force at a Point in the Interior of a Semi-Infinite Solid," *Physics,* Vol. 7, pp. 195–202.

Mindlin, R. D., and Cheng, D. H., 1950, "Nuclei of strain in the semi-infinite solid," *Journal of Applied Physics,* Vol. 21, pp. 926–930.

Mura, T., 1982, *Micromechanics of defects in solids,* Martinus Nijhoff, Dordrecht, Netherlands.

Papkovich, P. F., 1932, "Solution générale des équations différentieles fondamentales d'élasticité, exprimée par trois fonctions harmoniques," *Comptes Rendus Academie des Sciences,* Vol. 193, pp. 513–515.

Rongved, L., 1955, "Force Interior to One of Two Joined Semi-Infinite Solids," *Proceedings of the Second Midwestern Conference on Solid Mechanics,* pp. 1–13.

Salamon, N. J., and Dundurs, J., 1971, "Elastic Fields of a Dislocation Loop in a Two-Phase Material," *Journal of Elasticity,* Vol. 1, pp. 153–164.

Yu, H. Y., and Sanday, S. C., 1990, "Axisymmetric Inclusion in a Half Space," ASME Journal of Applied Mechanics, Vol. 57, pp. 74–77.

Thermal Post-buckling Analysis of Imperfect Laminated Plates on Two-Parameter Elastic Foundations

Hui-Shen Shen[7] **and F. W. Williams**[8]

1 Introduction

Composite laminated structures are being increasingly used in aeronautical and aerospace construction. Their components are subjected to severe aerothermal loads due to kinetic heating. Component plates may be supported by an elastic medium and have significant and unavoidable initial geometrical imperfections. Moreover, because of the boundary constraints the thermal loads induce compressive stresses which may cause buckling, particularly for thin-walled members. Therefore, there is a need to understand the thermal buckling and post-buckling behavior of imperfect composite laminated plates resting on elastic foundations. Such solutions have important potential applications in analyzing the face behavior of certain types of foam-filled sandwich panels. The simplest model for elastic foundations is the Winkler one, but for many practical foundations it is not sufficiently accurate. This has led to the development of more accurate foundation models, including the so-called two-parameter, i.e., Pasternak-type, model.

Raju and Rao (1988) calculated the thermal post-buckling response of isotropic square plates resting on Winkler elastic foundations by the finite element method. In contrast, Dumir (1988) used the Galerkin method to analyze the thermal post-buckling of isotropic rectangular plates resting on Pasternak-type elastic foundations, but he only gave numerical results for the Winkler elastic foundation case. Also recently, Shen (1995a, 1995b) analyzed the post-buckling of uniaxially compressed, perfect and imperfect, isotropic and anisotropic plates resting on two-parameter elastic foundations, from which results for Winkler elastic foundations follow as a limiting case. However, the authors are not aware of any published information on the thermal post-buckling behavior of imperfect composite laminated plates resting on two-parameter elastic foundations.

Therefore, this study deals with simply supported, perfect and imperfect, composite laminated plates subjected to uniform or parabolically nonuniform thermal loading and resting on two-parameter elastic foundations. The analysis uses a mixed Galerkin-perturbation technique to determine the required thermal buckling loads and the post-buckling equilibrium paths, with the material properties assumed to be independent of temperature. The initial geometrical imperfection of the plate is taken into account but, for simplicity, its form is taken as the buckling mode of the plate. The theory presented is for plate thermal post-buckling response and accounts for the combined effects of an initial geometrical imperfection and of plate-foundation interaction.

2 Analysis

Consider a thin rectangular plate of length a, width b, and thickness t which consists of N plies of any kind, is subjected to thermal loading and rests on a two-parameter elastic foundation. This type of foundation yields the load-displacement relation $p = \bar{K}_1\bar{W} - \bar{K}_2\nabla^2\bar{W}$, where ∇^2 is the Laplace operator in X and Y, p is the force per unit area, $\bar{K}_1$ is the elastic spring constant, and $\bar{K}_2$ is a constant showing the effect of the shear interactions of the vertical elements. $\bar{U}$, $\bar{V}$, and $\bar{W}$ are the plate displacements parallel to a right-hand set of axes (X, Y, Z), where X is longitudinal and Z is perpendicular to the plate. Denoting the initial deflection by $\bar{W}^*(X, Y)$, let $\bar{W}(X, Y)$ be the additional deflection and $\bar{F}(X, Y)$ be the stress function for the stress resultants, so that $N_x = \bar{F}_{,yy}$, $N_y = \bar{F}_{,xx}$ and $N_{xy} = -\bar{F}_{,xy}$.

The in-plane temperature variation is assumed as

$$T(X, Y, Z) = T_0 + T_1\left[1 - \left(\frac{2Y - b}{b}\right)^2\right] \tag{1}$$

and the thermal forces and moments are defined by

$$\begin{bmatrix} N_x^T, & M_x^T \\ N_y^T, & M_y^T \\ N_{xy}^T, & M_{xy}^T \end{bmatrix} = \sum_{k=1} \int_{t_{k-1}}^{t_k} (1, Z) \begin{bmatrix} A_x \\ A_y \\ A_{xy} \end{bmatrix}_k T(X, Y, Z)dZ. \tag{2}$$

[7] Professor of Civil Engineering, Shanghai Jiao Tong University, Shanghai 200030, China.

[8] Professor of Structural Engineering, University of Wales Cardiff, Cardiff CF2 1XH, UK.

Contributed by the Applied Mechanics Division of The American Society of Mechanical Engineers for publication in the ASME Journal of Applied Mechanics. Manuscript received by the ASME Applied Mechanics Division, July 8, 1996; final revision, Oct. 8, 1996. Associate Technical Editor: S. Kyriakides.

In Eq. (1), $T_1 = 0$ gives uniform temperature fields, and $T_0 = 0$ gives a parabolic temperature distribution. From Eqs. (1) and (2) it is noted that the thermal force N_{xy}^T and thermal moments M_x^T and M_y^T are zero.

Attention is confined to the four cases of (1) isotropic plates, (2) orthotropic plates and symmetrically cross-ply laminated plates, (3) antisymmetrically angle-ply laminated plates, and (4) symmetrically angle-ply laminated plates with more than 15 plies; i.e., $N > 15$, for which the results are only approximate. As mentioned in Shen (1995b), for these four cases the plate remains flat up to the bifurcation point unless there is an initial geometrical imperfection.

Before proceeding, it is convenient to first define the following dimensionless quantities for such plates, in which the alternative forms k_1 and k_2 are not needed until the numerical examples are considered,

$$x = \pi X/a, \quad y = \pi Y/b, \quad \beta = a/b,$$

$$(W^*, W) = (\bar{W}^*, \bar{W})/\sqrt[4]{D_{11}^* D_{22}^* A_{11}^* A_{22}^*},$$

$$F = \bar{F}/\sqrt{D_{11}^* D_{22}^*}, \quad \gamma_{12} = (D_{12}^* + 2D_{66}^*)/D_{11}^*,$$

$$\gamma_{14} = \sqrt{D_{22}^*/D_{11}^*}, \quad \gamma_{22} = (A_{12}^* + A_{66}^*/2)/A_{22}^*,$$

$$\gamma_{24} = \sqrt{A_{11}^*/A_{22}^*}, \quad \gamma_5 = -A_{12}^*/A_{22}^*,$$

$$(\gamma_{31}, \gamma_{33}, \gamma_{316}, \gamma_{326}) = (2B_{26}^* - B_{61}^*, 2B_{16}^* - B_{62}^*, B_{16}^*, B_{26}^*)/\sqrt[4]{D_{11}^* D_{22}^* A_{11}^* A_{22}^*},$$

$$(\gamma_{T1}, \gamma_{T2}) = (A_x^T, A_y^T)a^2/\alpha_0 \pi^2 \sqrt{D_{11}^* D_{22}^*},$$

$$\gamma_6 = (\gamma_{24}^2 \gamma_{T1} - \gamma_5 \gamma_{T2})/\gamma_{24}^2,$$

$$(K_1, k_1) = (a^4, b^4)\bar{K}_1/\pi^4 D_{11}^*, \ (K_2, k_2) = (a^2, b^2)\bar{K}_2/\pi^2 D_{11}^*,$$

$$(M_x, M_y) = (\bar{M}_x, \bar{M}_y)a^2/\pi^2 D_{11}^* \sqrt[4]{D_{11}^* D_{22}^* A_{11}^* A_{22}^*},$$

$$(\delta_x, \delta_y) = (\Delta_x/a, \Delta_y/b)b^2/4\pi^2 \sqrt{D_{11}^* D_{22}^* A_{11}^* A_{22}^*}. \quad (3)$$

Here Δ_x and Δ_y are the shortenings in the X and Y directions, $\bar{M}_x(\bar{M}_y)$ is the bending moment per unit width (length) of the plate, and for convenience $\lambda_T = \alpha_0 T_i$, where $i = 0$ for a uniform temperature distribution and $i = 1$ otherwise.

Also let the thermal expansion coefficients for each lamina be

$$\alpha_{11} = a_{11}\alpha_0, \quad \alpha_{22} = a_{22}\alpha_0 \quad (4)$$

where α_0 is an arbitrary reference value, and

$$\begin{bmatrix} A_x^T \\ A_y^T \end{bmatrix} = -\sum_{k=1} \int_{t_{k-1}}^{t_k} \begin{bmatrix} A_x \\ A_y \end{bmatrix}_k dZ \quad (5)$$

In the above equations $[A_{ij}^*]$, $[B_{ij}^*]$ and $[D_{ij}^*]$ $(i, j = 1, 2, 6)$ are reduced stiffness matrices the details of which, along with A_x, A_y, and A_{xy}, can be found in Stavsky (1963).

Note that in Eqs. (7) and (8) below, for the uniform thermal loading case, $C_1 = 0.0$, $C_2 = 1.0$, and $\lambda_T = \alpha_0 T_0$, whereas for the parabolic thermal loading case, $C_1 = 8\gamma_{24}^2 \gamma_6 \beta^2 \lambda_T/\pi^2$, $C_2 = [T_0/T_1 + 4(y/\pi - y^2/\pi^2)]$ and $\lambda_T = \alpha_0 T_1$.

Now by using classical laminated plate theory (i.e., transverse shear deformation is neglected) and including the plate-foundation interaction and thermal effects, the governing differential equations can be written in the dimensionless form

$$L_1(W) + \gamma_{14} L_3(F) + K_1 W - K_2 \nabla^2 W = \gamma_{14}\beta^2 L(W + W^*, F) \quad (6)$$

$$L_2(F) - \gamma_{24} L_3(W) - C_1 = -\tfrac{1}{2}\gamma_{24}\beta^2 L(W + 2W^*, W) \quad (7)$$

where

$$L_1(\ ) = \frac{\partial^4}{\partial x^4} + 2\gamma_{12}\beta^2 \frac{\partial^4}{\partial x^2 \partial y^2} + \gamma_{14}^2 \beta^4 \frac{\partial^4}{\partial y^4}$$

$$L_2(\ ) = \frac{\partial^4}{\partial x^4} + 2\gamma_{22}\beta^2 \frac{\partial^4}{\partial x^2 \partial y^2} + \gamma_{24}^2 \beta^4 \frac{\partial^4}{\partial y^4}$$

$$L_3(\ ) = \gamma_{31}\beta \frac{\partial^4}{\partial x^3 \partial y} + \gamma_{33}\beta^3 \frac{\partial^4}{\partial x \partial y^3}$$

$$L(\ ) = \frac{\partial^2}{\partial x^2}\frac{\partial^2}{\partial y^2} - 2\frac{\partial^2}{\partial x \partial y}\frac{\partial^2}{\partial x \partial y} + \frac{\partial^2}{\partial y^2}\frac{\partial^2}{\partial x^2}$$

$$\nabla^2(\ ) = \frac{\partial^2}{\partial x^2} + \beta^2 \frac{\partial^2}{\partial y^2}.$$

The unit end-shortening relationships are

$$\delta_x = -\frac{1}{4\pi^2\beta^2\gamma_{24}} \int_0^\pi \int_0^\pi \left\{ \left[\gamma_{24}^2 \beta^2 \frac{\partial^2 F}{\partial y^2} - \gamma_5 \frac{\partial^2 F}{\partial x^2} - 2\gamma_{24}\gamma_{316}\beta \frac{\partial^2 W}{\partial x \partial y} \right] - \frac{1}{2}\gamma_{24}\left(\frac{\partial W}{\partial x}\right)^2 - \gamma_{24}\frac{\partial W}{\partial x}\frac{\partial W^*}{\partial x} + (\gamma_{24}^2 \gamma_{T1} - \gamma_5 \gamma_{T2})\lambda_T C_2 \right\} dx dy \quad (8a)$$

$$\delta_y = -\frac{1}{4\pi^2\beta^2\gamma_{24}} \int_0^\pi \int_0^\pi \left\{ \left[\frac{\partial^2 F}{\partial x^2} - \gamma_5 \beta^2 \frac{\partial^2 F}{\partial y^2} - 2\gamma_{24}\gamma_{326}\beta \frac{\partial^2 W}{\partial x \partial y} \right] - \frac{1}{2}\gamma_{24}\beta^2\left(\frac{\partial W}{\partial y}\right)^2 - \gamma_{24}\beta^2 \frac{\partial W}{\partial y}\frac{\partial W^*}{\partial y} + (\gamma_{T2} - \gamma_5 \gamma_{T1})\lambda_T C_2 \right\} dx dy. \quad (8b)$$

All the edges are assumed to be simply supported and to be restrained against expansion in the in-plane directions, so that the boundary conditions are
$x = 0, \quad \pi;$

$$W = 0, \quad \delta_x = 0 \quad (9a)$$

$$F_{,xy} = 0, \quad M_x = 0 \quad (9b)$$

$y = 0, \quad \pi;$

$$W = 0, \quad \delta_y = 0 \quad (9c)$$

$$F_{,xy} = 0, \quad M_y = 0. \quad (9d)$$

By applying Eqs. (6)–(9), the thermal post-buckling behavior of a simply supported composite laminated plate resting on a two-parameter elastic foundation is now determined by a mixed Galerkin-perturbation technique suggested in Shen and Lin (1995). The essence of this procedure, in the present case, is to assume that

$$W(x, y, \epsilon) = \sum_{j=1} \epsilon^j w_j(x, y),$$

$$F(x, y, \epsilon) = \sum_{j=0} \epsilon^j f_j(x, y) \quad (10)$$

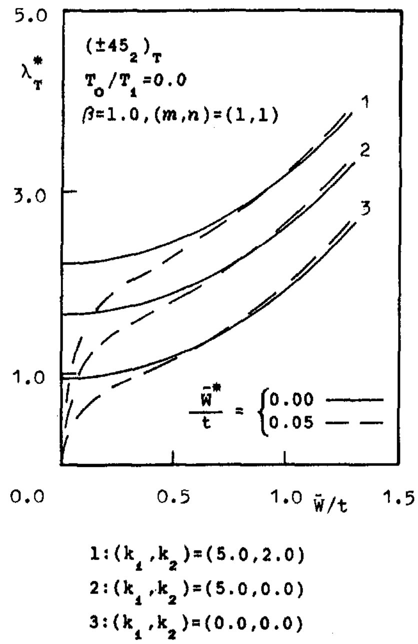

Fig. 1(*a*) $(\pm 45_2)_T$

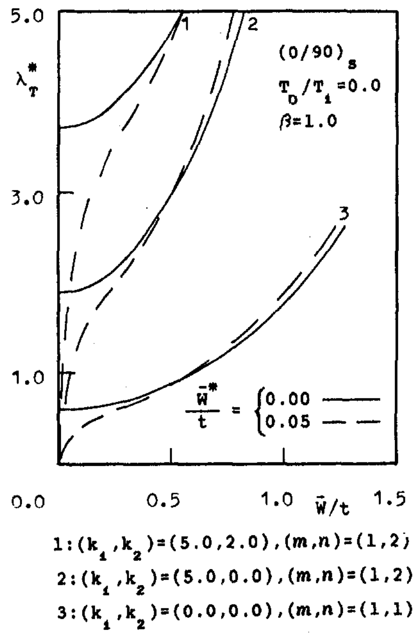

Fig. 1(*b*) $(0/90)_s$

Fig. 1 Thermal post-buckling load-deflection curves for laminated square plates with and without elastic foundations

where ϵ is a small perturbation parameter and the first term of $w_j(x, y)$ is assumed to have the form

$$w_1(x, y) = A_{11}^{(1)} \sin mx \sin ny. \tag{11}$$

The initial geometrical imperfection is assumed to have a similar form to $w_1(x, y)$, i.e.,

$$\begin{aligned} W^*(x, y, \epsilon) &= \epsilon A_{11}^* \sin mx \sin ny \\ &= \epsilon \mu A_{11}^{(1)} \sin mx \sin ny \end{aligned} \tag{12}$$

where μ is the imperfection parameter.

All the necessary steps of the solution methodology are described below, but the detailed expressions of the equations are not shown, for the sake of brevity, since they may be found in Shen (1995b) and Shen and Lin (1995).

First, the assumed solution form of Eq. (10) is substituted into Eqs. (6) and (7) to obtain a system of perturbation equations.

Then, Eqs. (11) and (12) are used to solve these perturbation equations of each order step by step. At each step the amplitudes of the components of $w_j(x, y)$ and $f_j(x, y)$ can be determined by the Galerkin procedure. Hence, the asymptotic solutions $W(x, y, \epsilon)$ and $F(x, y, \epsilon)$ are obtained.

Next, substituting $W(x, y, \epsilon)$ and $F(x, y, \epsilon)$ into the boundary conditions $\delta_x = 0$ and $\delta_y = 0$, the thermal postbuckling equilibrium path can be written as

$$\lambda_T = \lambda_T^{(0)} + \lambda_T^{(2)} W_m^2 + \lambda_T^{(4)} W_m^4 + \ldots \tag{13}$$

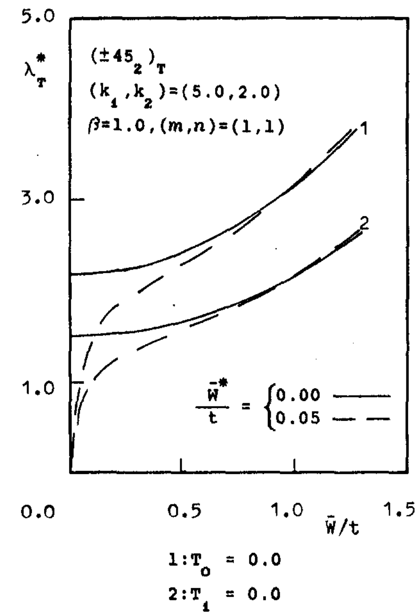

Fig. 2(*a*) $(\pm 45_2)_T$

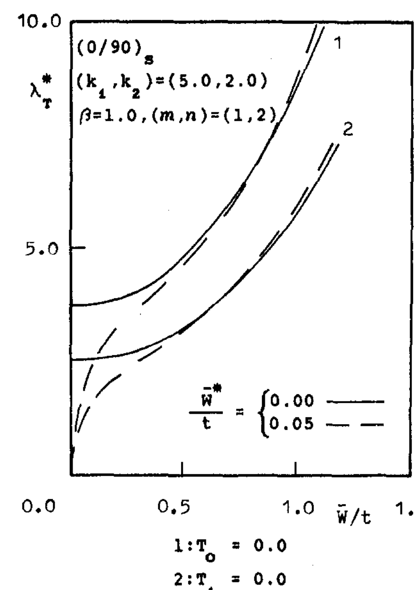

Fig. 2(*b*) $(0/90)_s$

Fig. 2 Thermal post-buckling load-deflection curves for laminated plates on two-parameter elastic foundations and subjected to uniform or parabolic thermal loading

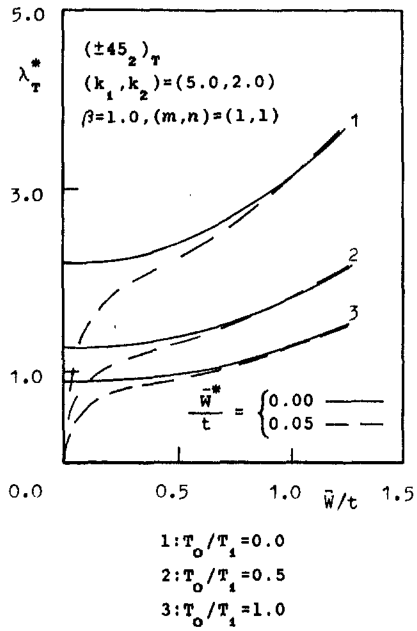

Fig. 3 Effect of thermal load ratio T_0/T_1 on the post-buckling of $(\pm 45_2)_T$ laminated plates on two-parameter elastic foundations

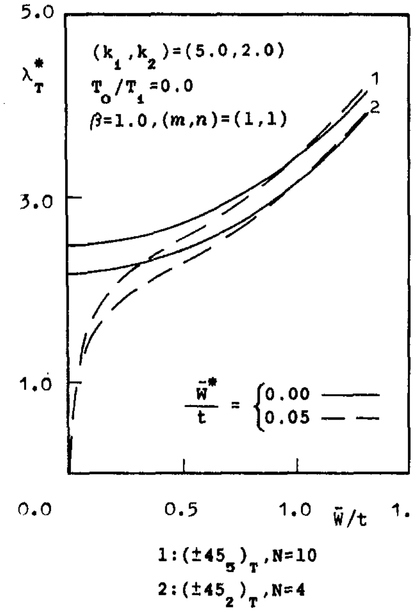

Fig. 5 Effect of total number of plies N on thermal post-buckling of antisymmetrically laminated plates on two-parameter elastic foundations

in which W_m is the dimensionless form of the maximum deflection of the plate, which is assumed to be at the point $(x, y) = (\pi/2m, \pi/2n)$.

It is noted that Eq. (13) has a similar form to that of Koiter (1963), but is an asymptotic solution for the large deflection thermal post-buckling response of the plate. Hence, Eq. (13) can be employed to obtain full-range thermal post-buckling load-deflection curves of composite laminated plates resting on two-parameter elastic foundations.

3 Results

Thermal post-buckling induced by uniform and nonuniform temperature distribution has been studied by a mixed Galerkin-perturbation method. A number of examples are now given to illustrate the application of the method presented. These cover the performance of perfect and imperfect, antisymmetrically angle-ply and symmetrically cross-ply laminated plates. Typical results are presented in dimensionless graphical form, in which $\lambda_T^* = 12(\alpha_{11} + \nu_{21}\alpha_{22})b^2\lambda_T/\alpha_0\pi^2t^2$. It should be remembered that, because of the definition of λ_T given beneath Eq. (3), this means that for a given plate λ_T^* is a constant times T_0 when $T_1 = 0$ but is otherwise the same constant times T_1. For all of the laminated plate examples $b/t = 100.0$, all plies are of equal thickness and the material properties used were $E_{11} = 130.3$ GPa, $E_{22} = 9.377$ GPa, $G_{12} = 4.502$ GPa, $\nu_{12} = 0.33$, $\alpha_{11} = 0.139 \times 10^{-6}$/°C, and $\alpha_{22} = 9.01 \times 10^{-6}$/°C.

Figure 1 gives the thermal post-buckling load-deflection curves for four-ply $(\pm 45_2)_T$ antisymmetrically angle-ply and $(0/90)_s$ symmetrically cross-ply laminated plates under nonuni-

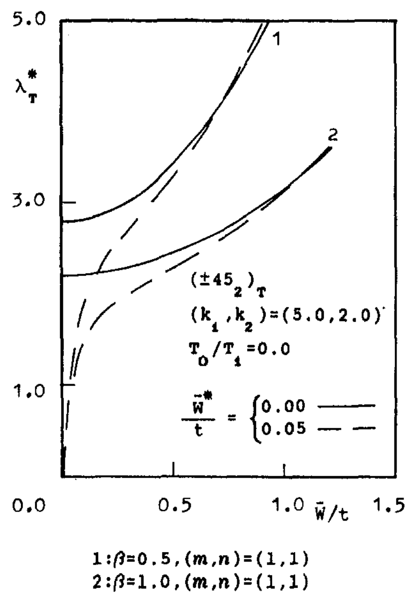

Fig. 4 Effect of plate aspect ratio β on thermal post-buckling of $(\pm 45_2)_T$ laminated plates on two-parameter elastic foundations

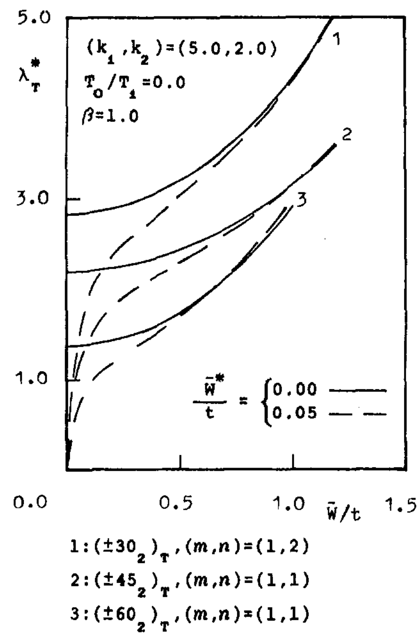

Fig. 6 Effect of fiber orientation on thermal post-buckling of antisymmetrically laminated plates on two-parameter elastic foundations

form temperature loading and either without foundations or resting on either Winkler or two-parameter elastic foundations. The stiffnesses for these three alternative foundations are, respectively, $(k_1, k_2) = (0.0, 0.0)$, $(5.0, 0.0)$, and $(5.0, 2.0)$. It can be seen that the foundation stiffness increases the buckling load and affects the post-buckling response of the $(0/90)_s$ plate more than that of the $(\pm 45_2)_T$ one. The buckling mode can also be seen to change as the foundation stiffness is increased for the $(0/90)_s$ plate, with $(m, n) = (1, 1)$ for the foundationless case, whereas $(m, n) = (1, 2)$ for the Winkler and two-parameter elastic foundation cases.

Figure 2 gives the thermal post-buckling load-deflection curves of the same two laminated plates under uniform or parabolic temperature loading and resting on two-parameter elastic foundations. It can be seen that the laminated plate under parabolic thermal loading has a higher initial buckling load and a higher post-buckling load than for a plate under uniform thermal loading.

Figures 3 and 4, show, respectively, the effects of the thermal load ratio T_0/T_1 and of the plate aspect ratio β (= 0.5, 1.0) on the thermal post-buckling response of four-ply $(\pm 45_2)_T$ antisymmetrically angle-ply laminated plates. Then Fig. 5 shows the influence of the total number of plies N (= 4, 10) on the thermal post-buckling response of antisymmetrically angle-ply laminated plates of constant thickness and resting on two-parameter elastic foundations. Finally, Fig. 6 compares together the thermal post-buckling load-deflection curves of square, four-layer $(\pm 30_2)_T$, $(\pm 45_2)_T$ and $(\pm 60_2)_T$ antisymmetrically angle-ply laminated plates resting on two-parameter elastic foundations.

In all of Figs. 2–6 the stiffnesses for the two-parameter elastic foundation are $(k_1, k_2) = (5.0, 2.0)$. The results show that the thermal buckling load and post-buckling strength are increased by increasing the total number of plies N, decreasing the plate aspect ratio β, or decreasing the thermal load ratio T_0/T_1. They also show that N has less effect than β or the ply orientation.

Thermal post-buckling load-deflection curves for imperfect as well as perfect plates are plotted in each of Figs. 1–6. The imperfect curves show that the effect of an initial geometrical imperfection on the thermal post-buckling response of laminated plates resting on an elastic foundation is substantial, as was already known to be the case (see Shen, 1995b) for laminated plates under in-plane compression both with and without elastic foundations.

4 Conclusions

A thermal post-buckling analysis has been presented for the previously unsolved problem of imperfect composite laminated plates under nonuniform temperature loading and resting on two-parameter elastic foundations. The numerical results show that the characteristics of thermal post-buckling are significantly influenced by foundation stiffness, plate aspect ratio, fiber orientation, thermal load ratio, and initial geometrical imperfection, whereas the total number of plies has rather less effect.

Acknowledgment

The authors are grateful for financial support from the Cardiff Advanced Chinese Engineering Centre.

References

Dumir, P. C., 1988, "Thermal postbuckling of rectangular plates on Pasternak elastic foundations," *Mechanics Research Communications*, Vol. 15, pp. 371–379.

Koiter, W. T., 1963, "Elastic stability and postbuckling behavior," *Proceedings of Symposium on Nonlinear Problem*, University of Wisconsin Press, Madison, WI, pp. 257–275.

Raju, K. K., and Rao, G. V., 1988, "Thermal post-buckling of a square plate resting on an elastic foundation by finite element method," *Computers and Structures*, Vol. 28, pp. 195–199.

Shen, H. S., 1995a, "Postbuckling of orthotropic plates on two-parameter elastic foundation," *ASCE Journal of Engineering Mechanics*, Vol. 121, pp. 50–56.

Shen, H. S., 1995b, "Postbuckling analysis of composite laminated plates on two-parameter elastic foundations," *International Journal of Mechanical Sciences*, Vol. 37, pp. 1307–1316.

Shen, H. S., and Lin, Z. Q., 1995, "Thermal post-buckling analysis of imperfect laminated plates," *Computers and Structures*, Vol. 57, pp. 533–540.

Stavsky, Y., 1963, "Thermoelasticity of heterogeneous aeolotropic plates," *ASCE Journal of Engineering Mechanics*, Vol. 89, pp. 88–105.

A Remarkable Tensor in Plane Linear Elasticity

Q.-C. He[9]

It is shown that any two-dimensional elastic tensor can be orthogonally and uniquely decomposed into a symmetric tensor and an antisymmetric tensor. To within a scalar multiplier, the latter turns out to be equal to the right-angle rotation on the space of two-dimensional second-order symmetric tensors. On the basis of these facts, several useful results are derived for the traction boundary value problem of plane linear elasticity.

Introduction

Formulated classically in terms of Airy's function, the traction boundary value problem of plane linear elasticity has four governing equations: Hooke's law, the stress field derivation equation, the compatibility equation, and the boundary condition. It has been known (see, e.g., Cherkaev et al. (1992) or Eqs. (24), (26), and (28)) that each of the latter three ones involves the fourth-order tensor

$$\mathbb{R} = \mathbf{1} \otimes \mathbf{1} - \mathbb{I} \tag{1}$$

where $\otimes$ designates the usual tensor product, $\mathbf{1}$ the identity tensor on the two-dimensional vector space $\mathcal{V}$, and $\mathbb{I}$ the identity tensor on the space Sym of two-dimensional second-order *symmetric* tensors. The present note, inspired by a recent work of Cherkaev et al. (1992), has two objectives. The first one is to show that $\mathbb{R}$ occurs equally in Hooke's law and coincides in reality with the "antisymmetric" part of any elastic tensor to within a scalar multiplier. The second one consists in using this result and certain properties of $\mathbb{R}$ to simplify the formulation of the traction boundary value problem in some particular but important cases and thus to derive, in an algebraically meaningful way, the stress invariance conditions given in Cherkaev et al. (1992) and Dundurs and Markenscoff (1993).

Right-Angle Rotation

We begin by introducing some notations. In what follows, Lin denotes the space of all linear transformations on $\mathcal{V}$ and $\mathcal{L}$ the space of all linear transformations on Lin. The inner inner products of $\mathcal{V}$, Lin and $\mathcal{L}$ will be symbolized by $\mathbf{a}.\mathbf{b}$ for $\mathbf{a}$, $\mathbf{b} \in \mathcal{V}$, $\mathbf{A}:\mathbf{B}$ for $\mathbf{A}$, $\mathbf{B} \in$ Lin, and $\mathbb{A}::\mathbb{B}$ for $\mathbb{A}$, $\mathbb{B} \in \mathcal{L}$. When fourth-order tensors are concerned, it has turned out to be fruitful to define, in addition to the usual tensor product $\mathbf{A} \otimes \mathbf{B}$ of $\mathbf{A} \in$

[9] Laboratory of Applied Mechanics, Department of Mechanical Engineering, Swiss Federal Institute of Technology, CH-1015 Lausanne, Switzerland.

Contributed by the Applied Mechanics Division of THE AMERICAN SOCIETY OF MECHANICAL ENGINEERS for publication in the ASME JOURNAL OF APPLIED MECHANICS. Manuscript received by the ASME Applied Mechanics Division, July 17, 1996; final revision, Nov. 15, 1996. Associate Technical Editor: X. Markenscoff.

form temperature loading and either without foundations or resting on either Winkler or two-parameter elastic foundations. The stiffnesses for these three alternative foundations are, respectively, $(k_1, k_2) = (0.0, 0.0)$, $(5.0, 0.0)$, and $(5.0, 2.0)$. It can be seen that the foundation stiffness increases the buckling load and affects the post-buckling response of the $(0/90)_s$ plate more than that of the $(\pm 45_2)_T$ one. The buckling mode can also be seen to change as the foundation stiffness is increased for the $(0/90)_s$ plate, with $(m, n) = (1, 1)$ for the foundationless case, whereas $(m, n) = (1, 2)$ for the Winkler and two-parameter elastic foundation cases.

Figure 2 gives the thermal post-buckling load-deflection curves of the same two laminated plates under uniform or parabolic temperature loading and resting on two-parameter elastic foundations. It can be seen that the laminated plate under parabolic thermal loading has a higher initial buckling load and a higher post-buckling load than for a plate under uniform thermal loading.

Figures 3 and 4, show, respectively, the effects of the thermal load ratio T_0/T_1 and of the plate aspect ratio β (= 0.5, 1.0) on the thermal post-buckling response of four-ply $(\pm 45_2)_T$ antisymmetrically angle-ply laminated plates. Then Fig. 5 shows the influence of the total number of plies N (= 4, 10) on the thermal post-buckling response of antisymmetrically angle-ply laminated plates of constant thickness and resting on two-parameter elastic foundations. Finally, Fig. 6 compares together the thermal post-buckling load-deflection curves of square, four-layer $(\pm 30_2)_T$, $(\pm 45_2)_T$ and $(\pm 60_2)_T$ antisymmetrically angle-ply laminated plates resting on two-parameter elastic foundations.

In all of Figs. 2–6 the stiffnesses for the two-parameter elastic foundation are $(k_1, k_2) = (5.0, 2.0)$. The results show that the thermal buckling load and post-buckling strength are increased by increasing the total number of plies N, decreasing the plate aspect ratio β, or decreasing the thermal load ratio T_0/T_1. They also show that N has less effect than β or the ply orientation.

Thermal post-buckling load-deflection curves for imperfect as well as perfect plates are plotted in each of Figs. 1–6. The imperfect curves show that the effect of an initial geometrical imperfection on the thermal post-buckling response of laminated plates resting on an elastic foundation is substantial, as was already known to be the case (see Shen, 1995b) for laminated plates under in-plane compression both with and without elastic foundations.

4 Conclusions

A thermal post-buckling analysis has been presented for the previously unsolved problem of imperfect composite laminated plates under nonuniform temperature loading and resting on two-parameter elastic foundations. The numerical results show that the characteristics of thermal post-buckling are significantly influenced by foundation stiffness, plate aspect ratio, fiber orientation, thermal load ratio, and initial geometrical imperfection, whereas the total number of plies has rather less effect.

Acknowledgment

The authors are grateful for financial support from the Cardiff Advanced Chinese Engineering Centre.

References

Dumir, P. C., 1988, "Thermal postbuckling of rectangular plates on Pasternak elastic foundations," *Mechanics Research Communications*, Vol. 15, pp. 371–379.

Koiter, W. T., 1963, "Elastic stability and postbuckling behavior," *Proceedings of Symposium on Nonlinear Problem*, University of Wisconsin Press, Madison, WI, pp. 257–275.

Raju, K. K., and Rao, G. V., 1988, "Thermal post-buckling of a square plate resting on an elastic foundation by finite element method," *Computers and Structures*, Vol. 28, pp. 195–199.

Shen, H. S., 1995a, "Postbuckling of orthotropic plates on two-parameter elastic foundation," *ASCE Journal of Engineering Mechanics*, Vol. 121, pp. 50–56.

Shen, H. S., 1995b, "Postbuckling analysis of composite laminated plates on two-parameter elastic foundations," *International Journal of Mechanical Sciences*, Vol. 37, pp. 1307–1316.

Shen, H. S., and Lin, Z. Q., 1995, "Thermal post-buckling analysis of imperfect laminated plates," *Computers and Structures*, Vol. 57, pp. 533–540.

Stavsky, Y., 1963, "Thermoelasticity of heterogeneous aeolotropic plates," *ASCE Journal of Engineering Mechanics*, Vol. 89, pp. 88–105.

A Remarkable Tensor in Plane Linear Elasticity

Q.-C. He[9]

It is shown that any two-dimensional elastic tensor can be orthogonally and uniquely decomposed into a symmetric tensor and an antisymmetric tensor. To within a scalar multiplier, the latter turns out to be equal to the right-angle rotation on the space of two-dimensional second-order symmetric tensors. On the basis of these facts, several useful results are derived for the traction boundary value problem of plane linear elasticity.

Introduction

Formulated classically in terms of Airy's function, the traction boundary value problem of plane linear elasticity has four governing equations: Hooke's law, the stress field derivation equation, the compatibility equation, and the boundary condition. It has been known (see, e.g., Cherkaev et al. (1992) or Eqs. (24), (26), and (28)) that each of the latter three ones involves the fourth-order tensor

$$\mathbb{R} = \mathbf{1} \otimes \mathbf{1} - \mathbb{I} \tag{1}$$

where $\otimes$ designates the usual tensor product, $\mathbf{1}$ the identity tensor on the two-dimensional vector space $\mathcal{V}$, and $\mathbb{I}$ the identity tensor on the space Sym of two-dimensional second-order *symmetric* tensors. The present note, inspired by a recent work of Cherkaev et al. (1992), has two objectives. The first one is to show that $\mathbb{R}$ occurs equally in Hooke's law and coincides in reality with the "antisymmetric" part of any elastic tensor to within a scalar multiplier. The second one consists in using this result and certain properties of $\mathbb{R}$ to simplify the formulation of the traction boundary value problem in some particular but important cases and thus to derive, in an algebraically meaningful way, the stress invariance conditions given in Cherkaev et al. (1992) and Dundurs and Markenscoff (1993).

Right-Angle Rotation

We begin by introducing some notations. In what follows, Lin denotes the space of all linear transformations on $\mathcal{V}$ and $\mathcal{L}$ the space of all linear transformations on Lin. The inner inner products of $\mathcal{V}$, Lin and $\mathcal{L}$ will be symbolized by $\mathbf{a}.\mathbf{b}$ for $\mathbf{a}$, $\mathbf{b} \in \mathcal{V}$, $\mathbf{A}:\mathbf{B}$ for $\mathbf{A}$, $\mathbf{B} \in$ Lin, and $\mathbb{A}::\mathbb{B}$ for $\mathbb{A}$, $\mathbb{B} \in \mathcal{L}$. When fourth-order tensors are concerned, it has turned out to be fruitful to define, in addition to the usual tensor product $\mathbf{A} \otimes \mathbf{B}$ of $\mathbf{A} \in$

[9] Laboratory of Applied Mechanics, Department of Mechanical Engineering, Swiss Federal Institute of Technology, CH-1015 Lausanne, Switzerland.

Contributed by the Applied Mechanics Division of THE AMERICAN SOCIETY OF MECHANICAL ENGINEERS for publication in the ASME JOURNAL OF APPLIED MECHANICS. Manuscript received by the ASME Applied Mechanics Division, July 17, 1996; final revision, Nov. 15, 1996. Associate Technical Editor: X. Markenscoff.

Lin by $\mathbf{B} \in$ Lin, the following two tensor products $\mathbf{A} \underline{\otimes} \mathbf{B}$ and $\mathbf{A} \bar{\otimes} \mathbf{B}$ (Curnier, 1993):

$$(\mathbf{A} \underline{\otimes} \mathbf{B})(\mathbf{u} \otimes \mathbf{v}) := (\mathbf{Au}) \otimes (\mathbf{Bv}), \quad \forall \mathbf{u}, \mathbf{v} \in \mathcal{V}, \quad (2a)$$

$$(\mathbf{A} \bar{\otimes} \mathbf{B})(\mathbf{u} \otimes \mathbf{v}) := (\mathbf{Av}) \otimes (\mathbf{Bu}), \quad \forall \mathbf{u}, \mathbf{v} \in \mathcal{V}. \quad (2b)$$

From these two definitions ensue the identities

$$(\mathbf{a} \otimes \mathbf{b}) \underline{\otimes} (\mathbf{c} \otimes \mathbf{d}) = \mathbf{a} \otimes \mathbf{c} \otimes \mathbf{b} \otimes \mathbf{d}, \quad (3a)$$

$$(\mathbf{a} \otimes \mathbf{b}) \bar{\otimes} (\mathbf{c} \otimes \mathbf{d}) = \mathbf{a} \otimes \mathbf{c} \otimes \mathbf{d} \otimes \mathbf{b}, \quad (3b)$$

$$(\mathbf{A} \underline{\otimes} \mathbf{B})\mathbf{X} = \mathbf{AXB}^{\mathrm{T}}, \quad (\mathbf{A} \bar{\otimes} \mathbf{B})\mathbf{X} = \mathbf{AX}^{\mathrm{T}}\mathbf{B}^{\mathrm{T}}, \quad (3c)$$

where $\mathbf{a}$, $\mathbf{b}$, $\mathbf{c}$, and $\mathbf{d}$ belong to $\mathcal{V}$ and the transposition $\mathbf{X}^{\mathrm{T}}$ of $\mathbf{X} \in$ Lin is defined by $\mathbf{X}^{\mathrm{T}}\mathbf{u}.\mathbf{v} = \mathbf{u}.\mathbf{Xv}$ for any $\mathbf{u}, \mathbf{v} \in \mathcal{V}$. It is immediate from (3c) that the identity tensors on Lin and Sym have the coordinate-free expressions

$$1 = \mathbf{1} \underline{\otimes} \mathbf{1}, \quad \mathbb{I} = \tfrac{1}{2}(\mathbf{1} \underline{\otimes} \mathbf{1} + \mathbf{1} \bar{\otimes} \mathbf{1}). \quad (4)$$

Further, if $\mathbf{Q} \in$ Lin is an orthogonal transformation on $\mathcal{V}$, i.e., $\mathbf{Qu}.\mathbf{Qv} = \mathbf{u}.\mathbf{v}$ for any $\mathbf{u}, \mathbf{v} \in \mathcal{V}$, then

$$\mathbb{Q} := \tfrac{1}{2}(\mathbf{Q} \underline{\otimes} \mathbf{Q} + \mathbf{Q} \bar{\otimes} \mathbf{Q})$$

is an *orthogonal transformation on* Sym, because $\mathbb{Q}\mathbf{U}:\mathbb{Q}\mathbf{V} = \mathbf{U}:\mathbf{V}$ for all $\mathbf{U}, \mathbf{V} \in$ Sym.

Next, let us deduce two properties of $\mathbb{R}$ for later use. Supposing that $\{\mathbf{e}_1, \mathbf{e}_2\}$ is an orthonormal basis of $\mathcal{V}$, the *right-angle rotation* $\mathbf{R}$ from $\mathbf{e}_2$ to $\mathbf{e}_1$ is then represented by

$$\mathbf{R} = \mathbf{e}_1 \otimes \mathbf{e}_2 - \mathbf{e}_2 \otimes \mathbf{e}_1. \quad (5)$$

This tensor also corresponds to the *two-dimensional alternator*, for $R_{11} = R_{22} = 0$ and $R_{12} = -R_{21} = 1$. Using (3a) and the fact that $\mathbf{1} = \mathbf{e}_1 \otimes \mathbf{e}_1 + \mathbf{e}_2 \otimes \mathbf{e}_2$, we arrive at relating $\mathbb{R}$ to $\mathbf{R}$:

$$\mathbb{R} = \mathbf{1} \otimes \mathbf{1} - \mathbb{I} = \tfrac{1}{2}(\mathbf{R} \underline{\otimes} \mathbf{R} + \mathbf{R} \bar{\otimes} \mathbf{R}). \quad (6)$$

Thus, $\mathbb{R}$ can be considered as the right-angle rotation on Sym. Such an interpretation for $\mathbb{R}$ seems to be given for the first time by Cherkaev et al. (1992). Another important property of $\mathbb{R}$ is that with its domain and range restricted to Sym,

$$\mathbb{R} = \mathbb{R}^{-1} = \mathbb{R}^{T}. \quad (7)$$

Here $\mathbb{R}^{-1}$ is understood to be such that $\mathbb{R}^{-1}\mathbb{R} = \mathbb{R}\mathbb{R}^{-1} = \mathbb{I}$, and $\mathbb{R}^{T}$ is defined by $\mathbb{R}^{T}\mathbf{U}:\mathbf{V} := \mathbf{U}:\mathbb{R}\mathbf{V}$ for $\mathbf{U}, \mathbf{V} \in$ Sym.

Orthgonal Decomposition of a Two-Dimensional Elastic Tensor

Now we proceed to show that $\mathbb{R}$ can be drawn out from any two-dimensional elastic tensor. Hereafter, an elastic tensor will refer to an element $\mathbb{C}$ of the space $\mathcal{C}$ of linear self-adjoint transformations on Sym; in other words, the defining property of $\mathbb{C}$ is that its Cartesian matrix components C_{ijmn} present the symmetries

$$C_{ijmn} = C_{jimn} = C_{mnij}. \quad (8)$$

In coordinate-free notations, (8) reads as $\mathbb{C} = (\mathbf{1} \bar{\otimes} \mathbf{1})\mathbb{C} = \mathbb{C}^{T}$.

In mechanics, we are familiar with the orthogonal decomposition of a 2nd-order tensor $\mathbf{L} \in$ Lin into a unique symmetric one $\mathbf{S} = (\mathbf{L} + \mathbf{L}^{T})/2$ and a unique antisymmetric one $\mathbf{A} = (\mathbf{L} - \mathbf{L}^{T})/2$. For a clue to as how to extend this decomposition to a tensor of order $n > 2$, we shall write the symmetry, $\mathbf{S}^{T} = \mathbf{S}$, of $\mathbf{S}$ and the antisymmetry, $\mathbf{A}^{T} = -\mathbf{A}$, of $\mathbf{A}$ in an equivalent but less familiar form. Denoting by $T_{(i_1 i_2 \ldots i_n)}$ the sum of the $n!$ terms obtained by permuting a component $T_{i_1 i_2 \ldots i_n}$ of a tensor of order $n \geq 2$ in all possible ways (see, e.g., Spencer, 1970) and putting $T_{[i_1 i_2 \ldots i_n]} = T_{(i_1 i_2 \ldots i_n)}/n!$, then the symmetry of $\mathbf{S}$ and the antisymmetry of $\mathbf{A}$ can be expressed as $S_{[ij]} = S_{ij}$ and $A_{[ij]} = 0$. With this in mind, we associate two tensors, $\mathbb{S}$ and $\mathbb{A}$, with a given elastic tensor $\mathbb{C}$ by setting

$$S_{ijmn} := C_{[ijmn]} = \tfrac{1}{4!} C_{(ijmn)}, \quad A_{ijmn} := C_{ijmn} - S_{ijmn}. \quad (9)$$

The tensors $\mathbb{S}$ and $\mathbb{A}$ thus defined can be referred to as the *symmetric and antisymmetric* parts of $\mathbb{C}$, since $S_{[ijmn]} = S_{ijmn}$ by construction and $A_{[ijmn]} = 0$ by verification. Moreover,

$$\mathbb{S}::\mathbb{A} = S_{ijmn}A_{ijmn} = 0, \quad (10)$$

since, due to the fact that S_{ijmn} is unaffected by permuting any pair of indices,

$$S_{ijmn}A_{ijmn} = S_{ijmn}A_{[ijmn]} = 0.$$

Clearly, all symmetric and antisymmetric tensors $\mathbb{S}$ and $\mathbb{A}$ belonging to $\mathcal{C}$ form the two respective subspaces of $\mathcal{C}$, which will be denoted as $\mathcal{S}$ and $\mathcal{A}$. At this stage, we can write

$$\mathbb{C} = \mathbb{S} + \mathbb{A}, \quad (11)$$

$$\mathcal{C} = \mathcal{S} \oplus \mathcal{A}, \quad \dim(\mathcal{C}) = \dim(\mathcal{S}) + \dim(\mathcal{A}). \quad (12)$$

Uniqueness of this orthogonal decomposition can be proved in the same manner as that used for $\mathbf{L} = \mathbf{S} + \mathbf{A}$.

Taking the symmetry property (8) of $\mathbb{C}$ into account in (9), we get

$$S_{ijmn} = \tfrac{1}{3}(C_{ijmn} + C_{imjn} + C_{inmj}), \quad (13)$$

$$A_{ijmn} = \tfrac{1}{3}(2C_{ijmn} - C_{imjn} - C_{inmj}). \quad (14)$$

While noting that $\mathbb{A}$ has the same symmetries as those of $\mathbb{C}$, (14) can be written out as follows:

$$3A_{1111} = 2C_{1111} - C_{1111} - C_{1111} = 0,$$

$$3A_{2222} = 2C_{2222} - C_{2222} - C_{2222} = 0,$$

$$3A_{1212} = 2C_{1212} - C_{1122} - C_{1212} = C_{1212} - C_{1122},$$

$$3A_{1122} = 2C_{1122} - C_{1212} - C_{1221} = 2(C_{1122} - C_{1212}),$$

$$3A_{1112} = 2C_{1112} - C_{1112} - C_{1211} = 0,$$

$$3A_{2212} = 2C_{2212} - C_{2122} - C_{2212} = 0.$$

In short,

$$A_{1111} = A_{2222} = A_{1112} = A_{2212} = 0, \quad (15a)$$

$$A_{1122} = -2A_{1212} = 2(C_{1122} - C_{1212})/3. \quad (15b)$$

The relation $S_{ijmn} = C_{ijmn} - A_{ijmn}$ gives

$$S_{1111} = C_{1111},\ S_{2222} = C_{2222},\ S_{1112} = C_{1112}, \quad (16a)$$

$$S_{2212} = C_{2212},\ S_{1212} = -2S_{1122} = 2(C_{1122} - C_{1212})/3. \quad (16b)$$

On the other hand, writing out the components of $\mathbb{R}$, we have

$$R_{1111} = R_{2222} = R_{1112} = R_{2212} = 0, \quad (17a)$$

$$R_{1122} = -2R_{1212} = 1. \quad (17b)$$

Comparing (15) with (17) gives

$$\mathbb{A} = \alpha\mathbb{R}, \quad \alpha = 2(C_{1122} - C_{1212})/3. \quad (18)$$

This means that *the antisymmetric part of any two-dimensional elastic tensor is identical to* $\mathbb{R}$ *to within a scalar multiplier.* This result is surprising in the sense that the antisymmetric tensor of either isotropic or anisotropic elastic tensor takes the *same* form. We observe that the scalar α in (18) is an *invariant* of $\mathbb{C}$ under orthogonal transformations, since

$$3\alpha = \mathbb{R}::\mathbb{C} = (\mathbf{1} \otimes \mathbf{1} - \mathbb{I})::\mathbb{C}. \quad (19)$$

So, (18) can be rewritten in the form

$$\mathbb{A} = \tfrac{1}{3}(\mathbb{R} \otimes \mathbb{R})\mathbb{C}. \tag{20}$$

This indicates that $(\mathbb{R} \otimes \mathbb{R})/3$ is the linear operator representing the perpendicular projection of C on $\mathcal{A}$ along S. In addition, (18) together with (12_2) implies that

$$\dim(\mathcal{A}) = 1, \quad \dim(S) = 5. \tag{21}$$

Before applying formulae (6), (10), (11), and (18) to the traction boundary value problem, it is interesting to remark that

$$C_{ijmn} = C_{imjn} \quad \Leftrightarrow \quad \alpha = 0 \quad \Leftrightarrow \quad \mathbb{A} = 0, \tag{22}$$

where $C_{ijmn} = C_{imjn}$ is the Cauchy condition (see, e.g., Novozhilov, 1961). Indeed, as S_{ijmn} is symmetric, this condition is equivalent to

$$\begin{aligned} 0 = C_{ijmn} - C_{imjn} &= A_{ijmn} - A_{imjn} \\ &= \alpha(R_{ijmn} - R_{imjn}) = 3\alpha(\delta_{ij}\delta_{mn} - \delta_{im}\delta_{jn})/2 \end{aligned}$$

and hence to $\alpha = 0$.

The General Two-Dimensional Traction Boundary Value Problem

We come now to applying the preceding algebraic results to the traction boundary value problem of plane elasticity. For this, consider a two-dimensional linearly elastic solid, which occupies in its reference configuration a bounded simply connected domain Ω of R^2, with the regular boundary $\partial\Omega$ subjected to equilibrated tractions $\mathbf{t}: \partial\Omega \to \mathcal{V}$. The behavior of the solid is by hypothesis described by Hooke's law:

$$\mathbf{E}(\mathbf{x}) = \mathbb{C}(\mathbf{x})\mathbf{T}(\mathbf{x}), \quad \mathbf{x} \in \bar{\Omega} = \Omega \cup \partial\Omega, \tag{23}$$

where $\mathbf{E}$ and $\mathbf{T}$ are the two-dimensional (infinitesimal) strain and stress tensors, and the compliance tensor field $\mathbb{C}$ on $\bar{\Omega}$ will be assumed to be twice continuously differentiable. Denoting by φ the regular (or more precisely four times continuously differentiable) Airy function on $\bar{\Omega}$, then the stress tensor derived from φ, i.e.,

$$\mathbf{T}(\mathbf{x}) = \mathbb{R}(\nabla \otimes \nabla)\varphi(\mathbf{x}), \quad (T_{ij} = R_{ijmn}\varphi_{,mn}), \tag{24}$$

automatically verifies the equilibrium equation without body forces:

$$\operatorname{div}(\mathbf{T}(\mathbf{x})) = \mathbb{R}(\nabla \otimes \nabla \otimes \nabla)\varphi(\mathbf{x}) = 0, \quad \mathbf{x} \in \Omega. \tag{25}$$

On the other hand, the strain tensor $\mathbf{E}$ obtained from (23) and (24) must verify the compatibility equation

$$[\mathbb{R}\mathbf{E}(\mathbf{x})]:(\nabla \otimes \nabla) = [R_{ijmn}E_{mn}(\mathbf{x})]_{,ij} = 0, \quad \mathbf{x} \in \Omega. \tag{26}$$

In passing, let us give a new interpretation to this equation by using (10). First, observe that $(R_{ijmn}E_{mn})_{,ij} = R_{ijmn}E_{mn,ij} = R_{ijmn}(E_{mn,ij} + E_{ij,mn})/2$ because of $R_{ijmn} = R_{mnij}$; then, denoting by $\mathbb{E}(\mathbf{x})$ the tensor whose matrix corresponds to the Hessian $E_{mn,ij}(\mathbf{x})$ of $\mathbf{E}(\mathbf{x})$, (26) amounts to writing $\mathbb{R}::(\mathbb{E} + \mathbb{E}^T) = 0$ or $(\mathbb{E} + \mathbb{E}^T) \in S$; so, (26) can be said to require that the Hessian of a strain tensor field $\mathbf{E}(\mathbf{x})$ plus its transpose be *symmetric.*

Introducing (23) and (24) into (26) and writing out the boundary condition, we get the classical formulation of the two-dimensional traction boundary value problem in terms of φ:

$$(P)\begin{cases} [\mathbb{R}\mathbb{C}(\mathbf{x})\mathbb{R}(\nabla \otimes \nabla)\varphi(\mathbf{x})]:(\nabla \otimes \nabla) = 0, \ \mathbf{x} \in \Omega, & (27) \\ [\mathbb{R}(\nabla \otimes \nabla)\varphi(\mathbf{x})]\mathbf{n}(\mathbf{x}) = \mathbf{t}(\mathbf{x}), \ \mathbf{x} \in \partial\Omega. & (28) \end{cases}$$

Above $\mathbf{n}(\mathbf{x})$ is the outward unit normal to $\partial\Omega$ at $\mathbf{x}$. Hereafter, the data $(\bar{\Omega}, \mathbb{C}, \mathbf{t})$ will be assumed to be such that (P) *has a unique solution to within an affine function of* $\mathbf{x}$. This hypothesis, implicitly made in both Cherkaev et al. (1992) and Dundurs and Markenscoff (1993) and essential to the subsequent development, should be kept in mind.

As $\mathbb{C}(\mathbf{x})$ does not occur in the traction boundary condition (28), from now on we shall focus our attention on the field equation (27). In view of (11) and (18), $\mathbb{C}(\mathbf{x})$ can be written as

$$\mathbb{C}(\mathbf{x}) = \mathbb{S}(\mathbf{x}) + \alpha(\mathbf{x})\mathbb{R}. \tag{29}$$

Introducing this partition into (27) while using (7), (27) becomes

$$\begin{aligned} 0 = [\mathbb{R}\mathbb{S}(\mathbf{x})\mathbb{R}(\nabla \otimes \nabla)\varphi(\mathbf{x})]&:(\nabla \otimes \nabla) \\ &+ [\alpha(\mathbf{x})\mathbb{R}(\nabla \otimes \nabla)\varphi(\mathbf{x})]:(\nabla \otimes \nabla). \end{aligned}$$

In developing the second term of the right-hand member, it is important to note that

$$\mathbb{R}::(\nabla \otimes \nabla \otimes \nabla \otimes \nabla)\varphi = R_{ijmn}\varphi_{,ijmn} = 0, \tag{30}$$

$$\mathbb{R}::[\nabla\alpha \otimes (\nabla \otimes \nabla \otimes \nabla)\varphi] = R_{ijmn}\alpha_{,i}\varphi_{,jmn} = 0. \tag{31}$$

Here, (30) is a direct consequence of (10), since $(\nabla \otimes \nabla \otimes \nabla \otimes \nabla)\varphi$ is a symmetric tensor according to the Schwartz theorem; (31) is due to the fact that $R_{ijmn}\alpha_{,i}\varphi_{,jmn} = R_{ijmn}(\alpha_{,i}\varphi_{,jmn} + \alpha_{,j}\varphi_{,imn})/2$ with $(\alpha_{,i}\varphi_{,jmn} + \alpha_{,j}\varphi_{,imn})$ being unaltered by permuting indices. Finally, (27) takes the following *equivalent* form

$$\begin{aligned} 0 = [\mathbb{R}\mathbb{S}(\mathbf{x})\mathbb{R}(\nabla \otimes \nabla)\varphi(\mathbf{x})]:(\nabla \otimes \nabla) + \Delta\alpha(\mathbf{x})\Delta\varphi(\mathbf{x}) \\ - [(\nabla \otimes \nabla)\alpha(\mathbf{x})]:[(\nabla \otimes \nabla)\varphi(\mathbf{x})], \end{aligned} \tag{27'}$$

where $\mathbf{x} \in \Omega$ and Δ is the Laplacian operator.

Some Particular Two-Dimensional Traction Boundary Value Problems

It is immediate from (27') that, if $\alpha(\mathbf{x})$ is an affine function of $\mathbf{x}$, (27') reduces to

$$0 = [\mathbb{R}\mathbb{S}(\mathbf{x})\mathbb{R}(\nabla \otimes \nabla)\varphi(\mathbf{x})]:(\nabla \otimes \nabla), \quad \mathbf{x} \in \Omega. \tag{32}$$

This implies that, if the inhomogeneity of the solid is such that the antisymmetric part $\mathbb{A}(\mathbf{x})$ of $\mathbb{C}(\mathbf{x})$ is affine with respect to $\mathbf{x}$, the solution to (P) is independent of $\mathbb{A}(\mathbf{x})$. More generally, even if the inhomogeneity of the solid is arbitrary, we can let $\mathbb{C}(\mathbf{x})$ undergo the following *affine shift:*

$$\mathbb{C}^*(\mathbf{x}) := \mathbb{C}(\mathbf{x}) + (\mathbf{a}.\mathbf{x} + b)\mathbb{R} \tag{33}$$

where the scalar b and vector $\mathbf{a} \in \mathcal{V}$ are constant, without changing the solution to (P) and hence the stress tensor field derived from it by (24). As a matter of fact, inserting (29) into (33) yields $\mathbb{C}^*(\mathbf{x}) = \mathbb{S}(\mathbf{x}) + [\alpha(\mathbf{x}) + \mathbf{a}.\mathbf{x} + b]\mathbb{R}$, so that

$$\mathbb{S}^*(\mathbf{x}) = \mathbb{S}(\mathbf{x}), \quad \mathbb{A}^*(\mathbf{x}) = \alpha^*(\mathbf{x})\mathbb{R}, \tag{34a}$$

$$\alpha^*(\mathbf{x}) = \alpha(\mathbf{x}) + \mathbf{a}.\mathbf{x} + b; \tag{34b}$$

then by noting that $\Delta\alpha^*(\mathbf{x}) = \Delta\alpha(\mathbf{x})$ and $(\nabla \otimes \nabla)\alpha^*(\mathbf{x}) = (\nabla \otimes \nabla)\alpha(\mathbf{x})$, we see that (27') is invariant under (33). Cherkaev et al. (1992) and Dundurs and Markenscoff (1993) were the first to show that the stress tensor field derived from the solution to (P) is unaffected by (33) with $\mathbf{a} = 0$ and $\mathbf{a} \neq 0$, respectively. This result, besides its own theoretical importance, has already been found to have a number of significant applications in the mechanics of composites (Thorpe and Jasiuk, 1992; Moran and Gosz, 1994). The alternative proof given above presents the advantage of allowing us to gain a deep insight into the result.

If the solid in question is *homogeneous,* then both $\alpha(\mathbf{x})$ and $\mathbb{S}(\mathbf{x})$ are independent of $\mathbf{x}$ and (27') can further be simplified into

$$(\mathbb{R}\mathbb{S}\mathbb{R})::(\nabla\otimes\nabla\otimes\nabla\otimes\nabla)\varphi(\mathbf{x}) = 0, \quad \mathbf{x}\in\Omega. \qquad (35)$$

It is physically sound to admit that $C_{1111} > 0$ and $C_{2222} > 0$. Thus, dividing (35) by C_{1111} gives

$$(\mathbb{R}\hat{\mathbb{S}}\mathbb{R})::(\nabla\otimes\nabla\otimes\nabla\otimes\nabla)\varphi(\mathbf{x}) = 0, \quad \mathbf{x}\in\Omega. \qquad (36)$$

Here the dimensionless tensor $\hat{\mathbb{S}} := \mathbb{S}/C_{1111}$ involves *at most* four constants, because $\mathbb{S}$ contains at most five constants and $\hat{S}_{1111} = S_{1111}/C_{1111} = 1$ in view of (16*a*). Consequently, *in the fully anisotropic case, the stress state of a linearly elastic homogeneous plane solid subjected to no body forces and to tractions on its boundary is dependent on four dimensionless parameters instead of the six elastic constants of* $\mathbb{C}$. However, remark that the strain tensor obtained by (23) continues depending on the latter.

The relation (6) can also be employed to simplify the field equation (27) or (27′) in several important cases. By (7) and the minor symmetries $\mathbb{C} = (\mathbf{1}\overline{\otimes}\mathbf{1})\mathbb{C} = \mathbb{C}(\mathbf{x})(\mathbf{1}\overline{\otimes}\mathbf{1})$, we have

$$\mathbb{R}\mathbb{C}\mathbb{R} = \mathbb{R}\mathbb{C}\mathbb{R}^T = (\mathbf{R}\underline{\otimes}\mathbf{R})\mathbb{C}(\mathbf{R}\underline{\otimes}\mathbf{R})^T. \qquad (37)$$

As $\mathbf{R}$ represents the right-angle rotation, (37) means that $\mathbb{R}\mathbb{C}\mathbb{R}$ in (27) or (27′) is nothing but $\mathbb{C}$ rotated through 90 deg. However, it has already been shown in He and Zheng (1996) that any two-dimensional elastic tensor $\mathbb{C}$ can be *only either fully anisotropic or orthotropic or square-symmetric or isotropic*. As a result, every two-dimensional elastic tensor $\mathbb{C}$, except the fully anisotropic one who has $\{\mathbf{1}, -\mathbf{1}\}$ as the symmetry group, is invariant under $\mathbf{R}$, i.e.,

$$\mathbb{R}\mathbb{C}\mathbb{R} = \mathbb{C}. \qquad (38)$$

Correspondingly, (27′) and (36) reduce to

$$0 = [\mathbb{S}(\mathbf{x})(\nabla\otimes\nabla)\varphi(\mathbf{x})]:(\nabla\otimes\nabla) + \Delta\alpha(\mathbf{x})\Delta\varphi(\mathbf{x})$$
$$- [(\nabla\otimes\nabla)\alpha(\mathbf{x})]:[(\nabla\otimes\nabla)\varphi(\mathbf{x})], \ \mathbf{x}\in\Omega; \qquad (39)$$

$$0 = \hat{\mathbb{S}}::(\nabla\otimes\nabla\otimes\nabla\otimes\nabla)\varphi(\mathbf{x}), \ \mathbf{x}\in\Omega. \qquad (40)$$

It is useful to write (40) in detail. According as the solid is isotropic, square-symmetric or orthotropic, (40) reads differently as

$$\varphi_{,1111} + \varphi_{,2222} + 2\varphi_{,1122} = 0, \qquad (41a)$$

$$\varphi_{,1111} + \varphi_{,2222} + 2\gamma\varphi_{,1122} = 0, \qquad (41b)$$

$$\varphi_{,1111} + \beta\varphi_{,2222} + 2\gamma\varphi_{,1122} = 0, \qquad (41c)$$

with

$$\beta = C_{2222}/C_{1111}, \quad \gamma = (C_{1122} + 2C_{1212})/C_{1111}.$$

Among (41*a*)–(41*c*), we recognize the usual biharmonic equation (41*a*). As neither (41*a*) nor (28) contains any material parameter, then the stresses associated with the solution (unique to within an affine function) of the traction boundary value problem of a plane isotropic homogeneous solid (with no body forces) are independent of the elastic constants. This result, known as Michell's theorem (see, e.g., Gurtin 1972), has recently been applied by Zheng and Hwang (1996) to the micromechanics of composite materials. As in the isotropic case, we can conclude from (41*b*)–(41*c*) together with (28) that *the stresses corresponding to the solution of the traction boundary value problem of a plane square-symmetric (orthotropic) homogeneous solid are dependent on only one (two) dimensionless elastic constant(s)*. This conclusion should also have applications in the micromechanics of (anisotropic) elastic composite materials.

References

Cherkaev, A. V., Lurie, K. A., and Milton, G. W., 1992, "Invariant Properties of the Stress in Plane Elasticity and Equivalence Classes of Composites," *Proc. R. Soc. Lond.*, Vol. A438, pp. 519–529.

Curnier, A., 1993, *Méthodes Numériques en Mécanique des Solides*, Presses Polytechniques et Universitaires Romandes, Lausanne, Switzerland.

Dundurs, J., and Markenscoff, X., 1993, "Invariance of Stresses under a Change in Elastic Compliances," *Proc. R. Soc. Lond.*, Vol. A443, pp. 289–300.

Gurtin, M. E., 1972, "The Linear Theory of Elasticity," *Handbuch der Physik*, Vol. VIa/2, Springer-Verlag, Berlin.

He, Q. C., and Zheng, Q. S., 1996, "On the Symmetries of 2D Elastic and Hyperelastic Tensors," *J. Elasticity*, Vol. 43, pp. 203–225.

Moran, B., and Gosz, M., 1994, "Stress Invariance in Plane Anisotropic Elasticity," *Modelling Simul. Mater. Eng.*, Vol. 2, pp. 677–688.

Novozhilov, V. V., 1961, *Theory of Elasticity*, Pergamon, Oxford, UK.

Spencer, A. J. M., 1970, "A Note on the Decomposition of Tensors into Traceless Symmetric Tensors," *Int. J. Egng. Sci.*, Vol. 8, pp. 475–481.

Thorpe, M. F., and Jasiuk, I., 1992, "New Results in the Theory of Elasticity for Two-Dimensional Composites," *Proc. R. Soc. Lond.*, Vol. A438, pp. 531–544.

Zheng, Q. S., and Hwang, K. C., 1997, "Two-Dimensional Elastic Compliances of Materials with Holes and Microcracks," *Proc. R. Soc. Lond*, Vol. A453, pp. 353–364.

Analysis of the Motion of a Frictional Elastic Ball Dropped on an Inclined Surface

S. V. Myagchilov[10,11] **and J. T. Jenkins**[10,11]

1 Introduction

In this paper we analyze plane motions of a frictional elastic sphere dropped on an inclined surface. We are interested in how sticking and sliding collisions occur as the bouncing proceeds. In particular, we are interested under what circumstances the collisions are eventually all sliding, all sticking, or exhibit intermittancy between sticking and sliding.

We introduce the following notation: σ is the diameter of the sphere, m is its mass, and I is the moment of inertia about its center, given for a homogeneous sphere by $I = m\sigma^2/10$. Prior to a collision, the sphere has translational velocity $\mathbf{v}$ and angular velocity ω; the corresponding post-collision quantities are denoted with hats. $\mathbf{J}$ is the impulse exerted by the wall upon the ball during impact, $\mathbf{n}$ is the unit normal to the wall directed upward, and $\mathbf{G}$ is the gravitational acceleration.

The velocities before and after a collision are related by

$$m(\hat{\mathbf{v}} - \mathbf{v}) = \mathbf{J}, \qquad (1)$$

and

$$(m\sigma^2/10)(\hat{\omega} - \omega) = -(\sigma/2)\mathbf{n}\times\mathbf{J}. \qquad (2)$$

In order to completely determine the impulse $\mathbf{J}$, we introduce the velocity $\mathbf{g}$ of the point of contact,

$$\mathbf{g} = \mathbf{v} - (\sigma/2)\omega\times\mathbf{n}, \qquad (3)$$

and note that $\mathbf{n}\cdot\mathbf{g} = \mathbf{n}\cdot\mathbf{v}$. We assume that the normal components of $\mathbf{g}$ before and after a collision are related through

$$\hat{\mathbf{g}}\cdot\mathbf{n} = -e(\mathbf{g}\cdot\mathbf{n}), \qquad (4)$$

where e is the coefficient of restitution in the normal direction.

[10] Theoretical and Applied Mechanics, Cornell University, 212 Kimball Hall, Ithaca, NY 14853.

[11] Mem. ASME.

Contributed by the Applied Mechanics Division of THE AMERICAN SOCIETY OF MECHANICAL ENGINEERS for publication in the ASME JOURNAL OF APPLIED MECHANICS. Manuscript received by the ASME Applied Mechanics Division, Jan. 31, 1996; final revision, March 6, 1997. Associate Technical Editor: L. T. Wheeler.

$$(\mathbb{R}\mathbb{S}\mathbb{R})::(\nabla \otimes \nabla \otimes \nabla \otimes \nabla)\varphi(\mathbf{x}) = 0, \quad \mathbf{x} \in \Omega. \quad (35)$$

It is physically sound to admit that $C_{1111} > 0$ and $C_{2222} > 0$. Thus, dividing (35) by C_{1111} gives

$$(\mathbb{R}\hat{\mathbb{S}}\mathbb{R})::(\nabla \otimes \nabla \otimes \nabla \otimes \nabla)\varphi(\mathbf{x}) = 0, \quad \mathbf{x} \in \Omega. \quad (36)$$

Here the dimensionless tensor $\hat{\mathbb{S}} := \mathbb{S}/C_{1111}$ involves *at most* four constants, because $\mathbb{S}$ contains at most five constants and $\hat{S}_{1111} = S_{1111}/C_{1111} = 1$ in view of (16*a*). Consequently, *in the fully anisotropic case, the stress state of a linearly elastic homogeneous plane solid subjected to no body forces and to tractions on its boundary is dependent on four dimensionless parameters instead of the six elastic constants of* $\mathbb{C}$. However, remark that the strain tensor obtained by (23) continues depending on the latter.

The relation (6) can also be employed to simplify the field equation (27) or (27′) in several important cases. By (7) and the minor symmetries $\mathbb{C} = (\mathbf{1} \bar{\otimes} \mathbf{1})\mathbb{C} = \mathbb{C}(\mathbf{x})(\mathbf{1} \bar{\otimes} \mathbf{1})$, we have

$$\mathbb{R}\mathbb{C}\mathbb{R} = \mathbb{R}\mathbb{C}\mathbb{R}^T = (\mathbf{R} \underset{=}{\otimes} \mathbf{R})\mathbb{C}(\mathbf{R} \underset{=}{\otimes} \mathbf{R})^T. \quad (37)$$

As $\mathbf{R}$ represents the right-angle rotation, (37) means that $\mathbb{R}\mathbb{C}\mathbb{R}$ in (27) or (27′) is nothing but $\mathbb{C}$ rotated through 90 deg. However, it has already been shown in He and Zheng (1996) that any two-dimensional elastic tensor $\mathbb{C}$ can be *only either fully anisotropic or orthotropic or square-symmetric or isotropic*. As a result, every two-dimensional elastic tensor $\mathbb{C}$, except the fully anisotropic one who has $\{\mathbf{1}, -\mathbf{1}\}$ as the symmetry group, is invariant under $\mathbf{R}$, i.e.,

$$\mathbb{R}\mathbb{C}\mathbb{R} = \mathbb{C}. \quad (38)$$

Correspondingly, (27′) and (36) reduce to

$$0 = [\mathbb{S}(\mathbf{x})(\nabla \otimes \nabla)\varphi(\mathbf{x})]:(\nabla \otimes \nabla) + \Delta\alpha(\mathbf{x})\Delta\varphi(\mathbf{x}) - [(\nabla \otimes \nabla)\alpha(\mathbf{x})]:[(\nabla \otimes \nabla)\varphi(\mathbf{x})], \ \mathbf{x} \in \Omega; \quad (39)$$

$$0 = \hat{\mathbb{S}}::(\nabla \otimes \nabla \otimes \nabla \otimes \nabla)\varphi(\mathbf{x}), \ \mathbf{x} \in \Omega. \quad (40)$$

It is useful to write (40) in detail. According as the solid is isotropic, square-symmetric or orthotropic, (40) reads differently as

$$\varphi_{,1111} + \varphi_{,2222} + 2\varphi_{,1122} = 0, \quad (41a)$$

$$\varphi_{,1111} + \varphi_{,2222} + 2\gamma\varphi_{,1122} = 0, \quad (41b)$$

$$\varphi_{,1111} + \beta\varphi_{,2222} + 2\gamma\varphi_{,1122} = 0, \quad (41c)$$

with

$$\beta = C_{2222}/C_{1111}, \quad \gamma = (C_{1122} + 2C_{1212})/C_{1111}.$$

Among (41*a*)–(41*c*), we recognize the usual biharmonic equation (41*a*). As neither (41*a*) nor (28) contains any material parameter, then the stresses associated with the solution (unique to within an affine function) of the traction boundary value problem of a plane isotropic homogeneous solid (with no body forces) are independent of the elastic constants. This result, known as Michell's theorem (see, e.g., Gurtin 1972), has recently been applied by Zheng and Hwang (1996) to the micromechanics of composite materials. As in the isotropic case, we can conclude from (41*b*)–(41*c*) together with (28) that *the stresses corresponding to the solution of the traction boundary value problem of a plane square-symmetric (orthotropic) homogeneous solid are dependent on only one (two) dimensionless elastic constant(s)*. This conclusion should also have applications in the micromechanics of (anisotropic) elastic composite materials.

References

Cherkaev, A. V., Lurie, K. A., and Milton, G. W., 1992, "Invariant Properties of the Stress in Plane Elasticity and Equivalence Classes of Composites," *Proc. R. Soc. Lond.*, Vol. A438, pp. 519–529.

Curnier, A., 1993, *Méthodes Numériques en Mécanique des Solides*, Presses Polytechniques et Universitaires Romandes, Lausanne, Switzerland.

Dundurs, J., and Markenscoff, X., 1993, "Invariance of Stresses under a Change in Elastic Compliances," *Proc. R. Soc. Lond.*, Vol. A443, pp. 289–300.

Gurtin, M. E., 1972, "The Linear Theory of Elasticity," *Handbuch der Physik*, Vol. VIa/2, Springer-Verlag, Berlin.

He, Q. C., and Zheng, Q. S., 1996, "On the Symmetries of 2D Elastic and Hyperelastic Tensors," *J. Elasticity*, Vol. 43, pp. 203–225.

Moran, B., and Gosz, M., 1994, "Stress Invariance in Plane Anisotropic Elasticity," *Modelling Simul. Mater. Eng.*, Vol. 2, pp. 677–688.

Novozhilov, V. V., 1961, *Theory of Elasticity*, Pergamon, Oxford, UK.

Spencer, A. J. M., 1970, "A Note on the Decomposition of Tensors into Traceless Symmetric Tensors," *Int. J. Egng. Sci.*, Vol. 8, pp. 475–481.

Thorpe, M. F., and Jasiuk, I., 1992, "New Results in the Theory of Elasticity for Two-Dimensional Composites," *Proc. R. Soc. Lond.*, Vol. A438, pp. 531–544.

Zheng, Q. S., and Hwang, K. C., 1997, "Two-Dimensional Elastic Compliances of Materials with Holes and Microcracks," *Proc. R. Soc. Lond*, Vol. A453, pp. 353–364.

Analysis of the Motion of a Frictional Elastic Ball Dropped on an Inclined Surface

S. V. Myagchilov[10,11] **and J. T. Jenkins**[10,11]

1 Introduction

In this paper we analyze plane motions of a frictional elastic sphere dropped on an inclined surface. We are interested in how sticking and sliding collisions occur as the bouncing proceeds. In particular, we are interested under what circumstances the collisions are eventually all sliding, all sticking, or exhibit intermittancy between sticking and sliding.

We introduce the following notation: σ is the diameter of the sphere, m is its mass, and I is the moment of inertia about its center, given for a homogeneous sphere by $I = m\sigma^2/10$. Prior to a collision, the sphere has translational velocity $\mathbf{v}$ and angular velocity ω; the corresponding post-collision quantities are denoted with hats. $\mathbf{J}$ is the impulse exerted by the wall upon the ball during impact, $\mathbf{n}$ is the unit normal to the wall directed upward, and $\mathbf{G}$ is the gravitational acceleration.

The velocities before and after a collision are related by

$$m(\hat{\mathbf{v}} - \mathbf{v}) = \mathbf{J}, \quad (1)$$

and

$$(m\sigma^2/10)(\hat{\omega} - \omega) = -(\sigma/2)\mathbf{n} \times \mathbf{J}. \quad (2)$$

In order to completely determine the impulse $\mathbf{J}$, we introduce the velocity $\mathbf{g}$ of the point of contact,

$$\mathbf{g} = \mathbf{v} - (\sigma/2)\omega \times \mathbf{n}, \quad (3)$$

and note that $\mathbf{n}\cdot\mathbf{g} = \mathbf{n}\cdot\mathbf{v}$. We assume that the normal components of $\mathbf{g}$ before and after a collision are related through

$$\hat{\mathbf{g}}\cdot\mathbf{n} = -e(\mathbf{g}\cdot\mathbf{n}), \quad (4)$$

where e is the coefficient of restitution in the normal direction.

[10] Theoretical and Applied Mechanics, Cornell University, 212 Kimball Hall, Ithaca, NY 14853.

[11] Mem. ASME.

Contributed by the Applied Mechanics Division of The American Society of Mechanical Engineers for publication in the ASME Journal of Applied Mechanics. Manuscript received by the ASME Applied Mechanics Division, Jan. 31, 1996; final revision, March 6, 1997. Associate Technical Editor: L. T. Wheeler.

When treating the tangential component of velocity two types of collisions must be distinguished: a sticking collision, in which the point of contact is brought to rest during the collision; and a sliding collision, in which the point of contact slides thoughout the collision. In a sticking collision, the tangential components of $\mathbf{g}$ are assumed to be related by a constant tangential coefficient of restitution β_0:

$$(\mathbf{n} \times \hat{\mathbf{g}}) = -\beta_0(\mathbf{n} \times \mathbf{g}), \tag{5}$$

where $0 \leq \beta_0 \leq 1$. In a sliding collision, the sliding is assumed to be resisted by Coulomb friction and the tangential and normal components of the impulse are related by the coefficient of friction μ:

$$|\mathbf{n} \times \mathbf{J}| = \mu(\mathbf{n} \cdot \mathbf{J}), \tag{6}$$

where $\mu \geq 0$.

The parameter that determines whether a sticking or sliding collision occurs is the angle γ between $\mathbf{g}$ and $\mathbf{n}$:

$$\cot \gamma \equiv (\mathbf{n} \cdot \mathbf{g})/|\mathbf{n} \times \mathbf{g}|. \tag{7}$$

When γ is greater than critical value γ_0 given by

$$\tan \gamma_0 = -\frac{7\mu(1+e)}{2(1+\beta_0)}, \tag{8}$$

we have sticking collision; otherwise, we have sliding collision. The angle γ_0 is between $\pi/2$ and π, so the tangent of γ_0 is negative.

Note that for a sliding collision, the collisional impulse is

$$\mathbf{J}^{(1)} = -m(1+e)(\mathbf{n} \cdot \mathbf{g})\mathbf{n} + \mu m(1+e) \times \cot \gamma[\mathbf{g} - (\mathbf{n} \cdot \mathbf{g})\mathbf{n}], \tag{9}$$

and the change of $\mathbf{g}$ is

$$\hat{\mathbf{g}} = \mathbf{g} - (1+e)(\mathbf{n} \cdot \mathbf{g})\mathbf{n} + \mu_0 \cot \gamma[\mathbf{g} - (\mathbf{n} \cdot \mathbf{g})\mathbf{n}], \tag{10}$$

where

$$\mu_0 \equiv (7/2)(1+e)\mu. \tag{11}$$

In a sticking collision the impulse is

$$\mathbf{J}^{(2)} = -m(1+e)(\mathbf{n} \cdot \mathbf{g})\mathbf{n} - (2m/7)(1+\beta_0)[\mathbf{g} - (\mathbf{n} \cdot \mathbf{g})\mathbf{n}], \tag{12}$$

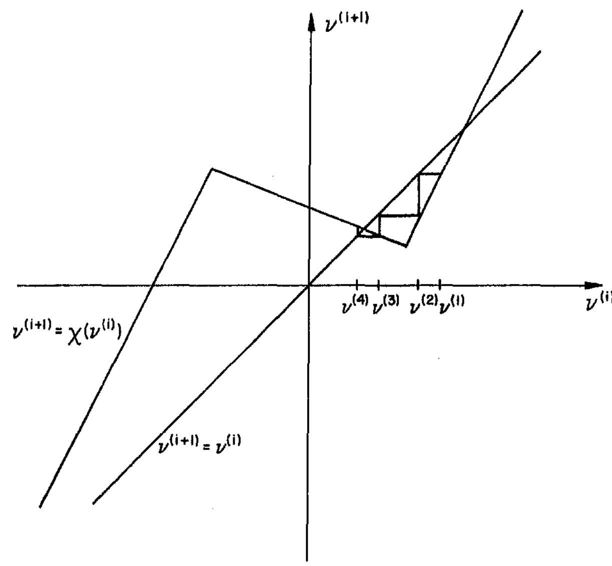

Fig. 2 Iterative mapping

and the change of $\mathbf{g}$ is

$$\hat{\mathbf{g}} = \mathbf{g} - (1+e)(\mathbf{n} \cdot \mathbf{g})\mathbf{n} - (1+\beta_0)[\mathbf{g} - (\mathbf{n} \cdot \mathbf{g})\mathbf{n}]. \tag{13}$$

We exploit the fact that after each bounce the normal component g_y is diminished by the factor $e < 1$. More precisely, for the ith bounce we have $\hat{g}_y^{(i)} = -eg_y^{(i)}$, where superscripts in parantheses indicate the bounce number. But we also have that $\hat{g}_y^{(i-1)} = -g_y^{(i)}$. Hence, $\hat{g}_y^{(i)} = e\hat{g}_y^{(i-1)}$. Analogously $g_y^{(i)} = eg_y^{(i-1)}$. We see that both $g_y^{(i)}$ and $\hat{g}_y^{(i)}$ form geometric sequences. Further, it is convenient for us to introduce normalized vector $\mathbf{f}^{(i)}$:

$$\mathbf{f}^{(i)} \equiv \frac{1}{e^i}\mathbf{g}^{(i)}. \tag{14}$$

If we assume that the ith collision is sticking, then $\hat{g}_x^{(i)} = -\beta g_x^{(i)}$. In this event, from the dynamics of the parabolic trajectory, g_x before $i+1$ collision is

$$g_x^{(i+1)} = -\beta g_x^{(i)} + \Delta g_x^{(i+1)}, \tag{15}$$

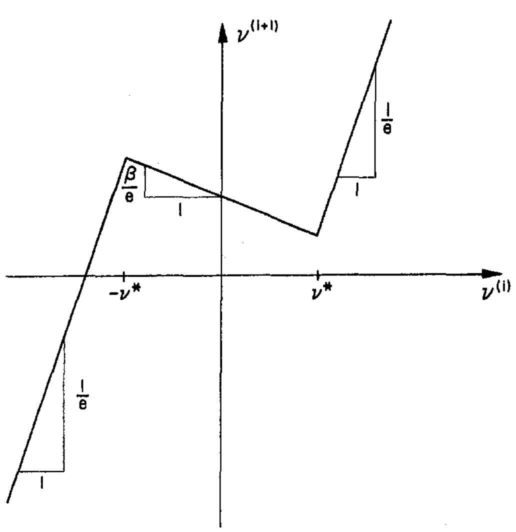

Fig. 1 Dependence $\nu^{(i+1)} = \chi(\nu^i)$

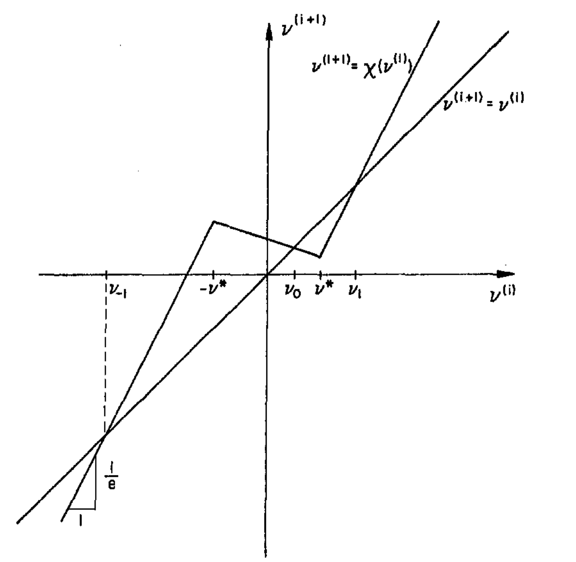

Fig. 3 Case $e < 1$

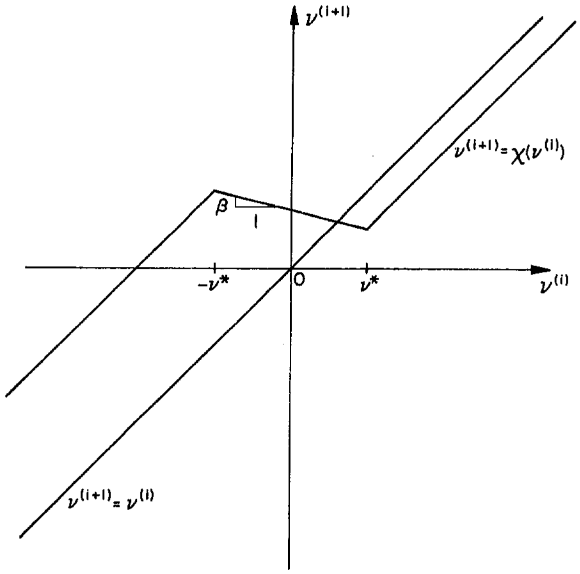

Fig. 4 Case e = 1

where

$$\Delta g_x^{(i+1)} \equiv \frac{2|g_y^{(i+1)}|}{G\cos\alpha} G \sin\alpha = 2|g_y^{(i+1)}| \tan\alpha. \quad (16)$$

From (14)–(16) we obtain the following equation:

$$f_x^{(i+1)} = -\frac{\beta}{e} f_x^{(i)} + 2|f_y^{(i+1)}| \tan\alpha. \quad (17)$$

Because $f_y^{(i+1)} = f_y^{(i)}$ for all i, from (17),

$$\frac{f_x^{(i+1)}}{|f_y^{(i+1)}|} = -\frac{\beta}{e}\frac{f_x^{(i)}}{|f_y^{(i)}|} + 2\tan\alpha. \quad (18)$$

We introduce

$$\nu^{(i)} \equiv \frac{f_x^{(i)}}{|f_y^{(i)}|} = \frac{g_x^{(i)}}{|g_y^{(i)}|}, \quad (19)$$

then (17) becomes

$$\nu^{(i+1)} = -\frac{\beta}{e}\nu^{(i)} + 2\tan\alpha. \quad (20)$$

We recall that Eq. (20) is valid only for sticking collision, for which $|\nu^{(i)}| < \nu^* \equiv -\tan\gamma_0$.

When there is a sliding, $g_x^{(i+1)}$ is a linear function of $g_x^{(i)}$ with slope one. It follows from this that during sliding collision, J_x depends only upon J_y and the collision parameters and does not depend on the relative velocity of the contact surfaces. Then $f_x^{(i+1)}$ is a linear function of $f_x^{(i)}$ with slope e^{-1}; and, finally, $\nu^{(i+1)}$ is a linear function of $\nu^{(i)}$ with slope e^{-1}. This, together with condition that the dependence between $\nu^{(i+1)}$ and $\nu^{(i)}$ should be continuous at the transition between sticking and sliding, permit us to obtain the function $\nu^{(i+1)} = \chi(\nu^{(i)})$ for $-\infty < \nu^{(i)} < +\infty$. The plot of $\chi(\nu^{(i)})$ is shown on Fig. 1.

Because $\nu^{(2)} = \chi(\nu^{(1)})$, $\nu^{(3)} = \chi(\nu^{(2)}) = \chi(\chi(\nu^{(1)}))$, etc., we see that we have an iterative mapping for determining $\nu^{(i+1)}$. This iterative mapping can be represented graphically by plotting the auxilliary curve $\nu^{(i+1)} = \nu^{(i)}$ as shown on Fig. 2. The resulting behavior of the ball depends significantly upon whether e is less than one or equal to one.

We consider plots $\nu^{(i+1)} = \chi(\nu^{(i)})$ for case $e < 1$ as shown on Fig. 3 and for case $e = 1$ as shown on Fig. 4 and consider intersection of those plots with line $\nu^{(i+1)} = \nu^{(i)}$. We see that when $e < 1$, we have up to three intersections of the curves $\nu^{(i+1)} = \chi(\nu^{(i)})$ and $\nu^{(i+1)} = \nu^{(i)}$. When $e = 1$ we have, in general, only one intersection. The point of intersection is a steady point of the iterative mapping. Physically, $\nu^{(i)} = \tilde{\nu}$, where $\tilde{\nu}$ is such a steady point, then in all subsequent bounces the ball will strike the wall at the same angle. It also means is that if $\tilde{\nu}$ is a sticking collision region then all subsequent collisions will be sticking, and if $\tilde{\nu}$ is within a sliding collision, then all subsequent collisions are sliding. We shall consider the cases $e < 1$ and $e = 1$ separately.

2 Perfectly Elastic Wall ($e = 1$)

By examining the graphs on Fig. 4, we conclude that a steady point exists when $|\alpha| < \alpha_{cr}$, where

$$\tan\alpha_{cr} = -\tan\gamma_0 \frac{\beta + e}{2e}$$
$$= \frac{7\mu(1+e)(\beta+e)}{4e(1+\beta)} \equiv \frac{7\mu}{2}. \quad (21)$$

Because β is always less than one (i.e., $\beta/e \le 1$), this steady point is also stable. Because this steady stable point is in a sticking region, it doesn't matter what $\nu^{(1)}$ is; after several collisions, which could be in sliding region, we will eventually end up in a sticking region.

When $|\alpha| > \alpha_{cr}$, there is no steady point. It doesn't matter where we start, we will eventually end up in a sliding mode. In this case $\nu^{(k)} \to \infty$ as $k \to \infty$.

3 Inelastic Wall ($e < 1$)

This is the case for all real balls. If $|\alpha| < \alpha_{cr}$, where α_{cr} is given by (21) with $e \ne 1$, we have three points of intersection, as it is shown on Fig. 3. We denote these points by ν_{-1}, ν_0, and ν_1. The steady points ν_{-1} and ν_1 are unstable, while the stability of ν_0 depends upon the magnitude of β/e. If $\beta/e > 1$, then ν_0 is unstable; if $\beta/e \le 1$ then ν_0 is stable.

If we start in the region $\nu^{(1)} < \nu_{-1}$ or $\nu^{(1)} > \nu_1$, our iterations will diverge, which physically means that we get all sliding collisions as $k \to \infty$. If we begin in the region $\nu_{-1} < \nu^{(1)} < \nu_1$ then the subsequent behavior depends on $\chi(\nu^{(i)})$. If $\chi(\nu_{-1}) < \chi(\nu^*)$ and $\chi(-\nu^*) < \chi(\nu_1)$, then we will never get out of this region. For all k we will have $\nu_{-1} < \nu^{(k)} < \nu_1$. The behavior in this case depends upon the stability of ν_0. If ν_0 is stable, then eventually we will obtain $\nu^{(k)} \to \nu_0$ as $k \to \infty$. Because ν_0 is in a sticking region, then eventually all collisions will be sticking as $k \to \infty$, although in this case there is some possibility of intermittance between sliding and sticking collisions in the beginning. If ν_0 is unstable and if $\nu_{-1} < \nu^{(1)} < \nu_1$ and $\nu^{(1)} \ne \nu_0$, chaos will occur in this iterative mapping. In this case we will have a chaotic intermittance between sticking and sliding collisions.

Acknowledgment

This research was supported by the Pittsburgh Energy Technology center of the Department of Energy as part of the Granular Flow Advanced Research Objective.

References

Jenkins, J. T., 1992, "Boundary Conditions for Rapid Granular Flows: Flat, Frictional Walls," ASME JOURNAL OF APPLIED MECHANICS, Vol. 59, pp. 120–127.

Eigenvalue and Eigenvector Determination for Damped Gyroscopic Systems

D. P. Malone[12,14,16], D. L. Cronin[13,14,15,17], and T. W. Randolph[12,14]

1 Introduction

Cronin (1990) developed an efficient perturbation-based series method to solve the eigenproblem for dynamic systems having a nonproportional damping matrix. To illustrate the general applicability of this method, Peres-da-Silva, Cronin, and Randolph (1995) applied it to determine the eigenvalues and eigenvectors of a damped gyroscopic system. Although the method was shown to work for gyroscopic systems, its usefulness is limited because it requires that the gyroscopic terms are small.

In the present note we derive and examine a new method that uses the undamped gyroscopic system as the unperturbed system. The accuracy and convergence of the new method are independent of the size of the gyroscopic terms. Furthermore, the method permits a numerically efficient solution of the eigenproblem for damped gyroscopic systems because it can use the approach of Meirovitch (1974) to solve the eigenproblem for the unperturbed system.

2 Method

The equation for the free vibration of an nth-order damped gyroscopic system is

$$[M]\{\ddot{x}\} + [D]\{\dot{x}\} + [K]\{x\} = \{0\} \tag{1}$$

where $[M]$ and $[K]$ are real and symmetric $(n \times n)$ matrices, and where

$$[D] = [G] + [C]. \tag{2}$$

The $(n \times n)$ matrices $[G]$ and $[C]$ are real. The gyroscopic matrix $[G]$ is skew symmetric, and the damping matrix $[C]$ is symmetric. It is assumed here that the mass matrix $[M]$ and the stiffness matrix $[K]$ are positive definite. The $(n \times 1)$ vector $\{x\}$ represents the unknown displacements, and $\{\dot{x}\}$ and $\{\ddot{x}\}$ are the vectors of unknown velocities and accelerations, respectively.

When a solution to Eq. (1) is assumed to have the form $\{x\} = \{u\}e^{st}$, the following algebraic problem arises:

$$(s^2[M] + s[D] + [K])\{u\} = \{0\}. \tag{3}$$

The problem defined by Eq. (3) belongs to a class described by Lancaster (1966) as the "latent root problem." Solutions to Eq. (3) can be obtained by reformulating the problem as an eigenproblem in a space having twice the dimension of the space of the original problem. To distinguish between these two formulations, we shall use the terms "latent root" or "latent vector" when referring to the solutions to Eq. (3) in n-space, and the terms "eigenvalue" or "eigenvector" when referring to the solutions to the $2n$-space formulation.

Let $[\Phi]$ be the matrix consisting of the latent vectors of Eq. (3) for the case $[D] = [0]$, and assume that it is normalized so that

$$[\Phi]^T[M][\Phi] = [I] \tag{4}$$

where $[I]$ denotes the identity matrix. Using the transformation $\{u\} = [\Phi]\{v\}$ and premultiplying by $[\Phi]^T$ result in the new latent root problem

$$(s^2[I] + s[\Gamma] + [\Lambda])\{v\} = \{0\} \tag{5}$$

where $[\Lambda]$ is a diagonal matrix: $[\Lambda] = \mathrm{diag}\,(\omega_1^2, \ldots, \omega_n^2)$. In this formulation, the matrix $[\Gamma]$ contains the transformed gyroscopic and damping terms

$$[\Gamma] = [\Phi]^T[D][\Phi] = [\Phi]^T([G] + [C])[\Phi]. \tag{6}$$

The matrix $[\Gamma]$ contains both gyroscopic and damping terms (see Eq. (6)). We write $[\Gamma]$ as

$$[\Gamma] = [\Gamma_0] + \epsilon[\Gamma_1] \tag{7}$$

where

$$[\Gamma_0] = [\Phi]^T[G][\Phi] \quad \text{and} \quad \epsilon[\Gamma_1] = [\Phi]^T[C][\Phi].$$

Here, $[\Gamma_0]$ is a real and skew symmetric, $\epsilon[\Gamma_1]$ is real and symmetric, and ϵ is our perturbation quantity. In this manner, we analyze Eq. (5) by viewing it as a perturbation of the system

$$(s^2[I] + s[\Gamma_0] + [\Lambda])\{v\} = \{0\}. \tag{8}$$

We wish to represent the jth latent root and latent vector of Eq. (5) using power series in ϵ

$$s_j = s_j(\epsilon) = \sum_{i=0}^{\infty} s_{ji}\epsilon^i \tag{9}$$

and

$$\{v_j\} = \{v_j(\epsilon)\} = \sum_{i=0}^{\infty} \{v_{ji}\}\epsilon^i. \tag{10}$$

Substituting Eqs. (7), (9), and (10) into Eq. (8) and manipulating lead to the equation

$$\sum_{i=0}^{\infty} \{B_{ji}\}\epsilon^i = \{0\} \tag{11}$$

where

$$\{B_{ji}\} = [A_{j0}]\{v_{ji}\} - \{\beta_{ji}\}, \quad i = 0, 1, \ldots \tag{12}$$

and where we have used the notation

$$[A_{j0}] = s_{j0}^2[I] + s_{j0}[\Gamma_0] + [\Lambda]$$

and

$$\{\beta_{j0}\} = \{0\}$$

$$\{\beta_{ji}\} = -s_{ji}(2s_{j0}[I] + [\Gamma_0])\{v_{j0}\} + \{\gamma_{ji}\}, \quad i = 1, 2, \ldots$$

where

$$\{\gamma_{ji}\} = -\sum_{l=1}^{i-1} s_{jl}s_{j,i-l}\{v_{j0}\} - [\Gamma_0]\sum_{l=1}^{i-1} s_{j,i-l}\{v_{jl}\} - [\Gamma_1]\sum_{l=1}^{i} s_{j,i-l}\{v_{j,l-1}\} - \sum_{l=1}^{i-1} b_{j,i-l}\{v_{jl}\}$$

---

[12] Department of Mathematics and Statistics.

[13] Department of Mechanical and Aerospace Engineering and Engineering Mechanics.

[14] University of Missouri, Rolla, MO 65409.

[15] Author for Correspondence. 130 Mechanical Engineering, University of Missouri-Rolla, 1870 Miner Circle, Rolla, MO 65409-0050.

[16] Assoc. Mem. ASME.

[17] Mem. ASME.

Contributed by the Applied Mechanics Division of THE AMERICAN SOCIETY OF MECHANICAL ENGINEERS for publication in the ASME JOURNAL OF APPLIED MECHANICS. Manuscript received by the ASME Applied Mechanics Division, June 6, 1996; final revision, Jan. 8, 1997. Associate Technical Editor: W. K. Liu.

and where the quantity b_{jl} is

$$b_{jl} = \sum_{m=0}^{l} s_{jm} s_{j,l-m}. \qquad (13)$$

If Eq. (11) holds for all ϵ in the interval of convergence, then $\{B_{ji}\} = \{0\}$ for all $i = 0, 1, \ldots$. Or, in view of Eq. (12),

$$[A_{j0}]\{v_{ji}\} = \{\beta_{ji}\}, \quad \text{for} \quad i = 0, 1, \ldots. \qquad (14)$$

For $i = 0$, Eq. (14) corresponds to the unperturbed equation, Eq. (8), whose latent roots and latent vectors are given, respectively, by s_{j0} and $\{v_{j0}\}, j = 1, \ldots, n$. This is the type of system for which Meirovitch proposed an efficient solution method. Therefore, it will be assumed that s_{j0} and $\{v_{j0}\}, j = 1, \ldots, n$, have been determined efficiently and at a low cost, and are available as needed.

We now turn to the problem of computing s_{ji} and $\{v_{ji}\}$, $i > 0$, in Eqs. (9) and (10). For $j = 1, \ldots, n$, we note that the rank of $[A_{j0}]$ is $n - 1$, and we note that $\{v_{j0}\}$ is the eigenvector of $[A_{j0}]$ corresponding to its eigenvalue $\lambda = 0$: $[A_{j0}]\{v_{j0}\} = \{0\}$. Since $[A_{j0}]$ is hermitian, it follows that $\{v_{j0}\}$ (being in the null space of $[A_{j0}]$) is orthogonal to the range of $[A_{j0}]$. Therefore

$$\{v_{j0}\}^*\{\beta_{ji}\} = \{v_{j0}\}^*[A_{j0}]\{v_{ji}\} = 0. \qquad (15)$$

The notation $[M]^*$ is used here and in the following to denote the conjugate transpose of any $m \times n$ matrix $[M]$.

Using the property described in Eq. (15) with the definition of $\{\beta_{ji}\}$, along with the observation that $\{v_{j0}\}^*[\Gamma_0]\{v_{j0}\} = 0$, we may write the ith term in the series for s_j as

$$s_{ji} = \frac{\{v_{j0}\}^*\{\gamma_{ji}\}}{2s_{j0}\|v_{j0}\|}. \qquad (16)$$

Solving Eq. (14) for $\{v_{ji}\}$ is straightforward. Indeed, since $[A_{j0}]$ is hermitian and of rank $n - 1$, a basis may be chosen of the form $\mathcal{B} = (\{v_{j0}\}, \{e_{j1}\}, \ldots, \{e_{j(n-1)}\})$ where $(\{e_{j1}\}, \ldots, \{e_{j(n-1)}\})$ forms a basis of the range of $[A_{j0}]$, and $\{v_{j0}\}$—a basis for the null space of $[A_{j0}]$—is orthogonal to each of these vectors. Since

$$\{v_j(\epsilon)\} - \{v_{j0}\} = \sum_{i=1}^{\infty} \{v_{ji}\}\epsilon^i$$

is in the range of $[A_{j0}]$, this vector can be expressed, relative to $\mathcal{B}$, as

$$\begin{Bmatrix} 0 \\ v_j^1(\epsilon) \\ \vdots \\ v_j^n(\epsilon) \end{Bmatrix}$$

for some scaler functions $v_j^1(\epsilon), \ldots, v_j^n(\epsilon)$. By uniqueness of the power series representation, it follows that each term in the series $\sum_{i=1}^{\infty} \{v_{ji}\}\epsilon^i$ is a vector in the range of $[A_{j0}]$. Since the restriction of $[A_{j0}]$ to its range is invertible, Eq. (14) can be solved uniquely and simply for $\{v_{ji}\}$.

3 Convergence

Having found explicitly the terms in the series, Eqs. (9) and (10), that represent the latent roots and latent vectors for the system described by Eq. (5), we wish to determine the conditions under which these series converge. To do this, we follow the technique used in Peres-da-Silva et al. and reformulate the system as a special eigenproblem in $2n$-space. We then obtain a convergence condition based entirely on the properties of $[\Gamma_1]$, defined in and below Eq. (7), and the spacing between the latent roots of Eq. (8).

Mimicking steps used in Peres-da-Silva et al., we rewrite Eq. (3) as

$$s\begin{bmatrix} I & 0 \\ 0 & \Lambda \end{bmatrix}\begin{Bmatrix} su \\ u \end{Bmatrix} + \begin{bmatrix} \Gamma & \Lambda \\ -\Lambda & 0 \end{bmatrix}\begin{Bmatrix} su \\ u \end{Bmatrix} = \begin{Bmatrix} 0 \\ 0 \end{Bmatrix}. \qquad (17)$$

Premultiplying Eq. (17) by

$$[H] = \begin{bmatrix} I & 0 \\ 0 & \Omega^{-1} \end{bmatrix}$$

where $[\Omega] = \text{diag}\,(\omega_1, \ldots, \omega_n)$, and using the change of variable

$$\begin{Bmatrix} su \\ u \end{Bmatrix} = [H]\{z\},$$

we obtain the special eigenvalue problem

$$\begin{bmatrix} -\Gamma & -\Omega \\ \Omega & 0 \end{bmatrix}\{z\} = s\{z\}. \qquad (18)$$

Using the decomposition $[\Gamma] = [\Gamma_0] + \epsilon[\Gamma_1]$ of Eq. (7), we may write

$$([T_0] + \epsilon[T_1])\{z\} = s\{z\} \qquad (19)$$

where

$$[T_0] = \begin{bmatrix} -\Gamma_0 & -\Omega \\ \Omega & 0 \end{bmatrix} \quad \text{and} \quad [T_1] = \begin{bmatrix} -\Gamma_1 & 0 \\ 0 & 0 \end{bmatrix}.$$

Here $[T_0]$ is real, skew symmetric and hence normal: $[T_0]^*[T_0] = [T_0][T_0]^*$. It follows from Theorem 3.9 of Kato (1982) that the perturbation series for the jth eigenvalue and eigenvector of Eq. (19) will converge provided

$$\|\epsilon T_1\| = \|\epsilon \Gamma_1\| < \frac{d_j}{2}$$

where d_j denotes the distance between the jth eigenvalue of $[T_0]$ and its closest neighbor.

In this note, if $[M]$ is an $n \times n$ matrix, then $\|M\|$ denotes the operator norm: $\|M\| = \max\{\|[M]\{v\}\| : \|\{v\}\| = 1\}$.

The convergence of these series implies the convergence of the latent root and latent vector series given in Eqs. (9) and (10), respectively, and so a radius of convergence for these series will be at least $|\epsilon|$, where ϵ satisfies

$$|\epsilon| < \frac{d_j}{2\|\Gamma_1\|}. \qquad (20)$$

4 Example

Meirovitch and Ryland (1979) worked with the following example; it was used subsequently by Peres-da-Silva et al. to illustrate the behavior of their series method

$$\begin{bmatrix} 1 & 0 \\ 0 & 1 \end{bmatrix}\{\ddot{x}\} + \left(\begin{bmatrix} 0 & -.2 \\ .2 & 0 \end{bmatrix} + \begin{bmatrix} .01 & 0 \\ 0 & 0 \end{bmatrix}\right)\{\dot{x}\} + \begin{bmatrix} 2 & 0 \\ 0 & 4 \end{bmatrix}\{x\} = \{0\}.$$

The gyroscopic matrix is

$$[G] = \begin{bmatrix} 0 & -.2 \\ .2 & 0 \end{bmatrix}$$

and the damping matrix is

$$[C] = \begin{bmatrix} .01 & 0 \\ 0 & 0 \end{bmatrix}.$$

For this system, the combined damping and gyroscopic matrix in the transformed space employed in this note and in Peres-da-Silva et al. is

$$[\Gamma] = \begin{bmatrix} .01 & -.2 \\ .2 & 0 \end{bmatrix}.$$

The L_1 and L_∞ norm of $[\Gamma]$ are both 0.21, and the natural frequencies of the unperturbed system are

$$\omega_1 = \sqrt{2} \quad \omega_2 = 2.$$

The condition given in Eq. (20) shows that the series of Peres-da-Silva et al. will converge for both latent roots and latent vectors provided that

$$|\epsilon| < \frac{d_j}{2\|\Gamma_1\|} = \frac{|\sqrt{2} - 2|}{(2)(.21)} \doteq 1.395.$$

As noted in Peres-da-Silva et al., when the exact latent roots of this system are calculated and compared to the approximations obtained from summing the first few terms of the series they derived, one finds that 12 terms are needed to achieve six decimal places of accuracy.

Reformulating the problem and using the series derived in this note result in a more efficient technique. Only two terms of these series are needed to achieve six decimal places of accuracy. Moreover, since $[\Gamma_1] = [C]$ has norm 0.01, and since the eigenvalues of $[T_0]$ are $\pm 1.40054i$ and $\pm 2.01953i$, the series will converge for both latent roots and latent vectors provided

$$|\epsilon| < \frac{d_j}{2\|\Gamma_1\|} = \frac{|1.40054 - 2.01953|}{(2)(0.01)} \doteq 30.95.$$

The larger radius of convergence is consistent with the improved convergence of the series.

5 Conclusion

Developed in this note is a series method for solving the latent roots/eigenproblem for generally damped gyroscopic systems. This method differs from that presented in Peres-da-Silva et al. in that the undamped gyroscopic system is the unperturbed system. Since both methods are furnished with a convergence test, it is straightforward to demonstrate that the new method offers the advantage of faster computation and the capability for the analysis of a wider range of physical systems. In particular, interesting gyroscopic systems—systems for which gyroscopic terms are not small—may be analyzed by this method.

With the exception of the eigenanalysis of the unperturbed system, which must be performed in $2n$-space—efficiently, however, thanks to Meirovitch—the method described in this note is worked in n-space, and it is, as a consequence, potentially low in cost.

As was pointed out in Peres-da-Silva et al., this approach to eigenanalysis has the particular advantage that the convergence criterion may be determined a priori for each latent root and latent vector, and that the decision can be made, based upon its value, whether there is a need to proceed further with the analysis for that latent pair, or whether the unperturbed latent root and latent vector are of sufficient accuracy. This capability suggests the possibility for a considerable savings in the cost of analysis.

References

Cronin, D. L., 1990, "Eigenvalue and Eigenvector Determination for Nonclassically Damped Dynamic Systems," *Computers and Structures*, Vol. 36, No. 1, pp. 133–138.

Kato, T., 1982, *A Short Introduction to Perturbation Theory for Linear Operators*, Springer-Verlag, New York.

Lancaster, P., 1966, *Lambda-matrices and Vibrating Systems*, Pergamon Press, New York.

Meirovitch, L., 1974, "A New Method of Solution of the Eigenvalue Problem for Gyroscopic Systems," *AIAA Journal*, Vol. 12, No. 10.

Meirovitch, L., and Ryland, G., II, 1979, "Response of Slightly Damped Gyroscopic Systems," *Journal of Sound and Vibration*, Vol. 67, No. 1, pp. 1–19.

Peres-da-Silva, S. S., Cronin, D. L., and Randolph, T. W., 1995, "Computation of Eigenvalues and Eigenvectors of Nonclassically Damped Systems," *Computers and Structures*, Vol. 57, No. 5, pp. 883–891.

Linear Systems Excited by Polynomials of Filtered Poisson Pulses

M. Di Paola[18]

The stochastic differential equations for quasi-linear systems excited by parametric non-normal Poisson white noise are derived. Then it is shown that the class of memoryless transformation of filtered non-normal delta correlated process can be reduced, by means of some transformation, to quasi-linear systems. The latter, being excited by parametric excitations, are first converted into Itô stochastic differential equations, by adding the hierarchy of corrective terms which account for the non-normality of the input, then by applying the Itô differential rule, the moment equations have been derived. It is shown that the moment equations constitute a linear finite set of differential equation that can be exactly solved.

1 Introduction

The study of mechanical and structural system under non-normal stochastic loads has become very popular in recent years. This is due to the fact that many excitations acting on the structures, such as moving loads on the bridges, quadratic drag terms in fluid mechanics, etc., show significant non-normal characteristics.

Nonlinear systems loaded by both external and parametric normal white noise excitation can be treated by means of the application of the Itô stochastic calculus (1951) which provides an easy procedure for deriving the differential equations in terms of moment or in terms of the probability density function (Arnold, 1973; Ibrahim, 1985; Gardiner, 1985; Soong-Grigoriu, 1993). It consists in modifying the drift coefficients taking into account the so-called Wong-Zakai (1965) correction term. In this way one takes full advantage of classical differential calculus retaining the nonanticipating function properties as well.

[18] Dipartimento di Ingegneria Strutturale e Geotecnica, Università degli Studi di Palermo, Viale delle Scienze, I-90128 Palermo, Italy.

Contributed by the Applied Mechanics Division of THE AMERICAN SOCIETY OF MECHANICAL ENGINEERS for publication in the ASME JOURNAL OF APPLIED MECHANICS. Manuscript received by the ASME Applied Mechanics Division, Oct. 31, 1994; final revision, September 14, 1996. Associate Technical Editor: M. Shinozuka.

The gyroscopic matrix is

$$[G] = \begin{bmatrix} 0 & -.2 \\ .2 & 0 \end{bmatrix}$$

and the damping matrix is

$$[C] = \begin{bmatrix} .01 & 0 \\ 0 & 0 \end{bmatrix}.$$

For this system, the combined damping and gyroscopic matrix in the transformed space employed in this note and in Peres-da-Silva et al. is

$$[\Gamma] = \begin{bmatrix} .01 & -.2 \\ .2 & 0 \end{bmatrix}.$$

The L_1 and L_∞ norm of $[\Gamma]$ are both 0.21, and the natural frequencies of the unperturbed system are

$$\omega_1 = \sqrt{2} \quad \omega_2 = 2.$$

The condition given in Eq. (20) shows that the series of Peres-da-Silva et al. will converge for both latent roots and latent vectors provided that

$$|\epsilon| < \frac{d_j}{2\|\Gamma_1\|} = \frac{|\sqrt{2} - 2|}{(2)(.21)} \doteq 1.395.$$

As noted in Peres-da-Silva et al., when the exact latent roots of this system are calculated and compared to the approximations obtained from summing the first few terms of the series they derived, one finds that 12 terms are needed to achieve six decimal places of accuracy.

Reformulating the problem and using the series derived in this note result in a more efficient technique. Only two terms of these series are needed to achieve six decimal places of accuracy. Moreover, since $[\Gamma_1] = [C]$ has norm 0.01, and since the eigenvalues of $[T_0]$ are $\pm 1.40054i$ and $\pm 2.01953i$, the series will converge for both latent roots and latent vectors provided

$$|\epsilon| < \frac{d_j}{2\|\Gamma_1\|} = \frac{|1.40054 - 2.01953|}{(2)(0.01)} \doteq 30.95.$$

The larger radius of convergence is consistent with the improved convergence of the series.

5 Conclusion

Developed in this note is a series method for solving the latent roots/eigenproblem for generally damped gyroscopic systems. This method differs from that presented in Peres-da-Silva et al. in that the undamped gyroscopic system is the unperturbed system. Since both methods are furnished with a convergence test, it is straightforward to demonstrate that the new method offers the advantage of faster computation and the capability for the analysis of a wider range of physical systems. In particular, interesting gyroscopic systems—systems for which gyroscopic terms are not small—may be analyzed by this method.

With the exception of the eigenanalysis of the unperturbed system, which must be performed in $2n$-space—efficiently, however, thanks to Meirovitch—the method described in this note is worked in n-space, and it is, as a consequence, potentially low in cost.

As was pointed out in Peres-da-Silva et al., this approach to eigenanalysis has the particular advantage that the convergence criterion may be determined a priori for each latent root and latent vector, and that the decision can be made, based upon its value, whether there is a need to proceed further with the analysis for that latent pair, or whether the unperturbed latent root and latent vector are of sufficient accuracy. This capability suggests the possibility for a considerable savings in the cost of analysis.

References

Cronin, D. L., 1990, "Eigenvalue and Eigenvector Determination for Nonclassically Damped Dynamic Systems," *Computers and Structures*, Vol. 36, No. 1, pp. 133–138.

Kato, T., 1982, *A Short Introduction to Perturbation Theory for Linear Operators*, Springer-Verlag, New York.

Lancaster, P., 1966, *Lambda-matrices and Vibrating Systems*, Pergamon Press, New York.

Meirovitch, L., 1974, "A New Method of Solution of the Eigenvalue Problem for Gyroscopic Systems," *AIAA Journal*, Vol. 12, No. 10.

Meirovitch, L., and Ryland, G., II, 1979, "Response of Slightly Damped Gyroscopic Systems," *Journal of Sound and Vibration*, Vol. 67, No. 1, pp. 1–19.

Peres-da-Silva, S. S., Cronin, D. L., and Randolph, T. W., 1995, "Computation of Eigenvalues and Eigenvectors of Nonclassically Damped Systems," *Computers and Structures*, Vol. 57, No. 5, pp. 883–891.

Linear Systems Excited by Polynomials of Filtered Poisson Pulses

M. Di Paola[18]

The stochastic differential equations for quasi-linear systems excited by parametric non-normal Poisson white noise are derived. Then it is shown that the class of memoryless transformation of filtered non-normal delta correlated process can be reduced, by means of some transformation, to quasi-linear systems. The latter, being excited by parametric excitations, are first converted into Itô stochastic differential equations, by adding the hierarchy of corrective terms which account for the non-normality of the input, then by applying the Itô differential rule, the moment equations have been derived. It is shown that the moment equations constitute a linear finite set of differential equation that can be exactly solved.

1 Introduction

The study of mechanical and structural system under non-normal stochastic loads has become very popular in recent years. This is due to the fact that many excitations acting on the structures, such as moving loads on the bridges, quadratic drag terms in fluid mechanics, etc., show significant non-normal characteristics.

Nonlinear systems loaded by both external and parametric normal white noise excitation can be treated by means of the application of the Itô stochastic calculus (1951) which provides an easy procedure for deriving the differential equations in terms of moment or in terms of the probability density function (Arnold, 1973; Ibrahim, 1985; Gardiner, 1985; Soong-Grigoriu, 1993). It consists in modifying the drift coefficients taking into account the so-called Wong-Zakai (1965) correction term. In this way one takes full advantage of classical differential calculus retaining the nonanticipating function properties as well.

[18] Dipartimento di Ingegneria Strutturale e Geotecnica, Università degli Studi di Palermo, Viale delle Scienze, I-90128 Palermo, Italy.

Contributed by the Applied Mechanics Division of THE AMERICAN SOCIETY OF MECHANICAL ENGINEERS for publication in the ASME JOURNAL OF APPLIED MECHANICS. Manuscript received by the ASME Applied Mechanics Division, Oct. 31, 1994; final revision, September 14, 1996. Associate Technical Editor: M. Shinozuka.

Both linear systems (Lin, 1965; Lutes, 1986, 1993; Lutes and Hu, 1986) and nonlinear systems (Roberts, 1972; Iwankievicz, 1990) under external non-normal Poisson pulses have been widely investigated in the past. Only recently the problem of nonlinear systems under parametric Poisson pulses has been framed in the stochastic differential calculus (Di Paola and Falsone, 1993a, b; Di Paola, 1993; Di Paola and Falsone, 1994). They extended the Itô calculus to this kind of input, showing that, in the case of parametric excitations, it is necessary to take into account some new hierarchy of corrective terms in order to convert the physical equation into Itô-type stochastic differential equations. In this frame, apart from some additional computational effort, the mathematical treatment remains very efficient and simple.

Nonlinear systems driven by external excitation handled by means of perturbation theory (Grigoriu, 1995), or by a pseudo force principle or by means of a variational principle (Rugh, 1981) belong to the very important class of linear systems excited by polynomials of filtered processes. The latter class has been investigated by Grigoriu and Arariatnam (1988) for normal white noise input and by Muscolino (1995) for non-normal Poisson white noise directly deriving the moment equation by the given systems and hence by considering the whole system driven by external excitation.

Here, by means of a suitable coordinate transformation, it is shown that linear systems excited by polynomials of filtered normal or non-normal white noise can be reduced to the class of quasi-linear systems (also called bilinear or simply linear), and then the moment equations can be easily derived and solved for both normal and non-normal white noise because they do not constitute an infinite hierarchy.

Because the quasi-linear system, equivalent to the physical nonlinear one (driven by external excitation), is loaded by a parametric-type excitation, a hierarchy of new corrective terms (Di Paola and Falsone, 1993a, b) (extension of the Wong-Zakai correction term) are needed to obtain the corresponding Itô stochastic differential equations. It is shown that the moments obtained directly on applying the modified Itô differential rule for external excitation (extended to account for the non-normality of the input process) and the moment equations, obtained by deriving the moments from the Itô equations of the equivalent quasi-linear system, are exactly the same.

2 Preliminary Concepts and Definitions

In this section some preliminary concepts and definitions will be introduced for clarity sakes and with the aim to introduce appropriate symbologies.

Let a Poisson delta correlated process be defined in the form

$$W(t) = \sum_{k=1}^{N(t)} P_k \delta(t - t_k) \tag{1}$$

where $N(t)$ is a homogeneous counting Poisson process, giving the total number of spikes $\delta(t - t_k)$ (Poisson distributed) in the interval $[0, t]$; P_k are identically distributed random variables which are mutually independent and independent of the time instant t_k. The correlations (cumulants of the process $W(t)$ evaluated at different time instances) of $W(t)$ are given as

$$R_w^{(r)}(t_1, t_2, \ldots, t_r) = \lambda E[P^r]\delta(t_2 - t_1)\cdot\delta(t_3 - t_1)\ldots\delta(t_r - t_1) \tag{2}$$

where $\lambda > 0$ is the mean arrival rate of impulses in unit time. It is well known that when λ approaches infinity and, at the same time $\lambda E[P^2]$ keeps a constant value, the Poisson white noise approaches the normal white noise, in the following, denoted as $W^0(t)$.

As a normal white noise $W^0(t)$ can be considered as formal derivative of the Wiener process $B(t)$, the Poisson delta correlated process can be considered as the formal derivative of the so-called compound Poisson process hereafter denoted as $C(t)$ defined as

$$C(t) = \sum_{k=1}^{N(t)} P_k U(t - t_k), \tag{3}$$

$U(\cdot)$ being the unit step function. So that increments of Wiener processes and increments of compound Poisson processes are characterized by having the following moments (or cumulants),

$$k_2(dB) = m_2(dB) = q_2 dt; \quad m_r(dB) = 0; \quad \forall r \neq 2 \tag{4}$$

$$k_r(dC) = m_r(dC) = q_r dt = \lambda E[P^r]dt; \quad r = 1, 2, 3, \ldots, \infty, \tag{5}$$

from Eq. (5) we recognize that also in the case in which P is normally distributed, increments of compound Poisson processes are not normal.

Now let a physical dynamic system be given in the general form

$$\dot{X} = a(X, t) + g(X, t)W(t) \tag{6}$$

where $a(X, t)$ and $g(X, t)$ are deterministic nonlinear functions of X and t, and $W(t)$ is a Poisson delta correlated process. Alternatively this equation can be rewritten in the differential form

$$dX = a(X, t)dt + g(X, t)dC. \tag{7}$$

The corresponding Itô differential equation, hereafter denoted as ΔX (Di Paola and Falsone, 1993a, b; 1994), is given a

$$\Delta X = dX + \sum_{j=2}^{\infty} \frac{1}{j!} g^{(j)}(X, t)(dC)^j \tag{8}$$

where the summation in Eq. (8) is the Di Paola-Falsone corrective term in passing from the integrals in Stratonovich sense to that in Itô sense, and $g^{(r)}(X, t)$ can be evaluated in recursive form as follows:

$$g^{(r)}(X, t) = \frac{\partial g^{(r-1)}(X, t)}{\partial X} g^{(1)}(X, t); \quad g^{(1)}(X, t) = g(X, t). \tag{9}$$

It will be noted that $(dC)^r$ is an infinitesimal of order dt so that the various terms in Eq. (8) cannot be neglected because all terms have the same order. It can be seen that if $dC \to dB$ then the summation on the right-hand side of Eq. (8) contains only the first terms ($j = 2$) and $\frac{1}{2}g^{(2)}(X, t)(dB)^2$ coincides with the well-known Wong-Zakai (1965) correction term. The primary concern in dealing with ΔX is the fundamental property of nonanticipating function of the Itô stochastic differential Eq. (8), that is

$$E[f(X, t)(dC)^k] = E[f(X, t)]E[(dC)^k]. \tag{10}$$

Once the physical Eq. (8) is converted into an Itô-type stochastic differential equation, the extended Itô differential rule for any scalar real-values function $\phi(X, t)$ can be used,

$$d\phi(X, t) = \frac{\partial \phi}{\partial t} dt + \sum_{j=1}^{\infty} \frac{1}{j!} \frac{\partial^j \phi}{\partial X^j} (\Delta X)^j. \tag{11}$$

If $C(t) \to B(t)$, then the summation on the right-hand side of Eqs. (8) and (11) can be truncated at the second term and we exactly obtain the classical Itô differential rule. At last we note that in the case of external excitation, that is if $g(X, t) = g(t)$, then $\Delta X \equiv dX$, because the summation in Eq. (8) disappears. Extension to multidegree-of-freedom systems is shortly reported in the Appendix.

As an example for the quasi-linear system, that is $f(X, t) =$

$a(t)X + \mu(t)$ and $g(X, t) = b(t)X$, the equation of motion is given as

$$dX = a(t)Xdt + \mu(t)dt + b(t)XdC. \quad (12)$$

The corresponding Itô equation can be written as

$$\Delta X = a(t)Xdt + \mu(t)dt + \sum_{j=1}^{\infty} \frac{b^j(t)}{j!} X(dC)^j. \quad (13)$$

On applying Eq. (11) for the special case $\phi(X, t) = X^k$, making the stochastic average, and dividing by dt, we obtain the equation of moments of every order in the form

$$\dot{m}_k(t) = ka(t)m_k(t) + k\mu(t)m_{k-1}(t) + \left(\sum_{j=1}^{k} \frac{k!}{(k-j)!j!} \psi_j(t)\right) m_k \quad (14)$$

where

$$\psi_1(t) = \sum_{r=1}^{\infty} \frac{b^r(t)}{r!} q_r(t);$$

$$\psi_2(t) = \sum_{r=1}^{\infty} \sum_{s=1}^{\infty} \frac{b^r(t)b^s(t)}{r!s!} q_{r+s}(t); \quad \ldots \quad (15)$$

From Eq. (14) we recognize that in the case of the linear system excited by parameters Poisson pulses the equation of moments of any order does not constitute an infinite hierarchy and then can be exactly solved. The system given in Eq. (12) is also called "quasi-linear" or "bilinear."

In the case of zero-mean normal white noise input, if $a(t)$, $\mu(t)$, $b(t)$ are constant quantities and the system operates from $t = -\infty$, then the response attains the stationary solution and the moments of every order are given in the simple form

$$m_k = (-1)^k \frac{\mu^k}{\prod_{j=1}^{k} a_j} \quad k = 1, 2, \ldots \quad (16)$$

where

$$a_j = a + \frac{j}{2} b^2 q_2. \quad (17)$$

It will be noted that also in the case of normal input the response X is not normal. In fact in the stationary case the higher order cumulants proves to be different from zero.

3 Linear Systems to Polynomials of Filtered Poisson White Noise and Quasi-Linear Systems

In this section a linear system with polynomial of filtered delta correlated process is treated, showing that such a class of systems can be reduced to quasi-linear ones.

Let a dynamical system be given in the form

$$\dot{X}_1 = \alpha(t)X_1 + \mu(t) + f(Y) \quad (18)$$

where $f(Y)$ is a deterministic function of a non-normal process obtained by filtering a delta correlated process, that is

$$\dot{Y} = \rho(t)Y + \gamma(t)W \quad (19)$$

where $\rho(t)$ and $\gamma(t)$ are deterministic coefficients and $W(t)$ is characterized by the correlations given in Eq. (4).

Let $f(Y)$ be given in the form

$$f(Y) = \sum_{j=1}^{n} a_j Y^j. \quad (20)$$

We now introduce the state variables $X_s = d^{s-2}f(Y)/dY^{s-2}$, $s = 2, 3, \ldots, n$, that is

$$X_2 = Y^n; \quad X_3 = nY^{n-1}; \ldots; \quad X_{n+1} = n!Y \quad (21)$$

by using the following relationships:

$$\dot{Y} = \frac{\dot{X}_{n+1}}{n!} = \frac{\rho X_{n+1}}{n!} + \gamma W; \quad X_k X_{n+1} = n!(n-k+3)X_{k-1}; \quad k = 3, 4, \ldots, n \quad (22)$$

and defining the differentials dX_k, $k = 2, 3, \ldots, n+1$ as follows:

$$dX_2 = nY^{n-1}dY; \quad dX_3 = n(n-1)Y^{n-2}dY; \ldots; \quad dX_{n+1} = n!dY. \quad (23)$$

Equations (18) and (19), with the aid of Eqs. (22) and (23), can be also rewritten in the differential form as follows:

$$\begin{aligned} dX_1 &= \alpha X_1 + a_n X_2 + \frac{a_{n-1}}{n} X_3 + \frac{a_{n-2}}{n(n-1)} X_4 + \ldots + \frac{a_1}{n!} X_{n+1} + \mu dt \\ dX_2 &= n\rho X_2 dt + \gamma X_3 dC \\ dX_3 &= (n-1)\rho X_3 dt + \gamma X_4 dC \\ &\vdots \\ dX_n &= 2\rho X_n dt + \gamma X_{n+1} dC \\ dX_{n+1} &= \rho X_{n+1} + n!\gamma dC. \end{aligned} \quad (24)$$

From these equations we recognize that the non-linear system of differential equations forced by external non-normal input has been transformed in a quasi-linear system forced by parametric-type excitations. The first step for obtaining the moment differential equations consists in transforming Eqs. (24) in the Ito stochastic differential equations by adding the Di Paola-Falsone correction terms. In order to do this we rewrite Eqs. (24) in compact form as follows:

$$d\mathbf{X} = (\mathbf{AX} + \mu\boldsymbol{\nu}_1)dt + (\mathbf{RX} + n!\gamma\boldsymbol{\nu}_{n+1})dC \quad (25)$$

where

$$\mathbf{A} = \begin{bmatrix} \alpha & a_n & \frac{a_{n-1}}{n} & \cdots & \frac{2a_2}{n!} & \frac{a_1}{n!} \\ \varnothing & n\rho & \varnothing & \cdots & \varnothing & \varnothing \\ \varnothing & \varnothing & (n-1)\rho & \cdots & \varnothing & \varnothing \\ \vdots & \vdots & \vdots & \ddots & \vdots & \vdots \\ \varnothing & \varnothing & \varnothing & \cdots & 2\rho & \varnothing \\ \varnothing & \varnothing & \varnothing & \cdots & \varnothing & \rho \end{bmatrix};$$

$$\mathbf{R} = \begin{bmatrix} \varnothing & \varnothing & \varnothing & \varnothing & \cdots & \varnothing \\ \varnothing & \varnothing & \gamma & \varnothing & \cdots & \varnothing \\ \varnothing & \varnothing & \varnothing & \gamma & \cdots & \varnothing \\ \vdots & \vdots & \vdots & \vdots & \ddots & \vdots \\ \varnothing & \varnothing & \varnothing & \varnothing & \cdots & \gamma \\ \varnothing & \varnothing & \varnothing & \varnothing & \cdots & \varnothing \end{bmatrix};$$

$$\boldsymbol{\nu}_k = \begin{bmatrix} \varnothing \\ \varnothing \\ 1 \\ \vdots \\ \varnothing \\ \varnothing \end{bmatrix} \leftarrow k\text{-th row}. \quad (26)$$

It can be easily seen that the vectors $\mathbf{g}^{(s)}(\mathbf{X})$ are simply given in the form

$$\mathbf{g}^{(1)}(\mathbf{X}) = \mathbf{R}\mathbf{X} + n!\gamma\boldsymbol{\nu}_{n+1}; \quad \mathbf{g}^{(2)}(\mathbf{X}) = \mathbf{R}^2\mathbf{X} + n!\gamma^2\boldsymbol{\nu}_n; \ \ldots; \quad \mathbf{g}^{(r)}(\mathbf{X}) = n!\gamma^n\boldsymbol{\nu}_2; \quad \mathbf{g}^{(s)}(\mathbf{X}) = \mathbf{0} \quad s > n. \tag{27}$$

Then the Itô stochastic differential equation correspondent to Eq. (24) can be written in the form

$$\Delta\mathbf{X} = (\mathbf{A}\mathbf{X} + \mu\boldsymbol{\nu}_1)dt + \left(\sum_{s=1}^{n-1}\frac{(dC)^s}{s!}\mathbf{R}^s\right)\mathbf{X} + n!\sum_{s=1}^{n}\frac{(dC)^s}{s!}\gamma^s\boldsymbol{\nu}_{n+2-s} \tag{28}$$

or in extended form

$$\Delta X_1 = \left(\alpha X_1 + a_n X_2 + \frac{a_{n-1}}{n}X_3 + \ldots + \frac{a_1}{n!}X_{n+1} + \mu\right)dt$$

$$\Delta X_2 = n\rho X_2 dt + \sum_{k=1}^{n-1}\frac{\gamma^k}{k!}X_{k+2}(dC)^k + \gamma^n(dC)^n$$

$$\Delta X_3 = (n-1)\rho X_3 dt + \sum_{k=1}^{n-2}\frac{\gamma^k}{k!}X_{k+3}(dC)^k + \gamma^{n-1}(dC)^{n-1}$$

$$\vdots$$

$$\Delta X_n = 2\rho X_n dt + \gamma X_{n+1}dC + (n-1)!\gamma^2(dC)^2$$

$$\Delta X_{n+1} = \rho X_{n+1}dt + n!\gamma dC. \tag{29}$$

Once the ΔX_s, $s = 1, 2, \ldots, n+1$ has been calculated, by appropriately using the differential rule described in the Appendix, the differential equations governing any order moments can be easily derived.

The described procedure can be better explained by means of a simple example: we will evaluate the response of the differential equation

$$\dot{X}_1 = \alpha X_1 + \mu + Y^2 \tag{30}$$

in which Y is the non-normal filtered Poisson process defined by the equation

$$\dot{Y} = \rho Y + \gamma W. \tag{31}$$

By putting $Y^2 = X_2$ and $2Y = X_3$, we can transform Eqs. (30) and (31) in the set of physical differential equations as follows:

$$dX_1 = (\alpha X_1 + \mu + X_2)dt$$

$$dX_2 = 2\rho X_2 dt + \gamma X_3 dC$$

$$dX_3 = \rho X_3 dt + 2\gamma dC \tag{32}$$

and in turn they can be converted into an Itô-type stochastic differential equation, (see the Appendix), as follows:

$$\Delta X_1 = (\alpha X_1 + \mu + X_2)dt$$

$$\Delta X_2 = 2\rho X_2 dt + \gamma X_3 dC + \gamma^2(dC)^2$$

$$\Delta X_3 = \rho X_3 dt + 2\gamma dC. \tag{33}$$

By using the Itô differential rule given described in the Appendix, the moment equations up to the second-order moment can be easily derived in the form

$$\dot{E}[X_1] = \alpha E[X_1] + \mu + E[X_2]$$

$$\dot{E}[X_2] = 2\rho E[X_2] + \gamma q_1 E[X_3] + \gamma^2 q_2$$

$$\dot{E}[X_3] = \rho E[X_3] + 2\gamma q_1$$

$$\dot{E}[X_1^2] = 2\alpha E[X_1^2] + 2\mu E[X_1] + E[X_1X_2]$$

$$\dot{E}[X_1X_2] = (2\rho + \alpha)E[X_1X_2] + \gamma E[X_1X_3]q_1 + \gamma^2 E[X_1]q_2 + \mu E[X_2] + E[X_2^2]$$

$$\dot{E}[X_1X_3] = (\rho + \alpha)E[X_1X_3] + 2\gamma E[X_1]q_1 + \mu E[X_3] + E[X_2X_3] \tag{34}$$

$$\dot{E}[X_2^2] = 4\rho E[X_2^2] + 2\gamma E[X_2X_3]q_1 + 2\gamma^2 E[X_2]q_2 + \gamma^2 E[X_3^2]q_2 + \gamma^4 q_4 + 2\gamma^3 E[X_3]q_2$$

$$\dot{E}[X_2X_3] = 3\rho E[X_2X_3] + 2\gamma E[X_2]q_1 + \gamma E[X_3^2]q_1 + 3\gamma^2 E[X_3]q_2 + 2\gamma^3 q_3$$

$$\dot{E}[X_3^2] = 2\rho E[X_3^2] + 2\gamma E[X_3]q_1 + \gamma^2 q_2.$$

From these equations we recognize that for the Itô Eq. (33) the moment equations up to the second order contain only the first and second order moments, and the same happens for higher order moments, that is for Eq. (33) the moment equation does not constitute infinite hierarchy.

On the other hand, if we directly approach Eqs. (30) and (31) we recognize that it is a non linear system excited by external delta correlated process, so that the physical differential equations coincide with the Itô differential equations, that is

$$\Delta X_1 = dX_1 = (\alpha X_1 + \mu + Y^2)dt$$

$$\Delta Y = dY = \rho Y dt + \gamma dC. \tag{35}$$

Using the approach proposed by Muscolino (1995) for this system by applying the extended Itô differential rule given in Eq. (15) and appropriately selecting the function ϕ, we can write the differential equation of moments in the form

$$\dot{E}[X_1] = \alpha E[X_1] + \mu + E[Y^2]$$

$$\dot{E}[Y] = \rho E[Y] + \gamma q_1$$

$$\dot{E}[X_1^2] = 2\alpha E[X_1^2] + 2\mu E[X_1] + E[Y^2X_1]$$

$$\dot{E}[X_1Y] = (\rho + \alpha)E[X_1Y] + \mu E[Y] + E[Y^3] + \gamma E[X_1]q_1$$

$$\dot{E}[Y^2] = 2\rho E[Y^2] + 2\gamma E[Y]q_1 + \gamma^2 q_2. \tag{36}$$

In these equations moments of order higher than two appear, so we need the third-order equation for $E[Y^3]$ and $E[Y^2X_1]$, these equations are

$$\dot{E}[Y^3] = 3\rho E[Y^3] + 3\gamma E[Y^3] + 3\gamma E[Y^2]q_1 + 3E[Y]\gamma^2 q_2 + \gamma^3 q_3$$

$$\dot{E}[Y^2X_1] = (2\rho + \alpha)E[Y^2X_1] + 2\rho E[YX_1]\gamma q_1 + \mu E[Y^2] + E[Y^4] + \gamma^2 E[X_1]q_2 \tag{37}$$

and in view of the presence of the fourth order moment $E[Y^4]$, we need the fourth order moment equation, that is

$$\dot{E}[Y^4] = 4E[Y^4] + 4E[Y^3]\gamma q_1 + 6E[Y^2]\gamma^2 q_2 + 4E[Y]\gamma^3 q_3 + \gamma^4 q_4. \tag{38}$$

Now the set of Eqs. (36)–(38) seems to be quite different from Eqs. (34). However, by accounting for these simple algebraic relationships

$$X_2 = Y^2, \quad X_3 = 2Y, \quad E[X_1Y] = E[X_1X_3]/2$$

$$E[X_1Y^2] = E[X_1X_2], \quad E[Y^2] = E[X_2] = E[X_3^2]/4$$

$$E[Y^3] = E[X_2X_3]/2, \quad E[Y^4] = E[X_2^2] \tag{39}$$

and putting them into Eqs. (36)–(38) we exactly obtain Eqs. (34).

Similar equations for higher order polynomials and higher order moment equations have been derived but are not here proposed for the sake of brevity.

Finally, we can make the following remarks: (i) the class of linear systems excited by nonlinear transformation of filtered (normal or non-normal) process can be reduced to the solution of quasi-linear systems—that is a linear system excited by parametric excitations. The equation of moments for such a kind of system can be exactly solved obtaining the moments of every order, also for the class of non-normal Poisson filtered process; (ii) because the quasi-linear system, equivalent to the original nonlinear one, is loaded by parametric excitations in accordance with Di Paola-Falsone (1993a, b), we have to take into account correction terms for deriving the Itô equations from the physical ones. These terms are essential in order to establish the equivalence between the original and the corresponding quasi-linear system.

4 Conclusions

The quasi-linear systems excited by non-normal Poisson white noise processes can be treated as linear systems, in the sense that the moment equations of any order are linear and involves moments of lower order only, although the response is non-normal even for normal white excitation.

To this class belong the class of linear systems excited by polynomials of filtered non-normal Poisson processes. It has been shown that for such a class the analytic treatment for deriving the moment equations of any order can be obtained by means of two different strategies. The first one consists of considering the nonlinear system excited by external noise, while the second consists in replacing the original system in an equivalent quasi-linear one. The latter, since parametric excitation appears, has to be first transformed from a set of physical differential equations into a set of Itô-type stochastic differential equations by adding the Di Paola-Falsone correction term to the physical equations. By applying the Itô differential rule, the moment equations for the quasi-linear system have been derived and compared with the equations of moments obtained by the original systems obtaining the coincidence of the moment equations for the two aforementioned systems. Moreover, because the moment equations of any order of quasi-linear systems does not constitute hierarchy, the probabilistic characterization of linear systems excited by polynomials of filtered non-normal Poisson processes can be exactly found also for this class of input.

References

Arnold, L., 1973, *Stochastic differential equations: Theory and applications*, John Wiley and Sons, New York.

Di Paola, M., 1993, *Stochastic differential calculus* (CISM Courses and Lectures No. 340), Casciati, ed., Springer-Verlag, New York, pp. 29–92.

Di Paola, M., and Falsone, G., 1993, "Ito and Stratonovich integral for delta correlated processes," *Probabilistic Engineering Mechanics*, Vol. 8, pp. 197–208.

Di Paola, M., and Falsone, G., 1993, "Stochastic Dynamics of Nonlinear Systems Driven by Non-Normal Delta Correlated Processes," ASME Journal of Applied Mechanics, Vol. 60, pp. 141–148.

Di Paola, M., and Falsone, G., 1994, "Nonlinear oscillators under parametric and external Poisson pulses," *Nonlinear Dynamics*, Vol. 5, pp. 337–352.

Di Paola, M., and Muscolino, G., 1990, "Differential moment equations of FE modelled structures with geometrical non-linearities," *Int. Journal of Nonlinear Mechanics*, Vol. 25, No. 4, pp. 363–373.

Di Paola, M., Falsone, G., and Pirrotta, A., 1992, "Stochastic response analysis of non-linear systems under Gaussian inputs," *Probabilistic Engineering Mechanics*, Vol. 7, pp. 15–21.

Dimentberg, M. F., 1988, *Statistical dynamics of nonlinear and time-varying systems*, Research Studies Press, U.K.

Gardiner, C. W., 1985, *Handbook of stochastic methods*, Springer-Verlag, New York.

Grigoriu, M., 1987, "White noise processes," *Journal of Engineering Mechanics*, Vol. 113, No. 5, pp. 757–765.

Grigoriu, M., and Ariaratnam, S. T., 1988, "Response of Linear Systems to Polynomials of Gaussian Processes," ASME Journal of Applied Mechanics, Vol. 55, pp. 905–910.

Grigoriu, M., Wall, W. A., and Bucher, C. G., 1995, "A novel algorithm for analyzing non linear systems by perturbation theory," *Computational Stochastic Mechanics*, P. D. Spanos, Ed., Balkema, Rotterdam.

Ibrahim, R. A., 1985, *Parametric random vibration*, John Wiley and Sons, New York.

Itô, K., 1951, "On a formula concerning stochastic differential equation," *Nagoya Mathematical Journal*, Vol. 3, pp. 55–65.

Iwankiewicz, R., Nielsen, S. R. K., and Christensen, P. T., 1990, "Dynamic response of non-linear systems to Poisson distributed pulse train Markov approach," *Nonlinear Structural System under Random Conditions*, F. Casciati, I. Elishakoff, and J. B. Roberts, eds., pp. 223–238.

Lin, Y. K., 1965, "Non stationary excitation and response in linear systems treated on sequence of random pulses," *Journal of the Acoustical Society of America*, Vol. 38, pp. 453–460.

Lutes, L. D., 1986, "Cumulants of Stochastic Response for Linear Systems," ASME Journal of Applied Mechanics, Vol. 112, No. 10, pp. 1062–1075.

Lutes, L. D., and Hu, S.-L., 1986, "Non-Normal Stochastic Response of Linear Systems," ASME Journal of Applied Mechanics, Vol. 112, No. 2, pp. 127–141.

Muscolino, G., 1995, "Linear systems excited by polynomial form of non-Gaussian filtered processes," *Probabilistic Engineering Mechanics*, Vol. 10, pp. 35–44.

Roberts, J. B., 1972, "Systems response to random impulses," *Journal of Sound and Vibration*, Vol. 24, pp. 23–34.

Rugh, W. J., 1981, *Non linear system theory: The Volterra/Wiener approach*, John Hobkins Press Ltd., London.

Soong, T. T., and Grigoriu, M., 1993, *Random vibration of mechanical and structural systems*, PTR, Prentice-Hall, Englewoods Cliffs, NJ.

Stratonovich, R. L., 1963, *Topics in the theory of random noise*, Vol. I, Gordon and Breach, New York.

Wong, E., and Zakai, M., 1965, "On the relation between ordinary and stochastic differential equations," *Int. Journal of Engineering Sciences*, Vol. 3, pp. 213–229.

APPENDIX

In this Appendix the extension of the theory outlined in the paper for the scalar sense is extended to multidegree-of-freedom systems.

Let the equation of motion given in the form

$$d\mathbf{X} = \mathbf{f}(\mathbf{X}, t)dt + \mathbf{g}(\mathbf{X}, t)dC \tag{A1}$$

where $\mathbf{f}(\mathbf{X}, t)$, $\mathbf{g}(\mathbf{X}, t)$ are deterministic n-vector of the vector response process $\mathbf{X}(t)$. The Itô equation can be written as

$$\Delta\mathbf{X} = \mathbf{f}(\mathbf{X}, t)dt + \sum_{j=1}^{\infty} \frac{1}{j!}\mathbf{g}^{(j)}(\mathbf{X}, t)(dC)^j \tag{A2}$$

where

$$\mathbf{g}^{(j)}(\mathbf{X}, t) = \nabla\mathbf{g}^{(j-1)}(\mathbf{X}, t)\mathbf{g}(\mathbf{X}, t);$$
$$\mathbf{g}^{(1)}(\mathbf{X}, t) = \mathbf{g}(\mathbf{X}, t) \tag{A3}$$

and where $\nabla\mathbf{g}^{(k)}(\mathbf{X}, t)$ is the gradient operator, that is

$$\nabla\mathbf{g}^{(k)} = \begin{bmatrix} \dfrac{\partial g_1^{(k)}}{\partial X_1} & \dfrac{\partial g_1^{(k)}}{\partial X_2} & \cdots & \dfrac{\partial g_1^{(k)}}{\partial X_n} \\ \vdots & \vdots & \cdots & \vdots \\ \dfrac{\partial g_n^{(k)}}{\partial X_1} & \dfrac{\partial g_n^{(k)}}{\partial X_2} & \cdots & \dfrac{\partial g_n^{(k)}}{\partial X_n} \end{bmatrix}. \tag{A4}$$

The Itô differential rule for any scalar real-valued function $\phi(\mathbf{X}) = \phi(X_1, X_2, \ldots, X_n)$, ∞ times differentiable on X_1, X_2, $\ldots$, X_n, can be written as

$$d\phi(\mathbf{X}) = \sum_{j=1}^{n} \frac{\partial \phi(\mathbf{X})}{\partial X_j} \Delta X_j + \frac{1}{2} \sum_{j=1}^{n} \sum_{k=1}^{n} \frac{\partial^2 \phi(\mathbf{X})}{\partial X_j \partial X_k} \Delta X_j \Delta X_k + \ldots . \quad (A5)$$

Then for quasi-linear multi-degree-of-freedom systems, that is

$$d\mathbf{X} = (\mathbf{A}(t)\mathbf{X} + \boldsymbol{\mu}(t))dt + (\mathbf{R}(t)\mathbf{X} + \boldsymbol{\beta}(t))dC, \quad (A6)$$

the Itô-type stochastic differential equation can be written as

$$\Delta \mathbf{X} = (\mathbf{A}(t)\mathbf{X} + \boldsymbol{\mu}(t))dt + \sum_{j=1}^{\infty} \frac{(dC)^j}{j!} \mathbf{R}^{(j-1)}(t)(\mathbf{R}(t)\mathbf{X} + \boldsymbol{\beta}(t)). \quad (A7)$$

The Order of Stress Singularities in Orthotropic Wedges

A. Selvarathinam[19] **and S. S. Pageau**[20]

A formulation for the determination of the order of the stress singularities at the tip of a re-entrant corner for anisotropic wedges was given by Bogy (1972). Results for orthotropic wedges were obtained as a special case, and it was concluded that the order of the stress singularities at the tip of re-entrant orthotropic wedges is always more severe than that of the corresponding isotropic wedge. It is shown here that the order of the stress singularities at the wedge tip can be above or below that of the corresponding isotropic wedge, depending on the material properties.

Introduction

Once Williams (1952) demonstrated the singular character of the stresses at the apex of re-entrant corners, many other papers related to the singular stress field at the apex of multimaterial isotropic wedges followed. The work of Hein and Erdogan (1972) and Theocaris (1974) are good examples of such studies. Bogy (1972) and Kuo and Bogy (1974a, 1974b) solved similar problems for anisotropic materials. Bogy (1972) made use of Mellin Transforms to solve for the order of the stress singularities at the apex of wedges subject to various in-plane loads. The results presented by Bogy (1972) and Kuo and Bogy (1974a, 1974b) utilize the notation of Green and Zerna (1954) to condense the results in terms of reduced material properties. The present study concentrates on the order of the stress singularities in orthotropic wedges first examined by Bogy (1972). Orthotropic wedges are defined as having their symmetry line coincident to one of the axes of orthotropy of the material. It will be shown here that the results which were presented by Bogy (1972) in terms of reduced material properties, although correct, do not cover the entire range of material properties. A discussion of the complete solution is presented below. The new results demonstrate that the order of the stress singularities in orthotropic wedges are not bounded below by the results obtained for isotropic materials.

Analysis

Bogy (1972) proposed a formulation to solve for the asymptotic stress and displacement fields at the apex of a reentrant linear elastic anisotropic wedge. The wedge is shown in Fig. 1 and is subjected to either symmetric normal and antisymmetric shear loading (case A) or antisymmetric normal and symmetric shear loading (case B). The formulation was derived using Mellin transforms in complex variable form. This formulation is considerably simplified when the principal axes of the material coincide with the axes of the wedge. This particular configuration was referred to by Bogy (1972) as an orthotropic wedge.

For these orthotropic wedges, the order of stress singularities are given by equations (61)–(62) of Bogy (1972). They are repeated here for convenience as

$$D^A = D_2^A - D_1^A, \quad D^B = D_2^B - D_1^B, \quad (1)$$

where

$$D_\lambda^A = \frac{1}{\alpha_\lambda} \tan\left[(s+1)\arctan\left(\frac{1}{\alpha_\lambda}\tan\beta\right)\right], \quad (2)$$

$$D_\lambda^B = \alpha_\lambda^2 D_\lambda^A, \quad \lambda = 1, 2. \quad (3)$$

The superscripts A and B denote the two types of loading indicated in Fig. 1. The values α_1 and α_2 are the roots of the characteristic equation

$$S_{22}^{22}\alpha^4 - 2(S_{11}^{22} + 2S_{12}^{12})\alpha^2 + S_{11}^{11} = 0, \quad (4)$$

as defined by Green and Zerna (1954), and which are directly obtainable from the properties of the material constituting the orthotropic wedge. The values α_1 and α_2 are condensed material properties. They can be real or complex. The case when these reduced material properties are complex adds to the difficulty of the formulation and will not be considered here. For a given wedge geometry, the order of the stress singularity, defined as $(s+2)$, (where s is the root of Eq. (1)) is a function of these two condensed material properties only. Bogy (1972) plotted solutions of the root s for different values of the wedge angle 2β and the two reduced material properties α_1 and α_2. The plots given by Bogy (1972) only consider $1/\alpha_1$ and $1/\alpha_2$ to vary between 0 and 1 and seem to imply that the full range of material properties was covered. This is not true, however, and the present results consider cases where one or both of these parameters are greater than one as well as the cases already considered by Bogy (1972). Some interesting properties arise from extending Bogy's (1972) results. In order to facilitate the discussion the following expressions, retrievable from Green and Zerna's (1954) formulation, are introduced:

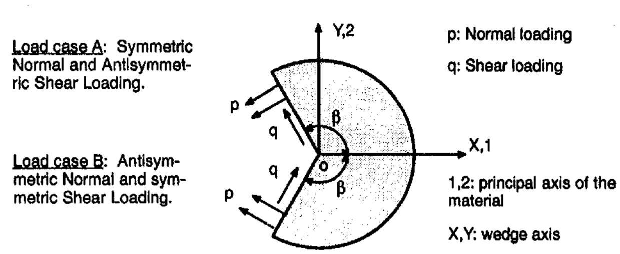

Fig. 1 Wedge of angle 2β under normal and shear loads

[19] Department of Mechanical Engineering and Aerospace Engineering and Engineering Science, 307 Perkins Hall, University of Tennessee, Knoxville, TN 37996. Mem. ASME.

[20] To whom all correspondence should be addressed. HKS, 1080 Main Street, Pawtucket, RI 02860. Mem. ASME.

Contributed by the Applied Mechanics Division of The American Society of Mechanical Engineers for publication in the ASME Journal of Applied Mechanics. Manuscript received by the ASME Applied Mechanics Division, Feb. 16, 1995; final revision, Apr. 10, 1997. Associate Technical Editor: M. Taya.

$$d\phi(\mathbf{X}) = \sum_{j=1}^{n} \frac{\partial\phi(\mathbf{X})}{\partial X_j}\Delta X_j + \frac{1}{2}\sum_{j=1}^{n}\sum_{k=1}^{n}\frac{\partial^2\phi(\mathbf{X})}{\partial X_j \partial X_k}\Delta X_j \Delta X_k + \ldots . \quad (A5)$$

Then for quasi-linear multi-degree-of-freedom systems, that is

$$d\mathbf{X} = (\mathbf{A}(t)\mathbf{X} + \boldsymbol{\mu}(t))dt + (\mathbf{R}(t)\mathbf{X} + \boldsymbol{\beta}(t))dC, \quad (A6)$$

the Itô-type stochastic differential equation can be written as

$$\Delta\mathbf{X} = (\mathbf{A}(t)\mathbf{X} + \boldsymbol{\mu}(t))dt + \sum_{j=1}^{\infty}\frac{(dC)^j}{j!}\mathbf{R}^{(j-1)}(t)(\mathbf{R}(t)\mathbf{X} + \boldsymbol{\beta}(t)). \quad (A7)$$

The Order of Stress Singularities in Orthotropic Wedges

A. Selvarathinam[19] and S. S. Pageau[20]

A formulation for the determination of the order of the stress singularities at the tip of a re-entrant corner for anisotropic wedges was given by Bogy (1972). Results for orthotropic wedges were obtained as a special case, and it was concluded that the order of the stress singularities at the tip of re-entrant orthotropic wedges is always more severe than that of the corresponding isotropic wedge. It is shown here that the order of the stress singularities at the wedge tip can be above or below that of the corresponding isotropic wedge, depending on the material properties.

Introduction

Once Williams (1952) demonstrated the singular character of the stresses at the apex of re-entrant corners, many other papers related to the singular stress field at the apex of multimaterial isotropic wedges followed. The work of Hein and Erdogan (1972) and Theocaris (1974) are good examples of such studies. Bogy (1972) and Kuo and Bogy (1974a, 1974b) solved similar problems for anisotropic materials. Bogy (1972) made use of Mellin Transforms to solve for the order of the stress singularities at the apex of wedges subject to various in-plane loads. The results presented by Bogy (1972) and Kuo and Bogy (1974a, 1974b) utilize the notation of Green and Zerna (1954) to condense the results in terms of reduced material properties. The present study concentrates on the order of the stress singularities in orthotropic wedges first examined by Bogy (1972). Orthotropic wedges are defined as having their symmetry line coincident to one of the axes of orthotropy of the material. It will be shown here that the results which were presented by Bogy (1972) in terms of reduced material properties, although correct, do not cover the entire range of material properties. A discussion of the complete solution is presented below. The new results demonstrate that the order of the stress singularities in orthotropic wedges are not bounded below by the results obtained for isotropic materials.

[19] Department of Mechanical Engineering and Aerospace Engineering and Engineering Science, 307 Perkins Hall, University of Tennessee, Knoxville, TN 37996. Mem. ASME.

[20] To whom all correspondence should be addressed. HKS, 1080 Main Street, Pawtucket, RI 02860. Mem. ASME.

Contributed by the Applied Mechanics Division of The American Society of Mechanical Engineers for publication in the ASME Journal of Applied Mechanics. Manuscript received by the ASME Applied Mechanics Division, Feb. 16, 1995; final revision, Apr. 10, 1997. Associate Technical Editor: M. Taya.

Analysis

Bogy (1972) proposed a formulation to solve for the asymptotic stress and displacement fields at the apex of a reentrant linear elastic anisotropic wedge. The wedge is shown in Fig. 1 and is subjected to either symmetric normal and antisymmetric shear loading (case A) or antisymmetric normal and symmetric shear loading (case B). The formulation was derived using Mellin transforms in complex variable form. This formulation is considerably simplified when the principal axes of the material coincide with the axes of the wedge. This particular configuration was referred to by Bogy (1972) as an orthotropic wedge.

For these orthotropic wedges, the order of stress singularities are given by equations (61)–(62) of Bogy (1972). They are repeated here for convenience as

$$D^A = D_2^A - D_1^A, \quad D^B = D_2^B - D_1^B, \quad (1)$$

where

$$D_\lambda^A = \frac{1}{\alpha_\lambda}\tan\left[(s+1)\arctan\left(\frac{1}{\alpha_\lambda}\tan\beta\right)\right], \quad (2)$$

$$D_\lambda^B = \alpha_\lambda^2 D_\lambda^A, \quad \lambda = 1, 2. \quad (3)$$

The superscripts A and B denote the two types of loading indicated in Fig. 1. The values α_1 and α_2 are the roots of the characteristic equation

$$S_{22}^{22}\alpha^4 - 2(S_{11}^{22} + 2S_{12}^{12})\alpha^2 + S_{11}^{11} = 0, \quad (4)$$

as defined by Green and Zerna (1954), and which are directly obtainable from the properties of the material constituting the orthotropic wedge. The values α_1 and α_2 are condensed material properties. They can be real or complex. The case when these reduced material properties are complex adds to the difficulty of the formulation and will not be considered here. For a given wedge geometry, the order of the stress singularity, defined as $(s + 2)$, (where s is the root of Eq. (1)) is a function of these two condensed material properties only. Bogy (1972) plotted solutions of the root s for different values of the wedge angle 2β and the two reduced material properties α_1 and α_2. The plots given by Bogy (1972) only consider $1/\alpha_1$ and $1/\alpha_2$ to vary between 0 and 1 and seem to imply that the full range of material properties was covered. This is not true, however, and the present results consider cases where one or both of these parameters are greater than one as well as the cases already considered by Bogy (1972). Some interesting properties arise from extending Bogy's (1972) results. In order to facilitate the discussion the following expressions, retrievable from Green and Zerna's (1954) formulation, are introduced:

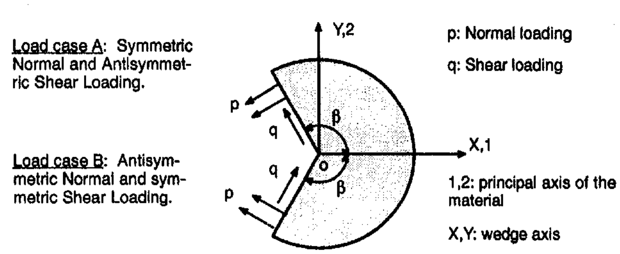

Fig. 1 Wedge of angle 2β under normal and shear loads

$$\frac{1}{\alpha_1^2} + \frac{1}{\alpha_2^2} = \frac{E_1'}{G_{12}} - 2\nu_{12}', \qquad 5(a)$$

$$\alpha_1^2 + \alpha_2^2 = \frac{E_2'}{G_{12}} - 2\nu_{21}', \qquad 5(b)$$

$$\left(\frac{1}{\alpha_1}\cdot\frac{1}{\alpha_2}\right)^2 = \frac{E_1'}{E_2'}, \qquad 5(c)$$

where

$E_1' = E_1$, $E_2' = E_2$, $\nu_{12}' = \nu_{12}$, $\nu_{21}' = \nu_{21}$ for plane stress and

$$E_1' = \frac{E_1}{1-\nu_{31}\nu_{13}},\ E_2' = \frac{E_2}{1-\nu_{32}\nu_{23}},$$

$$\nu_{12}' = \frac{\nu_{12}+\nu_{13}\nu_{32}}{1-\nu_{31}\nu_{13}},\ \frac{\nu_{12}'}{E_1'} = \frac{\nu_{21}'}{E_2'} \text{ for plane strain.}$$

Results

In order to demonstrate the singular behavior for a complete range of material and wedge geometry, results only need to be presented for the order of the stress singularity in a wedge of angle $2\beta = 200$ deg subjected to case A loading. First, numerical results are obtained using Eq. (1), (which was correctly derived by Bogy (1972) though its usage was restricted to $0 < [1/\alpha_1, 1/\alpha_2] < 1$) for diverse values of α_1 and α_2.

Figure 2 shows the roots, s, of Eq. (1) as a function of $1/\alpha_1$ and $1/\alpha_2$. The results match those obtained by Bogy (1972) for all load cases where $1/\alpha_1$ and $1/\alpha_2$ are both less than 1. Note, however, that only the results obtained for the load case A are represented here. Figure 2 extends the results to cases where $1/\alpha_1$ and/or $1/\alpha_2$ are greater than 1.

The solid lines represent curves of constant root s which are displayed for the range of values between -1.55 and -1.85. The constant root curves are symmetric about the principal diagonal. Curves for roots less than -1.85 have not been represented for clarity of the figure. In order to explain this complex figure the graph is divided into four regions limited by dashed lines. The curve (IJA) represents the case where $G_{12} = E_1'/(2(1+\nu_{12}'))$, i.e., the curve obtained by setting the left-hand side of Eq. (5a) equal to 2 (i.e., $1/\alpha_1^2 + 1/\alpha_2^2 = 2$). The curve (DJF) represents the case where $G_{12} = E_2'/(2(1+\nu_{21}'))$, i.e., the curve obtained by setting the left-hand side of Eq. (5b) equal to 2 (i.e., $\alpha_1^2 + \alpha_2^2 = 2$). The curve ($CJG$) is

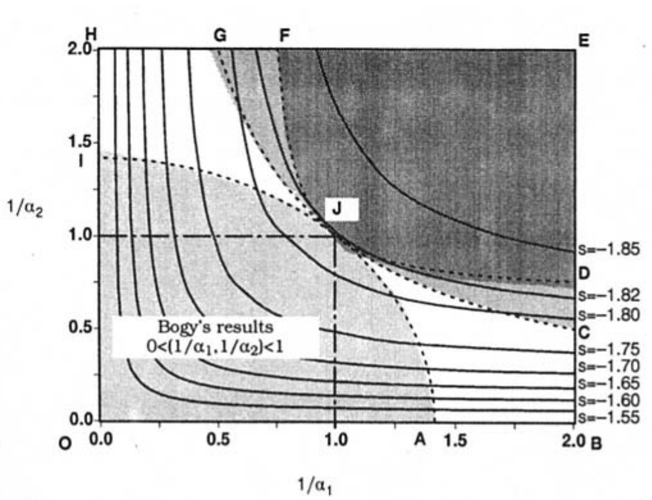

Fig. 2 Results for the order of the stress singularity for $1/\alpha_i$ from 0 to 2 and a wedge angle $2\beta = 200$ deg

obtained by setting the left-hand side of Eq. (5c) equal to 1, that is $E_1' = E_2'$ for all results lying on this curve. Note that the shear modulus satisfies the isotropic relationship only at point J.

In the region ($OAJIO$), $G_{12} > E_1'/(2(1+\nu_{12}'))$, and $E_2' > E_1'$. The root s is higher (in the negative sense) than that of the isotropic case ($s = -1.818$), i.e., it leads to a more singular stress state at the wedge apex. When E_1' and E_2' are inverted, the order of the stress singularity is located in the region ($DEFJD$) in which $G_{12} > E_2'/(2(1+\nu_{21}'))$. The root s in this region is lower than that of the isotropic case, i.e., it leads to a less singular stress state.

In the region ($ABCJGHIJA$), $G_{12} < E_1'/(2(1+\nu_{12}'))$ and $E_2' > E_1'$. The root s is greater than that of the isotropic case, i.e., it leads to a more singular stress state at the wedge apex. When E_1' and E_2' are inverted, the order of the stress singularity is located in the region ($CDJFGJC$) which is also a region in which $G_{12} < E_2'/(2(1+\nu_{21}'))$. For this region there is no way of telling, a priori, whether the order of the stress singularity is lower or higher than that of the isotropic wedge. This has to be to be determined based on where the material lies in the region, once Eq. (1) is solved. When the material can be located below the constant root curve $s = -1.82$ (which separates the region ($CDJFGJC$) into two parts), the root s is higher than that of the isotropic case, lower otherwise. For materials along the curve (CJG) which represents cases where $E_1' = E_2'$, the root s is always greater than the isotropic limit except of course at point J, where it is identical.

An interesting result for load case A and $2\beta = 200$ deg is that the roots s lie between $s = -1.50$ (which corresponds to $E_1' \ll E_2'$) and $s = -2.00$ (which corresponds to $E_1' \gg E_2'$). This is also true for other reentrant wedges, except for the special case where $2\beta = 360$ deg. The latter always leads to $s = -1.50$, independently of the material properties.

The above results demonstrate that the order of the stress singularity for an orthotropic wedge lies on either side of that obtained for an isotropic material, depending on the shear modulus value and the ratio E_2'/E_1'. Following the finite element formulation developed by Pageau, Joseph, and Biggers (1995a) these results were confirmed by Pageau (1995b).

Conclusions

The stress singularities at the apex of an orthotropic re-entrant wedge was investigated by using Bogy's (1972) formulation. It is shown that Bogy's (1972) conclusion, "...the least severe stress singularity occurs for the isotropic limit...," is too restrictive and that, for an orthotropic material whose principal axes of orthotropy coincide with the axes of the wedge, the least severe singularity does not always occur at the isotropic limit.

Acknowledgment

The support of AFOSR through Grant F49620-93-1-0256 (Dr. W. F. Jones, Monitor), NASA Langley Research Center through Grant NAG-1-1411 (Dr. J. H. Starnes, Jr., Monitor), and helpful suggestions of Prof. J. G. Goree of Clemson University are gratefully acknowledged by the authors. The authors would also like to thank Prof. D. B. Bogy for his valuable comments.

References

Bogy, D. B., 1972, "The Plane Solution for Anisotropic Elastic Wedges Under Normal and Shear Loading," ASME JOURNAL OF APPLIED MECHANICS, pp. 1103–1109.

Green, A. E., and Zerna, W., 1954, *Theoretical Elasticity*, Oxford University Press, Oxford, U.K.

Hein, V. L., and Erdogan, F., 1971, "Stress Singularities in a Two-Material Wedge," *International Journal of Fracture Mechanics*, Vol. 7, pp. 317–330.

Kuo, M. C., and Bogy, D. B., 1974a, "Plane Solutions for the Displacement and Traction-Displacement Problems for Anisotropic Elastic Wedges," ASME Journal of Applied Mechanics, pp. 197–202.

Kuo, M. C., and Bogy, D. B., 1974b, "Plane Solutions for the Displacement and Traction-Displacement Problems for Anisotropic Elastic Wedges," ASME *Journal of Applied Mechanics*, pp. 203–208.

Pageau, S. S., Joseph, P. F., and Biggers, S. B., Jr., 1995a, "Finite Element Analysis of Anisotropic Materials with Singular Inplane Stress Fields," *International Journal of Solids and Structures*, Vol. 32, No. 5, pp. 571–591.

Pageau, S. S., 1995b, Ph.D. dissertation, Clemson University, Clemson, SC.

Theocaris, P. S., 1974, "The Order of Singularity at a Multi-Wedge Corner of a Composite Plate," *International Journal of Engineering Sciences*, Vol. 12, pp. 107–120.

Williams, M. L., 1952, "Stress Singularities Resulting From Various Boundary Conditions in Angular Corners of Plates in Extension," ASME Journal of Applied Mechanics, pp. 526–528.

Journal of Applied Mechanics

Discussion

Local Stability of Gyroscopic Systems Near Vanishing Eigenvalues[1]

A. P. Seyranian.[2] The authors proposed a conjecture for gyroscopic systems that predicts whether the eigenvalue locus is imaginary or complex (with a nonzero real part) in the neighborhood of a vanishing eigenvalue. We will show that the conjecture is not true. For this purpose let us consider the simple gyroscopic system (see Seyranian et al., 1995)

$$I\ddot{u} + G\dot{u} + Ku = \begin{bmatrix} 1 & 0 \\ 0 & 1 \end{bmatrix}\ddot{u} + 2p\begin{bmatrix} 0 & -1 \\ 1 & 0 \end{bmatrix}\dot{u} + \begin{bmatrix} a_1 - p^2 & 0 \\ 0 & a_2 - p^2 \end{bmatrix}u = 0. \quad (1)$$

The characteristic equation for this system takes the form

$$\lambda^4 + \lambda^2(a_1 + a_2 + 2p^2) + (a_1 - p^2)(a_2 - p^2) = 0 \quad (2)$$

with solutions

$$\lambda_{1,2}^2 = (-(a_1 + a_2 + 2p^2) \pm \sqrt{D})/2,$$
$$D = (a_1 - a_2)^2 + 8(a_1 + a_2)p^2. \quad (3)$$

We shall study the case $0 < a_2 < a_1$. Then the system (1) is stable when $0 \le p^2 < a_2$, unstable (divergence) when $a_2 \le p^2 \le a_1$, and again stable when $a_1 < p^2$. Or expressed in behavior of eigenvalues: with the increase of p^2 two pure imaginary eigenvalues $\lambda = \pm i\omega$ (with smallest absolute value) collide in $\lambda = 0$ (double eigenvalue) at $p^2 = a_2$, and then split along the real axis into $\lambda = \pm\alpha$, as shown in Fig. 1. (When $p^2 = a_1$, a "reversed" collision in $\lambda = 0$ is happening.)

There exists only one eigenvector $\Phi_1 = [0\ \beta]^T$, $(\beta \neq 0)$, to the double eigenvalue $\lambda = 0$. According to [1], a solution to system (1) in this case is of the form $u = \Phi_2 + \Phi_1 t$ where $K\Phi_2 = -G\Phi_1$ such that $\Phi_2 = [2\sqrt{a_2}\,\beta/(a_1 - a_2)\gamma]^T$ (γ arbitrary). Therefore we are dealing with class I in the terminology of [1]. But the eigenvalues have no real parts for $p^2 < a_2$. Thus the conjecture is not true.

Notice also that the eigenvalues of a conservative gyroscopic system are placed in the complex plane symmetrically with respect to the real as well as to the imaginary axis. Therefore a double zero eigenvalue should, according to the conjecture, change into four complex eigenvalues with nonzero real part.

Finally, we would mention that the theory of interaction of eigenvalues in vibrational systems with finite degrees-of-freedom has been developed recently by Seyranian (1991, 1993a, b). This theory is essential to reveal the mechanism of transition between divergence, flutter, and stability for gyroscopic systems.

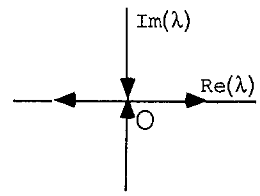

Fig. 1 Behavior of eigenvalues in the neighborhood of $\lambda = 0$

References

Seyranian, A. P., 1991, "Stability and Catastrophes of Vibrating Systems Depending on Parameters," lecture notes, Technical University of Denmark.

Seyranian, A. P., 1993a, "Sensitivity Analysis of Multiple Eigenvalues," *Mech. Struct. & Mach*, Vol. 21, No. 2, pp. 261–284.

Seyranian, A. P., 1993b, "Interaction of vibrational frequencies in gyroscopic systems," *Mechanics of Solids (MTT)*, Vol. 28, No. 4, pp. 33–41.

Seyranian, A. P., Stoustrup, J., and Kliem, W., 1995, "On gyroscopic stabilization," *Journal of Applied Mathematics and Physics (ZAMP)*, Vol. 46, pp. 255–267.

Author's Closure[3]

We thank Dr. Seyranian for his interest in our paper, but the example he gives supports the conjecture we proposed rather than prove it false.

The conjecture states that when the eigenfunction of a vanishing eigenvalue has a nonzero velocity (class I), such as the eigenfunction described in his Discussion example, then the eigenvalue locus plotted as a function of a system parameter will have a nonzero real part in the neighborhood of the vanishing eigenvalue, indicating instability. This nonzero real part may occur when the system parameter is either increased or decreased, as explicitly stated in the conjecture.

In the Discussion example, the eigenvalues have no real parts for $p^2 < a_2$, but they do have nonzero real parts for $p^2 > a_2$. Hence, in the neighborhood of $p^2 = a_2$ the eigenvalue locus has a nonzero real part and is unstable, as predicted by the conjecture.

Several of the examples given in the paper show the same eigenvalue behavior as the Discussion example, specifically, the first critical speeds of the axially moving beam (example 1), and the axisymmetric rotating disk with spring loading (example 3). In each case, the eigenvalues below the first critical speed must be imaginary because the operator K is positive definite at these speeds. In these cases, as in the Discussion

[1] Renshaw, A. A., and Mote, C. D., Jr., 1996, "Local Stability of Gyroscopic Systems Near Vanishing Eigenvalues," ASME JOURNAL OF APPLIED MECHANICS, Vol. 63, pp. 116–120.

[2] Institute of Mechanics, Moscow State Lomonosov University, Moscow, 117192, Russia.

[3] A. Renshaw, Department of Mechanical Engineering, Columbia University, 220 Mudd Building, 500 W. 120th Street, New York, NY 10027.

example, the conjecture predicts correctly whether the repeated eigenvalue is a simple, eigenvalue crossing or whether divergence instability is impending as the speed or p is increased.

The Elastic Field in a Half-Space With a Circular Cylindrical Inclusion[4]

H. Y. Yu[5]. This paper presents a method to obtain analytical solutions of the elastic field due a cylindrical inclusion with uniform eigenstrain in a half-space. The solutions are expressed as functions of the complete elliptic integrals of the first, second, and third kind that represent the harmonic and biharmonic potentials due to the inclusion and its mirror images. The method for obtaining these potentials and their derivatives was given by the authors in two previous papers (Wu and Du, 1995a, 1995b) for a cylindrical inclusion in an infinite solid. The writer would like to point out that by using the method given by the authors for expressing the potentials and their derivatives in terms of complete elliptic integrals, the solutions of the elastic field due to a cylindrical inclusion in two joined isotropic semi-infinite solids, in an infinite transversely isotropic solid, and in two joined semi-infinite transversely isotropic solids can be readily obtained after proper, simple coordinate transformations (Yu and Sanday, 1991; Yu et al., 1994, 1995).

In addition to this, the writer has two points to discuss regarding the methodology used in all three papers by the authors. First, when $s = -z^2$, the denominator $h + k^2$ in Eq. (24) (Wu and Du, 1995a) is zero. To avoid the tedious tasks for obtaining the stress and strain by using Eqs. (24) and (A3) (ibid.), the expressions for the function I^3 given by Eq. (A3) can be obtained directly from the table of integrals (Gradshteyn and Ryzhik, 1980) as

$$I^3(x_1, x_2, z, s) = \frac{2}{(t_1 + z^2)\sqrt{t_2 + z^2}} E\left(\sqrt{\frac{t_2 - t_1}{t_2 + z^2}}\right)$$

when $s = -z^2$. Secondly, to simplify the expressions and to reduce the number of integrations ($I_{ij}, \bar{I}_{ij}, \ldots, \bar{T}_{ij}, \bar{T}_{ijk}\bar{T}_{ijkl}, \ldots,$ where $i, j, k, l = 1, 2, 3$) needed for the solutions, one could perform the integration of the Green's functions over the volume of the inclusion first and then differentiate them with respect to x_1, x_2, and x_3. For example

$$I_{ij} = I\delta_{ij} - \frac{\partial^2}{\partial x_i \partial x_j}\Gamma$$

where

$$\begin{aligned}\Gamma(x_1, x_2, z) &= \iint_{\Omega_1} |\mathbf{x} - \mathbf{x}'|\, dx_1' dx_2' \\ &= \tfrac{1}{3}\{(a^2 - x_1^2 - x_2^2)[I^1 + 2z^2 I^2 + z^4 I^3(x_1, x_2, z, 0)] \\ &\qquad + (I^0 + 2z^2 I^1 + z^4 I^2) - 2\pi|z^3|\}.\end{aligned}$$

Finally, possibly misprinted, the coordinate r, shown as equal to $|\mathbf{x} - \mathbf{x}'|$ should have been equal to $[(x_1 - x_1')^2 + (x_2 - x_2')^2]^{1/2}$.

References

Gradshteyn, I. S., and Ryzhik, I. M., 1980, *Table of Integrals, Series, and Products,* Academic Press, New York.

Wu, L. Z., and Du, S. Y., 1995a, "The Elastic Field Caused by a Circular Cylindrical Inclusion—Part I: Inside Region $x_1^2 + x_2^2 < a^2$, $-\infty < x_3 < \infty$ where the Circular Inclusion is Expressed as $x_1^2 + x_2^2 \le a^2$, $-h \le x_3 \le h$," ASME JOURNAL OF APPLIED MECHANICS, Vol. 62, pp. 579–584.

Wu, L. Z., and Du, S. Y., 1995b, "The Elastic Field Caused by a Circular Cylindrical Inclusion—Part II: Inside Region $x_1^2 + x_2^2 > a^2$, $-\infty < x_3 < \infty$ where the Circular Inclusion is Expressed as $x_1^2 + x_2^2 \le a^2$, $-h \le x_3 \le h$," ASME JOURNAL OF APPLIED MECHANICS, Vol. 62, pp. 585–589.

Yu, H. Y., and Sanday, S. C., 1991, "Elastic Field in Joined Semi-Infinite Solids with an Inclusion," *Proceedings of the Royal Society of London,* Vol. A434, pp. 521–530.

Yu, H. Y., Sanday, S. C., and Chang, C. I., 1994, "Elastic Inclusions and Inhomogeneities in Transversely Isotropic Solids," *Proceedings of the Royal Society of London,* Vol. A444, pp. 239–252.

Yu, H. Y., Sanday, S. C., Chang, C. I., and Rath, B. B., 1995, "Elastic Field due to Defects in Transversely Isotropic Bimaterials," *Proceedings of the Royal Society of London,* Vol. A449, pp. 1–30.

Author's Closure[6]

The authors are indebted to Dr. Yu for his comment where two points concerning the methodology used in the papers are discussed. First, Dr. Yu points out that when $s = -z^2$, $I^3(x_1, x_2, z, s)$ can be expressed by the complete elliptic integral of the second kind. In fact, this special case has been included in Eq. (A3) (Wu and Du, 1995a) and can be obtained by the relation

$$\frac{E(k)}{1 - k^2} = \Pi(-k^2, k).$$

To avoid excessive formulations, we did not represent the degenerate expression of Eq. (A3) in the paper. When $s = -z^2$, if the above equation is substituted in Eq. (24) (Wu and Du, 1995a), we find that there is no singularity.

Secondly, it seems that a simple method is given in performing the integration of Green's functions. However, I doubt that it is not easy to solve the second derivative of function Γ. Finally, Dr. Yu points out that there is a typing error in Wu and Du (1995a). The authors then notice a similar typing error in Wu and Du (1995b) where r, shown as equal to $|\mathbf{x} - \mathbf{x}'|$, should have been equal to $[(x_1 - x_1')^2 + (x_2 - x_2')^2]^{1/2}$.

References

Wu, L. Z., and Du, S. Y., 1995a, "The Elastic Field Caused by a Circular Cylindrical Inclusion—Part I: Inside Region $x_1^2 + x_2^2 < a^2$, $-\infty < x_3 < \infty$ Where the Circular Inclusion is Expressed as $x_1^2 + x_2^2 \le a^2$, $-h \le x_3 \le h$," ASME JOURNAL OF APPLIED MECHANICS, Vol. 62, pp. 579–584.

Wu, L. Z., and Du, S. Y., 1995b, "The Elastic Field Caused by a Circular Cylindrical Inclusion—Part II: Inside Region $x_1^2 + x_2^2 > a^2$, $-\infty < x_3 < \infty$ where the Circular Inclusion is Expressed as $x_1^2 + x_2^2 \le a^2$, $-h \le x_3 \le h$," ASME JOURNAL OF APPLIED MECHANICS, Vol. 62, pp. 585–589.

An Integral-Equation Formulation for Anisotropic Elastostatics[7]

C. Song and J. P. Wolf.[8] This paper describes an efficient integral-equation formulation for the numerical analysis of homogeneous anisotropic linear elastic problems. As the fundamental solution of isotropic elastostatics is used, the boundary integrals are evaluated more straightforwardly and efficiently than when the fundamental solution of anisotropic elastostatics is applied. However, besides the discretization on the boundary, it is necessary to discretize the domain into internal cells, but the number of variables is not increased.

[4] Wu, L. Z., and Du, S. Y., 1996, "The Elastic Field in a Half-Space With a Circular Cylindrical Inclusions," ASME JOURNAL OF APPLIED MECHANICS, Vol. 63, pp. 925–932.

[5] Mechanics of Materials Branch, Naval Research Laboratory, Washington, DC 20375.

[6] Lin Zhi Wu, Research Lab of Composite Materials, School of Astronautics, Harbin Institute of Technology, Harbin 150001, P. R. China.

[7] Perez, M. M., and Wrobel, L. C., 1996, "An Integral-Equation Formulation for Anisotropic Elastostatics," ASME JOURNAL OF APPLIED MECHANICS, Vol. 63, pp. 891–902.

[8] Institute of Hydraulics and Energy, Department of Civil Engineering, Swiss Federal Institute of Technology Lausanne, CH-1015 Lausanne, Switzerland.